

NBS
PUBLICATIONS

A11102 874374

NAT'L INST OF STANDARDS & TECH R.I.C.



A11102874374

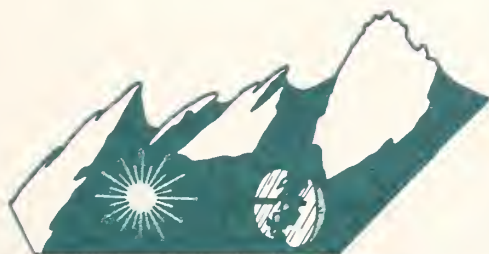
/Laser induced damage in optical materia
QC100 .U57 NO.746 1988 V1988 C.2 NBS-PUB



NBS SPECIAL PUBLICATION **746**

U.S. DEPARTMENT OF COMMERCE/National Bureau of Standards

Laser Induced Damage in Optical Materials: 1985



BOULDER DAMAGE SYMPOSIUM



STP 1015

The National Bureau of Standards¹ was established by an act of Congress on March 3, 1901. The Bureau's overall goal is to strengthen and advance the nation's science and technology and facilitate their effective application for public benefit. To this end, the Bureau conducts research to assure international competitiveness and leadership of U.S. industry, science and technology. NBS work involves development and transfer of measurements, standards and related science and technology, in support of continually improving U.S. productivity, product quality and reliability, innovation and underlying science and engineering. The Bureau's technical work is performed by the National Measurement Laboratory, the National Engineering Laboratory, the Institute for Computer Sciences and Technology, and the Institute for Materials Science and Engineering.

The National Measurement Laboratory

Provides the national system of physical and chemical measurement; coordinates the system with measurement systems of other nations and furnishes essential services leading to accurate and uniform physical and chemical measurement throughout the Nation's scientific community, industry, and commerce; provides advisory and research services to other Government agencies; conducts physical and chemical research; develops, produces, and distributes Standard Reference Materials; provides calibration services; and manages the National Standard Reference Data System. The Laboratory consists of the following centers:

- Basic Standards²
- Radiation Research
- Chemical Physics
- Analytical Chemistry

The National Engineering Laboratory

Provides technology and technical services to the public and private sectors to address national needs and to solve national problems; conducts research in engineering and applied science in support of these efforts; builds and maintains competence in the necessary disciplines required to carry out this research and technical service; develops engineering data and measurement capabilities; provides engineering measurement traceability services; develops test methods and proposes engineering standards and code changes; develops and proposes new engineering practices; and develops and improves mechanisms to transfer results of its research to the ultimate user. The Laboratory consists of the following centers:

- Applied Mathematics
- Electronics and Electrical Engineering²
- Manufacturing Engineering
- Building Technology
- Fire Research
- Chemical Engineering³

The Institute for Computer Sciences and Technology

Conducts research and provides scientific and technical services to aid Federal agencies in the selection, acquisition, application, and use of computer technology to improve effectiveness and economy in Government operations in accordance with Public Law 89-306 (40 U.S.C. 759), relevant Executive Orders, and other directives; carries out this mission by managing the Federal Information Processing Standards Program, developing Federal ADP standards guidelines, and managing Federal participation in ADP voluntary standardization activities; provides scientific and technological advisory services and assistance to Federal agencies; and provides the technical foundation for computer-related policies of the Federal Government. The Institute consists of the following divisions:

- Information Systems Engineering
- Systems and Software Technology
- Computer Security
- System and Network Architecture
- Advanced Systems

The Institute for Materials Science and Engineering

Conducts research and provides measurements, data, standards, reference materials, quantitative understanding and other technical information fundamental to the processing, structure, properties and performance of materials; addresses the scientific basis for new advanced materials technologies; plans research around cross-cutting scientific themes such as nondestructive evaluation and phase diagram development; oversees Bureau-wide technical programs in nuclear reactor radiation research and nondestructive evaluation; and broadly disseminates generic technical information resulting from its programs. The Institute consists of the following Divisions:

- Ceramics
- Fracture and Deformation³
- Polymers
- Metallurgy
- Reactor Radiation

¹Headquarters and Laboratories at Gaithersburg, MD, unless otherwise noted; mailing address Gaithersburg, MD 20899.

²Some divisions within the center are located at Boulder, CO 80303.

³Located at Boulder, CO, with some elements at Gaithersburg, MD

Laser Induced Damage in Optical Materials: 1985

Proceedings of a Symposium Sponsored by:
National Bureau of Standards
American Society for Testing and Materials
Office of Naval Research
Department of Energy
Defense Advanced Research Project Agency
Air Force Office of Scientific Research

October 28-30, 1985

NBS, Boulder, Colorado 80303

Edited by:

Harold E. Bennett

Naval Weapons Center
China Lake, California 93555

Arthur H. Guenther

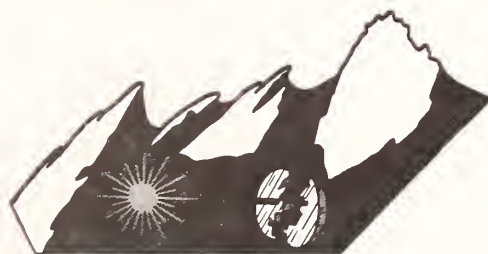
Air Force Weapons Laboratory
Kirtland Air Force Base, New Mexico 87117

David Milam

Lawrence Livermore National Laboratory
Livermore, California 94550

Brian E. Newnam

Los Alamos National Laboratory
Los Alamos, New Mexico 87545



BOULDER DAMAGE SYMPOSIUM

U.S. DEPARTMENT OF COMMERCE, C. William Verity, Secretary

NATIONAL BUREAU OF STANDARDS, Ernest Ambler, Director

Issued July 1988

Library of Congress Catalog Card Number: 88-600557

National Bureau of Standards Special Publication 746
Natl. Bur. Stand. (U.S.), Spec. Publ. 746, 576 pages (July 1988)
CODEN: XNBSAV

U.S. GOVERNMENT PRINTING OFFICE
WASHINGTON: 1988

For sale by the Superintendent of Documents, U.S. Government Printing Office, Washington, DC 20402-9325

Foreword

The Proceedings contain the papers presented at the Seventeenth Symposium on Optical Materials for High-Power Lasers held at the National Bureau of Standards in Boulder, Colorado, on October 28-30, 1985. The Symposium was jointly sponsored by the National Bureau of Standards, the American Society for Testing and Materials, the Office of Naval Research, the Defense Advanced Research Project Agency, the Department of Energy, and the Air Force Office of Scientific Research. The Symposium was attended by over 215 scientists from the United States, Israel, India, the United Kingdom, Japan, Federal Republic of Germany, and the Soviet Union. It was divided into sessions devoted to the following topics: Materials and Measurements, Mirrors and Surfaces, Thin Films, and finally, Fundamental Mechanisms. The Symposium Co-Chairmen were Dr. Harold E. Bennett of the Naval Weapons Center, Dr. Arthur H. Guenther of the Air Force Weapons Laboratory, Dr. David Milam of the Lawrence Livermore National Laboratory, and Dr. Brian E. Newnam of the Los Alamos National Laboratory. They also served as editors of this report.

The editors assume full responsibility for the summary article which contains an overview of the Symposium. The manuscripts of the papers presented at the Symposium have been prepared by the designated authors, and questions pertaining to their content should be addressed to those authors. The interested reader is referred to the bibliography at the end of the summary article for general references to the literature of laser damage studies. The Eighteenth Annual Symposium on this topic will be held in Boulder, Colorado, November 3-5, 1986. A concerted effort will be made to ensure closer liaison between the practitioners of high-peak power and the high-average power community.

The principal topics to be considered as contributed papers in 1986 do not differ drastically from those enumerated above. We expect to hear more about improved scaling relations as a function of pulse duration, area, and wavelength, and to see a continuing transfer of information from research activities to industrial practice. New sources at shorter wavelengths continue to be developed, and a corresponding shift in emphasis to short wavelength and repetitively-pulsed damage problems is anticipated. Fabrication and test procedures will continue to be developed, particularly in the diamond-turned optics and thin film areas.

The purpose of these symposia is to exchange information about optical materials for high-power lasers. The editors will welcome comment and criticism from all interested readers relevant to this purpose, and particularly relative to our plans for the Eighteenth Annual Symposium.

H. E. Bennett, A. H. Guenther,
D. Milam, and B. E. Newnam
Co-Chairmen

Disclaimer

Certain papers contributed to this publication have been prepared by non-NBS authors. These papers have not been reviewed or edited by NBS; therefore, the National Bureau of Standards accepts no responsibility for comments or recommendations contained therein.

Certain commercial equipment, instruments, and materials are identified in this publication in order to explain the experimental procedure adequately. Such identification in no way implies approval, recommendation, or endorsement by the National Bureau of Standards, nor does it imply that the equipment, instruments, or materials identified are necessarily the best available for the purpose.

CONTENTS

	<u>Page</u>
Foreword	iii
H.E. Bennett, A.H. Guenther, D. Milam, and B.E. Newnam	
Disclaimer	iv
Symposium Welcome	xii
H.E. Bennett	
Summary of Meeting	1
H.E. Bennett, A.H. Guenther, D. Milam, and B.E. Newnam	
1.0 Introduction	1
2.0 Overview	2
3.0 Acknowledgments	6
4.0 References	6

Materials and Measurements

A Versatile Laser Glass Inspection and Damage Testing Facility	8
J.E. Marion, G.J. Greiner, J.H. Campbell, P.H. Chaffee, J.S. Hildum, J.Z. Grens, C.L. Weinzapfel, S.M. Winfree, and D.Milam	
Computer-Controlled Facility for Laser Switching and Damage Testing	12
Jay S. Chivian, W.D. Cotten, D.F. Fuller, R. B. Hemphill, and M.W. Scott	
Damage Testing in Optics Production and Procurement	33
S.C. Seitel and E.A. Teppo	
A Computer Automated Laser Damage Laboratory	34
Martin R. Sweet, L.J. Jolin, and S.R. Foltyn	
U.V. Laser Beam Diagnostics Using a Computer Controlled Video Frame Store System	35
S.E. Clark, I. Laidler, D.C. Emmony, B.A. Omar, and M.J. Shaw	

Beam Profiling Characteristics of a Sensitivity-Enhanced Silicon Vidicon System at 1.06 Microns	44
R.M. O'Connell, R.A. Vogel	
A.F. Stewart and D.A. Smith	
Digital Fluence Profiling System and Software	53
S.C. Seitel and R.L. Rypma	
Simple Accurate Inversion of Knife-Edge Data from Radially Symmetric Laser Beams	54
R.M. O'Connell and R.A. Vogel	
Investigation of Optical Damage via Resonance Ionization Mass Spectrometry	61
R.C. Estler and N.S. Nogar	
Laser Mirror Profilometry by High-Q Interferometry	68
J.R. Rotge'	
Design and Construction of a Single Polarizer Infrared Ellipsometer/Reflectometer for Characterization of Highly Curved Surfaces	72
Jack B. Stubbs, John S. Loomis, and Thomas A. Leonard	
Direct n_2 Measurement in Yttria Stabilized Cubic Zirconia	80
Shekhar Guha, Nastaran Mansour, and M.J. Soileau	
Measurement of Optical Damage Threshold of Wire Grid Polarizers at 10.6 Microns	84
M. Mohebi, A. Said, and M.J. Soileau	
Laser Damage Studies of Several Acrylic Polymers	92
A.B. Romberger, B.W. Mullins, A.A. Shaffer, J.F. Hilbing,	
K.E. Siegenthaler, T.F. Deaton, and Y. Chang	
Improvement of the Bulk Laser Damage Threshold of Potassium Dihydrogen Phosphate Crystals by Ultraviolet Irradiation	101
A. Yokotani, T. Sasaki, K. Yoshida,	
T. Yamanaka, and C. Yamanaka	
Laser-Induced Damage in Doped and Undoped Fluorozirconate Glass	108
Nastaran Mansour, Shekhar Guha, M.J. Soileau,	
Bernard Bendow, and Diane Martin	

Platinum Particles in the Nd:doped Disks of Phosphate Glass in the Nova Laser	120
D. Milam, C.W. Hatcher, and J.H. Campbell	
Evolution during Multiple-Shot Irradiation of Damage Surrounding Isolated Platinum Inclusions in Phosphate Laser Glasses	128
R.P. Gonzales and D. Milam	
Multiple Pulse Damage Studies of BK-7, KCl, and SiO ₂ at 532 nm	138
D. Kitriotis, L.D. Merkle, and A. Dodson	
Picosecond Nonlinear Investigation of Accumulated Damage in Molecular Crystals	146
Thomas J. Koscic, Jeffrey R. Hill, and Dana D. Dlott	
Laser Photoconductivity in Alkali Halides	152
Alexander Epifanov	

Mirrors and Surfaces

The Scratch Standard is only a Cosmetic Standard	153
Matt Young	
Ion Exchange Strengthening of Nd:Doped Phosphate Laser Glass	159
Kathleen A. Cerqua, Stephen Jacobs, Brian L. McIntyre, and William Zhong	
Infra-Red Absorption Spectroscopy of Nd:YAG and Nd:GSGG Surface Contaminants	170
M.A. Acharekar	
Excimer Radiation Colouration Processes and Surface Damage to Single Crystal CaF ₂ Substrates	182
I. Laidler and D.C. Emmony	
Analysis of Optical Surfaces by Laser Ionization Mass Spectrometry: Spatial Variation of the Laser Damage Threshold and its Relationship to Polishing Compound Incorporation	190
Wigbert J. Siekhaus	
Laser Induced Damage and Ion Emission of GaAs at 1.06 μ m	191
A.L. Huang, M.F. Becker, and R.M. Walser	

CO ₂ Laser Induced Damage to Germanium: Relation to Surface Preparation	203
D.R. Gibson, C.M. MacDonald, and A.D. Wilson	
Study of Mo, Au, and Ni Implanted Molybdenum Laser Mirrors by Spectroscopic Ellipsometry	215
Paul G. Snyder, George H. Bu-Abbud, Jae Oh, John A. Woollam, David Poker, D.E. Aspnes, David Ingram, and Peter Pronko	
Glancing Incidence Absorption Measurements of Metal Mirrors	227
W.D. Kimura and D.H. Ford	
N-on-1 Testing of Single Crystal Metal Surfaces at 1.06 μm	236
Yong Jee, Michael F. Becker, and Rodger M. Walser	
Laser Induced Mo Mirror Damage for High Power CO ₂ Laser	248
H. Okamoto, N. Matsusue, K. Kitazima, K. Yoshida, Y. Ichikawa, M. Yamanaka, T. Yamanaka, and Y. Tsunawaki	

Thin Films

Multifacet, Metal Mirror Design for Extreme-Ultraviolet and Soft X-Ray Free-Electron Laser Resonators	261
Brian E. Newnam	
The Design of Optimum Reflectivity Coatings for Grazing Angles of Incidence	270
Jeffrey B. Shellan	
Phase Control Coating Design Analysis	282
M. McGuirk and R.D. Poirier	
Thermal Conductivity of Enhanced High Reflectors	283
M. McGuirk and R.D. Poirier	
Yttrium Oxide Coatings for High Power Lasers at 351 nm	284
D.J. Smith, C.J. Hayden, B.U. Krakauer, A.W. Schmid, and M.J. Guardalben	
Self-Consistent Dependence of Porosity and Refractive Index on Composition in Co-Evaporated Films	299
A. Feldman, E.N. Farabaugh, and R.A. Stempniak	

The Formation and Development of Nodular Defects in Optical Coatings	305
Bangjun Liao, Douglas J. Smith, and Brian McIntyre	
Interfacial Structure of Ion-Beam Sputter Deposited $\text{SiO}_2/\text{TiO}_2$ Coatings	319
J.R. Sites and H. Demiryont	
Ion Beam Deposited Oxide Coatings	325
T. Raj, J.S. Price, and C.K. Carniglia	
Properties of IAD $\text{Al}_2\text{O}_3/\text{SiO}_2$ and $\text{Ta}_2\text{O}_5/\text{SiO}_2$ Thin Film AR Structures	333
J.J. McNally, F.L. Williams, S.R. Wilson, and J.R. McNeil	
Ion Assisted Deposition of Optical Films on Heavy Metal Fluoride Glass Substrates	342
J.J. McNally, G.A. Al-Jumaily, and J.R. McNeil	
Highly Damage Resistant Porous Dielectric Coating for High Power Lasers in the Ultraviolet to Near-Infrared Wavelength Region	350
K. Yoshida, H. Yoshida, Y. Kato, and C. Yamanaka	
Ion Beam Characterization of Multi-Layer Dielectric Reflectors	355
J.G. Beery, M.G. Hollander, C.J. Maggiore, A. Redondo, R.T. Westervelt, and T.N. Taylor	
Raman Scattering Analysis of Thin Film Coatings Using Guided Waves	362
Alan F. Stewart, David R. Tallant, and Karen L. Higgins	
Raman Microprobe of Laser-Induced Surface Damage Regions in TiO_2 and ZrO_2 Coatings	374
Donald M. Friedrich and Gregory J. Exarhos	
Probing Structural Properties of Amorphous Films with Raman Spectroscopy	383
C.Y. She and L.S. Hsu	
Detection of Laser Damage by Raman Microscopy	388
P.M. Fauchet, I.H. Campbell, and F. Adar	
Time-Resolved Temperature Determinations from Raman Scattering of TiO_2 Coatings During Pulsed Laser Irradiation	395
Gregory J. Exarhos	

Effect of Molecular Fluorine on the Performance of Excimer Laser Optics	403
S.R. Foltyn, L.J. Jolin, and G. Lindholm	
Thresholds Measured with 350-nm Pulses at 25-100 Hz for Bare Polished Crystals of CaF ₂ and for Silica Sol-gel AR Coatings on Silica Substrates	404
M.C. Staggs, D. Milam, I.M. Thomas, and J.G. Wilder	
Study of Temporal and Spatial Intensity Variations and Intracavity Damage Thresholds of Alexandrite Lasers	412
D.J. Harter, H. Rainee, and A.J. Heiney	
Investigation of Metal Coatings for the Free Electron Laser	419
Marion L. Scott, Paul N. Arendt, Robert W. Springer, Richard C. Cordi, and William J. McCreary	
Influence of Deposition and Post Deposition Conditions on Laser Induced Damage in Electron Beam Evaporated TiO ₂ and SiO ₂ Films	429
K. Narasimha Rao, M. Adinarayana Murthy, S. Mohan, and M. Ramakrishna Rao	
Dependence of Damage Threshold of Anti-Reflection Coatings on Substrate Surface Roughness	438
Y. Nose, Y. Kato, K. Yoshida, and C. Yamanaka	
Correlation between Local HeNe Scatter and Defect-Initiated Laser Damage at 2.7 μ m	449
J.O. Porteus, C.J. Spiker, and J.B. Franck	
CO ₂ Laser Induced Damage in a Model Thin Film System: ZnS on Ge	460
D.R. Gibson and A.D. Wilson	
Laser Induced Damage in Dense Optical Thin Films	472
K.L. Lewis, A.M. Pitt, A.G. Cullis N.G. Chew, and L. Charlwood	
<u>Fundamental Mechanisms</u>	
Transient Absorption of Light Induced by Radiation	480
R. Godwin, F.B. Harrison, and A. Larson	
Effects of Radiation Induced Defects on Laser-Induced Breakdown in SiO ₂	486
M.J. Soileau, Nastaran Mansour, Edesly Canto, and D.L. Griscom	

Fundamental Mechanisms of Optical Damage in Short-Wavelength High-Power Lasers	497
R.F. Haglund, Jr., N.H. Tolk, and G.W. York	
Temporal Distribution of Electron and Ion Emission Caused by Laser Excitation of Optical Surfaces in Ultra-High Vacuum	509
W.J. Siekhaus, L.L. Chase, and D. Milam	
Anomalous Absorption in Optical Coatings	515
M.R. Lange, J.K. McIver, and A.H. Guenther	
Time of Damage and the Effect of the Pulse Repetition Frequency on the Laser Induced Damage Threshold	529
R.M. Wood, S.K. Sharma, P. Waite, E.K. Gorton, and K. Lewis	
Modeling Laser Damage Caused by Platinum Inclusions in Laser Glass	537
John H. Pitts	
CO ₂ Laser-Induced Air Breakdown near Metal Mirror Surfaces	547
Vitaly Konov	
APPENDIX I. List of Attendees	548

WELCOME

H. E. Bennett

Michelson Laboratory, Naval Weapons Center

China Lake, CA 93555

On behalf of co-chairmen Art Guenther, Brian Newnam, Dave Milam, and myself, I welcome you to the Seventeenth Annual Symposium on Optical Materials for High-Power Lasers. We have a record number of papers this year and a record attendance also; it promises to be an excellent conference. We especially want to welcome our many foreign guests, most of whom are contributing papers to the meeting. Many of them have come a long way and it is a commentary on the quality of this meeting that scientists from around the world will arrange to come here and share with us their insights into the difficult questions surrounding laser damage to materials. Some of their contributions have been quite significant too. For example, Professor Manenkov of the Soviet Union started a whole new line of investigation with his paper on NaCl damage limits a few years ago. Professor Yoshiharu Namba of Japan started us to thinking about float polishing, Dr. Achim Bubenzer and his colleagues from West Germany helped to clarify the science behind hard, diamondlike carbon coatings, and last year, Dr. Keith Lewis from Great Britain encouraged us to think that, using MBE techniques, thin films can be prepared which exhibit bulk properties instead of having several orders-of-magnitude more absorption than bulk material and so on. I could easily name many others from outside the United States who have contributed greatly to the well-deserved reputation of this conference for being a must for anyone who is interested in laser damage to optical components. We are proud of the international cooperation shown here in attacking problems in fundamental science, which knows no boundaries. In this spirit let me caution those of you who are engaged in applied research and development as well as more fundamental studies to avoid embarrassing our foreign guests and jeopardizing the excellent reputation of this conference by engaging in inappropriate discussions in the halls. These are not cleared areas. Let us concentrate our efforts in the next three days on understanding the fundamental problems associated with optical materials and laser damage to them. In this we can all work together.

Optics is a fashionable field to work in now. I remember in the fifties that it was suggested to me that research on optical properties of materials had no future, everything had been discovered which was of any useful interest, and only adding more decimal points to the optical constants remained to be done. The laser came along about then and was regarded as a new and interesting curiosity; a solution looking for a problem. Since then it has been used to solve many problems. Surgery, communications, data recording, laser welding, surface modification, and space applications are a few that come to mind. In all of them we are dealing with optical trains which, although they may not transmit high energies, do have to handle high powers. Lasers have introduced a new dimension into optical systems which we may call power optics. Electrical engineers have an analogous field, power engineering, where

they study how to handle the output of hydroelectric dams and other sources of power. Electrical engineering also encompasses small-signal processing in the radio and microwave fields. The analogous field in optical design deals with telescopes, microscopes, cameras, etc. and is often referred to as classical optics. With the advent of power optics, for which this conference is one of the main forums, we enter a new kind of optical design, one in which the underlying physics is not well understood.

At first glance the problem seems simple enough. A high enough intensity of laser energy causes either reversible or irreversible damage to the optical components reflecting or transmitting the laser energy. But why do components damage and why do damage thresholds of similar samples vary by as much as one or two orders-of-magnitude? The absorption coefficients of the component substrate and coating obviously should be related to the damage threshold, but frequently they are not. Even so, what makes the materials absorb? Figure 1 shows some of the mechanisms which have been studied as causes of intrinsic absorption in low absorption dielectrics. Other mechanisms have also been proposed, but these will suffice to demonstrate that even intrinsic absorption is not necessarily simple. On the other hand, there is considerable evidence that extrinsic effects dominate laser damage in low absorption regions, and these may be even more complicated. Worse yet, absorption from extrinsic or intrinsic effects may be completely unimportant. Structural effects may be the key, or the high-field strengths involved in laser beams may cause dielectric breakdowns or non-linear effects. Sub-picosecond pulses get us down to the time intervals characteristic of atomic processes, with consequent changes in the rules, and one concludes that laser damage is not so simple after all.

We have made many important advances over the years in our understanding of laser damage. Most have been reported here first, and the back issues of the Conference Proceedings are regarded by most of the community as a gold mine of information on the subject. Many of the back issues can be obtained from the American Society for Testing Materials, the professional sponsor for this conference. Some advances which come to mind are the understanding of self focussing (which is not yet perfect), the effect of scratches and voids on damage thresholds (also not complete), the asymmetry of laser damage thresholds for the front and back surfaces of windows caused by standing-wave fields, the development of experimental techniques to measure various key parameters. We still do not understand the origin of surface absorption, but at least we can measure it and scale damage thresholds for small spot-sizes to larger beam diameters for some types of surfaces. To understand laser damage phenomena, diverse disciplines such as crystal growth, thin film technology, surface finishing technology and others are required, and some notable advances have been reported here in these fields. One I remember was the achievement of absorption coefficients of 10^{-4} cm^{-1} range at $10.6 \mu\text{m}$ wavelength for both KCl and ZnSe, orders-of-magnitude better than had been possible previously. Many other examples of progress could be mentioned and some of these fields are among the most well-represented at this year's Symposium. Thin film technology, for example, is now consistently the subject of more than one quarter of all the papers presented in these Symposia.

Plenty of technical problems remain to be solved. One of the most puzzling is the reason for the decrease in damage threshold seen for multiple pulses, and the general behavior of components to rep-rate pulses. The subject of short-wavelength laser components is a fascinating one and brings in all the physics of multiphoton processes and the happy discovery that things are not as hopeless as they seemed at first. Many other topics could be mentioned, and indeed are in the Conference Program which you all have. This is the largest conference we have ever had, let us hope that it will also be seen in future years as one of the best. Enjoy and profit by the 2 1/2 days that we are about to embark on.

Let me close by mentioning some items of which you all should be aware. First, save Tuesday evening. There will be a Wine and Cheese Tasting extravaganza that evening, and I hope that you all can come, get to know each other on a more personal basis, exchange ideas, and enjoy some fine wine and unusual cheeses and goodies.

Let us take this opportunity to thank our professional sponsor of this conference, the American Society for Testing Materials, often familiarly known as the ASTM, and also our financial sponsors. They are (1) the Air Force Office of Scientific Research, (2) the Office of Naval Research through the Naval Weapons Center, (3) Lawrence Livermore National Laboratory, (4) Los Alamos National Laboratory, (5) The Defense Advanced Research Projects Agency, and (6) the National Bureau of Standards. The Bureau does a great deal to make this meeting possible, and we particularly acknowledge the support of Robert A. Kamper, Director of the Boulder Laboratories of NBS, and Aaron A. Sanders, Group Leader of the Electromagnetic Technology Division, who performs the functions of Conference Coordinator and Fundraiser. His secretary, Ms. Susie Rivera continues to perform an outstanding job in managing the conference manuscripts, sending out notices, typing editors comments, and generally keeping the show on the road. She is aided by several other secretaries here at the Bureau. Ann Mannos here at the Bureau handles the finances. No set of acknowledgments would be complete without reference to the outstanding work done by Pat Whited, Art Guenther's secretary, in making this Symposium happen. Finally, and most importantly, my cochairmen Brian Newnam, Dave Milam and I want you to join with us in thanking Art Guenther, who with Alex Glass started these Symposia and who, in spite of his impossibly busy schedule as Chief Scientist of the Air Force Weapons Laboratory, is still supplying much of the motive force to keep it going. We hear that he is to be awarded the Distinguished Senior Executive Award in Washington, D.C. and that it will be presented personally to him by President Reagan. Let us all stand and give a round of applause.

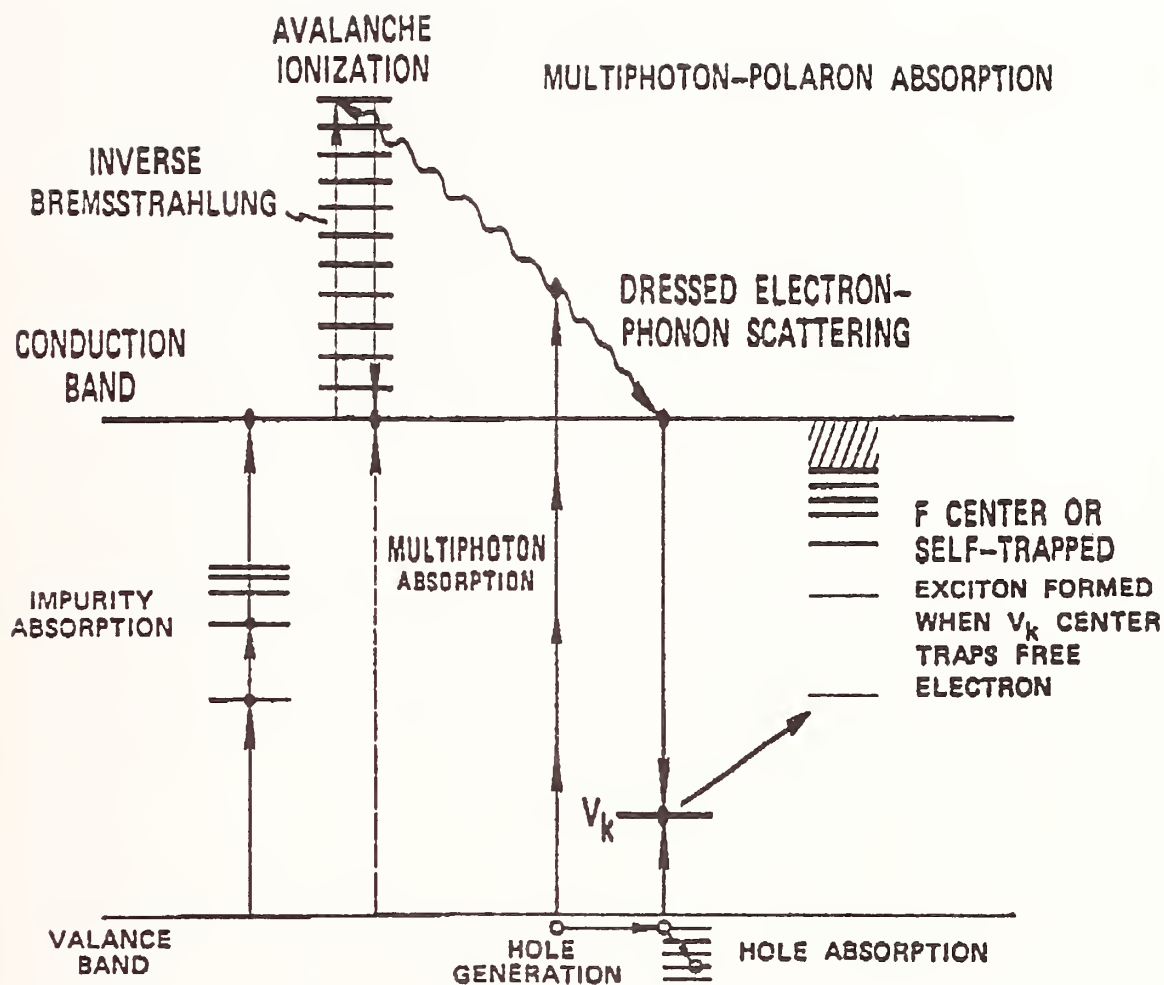


Fig. 1 Some suggested mechanisms for laser damage in solids.

Laser-Induced Damage in Optical Materials
Seventeenth ASTM Symposium
October 28-30, 1985

The Seventeenth Annual Symposium on Optical Materials for High Power Lasers (Boulder Damage Symposium) was held at the National Bureau of Standards in Boulder, Colorado, October 28-30, 1985. The Symposium was held under the auspices of ASTM Committee F-1, Subcommittee on Laser Standards, with the joint sponsorship of NBS, the Defense Advanced Research Project Agency, the Department of Energy, the Office of Naval Research, and the Air Force Office of Scientific Research. Over 215 scientists attended the Symposium, including representatives from the United States, the United Kingdom, Israel, India, Japan, the Federal Republic of Germany, and the Soviet Union. The Symposium was divided into sessions concerning Materials and Measurements, Mirrors and Surfaces, Thin Films, and Fundamental Mechanisms. As in previous years, the emphasis of the papers presented at the Symposium was directed toward new frontiers and new developments. Particular emphasis was given to materials for high-power apparatus. The wavelength range of prime interest was from 10.6 μm to the uv region. Highlights included surface characterization, thin film-substrate boundaries, and advances in fundamental laser-matter threshold interactions and mechanisms. Harold E. Bennett of the Naval Weapons Center, Arthur H. Guenther of the Air Force Weapons Laboratory, David Milam of the Lawrence Livermore National Laboratory, and Brian E. Newnam of the Los Alamos National Laboratory were co-chairmen of the Symposium. The Eighteenth Annual Symposium is scheduled for November 3-5, 1986, at the National Bureau of Standards, Boulder, Colorado.

Key Words: laser damage; laser interaction; optical components; optical fabrication; optical materials and properties; thin film coatings.

1. Introduction

The Seventeenth Annual Symposium on Optical Materials for High Power Lasers (Boulder Damage Symposium) was held, as in previous years, at the National Bureau of Standards in Boulder, Colorado, October 28-30, 1985. The Symposium was held under the auspices of the ASTM Committee F-1, Subcommittee on Laser Standards, with the joint sponsorship of NBS, the Defense Advanced Research Projects Agency, the Department of Energy, the Office of Naval Research, and the Air Force Office of Scientific Research. Over 215 scientists attended the Symposium, including representatives from the United States, the United Kingdom, Israel, India, Japan, the Federal Republic of Germany, and the Soviet Union. The Symposium was divided into sessions concerning Materials and Measurements, Mirrors and Surfaces, Thin Films, and finally, Fundamental Mechanisms. In all, approximately 70 technical presentations were made. Harold E. Bennett of the Naval Weapons Center, Arthur H. Guenther of the Air Force Weapons laboratory, David Milam of the Lawrence Livermore National Laboratory, and Brian E. Newnam of the Los Alamos National Laboratory were co-chairmen of the Symposium. Alexander J. Glass of KMS Fusion is Conference Treasurer and Aaron A. Sanders of the National Bureau of Standards acts as Conference Coordinator.

The purpose of these symposia is to exchange information about optical materials for high-power lasers. The authors welcome comments and criticism from all interested readers relevant to this purpose and particularly relative to our plans for the Eighteenth Annual Symposium, scheduled for November 3-5, 1986, at the National Bureau of Standards, Boulder, Colorado.

2. Overview

Our objective in this section is to give the reader a sense of the emphases and general concerns of this year's symposium. Although we do not review all of the excellent work presented, some of the highlights are touched upon briefly.

Materials and Measurements

A sizeable fraction of this 21-paper session described damage testing facilities with significant automation and computer manipulation of the test parameters. Automated beam profiling received the most attention. For example, one paper reported computer-assisted profiling of the laser fluence from 193 nm to 10.6 μm using fluorescence in a thin slab of BK glass for the uv, solid-state video camera direct response for 0.45 to 1.06 μm , and laser-induced emission from graphite films for 10.6 μm . Another paper described highly automated, computer-controlled operation of CO₂ and HF lasers with pulse durations from 50 μs to fractional cw times, collection of laser power readings and beam profiles (automated pinhole scan), control of sample position (x,y,z), and sample temperature ranging from 77 to 370° K.

A second group of three papers was stimulated by recent Lawrence Livermore National Laboratory experience of reduced damage thresholds in laser glass discs caused by platinum inclusions. These concerned characterization of the damage and its growth under repeated irradiation at 1064 nm, dependence on the laser pulsewidth, and destructive inspection by rastering a laser beam over the 46-cm discs.

Of great interest to researchers in this field was the diagnostic system that featured two synchronized, picosecond dye lasers as multiwavelength probes to identify causes of multiple-pulse damage. The lasers were used both to cause damage and sample accumulation of defects. Another experimental study identified bacterial growth in starting aqueous solutions as the cause of increased absorption and lower bulk damage thresholds for KDP crystals. Irradiation with a uv lamp during crystal growth killed the bacteria and resulted in dramatically higher damage resistance material.

Surfaces and Mirrors

Of the eleven papers in this session, three addressed methods of surface preparation to maximize the damage resistance. One study determined, not surprisingly,

that 355-nm damage to surfaces of fused silica is very dependent on the polishing compound. Highest thresholds were attained by using yttrium oxide, followed by silicon carbide, and least with iron oxide. Spectral analysis of the surface plasmas always revealed elements of the polishing compound. In a systematic study of the role of surface preparation on damage to Ge, alumina polish followed by an argon-ion sputter etch generally yielded the highest threshold. Diamond-turning was second-best, but this caused higher absorption in the top Ge layer due to mechanically induced changes in the work function.

Implantation of 150-keV Mo ions into polished Mo laser mirrors was found to increase the reflectivity by surface smoothing. With an appropriate Mo^+ fluence, a nearly atomically smooth surface was attained. Other ions, such as 1-MeV Au and 3-MeV Ni, caused some surface roughening. A second paper reported successful use of an ion-exchange process to toughen phosphate laser glass for high-average power applications. This process produced a compressive surface layer that raised the thermal shock resistance by a factor of five.

Several papers examined multiple-pulse effects. An important study of N-on-1 irradiation of single-crystal surfaces of Cu, Ni, and Al using a 1- μm laser revealed two damage mechanisms: 1) defect-related local melting at low pulse numbers and 2) plastic deformation at high pulse numbers. A second paper discovered multiple-shot accumulation damage in GaAs irradiated by a 1- μm laser at levels 25% to 50% of the single-shot threshold. No predamage correlation with ion emission was found.

The need for grazing-incidence, intracavity mirrors in free-electron laser resonators motivated a study of the optical properties of a variety of metal surfaces. Absorption was measured directly at 0.5 μm and 10.6 μm for angles up to 89°. Except for the highest angles, where complications due to surface topography were manifest, the measured absorption of freshly coated mirrors agreed with that predicted by Fresnel's equations.

Thin Films

Thin film coatings are generally the weakest components of high-power laser systems and, because of their complex nature, they have been the most difficult to improve. In recent years, the amount of effort directed toward coating development has steadily increased, and at this year's Symposium just over 40% of the total number of papers presented concerned optical coatings. These 28 papers can be categorized in seven groups: 1) advanced coating diagnostics, 2) defect analysis and detection, 3) methods to improve coating structure, 4) optimization of coating deposition parameters, 5) survival in hostile environments, 6) performance of porous coatings, and 7) new reflector designs.

As an indication of the popularity of Raman spectroscopy as a diagnostic in thin film analysis, four papers described its application to measurements of laser-induced

stress and strain, crystallinity, and phase changes in real-time with 1- μm spatial resolution (better than Nomarsky microscopy). A fifth paper described how Raman scattering can detect temperature increases on SiO_2 and glass substrates and in TiO_2 coatings by simultaneous measurement of Stokes and anti-Stokes intensities; higher anti-Stokes intensities were seen above threshold; no effect occurred below threshold. Yet another paper demonstrated how to increase the sensitivity of Raman analysis by launching the probe laser as a guided wave within the thin film under investigation, with the additional benefit of eliminating substrate interference.

X-ray photoelectron spectroscopy (XPS) was exploited in the analysis of the interfacial structure of ion-beam-deposited $\text{TiO}_2/\text{SiO}_2$ coatings. Intermixing of these materials was detected over a 7-nm range at the film boundaries, oxygen deficiency was evident for films in contact with the Si substrate, and the outer free surface apparently contained water vapor. Another paper described the use of MeV-ion beams (alpha particles) to characterize multilayer dielectric reflectors. These were employed in Rutherford Backscattering (RBS) to measure the composition as a function of depth, detect laser damage-induced structural changes, and by particle-induced x-ray emission (PIXE), to measure the presence of low-concentration impurities.

Under the topic of coating-defect detection and analysis, one paper described a positive correlation between local He-Ne laser scatter and defect-initiated laser damage at 2.7 μm for certain sample types. Another group described microscopic observation of damage-initiating sites of $\sim 1 \mu\text{m}$ diameter at the boundary between an antireflection coating and the substrate and a good correlation of substrate roughness with the number of initiator sites.

Seven papers were concerned with coating microstructure, e.g. how to eliminate columnar structure and decrease porosity. One group reported use of metal/dielectric laminates of silver and thin TiO_2 coatings to prevent columnar microstructure. This had the positive result of increased laser damage thresholds at 351 nm. Use of stratified films was also found effective in controlling the microstructure of $(\text{ZnS}/\text{ZnSe})_2$ films deposited by molecular-beam epitaxy. Remarkably, these films had the same damage threshold as the uncoated substrates.

Co-evaporation of zirconia and silica films was reported to decrease porosity and columnar structure. Furthermore, a second paper reported that the porosity of ZnS films is correlated with the damage threshold at 10.6 μm : denser films attained by deposition at high substrate (Ge) temperature (200° C) had substrate-limited thresholds!

Confirming the report by Decker, et al. at the 1984 Symposium, a second group determined that the thermal conductivity of coatings can be much less than the bulk value. The measured conductivity of an enhanced high reflector was found to be a factor of 30 lower than predicted by use of bulk values. Especially for cw-laser

applications, methods to alter coating structure to more nearly match that of bulk material will greatly improve the thermal performance.

Five papers reported experimental studies to optimize the deposition parameters for particular coating processes and film materials. For example, ion-assisted deposition (IAD) was uniquely able to produce durable films of MgF_2 , SiO_2 , and $\text{Al}_2\text{O}_3/\text{SiO}_2$ near room temperature on heavy-metal fluoride glasses.

Valuable data on the effect of molecular fluoride on optics for excimer lasers, in particular at 351 nm, was presented. (Regrettably, the manuscript of this paper was not supplied for this proceedings.) Coatings were exposed to a XeF excimer gas mix containing 0.5% dry F_2 at 760 Torr. All coatings with SiO_2 layers failed quickly and catastrophically, and after 48-hours exposure, the transmittance of bare Suprasil fused silica decreased by 7%. Multilayer reflectors of Al_2O_3 /cryolite on SiO_2 exhibited good resistance for F attack and had high damage resistance; similar performance was observed for Al_2O_3 /MgF antireflection coatings on CaF_2 .

The properties and obvious advantages of graded-index AR coatings made of porous silica were presented by two groups. A new fabrication method developed in Japan involves electron-beam codeposition of NaF and SiO_2 followed by dissolving the NaF with water. These coatings feature 0.17% reflectance at 355 nm, surface roughness no greater than that of the substrate (11 Å rms), and very high damage thresholds. A second paper by Lawrence Livermore Laboratory scientists presented results of multiple-shot tests at 351 nm at 25 to 100 Hz. Porous-silica AR coatings on fused silica had damage thresholds double those reported for films prepared by physical vapor deposition processes.

Finally, three papers presented theoretical designs for advanced coatings. One analyzed designs for multilayer dielectric coatings for phase control, while a second maximized the theoretical reflectance of dielectric coatings set at grazing incidence for possible use in free-electron laser resonators. Extending even further into the future was a proposed reflector design for free-electron lasers that will operate in the extreme ultraviolet below 100 nm. Total external reflection at multiple, flat-metal surfaces, e.g. Al and Si, was shown to be a feasible way to turn the light beam by 180° with broadband reflectance exceeding 40% for wavelengths greater than 35 nm.

Fundamental Mechanisms

Of the eight papers in this session, two were experimental studies of the effects of high-energy radiation on the absorption and laser damage of fused silica. First, irradiation with 2-MeV electrons caused transient absorption at 250 nm which had two recovery paths as indicated by two time constants, 50 ns and 1 μs . Second, defects induced by 1-MeV gamma rays reduced the pulsed-laser damage threshold at 532 nm by as much as 40% due to two-photon absorption, but little change in thresholds was measured for 1064-nm laser pulses.

Complementing the aforementioned experimental studies on the same topic, the fracture mechanics of glass due to absorption at Pt inclusions were analyzed theoretically. The author considered crack formation based on shock-wave propagation when the temperature of the Pt exceeds the boiling point.

Observation of lower damage thresholds at moderate pulse-repetition frequencies (PRF) is not yet well understood. In pursuit of an explanation, one experimental paper reported the effect of ≤ 100 Hz prf on pulsed- CO_2 laser damage to a number of infrared-transmitting materials. For some of the materials, including Si, ZnS, and ZnSe, the damage thresholds dropped monotonically for prf's from 1 to 10 Hz and then remained constant from 10 to 100 Hz. The authors believed that such behavior might be explained by anomalously low thermal conductivity at the surface due to polishing-induced structure changes or grain size.

For further information on the topics reported at this Symposium, the interested reader should consult the individual manuscripts contained in this Proceedings.

3. Acknowledgments

The editors would like to acknowledge the invaluable assistance of Mr. Aaron A. Sanders and the other involved staff members of the National Bureau of Standards in Boulder, Colorado, for their interest, support, and untiring efforts in the professional operation of the Symposium. Particular thanks to Ms. Susie Rivera for her lead in the preparation and publication of the proceedings as well as to Ms. Edit Haakinson and to Ms. Pat Whited of the Air Force Weapons Laboratory for conference coordination.

4. References

- [1] Glass, A.J.; Guenther, A.H., eds. Damage in Laser Glass, ASTM Spec. Tech. Pub. 469, ASTM, Philadelphia. PA; 1969.
- [2] Glass, A.J.; Guenther, A.H., eds. Damage in Laser Materials, Nat. Bur. Stand. (U.S.) Spec. Publ. 341; 1970.
- [3] Bloembergen, N. Fundamentals of Damage in Laser Glass, National Materials Advisory Board Publ. NMAB-271, National Academy of Sciences; 1970.
- [4] Glass, A.J.; Guenther, A.H., eds. Damage in Laser Materials: 1971, Nat. Bur. Stand. (U.S.) Spec. Publ. 356; 1971.
- [5] Bloembergen, N. High Power Infrared Laser Windows. National Materials Advisory Board Publ. NMAB-292; 1972.
- [6] Glass, A.J.; Guenther, A.H., eds. Laser Induced Damage in Optical Materials: 1972, Nat. Bur. Stand. (U.S.) Spec. Publ. 372; 1972.
- [7] Glass, A.J.; Guenther, A.H., eds. Laser Induced Damage in Optical Materials: 1973, Nat. Bur. Stand. (U.S.) Spec. Publ. 387; 1973.
- [8] Glass, A.J.; Guenther, A. H. Laser Induced Damage in Optical Materials: A Conference Report. Appl. Opt. 13 (1): 74-88; 1974.

- [9] Glass, A.J.; Guenther, A.H., eds. Laser Induced Damage in Optical Materials: 1974, Nat. Bur. Stand. (U.S.) Spec. Publ. 414; 1974.
- [10] Glass, A.J.; Guenther, A.H. Laser Induced Damage in Optical Materials: 6th ASTM Symposium, Appl. Opt. 14 (3): 698-715; 1975.
- [11] Glass, A.J.; Guenther, A.H., eds. Laser Induced Damage in Optical Materials: 1975, Nat. Bur. Stand. (U.S.) Spec. Publ. 435; 1975.
- [12] Glass, A.J.; Guenther, A.H. Laser Induced Damage in Optical Materials: 7th ASTM Symposium, Appl. Opt. 15 (6): 1510-1529; 1976.
- [13] Glass, A.J.; Guenther, A.H., eds. Laser Induced Damage in Optical Materials: 1976, Nat. Bur. Stand. (U.S.) Spec. Publ. 462; 1976.
- [14] Glass, A.J.; Guenther, A.H. Laser Induced Damage in Optical Materials: 8th ASTM Symposium, Appl. Opt. 16 (5): 1214-1231; 1977.
- [15] Glass, A.J.; Guenther, A.H., eds. Laser Induced Damage in Optical materials: 1977, Nat. Bur. Stand. (U.S.) Spec. Publ. 509; 1977.
- [16] Glass, A.J.; Guenther, A.H. Laser Induced Damage in Optical Materials: 9th ASTM Symposium, Appl. Opt. 17 (15): 2386-2411; 1978.
- [17] Glass, A.J.; Guenther, A.H., eds. Laser Induced Damage in Optical Materials: 1978, Nat. Bur. Stand. (U.S.) Spec. Publ. 541; 1978.
- [18] Glass, A.J.; Guenther, A.H., eds. Laser Induced Damage in Optical Materials: 10th ASTM Symposium, Appl. Opt. 18 (13): 2212-2229; 1979.
- [19] Bennett, H.E.; Glass, A.J.; Guenther, A.H.; Newnam, B.E., eds. Laser Induced Damage in Optical Materials: 1979, Nat. Bur. Stand. (U.S.) Spec. Publ. 568; 1979.
- [20] Bennett, H.E.; Glass, A.J.; Guenther, A.H.; Newnam, B.E. Laser Induced Damage in Optical Materials: 11th ASTM Symposium, Appl. Opt. 19 (14): 2375-2397; 1980.
- [21] Bennett, H. E.; Glass, A.J.; Guenther, A. H.; Newnam, B.E., eds. Laser Induced Damage in Optical Materials: 1980, Nat. Bur. Stand. (U.S.) Spec. Publ. 620; 1981.
- [22] Bennett, H.E.; Glass, A.J.; Guenther, A.H.; Newnam, B.E. Laser Induced Damage in Optical Materials: 12th ASTM Symposium, Appl. Opt. 20 (17): 3003-3019; 1981.
- [23] Bennett, H.E.; Guenther, A.H.; Milam, D.; Newnam, B.E., eds. Laser Induced Damage in Optical Materials: 1981, Nat. Bur. Stand. (U.S.) Spec. Publ. 638; 1983.
- [24] Bennett, H.E.; Guenther, A.H.; Milam, D.; Newnam, B.E. Laser Induced Damage in Optical Materials: 13th ASTM Symposium, Appl. Opt. 22 (20): 3276-3296; 1983.
- [25] Bennett, H.E.; Guenther, A.H.; Milam, D.; Newnam, B.E., eds. Laser Induced Damage in Optical Materials: 1982, Nat. Bur. Stand. (U.S.) Spec. Publ. 669; 1984.
- [26] Bennett, H.E.; Guenther, A.H.; Milam, D.; Newnam, B.E. Laser Induced Damage in Optical Materials: 14th ASTM Symposium, Appl. Opt. 23 (21): 3782-3795; 1984.
- [27] Bennett, H.E.; Guenther, A.H.; Milam, D.; Newnam, B.E., eds. Laser Induced Damage in Optical Materials: 1983, Nat. Bur. Stand. (U.S.) Spec. Publ. 688; 1985.
- [28] Bennett, H.E.; Guenther, A.H.; Milam, D.; Newnam, B.E. Laser Induced Damage in Optical Materials: 15th ASTM Symposium, Appl. Opt. 25 (2): 258-275; 1986.
- [29] Bennett, H.E.; Guenther, A.H.; Milam, D.; Newnam, B.E., eds. Laser Induced Damage in Optical Materials: 1984, Nat. Bur. Stand. (U.S.) Spec. Publ. 272; 1986.
- [30] Bennett, H.E.; Guenther, A.H.; Milam, D.; Newnam, B.E. Laser Induced Damage in Optical Materials: 16th ASTM Symposium, Appl. Opt. 26 (5): 813-827; 1987.

A Versatile Laser Glass Inspection and Damage Testing Facility*

J. E. Marion, G. J. Greiner, J. H. Campbell, P. H. Chaffee, J. S. Hildum,
J. Z. Grens, C. L. Weinzapfel, S. M. Winfree and D. Milam

Lawrence Livermore National Laboratory
University of California
P.O. Box 5508, L-490
Livermore, California 94550

Most glass optical components for high power lasers are melted and homogenized in platinum-lined crucibles leading to the potential presence of microscopic platinum inclusions. In situations where large optics are exposed to high laser fluences, a significant problem can be created by an extremely low density of inclusions, as low as one per component. Previously, direct visual examination or optical microscopy was used to inspect for these particles, limiting reliable detection to inclusions greater than $10\mu\text{m}$ diameter. Unfortunately, much smaller inclusions can initiate damage in modern lasers operated at high fluences.

A test facility is described which detects small opaque inclusions in large transparent components by using a commercial laser which delivers high energy pulses to the test sample at moderate frequency in a small diameter beam. The sample is automatically scanned such that each point in the volume is irradiated with ten pulses at twice the inclusion damage threshold--an amount sufficient to cause visible damage at inclusion sites. This approach permits detection of opaque inclusions in the parts per trillion and lower concentration range. The specifics of the device design, and its performance are discussed in the context of automatic inclusion inspection and mapping in large laser optics.

Key words: inspection techniques, laser glass, laser-induced damage, metallic inclusions, platinum

1. Introduction

Modern fusion research lasers and proposed defensive laser weapons use very large optics which are exposed to high laser fluences.¹ If present, opaque microscopic inclusions cause unacceptable damage. A simple device for performing large scale inspection of optical components for the presence of inclusions is described. Our present application requires a system capable of rapid and reliable inspection of Nd:phosphate glass samples for inclusions which absorb at $1.06\mu\text{m}$, such as platinum and carbon. The samples include finished amplifier disks, ranging in volume up to about 10 liters, as well as numerous test samples. The size of the inclusions which must be located extend into the sub-micron region--a territory in which conventional optical microscopy is ineffective. Light scattering methods are unwieldy because hubbles, surface imperfections and dust are indistinguishable from inclusions even when the sample is of high optical quality. Signals from these imperfections can swamp the signals of interest because the inclusion number density is quite low, in the $10^{-4}/\text{cm}^3$ range.

We adopt a destructive technique for locating inclusions as the only reliable method available. A commercial Q-switched YAG laser (JK Model HY 750) gives a focussed beam 2 mm diameter on the sample which is scanned in X and Z directions by a commercial stage drive (Daedal Models 47215 LH and MLH, Fig. 1). In order to assure adequately large damage sites at each inclusion (to facilitate subsequent optical inspection) each site in the sample is irradiated at normal incidence with ten shots; each above $10\text{ J}/\text{cm}^2$. This fluence corresponds to twice the damage threshold for platinum inclusions in glass at the 8 ns pulsewidths used here.² In practice, the device is capable of scanning a 46 cm aperture phosphate glass amplifier disk (7000 cm^3 volume) in about four hours using ten shots per site. Reducing the number of shots proportionately reduces the scan time. The optical examination of the damaged disk takes an additional hour or so depending on the number of damage sites which must be characterized and mapped.

*Work performed under the auspices of the U.S. Department of Energy by Lawrence Livermore National Laboratory under Contract No. W-7405-ENG-48.

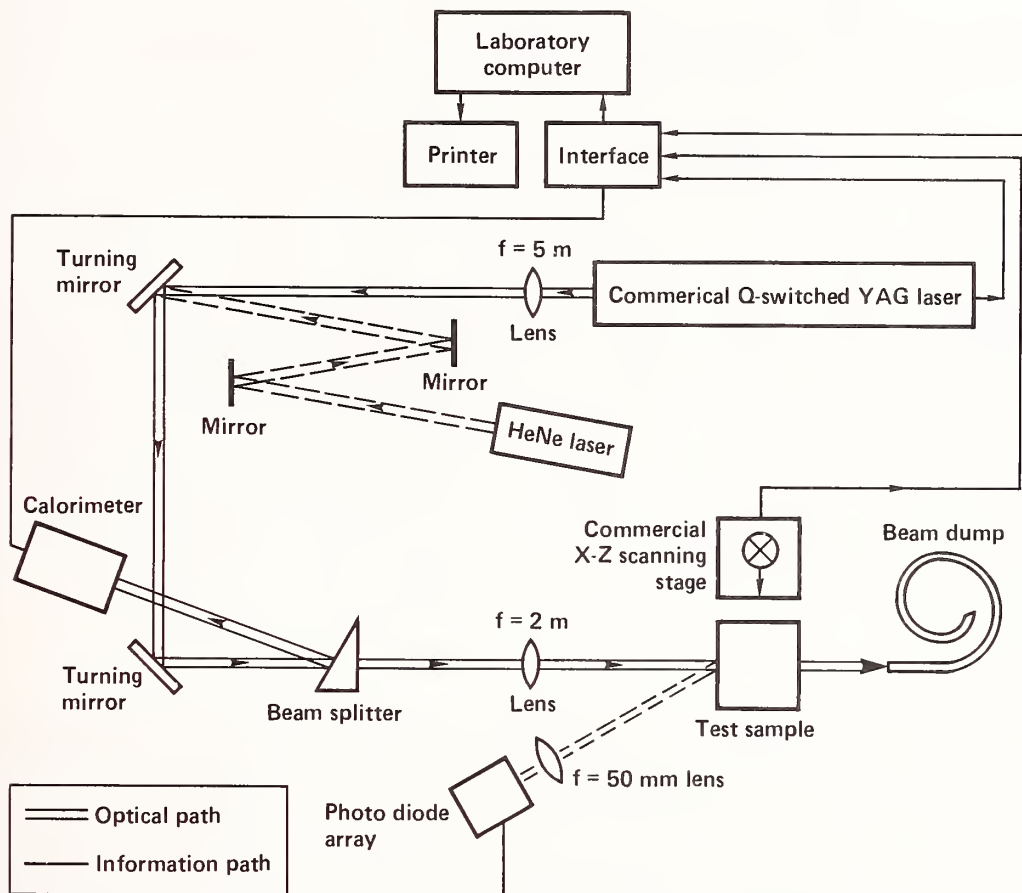


Figure 1. Schematic of the inspection test device, as described in the text.

2. Device Description

The device is located in a class 1000 clean room in order to avoid dust contamination and subsequent damage to the device optics as well as the test sample. The laser is quite stable with better than 99% of the shots within 1% of the mean shot energy. The beam profile is adequately uniform to insure that the sample is irradiated at the desired fluence (Fig. 2). The output energy is 800 mJ at 8 ns pulsewidth and 20 Hz PRF. The slightly diverging 8 mm diameter output beam is approximately collimated by a five meter lens and directed toward the sample by high power dielectric-coated mirrors. It is then focussed by a two meter positive lens into a mildly converging beam. A collinear HeNe alignment beam is introduced before the positive lens to aid in sample positioning. A beam splitter (with the front surface anti-reflection coated) is located after the two meter lens, and a calorimeter monitors the second surface reflection as a continuous check of laser performance. After the beam splitter, the laser beam, now 2 mm in diameter, strikes the sample which is mounted on a X-Z motor driven stage.

The laser and the stage drive are controlled by a laboratory computer (Hewlett Packard 9816S), interfaced through a general purpose data acquisition control unit (HP 3421A). If dust or damage occurs upstream, leading to a degradation in the laser energy, the test is interrupted by the computer monitoring the calorimeter. Automatic shut off of the laser and stage drive can also occur if the sample reaches position limit triggers, or if there is a high laser cooling water temperature.

The use of the computer also offers the possibility of real time inclusion mapping. When irradiated, the damaging inclusions give a distinct optical signal associated with plasma emission. This signal can be readily detected by focussing onto a photodiode array. This information is combined with X-Z position coordinates to give an inclusion map. Although the detection system has been demonstrated,³ it is not yet sufficiently reliable to replace optical inspection. Incorporation of this mapping option will reduce the inspection time by an order of magnitude because only one shot at each site will be required. The post mortem optical inspection will also be eliminated along with its inherent operator subjectivity.

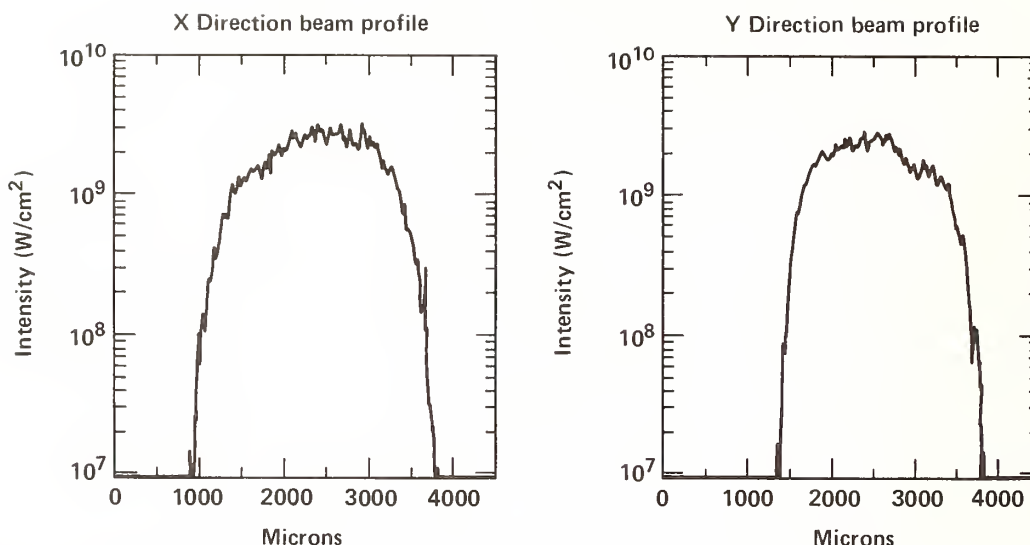


Figure 2. Beam profiles obtained from microdensitometer traces of the photographed beam. The beam shape is reasonably Gaussian.

3. Device Applications

We believe that this facility offers a unique capability in materials damage assessment. Prior damage testing has generally fallen into one of two categories. Previously, small (mm^2 or smaller) beams at high fluences were used to test several spots on the sample, in conjunction with a statistical treatment of the data.⁴ The limitations of that method in situations where the damaging entities have a very low spatial density are obvious. A second approach uses a research tool such as the Nova laser to give high fluences over an entire area in single shots, but at very low repetition rate.⁵ Aside from the expense of the latter method, our new device is faster and less cumbersome. Large optics can now be quickly and reliably inspected for inclusion volume concentrations in the parts per quadrillion range (10^{15}) (i.e., several one micron diameter inclusions in a 7000 cm^3 optical component.)

A further advantage of this testing device is its ability to rapidly perform multiple shot damage characterization on inclusions that have been carefully analyzed prior to testing. Damage growth rate data on single inclusions subjected to ten thousand shots or more can be obtained readily, helping to relieve the paucity of information in that area.

Finally, it has not escaped the attention of the authors that this device has useful applications in other fields of materials science and chemistry, for example, in any application in which small concentrations of microscopic contaminants must be detected. In principle, any laser wavelength may be used where the samples are reasonably transparent. The primary requirement is that the microscopic inclusions or defects have a higher absorption than the surrounding matrix at the laser wavelength.

4. Summary

Our requirement for rapid inspection of large optics for the presence of microscopic inclusions has led us to construct a simple damage device using a Q-switched YAG laser and a computer controlled X-Z motor driven stage. Each point in the volume of the test sample receives ten pulses at twice the damage threshold, permitting straightforward post mortem visual determination of inclusion spatial density. An automatic detection scheme, in development, will permit automatic mapping.

In addition to automated inspection, straightforward damage growth characterization to high shot numbers is being pursued. This information is of interest for assessing optical component reliability both for fusion research lasers as well as defensive laser weapon systems.

5. References

- [1] Laser Program Annual Report, Lawrence Livermore National Laboratory, Livermore, CA, Eds. M. L. Rufer, P. W. Murphy, 1984.
- [2] R. P. Gonzales and D. Milam, "Evolution during multiple-shot irradiation of damage surrounding isolated platinum inclusions in phosphate laser glass", elsewhere in these proceedings.
- [3] J. E. Marion, unpublished.
- [4] Statistical aspects of laser-induced damage were first treated in: M. Bass and H. H. Barrett, "The probability and dynamics of damaging optical materials with lasers", Proceedings of Damage in Laser Materials: 1971, NBS Spec. Pub. 356, pp. 76, issued Nov. 1971. The first treatment of the probability of encountering isolated defects with a small test beam was: L. G. deShazer, B. E. Newnam and K. M. Leung, "The role of coating defects in laser-induced damage to thin films", Proceedings of Laser-Induced Damage in Optical Materials: 1973, NBS Spec. Pub. 387, pp. 114, issued Dec. 1973.
- [5] D. Milam, C. W. Hatcher and J. H. Campbell, "Platinum particles in the Nd:doped disks of phosphate glass in the Nova laser", elsewhere in these proceedings.

DISCLAIMER

This document was prepared as an account of work sponsored by an agency of the United States Government. Neither the United States Government nor the University of California nor any of their employees, makes any warranty, express or implied, or assumes any legal liability or responsibility for the accuracy, completeness, or usefulness of any information, apparatus, product, or process disclosed, or represents that its use would not infringe privately owned rights. Reference herein to any specific commercial products, process, or service by trade name, trademark, manufacturer, or otherwise, does not necessarily constitute or imply its endorsement, recommendation, or favoring by the United States Government or the University of California. The views and opinions of authors expressed herein do not necessarily state or reflect those of the United States Government thereof, and shall not be used for advertising or product endorsement purposes.

Computer-Controlled Facility for
Laser Switching and Damage Testing

Jay S. Chivian, W. D. Cotten, D. F. Fuller,
R. B. Hemphill and M. W. Scott

LTV Aerospace and Defense Company
Dallas, Texas 75265-0003

Apparatus has been assembled for mostly-automatic laser switching and damage measurements in which dynamic events are followed in real time. Lasers, optical elements, and detectors are available for operation at 2.8 μm and at 10.6 μm . Sample exposure time is variable from 50 μs to cw. Sample positioning in X:Y:Z is controllable to 0.2 μm . Testing can be done with static beam position or with a scanning beam. Samples can be tested at ambient temperature, or from near 77°K to 370°K.

Software provides for test control, data processing, and graphic, hard copy output. Beam profiling can be done automatically at the sample position, and the profile fit to a Gaussian of the same $1/e^2$ width. Sample data acquisition is sequenced by the computer after an enable pulse is given at the discretion of the experimenter. The computer records and processes the incoming data, presents intermediate data display, completes data manipulation, and compares processed measurement data with internally available prediction models in graphic form. Representative output for a thin film nonlinear optical material is shown.

Key words: automated testing; dynamic real time testing; laser-induced damage; laser-induced switching.

1. Introduction

It has been our objective to assemble versatile apparatus to make accurate and reproducible measurements in real time of fast, dynamic processes occurring under intense laser irradiation. We wished to examine laser-induced switching and damage in nonlinear materials, and in a more general sense, do damage characterization of any thin film material/substrate pair. For these purposes, we define "nonlinear material" as one for which its optical properties change abruptly at some fixed condition, such as at a phase transition occurring at a given temperature.

Present and projected capabilities are summarized in tables 1 and 2. Hardware is reviewed in section 2, first in a generalized form, after which specific embodiments are discussed. The procedural sequence, during which the experimenter interacts with the coordinating software, is covered in section 3. Data samples are shown at various stages of processing, as is representative output for switching and damage events.

2. Hardware

The apparatus and instrumentation are shown in general form in figures 1 and 2. The block labeled Beam Handling in figure 1 is a convenient way of describing a collection of items distributed throughout the optical path which direct and shape the beam. These typically include mirrors, lenses, windows, beamsplitters, and apertures. These optical components are usually positioned during setup and alignment, and do not interface with the computer. The Pulse Selection components are also distributed at convenient locations; included are a shutter, light chopper, and scan mirror (if used). The chopper is often placed at the internal focal plane of a beam expander, which thus allows for fast rise times and short pulse lengths. The power meter shown in two positions is used during the calibration of the detectors. A pinhole (of appropriate size) can be

placed at the position of the sample for beam profiling of a stationary beam. Two pinholes separated by a known distance are used to measure scan speed.

The available hardware is listed in more detail in table 3. Schematics for a stationary spot experiment at $2.8 \mu\text{m}$, and for a scanned spot test at $10.6 \mu\text{m}$ are shown in figures 3 and 4 respectively. Figures 5 and 6 are photographs of the actual apparatus, in the same order. Figure 7 shows the overall test instrumentation configured for a single short pulse; the lock in amplifiers are used only for repetitive pulses, as in long exposures. Figure 8 and 9 show the timing electronics for long exposures (50% duty cycle at 20 kHz) and for the scanning test, respectively. The timing sequence for a scanning laser pulse is given in figure 10 as an example. The timing sequence for a single short pulse is similar to figure 10, but without the scanner or variable delay sequence (pulse trains at locations 3-7 only). The timing sequence for long exposure is even simpler; the chopper is free running and the manually triggered shutter is open long enough to include many cycles of the 50% duty cycle chopper. The laser isolator feature has proved to be essential to prevent feedback causing modulation of the laser output power when a scanning beam is involved; its effect is shown in figure 11.

3. Experimental procedure and representative results

An outline of the experimental sequence is shown in figure 12. The mathematical quantities will be defined in context.

The spatial distribution of the laser beam at the location of the sample is determined by stepping an appropriately sized pinhole across the beam in a number of steps while measuring the power transmitted by the pinhole. This is done automatically by the controller at the same time that a graph of relative power versus position is plotted on the printer. Figure 13 is a typical laser beam profile map with a theoretical Gaussian fit to the same $1/e^2$ diameter (also generated by the computer). Circular symmetry is assumed, although symmetry is easily monitored with an IR image plate or by additional profiles.

The apparatus is calibrated with no sample in the system using power meter and programmable digitizer. Calibration is done at or near operating power conditions. The ratio of the average power to the transmitted detector system \bar{P}_T (power at meter position 2) to the average power to the incident detector \bar{P}_I (power at meter position 1) is measured at the beginning of the experiment by recording the power in front of the incident detector system and then in front of the transmitted detector system several times to arrive at an average of the beamsplitter ratio

$$B = \bar{P}_T / \bar{P}_I.$$

The error on this measurement does not affect the final results, as it will be absorbed into the responsivity calculation.

The incident detector is calibrated with the power meter in front of the transmitted detector system (position 2); the chopper is turned off and held open to read the transmitted cw power. Next, the chopper is turned on and 32 pulses from the incident detector are averaged by the programmable digitizer. Using the digital cursors, the average voltage \bar{V}_I from the incident detector differential amplifier is measured. This is repeated several times. The responsivity (in V/W) of the incident detector system is then calculated from

$$R_I = \bar{V}_I B / (G_I \bar{P}_T),$$

where G = gain on the detector differential amplifier.

The transmitted detector system is calibrated from the incident detector:

$$R_T = \frac{\bar{V}_T}{G_T \bar{P}_T} = \frac{\bar{V}_T G_I R_I}{G_T B \bar{V}_I}.$$

To calibrate for long exposures, the procedure is the same except the 50% duty cycle chopper is not stopped for power measurements. Also the outputs of the lock-in amplifiers are treated as the detector outputs.

Data is acquired after a sample has been inserted into the system. It is assumed that pulse length, digitize rate, power level, and amplifier gain setting have been selected. An enable pulse from the computer starts the sequence and the sample is irradiated. Data is taken into the digitizer and voltages from the incident detector amplifier $V_I(t)$ and the transmitted detector amplifier $V_T(t)$ are displayed versus time, giving a dynamic record of the sample characteristic during irradiation. At this point, the experimenter can repeat the test, or accept the data and instruct the computer to continue. The computer next locates the beginning and end of the exposure, and corrects for dc shift and ac coupled signal droop. Options exist to display voltage or power versus time, and to print or not print the data in tabular form.

The power to the transmitted detector system $P_T(t)$ is calculated by the computer from

$$P_T(t) = \frac{V_T(t)}{G_T P_T}$$

and now includes the transmission of the sample $T(t)$. The power incident on the sample $P_I(t)$ is predicted by the incident detector from

$$P_I'(t) = \frac{V_I(t) B}{G_I R_I}$$

$T(t)$ can then be calculated from

$$T(t) = \frac{P_T(t)}{P_I'(t)}.$$

The peak irradiance $I_0(t)$ on the sample is determined from

$$I_0(t) = \frac{P_T'(t) K_0}{A_0},$$

where A_0 = transmission of the optical elements between the sample and the transmitted detector system. $A_0 \approx 0.96$ (typical). The peak fluence incident on the sample from pulse initiation time t_i to time t is calculated by the computer from

$$F(t) = \int_{t_i}^t I_0(t) dt.$$

The computer then displays the percent transmission and integrated peak fluence versus time. Sample plots of $V_I(t)$, $V_T(t)$, $T(t)$, and $F(t)$ for a switching event and for a damage event are shown in figure 14 for two different samples. For the switching event, the abrupt change in the transmitted signal occurs when the nonlinear material switches from a high transmission state to high reflectance. In the damage event, the sample switches early in the pulse (high transmission to low transmission); the transmission is seen to increase roughly midway in the irradiance pulse due to film removal from the substrate. The operator sets the vertical (time) cursor on the $T(t)$ plot at the time the event starts. The computer sets the horizontal cursor where the time cursor crosses the fluence curve, displays the indicated lapsed time to the event, and calculates and displays the integrated fluence up to event initiation (threshold fluence).

The experimenter can now repeat the sequence for different power levels or pulse widths (gather more data), or proceed with computation.

When enough data has been acquired, the computer is instructed to calculate values of threshold fluence versus time for specified conditions from a stored predictive thermal model. The thermal model is based on solutions of the diffusion equation for a thin film on a semi-infinite substrate; solutions of arbitrary sophistication can be used. The conditions involve material constants and test conditions including switch or damage temperature, bias temperature, beam spot size at the sample, and scale ranges. As a final step, the computer plots the experimental data points on the same sheet as the theoretical curve. Examples of a switching curve and a damage curve (for the same sample) are shown in figures 15 and 16. Note that the damage data point from figure 14 is the solid data point in figure 16.

4. Summary

The apparatus and techniques described are obviously not limited to application with nonlinear material films, but can be used with any material which damages when subjected to intense laser radiation. Samples can be examined under dynamic conditions, and before and after maps can be made of damage regions without losing the ability to do structural studies after removal from the test apparatus. Thus the goal stated earlier has been achieved.

We wish to thank M. O. Gracey and J. H. Nickelson for valuable technical assistance. J. D. Ward contributed greatly to apparatus development and assembly. D. S. Smith helped considerably with procedural and software development, as did cooperative student employees L. E. Godwin, C. D. Murphy, and L. Valdez.

Table 1. Present Capability

-
- o Multiple wavelength - ~50W cw at 2.8 μm (HF) and 10.6 μm (CO₂)
 - o Gaussian irradiance distribution
 - o Diffraction-limited focusing - ~ 50 μm 1/e² diameter spot
 - o Peak irradiance range - up to ~ 10⁶ W/cm²
 - o Variable exposure - single pulse at 50 μs to cw (50% duty cycle at 20 kHz) - 5 μs minimum rise time
 - o Stationary beam position or swept beam (multiple scan option)
 - o Sample positioning in X:Y:Z - 1 in. travel in 0.2 μm steps - computer interfaced
 - o Sample temperature control - ambient, or 77°K to 370°K
 - o Calibration for absolute measurement of fluence
 - o Dynamic, real time record of sample characteristic during irradiation
 - o Automated data collection, analysis, plotting
 - o Comparison of results with theory for switching and damage thresholds
-

Table 2. Projected additions to capability

-
- Lasers available
- o TEA CO₂(pulsed) - 0.5J/pulse, pulse width ~ 50 ns
 - o Transverse flow CO₂(cw) - ~ 800 W
 - o Nd:YAG (pulsed) - 1.2J/pulse, pulse width ~ 10 ns
-

Table 3. Hardware

Sources

- o 2.8 μm - 50W cw, TEM₀₀ (grating tuning available)
- o 10.6 μm - 50W cw, TEM₀₀ (500W pulsed capability)
 - amplitude stabilized
 - grating tuned capability

Detectors

- o InSb photovoltaic cooled to LN₂
- o HgCdTe photoconductive cooled to LN₂
- o Integrating spheres - adjustable attenuation factor by variable iris

Optical Elements

- o Mirrors and beam directors - high reflectance metallic
- o Lenses - CaF₂, Si(AR/AR), ZnSe(AR/AR)
- o Beamsplitters - Al₂O₃(bare/AR), ZnSe(coated/AR)
- o Isolator-attenuator for 10.6 μm - polarizer/analyzer (ZnSe Brewster angle plates), ZnSe Fresnel rhomb (AR coated)

Sample inspection

- o Fiber optic probe and photomultiplier for flash detection - can be used to verify and time catastrophic failure
 - o Microscope and video monitor - before and after snapshot capability
-

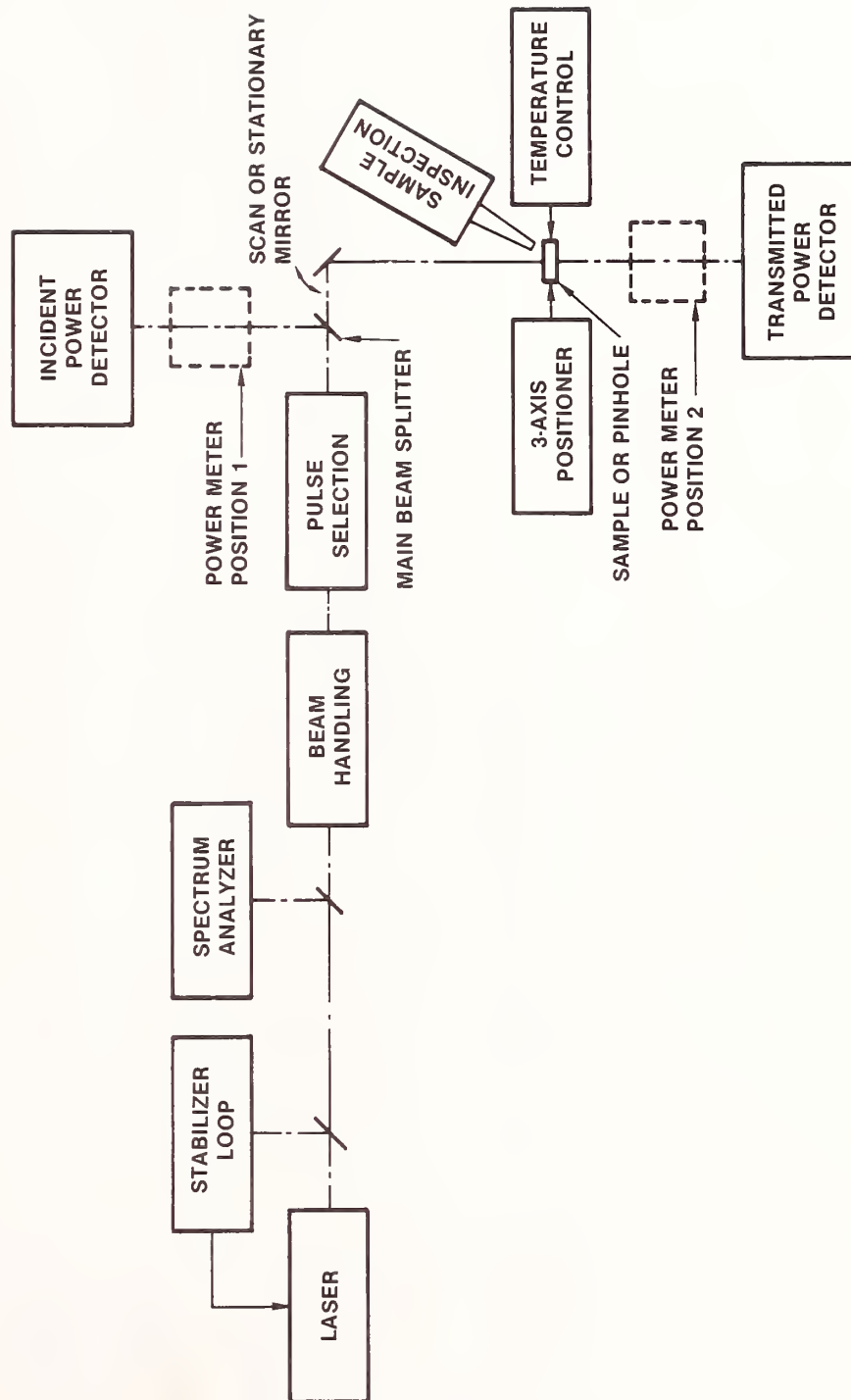


Figure 1 Generalized Apparatus Setup

MP5-3031-1

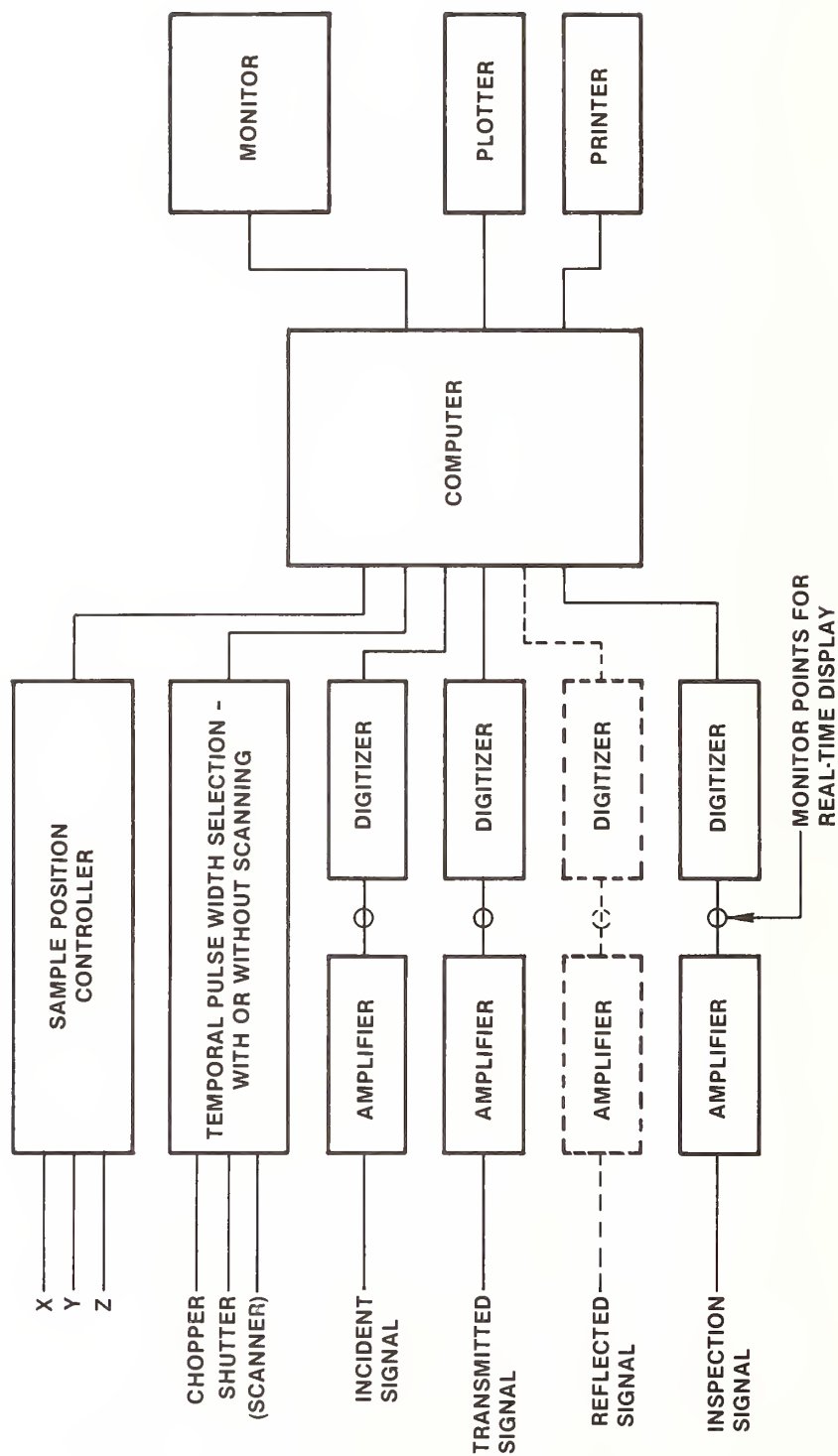


Figure 2 Generalized Instrumentation Setup

MP5-3031-2

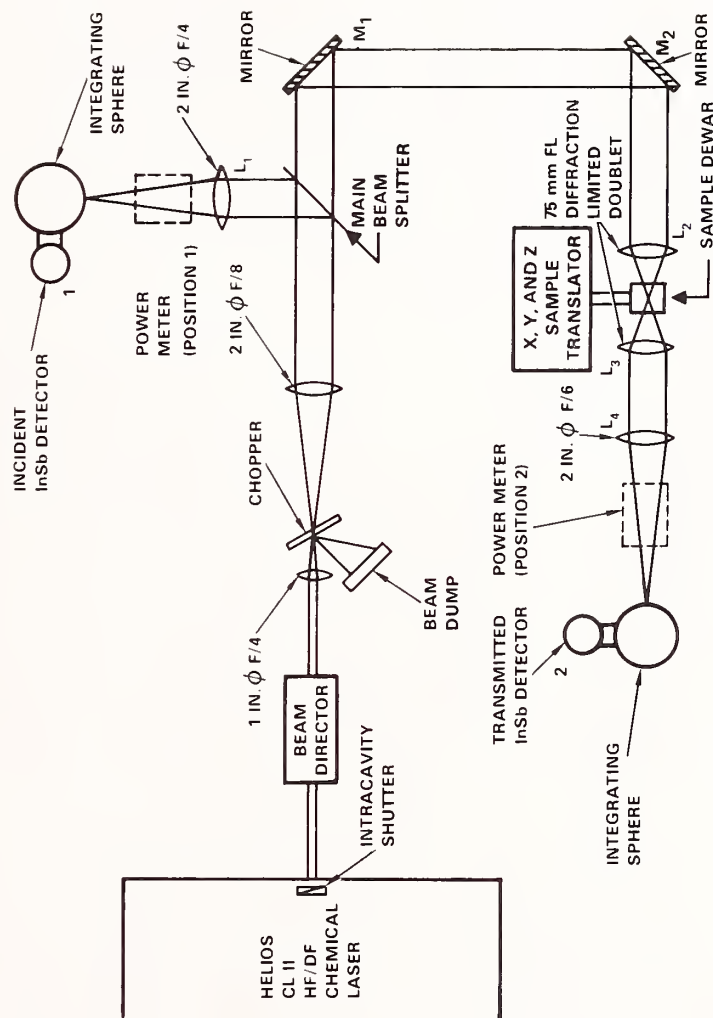


Figure 3 Stationary spot apparatus for 2.8 μm

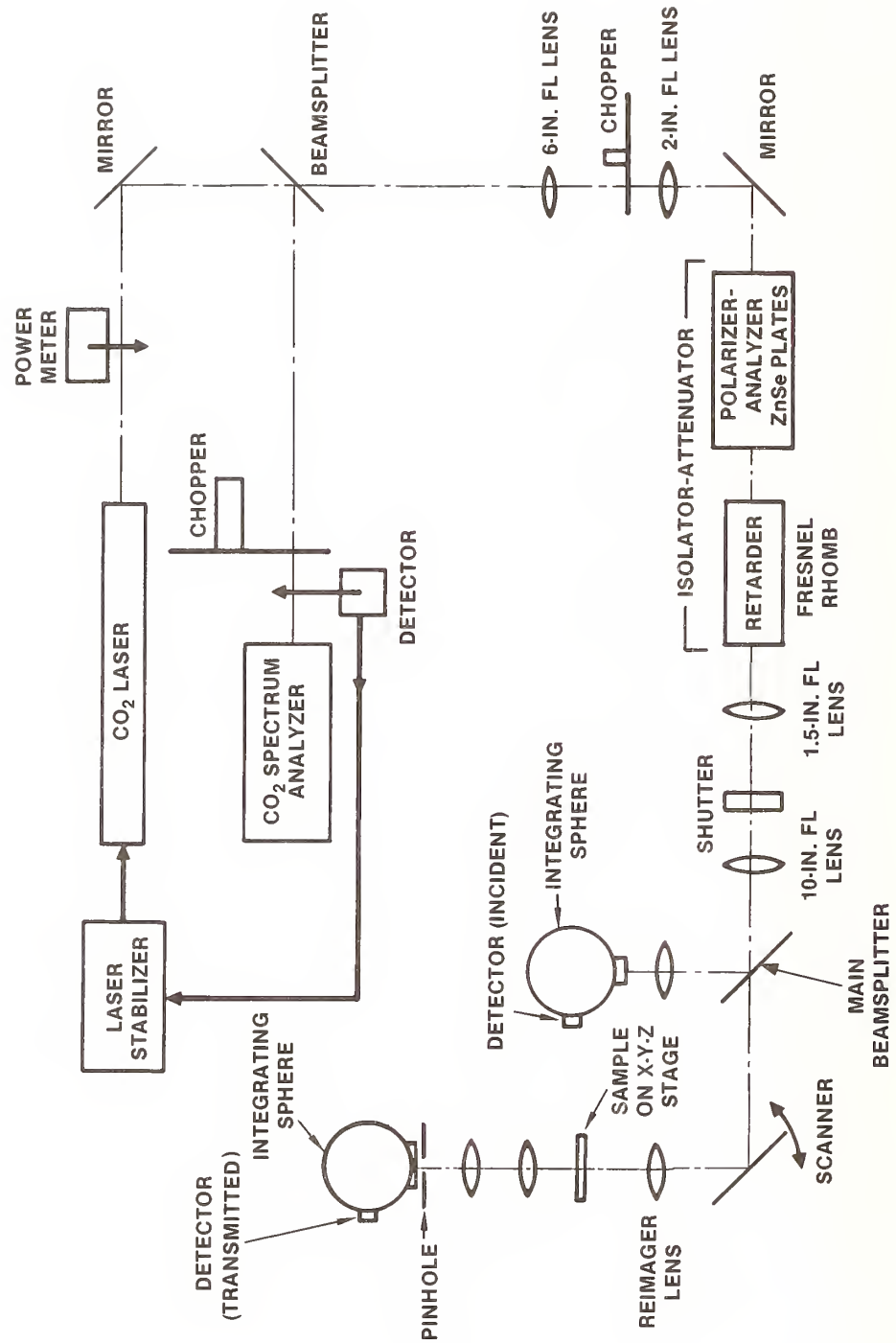
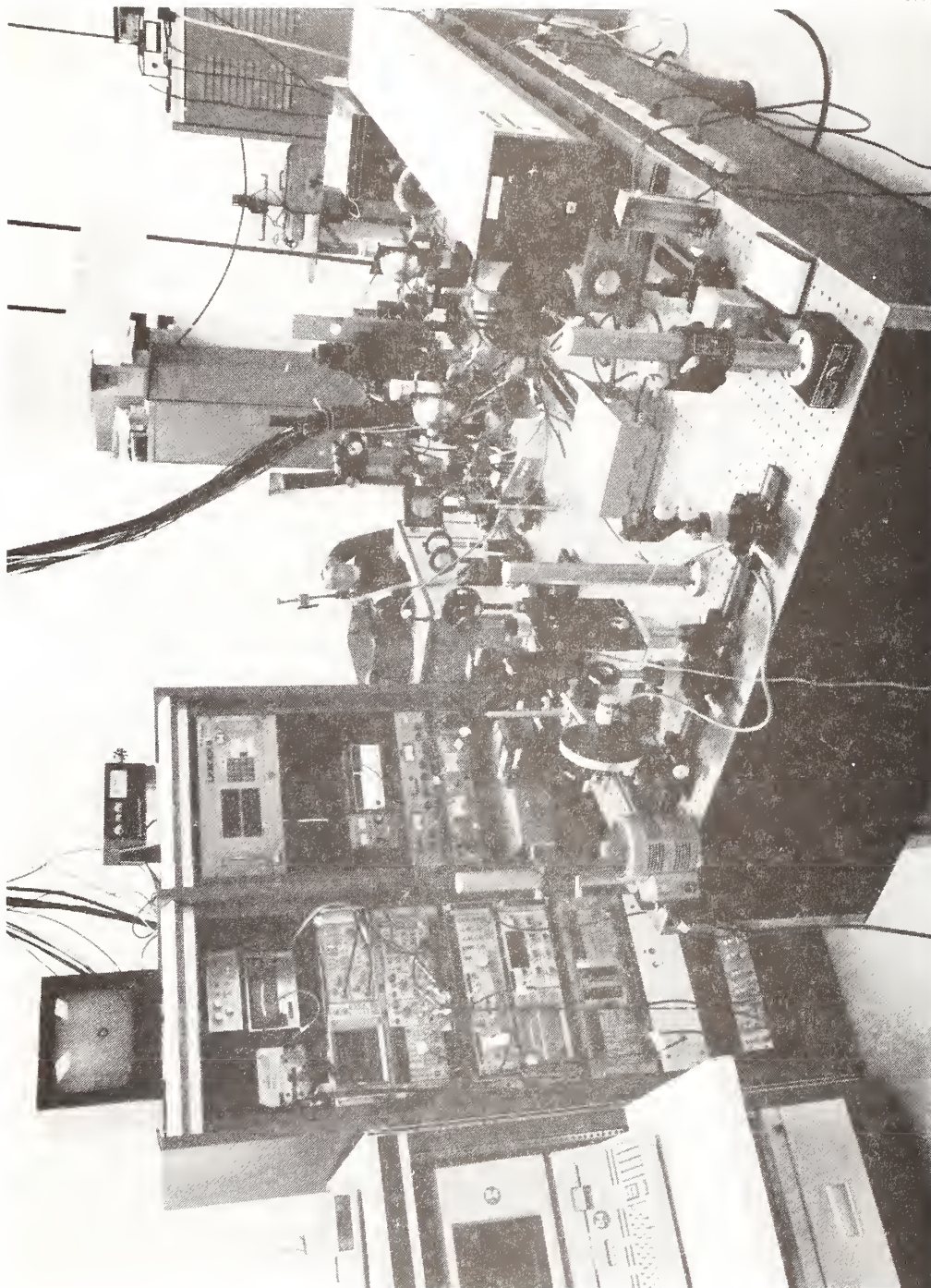


Figure 4 Scanning spot laser tests



Figure 5 Stationary Spot Apparatus at $2.8\ \mu\text{m}$

MB5-2235-18



MP5-3031-25

Figure 6 Scanning Spot Apparatus at 10.6 μm

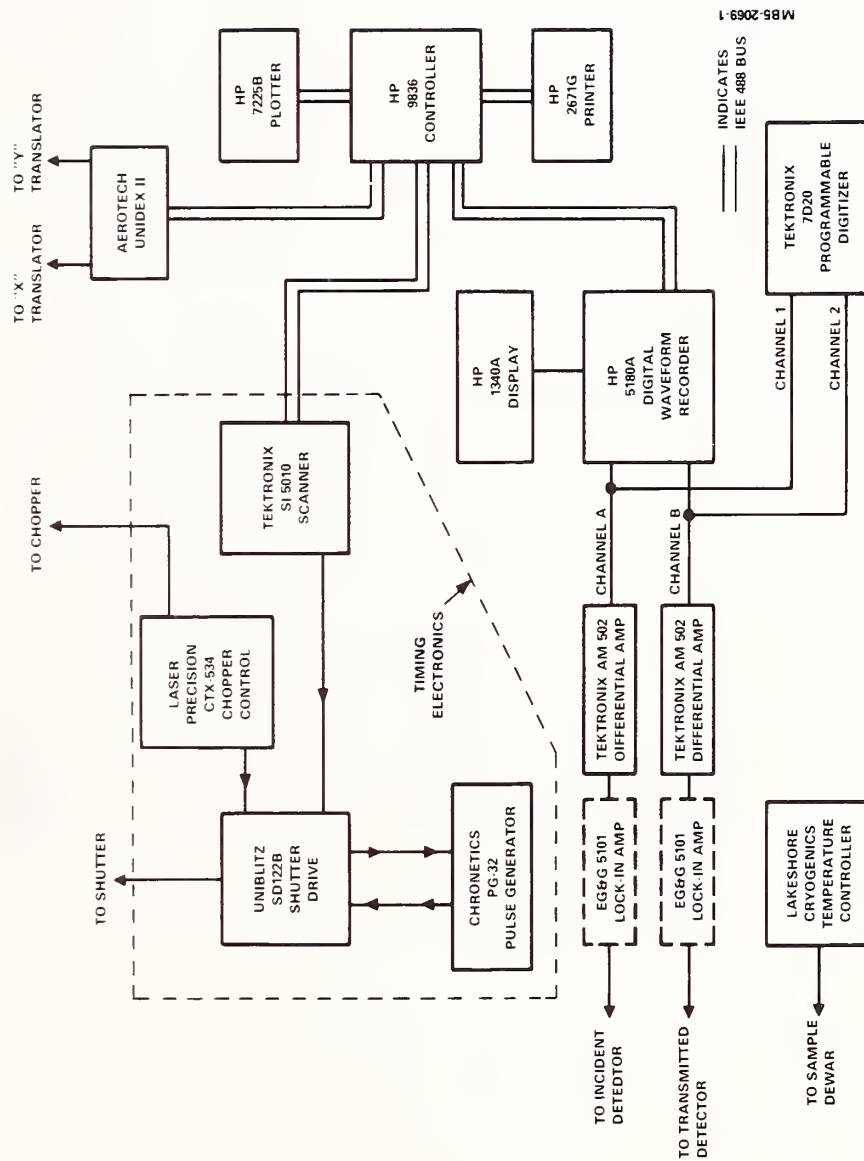


Figure 7 Laser test electronics for single pulse

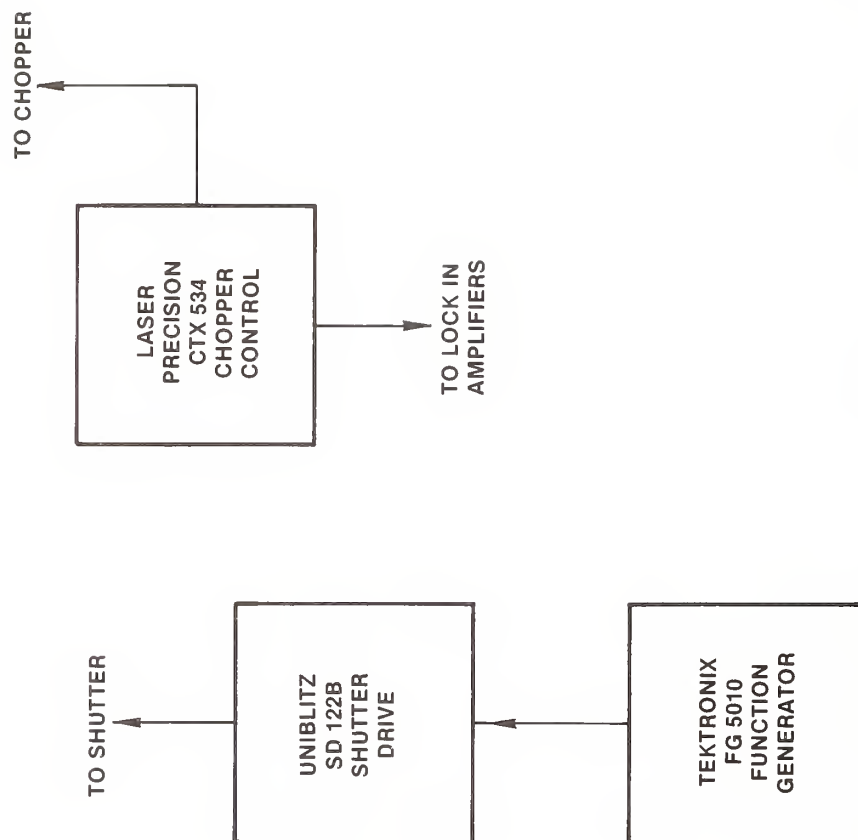


Figure 8 Timing Electronics for Long Exposure (≥ 20 ms)

MP5-3031-6

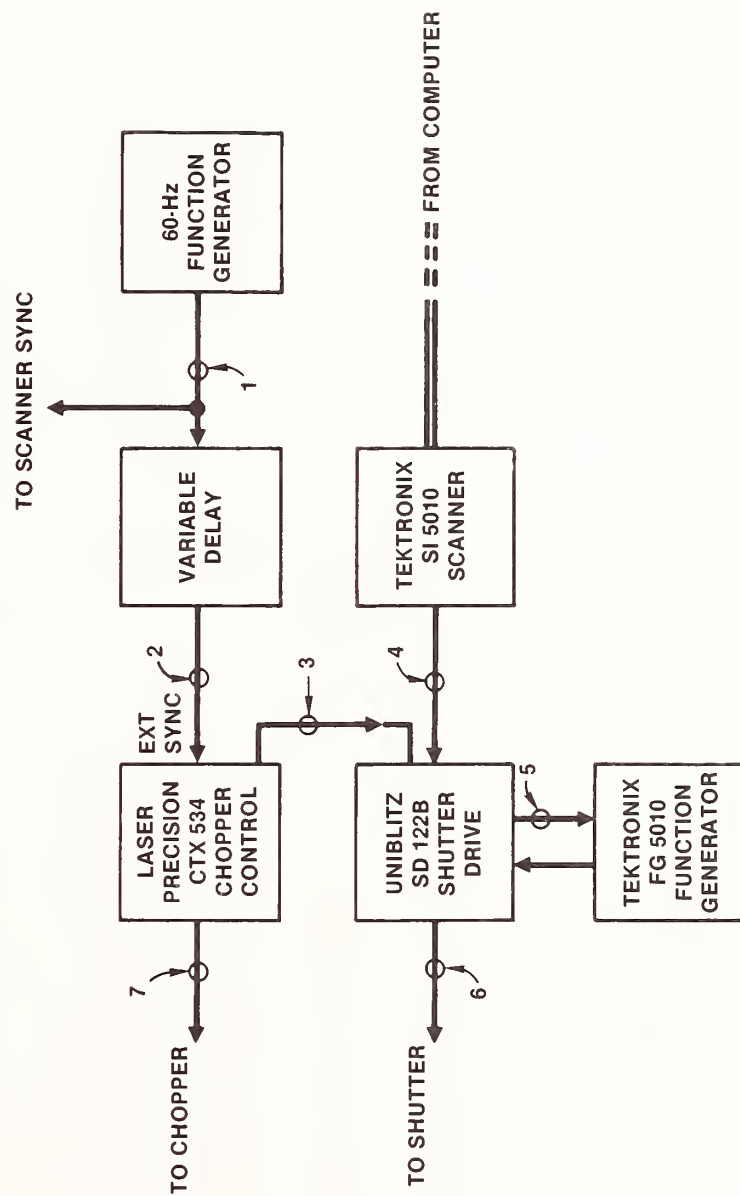


Figure 9 Timing Electronics for Scanning Laser Pulse

MP5-3031-7

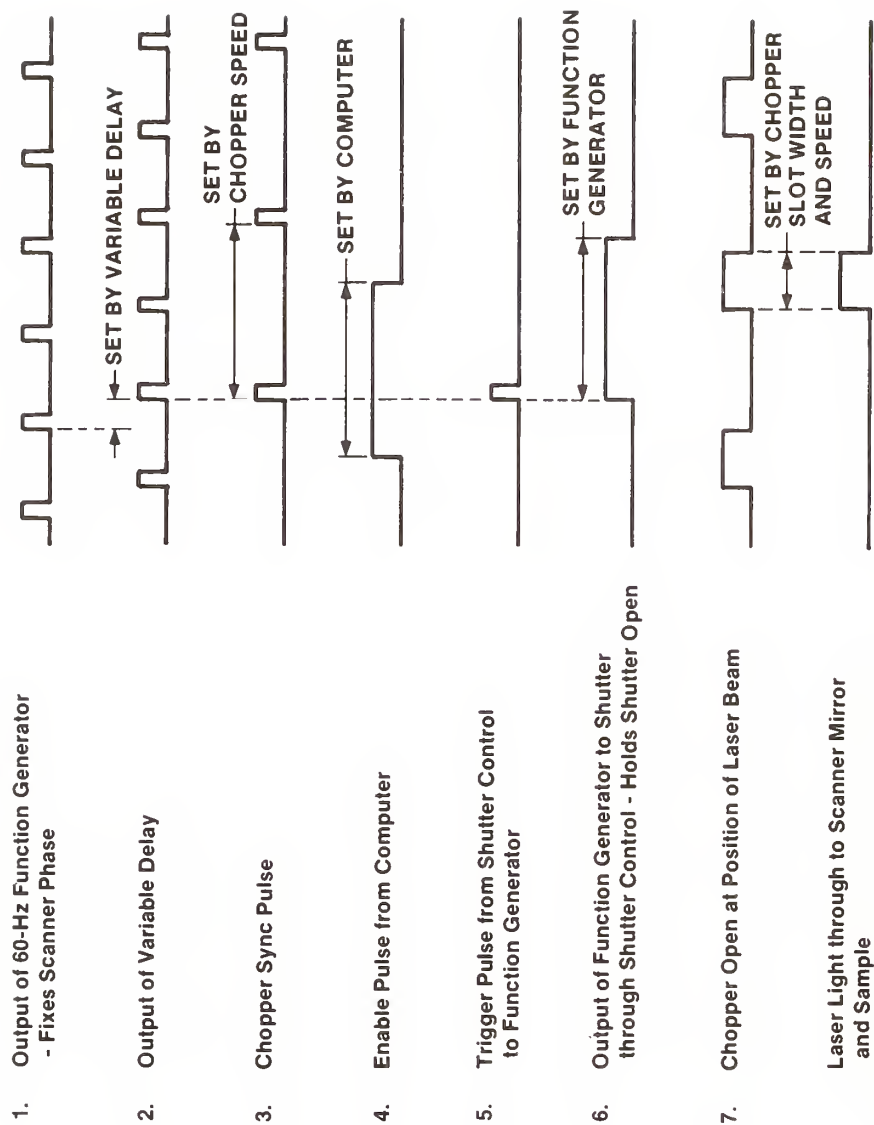


Figure 10 Timing sequence for scanning laser pulse

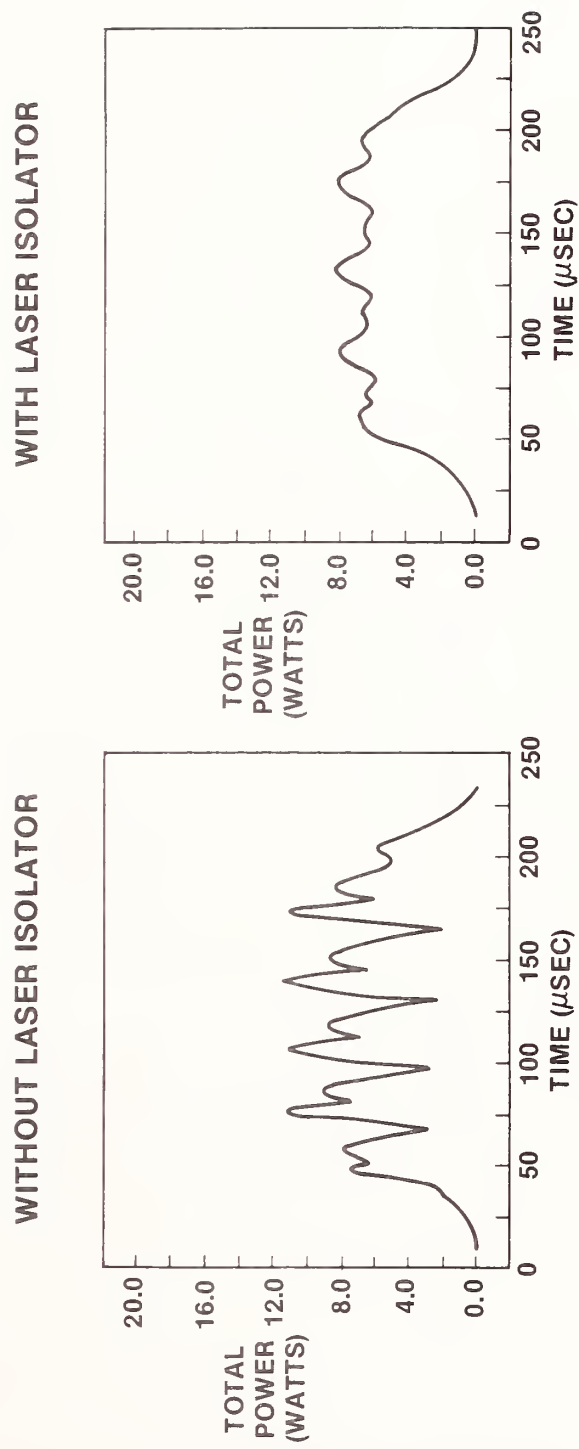


Figure 11 Effect of laser isolator

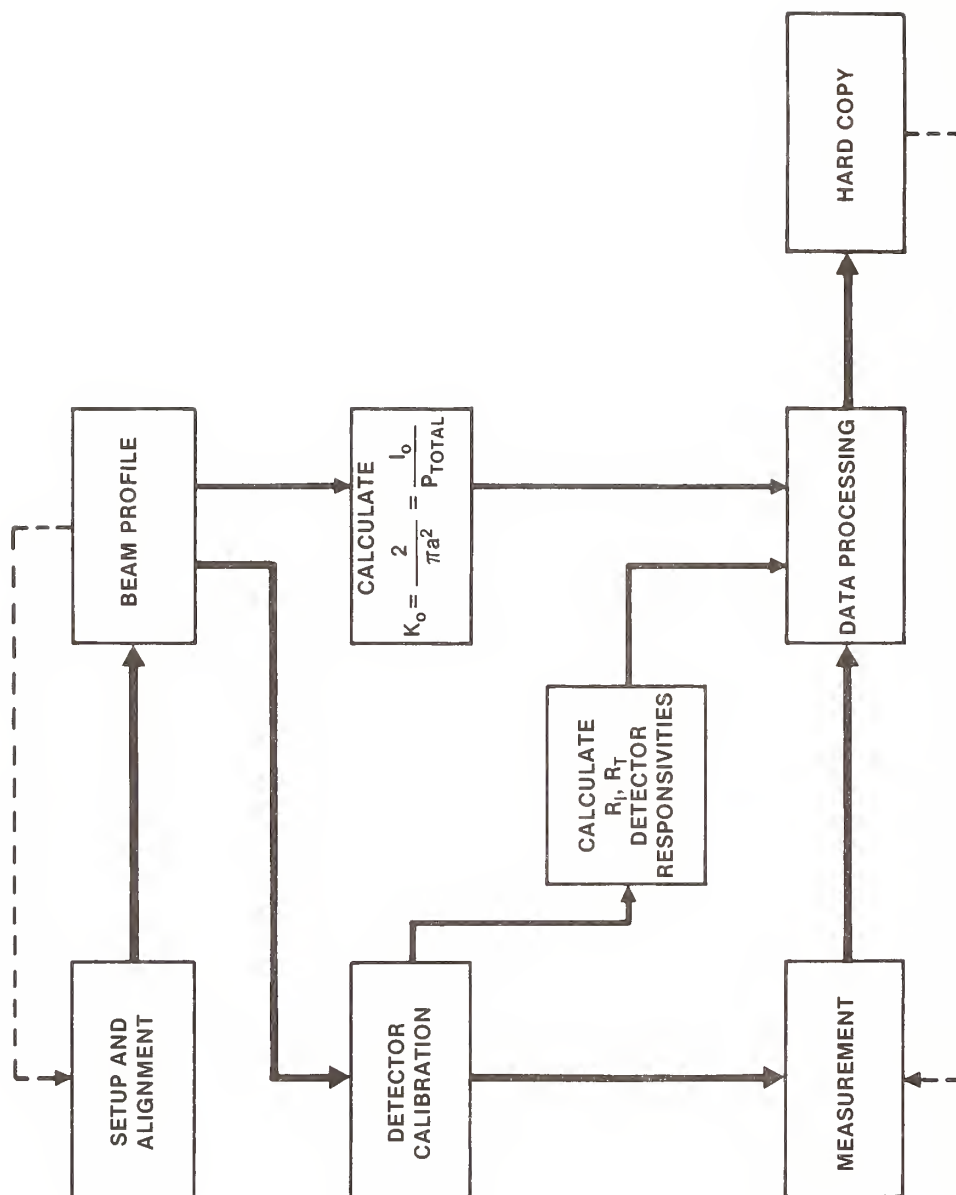
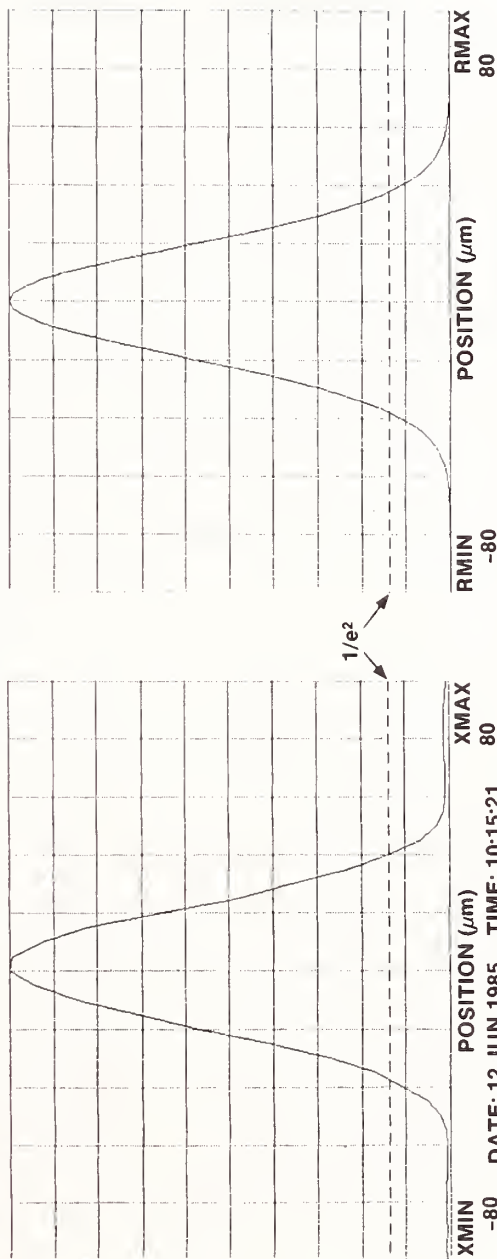


Figure 12 Experimental Sequence

MP5-3031-10

GAUSSIAN BEAM CALCULATIONS—
 GAUSSIAN PROFILE—
 THE HALF WIDTH OF BEAM AT THE $1/e^2$ INTENSITY POINT (MICRONS) = 30.5
 MAX NORMALIZED IRRADIANCE = 68435.3423668 W/cm² PER INCIDENT WATT.
 DATE: 12 JUN 1985 TIME: 10:16:09



PINHOLE STEPPED ACROSS BEAM

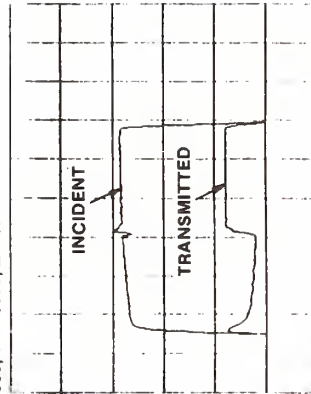
GAUSSIAN FIT TO SAME $1/e^2$ RADIUS
 $a = 30.5 \mu\text{m}$

K_0 MAX NORMALIZED IRRADIANCE

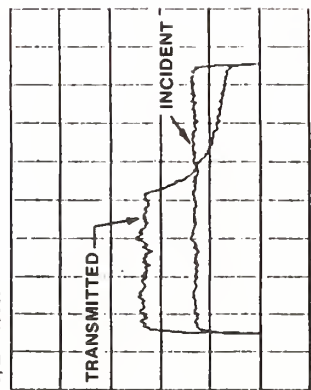
$$K_0 = \frac{2}{\pi a^2} = \frac{I_0}{P_{\text{TOTAL}}} \frac{W/\text{cm}^2}{W(\text{INCIDENT})}$$

Figure 13 Beam profile

DATE: 7 JUN 1985 TIME: 13:56:01
 INC RESP: 1.442E+00 TRANS RESP: 4.026E-01 IRRAD(W/cm² PER W): 5.846E+04
 INCIDENT GAIN: 2 TRANSMITTED GAIN: 1
 POWER 2.462E-00 W/DIV. IRRAD: 1.440+05 W/cm²/DIV
 COMMENT: X = -2000, Y = -8000, Z = 0;



DATE: 13 FEB 1985 TIME: 17:38:50
 INC RESP: 5.260E+02 TRANS RESP: 8.000E+01 IRRAD(W/cm² PER W): 2.550E+02
 INCIDENT GAIN: 0.1 TRANSMITTED GAIN: 0.4
 POWER 7.605E-02 W/DIV. IRRAD: 1.939+01 W/cm²/DIV
 COMMENT: X = 0, Y = 0, Z = 4600;



(a)

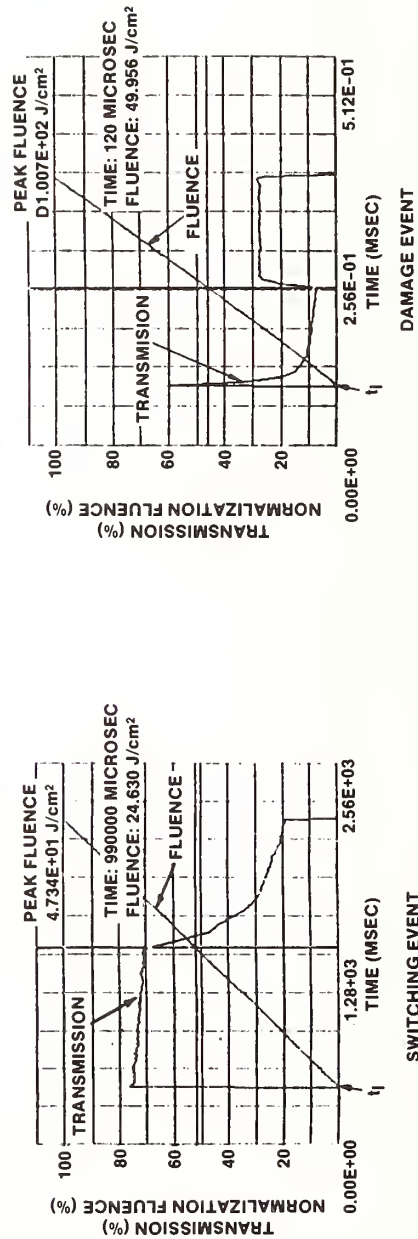


Figure 14 Typical switching and damage events for two different samples/Upper traces show $V_I(t)$ and $V_T(t)$; lower, $T(t)$ and $F(t)$.

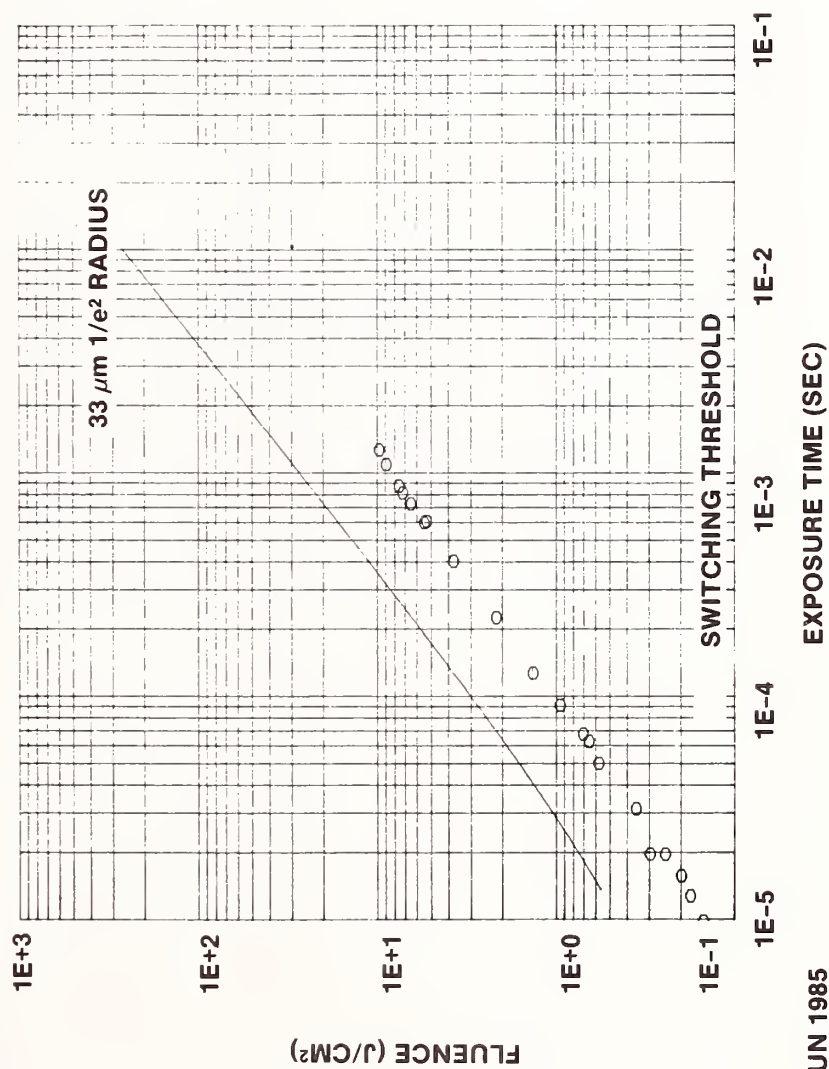


Figure 15 Sample switching curve and data



Figure 16 Sample damage curve and data

- Manuscript Not Received -
=====

DAMAGE TESTING IN OPTICS PRODUCTION AND PROCUREMENT

S. C. Seitel and E. A. Teppo
Montana Laser Optics, Inc.
Bozeman, MT 59715

ABSTRACT

Laser-induced damage studies reported at these symposia have emphasized basic understanding of the light-matter interaction physics, and development of new, more durable materials and coatings. This paper reports a parallel trend toward routine use of damage testing in the procurement and production of reliable optics for low energy, high peak power military and commercial laser systems. Materials and coating designs are conventional, and in practice, in-service failures are as often due to system design effects and contamination as to improper finishing or coating design errors.

The emerging roles of damage testing as a production process-control tool, in acceptance testing, and in failure diagnostics, are discussed and illustrated with specific examples and color photomicrographs. Particular attention is paid to the problems of (1) meeting widely varying test requirements, often on deliverable part of complex geometry, in timely and cost-effective fashion; and (2) relating calibrated single-mode damage test results to optics durability in highly multimode military systems. A brief review of a new repetitively pulsed dual-wavelength damage test station with exceptional configurational flexibility and advanced digital fluence profiling features is included.

Key Words: computer control; laser damage; laser beam diagnostics;
laser fluence measurement.

- Manuscript Not Received -
=====

A COMPUTER AUTOMATED LASER DAMAGE LABORATORY

M. R. Sweet, L. J. Jolin, S. R. Foltyn
Los Alamos National Laboratory
Chemistry Division
Los Alamos, New Mexico 87545

ABSTRACT

The UV Laser Damage Program has been in existence at Los Alamos for over five years. Recently, the damage laboratories have been upgraded by using a computer system to control and monitor testing parameters, and to display and store the damage data.

The system was designed around already existing testing equipment merged with an IBM-XT for cost effectiveness. The damage fluence is set by a programmable beam attenuator configured in a closed-loop control system with the computer and an energy meter. A matrix of damage sites is set up at the test plane such that the operator can move the sample sequentially between sites or pick sites at random. To aid the operator in choosing test fluence values, a damage plot may be generated on the monitor or on a high resolution plotter.

By automating the Laser Damage Laboratory with a computer, consistent results can be achieved over a short testing time.

Key Words: computer-control; laser damage; laser diagnostics ultraviolet;

U.V. Laser Beam Diagnostics using a Computer
Controlled Video Frame Store System

S.E. Clark, I. Laidler and D.C. Emmony
Department of Physics, University of Technology
Loughborough, Leics., England

and

B.A. Omar and M.J. Shaw
Rutherford Appleton Laboratory
Chilton, Didcot, Oxon, England

In the past the spatial intensity profile of a laser beam has been measured using such techniques as scanning pinholes, detector arrays and photography.

This new system converts the Excimer beam into visible light using a glass fluorescer with a very small penetration depth giving a good 2D image of the beam. The fluorescence has been found to be linear over a wide range of input energy and is imaged by a CCD camera linked to the computer controlled video frame store.

The digitised information is then computer processed to yield such results as the intensity profile along an arbitrary line, peak fluence, the difference between two images and various statistical values.

This new technique has been applied to beams with widely varying diameters including analysis in the focal region and in the early detection of damage in materials.

Keywords:- Video frame store; computer controlled; 2D image; linearity; calibrated.

1. Introduction

The problem of beam profiling is as old as the laser itself. Previous techniques have included direct photography, scanning pinholes and detector arrays, all of which suffer from significant problems.

Photography has the two main problems of chemical (wet) processing and image linearity. It is not a trivial task to obtain a truly linear intensity representation of an object on film. If the image is not linear calibration becomes not only far more tedious but subject to greater error. Even with a linear image it is a time consuming problem to obtain the data from the film by such instruments as micro-densitometers. The slightly redeeming feature is that a 2D image is recorded at one go.

The main problem with a pinhole is that it provides information about a point, thus a time consuming rastering process must be used to obtain a 2D profile. In order to allow for shot to shot variation an average of several shots must be taken at each point.

Detector arrays are a logical step forward but have often suffered from poor spatial resolution and require complex driver electronics.

Using a video camera allows a 2D linear image to be obtained in one shot with good spatial resolution due to the high packing of detectors on the camera chip. Typically without external optics resolution of around 25 μ m and with external optics of 1 μ m is routinely obtainable.

2. The System

Figure 1 shows how the various components of the system are inter-connected and figure 2 a practical arrangement for imaging the beam.

Since the camera does not respond to light with a wavelength below 400nm a fluorecser is used to convert the U.V. (usually KrF at 249nm) to visible fluorescence which the camera can then image.

A boro-silicate glass is used as the fluorecser. To avoid problems of image distortion the glass in the form of a thin slab (less than 150 μ m thick) with a U.V. penetration depth of less than 1 μ m. The response of the glass to incident radiation was measured and found to be linear over a range of fluences from 10 μ J/cm² to above 10mJ/cm². The normal operating fluence is in the 2mJ/cm² range so as to use the full dynamic range of the frame store.

The camera used was a commercially available solid state device which was checked for linearity of response and for the effects of automatic gain control. The device was found to have essentially no automatic gain control and to be linear over a dynamic range of approximately 100 at the operating fluences.

The fluorescence is imaged by the camera and the video output goes both to the frame store and a specially developed trigger box.

The trigger box is required to ensure that the image is always captured by the system for without it between 10 - 90% of the shots, depending upon the type of camera being used, would not be recorded. The box works by synchronizing the triggering of the frame store and the firing of the laser to the video frame (field) sync pulses produced by the camera so that the laser is fired at the correct point in the frame that the store is set to capture.

The frame store is a commercially available unit, the Eltime Image III with slight hardware modifications so that both the controlling computer and an output from the trigger box can initiate a frame snatch.

The store is set up to hold two pictures each 256 x 512 pixels simultaneously in memory each with 64 levels of intensity resolution (greylevels). The incoming data is digitised and stored in the frame store memory in a grid format so that any point in the picture can be addressed using cartesian type co-ordinate addressing.

An Apple IIe computer is used to control the system and it is this which makes the system particularly powerful and versatile.

A suite of programs was written to perform the following tasks.

- a) Aquisition, storage and display of data.
- b) Image processing.
- c) Intensity profiling in X, Y and θ directions.
- d) Radially averaged profiling.
- e) Numerical integration.
- f) Statistical analysis.

By using options e and f it is possible to calibrate an image in absolute units and so obtain the fluence (J/cm²) at any point in the image. Option f will also give such parameters as average fluence, fluence per intensity level recorded and standard deviation of fluence.

The profiling program allows the user to select the location of the profile and whether it is a line profile or a radial profile and produces graphs of recorded intensity versus position along the profile.

The image processing routines include removal of background (dark level) noise, image enhancement and a routine to display the difference (in intensity levels) between two frames. There are also routines to store an image on disc for future reference and processing.

3. Experimental Considerations

The main drawback of the system is the limited dynamic range of the frame store and care must be used to ensure that the fluence incident on the fluorescer is sufficient to fully use the available dynamic range. The 64 levels are more than enough to determine the $1/e^2$ points which are down by a factor of 7.4 on the maximum.

The arrangement of the fluorescer and camera in figure 2 is not practically the most convenient as it is impossible to both profile and damage at the same time since the fluorescer is sitting where the damage sample should be. A more convenient set-up would be to insert a beam splitter between the lens and target plane and profile the beam away from the damage plane. However care is needed, since the beam is a converging one unless the beam splitter is very thin it will introduce significant distortion in the transmitted beam.

For calibration the following data is required.

1. Beam energy per shot as measured for example by a calorimeter and
2. the relation between pixel size on screen and real object size. This can be measured by observing calibrated gratings at the place where the fluorescer is to be placed.

4. Applications and Uses

The main application of the system is in profiling the beam from the Excimer laser here at Loughborough University of Technology which is operated at wavelengths between 193 and 308nm. By suitable fluorescers the system can work in the infra red, e.g. graphite for $10.6\mu\text{m}$ CO_2 radiation. Between 450 and 1060nm (Nd:YAG) no fluorescer is needed as the camera will respond directly.

The system has also been used in conjunction with other techniques to look at the early detection of laser damage where it enables an actual image of an area to be recorded rather than giving a spatially averaged result as a photodiode would do.

5. Results

Figures 3 to 11 represent typical data from the system. Figures 3 to 5 are from a 5mW He-Ne laser operating at 633nm. Figures 6 to 11 are for a nominal 1J 30ns KrF excimer laser.

Figures 10 and 11 show how use of the statistical analysis package can enable the system to be calibrated yielding several important parameters.

Comparisons between profiles taken from this system and those by using a scanning pinhole are in near perfect agreement.

6. Summary

The system can provide a two-dimensional beam profile much faster than previous methods and can process the data to yield much more information about the profile than with current methods. In short this is a highly versatile system capable of providing high quality 2D beam profiles with associated data in near real time.

S.E. Clark and I. Laidler would like to acknowledge the financial support given by the United Kingdom Science and Engineering Research Council.

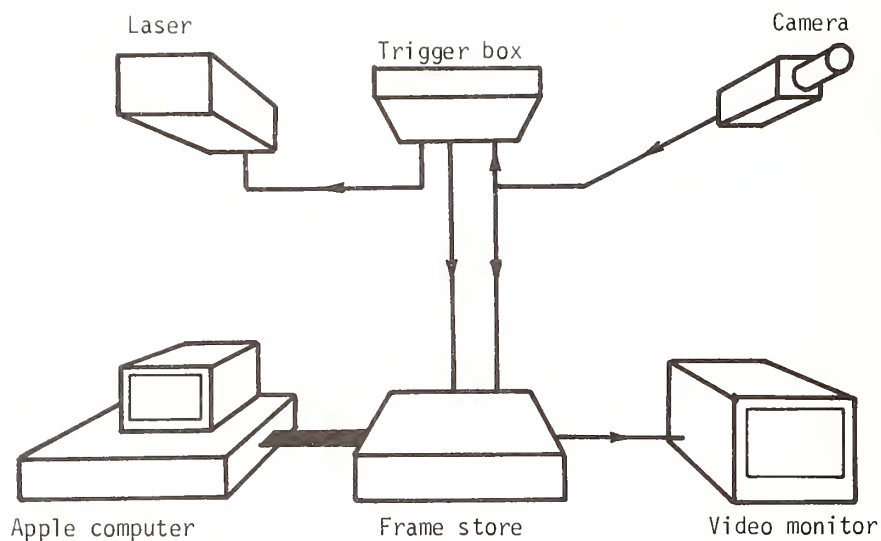


Figure 1.

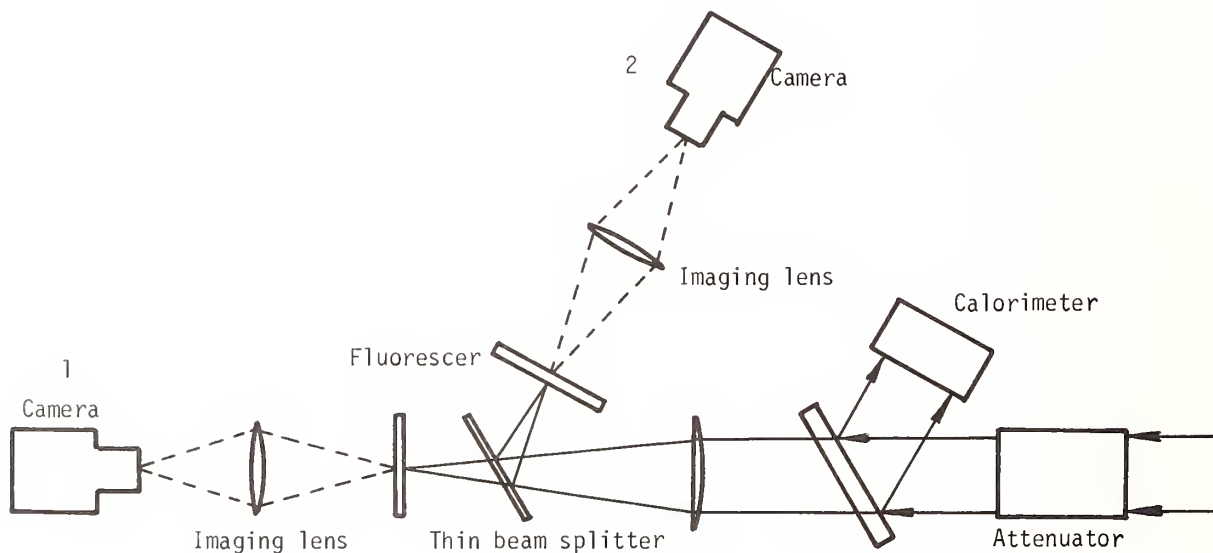


Figure 2.

With camera and lens in position 1 the thin beamsplitter is not required. This avoids the problems of distortion associated with the beam splitter but means that both damage and profiling cannot be done together. In position 2, both damage and profiling can be done together but as the thin beam splitter has to be used there are problems of distortion on the transmitted beam.

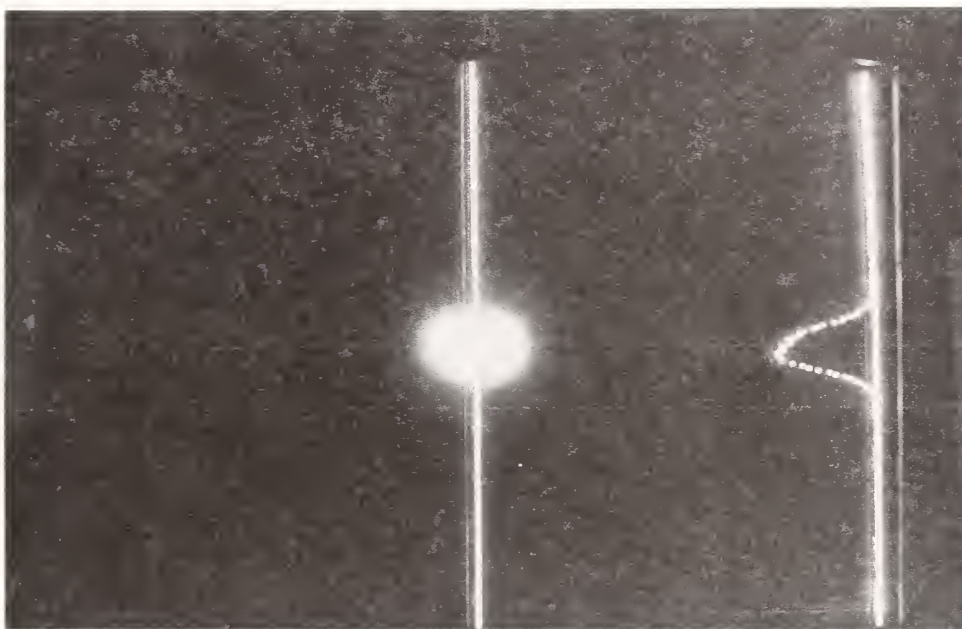


Figure 3. He-Ne Laser
Vertical profile

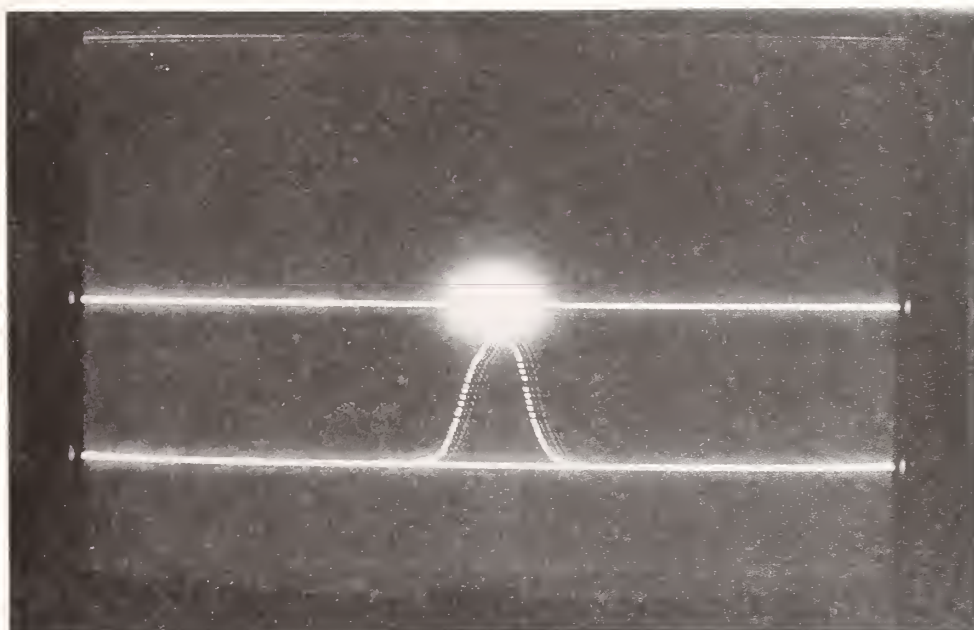


Figure 4. He-Ne Laser
Horizontal profile

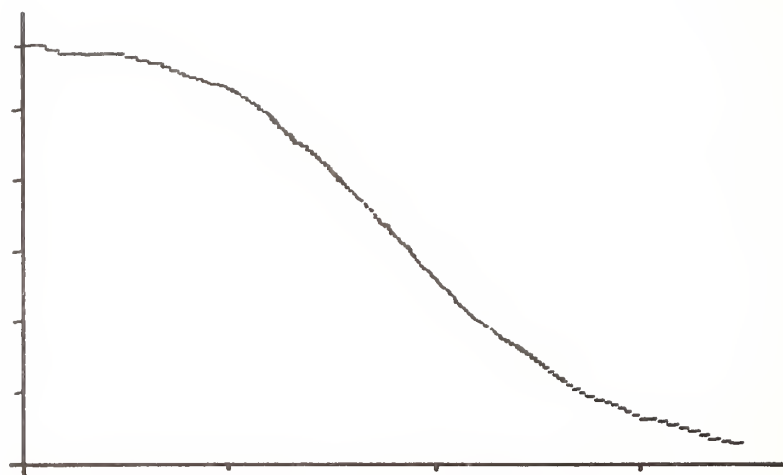


Figure 5.
He-Ne laser 633nm radially averaged profile from beam
centroid

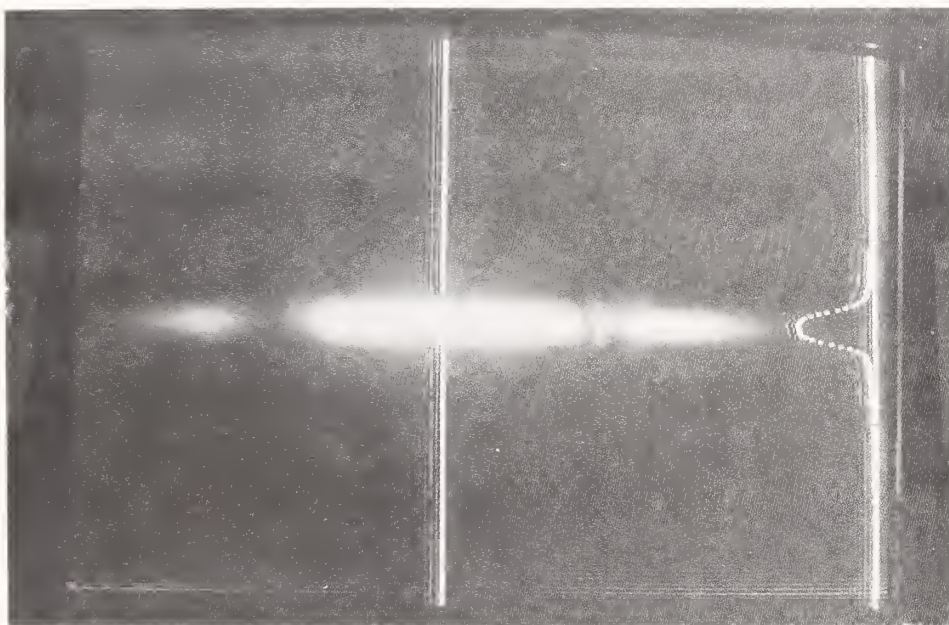


Figure 6. Excimer Laser 249nm
Vertical profile

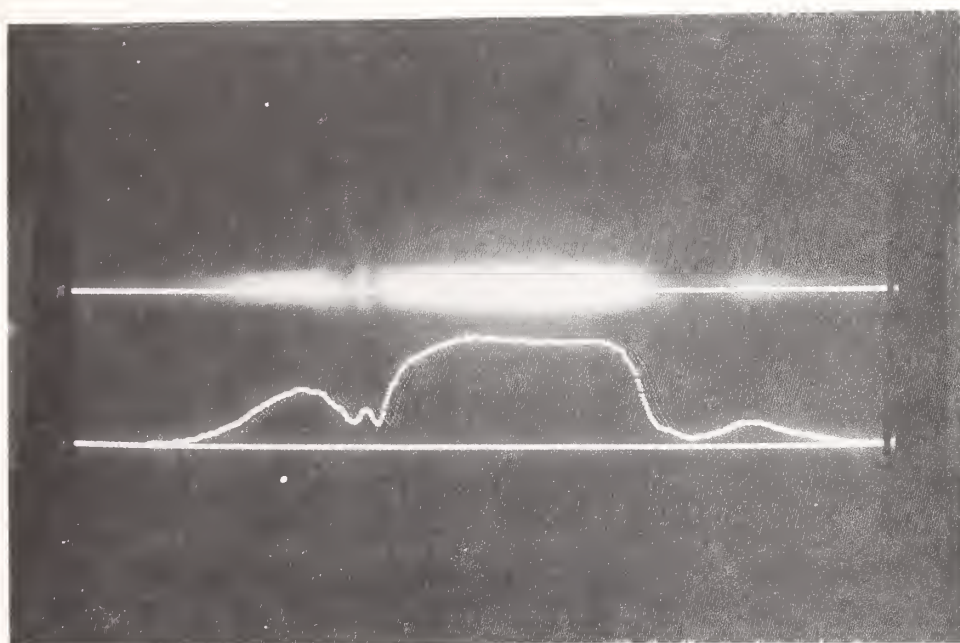


Figure 7. Excimer Laser
Horizontal profile

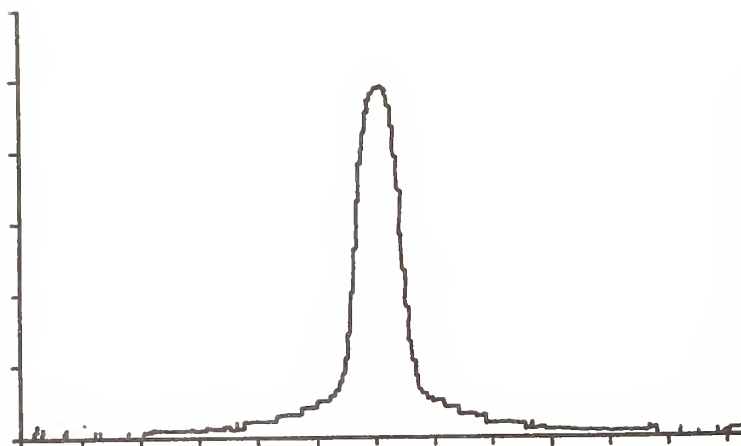


Figure 8.
KrF laser 249nm vertical profile

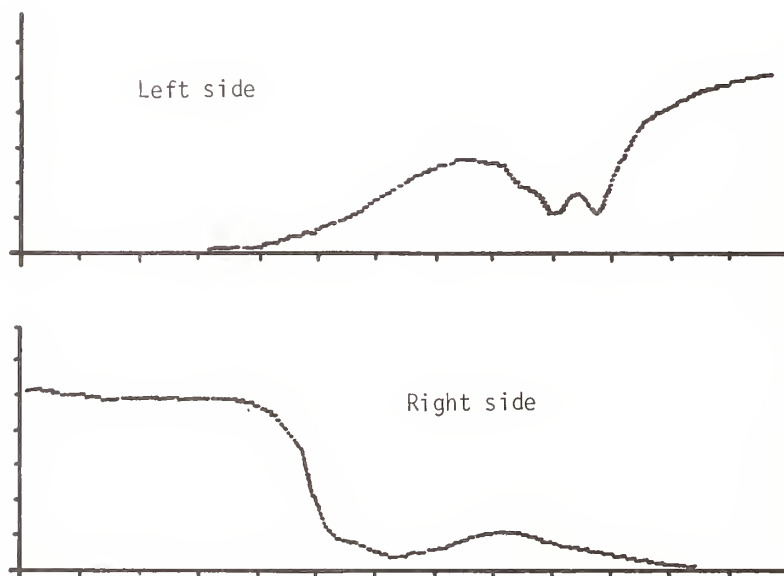


Figure 9.
KrF laser 249nm horizontal profile



Figure 10.
KrF laser 249nm unprocessed histogram

Starting level = 0

Excimer profile
Sampling started at level = 5
Background level subtracted off = 5
Fluence per greylevel = 1.60860 J/sq.cm
Average fluence = 2.13154E1 J/sq.cm
Standard deviation of fluence = 2.40314E1 J/sq.cm
Highest fluence = 8.36470E1 J/sq.cm
Most frequent fluence = 8.04298 J/sq.cm

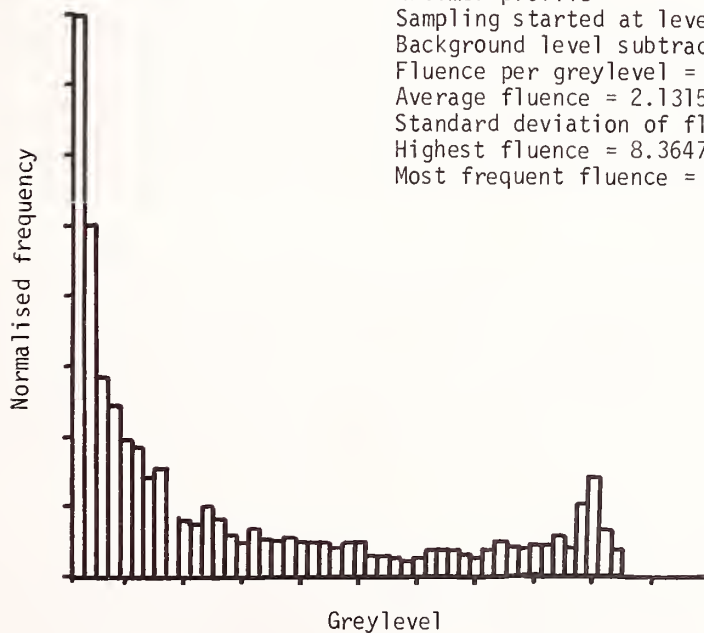


Figure 11.
KrF laser 249nm
Processed histogram: background levels removed

Beam Profiling Characteristics
of a Sensitivity-Enhanced Silicon Vidicon System
at 1.06 Microns

R. M. O'Connell* and R. A. Vogel*
Electrical and Computer Engineering Department
University of Missouri
Columbia, MO 65211

A. F. Stewart and D. A. Smith
Air Force Weapons Laboratory
Kirtland AFB, NM 87117

A beam profiling system consisting of a silicon vidicon detector and an image processing computer is described, and results of measurements to characterize the system are presented. For the transmission and display of geometrically accurate images, a unique relationship was found to exist between pixel clock frequency, channel time and channel length. The vidicon target's dark current and 1.06 μm detection sensitivity were found to have peak-to-peak variations of 5.6% and 3.75%, respectively, throughout the target's central 3.75 x 3.13 mm region. Signal-to-noise levels were optimum at a target temperature near 0° C. Without being optimized, cathode voltage switching improved the pulsed-mode dynamic range of the system to approximately 4.

Key Words: beam profiling; dark current; detector target uniformity; dynamic range; transient response.

1. Introduction

Two-dimensional electronic imaging devices are a potentially powerful beam profiling tool for laser damage experiments. For beams that are neither too tightly focused (diameters less than approximately 1 mm) nor too rapidly pulsed (pulse repetition period less than approximately 30 seconds) these devices can provide real-time profile information on a pulse-to-pulse basis[1]. Since no averaging is required, it is unnecessary to make the often questionable assumption that the laser is absolutely stable from pulse-to-pulse. Such a requirement is necessary when masking methods such as the knife-edge are used to profile a beam[2]. With these advantages in mind, a beam-profiling system, which combines various two-dimensional imaging devices with an image processing computer, has been developed and incorporated into a laser damage facility at the Air Force Weapons Laboratory (AFWL).

In this paper, the results of a study to characterize the use of a silicon vidicon detector in the AFWL beam-profiling system are presented. After a brief description of the entire system in section 2, a discussion of those system parameters that control the reproduction of vidicon images on the computer display monitor follows in section 3. Results of measurements made at various temperatures to characterize the system's ability to profile fast (10 nsec) 1.06 micron pulses are then presented and discussed in sections 4 and 5. Included are measurements of the spatial variations of vidicon dark current and detection sensitivity in Section 4 and system linearity and dynamic range in section 5.

2. Silicon Vidicon Beam Profiling System

The AFWL beam profiling system is shown schematically in figure 1. The PAR 1252E silicon vidicon [3] was chosen for the study because its target offers several attractive features: it is thicker to provide for enhanced sensitivity at 1.06 μm ; it is wedged to suppress Moire' interference; and its area (12.5 mm x 12.5 mm) is large enough to permit profiling of a wide range of laser beam sizes.

The PAR 1216 vidicon controller shown in figure 1 performs several functions. First of all, it is the interface for operator control of vidicon scanning conditions, including channel length in pixels, channel time, and the number of channels per frame. Thus, the vidicon reads images in an

operator-determined non-standard video format. The "video" output of this system is approximately a voltage-inverted RS 170 format with non-standard timing.

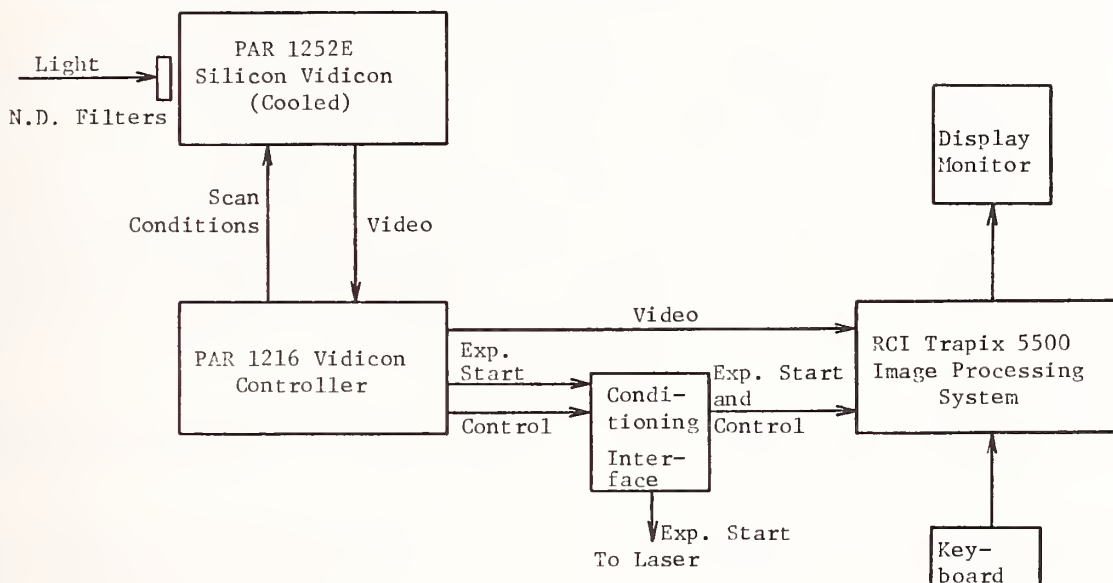


Figure 1. Silicon vidicon beam profiling system.

The second function of the vidicon controller is to transmit images from the vidicon to the Trapix computer [4]. For the computer to properly accept a non-standard video image, the image must be transmitted via a set of control signals which serve as a pixel clock and channel and frame synchronization flags. These signals are provided by the controller in the form of its 4.0 MHz master clock, its clock-out signal, and its trigger-1 signal, respectively. In considering various clock sources, it was found that unless the 4.0 MHz master clock from the controller was used, an interference signal was always present in the displayed image. Use of the 4.0 MHz master clock eliminated the interference signal, evidently because the clock-out and trigger-1 signals are derived from, and thereby phase-locked to it. The three control signals, illustrated in figure 2, must reach the computer in TTL-compatible, differential form. Thus they are first processed at the signal conditioning interface shown symbolically in figure 1 and detailed in figure 2.

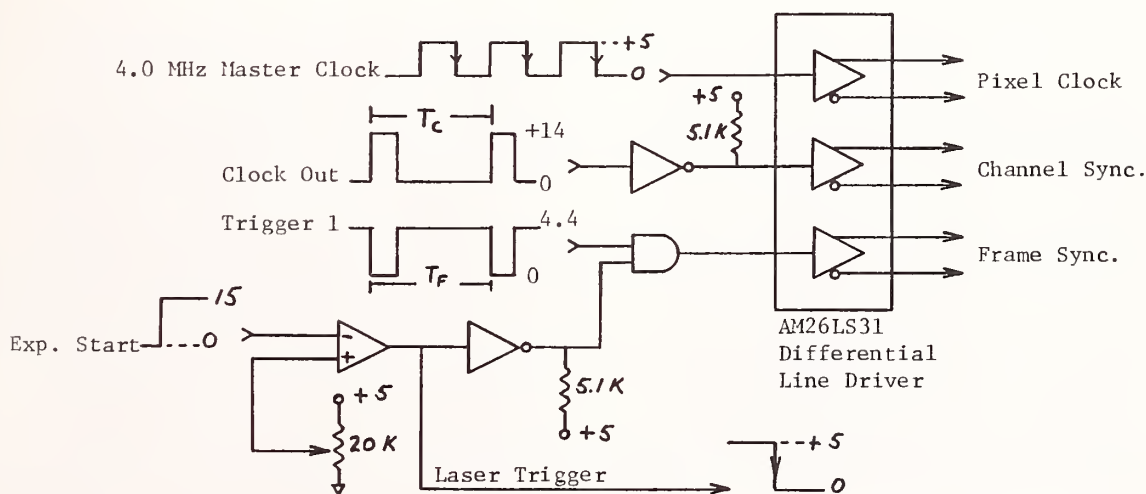


Figure 2. Control and timing signal conditioning interface: signals and conditioning circuitry. T_C = channel time, T_F = frame time.

The vidicon controller also provides a timing signal for frame synchronization, allowing measurements with single laser pulses. When the system is used to characterize a pulsed laser, the vidicon target is allowed to pre-equilibrate for 15 preparatory (prep) frames at the programmed scanning conditions. The laser is then fired at the start of the next frame, which is transmitted to the Trapix computer. Since the computer is programmed to capture and store the first frame transmitted to it, image transmission from the controller to the computer must be delayed until the laser is fired. This is accomplished with the controller-generated experiment-start signal, which automatically turns on at the completion of the prep frames. As shown in figure 2, after some compatibility conditioning, the experiment-start signal simultaneously fires the laser and enables the frame synchronization control signal (trigger-1). Since all three control signals must be present for data transmission, a single laser pulse image is thus captured by the image processor.

The RCI Trapix 5500 image processing system shown in figure 1 completes the AFWL beam profiling system. It is used to digitize, store, and display the non-standard video image from the vidicon, and to perform image analysis and/or processing operations such as pixel grey level averaging, contrast inversion, production of grey level histograms, and image profiling.

3. Transmission and Display of Geometrically Undistorted Images.

Since all image analysis and processing is performed on the image stored in the Trapix computer memory and displayed on the display monitor, it is essential that this image be as true a reproduction of the vidicon image as possible. During the course of the study it was found that this would be ensured if three conditions were satisfied.

First, it was essential to adjust the display monitor for square pixels. The Trapix software program "ROZ" allows the operator to magnify the display up to eight times, enabling the physical measurement of the dimensions of a 40 x 40 pixel region. Adjustments were made via the display monitor pixel-width potentiometer.

Next, the controller must be programmed for symmetric image sampling, so that channels and pixels on the display monitor correspond to channels and pixels on the vidicon target. The correspondence of channels is assured by the channel synchronization control signal, but pixel correspondence requires more care. Since one pixel of vidicon information is transmitted per period of the pixel clock, it was observed that pixel correspondence is assured if the programmed channel length in pixels N_C is equal to the transmitted number of pixels per channel N_T , which in turn is set by the programmed channel time T_C according to

$$(1) \quad N_T = (T_C - 10 \text{ } \mu\text{sec}) f_{cl}.$$

The 10 μsec in equation (1) represents the non-scanning retrace time during each channel, and f_{cl} is the pixel clock period, which was kept at 4.0 MHz throughout the study. Setting $N_T = N_C$ in equation (1) gives

$$(2) \quad N_C = (T_C - 10 \text{ } \mu\text{sec}) f_{cl},$$

which is the condition that the programmable quantities N_C and T_C must satisfy for symmetric image sampling.

The third condition to be satisfied for the optimum reproduction of a vidicon image on the display monitor is that the vidicon channel deflection voltage must be set for symmetric image transmission. If necessary, adjustment can be accomplished by first satisfying the previous two conditions, and then by displaying the image of a circular or square object and adjusting the vidicon channel deflection voltage for a circular or square image. The Trapix software program "CUR" can be used to surround the image with a rectangular cursor and count the number of pixels in the x and y directions. When the two numbers are equal, adjustment is complete.

If the display monitor pixel-width potentiometer and the vidicon channel deflection voltage are properly set, any (T_C, N_C) pair that satisfies equation (2) will result in the transmission and display of a geometrically undistorted image. The PAR 1216 vidicon controller provides a choice of seven channel times. They are listed in table 1 along with the corresponding programmed channel lengths that satisfy equation (2). The vidicon has a maximum of 512 pixels per channel; thus, the 140 μsec channel time, which requires 520 pixels per channel (see table 1), can not be used for symmetric sampling. All the other channel times can be used.

Table 1. Channel time/channel length pairs that result in symmetric image sampling

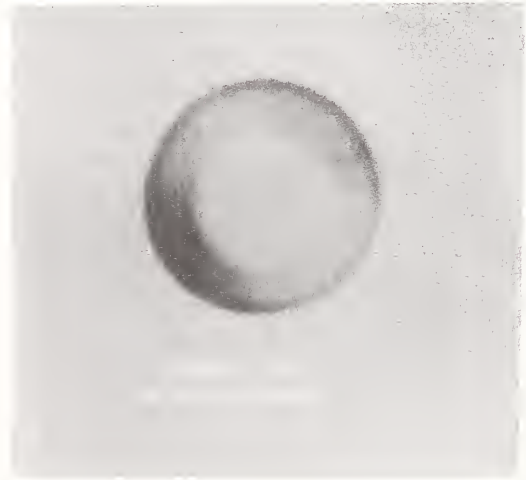
T_C (μsec)	20	40	60	80	100	120	140
N_C (pixels)	40	120	200	280	360	440	520

The photos in figure 3, which show the circular image of a laser diode transmitted through an optical fiber onto the vidicon target, illustrate the effects of various choices of T_C and N_C on sampled image symmetry. The circular geometry of the object was verified by rotating it 90° (at any T_C, N_C pair) and observing no change in image dimensions. Note that in each photo the Y/X ratio of image dimensions is equal to the ratio N_C/N_T , as expected. Also, the X dimension of the uniform background of each image is proportional to N_C . This is as expected, also, because the x and y axes of the vidicon are transposed on the Trapix display monitor.

A) Symmetric sampling: $T_C = 80 \mu\text{sec}$,
 $N_C = N_T = 280$ pixels.



B) Symmetric Sampling: $T_C = 100 \mu\text{sec}$,
 $N_C = N_T = 360$ pixels.



C) Undersampling: $T_C = 100 \mu\text{sec}$,
(so $N_T = 360$ pixels), $N_C = 512$ pixels.



D) Oversampling: $T_C = 100 \mu\text{sec}$,
(so $N_T = 360$ pixels), $N_C = 254$ pixels.



Figure 3. Effects of controller programming on image symmetry.

4.1 Dark Current and 1.06 μm Detection Sensitivity Measurements

4.1 Spatial Uniformity

To be useful in two-dimensional beam profiling, the vidicon target's dark current and detection sensitivity at the wavelength of interest should be reasonably uniform throughout the region of interaction with the beam. To measure these quantities, the vidicon was programmed for a 100 μsec channel time and a 512 pixel channel length. While this (T_c, N_c) pair does not satisfy the symmetric sampling criterion of equation (2), it is preferred in this measurement because it allows a uniform survey of the entire target rather than the lower 70%, which would result if N_c were programmed for symmetric sampling, i.e., 360 pixels. Approximately uniform illumination of the target at 1.06 μm was provided by illuminating it with a fiber-optic illuminator through a frosted glass window and a 1.06 μm band-pass filter. Since measurements were to be made with a fixed illumination of the target at three different temperatures (24° C, 0° C, and -30° C), it was necessary to ascertain that the chosen illumination level did not cause target saturation at any of the three temperatures. At each temperature, single frames of the illuminated and unilluminated target were stored in Trapix memory. The unilluminated frames provided dark current information.

To analyze the data, the mean gray level (ranging from 0 to 83) was calculated in each of 63 equally spaced 27 x 27 pixel cells throughout each frame. The dark current value was then subtracted from the corresponding illuminated value at each of the 63 cells to give background-corrected signal levels. This procedure resulted in a pair of maps such as those shown in figure 4 for the case of a target temperature of 0° C. Note that the target response is maximum in the center, which illustrates the greater efficiency of the reading electron beam in that portion of the target.

Dark current	14.3	14.9	15.3	15.0	15.1	14.6	15.0
	14.5	15.1	15.5	15.2	15.3	14.8	15.2
	14.5	15.1	15.4	15.1	15.3	14.7	15.2
	14.6	15.3	15.6	15.3	15.4	14.9	15.3
	15.0	15.6	16.0	15.7	15.9	15.4	15.7
	14.7	15.3	15.7	15.4	15.7	15.2	15.5
	15.4	16.0	16.2	15.9	16.2	15.8	16.0
	15.0	15.4	15.6	15.4	15.6	15.2	15.6
	14.6	15.7	15.7	15.4	15.7	15.4	15.7
Background-subtracted signal	27.6	35.1	37.0	37.4	37.0	35.9	34.5
	27.2	34.9	36.8	37.0	36.7	35.7	34.2
	27.3	34.9	36.9	37.2	36.7	35.8	34.3
	27.3	34.7	36.7	37.1	36.7	35.6	34.1
	27.1	34.6	36.7	37.0	36.2	35.6	34.0
	26.8	34.6	35.9	36.5	36.5	35.2	33.2
	25.9	33.0	34.4	35.1	34.5	33.0	30.2
	26.3	32.8	34.5	34.8	33.7	31.3	29.0
	25.7	32.3	32.9	32.1	30.3	29.0	28.3

Figure 4. Mappings of vidicon target dark current and background - corrected signal in trapix grey levels (0-83) at $T=0^\circ\text{C}$. The bracketed 3 x 4 cell region corresponds approximately to the central 3.75 x 3.13 mm region of the target.

Table 2 contains summaries of the peak-to-peak variation of the data in figure 4 for both the entire target and the bracketed 3 x 4 cell region shown in figure 4. This region corresponds to a 3.75 x 3.13 mm region near the center of the target.

Table 2. Peak-to-peak variation of target response at T = 0° C

	Dark Current	Background-Subtracted Signal
Whole Target	11.7%	31.3%
Central 3.75 x 3.13 mm	5.6%	3.75%

The numbers in table 2 suggest that while the whole-target variations are rather excessive, those in the central 3.75 x 3.13 mm region, an area large enough to profile many typical laser beams, are quite acceptable. Results similar to these were obtained at the other two measurement temperatures.

4.2 Temperature Dependence

The temperature dependence of target sensitivity was studied using data from figure 4 and the corresponding mappings (not shown) for T = 24° C and -30° C. In each case, dark current and corrected-signal values from three adjacent 27 x 27 pixel cells near the center of the target were averaged and plotted as shown in figure 5. The results show that while the target's signal response decreases quite linearly with cooling over the entire 3-temperature range, the dark current improves very little below 0° C. The widest gap between the two curves is in the vicinity of 0° C, which indicates that the signal-to-noise ratio is optimum at that temperature.

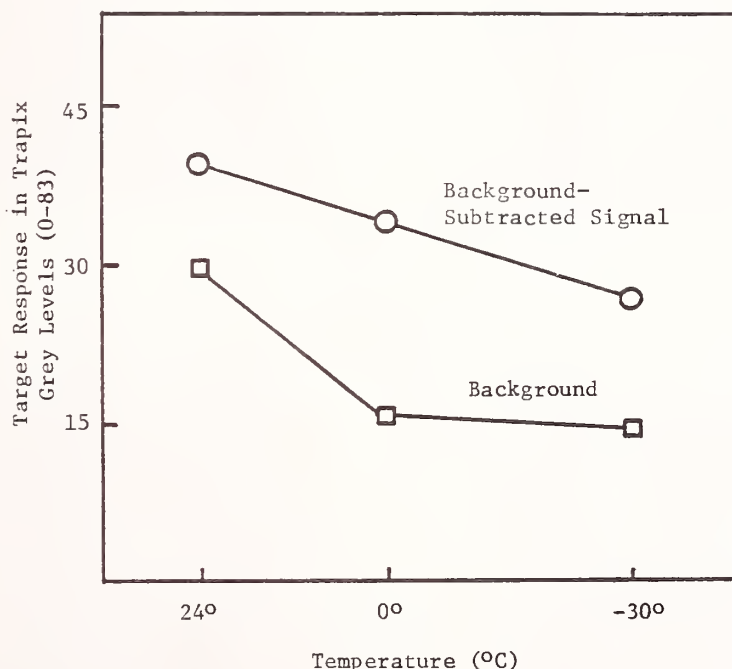


Figure 5. Temperature dependence of target response using mean data from three adjacent 27 x 27 pixel cells near the center of the target.

5. Pulsed Measurements at 1.06 μm

5.1 Linearity Improvement by Cathode Voltage Switching

The main drawback to the use of vidicons in pulsed applications is their nonlinear response [5]. This is known to be caused by the capacitive "lag" that is inherent in all electron beam readout devices [6]. To combat the problem, the method of frame summations has proven very useful in the past [5]. More recently, however, a cathode voltage switching method was developed and shown to be superior to frame summation [7,8]. Thus, the effects of cathode voltage switching on the pulsed-mode linearity of the PAR 1252E vidicon were studied.

To incorporate cathode voltage switching into the beam profiling system, the vidicon controller was modified to include a switching circuit [9] to raise the vidicon target voltage immediately after the prep frames and before the read frames. The idea is to pre-equilibrate the target at a low voltage, which establishes a relatively low background level, and to read the signal at a higher voltage, which increases the saturation level of the vidicon photodiodes [7,8]. The net effect should be a greater dynamic range, i.e., the ratio between the optical signal level that initiates vidicon saturation and that at which the vidicon response is just discernible from the background.

For the measurements, the vidicon was programmed for symmetric image sampling with $T_c = 100$ μsec and $N_c = 360$ pixels. It was illuminated with 1.06 μm , 5 nsec pulses from a Q-switched Nd:YAg laser. The beam was focused to approximately 1 mm diameter on the vidicon target and adjusted for various intensities with a wave plate attenuator. The vidicon controller was programmed to pre-equilibrate the target at 5 volts for 15 prep frames, fire the laser at the start of the next frame, and transmit that frame to the Trapix computer for storage and analysis. With the switching circuit [7] set for cathode voltage switching, the target voltage increased to 6.5 volts on the 16th (illumination) frame. Otherwise it remained at 5.0 volts.

To extract vidicon response data from the stored pulse images, a software program was written to calculate the average gray level of all pixels with gray level values greater than 90% of the maximum value. This is illustrated in the inset of figure 6. The two curves shown there are the

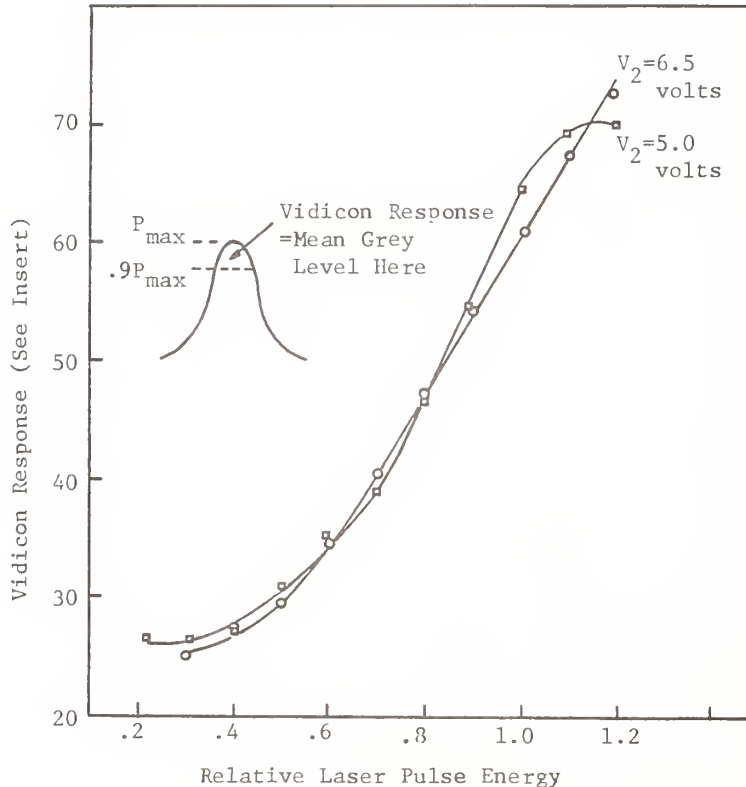


Figure 6. Comparison of linearity of vidicon response with cathode voltage switching (6.5 volt curve) and without it (5.0 volt curve).

result of averaging approximately 10 such values at each pulse energy level, both with cathode voltage switching ($V_2 = 6.5$ volt curve) and without it ($V_2 = 5.0$ volt curve). The greater linearity and increased saturation level of the $V_2 = 6.5$ volt curve show that significant improvement is possible with cathode voltage switching. The dynamic range in figure 6 is improved by more than a factor of 2 to approximately 4.

It appears from figure 6 that greater V_2 cathode voltages will improve the linearity even further. Investigation of this was not possible for the following reason. In generating the curves of figure 6, laser pulses were not used in the statistics if they caused saturation of even one pixel on the display monitor. Thus the saturation obvious on the $V_2 = 5.0$ volt curve and possibly just beginning on the $V_2 = 6.5$ volt curve are evidence of vidicon target saturation. The saturation level of the display pixels was not much higher, however, because with relative pulse energies higher than the upper level shown in figure 6, significant numbers of display pixels did saturate. This is why the upper end of the $V_2 = 6.5$ volt curve is not extended further, and why higher V_2 cathode voltages were not investigated. To do so would require raising the display monitor pixel saturation level, which was beyond the scope of the study. The results in figure 6 were obtained with the vidicon target cooled to 0°C . Similar results (not shown) were obtained at 24°C and -30°C .

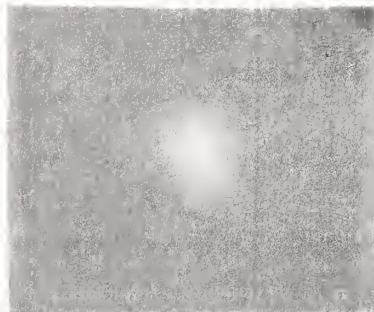
5.2 1.06 μm Laser Pulse Images and Analysis

Figure 7 shows the image of a typical pulse from the laser used in this study, including some ways of processing and analyzing the image. The results of the image inversion (figure 7b) and profile smoothing software routines (figure 7d) are available approximately 30 seconds after firing the laser. Thus, the system can provide real-time feedback in many laser damage experiments.

- A. Pulse image. Negative video causes Trapix pixels to saturate at zero grey level.



- B. Pulse image inverted so Trapix grey levels vary from zero at low energy to 83 at saturation.



- C. Profile of the inverted pulse through the section indicated by the cursor.



- D. Smoothed profile obtained by averaging the pixels in the thin region outlined by the cursor.

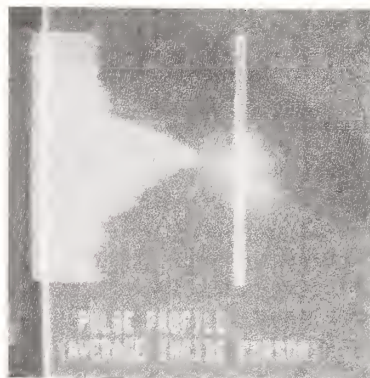


Figure 7. Processed, analyzed image of a 1.06 μm , Q-switched laser pulse.

6. Summary and Conclusions

A PAR 1252E vidicon and 1216 vidicon controller were successfully interfaced with a Trapix 5500 image processing system for the acquisition, display, and analysis of fast 1.06 μm laser pulses. Procedures were established for minimizing geometric distortion of displayed images. It was found that each channel time has a unique channel length in pixels which must be programmed via the vidicon controller. Several useful image analysis routines require less than 30 seconds, thereby providing real-time feedback in some types of laser damage experiments.

The peak-to-peak variations of dark current and 1.06 μm detection-sensitivity are 5.6% and 3.75%, respectively, in the central 3.75 x 3.13 mm region of the target. These variations are small enough and the area large enough for the system to be useful in profiling many laser beams. Temperature-dependence measurements of dark current and detection sensitivity show that the vidicon target has an optimum signal-to-noise ratio near 0° C.

Cathode voltage switching improves pulsed-mode linearity and raises the vidicon saturation level. A factor of 2 improvement (to 4) in dynamic range was shown here, but the system was not optimized because display monitor pixel saturation prevented investigation of higher V_2 cathode voltages. It is doubtful whether an ultimate dynamic range greater than 20, measured previously with an RCA C23250-NTD vidicon [1] will be achievable for this system in its present form.

*Research sponsored by the Air Force Office of Scientific Research/AFSC, United States Air Force, under Contract F49620-85-C-0013. The United States Government is authorized to reproduce and distribute reprints for governmental purposes notwithstanding any copyright notation hereon.

7. References

- [1] Smith, W.L.; DeGroot, A.J.; Weber, M.J. Silicon Vidicon System for Measuring Laser Intensity Profiles. Appl. Opt. 17(24): 3938; 1978.
- [2] O'Connell, R.M.; Deaton, T.F.; Saito, T.T. Single- and Multiple-Shot Laser-Damage Properties of Commercial Grade PMMA. Appl. Opt. 23(5): 682; 1984.
- [3] EG and G Princeton Applied Research, P.O. Box 2566, Princeton, NJ 08540.
- [4] Recognition Concepts, Inc., 924 Incline Way, P.O. Box 8510, Incline Village, NV 89450.
- [5] Fleming, G.R.; Morris, J.M.; Robinson, G.W. Picosecond Fluorescence Spectroscopy with a Streak Camera. Aust. J. Chem. 30: 2337; 1977.
- [6] Redington, R.W. The Transient Response of Photoconductive Camera Tubes Employing Low-Velocity Scanning. IRE Trans. Electron Devices Ed-4: 220; 1957.
- [7] Liesegang, G.W.; Smith, P.D. Improving Vidicon Linearity in the Pulsed Illumination Mode. Appl. Opt. 20(15): 2604; 1981.
- [8] Liesegang, G.W.; Smith, P.D. Vidicon Characteristics under Continuous and Pulsed Illumination. Appl. Opt. 21(8): 1437; 1982.
- [9] Cascio, H.E.; Smith, P.D.; Liesegang, G.W. Simple Switching Circuit to Improve Vidicon (OMA2) Linearity. Rev. Sci. Instrum. 53(7): 967; 1982.

- Manuscript Not Received -
=====

DIGITAL FLUENCE PROFILING SYSTEM AND SOFTWARE

S. C. Seitel
Montana Laser Optics, Inc.
Bozeman, MT 59715

and

R. L. Rypma
Big Sky Software Corp.
Bozeman, MT 59715

ABSTRACT

An advanced digital fluence profiling system based on a windowless GE TN2502 or TN2509 silicon array camera and Poynting Products 505RM frame grabber is described. The camera array is located precisely in the target plane or equivalent, and synchronized to the pulsed laser source with a flashlamp radiation sensor circuit. Data acquired by the frame grabber are transferred to an HP Series 200 computer for analysis.

Analysis is performed with BEAMCODE 2.0 software which permits near real time extraction of the peak fluence to total energy ratio in a single pulse to better than 20 percent. When corrected to camera non-uniformity and compared to large-aperture calorimetry, accuracy exceeds 10 percent. Other functions include measurement of pointing stability (beam wander) and divergence, fit-to-gaussian, and graphics data displays in contour and pseudo-3D formats.

Key Words: computer control; laser beam profile; laser diagnostics;
laser fluence measurement.

SIMPLE ACCURATE INVERSION OF KNIFE-EDGE DATA
FROM RADIALLY SYMMETRIC LASER BEAMS

R. M. O'Connell and R. A. Vogel
Electrical and Computer Engineering Department
University of Missouri
Columbia, Missouri 65211

The intensity profile of a radially symmetric beam is shown to be related to the inverse Abel transform of knife-edge-scan data. Two inversion algorithms, previously applied to problems in plasma diagnostics, are described and applied to knife-edge data from a confocal unstable resonator laser. The resulting profiles are shown to be in good agreement with each other but significantly different from the profile obtained by assuming the beam to be approximately Gaussian. As a beneficial consequence, the results are shown to imply a significantly higher laser damage threshold for polymethylmethacrylate than previously reported.

Key Words: beam profiles; inverse Abel transform; knife-edge scan; laser damage threshold; polymethylmethacrylate;

1. Introduction

Because it is experimentally simple to implement and offers excellent spatial resolution ($< 2 \mu\text{m}$) and dynamic range (10^6), the knife-edge method is frequently used to obtain beam profile information of narrowly focused ($< 100 \mu\text{m}$) high intensity ($> 1 \text{ GW/cm}^2$) laser beams, which are used in some laser damage studies. Knife-edge data does not replicate a beam profile; it must subsequently be inverted. The proper data-inversion method to be used depends on the functional form of the beam. For a Gaussian beam, simple differentiation of a knife-edge scan is sufficient to produce the required beam profile [1,2]. For this reason, non-Gaussian beams are also often approximated as Gaussian, a simplification which, as we will show, can lead to erroneous beam profiles.

In this paper we consider the problem of knife-edge data inversion for the class of beams that are radially symmetric. This important group includes the Airy pattern, the focused annulus, and even the Gaussian beam as a special case. In section 2 we show that the knife-edge scan of a radially symmetric beam has a simple relationship to the Abel transform of the beam profile. Thus, in principle, exact data inversion is possible. However, because the knife-edge scan consists of discrete data, the inversion must be done numerically. In section 3, we describe two numerical inversion algorithms, previously applied to problems in plasma diagnostics, which we applied to an appropriate set of knife edge data. We then present the resulting beam profiles and compare them to the result obtained using the Gaussian approximation. Finally, in section 4 we discuss the implications of these results for the single-shot bulk laser damage threshold of polymethylmethacrylate (PMMA).

2. Knife-Edge Data Inversion

2.1 Edge and Line Response Functions

In knife-edge scanning, illustrated in figure 1a, a straight-edge such as a razor blade is stepped across the focal plane of the beam and the total unclipped energy or power is measured at each position of the knife-edge. In the case of pulsed beams, the knife-edge is maintained at each position for several pulses. The average pulse energy at each position is then related to either the average measured power (through the pulse repetition frequency) or the total measured energy (through the number of pulses integrated). The result is a monotonically decreasing function such as that illustrated in figure 1b. If the knife-edge step increment is very small compared to fluctuations in the beam's spatial energy density (fluence), the measured data will closely approximate the mathematical edge response function $E(x)$ [3], the negative first derivative of which is the line response function $L(x)$ [3], illustrated in figure 1c. That is,

$$L(x) = - E'(x). \quad (1)$$

The line response function would be approximated by the measured "slit-scan" that would result if the knife-edge were replaced with a thin slit having a much narrower width than the beam's fluence fluctuations.

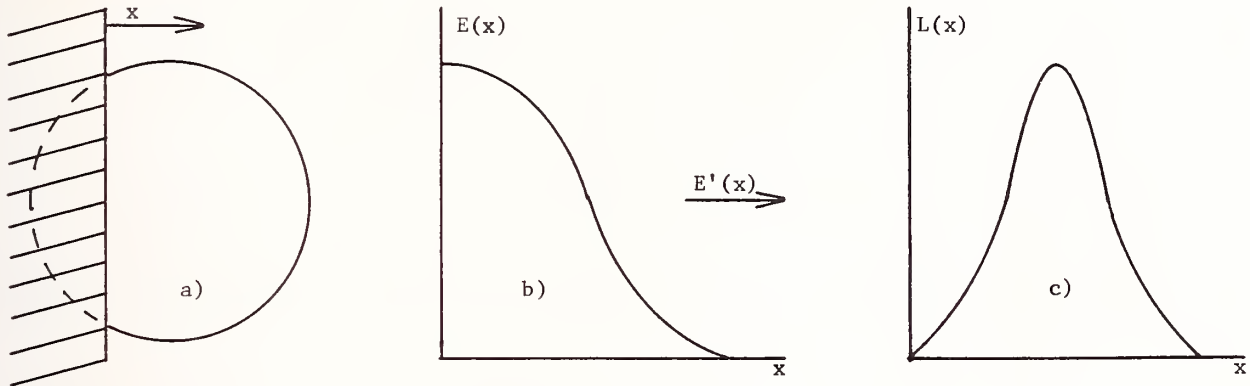


Figure 1. Relationship between the knife-edge scan(a), the edge-response function $E(x)$ (b), and the line-response function $L(x)$ (c).

2.2 The Abel Transform Pair for Radially Symmetric Beams

The relationship between the line response function and the profile of a radially symmetric beam can be obtained with the aid of figure 2. The circle of radius R represents the beam cross-section

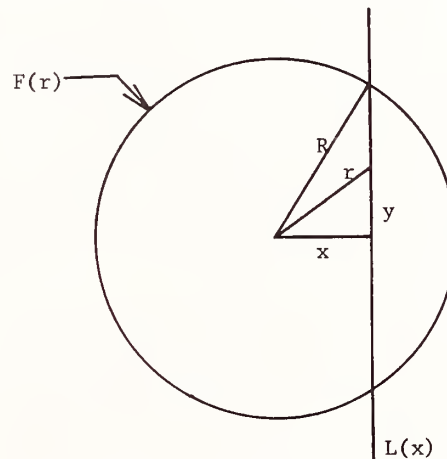


Figure 2. Geometry used to determine the relationships between the line response function $L(x)$ and the profile of a radially symmetric beam $F(r)$.

in the measurement plane at either a specific instant in time or under the assumption of time independence. Thus, it is a mapping of radially varying fluence, $F(r)$. The line response function $L(x)$ is just a line integral at each position x . In terms of the geometry shown in figure 2,

$$L(x) = 2 \int_0^{(R^2 - x^2)^{1/2}} F(r) dy. \quad (2)$$

To express dy and the limits of integration in terms of r , note that

$$x^2 + y^2 = r^2 , \quad (3)$$

from which

$$dy = \frac{rdr}{(r^2 - x^2)^{1/2}} , \quad (4)$$

and the lower and upper limits of integration become x and R , respectively. Thus, eq (2) becomes

$$L(x) = 2 \int_x^R \frac{F(r)rdr}{(r^2 - x^2)^{1/2}} , \quad (5)$$

which can be recognized as the Abel transform of $F(r)$ [4]. The solution of eq (5), known as the inverse Abel transform relation [4], is

$$F(r) = -\frac{1}{\pi} \int_r^R \frac{L'(x)}{(x^2 - r^2)^{1/2}} dx . \quad (6)$$

In eq (6), $L'(x)$ is the first derivative of the line response function. Using eq (1), eq (6) becomes

$$F(r) = \frac{1}{\pi} \int_r^R \frac{E''(x)}{(x^2 - r^2)^{1/2}} dx , \quad (7)$$

which is the desired relationship between the radially symmetric beam profile and the knife-edge scan.

2.3 Gaussian Beams: A Special Case

Gaussian beams are radially symmetric and therefore invertible from knife-edge data via eq (7). However, because the Gaussian function is also separable in the x and y coordinate variables, a much simpler result can be obtained by evaluating eq (2) specifically for the Gaussian case. In the plane of its waist, the fluence function of a Gaussian beam is expressible as

$$F(r) = F_0 \exp(-2r^2/w_0^2), \quad (8)$$

where F_0 is the peak fluence in the beam and w_0 is the $1/e^2$ energy radius, i.e., the beam waist or spot size. Since the Gaussian beam has an infinite radial extent, eq (2) can be written as

$$L(x) = \int_{-\infty}^{\infty} F(r) dy . \quad (9)$$

Substituting eq (8) into eq (9) and using eq (3) gives

$$L(x) = F_0 \exp(-2x^2/w_0^2) \int_{-\infty}^{\infty} \exp(-2y^2/w_0^2) dy. \quad (10)$$

The integral in eq (10) is the constant $F_0 w_0 \pi^{1/2}/2$. Therefore

$$L(x) = F_0 w_0 \pi^{1/2}/2 \exp(-2x^2/w_0^2), \quad (11)$$

which is just a scaled replica of the Gaussian function in eq (8). Thus, the line response function $L(x)$ gives the profile of a Gaussian beam directly. Recalling eq (1), it is then seen that the edge response function $E(x)$, i.e., the knife-edge scan, need only be differentiated to produce the desired profile. Because this procedure is so simple, non-Gaussian beams are often approximated as Gaussian and inverted accordingly.

3. Application to Experimental Knife-Edge Data

3.1 Inverse Abel Transform Algorithms

Returning to the more general case of radially symmetric but non-Gaussian beams, the correct inversion rule is given by eq (7). Since the edge response function $E(x)$ in the equation is approximated by the discrete knife-edge scan, the equation must be evaluated numerically. Several methods have been developed to do this, and complete summaries can be found in references [5] and [6]. Here, we briefly describe two of these methods, the popular data inversion algorithms of Nestor and Olsen [7] and Cremers and Birkebak [8], both of which we applied to a measured knife-edge scan. The measured data and the results of the inversion process are presented and discussed subsequently.

In the Nestor/Olsen algorithm, a transformation of variables is made and the x axis is divided into small segments, in each of which $E''(x)$ is assumed to be constant. This reduces eq (7) to a series of easily solved and summed integrals. One problem with the algorithm is that the second derivative function $E''(x)$ is formed by taking second differences of the discrete knife-edge data values. Nestor and Olsen showed that this step amplifies errors. Thus, for data with appreciable scatter, the resulting profile can be seriously flawed.

To make the data less sensitive to fluctuations, the Cremers/Birkebak algorithm divides slit-scan data (rather than knife-edge data) into a small number of zones and least-squares-fits a fourth order polynomial to the data in each zone. This provides an expression for $L(x)$ that can be differentiated analytically to give $L'(x)$ in eq (6), which can then be integrated exactly. The weakness of this algorithm is that the optimum size and number of zones for a given set of data need to be found empirically.

Despite their shortcomings, both of these algorithms were found to give good results when applied to test data produced by deliberately introducing round-off error to line and edge response function values generated with a polynomial profile function [7,8].

3.2 Experimental Data

Because they can give good results with artificial data, we applied both of the above described algorithms to previously measured knife-edge data from a narrowly focused 1.06 μm wavelength, Q-switched Nd:YAG laser [9]. The resonator in the Nd:YAG laser is of the confocal unstable variety.

Thus, its ideal output is a uniformly illuminated annulus [10] which focuses to a radially symmetric pattern similar to the Airy function [11]. The main difference between the two functions is that the secondary lobes of the focused annulus may contain a much larger fraction of the total energy than those of the Airy function. For example, whereas the main lobe of the Airy function contains approximately 84% of the total energy, the main lobe of a typical focused annulus may contain less than half of the total energy. Thus, the secondary lobes of the focused annulus should not generally be neglected, which is done when such a beam is assumed to be approximately Gaussian.

The knife-edge data, shown in figure 3, were obtained as described in section 2.1 with the laser free-running at 10 pps. The knife-edge, a 1/16-inch thick steel plate, was stepped across the beam in 2.54 μm increments and maintained at each position for at least 100 pulses of the beam. An S-1 photodiode recorded relative pulse energies and showed that the pulse-to-pulse variation was <5% rms. Note that because the two data inversion algorithms assume radial symmetry, they can only be applied to half-beam data, i.e., from 50% occlusion (at the $r=0$ point) to 100% occlusion (at the $r=R$ point). Therefore figure 3 shows only that portion of the full knife-edge scan needed by the two algorithms. Furthermore, since the Cremers/Birkebak algorithm requires line response or slit-scan data, the knife-edge data of figure 3 had to be differentiated first, according to eq (1). Since the impetus behind the Cremers/Birkebak algorithm was to eliminate differentiation by finite differences, we performed the operation by least-squares-fitting a quadratic equation to the five point segment centered on each data point [9] and evaluating the derivative at each point analytically. The right half of the resulting curve was then divided into five zones and used to approximate the slit-scan required by the Cremers/Birkebak algorithm. No attempt was made to optimize the number of zones.

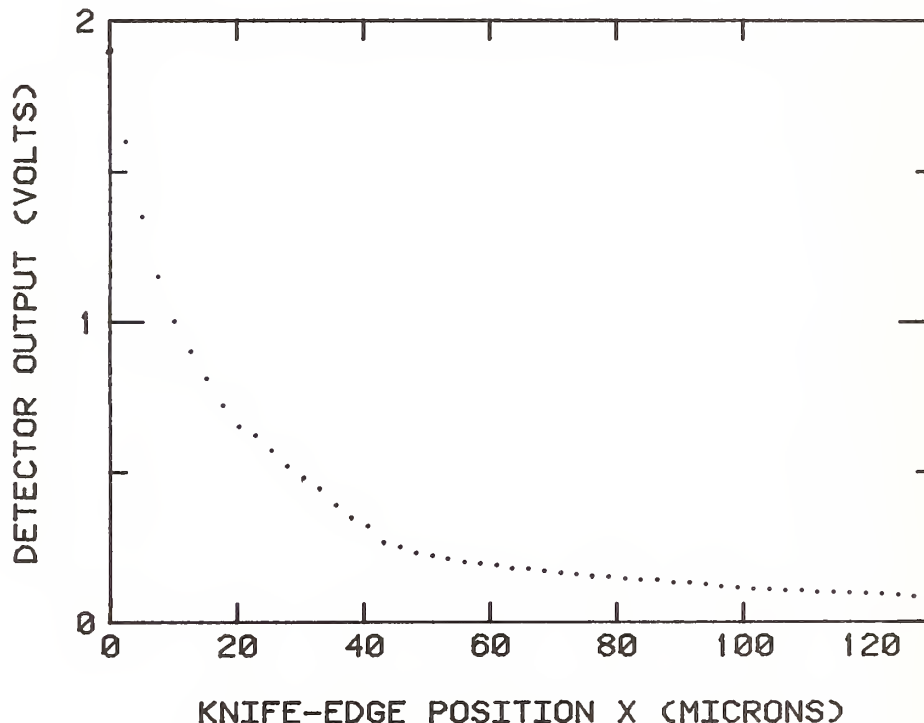


Figure 3. Measured knife-edge data from a 1.06 μm , Q-switched Nd:YAG laser.

3.3 Results

Figures 4a and 4b show the beam profiles that result from applying the Nestor/Olsen and Cremers/Birkebak algorithms, respectively, to the knife-edge data of figure 3. Except for the three nulls present in figure 4a but missing in figure 4b, the two profiles are very similar; the $1/e^2$ radii of their main lobes are 12 μm and 14 μm , respectively; and they both have significant and similar energies outside the main lobe, extending to the same 46 μm radius. The lack of detail outside the main lobe in figure 4b is probably due to excessive data smoothing introduced by the

quadratic fit/differentiation, which we used to convert the knife-edge data to slit-scan data, and the zonal polynomial fit/differentiation done in the Cremers/Birkebak algorithm itself.

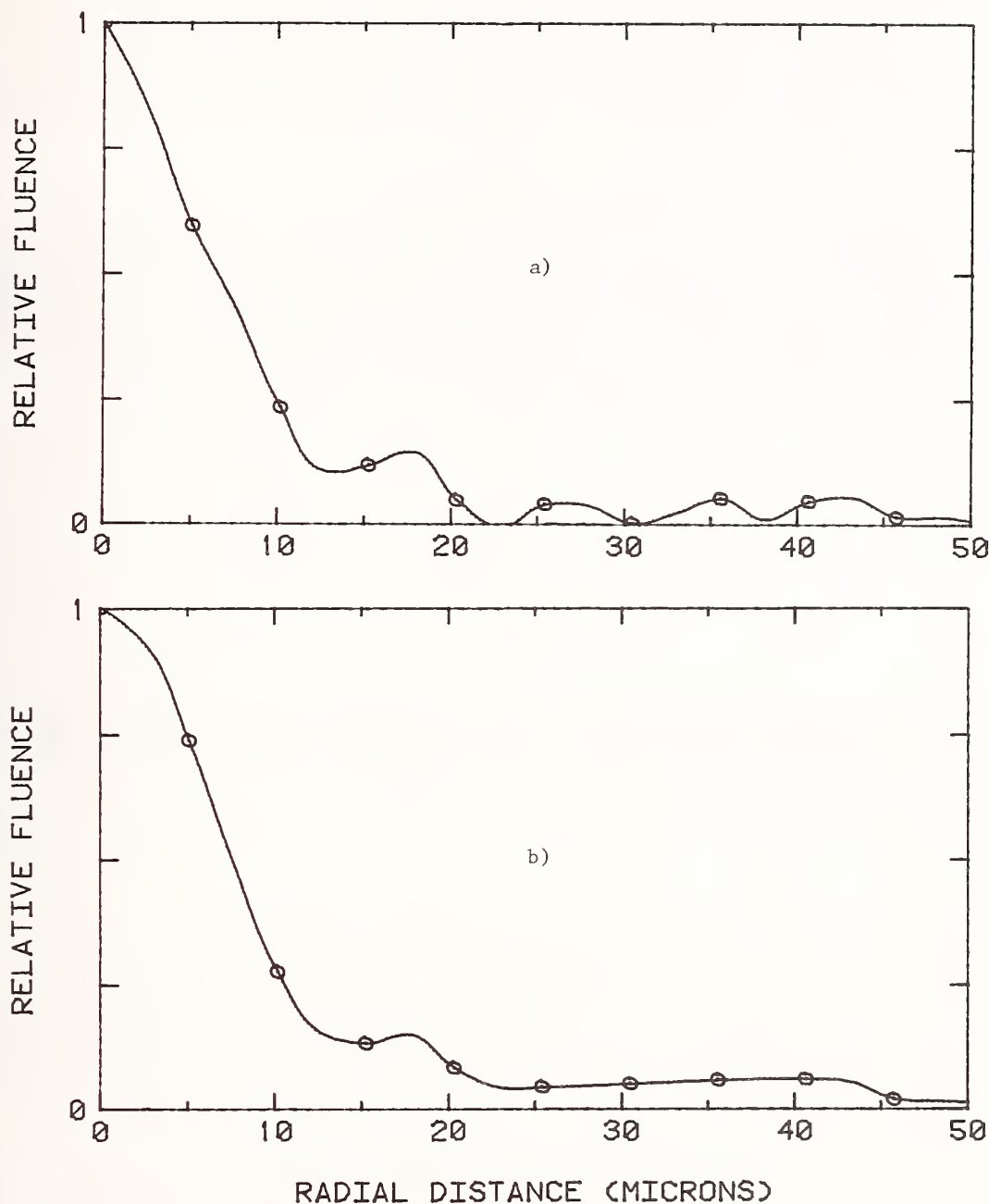


Figure 4. Beam profiles obtained by inverting the knife-edge data of figure 3 with the Nestor/Olsen (a) and Cremers/Birkebak (b) algorithms.

We also inverted the knife-edge scan of figure 3 using the Gaussian approximation. Since in that case the knife-edge data needs only to be differentiated to produce the beam profile, the result was already available in the $1/e^2$ form of the quadratic fit/differentiated data used with the Cremers/Birkebak algorithm. The $1/e^2$ radius of the resulting profile (not shown here) is approximately 23 μm , roughly twice as large as those in figure 4. Also, the profile has significantly secondary lobe energy extending beyond a 50 μm radius. Thus, the beam profiles produced using the

two algorithms for implementing the correct inversion procedure are both similar to each other and quite different from the profile obtained by assuming the beam to be approximately Gaussian.

Although it would be desirable to compare the profiles in figure 4 to an expected, calculated profile, an accurate calculation would be very difficult to perform. First of all, film burns of the laser output showed that it was not an ideal uniformly illuminated annulus, but only approximately so. Secondly, in taking the knife-edge data, it was difficult to locate the focal plane precisely. Thus, the standard Fraunhofer (focal plane) diffraction pattern of a uniformly illuminated annulus can not be relied upon for accurate comparison. A more general and difficult diffraction calculation would be needed.

4. Implications for the Laser Damage Threshold of PMMA

Pulsed laser damage thresholds are usually obtained from plots of measured damage probability versus laser pulse energy. The damage threshold is then defined as the peak fluence associated with the pulse energy causing a certain probability of damage; the onset (or 0%) and 50% levels are frequently used [12,13]. Accurate beam profiles are needed in this because they provide a calibration constant for relating peak fluences to pulse energies [9]. The calibration constant is found by rotating the profile $F(r)$ about its relative fluence axis, integrating with respect to area to obtain a total relative energy E_{TP} , and then normalizing to the peak relative fluence F_{PP} in the profile. The resulting calibration constant A has the units of area, i.e.,

$$A = \frac{E_{TP}}{F_{PP}} = \frac{2\pi \int_0^R F(r) r dr}{F_{PP}} . \quad (12)$$

If the laser is reasonably stable from pulse to pulse (see Sec. 3.2), the measured beam profile will be a scaled replica of any pulse from the laser. The peak fluence F_P in each pulse is then just the ratio of the measured energy E_T in the pulse to A , i.e.,

$$F_P = \frac{E_T}{A} . \quad (13)$$

If E_T in eq (11) is the damage threshold pulse energy, F_P is the required threshold peak fluence.

Since the calibration constant A is determined from a beam profile, it is clear from eq (13) that different beam profiles obtained from the same set of knife-edge data will result in different values of the peak fluence damage threshold being associated with a single threshold pulse energy. Alternate threshold values F_{P2} and F_{P1} simply scale with their respective beam profile calibration constants A_1 and A_2 via the relation

$$F_{P2} = F_{P1} \frac{A_2}{A_1} , \quad (14)$$

which follows from eq (13). In the study in which the knife-edge scan of figure 3 was measured [9], the beam was assumed to be approximately Gaussian and the data was inverted accordingly. From the resulting beam profile and the threshold pulse energy, the single-shot bulk damage threshold of polymethylmethacrylate (PMMA) was reported as 41 j/cm^2 . Using eq (14) and the calibration constants obtained as described above from figures 4a and 4b, the laser damage threshold of PMMA becomes 187 j/cm^2 and 136 j/cm^2 , respectively, according to the Nestor/Olsen and Cremers/Birkebak algorithms.

Investigation of Optical Damage via Resonance Ionization Mass Spectrometry

R. C. Estler* and N. S. Nogar

Chemistry Division
Los Alamos National Laboratory
Los Alamos, New Mexico 87545

Resonance ionization mass spectrometry (RIMS) has been used as a diagnostic for interrogating optical damage events. RIMS involves multistep laser photoionization, generally through real intermediate states, followed by mass separation and detection. It is a sensitive and selective means of detection, and has the potential for detection of ultratrace inclusions in substrates and/or coatings.

In initial experiments, damage on uncoated CaF_2 substrates was initiated by pulses of 1.06- μm light from a Q-switched Nd^{+3} :YAG laser. Interrogation of the spalled plume revealed CaF radicals only when damage events occurred. No Ca atoms were observed, and no attempt was made to detect F atoms or CaF_2 . In subsequent experiments conducted at laser intensities below the damage threshold, we observed the presence of surface adsorbents and a correlation between the presence of the adsorbents and the occurrence of optical damage.

Key Words: calcium fluoride; laser-induced damage; optical damage; photoionization; resonance ionization mass spectrometry (RIMS).

1. Introduction

Laser-induced desorption and laser-based detection of ablated or sputtered species are both becoming widely used techniques in a variety of studies, including surface chemistry, sputtering, and optical damage. Much work has concerned laser-desorption of adsorbed species from substrate surfaces as detected by a variety of mass spectroscopic techniques [1-10]. Other experiments have concentrated on probing the basic processes related to laser-ablation of the substrate material itself [11-16]. Laser detection of desorbed particles via fluorescence or ionization is also becoming a widely used technique in more traditional particle-induced sputtering experiments [17-20].

Few investigations have, however, coupled the advantages found in laser-induced desorption to those of the sensitive and specific laser-based schemes now available for the detection of the desorbed material [21-24]. We report here, the use of resonance ionization mass spectrometry (RIMS) as a diagnostic for interrogating laser-induced optical damage events. RIMS is a sensitive and selective means of detection, and has the potential for detection of ultratrace inclusions in substrates and/or coatings as well as the detection of active sites on the surface where subsequent damage is likely to occur.

2. Experimental

The damage/desorption experiments described below took place in the source region of a time-of-flight mass spectrometer described in detail previously [25]. Figure 1a depicts a schematic of this region, while figure 1b describes a typical timing sequence used. Briefly, the Q-switch synch-out from the Nd^{+3} :YAG damage/desorption laser (Quanta Ray/Spectra Physics Model DCR 1A) was used to master the timing sequence. The laser output, initially frequency doubled to provide a visible beam, was focused onto the substrate surface with the aid of beam-steering prisms and a 250-mm focal length lens. Once alignment was completed, the frequency doubler was detuned, the residual 532-nm light removed with a dichroic mirror, leaving only (>99%) the fundamental 1.06- μm beam. The 10-ns pulses from this laser typically arrived at the substrate ~100 ns after the Q-switch synch-out trigger. Beam size at the substrate was approximately 0.47 mm^2 , and pulse energies ≥ 25 mJ were used producing fluences ≥ 5.3 J cm^{-2} . These values must be regarded as approximations, since the "doughnut" shaped output of the 1.06- μm laser produces a nonuniform intensity distribution. No attempt was made in this preliminary study to modify the spatial distribution of this laser.

*Permanent address: Department of Chemistry, Fort Lewis College, Durango, Colorado 81301

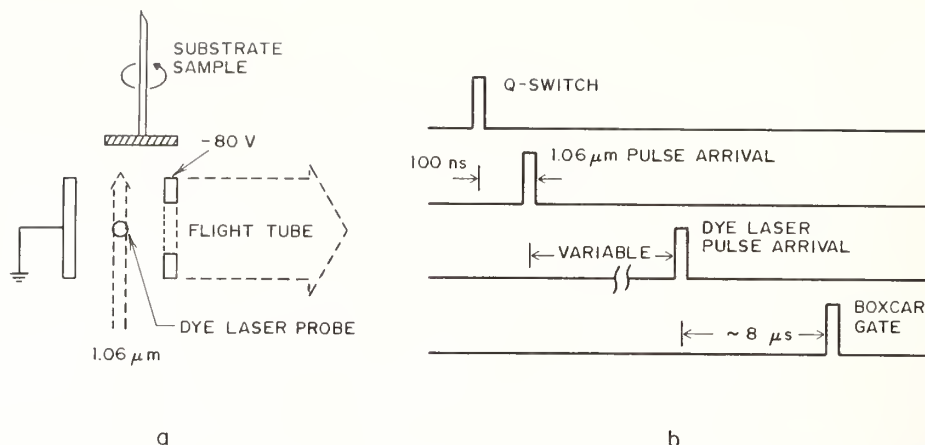


Figure 1. Schematic of the experimental apparatus. The 1.06- μm damage pulse is typically focused to a beam diameter of 0.7 mm at the substrate surface. The delay time to the dye laser probe pulse was $\sim 30\text{--}50\text{ }\mu\text{s}$.

The CaF_2 substrates (Janos Optical) were polished flats, 1.9 cm in diameter and 3 mm thick. Each was cemented to a 15-cm stainless steel rod for mounting within the mass spectrometer source region. The substrates could be translated and rotated while in the source region via a high vacuum feedthrough (Varian Model 1371). The rotation axis of the substrate was parallel but not coincident with the 1.06- μm laser beam axis. A displacement of 5 mm between these two axes allowed the interrogation of different substrate sites via substrate rotation. Rotation rates varied from 1 revolution/15 minutes to 1 revolution/60 minutes. The long substrate mounting rods were required to prevent metal ion formation near the source region from the focused 1.06- μm laser striking the surfaces of the vacuum chamber.

A gas inlet system facilitated gas-phase RIMS studies and provided a means of introducing adsorbents onto the surface of the substrate. A stainless steel nozzle opposite the surface being interrogated directed the adsorbents to this surface. The inlet system was also constructed in such a manner as to allow adsorbent purification via distillation prior to deposition. All adsorbents were triply distilled prior to use.

Pulses from an excimer-pumped dye laser (Lambda Physik, Models 101/2002) were used to effect ionization. Ions were generated from ground electronic states of the detected species in a variety of multiphoton transition sequences. The excimer laser typically produced 100-mJ, 15-ns pulses and was triggered after a variable delay. Dye laser pulses (2 mJ, 10 ns) were spatially filtered and loosely focused (0.07 cm diam) through the ionization region. The laser beam propagated parallel to the substrate surface, at a distance of 2.5 cm. The extraction field was approximately 110 V/cm, perpendicular to the paths of both laser beams. This was followed by a drift tube at $\sim 1000\text{ V}$; the flight path was 0.4 m. A pair of deflection plates between the extractor and flight tube maximized the transmission of ions to the detector and minimized any transmission variation due to ion velocity components perpendicular to the flight tube. Detection electronics consisted of a channel electron multiplier, a preamplifier, an amplifier, and a boxcar averager whose gate delay was set to the flight time of the ion of interest. The boxcar gate width was adjusted so as to encompass only a few mass units about that of the detected specie. An oscilloscope was used to observe simultaneously the arrival of the damage/desorption laser pulses, the ion signal, and the boxcar gate.

3. Results and Discussion

In initial experiments, damage on uncoated, polished substrates was initiated by pulses of the 1.06- μm laser. Dielectric breakdown was observed at thresholds fundamentally consistent with previous measurements on CaF_2 [26]. However, the breakdown threshold was surface site dependent, possibly due to defects or surface contamination. Neither Ca atoms nor CaF radicals could be detected prior to breakdown. Upon breakdown, however, CaF radicals were easily detected via a two-photon transition to the $F^2\Pi$ excited state (37548 cm^{-1}) from the $X^2\Sigma^+$ ground state. Absorption of a third photon of the same color results in ionization (ionization potential $\sim 6.0\text{ eV}$) [27]. Figure 2 shows the resulting excitation spectrum for this $2 + 1$ ionization of CaF through the multi-branched $\Delta v = 0$ transitions of the F state at flight time delay of 50 μs . In addition to the major features of the $F^2\Pi \leftarrow X^2\Sigma^+$ $2 + 1$ ionization process, smaller features due to a $1 + 2$ ionization process via the $B^2\Sigma^+ \leftarrow X^2\Sigma^+$ $\Delta v = 0$ transitions are also observed. We believe that this is the first reported multiphoton photoionization spectrum of CaF.

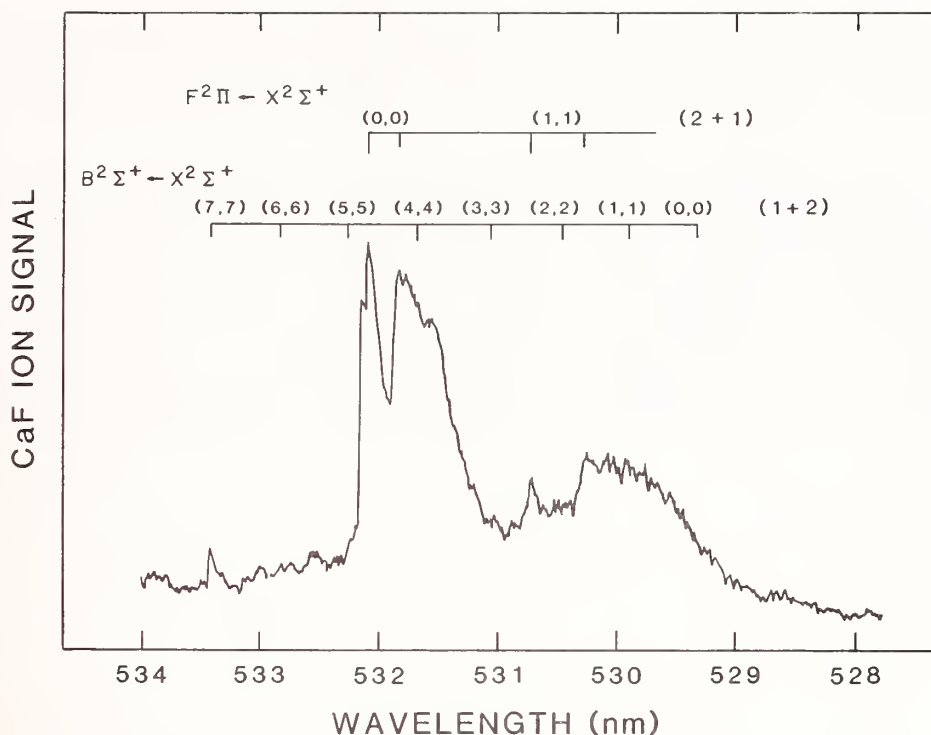


Figure 2. Optical MPI spectrum of desorbed CaF, obtained at a 50- μ s delay after the desorption pulse. Bandhead positions are indicated for the $\Delta v = 0$ sequences for the electronic transitions observed.

Time-of-flight spectra of the CaF radicals could not be recorded due to a large nonresonant signal from ions of many different masses at shorter flight times. The source of this contaminating signal is the intense UV-light pulse generated at the substrate surface during breakdown. The source of the interference was confirmed by placing electron/ion deflectors in the flight path of the spalled material. All attempts to reduce this signal by particle deflection failed, although ions are certainly generated in such a breakdown event. The breakdown-generated light pulse was easily visible to the naked eye and sometimes generated overloads in the electronics due to the formation of many ions as it struck the optic elements of the ion spectrometer. Such light-generated signals have been observed previously [2]. Direct inversion of spectral intensities to state populations is not currently possible (as in much laser-induced fluorescence work) due to the lack of knowledge of the two-photon line strengths of the transitions involved [28]. However, it is clear that several low-lying vibrational states of the ground electronic state have been populated in the damage event. No Ca atoms could be detected after the onset of breakdown, even though detection sensitivity for desorbed alkaline earth atoms is high [29]. This suggests that the mechanism for breakdown at 1.06 μ m is thermal, or hydrodynamic in nature, since previous observations [20,30] suggest that an electronic or photophysical interaction leads to the production of free metal atoms. No attempt was made to observe either F atoms or CaF₂.

In an attempt to correlate surface contamination with low breakdown threshold, a series of adsorption/desorption experiments were performed. In previous work [5,9], water aggregation appeared correlated to low damage thresholds at a particular site. However, water is not a good RIMS candidate due to its high ionization potential and sparse electronic structure. Only recently has the multiphoton ionization spectrum of water been obtained at the relatively high pressure of 100 torr [31]. In the experiments reported below, nitrogen dioxide (NO₂) was chosen for the adsorbent for several reasons. First, at wavelengths at and below 380 nm, NO₂ dissociates efficiently to NO + O, the NO being easily detected via multiphoton ionization due to its low ionization potential [32]. Second, if the NO₂ reacts with surface water, several of the possible reaction products, like NO₂, have dissociating UV absorptions at the NO resonance wavelengths. Lastly, NO₂, like water, is polar and seeks the same high potential sites where damage is likely to occur [33]. In addition, at the wavelength chosen for this preliminary study, 365 nm (corresponding to the large Franck-Condon factor transition C²Π ($v = 1$) ← X²Π² ($v = 0$) in NO, i.e., the δ (1,0) transition, high efficiency laser dyes are available. This technique of dissociation and fragment probe within a single laser pulse has been used previously in several dynamic studies [31,34].

Following the substrate mounting, samples were placed within the mass spectrometer and evacuated to 10^{-7} torr for several hours. The substrates were then exposed to NO_2 at low pressure (10^{-6} torr) for sufficient time to form several monolayers. Substrates were then again returned to 10^{-7} torr. The RIMS sensitivity for detecting NO from NO_2 is very high, requiring another several-hour period of pumping to eliminate background nitric oxide RIMS signals prior to a desorption experiment.

Each area on the substrate was then sequentially exposed to low intensity and high intensity laser pulses. At $1.06\text{-}\mu\text{m}$ intensities below the damage threshold (typically $0.4\text{--}0.6\text{ J cm}^{-2}$) the ion signal at the bandhead wavelength of the $\text{NO } \delta(1,0)$ was recorded as a function of substrate rotation angle. Such records are shown for two samples in figure 3b. On a second pass, at intensities near or above the damage threshold (approximately 5 J cm^{-2}), a signal due to breakdown was recorded as a function of substrate rotation angle. These spectra are shown for the same two samples in figure 3a. Only a single pass below the damage threshold was made, since laser annealing was observed for sites receiving multiple exposures below these thresholds. This annealing effect and the low signal-to-noise ratio in these experiments prevented time-of-flight spectra from being recorded for the adsorbent. The NO signals of figure 3 were recorded at a $50\text{-}\mu\text{s}$ flight time

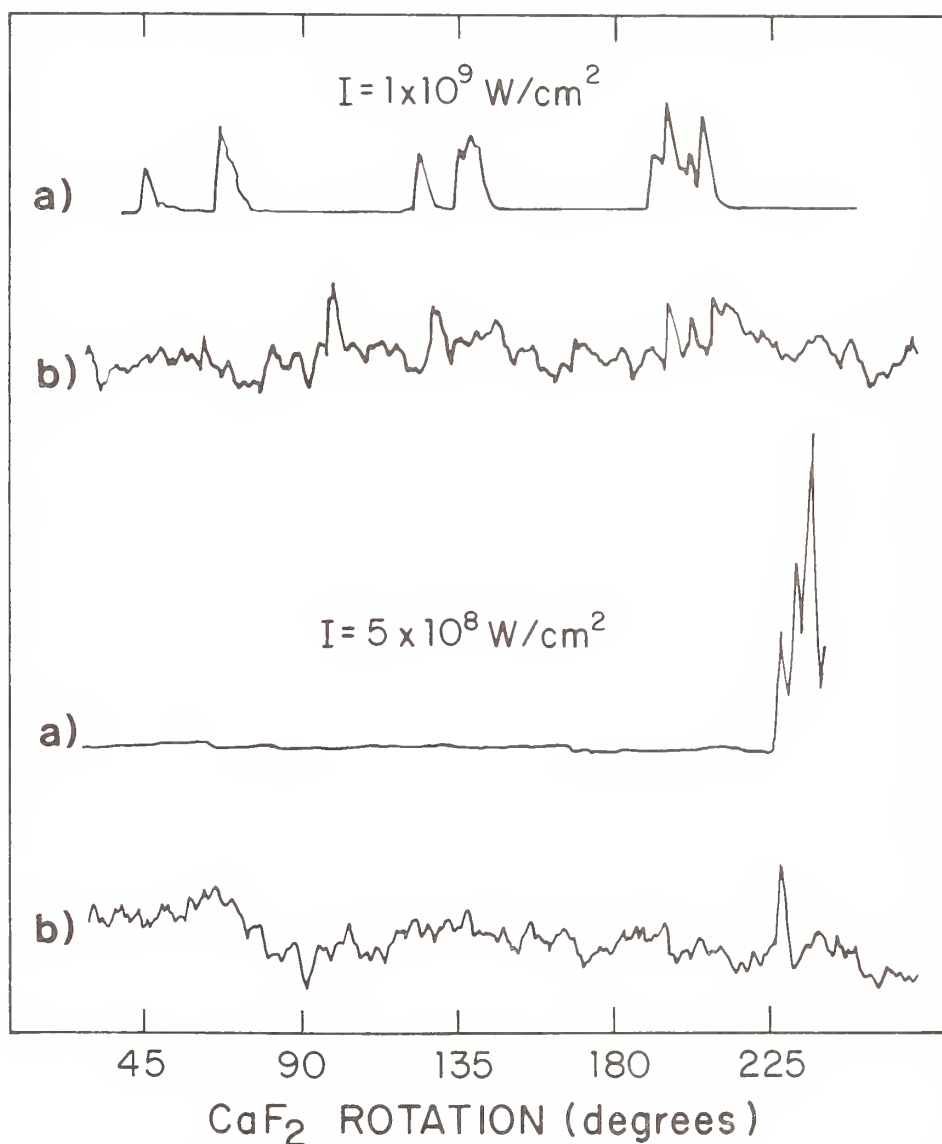


Figure 3. Correlation between breakdown and adsorbent concentration for two different damage intensities ($10^9\text{ W/cm}^2 \sim 10\text{ J/cm}^2$). (a) Breakdown (damage) signal as a function of substrate rotation following the nondestructive desorption of adsorbent (Pass 2). (b) NO desorption signal as a function of substrate rotation (Pass 1).

between desorption and ionization. The correlations observed between damage and desorbent concentration for the two samples are representative of the correlations observed for all samples interrogated. Not all sites showing higher concentrations of adsorbent produce breakdown; however, most all breakdown sites exhibited higher adsorbent concentrations.

The efficiency of detecting the active sites by adsorbent aggregation could be improved over that observed above by using a desorbing wavelength in resonance with the adsorbent [5,9]. This is not the case for the experiments described above. From our static gas phase NO_2 experiments, we estimate (incorporating observed signal-to-noise, detection volume, etc.) a lower detection limit of $\sim 6 \times 10^5$ molecules of NO_2 . Using this number, a rough calculation of our desorption efficiency yields $\sim 10\%$, assuming a temporal and spatial overlap of 10^{-3} , a partition function of 10^{-2} , and a dissociation and ionization efficiency of 10^{-1} . Although this desorption efficiency certainly represents an upper bound for this nonresonant process, it could be dramatically improved via vibrational resonant frequencies. RIMS is inherently more sensitive for such studies than the traditional residual gas analyzers due to its order of magnitude better ionization efficiency over electron bombardment. Further improvement in the present apparatus can be made by providing a line-of-sight path between substrate surface and detectors. Such improvements will be incorporated into future instrumentation.

Since the neutral/ion production ratio ranges from 10^2 to 10^{-5} in laser desorption of adsorbents and substrates [11,16,21,22], efficient detection of the neutral major product channel is imperative to our understanding of such processes. RIMS provides such a sensitive, specific detection scheme. It shows potential for monitoring ultratrace inclusions in substrates and/or coatings, as well as for nondestructively locating active surface sites where subsequent damage is probable.

Note added in proof:

Since recording this data, beam-filling optics have been installed into the Nd^{+3} :YAG laser, allowing for smaller spot sizes with smoother spatial profiles. With these optics installed, Ca atoms have been detected after breakdown in addition to the CaF molecules. These results, as well as those observed at 266 nm and 355 nm desorbing wavelengths will be discussed elsewhere.

4. References

- [1] Levine, L. P.; Ready, J. F.; Bernal G., E. J. Appl. Phys. 38, 331 (1967).
- [2] Levine, L. P.; Ready, J. F.; Bernal G., E. IEEE J. Quant. Electron. QE-4, 18 (1968).
- [3] Antonov, V. S.; Letokhov, V. S.; Shibarov, A. N. Appl. Phys. 25, 71 (1981).
- [4] Chuang, T. J. J. Chem. Phys. 76, 3828 (1982).
- [5] Allen, S. D.; Porteus, J. O.; Faith, W. N. Appl. Phys. Lett. 41, 417 (1982).
- [6] Egorov, S. E.; Letokhov, V. S.; Shibarov, A. N. Chem. Phys. 85, 349 (1984).
- [7] Hussla, I.; Chuang, T. J. Mat. Res. Soc. Symp. Proc. 29, 341 (1984).
- [8] (a) Burgess, Jr., D. R.; Hussla, I.; Stair, P. C.; Viswanathan, R.; Weitz, E. J. Chem. Phys. 79, 5200 (1983); (b) _____, Rev. Sci. Instrum. 55, 1771 (1984).
- [9] Allen, S. D.; Porteus, J. O.; Faith, W. N.; Franck, J. B. Appl. Phys. Lett. 45, 997 (1984).
- [10] Sherman, M. G.; Kingsley, J. R.; Dahlgren, D. A.; Hemminger, J. C.; McIver, Jr., R. T. Surface Sci. 148, L25 (1985).
- [11] Olstad, R. A.; Olander, D. R. J. Appl. Phys. 46, 1499 (1975).
- [12] For a review of much work see Smalley, R. E. Laser Chem. 2, 167 (1983).
- [13] Davis, G. M.; Gower, M. C.; Fotakis, C.; Efthimiopoulos, T.; Argyrakis, P. Appl. Phys. A36, 27 (1985).
- [14] Kelly, R.; Cuomo, J. T.; Leary, P. A.; Rothenberg, J. E.; Braren, B. E.; Aliotta, C. F. Nucl. Instr. and Meth. B9, 329 (1985).

- [15] (a) Rothenberg, J. E.; Kelly, R. Nucl. Instr. and Meth. B1, 291 (1984); (b) ____ Nucl. Instr. and Meth. B7/8, 755 (1985).
- [16] Kang, H.; Beauchamp, J. L. J. Phys. Chem. 89, 3364 (1985).
- [17] Pellin, M. J.; Wright, R. B.; Gruen, D. M. J. Chem. Phys. 74, 6448 (1981).
- [18] Kimock, F. M.; Baxter, J. P.; Winograd, N. Instr. and Meth. in Phys. Res. 218, 287 (1983).
- [19] Kimock, F. M.; Baxter, J. P.; Pappas, D. L.; Kobrin, P. H.; Winograd, N. Anal. Chem. 56, 2782 (1984).
- [20] Tolk, N. J. Luminescence 31/32, 913 (1984).
- [21] Beekman, D. W.; Callcott, T. A.; Kramer, S. D.; Arakawa, E. T.; Hurst, G. S.; Nussbaum, E. Int. J. Mass. Spectrom. Ion Phys. 34, 89 (1980).
- [22] Selter, K. P.; Kunze, H. -J. Physica Scripta. 25, 929 (1982).
- [23] Leismann, P.; Henc-Bartolic, V.; Rebhan, U.; Kunze, H. -J. Physica Scripta. 30, 186 (1984).
- [24] Nogar, N. S.; Estler, R. C.; Miller, C. M. Anal. Chem. 57, 2441 (1985).
- [25] Downey, S. W.; Nogar, N. S.; Miller, C. M. Int. J. Mass Spec. Ion Proc. 61, 337 (1984).
- [26] Smith, W. L.; Bechtel, J. H.; and Bloembergen, N. Phys. Rev. B12, 706 (1975).
- [27] Hildenbrand, D. L.; Murad, E. J. Chem. Phys. 43, 1400 (1965).
- [28] Zare, R. N.; Dagdigian, P. J. Science 185, 739 (1974).
- [29] Estler, R. C.; Nogar, N. S. to be published.
- [30] Stoffel, N. G.; Riedel, R.; Colavits, E.; Margaritondo, G.; Haglund, R. F.; Taglaner, E.; Tolk, N. H. Phys. Rev. B32, 6805 (1985).
- [31] Ashfold, M. N. R.; Bayley, J. M.; Dixon, R. N. Chem. Phys. 84, 35 (1984).
- [32] Radhakrishnan, G.; Ng, D.; Estler, R. C. Chem. Phys. Lett. 84, 260 (1981).
- [33] Radhakrishnan, G.; Estler, R. C. Chem. Phys. Lett. 100, 403 (1983).
- [34] Bloembergen, N. Appl. Opt. 12, 661 (1973).

5. Summary and Conclusions

We have shown that knife-edge data from a radially symmetric but non-Gaussian beam is properly inverted by an inverse Abel transform of the derivative of the knife-edge data. The frequently used method of simple differentiation is strictly correct only with Gaussian beams.

The Nestor/Olsen and Cremers/Birkebak algorithms for implementing the correct data inversion procedure gave similar and reasonable beam profiles when applied to the measured knife-edge scan of a focused annulus beam. Thus, despite some shortcomings, both algorithms appear to be useful for inverting knife-edge data from those radially symmetric beams with pulse-to-pulse stability similar to that of the laser used to generate the data of figure 3. For data with greater scatter, certain newer algorithms [5] may give better results. In contrast with the beam profiles produced by the Nestor/Olsen and Cremers/Birkebak algorithms, the one produced by the quadratic fit/differentiation procedure was significantly different, suggesting that the focused output of lasers based on confocal unstable resonators should not be approximated as Gaussian.

Values for the 1.06 μm single-shot bulk laser damage threshold of PMMA implied by the beam profiles produced by the Nestor/Olsen, Cremers/Birkebak, and quadratic fit/differentiation algorithms are, respectively, 187 j/cm^2 , 136 j/cm^2 , and 41 j/cm^2 . The average of the first two values is 161 j/cm^2 . This fact and the apparent improvement in accuracy of the first two profiles over the third lead to the conclusion that the laser damage threshold of PMMA is approximately four times as large as previously reported [9].

6. References

- [1] Arnaud, J.A.; Hubbard, W.M.; Mandeville, G.D.; de la Claviere, B.; Franke, E.A.; Franke, J.M. Technique for fast measurement of Gaussian laser beam parameters. Appl. Opt. 10(12): 2775; 1971.
- [2] Mauck, M. Knife-edge profiling of Q-switched Nd:YAG laser beam and waist. Appl. Opt. 18(5): 599; 1979.
- [3] Gaskill, J.D. Linear systems, Fourier transform, and optics. New York: Wiley; 1978.
- [4] Bracewell, R.N. The Fourier transform and its applications. New York: McGraw-Hill; 1965.
- [5] Hansen, E.W.; Law, P. Recursive methods for computing the Abel transform and its inverse. J. Opt. Soc. Am. A. 2(4): 510; 1985.
- [6] Minerbo, G.N.; Levy, M.E. Inversion of Abel's integral equation by means of orthogonal polynomials. SIAM J. Numer. Anal. 6(4): 598; 1969.
- [7] Nestor, O.H.; Olsen, H.N. Numerical methods for reducing line and surface probe data. SIAM Rev. 2(3): 200; 1960.
- [8] Cremers, C.J.; Birkebak, R.C. Application of the Abel integral equation to spectrographic data. Appl. Opt. 5(6): 1057; 1966.
- [9] O'Connell, R.M.; Deaton, T.F.; Saito, T.T. Single- and multiple-shot laser damage properties of commercial grade PMMA. Appl. Opt. 23(5): 682; 1984.
- [10] Krupke, W.F.; Sooy, W.R. Properties of an unstable confocal resonator CO_2 laser system. IEEE J. Quantum Electron. 5(12): 575; 1969.
- [11] Born, M.; Wolf, E. Principles of optics. New York: MacMillan; 1964.
- [12] Foltyn, S.R. Spotsize effects in laser damage testing. Nat. Bur. Stand. (US) Spec. Publ. 619; 1982. p. 368.
- [13] Porteus, J.O.; Seitel, S.C. Absolute onset of optical surface damage using defect ensembles. Appl. Opt. 23(21): 3796; 1984.

Laser Mirror Profilometry by High-0 Interferometry

J.R. Rotge'
Frank J. Seiler Research Laboratory
USAF Academy
Colorado Springs, Colorado 80840-6528

A novel interferometric technique is described which exploits the relationship between an optical resonator's length and resonant frequency. This concept has potential for measuring length variations of an order of $\ll 1 \text{ \AA}$. This paper briefly describes the concept, the experiment performed to demonstrate the concept, and the experimental results. Results obtained indicate a repeatability in the measured data to $\sim 5 \text{ \AA}$ rms.

Key Words: heterodyne interferometer; interferometry; laser mirror profilometry; mirror figure; profilometry; surface figure.

1. INTRODUCTION

Traditional optical interferometry involves splitting a beam of light and then recombining the beam after the two partial beams have traversed different optical paths. The length of one path acts as a reference against which the other (signal) path is compared. This comparison is usually done by means of measuring the relative phase difference (i.e., optical fringe shift) between the two paths. There are at least two major characteristics which may be associated with our idea of "traditional" interferometry: (1) a single light source (arc lamp or laser) is used to insure proper phase coherence and (2) the concept is based upon the precise measurements of relative phase. In practice this is done by measuring relative changes in intensity as measured by some photosensitive medium (film, photodiode, photocathode, etc.). This concept works well for most applications, but when very small displacements ($\delta\ell \ll \lambda$) are to be measured the experimentalist must be very careful to account for errors and/or ambiguities which may arise. These may be due to such things as low fringe contrast, time variations of fringe contrast, detector/film non-linear response and finally the limit of detectability (i.e., how precisely can fringe positions/spacings be determined?).

2. BACKGROUND

The concept discussed in this paper is based upon the relationship between the output frequency of a laser and its effective cavity length.¹ This relationship results from the boundary conditions applying to a resonant cavity, namely an integral number (N) of wavelengths (λ) must equal twice the cavity length (ℓ).

$$N\lambda = 2\ell \quad (1)$$

In a HeNe laser the (Doppler broadened) gain curve has a width of $\sim 1500 \text{ Mhz}$. From equation one we derive a longitudinal inter-mode spacing (Δ)

$$\Delta = \frac{c}{2\ell} \quad (2)$$

That is, by holding ℓ constant and varying N ($N \rightarrow N + 1$), the laser wavelength (frequency) changes to maintain the boundary conditions of equation one.

Conversely, if we consider a given longitudinal mode (N) and let the cavity length vary slightly (if the variation in ℓ is excessive the longitudinal mode corresponding to N will drift from under the gain curve, i.e., the laser "mode hops" as discussed above) the output frequency variation (δf) goes according to the relationship

$$\delta f = f \frac{\delta\ell}{\ell} \quad (3)$$

The potential sensitivity of this concept to small variations in cavity length becomes obvious when we plug typical numbers into equation three. Assuming a cavity length of one meter, nominal frequency of $5 \times 10^{14} \text{ hz}$, and a displacement ($\delta\ell$) of one Angstrom (10^{-10} m), the resulting shift in the laser's output frequency is about five kilohertz.

To detect this frequency shift a reference (fixed) frequency source can be used. By employing another HeNe laser oscillator as this reference we can be assured that the reference frequency (f_0) will lie within a few hundred megahertz of the signal laser frequency (f). This

difference frequency ($f_0 - f$) can be electronically monitored by interfering the beams from the two lasers on a high-speed photodetector (Figure 1) and feeding the detector output into an electronic spectrum analyzer.

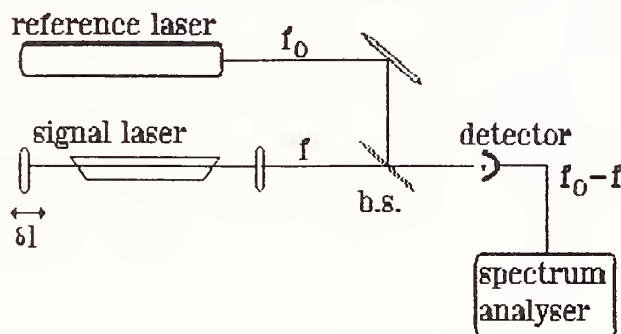


Figure 1. Heterodyne interferometry

A recording of the spectrum analyzer output as a function of time will, after proper scaling according to equation three, produce a time history of the variations in effective signal laser cavity length.

3. EXPERIMENT

The surface profilometry experiment is relatively simple in concept if not in practice. The mirror under test serves as the flat mirror of a folded spherical (half-symmetric) Fabry-Perot resonator cavity. This cavity acts as the stable resonator for a helium-neon (.633 μm) laser. The flat mirror in question is mounted on an air bearing and is rotated in a plane perpendicular to the laser optical axis (Figure 2). As the bearing rotates the laser spot traverses a circle on the surface of the test mirror. The radius of this circle is adjustable by translating the mirror-bearing assembly in a direction transverse to the optic axis. The output frequency from this laser is compared to that of a reference laser and the difference frequency is monitored as a function of bearing rotation phase angle. As the mirror rotates, deviations of its surface from a plane cause cavity length excursions in the "signal" laser. These length changes are manifest as changes in the inter-laser beat frequency. By taking data over many revolutions any random frequency excursions can be averaged out, leaving a relief map of the mirror surface at that radius. This surface map is completed by compiling data at several discrete values of radius.

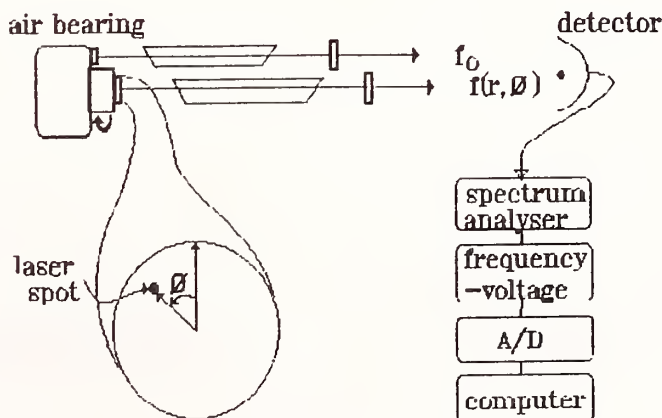


Figure 2. Differential cavity profilometer

4. APPARATUS

The first version of the apparatus consisted of the signal laser as described above and a commercial (Spectra-Physics model 133) HeNe laser as the reference frequency source. The noise levels (random excursions in the inter-laser beat frequency) were excessive with this configuration and it was replaced with a differential cavity arrangement (Figure 2). The experiment was mounted atop a granite slab which was supported by inflated inner-tubes to provide some degree of vibration isolation.

In this configuration the reference laser is an open cavity as is the signal laser. The advantage is that by having the cavities in a common mounting arrangement, common mode vibrations will affect both lasers similarly and thereby have a diminished effect on the inter-laser beat signal. This is especially important for the air-bearing mounted mirror since significant levels of vibration originate in the rotating bearing assembly. The beat signal developed by combining the beams from the reference and signal lasers on a high-speed (bandwidth ~ 1 GHz) photodiode is displayed on the CRT of a spectrum analyzer and stored in digital form on an Apple IIe computer. Details of the apparatus, techniques and circuitry developed to carry out these steps are described elsewhere.²

5. RESULTS

Figure 3 shows a mirror surface "profile" constructed by taking data at five radial distances from the center of a mirror under test. Run-to-run repeatability in the data was shown to be approximately 5 \AA rms, for averages of at least 50 samples per data point. "Profile" is set in quotes since the data does not support the registering of one radial data set to the next. The scans are azimuthal at constant radius so the data is insensitive to spherical aberrations. In this instance the data is arbitrarily registered at a fixed azimuthal position. This deficiency could be removed by replacing the micrometer stage with a (linear) air bearing to provide radial data scans.

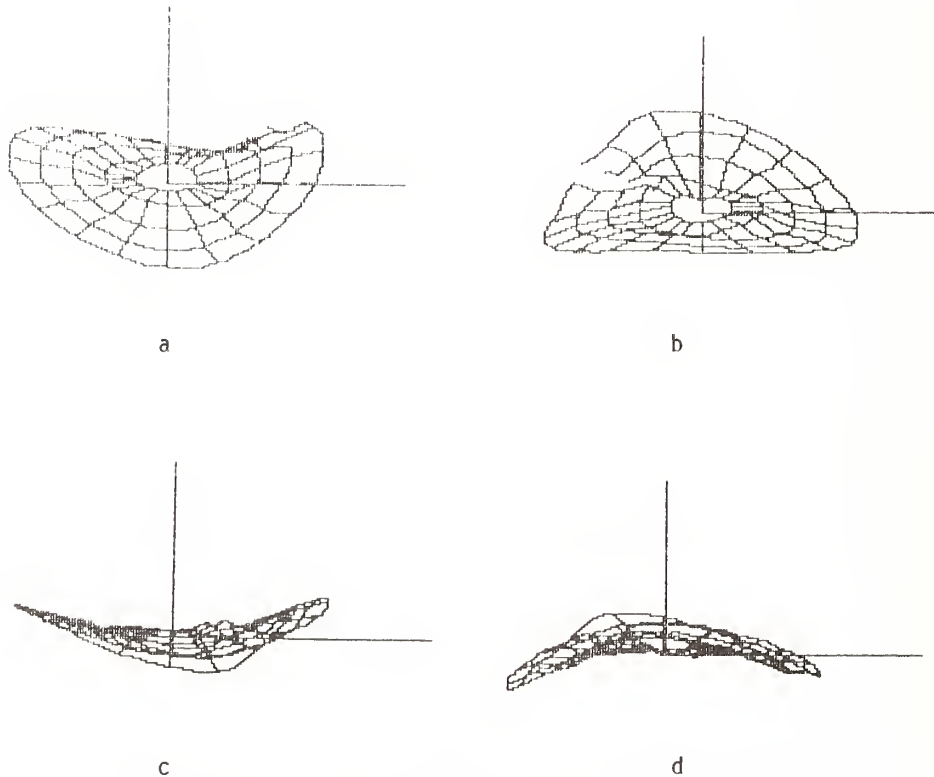


Figure 3. Surface contour generated from data taken at five radii and displayed at different aspect angles. The total surface relief is 303 Angstroms. (b and d are rotated 90°.)

6. CONCLUSIONS

We have demonstrated the sensitivity of the high-finesse (high-Q) interferometric technique, having made surface contour measurements repeatable to $\sim 5 \text{ \AA}$ rms with a relatively crude experimental apparatus. Further improvements to the experiment should provide a non-contact technique to measure surface height variations to levels approaching 0.01 \AA , with lateral resolution approaching $10 \text{ }\mu\text{m}$. The requirement for highly reflective surfaces can be reduced somewhat by passive cavity techniques (i.e., the test surface would constitute an element of a passive cavity pumped by a laser locked to the passive cavity resonance).

7. ACKNOWLEDGEMENT

I would like to thank Dr. Jim Small for his valuable insights and suggestions during the course of this work. This experiment was accomplished as a part of PhD dissertation research at the University of New Mexico.

8. REFERENCES

1. First proposed by Dr. J. Small in an unpublished white paper at the University of New Mexico. J. Small, "High-Q Interferometry."
2. J.R. Rotge', "Laser Heterodyne Interferometry for the Measurement of Small (Angstrom Level) Displacements," PhD Dissertation, University of New Mexico, Department of Physics and Astronomy. Publication pending.

Design and Construction of a Single Polarizer Infrared
Ellipsometer/Reflectometer for Characterization
of Highly Curved Surfaces

Jack B. Stubbs, John S. Loomis, and Thomas A. Leonard*
University of Dayton Research Institute
KL-464
Dayton, OH 45469
(513)229-3724

ABSTRACT

The University of Dayton has designed and built an Infrared Ellipsometer/ Reflectometer (E/R) to characterize curved surfaces in support of the ALPHA Laser Program. The instrument is tunable in wavelength and angle of incidence, is remotely controlled by a dedicated microcomputer, is positioned and scanned by a six-degree-of-freedom translation stage, and makes simultaneous measurements of R_p , R_s , ψ , and Δ .

A return path configuration was chosen to provide the versatility necessary for the variety of curved surfaces to be used in the ALPHA laser. This E/R is capable of measuring R_p and R_s to 0.1% accuracy and Δ to better than 0.1° accuracy on curved surfaces to 1.0 centimeter radius of curvature.

The optical design and theory of operation as well as automatic alignment and focusing features are discussed. Data taken with this instrument are presented.

Key Words: ellipsometer; infrared ellipsometry; infrared reflectometry; reflectometer.

1. Introduction - Design Considerations

The design specifications for the combined Ellipsometer/Reflectometer were to measure the reflectance of both P and S polarized light and the differential phase shift (Δ) to an accuracy of 0.1% and 0.1 degree respectively. These measurements are to be made at discrete wavelengths between 2.5 and 3.1 microns at angles of incidence between 20 and 55 degrees. The optics to be measured by this instrument are, in general, thick circular disks, cones, and rings varying from 28 to 142cm diameter. Reflectivities on the order of 96% to 99.7% are to be expected from these surfaces, implying a value of ψ near 45°. Delta values will vary from + 45° to - 45°. The small radii of curvatures near the truncated tips of the reflaxicon (0.76cm) and waxicon (0.36cm) are the most difficult areas to measure.

2. Instrument Configuration

The combined E/R instrument is configured as a return path, single rotating polarizer instrument capable of simultaneously measuring parallel and perpendicular reflectances (R_p and R_s) as well as the ellipsometric parameters ψ and Δ . The Spinning Polarizer Infrared Reflectometer/Ellipsometer (SPIRE) is configured to measure both flat and highly curved surfaces with focused light but may also be configured to measure flat surfaces with collimated light. SPIRE has been designed with a broad-band light source and narrow-bandpass, wavelength-selection filters. SPIRE can be used to make reflectance and ellipsometric measurements at 1.0 to 5.0 microns wavelength by substitution of the appropriate optical filter and can also be used to make measurements in the visible spectrum by substitution of an appropriate polarizer and detector.

SPIRE operates remotely and is controlled by a Hewlett-Packard 9836 microcomputer. Video cameras and monitors allow for the precise positioning and alignment of the instrument with respect to the optics to be characterized. Wavelength selection, angle of incidence positions (defined by the retro-arm position), data taking, and analysis are all performed by the dedicated computer.

*Thomas A. Leonard is currently at Analytic Decisions Inc., 5100/211 Springfield Pike, Dayton OH 45431 (513)258-1192

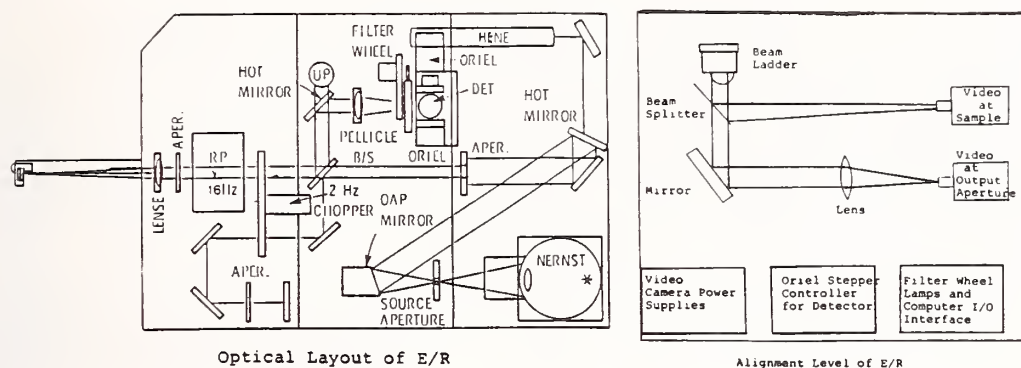


Figure 1. The optical layout for the return path, double bounce ellipsometer/reflectometer. The retro-arm is shown in the calibrate position. The alignment level provides auto-alignment and focusing.

Figure 1 is a view of the optical layout of the E/R and alignment shelf. The Helium-Neon Laser is used for visible alignment of all the internal optics. All optics are reflective except for the output lens, the Nernst glower lens, and the lens directly before the detector, so the only offset between the visible and infrared focal planes appears at these optics.

The light source is a Nernst glower shown in the lower right corner of figure 1. The unpolarized light from the glower is focused onto a 1-millimeter pinhole by an A/R coated, CaF_2 , 4-inch focal length lens. The light from the pin hole is collimated by a six-inch focal length off-axis parabolic mirror. The hot mirror directs the infrared light from the Nernst to the main optical axis on the center of the table. The hot mirror also allows the He-Ne beam to be transmitted from the back side, making it co-aligned with the Nernst light. The two apertures define the optical axis which passes through the measurement point (MEPO), which is defined by the retro-arm. A beamsplitter divides the incoming source beam into a reference beam and sample beam. The beam splitter is a coated pellicle, approximately seven microns thick, which eliminates secondary reflections. Both beams are directed through a rotating chopper wheel with a single aperture. The geometry is such that the reference beam and the sample beam alternately pass through the chopper. Background radiance measurements are made when neither beam is passing through the chopper.

After the reference beam passes through the chopper, it is reflected back along its original path. At the beamsplitter, it is again divided into two components. The reflected component is discarded while the transmitted component proceeds to the detector. The function of the reference beam is to provide a reference measurement of the source intensity.

After the sample beam passes through the chopper, it is converted to linearly polarized light by a polarizer. The 10-inch focal length Calcium Fluoride (CaF_2) lens at the front of the table focuses the infrared light to a 1.6 millimeter spot at the MEPO, from which it is collected by the 1.25 inch focal length spherical retro mirror (one inch diameter). The light then returns back through the same optics to the pellicle beamsplitter where it is reflected toward the detector. As the return beam passes through the polarizer, it is again converted to linearly polarized light. The path lengths of the reference arm and sample arm are equal. After returning to the beamsplitter both components follow an identical path to the detector, although not at the same time. From the beamsplitter the light travels to a second hot mirror where the visible light transmits to the upper table with the alignment cameras. The infrared light reflects from the hot mirror to a 4-inch focal length CaF_2 lens. The light is focused to the detector surface through the wavelength selection filters.

The reference beam remains unpolarized for its entire path. The sample beam is linearly polarized by the polarizer before the second pass through the beamsplitter. The fraction of the sample beam reflected to the detector is sensitive to its polarization state and in particular will depend on the orientation angle of the linearly polarized light.

The signal measured by the detector is repetitive, with its fundamental frequency determined by the rotation speed of the chopper wheel. The waveform, as it might be observed on an oscilloscope, is shown in Figure 2. The signal is AC coupled and inverted by the detector amplifier. Amplification is adjusted to cover the range -10 to +10 volts. A full period, or one chopper cycle, is divided into four parts, labeled B1, PR, B2, and PS. The chopper passes the sample beam during PS and the reference beam during PR. During B1 and B2, the chopper blocks both the sample and the reference beam. The width of the transition region between constant levels is determined by the time needed for a chopper edge to sweep across the corresponding beam. An A/D converter within the H-P computer system is used to sample the detector waveform. One channel on the encoder has a single pulse per revolution (PPR) which is used in the synchronization of the polarizer and chopper rotations. A second channel on the encoder contains 128 PPR. The 128 PPR are equally spaced and correspond to 2.8 degrees rotation of the polarizer. As shown in the waveform plot there are 8 complete cycles of the polarizer for each cycle of the chopper. This corresponds to 1024 pulses per waveform (1 chopper cycle).

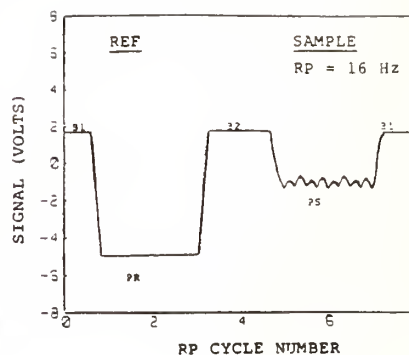


Figure 2. Example of the waveform for one complete chopper cycle. The chopper rotation rate is 2.5 Hz and the rotating polarizer rate is 20 Hz.

The background levels are averaged and subtracted from both the reference and sample levels to produce intensity values. The ratio of sample intensity to reference intensity is taken to cancel the effects of source intensity variation. A calibration measurement is required at each polarizer orientation to factor out the effects of the beamsplitter and retro mirror.

In actual operation, the polarizer rotates at a rate of 20 Hz while the chopper rotates synchronously at exactly one-eighth of the polarizer frequency. During each sample period PS, measurements are obtained for a series of polarizer positions. An angle encoder on the rotating polarizer ensures that the same polarizer positions are measured for any cycle. The encoder clocks each A/D conversion so that there are 128 measurements per cycle. This allows a Fourier decomposition using a Fast Fourier Transform. The amplitudes of the constant term and the second and fourth harmonics are used to calculate reflectance, ψ and Δ .

Two mechanisms worthy of further comment are the retro arm and the phase lock loop circuit which synchronizes the rotations of the polarizer and the light chopper.

The retro-arm is necessary to return the reflected light from the sample to the E/R pallet where the detector is mounted. The retro-arm must rotate about a point in space (MEPO) and allow the retro-mirror axis to always pass through that point. This is necessary to measure a defined location at any angle of incidence. The retro-arm design is shown in Figure 3. It incorporates an Aerotech rotary stage with 0.01 degrees rotation per step. This acts as a pivot for the lever arm action. A belt between the two pivot points allows for rotation of the retro-mirror about the pivot as well as about the measurement point.

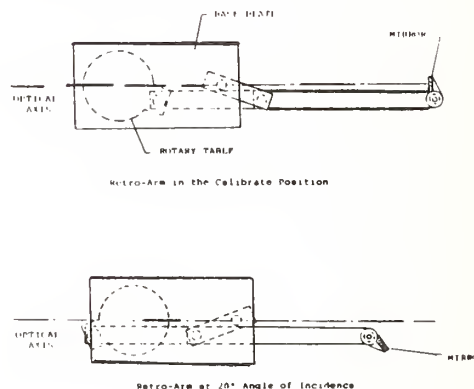


Figure 3. The retro-arm is shown in the calibrate position and at 20° angle of incidence. The retro-mirror may be positioned between 25° and 90° with 0.01° accuracy.

The chopper phase lock loop (shown in Figure 4) requires two input signals and produces an analog voltage to drive the chopper motor to the correct speed and angular position relative to the rotating polarizer. The one pulse per revolution (1 PPR) input coming from the rotating polarizer is connected to the 4040 counter. This divides the 1 PPR input by 2 to the N power where N is between 1 and 12 (1,2,4,8...4096).

The output of the divider is compared with the chopper input by the 4046 phase-locked loop-integrated circuit which generates two outputs. The first output generates a train pulse with a duty cycle proportional to the frequency difference and phase difference of the input signals. If the frequency at pin 14 is higher than at pin 3, then the output at pin 13 goes high or, conversely, if pin 14 is lower frequency than pin 13 then pin 3 goes low. When pin 14 and pin 3 are equal in frequency but differ in phase then the duty cycle is

proportional to the phase difference. A filter on pin 13 removes the AC component of the signal leaving the average (DC) to control the chopper motor speed. The amplifier is used to buffer this signal to prevent loading by the chopper controller. The voltage divider on the output of the buffer is necessary to allow the 4046 to operate in its linear region. It will not operate close to the negative supply (ground in this case).

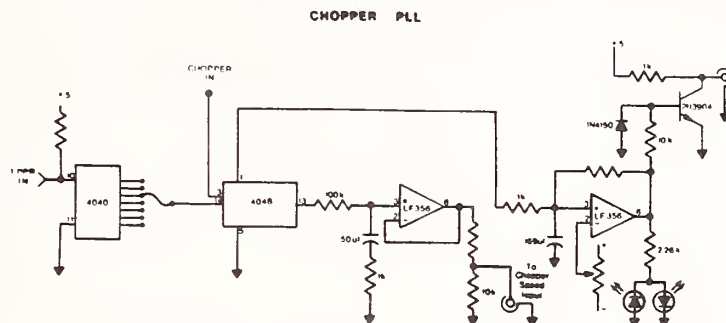


Figure 4. The chopper phase lock loop circuit controls the synchronization of the chopper and rotating polarizer to allow for data acquisition.

An ellipsometric measurement is concerned with the ratio of the principal amplitude reflectances ρ_D and ρ_S :

The angles ψ and Δ are called the ellipsometric angles.

$$E_1 = \begin{pmatrix} \sin(\theta) \\ \cos(\theta) \end{pmatrix}$$

The angle θ is the instantaneous polarizer orientation given by

where ω is the angular rotation rate and θ is the orientation at time zero.

$$E_2 = \begin{vmatrix} \rho_p^2 & 0 \\ 0 & \rho_s^2 \end{vmatrix}$$

where E_2 is the Jones vector after the second reflection.

The return beam can be projected onto the position of the polarizer to find the magnitude E of the Jones vector after the second pass through the polarizer.

$$E = [\sin(\theta) \cos(\theta)] E_2$$

This expression can be simplified to

$$E = \rho_p^2 \sin^2(\theta) + \rho_s^2 \cos^2(\theta)$$

The intensity I measured by the detector is given by

$$I = EE^*$$

The following equation is obtained by substituting for E to obtain

$$I = \rho_p^4 \sin^4(\theta) + \rho_s^4 \cos^4(\theta) + \frac{1}{2} \rho_p^2 \rho_s^2 \cos(2\theta) \sin^2(2\theta)$$

Reflectances and phase shift Δ are based on a harmonic analysis of the intensity I of the form:

$$I = b_0 + b_2 \cos(2\theta) + b_4 \cos(4\theta)$$

where

$$b_0 = 3(\rho_s^2 + \rho_p^2)/8 + \frac{1}{4} \rho_p^2 \rho_s^2 \cos(2\theta)$$

$$b_2 = \frac{1}{4} (\rho_s^2 - \rho_p^2)$$

$$b_4 = (\rho_s^2 + \rho_p^2)/8 - \frac{1}{4} \rho_p^2 \rho_s^2 \cos(2\Delta)$$

In the harmonic analysis, the offset angle θ_0 between the zero position of the rotating polarizer and the plane of incidence is contained in the phase terms. The magnitude of the harmonic coefficients is independent of the offset angle. Each harmonic analysis, therefore, implicitly includes a determination of the plane of incidence. The plane of incidence is then equal to the difference between the zero angle and half of the phase of the second harmonic.

The principal reflectances and the ellipsometric angles ψ and Δ can be obtained from the following equations:

$$\rho_s^2 = b_0 + b_4 + b_2$$

$$R_p^2 = b_0 + b_4 - b_2$$

$$\cos(2\Delta) = (b_0 - 3b_4)/(R_p R_s)$$

$$\tan^2 \psi = R_p/R_s.$$

The harmonic coefficients are non-negative because they represent magnitudes. Thus, the above equations explicitly assume that R_s will be greater than R_p . If this is not the case, the phase of the second harmonic will be 90° shifted from its normal value, indicating that R_p is greater than R_s . The second harmonic becomes zero when R_p is equal to R_s .

In ellipsometers without compensators, the phase shift Δ appears as $\cos(\Delta)$. Taking the inverse cosine leads to an ambiguity in determining Δ . Angles in the lower half plane have the same cosine as those in the upper half plane. In a double-bounce ellipsometer, the phase shift appears as $\cos(2\Delta)$. The sensitivity in measuring phase shift is increased because the sample is traversed twice, but the ambiguity also increases. The cosine function has a principal range of 0° to 180° . Removing the factor of two reduces the principal range to 0° to 90° . Thus, all phase shifts are folded into the first quadrant. This folding process must be kept in mind when interpreting the results of a SPIRE measurement.

Another implication of the cosine dependence on Δ is that the measurement varies quadratically for angles near 0° to 180° . The lack of a linear term means that the precision of the measurement decreases as the cosine argument approaches either 0° or 180° .

After some trigonometric manipulation, it is possible to write the equations for the harmonic coefficients in a form where the ellipsometric angles appear explicitly:

$$b_0 = \frac{1}{2}(R_s^2 + R_p^2) + \frac{1}{2}R_p R_s [\cos^2(2\Delta) - \csc^2(2\psi)]$$

$$b_2 = R_p R_s [\cot^2(\psi) - \tan^2(\psi)]$$

$$b_4 = \frac{1}{2}R_p R_s [\sin^2(2\Delta) + \cot^2(2\psi)]$$

In this form, the ellipsometric dependence of the second harmonic is only on ψ . The other harmonics depend on a mixture of ψ and Δ . There is some additional simplification for the case $R=R_p=R_s$, where the angle ψ is 45° and the harmonic equations reduce further to the form

$$b_0 = \frac{1}{2}R^2 + \frac{1}{2}R^2 \cos^2(2\Delta)$$

$$b_2 = 0$$

$$b_4 = \frac{1}{2}R^2 \sin^2(2\Delta)$$

b_0 , b_2 and b_4 are the coefficients for the modulus, and the second and fourth harmonic terms of the harmonic series which describes the E/R waveform. Now the fourth harmonic depends only on Δ . Measurements on metal reflectors, where ψ is approximately 45° , essentially satisfies these conditions. Then the second harmonic measures the departure of ψ from 45° and the fourth harmonic measures the value of Δ .

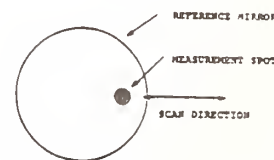
The equations used to obtain the ellipsometric angles involve ratios of the harmonic coefficients. It is possible to obtain accurate ellipsometric values under conditions where the reflectance measurements are not accurate because of light lost to the measuring

instrument. Ellipsometric angles are obtained as the ratio of reflectances. If a fixed fraction of the reflected beam is blocked or otherwise removed from the measurement, an ellipsometric measurement is still possible. This vignetting affects each polarization component equally. Therefore, the ratio is not affected.

4. Edge Detection

When the SPIRE instrument is coupled with a manipulator system, the combined system offers a mechanism for alignment. The basic measurement is that of edge detection. During edge detection, the measurement spot is stepped across the edge and the reflectance is measured as a function of position. The reflectance is obtained by averaging the ratio measurements for all polarizer positions. The averaging operation is equivalent to using the zero harmonic as a measure of reflectance, but does not require as much time as an explicit Fourier transform.

To make an edge measurement, one endpoint of the scan must be entirely on the mirror. This is the position of maximum reflectance. The other endpoint must be entirely off the mirror. The test geometry is shown in Figure 5. This is the position of minimum reflectance. Between these two positions, as shown in Figure 5, the reflectance remains constant except for the transition positions where the measurement spot overlaps the edge. In the transition region there will be two shoulders and a middle linear portion. The linear portion is centered on the inflection point of the edge scan. This inflection point represents the edge of the mirror. For a symmetric measurement situation, the inflection points occur when the measurement spot is half on the mirror so that the reflectance is halfway between the maximum and minimum values. In addition, the shape of the curve will be symmetric about the inflection point.



Test geometry for edge detection.



Figure 5. Test geometry and components of an edge scan.

In analyzing an edge scan, the endpoints of a measurement sequence are used to determine the reflectance span (R_{span}) between minimum and maximum reflectance. The target reflectance (R_e) is the average of the endpoints. The limits of the linear portion are assumed to be a fixed fraction of the reflectance span. The default fraction is 0.5. The linear region is then defined as all points within the range

$$|R - R_e| \leq 0.5 R_{span}$$

where R_e is the target reflectance, and R_{span} is the reflectance span.

In finding the edge, the software first determines whether the scan starts high or low. Then it locates the point along the scan where the previous point is above (below) R_e and the current point is below (above) R_e . These points are sufficient to provide a linear interpolation of the edge position. However, the software examines the points in the vicinity of the transition point and uses those within the linear limit to make a least-squares linear fit of the edge position. This process ensures a successful edge measurement even if the scan points are unequally spaced or spaced too far apart compared to the extent of the linear region. Maximum precision is obtained when a number of measurement points lie within the linear region and the endpoints are sufficiently away from the edge to eliminate the effects of the edge.

A single edge measurement determines both the position of the edge and the width of the measurement spot. The location of the point R_e along the scan determines the edge location. The slope of the reflectance scan at the edge determines the beam width. A working definition of beam diameter d is given by

$$d = R_{span} / \text{slope}$$

An explicit definition depends on a model of the beam profile. A Gaussian profile, for example, may be an adequate representation of the beam profile, in which case the measured beam diameter can be related to the e^{-2} energy point.

This edge scanning routine is used with various modifications to perform system focus scans, detector centering, sample positioning, and various internal alignments.

5. Measurements and Results

There are no other instruments to date capable of measuring reflectance and ellipsometric data on highly curved surfaces, so determining the accuracy of the E/R became a very detailed task. Confirmation of accuracy on flat surfaces was accomplished by measuring bare metal flats and comparing to theoretical value, and other reported measurements.

The reflectance accuracy on flat surfaces was determined by measuring copper samples, comparing to theoretical values, and also making absorption measurements on the same samples. The ellipsometric accuracy was determined by comparing measurements with those made on a four-zone null ellipsometer.

The accuracy for reflectance and ellipsometric measurements on flats is $\pm 0.1\%$ in reflectance and 0.1 degrees in differential phase. The accuracy in reflectance and ellipsometric parameters on curved surfaces was determined by manufacturing a conical mirror with a flat surface on approximately 5% of the surface. This permits the measurement of flat surfaces and curved surfaces on one uniformly gold-coated sample. The accuracy for reflectances measurements is 0.2% on conical surfaces with curvature down to 20 millimeters radius. Ellipsometric accuracy is 0.1°. The ellipsometric data taken in a photometric mode is not sensitive to light losses as are reflectance measurements. Phase is determined from a ratio and the ratio is unaffected by some light loss. A summary of the instrument performance is shown in Table 1.

Table 1. Ellipsometer/Reflectometer Performance Summary

PARAMETER	PERFORMANCE
Measurement wavelength	$\lambda_1 = 2.622 \mu\text{m}$ $\lambda_2 = 2.745$ $\lambda_3 = 2.820$ $\lambda_4 = 2.995$ $\lambda_5 = 3.129$
Spectral Bandwidth	FWHM = $2\% \pm .1\%$ center λ
Reflectance	measure R_p & R_s separately
Range in R	40 + % to 100%
Accuracy in R	$\pm 0.1\%$ flats; $\pm 0.2\%$ conics
Range in Δ	$\pm 45^\circ \phi_s - \phi_p$
Accuracy in Δ	$\pm 0.1^\circ$
Angle of incidence range	$20^\circ - 55^\circ$
Accuracy in setting angle of incidence	$< \pm 0.1^\circ$
Autocollimation accuracy	$\sim 0.01^\circ$
Edge locating accuracy	$\sim \pm 10 \mu\text{m}$

Direct n_2 Measurement in Yttria Stabilized Cubic Zirconia

Shekhar Guha,* Nastaran Mansour, and M. J. Soileau

Center for Applied Quantum Electronics
Department of Physics
North Texas State University
Denton, TX 76203

We present here the results of direct measurement of the nonlinear refractive index, n_2 , of yttria doped cubic zirconia at $1.06 \mu\text{m}$ using external self-focusing. The value of n_2 was found to be independent of the yttria concentration. The measured value (6×10^{-13} esu) compares well with that calculated from the breakdown measurements [1].

Key words: external self-action; laser induced damage; nonlinear refractive index; psec pulses; yttria stabilized cubic zirconia; $1.06 \mu\text{m}$.

1. Introduction

Cubic zirconia is an attractive candidate for window material in high power laser systems because of its transparency, mechanical strength, and stability when doped with yttria (Y_2O_3). A knowledge of the nonlinear refractive index n_2 is therefore necessary in the design of such laser systems to properly account for the nonlinear beam propagation effects as well as in evaluating the role of self-focusing in laser-induced damage process. n_2 of yttria stabilized zirconia (YSZ) has previously been inferred from breakdown critical power. We present here a description of an analysis and experiments used to directly determine n_2 in the YSZ using picosecond pulses of different states of polarization.

2. Analysis

The mechanism used to measure n_2 is that of external self-focusing [2] in which a collimated laser beam of Gaussian temporal and spatial profile is incident on a thin sample. (The sample thickness is much less than the confocal parameter of the laser beam.) In this case the diffraction of the laser beam inside the nonlinear medium can be ignored and the irradiance I and phase of the electric field

$$E = \sqrt{\frac{2I}{n_o \epsilon_o c}} e^{i\phi} \quad (1)$$

of frequency ω follow the propagation equations:

$$\frac{dI}{dz} = -\alpha I \quad (2)$$

$$\frac{d\phi}{dz} = \beta_1 I \quad (3)$$

where α is the linear absorption coefficient and β_1 is related to n_2 through

$$\beta_1 = \frac{40\pi\delta}{c^2 n_o} n_2 \text{ (esu)} \quad (4)$$

*Present address: Martin Marietta Laboratories, Baltimore, MD 21227

The laser beam is assumed to be Gaussian in temporal and spatial profile and incident on the sample at $z=0$ with irradiance

$$I(0,r,t) = I_0 \exp [-(r/r_0)^2 - (t/t_0)^2] \quad (5)$$

For a medium of length l and reflectivity R , the transmitted irradiance is given by

$$I(l,r,t) = (1-R)^2 \exp(-\alpha l) I(0,r,t) \quad (6)$$

and the phase change on transmission through the sample is given by

$$\phi(l,r,t) - \phi(0,r,t) = \beta_l \left(\frac{1 - (1-R)^2 e^{-\alpha l}}{\alpha} \right) I(0,r,t) \quad (7)$$

The irradiance and the phase obtained from equations 6 and 7 completely determine the electric field $E(l,r,t)$ at the exit plane of the sample from which the field at any point $(l+z,r,t)$ can be determined using the Huygens-Fresnel propagation formalism [3]

$$E(l+z,r,t) = \frac{2\pi}{i\lambda z} \exp(i\pi r^2/\lambda z) \int_0^\infty E(l,r',t - z/c) \times \exp(i r'^2/\lambda z) J_0(2\pi r r'/\lambda z) r' dr' \quad (8)$$

The experimentally measured quantity is the fluence at the observation plane at a distance z from the sample. The fluence is

$$F = \frac{c\epsilon_0}{2} \int_{-\infty}^\infty |E(l+z,r,t)|^2 dt \quad (9)$$

3. Experiment

The apparatus used is described in greater detail elsewhere [4]. Single pulses of measured Gaussian spatial and temporal profiles were obtained from a microprocessor-controlled, passively mode-locked Nd:YAG laser system operated at 0.5 Hz. Single pulses were switched out of the mode locked pulse train and amplified. About 1 mJ of energy in the infrared was routinely available in pulses of 30 ps to 200 ps width. The pulsewidth was varied by using etalons of different thickness as the output coupler of the laser. Attenuation of the energy in the pulse was achieved by using a half-wave plate polarizer combination which produced no measurable aberrations on the spatial profile of the beam. The shot-to-shot variations of both the energy and the pulsewidth were monitored. The change in the spatial profile of the laser beam transmitted through the sample with increased incident irradiance was determined by using a vidicon tube interfaced with a microprocessor controlled optical multichannel analyzer (PARC 1215). By using a pinhole (25 μm diameter) mounted on a photodetector, the on-axis fluence of the transmitted signal was also measured as a function of the incident irradiance.

4. Results

Figures 1 and 2 show the result of measuring the transmitted on-axis fluence in the near field as a function of irradiance for 30 psec, 1.06 μm pulses of linearly and circularly polarized light incident on 1 cm long samples of YSZ. Up to the highest irradiance used, no nonlinear absorption was observed in the sample. Three samples of YSZ were studied, with yttria concentrations of 9.4%, 12%, and 21%, respectively. The measured n_2 was found to be independent of the yttria concentration. The solid lines in figures 1 and 2 are the theoretical fit obtained from equations 6 and 7, with the value of n_2 as the only free parameter. The best fit to figure 1 was obtained for

$n_2 = 6 \times 10^{-13}$ esu. For comparison, in figure 3 we show the results of the same experiment performed on a sample of sodium chloride. The value of n_2 in YSZ was found to be 9.5 times more than that of sodium chloride. The ratio of n_2 (linear)/ n_2 (circular) was found to be close to 1.5 for each sample. The value of n_2 obtained by this method compares well with the value of 8×10^{-13} esu estimated from the measurement of the breakdown power (P_B) of 400 kW.

5. Summary

External self-action provides a relatively simple procedure for estimating the nonlinear refractive index, n_2 . This method was used to determine n_2 for yttria doped cubic zirconia. The value obtained compares well with that determined by other methods.

6. References

- [1] Mansour, N.; Soileau, M. J.; Van Stryland, E. W. "Picosecond damage in Y_2O_3 stabilized cubic zirconia." Natl. Bur. Stand. (U.S.) Spec. Pub.; 1984.
- [2] Weaire, D.; Wherrett, B.S.; Miller, D. A. B.; Smith, S. D. "Effect of low-power nonlinear refraction on laser-beam propagation in InSb." Opt. Lett. 4(10): 331-333; 1979.
- [3] Born, M.; Wolf, E. "Principles of optics," 5th ed. Oxford, U.K.; Pergamon Press; 383; 1975.
- [4] Van Stryland, E. W.; Soileau, M. J.; Smirl, A. L.; Williams W. E. "Pulsewidth and focal volume dependences of laser-induced breakdown." Phys. Rev. B 23(5): 2144-2151; 1981.

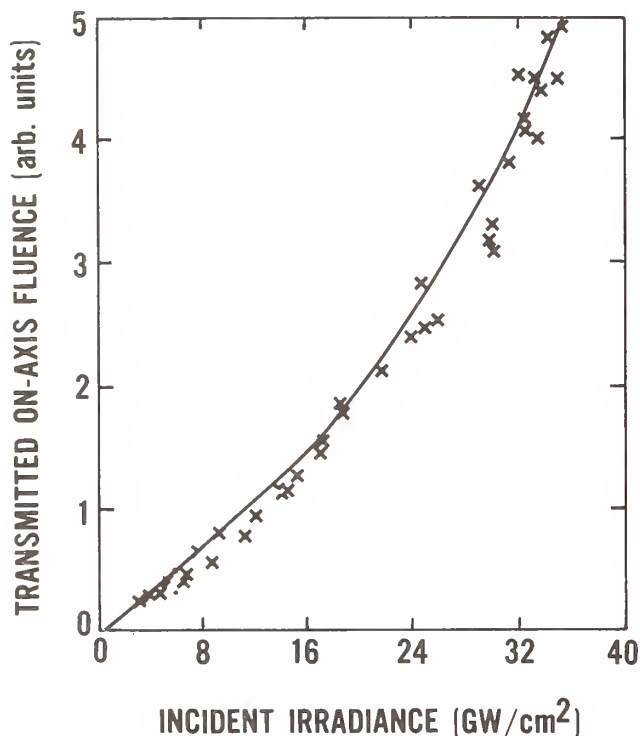


Figure 1. The transmitted on-axis fluence measured as a function of incident irradiance for zirconia, using $1.06 \mu\text{m}$, 30 psec, linearly polarized pulses. The measurement was performed in the near-field region. The solid line is the theoretical fit with $n_2 = 6 \times 10^{-13}$ esu.

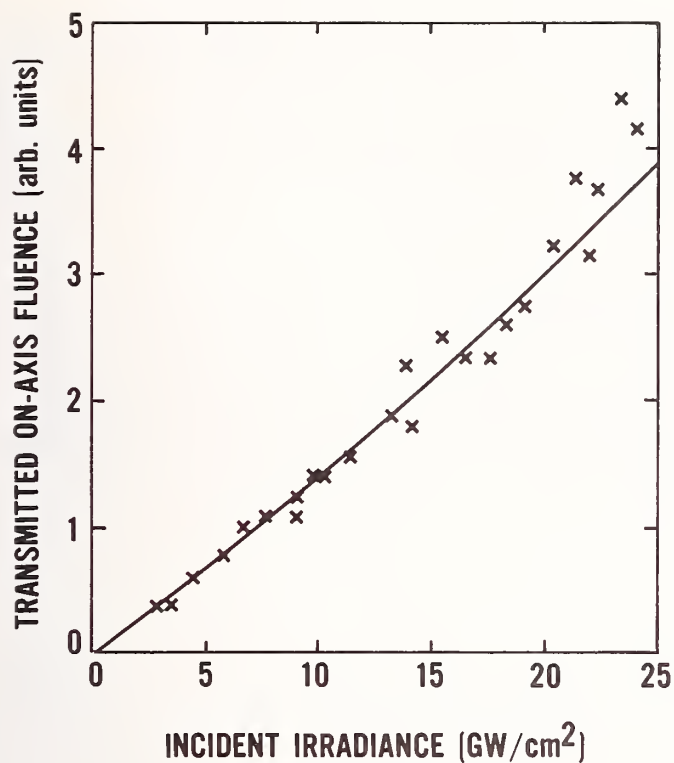


Figure 2. The transmitted on-axis fluence measured as a function of incident irradiance for zirconia, using 1.06 μm , 30 psec, circularly polarized pulses. The measurement was performed in the near field. The solid line is the theoretical fit.

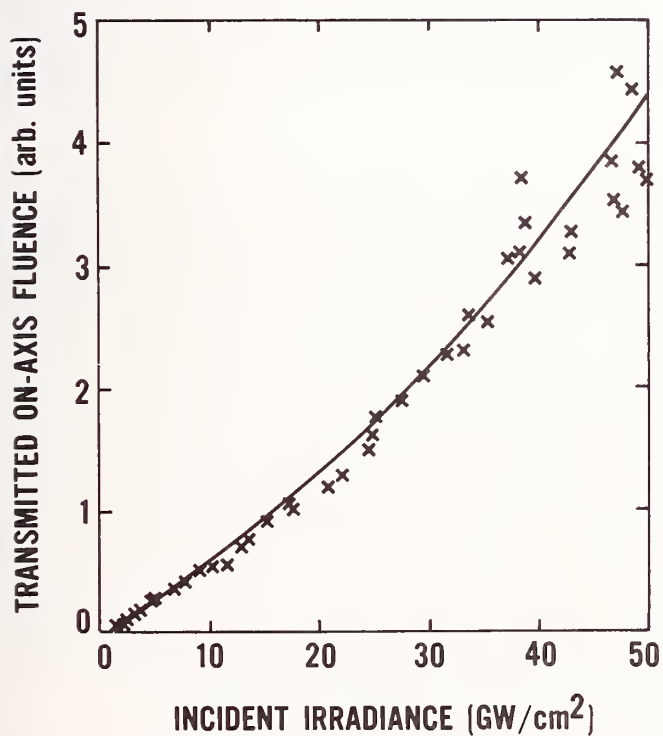


Figure 3. The transmitted on-axis fluence measured as a function of incident irradiance for zirconia, using 1.06 μm , 30 psec, linearly polarized radiation. The measurement was performed in the near field. The solid line is a theoretical fit with $n_2 = 4.5 \times 10^{-12}$ esu.

Measurement of Optical Damage Threshold of Wire Grid Polarizers at $10.6\text{ }\mu\text{m}$

M. Mohebi, A. Said, and M. J. Soileau

Center for Applied Quantum Electronics
Department of Physics
North Texas State University
Denton, Texas 76203

We report the results of measurement of laser induced surface damage threshold of wire grid polarizers at $10.6\text{ }\mu\text{m}$ as a function of orientation of the wires and polarization of light. We also measured the absorption of wire grids at $10.6\text{ }\mu\text{m}$, 1.06 , and $0.53\text{ }\mu\text{m}$. The results of surface damage thresholds are consistent with the results of absorption measurements and theory.

Key words: absorption; damage threshold; photoacoustic; polarization; wire grid.

1. Introduction

Microscopic wire grids deposited on a dielectric grating at grazing angle are useful polarizers. They are compact, easily rotatable, can be used with converging and diverging beams, and work with all wavelengths at least four times smaller than the period of the grid, as long as the substrate's transmission permits. Gratings with a period as small as $0.4\text{ }\mu\text{m}$ are commercially available. (Wire grid polarizers used in this work were acquired from PTR Optics Corporation, 145 Newton, Waltham, MA 02454.) With proper choice of the substrate, wire grid polarizers can be fabricated for use at any wavelength for $2\text{ }\mu\text{m}$ to far infrared. However, their principal limitation for use with high power lasers is their damage properties. In this work we have measured laser induced surface damage threshold of wire grid polarizers for pulsed radiation at $10.6\text{ }\mu\text{m}$ as a function of orientation of wires with respect to the polarization of laser beam. In addition, we measured absorption vs. λ and orientation.

2. Experimental Results

The polarizers used in our experiment were two wire grids of aluminum deposited on ZnSe substrates, one of the samples was overcoated with an antireflection (AR) coating on both surfaces. The period of wire grids was $0.84\text{ }\mu\text{m}$ with a symmetric 90° sawtooth groove shape. The measurements were performed using linearly polarized, normal incident pulses from a hybrid CO_2 TEA laser. The laser was operated in the TEM_{00} spatial mode and single longitudinal mode with 130 ns (FWHM) pulses. Figure 1 shows a pinhole beam scan of the spatial profile of the beam as well as a temporal profile detected by a photon drag detector (500 MHz response). The beam scan was performed just before a lens ($F=25.4\text{ cm}$) which focused the beam on the wire grid to a beam size of 0.36 mm (FWHM). Each site was irradiated only once (one-on-one measurement). Figure 2a shows the experimental results for the sample with no AR coating for orientation of the wires parallel and perpendicular to the incident electric field. The damage threshold for this sample was 2 J/cm^2 (corresponding to a peak-on-axis irradiance of 15 MW/cm^2) when the wires were parallel to the incident electric field. Here we have defined the damage threshold as the lowest incident fluence (or irradiance) for which damage occurred. The relatively large overlap region for this sample was because of nonuniformities of the surface structure. Figure 2b shows the results for the sample with AR coating on both sides. The damage threshold for this sample was 0.8 J/cm^2 (6 MW/cm^2) when the wires were parallel to the incident polarization. The damage threshold of both samples increased by more than a factor of two when the wires were oriented perpendicular to the incident electric field (i.e., the orientation for maximum transmission).

In order to study the effects of orientation of wires on the absorption of the wire grids we monitored the photoacoustic (PA) signal generated in the wire grid by coupling a transducer to the side of the sample. The beam size on the front surface of the sample was kept large (3.2 mm FWHM), in order to avoid surface damage. Figure 3 shows the PA signal as a function of incident power for both orientations. The absorption of wire grid was greater by a factor of ~ 3.6 when the polarization was parallel to the wires. This is consistent with the measurement of damage threshold in the parallel and perpendicular orientation. It is well known [1,2] that the optical properties of wire grids are strongly dependent on the ratio of wavelength to the period

of wires (λ/d). The wire grids are effective polarizers only when $\lambda/d \gg 1$. Both polarizations tend to be equally transmitted or reflected for λ/d close to or smaller than one. We used 30 ns pulses from YAG laser at $1.06 \mu\text{m}$ and its second harmonic ($0.53 \mu\text{m}$) to change λ/d in our experiment. Figure 4a shows the PA signal versus incident power at $1.06 \mu\text{m}$ for both orientations. The absorption is smaller by a factor of 0.6 when the wires are parallel to the electric field. Figure 4b is the result of the same measurement at $0.53 \mu\text{m}$. It shows that absorption is smaller by a factor of 0.8 when the wires are parallel to electric field.

3. Theory and Discussion

The theory of operation of wire grid polarizers has been the subject of investigations by many researchers [3-5] in the past. All theoretical treatments start by assuming an ideal cross section for the wires. Flat strips [3] and cylindrical wires [4-5] have been considered. The effect of nonuniformities in the wires cannot be easily treated. Only the plane wave approximation has been considered. The problem of incident electric field with polarizations other than parallel to the wires, including ohmic loss has not been considered before. The reflected wave is regarded as originating from the currents induced in the wires, while the transmitted wave is the superposition of the induced and incident fields. Absorption is considered as the difference between incident and sum of transmitted and reflected waves. The current in wires all have the same magnitude (for plane wave illumination), but differ in phase from wire to wire by $Kd \sin \alpha$, where $K=2\pi/\lambda$ and α is the angle of incidence. When the electric field is parallel to the wires the current has the same phase everywhere along any given wire. The effect of adding ohmic loss of conducting wires to this picture is to decrease the amplitude of reflection coefficient and the phase of the transmission coefficient. Cassey's [5] calculations show that the loss in the wires depends directly on the square of reflection coefficient, that is, the absorption of wire grid is greater when its reflection is greater. This is consistent with the results of measurements of absorption vs. orientation in this work. Bird and Parrish [1] investigated the wire grids experimentally and found that the transmission curves for parallel and perpendicular polarization cross one another when λ/d is decreased to a value of one. Their result was in agreement with the theoretical work of Baldwin [3]. This suggests that reflection, and therefore absorption, curves for parallel and perpendicular polarization cross over when λ/d is close to one. This is also consistent with the measurement of absorption at three different wavelengths in this work. This qualitative agreement is striking, considering that in this experiment we have a Gaussian profile beam, and the fact that wire cross section is neither a flat strip nor a cylinder.

4. Summary

We have measured the surface damage thresholds of wire grid polarizers at $10.6 \mu\text{m}$. Damage thresholds were maximum when the polarization of light was perpendicular to the wires, and the damage thresholds were greater for the uncoated wire grid. The ratio of absorption of parallel polarized light to the absorption of perpendicular polarized light depends on λ/d . The ratio of these two absorption is greater than one for $\lambda/d \gg 1$ and it is less than one for λ/d close to or smaller than one. Measured absorptions at three different wavelengths are in agreement with the theory.

5. References

- [1] G. Bird and M. Parish, J. Opt. Soc. Am. 50(9), 886-891 (1960).
- [2] M. Hass and M. O'Hara, App. Opt. 4(8), 1027-1031 (1965).
- [3] G. Baldwin and A. E. Heins, Math. Scand. 2, 103-118 (1954).
- [4] E. A. Lewis and J. P. Casey, J. Appl. Phys. 23(6), 605-608 (1952).
- [5] J. P. Casey and E. A. Lewis, J. Opt. Soc. Am. 42(12), 971-977 (1951).

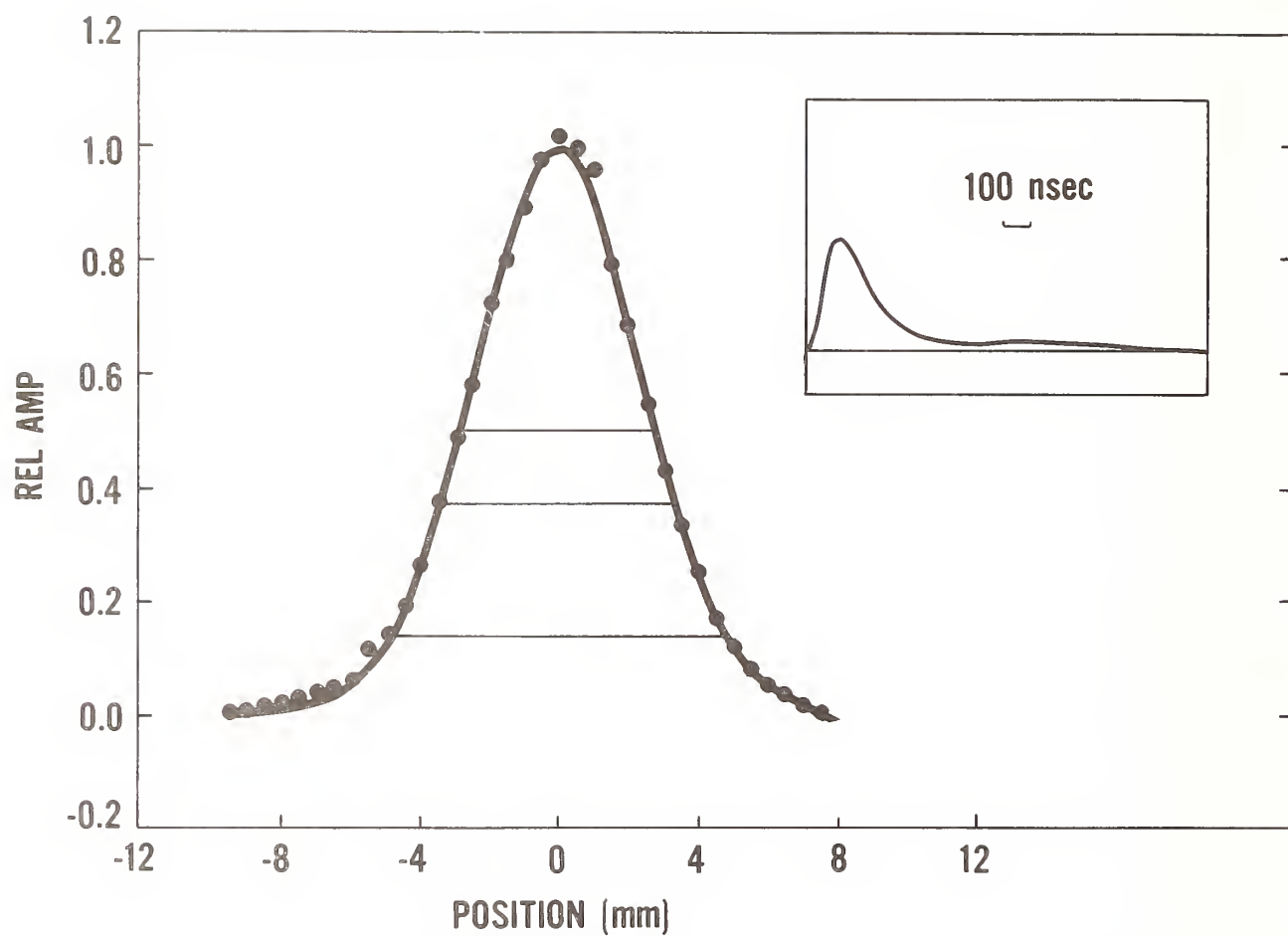


Figure 1. The 200 μm pinhole beam scan performed just before the focusing lens ($F=25.4$ cm). The inset shows the temporal profile of the pulse.

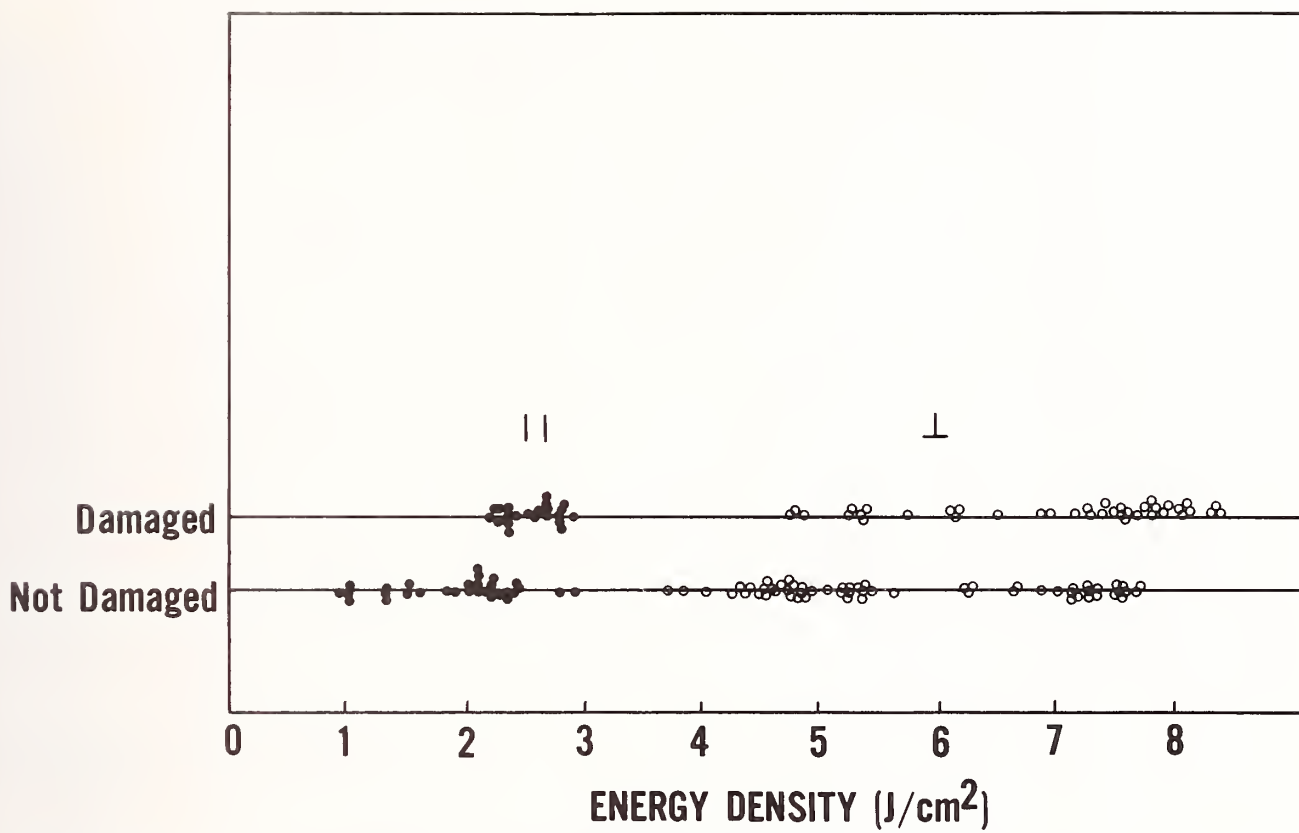


Figure 2a. Damage data for the wire grid without AR coating. Each point represents a single shot. Open circles are for polarization perpendicular to the wires. Closed circles are for polarization parallel to the wires.

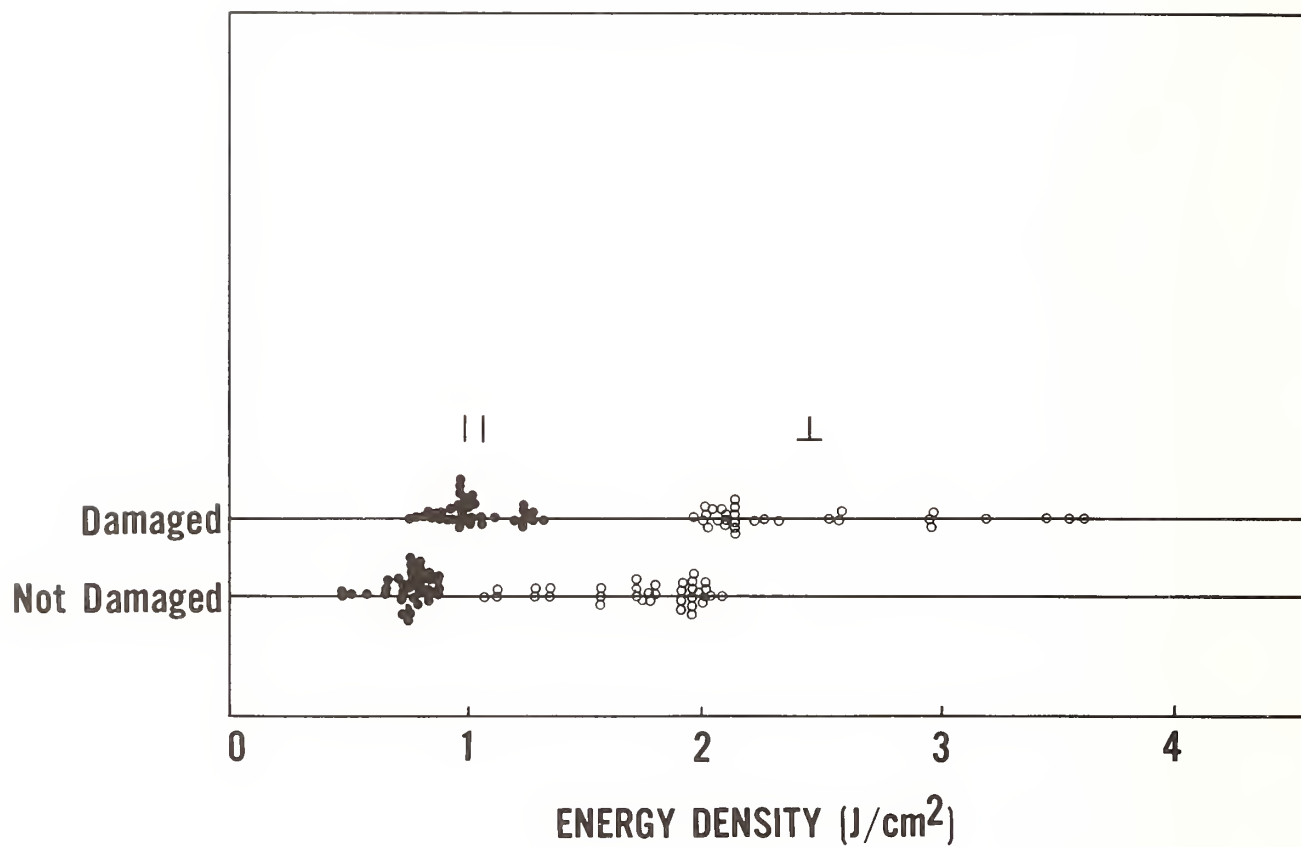


Figure 2b. Damage data for the wire grid with AR coating. The damage threshold for this sample was less than the sample without AR coating by more than a factor of two.

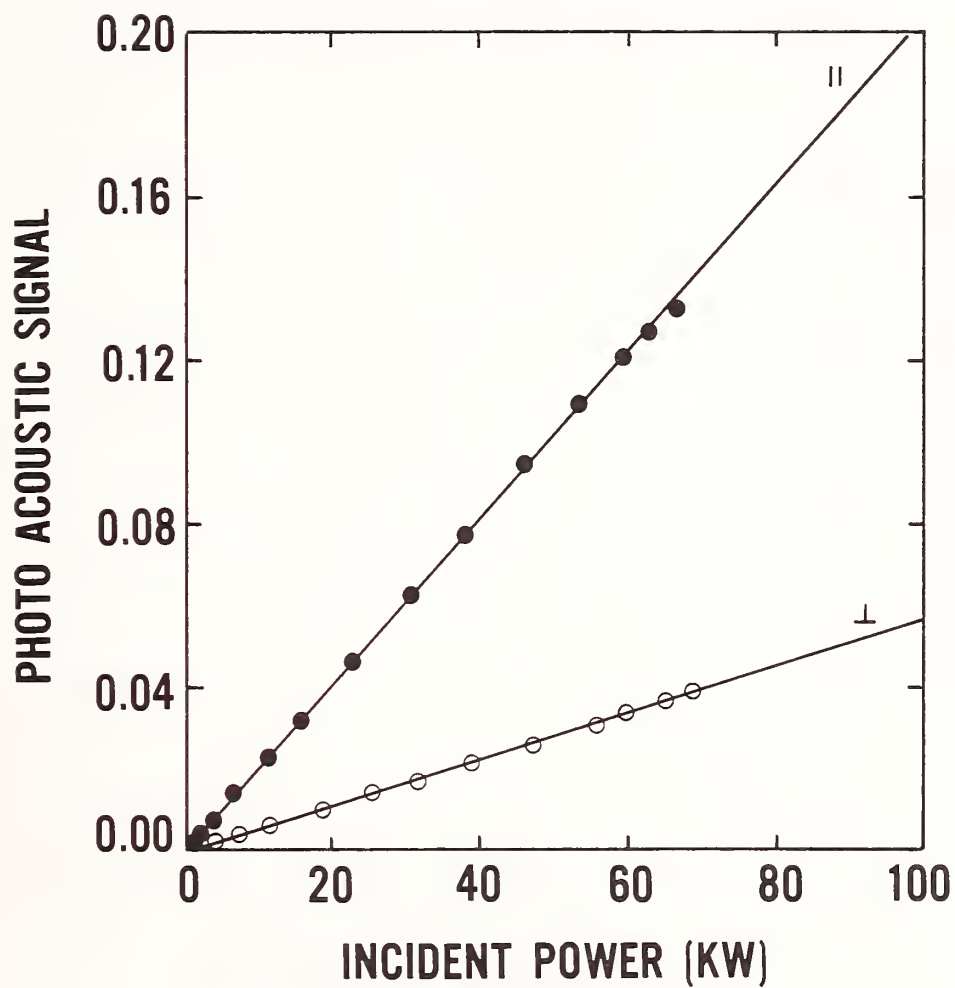


Figure 3. Absorption of the wire grid at $10.6\ \mu\text{m}$. The photoacoustic signal indicates greater absorption when the wires are parallel to the polarization of the incident electric field.

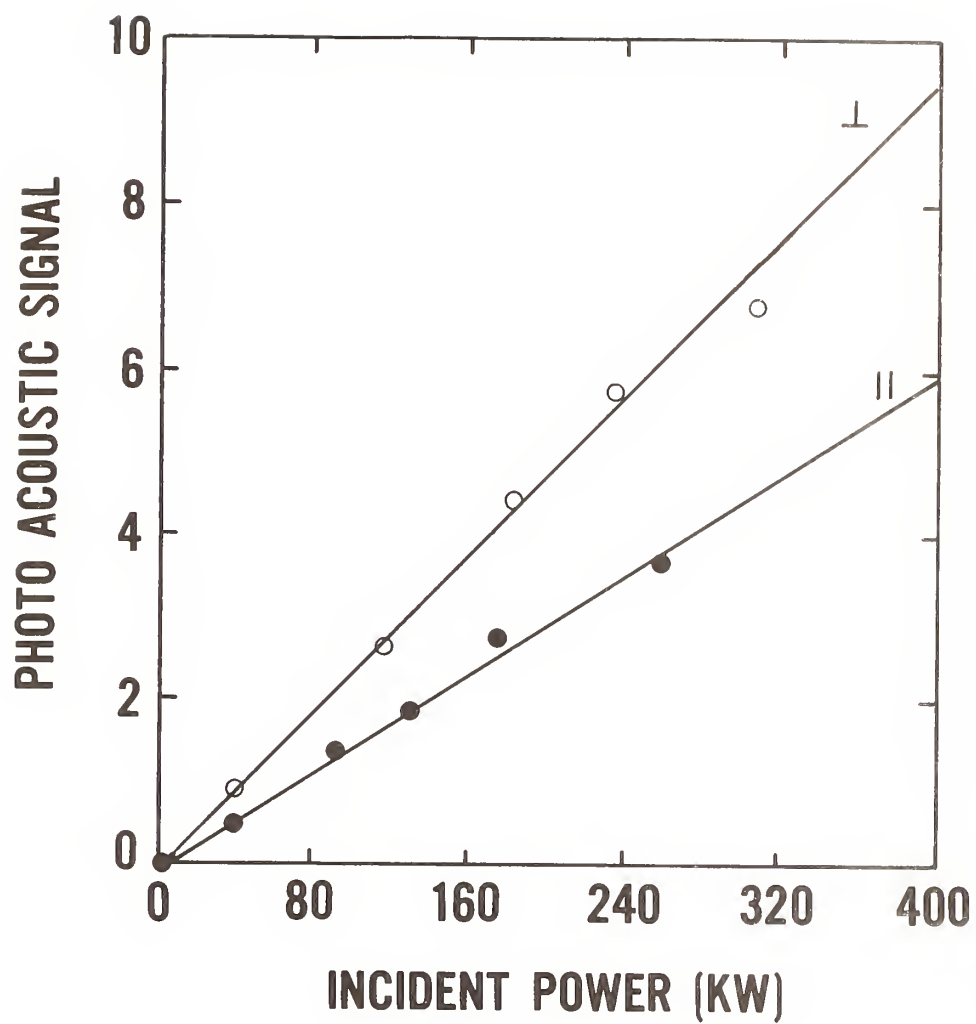


Figure 4a

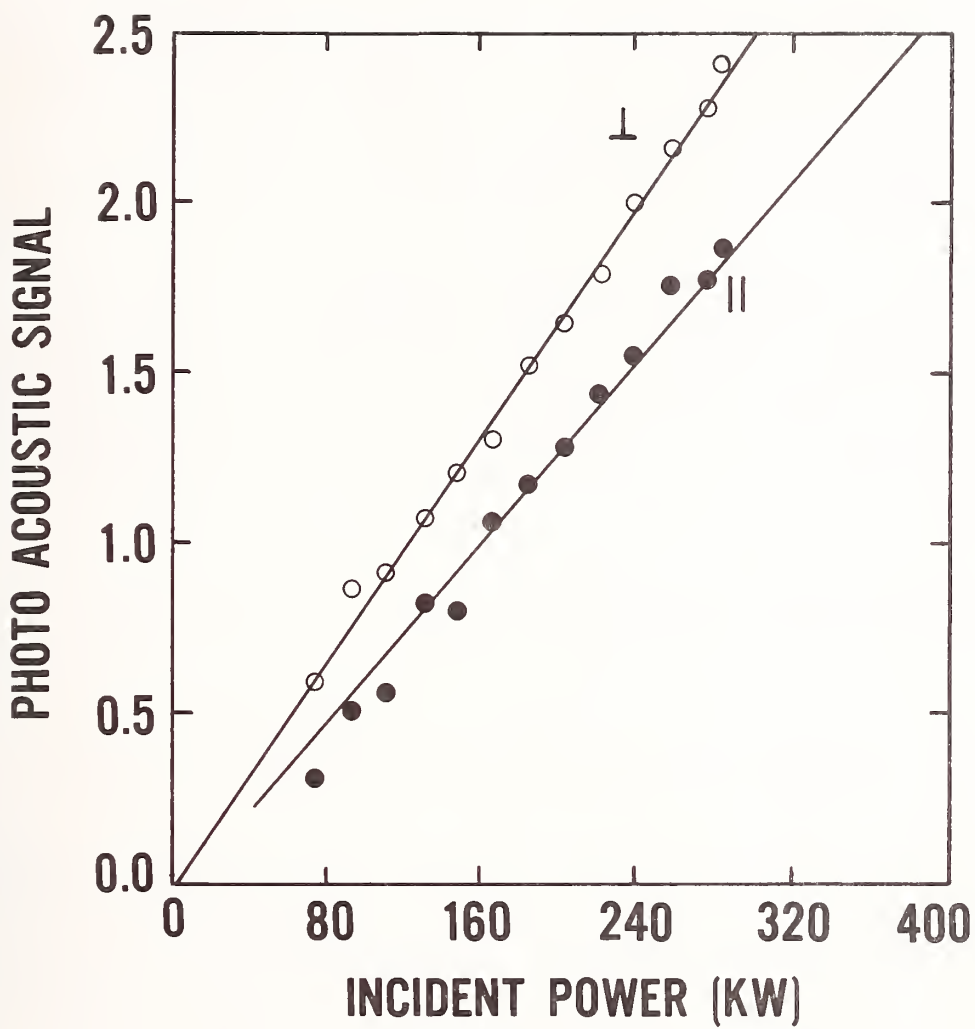


Figure 4b

Figure 4. Absorption of the wire grid at $1.06 \mu\text{m}$ (4a) and $0.53 \mu\text{m}$ (4b). The photoacoustic signal indicates greater absorption when the wires are perpendicular to the electric field.

Laser Damage Studies of Several Acrylic Polymers

A.B. Romberger

Pennsylvania State University, Berks Campus,
P.O. Box 2150, Reading, PA 19608

B.W. Mullins

Department of Physics, USAF Academy, Colorado Springs, CO 80840

A.A. Shaffer

Department of Chemistry, USAF Academy, Colorado Springs, CO 80840

J.F. Hilbing, K.E. Siegenthaler, T.F. Deaton and Y. Chang

Frank J. Seiler Research Laboratory, USAF Academy
Colorado Springs, Colorado 80840-6528

The bulk laser damage resistance of several acrylic copolymers and of pure poly(ethyl)methacrylate (PEMA) were investigated with a 1.06 μm wavelength pulsed Nd:YAG laser having a pulse length of 8 ± 2 ns and an e^{-2} radius spot size of 30 ± 0.7 μm . These materials were synthesized in the bulk after extensive filtration or distillation to remove absorbing dust particles. A correlation is made between the damage thresholds and the number of scattering centers per volume observed in a HeNe beam. The HeNe laser beam scattering in the sample was used as an indicator of the impurity content of the sample. In the course of this experiment a spatial filter was installed in order to make the focused YAG laser beam more nearly Gaussian. Comparison of results obtained from the filtered beam and the unfiltered beam (which is mathematically described as a sombrero function) indicated that previous characterization of the non-Gaussian beam provided an incorrectly low damage threshold value.

Key Words: beam profile; bulk laser damage; damage threshold; laser damage; multiple-shot; plastics; single-shot

1. Introduction

It has been suggested¹ that transparent organic glasses (plastics) would be an attractive optical material for use in laser systems if the laser-damage resistance of plastics could be improved relative to that of silicate glass. Besides being lightweight, low cost, diamond turnable, and castable, plastics are dye-impregnable and therefore potentially useful as simple, passive Q-switches or as dye-laser hosts.² As recent measurements have shown, however, the laser-damage resistance of commercially available silicate glass³ is significantly better than that of several commercially available transparent plastics, including polymethylmethacrylate (PMMA),⁴ bisphenol-A polycarbonate (PC),⁵ and cellulose acetate butyrate (CAR).⁵

Various copolymers have been proposed as candidates for laser optics.^{1,6,7} Modification of a chemically pure polymer by adding another polymerizing material to improve the material properties of the sample has been used in industry for a long time. One principal advantage of a copolymer is that a more elastic material can be obtained compared to a chemically pure

sample. For optical applications, improvement of a plastic by improving its viscoelastic properties has been proposed.^{1,6} One way of improving these plastics is by preparing copolymers. Both Emel'yanova, et. al.⁶ and Dyumaev, et. al.¹ report improvement for the copolymers they studied. Emel'yanova, et. al.⁶ report single-shot improvement in a polymethylmethacrylate (PMMA)-polybutylacrylate (PBA) copolymer. Dyumaev, et. al.¹ report minor single-shot improvement and significant multiple-shot improvement in some of the copolymers they studied.

As a continuation of the laser damage in plastics research at the Frank J. Seiler Research Laboratory, several copolymers were synthesized and their damage thresholds were studied.

2. The Damage Experiment

The laser and optical system used to perform the damage studies has been previously described and is shown in figures 1 and 2.^{4,8} The laser used was a Quanta-Ray DCR-2A Q-switched Nd:YAG system with an unstable confocal resonator having a linearly-polarized $1.06\text{ }\mu\text{m}$ wavelength output, and producing an $8 \pm 2\text{ ns}$ FWHM, 300 mJ maximum pulse with a variable repetition rate of up to 10 pulses per second (pps). The laser was pumped with a constant flashlamp energy and rate to foster thermal stability. The output was annular in shape and attenuated with optical density filters.

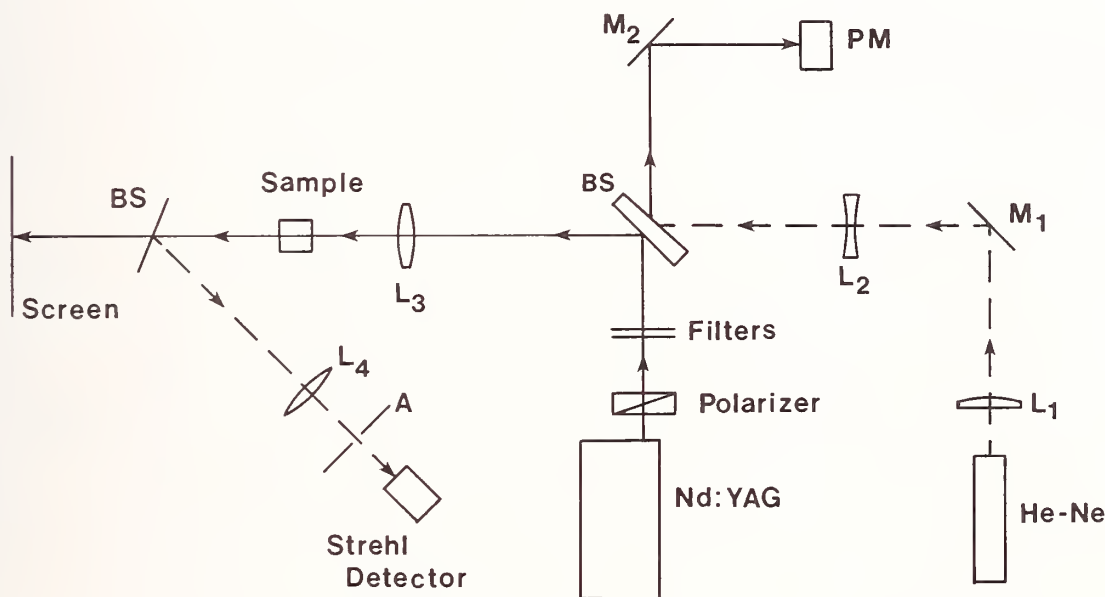


Figure 1. Optical layout for damage studies done with a sombrero-shaped beam profile

Figure 1 shows the optical system used for the damage studies using the sombrero-shaped beam from the unstable resonator. A bare silica wedge was used as a beam splitter with the 4% front surface reflection focused into the sample by a 24.7 cm focal length lens. The radiation transmitted by the wedge was collected by a Scientech power meter for monitoring the laser power.

In our previously-reported work^{4,8,3} we characterized the beam using the knife-edge technique described by Mauck⁹, and analyzed as described by O'Connell, et. al.⁴ This test resulted in an e^{-2} beam waist radius of $33\text{ }\mu\text{m}$. However, an annular beam should focus to a waist profile described by a sombrero function, and the differentiation of a knife-edge scan is inaccurate for this type of beam since the Bessel function is not separable into x and y coordinates as is a Gaussian function. The peak intensity calculated from this test is probably low, but the knife-edge technique was the only one available for much of our earlier work. We eventually performed checks of the validity of this technique by employing other beam profiling methods. A more accurate determination of the peak intensity of the sombrero beam is the measurement of the transmittance through a small pinhole (compared to the beam diameter)

centered on the beam. This test was performed using a $5\text{ }\mu\text{m}$ diameter pinhole, and the average fluence (or approximately the peak fluence) was calculated by multiplying the transmittance times the beam's total energy per pulse and then dividing by the pinhole area. Comparison of the data from these two methods indicates a discrepancy of a factor of approximately 2.3, as discussed below.

In order to avoid the beam profile problems described above, a spatial filter was placed in the beam so as to transmit only the central disk of the sombrero profile. The output from the spatial filter is thus approximately described by a Gaussian function. Figure 2 shows the optical layout for the damage studies done with this Gaussian beam. The output from the Nd:YAG was focused into a vacuum spatial filter by a 30 cm focal length lens. The filtered beam was recollimated by a second 30 cm focal length lens and attenuated by neutral density filters. The beam splitter transmitted a portion of the beam to the Scientech power meter to monitor the beam's power. The reflected beam was focused into the sample by the 24.7 cm focal length lens.

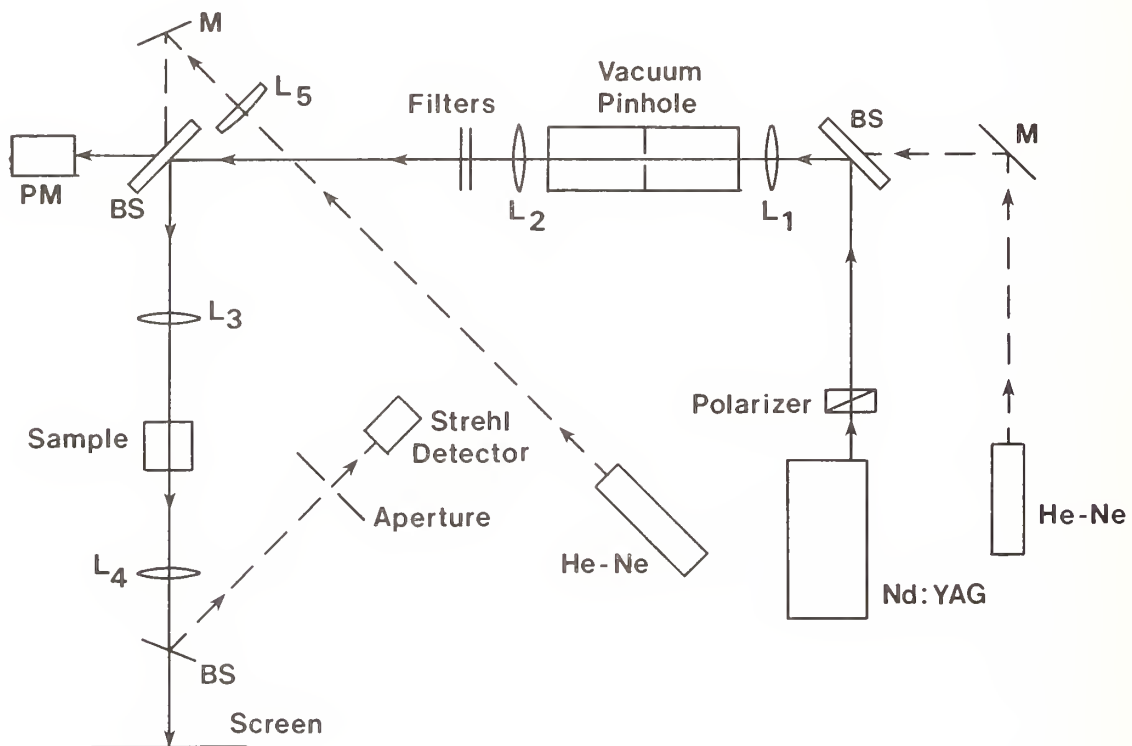


Figure 2. Optical layout for damage studies done with a spatially filtered beam

The spatially filtered Nd:YAG beam was determined to have a focused e^{-2} waist radius of $30 \pm 0.7\text{ }\mu\text{m}$. The characterization was carried out by again using the knife-edge technique mentioned above.

The samples used for both experiments were approximately 1.5 cm thick, with the waist of the Nd:YAG laser beam located nominally in the center of the sample. The Nd:YAG beam entered the sample surface at near normal incidence.

A 2 mW HeNe laser was used as a source for the Strehl detector¹⁰ and was aligned to be collinear with the $1.06\text{ }\mu\text{m}$ beam. Since the 24.7 cm focal length lens would focus the HeNe beam to a different point in space than the $1.06\text{ }\mu\text{m}$ beam, two lenses preconditioned the HeNe beam to bring the two laser beams to a focus at approximately the same point. A knife edge test of the

HeNe beam yielded an e^{-2} radius of $36\text{ }\mu\text{m}$ located approximately 6.5 mm in front of the Nd:YAG beam's waist. A dielectrically coated mirror, having a reflectivity of 70% at 632.8 nm and a transmissivity of 99% at $1.06\text{ }\mu\text{m}$, was used to separate the two beams, and to allow observation of the diffraction pattern from the damage site on the screen.

The reflected HeNe beam was then sent through the optics comprising the Strehl detector. The Strehl detector consisted of a 5 mm aperture centered on the HeNe beam, a 2.5 cm focal length lens, a KG-3 crystal to block any stray $1.06\text{ }\mu\text{m}$ radiation, and an unbiased pin photodiode detector. The photodiode output voltage was then displayed on a digital voltmeter and recorded on a strip chart recorder.

The Strehl detection system was used exclusively to determine the presence of damage. Past work has shown excellent agreement ($>95\%$) between the Strehl detector and a post-irradiation examination under a 100X microscope.^{10,11} The microscope examination was therefore deemed unnecessary. A post-irradiation Strehl intensity of less than 0.995 was used to determine if damage had occurred. This corresponds to the formation of a $2\text{ }\mu\text{m}$ diameter, or larger, damage site.¹⁰

Prior to performing the damage experiment, each sample was examined to determine the relative number of inclusions. The use of the scattered light from a HeNe beam (other than as a Strehl detector) has been previously used successfully as an indication of the number of inclusions in various samples.^{8,12} In order to attempt to compare our current samples with each other and to compare these results with the previous work done at Seiler, the current samples were also studied to determine the average number of scattering centers/volume. A 5 mw HeNe beam was focused into the sample by a 30 cm lens. The depolarized scattered light was observed through a 30X microscope. The average number of micron-size particles (bright scattering centers) within the 0.4 mm^3 volume of the HeNe track was observed with the microscope. These results are incorporated in table 1.

Table 1. Summary of the Damage Results (peak fluences at 50% probability of damage)

Sample	Content	# Scatt Centers/ mm^3	F_{TH}	F (10 pps, $N_{cr}=1000$)	F/ F_{TH}
S-61	MMA +5.0% nBA	13	67 J/ cm^2	2.4 J/ cm^2	0.036
S-62 ¹	MMA +5.0% nBA	23	69	1.1	0.016
S-50	MMA +11% nBA	11	64 ²	1.2 ²	0.019
S-58	MMA +5.2% IDM	4	120	10.2	0.085
S-53	MMA +10% IDM	16	93 ²	--	--
S-52	MMA +20% IDM	7	101 ²	10.7 ²	0.106
S-56	MMA +5.3% EA	6	103	--	--
S-57 ¹	MMA +5.1% EA	14	73	1.6	0.022
S-63	MMA +5.1% CHM	23	56	3.1	0.055
S-54 ³	PEMA	3.4	105 ²	--	--
S-55 ⁴	PEMA	52	56 ²	3.4 ²	0.061

NOTES: 1. uv polymerized. Unless noted sample was thermally polymerized.
2. old beam profile used; values converted (see text).
3. filtered and polymerized thermally over 2 1/2 months
4. filtered with AIBN initiator added.

3. Sample Preparation

The several copolymers studied were prepared from the dried (with CaH_2) bulk monomer. All the copolymer samples were fractionally or vacuum distilled to remove the hydroquinone inhibitor and then filtered with a $0.22\ \mu\text{m}$ porosity membrane filter to remove as much dust as possible. The copolymer components were then placed in the polymerizing ampoule. The weight of each component was recorded. The copolymers were then sealed in their cylindrical ampoules (17 mm dia x 6 cm long) and either polymerized in a 40°C thermal bath (most samples) or polymerized by the uv (300-400 nm) radiation (Samples S-57 & Samples S-62) from a laboratory mercury lamp. All these samples polymerized in approximately three days. The PEMA samples were only filtered and placed in the temperature bath. S-55 had 4.03 mg azoisobutyronitrile added as an initiator; S-54 did not. S-55 polymerized quickly (one day) while S-54 took two and one half months to polymerize, presumably due to the presence of the inhibitor and lack of initiator.

4. Results of the Damage Experiment

The damage results reported in table 1 were analyzed by the following methods which have been described previously.^{8,12} The single-shot damage at five or more sites for each peak fluence was reduced to a probability of damage for that fluence. The peak fluence F_{TH} corresponding to 50% probability of damage was determined by generating a linear least squares fit (LSF) to the data (figure 3).

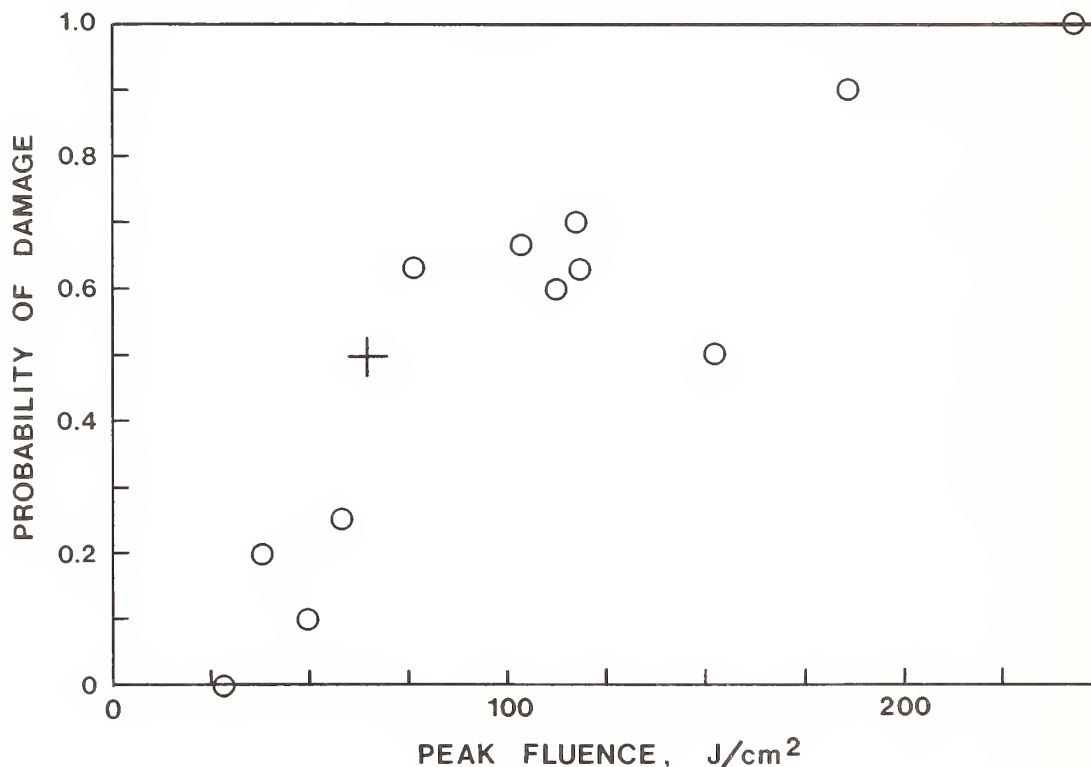


Figure 3. Single-shot damage data for sample 56; the + indicates the threshold fluence level

The 10 pulse per second (pps) multiple-shot data was similarly treated according to the method reported at the 16th Laser Damage Symposium.¹² The probability of damage at a given fluence for $N=10, 25, 75, 100, 200$ and 1000 shots was first determined. Each probability set for a given N was analyzed for the 50% probability peak fluence according to the single shot method described above. A plot of N vs. peak fluence level was then made (figure 4).

All the reported damage thresholds have been converted to the values expected for a spatially filtered Gaussian beam (S-50 through S-55 and previously published PMMA data in table 2), or were actually determined using the filtered, Gaussian beam (S-56 through S-63). A factor of 2.27 ± 0.07 was used to convert the data obtained with the non-Gaussian beam to compare them to the Gaussian beam data. This factor was obtained by comparing threshold peak fluence levels for the same sample in both types of beams, and it was checked against the pinhole data for the non-Gaussian beam.

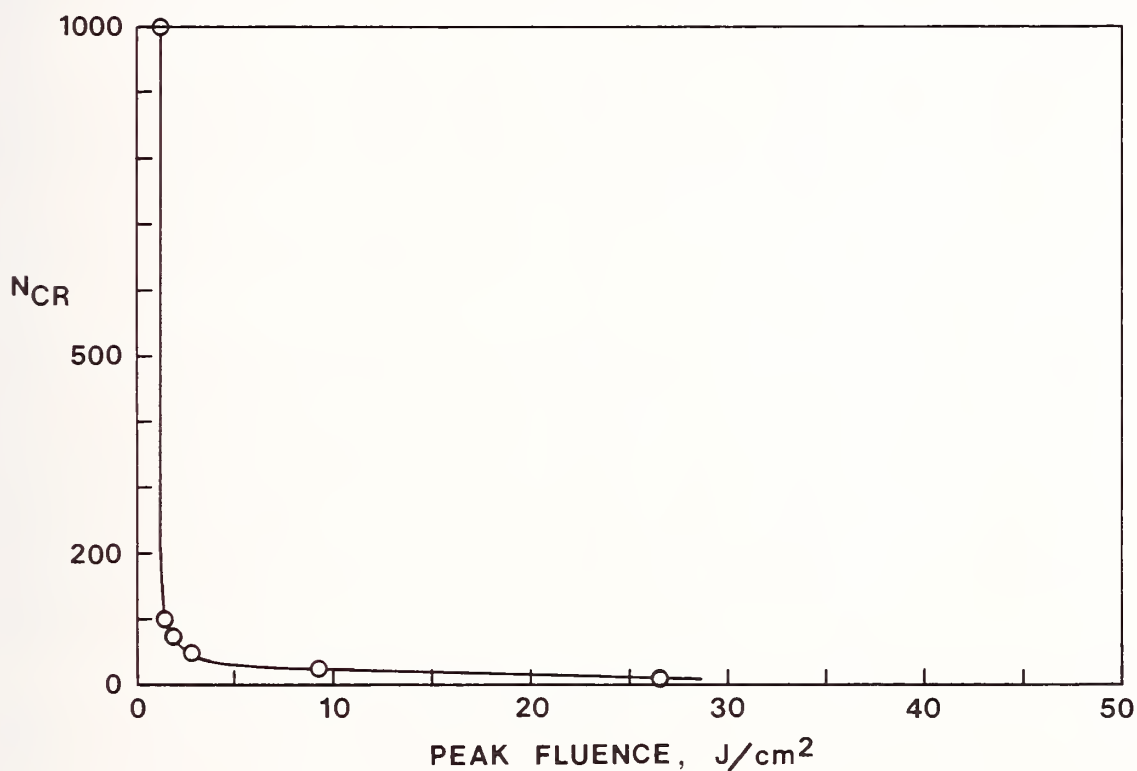


Figure 4. Multiple-shot, 10 pps data for sample 62

Table 2. Comparison of Copolymer Samples and PEMA with Previously Reported¹² PMMA of Similar Inclusion Density

Sample	# Scatt. Centers/mm ³	Single-Shot F _{TH} (J/cm ²)	PMMA Sample	# Scatt. Centers/mm ³	Single-Shot F _{TH} *(J/cm ²)
S-61	13	67	E-20	7.1	66
S-62	23	69	R0-1	20	73
S-50	11	64	E-20	7.1	66
S-58	4	120	S-43	1.7	111
S-53	16	93	R0-1	20	73
S-52	7	101	E-20	7.1	66
S-56	6	103	E-20	7.1	66
S-57	14	73	E-20	7.1	66
S-63	23	56	R0-1	20	73
S-54	3.4	105	S-43	1.7	111
S-55	52	56	R0-3	31	73

*Previously reported data¹² converted to equivalent values for filtered Gaussian beam profile.

It is apparent that our ability to reduce the impurity content (as indicated by the number of scattering centers observed) was not good for the 11 copolymers and PEMA shown here. We have shown previously^{10,14} that there is a strong correlation between scattering centers and the damage thresholds. However, within the above restriction it also seems that varying the copolymer content does little to influence the damage resistance of the sample. S-61 and S-50 have increasing amounts of n-butylacrylate (nBA) (5% and 11% by weight, respectively), and S-58, S-53 and S-52 have increasing amounts of isodecyl methacrylate (IDM) (5.2%, 10% and 20% by weight, respectively), but neither copolymer conclusively demonstrates an increasing damage threshold. In fact, the opposite is true for the nBA copolymers and nothing can be concluded for the IDM copolymers.

IDM does have the largest and heaviest side group, thus it will spread apart the polymer chains and make the entire polymer more elastic. This is a desired effect, because it will improve the viscoelastic properties of the sample and thus should increase the damage threshold of the material as indicated by Dyumaev, et. al.¹ The same comparison should be true for the nBA (S-61 or S-62) copolymers vis-a-vis the ethylacrylate (EA) copolymers (S-56 or S-57) but does not hold.

It is probable that the inclusion content is so large that only a big change (i.e., nBA or EA to IDM) in the copolymer will have a significant effect.

A comparison of polymerization methods was attempted with S-56 (thermal) and S-57 (uv) and also with S-61 (thermal) and S-62 (uv) with the expected result that S-57 and S-62 would exhibit improved thresholds based on our previous work with PMMA.¹² This is not true, but it should also be noted that the particulate content of S-57 and S-62 is higher than their thermally polymerized counterparts, even though all samples were prepared under conditions as identical as possible. It is clear that the inclusion content has the greater influence and no trend can be established for these samples.

The two samples (S-54 and S-55) of PEMA recorded were the initial attempts at making these samples. The inhibitor was not removed, and initiator was added to S-55. It is clear that adding the initiator added inclusions and decreased the damage thresholds of S-55. This was expected. PEMA is interesting however, because it is still relatively hard, but is softer than PMMA. PEMA should therefore have improved viscoelastic properties and greater damage resistance.

S-63 is a copolymer of MMA and cyclohexyl methacrylate (CHMA). Both materials alone make a hard polymer and PCHMA additionally tends to crystallize and become milky in appearance. The copolymer sample studied was slightly cloudy, and there is little in its results to indicate any improvement over the other samples. In fact, its single-shot behavior is relatively worse than the other samples, while its multiple-shot behavior is not much better than several other samples.

Finally, a comparison of the samples with PMMA of similar inclusion content is shown in table 2. It appears that the copolymer material, or PEMA, has a somewhat higher single-shot damage threshold. However, the differences are not very great, and certainly no sample had damage thresholds greater than some of the PMMA samples previously reported.¹²

It is thus unclear whether copolymers or a different methacrylate polymer will have a significantly improved laser damage threshold.

5. Conclusions

The apparent improper characterization of the sombrero function beam's peak fluence yields a significantly lower damage threshold than those obtained with a properly determined Gaussian peak fluence. The high inclusion density present in our samples probably masks the bulk material properties that would influence the damage threshold. The copolymers and PEMA shows a modest improvement in single-shot threshold level over PMMA, which agrees with the Soviet literature.^{6,7} The multi-shot threshold improvement of copolymers over that of PMMA is inconclusive for our samples. We did not observe the improved multi-shot threshold performance of the copolymers as was reported by Dyumaev, et. al.⁷ Finally, due to the large number of inclusions in our samples, work in this area needs to be continued with better prepared samples.

6. References

- [1] K.M. Dyumaev, A. A. Manenkov, A. P. Maslyukov, G. A. Matyushin, V. S. Nechitailo, and A. M. Prokhorov, "Transparent polymers: A New Class of Optical Materials for Lasers," Sov. J. Quantum Electron., **13**, (4), 503 (1983).
- [2] D. A. Gromov, K. M. Dyumaev, A. A. Manenkov, A. P. Maslyukov, G. A. Matyushin, V. S. Nechitailo, and A. M. Prokhorov, "Efficient Plastic-Host Dye Lasers," J. Opt. Soc. Am. B, **1**, 431 (A) (1984).
- [3] L. D. Merkle, M. Bass, and R. T. Swimm, "Multiple Pulse Laser-Induced Bulk Damage in Crystalline and Fused Quartz at 1.064 and 0.532 μm ," Opt. Eng., **22**, 405 (1983).
- [4] R. M. O'Connell, T. F. Deaton, and T. T. Saito, "Single- and Multiple-Shot Laser-Damage Properties of Commercial Grade PPMA," Appl. Opt., **23**, 682 (1984).
- [5] R. M. O'Connell, T. T. Saito, T. F. Deaton, K. E. Siegenthaler, J. J. McNally, and A. A. Shaffer, "Laser Damage in Plastics at the Frank J. Seiler Research Laboratory," presented at the Fifteenth Annual Symposium on Optical Materials for high power lasers, Boulder, Colorado, November 14-16, 1983 NBS Spec. Pub. (to be published).
- [6] B. M. Emel'yanova, T. F. Ivanova, M. P. Votinov, V. M. Ovchinnikov, V. D. Piterkin, and Z. A. Smirnova, "Optical Strength of Copolymers of Methyl Methacrylate and Butyl Acrylate," Sov. Tech. Phys. Lett., **3** (7), 280 (1977).
- [7] V. I. Bezrodnyy, O. V. Przhonshaya, Ye. A. Tikhonov, M. V. Bondar, M. T. Shpak, "Polymer Active and Passive Laser Elements Based on Organic Dyes," Kvantovaya Elektronika, **9** (12), 2455 (1982).
- [8] R.M. O'Connell, A.B. Romberger, A.A. Shaffer, T.T. Saito, T.F. Deaton, and K.E. Siegenthaler, "Improved Laser-Damage-Resistant Polymethylmethacrylate," JOSA B, **1**, 853. (1984)

- [9] M. Nauck, "Knife-Edge Profiling of a Q-Switched Nd:YAG Laser Beam and Waist," Applied Optics, 18, 599. (1977)
- [10] B.W. Mullins and A.B. Romberger, "Real Time Laser Damage Detection in Bulk Materials by Strehl Intensities," Proc. Southwest Conference on Optics: 1985, R.S. McDowell and J.B. Gerardo, editors, accepted for publication, (1985).
- [11] B.W. Mullins and B.A. Richert, "Strehl Ratio Measurements of Laser Damaged Plastics," Proc. 15th Annual Symposium on Laser Induced Damage in Optical Materials, A. Guenther and H. Bennet, editors, accepted for publication.
- [12] R.M. O'Connell, R.V. Ellis, A.B. Romberger, T.F. Deaton, K.E. Siegenthaler, A.A. Shaffer, B.W. Mullins, and T.T. Saito, "Laser Damage Studies of Several Methacrylate Polymeric Materials," in Proceedings of the 16th Annual Symposium on Optical Materials for High Power Lasers, Boulder, CO, 15-17 Oct 84.

Improvement of The Bulk Laser Damage Threshold of Potassium Dihydrogen Phosphate Crystals by Ultraviolet Irradiation

A. Yokotani, T. Sasaki, K. Yoshida, T. Yamanaka and C. Yamanaka

Institute of Laser Engineering, Osaka University,
Suita, Osaka, 565, Japan.

Potassium dihydrogen phosphate (KDP) crystals were grown under the irradiation of ultraviolet light. The bulk laser damage threshold was improved two to three times (15 - 20 J/cm²) compared to the case of crystals grown by conventional methods. Microbes such as germs and bacteria are frequently generated in the KDP solution with the usual growth method, causing a low damage threshold. A main reason of the low damage threshold is due to the organic materials such as microbes or their carcass which are incorporated in the growing KDP crystals.

Key words : potassium dihydrogen phosphate; crystal; harmonic generation; high power laser; laser fusion; damage threshold; ultraviolet light; microbes; germs; bacteria; pasteurization; dissociation.

1. Introduction

Potassium dihydrogen phosphate (KDP) crystals which can withstand the irradiation over 10 J/cm² with a 1 ns pulse at 1.053 μ m laser wavelength are necessary for the harmonic generation of fusion lasers. Typically as-grown crystals have the bulk laser damage threshold of 6-9 J/cm². [1,2] Swain showed that the baking and pulsed laser irradiation of KDP crystals improved the laser damage threshold without describing the reason. [3]

The KDP crystals are usually grown from the aqueous solution at the temperature range between 60°C and 20°C. Microbes are sometimes observed in the KDP solution during the long growth term in spite of stirring of the solution. If these microbes or their carcass are incorporated into the growing crystals, the damage threshold will show the lower values than the intrinsic value, because the damage threshold of the organic material is much lower compared to the inorganic material. To prevent the creation of the microbes in the KDP solution we have grown KDP crystals under the irradiation of ultraviolet (UV) light.

The KDP crystals which have been grown by this method showed the increase of the damage threshold two to three times (15 - 20 J/cm²). We have also performed the experiment of the effect of the ultraviolet irradiation on the bulk laser damage threshold of KDP crystals after growth.

2. Damage threshold of KDP crystals grown under the UV irradiation

2.2. Crystal growth unit

Figure 1 shows the crystal growth unit. The inner vessel was made of glass which was durable against the UV radiation. Low pressure mercury lamps with Suprasil quartz tubes of which input power were 10 and 20 W were used to pasteurize the KDP solution. The mother liquor was 9 liters and the temperature falling method was adopted to grow crystals. The starting temperature was 45°C. The solution was filtered with 0.2 μ m membrane before starting of crystal growth. Z-cut seed crystals of which cross section was 5cm x 5cm were used. The growth rate of Z-axis was 3 - 8 mm/day. The technique of crystal habit control by metal impurities such as Cr and Al was used. [4] The growth term was approximately one month.

2.2. Investigation of microbes in KDP solution

The microbes in KDP solution were studied by using Water Sampler from Millipore Limited (SPC Total-Count Sampler). This is a standard method for total bacteria count in water. In the case of solution unpasteurized by the UV lamps, a number of colonies of gel-like germs appeared on the sampler after one or two days of incubation. Figure 2 illustrates a typical photograph of such germs. The gathering of white strings are certain kind of mold which generated in the air atmosphere from the gel-like germs.

We could not observe such germs from the solution pasteurized with the UV lamps even after four or five days of incubation.

2.3. Laser damage test facility

Figure 3 shows the experimental setup of glass laser damage test facility. The measurement of the bulk laser damage threshold was performed using a Q-switched YLF laser ($1.053 \mu\text{m}$) of transverse and longitudinal single mode with a 1 nsec pulse. The pulse was focused into Z-cut KDP samples by a lens of which focus length was 3.5 cm. The surfaces of KDP crystals were finished with combination of diamond turning and wet polishing with $0.05 \mu\text{m}$ aluminum oxide powder. The damage was observed by eyes. A He-Ne laser was also used to find the small damage spots by utilizing the scattering from the damage spots. The focus spots was moved shot by shot.

2.4. Results of damage test

The results of the damage threshold measurement are shown in figure 4. The abscissa is damage threshold and the ordinate shows number of samples. The empty squares illustrate the samples grown without the UV irradiation. The shaded squares shows the samples with the UV irradiation. In the case without the UV irradiation, most samples showed the damage thresholds of $6-10 \text{ J/cm}^2$, whereas, for the samples with the UV irradiation showed considerably higher damage thresholds ($10-22 \text{ J/cm}^2$). There is a tendency that larger the intensity of UV irradiation is, higher the damage threshold becomes.

In a few cases without the UV irradiation, very high damage thresholds (20 J/cm^2) were also observed. We consider that one reason of the wide spread of the damage thresholds may be due to the differences of the initial conditions of the KDP powders. We did not investigate the quantity of microbes or other organic impurities in the KDP powder before dissolving in pure water.

3. Effect of the UV irradiation on KDP crystals after growth

We have investigated the effect of the UV irradiation on KDP crystals after growth. Lowrence Livermore Laboratory reported that the repetitive Xenon flashes were not effective.[2]

We used the UV light from continuous high pressure Xenon lamp of which input power was 500 W. The experimental setup is shown in figure 5. The KDP sample whose dimension was $1.5 \text{ cm} \times 1.5 \text{ cm} \times 4 \text{ cm}$ was set at the distance of 5 cm from the Xenon lamp. This sample was cut from the crystal grown at the growth rate of 8 mm/day with addition of Cr and Al ions to the solution. The bulk damage threshold were measured as a function of the distance from the UV irradiated surface, which is illustrated in figure 6. Exposure time of the Xe lamp was 3 hours. The damage threshold decreased almost exponentially with the distance. The temperature of the sample became almost 50°C due to the irradiation of Xe lamp but there was no temperature distribution in the sample. Therefore we can say that the increase of the damage threshold was induced mainly by the UV light and not by the thermal effect. Figure 7 shows the damage threshold as a function of the UV exposure time. The data were taken at a distance of 5mm from the UV irradiated surface.

Although we tried to measure the difference of the absorption spectra of KDP crystals grown with and without the UV lamps, it was too small to measure. Instead, we have measured the change of the absorption spectra of a KDP solution which was kept for a long term (approximately one month) at room temperature and had much microbes. The results are shown in Figure 8. A continuous high pressure Xe lamp whose input power was 500 W again used for the UV irradiation. The transmittance increased only by filtration of the solution with $0.22 \mu\text{m}$ membrane and more

increased by the further UV irradiation. The germs and bacteria generally have the absorption in UV regions(3000 Å -2000 Å). So it can be said that a dissociation in these organic material induced due to the UV light and the absorption decreased. Although the quantity of these organic material in KDP crystal is fewer than this KDP solution, the same dissociation may be induced in KDP crystal by the UV irradiation and as a result the damage threshold may increase.

We could not obtain this improvement of the damage threshold in every grown crystal. The samples from other runs, at most 20 % improvement or not at all. At this moment we don't know the reason.

4. Conclusions

Two types of experiments were performed to improve the bulk laser damage threshold of KDP crystals. One was to grow KDP crystals under the UV irradiation. The other was to irradiate KDP crystals which had finished growing by the UV light. The present works are summerized as follows;

1) The damage threshold of the KDP crystal improved two to three times (15-22 J/cm²) by growing crystals under the irradiation of the UV light compared to the case of the crystals grown by conventional methods.

2) A main reason of the low bulk laser damage thresholds of as-grown KDP crystal is due to the incorporation of organic materials such as germs and their carcass which were generated in the mother solution during the growth.

3) In some cases, the UV irradiation on KDP crystal after growth was effective. In this case, the damage threshold decreased almost exponentially with the distance from the UV irradiated surface. This effect was induced by the dissociation of the UV light and not by the heat.

4) Enough attention must be paid for the KDP crystals growth not to incorporate the organic materials such as germs, bacteria and their carcass in the KDP solution.

This technique can be adopted for other crystal growth from solution for high power lasers.

5. References

- [1] Swain, J. E.; Stokowski, S. E.; Millam, D.; Rainer, F. Improving the bulk laser damage resistance of potassium dihydrogen phosphate crystals by pulsed laser irradiation. Appl. Phys. Lett. 40; 1982 February. 350 p.
- [2] Newkirk, H.; Swain, J. E.; Stokowski, S. E.; Millam, D. X-ray topography of laser-induced damage in potassium dihydrogen phosphate crystals. J. crystal growth 65; 1983. 651 p.
- [3] Swain, J. E.; Stokowski, S. E.; Millam, D.; Kennedy, G. C. The effect of baking and pulsed laser irradiation on the bulk laser damage threshold of potassium dihydrogen phosphate crystals. Appl. Phys. Lett. 41; 1982 July. 12 p.
- [4] Yokotani, A.; Koide, H.; Yamamuro, K.; Sasaki, T.; Yamanaka, T.; Yamanaka, C. Solution growth of large KDP crystals by rotation fluid method. Technol. Repts. Osaka University 33; 1983 October. 301 p.

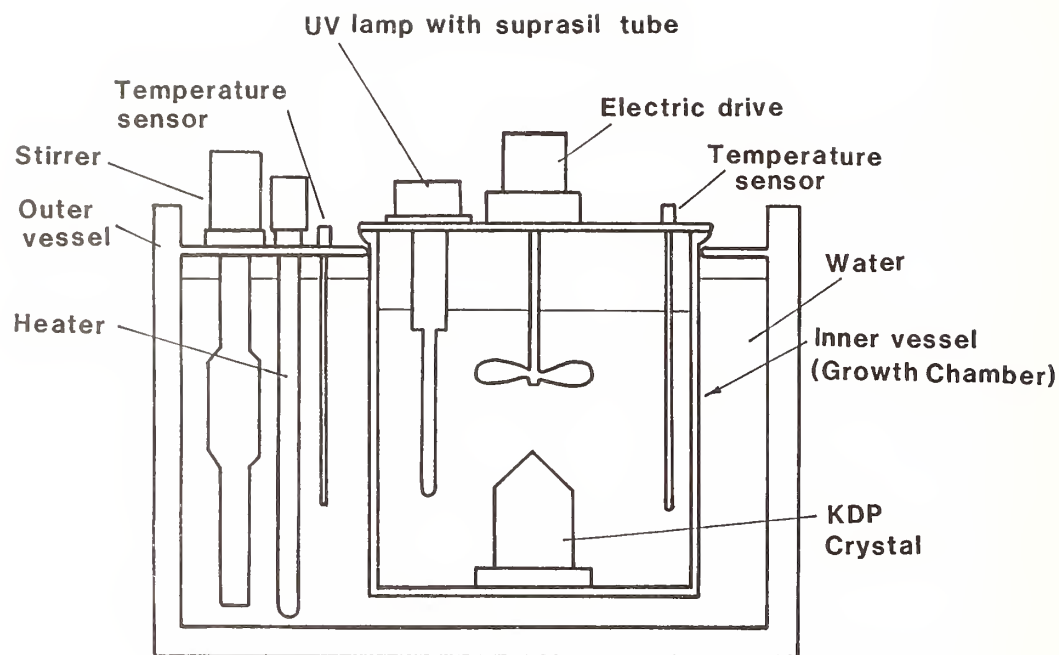


Figure 1. Schematic diagram of crystal growth unit with the UV lamp.

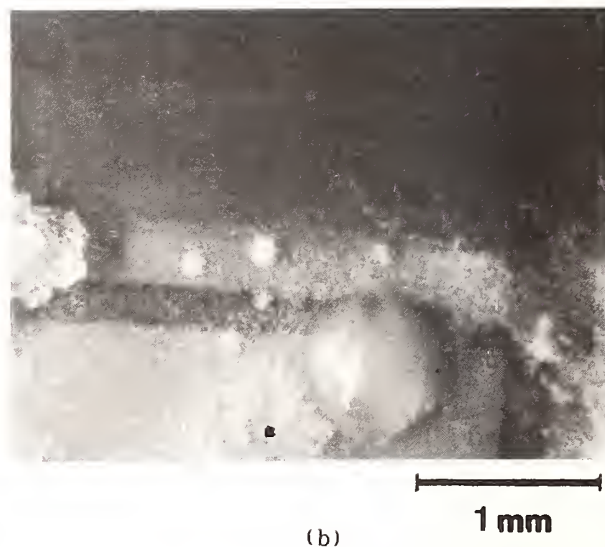
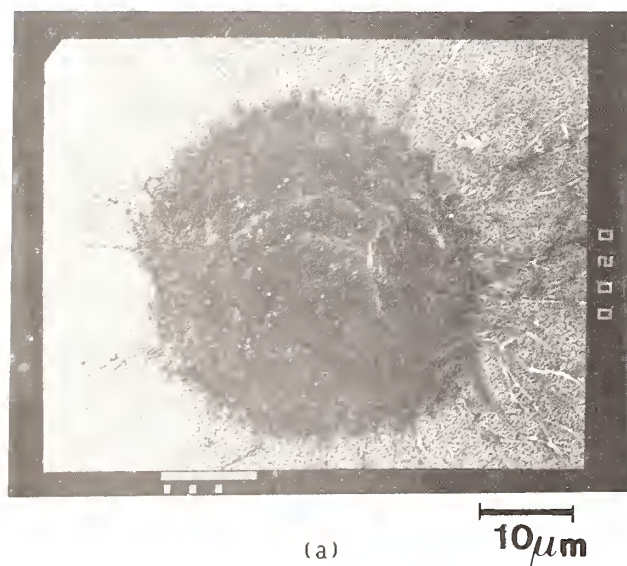


Figure 2. Typical colony of the gel-like germs on the water sampler after two days of incubation of KDP solution without pasteurization by the UV light. (a) with optical microscope (b) with scanning electron microscope.

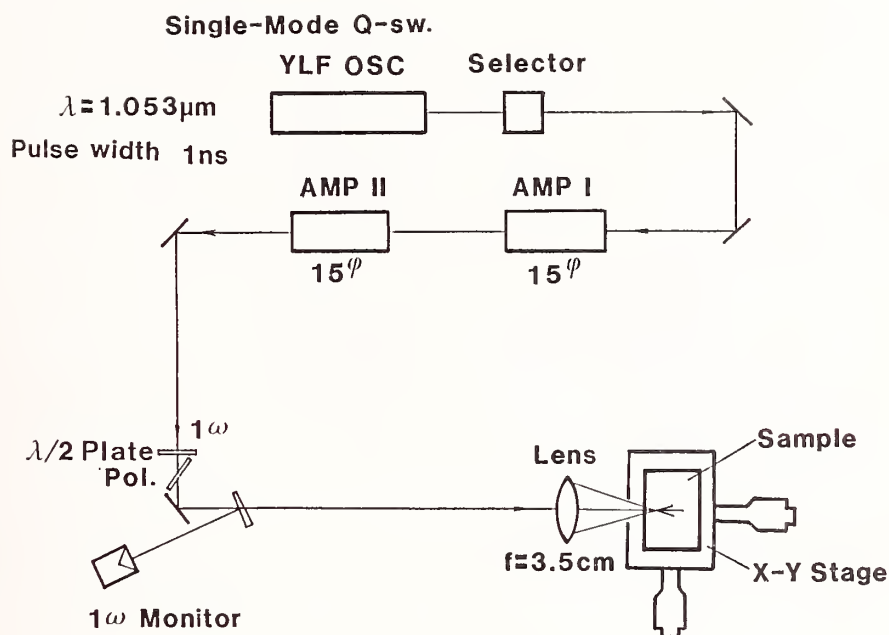


Figure 3. Experimental setup of the glass laser damage test facility.

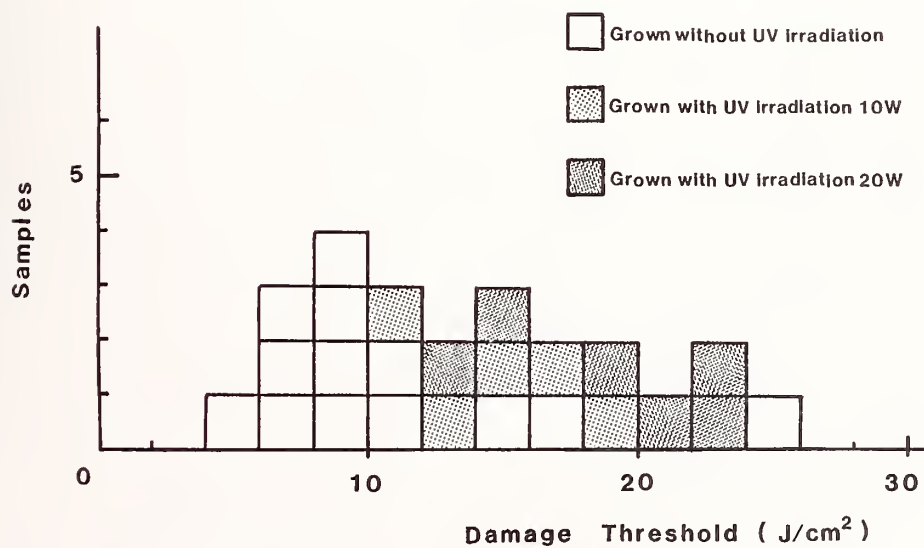


Figure 4. Histogram of the bulk laser damage threshold measured for KDP crystals which were grown in the solution with and without the UV irradiation (laser: 1 ns, 1.053 μm).

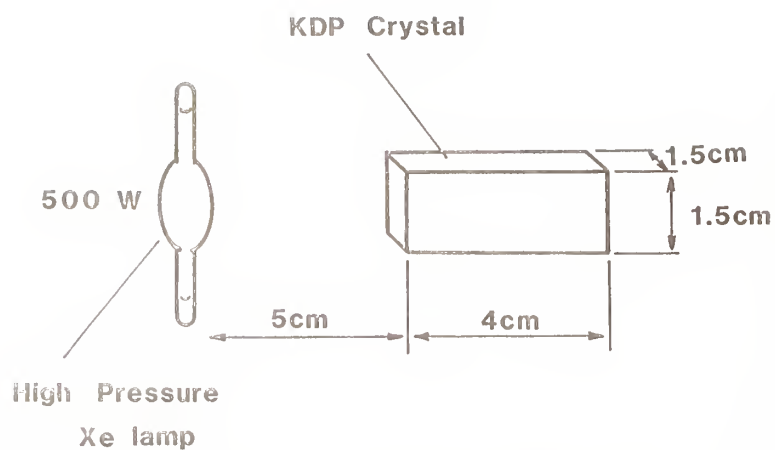


Figure 5. Experimental setup for the UV irradiation to KDP crystal. A high pressure Xenon lamp whose input power was 500W was used.

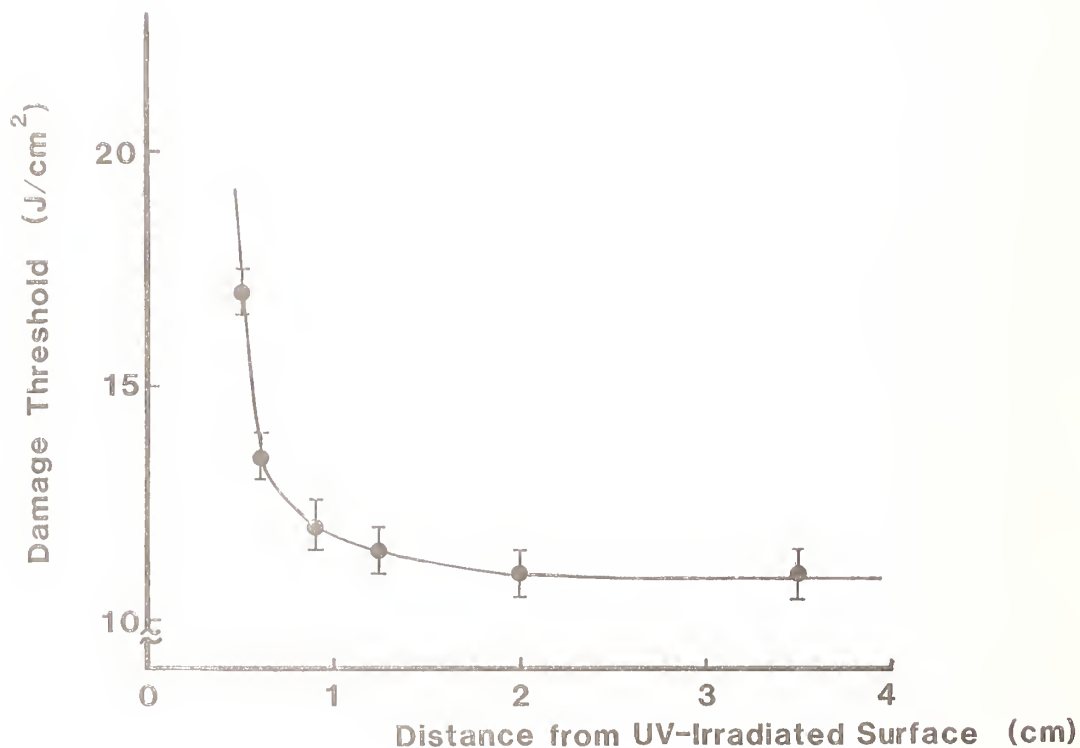


Figure 6. Changes of damage threshold as a function of the distance from the UV irradiated surface. Exposure time of the Xe lamp was 3 hours.

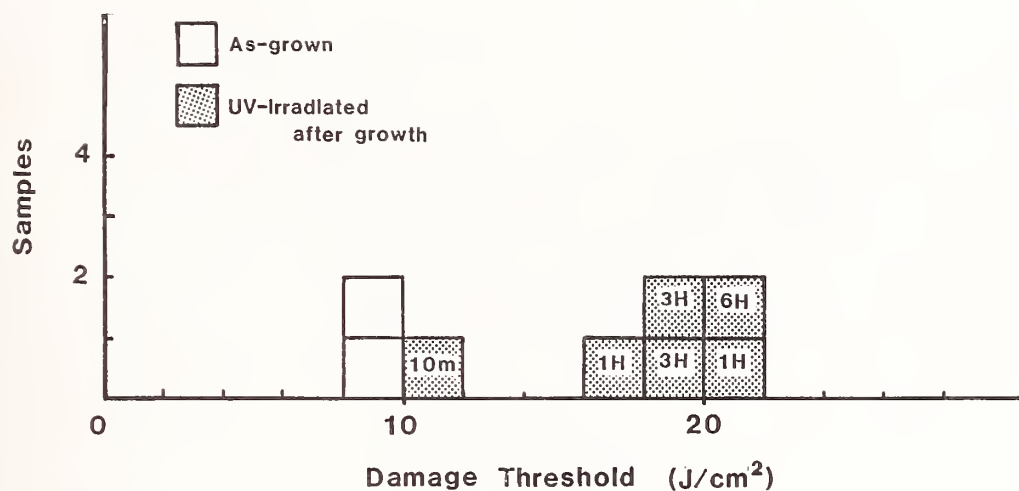


Figure 7. Damage threshold of KDP crystals which was irradiated by the UV light after the growth. The data indicated here include the results from crystals as-grown, irradiated 10 min., 1 hour, 3 hours and 6 hours.

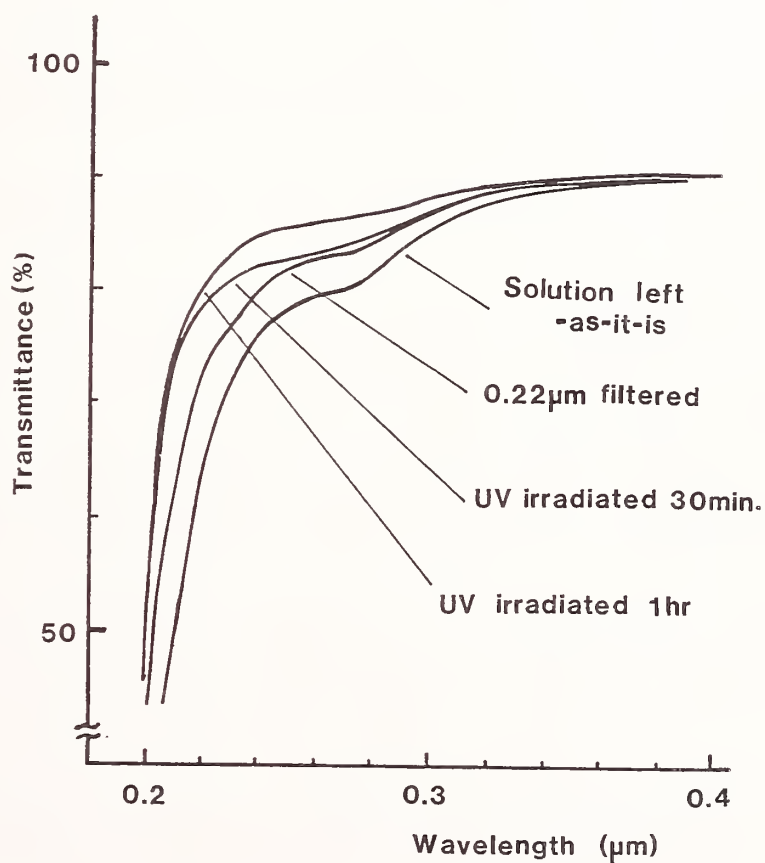


Figure 8. Changes of absorption spectra of KDP solution. Curves include the results from a solution -as-it-is, a solution filtered with a 0.22 μm membrane, a solution UV-irradiated for 30 min. and a solution UV-irradiated for one hour.

Laser-Induced Damage in Doped and Undoped Fluorozirconate Glass

Nastaran Mansour, Shekhar Guha, and M. J. Soileau

Center for Applied Quantum Electronics
Department of Physics
North Texas State University
Denton, Texas 76203

Bernard Bendow
BDM Corporation
1801 Randolph Road, SE
Albuquerque, NM 87106

and

Diane Martin
Air Force Weapons Laboratory
Kirtland AFB, NM

Results of laser-induced damage studies in doped and undoped fluorozirconate (FZ) glass in the system of $\text{ZrF}_4\text{-BaF}_2\text{-LaF}_3\text{-AlF}_3$ are reported. Measurements were made at 1.06 and 0.53 μm for pulsewidths of 45 psec and 20 nsec (FWHM), respectively. The breakdown thresholds are significantly reduced for material doped with Cr, Mn, Ni, and Nd. The decrease in breakdown thresholds at the fundamental wavelength (λ) for the doped material was found to be roughly proportional to the linear absorption of the specimen at the second harmonic ($\lambda/2$). This suggests that two-photon absorption (2PA) is instrumental in initiating damage in the doped specimens.

Key words: avalanche breakdown; fluorozirconate glasses; laser-induced damage; nanosecond pulses, picosecond pulses; two-photon absorption.

1. Introduction

Heavy-metal fluoride (HMF) glasses [1-3] have attracted considerable interest in recent years as potential multispectral materials for a broad range of components such as laser windows, IR domes, laser hosts, lenses, prisms, filters, and optical fibers. While many HMF glasses have been synthesized, probably the most attention to date has been directed towards three types of HMF glasses, namely fluorozirconate-type (FZ), rare-earth (RE), and transition-metal (TM) fluoride glasses. FZ-type glasses are composed primarily of ZrF_4 or HfF_4 , in combination with BaF_2 and a variety of tertiary components such as LaF_3 , ThF_4 , and alkali-fluorides. RE glasses [4,5], which are usually based on ThF_4 and BaF_2 , in combination with ZnF_2 , YbF_3 , YF_3 , AlF_3 and/or LiF_3 , offer extended IR transparency [6] and improved chemical durability relative to FZ glasses. Another less studied group of glasses are the TM fluorides [7,8], with typical compositions consisting of combinations of the fluorides of bivalent metals such as Mn, Co, Ni, or Zn; trivalent metals such as Cr, Ga, or In; and other constituents such as PbF_2 and AlF_3 . From a practical standpoint, the fabrication technology for FZ glasses is the most advanced of these, and some fairly large (> 20 cm) size components with good optical quality have been produced. FZ-type glasses can be continuously transparent from about 0.3 μm in the near-UV (fig. 1) to about 7 μm in the mid-IR (fig. 4). They are readily doped with a variety of RE and TM ions for active applications.

The objective of this investigation is to obtain information on laser-induced damage in fluorozirconate glasses (FZ). Measurements were conducted using picosecond pulses at 1.06 μm and nanosecond pulses at 0.53 μm . To date, there have been no reports in the literature on these measurements. FZ glasses were chosen for this study because of their good optical quality and their technological importance.

For the present study, doped and undoped FZ glasses with the compositions indicated in table 1 were acquired from Le Verre Fluore, St. Erblon, France. These samples were prepared by standard melting techniques starting from oxides and/or fluoride constituents [2]. Polished samples in the form of discs (diameter=2.5 cm and thickness=3.5 mm) were used in the experiments.

2. Experiment

The laser source used in the picosecond regime was a passively mode-locked, microprocessor-controlled, neodymium:yttrium aluminum garnet (Nd:YAG) oscillator-amplifier laser system operating at $1.06\text{ }\mu\text{m}$. A single pulse of measured Gaussian spatial irradiance distribution was switched from the mode-locked train and amplified. The temporal pulsewidth was 45 psec [full width at half maximum (FWHM)]. The width of each pulse was monitored by measuring the ratio of the square of the energy in the fundamental ($1.06\text{ }\mu\text{m}$) to the energy in the second harmonic, produced in a LiIO_3 crystal [9]. The ratio was calibrated by measuring the pulsewidth using an autocorrelation scan. For the nanosecond pulses the laser source was an actively Q-switched Nd:YAG laser system operating at fundamental wavelength ($1.06\text{ }\mu\text{m}$) with an oscillator and one amplifier. Single pulses of measured Gaussian spatial profile were produced by the oscillator and amplified by a single pass through the amplifier. A KDP* crystal was used with the Nd:YAG laser to produce pulses at $0.53\text{ }\mu\text{m}$. The crystal was temperature controlled for long-term energy stability at the second harmonic. Residual $1.06\text{ }\mu\text{m}$ radiation was eliminated by reflection off three dichroic mirrors. The temporal pulsewidth was approximately 20 nsec (FWHM) at $0.53\text{ }\mu\text{m}$. The width of each pulse was monitored by a PIN photodiode detector and fast Tektronix storage oscilloscope (Model 7834).

The experimental setup at $1.06\text{ }\mu\text{m}$ is shown in figure 5. At $0.53\text{ }\mu\text{m}$ the experiment was performed in a similar setup as given elsewhere [10]. The spatial beam spot size (of the unfocused beam) was determined by pinhole scans. A 40 mm focal length lens, designed for minimum spherical aberration, was used to focus the light into the bulk material. A rotating half wave plate/polarizer combination was used to vary the irradiance on the sample. The energy incident on the sample was continuously monitored by a sensitive photodiode peak-and-hold detector, and was calibrated to a Gentec (ED-100) pyroelectric energy monitor. The incident beam polarization on the sample was changed from linear to circular by adding a quarter-wave plate in front of the focusing lens. Each site was irradiated only once, and damage was determined by the observation of scattered light from a coaxial HeNe laser as viewed through a 10x microscope.

3. Results and Discussion

Tables 2 and 3 summarize the results of measurements of the laser-induced breakdown threshold for fluorozirconate (FZ) glasses, undoped and doped with Cr, Mn, Ni, and Nd. The doped and undoped FZ glasses were studied with linearly and circularly polarized light at $1.06\text{ }\mu\text{m}$. The uncertainties listed in the tables of data are relative error obtained by the method used in reference 11. All the data presented in tables 1 and 2 were taken using 45 psec (FWHM) pulses and a calculated $6.2\text{ }\mu\text{m}$ focused spot size ($\text{HW1/e}^2\text{M}$ in irradiance). The values given for the electric field are rms fields corresponding to the peak-on-axis irradiance. As indicated in the table of data, the breakdown fields decrease significantly for all the doped FZ glasses. However, the most reduction in laser-induced breakdown at $1.06\text{ }\mu\text{m}$ is observed in the FZ samples B, C, and D (fig. 6) which are doped with the same molar percent (table 1) of trivalent metal Cr. In these three samples (B, C, and D) the breakdown field decreases roughly by a factor of 2 compared to undoped FZ sample A. From this, we conclude that doping with Cr significantly reduces the optical breakdown of FZ glasses at $1.06\text{ }\mu\text{m}$.

We carried out the same measurements for circularly as well as linearly polarized light in order to confirm the absence of self-focusing in these measurements. The breakdown field for linearly and circularly polarized light are displayed in figure 7. As clearly represented by bar graphs, the breakdown field remains unchanged (to within $\pm 5\%$) for undoped and doped FZ glasses. Thus, we conclude that self-focusing was not a major contributor to the observed laser-induced damage [10].

In the nanosecond regime, results of the laser induced breakdown measurements at $0.53\text{ }\mu\text{m}$ for the undoped and doped FZ glasses are given in table 4. For all data summarized in this table (4) we used 20 nanosecond (FWHM) pulses and a calculated focused spot size equal to $2.7\text{ }\mu\text{m}$ ($\text{HW1/e}^2\text{M}$ in irradiance). As shown in figure 8 the optical breakdown thresholds decrease for doped FZ glasses with Cr, Mn, Ni, and Nd. At this wavelength ($0.53\text{ }\mu\text{m}$) the decrease in thresholds was larger in samples doped with Cr, Mn, and Nd.

Figures 1, 2, and 3 are the linear spectra for the undoped and doped FZ glasses for wavelengths ranging between 0.2 and $1.2\text{ }\mu\text{m}$. These linear spectra were acquired using a Perkin-Elmer spectrophotometer (Model 330). The existence of impurity states within the energy gap for FZ glasses doped with Cr, Mn, Ni, and Nd can result in two-photon absorption which in turn can initiate laser induced breakdown in these materials. Our experimental results were found to be in good agreement with a two-photon assisted electron avalanche breakdown model as given in reference 10. In this model it is assumed that laser-induced breakdown occurs when the density of free carriers generated by a combination of two-photon and avalanche processes reaches some critical

value, N_B . In the avalanche process the buildup of free carrier density is given by

$$N_B = N_0 e^{\eta_B t} \quad (1)$$

where η_B = net ionization rate

N_0 = initial free carrier

The net ionization rate for laser-induced damage is a function of the breakdown field, E_B . Some authors have proposed models [13-15] which predict an ionization rate given by:

$$\eta_B \propto E_B^2$$

Then eq. (1) can be written as

$$N_B = N_0 e^{a E_B^2}, \quad (2)$$

where "a" for our experiment is a constant related to many factors such as: frequency of light, pulsewidth of laser light, the momentum transfer collision time, effective mass and electron charge. The model proposed in reference 10 assumed that the initial free carriers are generated by two-photon absorption from impurity states within the bandgap. Therefore, N_0 can be written as:

$$N_0 \propto n$$

where n = density of two-photon allowed impurity states.

Taking the natural log of eq. (2) yields:

$$a E_B^2 = -\ln n + \text{const} \quad (3)$$

The final assumption is that the density of two-photon allowed states at the fundamental wavelength (λ) is proportional to the linear absorption at the second harmonic ($\lambda/2$). For that assumption eq. (3) gives:

$$E_B^2 \left| \begin{array}{l} \propto \\ \text{at } \lambda \end{array} \right| = -\ln(\alpha l) \left| \begin{array}{l} \\ \text{at } \lambda/2 \end{array} \right| \quad (4)$$

where α = linear absorption coefficient at the second harmonic wavelength

l = length of sample

This analysis [eq. (4)] predicts that the breakdown field at 1.06 μm should be proportional to the natural log of the absorption at 0.53 μm . Figure 9 is a plot of the square of the breakdown field at 1.06 μm [(MV/cm)²] versus the negative natural logarithm of the linear absorption at 0.53 μm for the undoped and doped FZ glasses. A similar plot, for the breakdown field squared at 0.532 μm versus the $-\ln$ of the linear absorption at 0.266 μm is given in figure 10. The linear absorption was calculated from the linear spectra of these material (figs. 1, 2, and 3) using the assumption that the change in index of refraction is negligible in the wavelength range between 0.532 and 0.266 μm . The agreement with the prediction of eq. (4) is quite good considering the relative simplicity of the model and the assumptions made. Note that we measured the laser induced damage for the undoped and doped FZ glasses at 1.06 μm in the picosecond regime; however, the

measurements at 0.53 μm were performed in the nanosecond regime. In spite of the complexity associated with laser-induced damage mechanisms for dielectric materials, our experimental results are quite consistent with two-photon-assisted electron avalanche processes.

4. Summary

Laser-induced breakdown was studied for undoped and doped fluorozirconate glasses at 1.06 and 0.53 μm . Samples doped with Cr, Mn, Ni, and Nd were investigated. Laser-induced damage thresholds decrease significantly for doped FZ glasses. The breakdown threshold field for sample A is approximately 25% lower than that of SiO_2 in similar conditions for 1064 nm. However, all samples have substantially lower threshold fields (on the order of a factor of 5 lower) at 532 nm [9,15]. The reduction of the damage thresholds at 1.06 and 0.53 μm was found to be related to the increase in linear absorption at the second harmonic of the light used to produce the damage. The experimental results are consistent with a model that assumes that damage is caused by two-photon absorption initiated avalanche breakdown. The two-photon absorption is assumed to be associated with states within the bandgap which are due to the added dopants.

The authors from North Texas State University acknowledge support of the Office of Naval Research, the National Science Foundation (ECS #8310625), and the NTSU Faculty Research Fund. Research of B. Bendow was supported by the U.S. Air Force Weapons Laboratory under Contract #F29601-81-C-0012.

5. References

- [1] Tran, D.; Sigel, G.; Bendow, B. J. Lightwave Technol. LT-2(5):566-586; 1984.
- [2] Drexhage, M. in Glass IV, Tomozawa, M.; Doremus, R., eds. New York; Academic Press; 1985.
- [3] Digest of Extended Abstracts of the First International Symposium on Halide and Other Non-Oxide Glasses, Churchill College, Cambridge, U.K., 1982; of the Second International Symposium on Halide Glasses, RPI, Troy, NY, 1983; and of the Third International Symposium on Halide Glasses, Rennes, France, 1985.
- [4] Poulain, M.; Poulain, M.; Matecki, M. Materials Research Bulletin 16(5):555-564; 1981.
- [5] Drexhage, M.G.; El-Bayoumi, O.; Moynihan, C. T.; Bruce, A. J.; Chung, K.-H.; Gavin, D. L.; Lorentz, T. J. J. Amer. Ceram. Soc. 65(10):C168-C171; 1982.
- [6] Drexhage, M.G.; Bendow, B.; Brown, R.N.; Banerjee, P.K.; Lipson, H.G.; Fonteneau, G.; Lucas, J.; Moynihan, C.T. Rapid Communication. Appl. Opt. 21(6):971-972; 1982.
- [7] Miranday, J.P.; Jacoboni, C.; de Pape, R. Rev. Chim. Min. 16(4):277-282; 1979.
- [8] Miranday, J.P.; Jacoboni, C.; de Pape, R. J. Non-Cryst. Solids 43:393-401; 1981.
- [9] Van Stryland, E. W.; Soileau, M. J.; Smirl, A. L.; Williams, W. E. "Pulsewidth and focal volume dependences of laser-induced breakdown." Phys. Rev. B 23(5):2144-2151; 1981.
- [10] Soileau, M. J.; Mansour, N.; Canto, E.; Griscom, D. L. "Effect of radiation induced defects on laser-induced breakdown in SiO_2 ." To be published in the Proceedings of the 1985 MRS Meeting.
- [11] Porteus, J. O.; Jernigan, J. L.; Faith, W. N. "Multithreshold measurement and analysis of pulsed laser damage on optical surface." Natl. Bur. Stand. (U.S.) Spec. Pub. 568; 507-515; 1979.
- [12] Williams, W. E.; Soileau, M. J.; Van Stryland, E. W. "The effect of self-focusing on laser-induced breakdown." Natl. Bur. Stand. (U.S.) Spec. Pub.; 1983.
- [13] Yablonovitch, E.; Bloembergen, N. "Avalanche ionization and the limiting diameter of filaments induced by light pulses in transparent media." Phys. Rev. Lett. 29(14):907-910; 1972.
- [14] Sparks, M.; Holstein, T.; Warren, R.; Mills, D. L.; Maradudin, A. A.; Sham, E. Loh, Jr.; King, F. "Theory of avalanche breakdown in solids." Natl. Bur. Stand. (U.S.) Spec. Pub. 568; 467-

478; 1979.

- [15] Soileau, M. J.; Williams, W. E.; Van Stryland, E. W.; Boggess, T. F.; Smirl, A. L. "Pico-second damage studies at 0.5 and 1 μm ." Opt. Eng. 22(4):424-430; 1983.

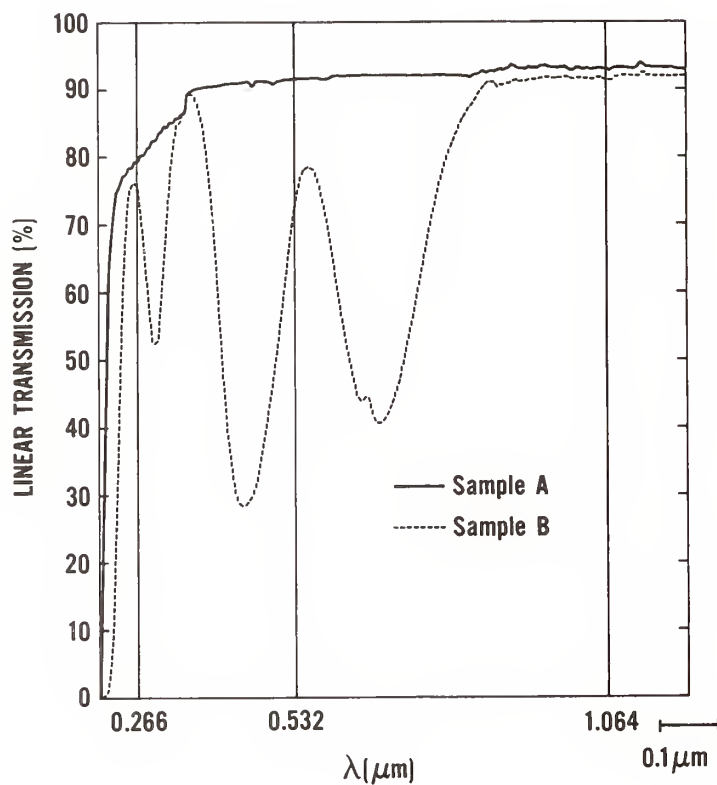


Figure 1. Linear transmission spectra for FZ glass samples A and B for a wavelength range between 0.2 to 1.2 μm .

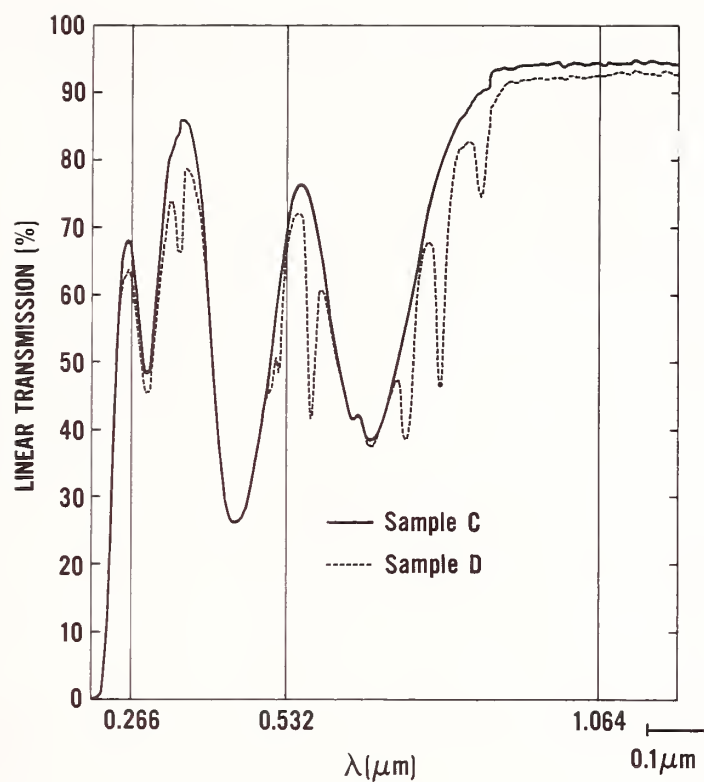


Figure 2. Linear transmission spectra for FZ glass samples C and D for a wavelength range between 0.2 to 1.2 μm .

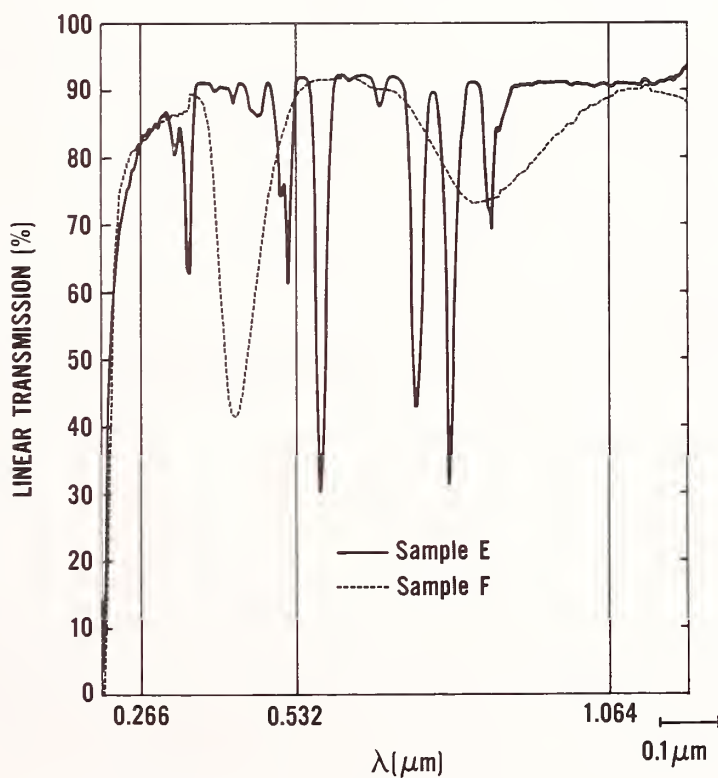


Figure 3. Linear transmission spectra for FZ glass samples E and F for a wavelength range between 0.2 to 1.2 μm .

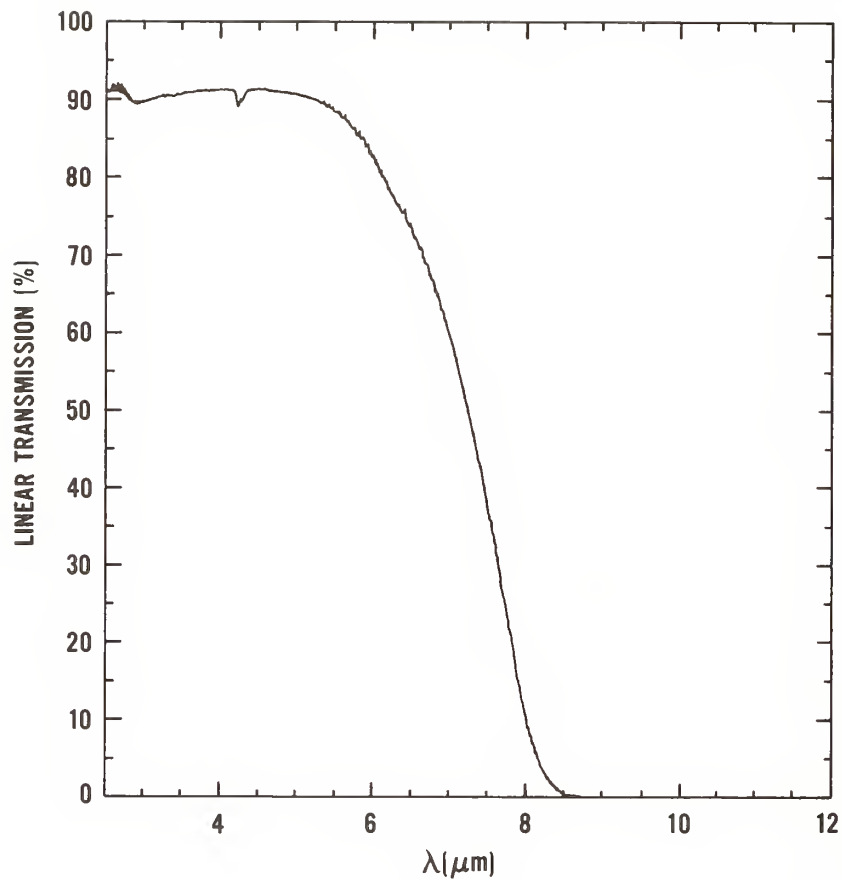


Figure 4. Infrared transmission spectra of fluorozirconate glass (sample A). Similar infrared spectra were acquired for the other FZ glass samples.

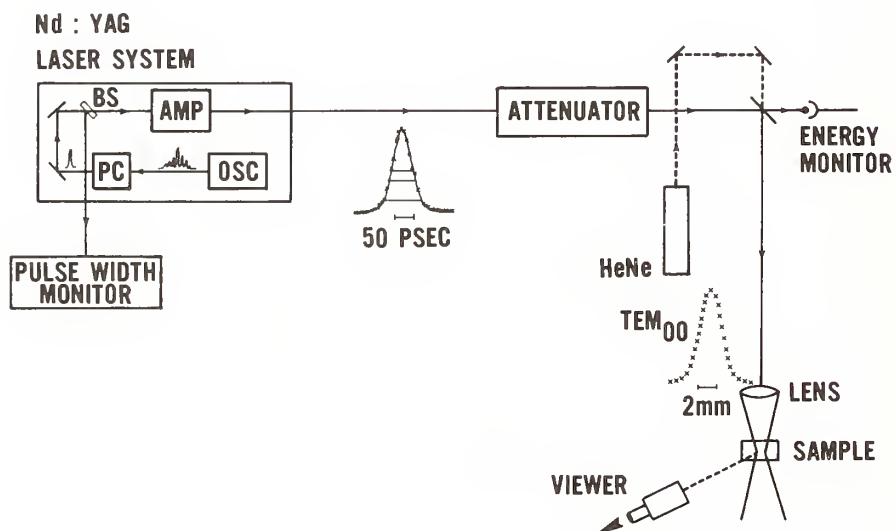


Figure 5. The experimental setup used for the picosecond pulse 1.06 μm damage measurements.

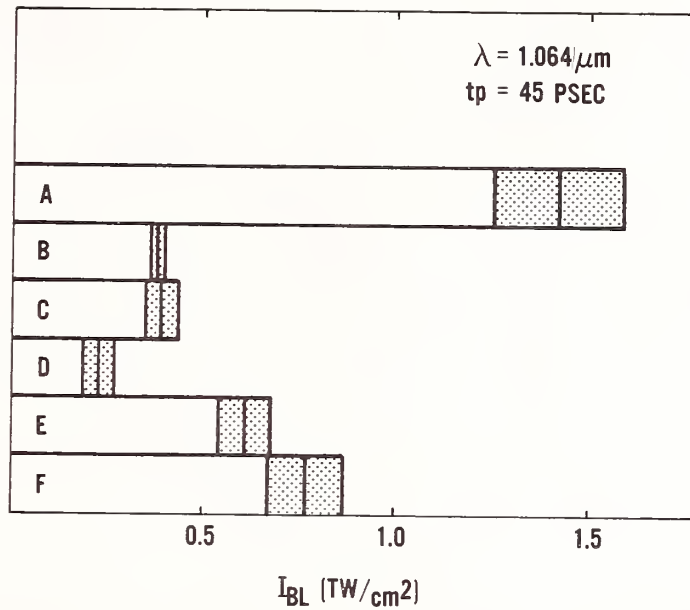


Figure 6. Experimentally determined breakdown irradiance (peak-on-axis irradiance) for undoped and doped FZ glasses at $1.06 \mu\text{m}$ for a laser pulsewidth of 45 ps.

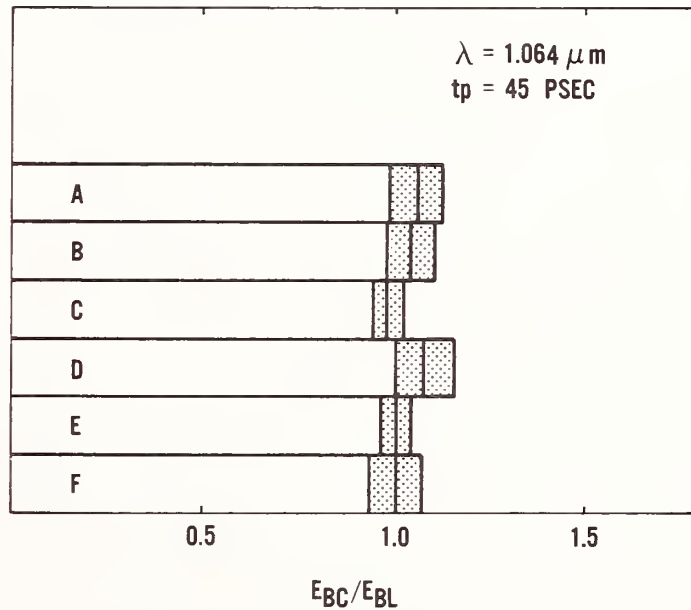


Figure 7. Experimentally determined ratio of breakdown electric field for circularly and linearly polarized light, E_{BC}/E_{BL} , for undoped and doped fluorozirconate glass samples (E_{BC} is the breakdown field for circularly polarized light and E_{BL} is the breakdown field for linearly polarized light). Note that $E_{BC} \sim E_{BL}$. The lack of polarization dependence indicates effects of self-focusing are negligible for the observed laser-induced damage.

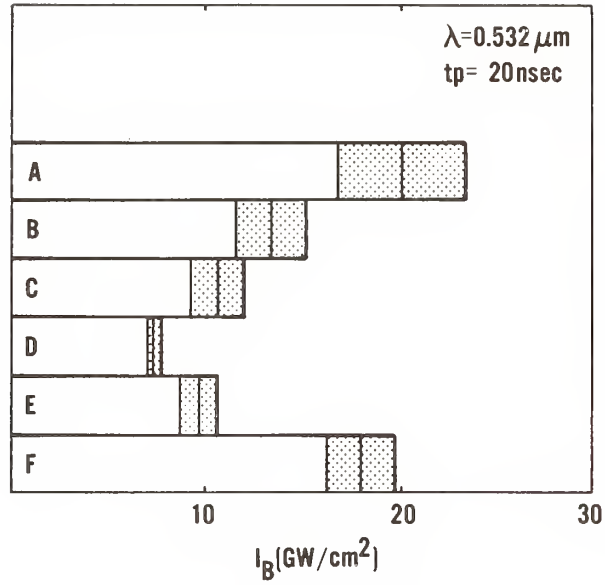


Figure 8. Experimentally determined breakdown irradiance (peak-on-axis irradiance) for undoped and doped fluorozirconate glass samples at $0.53 \mu\text{m}$ for a laser pulsewidth of 20 ns.

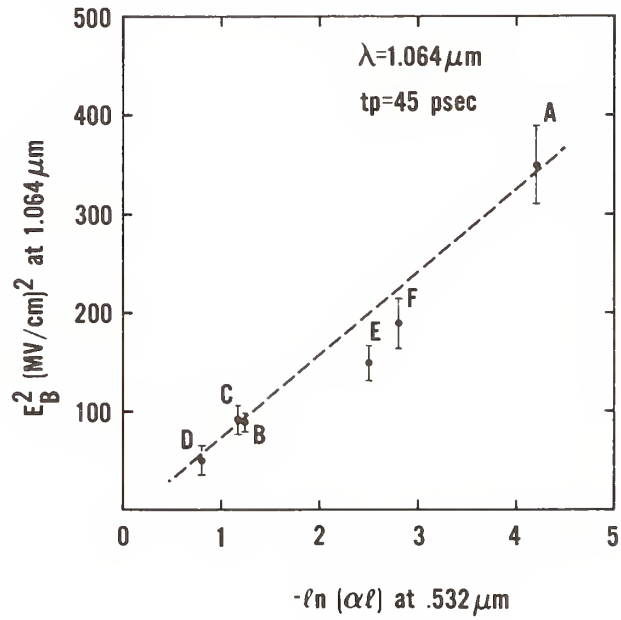


Figure 9. Square of breakdown electric field $(\text{MV}/\text{cm})^2$ at $1.06 \mu\text{m}$ versus the negative natural logarithm of absorption at $0.53 \mu\text{m}$.

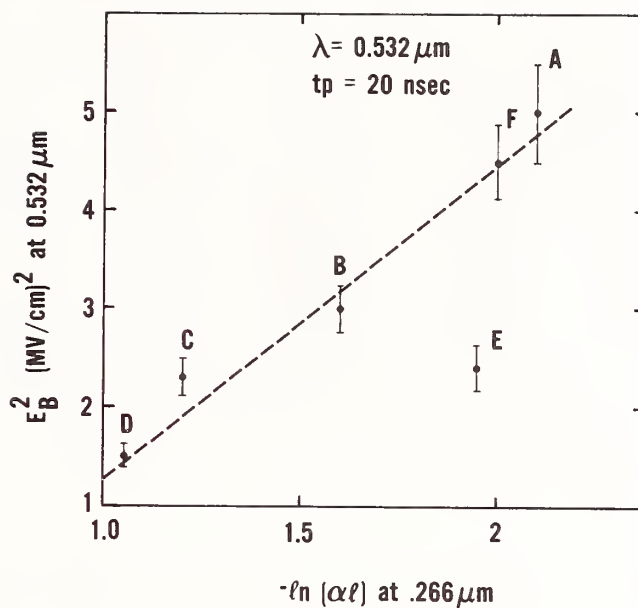


Figure 10. Square of breakdown electric field (MV/cm) 2 at 0.532 μm versus the negative natural logarithm of the linear absorption at 0.266 μm . Note that sample E has sharp absorption bands near to 0.532 μm (fig. 3).

Table 1. Compositions of fluorozirconate glass samples.

Sample	Color	ZrF ₄ (molar %)	BaF ₂ (molar %)	LaF ₃ (molar %)	AlF ₃ (molar %)	CrF ₃ (molar %)	MnF ₂ (molar %)	NiF ₂ (molar %)	NdF ₃ (molar %)
A	Clear	57	34.5	4.5	4				
B	Green	56.75	34.25	4.5	4	0.5			
C	Green	56.5	34	4.5	4	0.5	0.5		
D	Green	56.5	34	4.5	4	0.5			0.5
E	Violet	55.75	33.75	4.5	4		1		1
F	Yellow	56.75	34.25	4.5	4			0.5	

Table 2. Laser-induced damage data for undoped and doped Fluorozirconate glass at 1.06 μm using linearly polarized light. The laser pulsewidth was 45 ± 15 picosecond (FWHM).

Sample	I_{BL} GW/cm ²	E_{BL} MV/cm	P_{BL} KW	F_{BL} J/cm ²
A	1418 ± 173	18.68 ± 1.14	847 ± 103	68.02 ± 8.31
B	384 ± 12	9.72 ± 0.15	229 ± 7	18.42 ± 0.57
C	398 ± 45	9.90 ± 0.56	238 ± 27	19.10 ± 2.16
D	226 ± 48	7.47 ± 0.79	135 ± 29	10.87 ± 2.32
E	612 ± 75	12.28 ± 0.76	366 ± 45	29.37 ± 3.61
F	767 ± 109	13.74 ± 0.98	458 ± 65	36.80 ± 5.25

I_{BL} = breakdown irradiance (peak on-axis irradiance)

E_{BL} = breakdown field

P_{BL} = breakdown power

F_{BL} = breakdown fluence

Table 3. Laser-induced damage data for undoped and doped Fluorozirconate glass at 1.06 μm using circularly polarized light. The laser pulsewidth was 45 ± 15 picosecond (FWHM).

Sample	I_{BC} GW/cm ²	E_{BC} MV/cm	P_{BC} KW	F_{BC} J/cm ²
A	1611 ± 271	19.92 ± 1.67	962 ± 162	77.28 ± 13.00
B	416 ± 52	10.12 ± 0.63	248 ± 31	19.96 ± 2.49
C	380 ± 32	9.67 ± 0.41	227 ± 19	18.23 ± 1.54
D	269 ± 38	8.13 ± 0.57	161 ± 22	12.89 ± 1.81
E	627 ± 43	12.43 ± 0.42	375 ± 26	30.09 ± 2.06
F	786 ± 54	13.91 ± 0.48	470 ± 32	37.73 ± 2.59

I_{BC} = breakdown irradiance (peak on-axis irradiance)

E_{BC} = breakdown field

P_{BC} = breakdown power

F_{BC} = breakdown fluence

Table 4. Laser-induced damage data for undoped Fluorozirconate glass at 0.53 μm for a pulsewidth of 20 nanosecond (FWHM).

	I_B	E_B	P_B	F_B
SAMPLE	GW/cm ²	MV/cm	kw	J/cm ²
A	20.1 ± 3.40	2.26 ± 0.19	2.33 ± 0.40	427 ± 72
B	13.4 ± 1.83	1.86 ± 0.12	1.55 ± 0.21	284 ± 39
C	10.6 ± 1.38	1.65 ± 0.11	1.23 ± 0.16	225 ± 29
D	7.31 ± 0.28	1.36 ± 0.03	0.85 ± 0.03	155 ± 6
E	9.60 ± 0.96	1.57 ± 0.08	1.11 ± 0.11	204 ± 21
F	18.1 ± 1.83	2.15 ± 0.07	2.09 ± 0.21	384 ± 39

I_B = breakdown irradiance (peak on-axis irradiance)

E_B = breakdown field

P_B = breakdown power

F_B = breakdown fluence

Platinum Particles in the Nd:doped Disks of Phosphate Glass in the Nova Laser*

D. Milam, C. W. Hatcher and J. H. Campbell
Lawrence Livermore National Laboratory
P.O. Box 5508, L-490
Livermore, California 94550

The disks of Nd:doped phosphate glass in the amplifiers of the Nova laser contain platinum particles with sizes ranging from $< 5\mu\text{m}$ (detection limit) to about $100\mu\text{m}$. The particle density varies from about 0.01 to 1.0 cm^{-3} . These particles cause fractures when irradiated at fluences $> 2.5\text{ J/cm}^2$ delivered in 1-ns, 1064-nm pulses. Under repeated irradiation at $5\text{--}7\text{ J/cm}^2$, damage from small ($< 5\mu\text{m}$) particles asymptotically approaches a limiting size, but damage surrounding the larger particles grows steadily. The damage threshold fluence, 2.5 J/cm^2 , corresponds to operation of Nova at one-half the desired output for pulse durations longer than 1 nsec. Operation at higher fluences causes accumulation of damage in the output amplifiers and requires replacement of the disks in those amplifiers on an accelerated schedule.

Large-area damage tests have been used to characterize samples from recent melts made to reduce the number of platinum particles. The 500-J, 1-ns pulses available at the midpoint of an arm were used to produce fluences of $7\text{--}10\text{ J/cm}^2$ over test areas 6-9 cm in diameter. Similar irradiations of areas 25-30 cm in diameter were accomplished using 5-kJ, 1-ns pulses available at the output of an arm. Preliminary results from these experiments indicate that a significant reduction of the inclusion density can be obtained through changes in the vendor's glass melting conditions.

Key words: platinum inclusions, phosphate glass, borosilicate glass, large-area damage tests.

1. Introduction

Isolated bulk damage sites caused by laser irradiation of platinum inclusions have been observed in the components of the Nova laser and its predecessor, Novette. These damages occurred in amplifier disks made of Nd-doped phosphate laser glass and in lenses made of borosilicate glass. This problem was first encountered in operation of Novette, a laser with two beam lines (each arm with 10 kJ, 1 ns output), each identical to one of the ten beams of Nova.

The output stage of a beam line arm of either of these lasers contains groups of Nd:glass amplifiers with apertures of 20.8, 31.5 or 46 cm (Fig. 1).^{1,2} Each group of amplifiers is followed by a vacuum spatial filter. A laser pulse passing along the beam line is amplified at one beam diameter to the desired pulse energy, and then focussed into a spatial filter which removes small-scale spatial ripple and enlarges the beam diameter to properly match that of the next group of amplifiers. A spatial filter at the output of the 46-cm amplifiers provides a final cleaning of the beam and increases its diameter to 74 cm which is maintained over the final path to the target chamber.

As a result of this series of amplifications and beam expansions, the variation of pulse energy or beam fluence with position along the chain is an approximately sawtoothed function (Fig. 2), with the largest fluence occurring at the output of the last 46-cm amplifier. During generation of 10 kJ, 1-ns pulses, the average fluence over the effective area of the 46-cm beam (1330 cm^2) is 7.5 J/cm^2 . Because this large fluence exists at the input to the final spatial filter, the fluence at the maxima of beam ripples may be more than 1.5 times the spatially averaged fluence. The components in this region of high fluence are the output 46-cm amplifier disks and the 46-cm input lens to the final filter. The lens is positioned normal to the beam and experiences the full beam fluence. Note, however that the fluence is lower in the 46-cm amplifier disks because they are positioned at Brewsters angle.

*Work performed under the auspices of the U.S. Department of Energy by Lawrence Livermore National Laboratory under Contract No. W-7405-ENG-48.

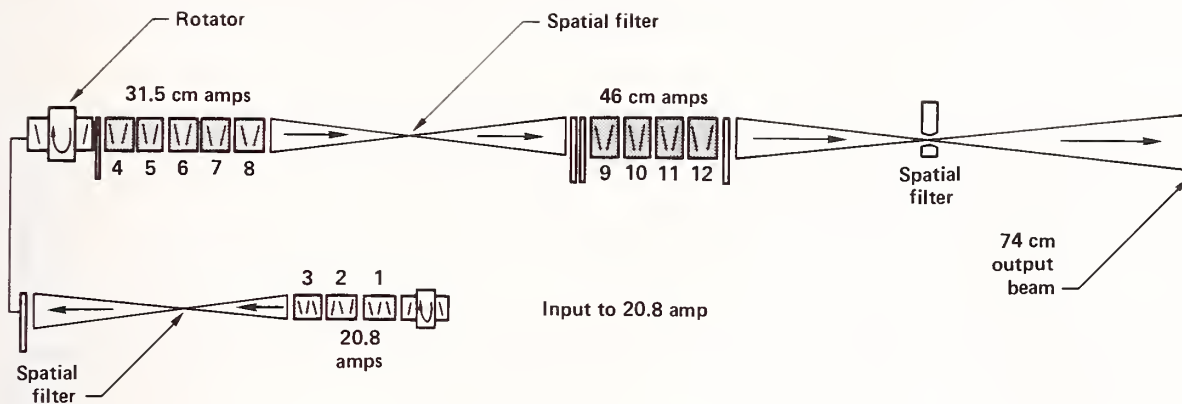


Figure 1: Schematic diagram of the final 3 amplifier stages (20.8 cm, 31.5 cm and 46 cm) and spatial filters that are a part of each one of the 10 beam lines on Nova.

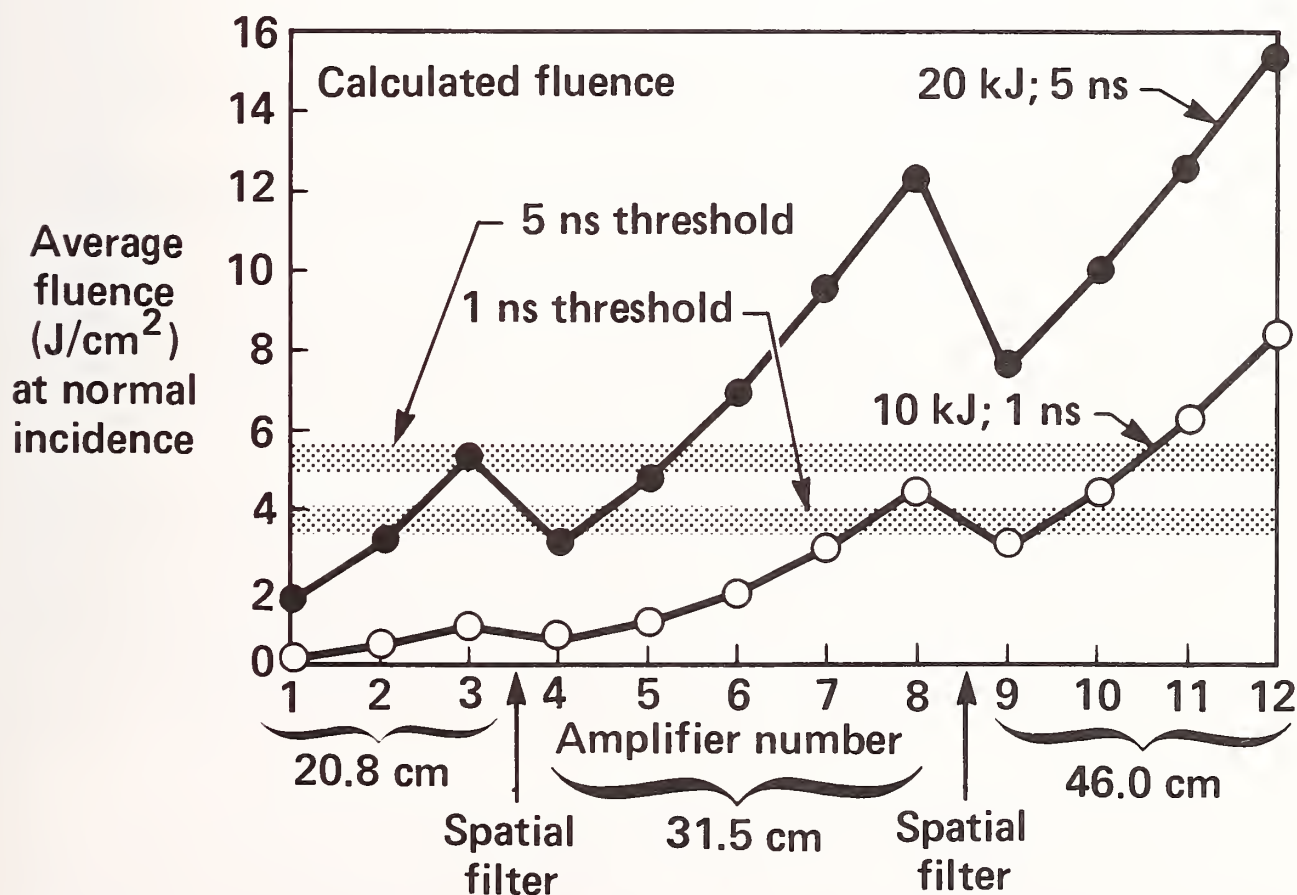


Figure 2: Beam fluence at normal incidence as a function of position along the final 3 amplifier stages of a Nova beam line.

Internal damage in a 46-cm spatial filter lens occurred during the initial full power pulses generated by Novette. Several small volumes each containing an internal damage were cored from the lens and broken to expose the centers of the damages. When these locations were examined by scanning electron microscopy, each was found to contain a platinum particle.

Because the glass was purported to be platinum free, this failure was initially believed to be an isolated incident caused by an identified degradation of a platinum stirrer used in production of the glass. However, replacement lenses made from glass purchased from two other vendors also damaged, indicating that platinum was probably present in most of the available homogeneous glass, all of which had been produced in platinum crucibles. The problem of damage to borosilicate glass was circumvented by fabricating the heavily loaded lenses from high purity fused silica. To date, bulk damage has not been detected in these silica lenses.

A more serious problem arose when bulk damage was observed in the phosphate glass amplifier disks in Novette. This problem could not be solved by substitution of materials because all presently available laser glasses are melted in platinum. A group of chemists, physicists and engineers was assembled to address the task of eliminating platinum. There were five major goals of the group:

- (1) measure the thresholds for damage to selected individual platinum inclusions and the rate of growth of the damaged volume surrounding the inclusions,
- (2) develop an accurate model for the damage caused by laser heating of Pt inclusions,
- (3) assess the damage on Nova and determine a safe operating range during the period of amplifier repair,
- (4) develop a reliable quality assurance technique for inspecting large volumes of glass for the presence of Pt inclusions, and
- (5) work with the glass vendors to quantify the mechanisms for platinum introduction and develop processing conditions to eliminate or minimize it.

The first four of these tasks are completed and significant progress has been made on item 5 to make us confident that Pt particles can be eliminated from the laser glass. The primary intent of this paper is to review the currently operating status of Nova and progress on understanding the Pt damage mechanism. The results from other aspects of the work will be briefly summarized to provide necessary background information.

Platinum inclusion damage in laser and optical glasses has been a recurrent problem throughout history of high power lasers. In particular, platinum damage in silicate laser glass has been well known for many years (see, for example, the review in Ref. 3). In some laser systems, the platinum inclusions were not a problem. Our previous high power laser, Shiva, used a Nd:silicate glass and we observed no damage in that system. However, results from current studies of the Nova glass indicate that Shiva operated just below the Pt damage threshold.

It was anticipated that use of a phosphate based laser glass would cause a reduction of the problem with platinum inclusions, because the solubility of Pt is much greater in phosphate glasses than in silicates. When phosphate glass was selected for use in Nova, five 15 cm x 15 cm x 2 cm samples were tested with 1-ns, 1064-nm pulses at 12 J/cm² using a 6-cm diameter beam produced by an arm of the Argus laser. These experiments indicated that the glass might typically contain one small (< 10 μ m) inclusion in each 10 cm³. This estimate of inclusion density appears to be correct for all but a few of Nova's disks. However, these qualification studies did not correctly predict the large sizes (up to 250 μ m) of some of the inclusions that have been found in glass supplied for Nova, or the growth of the damaged volume that would result from repeated irradiation of those large inclusions.

2. Results from Platinum Inclusion Damage Studies

2.1 Experimental Studies of Individual Inclusions

Individual inclusions with major dimensions ranging from 4 to 75 μ m were tested with 1064-nm pulses having durations of 1.3, 9 or 50 ns. Thresholds for initiation of damage were $2.5 \pm .3$, $4 \pm .4$ and 8 ± 1 J/cm², respectively, at these three pulse durations. These thresholds scaled with pulse duration (τ) as $\tau^{0.31}$ (Fig. 3) and, as expected for particles greater than one micron, the thresholds were independent of particle size. Damage surrounding small ($\lesssim 5$ μ m)

inclusions generally grew to stable dimensions of $< 250 \mu\text{m}$, while damage surrounding larger inclusions ($> 5 \mu\text{m}$) grew to dimensions of $400\text{--}1000 \mu\text{m}$ during irradiation by 5-10, 1-ns pulses at $5\text{--}9 \text{ J/cm}^2$.⁴

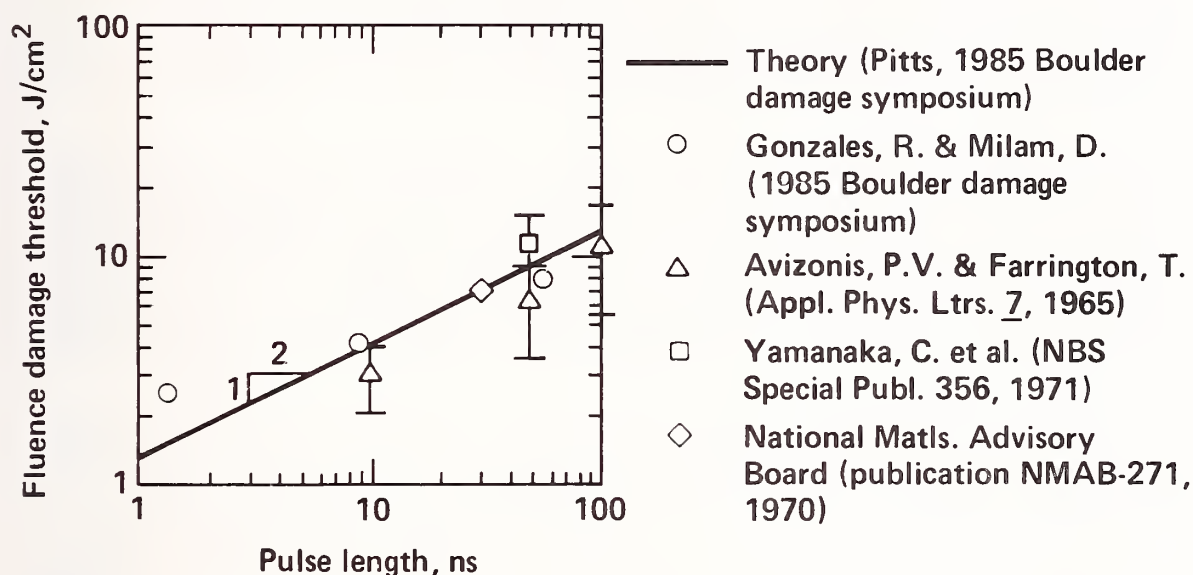


Figure 3: Measured damage threshold due to Pt^0 inclusions for laser pulses of several durations. The open circles represent the results from our study and the line represents the threshold calculated by Pitts.⁵

2.2 Modeling Inclusion Damage

The temperature of a laser-irradiated platinum particle was calculated using a numerical heat transport code (Topaz^{5,6}) that allowed heat conduction into the interior of the irradiated particle and into the surrounding glass, and cooling of the particle by radiation. Literature values were used for the absorption coefficient of platinum and for the heats of fusion and vaporization. Temperature dependence of the absorption coefficient was not treated. The Pt vapor state was described using the equation of state employed in the LASEX laser fusion computer code.⁷ Details of these calculations are given in the paper by Pitts.⁶

For pulses with duration of 9 or 50 ns, the calculated values of the fluences necessary to heat the surface of the particle to the vaporization temperature of platinum agreed with experimentally measured thresholds for initiation of damage. For 1-ns pulses, the calculated vaporization fluence was about one half of the measured threshold (Fig. 3). Calculated vaporization fluences were independent of particle size (for particles with dimensions $> 1.0 \mu\text{m}$) and varied with pulse duration as $\tau^{0.5}$. While the discrepancy between calculated and measured 1-ns threshold has not been resolved, there is close agreement between the results of Pitt's calculations⁶ and the experimental results obtained both at LLNL and in other studies (Fig. 3). The model calculation suggests that the damage surrounding a platinum particle occurs as a result of fracture driven by the pressure of Pt vaporized from the particle surface. Efforts are underway to model the growth of the damage during repeated irradiation.

2.3 Status of Nova

A schematic diagram of the components in an arm of Nova is given in Fig. 1. The 12 disk amplifiers are identified by numerals. Figure 2 gives the spatially averaged fluences present in each amplifier during generation of nominal 10-kJ, 1-ns and 20-kJ, 5-ns pulses. Fluence values are those in a plane normal to the beam. Fluences inside a given disk are lower by a factor of n^{-1} , where n is the refractive index of the glass ($n = 1.53$). Also shown are bands representing the measured thresholds for damage to platinum inclusions induced by pulses with durations of either 1 or 5 ns. The displayed thresholds are larger by a factor of 1.53 than the actual measured thresholds (Fig. 3). Recall that the thresholds were measured in samples oriented

normal to the test beam. We assume that it would be necessary to increase the beam fluence by a factor of n to damage inclusions inside the Brewster oriented disks.

At the time we began evaluating Nova, each of the ten arms had been used to produce 1-ns pulses with energies in excess of 8 kJ. If the experimental data (Fig. 3) correctly represented the damage thresholds for the glass in Nova, damage should have occurred in each arm in the last three 46-cm amplifiers (numbers 10, 11, 12) and the last 31.5-cm amplifier. Because the local fluence values exceed spatially averaged fluences, some damage might have occurred in the input 46-cm amplifier (#9) and the fourth 31.5-cm amplifier (#7). The 20.8-cm amplifiers and the first three 31.5-cm amplifiers should not have damaged.

Several disks were removed from Nova and inspected. For each of these disks a map was constructed giving the locations and approximate sizes of the damage sites. Similar inspections were made of disks removed from the two-arm laser, Novette, when it was disassembled and moved into place as the final two arms of Nova. Almost all of the 46-cm disks and many 31-cm disks contained damage. The volume density of damages ranged from about 1 to 0.01 cm^{-3} , with typical densities being 0.05 to 0.1 cm^{-3} . None of the 20.8-cm disks were damaged. The sizes of the damage sites depended on the fluences that had been experienced by the disks. This is illustrated in Fig. 4 which gives (for four 46-cm disks) normalized plots of the fraction of sites exceeding a given dimension and in Fig. 5 which gives the median size of damages in seven disks as a function of fluence.

The size of the damages is the parameter that most strongly effects the operation of Nova. Codes that model Nova operation indicate that the beam quality is not seriously degraded if the components contain a low volume density of beam obscurations with sizes $< 250 \mu\text{m}$. Larger obscurations produce beam ripple that can damage optical elements lying downstream, and very large ($>> 1 \text{ mm}$) obscurations block a significant fraction of the beam. Data indicate that disks used at fluences near threshold contained damage smaller than the $250 \mu\text{m}$ limit. In disks subjected to fluences well above the damage threshold, the median size was greater than $250 \mu\text{m}$, and the largest damages had diameters $> 10 \text{ mm}$ (Fig. 4).

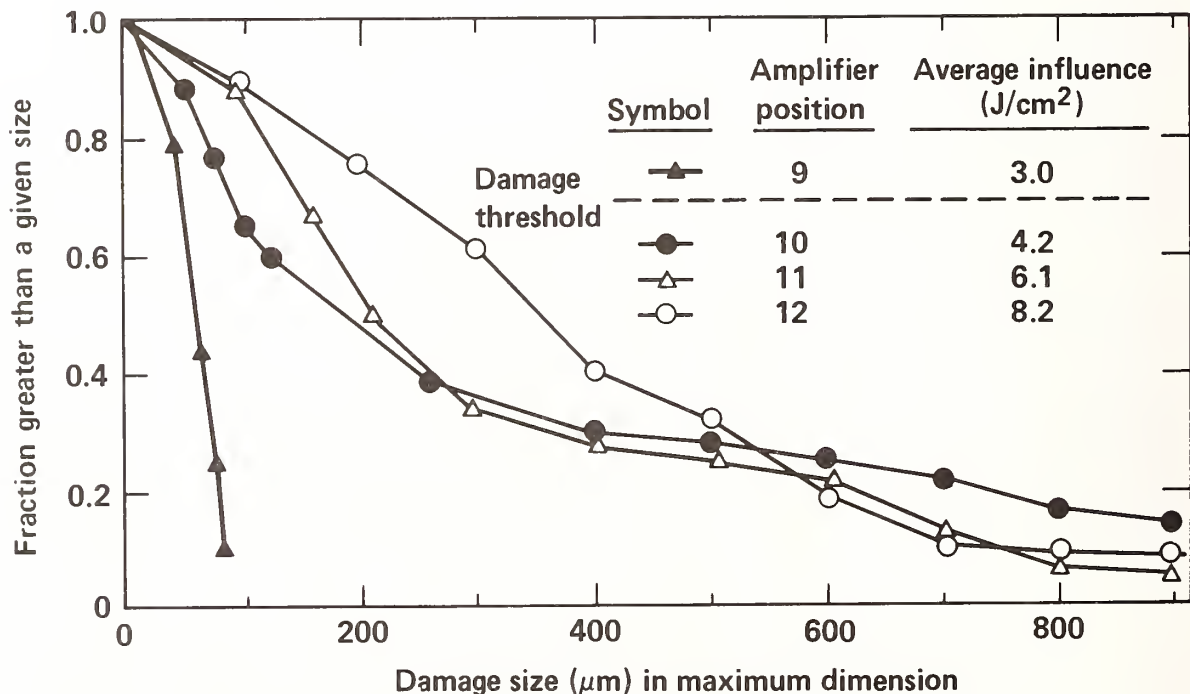


Figure 4: Normalized plot of fraction of damage sites (in Nova 46cm disks) that exceed the dimension shown on the abscissa. The disk amplifier positions are indicated by the numbers 9, 10, 11 and 12 corresponding to the locations shown in Fig. 1.

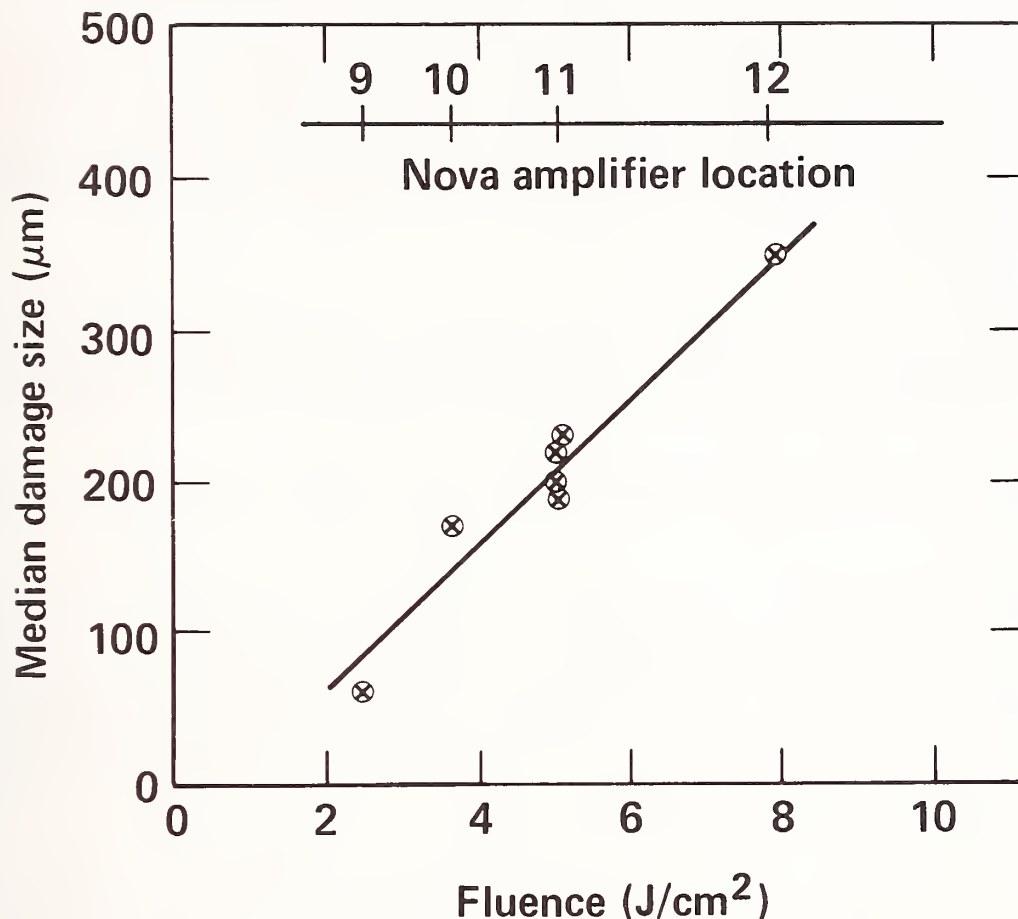


Figure 5: Median damage size found upon inspection of Nova disks vs. the average fluence at that disk location.

The correlation between the level of damage found in several of the Nova disks and the experimental data that we have recently generated can be used to predict which disks are likely to be damaged by a particular use of the laser. For safe operation at 1-ns and 10 kJ per beam (100 kJ total output), replacement of the eight 46-cm disks and of at least eight 31.5 cm disks in each arm is required. If each arm is to safely produce 20 kJ, 5-ns pulses, replacement of almost all 46 and 31.5 disks and the final 20.8-cm disks will be required. Until replacement glass is available, the laser can be safely operated at 5 kJ/arm (50 kJ total) with the existing glass. Currently we have about 2 years of experiments that require less than the 50 kJ output. This is sufficient time for us to replace the current glass with platinum free glass.

2.4 Inspection of Glass

Certification that Pt⁰ inclusion-free glass has been obtained will require an improved inspection procedure. Previously, the most effective technique for finding a low volume density of inclusions in a large volume of glass was to illuminate the sample from the back or through its edges and visually search for scattering centers. Even after the inclusion problem had become apparent and the visual inspections were being executed with great care, less than 50% of the inclusions were identified in most samples. Detailed microscopic examinations required too much time and were sometimes no more successful. Automated light scattering experiments are probably capable of detecting inclusions, but do not readily distinguish between inclusions and other bulk defects such as bubbles or surface defects. The only procedure known to be completely successful is a destructive damage test. Irradiating an inclusion with 5-10 pulses having fluences well above threshold produces a damaged volume that is readily visible.

To guide the initial experiments aimed at improving glass, two large-area damage experiments were attached to the Nova laser. One was positioned at the midpoint of an arm and allowed irradiation at fluences of 7-10 J/cm² of areas with diameters of 6-9 cm. The second was at the output of an arm and allowed similar experiments over areas 25-30 cm in diameter. These experiments have been very successful in determining the damage susceptibility of large glass samples, but use of Nova as a damage tester is highly impractical. To minimize shot time required from Nova, a separate system was built to allow rapid scanning of a glass sample with the beam of a commercially available 20-Hz Q-switched Nd:YAG laser. The beam from the laser is slightly focussed so that the fluence at the sample is about twice the damage threshold for the 8-ns pulses. Successful use of this system to locate platinum inclusions in glass is described in a separate paper by Marion et. al.⁸

2.5 Progress on Improved Glass Melting

Staff members at LLNL are working with scientists at the two Nova laser glass vendors (Hoya Optic, Inc. and Schott Glass Technologies, Inc.) to eliminate the Pt inclusion problem in phosphate laser glass. Details of glass manufacture at both these facilities are proprietary, so progress can only be discussed in general terms.

In brief, both companies have sought to control the Pt problem by (a) reducing or eliminating possible outside sources of Pt contamination and (b) adjusting process conditions to put or keep all Pt in solution, i.e. as ionic Pt (which does not damage) rather than as metallic inclusions (which do damage).

Considerable progress has been made in both areas. Recently we have tested 7 large pieces of glass having a total volume of about 17-18ℓ and found an average of less than 0.20 inclusions per liter of glass. (Four pieces of glass were completely Pt⁰ free).⁸ These new pieces were prepared under conditions designed to convert any metallic Pt⁰ to its ionic form. The samples were tested using both Nova and our new QA inspection tool at 2-4 times the damage fluence. A series of further process changes are in progress that should reduce the Pt inclusion level to less than 0.1 per liter⁹ thus meeting our design specifications. For comparison, the current Nova disks have Pt⁰ inclusion concentrations of between 10 to 1000 per liter, thus the current new glass represents a 50 to 5000 fold improvement.

We have begun procurement procedures necessary for the replacement of the Nova glass. Our present plans show construction of production melting facilities beginning in January of 1986 and being completed by about May. Production melting should begin in May or June, and the first replacement glass is expected to arrive at LLNL in Sept. or Oct. The complete replacement process will take about 18 to 24 months.

The large-area damage test facilities at Nova were designed and installed by the mechanical engineering staff of the fusion laser program. We are especially grateful to Brigitte Gim and Daniel Clifton for their major roles in that installation. Large-area experiments required the assistance of the Nova operations crews (shift leaders are Glenn Hermes, Gary Ross, and Timothy Wieland), and of two individuals, Janice Lawson and Carolyn Weinzapfel, who conducted some of the large-area testing. Inspections of disks removed from lasers for evaluation were done by Gary Edwards and Donald Gemmell of the Nova clean room staff. The authors also benefited from the council of Stanley Stokowski, Perry Wallerstein, Ian Thomas, Howard Patton, John Marion, John Pitts and Frederick Ryerson, who are members of the group working on this problem.

3. References

- [1] K. Manes and W. W. Simmons, "Statistical Optics Applied to High-Power Glass Lasers." J. Opt. Soc. Am. A 2, 1985, pg. 528.
- [2] J. T. Hunt and R. J. Foley "Laser Systems and Operations" in Laser Program Annual Rept, UCRL-50021-84, LLNL, (1985).
- [3] "Fundamentals of Damage in Laser Glass" National Materials Advisory Board, Division of Engineering, National Research Council; report NMAR-271, Washington, D. C. July 1970.

- [4] Ray Gonzales and Dave Milam "Evolution During Multiple-shot Irradiation of Damage Surrounding Isolated Pt Inclusions in Phosphate Laser Glass." 17th Boulder Damage Symposium, Oct. 1985.
- [5] A. B. Shapiro "Topaz - A finite element heat conduction code for analyzing 2-0 solids" UCID-20045, LLNL, March, 1984.
- [6] J. H. Pitts "Modeling laser damage caused by platinum inclusions in laser glass", 17th Boulder Damage Symposium, Oct. 1985, Boulder, CO.
- [7] C. Orth, Lawrence Livermore National Laboratory, Livermore, CA, Private Communication, July 1985.
- [8] J. E. Marion, P. H. Chaffee, G. J. Greiner and J. H. Campbell "A versatile laser glass inspection and damage testing facility", 17th Boulder Damage Symposium, Oct. 1985, Boulder, CO.
- [9] C. W. Hatcher, LLNL, 1985, unpublished results.

DISCLAIMER

This document was prepared as an account of work sponsored by an agency of the United States Government. Neither the United States Government nor the University of California nor any of their employees, makes any warranty, express or implied, or assumes any legal liability or responsibility for the accuracy, completeness, or usefulness of any information, apparatus, product, or process disclosed, or represents that its use would not infringe privately owned rights. Reference herein to any specific commercial products, process, or service by trade name, trademark, manufacturer, or otherwise, does not necessarily constitute or imply its endorsement, recommendation, or favoring by the United States Government or the University of California. The views and opinions of authors expressed herein do not necessarily state or reflect those of the United States Government thereof, and shall not be used for advertising or product endorsement purposes.

Evolution During Multiple-Shot Irradiation of Damage Surrounding
Isolated Platinum Inclusions in Phosphate Laser Glasses*

R. P. Gonzales and D. Milam
Lawrence Livermore National Laboratory
University of California
P.O. Box 5508, L-490
Livermore, California 94550

Platinum inclusions in samples of laser glass were placed in the center of a 2-mm-diameter beam and repeatedly irradiated with 1064-nm laser pulses having durations of 1.3, 9 or 50 ns. The initial major dimensions of the particles ranged from 4-75 μm . The thresholds for initiation of damage were 2.5 ± 0.3 , 4 ± 0.4 and 8 ± 0.8 J/cm², respectively, for the three pulse durations used in the tests. Thresholds were independent of particle size. Three particles with initial dimensions of 4, 5 and 8 μm caused damage smaller than 250 μm . One 6 μm particle and all particles larger than 10 μm caused larger damage.

Key words: platinum inclusions, bulk laser damage, phosphate laser glass

1. Introduction

Although it is desirable that glasses used in large lasers should be free of inclusions, the presence of a few small inclusions might be acceptable. For example, the codes that model the NOVA laser predict that the quality of this laser's output beam would not be seriously effected if the laser's components contained a low volume density of beam obscurations with sizes below ~ 250 μm .¹ All of the platinum inclusions that we have located in samples of Nd:phosphate glass initially had sizes well below this limit. However, when these inclusions were repeatedly irradiated by laser pulses, the sizes of the damaged volumes surrounding some inclusions were much larger than 250 μm . This growth of damage complicates the development of adequate specifications for the inclusion content of laser glass. The preferred option is to insist on complete elimination of metallic inclusions, but this may be difficult to achieve in large melts. Another option is to eliminate only those inclusions that will cause unacceptably large damages, but exercising this option requires an understanding of the relationship between the initial size of an inclusion and the ultimate size of the damage volume produced by repeated irradiation of the inclusion. The primary purpose of the experiments described in this paper was investigation of that relationship. Additionally, we needed to measure the dependence of the threshold for initiation of damage on both the duration of the laser pulse and the size of the inclusion.

2. Samples

John Marion and Susan Winfree of Lawrence Livermore National Laboratory provided small glass samples each containing one or more platinum inclusions. In their inspection of several liters of Nd:doped phosphate glass, they located three types of inclusions: spherical bubbles, irregularly shaped transparent objects believed to be microcrystals, and opaque inclusions. In each instance that an opaque inclusion was exposed and analyzed, it was found to be metallic platinum. Because it was necessary to leave inclusions encased in glass during damage tests, opacity was used as a criterion for selecting inclusions for testing. After the damage tests were completed some of the inclusions that had been tested were exposed, analyzed, and found to be platinum. We are reasonably certain, therefore, that all inclusions studied were metallic platinum.

*Work performed under the auspices of the U.S. Department of Energy by Lawrence Livermore National Laboratory under Contract No. W-7405-ENG-48.

Sizes of the inclusions were determined by optical microscopy. Because the inclusions were opaque, this measurement gave only the linear dimensions in a plane normal to the direction of observation, and the thicknesses of the inclusions were unknown. The major dimensions of the tested inclusions ranged from 4-70 μm . Attempts to locate inclusions smaller than 4 μm were unsuccessful.

3. Damage Testing

The samples were mounted in the microscope station on our 1064-nm laser damage experiment, with the polished surface above the inclusion oriented normal to the incident beam.² The inclusions were centered in the beam which had almost Gaussian fluence distribution and was about 2 mm in diameter at the e^{-1} level. In such a beam, fluence over a central area with diameter of .65 mm is $> 90\%$ of the peak on-axis fluence. The beam was, therefore, large compared to the 250 μm size of interest. Peak on-axis fluences were determined to within $\pm 7\%$.

Each inclusion received a sequence of single-shot irradiations usually beginning at a fluence level near 1 J/cm^2 . Fluence was sequentially increased until the damage threshold was exceeded, and then increased additionally to a selected level which was sustained in additional irradiations until the size of the damage either stabilized or exceeded 250 μm . For tests with 1.3-ns pulses, the fluences used during these repetitive irradiations were 5-7 J/cm^2 , which are identical to the spatially averaged fluences existent inside the 46-cm amplifiers of an arm of Nova during production of pulses with output energies of 10-15 kJ. For experiments with either 9-ns or 50-ns pulses, the selected level for sustained irradiation was chosen to be about 2-2.5 times the threshold fluence.

Because threshold level damage was usually observed during the first few pulses of each sequence, these experiments did not determine whether damage could have been produced by a large number of irradiations at lower fluences. However, most of the inclusions tested were taken from a 20.8-cm amplifier disk that had operated at fluences of 0.5-1.0 J/cm^2 during more than 500 shots in the Novette laser, and this series of irradiations by pulses with durations ≤ 1 -ns had not caused damage at any of the inclusions in the disk. We infer from this that the multi-shot 1-ns threshold is not significantly below the typical 1-ns threshold ($\sim 2.5 \text{ J}/\text{cm}^2$) determined by use of a few irradiations.

The occurrence and growth of damage at an inclusion was observed by using a microscope to inspect the inclusion after each irradiation. Most of the larger inclusions had irregular shapes, and damage at threshold consisted of one or more small fractures extending a few microns into the glass surrounding the inclusion. These initial fractures usually had shapes that were peculiar to individual inclusions. During a few irradiations at fluences above threshold, the damage evolved into a circular planar fracture oriented normal to the incident beam. This is believed to be the typical geometry of damage surrounding an inclusion, although additional or more intense irradiations sometimes produce complex damage consisting of intersecting planar fractures and lobes of damage lying along the direction of the incident beam.

4. Data

In most of the experiments, repeated irradiation of the inclusion caused damage larger than 250 μm . Data obtained in the test of the largest inclusion studied (major dimension of 75 μm) are given in Figs. 1 and 2. The inclusion survived three irradiations at fluences up to 2.4 J/cm^2 , and damaged during the fourth shot at 3.8 J/cm^2 . Two additional irradiations at higher fluences caused rapid growth of the fracture surrounding the inclusion, but the growth ceased when the fluence was reduced to $< 2.5 \text{ J}/\text{cm}^2$. Four additional irradiations at higher fluences caused damage much larger than 250 μm . Photographs of the damage are shown in Fig. 2.

For three of the inclusions, the damage grew to a size that remained stable under repeated irradiation. Data obtained in the test of an 4- μm particle are given in Figs 3 and 4. The particle survived 5 irradiations at fluences as large as 2.5 J/cm^2 . The damage stabilized after the fourteenth shot at 12 J/cm^2 , and did not grow during the final 27 shots.

All of the data generated in these experiments are summarized in Table 1.

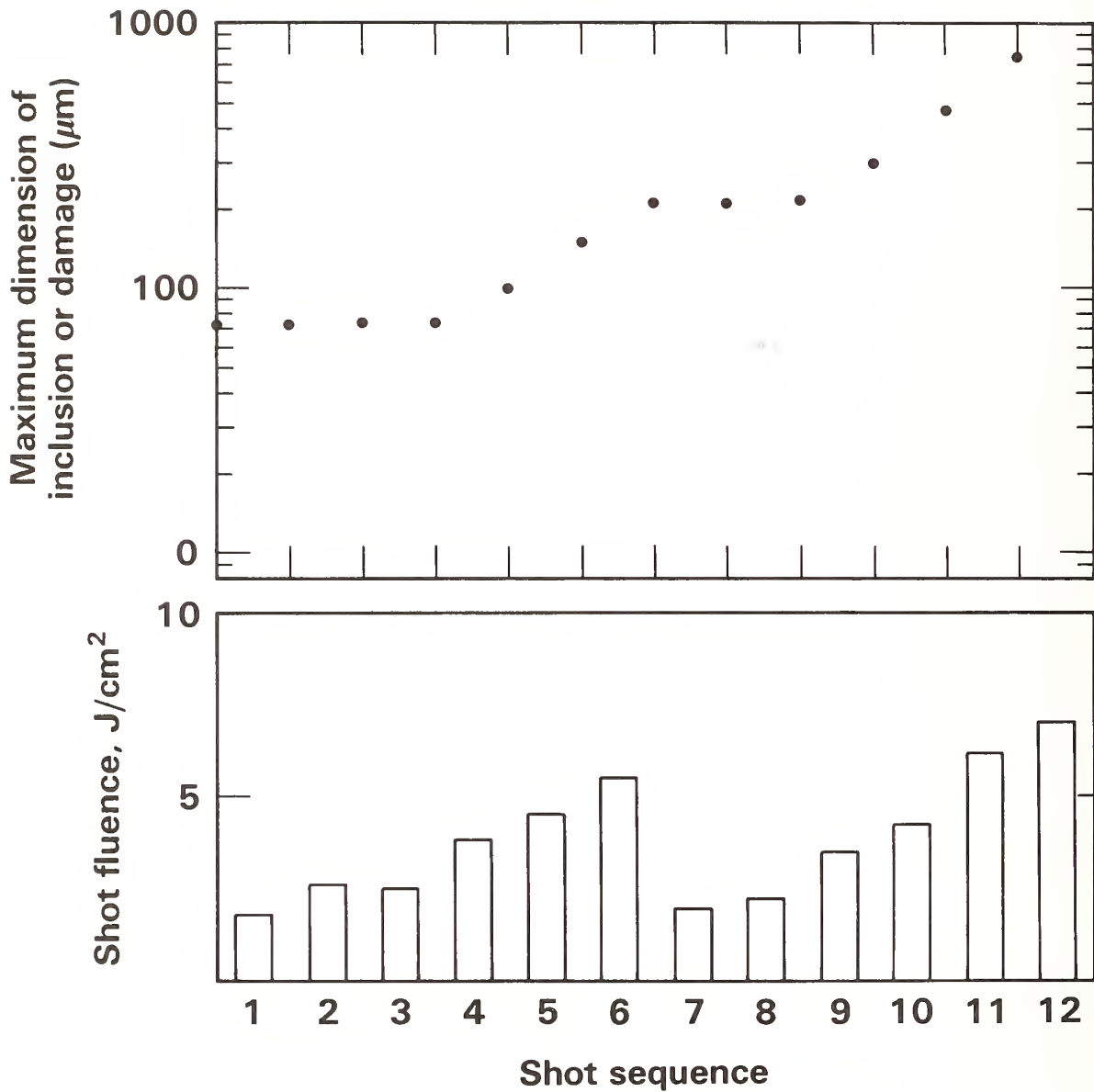
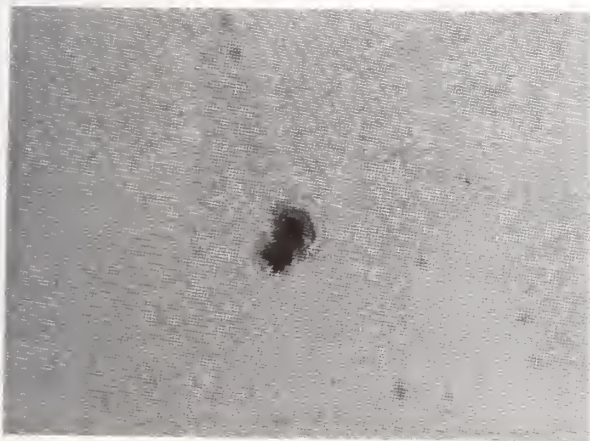


Figure 1: Evolution of damage surrounding a bar-shaped inclusion with initial major dimension of 75 μm . Damage was initiated during shot 4 at 3.8 J/cm^2 , and grew rapidly during each shot at fluences $> 4 \text{ J}/\text{cm}^2$. See associated photographs in Fig. 2.



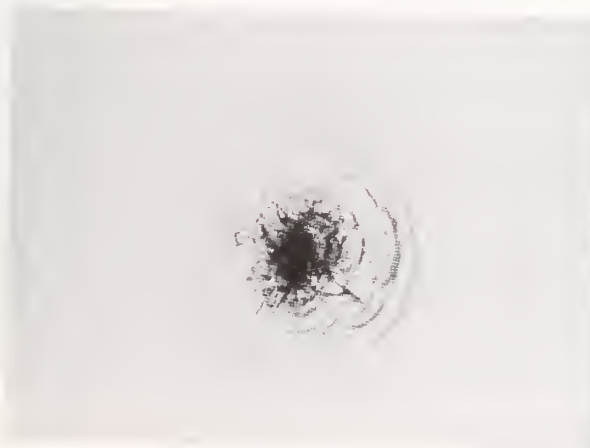
initial appearance



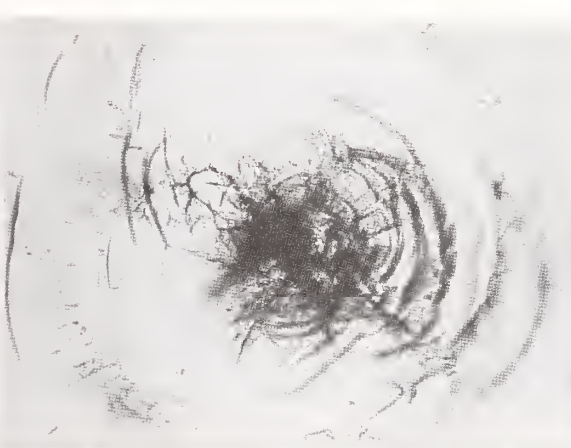
After shot 4 at 3.8 J/cm²



After shot 6 at 5.5 J/cm²



After shot 10 at 4.3 J/cm²



After shot 12 at 7 J/cm²

Figure 2: Photographs of damage surrounding an inclusion with initial major dimension of 75 μm . Physical dimensions are given in the associated data, see Fig. 1.

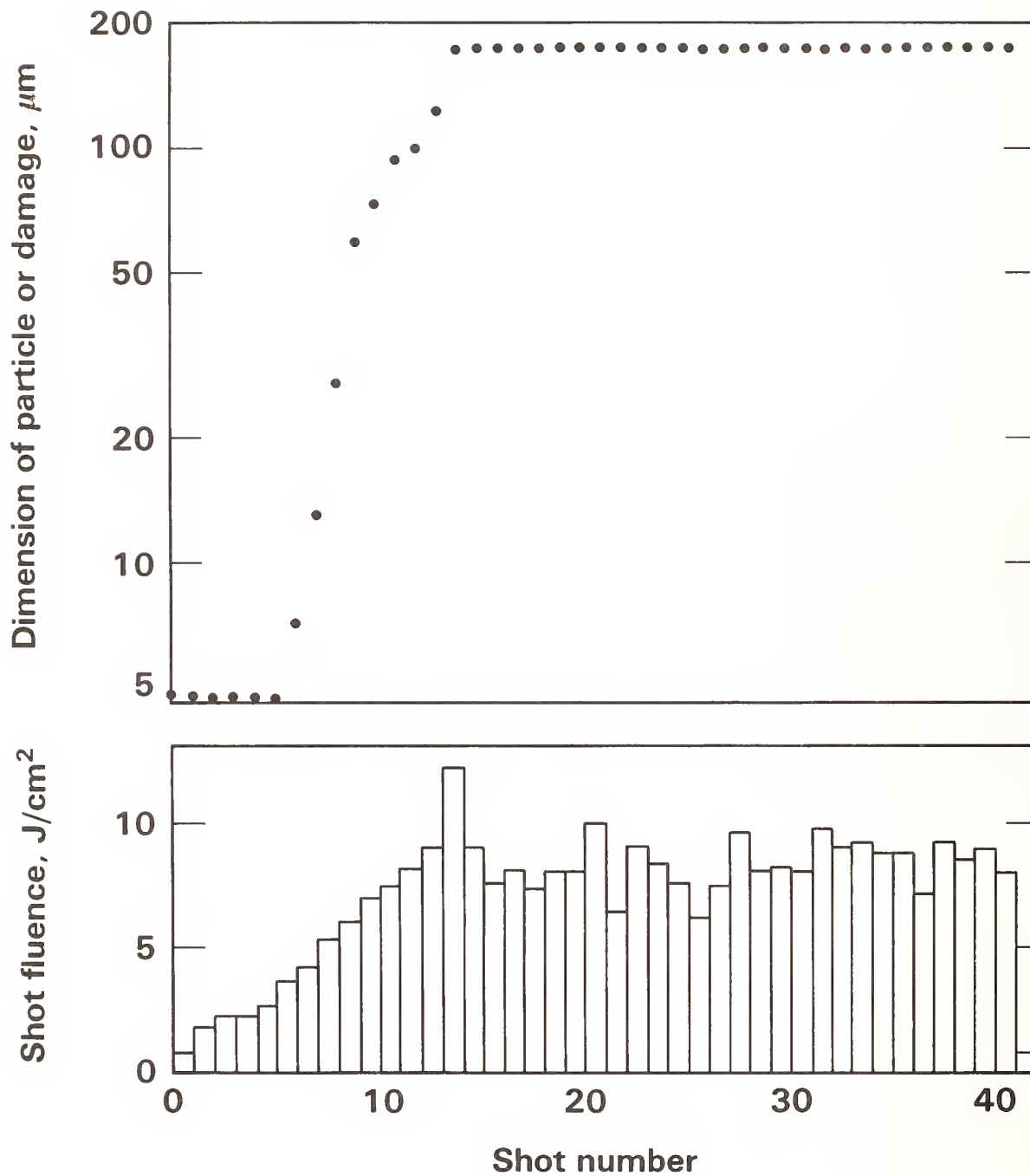


Figure 3: Evolution of damage surrounding an inclusion with initial dimension of 4 μm . Damage was initiated during shot 6 at 3.7 J/cm^2 and reached its stable size during shot 14 at 12.3 J/cm^2 . See associated photographs in Fig. 4.



initial appearance



After shot 6 at 3.7 J/cm^2

After shot 9 at 6.1 J/cm^2

After shot 11 at 7.6 J/cm^2



After shot 13 at 9.1 J/cm^2

After shot 14 at 12 J/cm^2

After shot 41

Figure 4: Photographs of damage surrounding an inclusion with initial dimension of $4 \mu\text{m}$. The size remained stable after shot 14. Major dimensions of damage sites are given in the associated data, see Fig. 3.

Table 1
Size of Damage Surrounding Particles with Varied Initial Dimensions.

Laser Pulse duration, ns	Test(a) Fluence J/cm ²	Number(b) of shots	Initial Particle size, μm	Final Size of Damage, μm (b)	
				stabilized	unstabilized
1	6-10	36(9)	4	176	
1	5-7	20(14)	6	240	
1	5-7	49(6)	8	75	
1	5-7	9	18		410
1	3-9	8	25		750
1	4-7	7	70		1000
9	5-9	9	17		380
9	5-9	8	18		440
55	8-20	6	6		340
55	9-20	5	18		390
55	8-20	6	19		500

(a) Range of fluences for which growth of damage was observed.

(b) Number of shots applied at fluences within the stated range. Bracketed values are numbers of shots during which damage grew prior to stabilization.

5. Discussion of Results

5.1 Maximum Allowable Size for Platinum Inclusions

We did not find a monotonic relationship between the initial size of an inclusion and the stable size for the damaged volume surrounding the inclusion. One particle with initial dimension of 6 μm and all the particles larger than 10 μm caused damage larger than 250 μm . Three particles with initial dimensions of 4, 5, and 8 μm caused damage that remained smaller than 250 μm . The fluence at which growth of damage ceased was 5-7 J/cm² delivered in 1.3-ns 1064-nm pulses. Therefore, the limited data indicates that repeated irradiations at 5-7 J/cm² of an inclusion with initial size of 4-6 μm might not cause damage larger than 250 μm . We believe that larger damage might be produced at larger fluences.

Several mechanisms have been proposed to describe the termination of the growth. It is known that platinum is distributed onto the fractured surfaces surrounding an inclusion.³ During multiple shots, the platinum might eventually become so thinly distributed that the net absorption of light was reduced below that required to produce additional fracturing. This mechanism could explain why the damage surrounding an 8- μm inclusion was smaller than that surrounding a 4- μm particle. It is possible that the 8- μm particle was a thin platelet whereas the apparent 4- μm size was the projected view of a particle with relatively large volume.

The calculations by Pitts⁴ suggest that the damage is driven by high pressure vapor boiled from the heated surface of the particle. Under this model, the fractured volume becomes a more effective vent for the vapor, and the crack tips to which force must be applied become more distant, as the damage grows. While this allows limitation of growth, the quantity of vapor to be vented should be proportional to the irradiated area of the particle, so this model has some difficulty accounting for the nonmonotonic relationship between the sizes of particles and damage.

5.2 Threshold vs. Particle Size

The 1.3-ns thresholds were $2.5 \pm 0.3 \text{ J/cm}^2$ for inclusions with initial major dimensions ranging from 4-75 μm , and the 50-ns thresholds were $8 \pm 0.8 \text{ J/cm}^2$ for inclusions with initial sizes ranging from 6 to 19 μm . Therefore, thresholds were independent of particle size. All models for inclusion damage, beginning with the earliest major treatment of the subject,⁵ predict this result which is caused by the limited dimension for heat flow during short time intervals. In a material with thermal diffusivity D , the characteristic dimension for heat flow in time t is $x = \sqrt{Dt}$. For platinum, $D = 0.24 \text{ cm}^2 \text{ sec}^{-1}$, and $x = 0.15 \mu\text{m}$ for $t = 1 \text{ ns}$ and $1.1 \mu\text{m}$ for $t = 50 \text{ ns}$. The heat deposited in 1-50 ns cannot be distributed across the surface of a particle with size $> 4 \mu\text{m}$, so the heating at each point on the surface of such large particles is almost independent of heat deposition at other points on the remainder of the surface.

Analytical models also predict that inclusions with diameters of about 0.1 μm would be most effectively heated by 1-ns pulses, and we initially suspected that laser glass containing large, visible particles might contain many particles with sizes below 1 μm . With a single exception, results of damage tests of large volumes of laser glass indicate that about 50% of the bulk damages occurred at sites containing rather large inclusions that had been located during pre-test inspections. A large fraction of the additional 50% contained large ($> 5 \mu\text{m}$) inclusions that had not been detected before they were made more visible by damage. Therefore, we must assume that the existing laser glass is either free of very small inclusions, or that repeated irradiation of very small inclusions fails to cause damaged volumes large enough to be readily detected.

5.3 Variation of Threshold with Pulse Duration

Thresholds measured at the three pulse durations, 1.3, 9 and 50 ns, were 2.5 ± 0.3 , 4 ± 0.4 and $8 \pm 0.8 \text{ J/cm}^2$. As shown in Fig. 5, these thresholds scale with pulse duration τ as τ^α with $\alpha = 0.3$. However, all theoretical models^{4,5} predict the scaling should be $\tau^{0.5}$.

If the smaller scaling rate of the experimental data is due to measurement error, then the actual 1.3-ns threshold must be less than the assigned value of 2.5 J/cm^2 , or the 50-ns threshold must be greater than 8 J/cm^2 . The latter possibility is readily dismissed. Damage was observed at 8 J/cm^2 in the 50-ns tests, and fluence measurements in that test were accurate to within $\pm 7\%$. It is possible that the assigned 1.3-ns threshold is too large. Pitts estimates that the damage produced by threshold level 1.3-ns irradiation might consist only of cracks extending $\sim 1 \mu\text{m}$ away from the inclusion. One could argue that our assigned value, 2.5 J/cm^2 , is the fluence necessary to produce a detectable level of damage, and not a true threshold.

There are additional facts that assist in bounding the 1.3-ns threshold. The inclusions tested in these experiments were taken from a Novette amplifier that had survived many irradiations at $\sim 1 \text{ J/cm}^2$, so the 1.3-ns threshold is not less than this value. Secondly, the level of damage found during examination of selected components in Nova can be explained if the 1.3-ns threshold is near 2.5 J/cm^2 . It is also generally true that inclusion damage has not been a problem in large glass lasers operating at fluences below 2 J/cm^2 . The Shiva and Argus laser, for example, were free of inclusion damage. Therefore, all evidence available suggests that the 1.3-ns threshold is 2.5 J/cm^2 , and additional experiments and modeling will be required to understand the discrepancy between experimental and theoretical values of the threshold scaling parameter for 1.3-ns pulses.

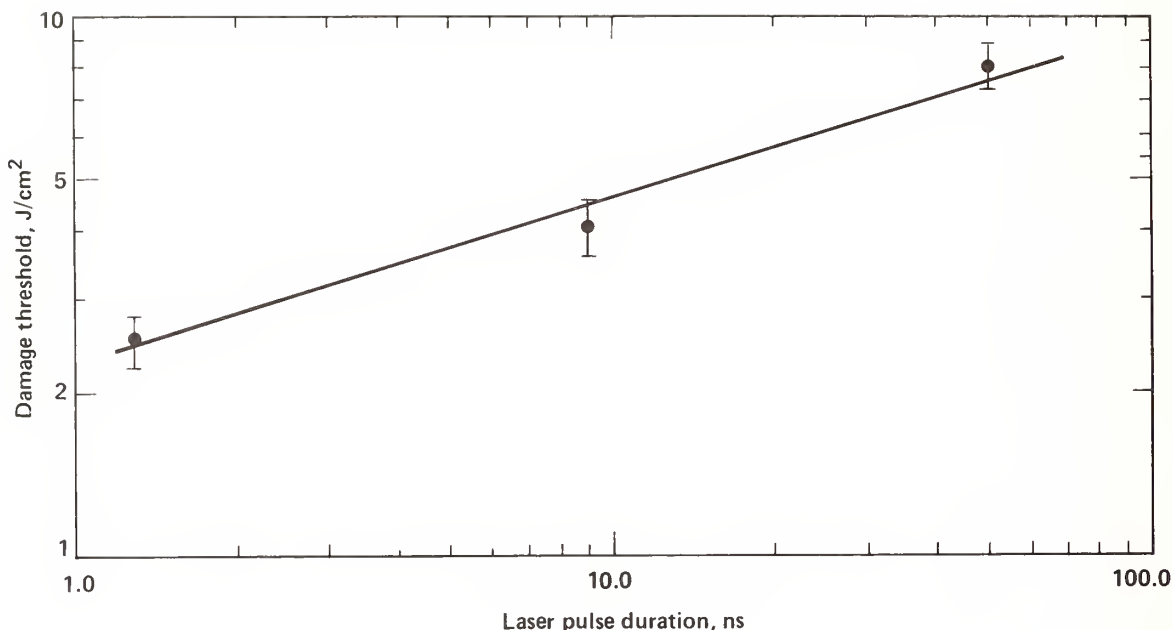


Figure 5: Variation of damage threshold of platinum inclusions in laser glass as a function of pulse duration. Data are average values for the inclusions tested. The curve is pulse duration raised to the 0.3 power ($\tau^{0.3}$).

6. Summary

Particles with initial dimensions greater than 4-6 μm will cause damage larger than 250 μm when the particles are irradiated by 1-ns pulses at fluences of 5-7 J/cm^2 . Damage around smaller particles may remain acceptably small. The size range of acceptable particles is based on a few measurements, so it is somewhat uncertain and it also probably depends on the fluence level at which the particles are irradiated.

For the large particles, the threshold for initiation of damage was independent of particle size, and for pulse durations between 1.3 and 50 ns, varied with pulse duration as $\tau^{0.3}$.

We are grateful to several co-workers for assistance during this study. John Marion and Susan Winfree prepared test samples containing inclusions. Numerous helpful discussions were held with members of the group (headed by Jack Campbell) formed to study elimination of platinum from glass.

7. References

- [1] Calculation of the maximum size for beam obscurations in Nova was done by W. E. Warren of LLNL using the code MALAPROP.
- [2] D. Milam, "Measurement and identification of laser-damage thresholds in thin films", SPIE Vol. 140, Optical Coatings-Applications and Utilization II, 52-61, 1978.
- [3] The observation of the distribution of platinum into cracks surrounding an inclusion was attributed by Hopper and Uhlmann (see Ref. 5) to R. W. Woodcock of American Optical Company; recent work by J. E. Marion of LLNL confirms this observation.

- [4] J. H. Pitts, "Modeling laser damage caused by platinum inclusions in laser glass", elsewhere in these proceedings.
- [5] The extensive literature on laser heating of inclusions appears to stem primarily from two early papers: R. W. Hopper and D. R. Uhlmann, "Mechanism of inclusion damage in laser glass", J. Appl. Phys., 41(10), 4023, Sept. 1970; Yu. K. Danileiko, A. A. Manenkov, A. M. Prokhorov and V. Ya. Khaïmov-Malkov, "Surface damage of ruby crystals by laser radiation", Sov. Phys. JETP, 31(1), 18, July 1970.

DISCLAIMER

This document was prepared as an account of work sponsored by an agency of the United States Government. Neither the United States Government nor the University of California nor any of their employees, makes any warranty, express or implied, or assumes any legal liability or responsibility for the accuracy, completeness, or usefulness of any information, apparatus, product, or process disclosed, or represents that its use would not infringe privately owned rights. Reference herein to any specific commercial products, process, or service by trade name, trademark, manufacturer, or otherwise, does not necessarily constitute or imply its endorsement, recommendation, or favoring by the United States Government or the University of California. The views and opinions of authors expressed herein do not necessarily state or reflect those of the United States Government thereof, and shall not be used for advertising or product endorsement purposes.

Multiple Pulse Damage Studies of BK-7, KCl
and SiO₂ at 532 nm

D. Kitriotis, L. D. Merkle and A. Dodson

Department of Physics
University of Arkansas
Fayetteville, AR 72701

We report the results of damage studies at 532 nm on BK-7 glass, KCl, fused silica and two grades of crystalline quartz using a frequency doubled, Q-switched YAG laser. This work represents the initial stages of a program to investigate the mechanisms of multiple pulse laser-induced bulk damage in transparent solids. Comparison of BK-7 damage behavior with that of fused silica shows little effect due to the color center generation which occurs in BK-7 due to its small band gap. Commercially grown KCl exhibits multiple pulse catastrophic damage at fluences significantly below single pulse "threshold", probably due to grown-in defects. Laser-induced damage behavior has been compared between two grades of crystalline quartz, with the surprising result that the nominally less perfect material is the more resistant to damage. The presence of "etch tunnels" may be involved, but considerably more study is required.

Key words: borosilicate glass; crystalline quartz; fused silica; multiple pulse damage; potassium chloride; pulse repetition frequency.

1. Introduction

In this paper we report the first results of a research program being undertaken at the University of Arkansas to study multiple pulse bulk damage and the spectroscopic properties of laser-irradiated transparent materials. The purpose of this program is to investigate the influence of microscopic defects, both pre-existing and laser-induced, on catastrophic damage properties of solids. It is believed that such investigations will contribute to understanding of the mechanisms of multiple pulse damage, which several recent studies have shown to involve gradual, perhaps transient, and very elusive laser-induced property modifications prior to catastrophic damage [1-5].

This paper contains early results of a study using 532 nm light to damage BK-7 borosilicate glass, single crystalline KCl and both fused and crystalline SiO₂. These materials were chosen to permit comparisons between substances with band gaps far larger than twice the energy of the incident photons and one with a gap of less than two 532 nm photons (BK-7). In addition, two grades of crystalline quartz were studied, permitting investigation of the influence of pre-irradiation defects and impurities on damage resistance.

In section 2 the experimental technique and apparatus are described. Section 3 presents and discusses damage data on crystalline quartz, including the most striking observation of this study: the dramatic difference in damage behavior between two samples of quartz differing only modestly in concentrations of the most common impurities. In section 4 damage data on fused silica and BK-7 are compared for evidence of the influence of their very different band gaps, and in section 5 the observation of multiple pulse damage in KCl is reported. In the final section the interpretations of all these results are discussed, as are the needed directions of future work.

2. Experiment

The experiments reported in this paper are straightforward multiple pulse damage experiments in which a sample is irradiated with a train of nominally identical laser pulses and the number of pulses required to induce catastrophic damage is noted. The irradiating laser beam is focused tightly into the bulk of the sample so that only bulk damage is obtained. In this work "catastrophic damage", or simply "damage", is defined as the event in which a flash of light, a sudden increase in light scattering as observed by eye, a sudden decrease in transmission and the generation of a bubble-like damage track occur. These indicators of "damage" are all found to occur on the same pulse, so that the above definition can be applied unambiguously.

The experimental apparatus is diagrammed in figure 1. Irradiating pulses were produced at a

pulse repetition frequency of 10 Hz by a Q-switched, unstable cavity Quanta Ray DCR-1 Nd:YAG laser. In these experiments the output was frequency doubled and the 532 nm light separated from the residual 1064 nm light by a prism. The annular cross section of the output beam was converted to a smooth central spot with only several percent of the light remaining in concentric diffraction rings by means of a spatial filter and subsequent apertures. The spatial filter was assembled using two positive and two negative lenses to produce a very long focal depth and large enough focal spot radius that air breakdown could not occur. The beam was focused tightly into the sample using a 25 mm focal length plano-convex lens.² The resulting focal spot was found by knife edge scans to be adequately fit by a Gaussian with $1/e^2$ radius in the range 5.7 microns to 11.7 microns, depending on configuration of the spatial filter and apertures.

The temporal profile of the laser pulse is not well characterized. The laser operates in multiple modes with a band width of about one inverse centimeter, so that the pulse of nominally 10 nsec duration contains large spikes unresolvable by available detectors. For this reason all results are presented in terms of fluence rather than intensity.

The scatter from a coaxial He-Ne laser beam was employed as a convenient real-time indicator of catastrophic damage.

Several aspects of the experiment were controlled or monitored by a microcomputer (LSI-11) by means of a CAMAC crate. Pulses were counted and the incident pulse energy was monitored using a calibrated Hamamatsu S1723-02 photodiode. Due to the small focal size, energies of only 10 μ J to 300 μ J were required. The energy stability during multiple pulse experiments was typically $\pm 15\%$, and experiments in which variability exceeded $\pm 20\%$ were rejected. A Hewlett-Packard 5082-4220 photodiode monitored the transmitted energy, and a computer controlled shutter was used to start and stop each experiment and to provide pulse repetition frequencies lower than 10 Hz.

3. Crystalline Quartz

A comparison of multiple pulse damage in two grades of single crystal quartz has been undertaken to investigate the influence of pre-existing impurities and defects on damage in SiO_2 . Samples of "Premium Q" grade and "Electronic" grade quartz from Thermo Dynamics, Inc., were cut and polished for beam propagation along the z-axis. Premium Q quartz has a lower concentration of OH ions than Electronic grade, and typically has lower concentrations of Al and the dislocations which give rise to "etch tunnels" as well [6]. Such impurities and defect structures may well affect the damage behavior of the material.

The results of damage tests on these materials due to 532 nm irradiation are shown in figures 2 and 3. In each case each data point represents an experiment in which a previously unirradiated section of the sample was exposed to the number of laser pulses indicated on the logarithmic vertical scale at the average on-axis fluence indicated on the horizontal scale. Different symbols indicate experiments terminated by catastrophic damage and those ended without such damage, as indicated in the captions. The focal spot radii employed are also noted.

The most striking feature of the data is the dramatic difference in damage resistance between the two samples. The Electronic grade sample was found to be considerably stronger against laser damage, both single and multiple pulse, than the Premium Q grade at 532 nm. The scatter in the data is too large to yield well-defined single pulse damage thresholds, particularly for the Electronic grade sample, but the approximate "threshold" for Electronic grade is clearly about twice that of the Premium Q grade.

Two other observations may be made regarding the Premium Q damage. The dependence upon focal spot size evident in figure 2 is qualitatively similar to that commonly observed in many materials and widely attributed to randomly distributed damage-promoting impurities or defects. Data were taken with pulse repetition frequencies of both 1 Hz and 10 Hz with indistinguishable results, so the laser-induced property changes which lead to damage after many pulses must live much longer than one second.

In an attempt to identify the pre-irradiation properties responsible for the very different damage resistances of the Premium Q and Electronic grade samples, comparisons of their concentrations of OH, Al and etch tunnels have been made. Estimates of the relative OH concentrations were made by comparison of the absorption coefficients of the two samples at two OH absorption wave numbers: 3410 cm^{-1} and 3500 cm^{-1} . Aluminum concentrations were measured by Larry Halliburton of Oklahoma State University using electron spin resonance on small samples cut from the material adjacent to each damage sample. Adjacent pieces were also cut and polished, then subjected to an etch in saturated ammonium bifluoride solution by a technique similar to that reported by Vig, et al. [6] All measurements were made on z-growth material, as were the damage tests themselves. The results

are summarized in table 1. Note that the approximate densities of pits on the etched surfaces are listed. The density and size of the etch pits made it difficult to see etch tunnels extending into the bulk with a standard microscope, but according to Vig and coworkers most etch pits should be the surface terminators of etch tunnels [6]. Note that the Premium Q sample has the lower concentrations of OH and Al, as expected. However, these subtly different concentrations appear unlikely to account for the large difference in damage resistance between the two materials.

Table 1. Comparison of OH, Al, and etch pit densities in Thermo Dynamics 11-7-83-85 (Premium Q) and Thermo Dynamics 11-14-83-29 (Electronic grade) quartz samples.

Impurity	Absorption Coefficient or Concentration in Premium Q	Absorption Coefficient or Concentration in Electronic	$\frac{C(\text{Premium Q})}{C(\text{Electronic})}$
OH	$\alpha_{3410} \doteq 0.245 \text{ cm}^{-1}$ $\alpha_{3500} \doteq 0.17 \text{ cm}^{-1}$	$\alpha_{3410} \doteq 0.26 \text{ cm}^{-1}$ $\alpha_{3500} \doteq 0.175 \text{ cm}^{-1}$	0.94-0.97
Al	3.7 ppm atomic	4.4 ppm atomic	0.84
etch pits on surface	$10^3\text{-}10^4 \text{ cm}^{-2}$	$10^2\text{-}10^3 \text{ cm}^{-2}$	~ 10

The very different damage behaviors may be related to the large difference in etch pit concentrations. The dislocations which give rise to etch tunnels contain broken or strained bonds and are thought to contain high concentrations of alkali impurities. Thus they may contain electronic states which could couple to the irradiating light to promote damage. The low density of such tunnels implied by table 1 dictates that damage dependent upon irradiation of such structures would be initiated at coarsely distributed locations, particularly in the Electronic grade sample. However, microscopic inspection of the damage tracks indicates that 85-90% of the damage events initiate within significantly less than 100 μm of the focal plane. Note also that microscopy provides no evidence of inclusion-controlled damage. Thus it remains unclear what defect or impurity gives rise to the dramatic difference in damage behavior between these two quartz samples.

4. Fused Silica and BK-7 Glass

It is known that BK-7 borosilicate glass, due to its small band gap, undergoes two photon absorption when irradiated by 532 nm laser light and that the resulting excitations form color centers which absorb linearly in the visible [7]. Irradiation in the green thus has channels for the excitation of electrons and the deposition of energy in BK-7 not available in fused silica, a glass with a far larger band gap. For this reason it is interesting to compare the single and multiple pulse damage properties of these glasses.

Damage data taken on these materials are summarized in figures 4 and 5. The single pulse damage threshold in BK-7 is considerably lower than in fused silica: about 65 j/cm^2 versus 175 j/cm^2 , respectively, when equal spot sizes are compared. This may reflect the easier generation of electron-hole pairs in BK-7 than in fused silica. The shapes of the pulse number versus fluence curves are very similar, however. For example, the fluence required to cause catastrophic damage in 1000 pulses is about 45% of single pulse threshold in both materials. This is perhaps surprising in view of the generation of color centers in BK-7, which should let successive pulses encounter a progressively less transparent material.

White, et al., found that the linear absorption at 532 nm induced by two photon color center generation in BK-7 saturated at a value proportional to the irradiating fluence [7]. Their data extend to 26 j/cm^2 , at which we observe damage after several thousand pulses. To estimate the heat deposition due to color center absorption at that fluence, assume that the absorption coefficient equals a constant, α , within the focal volume of the laser beam and is zero outside that volume. If it is also assumed that all absorbed energy is converted to heat, then noting that $1/\alpha$ is large compared to the focal depth and that $\sqrt{4Dt_{\text{pulse}}} \ll w_0$ for a spot radius, w_0 , of several microns and thermal diffusivity, D , about 0.005 cm^2/sec , the maximum temperature rise due to a single pulse is

$$\Delta T = \frac{Q}{VC_p} = \frac{3\alpha E}{4\pi\rho C_p w_0^2}.$$

Here Q is the heat absorbed, E is the incident pulse energy, V is the focal volume, ρ is the mass density and C_p the specific heat. Using standard room temperature values for the BK-7 properties and $\alpha=0.08 \text{ cm}^{-1}$ for a fluence of 26 J/cm^2 from White, et al. [7], the single pulse temperature rise is only 0.5 K. Buildup of temperature from pulse to pulse is insignificant with a focal spot size of several microns, since $\sqrt{4D \cdot 0.1 \text{ sec}} \gg w_0$.

This estimate may be too conservative due to the spikes in the temporal waveform of the laser used in this work. Comparison of figures 2, 3 and 4 with the data of Merkle, et al. [2] suggests that the peak intensities obtained in the present work may be an order of magnitude above those which would obtain at the same fluence with a smooth pulse of equal duration. Using the linear intensity dependence of the saturated absorption coefficient observed by White, et al. [7], this still gives a temperature rise of only several degrees. Thus heating due to color center absorption cannot significantly affect the damage process.

It is likely that absorption of a photon by an excited color center would produce a free conduction band electron. Thus, the presence of color centers generated on earlier pulses should promote the production of conduction band electrons to aid electron avalanche. For this reason the fact that multiple pulse damage occurs in about the same number of pulses at a given fraction of single pulse threshold fluence in BK-7 as in fused silica may indicate that the damage process in BK-7 is not sensitive to the concentration of easily freed electrons.

5. Potassium Chloride

Multiple pulse damage has also been investigated in KCl from Harshaw. Catastrophic damage of this material by repeated $10.6 \text{ }\mu\text{m}$ pulses was reported by Wu, et al., who attributed the effect to the growth of damage from microscopic inclusions [8]. It is of interest to study damage at other wavelengths where different mechanisms may be operative.

Figure 6 summarizes damage experiments performed at 532 nm using both 1 Hz and 10 Hz pulse repetition frequencies. It is clear that multiple pulse damage does occur at this wavelength. The scatter in the data make it evident that the damage mechanism involves interaction with inhomogeneously distributed defects. This is supported by microscopic inspection of damage tracks, many of which initiate more than $100 \text{ }\mu\text{m}$ from the focal plane. In addition, although the majority of each damaged volume is spindle-shaped as in the other materials, in KCl the damage tracks frequently begin with a line of "bubbles" extending up to several hundred microns. Another possible cause of scatter in the damage data would be surface roughness. However, comparison of data taken on samples cleaved and etched in HCl with data on samples only cleaved tend to rule out this possibility. Thus, although routine microscopy does not reveal inclusions in the unirradiated material, it is probable that very small inclusions or other defects control the damage behavior, much as was found to be true in the $10.6 \text{ }\mu\text{m}$ data.

6. Discussion and Future Directions

It has been known since the early years of the Boulder Damage Symposium that microscopic defects such as inclusions are important causes of laser-induced damage [9,10]. The subtleties of multiple pulse damage observed in various studies [1-5] and the importance of color centers to damage in at least one study [11] indicate that submicroscopic defects and impurities, even at the individual-atom scale, must also be considered. The studies reported here provide mixed evidence regarding the importance of such point defects, but may give indications as to the directions which further work should take.

In commercially grown potassium chloride it appears evident that inhomogeneously distributed defects or impurities such as inclusions control laser damage at 532 nm. It is worth noting, however, that F-centers in this material absorb strongly at 532 nm. It may thus be possible to investigate their effect on damage properties in highly pure samples.

The comparison of multiple pulse damage behavior in BK-7 and fused silica provides indirect evidence that the presence of color centers in BK-7 is not important to the bulk damage problem. Further work will be needed to confirm this conclusion. If it is true, the reason may be that the two photon absorption possible in this material at 532 nm provides sufficient absorption and conduction band electron density to initiate damage without the participation of color centers.

The most striking evidence of the influence of pre-existing defects on laser-induced damage is seen in the comparison of two crystalline quartz grades. The greatest difference in known properties which may be correlated with the damage behaviors is found in the density of etch pits (and thus presumably of etch tunnels), but the observed damage morphologies do not seem to support such a mechanism. It is possible that differing concentrations of more densely distributed point defects may control the damage behavior of quartz. This could be consistent with the higher damage "threshold" of the Electronic grade sample if impurities such as Al or OH impede electron multiplication. In addition, numerous less common impurities may play a role.

The quartz study is being extended by the acquisition of samples varying more widely in the concentrations of known impurities and defects. In addition, certain of these defects can be modified by ionizing irradiation, further extending the range over which the defect parameters can be varied. Systematic damage studies on quartz with differing defect content should reveal which species or structures strongly affect laser damage, and may lead to an understanding of the mechanism.

In addition, spectroscopic measurements are being prepared to detect the absorption, luminescence and radiative recombination of laser-induced point defects. These studies should probe the influence of point defects upon catastrophic damage much more directly.

This work was supported in part by a grant from Research Corporation. The authors wish to thank Aaron Murray and Thermo Dynamics, Inc. for providing the quartz samples, and Larry Halliburton of Oklahoma State University for measurements of aluminum content in the quartz samples as well as for helpful discussions.

7. References

- [1] Merkle, Larry D.; Bass, Michael; Swimm, Randall T. Nat. Bur. Stand. (U.S.) Spec. Publ. 669; 50-59; 1982.
- [2] Merkle, Larry D.; Koumvakalis, N.; Bass, N. J. Appl. Phys. 55(3); 772-775; 1984.
- [3] O'Connell, Robert M.; Deaton, Terrence F.; Saito, Theodore T. Appl. Opt. 23(5); 682-688; 1984.
- [4] Wood, R. M.; Sharma, S. K.; Waite, P. Nat. Bur. Stand. (U.S.) Spec. Publ. 669; 44-49; 1982.
- [5] Jhee, Y. K.; Becker, M. F.; Walser, R. M. J. Opt. Soc. Am. B2(10); 1626-1633; 1985.
- [6] Vig, John R.; LeBus, John W.; Filler, Raymond L. Proc. of the 31st Ann. Sym. on Freq. Control; 1977. 131-143.
- [7] White III, W. T.; Henesian, M. A.; Weber, M. J. J. Opt. Soc. Am. B2(9); 1402-1408; 1985.
- [8] Wu, S.-T.; Bass, M.; Stone, J. P. Nat. Bur. Stand. (U.S.) Spec. Publ. 638; 152-159; 1981.
- [9] Glass, A. J.; Guenther, A. H. Damage in Laser Glass. Am. Soc. for Test. and Mater. Spec. Publ. 469; 1969.
- [10] Glass, A. J.; Guenther, A. H. Damage in Laser Materials. Nat. Bur. Stand. (U.S.) Spec. Publ. 341; 1970.
- [11] Soileau, M. J.; Mansour, Nastaran; Canto, Edesly; Griscom, D. L. Proc. of Seventeenth Symp. on Opt. Mater. for High Power Lasers; to be published by Nat. Bur. Stand. (U.S.).

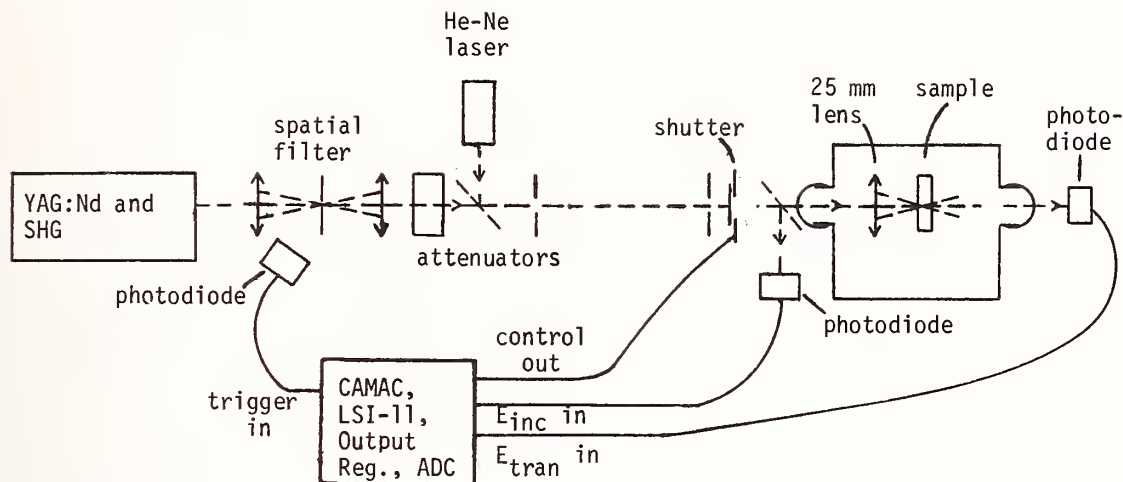


Figure 1. Experimental apparatus.

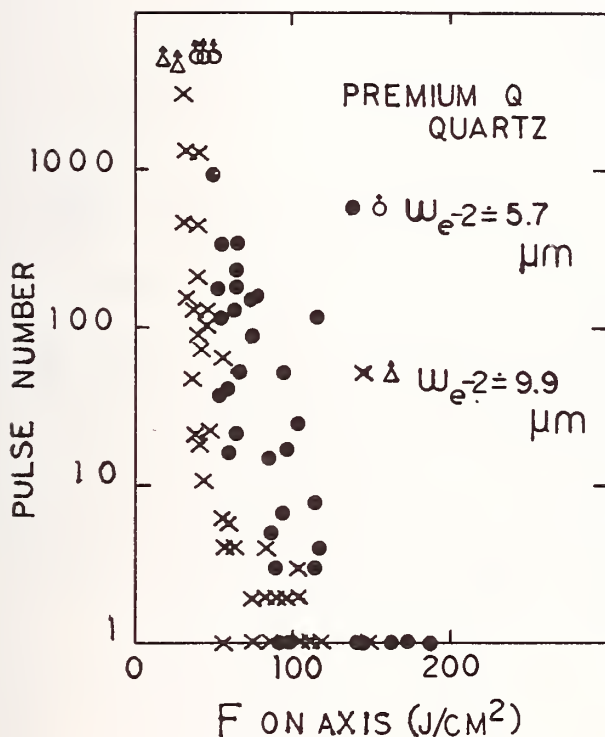


Figure 2. 532 nm multiple pulse damage data on "Premium Q" quartz (Thermo Dynamic 11-7-83-85). The data are indistinguishable for pulse repetition frequencies of 1 Hz and 10 Hz. Filled circles and crosses represent experiments in which catastrophic damage was observed at the indicated number of pulses, open circles and triangles representing experiments terminated without catastrophic damage. The vertical arrows on the latter indicate the obvious fact that the pulse numbers at which these experiments were terminated represent lower limits on the survival time of the material in those experiments.

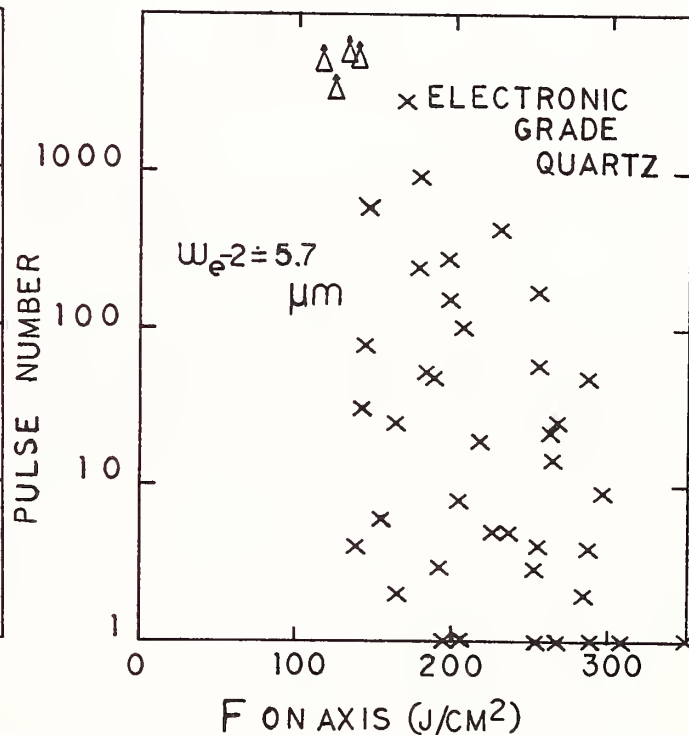


Figure 3. 532 nm multiple pulse damage data on "Electronic Grade" quartz (Thermo Dynamics 11-14-83-29). All data were taken at a pulse repetition frequency of 10 Hz. Experiments in which catastrophic damage was observed are indicated by crosses, experiments without such damage by triangles.

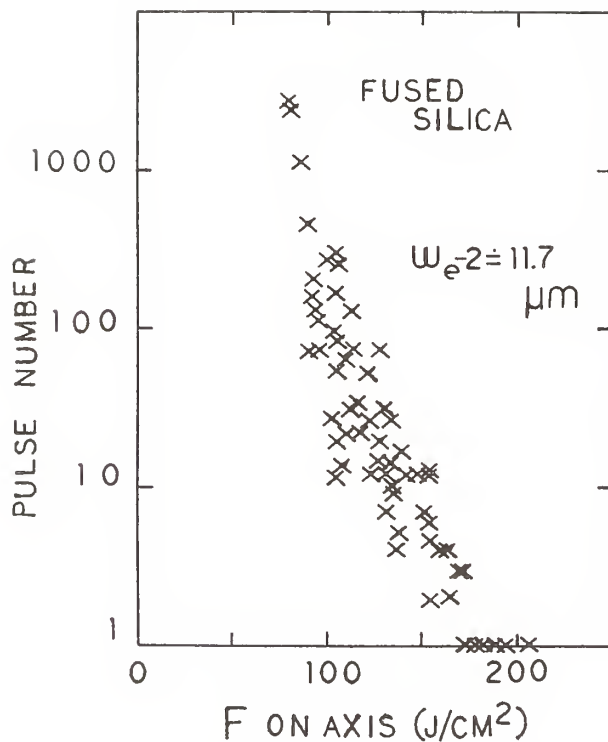


Figure 4. 532 nm multiple pulse damage data on fused silica (Corning 7940) at a pulse repetition frequency of 10 Hz. Each cross represents an experiment in which catastrophic damage was observed at the indicated number of pulses.

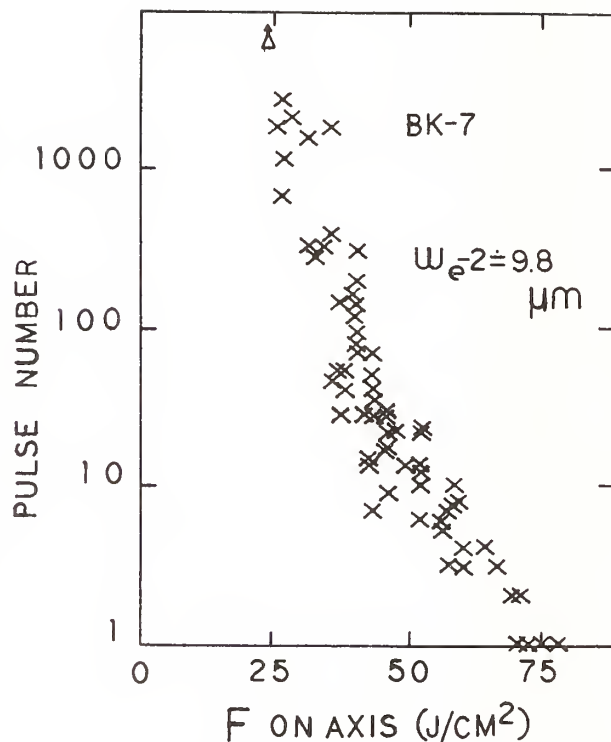


Figure 5. 532 nm multiple pulse damage data on BK-7 borosilicate glass at a pulse repetition frequency of 10 Hz. The data for a PRF of 1 Hz are indistinguishable from these. Data taken with a spot size of $11.7 \mu\text{m}$ give the same single pulse threshold (65 J/cm^2) and give $N=1000$ pulses for approximately the same fluence. Crosses represent catastrophic damage events, the triangle an experiment terminated without catastrophic damage.

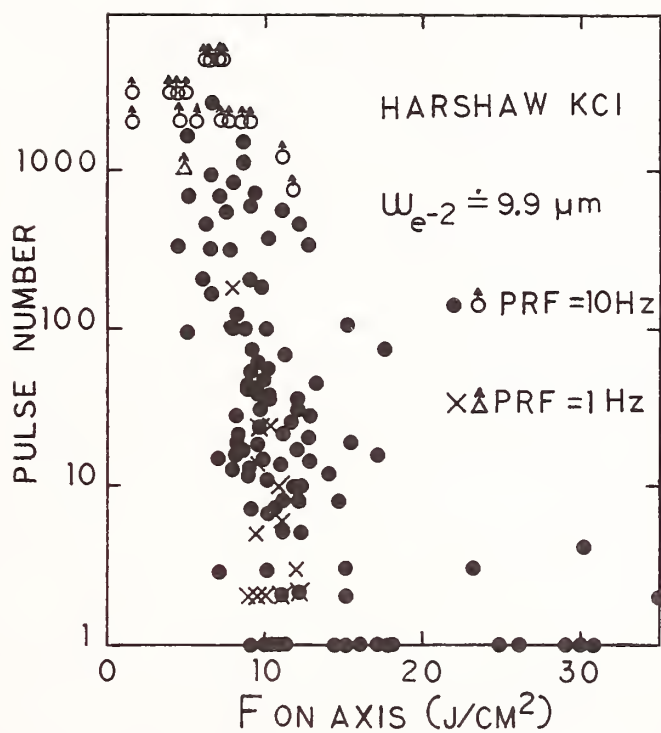


Figure 6. 532 nm multiple pulse damage data on Harshaw KCl. Experiments in which catastrophic damage was observed are indicated by filled circles and crosses, experiments without such damage by open circles and triangles.

Picosecond Nonlinear Investigation of Accumulated
Damage in Molecular Crystals

Thomas J. Kosic[#], Jeffrey R. Hill and Dana D. Dlott*

School of Chemical Sciences
University of Illinois
Urbana, Illinois 61801

Accumulated damage in aromatic molecular crystals at low temperature is studied by a variety of novel picosecond laser techniques. Damage in these materials is qualitatively different than in fused quartz, where dielectric breakdown is the predominant mechanism. In the aromatic crystals, multiphoton ionization creates reactive chemical fragments which are stabilized by the low temperature crystal matrix. These species accumulate until a high concentration is reached. At that point, phonon and photon assisted interactions release enough energy to damage the crystal. In a sense the process can be viewed as a chemical explosion.

The picosecond YAG--dual dye laser system used for these experiments is described. With this system we have demonstrated new methods to study damage. Subnanosecond damage is time-resolved with a sampling technique. The mechanism of defect production and crystal destruction is probed using damage detected spectroscopy. Scattering of the optical phonons by the accumulating defects is detected via picosecond time-delayed coherent Raman scattering.

Key words: accumulated damage; molecular crystals; nonlinear optics; picosecond lasers; time-resolved coherent Raman scattering.

1. Introduction

We are a group of solid-state chemists who have recently begun investigating optical damage in chemical materials. Most solid state chemical reactions are initiated at nucleation centers, and the extreme conditions of optical damage in chemical materials simulates the initiation of solid explosives. Our initial experiments were performed on acetanilide crystals at low temperature [1,2]. Acetanilide crystals consist of hydrogen bonded chains of aromatic phenyl groups. The phenyl group can be ionized to produce several reactive chemical species which are stabilized in the low temperature crystal matrix. When these species accumulate to high concentration, they begin to interact in photon and phonon assisted reactions, which produce damage in the crystal.

In this work, we contrast the behavior of cold organic systems with optical damage in inorganic glass at ambient temperature. We also describe our advanced picosecond spectrometer and some novel techniques for studying the fundamental mechanisms of accumulated damage.

2. Optical damage: organic versus inorganic

When a nonabsorbing glass is irradiated with intense pulses, bulk optical damage is caused by dielectric breakdown [3]. The single pulse damage threshold is typically comparable to the static breakdown voltage [3]. In accumulated damage, a material is irradiated with pulses below the single pulse damage threshold. These pulses create defects which lower the single pulse damage threshold. When this threshold is low enough, the material is damaged by the pulses [4,5]. In most cases, only a small concentration of defects is created before the damage is observed [4,5].

[#] Current address: Hughes Aircraft Corporation, El Segundo, California 90245.

* Author to whom correspondence should be addressed.

In low temperature acetanilide crystals, multiple pulse optical damage is more like a chemical explosion. The defects in acetanilide are very high energy centers ($E = 3-9$ eV) in the vicinity of radicals or ions created by multiphoton ionization. These defects are stabilized by the low temperature crystal matrix and tend to reach very high concentrations (several percent) before damage occurs. At a critical concentration, the metastable crystal is destroyed by phonon and photon assisted processes which release the stored energy [1,2].

In our experiments, we used a $25\ \mu$ laser spot size. Microscopic examination of damaged crystals showed an inclusion of roughly the same diameter. To create a cavity of volume $\sim 10^{-8}$ cm³, about 20 μ J of irreversible work must be performed on the crystal. Thus the damage process releases about 2000 J/cm³ of translational energy [2]. This is comparable to a TNT explosion; the heat of combustion of TNT is 22,000 J/cm³ of which about 10% is released as translational excitation. This "solid state explosion" is confined to a small volume within a cold crystal, and typically occurs on the time scale of about 1 ns.

3. Time-resolved laser experiments

3.1 Laser system

Figure 1 is a block diagram of the laser system we used for our experiments. The Nd:YAG laser, shown in the inset, is continuously pumped and is pulsed with an acousto-optic Q-switch and mode locker. It produces a very stable pulse burst of about 50 pulses, each 120 ps in duration, and the largest about 80 μ J. The repetition rate can be varied from single shot to 1000 Hz. The pulses are gaussian in time and in spatial profile, and are transform limited. This system provides a particularly clean, reproducible source for damage measurements, especially multiple pulse measurements. The gaussian beam can be focussed to a spot size of $5\ \mu$. This corresponds to a fluence level of about 100 J/cm², and a power density of 10^{12} W/cm², values which are above the damage threshold of most materials.

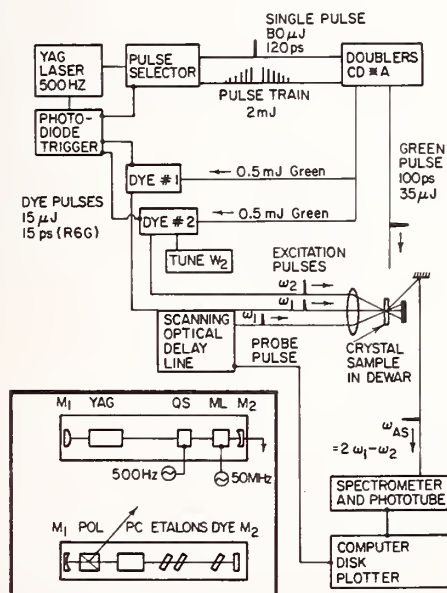


Figure 1. High repetition rate high power picosecond laser system for optical damage experiments. The inset shows the details of the YAG and dye lasers. In the experimental arrangement shown, a crystal in a cryostat is damaged by the green pulses. The crystal phonon dynamics are studied by time-resolved CARS. In this technique, a phonon is excited by simultaneous pulses at ω_1 and ω_2 , and the intensity of anti-Stokes emission produced by a delayed probe pulse is detected versus delay. Key: M = mirror, Pol = polarizer, PC = pockels cell, QS = acousto-optic Q-switch, ML = acousto-optic mode locker.

The frequency doubled laser is used to pump two synchronous cavity dumped dye lasers shown in the inset. The dye laser pulses are transform limited and spatially gaussian. A single pulse from the YAG pulse burst is selected with a pockels cell at the same time that the cavity dumpers in the dye lasers are triggered. The dye lasers and the fundamental and harmonics of the YAG laser can be mixed in nonlinear crystals to provide a tuneable pump and probe pulse in the ultraviolet, visible, and near IR. Although this laser system was home built in 1980, similar lasers are now commercially available.

3.2. Time resolving optical damage

Using a sampling technique, we have time resolved the damage process [1,2]. The sample is irradiated with successive pulses of 85 ps FWHM, and the rate of damage is determined by counting pulses. There is no fundamental limitation to extending this technique to the 10 fs time scale. The apparatus we used is shown in figure 2. Photodiodes and sample-and-hold circuits detect and normalize the incident and transmitted pulses. In a typical run, thousands of pulses are transmitted through the crystal before damage occurs. The computer acquires the time-dependent optical density of the crystal during the accumulated damage process.

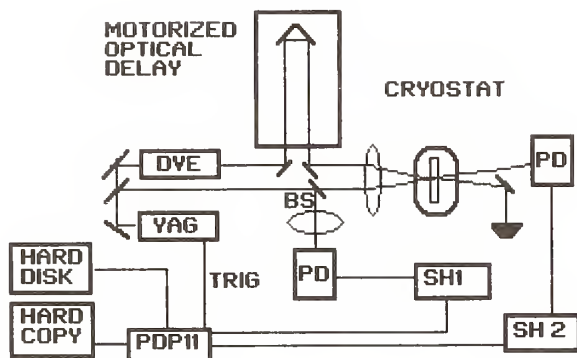


Figure 2. Apparatus used for time-resolved damage studies and "damage-detected spectroscopy". The optical damage is time-resolved by measuring the optical density change of the damage pulses with photodiodes (PD) before and after the crystal. Sample-and-hold circuits (SH) and a computer (PDP11) acquire the data. Each pulse irradiates the sample for 85 ps.

The crystal may be damaged by time-sequenced multicolor excitations which are designed to pump a particular vibrational or electronic level. The rate of damage for each pulse sequence is used to investigate the coupling between light and mechanical excitations of the crystal.

Two such runs are shown in figure 3. Only the final 100 pulses of each run are shown in the figure, corresponding to 8.5 ns of irradiation. In the upper run, there is no apparent change in optical density for several μ s (not shown). About 4 ns before destruction, some small fluctuations are observed. The catastrophic damage event takes 5 pulses, or roughly 400 ps of irradiation. In the lower trace, an oscillatory damage event is seen. Under the conditions we used, this mode occurred on 10% of the runs. We believe that the oscillations in the optical density of the metastable crystal are driven by fluctuations in the defect pumping rate.

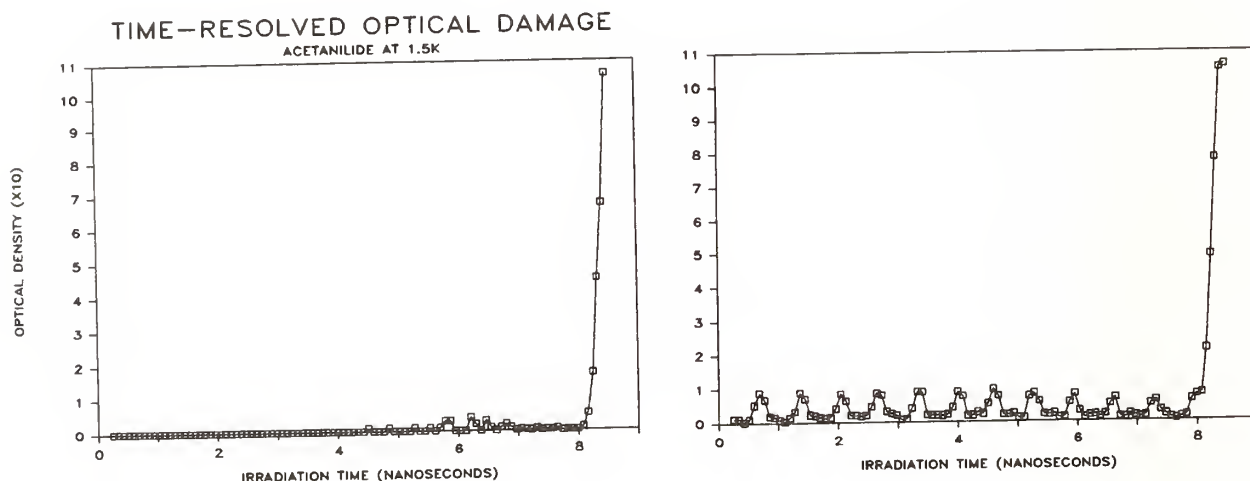


Figure 3. The time development of two damage events. Only the final 100 pulses of 85 ps duration are shown. Each event was preceded by several thousand pulses (not shown). The left figure shows the abrupt damage mode and the right figure shows an oscillating damage mode.

Time resolution of the optical damage introduces a new dimension to our measurements. Since defect accumulation is the rate limiting step in accumulated damage, conventional N-on-1 testing determines only the rate of defect producing processes. With our method, we determine the rate of crystal destruction processes as well. We can distinguish between models where these two processes occur by different mechanisms.

3.3. Damage detected spectroscopy

"Damage detected spectroscopy" involves setting up a time sequenced multicolor pulse train which pumps a specific electronic or vibrational level, and determining the effect of this pumping on the rate of defect production and damage. The apparatus in figure 2 is used. Usually we damage a number of identical volumes in a single crystal and average the result. The goal of these experiments is to determine how the radiation field couples into destructive mechanical excitations of the crystal.

In a series of damage detected spectroscopy experiments, we have shown that the defects in acetanilide are created by a 4-photon ionization process involving two sequential 2-photon absorptions [2]. The energy level diagram for acetanilide is shown in figure 4. Using the combinations shown in the figure, we determined that the first step in defect accumulate was excitation of the S_1 state. We also determined that the ionization process was stepwise, rather than simultaneous, by delaying the ionizing pulses behind the exciting pulses. In general, any proposed pumping scheme can be investigated in this manner.

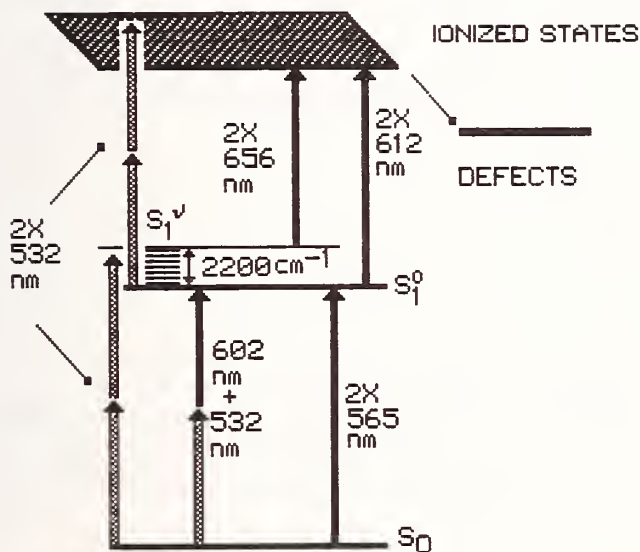


Figure 4. Energy level diagram for acetanilide. By using the one and two-color combinations shown in the figure, we have determined that the defects are created by 2-photon absorption to the S_1 state, and subsequent 2-photon ionization.

Since the crystal damage process occurs on a time scale which is faster than many vibrational relaxation rates in this material [6], nonequilibrium vibrational populations must play an important role. In a preliminary experiment, we have demonstrated the feasibility of studying the optical damage produced by pumping a specific molecular vibration or phonon with wavevector aligned along a particular crystallographic axis [1,2]. Using simultaneous pulses at 532.0 and 561.9 nm, the 1000 cm^{-1} vibration of the phenyl group was excited via stimulated Raman scattering. Compared to a control experiment where this mode was not excited, vibrational excitation reduced the damage rate by one half. Most likely there are other modes which increase the rate of damage. This will depend on the degree of coupling of a vibration with the translational degrees of freedom and the defects.

3.4. Phonon dynamics and optical damage

The Raman active phonons in a crystal are sensitive probes of changes in crystal structure during damage. Fauchet et al have used Raman spectroscopy to study structural damage in silicon crystals [7]. The damage caused a shift and broadening of the phonon spectrum. With a conventional Raman spectrometer, the resolution is typically 1 cm^{-1} . In silicon, a 1 cm^{-1} shift can be brought about by pressure gradients of order of a few kilobars [7].

In our lab, we use ps CARS spectroscopy [6] to measure the decay of phonons excited by short laser pulses. At low temperature, this decay is related to the width of the phonon Raman spectrum by T_1 (ps) = 5.3/(width in cm^{-1}). With our spectrometer, the resolution is better than 0.001 cm^{-1} . In this case, pressure gradients on the order of a few bars are detectable [6].

Figure 5 shows some ps CARS data on low temperature acetanilide crystals [1]. The phonon lifetimes constantly decrease as the crystal is irradiated. This crystal was damaged at $29 \mu\text{s}$ of irradiation. During the first $5 \mu\text{s}$, one phonon lifetime decreased from 674 to 540 ps, corresponding to a broadening of the Raman spectrum of 0.00791 cm^{-1} . This broadening is caused by phonon scattering from the accumulating defects and strain in the crystal [2].

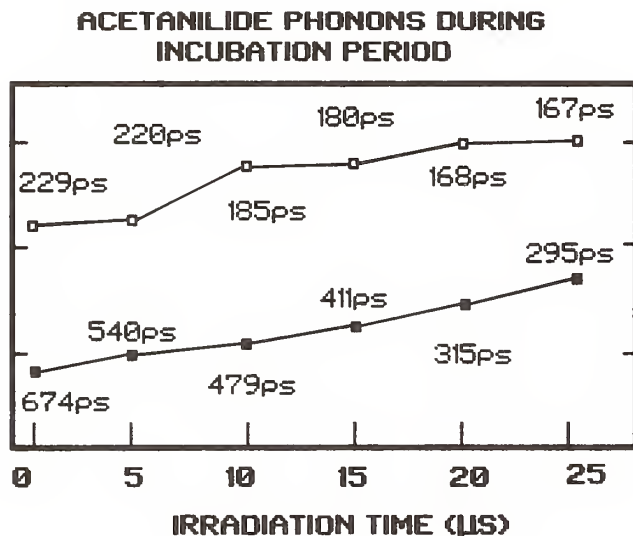


Figure 5. As defects accumulate in the lattice, the optical phonon lifetimes measured by ps CARS decrease. The phonon lifetime is a very sensitive probe of the predamage environment. The open squares are for the 38 cm^{-1} phonon and the filled squares are for the 39 cm^{-1} phonon. The crystal was damaged at $29 \mu\text{s}$ of irradiation.

This very sensitive probe of the predamage environment can be used to determine the efficiency of various damaging or annealing processes. Using psCARS as a noninvasive, nondestructive probe of the damage, the crystal can be irradiated until it is about to damage (the "brink of destruction"). At this point the crystal is a very interesting metastable system. It may prove possible to anneal these metastable crystals, either through optical or thermal processes. Annealing would be detected by an increase in the phonon lifetimes.

4. Conclusions

In a series of experiments made possible by our development of an advanced picosecond laser system, we have characterized damage in low temperature molecular crystals and demonstrated novel time-resolved diagnostic techniques to study this "solid-state explosion". Our work includes 1) First detailed study of optical damage in aromatic molecular crystals, 2) First picosecond time resolution of the destruction process in an accumulated damage system, 3) First use of phonon dynamics and ps CARS to detect the onset of damaging states, 4) First use of picosecond multicolor pulse sequences to investigate the mechanism of damage production, and 5) First demonstrate of the effect of non-equilibrium vibrational populations on optical damage.

This research was supported by the National Science Foundation, Solid State Chemistry through grant NSF DMR 84-15070. Dana D. Dlott is an Alfred P. Sloan fellow.

5. References

- [1] Hill, J.R., Kosic, T.J., Chronister, E.L., Dlott, D.D. Picosecond vibrational dynamics of hydrogen bonded solids: phonons and optical damage. Springer Ser. Phys. 4: 107-111; 1985.
- [2] Kosic, T.J., Hill, J.R., Dlott, D.D. Phonons, defects and optical damage in crystalline acetanilide. Chemical Physics (in press).
- [3] Bloembergen, N. Laser-induced electric breakdown in solids. IEEE J. Q. E. QE-10: 375-386; 1974.
- [4] Manekov, A.A., Matyushin, G.A., Nechitailo, V.S., Prokhorov, A.M., Tsaprilov, A.S. On the nature of the accumulation effect in laser-induced damage to optical materials. Opt. Eng. 22: 400-404, 1983.
- [5] Merkle, L.D., Bass, M., Swimm, R.T. Multiple pulse laser-induced bulk damage in crystalline and fused quartz at 1.064 and 0.532 μm . Opt. Eng. 22: 405-410; 1983.
- [6] Kosic, T.J., Cline, R.E., Jr., Dlott, D.D. Picosecond coherent Raman investigation of the relaxation of low frequency vibrational modes in amino acids and peptides. J. Chem. Phys. 81: 4932-4949 (1984).
- [7] Fauchet, P.M., Campbell, I.H., Adar, F. Long range material relaxation after localized laser damage. Appl. Phys. Lett. 47: 479-481; 1985.

- Manuscript Not Received -
=====

LASER PHOTOCONDUCTIVITY IN ALKALI HALIDES

Alexander Epifanov
Institute of General Physics
Moscow, USSR

Key Words: alkali halides; laser damage; laser-induced
photoconductivity; photoconductivity.

THE SCRATCH STANDARD IS ONLY A COSMETIC STANDARD

Matt Young
National Bureau of Standards
Boulder, Colorado

In this paper, I present a history of the scratch and dig standard for optical surface quality and show that this standard has since its inception been recognized as a cosmetic standard and not as an objective or performance standard. In addition, I attempt to dispel the myth that the scratch standard was changed during the 1960's and show that scratch number cannot be related to scratch width. Finally, I describe a preliminary aging experiment that suggests that the scratch standards have not aged with time and are, in fact, extremely stable.

Key Words: optical polishing; scratch-and-dig standards; surface figure.

Since learning that I was to give this paper at 5:30, I have had the recurring fantasy that there would be only one person left in the audience. I would give my presentation and conclude, "Thank you very much for listening," and she would reply, "Quite all right; I am the next speaker."

This paper is about the scratch and dig standard, mostly about its history. Those who do not remember this history are perhaps not condemned to repeat it, but rather to misunderstand or misuse the standard.

The scratch and dig standard was proposed in the mid forties by McLeod and Sherwood, who made clear that the standard is cosmetic. They prepared comparison standards numbered 10 through 120 and commented, "*If the scratch is made in a certain manner the numbers are the widths of the sample scratches in microns.*" They went on to note "that there is little correlation between the appearance or visibility of a scratch and its measured width. The shape of a scratch has a lot to do with its visibility The samples . . . have been selected to look alike, not necessarily to have the same measured widths." Likewise, in 1945, Frankford Arsenal stated unequivocally, "These numbers are arbitrary, and are *not to be assumed as denoting the width of the scratch.*" (All italics mine.)

The standard we use today, MIL-O-13830A, is based on a set of glass artifacts that may have been prepared as early as 1954. These artifacts are the primary or master standards against which secondary or submaster standards are calibrated and sent into the field for inspection of many kinds of optical element, whether transmitting or reflecting, transparent or metallic. The scratch and dig standard is the most widely used indicator of optical quality in the United States.

The dig standard is based on the diameter of the dig and so presents no problem. The secondary scratch standards, however, are certified by a subjective brightness comparison with the master standards. The standards are backlighted and viewed with the naked eye, by dark field illumination, and usually within a few degrees of the incident beam. Primary standards with a certain designation or scratch number (such as S-20) come in pairs with high (S-20H) and low (S-20L) visual brightness. A specimen that falls between the high and low primary standards is given their scratch number (in this example, S-20). A certified set of submasters is then boxed but not hermetically sealed. (It must therefore be resubmitted periodically for recertification.) This set is in turn used for naked eye comparisons with scratches on optical surfaces.

The light scattered by an isolated scratch no more than a few micrometers wide is a small fraction of the total light scattered by any surface. In part for that reason, the scratch standard can (with minor exception, such as inspection of reticle blanks) never be more than cosmetic. In addition, the scratches are almost invariably much narrower than the limit of resolution of the eye; since they can have almost any cross section, the naked eye can never, never, never! estimate the width or depth of any scratch by a simple brightness comparison.

The standards document, MIL-O-13830A, was adopted in 1954 and revised in 1963. It contains no specifications but rather refers to a 1945 drawing whose earliest versions apparently have been lost. Originally, this drawing showed only how the sets were to be boxed. The earliest version I could locate, Revision E (1956), has no relevant notes, but in 1960 a note was added saying, "Scratch numbers *do not denote width* of scratch. The numbers indicate that the scratch has the

same . . . visual appearance as the master scratch" This is perfectly clear. Confusion began with Revision H (1974), which states that the number of a scratch is *equal* to its width in micrometers. This revision probably resulted from a desire to define the standard so that the user could manufacture his own masters, but within two years another revision proclaimed that the scratch width was *one tenth* the scratch number and that, in any case, "Manufacturer-generated standards must be calibrated by Frankford Arsenal." This calibration was effected by the same old visual brightness comparison.

During all this time, absolutely nothing in the certification procedure had changed, nor has it changed to this day. The current revision, Revision L (1979), uses the parenthetical and enigmatic remark, "Dimensions are for reference only."

I argue that all reference to scratch width should be removed from the drawing. At best, a width specification can provide a starting point for the manufacture of artifacts; at worst, it can cause hopeless confusion. In any case, to be legitimate secondary standards these artifacts must still be compared visually with the primary standards located at Picatinny Arsenal. These primary standards were sent there when Frankford Arsenal closed in 1976 and are believed to be the set used since the inception of the standard.

The effort to correlate the scratch's number with its width ended with the closing of Frankford Arsenal but was probably doomed to failure anyway. Unfortunately, it contributed to three distinct misconceptions: (a) that the number of the scratch is somehow related to its width (or that it can be), (b) that the widths of the standard scratches somehow decreased by a factor of 10 and the standard had therefore become more stringent over the years, and (c) that width may be measured instead of appearance (Fig. 1).

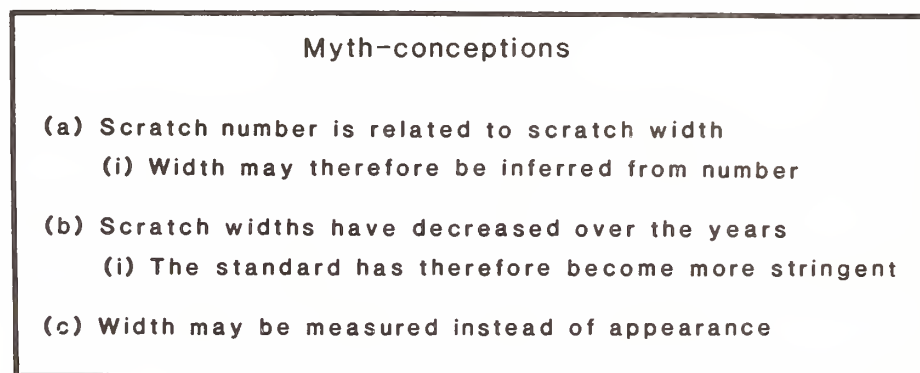


Figure 1. The most common misconceptions about the scratch standard.

Additionally, the startling factor-of-10 change between Revisions H and L has caused some users to speculate that the primary standards may have healed with the passage of time. Certainly the glass around a scratch cannot flow, but chemical weathering of the surface due to water vapor in the air is a possibility that could cause the primary standard either to heal or to worsen. There is evidence, however, that most weathering would take place and stabilize within a few hours or days. In any case, a change has to be quite substantial before it is apparent to the naked eye and, I think, would be picked up by the trained inspectors when they make repeated comparisons with secondary standards. More probably, it seems to me, small scratches that are reported to have "disappeared" have been contaminated by the volatile constituents of their wooden boxes and merely required a good degreasing.

Nevertheless, I performed a "preliminary" experiment on aging. Figure 2 shows polar scans of the scattering by a scratch that I made in a microscope slide. This scratch was rejected because of the asymmetry in the scan. The sharp peak is the unscattered or undiffracted light, and the rest of the curve is the logarithm of the power scattered by the scratch as a function of angle. The interesting part, as far as the scratch standards are concerned, is the region between about 5 and 10 degrees. This scratch has a side crack that gives rise to a two beam interference pattern beyond -20 degrees. Before placing some good samples into high humidity environments, I dumped this one into a beaker of de-ionized water for a bit over one day. If we make the naive assumption that concentration of water molecules is the only important factor, then this corresponds to aging over a period of about 150 years, assuming that each month is July and the location is New Jersey. Despite the dramatic change at the larger angles, the scattering at 5 degrees -- where it matters -- remains very nearly constant. With drying, even the large angle scatter recovers somewhat.

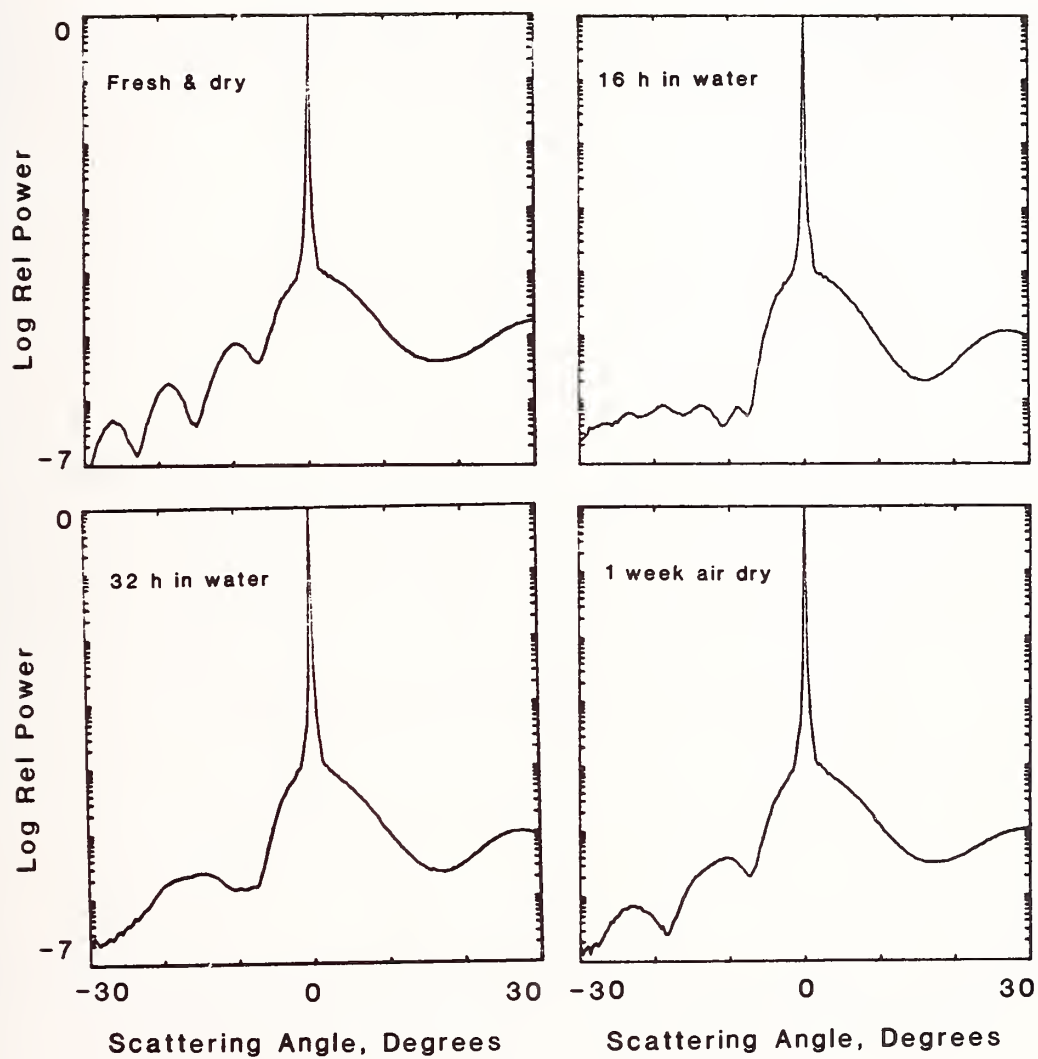


Figure 2. Power scattered by a scratch as a function of angle, on semi-logarithmic scale. Scratch has been immersed in de-ionized water, as stated. Periodic pattern beyond -10 degrees is two beam interference pattern resulting from undesirable side crack.

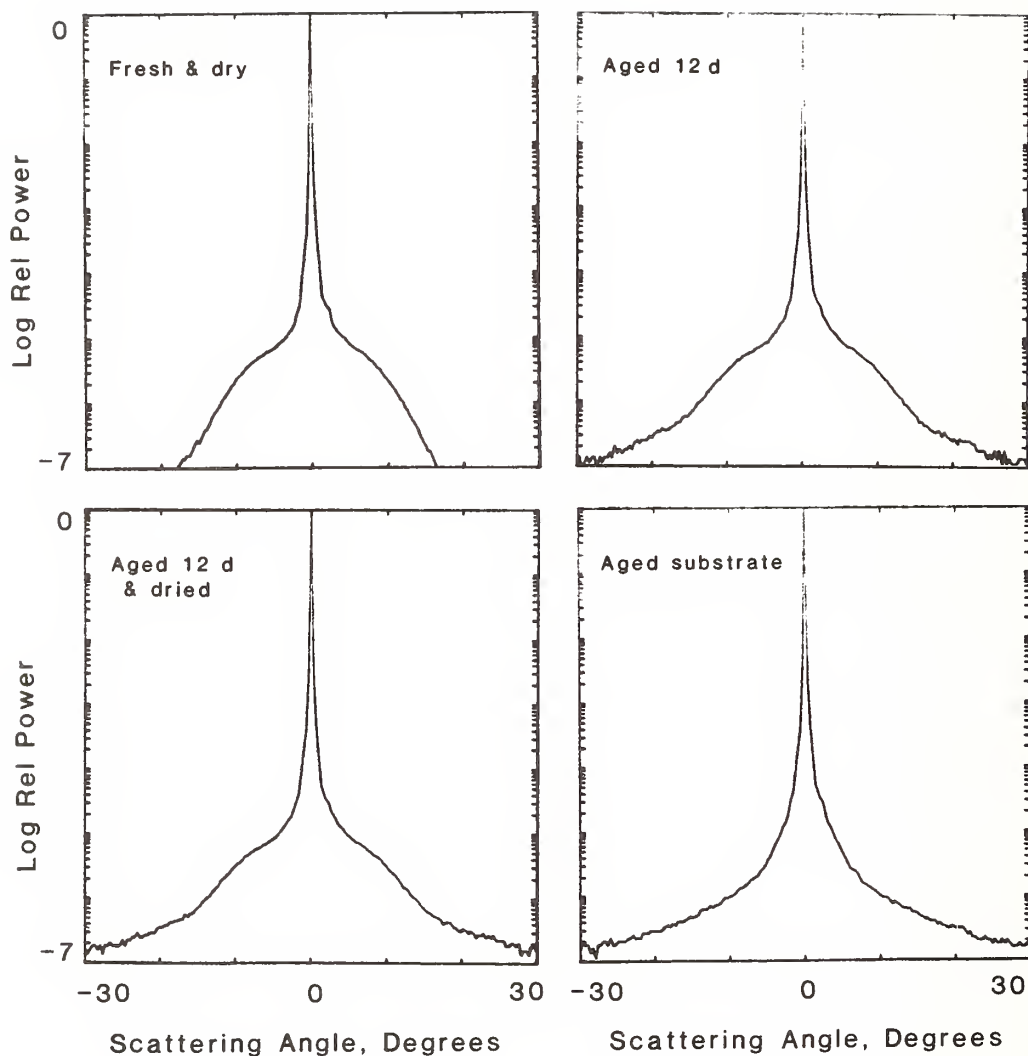
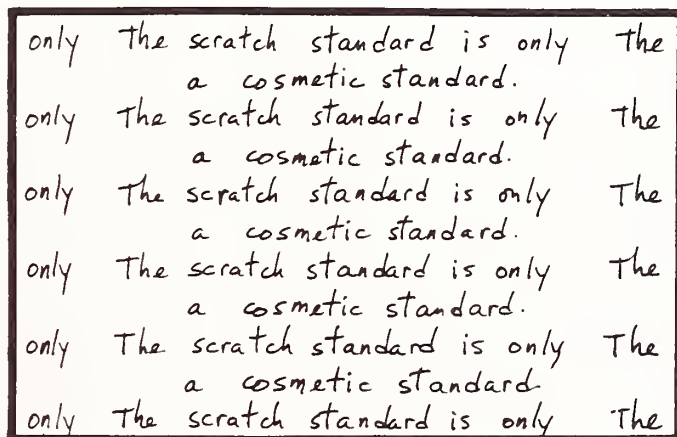


Figure 3. As in Figure 2. Scratch has been aged for 12 days in high humidity environment at 70 degrees Celsius. Scattering between 5 and 10 degrees is not measurably affected by aging. Lower right shows scattering by substrate alone and demonstrates that increased scattering at higher angles is due to etching of the substrate.

I subjected many other scratches (which had acceptable scattering profiles) to various stresses such as high humidity at 5, 20, and 70 degrees Celsius, and dry heat at 70 degrees for 12 days, and immersion in water for one or two nights. Only the scratches exposed to moist heat for 12 days showed measurably changed scattering patterns.

Figure 3 shows one such scratch, roughly an S-30, that was aged in a high humidity environment at approximately 70 degrees Celsius for 12 days. The substrate was severely etched and showed comparatively high scattering (lower right); nevertheless, the power scattered by the scratch itself is not measurably affected at angles less than 10 degrees. This suggests that the scratches must be extremely stable over long periods of time.

In recent years, I have heard speculation that laser damage threshold is related to the width of surface defects; this quite plausible speculation has unfortunately led to the rebirth of misconception (a). I therefore recommend (Fig. 4) that all those introduced to the standard after October 29, 1985 be required to write 50 times, "The scratch standard is only a cosmetic standard." All the rest of us should write it 100 times.



only The scratch standard is only The
a cosmetic standard.
only The scratch standard is only The
a cosmetic standard.
only The scratch standard is only The
a cosmetic standard.
only The scratch standard is only The
a cosmetic standard.
only The scratch standard is only The
a cosmetic standard.

Figure 4. And it isn't a width standard, either!

The history portions of this paper were published roughly concurrently in Laser Focus, November, 1985, pp. 138, 140. Based in part on a paper presented to the Workshop on Optical Fabrication and Testing, June 12-14, 1985. I am indebted to Dick Goldgraben, Jack Feeney, Jack Stateler, Jim Shean, and Hans Guttwein for helping me with the history of the standard, and to George McLellan and Brian Lawn for their explanations of crack formation and surface weathering. Keith Masterson encouraged the aging tests, and Edie DeWeese prepared the manuscript with her usual care. Any errors in this paper are, unhappily, my own. Contribution of the National Bureau of Standards, not subject to copyright.

Bibliography

1. J. H. McLeod and W. T. Sherwood, "A Proposed Method of Specifying Appearance Defects of Optical Parts," J. Opt. Soc. Amer. 35, 136-138 (1945).
2. M. Young, "Scratch Standards Should Not Be Used to Predict Damage Threshold," Proc. Conf. Laser Induced Damage in Optical Materials, 1982, Nat. Bur. Stand. (U.S.) Spec. Publ. 669, 151-155 (1982).
3. M. V. Swain, "Microfracture about Scratches in Brittle Solids," Proc. Roy. Soc. London A366, 575-597 (1979).

4. For a summary of our work relating the appearance of the scratches to their physical characteristics, see M. Young and E. G. Johnson, Jr., "Redefining the Scratch Standards," Nat. Bur. Stand. (U.S.) Tech. Note 1080 (1985); M. Young, E. G. Johnson, Jr., and R. Goldgraben, "Tunable Scratch Standards," Proc. Soc. Photo-Opt. Instr. Engrs. 525, 70-77 (1985); M. Young, "Objective Measurement and Characterization of Scratch Standards," Proc. Soc. Photo-Opt. Instr. Engrs. 362, 94-100 (1983).
5. For additional background material on optical surface quality measurements, see M. Young, "Can You Describe Optical Surface Quality with One or Two Numbers?" Proc. Soc. Photo-Opt. Instr. Engrs. 406, 12-22 (1983); see also pp. 119-131.

Table 1. An abbreviated history of the scratch and dig standard.

McLeod & Sherwood, 1945	"Samples . . . have been selected to look alike, not necessarily to have the same measured widths."
FED 1304, 1945(?)	"These numbers are arbitrary, and are not . . . the width of the scratch."
MIL-O-13830, 1954 and MIL-O-13830A, 1963	[Refer to Drawing C7641866]
Drawing C7641866, Revision E, 1956	[No statement]
Revision E-3, 1960	<u>Added Note 2:</u> "Scratch numbers do not denote width of scratch. The numbers indicate that the scratch has the same weight or visual appearance as the master scratch bearing the same weight number"
Revision F, 1965	<u>Added to Note 2:</u> "(Master scratch samples are maintained by the Frankford Arsenal.)" <u>Added Note 6:</u> "Only the item listed in this drawing . . . has been approved by Frankford Arsenal Substitute item shall not be used without prior approval."
Revision H, 1974	<u>Changed Note 2:</u> "Scratch number denotes width of scratch in microns." <u>Changed Note 6:</u> "Manufacturer has option to measure scratch width . . . or to utilize comparison standards identical to those illustrated herein. (Master scratch standards are maintained by the Frankford Arsenal.)"
Revision J, 1976	<u>Changed Note 2:</u> "Scratch standards width are (sic): (Dimensions are for calibration purposes only.) "#10 Scratch 1 mm \pm .1 "#20 Scratch 2 mm \pm .2" <u>Changed Note 6:</u> "Manufacturer has option to generate visual comparison standards . . . or to utilize Frankford Arsenal visual comparison standards. <i>Manufacturer generated standards must be calibrated by Frankford Arsenal . . .</i> " (my italics).
Revision L, 1980	<u>Changed Note 2:</u> "(Dimensions are for <i>reference</i> only.)" (My italics.) Note 6 unchanged except for replacement of Frankford Arsenal by ARRADCOM.

Ion Exchange Strengthening of Nd Doped Phosphate Laser Glass

Kathleen A. Cerqua and Stephen Jacobs
Laboratory for Laser Energetics
and

Brian L. McIntyre

New York State Center for Advanced Optical Technology of the Institute of Optics
University of Rochester
250 East River Road
Rochester, New York 14623-1299
716-275-5101

and

William Zhong
Kigre, Inc.
5333 Secor Road
Toledo, Ohio 43623

Recent advancements in high repetition rate and high average power laser systems have put increasing demands on the development of solid state laser materials with high thermal loading capabilities.

We have investigated strengthening of commercially available Nd doped phosphate glass via an ion-exchange process. Introduction of a compressive layer to the glass' exterior surfaces through this exchange, results in dramatically improved (approximately 4-5x) thermal shock resistance for specific sample geometries. This resulting increase in strength was directly measured through thermal shock resistance tests.

Our thermal shock test data showed extremely small (approximately $\pm 5\%$) standard deviations compared with data acquired through conventional mechanical fracture techniques. Additional topics investigated were strengthened layer thickness and effectiveness as a function of treatment time and the relationship of strengthening to the overall optical quality of the strengthened sample's surface.

Key Words: fracture strength; high-average power lasers; ion-exchange surface treatment; phosphate glass; solid-state laser glass; surface compression; surface strengthening; thermal shock resistance.

1. Introduction

Recent advances in high repetition rate and high-average-power (HAP) laser systems have put increasing demands on the thermal-loading capabilities of solid-state laser materials. In addition to the material's thermal properties, mechanical and optical limitations must also be identified if a reliable, high-performance system is to be maintained. After considerable effort in materials research at LLE and elsewhere, the physical limitations of various solid-state laser materials have become better understood. This article describes specific efforts to increase the thermal-shock resistance of a commercially available, Nd-doped phosphate laser glass. Improvements in this physical property permit a glass to be pumped at levels that may previously have led to its fracture, resulting in a capability for higher-average output powers.

A recently completed HAP laser system at LLE, which serves as a high repetition rate source for the in-house damage-testing facility, consists of a Nd:glass oscillator, rod preamp, and a phosphate-glass slab through which a beam propagates in a series of zig-zag, total internal reflections. Total internal reflection (TIR) makes efficient use of the entire gain medium. The slab is pumped and cooled on the two TIR sides, which reduces thermal beam distortion often present in alternative geometries. The slab is operated in a multi-pass configuration to additionally amplify the oscillator output. These features illustrate how the slab geometry lends itself well to HAP applications.

With renewed interest in HAP systems, emphasis needs to be placed on those properties of glass that make it a better HAP lasing gain medium. It is essential that the gain of the glass be high if a compact system is to be capable of high average powers. The requirement for a low nonlinear index is not as relevant for these systems, since longer pulses (nanosecond vs picoseconds) are frequently used. However, the issues of chemical compatibility and ease of fabrication become increasingly important. Slabs in most HAP systems utilize continuous cooling provided by a liquid flowing at a relatively high velocity across the pump faces of the glass. The gain medium must be durable, as chemically induced degradation to the precision-polished TIR surfaces would adversely affect output performance.

Fabrication issues become exceedingly important with HAP systems. Slab geometries, in particular, require very tight tolerances. Large polished faces with sharp edges are required to be extremely parallel, flat, and of excellent surface (scratch/dig) quality. Polished Brewster-angle end faces need to be parallel to within arc seconds and of comparable, if not better, quality than the pump faces. For high-performance slabs these stringent fabrication requirements frequently lead to high costs and long fabrication times.

In attempting to optimize the physical properties of a material to be used in a HAP system, it is necessary to define those properties which limit its performance. The primary limitation of glass is its thermal-loading capability, or more specifically, its relatively low thermal-shock resistance. Byer [1] expresses the average laser power a HAP solid-state gain medium can withstand as the product of the material's thermal-shock resistance and the ratio of plate area to plate thickness. A material's thermal-shock resistance is directly related to its strength, via its modulus of elasticity, thermal expansion, and thermal conductivity. These physical constants determine the stress limit, the fracture stress, at which a material will fail.

The thermal-shock resistance of a material, T_{SH} , is the temperature difference (ΔT) at which the fracture stress (commonly called the tensile yield-stress) is reached and failure occurs. This relationship is illustrated in Eq. 1, [2]

$$T_{SH} = \frac{\sigma_f (1 - \mu)k}{\alpha E} \quad , \quad (1)$$

where σ_f is the fracture stress, μ , k , E , and α are the material's Poisson ratio, thermal conductivity, Young's modulus, and linear coefficient of thermal expansion, respectively. Krupke [3] examined the $(1 - \mu)k/\alpha E$ portion of the term as a material figure of merit (FOM). Data compiled for a number of crystalline and noncrystalline materials show that the FOM is much larger for crystals than for glasses. The FOM, coupled with each material's known tensile yield-stress, indicate that crystals are several times more thermal shock resistant than glasses. While this is a plus, crystalline materials of high optical quality and homogeneity are considerably more expensive than their glass counterparts and are in some cases simply unavailable. Because of these limitations, we have chosen to examine the potential of external treatments for improving the strength of commercially available high-performance laser glass. Here we confine the discussion to Q-89, a high gain phosphate-composition glass manufactured by Kigre, Inc. [4]

2. Ion Exchange Strengthening

The goal of any external strengthening treatment is to introduce a compressive stress at the glass' surface, so as to increase the stress required to fracture the glass in tension. Marion [5] has shown that by reducing surface and subsurface damage, present in the form of microcracks (point sources where failure begins) via an acid etch, one can increase the fracture strength of a material. This benefit comes, however, at the expense of a thickness of $\sim 200 \mu m$ of material and leaves a surface of relatively poor optical quality. Our alternative approach is to chemically treat the surface by way of an ion-exchange process (cracks included), in which the surface becomes stronger through the introduction of a layer of compressive stress to the glass surface. In principle, ion-exchange strengthening can be performed without sacrificing the optical surface quality of the glass part.

Ion-exchange processing is routinely utilized by the glass industry for strengthening various products. The mechanism involves the exchange of a mobile alkali-ion A^+ that is present throughout the bulk material with a slightly larger ion B^+ of identical valence. The exchange is carried out in a molten-salt bath at an elevated temperature to accelerate the exchange of diffusing ions. The mobile A^+ ions readily diffuse out of the bulk, leaving vacancies behind. The larger B^+ ions migrate from the salt bath into the glass by occupying the small A^+ vacancies. The important feature of this "crowding" mechanism, as outlined by Kistler, [6] is that it is performed at temperatures sufficiently below the strain point of the glass. An optimized

treatment schedule prohibits structural relaxation from occurring and the surface, as a result of the larger ions, is "expanded" into compression. A number of factors will control the net compressive stress that results from the process: [7]

- o the radius ratio of the exchanging ions
- o the degree to which the exchange occurs
- o stress relaxation due to structural rearrangement of the surface
- o any change in thermal expansion coefficient
- o localized densification
- o the depth of the compressive layer.

Of these factors, the depth of the compressive layer is the most important. The layer can be thought of as a physical barrier that impedes the propagation of cracks. A thick layer will be more resistant to crack initiation and thus failure, since any flaw would have to penetrate past this depth to initiate fracture.

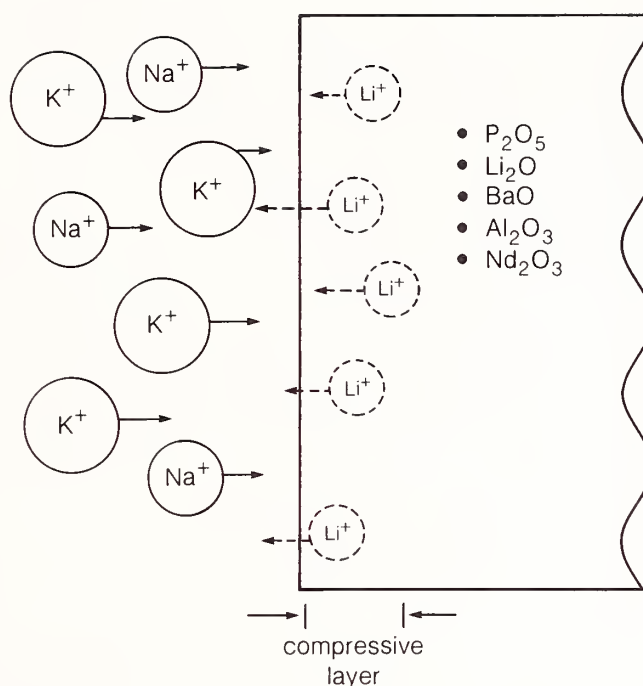
Considerable work has been done on the strengthening of silicate glass. To our knowledge, the process has not previously been extended to phosphate laser glass. While the basic mechanism remains the same, the composition of the base glass network determines the efficacy of the treatment. Silicates lend themselves well to ion exchange, because their network consists of openly spaced SiO_4 tetrahedra. This open network creates channels through which alkali ions can easily migrate.

The structure of phosphate glass is more complex. Whereas SiO_4 tetrahedra are able to bond exclusively to each other to form a network, phosphate glasses are composed of PO_4 tetrahedra, which are limited in that they can only bond to three like structures during network formation. [8] For this reason, Al_2O_3 is frequently added to assist as a network former in a phosphate-glass matrix. This, coupled with relatively large amounts of another network modifier, BaO , leads to a much more closed structure. This tighter matrix impedes the diffusion of alkali ions deep into the glass. Silicate glass systems strengthened via ion exchange are known to develop thicker compressive layers than phosphates.

The diffusion process that controls the exchange mechanism is very sensitive to changes in the exchange bath. Physical variations due to particulate, moisture, ion concentration, and other forms of bath contamination severely decrease the effectiveness of the process. In this work the primary A^+ alkali ion is Li^+ , a major constituent in Q-89 in the form of Li_2O . The exchanging B^+ ions are Na^+ and K^+ , present in the bath as nitrate salts. Figure 1 depicts the ion-exchange mechanism in Q-89 and lists the other major constituents of this glass. The stoichiometry of the nitrate salts used in the bath is important; a large Na^+/K^+ ratio would be desired since Na^+ is the predominant exchanging ion. However, Na^+ is corrosive, and in applications such as these, where post-treatment surface quality is critical, a tradeoff must be made.

3. Characterization of Exchange Process and Experimental Results

Several experiments have been conducted to examine methods for optimizing the strengthening process. The various test geometries and results are described as follows:

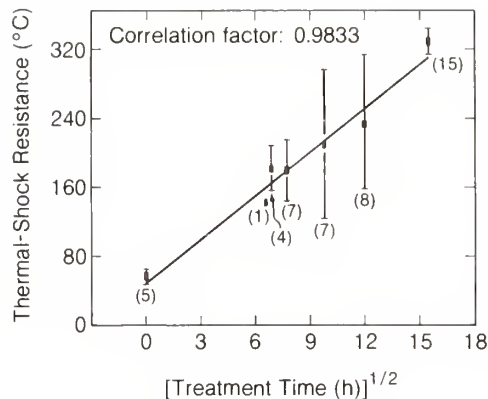


G1665

Fig. 1 Ion-exchange mechanism in Kigre Q-89. Mobile Li^+ ions diffuse out of the glass, leaving vacancies behind. Large Na^+ and K^+ ions preferentially diffuse from the bath into the small Li^+ vacancies, creating a compressive layer on the glass surface.

3.1. Thermal-Shock Tests

The improved strength through ion-exchange treatment was determined by a series of thermal-shock-resistance tests. Samples of Q-89 were fabricated into right-circular cylinders, $\frac{1}{4}$ " in diameter by $\frac{1}{4}$ " in length with fine ground surfaces (#400 grit) and acid etched in NH_4HF_2 for ~6 minutes prior to exchange treatment. The cylinders were then evaluated for their thermal-shock resistance through a soak/quench test. Treated cylinders were placed in an oven, raised to a prescribed temperature, and "soaked" at that temperature for ~30 minutes to guarantee sample-to-sample temperature uniformity. The samples were then removed and plunged into ice water ($\sim 5\text{--}7^\circ\text{C}$). Upon removal from the ice bath, each sample was visually inspected for fracture. If no fracture occurred, the $\Delta T(T_{\text{oven}} - T_{\text{water}})$ was recorded and the process repeated at a soak temperature increased by $+10^\circ\text{C}$. This continued until all samples had fractured. Results from these tests are shown in Fig. 2. Cylinders were treated in the exchange bath for 0, 2, 4, 6, and 10 days. The treatment time (in $(\text{hours})^{\frac{1}{2}}$) is plotted in Fig. 2 versus measured thermal-shock resistance, in degrees $^\circ\text{C}$. The treatment was carried out



() number of samples fractured

┃ first standard deviation

G1669

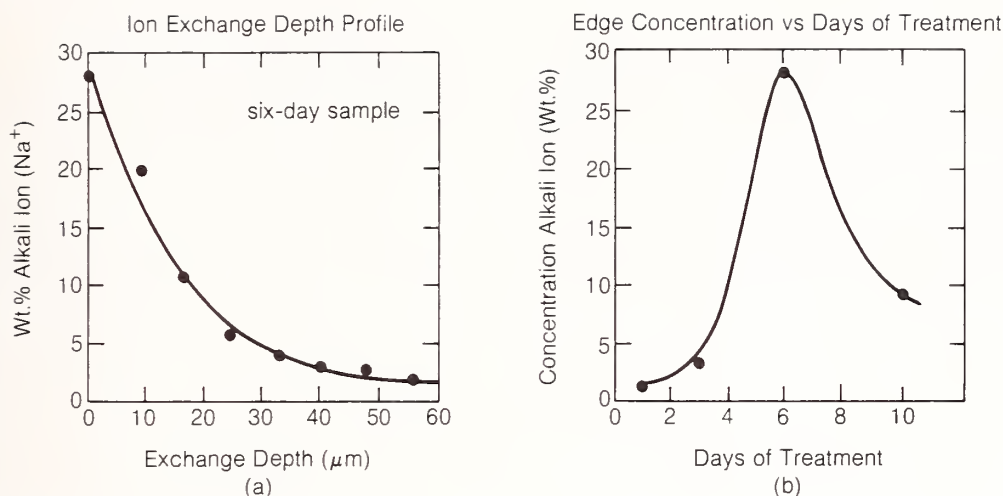
Fig. 2 Fivefold increase in thermal shock resistance in cylindrical, Q-89 samples. Excellent statistics ($\pm 5\%$) can be attributed to a clean, contamination-free bath.

at an exchange-bath temperature of 320°C, with samples treated statically (no agitation) and removed and rinsed with deionized water every other day to remove any residual material buildup on the sample surfaces.

Introduction of a compressive layer through ion exchange resulted in a fivefold increase in thermal-shock resistance. Our thermal-shock test data show extremely small (approximately $\pm 5\%$) standard deviations compared with the 50%-100% variation observed in data acquired through conventional mechanical-fracture techniques.

The widening spread in data for days 1-6 are a result of an increase in the level of bath contaminants. Depletion of diffusing ions and increased moisture content of the treatment bath are believed to have led to a larger standard deviation and poorer sample surface quality. The treatment of 15 samples for 10 days in a new, presumably dry bath restored the low standard deviation and improved sample surface quality. Although samples treated longer than 10 days were not tested, it is important to note in Fig. 2 that we did not observe any leveling off in the strength improvement data. Thus, the ultimate levels of strength improvement are not known at this point and deserve further investigation.

Ion penetration depths of approximately 60 μm were measured via electron microprobe analysis. [9] A depth profile for the light, highly mobile Na^+ ion that preferentially



G1671

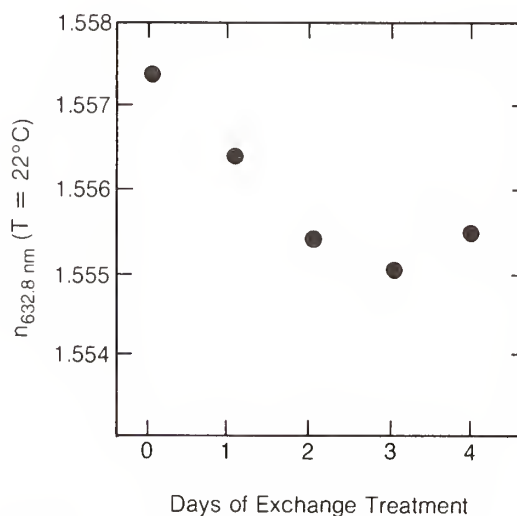
Fig. 3 (a) Ion-exchange depth profile for six-day treated sample, as determined by electron microprobe analysis.
 (b) Edge profile of alkali (Na⁺) ion concentration as a function of treatment time. Rollover after six days may be due to stress relaxation mechanism in glass network, which allows migration of Na⁺ ions away from surface and further into the bulk.

diffuses into the glass is shown for a six-day treated sample in Fig. 3a. Similar profiles for one-through four-day samples showed an alkali-ion dropoff to the detection limit at depths of 35 to 40 μm. However, six and ten-day samples remained at ~3%-5% levels considerably further into the bulk. This observation is useful in explaining alkali-ion edge concentration data shown in Fig. 3b. Here, we plot the edge concentration of alkali (Na⁺) ions as a function of days of treatment. The rollover that occurs after six days may be due to stress-relaxation processes occurring in the glass network at the elevated bath temperature of 320°C. This stress relaxation could allow ions in high concentrations at the material's edge to migrate further into the bulk, thus decreasing the concentration at the edge.

Current work is focused on answering a number of questions relating to the details of the exchange mechanism. Reproducible profiles of light-ion concentrations are difficult to obtain, and can be improved by fabricating samples with very clean edges. Supplemental analytical techniques will assist in confirming the details of the ion exchange, specifically in the analysis of the compressive layer.

3.2. Refractive-Index Variation in the Surface Layer

In examining the optical effects of the strengthening process, experiments were designed to investigate the "new" compressive surface layer. The surface refractive-index variations were measured as a function of days of treatment. A polished half cylinder was measured unstrengthened and then remeasured following additional one-day increments of treatment. These measurements were made on an Abbé refractometer, at $\lambda = 632.8$ nm and at a temperature of 22°C. The results of these tests are plotted in Fig. 4. The observed index decrease in the third



G1666

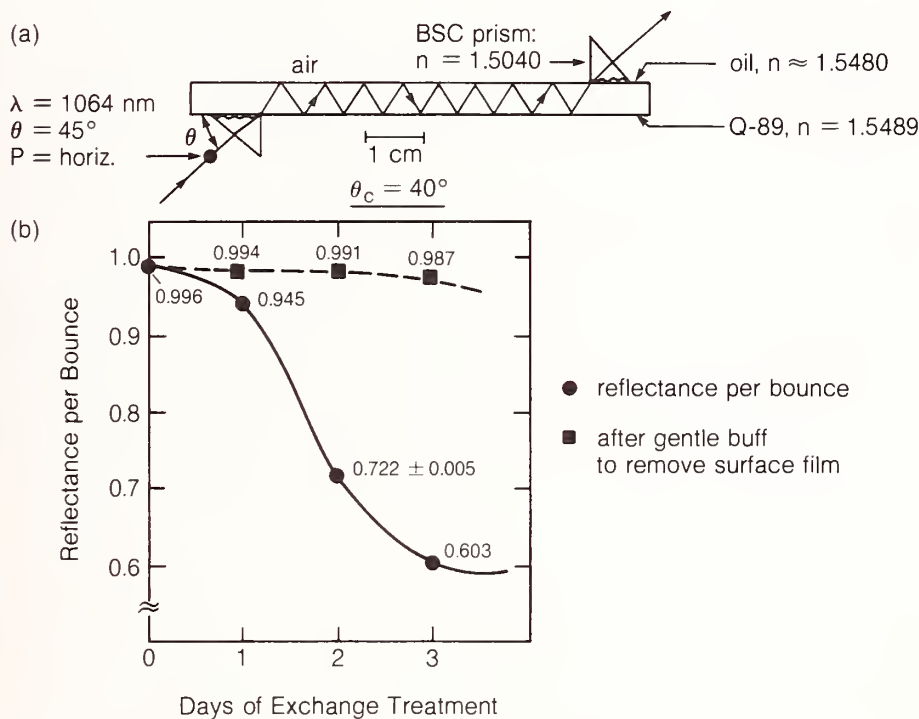
Fig. 4 Refractive-index variation in surface layer as a function of days of treatment. Measured index decreases as $\text{Li}_2\text{O}/\text{R}_2\text{O}$ ratio decreases.

decimal place is consistent with Kigre bulk-glass data for Q-89, which indicate a decrease in refractive index with decreasing $\text{Li}_2\text{O}/\text{R}_2\text{O}$ ratio. This decrease continues to occur in the strengthened layer with additional days of treatment. It is not expected that this small reduction in the surface index causes any deleterious effect on the TIR propagation of the beam through a strengthened slab.

3.3. TIR Transmission Tests

This experiment focused on treatment-induced degradation to optically polished surfaces. Thin slabs of Q-89, 15 x 75 x 3 mm, were fabricated for TIR transmission measurements, at

$\lambda = 1064$ nm at a glass-air interface. The objective was to examine surface degradation and increased scatter as well as possible limitations to TIR as a function of exchange-treatment time. Measurements on treated slabs were compared with the transmission through an untreated control sample. A YAG ($\lambda = 1064$ nm) laser was injected at $\sim 45^\circ$ ($>$ critical angle, $\theta_c = 40^\circ$) into the slab through a BK-7 prism, which was index-matched to the Q-89 surface, as shown in Fig. 5a.



G1667

Fig. 5 (a) TIR experiment on thin slabs of Q-89, $\theta = 45^\circ$, $\lambda = 1064$ nm. Measurements were made in air.
 (b) Reflectance per bounce decreases as a function of days of treatment. Gentle buff of treated surface restores TIR reflectance to the $>99\%$ level.

After a series of TIR bounces the beam exited the sample and the total transmission drop was monitored. From this observation the reflectance per bounce was calculated. The result is shown as a solid line in Fig. 5b.

Surface films may become apparent after as little as three days of treatment. Visible inspection of the samples after treatment showed a very irregular, mottled film, which gradually worsened with treatment time. This film caused the steady drop in reflectance that was observed as treatment time was lengthened. A gentle buff removing the surface film was found adequate to restore TIR reflectance to the 99% level (dotted line). Minimal (<0.5 μ m for three-day sample) material removal was required to achieve this improvement. We believe the results of this test to be based on a worst-case experiment, due to the use of an old, contaminated salt-bath. We

suspect that the observed surface film is the result of moisture contamination in the bath, [10] which can be eliminated with proper preventive measures.

4. Summary

The details of the process as outlined here support the claim that phosphate laser glass can be strengthened effectively. The demonstration of a fivefold increase in thermal-shock resistance of Q-89 illustrates the potential of this technique. A first step in assessing the impact of the ion-exchange process on the optical surface quality of fabricated parts is completed.

Ion-exchange strengthened phosphate glass is not yet available commercially. A number of materials scale-up issues are yet unresolved. Work is continuing to address the issues of bath contamination, optical surface degradation due to moisture, the effect of exchange treatment on the interferometric quality of fabricated parts (optical surface deformation due to compressive stress), and the compositional gradients of the compressive-stress layer. The scalability of the technology to larger, full size slabs will ultimately prove the feasibility of the process, and serve as a basis for increasing the capabilities of high average power laser systems.

This work was supported by the General Electric Company Advanced Laser Technology Group, Binghamton, New York under contract #A25-E-0580BS, the New York State Center for Advanced Optical Technology of the Institute of Optics, and the sponsors of the Laser Fusion Feasibility Project at the Laboratory for Laser Energetics whose sponsors are as follows: Empire State Electric Energy Research Corporation, General Electric Company, New York State Energy Research and Development Authority, Ontario Hydro, Southern California Edison Company, and the University of Rochester. Such support does not imply endorsement of the content by any of the above parties.

5. References

- [1] R. Byer, Slab Geometry Lasers presented at International Lasers and E-0 Exhibition, Tokyo, Japan, January 31, 1985.
- [2] W.D. Kingery et al., Introduction to Ceramics, Wiley, NY (1975), pg.823.
- [3] W.F. Krupke, Insulator Materials in High Power Lasers for Inertial Fusion: Present and Future, UCRL-89439 (1983).

- [4] Kigre, Inc., 5333 Secor Road, Toledo, Ohio 43623
- [5] J. Marion, Strengthened Solid State Laser Materials, UCRL-92680 (1985).
- [6] S.S. Kistler, J. Am. Ceram. Soc. 45, 59 (1962).
- [7] S.D. Stookey, High Strength Materials, pg. 669, V.F. Zackay, editor, Wiley, NY (1964).
- [8] W.D. Kingery et al., Introduction to Ceramics, Wiley, NY (1975), pg. 110.
- [9] Analysis performed by Xerox Analytical Laboratory, Jos. C. Wilson Center for Technology, Webster, NY.
- [10] Private communication, Dr. W. LaCourse, Institute for Glass Science and Engineering, Alfred University, Alfred, NY.

INFRA-RED ABSORPTION SPECTROSCOPY OF Nd:YAG AND
Nd:GSGG SURFACE CONTAMINANTS

Manuscript Received
12-4-85

BY

DR. M.A. ACHAREKAR
LITTON SYSTEMS, INC.
LASER SYSTEMS DIVISION
2787 SOUTH ORANGE BLOSSOM TRAIL
APOPKA, FL 32703

Neodymium doped yttrium aluminum garnet (Nd:YAG) is a commonly used laser material for solid-state high power, high PRF lasers. Gadolinium scandium gallium garnet doubled doped with neodymium and chromium (Nd:Cr:GSGG) shows higher efficiency than the Nd:YAG laser. We previously reported the bulk and surface damage thresholds of the Nd:Cr:GSGG crystal. It was shown that the bulk damage threshold of the Nd:Cr:GSGG was as high as the Nd:YAG crystal.

The surface damage threshold measurements for the Nd:YAG and the Nd:Cr:GSGG are reported in this paper. Infrared absorption spectroscopy was used to analyze surface contaminants. The data show that the organic contaminants, CH_n , derived from hydrocarbon (skin oil) associated with improper parts handling, significantly reduce the surface damage threshold.

Key Words: co-doped GSGG; infrared absorption spectroscopy; laser induced damage; Nd:Cr:GSGG; Nd:YAG; optical surface contaminants; solid-state laser; surface damage.

1. INTRODUCTION

Neodymium doped yttrium aluminum garnet (Nd:YAG) lasers have found numerous uses in scientific, military, and industrial applications. The typical overall efficiency for Nd:YAG is limited to 2-3 percent. Gadolinium scandium gallium garnet doubled doped with neodymium and chromium (Nd:Cr:GSGG) shows higher efficiency than the Nd:YAG laser. We previously reported [1] the bulk damage thresholds of Nd:Cr:GSGG crystal. It was shown that the bulk damage threshold of the Nd:Cr:GSGG was as high as the Nd:YAG crystal. In table 1, Nd:YAG and Nd:GSGG material properties [2],[3] are summarized.

The surface damage threshold data collected for Nd:Cr:GSGG material are reported in this paper. For the optical damage measurements, a stable, TEM₀₀, Q-switched, Nd:Cr:GSGG laser oscillator was set up. The unusual laser damage morphology is associated with Nd:Cr:GSGG samples. This statement follows from microscopic examination of hundreds of damage sites. Therefore, the samples were studied using infrared spectroscopy. The results of the infrared spectroscopy of the test specimen contaminants are also provided in this paper.

TABLE 1 GSGG and Nd:YAG Material Properties

PROPERTY	Cr:Nd:GSGG	Nd:YAG
Thermal Conductivity, κ	7-9 W/m°C (Conc. Dep.)	~13 W/m°C
Thermal Expansion, α	$7.8 \times 10^{-6}/^{\circ}\text{C}$	$7.8 \times 10^{-6}/^{\circ}\text{C}$
Young's Modulus, E	~21,000 kg/mm ²	~31,700 kg/mm ²
Breaking Strength† (4-pt bend), S_T	15-20 kg/mm ²	~20 kg/mm ²
Poisson's Ratio, ν	0.11-0.18	Not Reported
Thermal Shock*, R_T	~700 W/m	~800 W/m
Index of Refraction, 1060 nm	1.925	1.815
Density	6.46	4.55
Nd-Segregation Coeff.	0.65 ± 0.04	0.18
10 ns Damage Threshold (Bulk)	>28 J/cm ²	20 J/cm ²

* $R_T = (1 - \nu) \kappa S_T / \alpha E$

† Depends on Fabrication

2. SURFACE DAMAGE MEASUREMENTS

2.1 Test Specimens

For measuring the surface damage threshold of Nd:Cr:GSGG and Nd:YAG, optically polished discs of 0.38 cm diameter by 0.1 cm thick were prepared. The discs were prepolished prior to final polishing by the various methods. In the prepolysh, the discs were diamond lapped to a specular but sleek finish. The following three methods were used for the final polishing.

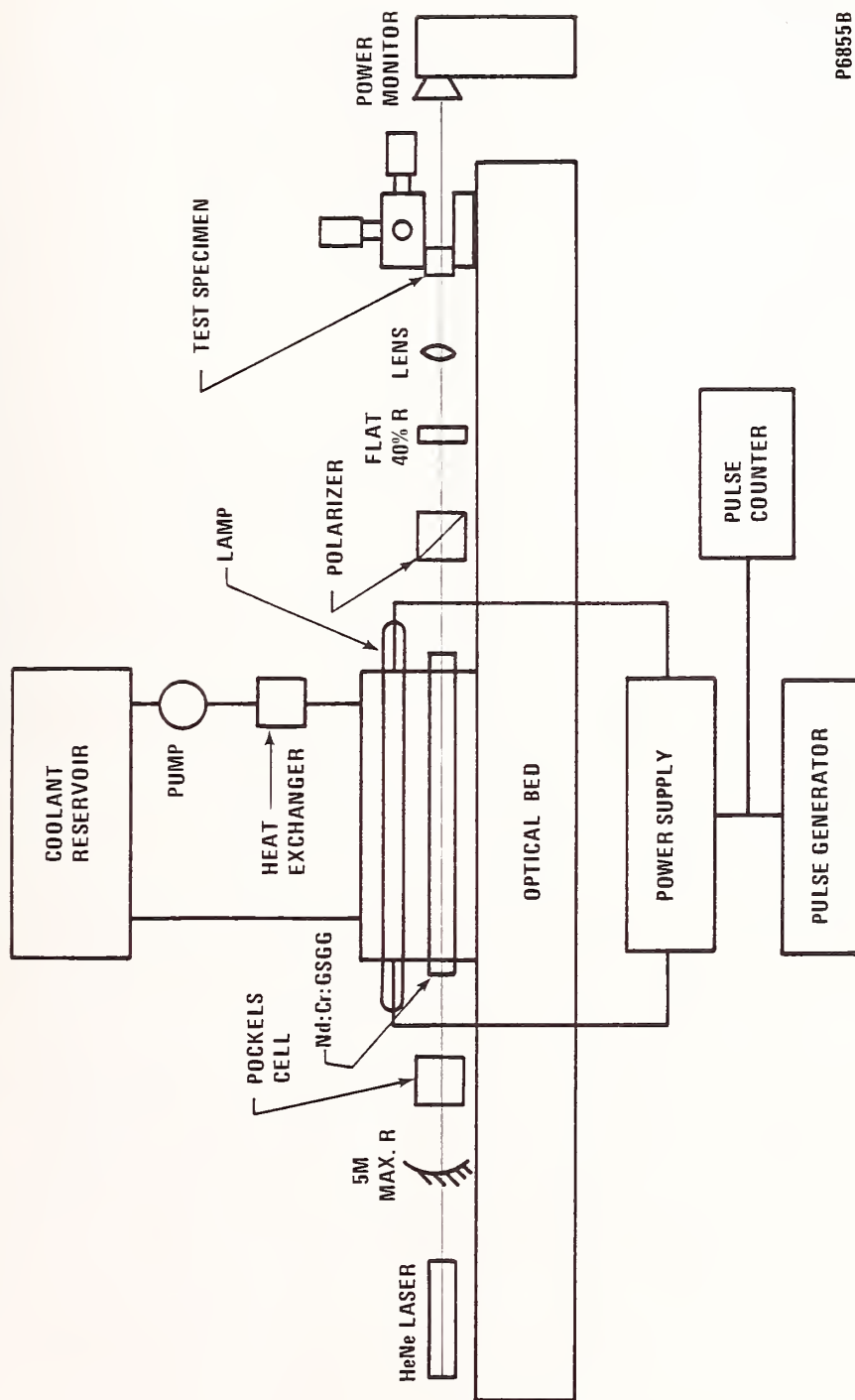
Test samples in Group "A" were fine polished on a lapping surface of medium hard polishing pitch on a planetary lap. The polishing agent was 0.3 μm alpha alumina mixed thin in water.

Test samples in Group "B" were fine polished on a lap of Pyrex (Tm Corning Glass). The lap was plane-ground with 30 μm alumina to an even roughness and cleaned. The polishing was done with 0.3 μm alpha alumina applied to the Pyrex lap. For this method the solid alumina content was high and a substantial part of the vehicle was a commercial ligand-surfactant. The polishing was done by hand in the traditional figure 8 stroke.

Test samples in Group "C" were polished by a hybrid of the other two polishing methods. The discs were substantially polished-out on the pitch polisher and then touched up to improve flatness on the Pyrex polisher. All the samples were flat within $\lambda/5$ at 632.8 nm.

2.2 Experimental Techniques

For the optical damage measurements, a stable, TEM₀₀, Q-switched, Nd:Cr:GSGG laser oscillator was set up. The experimental set up is shown in figure 1. In the pump cavity, 0.5 cm diameter by 6.50 cm long, the Nd:Cr:GSGG laser rod was pumped using a Xenon gas filled at 400 torr pressure in a cerium doped fused silica envelope flashlamp. The laser resonator consisted of a 5 meter radius mirror coated for maximum reflectivity, spaced 40 cm apart with an output coupling mirror of 40 percent reflectivity. In the resonator, a lithium niobate Pockels cell with a polarizer was used as the Q-switch. Q-switched output energy of 135 mJ was obtained in a beam divergence of 2.18 mR with 8 J/P input energy at 10 pps. The pulsewidth of the Q-switched pulses was measured using a EG&G 580 radiometer and a Tektronix Model 454A oscilloscope. The typical full width at half amplitude (FWHA) pulsewidth for the laser was 17.0 ns.



P6855B

Figure 1. Experimental Set Up.

The Q-switched, Nd:Cr:GSGG laser system described above was used for the surface damage threshold measurements. The desired power density on the test sample was obtained using focusing lenses of different focal lengths. The spot size was calculated and actually measured on photosensitive film; however, calculated spot size was used in obtaining the damage threshold.

The surface damage threshold measurements were conducted using single and multiple shots. In this work, "damage" is defined by the appearance of a flash of light and the attenuation of a transmitted HeNe beam through the sample. This definition and method are widely used in the study of single and multiple shot damage, and the details of the methods can be found in reference [4].

3. EXPERIMENTAL RESULTS

3.1

The Nd:YAG and Nd:Cr:GSGG Surface Damage Threshold was initially measured using the sample discs in Group "A" (pitch lap polished). The damage threshold for single and multiple shots was measured. It was observed that the Nd:YAG crystal single shot surface damage threshold was $13.51 \pm 1.26 \text{ J/cm}^2$, while the Nd:Cr:GSGG crystal single shot surface damage threshold was $16.38 \pm 3.11 \text{ J/cm}^2$. However, the multiple shot surface damage threshold for the pitch lap polished samples shows the Nd:YAG crystal at $9.74 \pm 0.95 \text{ J/cm}^2$ while the Nd:Cr:GSGG crystal was $11.03 \pm 1.07 \text{ J/cm}^2$.

The significant increase in mean deviation for the single shot damage threshold as compared to the multiple shot damage threshold is associated with the stability of the laser output. Generally, higher pulse-to-pulse stability is observed at 10 Hz repetition rate due to the thermal compensation in the resonator [5]. However, the mean deviation difference for the single shot surface damage threshold between the Nd:Cr:GSGG (± 3.11) and the Nd:YAG (± 1.26) led us to believe that the surface quality for the Nd:Cr:GSGG may not be as good as the Nd:YAG samples. Therefore, Nd:Cr:GSGG discs were Pyrex lap polished (Group "B" samples). The surface damage threshold of $15.62 \pm 0.72 \text{ J/cm}^2$ was observed for single shot and $10.58 \pm 0.72 \text{ J/cm}^2$ for multiple shot. It is clear that the single shot surface damage threshold for the Pyrex lap polished samples did not improve the higher mean deviation (± 3.01). Hence, a hybrid polishing technique of pitch and Pyrex lap was used (Group "C" samples). The data collected for all the samples are summarized in table 2. As seen in the table, the polishing technique did not seem to change the higher mean deviation observed for the single shot surface damage threshold of the Nd:Cr:GSGG crystal.

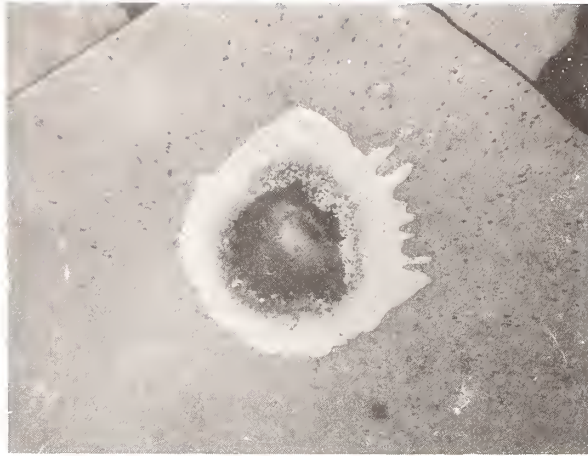
Table 2. Surface Damage Threshold in J/cm^2 for Nd:Cr:GSGG

Group "A"		Group "B"		Group "C"	
PITCH LAP POLISHED		PYREX LAP POLISHED		HYBRID PITCH + PYREX	
SINGLE SHOT	MULTIPLE SHOT	SINGLE SHOT	MULTIPLE SHOT	SINGLE SHOT	MULTIPLE SHOT
24.76	10.51	20.51	9.75	18.14	9.82
12.88	8.85	15.72	12.99	15.19	10.86
12.78	9.64	12.02	9.04	13.73	12.36
16.96	13.47	21.69	9.57	18.31	10.39
12.70	11.55	12.34	10.33	11.44	12.14
15.78	13.38	11.02	10.60	16.79	10.36
21.60	11.41	18.71	10.89	19.02	11.24
14.40	10.84	15.86	10.94	19.72	10.01
19.70	11.05	11.67	11.21	14.29	9.00
12.01	11.38	12.99	11.21	13.59	11.05
15.78	9.45	20.69	10.46	15.00	11.72
17.30	12.02	14.30	10.05	15.45	10.39
16.31 \pm 3.11	11.03 \pm 1.07	15.62 \pm 3.01	10.58 \pm 0.72	15.89 \pm 2.09	10.80 \pm 0.79

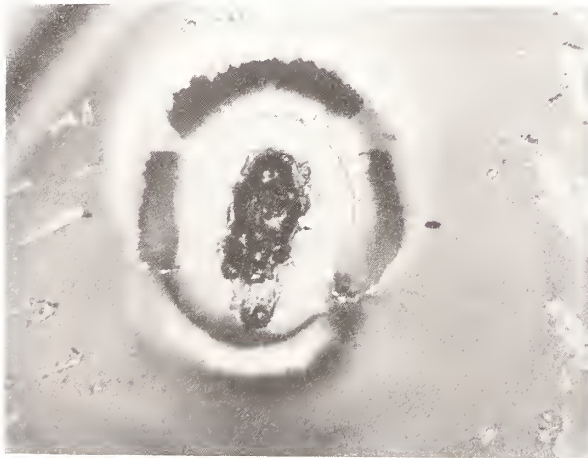
3.2 Damage Morphology

All the samples were examined with a microscope and scanned to find any outstanding surface defects at 10X magnification. Any areas that became suspect were then examined at 120X. Based on the microscope scan, less than two percent of the samples were rejected for the damage threshold measurements.

In figure 2A, a microscopic photograph for the Nd:YAG front surface damage with single shot at 1.061 μm (Nd:Cr:GSGG laser output wavelength) is shown. When this damage site is compared with the typical damage site on the Nd:Cr:GSGG, as seen in figure 2B, several differences are observed. It may be noted that the Nd:YAG crystal is pink-violet in color while the Nd:Cr:GSGG is green in color. The most notable difference in the damage sites was that the Nd:Cr:GSGG surface damage always was associated with dark color rings around the damage site. This fact led us to believe that the surface was contaminated with organic material.



A. Nd:YAG Front Surface Damage with Single Shot 1.061 μm (120X)



B. Nd:Cr:GSGG Front Surface Damage with Single Shot 1.061 μm (120X)

Figure 2. Damage Morphology Nd:YAG and Nd:Cr:GSGG

4. INFRARED SPECTROSCOPY

4.1 Typical Surface Contaminants

Typical surface contaminants of optical elements can be analyzed using infrared absorption spectroscopy. Using a titanium blade Micro-Spatula wetted with chloroform, the damage site is gently scraped, and if any contamination is present the chloroform will dissolve or soften it to adhere to the Micro-Spatula. The Micro-Spatula is then dipped into the 50 cc beaker which contains ~20 cc of Burdick & Jackson infrared spectroscopy grade chloroform. The contaminants are then dissolved into the beaker. This procedure is repeated until, using a 10X illuminated magnifier, as much of the contamination as possible is removed. The solvent in the beaker then is gently evaporated, using a warm hot plate, until approximately 200 μl remains. This quantity then is transferred while still warm to a potassium bromide infrared sampling plate using a 100 μl Micro-Pipet. Thus, a micro-cast film of the contaminants is prepared onto the plate.

This plate is now analyzed using a Perkin-Elmer Model 783 infrared spectrophotometer. The infrared spectrum from 4000-500 cm^{-1} is obtained from a six scan signal-average run, typically using a 5.4 cm^{-1} slit and noise suppression factor 4. The spectrum is analyzed using a Perkin-Elmer Model 7500 infrared data system. The spectrum is Computer Library searched for identification of all possible molecular structural units and spectral matching. In figure 3, the typical infrared spectra for organic contaminants, viz. skin oil, is shown. Using a similar method, infrared spectrum features were identified for $-\text{CH}_n$ vibrational modes associated with organic contaminants by Lewis and Arthur [6] at the Royal Signal and Radar establishment, Malvern, UK.

4.2 Test Specimens Contaminants

The method described above was used to identify surface contaminants on one disc of Nd:Cr:GSGG from Group "A" and one disc of Nd:YAG crystal. These samples were selected by a 10X microscope examination of the damage sites. The discs were selected particularly for the appearance of dark rings around the damage site. The infrared spectra collected from the contaminants is shown in figure 4. The infrared spectra collected for Nd:YAG and Nd:Cr:GSGG did not show a significant difference, indicating that organic contaminants were not the cause of the higher mean deviation observed in the Nd:Cr:GSGG surface damage threshold.

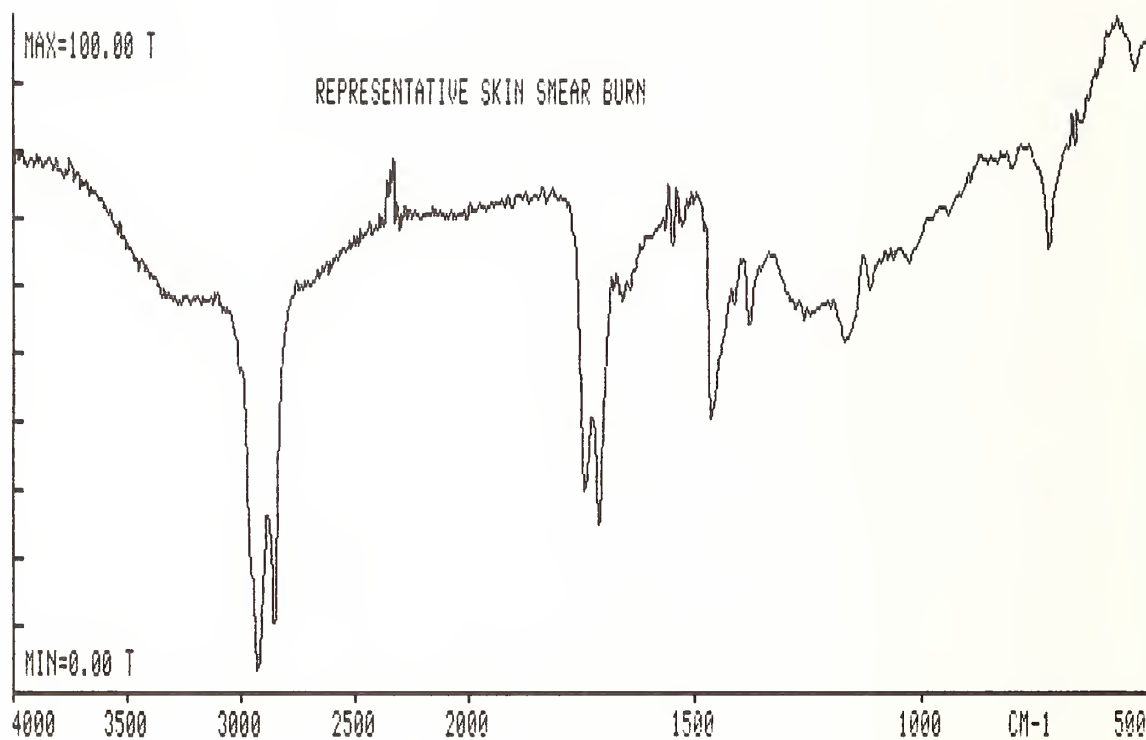


Figure 3. Typical Infrared Spectra for Organic Contaminant

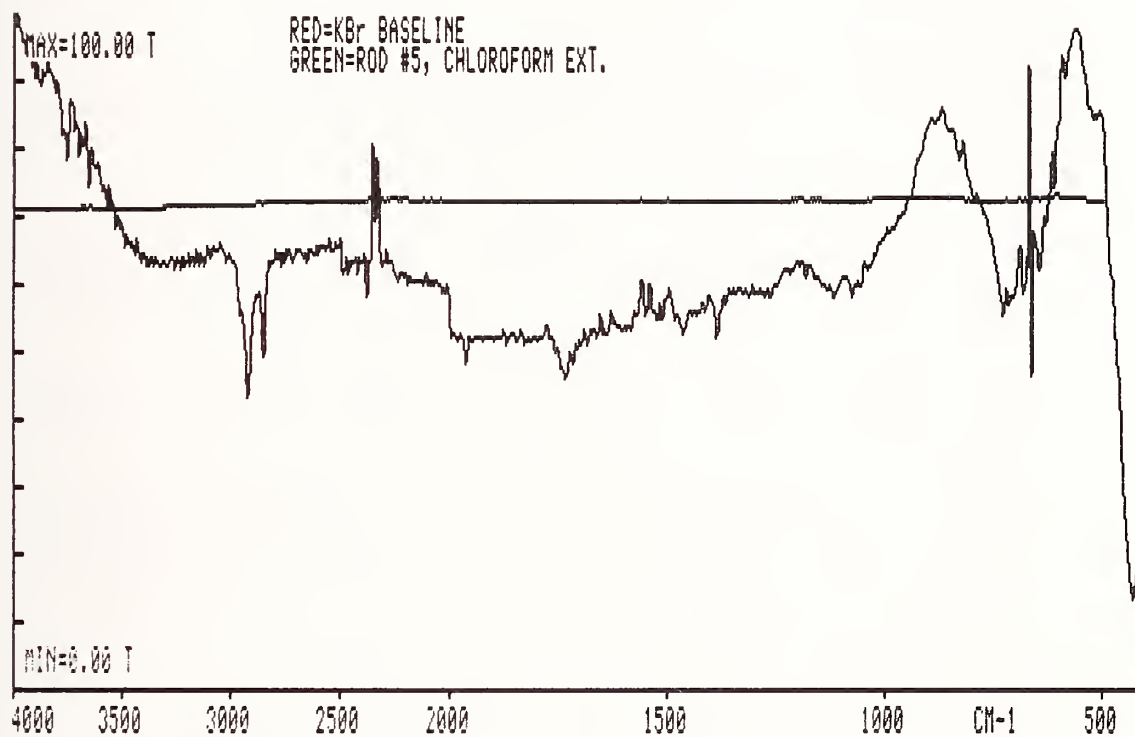


Figure 4. Infrared Spectra for Nd:Cr:GSGG Surface Contaminants

5. CONCLUSIONS

- a. The surface damage threshold for Nd:YAG, pitch lap polished, using 0.3 μm alpha alumina mixed thin in water, was measured to be $13.5 \pm 1.26 \text{ J/cm}^2$ for single shot and $9.74 \pm 0.95 \text{ J/cm}^2$ for multiple shots. For the damage measurements, a stable, TEM₀₀, Q-switched Nd:Cr:GSGG laser operating at 1.061 μm was used.
- b. The surface damage threshold for Nd:Cr:GSGG, pitch lap polished, using 0.3 μm alpha alumina mixed thin in water, was measured to be $16.38 \pm 3.11 \text{ J/cm}^2$ for single shot and $11.03 \pm 1.07 \text{ J/cm}^2$ for multiple shots at 1.061 μm .
- c. The higher mean deviation for the single shot surface damage threshold as compared to the multiple shot surface damage threshold is associated with poor shot-to-shot stability in the single shot operation of the laser.
- d. The mean deviation for the single shot surface damage threshold observed for Nd:Cr:GSGG (± 3.11) is substantially higher than the mean deviation for the single shot surface damage threshold observed for Nd:YAG (± 1.26).
- e. Three different methods of polishing used did not seem to make a difference in the single shot surface damage of the Nd:Cr:GSGG or the high mean deviation. The single shot surface damage threshold for pitch lap polished, Pyrex lap polished, and hybrid pitch plus Pyrex polished was measured at $16.31 \pm 3.11 \text{ J/cm}^2$, $15.62 \pm 3.01 \text{ J/cm}^2$, and $15.89 \pm 2.09 \text{ J/cm}^2$, respectively.
- f. The damage site comparison shows that the Nd:Cr:GSGG surface damage always was associated with dark color rings around the damage site.
- g. Infrared absorption spectroscopy of the damaged Nd:Cr:GSGG and Nd:YAG did not show significant difference in organic contaminants on the surface.
- h. Finally, the Nd:Cr:GSGG surface damage threshold is as high as the surface damage threshold of the Nd:YAG, but the mean deviation in the Nd:Cr:GSGG surface damage threshold is higher and the damage sites are surrounded by dark color rings.

6. ACKNOWLEDGEMENTS

This work is a part of an internal R&D program conducted at and supported by Litton Laser Systems, Orlando, FL. Thanks are due to Marvin Kaplan for assistance with Infrared Spectroscopy and Julie Trudell, Phyllis Milligan, and Jacqueline Wartell for preparation of this manuscript.

7. REFERENCES

- [1] Acharekar, M.A., McCarthy D.P.; Blackman R. Pulsed laser induced optical damage threshold in Nd:Cr:GSGG crystal, Laser induced damage in optical material, Boulder Damage Symposium, 1984 Sept., (Proceedings to be Published).
- [2] Zharikov, N.N. Laptev, V.V.; et.al., Sov. J. Quantum Electron. 13 (1), 82-85, 1983 Jan.
- [3] Krupke, W.F.; Modern solid state laser materials, Lawrence Livermore National Laboratory, Tech. Note UC1D-20119, 1984 June.
- [4] Merkle, L.D.; Bass, M. and Swimm, R.T.; Multiple pulse laser induced damage in crystalline and fused quartz at 1.064 and 0.532 μm , Nat. Bur. Stand. (U.S.) Spec. Publ. 669, 1982 Nov., 50 p.
- [5] Teppo E.A.; Nd:YAG laser technology, Naval Weapons Center, Tech. Note 4051-2, 1972.
- [6] Lewis, K.L.; Arthur, G.S.; Surface and free carrier absorption processes in CVD zinc selenide, Nat. Bur. Stand. (U.S.) Spec. Publ. 669, 1982 Nov., 86 p.

Excimer Radiation Colouration Processes and
Surface Damage to Single Crystal
CaF₂ Substrates

I. Laidler and D.C. Emmony
Department of Physics
Loughborough University of Technology
Loughborough, Leicestershire, LE11 3TU

This paper considers the effects of a 249nm excimer pulse on CaF₂ substrates and is concerned with both surface damage and bulk colouration processes.

The effect of different polishing procedures on the surface damage threshold of CaF₂ has been investigated.

CaF₂ has been shown to develop colour centres under prolonged U.V. irradiation. A technique has been developed to monitor the transient excited states created in the bulk material when irradiated with a 25ns excimer pulse. This involves a simultaneously pumped dye laser pulse probe operating at the absorption wavelengths of the excited species. From the results information about the photon absorption cross sections can be derived, the concentration of defect states at any time during the excimer pulse may be estimated and a knowledge of the maximum safe fluence levels established.

Key Words:- CaF₂ single crystal; surface finish; laser damage; colour centres; transient defects.

1. Introduction

Calcium fluoride is an important material for those working at the excimer wavelengths, both within and external to, the laser cavity. Damage in CaF₂ optics may manifest itself in one of two ways. Bulk and surface mechanical damage, or the long term degradation of the material's optical properties due to the irradiation induced generation of colour centres. Both these effects have been investigated using a 249nm, 30ns excimer laser with an output pulse energy of around 700mJ. The experimental configuration and beam characteristics can be seen in figures 1 and 2.

2. Sample Preparation

In order to study surface effects eight sample surfaces were prepared and the damage threshold and damage morphology of each studied. The surfaces were variations on a standardised polishing technique consisting of an alignment and cutting stage, an intermediate and then final polishing stage. Each surface was damage tested, then chemically etched and retested. The variations enabled conclusions to be drawn as to the effect of sample purity, surface stress induced during the cutting stage, the effect of surface scratches and chemical etching. The surfaces can be classified as follows and are given with their damage thresholds.

- | | |
|---------------------------------------------------------|---------------------|
| i) Standard Material and Standard Polish | 6Jcm ⁻² |
| ii) As in i) plus a chemical etch | 9Jcm ⁻² |
| iii) Optipur Material and Standard Polish | 6Jcm ⁻² |
| iv) As in iii) plus a chemical etch. | 9Jcm ⁻² |
| v) Standard Material but stress reduced Standard Polish | 5Jcm ⁻² |
| vi) As in v) plus a chemical etch | 11Jcm ⁻² |
| vii) Standard Material plus ultra fine Surface Polish | 7Jcm ⁻² |
| viii) As in vii) plus a chemical etch | 12Jcm ⁻² |

All figures have a $\pm 0.5J$ tolerance.

Damage has been defined as the fluence required to produce any visible damage (using a 1000 x Nomarski microscope) in 50% of the shots. The figures quoted are single shot thresholds and the spot size is large enough to remove any statistical dependence of damage threshold.

3. Discussion

As well as Nomarski microscope a Transmission Electron Microscope (T.E.M.) was used to look at the surfaces, both before and after damage testing. Prior to damage the surfaces looked identical except for samples vii) and viii) which were much more scratch free. No differences could be detected on the chemically etched surfaces. Visually they looked the same as the un-etched substrates. Practically, however the chemical etch raised the damage threshold by at least 50% and up to 100%. Figures 3a and 3b contrast a Standard Polish with an Ultra Fine Polish.

Observations of the damage sites has revealed the following points:-

- a) cleavage occurs along scratch lines or grooves. This was true on all surfaces.
- b) Sample v) with the lowest damage threshold has embedded impurities causing localised absorption and circular damage sites and cleavage centering on the impurity. See figure 4. The surrounding area was untouched by the radiation. The chemical etch appeared to have removed these impurities.
- c) Although cleavage was the most obvious form of damage in all samples it did not appear to be the first form except in sample v). All the other surfaces showed, without exception, that the onset of damage was light pitting and melting. The presence of scratches were irrelevant to this mechanism.
- d) All cleaved areas show that the actual cleaved surface has flowed, i.e. melted, again indicating that melting is the first form of damage.
- e) Samples vi) and viii) had a large difference in surface roughness as seen in figures 3a and 3b and yet only a 1J difference in damage threshold.

Firstly it would appear from these results that the purity of the bulk material is not significant in surface damage. Mass spectrographic analysis of the two grown sample materials show trace impurities of the rare earths in the ppm level of the naturally occurring fluorspar which is not present in the optipur material.

The cause of cleavage in CaF_2 has previously been discussed [1,2] and attributed to the plastic deformation of the material during heating. This causes slip planes to appear along the $\{111\}$ faces and specifically orientated $\{111\}$ surfaces to be pushed up out of the surface, figure 5, [3]. On cool down the plastic deformation results in a residual stress which may cleave the crystal, figure 6. We can assume that at room temperature CaF_2 can withstand a specific degree of internal stress but above this value it must yield and cleave. (Remember it can plastically deform at high temperatures). Around scratches and grooves the intrinsic stress is enhanced by a factor of the order $(\frac{\ell}{r})^{\frac{2}{3}}$ where ℓ is the length of the crack and r is the radius of the crack tip. For surface features characteristic to these polished samples an enhancement of 30x is typical. Thus cleavage, a stress related phenomena, first manifests itself around such features.

The results, however, would indicate that it is necessary for the surface first to melt before there is enough thermal energy to cause significant plastic deformation giving rise to residual stresses large enough to cause cleavage. Even around typical scratches the cleaved material has first flowed.

The exact role played by surface scratches is still uncertain, but does not seem all that great in CaF_2 , especially in the light of vi) and viii). Perhaps their most important role is as a trap for absorbing impurities. The scratches themselves would not appear to play a part in the damage initiating mechanism. The chemical etch has greatly increased the thresholds without significantly changing the volume of the surface features and it is suggested that it has acted purely as a thorough cleanser. Damage may be initiated by surface dirt or grease etc, heating the substrate to a sufficient temperature for some intrinsic temperature dependent effect to take over i.e. avalanche ionization. This mechanism may then take the whole surface to the melting point.

4. Colouration Processes

The role of colour centres in bulk damage processes is continually being debated [4]. With this in mind an experiment has been devised to monitor, during the damaging radiation pulse, the concentrations of primary defects produced by this pulse. This work has two aspects of interest. Firstly to try and understand if the laser induced, transient defects play any role in bulk damage phenomena. Then secondly to investigate the processes that lead to radiation induced colour centres in single crystal CaF_2 . With the increasing interest in large single crystal CaF_2 as an excimer window material the long term degradation of the window's transmission through colour centre generation is a frustrating and expensive problem.

5. Experimental Arrangement

The experimental arrangement can be seen in figure 7. It uses an identical damage facility as employed for the surface work. The samples are now, however, cubic in geometry. Immediately on leaving the laser the excimer beam is split, 15% of the 249nm light being used to pump a dye laser. The dye beam is T.E.M.₀₀ with a beam diameter of 2mm and a temporal profile corresponding to that of the excimer pumping pulse, though clipped in the wings. Figure 7 shows the dye beam split into two arms, a probe and a reference arm. The probe arm interrogates the crystal, entering perpendicularly to the excimer and passing concurrently in time through the excimer's focus. The reference arm traverses a 35ns delay line. Both beams are then incident upon a vacuum photodiode and the signal recorded by a fast oscilloscope capable of resolving their temporal profiles. Thus, direct comparison of the two pulses shown on the oscilloscope, the time dependent absorption of the dye beam can be ascertained. This beam is tuned to the absorption band of the excited species and primary defect of interest. The focussing optics of the probe beam is such that refractive index changes in the sample will not result in a loss of light and hence an apparent absorption.

The first excited state to be considered was that of the V_k centre or "self-trapped hole". In CaF_2 it is this state that leads to the production of metastable F and H centres. The V_k centre is formed every time an electron can be excited out of the valance band to the conduction band or to impurity traps. The hole relaxes to its lowest energy configuration, i.e. it forms a covalent X^- molecule with the nearest neighbour halogen ion. The V_k centre, providing a highly efficient electron trap, does not, in CaF_2 , directly revert back to the perfect lattice by straight forward recombination. Rather the V_k centres rotates into the (111) direction and a close F-H pair is the result [5]. The close F-H pair may then radiatively recombine or separate, depending upon the environment, forming the stable F centre and H centre and colouring the crystal. It is hoped that the experiment described will give us a better insight into the conditions for colour centre generation and ways of avoiding them.

The experiment was initially performed using two different grades of CaF_2 . Crystals were grown using optipur material and also a naturally occurring fluorspar. Mass spectrographic analysis of these materials showed the naturally occurring fluorspar to contain between 0.1 and 10ppm of the rare-earths whilst the optipur material, within the detection capability was free of these elements. The rare-earths will enter the fluorite lattice as a 3^+ ion sitting above the valance band and accessible to U.V. photons [6]. On trapping an electron the new 2^+ state now lies within a photon's reach of the conduction band. A method of V_k centre generation is thus available, and it can be seen that a single impurity may give rise to more than one V_k centre due to the cyclic nature of its production. The lifetimes of such states and formation rates need to be understood.

6. Results and Discussion

Figure 8 shows the increasing optical absorption caused by an increasing V_k centre concentration as the exciting pump fluence is raised. Trace A is that of the naturally occurring fluorspar, A_1 15 ns into the excimer pulse, A_2 10ns later. Trace B which indicates no optical absorption is that for the optipur material. Simultaneous fluorescence due to the first excited state of the V_k centre was observed in the fluorspar material but not in the optipur.

Analysis of the results using a knowledge of the excimer's spatial and temporal profile energy content and crystal impurity level enables an estimation of the V_k centre creation cross section (10^{-19}cm^2). The continuous lines on the graph represent a first order theory from which is derived the V_k centre creation cross section. It will be noted that the graphs tend to saturate at a level defined by the rare earth impurity concentration and exciting photon fluence. After saturation a gradual linear increase is experienced in V_k concentration. This is due to the cyclic nature of the rare-earth trapping process where the 2^+ state is ionized becoming a 3^+ impurity available for valence electron trapping. It would appear that the time for one cycle to be completed is of the approximate order of the excimer pulse.

7. Summary

Two forms of damage have been investigated. Work on surface finish of CaF_2 surfaces indicates that the damage threshold of the surfaces is not dependent upon ionic impurities, and not as dependent upon surface topography as believed. Surface cleanliness is by far the greatest factor affecting damage thresholds.

Colouration processes have been investigated and a sensitive technique developed to monitor the concentration of primary defects. So far work indicates the presence of rare earth 3^+ ions is crucial in the formation of both transient and metastable colour centres. It is hoped to continue the work to see how these states affect the bulk damage phenomena.

The authors would like to thank B.D.H. Chemicals, England, for their help and sponsorship of this work, through an SERC CASE award, for providing and preparing the crystals and most importantly, the initial impetus for the work.

8. References

- [1] Detrio, J.A.; Graves, G.A.; Wimmer, J.M. Failure criteria for laser window materials. Nat. Bur. Stand. (U.S.) Spec. Publ. 568; 1979. p.p. 151-158.
- [2] Loomis, J.S. Fourth conference on high power infra-red laser window materials. 1974
- [3] Porteus, J.O.; Soileau, M.J.; Fountain, C.W. Character of pulsed laser damage to Al at $10.6\mu\text{m}$ infra-red from single-crystal targets in vacuum. Nat. Bur. Stand. (U.S.) Spec. Publ. 462; 1976. p.p. 165-172.
- [4] Braunlich, P.; Brost, G.; Schmid, A.; Kelly, P. The role of laser induced primary defect formation in optical breakdown of NaCl. Nat. Bur. Stand. (U.S.) Spec. Publ. 620; 1980, p.p. 406-415.
- [5] Williams, R.T. Photochemistry of F-center halide crystals, Semiconductors and Insulators. Vol. 3 p.p. 251-283; 1978
- [6] Kiss, Z.J. Photochromatic materials for quantum electronics. I.E.E.E. Journal of Quantum Electronics, Vol. QE-5, No. 1, p.p. 12-17; 1969.

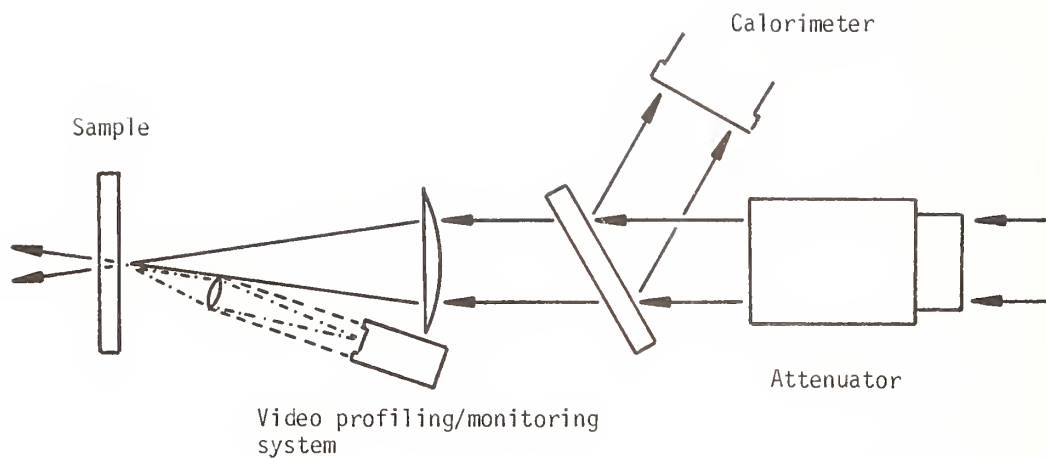


Figure 1. Damage configuration

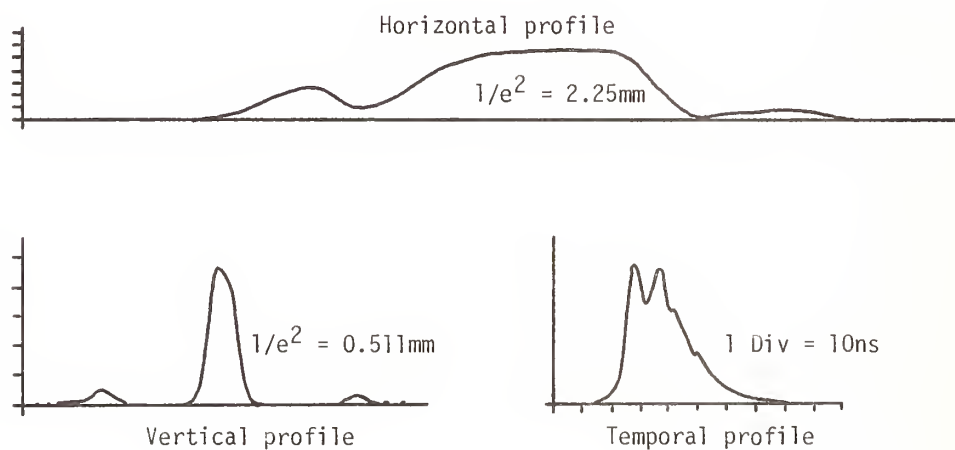


Figure 2. Focused beam characteristics



Figure 3a. Standard polish



Figure 3b. Ultra fine polish

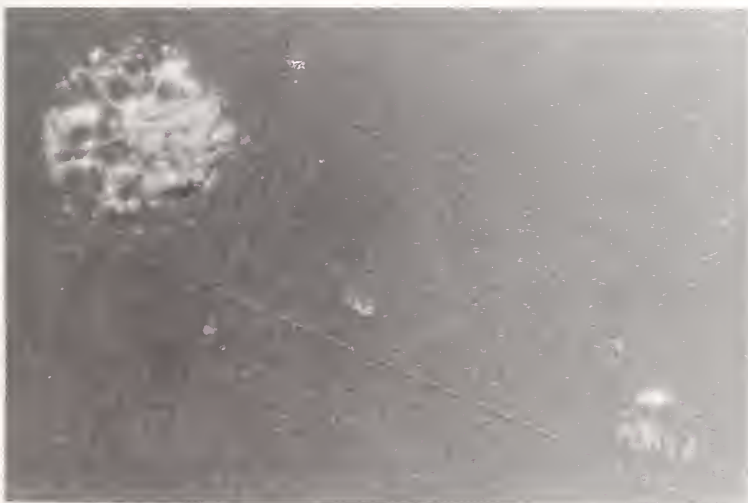


Figure 4. Impurity centre damage

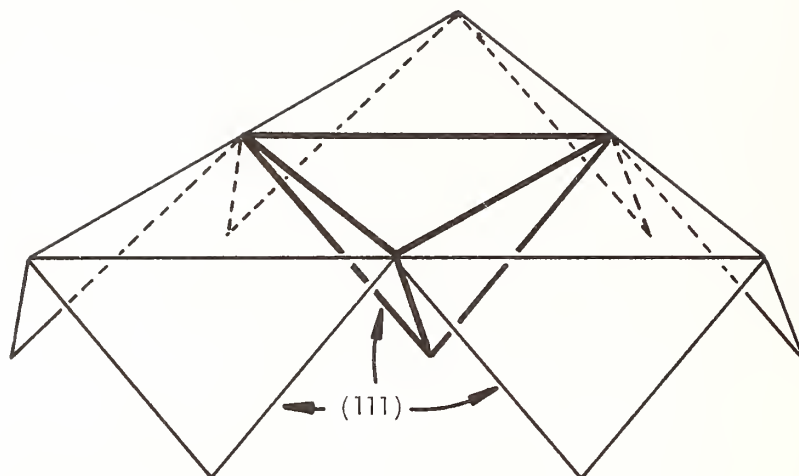


Figure 5. CaF_2 (111) surface and slip planes

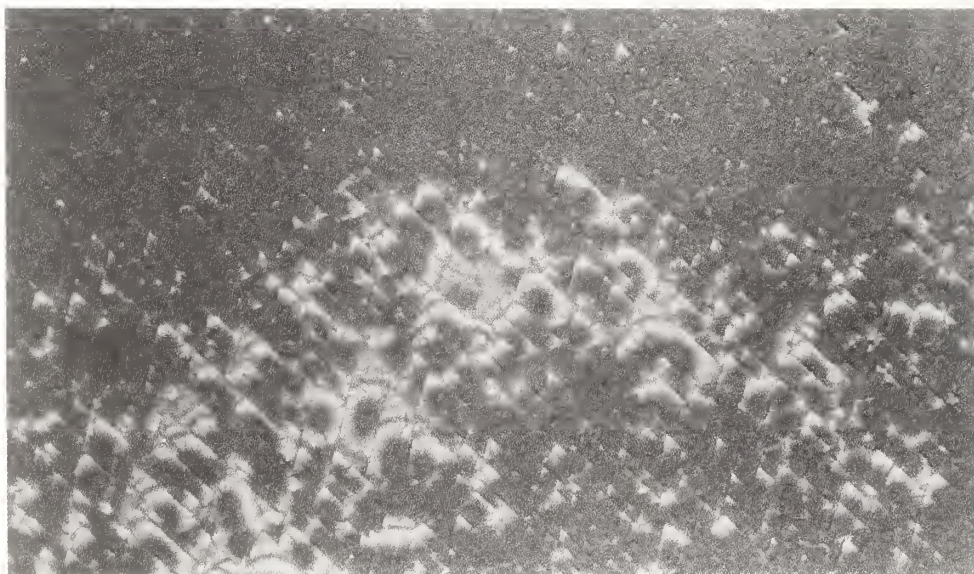


Figure 6. Cleaved surface of CaF_2 due to thermal expansion

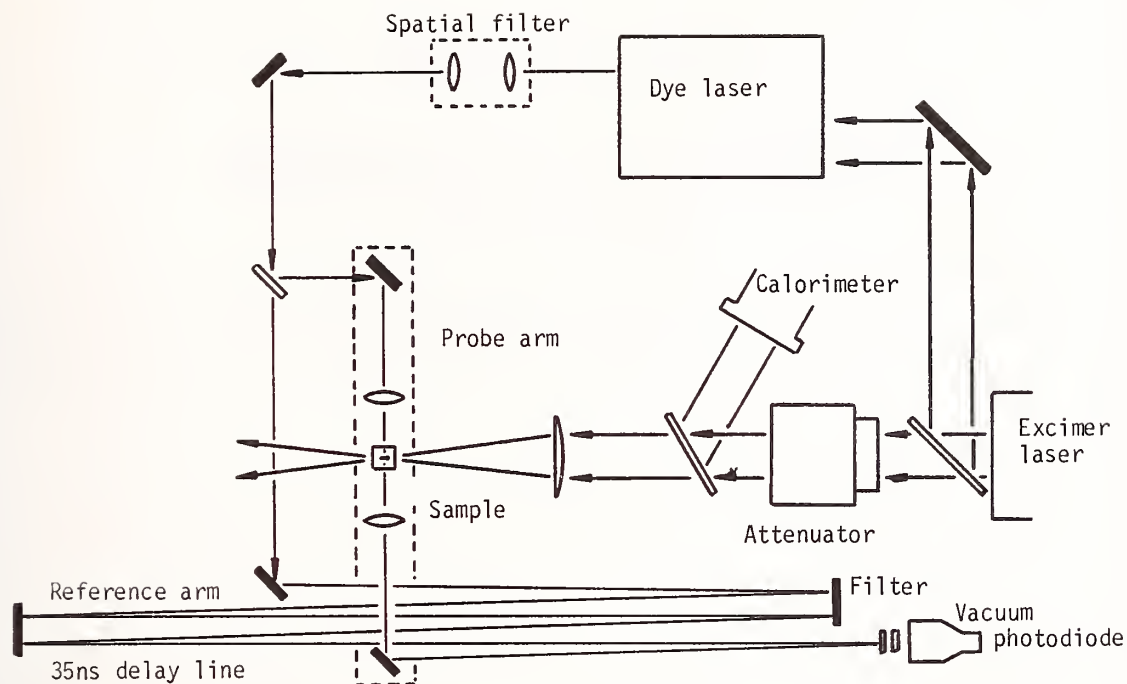


Figure 7. Experimental arrangement for monitoring transient absorption

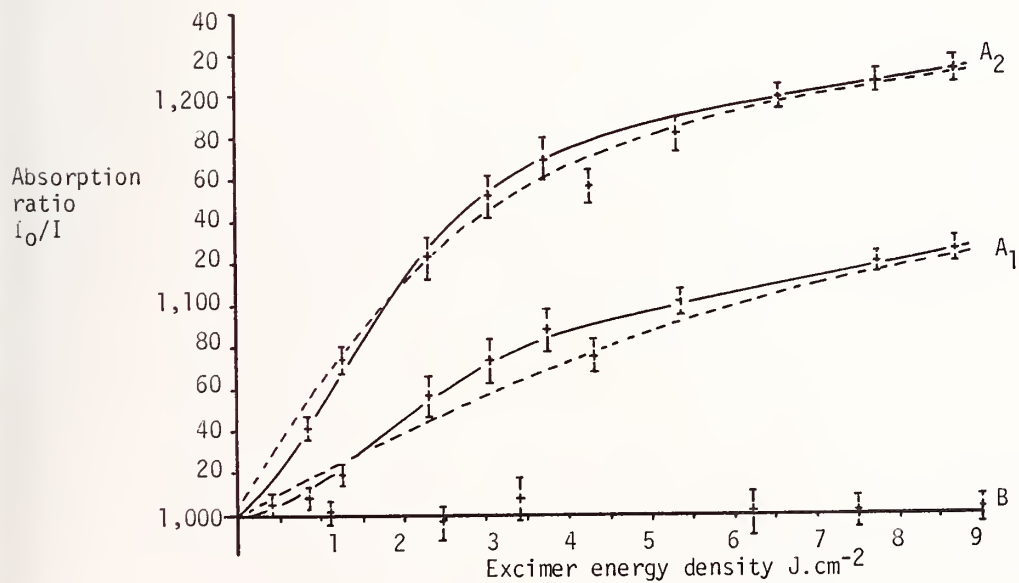


Figure 8. Absorption (V_{ic} centre concentration) growth as a function of energy density

- Manuscript Not Received -

=====

ANALYSIS OF OPTICAL SURFACES BY LASER IONIZATION MASS
SPECTROMETRY: SPATIAL VARIATION OF THE LASER DAMAGE
THRESHOLD AND ITS RELATIONSHIP TO POLISHING
COMPOUND INCORPORATION

Wigbert J. Siekhaus
Lawrence Livermore National Laboratory
Livermore, CA 94550

Laser Induced Damage and Ion Emission of GaAs at 1.06 μm

A. L. Huang, M. F. Becker, and R. M. Walser
Electrical and Computer Engineering Department and
Electronics Research Center
The University of Texas at Austin
Austin, Texas 78712

The experiments in this study were focused on the N-on-1 laser damage and sub-damage threshold ion emission of gallium arsenide. The initial goals were (1) to determine the N dependent damage threshold due to N-on-1 laser irradiance and (2) to correlate ion emission with surface damage events. A Q-switched Nd:YAG laser (1.064 μm , 45 nsec pulse, 580 μm spot diameter) was used to irradiate the <100> single crystal gallium arsenide samples.

Using values of N from 1 to 100, we obtained accumulation curves based on 50% damage probability. Corresponding damage threshold fluences were 0.4 - 0.8 J/cm^2 for $N > 1$ and approximately 1.5 J/cm^2 for $N = 1$. We observed large site-to-site fluctuations in ion emission, and emission occurred before surface damage was initiated. We found the onset of ion emission at a fluence of 0.2 J/cm^2 for all cases, whereas the damage threshold fluence was two to five times larger and dependent on N. Experimental measurements of linear and nonlinear absorption coefficients were made to check for anomalous absorption. The measured values were in agreement with those previously reported. Once surface damage occurred, ion emission was greatly increased. This type of behavior seems to support a surface cleaning model for ion emission which precedes surface damage.

Key words: gallium arsenide; charged particle emission; N-on-1 laser damage threshold.

1. Introduction

The interaction between laser radiation and solids has been a perplexing problem for many years. Often the lifetime of an optical device is determined by its susceptibility to optical damage. There has been much controversy and unexplained phenomena associated with the energy transfer mechanism of normal laser damage as well as the physical nature of surface damage.

The objectives of the experiments reported here were to characterize the statistical nature of surface damage for gallium arsenide, to observe the relationship of charged particle emission to surface damage, and to observe the damage morphology of gallium arsenide. In silicon it has been reported that charged particle emission is coincident with surface damage [1]. A relation between charged particle emission and surface damage has yet to be reported for gallium arsenide. To explore the statistical nature of surface damage of gallium arsenide, we performed various single shot and N-on-1 sub-threshold laser tests. We measured the positive charged particles emitted during each laser pulse to correlate the charge emission events with surface damage. Theoretical calculations for a thermal model, as well as an electron-hole production model, have been carried out to determine the mechanism responsible for the surface damage.

2. Experimental Setup and Apparatus

2.1. Samples

The gallium arsenide samples used in the experiment were supplied by the microwave integrated circuit production group at Texas Instruments in Dallas, Texas. The samples had a <100> orientation and were very lightly doped with chromium ($\approx 1 \times 10^{16} \text{ cm}^{-3}$), but otherwise undoped and unannealed. These samples were characterized by a resistivity of greater than $1 \times 10^7 \Omega\text{-cm}$ and an etch pit density of $40\text{-}60 \times 10^3 \text{ cm}^{-2}$. Only the front face of the wafer was polished to optical quality.

To prepare the sample for the vacuum tank we sequentially cleaned the gallium arsenide wafers in boiling solvents of trichlorethylene, acetone, and methanol to assure that all contaminants had been removed. While in each solvent, the wafer was ultrasonically cleaned before proceeding.

After the final cleaning in methanol, the wafer was rinsed in deionized water (less than 5 minutes at room temperature) and placed into the vacuum tank.

To measure the linear and non-linear absorption coefficients in the transmission tests, the gallium arsenide wafers were given an optical quality finish on both sides. The backside of the wafer was mechanically polished in a two step process. Rough polishing with a grinding pad with six micron diamond ferrous paste was used to initially buff the wafer. The finishing pad used a liquid, 0.05 micron alumina, non-ferrous, suspension as a grinding media. After polishing, the wafer was chemically cleaned as described above.

2.2. Experimental Setup

The experimental system is shown schematically in figure 1. It utilized a Q-switched Nd:YAG laser with a full width half maximum (FWHM) pulse length of 45 nanoseconds, TEM₀₀ mode, and wavelength of 1.064 μm . A knife edge scanning technique was used to measure the focused spot diameter on the sample surface which was found to be 580 μm . The laser stability fluctuated from pulse to pulse resulting in a 2-5 percent standard deviation in energy for each data run. The laser was operated at a 15 Hz repetition rate and the incident energy was attenuated by rotating a half-wave plate in front of a polarizer.

A computer was utilized to control and count the laser pulses striking the gallium arsenide sample and to record the charge collected. The computer had a Z80 microprocessor and supported several data acquisition ports via sample and hold amplifiers and a multi-channel A-to-D converter. The delay for the sample and hold amplifier was set to 130 μsec in hardware. This assured that the integrated values read for the charge emission were near the peak value, but were collected well after the laser noise burst. The electronics were triggered by a vacuum photodiode. A shutter, controlled by one of the computer's digital output ports, was used to select pulses for sample irradiation. To allow time for data computation and storage between pulses, the shutter selected every third pulse from the laser train.

A 760 mm focal length lens focused the beam onto the sample. The long focal length gave a region of constant spot size approximately 3 mm deep at the focal plane and permitted greater error in the placement of the sample. A system of 90° prisms was placed after the lens to scan the beam across the sample in the vacuum tank.

To detect charged particle emission the sample and detection device were placed into the vacuum environment. The system was dry pumped to achieve experimental pressures of less than 1×10^{-6} Torr. A Hamamatsu electron multiplier tube model R596 served as the ion detector and was placed inside the vacuum system at a 36° angle to the laser beam path. The sample surface was normal to the optical path. The output of the detector was connected to a capacitive voltage divider and amplifier. The dynamic range of the data acquisition system was increased by making one channel 100 times less sensitive than the other. The electron multiplier current gain was estimated to be approximately 0.75×10^6 at a voltage of -2kV. A data value of 1000 in the more sensitive A-to-D converter channel corresponded to a charge of approximately 1.5×10^{-17} Coulombs.

3. Data and Analysis

Three experiments were conducted on the cleaned samples: 1) an emission scan of the gallium arsenide sample at a fixed laser fluence, 2) an N-on-1 emission/damage threshold test, and 3) a transmission test. All of the tests were performed in vacuum with the exception of the transmission test. The calibration and beam profiles were checked at the start and end of each experimental session to assure accurate beam fluence measurements.

The emission scan of the gallium arsenide sample checked the uniformity of charge emission under constant laser fluence. The scan spots were separated by 0.8 millimeters and 42 samples were taken. The sample was irradiated with a constant fluence of 0.63 J/cm² ($\pm 7\%$). The results in figure 2 show a bi-level emission contour. A different pattern of emission variations was observed on each sample. Site-to-site fluctuations of the defect density in gallium arsenide have been previously noted [2] and could disrupt the statistics of charged particle emission and, possibly, the emission threshold. To minimize the effects of these site-to-site variations, we conducted the emission/damage tests over a small area of the wafer.

Other experiments were concerned with the multi-pulse and single pulse irradiance of gallium arsenide. In the multi-pulse experiments, fluences below the single pulse damage threshold were used to search for accumulation effects associated with either emission or damage. The objectives of these experiments were (1) to identify accumulation effects associated with surface damage, (2) measure a damage threshold based on 50% probability statistics, (3) search for correlations

inhomogeneous processes is made apparent by examining the laser absorption in the sample. From the slope and intercept of the linear fit of the inverse transmission versus intensity shown in figure 10, we extracted the nonlinear absorption coefficient, β_0 , and the linear absorption coefficient, α_0 . First α_0 was found from the equation:

$$T_0 = (1-R)^2 \exp(-\alpha_0 L) \quad (1)$$

where T_0 is the zero fluence transmission intercept, R is the reflectivity at the air-gallium arsenide wafer interface, and L is the thickness of the gallium arsenide sample. In our case T_0 was 0.447 (from figure 10), R was calculated to be 0.306, and $L = 0.0635$ cm. Substituting these values into eq. (1) and solving yields $\alpha_0 = 1.18 \text{ cm}^{-1}$. With α_0 known, the nonlinear absorption coefficient, β_0 , can be calculated from the following equation:

$$m = \beta_0 [\exp(\alpha_0 L) - 1] / [\alpha_0 (1-R)] \quad (2)$$

where m is the slope of the linear fit to the inverse transmission versus incident intensity data. Equation (2) was derived from eq. (3) as described in reference [6]. From figure 10, we obtained $m = 40.2$. Solving for β_0 in eq. (2) yields $\beta_0 = 0.42 \text{ cm/MW}$. When the pulse length is accounted for, the values of α_0 and β_0 are in agreement with those previously reported by Bechtel and Smith [7] and Lee and Fan [8]. Therefore there is no evidence of anomalous homogeneous absorption.

4.1. Thermal Model

To determine the mechanism responsible for the laser induced damage, we examine the temperature change of the surface. The linear and nonlinear absorption must be included in the heating model because the laser energy is absorbed throughout the gallium arsenide sample. For uniform illumination, the intensity relative to that at the surface is given by the differential equation:

$$dI/dx = -\alpha_0 I - \beta_0 I^2 \quad (3)$$

where $I = I(x)$ is the intensity at a depth x into the absorbing medium, α_0 and β_0 are the linear and nonlinear absorption coefficients, respectively. Assuming that all the absorbed energy is thermalized without diffusion, the peak surface temperature rise can be written

$$\Delta T = (dI/dx)_{\text{surf}} t_p / C_v \rho \quad (4)$$

where t_p is the pulse length, C_v is the heat capacity, and ρ is the mass density. Substituting eq. (3) into eq. (4), and taking the surface reflectivity into account gives

$$\Delta T = [\alpha_0 + \beta_0 I_0 (1 - R)] (1 - R) I_0 t_p / C_v \rho \quad (5)$$

where I_0 is the incident intensity. For gallium arsenide at room temperature, we have $C_v = 0.327 \text{ J/g-}^\circ\text{K}$ and $\rho = 5.32 \text{ g/cm}^3$. Using a typical damage intensity for the single shot case, $I_0 = 19 \text{ MW/cm}^2$, we obtain a maximum temperature rise of 2.3°C . This diffusionless model assumes homogeneous energy absorption and temperature independent reflection and linear and nonlinear absorption coefficients.

From the results of the previous calculation we conclude that uniform heating is not sufficient to explain the melting effects observed on the gallium arsenide surface. A similar conclusion has been reported for silicon by Merkle, Uebbing, Baumgart, and Phillipp [9]. However, this does not exclude the possibility of an abnormal absorption, or point absorption in defects at, or near, the gallium arsenide surface.

between surface damage and charged particle emission, and (4) determine the damage morphology as a function of fluence and number of pulses.

For each value of the number of pulses N used ($N = 1, 3, 10, 30$, and 100) we irradiated 150 to 200 different sites in order to obtain the statistics of surface damage. Surface damage on the front surface of the sample was identified by searching for surface changes with a Normarski optical microscope at 200X. The damage data for $N = 1, 10$, and 100 are plotted in figures 3-5, respectively. In each plot we used a linear curve fitting program to obtain the damage probability. From the linear fit we obtained the 50% probability fluence for each value of N , and used this value in the accumulation plot in figure 6.

For all values of N , we observed the onset of charged particle emission at an average fluence of 0.2 J/cm^2 ($\pm 0.069 \text{ J/cm}^2$). The values for the onset of emission and the 50% damage threshold are given in Table 1.

Table 1. Onset of Emission and 50% Damage Threshold Fluence of N-on-1 Experiments.

N	Charged Particle Emission Onset Fluence [J/cm^2]	50% Damage Fluence [J/cm^2]
1	0.18	1.518
3	0.15	0.7751
10	0.17	0.6357
30	0.32	0.7907
100	0.17	0.6781

From these damage fluence values and their plot in figure 6, it is apparent that an accumulation effect was present. As the number of laser pulses incident on the wafer increased, the 50% damage fluence decreased. Similar curves to the one shown in figure 6 have been reported for metals [3], polymethylmethacrylate and modified polymethylmethacrylate [4].

The positive charged particle emission data was collected on a pulse-by-pulse basis. A typical profile for $N = 30$ is shown in figure 7. The site from which this emission profile was obtained was damaged. From these data we note that the first few pulses (from 2 up to 10 depending on the case) induced a charge emission that decreased as the pulse number increased. After this, the emission increased greatly. We interpret the decrease in the first few pulses as a surface cleaning effect. These first pulses cleaned any residue left from either the chemical cleaning process or that had been ejected from previously laser irradiated sites. This emission could also be due in part to the depletion of the more volatile specie, As, from the surface atomic layers. Figure 7 also shows that, once the site experiences surface damage, charge emission is greatly increased. The emission at non-damaged sites always decreased with increasing number of pulses.

Figures 8 and 9 are SEM micrographs showing the development of laser induced surface damage morphologies. The initial surface was featureless and without contrast. In the Normarski microscope the initial surface change appeared as a depression with an area equal to that of the laser spot. Within this area there were several very small pitted regions (similar to those shown in figure 8 but not as well defined). As the fluence increased, or the number of pulses increased, the initial surface damage evolved into the melt pits shown in figure 8. The damage evolution ends with severe cratering as shown in figure 9. The theory of Fauchet and Siegman [5] would seem to apply in this case. They postulate that laser initiated ripple patterns on the surface of silicon and gallium arsenide are formed from the interaction of the incident laser wavefront with scattered optical surface waves. At $1.064 \mu\text{m}$, however, with a pulse length of 45 nsec and spot diameter of $580 \mu\text{m}$, no ripple patterns were seen in our experiments. Accordingly, the longer pulse lengths may inhibit ripple formation.

4. Discussion

Thermal models have been used in the past to explain both laser annealing processes and laser damage phenomena. These models assumed uniform heating, and the possibility of

4.2. Electron-hole Plasma Model

An alternative process that might lead to damage is heating caused by the electron-hole plasma produced during the laser-solid interaction. The relation of this process to silicon annealing has been reported previously [10-11]. To account for the heating by the plasma, one first calculates the peak number of electron-hole pairs produced by the inter-band absorption of photons. Sample heating results from the thermalization of the excess energy absorbed by the electrons raised to the conduction band.

The peak electron-hole pair density produced is calculated from the following differential equation describing the generation rate of electron-hole pairs,

$$dN/dt = (\alpha_0 I + \beta'_0 I^2) / (hf) - N/t_c \quad (6)$$

In eq. (6) f is the frequency of the laser, h is Planck's constant, t_c is the free carrier lifetime and β'_0 is the non-linear absorption coefficient reported by Bechtel and Smith [7] ($\beta'_0 = 0.0265 \text{ cm/MW}$). In eq. (6) Auger recombination was neglected due to the low expected carrier density involved, and ambipolar diffusion was neglected because of the short pulse length. A steady-state solution to eq. (6) gives the maximum electron-hole pair density produced and is given by:

$$N(I) = (\alpha_0 I + \beta'_0 I^2) t_c / (hf) \quad (7)$$

To obtain an upper bound for the electron-hole pair density, we used the incident intensity of a typical 1-on-1 damage pulse, $I=19 \text{ MW/cm}^2$, $\alpha_0=1.18 \text{ cm}^{-1}$, $t_c = 100 \text{ psec}$ (as given in [12] for similar conditions), and $\beta'_0=0.0265 \text{ cm/MW}$. Accounting for the reflectivity, we obtained a peak electron-hole density of $N=1.7 \times 10^{16} \text{ cm}^{-3}$. For comparison, the compensated intrinsic carrier concentrations were calculated. Accounting for the chromium dopant concentration ($\approx 1 \times 10^{16} \text{ cm}^{-3}$) and the resistivity of the sample ($\geq 1 \times 10^7 \text{ } \Omega\text{-cm}$), we calculated an electron concentration of $7.35 \times 10^7 \text{ cm}^{-3}$ and a hole concentration of $1.56 \times 10^9 \text{ cm}^{-3}$. Mobilities of $5000 \text{ cm}^2/\text{V-sec}$ and $300 \text{ cm}^2/\text{V-sec}$ were used for the electrons and holes, respectively. Although the photogenerated carrier density is much greater than the compensated intrinsic density, it is still quite small compared to the densities where plasma effects become important, $10^{19} - 10^{20} \text{ cm}^{-3}$. Therefore, we can disregard the plasma model from further consideration as a primary damage mechanism in gallium arsenide.

4.3. Other Models

To check for anomalous absorption, we compared the measured non-linear absorption coefficient, β_0 , to the reported value, β'_0 , with the following equation that accounts for the linear and non-linear absorption coefficient, and for free carrier absorption.

$$dI/dx = -(\alpha_0 + \beta'_0 I + N\Omega) I \quad (8)$$

In eq. (8), Ω is the free carrier absorption cross section. Substituting eq. (7) into eq. (8) for N yields

$$\frac{dI}{dx} = -\alpha_0 I + \left[\beta'_0 + \frac{\Omega \alpha_0 t_c}{hf} \right] I^2 + \frac{\Omega \beta'_0 t_c}{hf} I^3 \quad (9)$$

Since the transmission curve (figure 10) is linear, we can neglect the I^3 term in eq. (9). Therefore the β_0 determined from the transmission test measurements corresponds to the quadratic coefficient in eq. (9). Setting these terms equal to each other yields:

$$\beta_0 = \beta'_0 + (\Omega \alpha_0 t_c) / (hf). \quad (10)$$

Solving for Ω and substituting the corresponding numerical values into eq. (10) yields a free carrier absorption cross section of $\Omega = 6.3 \times 10^{-16} \text{ cm}^2$. This value agrees with those previously reported for gallium arsenide [13]. From this, we conclude that we have included the major homogeneous absorption mechanisms in our calculations and that no gross anomalous absorption was involved.

The charged particle detector system monitored the pulse-by-pulse charge emitted from the gallium arsenide sample. The magnitude of the emitted charge has been plotted in figure 7, on a pulse-by-pulse basis, for a site which exhibited surface damage. By examining the emission profiles, the emitted charge was observed to decrease after the first few pulses, and later increased at least two orders of magnitude. The relatively small, decreasing, emission profile of the initial pulses appears to be a surface cleaning effect. The later increase of charge emission, after the 5th pulse in this case, is attributable to surface damage. For gallium arsenide, only two types of charge emission profile were observed: either a cleaning effect without damage or a cleaning effect with damage. Damage in the absence of a cleaning effect was never observed, although at very high intensities the two profiles merged and became indistinguishable. This differs greatly from the emission characteristics of silicon as reported in [1]. For silicon, emission of charged particles coincided with surface damage initiation and no cleaning emission was observed. Furthermore, the emission of charge prior to damage in gallium arsenide did not affect the observed damage behavior in any detectable way.

It appears that neither the uniform heating model nor the electron-hole pair production model can adequately describe the damage mechanism of GaAs. In addition, it does not seem possible to relate the nature of the damage to surface cleaning, although the latter appears to be a necessary, and possibly essential, precursor to damage. From these results we are led to speculate on other possible influences that may cause, or enhance, surface damage. Lattice defects near the surface of the gallium arsenide wafer are possible energy absorption sites for nucleating damage. These lattice defects include anomalous vacancies, interstitials, and dislocations introduced during the crystal growth or surface preparation processes. A single point defect seems an improbable physical area for absorbing sufficient energy to cause a melt spot. It is more probable that a cluster of point defects will act as an efficient absorption site. This would result in a surface damage morphology of random melt points within the beam diameter of the laser.

Other possible sites for the nucleation of damage are physical surface defects caused by processing, or physical handling, of the wafer that scratch the surface. Surface defects on an optical surface will increase absorption and scattering, possibly creating absorption nuclei which could lead to damage.

5. Conclusion and Comments

We observed accumulation effects in gallium arsenide with multiple pulse laser irradiance below the 1-on-1 damage threshold intensity. These experiments also yielded various N-on-1 laser damage thresholds derived from the statistics of the surface damage. In the experiments we also measured the linear and nonlinear optical absorption constants for the gallium arsenide sample. With this information, calculations were performed to determine the mechanism responsible for the surface damage. The results for the uniform heating and electron-hole production models clearly show that these mechanisms could not be responsible for surface damage. There remains the possibility that non-uniform, localized heating and carrier generation may be involved in the damage process. An inhomogeneous heating model is supported by the observed damage morphologies. It is also possible that the sample contained absorbing defects, or defect clusters, that could contribute to the damage process, or surface defects (e.g., pits and scratches) that might cause a melt spot to nucleate.

By investigating the pulse-by-pulse history of the charged particle emission, a cleaning type profile was discovered. This cleaning emission proved to have no observable influence on the subsequent damage. Apparently, adsorbates remaining on the wafer surface after cleaning did not act as absorbing sites to cause surface damage. The charge emission proved to be very noisy from site-to-site. Although the emission did not strongly correlate with the event of surface damage, once surface damage commenced, an increase in charge emission was observed. This behavior is consistent with the idea of a hot, partially ionized, vapor being released from melt pits as damage proceeds.

Further investigation is needed to understand the mechanism of energy transfer that causes damage and emission. The relationship of the accumulation effect to lattice defects could prove to be a fundamental key in understanding the damage process. Another parameter which might influence the damage threshold is the dopant level of the semiconductor material.

We gratefully acknowledge support given by the DoD Joint Services Electronics Program under Research Contract AFOSR F49620-82-C-0033. We would also thank Dr. John Beall at Texas Instruments for providing the GaAs samples.

6. Bibliography

- [1] M. F. Becker, Y. K. Jhee, M. Bordelon, and R. M. Walser, "Charged Particle Exoemission from Silicon during Multi-Pulse Laser Induced Damage," 14th ASTM Laser Damage Symposium, NBS Special Publication #669, Boulder, CO, 1983; and Y. K. Jhee, M. F. Becker, and R. M. Walser, "Charge Emission and Precursor Accumulation in the Multi-pulse Damage Regime of Silicon," *Journal of the Optical Society of America B* 2, October 1985, pp. 1626-1633.
- [2] S. Dannefaer, B. Hogg, and D. Kerr, "Defect Characterization in Gallium Arsenide by Positron Annihilation," Thirteenth International Conference on Defects in Semiconductors, Eds. L. C. Kimerling and J. M. Parsey, Jr., pp. 1029-1033.
- [3] C. S. Lee, N. Koumvakalis, and M. Bass, "A Theoretical Model for Multiple-pulse Laser-induced Damage to Metal Mirrors," *Journal of Applied Physics* 54 (10), October 1983, pp. 5727-5731.
- [4] A. A. Manenkov, G. A. Matyushin, V. S. Nechitailo, A. M. Prokhorov, and A. S. Tsaprilov, "On the Nature of Accumulation Effect in the Laser-Induced Damage to Optical Materials," 14th ASTM Laser Damage Symposium, NBS Special Publication #669, Boulder, CO, 1983, pp. 436-447.
- [5] P. M. Fauchet and A. E. Siegman, "Surface Ripples on Silicon and Gallium Arsenide under Pico-second Laser Illumination," *Applied Physics Letters* 40 (9), May 1, 1982, pp. 824-826.
- [6] E. W. Van Stryland, H. Vanherzeele, M. A. Woodall, M. J. Soileau, A. L. Smirl, S. Guha, and T. E. Boggess, "Two Photon Absorption, Nonlinear Refraction, and Optical Limiting in Semiconductors," *Optical Engineering* 24 (4), July/August 1985, pp. 613-623.
- [7] J. H. Bechtel and W. L. Smith, "Two-Photon Absorption in Semiconductors with Picosecond Laser Pulses," *Physical Review B* 13 (8), April 15, 1976, pp. 3515-3522.
- [8] C. C. Lee and H. Y. Fan, "Second-Harmonic Generation in InSb, InP, and AlSb," *Physical Review B* 10 (2), July 15, 1974, pp. 703-709.
- [9] K. L. Merkle, R. H. Uebbing, H. Baumgart, and F. Phillipp, "Picosecond Laser Pulse Induced Damage in Crystalline Silicon," *Laser and Electron-Beam Interactions with Solids*, Eds. B. R. Appleton and G. K. Celler, 1982, pp. 337-342.
- [10] J. A. van Vechten and A. D. Compaan, "Plasma Annealing of Semiconductors; Plasmon Condensation to a Superconductivity Like State at 1000 K?" *Solid State Communication* 39 (2), (8), August 1981, pp. 867-873.
- [11] D. M. Kim, R. R. Shah, D. Von der Linde, and D. L. Crosthwait, "Picosecond Dynamics of Laser Annealing," *Laser and Electron-Beam Interactions with Solids*, Eds. B. R. Appleton and G. K. Celler, 1982, pp. 85-90.
- [12] V. K. Mathur and S. Rogers, "Relaxation of Photoexcited Carriers in GaAs," *Applied Physics Letters* 31 (11), December 1, 1977, pp. 765-768.
- [13] R. K. Willardson and A. C. Beer, *Semiconductors and Semimetals: Optical Properties of III-V Compounds* 3, New York: Academic Press, 1967, p. 409.

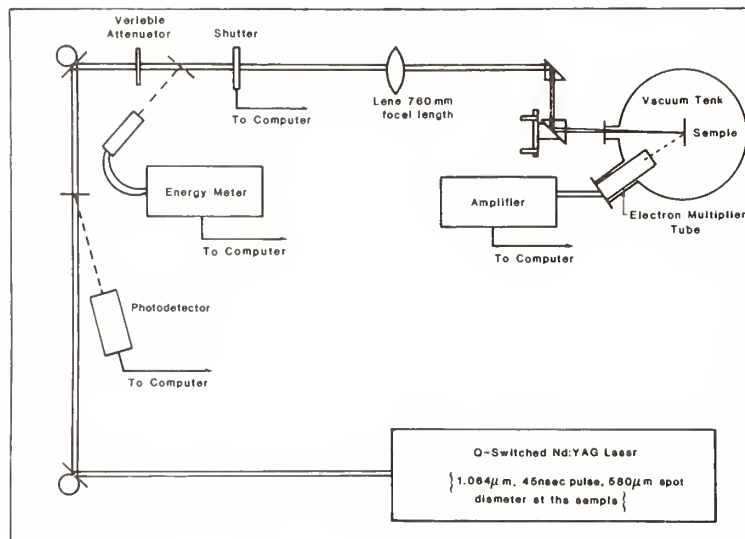


Figure 1. Experimental set-up

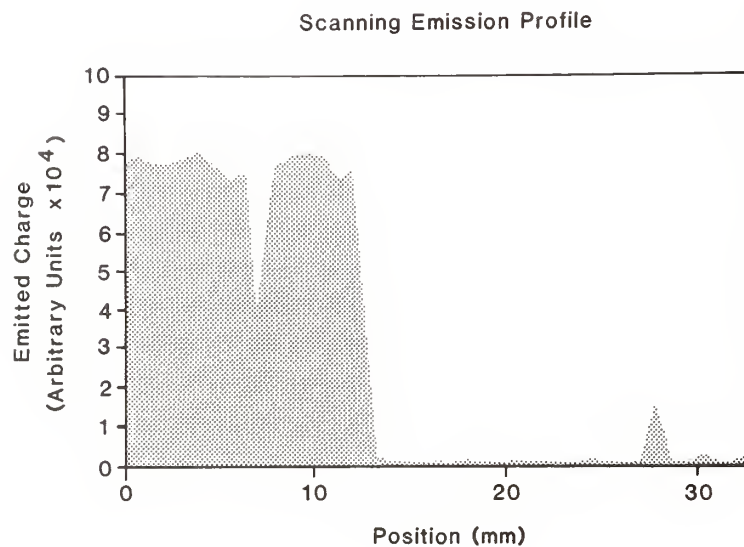


Figure 2. Charged particle emission versus position on wafer for a constant laser fluence of 0.63 J/cm^2 .

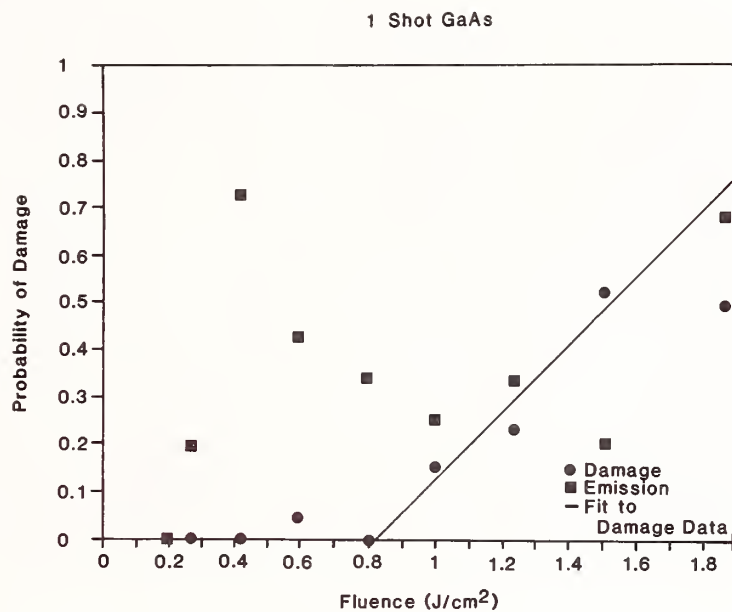


Figure 3. Damage and emission probabilities versus fluence for N=1.

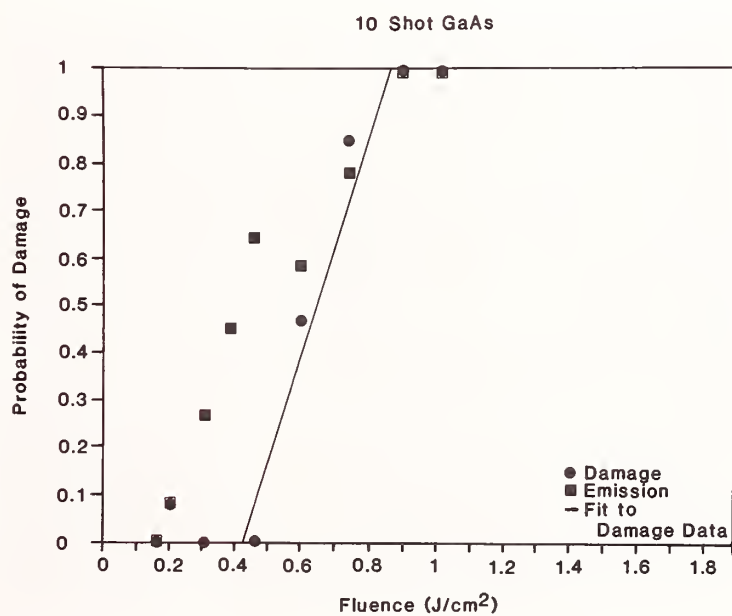


Figure 4. Damage and emission probabilities versus fluence for N=10.

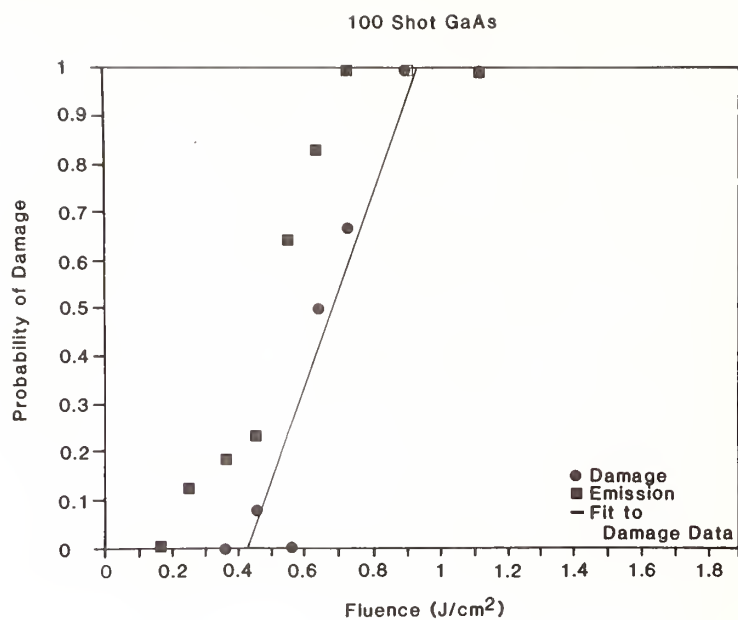


Figure 5. Damage and emission probabilities versus fluence for N=100.

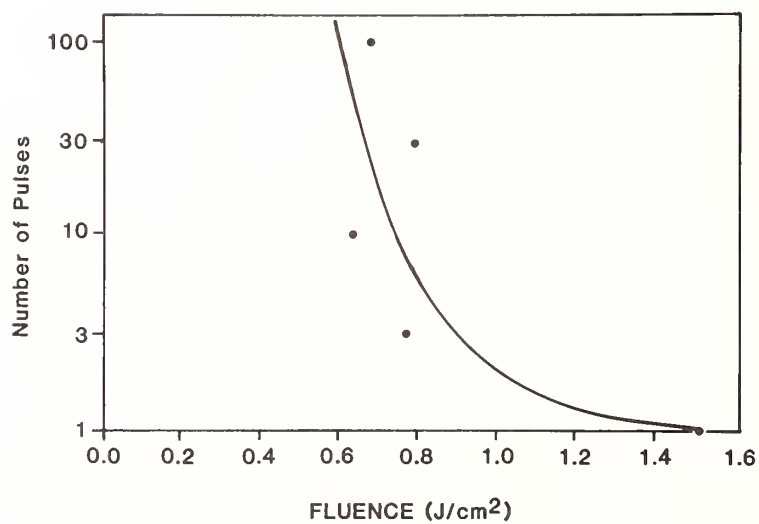


Figure 6. Number of pulses required to reach 50% damage probability versus fluence. The line was hand drawn to aid the viewer.

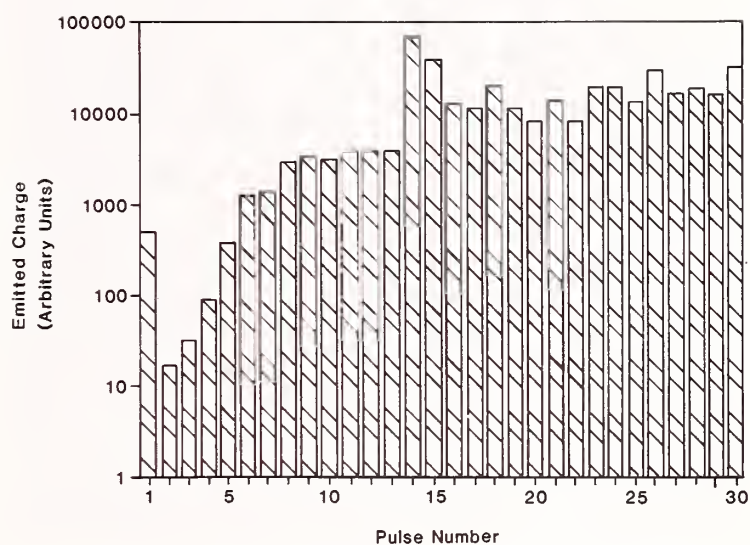


Figure 7. Pulse-by-pulse charged particle emission for $N=30$ at an average fluence of 0.46 J/cm^2 .

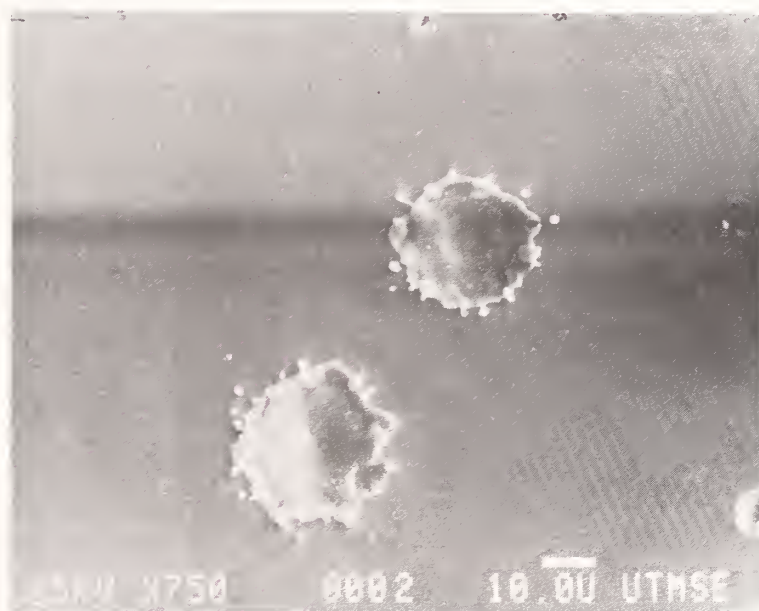


Figure 8. SEM micrograph of damage due to 3 pulses at an average fluence of 0.51 J/cm^2 .



Figure 9. SEM micrograph of damage due to 30 pulses at an average fluence of 0.38 J/cm^2 .

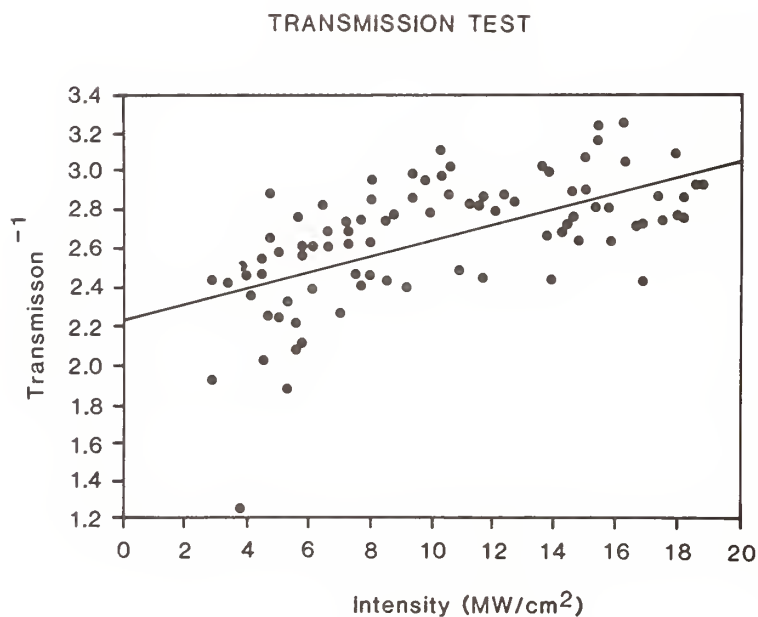


Figure 10. Inverse transmission versus intensity for a GaAs wafer polished on both sides. The solid line represents a least squares linear fit to the data.

CO₂ LASER INDUCED DAMAGE TO GERMANIUM : RELATION
TO SURFACE PREPARATION

D.R. Gibson, C.M. MacDonald and A.D. Wilson

Barr and Stroud Ltd.,
Applied Physics Group,
Caxton Street, Anniesland,
Glasgow G13 1HZ, U.K.

The laser damage behaviour of germanium is examined in relation to surface preparation methods including alumina polishing, "Syton" polishing, diamond machining and plasma etching. Data on laser damage threshold (LDT), damage morphology, surface absorption, surface roughness and the transmittance of the laser pulse (TLP) are used in conjunction with a thermal model in an attempt to identify the various mechanisms responsible for surface damage in Ge. Alumina and "Syton" polishing result in significantly different LDTs, morphologies and TLPs which can be directly correlated with the predictions of a thermal model based on laser heating of embedded polishing particles. Plasma etching removes polishing debris and thus increases the LDT. Diamond machining gives a wide range of LDTs related to variations in surface topography and work damage. A practical ranking of the effect of surface preparation method on LDT is presented.

KEY WORDS: CO₂ Laser Damage; Diamond Machining; Germanium; Plasma Etching; Polishing.

1. INTRODUCTION

In a previous paper [1] it was shown that CO₂ laser induced damage to alumina polished germanium occurred through a defect mechanism. The damage morphology consisted of localised sites, within the beam area, which showed clear evidence of gross melting of the Ge surface. Many sites followed the loci of surface or subsurface scratches suggesting that polishing debris may have been incorporated in the surface during the polishing process. Confirmation of the defect nature of the damage process was obtained by measuring the pulse length dependence of the laser damage threshold: a $t^{1/2}$ dependence was obtained [1,2].

For a standard 10.59 μ m CO₂ TEA laser pulse (100ns FWHM gain switched spike + $\approx 2\mu$ s relaxation tail) the front surface laser damage threshold (LDT) of alumina polished Ge was found to be $\approx 35 \text{ Jcm}^{-2}$ which is considerably lower than many of the "new" materials such as ZnS and ZnSe which typically have LDTs in the range 60 to 70 Jcm^{-2} . Since Ge is still preferred over ZnS and ZnSe for many IR optics applications due to its higher refractive index, lower dispersion, lower scatter (and, not least, its lower price) and since its CO₂ laser damage resistance is limited by extrinsic defects, a study of methods of laser-hardening Ge has been undertaken. Specifically, we have investigated the effect on the LDT of the surface preparation method since this directly affects the inclusion of defects in or the extent of work damage to the surface. The aim of the present investigation is to further understand the mechanisms responsible for CO₂ laser induced damage in Ge and to identify surface preparation methods which will lead to an increased LDT, hopefully, approaching those of ZnS and ZnSe.

Three alternative surface preparation methods have been investigated. Firstly, the effects of alumina and "Syton" polishing are directly compared. "Syton" [3] is a colloidal suspension of silica particles with typical diameters of $\approx 125\text{nm}$ [4]. In 1982, Hutchinson et al. [5] reported that "Syton" polished Ge had a lower surface absorptance than alumina polished Ge and thus the prospect of reduced thermal runaway. Presumably, an improved laser damage resistance could also be anticipated. Secondly, the effects of diamond machining are investigated. Diamond machining does not lead to particulate inclusion [6] but can give a highly structured surface and may give rise to significant levels of work damage. Finally, the possibility of removing the surface layer of alumina polished Ge is further investigated. In reference 1 we reported that ion beam planing increased the LDT. In the present work an argon ion RF sputter etch process is investigated.

2. EXPERIMENTAL

2.1 CO₂ TEA Laser Damage Test Facility

The CO₂ laser damage test facility has been described in detail previously [1]. For this work a standard spike (100ns FWHM) and tail ($\approx 2\mu\text{s}$) 10.59 μm pulse was used. Injection locking and cavity length tuning ensured a smooth temporal profile without longitudinal mode beating. The spatial profile at the sample was a near-Gaussian with a $1/e^2$ diameter of $> 0.9\text{mm}$. The pulse energies were measured using Scientech surface and volume calorimeters. The reported laser damage thresholds correspond to the incident peak energy densities required to cause an increase in the scatter of a He/Ne laser coincident with the damaging beam.

2.2 CO₂ Laser Calorimeter

A CO₂ laser rate calorimeter incorporating a grating-tunable CW rf waveguide laser giving an output from 9.2 to 10.8 μm was used to measure sample absorptances. The sample was held in a blackened chamber evacuated to 5mtorr to eliminate convection and conduction effects. Laser power is monitored in the incident and transmitted beams. The system is capable of measuring absorptances of the order of 0.05%.

2.3 Surface Profilometry

A stylus profilometry (Tencor, α -step) is used to characterise the topography of surfaces. The stylus tip radius is $\approx 2\mu\text{m}$ giving a lateral resolution of $< 2\mu\text{m}$ and the vertical resolution is $\approx 1 \text{ \AA}$ RMS. The raw data (vertical displacement vs horizontal position) are transferred to an HP85 computer for analysis. Standard output comprises the RMS roughness over the total scan length ($\approx 1.5\text{mm}$) and a frequency analysis (using the FFT technique) to obtain information on the spatial wavelength content of the surface. This latter output can be in the form of the power spectral density function [7] or a plot of equivalent sine wave amplitude vs spatial wavelength which we find allows a more direct "picture" of the surface. The range of spatial wavelengths obtained extends from $4\mu\text{m}$ to $> 500\mu\text{m}$.

2.4 Angle Resolved Scatter (ARS)

ARS provides a convenient means of examining surfaces for spatial wavelengths below the lower limit of the stylus profilometer. The scatter angle, θ , is related to spatial wavelength, λ_s , by the Bragg equation $\lambda/\lambda_s = \sin \theta$. For this study a He/Ne laser provided the illumination ($\lambda = 0.6328\mu\text{m}$).

3. COMPARISON OF ALUMINA AND "SYTON" POLISHED Ge

3.1 Absorptance Data

The absorptance of samples of Barr and Stroud 10 Ωcm n-type Ge of 4 thicknesses (1.5, 3.5, 6.5 and 10mm) cut from the same boule and polished with either alumina or "Syton" (W30 grade) were measured by laser calorimetry at 10.59 μm . The data were analysed to give the bulk absorption coefficient and the surface absorptance, A_s . The bulk absorption coefficient was estimated at 0.019 cm^{-1} in good agreement with other studies [5, 8]. For both polish types, A_s was $\approx 0.07\%$ per surface. The value for "Syton" is in good agreement with the best values measured by Hutchinson et al. [5] but the value for alumina is lower than the average value reported in that study ($0.47\% \pm 0.28\%$). The alumina polishing used in the present work was the standard production process at Barr and Stroud which uses, in the final polish stage, 0.3 μm diameter alumina and the value obtained for A_s is typical of those obtained for a large number of batches.

3.2 Laser Damage: Experimental Results

Front and rear surface laser damage thresholds of 1mm thick Ge samples are reported in Table 1. Several important points emerge:-

- (i) The "Syton" polished Ge has a lower front surface LDT value than the alumina polished material ($E(\text{"Syton"})/E(\text{alumina}) \approx 0.62$) ; (see Footnote)

Footnote: E denotes energy density not electric field.

- (ii) The rear surface LDT is higher than the front surface value for alumina polished Ge ($E_{\text{rear}}/E_{\text{front}} > 1.66$);
- (iii) The front and rear surface LDTs are similar for "Syton" polished material ($E_{\text{rear}}/E_{\text{front}} \approx 0.9$ to 1.1);
- (iv) Considering the electric field build up within the sample [9] the $E_{\text{rear}}/E_{\text{front}}$ ratio should be ≈ 0.4 in Ge ($n = 4$).

The relative ease of front surface damage with both polishing types indicates the existence of a mechanism which reduces the energy density at the rear surface. This effect has been observed but not explained in previous work [1, 10].

A further difference between polishing types is encountered in the form of the damage morphology, Figure 1. With "Syton" polishing the damage is localised predominantly along scratches, Figure 1a. At higher magnifications, these extended features are resolved into a number of discrete damage initiation sites from which extend surface ripple patterns, Figure 1b, of the type often associated with defect scattered waves [11, 12]. Although surface melting is obviously involved in the generation of the ripples, this morphology is quite distinct from that found for alumina polished material [1], which shows a gross melting of the surface, Figure 1c.

3.3 Laser Damage: Thermal Model

A simple thermal model is used in an attempt to explain the experimental data. It is assumed that polishing particles embedded in the Ge surface are responsible for the damage. The energy density needed to cause damage can be calculated using the theory of Goldenberg and Tranter [13] in which an absorbing, spherical particle is heated in a uniform radiation field: the non-absorbing host material is heated by thermal conduction from the hot particle. Damage is deemed to occur when either the particle temperature or host temperature, taken to be the temperature at the particle/host interface, exceed their respective melting points (T_p , T_h). The ratio of the laser damage thresholds of the particle (E_p) and the host (E_h) is given by (see Appendix)

$$\frac{E_p}{E_h} \approx 2 \frac{T_p}{T_h} \frac{k_p}{2k_p + k_h}$$

Using the property data of Table 2, this ratio is 1.13, indicating damage to the Ge host, for alumina polished Ge and is 0.06, indicating particle damage, for "Syton" polished material. It is clear that a low particle thermal conductivity results in particle damage. Based on this result, the ratio of the laser damage thresholds for "Syton" and alumina polished material is given by

$$\frac{E(\text{"Syton"})}{E(\text{alumina})} \approx 2 \frac{T_{m\text{SiO}_2}}{T_{m\text{Ge}}} \frac{k_{\text{SiO}_2}}{k_{\text{Ge}}} \frac{a_{\text{Al}_2\text{O}_3}}{a_{\text{SiO}_2}} \frac{Q_{\text{Al}_2\text{O}_3}}{Q_{\text{SiO}_2}}$$

where a is the particle radius and Q is the absorption efficiency factor obtained from Mie theory [14]. The calculated ratio is found to be 0.12 indicating that "Syton" polished material has the lower damage threshold, in qualitative agreement with experiment. The total energy transmitted through the Ge samples, measured as a function of the incident energy density, Figure 2, provides experimental corroboration of the results of the model. The constant transmittance observed for "Syton" polished material, until the LDT is exceeded, is expected if the particles are heated but the Ge remains relatively cold. The heating of the Ge predicted for alumina polished Ge is consistent with the observed gradual decrease in transmittance before damage occurs. The data for the best diamond machined (DM) Ge sample (see Section 4 for a detailed description) shows that Ge can be heated in the absence of particulate defects. In this case, the absorption initiators may be regions of work damage. Furthermore, since the relative decrease in transmittance ($\approx 40\%$) for alumina polished Ge is larger than the fraction of the surface area damaged ($\approx 10\%$) this further suggests that the Ge between the particulate defects is being heated, again, presumably through the effects of work damage. The constant transmittance observed for "Syton" polished Ge may indicate that

work damage is not significant for this polishing technique. We note that in addition to polishing debris the nature and effects of work damage may need to be considered in a more detailed model.

3.4 Discussion

The differences in damage morphology are consistent with the model. In alumina polished material, the Ge surrounding embedded polishing particles is heated and results in localised regions of gross melting. With "Syton" polished Ge, the SiO_2 particle damages and the Ge remains relatively cold. No gross melting is expected or observed. The ripple damage morphology observed for "Syton" polished Ge is of the type associated with defect scattered waves [11, 12]. A ripple pattern is often observed in a small region at the periphery of the gross melt damage site in alumina polished Ge but is never observed on its own. This suggests that gross damage and the ripple pattern are generated simultaneously (in energy or time) e.g. at the point where Ge adjacent to an alumina particle melts or the SiO_2 particle melts or otherwise damages.

It remains to explain the problem of the difficulty of rear surface damage. As noted previously, there must exist a mechanism which protects the rear surface of the germanium and which is more efficient with alumina than with "Syton" polished material. Firstly the effect of the Ge heating in alumina polished material is considered. The temperature dependence of the optical properties of Ge, as calculated using free carrier theory, Figure 3, reveals a significant increase in k and decrease in n for $T > 700\text{K}$. These changes will have significant effects on the electric field distributions within the sample. A tentative explanation of these effects is given below. Initially, the rear surface region (R) is heated ≈ 2.5 times faster than the front surface region (F) due to electric field enhancement at R [9]. When the R temperature exceeds $\approx 700\text{K}$ the field, and thence the heating rate at R, is reduced by the effect of the lower n value at R: since F is at a much lower temperature its heating rate is unaffected. When F exceeds 700K the interface transmission and F heating rate are increased. At higher temperatures the increase in the k value of F further increases the F heating rate but decreases the energy reaching R and thus the heating rate. Eventually the k value of F may become so large that reflection becomes significant reducing both the F and R heating rates. This behaviour is sketched in Figure 4 to illustrate how the temperature at F may exceed that at R and thus how damage to F may occur first.

With "Syton" polished material the lack of Ge heating means that the above mechanism does not apply and thus the E front/E rear ratio should be lower as is indeed observed. However the ratio is still larger than expected from theory [9]. To check whether defocussing was responsible for rear surface protection the transmitted spatial profile was measured but no significant broadening was observed. Thus the observed effect cannot be explained fully at this time.

4. DIAMOND MACHINED Ge

The samples were diamond machined on one surface, the other surface being alumina polished. The RMS surface roughness of all but one sample was in the range $78 \pm 18 \text{ \AA}$ measured perpendicular to the grooves: one sample had an RMS value of 446 \AA . The absorptance at $10.59 \mu\text{m}$ was measured with the radiation incident on the DM face with the electric field vector of the radiation both perpendicular and parallel to the diamond machining grooves. The bulk absorptance and rear surface absorptance were then subtracted to obtain the surface absorptance (A_s) of the diamond machined face. The lowest A_s value was 0.08% which is similar to the values for alumina and "Syton" polished material. More typical values ranged from 0.2% to 0.8%; a value of 4.2% was obtained for the very rough sample.

The LDT was also measured with the electric field vector perpendicular and parallel to the grooves. These data are presented as a plot of LDT against reciprocal surface absorptance, Figure 5, which reveals a good correlation between these parameters. Only the sample with the very low surface absorptance has a higher LDT than alumina polished material. Most samples are significantly poorer. The damage morphology consists of a single uniform melt site corresponding to the beam's spatial maximum, Figure 1d: there is no evidence of a localised defect-type damage morphology.

The variation of LDT with $1/A_s$ is not unexpected if the surface absorption is spatially uniform. The surface absorption may be related to the extent of work damage and/or the roughness and structure of the surface. The RMS roughnesses of all but one sample vary by only $\pm 25\%$. These variations cannot account for the absorption and laser damage data. However, the spatial wavelength distributions contributing to the roughness can vary significantly between samples. The differences in spatial wavelength distributions were investigated, in detail, for both the

"best" sample (lowest A_s , highest LDT) and for a typical sample with an LDT lower than for alumina polished material. Figure 6 shows profilometer derived spatial wavelength spectra and Figure 7 shows angle resolved scatter data. Both samples have significant roughnesses at long spatial wavelengths (>200 microns) corresponding to errors in "micro-figure" and at short spatial wavelengths (< 1.6 microns) which correlate with the tool feed rate. The "best" sample has no significant structure at spatial wavelengths between these limits whereas the typical sample shows a significant peak at a spatial wavelength of about 20 microns. Thus there are significant differences, between the two samples, in the content of spatial wavelengths close to the laser wavelength. Consequently, different radiation coupling efficiencies [15, 16], and hence laser damage thresholds, can be anticipated. That the "best" sample has the highest LDT is consistent with the lack of a suitable coupling surface structure.

The values of A_s and LDT were found to depend on the orientation of the electric vector and the diamond machining grooves: for 5 samples the LDT was higher (and A_s lower) for the parallel orientation; for 2 samples the reverse was true; 2 samples, including the "best" sample, were independent of the orientation used. For a grooved surface it is expected that the LDT will be reduced when the electric field vector is perpendicular to the grooves [17]. This is only observed for 5 out of the 9 samples. That the "best" sample does not show any dependence of the LDT on the electric vector/groove orientation can be explained by noting a lack of surface structure with a wavelength close to that of the radiation. However the remaining 3 samples show behaviour contrary to expectations. This may indicate that the effects of surface structure are more complex than envisaged or that the effects of work damage have a masking effect. A fuller examination of the spatial wavelength content of these diamond machined surfaces is underway in an effort to explain the apparently anomalous behaviour.

5. SPUTTER ETCHED Ge

An argon ion RF sputter etch (13.56 MHz, 100W, 5 mtorr) was used to remove approximately 2 microns from both surfaces of alumina polished Ge samples of varying thickness. The effect on the 10.59 micron absorptance is shown in Figure 8. The surface absorptance (intercept at zero thickness \div by 2) is reduced to negligible levels ($\approx 0.01\%$ per surface) suggesting the layer containing embedded alumina particles (and any work damage) has been removed. Profilometry showed that the etch process did not alter the surface microroughness or the "micro-figure". The front surface CO_2 laser damage threshold of the etched surfaces was $\approx 40 \text{ J cm}^{-2}$ which is an increase of $\approx 25\%$ over the value for alumina polished material.

6. SUMMARY AND CONCLUSIONS

The effects on the laser damage behaviour of Ge of a range of surface preparation methods have been assessed.

Particulate polishes, alumina and "Syton", show significantly different behaviour: (i) the front surface LDT is lower for "Syton" polished material (20 J cm^{-2} cf 32 J cm^{-2}); (ii) both result in defect type damage, comprising localised sites within the beam area, but with distinct local-scale morphologies (local melting for alumina, surface ripple for "Syton"); and (iii) the front surface/rear surface LDT ratio is higher for alumina than "Syton" polishing and is higher than predicted by simple theory [9]. A thermal model based on the assumption that polishing particles embedded in the Ge surface are responsible for laser heating predicts that the SiO_2 particles damage in the case of "Syton" polished material but that the Ge host damages in the case of alumina polishing. These predictions, which are supported by data on transmission of the laser pulse, allow a qualitative explanation of the differences in front surface LDTs and damage morphologies. (Conversely, the agreement between experiment and theoretical prediction is evidence that damage is initiated at embedded polishing particles.) In addition, an attempt is made to explain the front/rear LDT ratio "anomaly" for alumina polished material. It is suggested that the field distribution, which initially favours rear surface damage, is modified by the heated Ge surfaces, which are expected to show a significant decrease in n and increase in k , such that heating of the front surface is enhanced. However when the Ge host is not heated significantly, as with "Syton" polished material, the fact that the front/rear anomaly, persists, albeit to a lesser numerical extent, cannot yet be explained. Measurements suggest that defocussing does not lead to a significant reduction in rear surface energy density and thus cannot explain the results. Clearly, a more comprehensive theoretical model is required perhaps also taking into account the effects of work damage in introducing absorbing centres and the temperature dependent growth of absorbing regions. Diamond machining (DM), although not introducing particulate contamination, does lead to significant levels of surface absorption. Generally, front surface LDTs are lower than for alumina polished material. For one sample, only, the surface absorptance was low and an LDT 40% higher than for alumina polished material

was obtained. The reasons for the typical low LDTs could not be determined unambiguously but probably involve both the effects of the periodic structure produced by the DM (i.e. grooves) in coupling the laser radiation to the sample when periodicities are close to the laser wavelength and also the effects of work damage. A more detailed study of the surface topographies of the samples is planned to elucidate which effect predominates.

Argon ion sputter etching has been used to remove the surface layer of alumina polished samples. As expected, removal of defects led to a decrease in surface absorptance and a significant increase in laser damage threshold.

From a practical viewpoint, the various surface preparation methods can be ranked as follows:

highest LDT	diamond machined (exceptional)
	argon ion sputter etched (alumina pre-polish)
	alumina polished
	diamond machined (typical)
	"Syton" polished
lowest LDT	diamond machined (poor)

The authors thank the Management of Barr and Stroud for permission to publish this paper.

REFERENCES

- [1] D.R. Gibson and A.D. Wilson, "Studies of CO₂ laser induced damage to infrared optical materials and coatings", paper presented at the 16th Annual Symposium on Optical Materials for High Power Lasers, Boulder, Col., Oct. 1984.
- [2] D.R. Gibson and A.D. Wilson, Appl. Phys. Lett., 47, 914 (1985).
- [3] Monsanto Technical Bulletin, "Syton Colloidal Silica", 53-3 (E) M-E-4 (1979).
- [4] We have deposited the particles of a "Syton" suspension onto a Ge disc and measured the infrared transmission spectrum. The major absorption peak at 9.15 microns with a shoulder at ≈ 8.4 microns and a subsidiary peak at 12.5 microns indicate that the particles are very close in composition to SiO₂.
- [5] C.J. Hutchinson, C. Lewis, J.A. Savage and A. Pitt, Appl. Opt., 21, 1490 (1982).
- [6] D.L. Decker, in proceedings of "Workshop on Optical Fabrication and Testing", paper FE1 (1981).
- [7] E.L. Church and H.C. Berry, Wear, 83, 189 (1982).
- [8] P.J. Bishop and A.F. Gibson, Appl. Opt., 12, 2549 (1973).
- [9] N.L. Boling, M.D. Crisp and G. Dube, Appl. Opt., 12, 650 (1973).
- [10] B.E. Newnam and D.H. Gill, NBS Spec. Publ., 509, 298 (1977).
- [11] C.T. Walters, Appl. Phys. Lett., 25, 696 (1974).
- [12] M.J. Soileau, IEEE J. Quantum Electron., QE-20, 464 (1984).
- [13] H. Goldenberg and C. Tranter, Brit. J. Appl. Phys., 3, 296 (1952).
- [14] H. van de Hulst, "Light Scattering by Small Particles", Chapman Hall (London), p270 (1957).
- [15] M. Bass and L. Liou, J. Appl. Phys., 56, 184 (1984).
- [16] I. Ursu, I.N. Mihailescu, Al. Popa, A.M. Prokhorov, V.I. Konov, A.P. Ageev and V.N. Tokarev, Appl. Phys. Lett., 45, 365 (1984).
- [17] M.J. Soileau, J.O. Porteus and D.L. Decker, NBS Spec. Publ., 568, 195 (1979).
- [18] M.L. Lang and W.L. Wolfe, Appl. Opt., 22, 1267 (1983).

APPENDIX

Using the expressions of Goldenberg and Tranter [13] the energy, E_p , required to melt the centre of the absorbing particle is given by

$$E_p = \frac{8T_{mp} k_p k_h}{aQ} \frac{t}{(2k_p + k_h - 6k_h I_1)} \quad \text{.....A1}$$

and the energy required to melt the host adjacent to the particle, E_h , is given by

$$E_h = \frac{4T_{mh} k_p k_h}{aQ} \frac{t}{(k_p - 3k_h I_2)} \quad \text{.....A2}$$

where

$$I_1 = \frac{2\pi}{b} \int_0^\infty F(y) dy$$

$$I_2 = \frac{2\pi}{b} \int_0^\infty \frac{F(y) \sin y}{y} dy$$

$$F(y) = \frac{\exp(-y^2 t / \gamma) (\sin y - y \cos y)}{y (c \sin y - y \cos y) + b \sin y}$$

$$b = \frac{k_h}{k_p} \left(\frac{D_p}{D_h} \right)^{\frac{1}{2}} \quad c = 1 - k_h / k_p \quad \gamma = a^2 / D$$

k_i is the thermal conductivity, D_i is the thermal diffusivity, T_{mi} is the melting point of material i , a is the radius of the absorbing particle, and t is the pulse length. Q is the absorption efficiency factor obtained from Mie theory [14] and for Ge ($n = 4$) at 10.59 microns is given by

$$Q \approx \frac{910 n k a}{(n^2 + 32)^2} \quad \text{.....A3}$$

where n and k are, respectively, the refractive index and extinction coefficient of the particle.

For the pulse length ($t > 100\text{ns}$) and material properties (Table 2) under consideration the integrals (I_1, I_2) may be neglected to a first approximation ($< 5\%$ error). Equations A1 and A2 then reduce to

$$E_p \approx \frac{8T_{mp} k_p k_h}{aQ} \frac{t}{(2k_p + k_h)}$$

and

$$E_h \approx \frac{4T_{mh} k_h t}{aQ}$$

and thus the ratio of particle to host LDTs is given by

$$\frac{E_p}{E_h} \approx 2 \frac{T_{mp}}{T_{mh}} \frac{k_p}{2k_p + k_h}$$

The ratio for particle damage for "Syton" polished Ge to host damage in alumina polished material is given by

$$\frac{E(\text{"Syton"})}{E(\text{alumina})} \approx 2 \frac{T_{m\text{SiO}_2}}{T_{m\text{Ge}}} \frac{k_{m\text{SiO}_2}}{k_{\text{Ge}}} \frac{a_{\text{Al}_2\text{O}_3}}{a_{\text{SiO}_2}} \frac{Q_{\text{Al}_2\text{O}_3}}{Q_{\text{SiO}_2}}$$

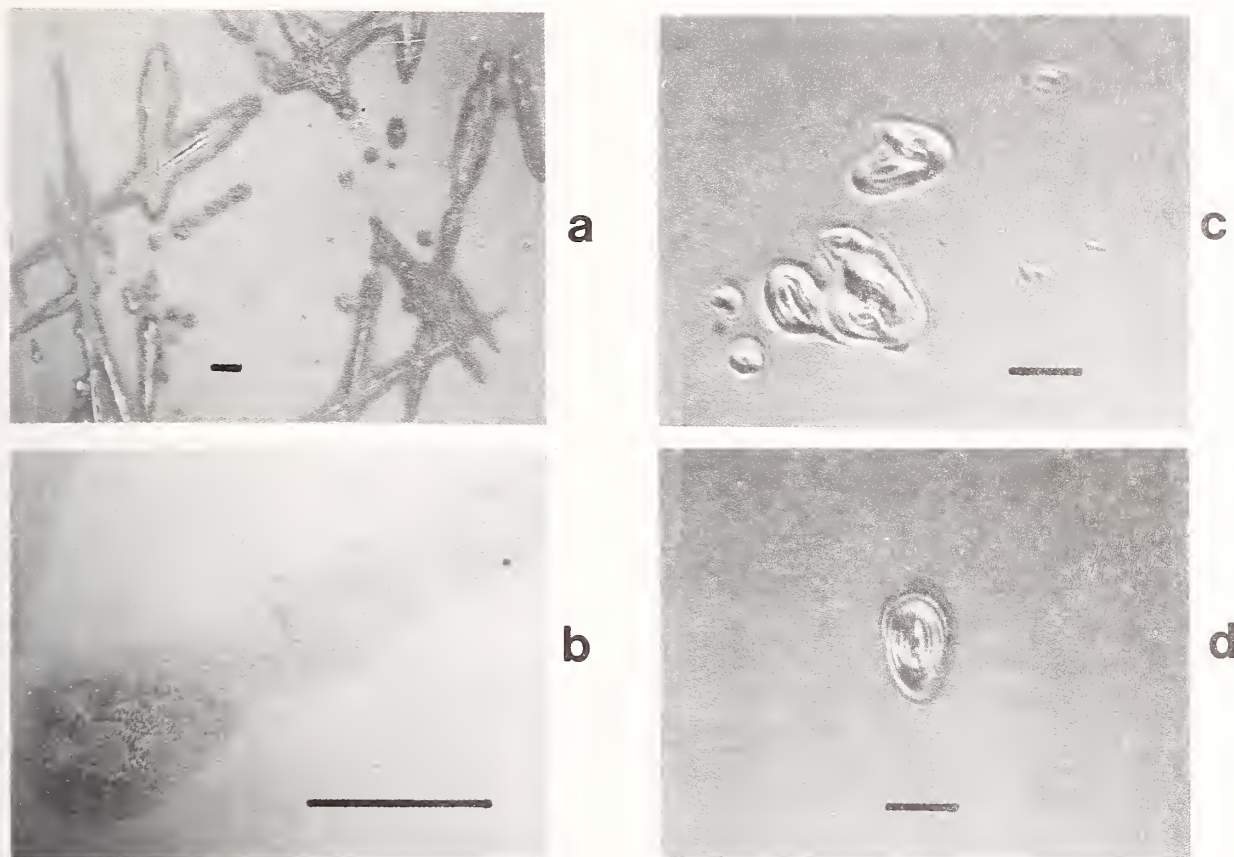
1. CO₂ LASER DAMAGE THRESHOLDS FOR ALUMINA AND SYTON POLISHED Ge

Polishing Material	Front Surface LDT (J cm ⁻²)	Rear Surface LDT (J cm ⁻²)
Alumina (Linde "A")	32	>53
"Syton" (w30)	20	≈ 20

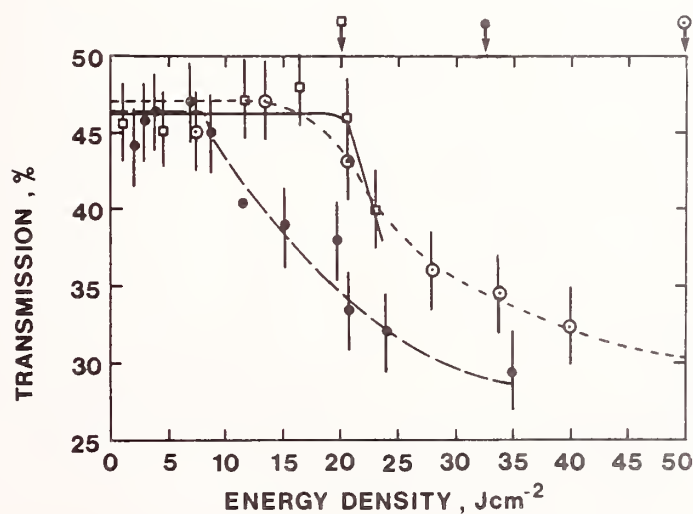
2. MATERIAL PROPERTIES USED IN THERMAL MODEL

Property \ Materials	Ge	SiO ₂	Al ₂ O ₃
Refractive index at 10.6μm	4	2.0	1.0
Extinction coefficient at 10.6μm	1.3 × 10 ⁻⁶	0.14	0.08
Thermal conductivity at 300K (Wm ⁻¹ K ⁻¹)	50	1	40
Melting Point (K)	1260	1990	2320
Particle radius (μm)	-	0.063	0.15

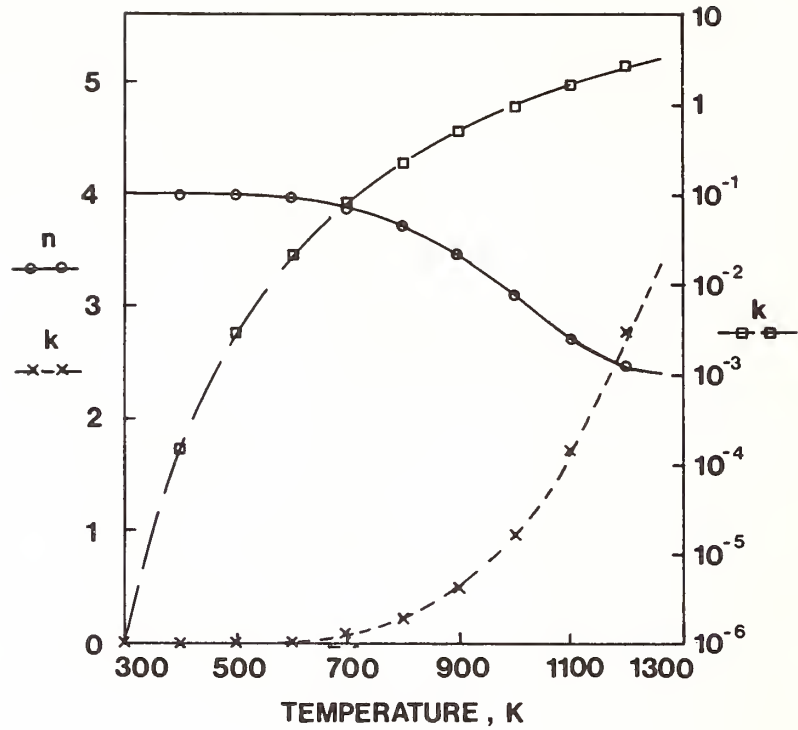
N.B. SiO₂ and Al₂O₃ optical data are taken from reference [18].



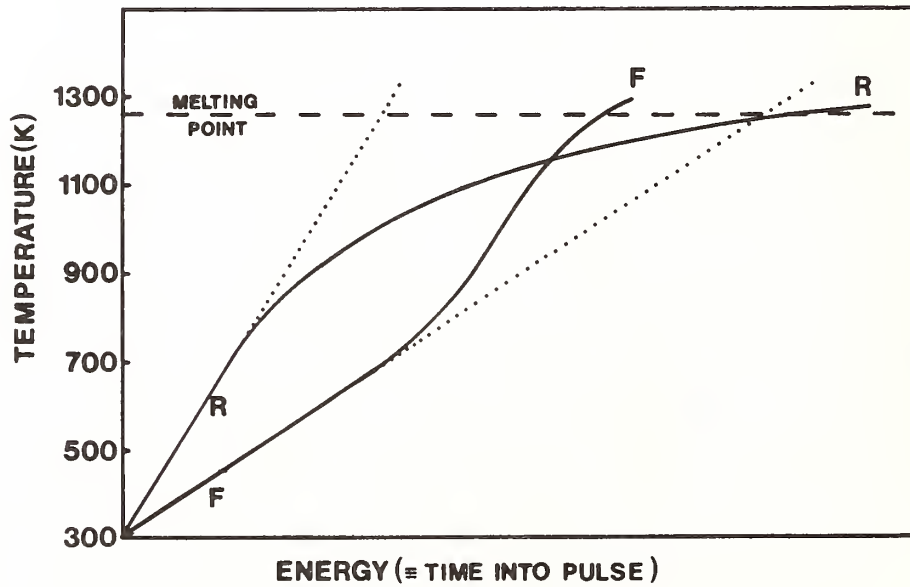
1. Nomarski photomicrographs of CO₂ laser induced damage sites on Ge: a) and b), "Syton" polished; c), alumina polished; d), diamond machined. Scale bar corresponds to 100 microns.



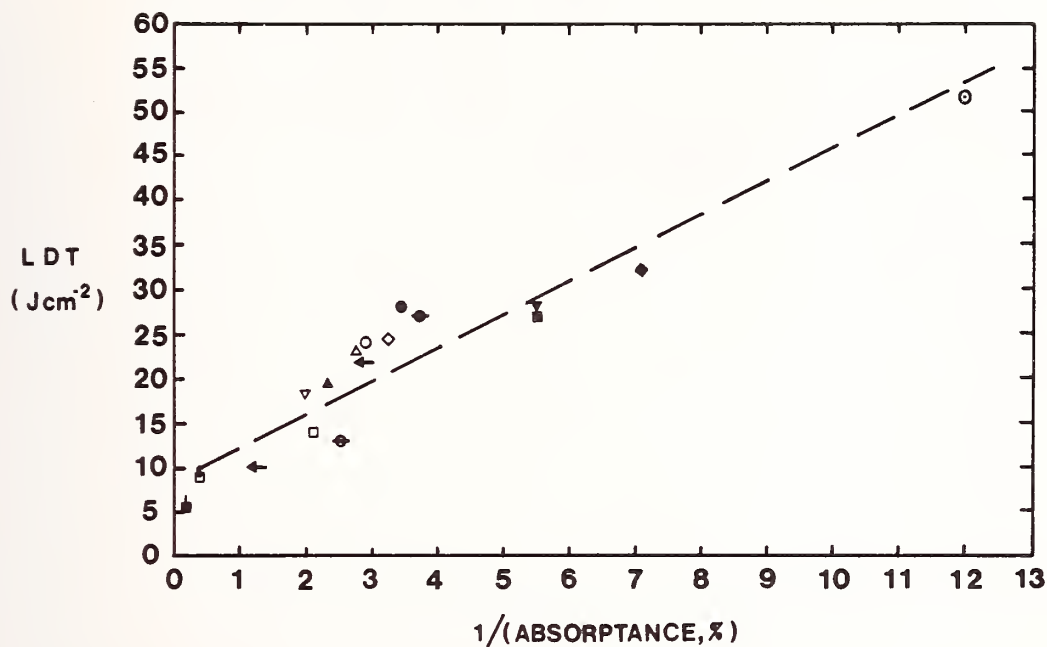
2. Total energy transmission as a function of incident peak energy density for Ge: ●, alumina polished; □, "Syton" polished; ○, diamond machined. The arrowed symbols indicate damage thresholds.



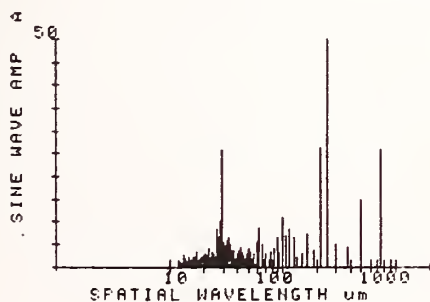
3. Variation of refractive index (n) and extinction coefficient (k) of Ge with temperature as calculated using free carrier theory.



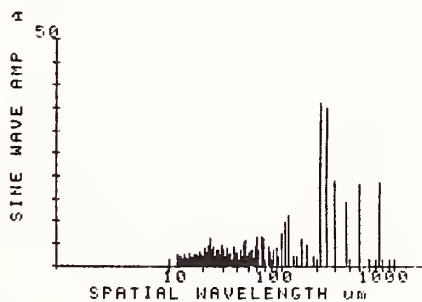
4. Schematic diagram showing variation of front (F) and rear (R) surface temperatures with energy (\equiv to time into a constant intensity pulse): dotted lines drawn assuming field build-up for a dielectric medium with $n = 4$; full lines for modified field distribution as discussed in text.



5. Relationship between laser damage threshold (LDT) and the reciprocal of the surface absorptance for diamond machined (DM) Ge; open symbols, electric field vector parallel to grooves; closed symbols, electric field vector perpendicular to grooves; \odot , the "best" DM sample for which both electric field/groove orientations gave same LDT and surface absorptance values.

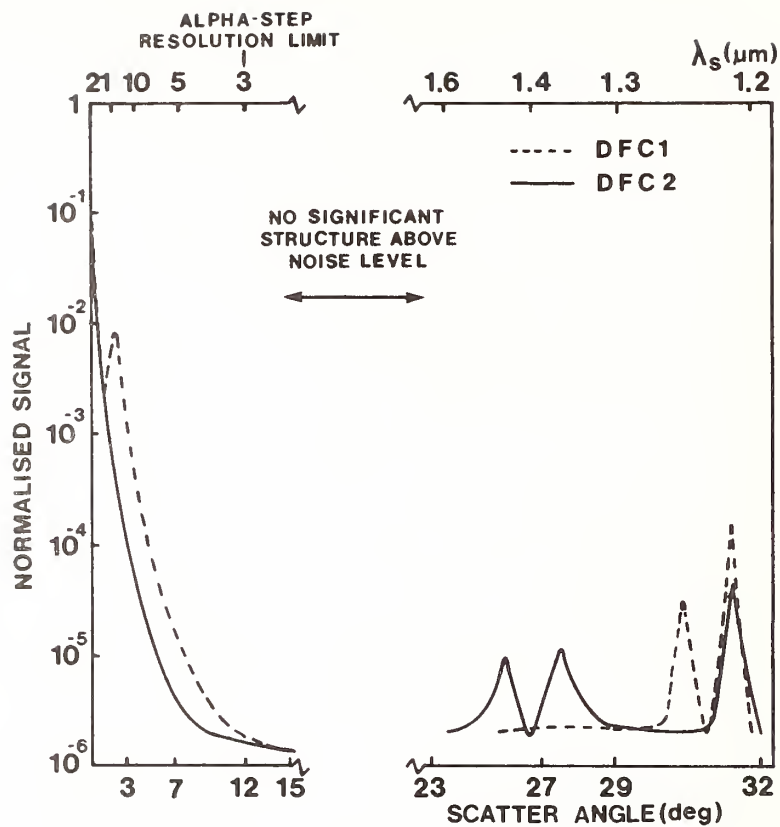


DFC1

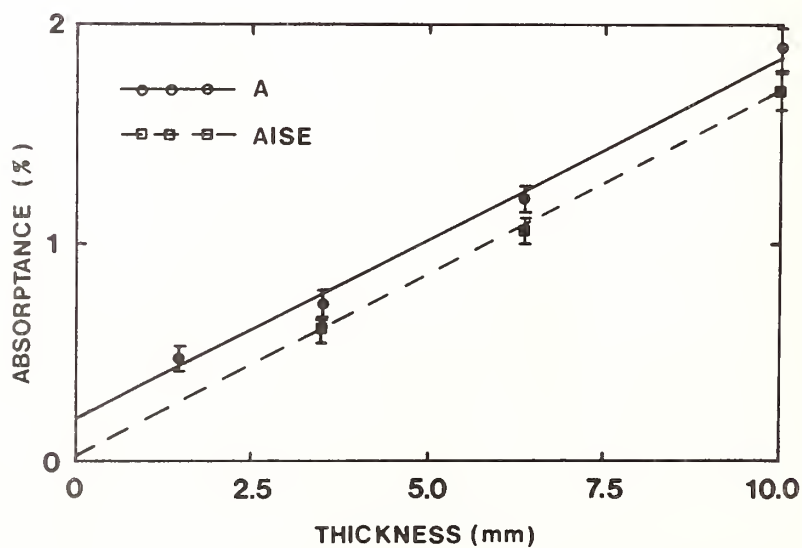


DFC2

6. Comparison of the spatial wavelength spectra obtained from stylus profilometer data for a typical (DFC1) and the best (DFC2) diamond machined Ge sample.



7. Angle resolved scatter data for a typical (DFC1) and the best (DFC2) diamond machined Ge sample.



8. Absorption data for Ge alumina polished (A) and pre-polished with alumina then argon ion sputter etched (AISE).

Study of Mo, Au, and Ni Implanted Molybdenum Laser Mirrors
By Spectroscopic Ellipsometry*

Paul G. Snyder, George H. Bu-Abbud,⁺ Jae Oh, and John A. Woollam

University of Nebraska, Lincoln, NE 68588-0511

David Poker

Oak Ridge National Laboratory, Oak Ridge, TN 37830

D. E. Aspnes

Bell Communications Research, Inc., Murray Hill, NJ 07974

David Ingram and Peter Pronko

Universal Energy Systems, Dayton, OH 45432

The implantation of 150 keV molybdenum ions into polished molybdenum laser mirrors is found to increase the complex dielectric constant in the visible spectrum. Analysis using the Bruggeman effective medium approximation demonstrates that the increase is due to surface smoothing, and that the surface is made nearly atomically smooth by a fluence of $5 \times 10^{15}/\text{cm}^2$. Implantation of Au at 1 MeV caused considerable microscopic roughening, as well as a change in the bulk optical properties. 3 MeV Ni ion implantation caused only a slight surface roughening. A thin dielectric film (probably a hydrocarbon) is found to condense in a laboratory atmosphere, reducing the reflectivity, and is removable by rinsing with methanol and distilled water.

Key Words: Molybdenum laser mirrors; spectroscopic ellipsometry; ion implantation; surface smoothing.

1. Introduction

Molybdenum is of interest as a laser mirror material because it possesses desirable thermal properties [1]. Various techniques for producing very smooth, highly reflecting surfaces have been investigated, including mechanical and electrochemical polishing [1,2], chemical vapor deposition [3], and ion implantation [4,5]. The optical properties of Mo prepared by bulk and thin film techniques have been studied using several methods [6], among them ellipsometry [5,6,7], reflectance [6,8], and reflectance and transmittance [9] measurements. Roughness and microstructure of molybdenum surfaces have been studied by Nomarski imaging, profilometry, and total integrated scattering [1,2,5,10,11]. In this paper we present the results of single and multiple angle of incidence spectroscopic ellipsometric measurements in the visible to near ultraviolet on polished Mo mirrors which have been implanted with 150 keV Mo, 1 MeV Au, or 3 MeV Ni ions. We describe the effect of implantation on the Mo mirror optical properties for a wide range of fluences.

2. Samples and Experiment

Three commercially prepared vacuum arc cast [1] molybdenum mirrors, about 4 cm in diameter, were mechanically polished with alumina to a final grit size of 0.3 micron. Chemical analysis of

*Research supported in part by the U.S. Department of Energy under contract DE-AC05-84OR21400 at ORNL, NSF/SBIR Grant PHY-8318798, and the College of Engineering, UNL.

⁺Present Address: Reliance Comm/TEC, Advanced Development Lab, Richardson, TX 75081

the starting molybdenum surfaces showed there to be less than the following percentages of impurities: 0.005 carbon, 0.008 iron, 0.002 nickel, 0.008 silicon, 0.0015 oxygen, 0.0005 hydrogen, 0.002 nitrogen. Six $1 \times 3 \text{ cm}^2$ regions on each mirror were implanted at room temperature with fluences from 1×10^{14} to $5 \times 10^{15} \text{ cm}^{-2}$, the first mirror with 150 keV Mo ions, the second with 1 MeV Au ions, and the third with 3 MeV Ni ions. All implantations were made at room temperature, because it was found in previous work that heating the substrate during implantation caused an increase in the surface roughness [5]. The Mo implantation was performed at Oak Ridge National Laboratories on a 200 keV Varian "Extrion", and Au and Ni were implanted on a 6 MeV General Ionex "Tandetron" at Universal Energy Systems. Reflection of a helium-neon laser beam from all of the implanted surfaces was specular, with no distortion of the beam.

Two automatic rotating analyzer ellipsometers were used. One, at Bell Communications Research Inc., had an angle of incidence ϕ fixed at 67.08° and a photon energy scanning range of 1.5 to 6 eV [12]. It was used to measure the ellipsometric parameters $\tan\psi$ and $\cos\Delta$ for the various regions on the Mo implanted mirror. Contamination effects were minimized by optically prealigning the mirror in a windowless cell, cleaning its surface by rinsing in sequence with distilled water, methanol, and distilled water, and then maintaining its surface in dry filtered N_2 during measurement.

The other ellipsometer, at the University of Nebraska-Lincoln, was similar in design to the first, but had a variable angle of incidence [5]. It was used to collect all of the data for the Au and Ni implanted mirrors, and some data for the Mo implanted mirror. Measurements were made at angles of incidence from 71° to 79° , and at photon energies from 1.8 to 3.8 eV. The Au implanted mirror was prealigned and rinsed as described above, then blown dry with high purity Argon. Data were obtained within several minutes of rinsing. The Ni implanted mirror was not rinsed at all before measuring. When the rinsing procedure was performed on the Mo implanted mirror, the two ellipsometers produced almost identical pseudodielectric function data for this carefully cleaned sample in the overlapping energy range, as shown in figure 1, despite the fact that data were obtained at different angles of incidence. This demonstrates that data from the Bellcore and UNL ellipsometers agree with each other to better than one percent when proper surface preparation procedures are followed. Multiple angle of incidence data provided additional information about the surface and bulk optical properties, as described below.

3. Mo Implanted Mirror

The pseudodielectric function is the effective, or apparent, dielectric response calculated from the measured ψ and Δ values at any given photon energy and angle of incidence, ϕ , by assuming a two-phase (smooth substrate-ambient) model [13]:

$$\langle \epsilon \rangle = \langle \epsilon_1 \rangle - j \langle \epsilon_2 \rangle = \sin^2 \phi \left[1 + \frac{1 - \tan \psi e^{j\Delta}}{1 + \tan \psi e^{j\Delta}} \right]^2 \tan^2 \phi \quad (1)$$

Pseudodielectric functions $\langle \epsilon \rangle$ for the various regions on the Mo implanted mirror surfaces, for fluences from $1 \times 10^{14} \text{ cm}^{-2}$ to $5 \times 10^{15} \text{ cm}^{-2}$, are shown in figure 2. There is little apparent change in $\langle \epsilon \rangle$ as the fluence is increased from $1 \times 10^{14} \text{ cm}^{-2}$ to $1 \times 10^{15} \text{ cm}^{-2}$, but at $2 \times 10^{15} \text{ cm}^{-2}$ both $\langle \epsilon_1 \rangle$ and $\langle \epsilon_2 \rangle$ are significantly changed over the entire spectrum. Increasing the fluence to $5 \times 10^{15} \text{ cm}^{-2}$ causes a slight further increase in $\langle \epsilon_2 \rangle$.

The changes in $\langle \epsilon \rangle$ described above could be due to thickness changes of a dielectric overlayer, or to changes in the substrate microstructure (as in a loss of crystallinity), or to changes in the surface microscopic roughness. While we have observed thin films to physisorb onto Mo surfaces, such films are completely removable by the rinsing procedure described above. A very thin passivating layer of natural oxide [14] is also known to grow on Mo. In a previous study [5] electron spectroscopy for chemical analysis (ESCA) measurements detected less than 10 Å of MoO_2 on Mo surfaces. No attempt was made to remove the oxides from our samples, because the necessary reactants would also have attacked the metal and roughened the surface. Even a very thin (monolayer) oxide will have a small effect on the $\langle \epsilon \rangle$ data, but this effect should be essentially the same for all samples. Thus physisorbed films or natural oxides cannot explain the differences in figure 2. Secondly, there is no broadening or shifting of the $\langle \epsilon \rangle$ spectral features with increasing fluence, which indicates that there is no implantation-induced change in crystallinity or grain size near the surface [15]. We conclude that the changes in $\langle \epsilon \rangle$ with implantation fluence are due to changes in microscopic roughness.

We call attention to the fact that we are using the terminology "microstructure" in the standard materials science convention, that is, to refer to inhomogeneities on a length scale of

the order of 1 to 100 nm [16]. In the optics literature, "microstructure" is commonly used to refer to what we would call macrostructural inhomogeneities, with length scales greater than 1000 nm, i.e., to inhomogeneities that can be resolved with an optical microscope (see, e.g., ref. 1). The distinction is important because quite different physical properties are involved: microstructure determines the dielectric discontinuity at the material-ambient interface, i.e., the reflectance properties or light loss from transmission into the substrate material, whereas macrostructure determines light loss from scattering. Ellipsometric data are essentially unaffected by macrostructure, while scattering data are essentially unaffected by microstructure.

The increase in magnitude of $\langle \epsilon \rangle$ with increasing fluence indicates microscopic smoothing of the surface by Mo ion implantation. To verify this and to quantify the changes in microscopic roughness, a single-parameter model was fit to the measured (ψ, Δ) data using the Marquardt minimization algorithm [17,18]. The three phases of the model were the molybdenum substrate, a "roughness" layer consisting of equal volume fractions of Mo and voids (absence of any material), and the air ambient. The size of the void regions is assumed to be much less than the wavelength of light. The Bruggeman effective medium approximation [19] (EMA) was used to model the effective dielectric response of the roughness layer, and the layer thickness was the model parameter.

The reference ϵ spectrum for Mo was taken to be the $\langle \epsilon \rangle$ spectrum for the Mo implanted region with a fluence of $5 \times 10^{15} \text{ cm}^{-2}$, which is seen in figure 2 to have the highest values of $\langle \epsilon \rangle$. This implies that the $5 \times 10^{15} \text{ cm}^{-2}$ region comes closest to realizing the sharp interface between bulk and ambient that is assumed with the two-phase model.

The roughness layer thicknesses obtained in the analysis are given in table I. The sharp drop in thickness above $1 \times 10^{15} \text{ cm}^{-2}$ correlates with the change in $\langle \epsilon \rangle$ seen in figure 2. In addition, the calculations show that Mo ion implantation at fluences higher than $2 \times 10^{15} \text{ cm}^{-2}$ does not significantly further decrease the surface roughness. These results are similar to those described in reference 5, in which the microscopic surface roughness of mechanically polished samples of molybdenum rolled sheet stock decreased when they were implanted at room temperature with 150 keV Mo ions at a fluence of $2 \times 10^{15} \text{ cm}^{-2}$, but did not decrease further when higher fluences were used.

A two phase (substrate, ambient) model was also investigated, in which the substrate was an effective medium containing voids, and the void fraction was the single variable parameter. As before, the $\langle \epsilon \rangle$ from the $5 \times 10^{15} \text{ cm}^{-2}$ fluence region was used as the substrate ϵ . This model, which excludes the possibility of surface roughness, produced a poor fit to the data. Furthermore, when the two models were combined to allow both substrate voids and surface roughness to be treated together, the calculated substrate void fraction converged to zero in all cases. This further indicates that the changes in $\langle \epsilon \rangle$ with fluence are due to changes in the surface rather than in the bulk microstructure.

4. Film Growth on Mirrors

When measurements were made with the sample surfaces in air or in unfiltered nitrogen from a high pressure gas cylinder, the ellipsometric data revealed the presence of a film growing on Mo surfaces. A small (<1%) decrease in $\langle \epsilon \rangle$ due to the growing film was often detectable within a few minutes after rinsing, and a film several days old lowered both $\langle \epsilon_2 \rangle$ and $\langle \epsilon_1 \rangle$ by almost 20 percent as shown in figure 3. Complete film removal by the distilled H_2O -methanol-distilled H_2O rinse was confirmed by analysis of data taken immediately after rinsing. The film was not an oxide, which would not be removed by the simple rinse procedure. The film is probably due to hydrocarbon contaminants from the nitrogen cylinder and/or in the laboratory air.

It was also inadvertently discovered that the film was not easily removed after the mirror had been left exposed to air in the lab for several months. This film was only slightly reduced in thickness by soaking for several hours in acetone and then rinsing with methanol and distilled H_2O . In contrast, the film on another polished Mo mirror which was kept in a desiccator jar over the same period of time was easily removed by rinsing. We suggest that the unremovable films are the result of catalytic decomposition of hydrocarbons on the Mo (or Mo-oxide) surface to form polymeric compounds, a process known to lead to contact failure in mechanical relays with transition metal contacts [20].

5. Au Implanted Mirror

The pseudodielectric functions of the Au implanted molybdenum mirror are shown in figure 4. These $\langle \epsilon \rangle$ spectra were derived from multiple angle of incidence measurements of $\tan \psi$ and $\cos \Delta$. At

each photon energy measurements were made at two angles of incidence near the principle angle. Each $\langle \epsilon \rangle$ spectrum of figure 4 (and also the UNL spectrum in fig. 1) is the average of the two spectra obtained by applying eq. 1 at each angle of incidence. The $\langle \epsilon \rangle$ spectra of the lowest fluence region are almost identical to those of the unimplanted region, and to those of the lowest fluence region on the Mo implanted mirror. Therefore Au or Mo implantation at a fluence of $1 \times 10^{14} \text{ cm}^{-2}$ or less has practically no effect on the polished mirrors. Au ion fluences above $5 \times 10^{14} \text{ cm}^{-2}$ caused a monotonic lowering of $\langle \epsilon_2 \rangle$, and also caused the structure in both $\langle \epsilon_2 \rangle$ and $\langle \epsilon_1 \rangle$ to be washed out. As discussed in the preceeding section the former effect is due to microscopic surface roughening, while the latter is due to changes in the bulk dielectric function of the mirror material near the surface.

In addition to calculating the pseudodielectric functions, we used the multiple angle of incidence ellipsometry data to simultaneously solve for the wavelength dependent Mo optical constants, and the thicknesses and void fractions of the surface roughness layers. This was possible because the system configuration was overdetermined, there being four data points (ψ and Δ at two angles of incidence) at each wavelength, and only two unknowns (ϵ_1 and ϵ_2) plus the wavelength independent roughness layer thickness and void fraction. Thus by using multiple angle of incidence, multiple wavelength data, we were able to eliminate the effect of surface roughness and to calculate the "true" dielectric function of the substrate material. It was assumed that the optical constants of the molybdenum metal in the substrate are identical to those of the Mo in the roughness layer. The optical constants (ϵ_1, ϵ_2) were allowed to vary, as well as the roughness layer thickness and void fraction, to obtain the best fit to the data. The Bruggeman EMA was again used to model the surface roughness layer. The thickness and void fraction solutions were 12Å and 0.5, respectively. In figure 5 the calculated substrate dielectric function of the $1 \times 10^{14} \text{ cm}^{-2}$ region is compared directly to the pseudodielectric function of the same region, and also to the pseudodielectric function of the $5 \times 10^{15} \text{ cm}^{-2}$ region on the Mo implanted mirror. If the $5 \times 10^{15} \text{ cm}^{-2}$ Mo implantation actually yields a nearly atomically smooth surface, and if the cleaning procedure really removes all surface overlayers, then the "substrate" and Mo implanted spectra should agree. Figure 5 shows that this is indeed the case. Thus the validity of the above assumptions is demonstrated.

Model "substrate" solutions for the higher fluence regions are shown in figure 6, and the corresponding thicknesses and void fractions of the roughness layers are given in table II. As with the Mo implanted mirror, the primary effect of roughness is to lower $\langle \epsilon_2 \rangle$. Note that even after correcting for surface roughness, the spectral features become broadened with increasing fluence. In addition, the ϵ_1 is shifted to more negative values. Both indicate a disruption of the electronic structure of the Mo grains, that is, amorphization of the near-surface material. However, electron microscopy analyses on similar samples have shown that there is little or no change in grain size in Mo-implanted Mo surfaces [21]. A more likely reason for the change in spectral structure is the formation of dense dislocation loops near the surface. In Rutherford backscattering measurements less than 0.1% Au was detected near the mirror surface, therefore the "washing out" of spectral features is not due to alloying. These points are discussed in more detail below.

6. Ni Implanted Mirror

The pseudodielectric functions of the Ni implanted surfaces are shown in figure 7. The mirror was not rinsed before measurements, and thus was covered by a thin dielectric film similar to that described above. The effect of the film is similar to that of roughness, namely, it lowers $\langle \epsilon \rangle$ (see fig. 3). However, because the optical constants of the film are different from those of Mo and from air, the thin dielectric film and roughness can be distinguished. Using the dielectric function of smooth Mo obtained in the previous section, we determined the thickness and dielectric function of the dielectric film and the thickness of the roughness layer as a function of fluence. A four-phase model was used, consisting of: a Mo substrate, a roughness layer (containing equal volumes of Mo and hydrocarbon material and modeled in the EMA), the hydrocarbon film, and the air ambient. The roughness corrected dielectric function in figure 5 was used to represent Mo in the model. The thickness of the roughness layer, as well as the thickness and dielectric function of the hydrocarbon films, were variables in the model. The hydrocarbon index of refraction was found to be 2.58 ± 0.1 over the entire photon energy range, and the results for the thicknesses are shown in table III. From the analysis we find that the Mo surface roughness decreases monotonically with increasing fluence to $1 \times 10^{15} \text{ cm}^{-2}$, at which point the trend reverses. In addition, a slight lowering and loss of optical structure was found for the Mo dielectric function at the highest fluence, indicating some disordering of the bulk crystalline structure near the surface. It is noteworthy that the initial smoothing trend with increasing fluence was not evident from the pseudodielectric functions. In contrast, for the Mo implanted mirror which had no film, the surface smoothing trend was observable in the pseudodielectric

function data of figure 2 as well as in the results of the analysis. Thus the effect of surface smoothing on $\langle \epsilon \rangle$ is masked by the presence of the film. The increase in hydrocarbon film thickness with fluence seen in table III is probably an artifact resulting from the time span of several days over which the mirror was exposed to air while measurements were made.

7. Discussion

The dielectric function data show that 150 keV Mo implantation improves the surface microstructure of the Mo mirrors, while 3 MeV Ni initially improves it, and 1 MeV Au or further Ni implantation degrades it. The fact that both improvement and degradation are seen for the same target material provides an opportunity to gain information on the mechanisms involved.

To proceed further we need the implantation parameters for each of the three systems. These are given in table IV. The values of the ranges x and straggles Δx , and the deposited energies in the near-surface region for both electronic and nuclear loss mechanisms were calculated with the TRIM simulation code [22] using the nominal implantation energies and standard bulk density data for Ni, Mo, and Au. TRIM uses a linear binary collision approximation and assumes that the energy lost by a moving ion may be separated into electronic energy loss and nuclear energy loss. The former is rapidly dissipated in metals by plasmons and causes no permanent damage.

Nuclear energy loss may result in permanent damage if the kinetic energy transferred to a lattice atom in a collision exceeds a threshold value. For metals a reasonable value is 25 eV but it is strongly dependent (within a factor of two) on the direction of displacement within the crystal lattice and the elemental nature of the target. Not all atoms which are displaced from a lattice site to an interstitial position during the adiabatic phase of each ion cascade (<100 ps) remain displaced; some return to their original site as the lattice relaxes. The remaining interstitials will diffuse away until they are trapped by another vacancy, dislocation, or grain boundary (including the boundary at the vacuum surface), if the temperature of the lattice is high enough. The preferred trapping locations for these diffusing interstitials at the surface will be those which will reduce the free energy of the surface, i.e., jogs, steps, etc. The surface should be smoothed on a microscopic scale by interstitials diffusing to the surface if no additional roughening takes place because of some other property of the bombardment.

Because the optical data are only sensitive to the material properties of the first 20 nm (approximately) of the solid, it is important to examine the spatial properties of the ion cascades generated by the three ion species in molybdenum. The range parameters in table IV indicate that at the highest doses employed, the nickel content of the surface will be less than 1 ppm, and the gold content about 200 ppm. Although there are no data in the literature on the effect of small amounts of these impurities on the optical properties of molybdenum, one may assume that the levels of gold or nickel present in the molybdenum mirrors should have a negligible effect on the reflectance. Therefore the broadening seen in the bulk optical structure is not likely to be due to alloying effects.

Another effect which may cause broadening of $\langle \epsilon \rangle$ spectra involves a change in grain size [15]. In a previous study [21], transmission electron microscopy was used to determine the grain size in molybdenum samples which had been polished mechanically, ending with a 1 μ m diamond paste polish. No difference was found between unirradiated samples and samples irradiated with 150 keV molybdenum ions to a dose of $1 \times 10^{16} \text{ cm}^{-2}$ at room temperature or 500° C. The mean grain size was 250 nm with some evidence of plastic deformation due to the polishing. Thus a change in grain size is also not likely to be the cause of the spectral broadening. The broadening may be due to the formation of dense dislocation loops near the surface, caused by the collapse of small voids generated during the ion cascade.

Sputtering, or the loss of target atoms from the first one or two atomic layers which receive sufficient energy during the ion cascade to overcome the surface barrier energy, can in principle roughen an originally flat surface [23]. The ion cascade and hence the sputtering, which ensues when the cascade intersects the surface, is a localized event and results in material loss in the form of microscopic pits if the cascade is sufficiently dense [24]. This roughening process can compete with the smoothing process described above.

If the depth at which the majority of interstitials are created is much greater than the mean free path between trapping sites then the flux of interstitials at the surface will be much less per incident ion for an ion which on average deposits its energy further below the surface than for an ion which on average deposits its energy nearer the surface. Thus the ion penetration depth will influence both the smoothing and roughening processes.

As an additional complicating effect, the sputtering rate can be greatly enhanced if the energy density of the ion cascades cannot be described by the "linear binary collision approximation". This can happen if the majority of atoms enveloped in each cascade are in motion and the cascade becomes nonlinear. This situation is referred to as an "energy spike".

For the ion target combinations examined here it is reasonable that the 150 keV molybdenum ions produce cascades which are "dilute" or "linear", and are sufficiently near the surface for the diffusing interstitials to smooth the surface faster than sputtering can roughen it. For 1 MeV gold the sputter rate is much larger than that for 150 keV molybdenum, which we speculate to be due to spike effects too large to be offset by the production of interstitials near the surface since the gold ion energy density is about twice that of the molybdenum ions. We postulate that the 3 MeV nickel ions in Mo produce deep diffuse cascades which generate interstitials which are trapped before reaching the surface. The sputtering that is generated causes the surface to roughen at a low rate compared to that of gold, and the sputtering rate for Mo is much lower than for both Au and Ni implants.

Thus the experimental data for Mo, Au, and Ni implants into Mo can be explained in terms of the ion energetics and competing smoothing and roughening processes.

8. Conclusion

The effects of ion implantation on the optical properties of highly polished molybdenum mirrors were determined using single and multiple angle of incidence spectroscopic ellipsometry. These measurements allowed us to obtain the bulk dielectric function of Mo from 1.5 to 6.0 eV as well as the thicknesses of surface roughness layers. The smoothest surfaces were obtained by implanting 150 keV Mo ions at a fluence of $5 \times 10^{15} \text{ cm}^{-2}$, which produced a microscopically smooth surface. In contrast to reflectance measurements, the ellipsometric measurements are found to be very sensitive to microscopic roughness. A thin dielectric overlayer (probably a hydrocarbon) condensed on mirror surfaces exposed to air, considerably lowering the apparent dielectric function and also reducing the reflectance.

9. References

- [1] J.M. Bennett, S.M. Wong and G. Krauss, *Appl. Opt.* 19, 3562 (1980).
- [2] J.M. Bennett, P.C. Archibald, J.P. Rohr and A. Klugman, *Appl. Opt.* 22, 4048 (1983).
- [3] G.E. Carver, *Thin Solid Films* 63, 169 (1979).
- [4] R.A. Hoffman and W.J. Lange, "Ion Polishing of Optical Surfaces", Final Report to Air Force Weapons Laboratory from Westinghouse Research Laboratories AFWL-TR-76-155, September 1976.
- [5] G.H. Bu-Abbud, D.L. Mathine, P.G. Snyder, J.A. Woollam, D. Poker, J.M. Bennett, D. Ingram and P.P. Pronko, *J. Appl. Phys.* 59, 257, (1986).
- [6] J.H. Weaver, C. Krafka, D.W. Lynch and E.E. Koch, in *Physics Data: Optical Properties of Metals I* (Fachinformationszentrum Energie, Physik, Mathematik GmbH, Karlsruhe, 1981), p. 139.
- [7] M.M. Kirillova, L.V. Nomerovannoya and M.M. Noskov, *Sov. Phys. JETP* 33, 1210 (1971).
- [8] B.W. Veal and A.P. Paulikas, *Phys. Rev.* B10, 1280 (1974).
- [9] J.E. Nestell, Jr. and R.W. Christy, *Phys. Rev.* B21, 3173 (1980).
- [10] J.M. Bennett and J.H. Dancy, *Appl. Opt.* 20, 1785 (1981).
- [11] J.M. Bennet, *Opt. Eng.* 24, 380 (1985).
- [12] D.E. Aspnes and A.A. Studna, *Appl. Opt.* 14, 22 (1975).
- [13] R.M.A. Azzam and N.M. Bashara, *Ellipsometry and Polarized Light*, North Holland Publishing Co., Amsterdam 1977.

- [14] E. Deltombe, N. deZoubov, and M. Pourbaix, in Atlas of Electrochemical Equilibria in Aqueous Solutions, ed. by M. Pourbaix (National Association of Corrosion Engineers, Houston, 1974), p. 272.
- [15] U. Kreibig, J. Phys. F4, 999 (1974).
- [16] D.E. Aspnes, J.B. Theeten and F. Hottier, Phys. Rev. B20, 3292 (1979).
- [17] D.W. Marquardt, J. Soc. Indus. Appl. Math. 11, 431 (1963).
- [18] G.H. Bu-Abbud, N.M. Bashara, and J.A. Woollam, Thin Solid Films 138, 27 (1986).
- [19] D.A.G. Bruggeman, Ann. Phys. 24, 636 (1935).
- [20] H.W. Hermance and T.F. Egan, Bell System Tech. J. 37, 739 (1958).
- [21] P. Pronko and D. Ingram, Phase 1 Report, "Ion beam processing for laser mirrors," NSF Award #PHY8260333, 1983.
- [22] J. P. Biersack, J. Nucl. Instrum. Meth. 174, 257 (1980).
- [23] J.E. Westmoreland and P. Sigmund, Radiation Effects 6, 187 (1971).
- [24] W. Jager and K.L. Merkle, 9th International Congress on Electron Microscopy, Vol. 1, p. 378 (1978).

Table 1. Mo Implanted Mo.

<u>Fluence</u>	<u>Roughness Layer</u>
$1 \times 10^{14} \text{cm}^{-2}$	$13\text{\AA} \pm 1\text{\AA}$
$2 \times 10^{14} \text{cm}^{-2}$	$13.5\text{\AA} \pm 1\text{\AA}$
$5 \times 10^{14} \text{cm}^{-2}$	$16\text{\AA} \pm 1\text{\AA}$
$1 \times 10^{15} \text{cm}^{-2}$	$14\text{\AA} \pm 1\text{\AA}$
$2 \times 10^{15} \text{cm}^{-2}$	$0.5\text{\AA} \pm 0.5\text{\AA}$

Table 2. Au Implanted Mo.

<u>Fluence</u>	<u>Roughness Layer</u>	<u>Void Fraction</u>
$1 \times 10^{14} \text{cm}^{-2}$	$12\text{\AA} \pm 1\text{\AA}$	0.5
$1 \times 10^{15} \text{cm}^{-2}$	$22\text{\AA} \pm 3\text{\AA}$	0.43
$2 \times 10^{15} \text{cm}^{-2}$	$62\text{\AA} \pm 10\text{\AA}$	0.39
$5 \times 10^{15} \text{cm}^{-2}$	$130\text{\AA} \pm 20\text{\AA}$	0.6

Table 3. Ni Implanted Mo.

Fluence	Roughness Layer	Film Thickness
$2 \times 10^{14} \text{cm}^{-2}$	$9\text{\AA} \pm 2\text{\AA}$	$23\text{\AA} \pm 2\text{\AA}$
$5 \times 10^{14} \text{cm}^{-2}$	$7\text{\AA} \pm 2\text{\AA}$	$23\text{\AA} \pm 2\text{\AA}$
$1 \times 10^{15} \text{cm}^{-2}$	$5\text{\AA} \pm 2\text{\AA}$	$26\text{\AA} \pm 2\text{\AA}$
$2 \times 10^{15} \text{cm}^{-2}$	$6\text{\AA} \pm 2\text{\AA}$	$29\text{\AA} \pm 2\text{\AA}$
$5 \times 10^{15} \text{cm}^{-2}$	$12\text{\AA} \pm 3\text{\AA}$	$33\text{\AA} \pm 3\text{\AA}$

Table 4. Implantation Parameters

Parameter	Ni	Mo	Au
Implantation energy (keV)	3000	150	1000
Range, \bar{X} (Å)	7450	295	1037
Straggle, $\overline{\Delta x}$ (Å)	1800	140	388
Estimated surface fraction	<0.001%		<0.1%
Deposited surface energy:			
electronic (eV/Å)	250	83	195
nuclear (eV/Å)	26	255	367
Integrated deposited surface energy:			
at $1 \times 10^{15} \text{ions/cm}^2$:			
electronic (eV/atom)	390	129	304
nuclear (eV/atom)	41	397	572

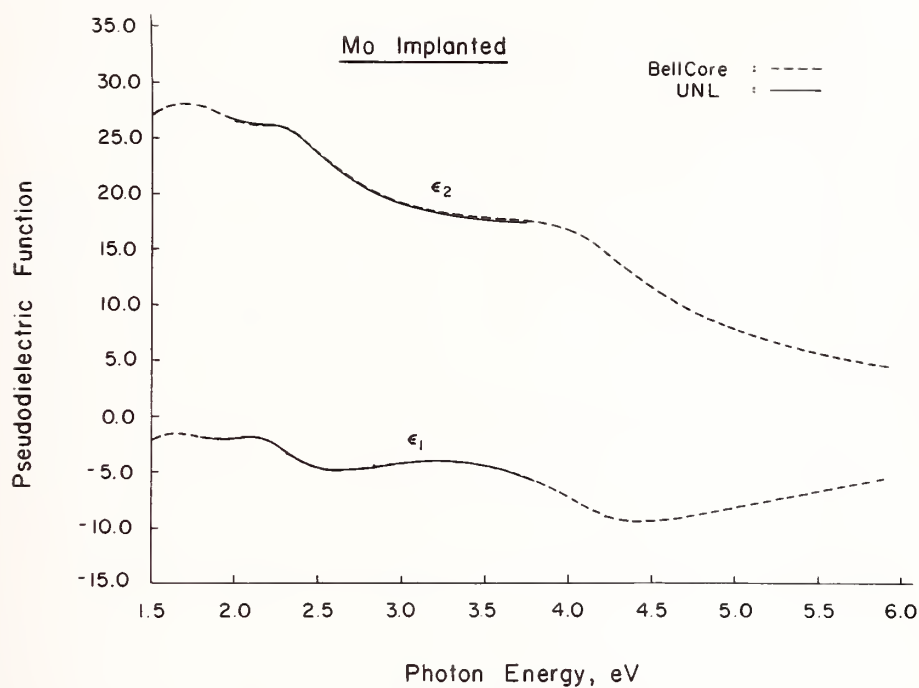


Figure 1. Pseudodielectric functions of the $5 \times 10^{14} \text{ cm}^{-2}$ fluence region of the Mo implanted mirror, measured by the two different ellipsometers used in this investigation, as described in the text.

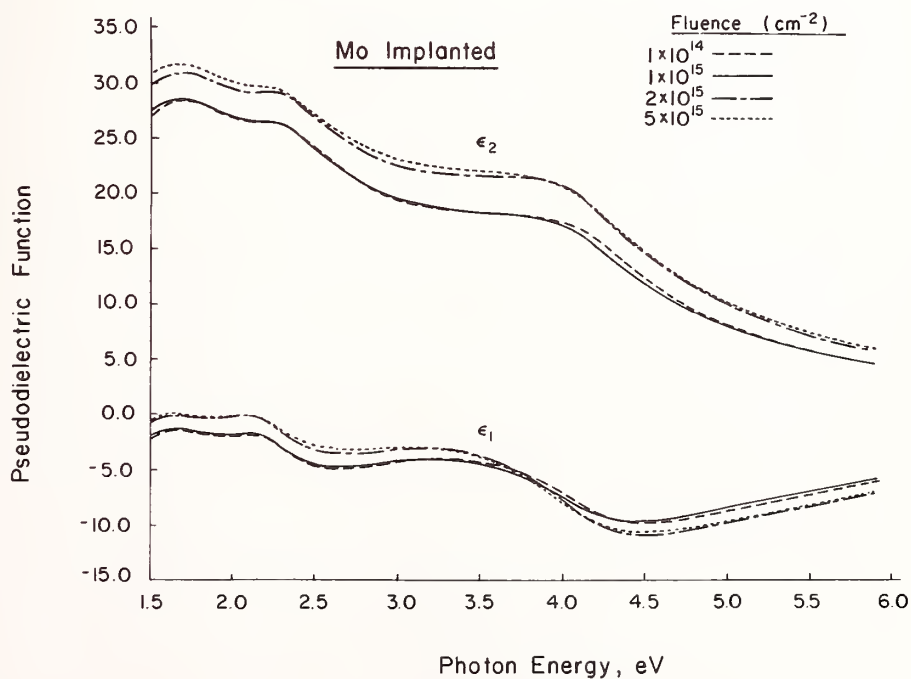


Figure 2. Pseudodielectric functions of the Mo implanted mirror as a function of fluence. (Bellcore ellipsometer)

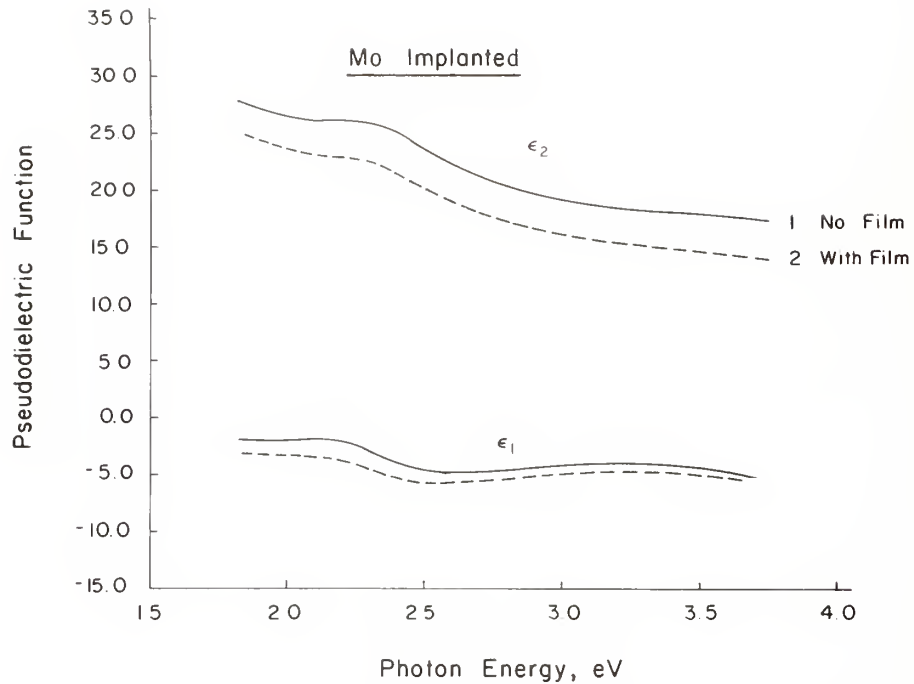


Figure 3. Pseudodielectric functions of an Mo surface after cleaning (solid lines), and of the same surface after several days in air (dashed lines).

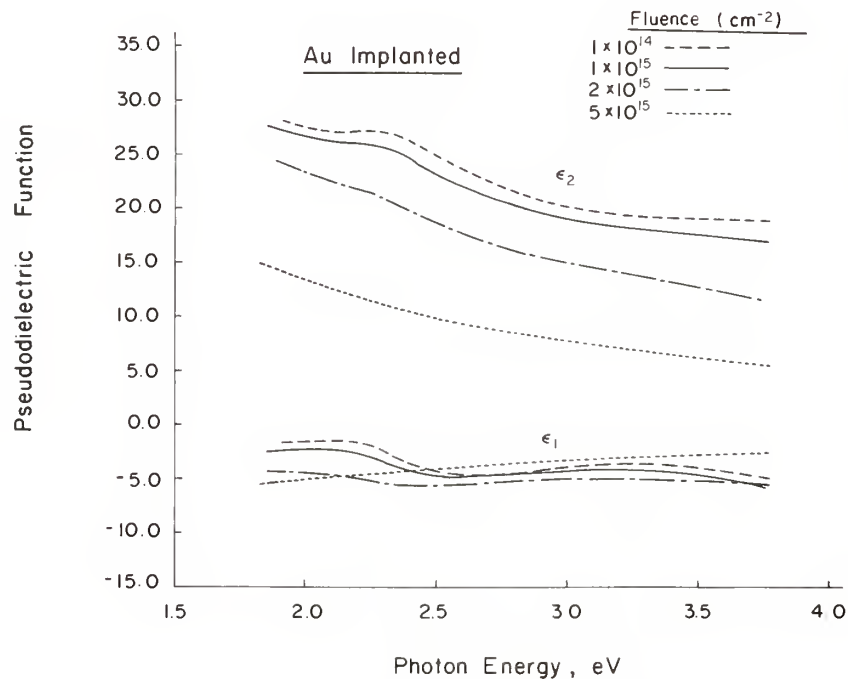


Figure 4. Pseudodielectric functions of the Au implanted mirror as a function of fluence. The $2 \times 10^{14} \text{ cm}^{-2}$ and $5 \times 10^{14} \text{ cm}^{-2}$ regions were almost identical to the $1 \times 10^{14} \text{ cm}^{-2}$ region (UNL ellipsometer).

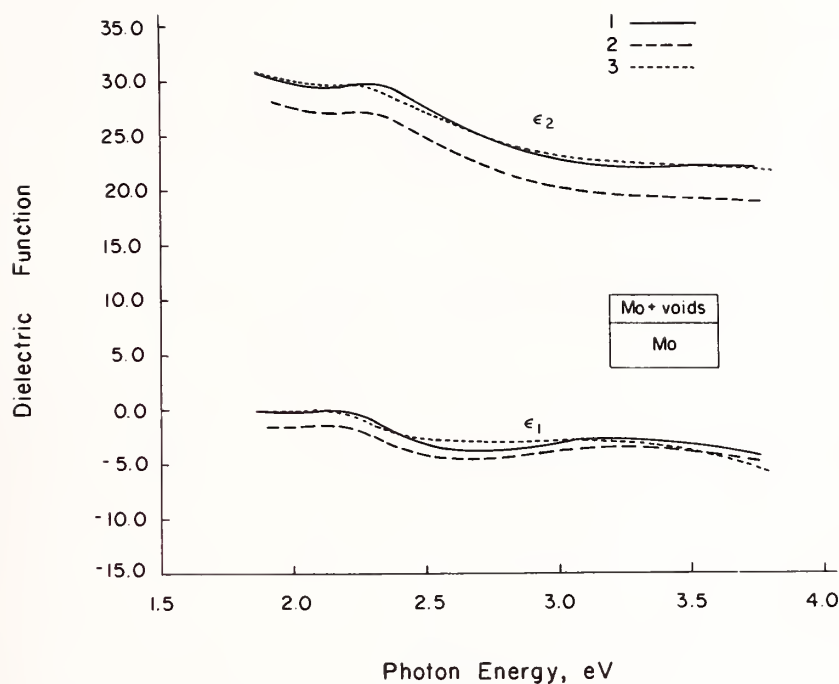


Figure 5. Dielectric function of the $1 \times 10^{14} \text{ cm}^{-2}$ fluence region of the Au-implanted mirror, calculated by correcting the data for 12Å roughness (curve 1); pseudodielectric function data of the same region (curve 2); pseudodielectric function data of the $5 \times 10^{15} \text{ cm}^{-2}$ fluence region of the Mo-implanted mirror (curve 3). Inset: 3 phase model used to correct data for surface microscopic roughness.

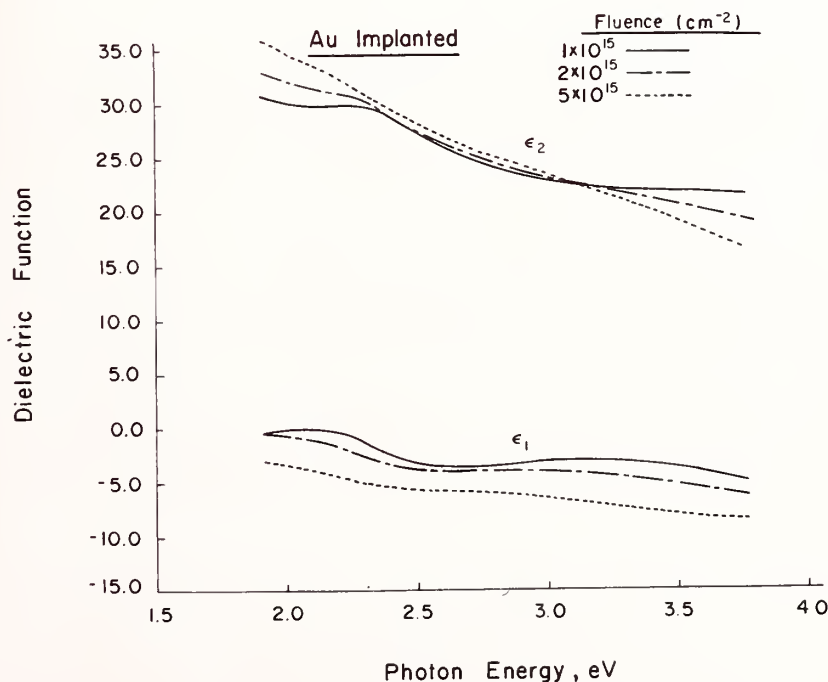


Figure 6. Dielectric functions of the Au implanted mirror, calculated by correcting the corresponding pseudodielectric function for microscopic roughness. The thicknesses and void fractions obtained from the calculations are given in Table II.

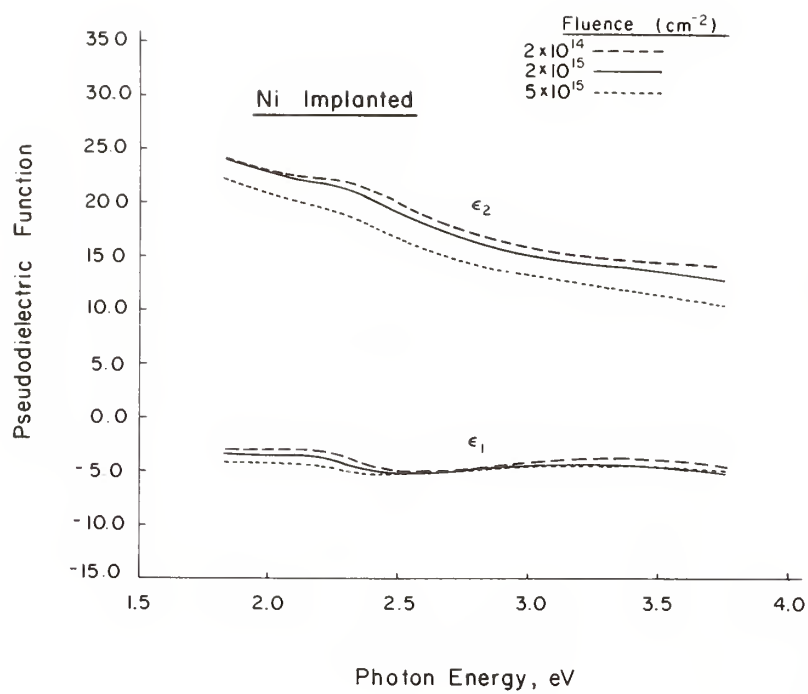


Figure 7. Pseudodielectric functions of the Ni implanted mirror, as a function of fluence (UNL ellipsometer).

Glancing Incidence Absorption Measurements of Metal Mirrors

W.D. Kimura and D.H. Ford

Spectra Technology, Inc., Bellevue, WA 98004
(formerly Mathematical Sciences Northwest)

Glancing incidence absorption measurements are performed on bare Cu, Mo, Au, Al, and Ag mirrors, and on Al and Ag mirrors with a protective dielectric overcoat. Data is obtained for angles of incidence from 0° to $\geq 89^\circ$. Wavelengths studied are $0.5 \mu\text{m}$ and $10.6 \mu\text{m}$ at both s and p polarizations. The absorption is measured using a photoacoustic calorimetry technique in which the transducer is attached directly to the back of the test mirror. Absolute calibration of the absorption data is obtained by using a radiometer to independently measure the absorption at near normal incidence.

The results are compared with the absorption predicted by Fresnel's equations for bare metals using values of n and k of the complex index of refraction measured by other sources. The absorption of a mirror at glancing incidence appears to be a sensitive function of its surface condition. New mirrors tend to agree with Fresnel's equations; while "old" mirrors have much higher absorption probably due to a layer of tarnish. The overcoated Al data deviates greatly from Fresnel's equations indicating that bare metal theory cannot be used and a thin film theory should be used instead. Representative results are given.

Key words: absorption; Fresnel equations; glancing incidence; metal mirrors; overcoats; photoacoustic calorimetry; polarization;

1. Introduction

Various concepts for laser particle accelerators (LPA) [1] require lasers with high average power (to provide high particle luminosity) and small beam diameters (for optimum mode matching). Thermal distortion and damage of the reflective optics used in such systems can become a critical issue. Glancing incidence mirrors can be used to overcome this problem; however, data on their performance is sparse. Previous experiments have primarily measured optical damage and were limited to $\leq 80^\circ$ angle of incidence [2,3].

In the work described in this paper, the thermal absorption characteristics of various mirrors are measured from 0° to $\geq 89^\circ$ angle of incidence for both s and p polarized laser light (perpendicular and parallel to the plane of incidence, respectively). Measurements are taken at two laser wavelengths: 0.5 and $10.6 \mu\text{m}$. Tested are commercially available bare metal mirrors (Cu, Mo, Au, Al, and Ag) and protected Al and Ag mirrors with thin overcoats on their surfaces.

In the next section, Fresnel's equations for the reflectivity of a metal surface is briefly reviewed. The experimental setup is described in Section 3 and sample results are given in Section 4. Section 5 concludes with a discussion of the results obtained thus far in this program.

2. Theory

The complex index of refraction, n , of a material is given by,

$$n(\lambda) = n(\lambda) + ik(\lambda) \quad [1]$$

where n is the index of refraction and k is the extinction coefficient. The values of n and k are in general a function of the wavelength of the light.

Beginning with Maxwell's equations and assuming a plane electromagnetic wave impinging from a dielectric medium (such as air) onto a conducting metal surface at an angle, θ , measured from the normal, one can solve for the amplitude, ρ_{\perp} and ρ_{\parallel} , of the reflected wave whose polarization is perpendicular and parallel to the plane of incidence, respectively. These are referred to as the Fresnel equations [4]. Assuming unity for the dielectric refractive index, Fresnel's equations are,

$$\rho_{\perp}^2 = \frac{(\cos\theta - u)^2 + v^2}{(\cos\theta + u)^2 + v^2} \quad [2]$$

$$\rho_{\parallel}^2 = \frac{[(n^2 - k^2)\cos\theta - u]^2 + [2nk\cos\theta - v]^2}{[(n^2 - k^2)\cos\theta + u]^2 + [2nk\cos\theta + v]^2} \quad [3]$$

where

$$2u^2 = [n^2 - k^2] - \sin^2\theta + \left\{ [[n^2 - k^2] - \sin^2\theta]^2 + 4n^2k^2 \right\}^{1/2}$$

$$2v^2 = -[n^2 - k^2] + \sin^2\theta + \left\{ [[n^2 - k^2] - \sin^2\theta]^2 + 4n^2k^2 \right\}^{1/2}$$

During this program, a computer code solves for the absorption at the mirror surface, i.e. $1 - \rho_{\perp}^2$ and $1 - \rho_{\parallel}^2$, using Equations 2 and 3.

When comparing our data to theory, values of n and k at the wavelength of interest must be chosen to substitute into Equations 2 and 3. A number of different sources [5]-[8] are used for values of n and k . It is important to realize that often these sources do not agree with one another on the values of n and k for the same material. This is not totally surprising when one considers that different forms of the same material may have been tested (e.g., films versus bulk), the condition of the surfaces may vary from author to author, and the various measurement techniques are susceptible to different systematic errors.

Fortunately, the overall shape of the absorption curves as a function of the angle of incidence for a material do not change significantly for small changes in n and k . The magnitude of the absorption at normal incidence, however, does change significantly for small changes in n and k . Hence, when comparing our data with theory, it is important to compare both the overall shape of the curves and their absolute magnitudes. As will be shown, there are times when the overall shape agreement between the data and theory is excellent, but there may be a disagreement with the absolute magnitude of the absorption.

As will be explained in the next section, during the experiment the absolute magnitude of the absorption at near normal incidence is measured independently with a radiometer energy meter. Therefore, any disagreement between the data and theory in regards to the absolute magnitude of the absorption is probably due to differences in the mirror surface condition rather than disagreement with the theory itself. Viewed with this perspective, it is more important that the overall shapes agree rather than the absolute magnitudes.

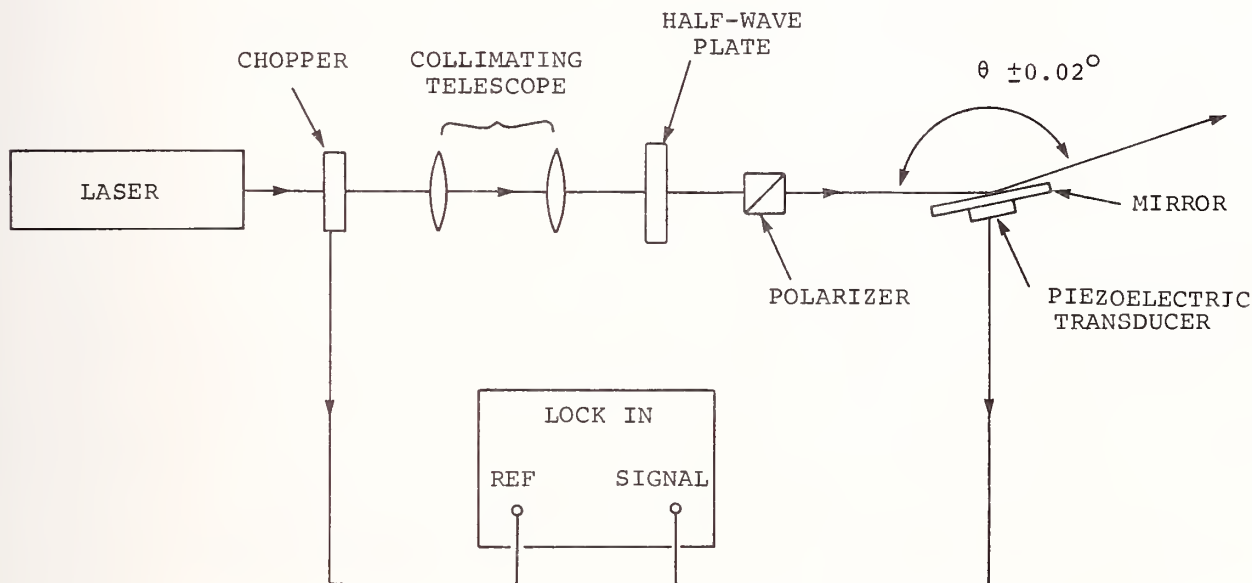
Finally, in regards to the practical usage of these mirrors at glancing incidence, it is the magnitude of their absorption at glancing incidence that is important. Since our data, once it is calibrated with the radiometer measurements, provides the absolute magnitude of the absorption for all angles, our experimental results are still valid despite any disagreements with theory.

3. Description of Experiment

Photoacoustic calorimetry is used to measure the very small absorptance expected at glancing incidence. The basic technique is well established [9]; a modified version [10] is being used in this experiment where the acoustic transducer is attached directly to the back of the mirror rather than on the test chamber wall. This modification greatly enhances the sensitivity of the technique; absorption coefficients (absorbed light/incident light) of 10^{-4} to 10^{-5} are detectable.

Briefly, in photoacoustic calorimetry, energy from a laser beam incident upon a mirror is absorbed at the mirror surface. This absorbed energy generates an elastic strain wave (acoustic wave) which propagates through the mirror substrate. This strain wave passes through the piezoelectric transducer rigidly attached to the back of the mirror substrate. The strain induced in the piezoelectric causes a voltage to be generated across the transducer electrodes which is directly proportional to the magnitude of the strain wave. Thus, the voltage gives a direct indication of the amount of energy absorbed at the mirror surface.

Figure 1 is a schematic of the glancing incidence measurement system. Two different cw, vertically polarized lasers are used: an argon ion laser ($0.5145 \mu\text{m}$) and a CO_2 laser ($10.6 \mu\text{m}$). The output from the lasers is sent through a chopper, a collimating telescope, a half-wave plate to rotate the polarization, and a "clean-up" polarizer which rejects all light not rotated by the half-wave plate. The laser light then reflects off the test mirror mounted on a rotation stage. A phase sensitive lock-in amplifier measures the piezoelectric transducer output which may be as low as 10–100 nV at glancing angles.



85 09482

Figure 1. Schematic of glancing incidence measurement apparatus.

There is a small dependence of the transducer output on the shape of the laser footprint on the mirror surface. At glancing incidence, the laser footprint on the mirror becomes very elongated and much longer than the diameter of the transducer. This footprint dependence can be easily determined by directing the laser beam at normal incidence to the test mirror surface and using a cylindrical lens to create an elongated beam spot on the mirror. The absorption at the mirror surface is relatively constant as the footprint size is varied because the angle of incidence of the laser beam never exceeds 10° as the beam expands from the cylindrical lens. Knowing the length of the footprint and the diameter of the laser beam, the equivalent angle that corresponds to the footprint can be calculated.

The correction for footprint dependence is found to be negligible for angles less than about 80° . Even at 89° the correction is typically only a factor of two which is small when compared with the orders of magnitude changes in reflectivity that occur at glancing incidence. The footprint calibration curve is obtained for every mirror tested and at the two wavelengths investigated.

Absolute calibration of the photoacoustic calorimeter is obtained by using a dual-head laser energy radiometer. Using the same laser as used for the angle dependence measurements, the calibration is performed by measuring the amount of energy absorbed on the mirror surface at near normal incidence. A beamsplitter reflects a portion of the incident laser light into one of the radiometer sensing heads which is used as a reference source in order to eliminate fluctuations in the

laser output energy. The other ratiometer head is positioned alternately before and after the mirror to measure the incident and reflected light, respectively. The ratiometer automatically averages over hundreds of light pulses.

4. Experimental Results

Figure 2 shows the absorptance characteristics of bare silver at $0.5145 \mu\text{m}$. To minimize tarnishing of the bare silver mirror, the mirror was shipped to Spectra Technology from the coating vendor in a leak-tight container filled with an inert gas and was tested in a nitrogen purged environment. Error bars on the data indicate the reproducibility of the data. The calibration at normal incidence is uncertain by approximately $\pm 1\text{-}2\%$ absolute absorptance. The solid curve is Fresnel's equations (eq. 2 and 3) using the values of n and k given in reference 5. There is a slight disagreement between the data and theory in regards to the absolute value of the absorptance; however, there is excellent agreement in overall curve shapes.

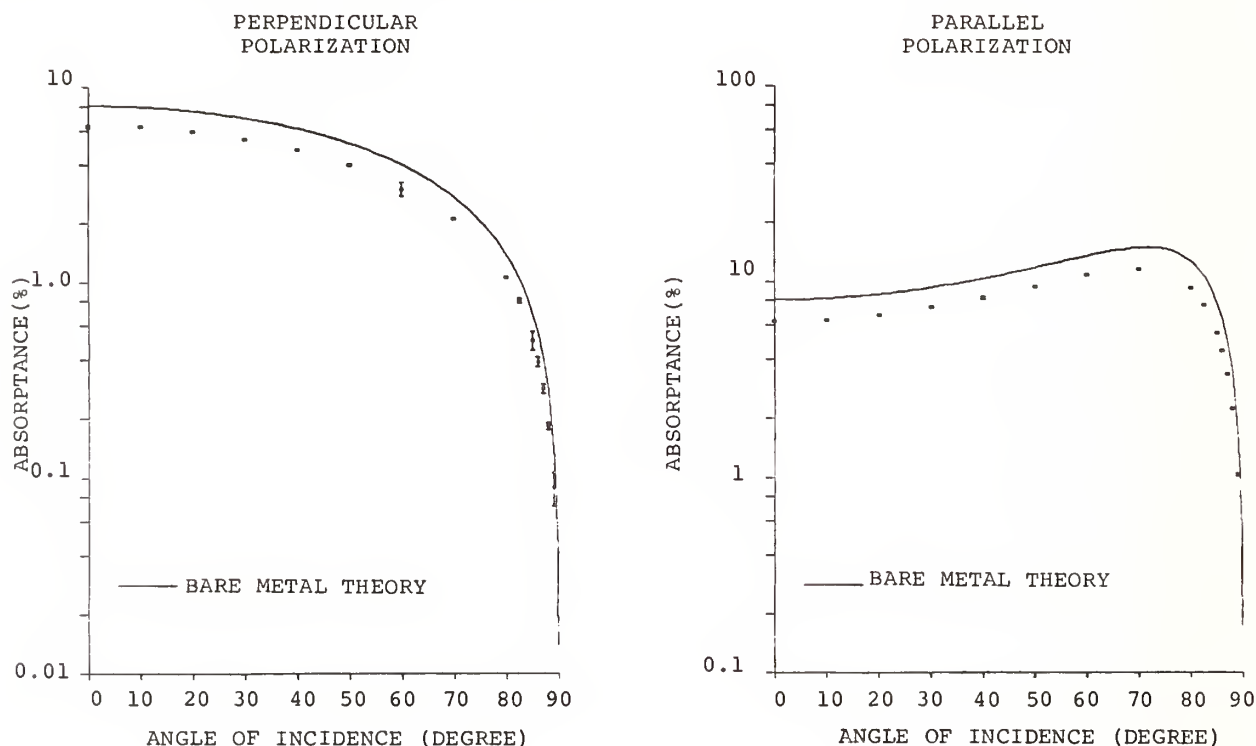


Figure 2. Absorptance curves for bare silver at $0.5145 \mu\text{m}$ for both s and p polarizations. The solid curve is Fresnel's equations using the values of n and k given in reference 5.

85 09888

The effects of a protective overcoat (≈ 1000 angstrom thick layer of ThF_4) on the silver surface is shown in figure 3. The protected silver mirror appears to have slightly higher absorptance at glancing angles than the bare silver mirror. This is true for both polarizations and may be related to a "trapping" of the laser radiation between the dielectric layer and the metal surface at high angles of incidence.

In general, for the metals and wavelengths tested, either $(\sin\theta/n)^2 \ll 1$ and/or $(\sin\theta/k)^2 \ll 1$. Then, for the perpendicular polarization case, eq. (2) simplifies to first order to a simple $\cos\theta$ dependence [2]. Hence, a simple comparison of the experimental absorptance curve shape can be made with the theoretical one by calculating the deviation of the data from the $\cos\theta$ dependence.

Figure 4 is a plot of the percentage deviation from this $\cos\theta$ dependence of the data for the bare and protected Ag mirrors. If the data followed exactly the $\cos\theta$ dependence, the points would lie on a straight line at zero deviation. The bare silver (fig. 4a) does exhibit a low deviation until approximately 85° , at that point the data actually indicates lower absorption than theory predicts.

However, since the error bars are also relatively large for these points, it is more likely that the absorption is very close to that predicted by theory.

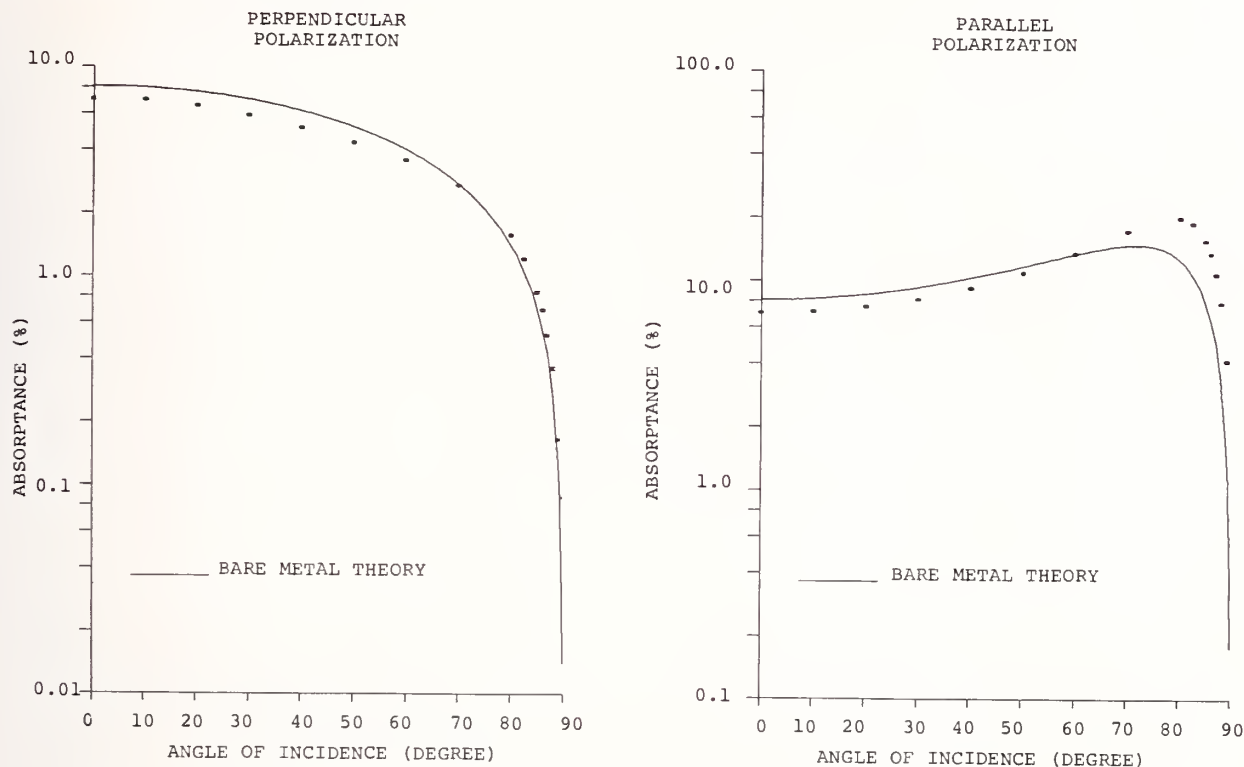


Figure 3. Absorptance curves for protected silver at $0.5145 \mu\text{m}$ for both s and p polarizations. The overcoat is an ≈ 1000 angstrom thick layer of ThF_4 . The solid curve is Fresnel's equations using the values of n and k given in reference 5 for bare silver.

The protected silver mirror (fig. 4b) displays clear deviations away from the $\cos\theta$ dependence. At approximately 40° it has lower absorptance than predicted, and for angles greater than 70° it has significantly higher absorptance.

Absorptance results for bare gold and copper mirrors at $10.6 \mu\text{m}$ are given in figures 5 and 6. Values of n and k for the theoretical curve are from references 5 and 6 for the bare gold and copper cases, respectively. The bare copper mirror is an example of the results when testing a "old" mirror; that is, a mirror which, although undamaged, has a tarnished surface as a natural result of aging. The copper data displays a curious increase in absorption at around 82° – 86° ; this may be related to the effects of the tarnish layer.

Figure 7 shows the deviation of the bare gold and copper data from the $\cos\theta$ dependence. The bare gold follows the dependence quite well until approximately 80° ; at higher angles the absorptance tends to be higher than that predicted by theory. At glancing angles, the absorptance of the tarnished copper mirror is significantly higher than theory predicts. The tarnish layer is probably largely responsible for this higher absorptance.

Finally, figure 8 gives an example of how an overcoat can dramatically alter the absorption characteristics of a mirror. The results are for a protected aluminum mirror with a MgF_2 overcoat measured at $0.5145 \mu\text{m}$. It is clear the data does not follow theory [7,8]; however, this simply implies a theory which incorporates the effects of a thin dielectric film needs to be used.

$\lambda = 0.5145 \mu\text{m}$
PERPENDICULAR POLARIZATION

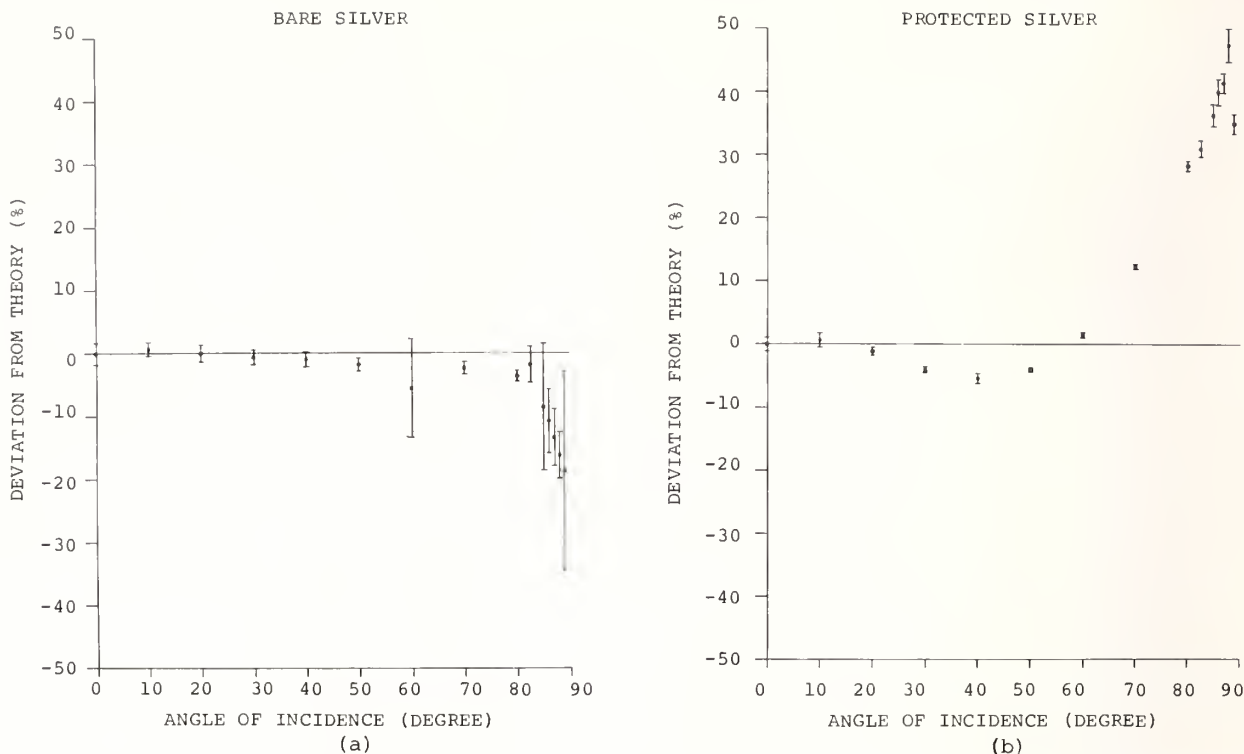


Figure 4. Deviation of data shown in figures 2 and 3 from the first order $\cos\theta$ dependence as predicted from Fresnel's equations.

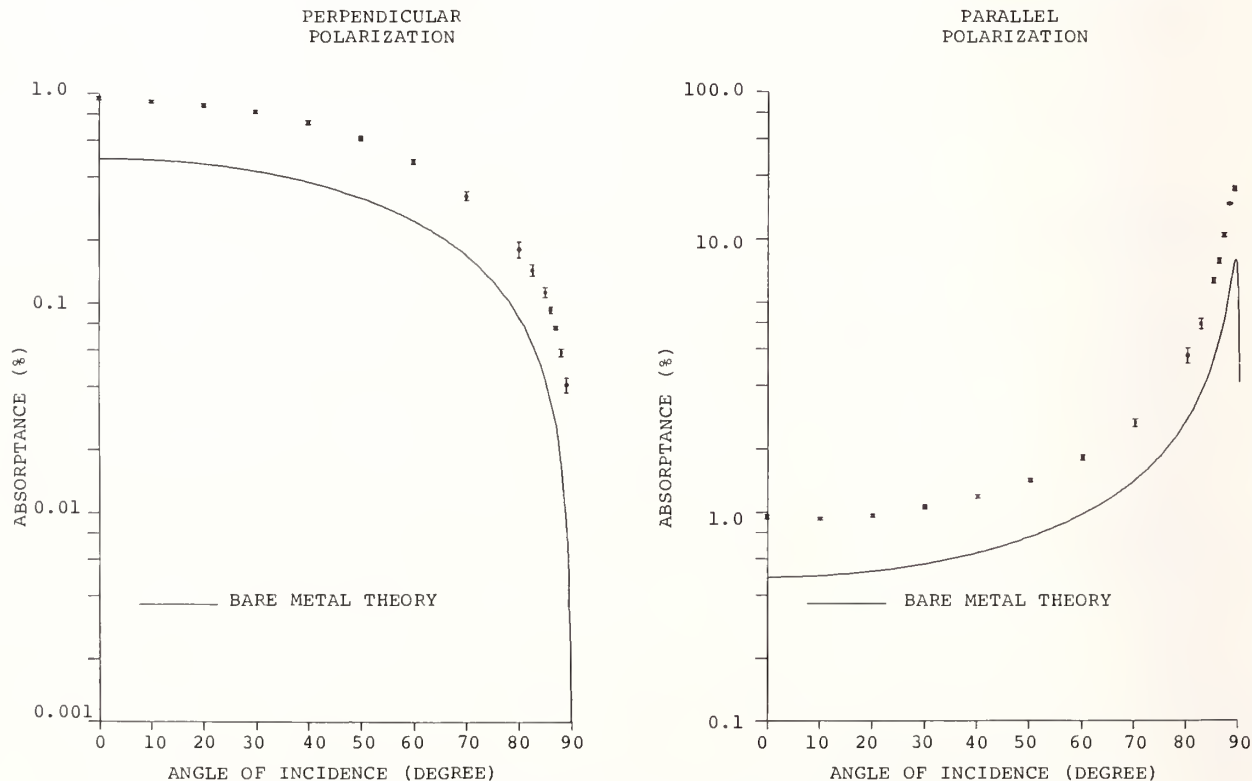


Figure 5. Absorptance curves for bare gold at $10.6 \mu\text{m}$ for both s and p polarizations. The solid curve is Fresnel's equations using the values of n and k given in reference 5.

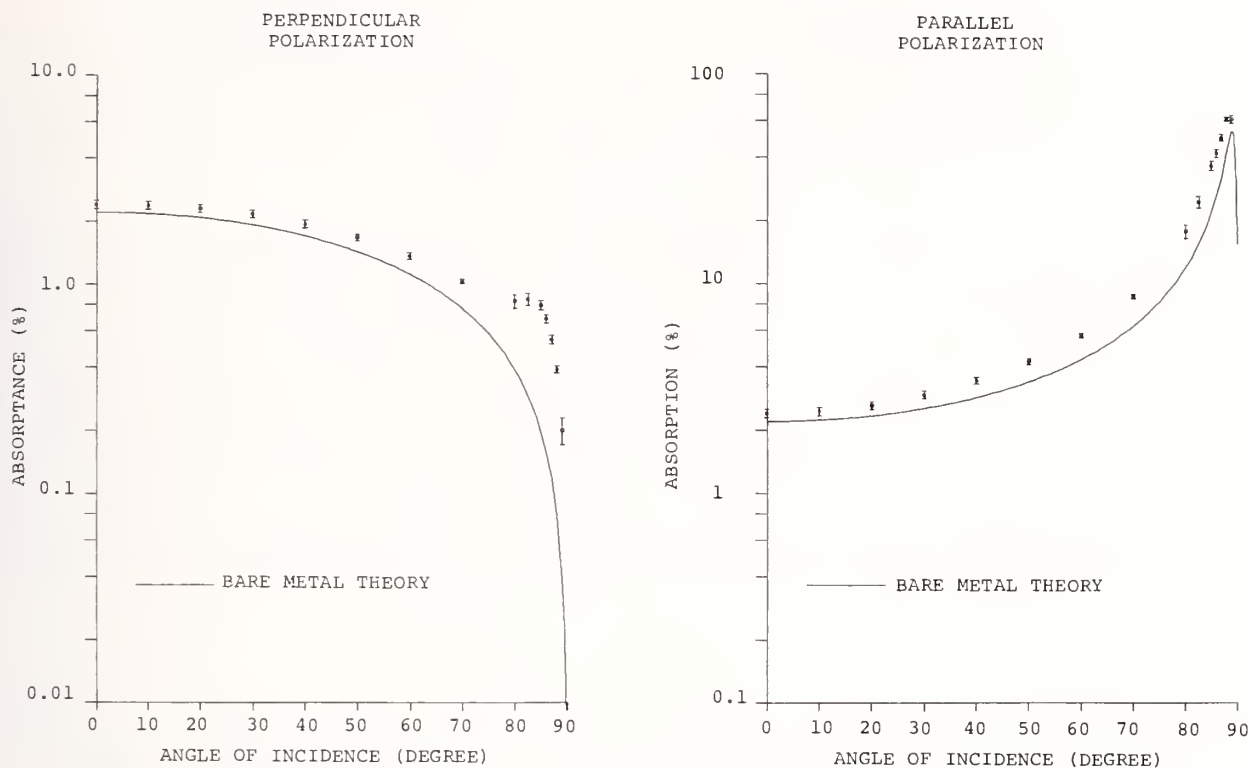
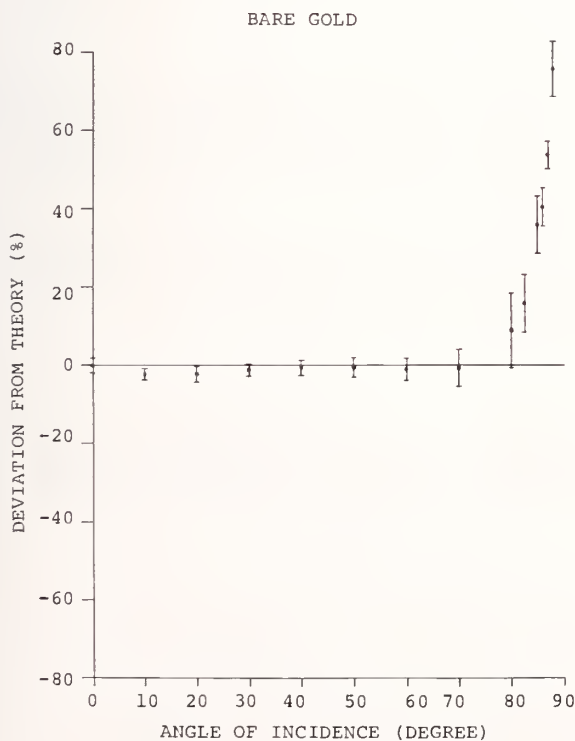


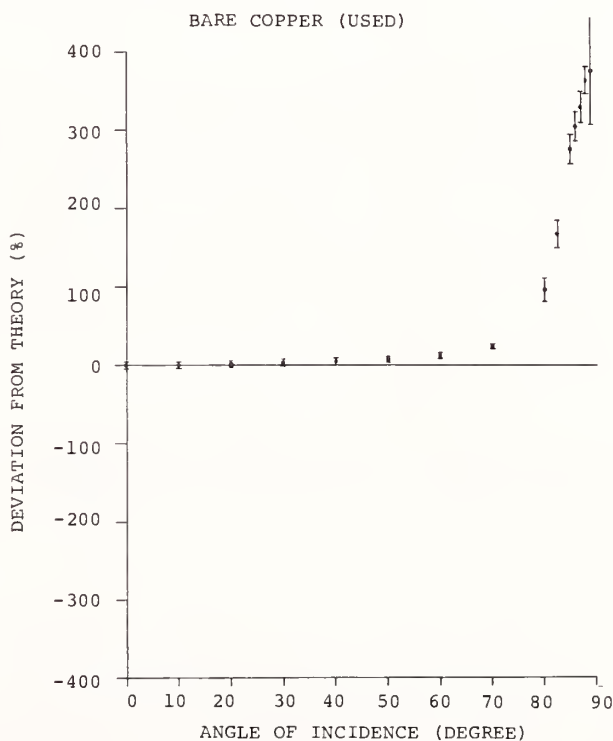
Figure 6. Absorbance curves for a bare but tarnished copper mirror at $10.6 \mu\text{m}$ for both s and p polarizations. The solid curve is Fresnel's equations using the values of n and k given in reference 6.

$$\lambda = 10.6 \mu\text{m}$$

PERPENDICULAR POLARIZATION



(a)



(b)

Figure 7. Deviation of data shown in figures 5 and 6 from the first order $\cos\theta$ dependence as predicted from Fresnel's equations.

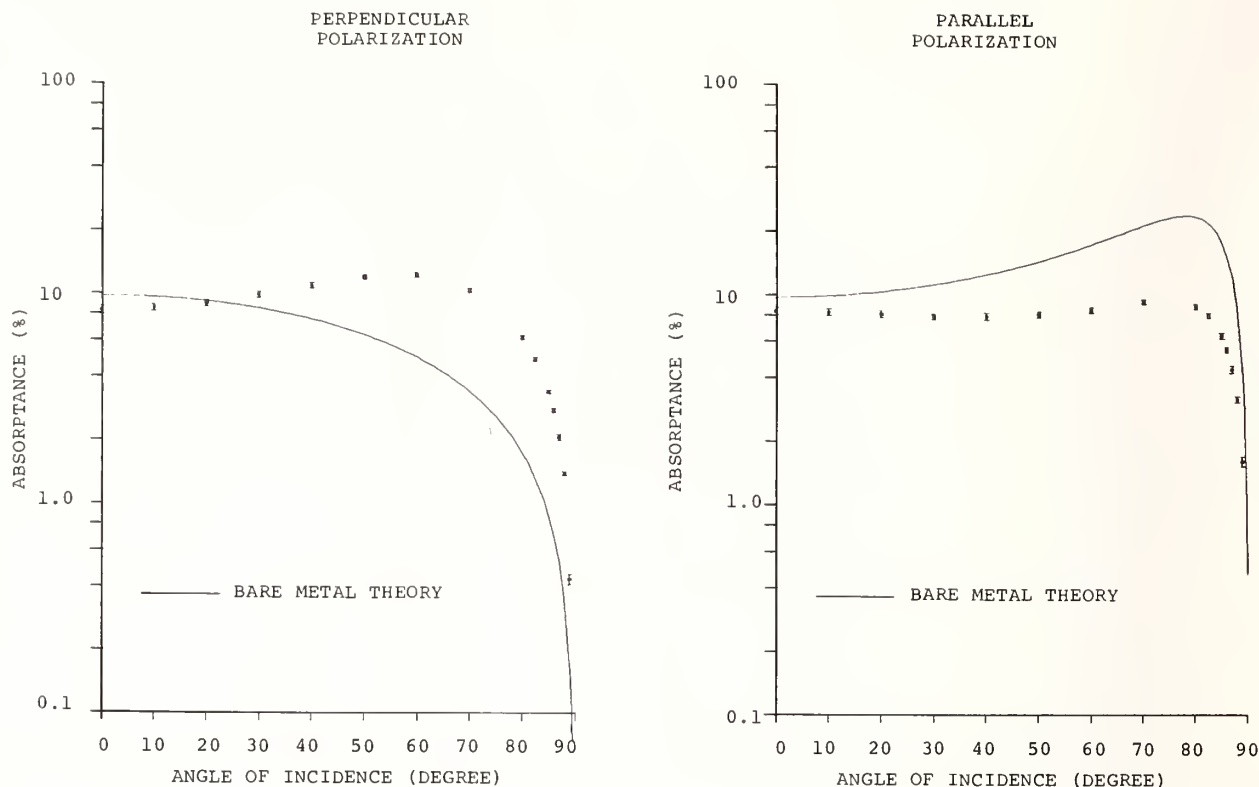


Figure 8. Absorptance curves for protected aluminum at $0.5145 \mu\text{m}$ for both s and p polarizations. The overcoat is a thin layer of MgF_2 . The solid curve is Fresnel's equations using the values of n and k given in references 7 and 8 for bare aluminum.

5. Conclusion

Glancing incidence absorption measurements have been performed at angles $\geq 89^\circ$ on a number of different bare metal and overcoated metal mirrors. Absorptions as low as 0.04% have been measured at 89° . While agreement between the data and Fresnel's equations for a bare metal surface is generally good for new bare metal mirrors, there is occasionally great disagreement when the mirror is either tarnished or has a protective overcoat.

Codes are available which predict the absorptance of mirrors with thin films [11]. Efforts are under way to compare the data obtained during this program with some of those code predictions. Work is also continuing on further measurements and reduction of the data.

6. Acknowledgments

The authors wish to thank Drs. J.M. Slater and D.D. Lowenthal for their technical advice during this program. They also wish to acknowledge J.S. Demboski for his assistance during some of the measurements. This work was sponsored by the Department of Energy, Contract No. DE-AC06-83ER40128.

7. References

1. Channell, Paul J., ed. Laser acceleration of particles. AIP conference proceedings, No. 91. New York: American Institute of Physics; 1982.
2. Figueira, J.F. and Thomas, S.J. Damage thresholds at metal surfaces for short pulse IR lasers. IEEE J. Quan. Elec. QE-18 (9): 1381-1386; 1982.
3. Mumola, P. and Jordan, D. Glancing incidence optics for high power lasers. Proceedings of the Society of Photo-Optical Instrumentation Engineers; 228: 54; 1981.

4. Born, Max and Wolf, Emil. Principles of optics. Oxford: Pergamon Press; 1975. 628-630.
5. Weaver, J.H., Krafka, C., Lynch, D.W., and Koch, E.E., ed. Physics data: optical properties of metals, pts. I and II. Federal Republic of Germany: Fachinformationszentrum; 1981.
6. Hagemann, H.J., Gudat, W., Kunz, C. Optical constants from the far infrared to the x-ray region: Mg, Al, Cu, Ag, Au, Bi, C, and Al_2O_3 . J. Opt. Soc. Am. 65(6): 742-744; 1975.
7. Schulz, L.G. The optical constants of silver, gold, copper, and aluminum. I. The absorption coefficient k. J. Opt. Soc. Am. 44(5): 357-362; 1954.
8. Schulz, L.G. and Tangherlini, F.R. The optical constants of silver, gold, copper, and aluminum. II. The index of refraction n. J. Opt. Soc. Am. 44(5): 362-368; 1954.
9. Parker, J.G. Optical absorption in glass: investigation using an acoustic technique. Appl. Optics. 12(12): 2974-2977; 1973.
10. Hordvik, A. and Schlossberg, H. Photoacoustic technique for determining optical absorption coefficients in solids. Appl. Optics. 16(1): 101-107; 1977.
11. Stanford, J.L., Michelson Laboratory, China Lake, CA, Woodberry, F.J., Rocketdyne Division, Canoga Park, CA, and Stubbs, J.B., University of Dayton, Dayton, OH. private communication.

N-on-1 Damage Testing of Single Crystal Metal Surfaces at 1.06 μm

Yong Jee, Michael F. Becker and Rodger M. Walser

Electronics Research Center
and
The Department of Electrical and Computer Engineering
The University of Texas at Austin
Austin, Texas 78712

We examined the accumulation dependence of laser damage on single crystal metal surfaces under Q-switched Nd:YAG laser irradiation (1.064 μm , 20 nsec pulses with a 200 μm spot diameter). The samples were chemically polished, electro-polished, and single point diamond machined Al, Cu and Ni single crystal surfaces of several crystallographic orientations. The single point diamond machined samples did not have single crystal surfaces as detected by electron channeling patterns, whereas the other samples had good single crystal surfaces.

Damage probability curves and accumulation curves were plotted to investigate N-on-1 damage behavior. The slope of the damage probability curve increased with the number of pulses required for damage. Accumulation curves, derived from 50% damage fluences, often had two regions showing different slopes. We interpret these measurements to indicate two different damage mechanisms, a defect related local melting at low pulse numbers and plastic deformation damage at high pulse numbers. These observations correlate with typical damage morphologies obtained by a Nomarski optical microscope and by SEM.

Key Words: accumulation; aluminum; copper; nickel; damage probability; single crystal metal surfaces

1. Introduction

The interaction of high power laser beams with metal surfaces has a variety of damage phenomena such as slip band formation, melting and evaporation. The difficulty of making the determination of a unique damage phenomenon has led to the study of the effect of spot-size [1,2] and pulse width [3] on the single shot damage of metal mirrors.

Several models were proposed to analyze these damage mechanisms. Sparks and Loh's thermodynamic model has been successfully applied to analyze 1-on-1 damage testing data [3]. But the accumulation effect has not been studied fully on metal surfaces, particularly at 1.06 μm . Lee, Koumvakalis and Bass have studied the accumulation effect on diamond machined Cu at 10.6 μm and proposed a model based on plastic deformation damage. Musal's model [4] was another, similar explanation which related damage to the thermal stress field induced by the laser pulse at the metal surface. Figueira et al. [5,6] have also investigated N-on-1 damage to metal surfaces at 10.6 μm and have observed anomalous, reversible fluence dependent damage.

The purpose of the present work is to measure single and multiple pulse damage thresholds for metal surfaces of single crystal Cu, Al and Ni under 1.06 μm irradiation. Because of the close relation of damage to surface preparation, we have also studied the effect of different polishing methods on the damage of single crystal surfaces. We have examined the slope of damage probability curves with several different polishing conditions, and have studied the accumulation effect by varying the incident number of pulses. Damage morphologies near threshold with various incident number of pulses will be discussed. Finally, the correlation between the cumulative effect of laser damage on metal surfaces and the linear slope regions of the accumulation curves will be investigated. The accumulation curves are plots of $\log(F_N/N)$ vs. $\log N$ where F_N is N-pulse damage threshold fluence and N is the incident number of pulses. From accumulation curves and damage morphologies, N-pulse damage can be explained in terms of a cumulative process which is dependent on the incident number of pulses. The metal samples were found to have a storage cycle dependent on preceding pulses if the incident energy was larger than the plastic yield threshold.

2. Experimental Procedures

The laser source used in these experiments was a Q-switched Nd:YAG laser with a 20 nsec pulse width and with pulse energy fluctuations of less than 3%. Incident pulses were attenuated by a rotating half-wave plate followed by a polarizer, and monitored by an energy meter whose output value was recorded by the computer. This energy meter was calibrated using a second energy meter before and after each testing session. The incident number of pulses was selected by an electro-mechanical shutter whose open and close operation was also automatically controlled.

The laser was operated at a pulse repetition frequency of 10-20 Hz. Output pulses were monitored by a vacuum photodiode and the pulse shape was displayed on a Tectronix 519 oscilloscope. Test samples were placed at the actual focal plane of a 50 cm focal length lens.

The beam spatial profile was measured with the knife-edge scanning method at the beginning and at the end of each session [7]. In this measurement, we calculated an equivalent Gaussian FWHM (Full Width at Half Maximum) from the detected error function data and then obtained the beam spot size using the equation $2W_0 = \text{FWHM}/\sqrt{\ln 2/2}$, where W_0 is the beam radius of $1/e^2$ in intensity. The actual operating beam spot diameter was around $200\mu\text{m}_0$, with a measurement error less than 3%.

In the damage testing process, a predetermined number of laser pulses were incident on the sample surface, the energy of each pulse was recorded, and the laser beam was blocked by the shutter. A new site was then selected by the step-motor stage controlled by the computer system. Testing sites were separated by 0.7-1 mm in order to avoid overlap. As it was tested, each site was viewed under an 80X optical microscope mounted on the experimental apparatus. Finally the sample was removed from the sample holder and examined under a 200X optical Nomarski microscope to determine whether there was a permanent change on the metal surface. The damage features were also examined using a scanning electron microscope (SEM) and a photograph was taken if needed. All damage thresholds presented here correspond to the energy fluence on-axis of a focused beam and represent 50% damage probability thresholds as determined by examination under the 200X optical Nomarski microscope.

The prepared samples were single point diamond machined, chemically polished and electro-polished single crystal Al, Cu and Ni surfaces. The single point diamond machined samples were prepared at the Los Alamos National Laboratory. Chemically polished and electro-polished samples were prepared using the solutions shown in table 1. The samples were then placed in the sample holder, blown off with a freon dust chaser, and damage tested.

Table 1. Sample Preparation Techniques

Sample	Single Point Diamond Turned Surface	Chemically Polished		Electro-polished Surface		
		Solution	Temp	Solution	Volt.	Time
Al	Los Alamos National Lab	H ₂ SO ₄ 25ml	293K	Ethanol(95%)800ml	35V	55s
		H ₃ PO ₄ 70ml		Water 140ml		
		HNO ₃ 5ml		HClO ₄ (60%) 60ml		
Cu	Los Alamos National Lab	HNO ₃ 66ml	293K	Water 175ml	1.6V	30m.
		H ₃ PO ₄ 66ml		H ₃ PO ₄ (85%) 825ml		
		CH ₃ COOH66ml				
Ni	Los Alamos National Lab			Water 250ml	6V	5m.
				H ₂ SO ₄ 600ml		

In order to investigate the surface crystal quality, electron channeling patterns (ECP), a Laue camera and an X-ray diffractometer were used. Since the electron channeling pattern can provide crystal orientation and crystal perfection information from a surface layer less than 50nm thick, sample surfaces can be checked effectively with this instrument [8]. The X-ray beam of the diffractometer and Laue camera penetrates more deeply into the material, up to 20µm. An X-ray diffractometer or a Laue camera is recommended for examining bulk crystals. Chemically polished or electro-polished surfaces exhibited good single crystal quality for either the ECP, X-ray diffractometer or Laue camera. However, when we examined single point diamond machined surfaces with ECP, they did not exhibit good single crystal qualities within a 0.1µm depth. Only with X-ray techniques could we see their single crystal quality.

3. Experimental Data

3.1 Damage Probability Curves

When each sample was damage tested, we determined the damage probability curve which plotted damage probability versus incident fluence as shown in figure 1. This sample was single point diamond machined <110> Cu tested with $N = 3$ pulses. Damaged and undamaged data points are overlapped within the interval between the maximum nondamaged and minimum damaged fluences. The linear curve is obtained from these overlapped data points by a least square curve fit. From this linear fit, we obtain the 50% damage threshold (F_N) for N pulses, and the damage onset, which is the zero intercept fluence for the linear fit. We also extracted the slope of the linear fit for later correlation with the surface defect density [1].

3.2 Accumulation Curves

We have repeatedly tested samples at different incident numbers of pulses, taken similar damage probability curves, and put the 50% probability threshold data on one graph as shown for <110> Al in figure 2. This damage fluence curve indicates a decreasing damage threshold for increasing incident number of pulses. The error bars indicate the minimum damaging fluence and the maximum nondamaging fluence.

If we redraw the damage fluence curve in another way, we can get a damage accumulation curve. This accumulation curve is used to examine the effect of cumulative laser action on metal surfaces. The y-axis is the log of the product of the N -pulse damage threshold, F_N , and the incident number of pulses, N , [$\log(F_N N)$]; and the x-axis is the log of the incident number of pulses, [$\log N$]. This plot, figure 3, shows two straight lines for the <110> Al surface shown previously in figure 2. Below $N = 10$ pulses, the curve has a smaller slope of $S = 0.558$; and above $N = 10$, the curve has a steeper slope of $S = 0.902$. Correspondingly, in figure 2, the curve below $N = 10$ has a steep decline, which means that the additional energy required to damage the surface is increasing rapidly as N decreases. Above $N = 10$, the curve becomes nearly flat, indicating that there is no great change in the additional energy to damage the surface with decreasing N . In figure 3, the slope for large N , $S = 0.902$, approaches the limit of $S = 1$. A slope of one means that the damage threshold does not change at all with increasing pulse number and that there is no accumulation effect.

From the linear segments of the damage accumulation curve, we can derive the following N -pulse damage threshold equation:

$$F_N = F_{th} N^{S-1} \quad (1)$$

For this Al example, when $N \leq 10$, $S = S_m = 0.558$, and $F_{th} = F_1$ represents single shot damage threshold. When $N \geq 10$, $S = S_p = 0.902$, and F_{th} is replaced with F_{pd} which is the threshold for plastic deformation damage. F_{pd} is obtained from the $N = 1$ intercept of the $N \geq 10$ line and is given by

$$F_{pd} = F_{th} 10^{(S_m - S_p) \log N_t} \quad (2)$$

where N_t is the turning point. Using $N_t = 10$ and the above values for S_m and S_p , $F_{pd} = 0.45F_1 = 0.8 \text{ J/cm}^2$. This means that the extrapolated single shot damage threshold for plastic deformation is approximately half of single shot damage threshold for this diamond machined Al sample. For the case of Cu, a similar accumulation curve is obtained, but there is just a single straight line as shown in figure 6. In this case $S_m = S_p$ and $F_{pd} = F_{th}$. The interpretation of these linear regions on the accumulation curves will be discussed in a subsequent section.

3.3 Damage Morphology

For small N , higher fluences are required for damage, and surface defects are damaged easily. Figure 7 shows single shot damage and local melting pits on diamond machined Cu at a fluence of 9.06 J/cm^2 . This picture was taken by a 500X optical Nomarski microscope. This morphology near the damage threshold illustrates the form of defect related local melting. However, when the threshold for slip formation is significantly lower than that for defect damage, visible slip lines appear on the surface prior to catastrophic damage or melting. Figure 4 shows slip lines on an Al surface produced by the thermal stress field induced by 1-on-1 laser tests. The photograph was taken by a optical Nomarski microscope from a single point diamond machined $\langle 111 \rangle$ Al sample irradiated at a fluence of 1.5 J/cm^2 with a beam spot diameter of $460 \mu\text{m}$. These slip lines are not ripple patterns and are not periodic. Similar slip lines on Ni are shown in figure 5. These slip lines represent slip along $\langle 111 \rangle$ direction surfaces. This picture was taken by SEM from an electro-polished $\langle 111 \rangle$ Ni sample.

We observed that in the low pulse number regime, defect damage and plastic deformation damage are competitive. If the defect damage threshold is lower than, or of the same order as, the plastic deformation threshold, then defect damage appears first on the surface, and slip is minimal and invisible. If the plastic deformation threshold is significantly lower than that for surface defect damage, then visible slip lines will appear first. In the high pulse number regime where damage fluences are lower, plastic deformation is dominant near threshold as shown in figure 8. This typical picture, taken from a 3000 pulse damage site on diamond machined Cu, suggests damage by plastic deformation. This is strong evidence for the cumulative effect of thermo-mechanical stress induced by repetitive laser pulses on the sample. Prior to catastrophic failure (i.e., before a flash or a spark was observed) [2], the irradiated sites became roughened and the degree of roughness increased with the incident number of pulses. Visible surface roughness was observed after a large number of pulses without the emission of light.

3.4 Damage Tests Results

For different materials and polishing methods, the slope of the accumulation curves and single shot threshold data are summarized in table 2. For a single point diamond machined Al sample, the single shot damage threshold was 1.77 J/cm^2 , damage onset was 1.62 J/cm^2 , and the slope of the accumulation curve was 0.71 for $N \leq 10$ and 0.88 for $N \geq 10$. For Cu samples, the single shot damage threshold was about 10 J/cm^2 . Although the damage threshold of Cu surfaces changed with the polishing method, there was only one slope to the accumulation curves.

4. Discussion

When we drew the various damage probability curves, the slope was found to increase with the incident number of pulses and decrease with increasing numbers of defect damage spots in the beam. This is in agreement with Foltyn's findings [1] that the slope is dependent on the beam spot size and surface defect density, and that surface defects can be probed using damage probability curves.

Theoretical melt thresholds and measured 1-on-1 damage thresholds are compared for a pulse width of 20 nsec in table 3. In the second column, $\langle A \rangle$ is the average optical absorptance which is obtained from the integral equation of Sparks and Loh [3].

$$\langle A \rangle = \frac{\int_{T_0}^{T_m} A_0 (1 + \alpha T) dT}{(T_m - T_0)} \quad (3)$$

Table 2. Test Data Summary

SAMPLE	Al		Cu		Ni
	D.T.	CH.P.	D.T.	E.P.	D.T.
	8/5/84 Sr.84151	5/22/85	8/12/85 Sr.85055	6/23/84	5/22/85 Sr.84156
1-on-1 50% Prob. (J/cm ²)	1.77±.15	7.66±.9	9.40±.79	10.2	2.72
1-on-1 onset (J/cm ²)	1.62	6.84	8.24		1.81
Slope of 1-on-1 damage Probability Curve	330.3		46.1 (%cm ² /J)		
Slope of Accumulation Curve S	0.709 N<10 0.878 N>10	0.732 N<30	0.980 N<10 0.960 N>10	0.942 1<N<10 ⁴	0.75 N<5 0.880 N>1

Table 3. Theoretical Melt Thresholds vs. 1-on-1 Damage Thresholds

Sample	A (average)	Theoretical values Melting threshold (20nsec, 1.06μm) (J/cm ²)	Measured values Diamond turned surface	
			20nsec (J/cm ²) (with spot size as noted)	47nsec (J/cm ²)
Al	0.0704	2.74	1.77±0.15 (200μm)	3.83±0.06 (68.5μm)
Cu	0.0253	19.52	9.40±0.79 (208μm)	-
Ni	0.3175	0.77	0.93±0.2 (68.7μm)	2.72±0.07 (80.2μm)

where A_0 is the surface optical absorptance at room temperature, α is the coefficient of temperature dependent absorption, T_m is the melting temperature, and T_0 is the ambient temperature ($^{\circ}\text{K}$). When an intense laser beam interacts with a normal metal surface, a fraction of incident energy penetrates the metal to a skin depth and is absorbed by the free carriers in the metal. This absorbed energy is converted to a thermal distribution which generates a thermal stress field. It is the stress field which contributes to the cumulative effect of deformation and slip in multiple pulse damage. If the incident radiation is intense enough, the absorbed energy can raise the surface temperature to melting. The threshold for single shot surface melting is given by [3].

$$F_m = \frac{(T_m - T_0) (\pi K C t_p)^{\frac{1}{2}}}{2 < A >} \quad (4)$$

where F_m is the fluence (J/cm^2) required to melt the surface, t_p (sec) is the pulse duration, C is the volumetric specific heat capacity in ($\text{J}/\text{cm}^3\text{K}$), and K is the thermal conductivity ($\text{W}/\text{cm}^{\circ}\text{K}$).

In the case of Al and Ni, the theoretical melt threshold and measured single pulse damage threshold values are nearly identical. The agreement is not as good for Cu where the theoretical melt threshold is near $20 \text{ J}/\text{cm}^2$, but the measured damage threshold is only $10 \text{ J}/\text{cm}^2$.

For the case of N-on-1 damage, we will consider cyclic thermomechanical stress induced by the laser pulse as a possible explanation of the accumulation effect. The thermal expansion of metal surfaces resulting from the transient temperature rise generates compressive stress, followed by tension during the cool-down period. If the temperature rise and the coefficient of thermal expansion are large enough, a permanent irreversible plastic strain will remain due to the compression and tension process. The fluence corresponding to the plastic yield (slip) threshold (F_y) is given by [4]

$$F_y = \frac{(\pi K C t_p)^{\frac{1}{2}} (1-v) Y}{2 < A > \beta E} \quad (5)$$

where v is Poisson's ratio, Y is the yield stress, β is the coefficient of thermal expansion and E is Young's modulus of the metal for an idealized case of strain being linearly dependent on the stress. The experimental threshold for visible plastic deformation, F_{pd} , identified in equation (2) was $F_{pd} = 0.8 \text{ J}/\text{cm}^2$ for $\langle 110 \rangle$ diamond machined Al. The calculated yield threshold at the free surface [4] for the same material is $0.12 \text{ J}/\text{cm}^2$. When we compared these two values, the experimental threshold for visible plastic deformation was 6.7 times larger than the theoretically predicted yield threshold. According to Musal's model [4], the predicted free surface elastic displacement is approximately 12 nm per incident J/cm^2 for the case of high quality Al mirror surfaces. If we use the same argument for our diamond machined Al surfaces, the predicted free surface displacement will be approximately 1.4 nm at the fluence of $0.12 \text{ J}/\text{cm}^2$, and about 6.7 times larger for the experimental case or approximately 9.6 nm. The distinction between these two cases appears consistent with the expected vertical detectivity threshold in Nomarski microscopy. In other words, the threshold for visibility and for subsequent damage due to plastic deformation might be larger than the threshold for the initiation of plastic deformation. Surface deformation above this threshold is distinguished by an increase in absorptance sufficient to lead to catastrophic surface damage to microscopically visible surface roughening. This cyclic thermomechanical effect can lead to the accumulation observed in N-on-1 damage.

In the previous section, we have shown that the accumulation curves and damage morphologies suggest two damage regimes for low N and high N , where in both cases the N pulse damage threshold, F_N , is in the form of equation (1). The N-on-1 damage threshold decreased with increasing N suggesting an energy storage cycle produced by the thermomechanical stress-strain field of the absorbed laser beam.

For cases such as Cu having a single slope in the accumulation curve, these results may be combined with the equation for the theoretical melt threshold. The result is an equation for N-on-1 damage threshold in terms of material constants, as shown below.

$$F_n = \frac{(T_m - T_o) (\pi K C t_p)}{N^{1-S} 2\langle A \rangle} \quad (6)$$

If S is 0.9 and N is 1000, then the 1000 pulse damage threshold is reduced by a half. Thus the N-pulse damage threshold may be predicted using equation (6) when a typical value of S for the material is known.

5. Conclusions

Single and multiple pulse damage threshold measurements have been performed on single crystal Cu, Al, and Ni single point diamond machined, chemically polished, and electro-polished surfaces with a 1.06 μm laser beam in air. Our findings imply that plastic deformation is an important contributor to the nanosecond pulse laser damage of these metal surfaces even at fluences well below their melting or their defect damage thresholds.

The crystal quality of the samples was checked with electron channelling patterns and X-ray diffraction. Diamond machined surfaces had a disordered layer at least 0.1 μm in depth, but the electro-polished and chemically polished surfaces were single crystals. It is well known that the diamond machining process involves high stresses at the surface, so this disorder is not unexpected.

The slope of the damage probability curve is related to the surface damaged defect density and the incident number of pulses. We found that in addition to the expected decrease in slope with increasing defect damage densities, the slope increased with increasing N in N-on-1 experiments.

Accumulation was observed in all samples and the accumulation curves indicated that the damage mechanism had two different regimes -- a low pulse number regime and a high pulse number regime. In the low pulse number regime, the morphology suggests defect dominated local melting; and in the high pulse number regime, the morphology suggests plastic deformation mediated by energy storage cycles from previous pulses. In some cases where the threshold for plastic deformation or yield was extremely low, plastic deformation damage was dominant even for N = 1.

The accumulation effect for all the samples could be described by the experimentally derived equation (1) which indicates decreasing N-pulse damage thresholds with increasing pulse numbers.

The thermal stress field produced by the incident laser pulse appears to drive cyclic thermo-mechanical behavior involving energy storage by nonconservative circuits around the stress-strain curve. Slip lines form when the absorbed energy exceeds the yield (slip) stress threshold. Under repeated laser irradiation this is manifested in surface roughness, and eventually the surface damages.

This research was supported by the DoD Joint Services Electronics Program under research contract AFOSR F49620-82-C-0033. We also are grateful to Dick Rohrer at the Los Alamos National Laboratory for his assistance with the diamond machined samples.

6. References

- [1] S.R. Foltyn, "Spotsize Effects in Laser Damage Testing." Nat. Bur. Stand. (US) Spec. Publ. #669; 368, 1982.
- [2] C.S. Lee, N. Koumvakalis, M. Bass, "Spot-size Dependence of Laser-Induced Damage to Diamond Turned Cu Mirrors," Appl. Phys. Lett. 48(7); 625 (1982); "A Theoretical Model for Multiple-pulse Laser Induced Damage to Metal Mirrors." J. Appl. Phys. 54(10); 5727 (1983).

- [3] M. Sparks, E. Loh, Jr., "Temperature Dependence of Absorptance in Laser Damage of Metallic Mirrors: I. Melting." J. Opt. Soc. Am.; 69(6), 847 (1979).
- [4] H.M. Musal, Jr., "Thermomechanical Stress Degradation of Metal Surfaces under PULsed Laser Irradiation." Nat. Bur. Stand. (US) Spec. Publ. #568; 159 (1980).
- [5] J.F. Figueira, S.J. Thomas, "Damage Thresholds at Metal Surfaces for Short Pulse IR Lasers." IEEE J. Quantum Electron; QE-13, 1381 (1982).
- [6] S.J. Thomas, R.F. Harrison, J.F. Figueira, "Observations of the Morphology of Laser-induced Damage in Copper Mirrors." Appl. Phys. Lett.; 40(3), 200 (1982).
- [7] D.C. Cohen, B. Little, F.S. Lueche, "Techniques for Measuring 1- μ m Diameter Gaussian Beams." Appl. Opt.; 23(4), 637 (1984).
- [8] J.I. Goldstein, H. Yakowitz, Practical Scanning Electron Microscopy. Plenum Press, New York; 149-210 (1975).

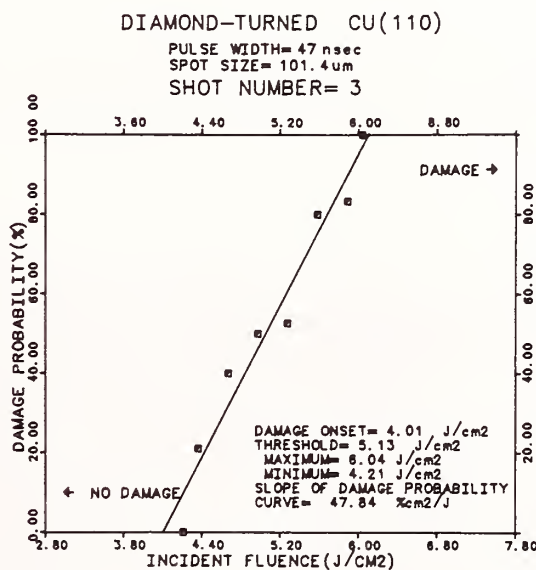


Figure 1. Damage probability curve for single point diamond machined <111> Cu, N=3.

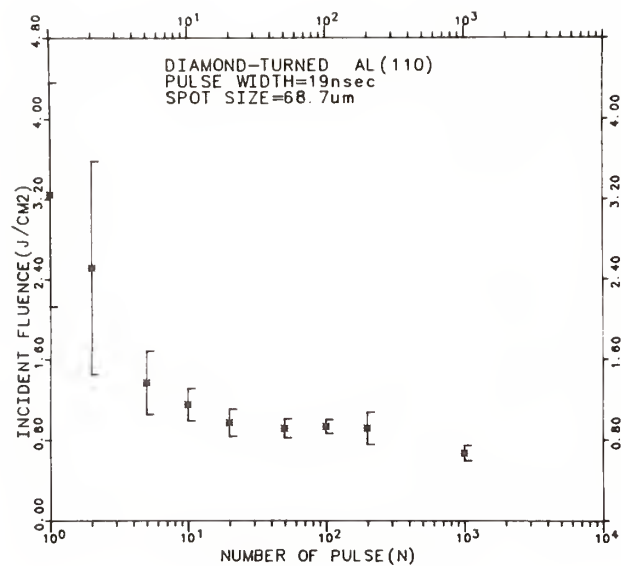


Figure 2. Damage fluence versus N for single point diamond machined <110> Al.

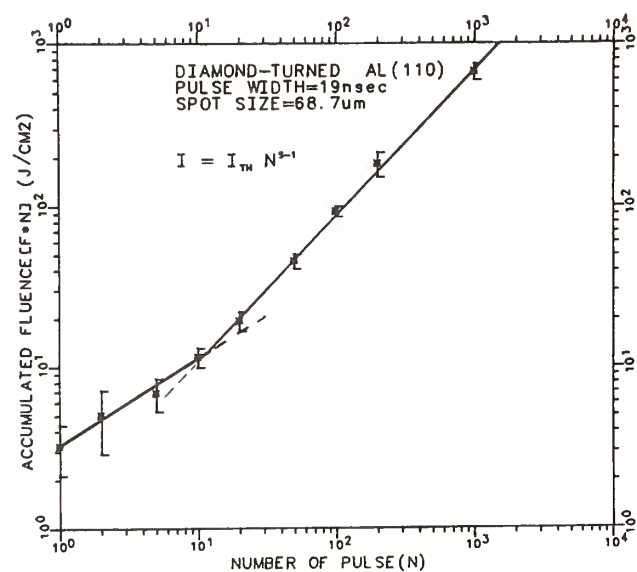


Figure 3. Accumulation curve (replotted data) for the same Al sample as figure 2.

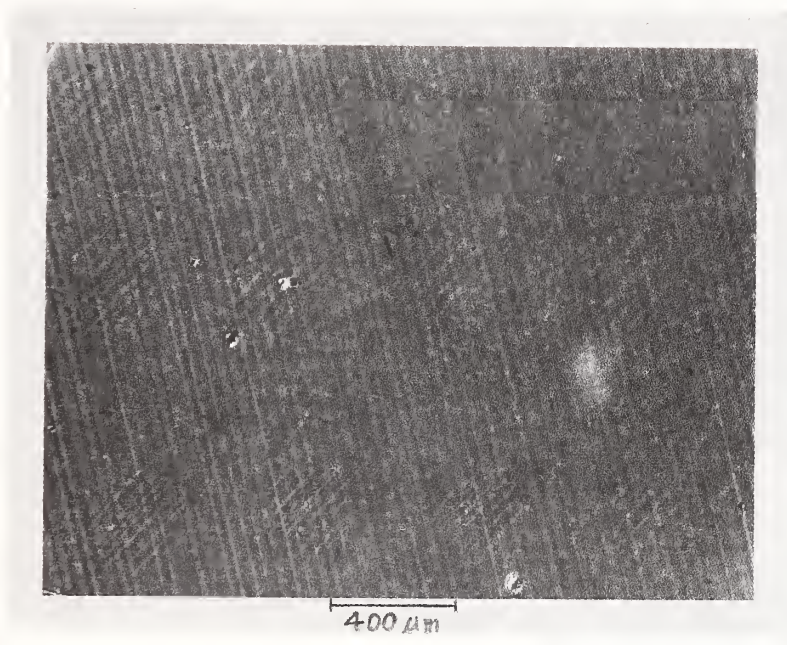


Figure 4. Optical Nomarski micrograph of the damage morphology on a diamond machined $\langle 111 \rangle$ Al surface. All the spots have been single shot damage tested at 1.5 J/cm^2 .

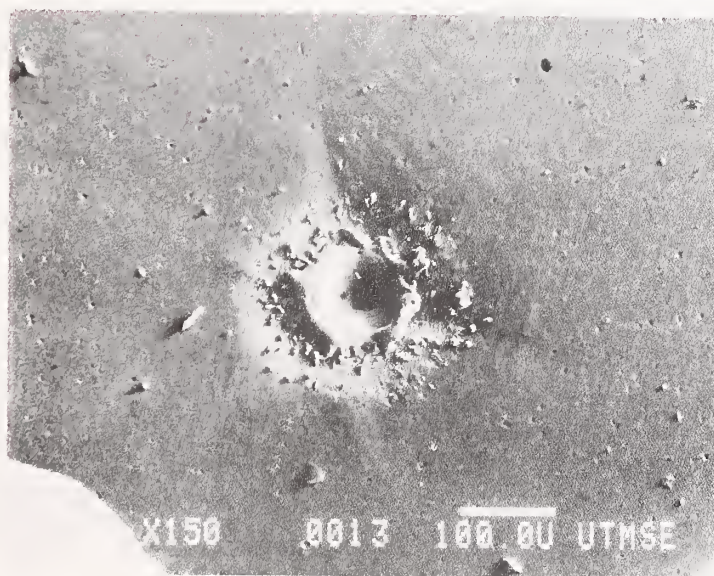


Figure 5. SEM micrograph of slip line formation on an electro-polished $\langle 111 \rangle$ Ni surface, $N = 245$ at 1.3 J/cm^2 .

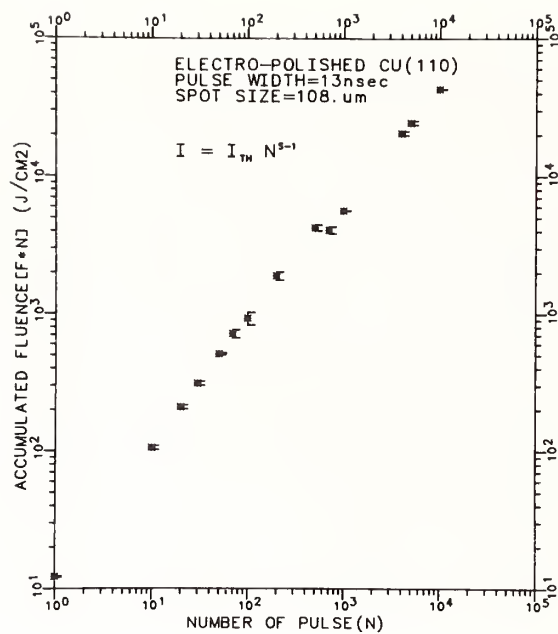


Figure 6. Accumulation curve for electro-polished <110> Cu.

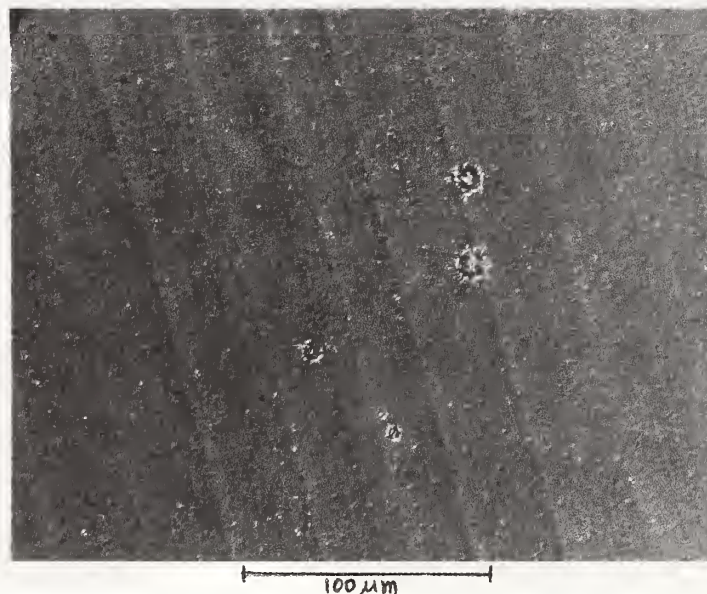


Figure 7. Optical Nomarski micrograph of damage on single point diamond machined <100> Cu which shows defect related local melting pits, N = 1 at 9.06 J/cm².

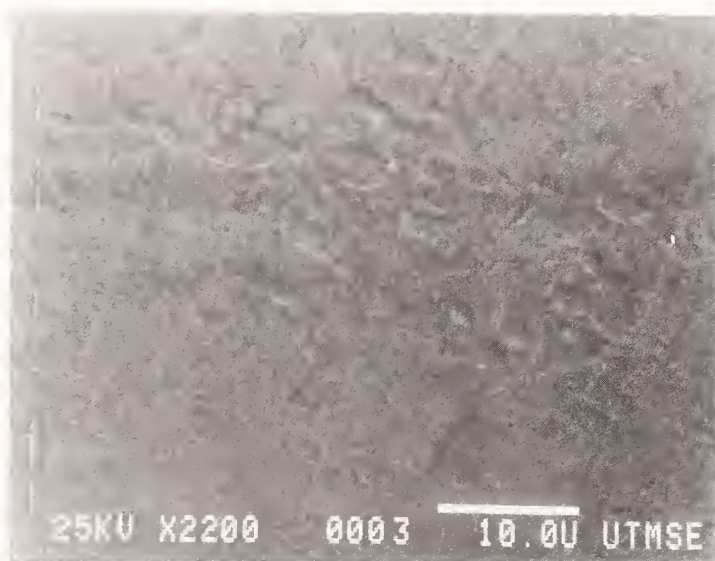


Figure 8. SEM micrograph of plastic deformation on a single point diamond machined $\langle 110 \rangle$ Cu surface, $N = 3000$ at 3.28 J/cm^2 .

LASER INDUCED MO MIRROR DAMAGE FOR HIGH POWER CO₂ LASER

H. Okamoto, N. Matsusue, K. Kitazima
Central Research Laboratory, Nippon Mining Co., Ltd.
3-17-35 Niizominami, Toda-shi, Saitama, 335, Japan

K. Yoshida, Y. Ichikawa, M. Yamanaka, T. Yamanaka
Institute of Laser Engineering, Osaka University
2-6 Yamadaoka, Suita-shi, Osaka, 565, Japan

and

Y. Tsunawaki
Osaka Industrial University
3 Nakagaito, Daito-shi, Osaka, 574, Japan

ABSTRACT

We have developed a high-purity molybdenum (Mo) mirror by electron-beam melting method (e.b.m. Mo mirror). Its high laser-damage threshold has been demonstrated for the high-power TEA CO₂ laser system. The e.b.m. Mo mirror has a damage threshold of 2 to 4 times higher than that of an Au coated glass mirror and had a life time of 3 times longer than that of a powder metallurgy Mo mirror (p.m. Mo mirror) when the laser energy density of higher than 60 J/cm² was irradiated. We found that on the laser-damage threshold the difference between the e.b.m. Mo mirror and the p.m. Mo mirror was due to the fine surface without voids and the small amount of impurities.

Key words: Laser mirror; molybdenum; CO₂ laser; laser damage; polished surfaces; surface roughness; optical characterization.

I. Introduction

We have been developing an optically pumped high power far infrared (FIR) laser system for plasma diagnostics.^{1,2} The maximum output power of this laser is limited mainly by low laser-damage threshold of optical components. Although Au coated glass mirrors are usually used in a high power TEA CO₂ laser system for pumping the FIR lasing molecules, metallic mirrors are more suitable for such a laser system because of the higher laser-damage threshold. Especially, molybdenum (Mo) is a material of interest as high power laser mirrors because it has a good heat conductivity, a low thermal expansion, a high melting point, a high reflectivity, and a high hardness of the surface.³ Conventional Mo mirror produced by sintering method has many voids on the surface, which are considered to cause the damage threshold lower than the expected value. We had newly developed Mo materials by electron-beam melting method to obtain a voidless mirror.

In this paper, a laser induced damage on electron-beam melting (e.b.m.) Mo mirror was studied comparing with powder metallurgy (p.m.) Mo mirror and Au coated glass mirror by using the TEA CO₂ laser (100 mJ, 50 ns).

II. Experimental Method

The e.b.m. Mo mirrors with high purity of 99.999% used in this test were prepared for target materials in semiconductor industry. The surface of the e.b.m. and p.m. Mo mirrors were polished by an oscillation type machine. The surface roughness was measured by a Talystep (Rank Taylor Hobson Limited) which had a conical 12.5 μ m tip radius for height measurement. The Au coated glass mirror consisted of Au and Cr layers with few micrometers of thickness on glass substrate.

The reflectivity of the Mo mirror was measured using 6328-Å He-Ne laser, 1.06- μ m YAG laser and an infrared spectrometer.

The laser damages against a high power TEA CO₂ laser were studied for three kinds of mirrors. The 9.26- μ m R(22) beam with pulse width of 50 nsec from TEA CO₂ laser oscillator (Lumonics K-921S)⁴ was focused with a 100 mm foocal length ZnSe lens onto the mirror set on an XYZ-stage. The incident energy of TEA CO₂ laser was varied from 10 to 65 mJ by changing the charging voltage and the mixing ratio of CO₂ laser gas components of CO₂, He and N₂. The beam spot size was estimated by Nomarski microscopic observation of damaged pattern on the plastic film and silicon wafer. The damage threshold was defined through microscopic observation as the minimum laser energy density when the surface states changed slightly. The plasma light produced by the laser irradiation on the mirror surface was observed by eyes. The plasma-production threshold was defined as the minimum laser energy density when plasma light was observed. The damage threshold of Mo mirror surface was, furthermore, studied for the multi-shots irradiation onto the same site of the sample.

III. Experimental Results and Discussion

A. Surface Characteristics of Mo Mirrors

The surface roughness of the p.m. and the e.b.m. Mo mirrors was measured by the Talystep as shown in Figs. 1(a) and (b). The surface roughness (peak to valley value) of the p.m. and e.b.m. Mo mirrors were about 250 Å and 120 Å respectively. Although the tip diameter was 25 μ m, a difference of the roughness of these two kinds of Mo mirrors was well distinguished. The surface flatness of both Mo mirrors was measured by Zygo interferometer to be less than $\lambda/5$ ($\lambda=6328$ Å).

Table I shows the chemical compositions of the p.m. and e.b.m. Mo, respectively. It can be seen that the impurities of Na, K, Al, Si, Fe and Ni included in the e.b.m. Mo. is considerably less than that of the p.m. Mo. From this analysis, we can expect that the laser induced damage threshold of the e.b.m. Mo mirror has higher value than that of the p.m. Mo mirror.

The reflectivity of the Mo mirror at three wavelengths is shown in Table 2. The reflectivity for He-Ne laser and YAG laser was obtained with nearly normal incident angle. The e.b.m. Mo mirror had a reflectivity higher than the p.m. Mo one. At the wavelength of 9.26 μ m, the reflectivity of both Mo mirrors was comparable to that of the Au coated glass mirror.

B. Anger Electron Spectroscopy Scan of the Mo Mirror

We have measured the contamination of the polished Mo mirror surface, and the impurities segregation of the Mo fracture surface by using the Anger electron spectroscopy method to investigate the corelativity with the laser induced damage. Fig 2 shows the Anger scan of the as-polished surface of the p.m. Mo mirror and the e.b.m. Mo mirror, respectively.

The Anger scan of the Mo mirrors after 10 mins sputter etch with argon is shown in Fig. 3. By using the argon sputter etch, the Na contamination on the surface is completely removed, but the C and O is considerably decreased. Anger scan for the fracture surface of the void in p.m. Mo and the grain boundary of the e.b.m. Mo is shown in Fig. 4. We found that the alkali metals of K and Na, and C, N, O was deposited of the void in p.m. Mo, and N and traces of O was deposited in grain boundary of the e.b.m. Mo.

C. One-Shot Laser Damage

The micrographs of the mirror surface damaged by one shot irradiation of the TEA CO₂ laser are shown in Figs. 5, 6 and 7, for the Au coated glass, the p.m. Mo and the e.b.m. Mo mirrors, respectively.

In Fig. 5, the Au coated glass mirror was irradiated by TEA CO₂ laser energy of 53.3 J/cm² and it is seen that the two coated layers of Au and Cr on the glass substrate is broken by the laser beam. The Au coated glass mirror with the irradiated energy density of larger than 17.6 - 21.6 J/cm² was always damaged.

Figures 6 and 7 show the micrograph of the p.m. and e.b.m. Mo mirrors damaged by 146.3 and J/cm², respectively. It is seen that the p.m. Mo mirror melted inhomogeneously; on the contrary e.b.m. Mo mirror melted homogeneously. For the less fluence of TEA CO₂ laser, the e.b.m. Mo mirror was melted along the grain boundary, and the grain was clearly observed in the damaged spot as

shown in Fig. 8.

The surface damage threshold and the plasma production threshold for three kinds of mirrors under the one shot irradiation of TEA CO₂ laser are summarized in Table 3. The surface damage threshold of the e.b.m. Mo mirror was 2 to 4 times higher than that of the Au coated glass mirror. The damage threshold of the p.m. Mo mirror decided by the surface observation using a microscope is higher than that of the e.b.m. Mo mirror. However, the threshold of energy density that the laser light reflected by the e.b.m. Mo mirror abruptly decreased due to the absorption of radiation by strong plasma on the surface is about 30% higher than that of the p.m. Mo mirror. This fact means that the e.b.m. Mo mirror is more resistant against high power TEA CO₂ laser irradiation than p.m. Mo mirror. The plasma-production threshold of the e.b.m. Mo mirror was, however, about 3 times and about 5 times higher than that of the p.m. Mo mirror and the Au coated glass mirror, respectively. It seems that the difference of these thresholds between the e.b.m. and p.m. Mo mirrors is due to the surface condition with and without voids which causes the plasma production.

D. Multi-Shots Laser-Damage for Mo Mirrors

For practical use of the Mo mirror, the study on the damage due to multi-shot irradiation of TEA CO₂ laser is very important.

In this study, the focused TEA CO₂ laser beam was irradiated with 0.5 pps at an incident angle of about 15°, and the energy of the reflected laser beam was measured by a pyroelectric detector. The reflected laser beam from the ZnSe lens surface was monitored by another pyroelectric detector.

Figure 9 shows the variation of the reflectivity to the shot number of TEA CO₂ laser with various incident laser energy densities for the e.b.m. Mo mirror. The similar tendency was also observed for the p.m. Mo mirror. At a certain shot number depending on the incident energy density, the strong plasma produced with a sound on the mirror surface and then the reflectivity decreased abruptly to about half value due to the absorption of radiation by plasma. After that, bright plasma was always observed and the reflectivity kept constant value. The shot number where the reflectivity reduced suddenly with plasma is plotted in Fig. 10 as a function of the incident laser energy density. It was found that the e.b.m. Mo mirror had a longer life time than the p.m. Mo mirror. Especially, for the incident laser energy density higher than 60 J/cm², the life time of the e.b.m. Mo mirror was about 3 times longer than that of the p.m. Mo mirror.

The micrograph of the p.m. Mo mirror surface, for example, after 480 shots irradiation of 60.7 J/cm² is shown in Fig. 11. The microscopic observation of a series of damaged p.m. Mo mirror surface with multi-shot irradiation of TEA CO₂ laser suggested that the voids on the mirror surface gradually began to melt by weak plasma and the melting area extended until the reflectivity decreased suddenly. Figure 12 shows the micrograph of the e.b.m. Mo mirror surface damaged after 26 shots irradiation of 72 J/cm². In this case, it is seen that the smaller grain is formed in the damaged surface due to the recrystallization based on thermal effect with repetitive laser irradiation. We are now pursuing the production mechanism of this phenomenon. This phenomena would be due to the relative lower melting point at the grain boundaries because the impurity is generally easy to gather at the grain as can be seen from the Auger scan of Fig. 4 and results in making the melting point lower.

IV. Conclusion

We showed the availability of the e.b.m. Mo mirror for the high power TEA CO₂ laser system. For wavelength at 9.26 μm, the Mo mirror had almost same reflectivity as the Au coated glass mirror. The surface damage threshold of the e.b.m. Mo mirror for one-shot irradiation of TEA CO₂ laser was 2 to 4 times higher than that of the Au coated glass mirror. For multi-shots irradiation of TEA CO₂ laser, the e.b.m. Mo mirror had a life time of 3 times longer than that of the p.m. Mo mirror for the laser energy density of higher than 60 J/cm². The laser damages on the Mo mirrors mainly depends on the surface condition; on the p.m. Mo mirror, a number of voids on the mirror surface originates and extends the damage, while on the e.b.m. Mo mirror, the impurities at the grain boundaries of polycrystalline mirror surface are the cause of the laser damage. Therefore we would be able to expect much higher damage threshold and longer life time with a single crystal Mo mirror.

Acknowledgements

The authors would like to thank S. Suzuki and K. Abico of the Institute of Metals, Tohoku Univ. for testing of Auger electron spectroscopy scans in ultra high vacuum of the Mo fracture surfaces and helpful discussions.

References

- [1] Y. Tsunawaki, M. Yamanaka, Y. Ichikawa, L. Wu, S. Okajima, T. Iwasaki, A. Mitsuishi, T. Yamanaka and C. Yamanaka, 9th Int. Conf. on Infrared Millimeter Waves (Takarazuka, Japan, 1984) Th7-4.
- [2] Y. Ichikawa, L. Wu, Y. Tsunawaki, M. Yamanaka, S. Okajima, T. Iwasaki, T. Yamanaka and C. Yamanaka, Technol. Repts. Osaka Univ. 35, No. 2 (1985) (in press).
- [3] S.M. Wong, G. Krauss, and J.M. Benett, "Laser Induced Damage in Optical Materials", A.J. Glass and A.H. Guenther, Eds. (NBS. Spec. Publ., 1978), pp. 132-163.
- [4] Y. Ichikawa, Y. Tsunawaki, M. Yamanaka, T. Yamanaka, A. Mitsuishi and C. Yamanaka, Infrerad Phyc. 35, No. 4, 633 (1985).

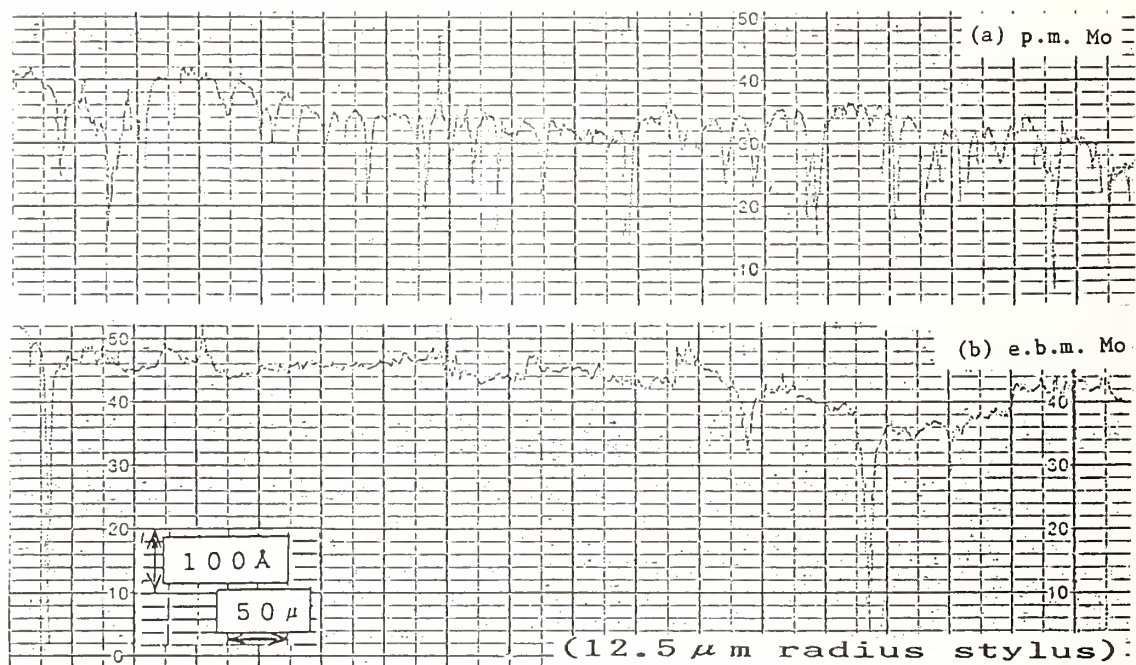


Figure 1. Surface scans of the Mo mirror; (a) p.m. Mo mirror and (b) e.b.m. Mo mirror.

Table 1. Chemical compositions of the p.m. and e.b.m. Mo mirrors.

	(ppm)								
	C	O	N	Na	K	Al	Si	Fe	Ni
p.m.Mo	30	30	3	12	46	7	15	50	24
e.b.m.Mo	10	30	10	0.001	0.005	0.004	0.4	<0.5	0.2

Table 2. The reflectivity of p.m. and e.b.m. Mo mirrors for wavelengths of 6328 Å (He-Ne laser), 1.06 μm (YAG laser) and 9.26 μm (infrared spectrometer).

WAVELENGTH	Reflectivity (%)	
	p.m. Mo	e.b.m. Mo
6328 Å	58	65.8
1.06 μm	61.2	70
10 μm	almost same as Au coated mirror	

Table 3. The threshold of surface-damage and plasma-production against 9.26-μm R(22) TEA CO₂ laser beam (50 ns) for the e.b.m. Mo mirror, p.m. Mo mirror and Au coated glass mirrors.

mirror	threshold energy density (J/cm ²)	
	damage	plasma
(i) e.b.m. Mo mirror	45.5 - 59	94
(ii) p.m. Mo mirror	87	30
(iii) Au coated on glass mirror	17.6 - 21.6	17.6 - 21.6

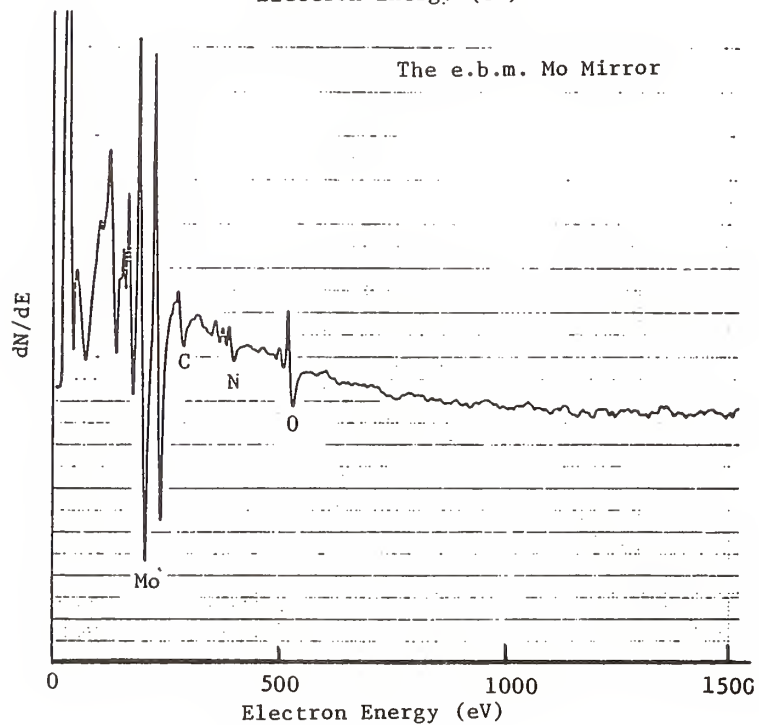
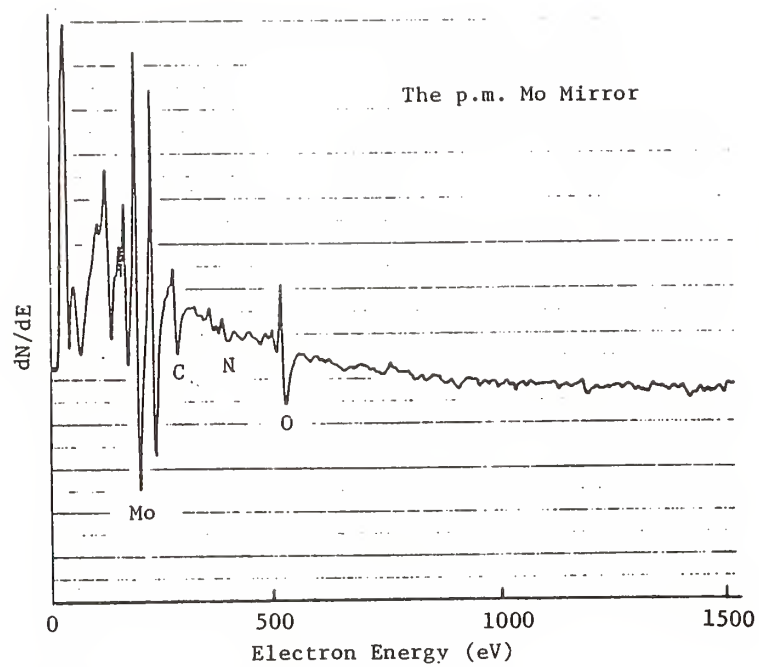


Figure 3. Auger electron spectroscopy scans of the after 10 mins. sputtered surface of the p.m. and e.b.m. Mo mirrors.

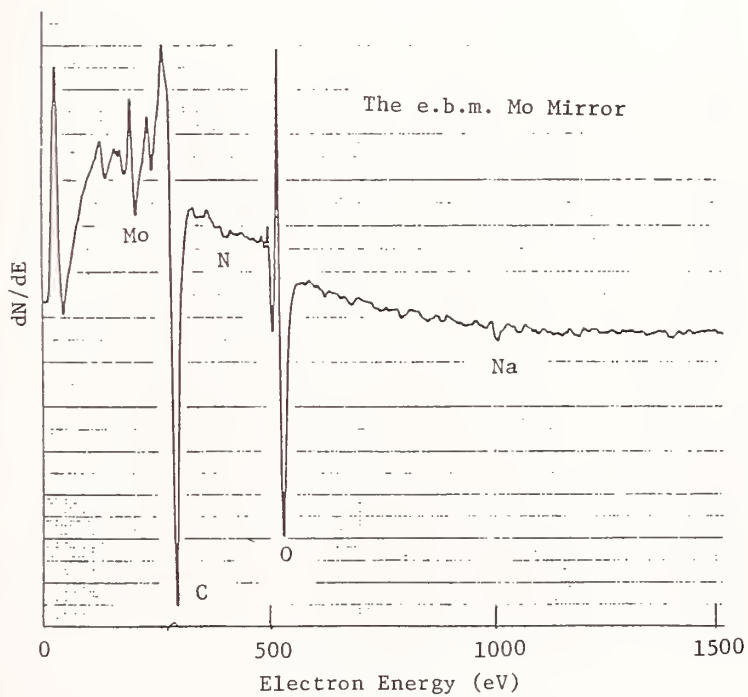
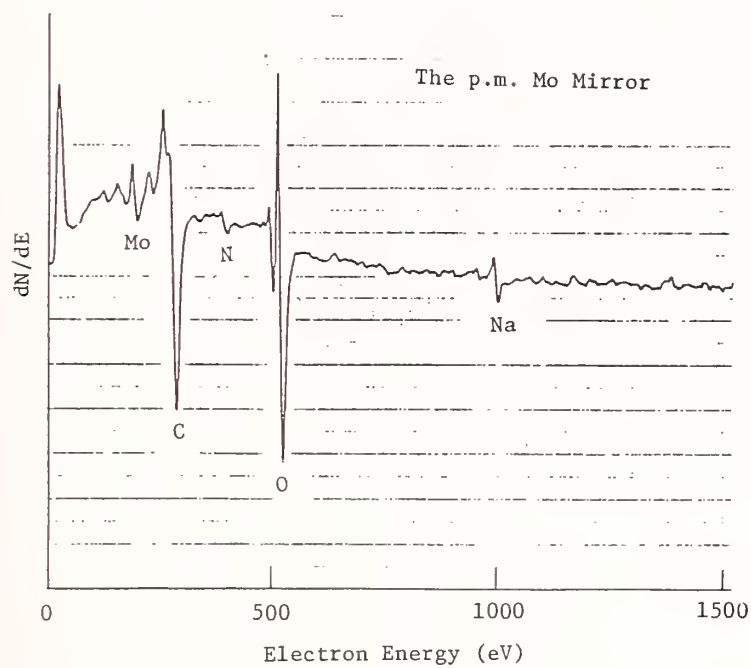


Figure 2. Auger electron spectroscopy scans of the as-polished surface of the p.m. and e.b.m. Mo mirrors.

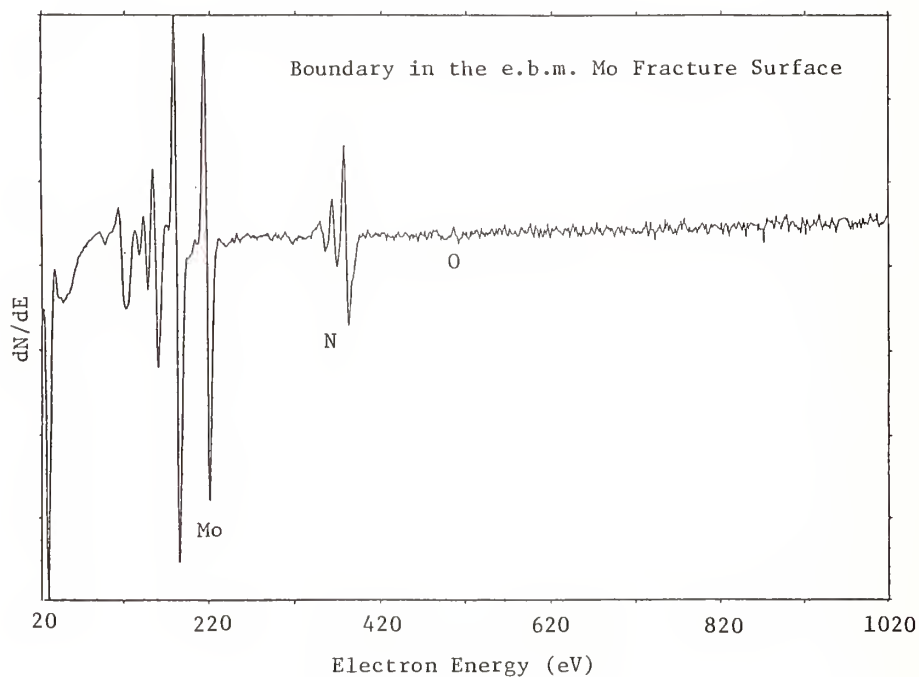
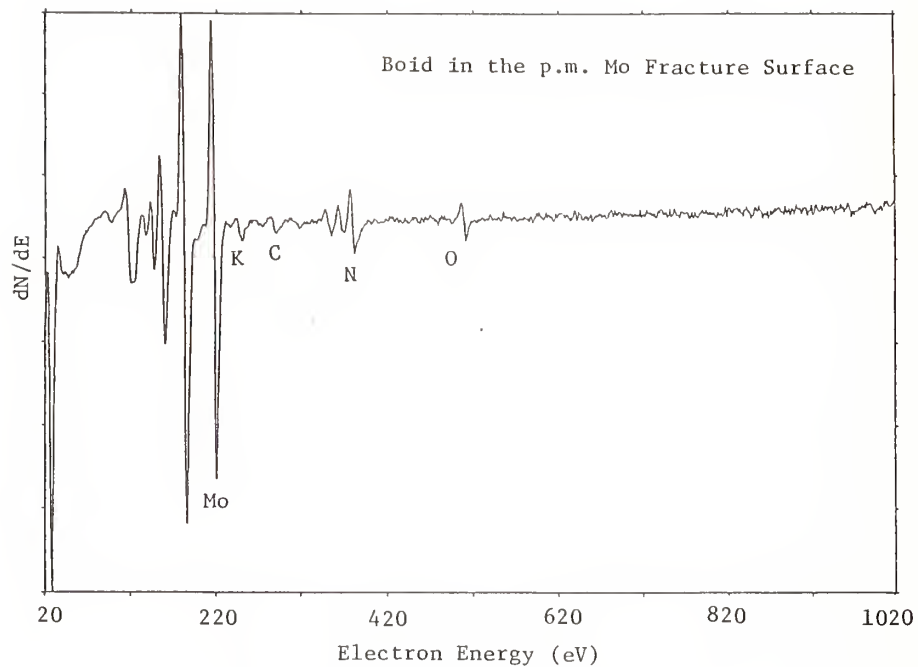


Figure 4. Auger electron spectroscopy scans of the fracture surface of the p.m. and e.b.m. Mo in ultra high vacuum. (Tested by Tohoku Univ.)

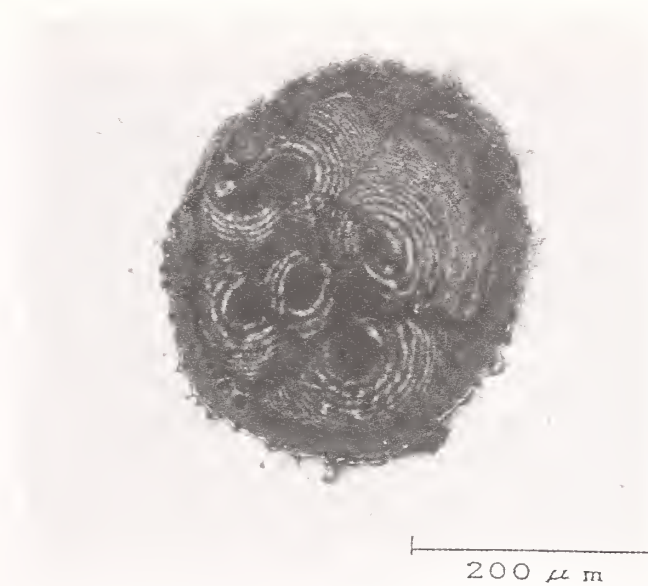


Figure 5. Microstructure of Au coated glass mirror damaged by TEA CO₂ laser of 53.3 J/cm². The mirror consisted of the two coated layers Au and Cr on the glass substrate.



Interference Contrast Image

Figure 6. Microstructure of the p.m. Mo mirror damaged by TEA CO₂ laser of 146.3 J/cm².



Interference Contrast Image 100 μ m

Figure 7. Microstructure of the e.b.m. Mo mirror damaged by TEA CO_2 laser of 152 J/cm^2 .



Interference Contrast Image 100 μ m

Figure 8. Microstructure of the e.b.m. Mo mirror damaged by TEA CO_2 laser of 95.6 J/cm^2 .

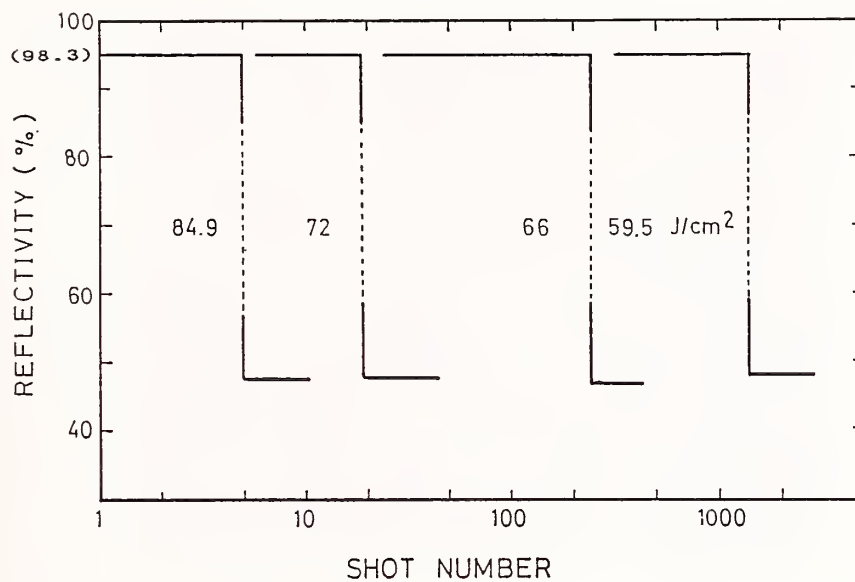


Figure 9. The dependency of the reflectivity on the number of TEA CO₂ laser shots for the e.b.m. Mo mirror.

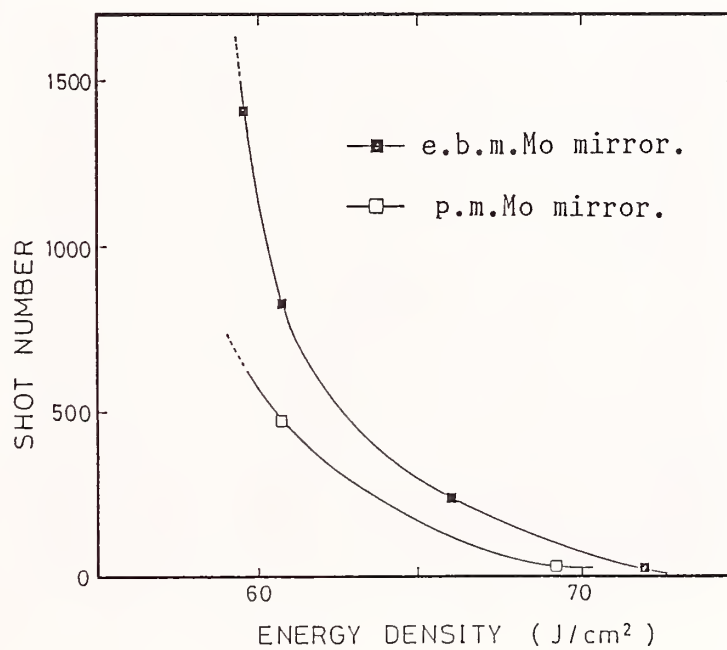


Figure 10. The relation between the shot number and the threshold of energy density that the laser light reflected by Mo mirror abruptly decreased due to the absorption of radiation by plasma on the mirror surface.

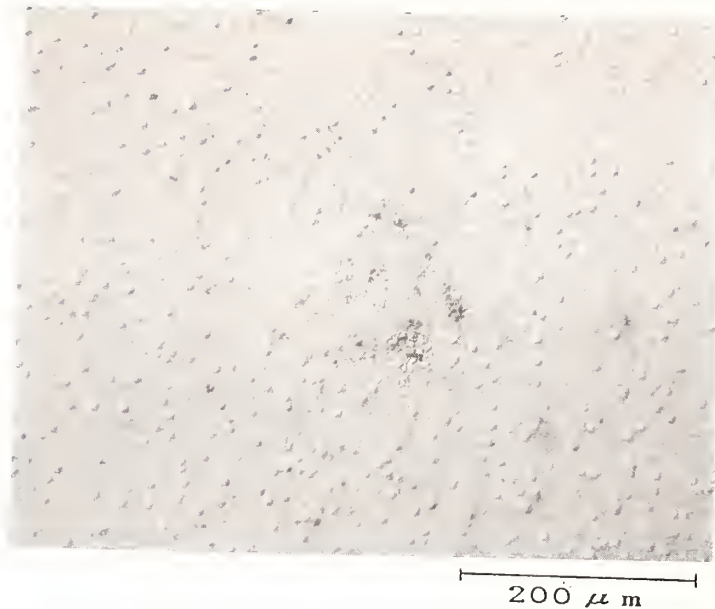


Figure 11. Damaged microstructure of the p.m. Mo mirror surface after the repetitive irradiation of 480 shots.



Interference Contrast Image

Figure 12. Damaged microstructure of the e.b.m. Mo mirror surface after the repetitive irradiations of 26 shots.

Multifacet, Metal Mirror Design for Extreme-Ultraviolet and Soft
X-Ray Free-Electron Laser Resonators*

Brian E. Newnam
Los Alamos National Laboratory
Chemistry and Laser Sciences Division
Los Alamos, New Mexico 87545

Resonator mirrors with reflectance greater than ~40% are required if free-electron laser (FEL) oscillators are to be extended to wavelengths below 100 nm. The principle of total-external reflection has been used to design multifacet mirrors of several metal films that surpass this requirement between 10 and 100 nm. These reflectors have high reflectance over a relatively broad band which suits well the inherent FEL wavelength tunability. The practical limitations to achieving and maintaining high reflectance include oxide- and carbon-contamination, scattering, and surface-plasmon absorption.

Key words: aluminum films; carbon contamination; extreme-ultraviolet reflectors; free-electron lasers; metal reflectors; multifacet reflectors; oxide contamination; rhodium films; silicon carbon; silicon films; soft x-ray reflectors.

1. Introduction

The recent successful operation of several free-electron laser (FEL) oscillators in the visible and near-infrared spectral ranges [1,2] has encouraged researchers to examine the possible short-wavelength limits for these devices [3,4]. One of the major technological constraints presently blocking their extension into the extreme-ultraviolet (XUV) is the inherently low reflectance of available resonator mirrors, of the order of 10 to 20%. Unless this limitation is overcome, very high values of single-pass optical gain will be needed. For example, if each resonator mirror were to have a reflectance of only 25%, the small-signal gain would have to exceed 1600% just to begin oscillation, a value which may be difficult to achieve. Development of resonator mirrors with reflectance $\geq 40\%$ appears to be a prerequisite for future operation of FEL oscillators at wavelengths below 100 nm.

2. Present Status of Reflectors for the XUV

There are four types of normal-incidence reflectors under development for the XUV. First, smooth surfaces of chemically vapor-deposited (CVD), single-crystal, silicon carbide (SiC) have been produced and used successfully in synchrotron radiation beam lines. The highest measured values of the normal-incidence reflectance for SiC have varied between 40 to 50% for wavelengths between 60 and 220 nm [5,6]. Below 60 nm, SiC reflectance drops rapidly to less than 10%, as shown in figure 1.

Simple metallic films represent a second type of reflector, and the reflectance properties of two examples, platinum and gold, are compared in figure 1. Only for wavelengths longer than 250 nm does their reflectance exceed our minimum 40% requirement. The notable exception are aluminum films freshly deposited on smooth substrates in ultra-high vacuum (10^{-9} to 10^{-10} torr). With care, the normal-incidence reflectance can exceed 40% for wavelengths as short as 80 nm [7,9]. However, even in high vacuum the reflectance gradually decreases with time as an oxide forms on the surface. Overcoating with a layer of MgF_2 does prevent the oxidation, but high reflectance ($\geq 80\%$) is then limited to wavelengths longer than 120 nm. We will revisit the use of Al films in following sections.

The third class of reflector includes multilayer thin-film structures which operate on the principle of standing-wave interference of multiple reflections from the film interfaces. Since all dielectric materials are absorbing for wavelengths shorter than 110 nm, alternating metal layers having differing absorption coefficients are used. For the soft x-ray and XUV spectral regions from 10 nm to 110 nm, this technology generally has yielded reflectances less than 50%

*Work performed under the auspices of the U.S. Department of Energy.

for near-normal incidence over a bandwidth limited to $\leq 10\%$ [10]. The status of normal-incidence reflectors as of 1983 was summarized by Attwood et al. [11], which is reproduced here as figure 2.

Multifacet reflectors, the fourth type of XUV reflector and the subject of this paper, involve multiple reflections from a series of metal mirrors. These make use of the principle of total external reflectance (TER) which is possible only when the refractive index is less than unity. We have determined that semi-TER ($R < 100\%$) is possible for a few metals over certain spectral ranges in the XUV. Surprisingly high values of retroreflectance (redirection of the optical beam by 180°) are possible, especially with S-plane reflections at large angles of incidence. In addition, the high reflectance extends over a relatively broad range, a feature that well suits the inherent tunability of FEL oscillators. Since the reflectance at each facet can exceed 95% for large angles of incidence, such as 80° , these reflectors offer another advantage: relatively high resistance to laser damage and thermal distortion.

In the following sections, we review the potential for the multifacet, vacuum-deposited metal films, the risks due to practical fabrication limitations and environmental contamination, and how they would be used in a ring-resonator configuration.

3. Requirements for Total-External Reflectance Mirrors

We first describe the fundamentals of total external reflection. When light travels across the boundary from one medium of refractive index n_1 into a second medium of index n_2 in which the velocity is greater, total reflection occurs when the angle of incidence exceeds the critical angle ϕ_c defined by $\sin \phi_c = n_2/n_1$. If the first medium is vacuum for which $n_1 = 1.0$, TER can occur only if $n_2 < 1.0$. For metals, there are many spectral regions where the real part n of the refractive index $N = n + ik$ is less than unity. This is less common for dielectrics, however. A second requirement for total (100%) reflection is that the extinction coefficient k of the media be absolutely zero (which is never attained). Still, if the absorption is small ($k \ll 1.0$ while $n_2/n_1 < 1.0$), a very large reflection can occur. Finally, higher values of reflectance are achieved with S-polarized light rather than with P-polarization. Figure 3 visualizes the conditions for TER.

Soviet researcher A. V. Vinogradov and colleagues [11-13] were the first to analyze the potential for high-retroreflectance in the soft x-ray regime using multiple, grazing-incidence reflections beyond the critical angle. They considered a single, cylindrical mirror configuration of a variety of metals and used optical constants derived from the theoretical tables of Henke et al. [14]. For use as resonator mirrors, however, we suggest a multifacet, flat mirror configuration as indicated in figure 4. Flat mirrors will cause much less astigmatism which is essential in an FEL resonator to obtain maximum intensity within the magnetic undulator. Also, flats are easiest to fabricate with the required surface figure. (The final facet should be an off-axis paraboloid for collimating the beam.)

4. Examples for the XUV: Aluminum and Silicon Retroreflectors

We have scrutinized the available tabulations of optical constants [14,16] for the metallic elements and various compounds, searching for wavelengths for which both k and n are sufficiently less than unity. In the XUV spectral region ≥ 25 nm, we initially identified three candidates: Al, crystalline Si, and Mg. The spectral dependence of the optical constants of Al is shown in figure 5 for reference. Vacuum-deposited films of Al are especially attractive since they have been characterized by a number of researchers over the last 35 years. Also, since the films are transparent in this region, interference effects with the substrate, e.g. SiC, can enhance the reflectance slightly. Less information (but still adequate) is available for crystalline Si films in the XUV. Practical use of Mg films is doubtful since an absorbing oxide forms rapidly at the surface.

The reflecting properties of a smooth, uncontaminated Al film on SiC at the wavelength of 50 nm are shown in figure 6 as a function of the number of mirror facets. Optical constants from the critical review and tabulation of Smith et al. [8,9] were used in the computations. According to the analysis of Goldstein et al. [17] for an FEL conservatively designed for 50 nm, the predicted 60% retroreflectance indicated in figure 6 is above the level needed to reach laser oscillation. Interestingly, only six facets are needed to achieve this value. Figure 7 shows the calculated retroreflectance over the entire spectral range (25 to 130 nm) where TER is operative for various numbers of mirror facets. It is obvious that the reflectance of a multifaceted aluminum mirror greatly exceeds that of a single, normal-incidence Al mirror over most of this region.

Examination of the optical constants of crystalline-Si films [18] reveals that TER occurs over the same 25- to 80-nm spectral range as for Al. Figure 8 illustrates the spectral characteristics of the retroreflectance of multifacet reflectors of this element.

5. Example for Soft X-Ray Wavelengths - Rhodium Retroreflector

In the soft x-ray region below 14 nm, a variety of metal coatings may be useful as multifacet retromirrors in laser resonators. These and the approximate wavelengths for which maximum reflectance enhancement occurs include Rh (12 nm), Os (12 nm), Mo (12 nm), Ag (10 nm), Au (10 nm), In (7.5 nm), La (6.5 nm), and Ba (5.5 nm) [14,19]. The calculated retroreflectance (60 to 65%) of a multifaceted rhodium reflector at 12 nm (figure 9) is very encouraging as is the 30% spectral band (10 to 13.5 nm) over which the reflectance exceeds 40%. A corresponding plot of reflectance versus number of mirror facets at 12 nm is shown in figure 10. Rhodium films are especially interesting since the available tabulation of optical constants [19] is for films deposited in modest vacuum (10^{-5} torr). From this fact we expect that oxide growth may not be a serious problem.

6. Risks of Contamination and Surface Roughness

Unless great care is taken, the TER enhancement in retroreflectance of a multifacet mirror will not be realized. The hazards to be avoided are surface contamination by oxide and carbon films and surface roughness which represent potential losses by absorption or scattering. We now discuss the magnitudes of these hazards and the conditions necessary to minimize their effects.

Oxide Contamination. In general, the metal films must be deposited and maintained in high vacuum to minimize the formation of oxide layers that absorb strongly at all wavelengths below 150 nm. This is evident for aluminum in figure 11 in which Smith et al. [9] have summarized the normal-incidence reflection for a variety of Al surface conditions. In particular, our computations of the potential degradation of an Al retroreflector (figure 12) show that very little oxide formation can be allowed before the reflectance drops below 40%. Several researchers have determined that ultra-high vacuum (10^{-9} to 10^{-20} torr) and fast deposition rates are necessary to preclude oxide contamination [20,21]. At these vacuum pressures over the period of two days, H. E. Bennett [21] was not able to detect (via ellipsometry) the growth of an oxide layer on Al films. Oxide growth on Si and Rh is expected to be much less of a threat.

Carbon Film Contamination. Surface contamination by carbon compounds, which are normally present in all environments, must be prevented to minimize optical absorption. As shown in figure 13, a carbon layer of only a few angstroms thickness will seriously degrade the TER condition required for multifaceted Al retromirrors. We have also calculated the potential for degraded performance of a multifaceted Rh mirror at 12 nm due to growth of a carbon epifilm (see figure 14). From comparison of figures 13 and 14, we conclude that carbon contamination should have less serious consequences near 10 nm than near 50 nm. The presence of high-energy photons, such as produced by synchrotrons, has been observed to greatly increase carbon film growth (to ~10 nm thickness) on optical surfaces [22]. Synchrotron users have been able to control the rate of carbon accumulation on optical surfaces by use of ultra-high vacuums (10^{-10} to 10^{-11} torr). Of course, a superior solution is to eliminate all carbonaceous compounds from the vacuum environment. Recently, an rf plasma discharge of O_2 or H_2O vapor has been used to effectively remove all traces of such contamination on metallic diffraction gratings [23,24].

Scattering Losses. The third requirement is that the reflecting films be deposited on smooth substrates to minimize scattering losses. For wavelengths much greater than the rms surface roughness σ , that is $\lambda \gg \sigma$, the effect of scattering on the specular reflectance, $R(\phi)$, at some angle of incidence, ϕ , is approximately [25,27]

$$R = R_0(\phi) \exp[-(4\pi\sigma \cos\phi/\lambda)^2] \quad , \quad (1)$$

where R_0 is the reflectance of a perfectly smooth surface. For XUV wavelengths ≥ 30 nm, mirror substrates with rms surface roughness of ≤ 5 Å are sufficiently smooth to limit scattering losses to $\leq 4\%$ for normal incidence. When used at 80° incidence, the losses should decrease to $\leq 0.1\%$ according to equation (1).

Although the derivation of equation (1) should make its application at soft x-ray wavelengths less valid, we use it here for estimation purposes for relatively smooth surfaces at 12 nm (120 Å). For example, incidence at 80° on Rh films with 5 Å rms surface roughness would result in 0.8% scattering loss per reflector facet. The net drop in retroreflectance (nine facets) would be about 5% (from 65% to 60%).

Surface-Plasmon Absorption. Polished substrates with the above smooth surfaces are attained in practice on flat and spherical substrates of fused silica, glass, Si, and occasionally SiC. For large angles of incidence, such as 80° , and relatively long wavelengths ≥ 30 nm, still rougher surfaces, e.g. with σ equal to 10 to 15 Å, could be tolerated. However, at wavelengths near a surface plasmon resonance, surface roughness can produce absorption loss within the metal. For Al, such a resonance occurs at 10.54 eV (118 nm) [28], and the effect on reflectance is shown in figure 15. This motivates a tighter limit on the tolerable roughness when using Al reflectors in the vicinity of this wavelengths.

7. Practical Implementation

It is obvious that the practical application of multifacet metal reflectors will require deposition of the films in ultra-high vacuum with the reflector substrates mounted in place in the laser resonator. This is convenient for an FEL oscillator in which the reflectors are usually mounted in vacuum anyway. With this provision, it would be possible to periodically overcoat the metallic films as required to offset the effects of any gradual deterioration that may occur. Of course, the total thickness of the films must not become too great or else surface roughness will become a problem. It is conceivable, too, that an ion gun mounted in the vacuum chamber could be used to periodically sputter away aged films and then deposit fresh layers. Certainly, initial removal of carbonaceous compounds from the vacuum environment by use of a rf plasma discharge, cited above, will also be beneficial.

8. Plans for Implementation

Los Alamos researchers Scott, Arendt, and Newnam have begun a project to implement the multifaceted metal-mirror concept. Included in the research plans are ellipsometric measurements of the oxide- and carbon-contamination growth rates as a function of O_2 , H_2O , and CO partial pressures and reflectance measurements of single- and multiple-facet reflectors for vacuum environments from 10^{-8} to 10^{-10} torr. If the results are encouraging, the multifacet retroreflectors will be eventually used in an XUV FEL oscillator as shown in figure 16. Recent three-dimensional calculations of the single-pass, small-signal gain for a soft x-ray FEL at 12 nm have shown that the 60% net reflectance possible for Rh retromirrors should be sufficient to achieve laser oscillation. This is indeed an exciting prospect!

9. References

- [1] Newnam, B. E. Symposium welcome and perceptions of future research. Natl. Bur. Stand. (U.S.) Spec. Publ. 727; (to be published 1986). vii-x.
- [2] Newnam, B. E. Evolution of free-electron laser development. High Power and Solid State Lasers, Proc. SPIE 622; to be published 1986. 84-92.
- [3] Madey, J. M. J.; Pellegrini, C.; Eds. Free Electron Generation of Extreme Ultraviolet Coherent Radiation. AIP Conf. Proc. No. 118 (Amer. Inst. of Phys., New York); 1984.
- [4] Harris, S. E.; Lucatorto, T. B.; Eds. Laser Techniques in the Extreme Ultraviolet. AIP Conf. Proc. No. 119 (Amer. Inst. of Phys., New York); 1984.
- [5] Rehn, V.; Choyke, W. J. SiC mirrors for synchrotron radiation. Nucl. Instr. and Methods 177, 173-178 (1980).
- [6] Choyke, W. J.; Palik, E. D. Silicon carbide (SiC). Handbook of Optical Constants of Solids, E. D. Palik, Ed. (Academic Press, New York); 1985. 587-596.
- [7] Shiles, E.; Sasaki, T.; Inokuti, M.; Smith, D. Y. Self-consistency and sumrule tests in the Kramers-Kronig analysis of optical data: applications to aluminum. Phys. Rev. B 22, 1612-1628 (1980).
- [8] Smith, D. Y.; Shiles, E.; Inokuti, M. The optical properties and complex dielectric function of metallic aluminum from 0.04 to 10^4 eV. Argonne National Laboratory Report ANL-83-24; March 1983.
- [9] Smith, D. Y.; Shiles, E.; Inokuti, M. The optical properties of metallic aluminum. Handbook of Optical Constants of Solids, E. D. Palik, Ed. (Academic Press, New York); 1985. 369-406.

- [10] Barbee, Jr., T. W.; Mrowka, S.; Hettrick, M. C. Molybdenum-silicon multilayer mirrors for the extreme ultraviolet. *Appl. Opt.* 24, 883-886 (1985).
- [11] Vinogradov, A. V.; Konoplev, N. A.; Popov, A. V. Broad-band mirrors for vacuum ultraviolet and soft x-ray radiation. *Sov. Phys. Dokl.* 27, 741-742 (1982).
- [12] Vinogradov, A. V.; Kozhevnikov, I. V.; Popov, A. V. On wide-band mirrors for soft x-ray range. *Opt. Commun.* 47, 361-363 (1983).
- [13] Vinogradov, A. V.; Sagitov, S. I. New types of mirrors for the soft x-ray range (review). *Sov. J. Quantum Electron.* 13, 1439-1447 (1983).
- [14] Henke, B. L.; Lee, P.; Tanaka, T. J.; Simabukuro, R. L.; Fujikawa, B. K. Low-energy x-ray interaction coefficients: photoabsorption, scattering, and reflection ($E = 100-2000$ eV, $Z = 1-94$). *Atomic Data and Nuclear Data Tables* 27, N1, 1-144 (1982).
- [15] Hagemann, H.-J.; Gudat, W.; Kunz, C. Optical constants from the far infrared to the x-ray region: Mg, Al, Cu, Ag, Au, Bi, C, and Al_2O_3 . *J. Op. Soc. Am.* 65, 742-744 (1975); also DESY Report SR-74-7; May 1974.
- [16] Palik, E. D., Ed. Handbook of Optical Constants of Solids, (Academic Press, New York); 1985.
- [17] Goldstein, J. C.; Newnam, B. E.; Cooper, R. K.; Comly, Jr., J. C. An xuv/vuv free-electron laser oscillator. Laser Techniques in the Extreme Ultraviolet. AIP Conf. Proc. No. 119, (Amer. Inst. of Physics, New York); 1984. 293-303.
- [18] Edwards, D. F. Silicon (Si). Handbook of Optical Constants of Solids. E. D. Palik, Ed. (Academic Press, New York); 1985. 547-569.
- [19] Lynch, D. W.; Hunter, W. R. Comments on the optical constants of metals and an introduction to the data for several metals. Handbook of Optical Constants of Solids, E. D. Palik, Ed. (Academic Press, New York); 1985. 275-367.
- [20] Feuerbacher, B. P. Steinmann, W. Reflectance of evaporated aluminum films in the 1050-1600 Å region, and the influence of the surface plasmon," *Opt. Commun.* 1, 81-85 (1969).
- [21] Bennett, H. E. Naval Weapons Center, private communication. July 1985.
- [22] Boller, K.; Haelbich, R.-P.; Hogrefe, H.; Jark, W.; Kunz, C. Investigation of carbon contamination of mirror surfaces exposed to synchrotron radiation. *Nucl. Instr. and Methods in Physics Res.* 208, 273-279 (1983).
- [23] Samson, J. A. R., University of Nebraska, private communication, 1986.
- [24] Johnson, E. D.; Garrett, R. F.; Williams, G. P.; Knotek, M. L. In-situ reactive glow discharge cleaning of x-ray optical surfaces. Presented at the VUV8 Vacuum Ultraviolet Radiation Physics Conf., Lund, Sweden, August 1986; to be published in *Rev. Sci. Instr.*, 1987.
- [25] Bennett, H. E.; Porteus, J. O. Relation between surface roughness and specular reflectance at normal incidence. *J. Opt. Soc. A.* 51, 123-129 (1961).
- [26] Bennett, H. E. Specular reflectance of aluminized ground glass and the height distribution of surface irregularities. *J. Opt. Soc. Am.* 53, 1389-1394 (1963).
- [27] Haelbich, R.-P.; Segmuller, A.; Spiller, E. Smooth multilayer films suitable for x-ray mirrors. *Appl. Phys. Lett.* 34, 184-186 (1979).
- [28] Endriz, J. G.; Spicer, W. Study of aluminum films. I. Optical studies of reflectance drops and surface oscillations on controlled-roughness films. *Phys. Rev. B* 4, 4144-4159 (1971).

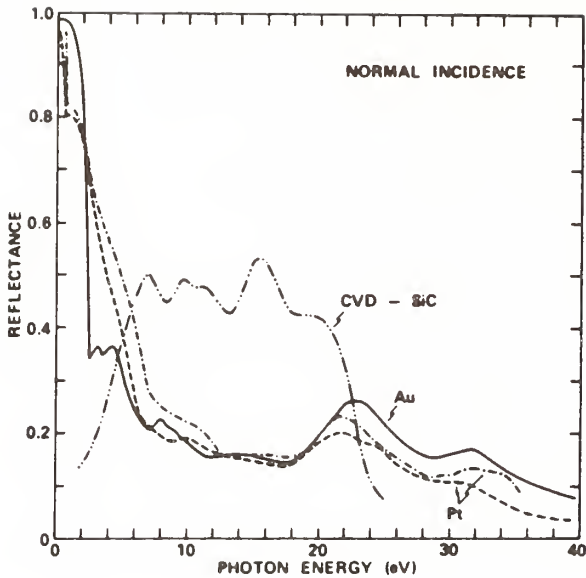


Figure 1. Reflectance of CVD-SiC at normal-incidence with comparison to platinum and gold films. After Rehn and Choyke [5].

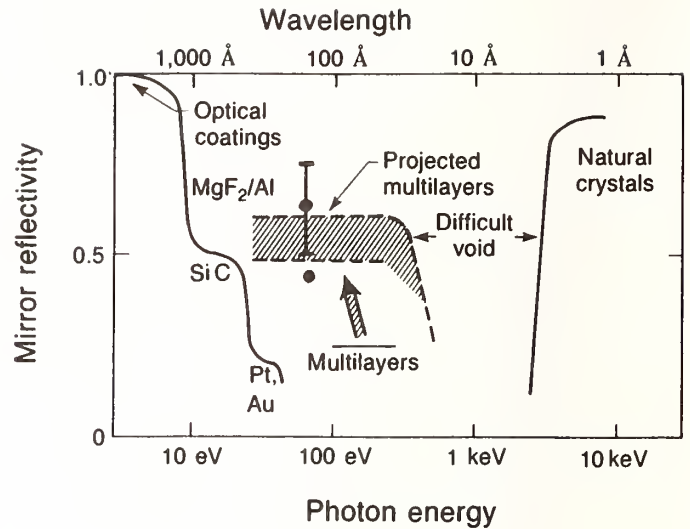


Figure 2. Present and projected reflectance of normal-incidence mirror configurations as compiled by Attwood, et al. [11]. Recent data points are those for Mo/Si multilayer reflectors produced by Barbee, et al. [10].

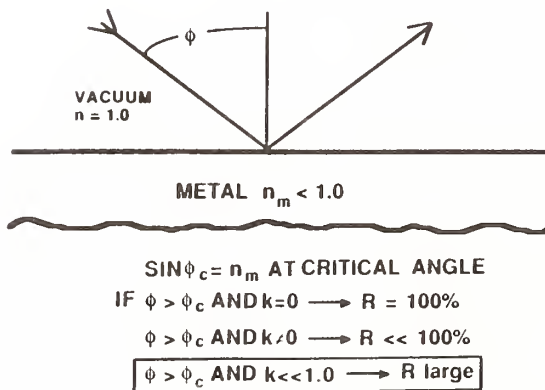


Figure 3. Reflection of an optical beam from a vacuum-metal interface for angles larger than the critical angle $\phi_c = \sin^{-1}n/n_0$. If $k = 0$ when $n < 1$, total external reflection occurs; with k sufficiently small, very large reflection can occur.

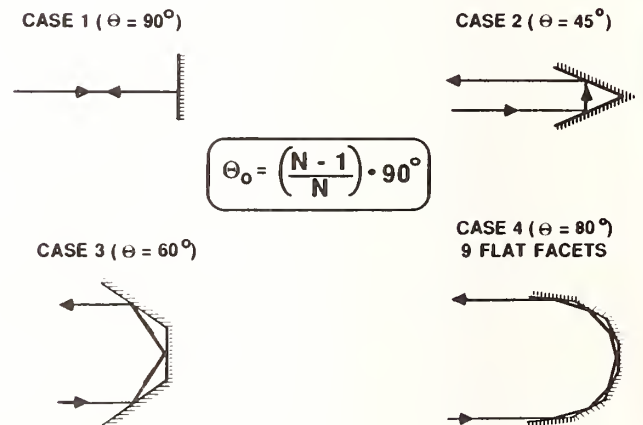


Figure 4. Multifacet retroreflector composed of N flat metallic reflectors. Total-external reflection is possible only when the number of mirror facets N is large enough so that the angle of incidence $\phi = 90^\circ \times (N - 1)/N > \phi_c$.

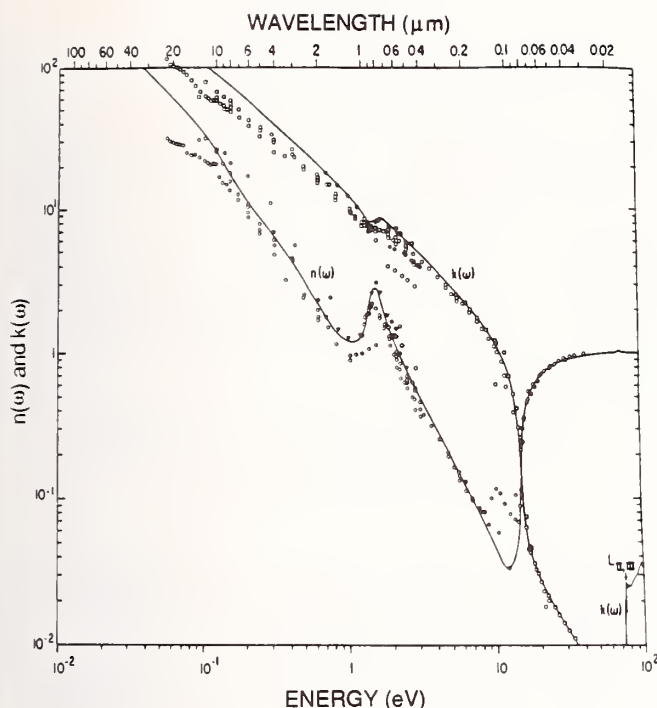


Figure 5. Spectral dependence of the complex refractive index of aluminum films deposited in high vacuum (after Smith, et al. [8,9]). Semi-total external reflectance is possible from 25 to 80 nm where both n and k are simultaneously less than unity.

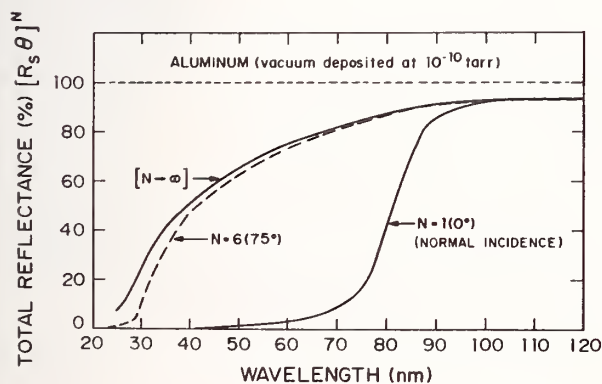


Figure 7. Total retroreflectance ($\phi=180^\circ$) versus XUV wavelength for multifacet aluminum mirrors deposited on smooth SiC in ultra-high vacuum. Calculations were made for S-polarization using the tabulation of optical constants by Smith, et al. [8,9]. Below 90 nm, the reflectance attainable with multifacet mirrors is much greater than that for a single ($N=1$), normal-incidence Al mirror.

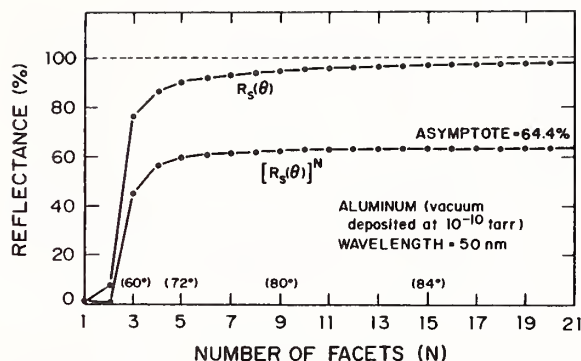


Figure 6. Calculated retroreflectance ($\phi=180^\circ$) and single-facet reflectance for S-polarized XUV radiation at 50 nm for multifacet aluminum films deposited on smooth SiC substrates in ultra-high vacuum. Calculations made use of the tabulation of optical constants by Smith, et al. [8,9]. Notably, only six mirror facets are needed to reach 60% reflectance with 64.4% being the maximum achievable.

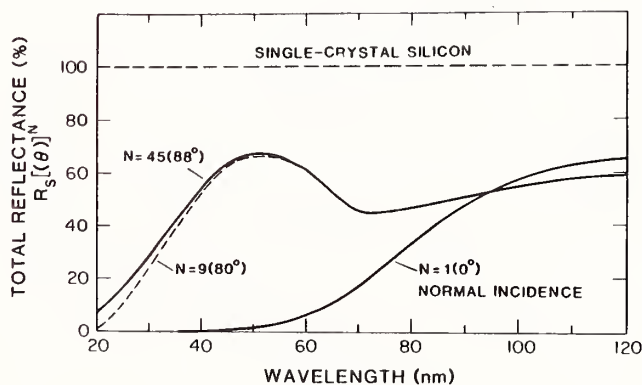


Figure 8. Total retroreflectance ($\phi=180^\circ$) versus XUV wavelength for multifacet, crystalline Si films deposited on smooth Si in ultra-high vacuum. Calculations were made for S-polarization using the optical constant compilation by Edwards [18]. Below 90 nm, the reflectance attainable with multifacet mirrors is much greater than that for a single ($N=1$) normal-incidence Si mirror.

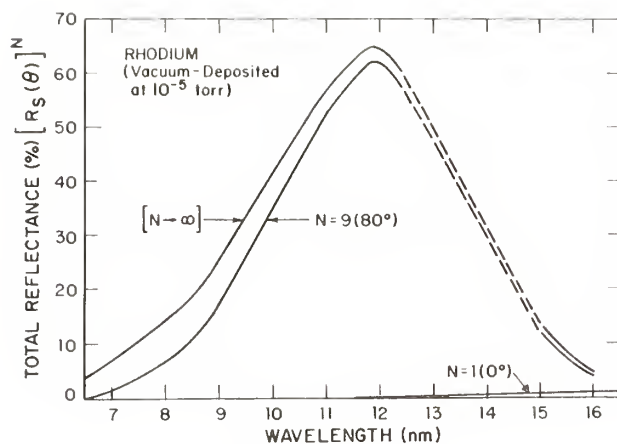


Figure 9. Retroreflectance of multifaceted rhodium coatings on smooth SiC substrates in the soft x-ray region for S-polarized radiation. Optical constants for Rh films deposited in a moderate vacuum (10^{-5} torr) were used in the calculations because oxidation is not serious for Rh at ambient temperatures [19]. Retroreflectance greater than 60% is calculated at 12 nm.

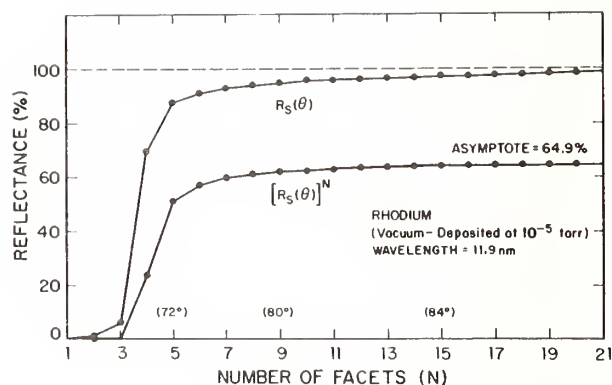


Figure 10. Calculated retroreflectance and single-surface reflectance of rhodium films on smooth SiC for S-polarized radiation at 11.9 nm as a function of the number of mirror facets. Only seven mirror facets are needed to reach 60% net reflectance with 64.9% maximum achievable. Optical constant tabulations by Lynch and Hunter [19] were used.

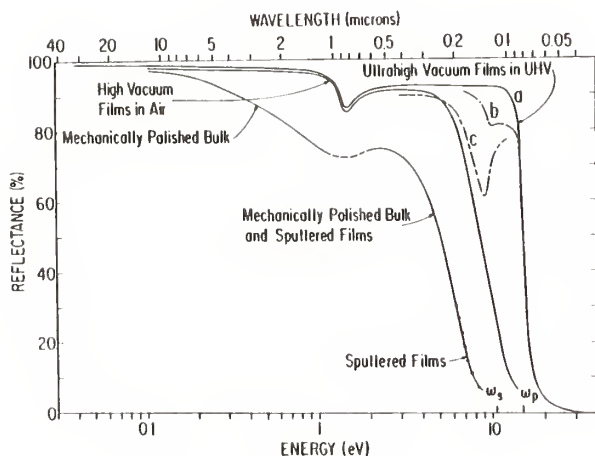


Figure 11. Reflectance of various types of aluminum surfaces at room temperature (after Smith, et al. [9]). Highest reflectance (curve a) is achieved with Al films deposited on substrates in ultra-high vacuum (10^{-9} to 10^{-10} torr) with high deposition rates. The effect of light scattering and surface plasmon absorption (at 10.6 eV) is shown by curves b and c. Curve b is for Al on a clean microscope slide and curve c is for a uhv film with rms roughness of 18 Å [15].

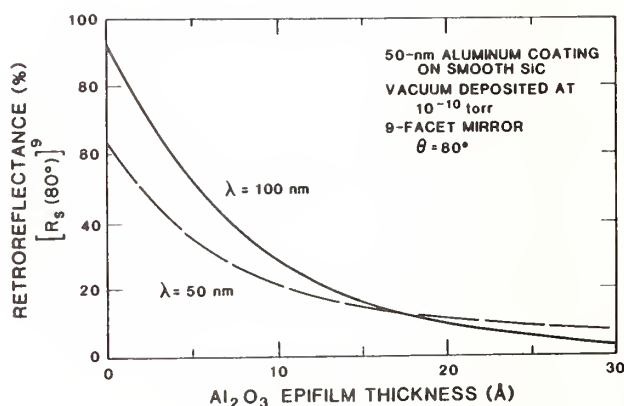


Figure 12. Influence of oxide thickness on the calculated retroreflectance (S-polarization) of a nine-facet aluminum mirror at XUV wavelengths of 50 and 100 nm. Optical constant tabulations for Al by Smith, et al. [8,9] and Al_2O_3 by Hagemann et al. [15] were used.

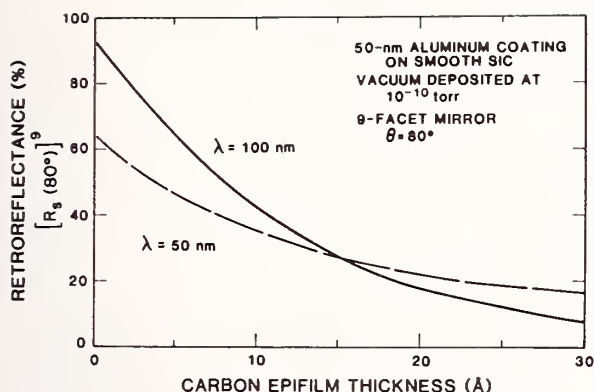


Figure 13. Influence of carbon film contamination on the calculated retroreflectance (S-polarization) of a nine-facet aluminum-coated mirror (smooth SiC substrate) at XUV wavelengths of 50 and 100 nm. Optical constant tabulations for Al by Smith, et al. [8,9] and C by Hagemann, et al. [15] were used.

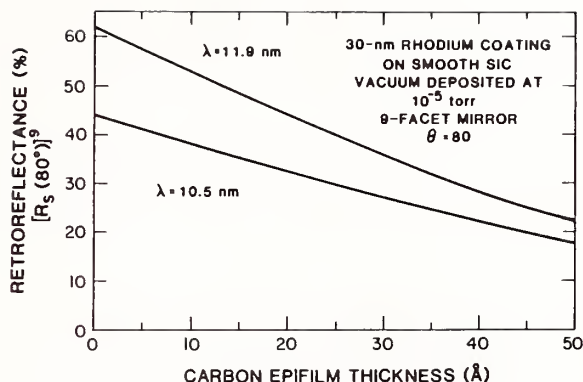


Figure 14. Influence of carbon film contamination on the calculated retroreflectance (S-polarization) of a nine-facet, rhodium-coated mirror (smooth SiC substrate) at soft x-ray wavelengths of 10.5 and 11.9 nm. Optical constant tabulations for Rh by Lynch and Hunter [19] and C by Hagemann, et al. [15] were used.

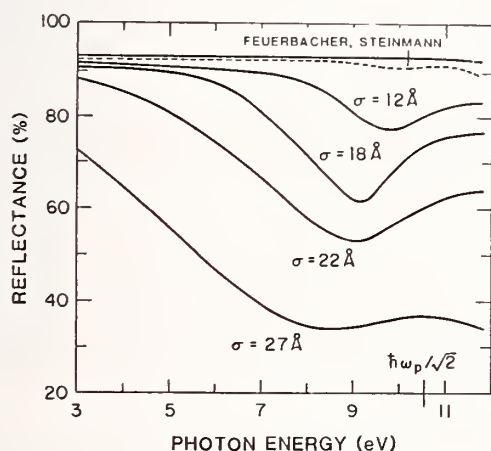


Figure 15. Degradation of the normal-incidence reflectance of uhv aluminum coatings on rough surfaces caused by the surface plasmon absorption resonance at 10.6 eV. Use of a fire-polished microscope slide (Feuerbacher and Steinmann [20]) or a bowl-feed polished glass substrate minimized plasmon absorption (after Endriz and Spicer [28]).

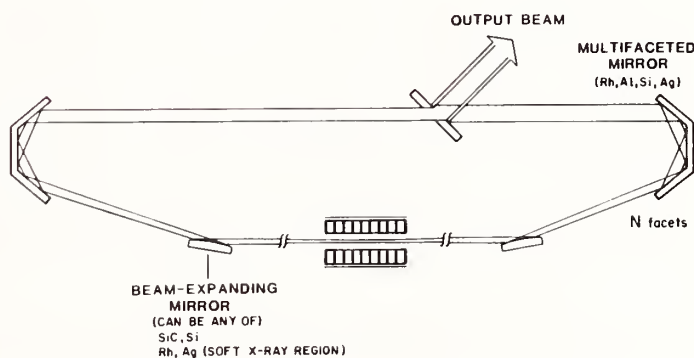


Figure 16. A free-electron laser ring-resonator design for extreme-ultraviolet and soft x-ray wavelengths has two unique features: (1) intra-cavity grazing-incidence mirrors (hyperboloids) to expand the beam incident on (2) multifaceted retroreflectors (N-1 flats and one off-axis paraboloid for beam collimation). Below 100 nm the multifaceted mirrors exhibiting semi-total external reflectance, e.g. Al, Si, Rh, Ag, Ru, Os are used to attain a retroreflectance $\geq 40\%$ in various XUV wavelength regions.

The Design of Optimum High Reflectivity Coatings
for Grazing Angles of Incidence

Jeffrey B. Shellan

W. J. Schafer Assoc., 22222 Sherman Way, #205
Canoga Park, CA 91303

Presented by Title only

Abstract

Although quarter-wave multilayer dielectric coatings (QW MLDCs) usually offer the highest reflectivity possible at a single wavelength, this may not be the case at grazing angles of incidence. For incident angles greater than the Brewster angle, the p polarization absorption can easily be several orders of magnitude higher than the s polarization absorption due to the destructive interference between the reflection from the superstrate - top layer interface and the rest of the coating. An analytic approach is developed for designing optimum reflectivity coatings at grazing angles of incidence, once the fraction of s and p polarized light is given. These coatings can give at least an order of magnitude reduction over QW MLDCs in total coating absorption, even for the case where less than 0.1% of the incident radiation is p polarized. The absorption of the designs found from the analytic results compare favorably with designs generated using numerical methods of non-linear optimization.

Key words: FEL optics; grazing angle of incidence coatings; optical coatings

1. Introduction

The purpose of this paper is to present analytic results that can be used to design multilayer dielectric coatings (MLDCs) with maximum reflectivity at grazing angles of incidence. The designs found can have absorptions orders of magnitude less than quarter-wave stack designs, since the p polarization reflectivity of quarter-wave stacks can be quite low at grazing angles. The closed form solutions found compare quite favorably with designs generated using numerical non-linear optimization procedures.

Grazing angle of incidence optics are used in numerous applications where ultra-high reflectivity, high damage thresholds, or reflectors in the far ultra-violet and soft x-ray are needed. For example, the high flux levels needed in the gain region of a free electron laser (FEL) are several orders of magnitude greater than can be handled by conventional optics. A possible solution to this problem is to use a grazing incident angle mirror (GIAM) to expand the beam geometrically before it strikes a mirror normally. If α is the grazing angle, defined as $\pi/2$ minus the incident angle, then the beam foot print will be increased by a factor $1/\alpha$ (for small α). In addition, the absorption will be shown to vary as α , giving an absorbed flux per area proportional to α^2 , and damage threshold proportional to $1/\alpha^2$. It has been shown by S. A. Mani and J. H. Hammond¹ that the optimum value of α , for minimizing the resonator length, is on the order of one to two degrees for high power FELs envisioned for the near future.

Another area where grazing incident optics are needed is for the reflection of very short wavelengths where the index of refraction of most dielectrics approaches 1 and reflection from bare metal at normal incidence is quite low.

For most applications where maximum reflectivity at a single wavelength is desired a quarter-wave MLDC is used, since it usually allows the coherent addition of the reflections from each dielectric interface. The advantages of deviating from a quarter-wave stack have been discussed for the case of slightly absorbing dielectric layers,^{2,3} as an attempt to increase the damage threshold by reducing the internal flux,⁴ and as a means of controlling the difference in s and p polarization phase shifts.⁵

Figure 1 illustrates the phase shifts experienced by a beam reflection from each of a number of dielectric interfaces. The O superstrate is usually air, the S layer represents the substrate, and H and L represent high and low index layers, respectively. In most cases the phase is shifted by π when radiation incident from a low index medium is reflected from a high

index medium. There is no phase shift when the light incident from a high index material is reflected by a low index material. Thus if the layer thicknesses in figure 1 are all quarter wave at the incident wavelength, maximum reflectivity will result for both s and p polarized light. The phase shifts shown in figure 1 hold for all incident angles ϕ in the case of s polarized light. They also hold for p polarized light if ϕ is less than the Brewster angle, ($\tan \phi_B \equiv n_H/n_0$, where n_H and n_0 are the indices of the high index layer and the superstrate respectively). For ϕ greater than ϕ_B , the superstrate - high index layer phase shift is 0 for p polarized light as shown in figure 2. Thus the quarter-wave stack will give poor p polarization reflectivity at grazing angles $\phi > \phi_B$.

From figures 1 and 2 it is clear that if only s polarization is present, then the quarter-wave design is best, while if only p polarization is present the top layer should be half-wave and the remaining layers quarter-wave thick ($\phi > \phi_B$). The purpose of this paper is to develop expressions for the coating design that will give the minimum total absorption as a function of the fraction of s and p light incident on the MLDC.

Section 2 will develop the theory used to find the optimum coating. A review will be given of work by Shellan⁶ in which simple expressions were found for the reflectivity of quarter-wave stacks at oblique angles of incidence. This analysis technique is then extended to the case of one layer being non-quarter wave thickness. Section 3 uses these results to find the coating with maximum reflectivity. Section 4 compares the results of sections 2 and 3 with exact computer results based on the matrix method. Numerical non-linear optimization solutions are compared with the analytic solutions and the reflectivities in the two cases are found to agree closely.

2. Analysis Approach

M. Sparks⁷, H. E. Bennett and D. K. Burge⁸, and Jeffrey B. Shellan⁶ have found simple but powerful techniques for calculating the optical properties of quarter-wave reflectors. The approach by Shellan⁶ is the most general since it is valid for arbitrary angle of incidence. The techniques will be reviewed and then extended to the case of a quarter-wave stack containing one layer of arbitrary thickness. Expressions can be developed to include the effects of substrate, volume, and interface absorption, as was done in references 6, 7, and 8, but only substrate absorption will be considered here. For high quality coatings, especially ones deposited with advanced deposition techniques such as ion beam sputtering, the substrate absorption will usually dominate unless many layers are used. For the grazing angles of primary interest in this paper, designs with 1, 2, or 3 layer pairs are probably sufficient.

Figure 3 illustrates the E field distribution and B field distribution for s and p polarized light, respectively, within a quarter-wave stack. The quantities O, H, L, and S designate the superstrate with index n_0 , high-index layer with index n_H , low-index layer of index n_L , and the substrate with index n_s . The E field with incident amplitude E_0 (normal to the plane of incidence) is shown by the solid line and the amplitude attenuation factor S_{ij} was shown⁶ to be given by

$$S_{ij} = n_i/n_j \quad (1)$$

$$\text{where } n_i \equiv (n_i^2 - n_0^2 \sin^2 \phi)^{1/2} \quad (2)$$

ϕ = angle of incidence from superstrate

The B field distribution, used to find the properties of p polarized light, is given by the dashed curve in figure 3 and its attenuation factor P_{ij} was shown to be equal to

$$P_{ij} = (n_i^2 n_j)/(n_j^2 n_i) \quad (3)$$

The fields are sinusoidal in each layer, and the thickness of layer i in the quarter-wave stack is

$$d_i = \lambda / (4n_i) \quad (4)$$

where λ is the wavelength in free space.

From figure 3, the electric field penetrating into the substrate for the S polarization is given by $S_{0H}S_{LH}^{N-1}S_{LS}^2E_0$, where $2N$ is the total number of layers and E_0 is the incident field. The incident flux is proportional to $n_0E_0^2\cos^2\phi$, whereas the flux penetrating into the substrate is proportional to $n_S(S_{0H}S_{LH}^{N-1}S_{LS}^2E_0)^2\cos\phi_S$, where ϕ and ϕ_S are the angle of incidence and the propagation angle in the substrate, respectively. The fraction of energy penetrating into the substrate, the absorption of the substrate, for $2N$ layers and S-polarized light is

$$\begin{aligned} A_S(2N) &= n_S(S_{0H}S_{LH}^{N-1}S_{LS}^2E_0)^2\cos\phi_S / (n_0E_0^2\cos^2\phi) \\ &= 4S_{0S}S_{LH}^{2N}. \end{aligned} \quad (5)$$

From the form of the B-field distribution for the P-polarized light in figure 3, the B field penetrating into the substrate is equal to $P_{LH}^{N/2}B_0$. The flux is proportional to $(1/n)B^2\cos\phi$, and the P-polarization substrate absorption for a coating with $2N$ layers is found to be

$$A_P(2N) = 4P_{0S}P_{LH}^{2N}. \quad (6)$$

If we consider the case of grazing incident angle mirrors (GIAMs) and neglect second order terms in the grazing angle α ($\alpha = \pi/2 - \phi$), then equations 5 and 6 can be rewritten as

$$\begin{aligned} A_S(2N) &\approx 4(S_{LH}^0)^{2N} S_{LS}^0 \frac{n_0}{n_L} \alpha \\ & \quad (7) \end{aligned}$$

$$\begin{aligned} A_P(2N) &\approx 4(P_{LH}^0)^{2N} \cdot P_{LS}^0 \frac{n_0 n_L^0}{n_L^2} \frac{1}{\alpha} \\ & \quad (8) \end{aligned}$$

where S_{ij}^0 , n_L^0 , P_{ij}^0 are equal to S_{ij} , n_L , and P_{ij} evaluated at $\phi = \pi/2$ ($\alpha=0$).

Equations 7 and 8 indicate that for a quarter-wave stack the s and p polarization are proportional to α and $1/\alpha$, respectively, for GIAMs. In deriving equations 5 and 6 it was assumed that the absorption is small and thus equation 8 will breakdown as α approaches zero.

Up to this point we have implicitly assumed that the substrate is a dielectric since we have taken n_j , n_i , S_{ij} , and P_{ij} to be real quantities. For a metal, these quantities are complex, but we can effectively make S_{ij} , and P_{ij} real by covering the metal substrate with a thin dielectric layer. The details of this are covered in Reference 6.

Although the s and p absorptions for bare metal can differ by almost two orders of magnitude in the visible, the difference in the two absorptions is even more pronounced for MLDCs at grazing angles. The ratio of the MLDC absorptions can be 3 to 5 orders of magnitude at $\alpha \sim 1^\circ 2''$. For this reason it is desirable to alter the quarter-wave stack slightly to improve the p polarization reflectivity. Expressions will now be derived for the s and p absorption for a modified quarter wave stack.

Figure 4 illustrates the effects on the internal electric field of including one layer, the n^{th} low index layer, of arbitrary thickness. The tangential component of the electric field is fixed at zero at the substrate interface, for most high reflectivity coatings containing a metal substrate. This has been verified by exact computer runs based on the matrix method^{9, 10}. The field distribution is the same as for a perfect quarter-wave stack between the substrate interface and the perturbed layer.

The thickness of the n^{th} low index layer (n is measured from the superstrate) is $\frac{\pi}{2} + \Delta_L^{(n)}$, measured in phase units. The actual thickness of the perturbed layer is thus

$$\lambda_L^{(n)} = (1 + 2\Delta_L^{(n)})/\pi \lambda_{1/4} \quad (9)$$

where $\lambda_{1/4}$ is the quarter wave thickness.

The perturbed layer has been expanded in the drawing for clarity, but its unperturbed width, from the LH interface to the vertically dashed line (of phase width $\pi/2$), is the same width as all the other unperturbed L layers. The distance $\Delta_L^{(n)}$ from the vertically dashed line to the HL interface is the perturbation. If we start from the substrate where the penetrating field has amplitude $2E_S$ and work backward to the n^{th} L layer, the amplitude of the sine wave in the perturbed layer is $2E_S S_{SL} S_{HL}^{N-n} (-1)^{N-n+1}$ for S-polarized light.

The equation for the field in the n^{th} L layer in a coordinate system whose origin is at the front surface of the layer (see fig. 4) is

$$D \cos[x - \Delta_L^{(n)}] = D \cos \Delta_L^{(n)} \cos x + D \sin \Delta_L^{(n)} \sin x, \quad (10)$$

where

$$D \equiv 2E_S S_{SL} S_{HL}^{N-n} (-1)^{N-n+1} \quad (11)$$

The $\cos x$ and $\sin x$ field components of $\cos[x - \Delta_L^{(n)}]$ have been drawn in dashed lines in figure 4. Equation (1) indicates that when the null of a sinusoidal wave is at an ij interface, the ratio of the wave amplitude on the i side to the j side is S_{ij} . On the other hand, if the peak of the sinusoidal wave is at the interface, the amplitude is the same in the i and j regions. Using this fact, we can easily find the amplitude of the $\sin x$ and $\cos x$ components at the mirror surface. At a y -coordinate system whose origin is at the mirror surface (see fig. 4), the field is

$$E(y) = (-1)^n D [S_{HL}^{n-1} S_{HO} \cos \Delta_L^{(n)} \sin y + S_{LH}^n \sin \Delta_L^{(n)} \cos y]. \quad (12)$$

This can be expressed as the sum of a forward-propagating wave and backward-propagating wave

$$C [e^{-iy} + (G - iF)/(G + iF) e^{iy}], \quad (13)$$

where

$$C = \frac{(-1)^n D}{2} [i S_{HL}^{n-1} S_{HO} \cos \Delta_L^{(n)} + S_{LH}^n \sin \Delta_L^{(n)}] \quad (14)$$

and F and G are defined as the coefficients of $\sin y$ and $\cos y$, respectively, in equation 12.

Since the incident intensity is equal to $|C|^2$, the absorption is proportional to $|E_S/C|^2$, with the constant of proportionality quickly found by comparing equation 5 with $|E_S/C|^2$ for the case $\Delta_L^{(n)} = 0$. The s polarization absorption for the case of quarter-wave stack where the n^{th} low index layer is perturbed by $\Delta_L^{(n)}$ is found to be

$$A_S(2N, \Delta_L^{(n)}) = \frac{4 S_{OS} S_{LH}^{2N}}{\cos^2 \Delta_L^{(n)} + [S_{LH}^{2N-1} S_{OH} \sin \Delta_L^{(n)}]^2} \quad (15)$$

In a similar manner, an expression can be found for the s polarization absorption, $A_S(2N, \Delta_H^{(n)})$, a quarter-wave stack with the n^{th} high index layer shifted by $\Delta_H^{(n)}$ phase units.

$$A_S(2N, \Delta_H^{(n)}) = \frac{4 S_{OS} S_{LH}^{2N}}{\cos^2 \Delta_H^{(n)} + [S_{LH}^{2(n-1)} S_{OH} \sin \Delta_H^{(n)}]^2} \quad (16)$$

The corresponding expressions for p polarization are

$$A_p(2N, \Delta_L^{(n)}) = \frac{4 P_{OS} P_{LH}^{2N}}{\cos^2 \Delta_L^{(n)} + [P_{LH}^{2(n-1)} P_{OH} \sin \Delta_L^{(n)}]^2} \quad (17)$$

$$A_p(2N, \Delta_H^{(n)}) = \frac{4 P_{OS} P_{LH}^{2N}}{\cos^2 \Delta_H^{(n)} + [P_{LH}^{2(n-1)} P_{OH} \sin \Delta_H^{(n)}]^2} \quad (18)$$

Equation 8 indicated that the p polarization absorption varies as $1/\alpha$ for small grazing angles and quarter-wave stacks. Since P_{OS} as well as P_{OH} vary as $1/\alpha$, equations 17 and 18 indicate that $A_p(2N, \Delta_L^{(n)})$ and $A_p(2N, \Delta_H^{(n)})$ will vary as α , not $1/\alpha$, for sufficiently small α , as long as $\sin \Delta^{(n)} \neq 0$. Equations 15 through 18 also indicate that the absorption is periodic in $\Delta^{(n)}$ with period equal to π (half wave thicknesses), as expected.

Equations 15 through 18 will now be used to find optimum GIAM reflectors.

3. Optimum Grazing Incidence Coatings

If we let A_t be the total substrate absorption due to both s and p absorption, and f_s be the fraction of s polarized light incident on the MLDC, then

$$A_t = f_s A_s(2N) + (1-f_s) A_p(2N) \quad (19)$$

where equation 15 or 16 is used for $A_s(2N)$ and equation 17 or 18 is used for $A_p(2N)$, depending on where a high or low index layer is perturbed.

If we differentiate equation 19 with respect to $\sin \Delta^{(n)}$, we find two solutions for the coating design giving lowest total absorption, $A_t^{(min)}$. The result is

$$\sin^2 \Delta_i^{(n)} = 0 \quad (20)$$

or

$$\sin^2 \Delta_i^{(n)} = \frac{[(1-f_s) P_{OS} P_{LH}^{2N} (P_{OH}^{(in)^2} - 1)]^{1/2} - [f_s S_{OS} S_{LH}^{2N} (1 - S_{OH}^{(in)^2})]^{1/2}}{(1 - S_{OH}^{(in)^2}) [(1-f_s) P_{OS} P_{LH}^{2N} (P_{OH}^{(in)^2} - 1)]^{1/2} + (P_{OH}^{(in)^2} - 1) [f_s S_{OS} S_{LH}^{2N} (1 - S_{OH}^{(in)^2})]^{1/2}} \quad (21)$$

where

$$i = L \text{ or } H, n = 1, 2, \dots, N$$

and

$$s_{OH}^{(Hn)} \equiv s_{LH}^{2(n-1)} s_{OH} \quad (22)$$

$$p_{OH}^{(Hn)} \equiv p_{LH}^{2(n-1)} p_{OH} \quad (23)$$

$$s_{OH}^{(Ln)} \equiv s_{LH}^{2n-1} s_{OH} \quad (24)$$

$$p_{OH}^{(Ln)} \equiv p_{LH}^{2n-1} p_{OH} \quad (25)$$

Equation 21 will give the minimum absorption design if two conditions are met. Otherwise equation 20, which defines the standard quarter-wave stack, will give the optimum coating. The first of these two conditions is that

$$p_{OH}^{(in)^2} > 1 \quad (26)$$

For the case of thickness adjustments to the outermost high-index layer, $p_{OH}^{(in)}$ = p_{OH} and the condition $p_{OH}=1$ defines the Brewster angle discussed in the introduction. The second condition that must hold for equation 21 to give the best coating is that the numerator be positive. This in effect defines a critical value for $f_p \equiv (1-f_s)$, the fraction of p polarized light.

If equations 15 through 19 and 21 are combined, the absorption can be found for the optimum MLDC for GIAMs, $A_t^{(min)}$. The result is

$$A_t^{(\min)} = 4 \left\{ \left[\frac{f_s s_{OS} s_{LH}^{2N}}{1 - s_{OH}^{(in)^2}} \right]^{1/2} + \left[\frac{(1 - f_s) p_{OS} p_{LH}^{2N}}{p_{OH}^{(in)^2} - 1} \right]^{1/2} \right\} .$$

$$\cdot \left\{ \frac{[(1 - s_{OH}^{(in)^2}) [(1 - f_s) p_{OS} p_{LH}^{2N} (p_{OH}^{(in)^2} - 1)]^{1/2} + (p_{OH}^{(in)^2} - 1) [f_s s_{OS} s_{LH}^{2N} (1 - s_{OH}^{(in)^2})]^{1/2}}{p_{OH}^{(in)^2} - s_{OH}^{(in)^2}} \right\} \quad (27)$$

$$i = L \text{ or } H, n = 1, 2, \dots, N$$

It can be shown that the best layer to adjust to achieve the lowest absorption is the outermost high index layer. Thus $s_{OH}^{(in)}$ and $p_{OH}^{(in)}$ should be replaced with s_{OH} and p_{OH} in equations 21 and 27.

Section 4. will compare the predictions of equations 15, 16, 17, 18, and 27 with numerical results. The $A_t^{(\min)}$ given in equation 27, which is based on a quarter-wave stack with only the outer layer adjusted, will be shown to compare quite favorably with that obtained using a numerical non-linear optimization procedure in which all layers can be adjusted.

4. Comparison Of Analytic And Exact Results

The accuracies of equations 15 through 19 can be verified by comparing them with numerical results. The computer results were obtained by using 2×2 matrices to represent the effects of dielectric discontinuities and propagation in a uniform dielectric layer.^{9,10} The relationship between left-and right-traveling light is established at each side of the dielectric discontinuities and at each end of uniform layers. The product of these matrices then gives a relationship between incident, reflected, and transmitted light for the entire system.

Figure 5 is a plot of A_s and A_p versus outer-layer thickness for the coating $\text{Si}(\text{Al}_2\text{O}_3/\text{ZnS})^N$ comparing the analytic results (equations 16 and 18) with exact results. The curves are indistinguishable for A_s and only differ for A_p in regions of high absorption. All layers, other than the top ZnS layer, are quarter-wave thick at the incident angle of 88° . There is almost a four order of magnitude change in the s absorption and more than a two order of magnitude variation in A_p as $\Delta_H^{(1)}$ is varied from 0 to π .

In order to assess the optimum MLDC design given in equation 21, the absorption given in equation 27 was compared with that of a quarter-wave stack ("substrate compensated design") as well as that generated using a numerical non-linear optimization procedure.

A $\text{Ag} (\text{SiO}_2/\text{ZrO}_2)^N$ "substrate compensated" quarter-wave stack at incident angle 89° with one adjustable layer was used ($\lambda=1.06\mu\text{m}$, $n_H=2.1$, $n_L=1.4$, $n_S=0.18+7.05i$). The absorption was calculated using equation 27 for $N = 1, 2, 3, 4, 5$ and $n = 1, 2, \dots, N$ for $f_s = 0.990$ to $f_s=0.999$. It was found in all cases that varying the thickness of the top layer gave the lowest absorptions and that the absorption was 6 to 100 times less than for the quarter-wave reflector, depending on the number of layers used.

There are many techniques of non-linear optimization used in coating synthesis.^{11,12,13,14} The one first suggested by Dobrowolski was used with the merit function equal to the total absorption, and compared with the analytic results.

Figure 6 compares the absorption for a quarter-wave design, the ideal coating found from equations 21 and 27, and the numerically generated design. In all cases the absorption of the analytic result is within 10% of that found using the non-linear optimization computer program.

5. Summary and Conclusion

Equations were derived for the reflectivity of quarter-wave stacks containing one layer of arbitrary thickness. The expressions were compared with exact numerical results and found to agree quite closely as long as the total absorption was small. These results were then used to find the MLDC with highest reflectivity at angles of incidence greater than the Brewster angle, once the fraction of s and p polarized light was specified. The designs found can have absorptions at least an order of magnitude less than QW designs, even if only 0.1% of the incident flux is p polarized. Good agreement was found between the absorptions of the analytically generated designs and that of coatings found using numerical methods.

References

- [1] S. A. Mani and J. H. Hammond, "Optics and resonator design issues for high-power free electron lasers," Proceedings of The International Conference on Lasers, New Orleans, La., December, 1981.
- [2] C. K. Carniglia and Joseph H. Apfel, "Maximum reflectance of multilayer dielectric mirrors in the presence of slight absorption," J. Opt. Soc. Am. 70, 523-534 (1980).
- [3] P. H. Lissberger, "The ultimate reflectance of multilayer dielectric mirrors," Opt. Acta 25, 291-298 (1978).
- [4] Joseph H. Apfel, "Optical coating design with reduced electric field intensity," Appl. Opt. 16, 1880-1885 (1977).
- [5] W. H. Southwell, "Multilayer coatings producing 90° phase change," Appl. Opt. 18, 1875 (1979).
- [6] Jeffrey B. Shellan, "Simple expressions for predicting substrate, volume, and interface absorption and reflective phase shifts in high-reflectance quarter-wave stacks at oblique angles of incidence," J. Opt. Soc. Am. 73, 1272-1281 (1983).
- [7] M. Sparks, "A simple method for calculating the optical properties of multilayer-dielectric reflectors," J. Opt. Soc. Am. 67, 1590-1594 (1977).
- [8] H. E. Bennett and D. K. Burge, "Simple expressions for predicting the effect of volume and interface absorption and of scattering in high-reflectance or anti-reflectance multilayer coatings," J. Opt. Soc. Am. 70, 268-276 (1980).
- [9] P. Yeh, A. Yariv, and Chi-Shain Hong, "Electromagnetic propagation in periodic stratified media. I. General Theory," J. Opt. Soc. Am. 67, 423-438 (1977).
- [10] M. Born and E. Wolf, Principles of Optics (MacMillan, New York, 1964).
- [11] Arnold L. Bloom, "Refining and optimization in multilayers," Appl. Opt. 20, 66-73 (1981).
- [12] William E. Case, "New synthesis method for optical thin-film coatings," Appl. Opt. 22, 4111-4117 (1983).
- [13] J. A. Dobrowolski, "Completely automatic synthesis of optical thin-film systems," Appl. Opt. 4, 937-946 (1965).
- [14] J. F. Tang and Q. Zheng, "Automatic design of optical thin-film systems - merit function and numerical optimization method," J. Opt. Soc. Am. 72, 1522-1528 (1982).

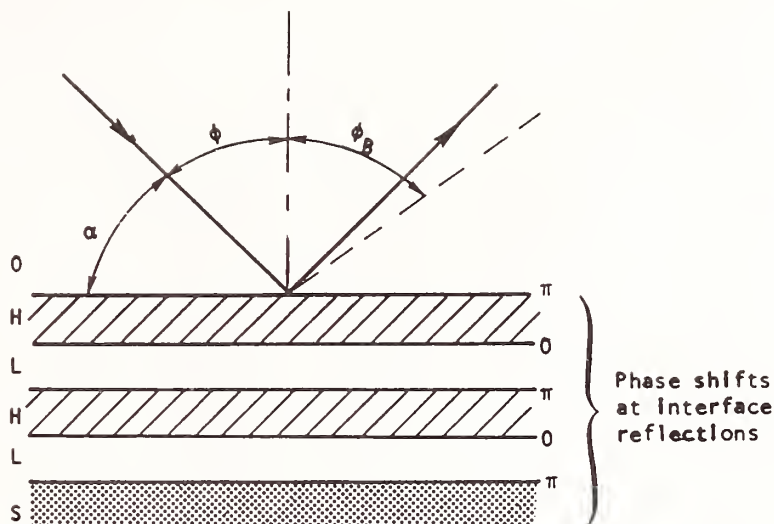


Figure 1. Phase shifts at each dielectric interface for s polarized light for all incident angles and for p polarized light if $\phi < \phi_B$, where ϕ_B is the Brewster angle. (H and L designate the high and low index layers, 0 represents a low index superstrate, and S is a high index substrate.)

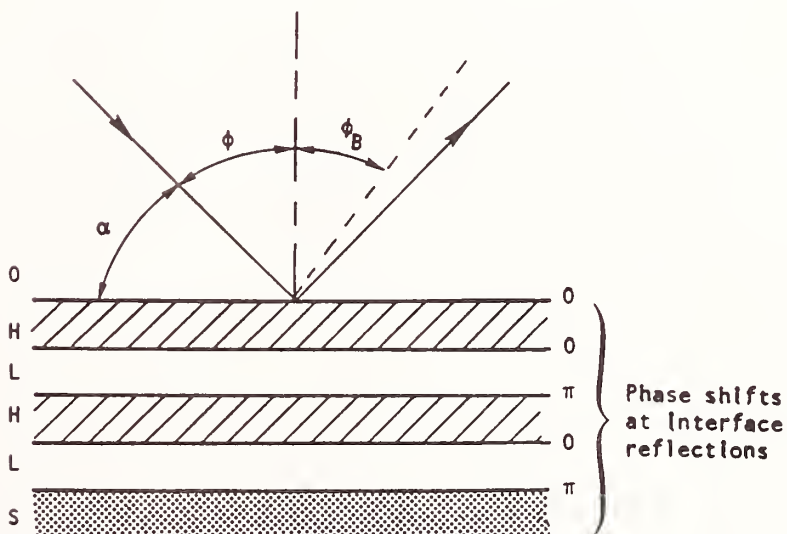


Figure 2. Phase shifts at each dielectric interface for p polarized light incident at $\phi > \phi_B$.

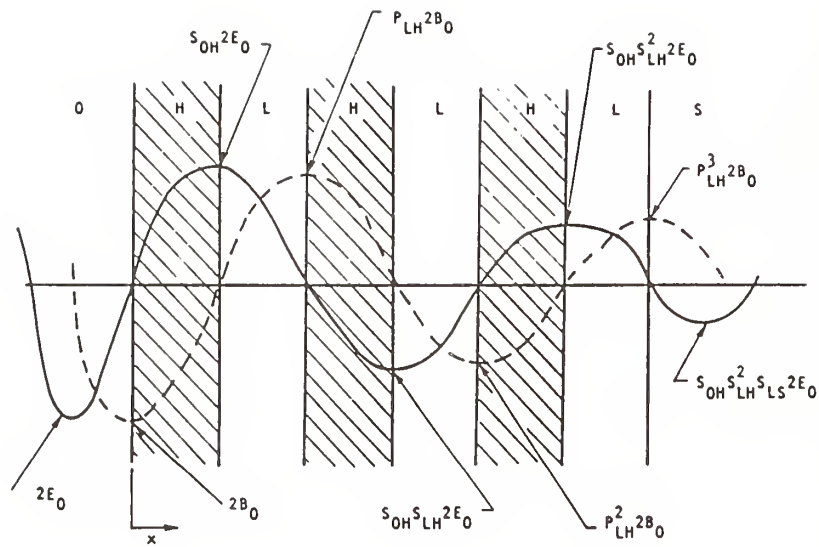


Figure 3. E-field distribution for S-polarized light and B-field distribution for P-polarized light in a high-reflectivity quarter-wave stack.

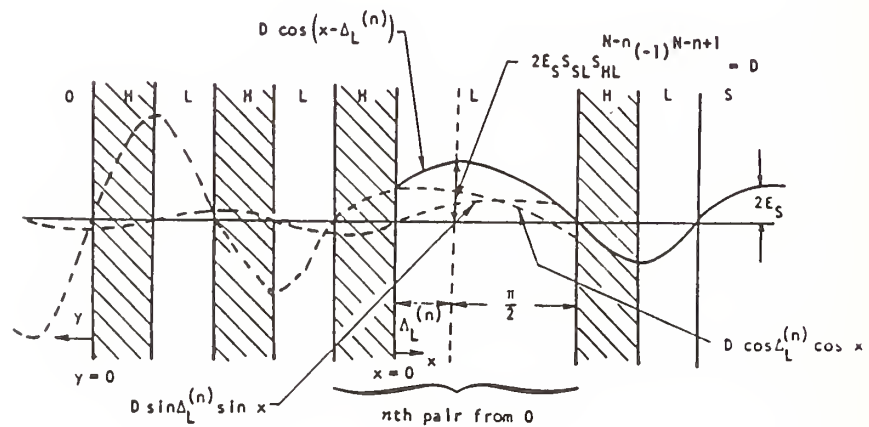


Figure 4. Geometry and field distribution for calculating the reflectivity of a quarter-wave stack with one layer of arbitrary thickness.

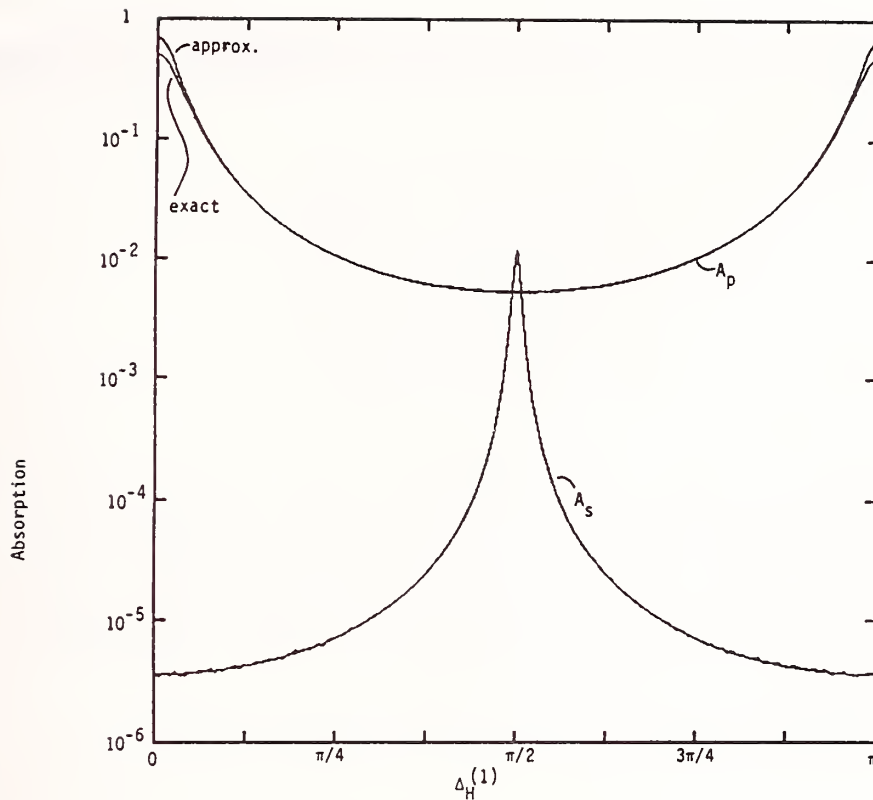


Figure 5. S and P polarization absorption as a function of top layer thickness $\Delta_H^{(1)}$ as calculated exactly and in the standing wave approximation for $\text{Si}(\text{Al}_2\text{O}_3/\text{ZnS})^9$. All layers, other than the top one, are quarter-wave thick at the incident angle of 88° . ($\lambda = 2.8\mu\text{m}$)

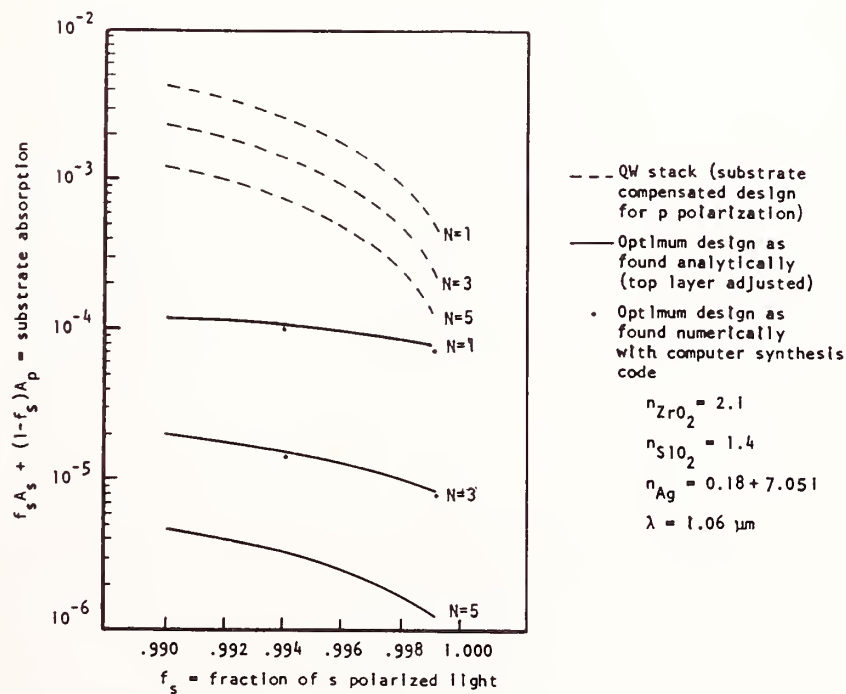


Figure 6. $\text{Ag}(\text{SiO}_2/\text{ZrO}_2)$ absorption as a function of the amount of s polarized light incident at 89° .

- Manuscript Not Received -

PHASE CONTROL DESIGN ANALYSIS

M. McGuirk and R. D. Poirier
The Perkin-Elmer Corporation
761 Main Avenue
Norwalk, CT 06859-0420

ABSTRACT

A novel graphical design technique was developed for two-wavelength achromatization of phase control coatings. The technique makes it possible to rapidly identify regions of approximate solutions for exact computer optimization. The technique gives an indication of the sensitivity of the design to thickness errors. The technique has been applied to design coatings yielding an average phase error of 0.3 phase degrees per mirror pair over a $\pm 5\%$ bandwidth.

Key Words: optical coating design; phase-control coatings;
thin film coatings.

- Manuscript Not Received -

=====

THERMAL CONDUCTIVITY OF ENHANCED HIGH REFLECTORS

M. McGuirk and R. D. Poirier
The Perkin-Elmer Corporation
761 Main Avenue
Norwalk, CT 06859-0420

ABSTRACT

Perkin-Elmer has designed and fabricated a simple thermal conductivity tester for thin film coatings. The work is motivated by the results Don Decker, et al., reported at this conference last year.¹ Our measurements confirm his finding that the thermal conductivity of thin films is substantially less than the thermal conductivity of the corresponding bulk material. In one case the measured thermal conductivity of an enhanced high reflectance coating is a factor of 30 less than the conductivity predicted from bulk values.

Perkin-Elmer has considered the theoretical reasons for the low conductivity, and methods for increasing the conductivity. Increased thermal conductivity should increase the laser damage threshold for CW applications.

Key Words: laser-damage resistance; thermal conductivity; thin film coatings.

¹ Decker, D.L., Ashley, E.J., and Koshigoe, L.G., "Thermal Properties of Optical Thin Film Materials" Poster Session 1984 Symposium on Laser Induced Damage in Optical Materials.

D. J. Smith, C. J. Hayden, B. U. Krakauer, A. W. Schmid, and M. J. Guardalben

LABORATORY FOR LASER ENERGETICS
and
NEW YORK STATE CENTER FOR ADVANCED OPTICAL TECHNOLOGY
THE INSTITUTE OF OPTICS
University of Rochester
250 East River Road
Rochester, New York 14623-1299

Yttrium oxide has proven to be a useful coating material for high power UV lasers. In combination with silicon dioxide it produces an effective dual wavelength antireflection coating at 351 and 1054 nanometers which has good resistance to damage at both wavelengths. While a durable coating material, yttrium oxide may be removed safely from a lightly damaged optic and reapplied. Index inhomogeneity of the material is investigated as well as modification of the film structure with ion-assisted deposition.

KEYWORDS: Antireflection coatings, thin film materials, inhomogeneity, coating damage, ion-assisted deposition.

1. Introduction

Yttrium oxide is useful for damage-resistant coatings in the ultraviolet primarily due to its low absorption edge and its moderately high refractive index. The material has been investigated by a number of groups for its damage resistance in various regions of the ultraviolet spectrum. [1-3] Coatings of yttrium oxide and silicon dioxide were used for the upgrade of the OMEGA laser at the Laboratory for Laser Energetics from 1054 nanometers to the frequency-tripled 351 nanometers. Yttria lends itself to simple two and three-layer designs which have a minimum of interfaces. These designs tend to reduce damage which propagates from impurities at the interfaces and from the intrinsic stress inherent in more complicated designs. While yttrium oxide forms hard and durable coatings, it is also removable under the appropriate conditions.

During production of the coatings the yttrium oxide films showed a significant degree of inhomogeneity as has been observed by Borgogno *et al.* [4] for other materials deposited by evaporation. The films also suffered from problems of reproducibility and, as a result, had to be made under stringent process conditions for the production of the OMEGA laser optics. These problems led to the study of the structure of yttrium oxide films.

Harris *et al.* [5] have developed a model which suggests the inhomogeneity in thin films is caused by a gradient in packing density of the columnar thin film. Klinger and Carniglia [11] have shown that inhomogeneity in zirconium dioxide thin films may also be the result of different crystalline phases becoming dominant during thin film growth. In this study, the origin of inhomogeneity in yttrium oxide appears to follow the Harris model as determined by electron diffraction.

Ion-assisted deposition techniques have been shown to favorably affect the structure of thin films with regard to stability, moisture absorption, stoichiometry and index homogeneity. [6-10] Preliminary experiments performed with Argon ion assist on yttrium oxide films indicate an improvement in homogeneity and film stability. Markedly different structure is seen in the ion-assist films.

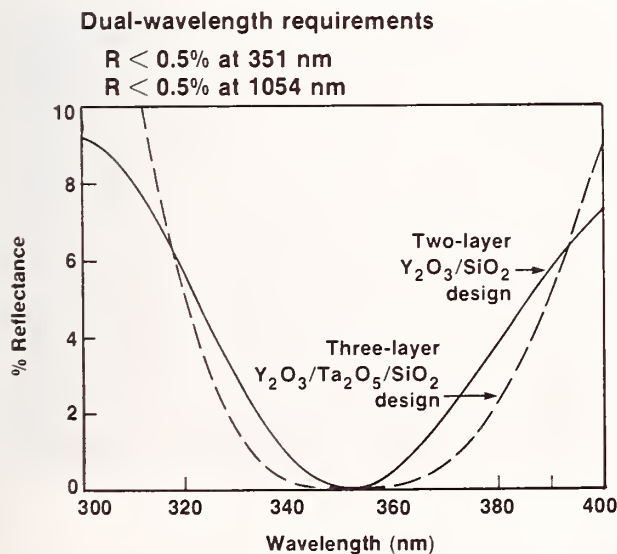
2.1 Design of Coatings for the OMEGA Laser

The OMEGA laser at the Laboratory for Laser Energetics is used primarily for experiments in inertial fusion. It is a 24 beam Nd:glass laser with an output aperture of 180 mm in each beamline. The primary 1054 nm radiation is converted to the third harmonic at 351 nm using a pair of KDP crystals. The system is capable of producing in excess of 2400 joules at 351 nm in one nanosecond pulses. Since the system uses the primary 1054 nm radiation for alignment purposes, all optics beyond the frequency conversion cells must perform at both the first and third harmonic.

The anti-reflection coatings for the OMEGA laser operate predominantly at normal incidence. The most straightforward designs used were those which consisted of quarter-wave optical thickness layers. These types of designs had several benefits: (1) a design which performs at the first harmonic will also perform at the third harmonic, (2) the designs have a minimal number of layers and interfaces, and (3) the coatings may be monitored during deposition by both optical and physical thickness methods.

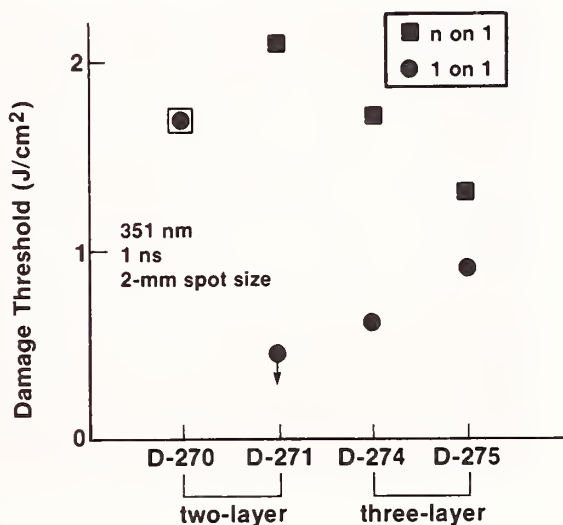
Selection of the final designs was determined by the results of damage tests. Abate et al. [1] had performed tests on similar coatings using Yttria at the appropriate wavelength and pulsewidth and found in general that a lower number of interfaces was beneficial for damage resistance. The improvement of damage threshold with the incorporation of an undercoat in the design as reported by Lowdermilk [15] was not observed by Abate, and was not used in this study.

The two design options were a two-layer design of yttrium oxide and silicon dioxide quarter-wave and a three-layer design consisting of a quarter-wave of yttrium oxide (next to the substrate), a half-wave of tantalum pentoxide, followed by a quarter-wave of silicon dioxide. The advantage of the three layer design is its broader low reflectance region, and the disadvantage is the higher absorption at 355 nm of the high index tantalum pentoxide layer (fig. 1). The wider AR band allows less stringent requirements on uniformity and is desirable due to the significant narrowing of the band which is characteristic of 3rd order interference effects. Despite this advantage, the two layer design was chosen on the basis of N-on-1 and 1-on-1 damage tests which favored the two layer design (fig. 2).



G1647

Figure 1: Two designs for the 351 nm/1054 nm AR were considered; a two layer coating similar to a V-coat, and a three layer quarter-half-quarter design.



G1648

Figure 2: Damage tests at 351 nm favored the two layer coating.

There are five optics with a clear aperture of 200 mm and seven surfaces in each beamline of the OMEGA laser which were coated with the dual wavelength AR. Eighteen of the twenty-four beamlines were coated at the University of Rochester coating facility along with the high-reflector coatings for beam transport to the target chamber.

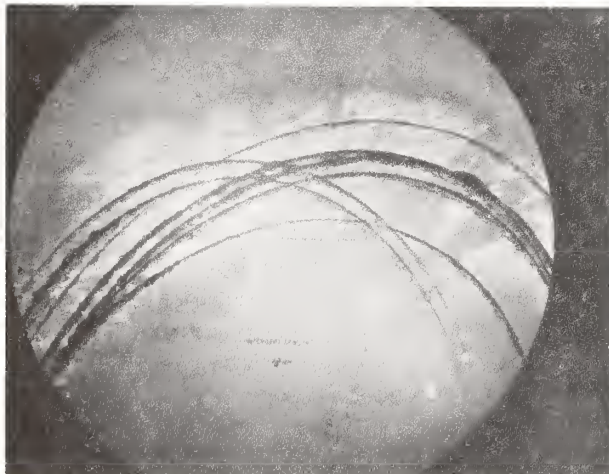
2.2 Fabrication and Performance of the Coatings

The optics were coated using conventional electron-beam evaporation techniques. The conditions of evaporation for the yttrium oxide are given in table 1. All substrates were prepared by a mechanical scrub followed by a wash in an aqueous ultrasonic bath. The parts were then rinsed in a series of water sprays and ultrasonic baths and finally dried with a solvent drier. The substrates were placed in the chamber as soon as possible after cleaning and it was immediately pumped.

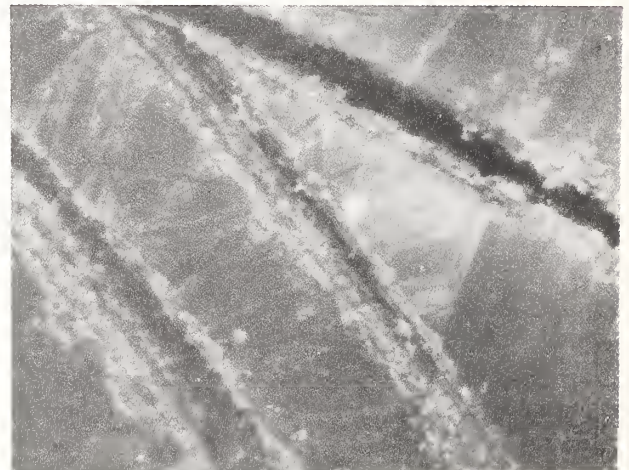
The majority of the coatings had good optical performance, although there was some variation in the index of the Yttria and the wavelength shift experienced upon exposure to atmosphere. These points are discussed in a subsequent section. Performance within specifications is essential in high power laser systems due to the danger of ghost image formation from residual reflection from curved surfaces.

As of November, 1985, the coatings in the OMEGA system had survived more than 450 system shots. The peak fluences seen by the coatings was $1.57 \pm 0.31 \text{ J/cm}^2$, at 351 nm, 1 ns. The coatings were carefully inspected after an extended shut-down for further upgrade. Few of the coatings showed signs of damage. Those that were damaged were located near regions of bulk damage in the fused silicon dioxide substrates. Since the damage threshold of the bulk fused silicon dioxide exceeds 9 J/cm^2 , [12] we assume most of these regions were formed by spurious ghost images. Figure 3A shows the highest level of damage seen in the OMEGA laser AR coatings to date. The two photomicrographs show the damage was not isolated to the coating but exists also in the substrate. The damage seen in Figure 3B extends 20 microns into the surface, which is a good deal further than the thickness of the coating (approximately 0.33 microns). Coating damage is seen only in the vicinity of the high fluence, as indicated by the bulk damage. The damage was caused by temporary misalignment of one beam with respect to the target. With the exception of this one optic, all the transmissive optics have remained intact in the system.

Focus Lens



— 1 mm —



— 100 μm —

G1649

Figure 3: Coating damage in the system was typically accompanied by bulk damage in the substrate indicating an extremely high local fluence due to ghost images.

Table 1: Evaporation Conditions for Yttrium Oxide

	54" System	28" System
Source of material	E. Merck	
Rotation	Planetary	Single
Source to substrate	66 cm	50 cm
Base pressure for consistant index Pa. (Torr)	9.31×10^{-5} (7.0×10^{-7})	2.66×10^{-4} (2.0×10^{-6})
Temperature	200 degrees	200 degrees
Rate	0.22 nm/sec	0.15 nm/sec
Oxygen Backfill Pa. (Torr)	6.7×10^{-3} (5×10^{-5})	1.1×10^{-2} (8×10^{-5})
Sweep	1 x 2 cm htz sweep manually moved over pot.	
Yttria pre-heat	2 min. burn-in at low beam power (0.05 A) followed by 3 min. of high beam power (0.2 A)	
Electron Beam Voltage	6 kV	5 kV
Ion Beam Gun Parameters: -----		
Beam Voltage		600 V
Beam Current		10 ma
Gas		Argon
Ion Impingment Ratio		1 Ar+/Yttria molecule

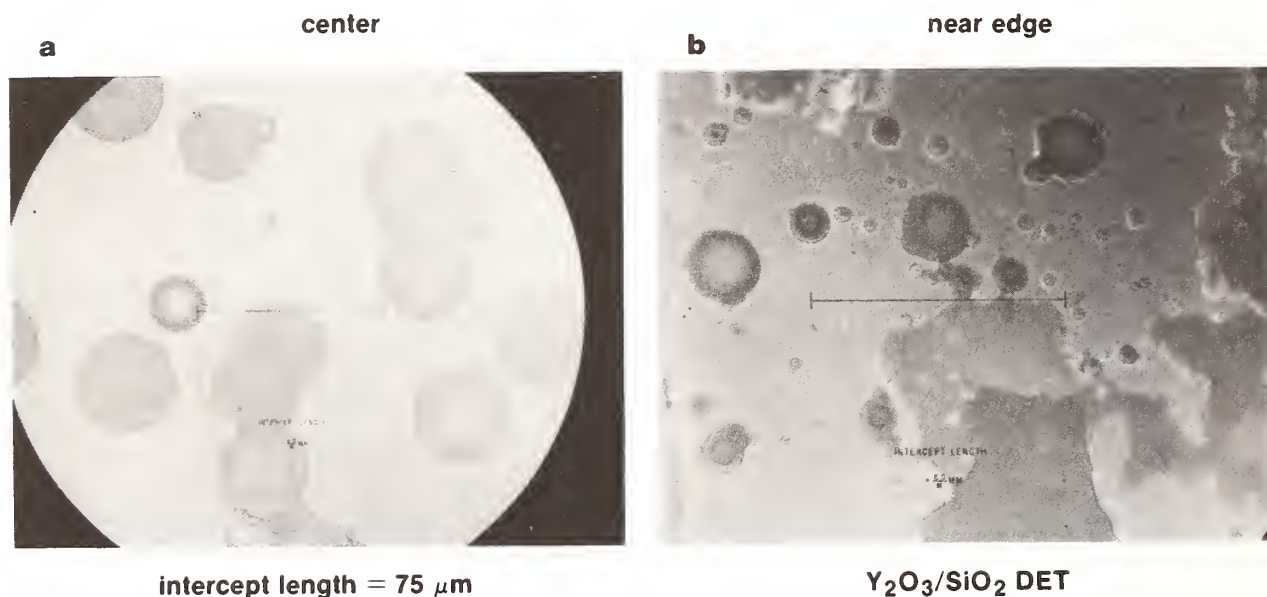
Table 2: Removal of Yttrium Oxide Coating by Various Solutions

Test	Result
100% humidity	no observed effect
50/50 2-propanol and water	deterioration/37 days
R.O. water	deterioration/6 days
NaCl solution	deterioration/5 days
5% micro	complete removal/2 days
1% HCl	complete removal/1 day

2.3 Removal of the Yttrium Oxide/Silica Coatings

In the process of fabricating the coatings we discovered an interesting aspect of yttrium oxide coatings; although it is a hard and durable coating, it is easily removed under certain conditions. Yttrium oxide is slightly soluble in an acid, and as a result the coatings will come off quite readily when soaked in an acid solution. An experiment was performed to test the durability of the coatings in various environments. Glass substrates were coated with 150 nm of yttrium oxide. The coated substrates were submerged in a variety of acidic solutions and solvents as well as kept in a high humidity environment.

The results are shown in table 2. The coatings kept in a humid atmosphere showed no deterioration after five weeks. Mild environments such as immersion in water, water/alcohol, and salt water produced slight deterioration of the coatings. Solutions of water and Micro (a commercial laboratory detergent) and weak acid solutions removed the coating completely in as little as four hours. In addition, coatings based on yttrium oxide in use on the OMEGA laser have proven to be durable in typical laboratory conditions.



G1651

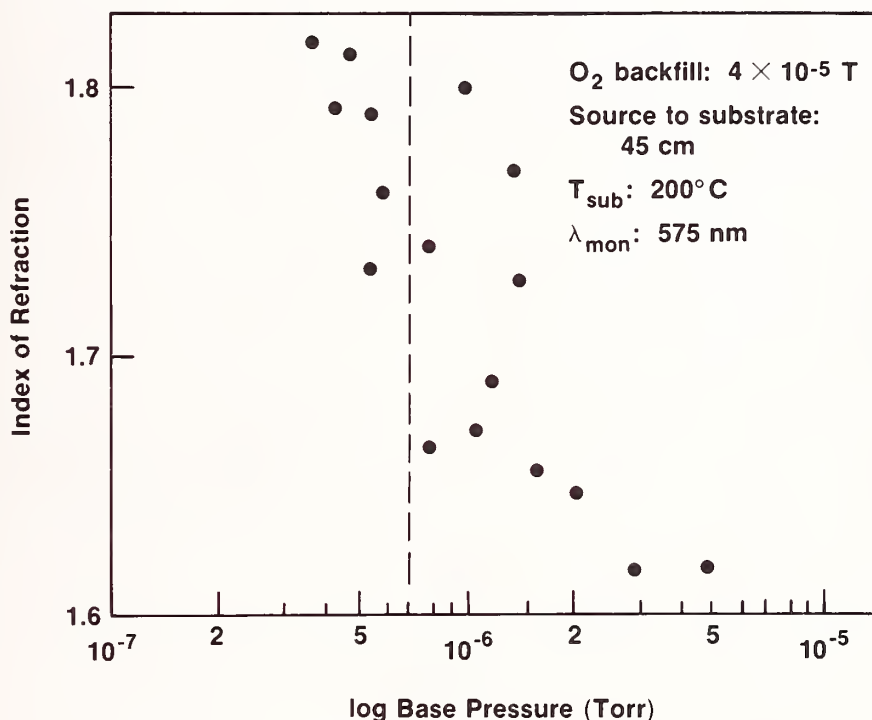
Figure 4: Both (a) and (b) show the three stages of coating removal in the yttrium oxide coatings: (1) Initial penetration through silica overlayer, (2) Dissolution of the yttrium oxide underneath the silica, (3) Fracture of the silica overlayer.

Figure 4 shows the mechanisms for the removal of a yttrium oxide/silicon dioxide anti-reflection coating. The yttrium oxide coating is next to the substrate and underneath the silicon dioxide layer. Three distinct stages of deterioration can be observed. (1) The acid solution penetrates through the pinhole and begins to corrode an area of yttrium oxide approximately 5 microns in diameter. (2) The yttrium oxide continues to dissolve underneath the silicon dioxide to an area as large as 35 microns. (3) The silicon dioxide layer finally breaks away and leaves the bare substrate exposed, and the solution continues to dissolve the yttrium oxide at the edges.

The removal process was used to strip both the coating and the target debris from the OMEGA laser target chamber blast shields. The contamination produced by the residual target materials has been difficult to remove from uncoated optics and impossible to remove from coated optics. Now the blast shields may be regularly removed, the coatings stripped, recoated, and replaced. Only bulk damage to the substrate will limit the life of the blast shields.

3.1 Properties of Yttria Films and Modification of Films with IAD

During the production of the coatings for the OMEGA laser, we observed some difficulties in the deposition of the yttrium oxide films. The first problem encountered was a significant variation of index of refraction for the first layer of yttrium oxide from different deposition runs. By compiling data from test and production runs, a correlation of index to base pressure of the system was noted. The data in figure 5 show that generally a lower index and a greater spread in index is obtained when the base pressure is above 1.0×10^{-6} Pa (7.7×10^{-7} Torr). The base pressure is the degree of high vacuum which a chamber is allowed to pump prior to backfilling the chamber with oxygen. No amount of careful substrate preparation could reduce the index variation.



G1654

Figure 5: Tests in a 54" chamber show the the index of refraction of the first quarter-wave is somewhat dependant on the base chamber pressure. The threshold for obtaining repeatable performance is $<7 \times 10^{-7}$ Torr.

Index variations in the first layer of a deposited material have been observed by Netterfield [13] as well as Behrndt and Doughty [14] for zinc sulphide. They perceived the variation as differences in nucleation of the first few layers of the film on the substrate. The problem was alleviated by first depositing a thin layer of another material with an index of refraction close to that of the substrate. The thin "Barrier" layer apparently produced evenly distributed nucleation sites and increased the sticking coefficient of the zinc sulphide. The "barrier" layer is reminiscent of the undercoat which has been used in various AR designs to increase damage thresholds. [16] In a similar manner uneven nucleation of the yttrium oxide, due to background gas contamination of the substrate may have caused the large spread in refractive index we observed. Generally, coatings made at lower pressures would see less contamination at the substrate, thereby promoting even nucleation of the film and the resulting higher index. Undercoats have not produced favorable damage results with this material and were not considered in this study although the topic merits further investigation. [1]

The second detrimental effect seen in the yttrium oxide films was inhomogeneity of the index of refraction of the films with thickness. Inhomogeneity in Yttria films was first observed by Borgogno et al. [4] They determined their yttrium oxide films showed an inhomogeneity $\Delta n/n = -1.5\%$. The yttrium oxide films deposited in this study had a much greater inhomogeneity with typical values being -5% . The index variation was determined *in situ* using a technique similar to Netterfield [13] and described in detail in the appendix. The results shown for some typical evaporation on hot and cool substrates are shown in figure 6. Each layer is marked by a steep drop in index in the first quarter-wave optical thickness layer (~ 50 nm) followed by a steady and gradual increase after the third quarter wave. These results are quite typical, although on occasion the initial drop was absent from a coating. The calculation of the index variation assumes that absorption in the films is negligible. A gradual increase in absorption as the layer is deposited could account for the gradual increase in index seen for the thicker coating, but would not affect the steep initial drop greatly. This is discussed in more detail in the appendix.

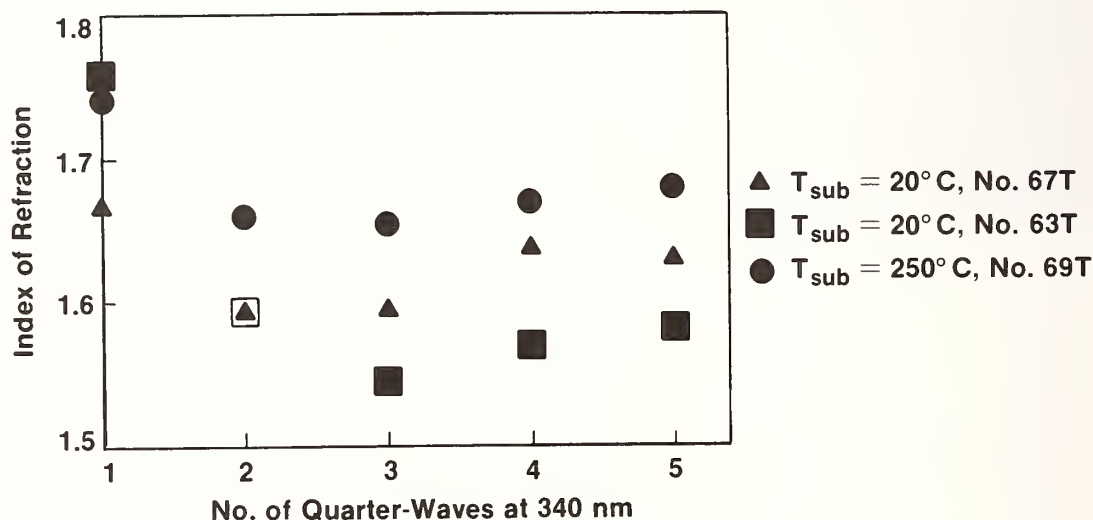


Figure 6: The index of refraction for conventional depositions changes with deposited thickness. Generally this index decreases sharply in the 1st quarter wave of optical thickness (~ 500 Angstroms).

The steep drop in the index in the first 50 nanometers of the film is a surprising but unfortunate result. A more gradual inhomogeneity was expected. The steeper drop (which is difficult to control) generally degrades the performance of an anti-reflection coating. The effect of the inhomogeneity on the damage threshold of a coating is not known. To understand the effect of inhomogeneity, a study was initiated to relate the physical structure to the optical characteristics. In addition, control of the inhomogeneity was attempted with ion assisted deposition techniques.

3.2 Experiment

A 28" vacuum coater was fitted with a series of shutters on its single rotation to allow a deposition of four discrete thicknesses on different sets of substrate without breaking vacuum. The chamber was fitted with a 10" diffusion pump topped by a liquid-nitrogen cooled baffle. All coating were deposited using reactive electron beam evaporation according to parameters given in table 1.

One fused silicon dioxide substrate in the center of the shutter assembly was used for optical monitoring of the films at 340 nm as they were being deposited. An Inficon quartz crystal head was mounted directly above the electron-beam source for monitoring rate and physical thickness of the film. The crystal head was outside the ion beam when the ion beam was used. Special considerations taken with the optical monitor are described in Appendix 2.

The ion source was a 3 cm, Kaufman source with a hot cathode and dual graphite grid optics. The operating parameters for the source are given in table 1. The power supply for the source was operated in the manual mode since electrons from the electron beam gun would interact with the beam and cause problems with the neutralizer feedback circuits in the ion source power supply. Argon gas was fed to the gun while Oxygen was let into the chamber in a 50/50 ratio with the argon. The profile of the ion source at the substrate was not characterized. The substrates were not exposed to the ion beam until the crystal monitor recorded a thickness of 2.0 nanometers deposited on the substrates. This was to allow for easy removal of the coating for analysis afterward.

The substrates for each thickness were two pieces of fused silicon dioxide for optical measurements and several pieces of mica. The freshly-cleaved mica was coated with ~5 nanometers of carbon prior to being mounted in the chamber. All substrates were within a 7 centimeter radius of the center of the holder. The substrate holder was rotated about its center during all depositions.

Three coatings under the above conditions were deposited under varying conditions of substrate temperature and ion impingement.

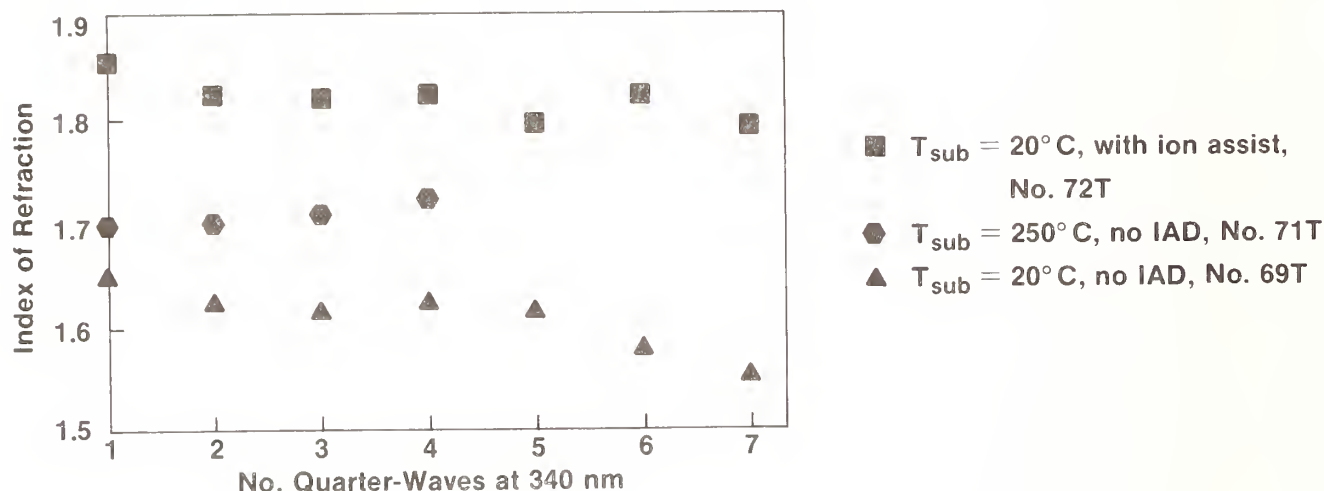
1. Cool substrate ($\sim 20^{\circ}\text{C}$), no ion assist.
2. Hot substrate (250°C), no ion assist.
3. Cool substrate ($\sim 20^{\circ}\text{C}$), with ion assist.

Except for temperature and ion assist, all substrate preparation and process procedures were as identical as possible. Coatings of 1, 2, 3, and 7 quarter-wave optical thickness at 340 nanometers were deposited on each set of substrates. Between each thickness the electron gun and the ion source were shut down while the respective shutter was positioned over the substrate set.

3.3 Analysis

Data from the optical monitor during the deposition was used to determine the index profile of the coating on the monitor piece. The index profile for the three runs is shown in figure 7. The index for the coating deposited on the cool substrate tended to be the lowest while the coating with ion assist had the highest index. In this particular data the initial sharp drop in index is missing from the conventionally deposited films. Based on experience, this is an infrequent exception to the behavior of the yttrium oxide films. However, the IAD runs always had a higher index and always drifted less in index throughout the deposition. An increase in absorption of the ion assisted film may account for some of the index drift seen in

the index (see appendix.) The hot substrate coating index starts at 1.7 and gradually drifts up until the fourth quarter-wave where data was lost from the optical monitor. The coating on the cold substrates drops only about 0.25 initially and gradually declines afterward to fairly low values. The ion assisted coating started at a much higher index of 1.85 and was fairly stable throughout the run dropping only a small amount in the last quarter waves.



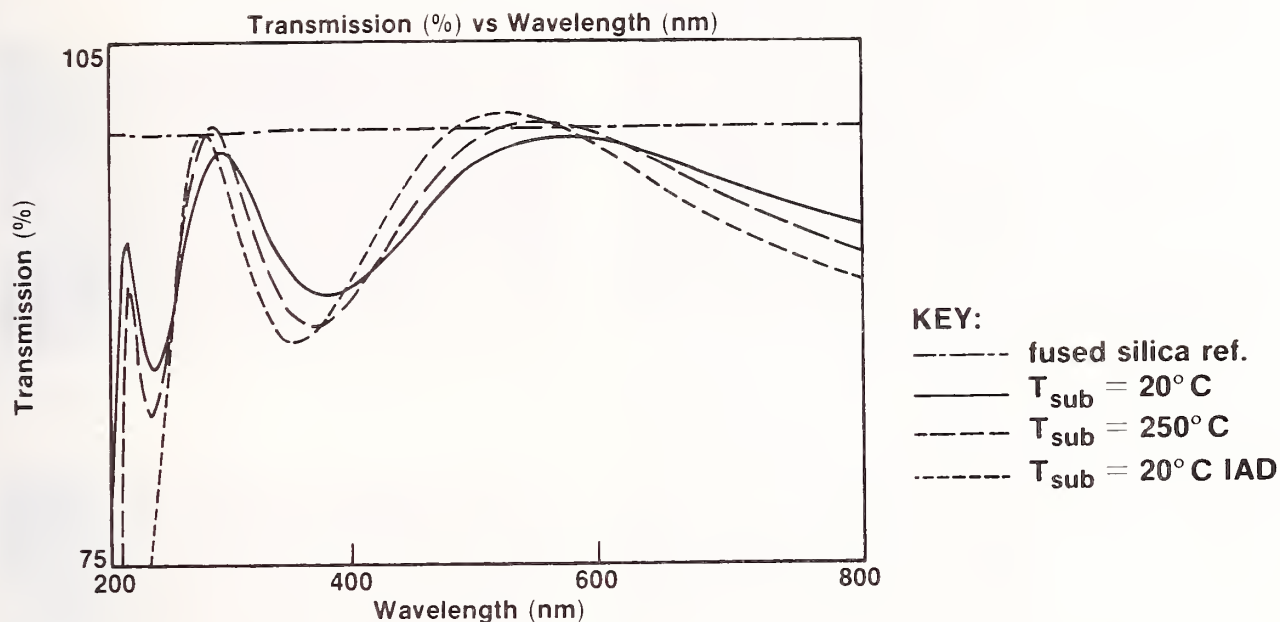
G1658

Figure 7: The IAD run had a significantly higher index as well being somewhat more stable than those films deposited by conventional E-Beam method on cool and hot (200°C) substrates.

The spectrum of each of the coatings for the 3 quarter-wave thicknesses is given in figure 8. Confirmation of some of the index measurements in figure 7 are seen in here. The transmission minimum of the ion-assist run is the lowest, indicating the highest index, followed by the heated run, and finally the cool run has the lowest index. Also evident is the reduced shift in wavelength for the ion-assisted coatings which is similar to the findings of Martin et al. [8]. All three depositions were stopped at the same optical thickness. The measurements, made in atmosphere, indicate the shift in wavelength each coating experienced when water entered the porous coatings and increased the effective optical thickness. The cold deposition, with the lowest packing density, shifted the greatest amount followed by the heated substrate, and finally by the ion-assisted coating with a shift of only 10 nanometers. The last bit of information from this figure is the longer wavelength UV cut-off exhibited for the ion-assist film. This result was consistent with the test runs made previous to the experiment. Also, the monitor piece, which was in the center and experienced a slightly higher ion flux, showed significantly higher absorption throughout the spectrum.

3.4 Structural Characteristics

The films deposited on the mica were floated off, placed onto TEM grids, and observed under bright field and dark field conditions in a transmission electron microscope. The same films were analyzed with wavelength dispersive spectroscopy in a Cambridge Instruments scanning electron microscope. Fractures of the coatings were also observed in the SEM but the detail in the coatings was too fine for this method. Using Pearson's [17] technique, replica cross-sections of the coating were generated and observed in the TEM.



G1659

Figure 8: Spectral scans of the coating indicate highest packing densities for the IAD coating as indicated by the small shift from the monitor wavelength of 350 nm. However, IAD coating also showed the highest absorption.

The bright field transmission electron micrographs and electron diffraction patterns for the single quarter-wave coatings are shown in figure 9. The instrument was operated at 100 kV with a tungsten filament. Three thicknesses (~50, 100, and 150 nm) of each coating were observed. While no changes in the structure were observed for the various thickness films in each deposition, there are striking differences between the micrographs of the three deposition conditions. The diffraction pattern of the hot substrate matches the powder diffraction files for cubic phase of yttrium oxide. This is a highly stable phase of this compound and no variation from it was seen. The diffraction pattern for the hot substrate is clearly defined indicating a well developed microcrystalline structure. The cold and IAD depositions both exhibit a pseudo-amorphous structure. The bright field micrographs show further differences. The grains in the hot sample are fairly uniform in size and are about 10-20 nm. Voids are observed in the coating. The grains in the cold deposition are also uniform in size but are smaller, less than 10 nm and voids also are observed. The IAD coating appears to have a background of a very fine structure with very large grains 30-50 nm superimposed on the finer structure. The lighter area appears to be depleted regions where a nucleation site has attracted a large radius of adatoms due to the increased mobility. This phenomena was observed by Marinov [18] for aluminum films. This work, although observed on thinner films, bears a strong resemblance to the IAD coatings. It is interesting to note that the finest and the largest grain structures are seen simultaneously on the IAD film.

Figures 9 also shows TEM micrograph cross-sections of the thickest films (~350 nm) for the three coatings. The hot films show a clear columnar growth and the interface with the substrate is clearly identified. The cold film shows only a faint columnar structure, although the interface is once again clearly identified. The IAD case shows some very peculiar features. There are very large "outcrops" in the cross-section which shadow the deeper regions of the cross-section. Secondly, no clear interface with the substrate is seen. Although the structures are larger in the film, they do not appear to affect the surface layer.

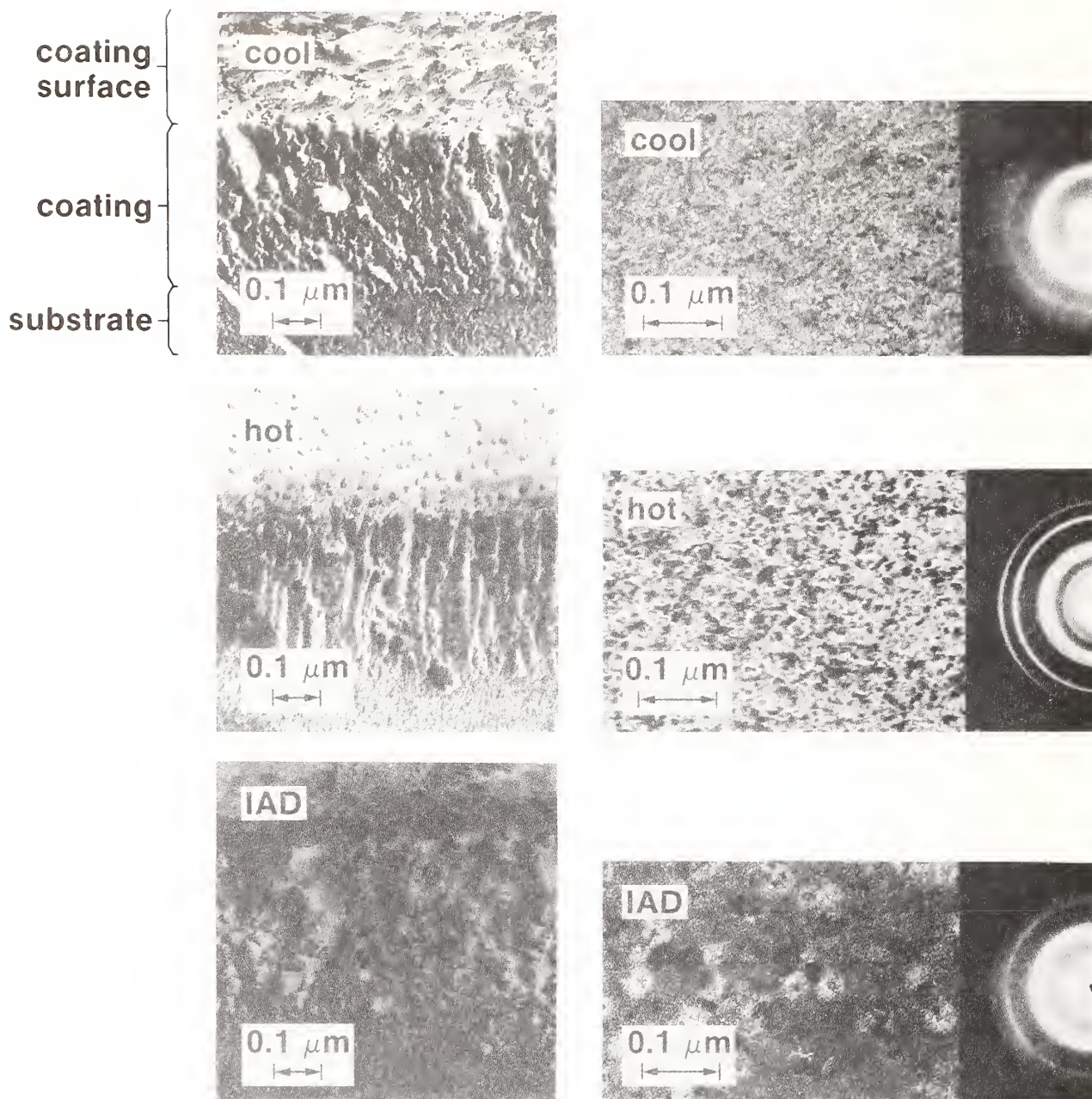


Figure 9: Structural analysis using cross-sectional replicas of a 350 nm film viewed with a TEM (left), bright field TEM images (center) and electron diffraction patterns (right) of the 50 nm films. The films deposited on the cool substrates showed a fine grain structure (10 nm) and had a pseudo-amorphous structure, while those deposited on hot substrates (200C) showed a larger grain size (10-20 nm) and a distinct cubic structure. Films deposited with ion-assisted deposition (IAD) had the largest grain size (30-50 nm) yet, they are dominated by an amorphous structure. Also note the disappearance of a distinct film/substrate interface in the IAD sample indicating enhanced adhesion.

The results from the wavelength dispersive spectroscopy are qualitative and preliminary. To use the data quantitatively requires a set of references of Yttria with the same thickness as the films. Currently some ultramicrotomy techniques are being investigated to produce these references. The data indicates that the films become Oxygen depleted as they become thicker. The films on the cold substrates showed the greatest tendency toward oxygen depletion.

4. Discussion

The steep index drop in the first fifty nanometers of the yttrium oxide coatings might be explained by the modeling techniques of Liao and Macleod. [20] The first layers of the model indicate a high packing density which decreases as the columnar structure formation begins. It is unusual that in yttrium oxide films the region where the packing density is high is thick enough to significantly affect the refractive index of the first quarter-wave at 351 nanometers. The model predicts the formation of the columnar growth within tens of monolayers of the surface. Experiments with undercoats of the same refractive index as the substrate may provide insight into the nucleation behavior of yttrium oxide. A relationship between index and stress as a function of coating thickness may provide additional insight into the film structure. Stress measurements are now being planned using the stress induced birefringence apparatus [21] at the Laboratory for Laser Energetics.

Our preliminary study confirmed that yttrium oxide inhomogeneity could be controlled through ion-assisted deposition. The physical microstructure of the IAD films was distinctly different than the films grown using conventional deposition techniques. Effects of reduced ion energy, oxygen ions, and beam intensity will be considered in the next phase of the study. Finally, ion-beam assisted coatings will be tested for damage susceptibility at 351 nm.

Verification of the steep index drop will be facilitated by a rapid scanning monochromator. This would also provide direct useful information on the shifts of the coating due to water absorption which relates to the packing density of the film. The data from the scanning monochromator would also confirm the cause of the apparent index increase for the thicker coatings. If absorption in the coatings is not the cause of the increase, then temperature fluctuations of the substrate during deposition must be considered.

Despite the many problems associated with the deposition of yttrium oxide, it remains an important material for high laser fluence coating applications. It is the intent of the authors to continue investigations of yttrium oxide to understand the effects of stress, inhomogeneity, absorption, and stoichiometry on the damage threshold of the film. Attempts will be made to improve the damage susceptibility of the films through ion-assisted deposition.

Acknowledgment

The work performed at Rochester was supported in part by the New York State Center for Advanced Optical Technology of The Institute of Optics, the U.S. Department of Energy Office of Inertial Fusion under agreement No. DE-FC08-85DP40200 and by the Laser Fusion Feasibility Project at the Laboratory for Laser Energetics which has the following sponsors: Empire State Electric Energy Research Corporation, General Electric Company, New York State Energy Research and Development Authority, Ontario Hydro, Southern California Edison Company, and the University of Rochester.

V. References

1. J.A. Abate, R. Roides, S.D. Jacobs, W. Piskorowski, and T. Chipp, "Laser Damage of Optical Coatings at 351 nm," NBS Special Publication 669, 282 (January 1984).
2. F. Rainer, W.H. Lowdermilk, D. Milam, C. Carniglia, T.T. Hart, and T.L. Lichtenstein, "Materials for Optical Coatings in the Ultraviolet," *App. Opt.* Vol. 24, No. 4, 496 (1985).
3. W.H. Lowdermilk, D. Milam, "Review of Ultraviolet Damage Threshold Measurements at Lawrence Livermore National Laboratory," Presented at SPIE Technical Symposium East '84, Arlington, Virginia, April 29 - May 4, 1984.
4. J.P. Borgogno, B. Lazarides, and E. Pelletier, "Automatic Determination of the Optical Constants of Inhomogeneous Thin Films," *Appl. Opt.*, Vol. 21, No. 22, 4020 (1982).
5. M. Harris, H.A. Macleod, S. Ogura, E. Pelletier, and B. Vidal, "The Relationship Between Optical Inhomogeneity and Thin Film Structure," *Thin Solid Films*, 57, p.173,178 (1979).
6. R.P. Netterfield, W.G. Sainty, P.J. Martin, and S.H. Sie, "Properties of CeO₂ Thin Films Prepared by Oxygen-Ion-Assisted Deposition," *Appl. Opt.*, Vol. 24, No. 14, 2267 (1985).
7. P.J. Martin, R.P. Netterfield, W.G. Sainty, G.J. Clark, W.A. Lanford, and S.H. Sie, "Ion-Assisted Deposition of Bulklike ZrO₂ Films," *Appl. Phys. Lett.* 43 (8), 711, (1983).
8. P.J. Martin, H.A. Macleod, R.P. Netterfield, C.G. Pacey, and W.G. Sainty, "Ion-Beam-Assisted Deposition of Thin Films," *Appl. Opt.*, Vol. 22, No. 1, 178 (1983).
9. J.R. McNeil, A.C. Barron, S.R. Wilson, and W.C. Herrmann, Jr., "Ion-Assisted Deposition of Optical Thin Films: Low Energy vs. High Energy Bombardment," *Appl. Opt.*, Vol. 23, No. 4, 552 (1984).
10. J.R. McNeil, G.A. Al-Jumaily, K.C. Jungling, and A.C. Barron, "Properties of TiO₂ and SiO₂ Thin Films Deposited Using Ion Assisted Deposition," *Appl. Opt.*, Vol. 24, No. 4, 486 (1985).
11. R.E. Klinger, and C.K. Carniglia, "Optical and Crystalline Inhomogeneity in Evaporated Zirconia Films," *Appl. Opt.*, Vol. 24, No. 19 (1985).
12. W.H. Lowdermilk, Laser Research and Development, LLNL Laser Progress and Annual Report, 1982, pp.7-28.
13. R.P. Netterfield, "Refractive Indices of Zinc Sulfide and Cryolite in Multilayer Stacks," *Appl. Opt.*, Vol. 15, No. 8, 1969 (1976).
14. K.H. Behrndt and D.W. Doughty, "Fabrication of Multilayer Dielectric Films," *J Vac. Sci. Technol.*, Vol. 3, 264 (1966).
15. W.H. Lowdermilk, D. Milam, "Laser Induced Surface and Coating Damage," *IEEE J. Quantum Electron.*, 17, 1888 (1981).
16. T. Hart, T. Lichtenstein, C. Carniglia, F. Rainer, "Effects of Undercoats and Overcoats on Damage Thresholds of 248 nm," NBS Special Publication No. 683 (September 1983).
17. J.M. Pearson, "Electron Microscopy of Multilayer Thin Films," *Thin Solid Films*, 6(1970) 349-358.
18. M. Marinov, "Effect of Ion Bombardment on the Initial Stages of Thin Film Growth," *Thin Solid Films*, 46 (1977) 267.
19. H.A. Macleod, Thin Film Optical Filters, Adam Higler Ltd. London (1969).
20. B. Liao and H.A. Macleod, "Thin Film Microstructure Modeling," presented at Southwest Conference in Optics, 4-8 March 1985, Albuquerque.
21. S. Jacobs, "Anisotropic Stress Around Defects in Thin Films," *LLE Review*, Vol. 10, 3 (March 1982).

Appendix - In-Situ Optical Monitoring of Refractive Index vs Coating Thickness

The characteristic matrix for a single film is given by Macleod, [19]

$$\begin{pmatrix} \cos \theta & (i \sin \theta)/n_j \\ i n_j \sin \theta & \cos \theta \end{pmatrix}$$

where n_j = complex refractive index for the j th layer

and θ = phase thickness of the layer = $\frac{2\pi nd}{\lambda} \cos \delta$

If we let $\theta = \pi/2$ (quarter-wave optical thickness) and assume zero absorption (i.e., n_j is real) in the films, then the matrix reduces to,

$$\begin{pmatrix} 0 & i/n_j \\ i n_j & 0 \end{pmatrix}.$$

The characteristic matrix is multiplied by the column vector from which the admittance, Y , is found.

$$\begin{pmatrix} 0 & i/n_j \\ i n_j & 0 \end{pmatrix} \begin{pmatrix} 1 \\ n_s \end{pmatrix} = \begin{pmatrix} \vec{k} \times \vec{E} \\ \vec{H} \end{pmatrix}$$

$$Y = \vec{H} / \vec{k} \times \vec{E}, \quad n_s = \text{substrate index.}$$

The value for the admittance in this simple layer case is,

$$Y = n_j^2 / n_s \quad (\text{Eq. 1})$$

Additional layers require only building up the characteristic matrix, multiplying the matrices, and solving for the admittance. So, for two and three layer, non-absorbing quarter waves we have,

$$Y = \frac{n_1^2 n_s}{n_2^2} \quad (\text{Eq. 2})$$

$$Y = \frac{n_1^2 n_3^2}{n_2^2 n_s} \quad (\text{Eq. 3})$$

The admittance may be found in this manner for any number of layers. The admittance may be found directly from reflectance measurements since,

$$R = \frac{(n_0 - Y)^2}{(n_0 + Y)^2} \quad \text{where } n_0 = \text{incident index.}$$

Taking the square root of the reflectance will yield two solutions, but only one has any physical significance and is quite obvious.

Equation (1) is easily solved for $n(1)$ if we know the reflectance at the quarter-wave thickness. Likewise, if $n(1)$ has been found, eq. (2) may be solved for $n(2)$ assuming R is known at the appropriate quarter-wave position. The process can continue for any number of layers as long as the reflectance is measured only at the quarter-wave points, and there is negligible absorption in the films.

The index profiles of the yttrium oxide films in this study were determined using the above method. Needless to say, it is imperative that the optical monitor for determining R be accurate (in this case transmission was measured and R was found using $R = 1 - T$). Considerable effort was made to insure that the optical monitor gave stable and accurate data. An absorption filter was used in the input slit of the monochromator to reduce the effect of scattered stray light from the grating. The monitor wavelength, 340 nm is close to the absorption edge of standard viewport materials and can be seen in the optical monitor as the absorption band of the glass moved up and back down the spectrum. So, fused silicon dioxide viewports were substituted for the original glass viewports. The viewports were carefully shielded to prevent an accumulation of coating which also would lead to inaccuracy.

There is a question of the validity of allowing the absorption to be zero for these measurements. In fact, post-deposition measurements did show that some of the films had significant absorption in the UV. A series of simulated depositions were made using existing programs, and the "optical monitor" data was extracted from the simulations. The model predicted the index profile of the nonabsorbing films as expected. However, in absorbing films, after the steep drop in index, there was often a gradual increase in index. The model with absorption also displayed this increase in index. Since a drop in index can only be caused by inhomogeneity, the initial drop is likely to be real, but the gradual increase may well be an artifact caused by absorption in the layer.

Self-Consistent Dependence of Porosity and Refractive Index on Composition in
Co-Evaporated Films*

A. Feldman, E.N. Farabaugh, and R.A. Stempniak**

Ceramics Division
Institute for Materials Science and Engineering
National Bureau of Standards
Gaithersburg, MD 20899

Zirconia:silica films grown by e-beam coevaporation show a decreased porosity compared to pure zirconia films. This decreased porosity causes an anomalous dependence of refractive index on composition. A maximum in refractive index occurs at about 20 percent by volume of silica, the concentration at which the films appear to become amorphous. A simple model which derives the porosity as a function of composition from the deposition parameters predicts the general compositional behavior of the refractive index. The results agree best with the Drude model of refractive index for mixed component systems.

Key words: coevaporation; porosity; refractive index; thin films; ZrO_2 ; SiO_2 .

1. Introduction

One approach suggested for obtaining optical coatings resistant to laser damage is to produce films that possess a bulk-like glassy structure. E-beam deposited films generally are not bulk-like in that they exhibit a columnar structure and a significant porosity. Because of this porosity, water is adsorbed and desorbed from the film depending upon the ambient atmospheric humidity. The net effect is an unstable refractive index. In addition water can seep between film layers leading to delamination. One method shown to decrease porosity is ion-assisted e-beam deposition [1]. In this work we show a similar decrease in porosity by e-beam coevaporation and without the need for an ion gun. This result is important because manufacturers of thin film coatings can use the current e-beam technology to produce bulk-like films without investing in the newer ion-beam technology.

Recent work has shown that mixed zirconia:silica films have varying structures depending on composition [2]. Pure zirconia films are polycrystalline with two crystalline phases present. Films with a silica content of up to 20 % by volume have a single crystalline phase. At volume fractions of silica >20 % the films show an amorphous structure as determined by x-ray diffraction.

In this work we show that some of these films appear to exhibit bulk-like densities. A simple model derives the porosity of the films as a function of composition. The model also is consistent with the observed anomalous compositional dependence of the refractive indices of the films. We find that the addition of silica to zirconia can produce films with larger refractive indices than pure zirconia films. The compositional dependence of the refractive index agrees best with the Drude model.

*This work was supported in part by the Air Force Office of Scientific Research under Grant Nos. AFOSR-84-00060 and AFOSR-ISSA-85-0006.

**Guest worker from Instituto Tecnológico de Aeronáutica, Brazil with partial support from CNPq.

2. Experimental Methods

Films in the system $(\text{ZrO}_2)_x(\text{SiO}_2)_{(1-x)}$ were produced by e-beam coevaporation from two independent sources onto fused silica substrates at a substrate temperature of 300 °C. The deposition system has been described elsewhere [3]. Each source was monitored by a separate quartz-crystal thickness monitor. Films were produced varying in composition from pure ZrO_2 to pure SiO_2 . The thickness monitors were calibrated on the basis of stylus measurements on the pure films. The target deposition rate for the sum of the constituents was 0.5 nm/s, however, a higher rate was used on the deposition of some of the films with a low fraction of one constituent because the monitors had to operate near the lower limit of their sensitivity range. Thicknesses were in the range 0.7 to 1.1 μm .

Two sets of films were produced. In the first set, the deposition rates were controlled manually; in the second set, the rates were controlled by a commercial controller. The results reported were similar for both sets of films.

The thickness of each film was measured by stylus profiling at several points around the film border. The reported results are based on the average value. The refractive index was obtained from a combination of channel spectra measurements [4] and the thickness measurements. Thickness and refractive index were also obtained by the method of m-line spectroscopy [5]. Although there appears to be some discrepancy between the two methods of obtaining refractive index, the agreement is sufficient to sustain our principal conclusions.

3. Symbols and Nomenclature

In order to expedite the discussion we introduce the following symbols and nomenclature:

t = measured film thickness,
 t_1 = monitored thickness of silica,
 t_2 = monitored thickness of zirconia,
 $D_n = (t_1 + t_2)/t$, nominal densification,
 f_1 = packing fraction of silica in film,
 f_2 = packing fraction of zirconia in film,
 $f = (f_1 + f_2)$, packing fraction of film,
 p = pore fraction in film,
 p_1 = pore fraction in pure silica film,
 p_2 = pore fraction in pure zirconia film,
 n = refractive index of film,
 n_1 = refractive index of silica, and
 n_2 = refractive index of zirconia.

The following relationships hold:

$$f = 1 - p \quad (1)$$

$$1 = f_1 + f_2 + p \quad (2)$$

4. Results and Discussion

Figure 1 shows a plot of refractive index as a function of the thickness fraction of silica, $t_1/(t_1+t_2)$, for film set one. If it is assumed that the volume fraction is proportional to the thickness fraction, then the behavior of the refractive index with composition is anomalous. On the basis of all theories of mixed component systems, the refractive index of the composite should have a value that falls between the values of the pure constituents. Thus, the addition of silica, a low index material, to zirconia, a high index material, would be expected to lower n . Instead, we find that initially n increases. A decrease in film porosity would account for this behavior.

In order to test this hypothesis, we have compared $t_1 + t_2$ with t for each film. In every case we find $t_1 + t_2 > t$. This is clearly demonstrated in figure 2 where we observe $D_n > 1$ for all mixed films. On the basis of a simple model, we are able to calculate the pore fraction of the coevaporated films as a function of composition. We can also model the compositional dependence of the refractive index.

5. Porosity Model

We make the following assumptions: 1) The sticking coefficient is independent of composition. This implies that the quantity of material deposited is proportional to the monitored thickness. 2) A given volume is associated with each type of molecular unit [6]. This implies that the deviations of $t_1 + t_2$ from t are due to porosity.

From these assumptions several relationships can be derived:

$$f = \frac{t_1(1-p_1) + t_2(1-p_2)}{t} \quad (3)$$

$$D_n = \frac{(1-p)(t_1+t_2)}{t_1(1-p_1) + t_2(1-p_2)} \quad (4)$$

From eq (3) we see that the packing fraction of a film can be obtained from the measured quantities t , t_1 , t_2 and assumed values for the pore fractions in pure films p_1 and p_2 . A theoretical expression for D_n can be obtained if we can assume a relationship between the pore fraction in the film and the fractions of the two constituents, f_1 and f_2 . The following expression was chosen as an empirical fit to simulate the experimental data:

$$p = p_2 \exp[-(f_1/A_1)]^2 + p_1 \exp[-(f_2/A_2)]^2 \quad (5)$$

The parameters A_1 and A_2 are chosen so that the porosities of the pure films are obtained, that is $A_1 \ll 1$, $A_2 \ll 1$. The expression implies that a small increasing fraction of one constituent acts to reduce the porosity. If we solve equations (1), (2), and (4) in a self-consistent manner we can obtain a curve for comparison with one set of experimental data. Figure 3 shows such a comparison with the experimental data of film set two. The values for p_1 , p_2 , A_1 , and A_2 are chosen so that the packing fraction did not exceed unity. We see that a reasonable fit is obtained with $p_1=0.10$, $p_2=0.25$, $A_1=0.15$, and $A_2=0.25$.

These results were used to calculate values of refractive index as a function of film composition on the basis of three different models, the Drude model, the Lorentz-Lorenz model, and the linear model. The Bruggeman effective media model agrees approximately with the linear model so it has not been used. Each of the models average the refractive indices in a different manner.

Drude:

$$n^2 = \sum_i f_i n_i^2 \quad (6)$$

Lorentz-Lorenz:

$$\frac{n^2-1}{n^2+2} = \sum_i f_i \frac{n_i^2-1}{n_i^2+2} \quad (7)$$

Linear:

$$n = \sum_i f_i n_i \quad (8)$$

In Figure 4, the results for each of the models are superposed on the experimental data of film set two. All of the models show the same general compositional behavior as the experimental data. Two data points are shown for each specimen; one point is obtained by m-line spectroscopy (x's), the other point by the method of channel spectra and stylus thickness measurements (dots). We believe the discrepancies are due to the different sensitivities of the measurement methods to compositional inhomogeneity. However, in spite of this difference, the two sets of data still display the same behavior and do not alter our conclusions. The best quantitative agreement appears to be provided by the Drude model.

6. Conclusions

The pore fractions in e-beam coevaporated zirconia:silica films are significantly smaller than in pure zirconia films. This results in an anomalous dependence of refractive index on composition. A porosity model, which requires estimates of porosity in pure films only, predicts the compositional dependence of the pore fractions in the films. This result is in reasonable agreement with the experimentally determined nominal densification of the films. Calculations of the compositional dependence of the refractive index agree with the behavior of the experimental data. Of the different models of refractive index in mixed component systems examined, the Drude model appears to agree best with the experimental data.

We thank T. Vorburger and C. Giauque of the Micro and Optical Technology Group for the diamond stylus measurements of specimen thicknesses.

7. References

- [1] Martin, P.J., Macleod, H.A., Netterfield, R.P., Pacey, C.G., and Sainty, W.G., Appl. Opt. 22, 178 (1983).
- [2] Farabaugh, E.N. and Sanders, D.M., J. Vac. Sci. Technol. A1, 356 (1983).
- [3] Sanders, D.M., Farabaugh, E.N., Hurst, W.S., and Haller, W.K., J. Vac. Sci. Technol. 18, 1308 (1981).
- [4] Feldman, A., Appl. Opt. 23, 1193 (1984).
- [5] Tien, P.K., Ulrich, R., and Martin, R.J., Appl. Phys. Lett. 14, 291 (1969).
- [6] Jacobsson, R., in Physics of Thin Films, 8, Hass, G., Francombe, M.H., and Hoffman, R.W., editors (Academic Press, New York, NY, 1975).

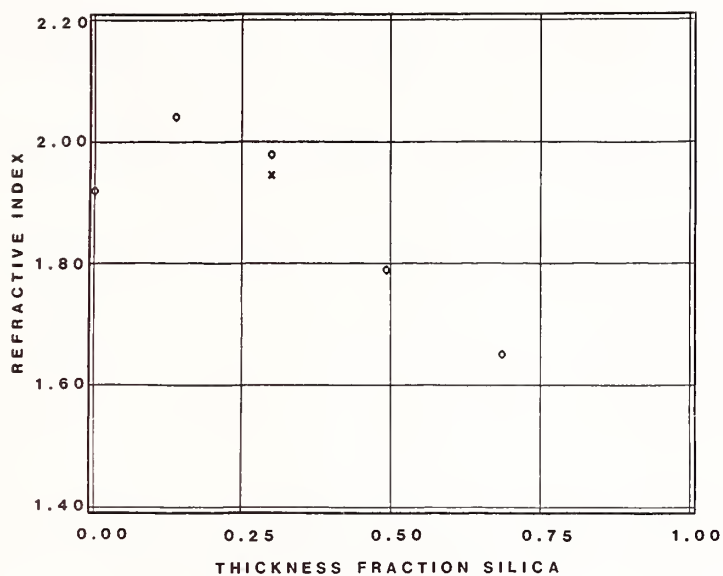


Figure 1. Refractive index of zirconia:silica films vs. thickness fraction of silica for film set one. The dots were obtained from channel spectra and stylus thickness measurements. The x was obtained by m-line spectroscopy.

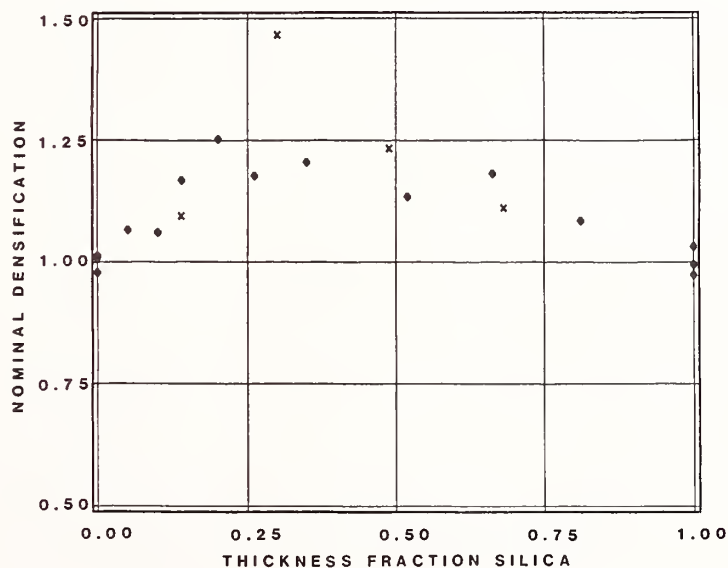


Figure 2. Nominal densification of zirconia silica films vs. thickness fraction of silica. The x's are for film set one, the dots for film set two.

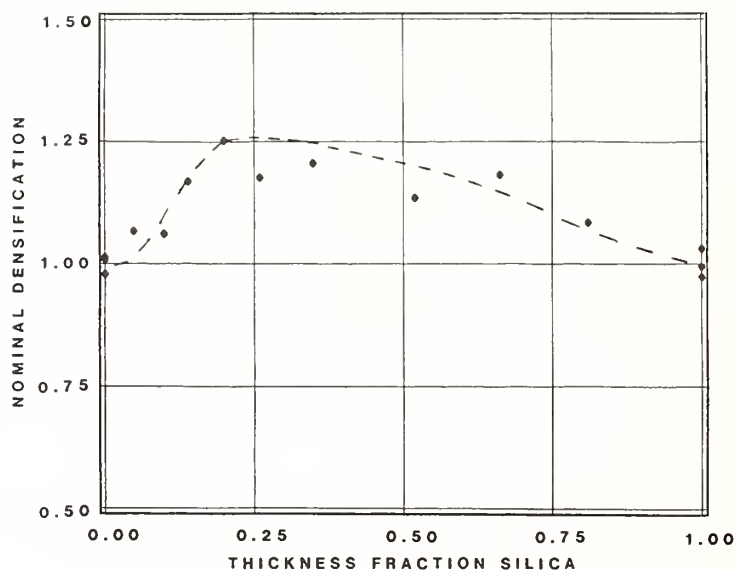


Figure 3. Nominal densification of zirconia:silica films vs. thickness fraction of silica. The curve is derived from the porosity model calculation with $p_1=0.10$, $p_2=0.25$, $A_1=0.15$, and $A_2=0.25$. The data are from film set two.

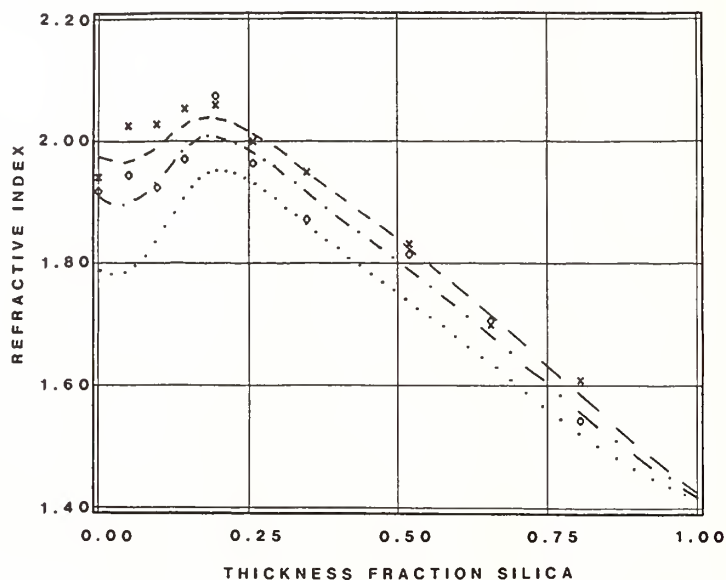


Figure 4. Refractive index of zirconia:silica films vs. thickness fraction of silica. The three curves shown were derived by insertion of the results of the porosity model into models of refractive index for mixed component systems. The topmost curve is for the Drude model, the middle curve is for the linear model, and the lowermost curve is for the Lorentz-Lorenz model. The data are from film set two. The x's were obtained by m-line spectroscopy, the dots from channel spectra and stylus measurements.

The Formation and Development of Nodular Defects in Optical Coatings

Bangjun Liao, Douglas J. Smith and Brian McIntyre

LABORATORY FOR LASER ENERGETICS
and
NEW YORK STATE CENTER FOR ADVANCED OPTICAL TECHNOLOGY
THE INSTITUTE OF OPTICS
University of Rochester
250 East River Road
Rochester, New York 14623-1299

We have investigated the nodular defect using computer simulations and experimental techniques. A modified version of the hard-disk model, in which the migration and attraction of atoms are introduced in simplified ways, is used to simulate the formation and development of nodules. This simulation reveals the self-extending nature of nodule growth and the dependence of the nodule shape and size upon the conditions of the coating's formation, including deposition geometry, migration, and capture length of atoms. By planting artificial seeds on substrate surfaces and overcoating with single and multilayer stacks, we have encouraged nodular formation under controlled and variable deposition conditions. Fractured cross-sections of these coatings have been examined by scanning microscopy (SEM). A comparison between our experimental observations and the modeling results help explain the mechanisms for nodule growth.

KEY WORDS: Coating defects; nodules; hard-disk model; laser damage; thin films; thin film structure.

1. Introduction

The nodule is a characteristic defect in optical coatings. It causes scattering and moisture penetration; in high energy laser coatings, the localized stress, [1] localized heat, [2] and micro-lens effects [3] generated by nodules are assumed to trigger laser-induced damage. Nodular defects have been found in various metal and dielectric films which are fabricated by sputtering, chemical vapor deposition, electroplating, thermal evaporation (both electron beam and thermal resistive) and ion plating. A number of reports have focused on this microstructure during the last 15 years. K. Guenther [4] outlined the importance of the nodule in optical coatings. Nodular defects [5] were thought to be formed by the same self-shadowing effects which cause columnar structure. [4,5] However, this effect alone can

explain neither the nodular growth in the films deposited at normal incidence nor the peculiar shapes of nodules. This paper investigates the character, formation, and development of nodular defects in thin films. Computer simulation and experimental verification are emphasized.

By using the modified version of the hard-disk model, the simulation maintains the simplicity which has made it possible to model the growth of a film on a large scale (up to 120,000 deposited disks). The modified model can accommodate different deposition conditions and material properties and thereby link the growth of nodules to these conditions.

2. Hard Disks with Multi-Jumping and Variable Capture Length

The starting point of our calculation is the two-dimensional hard disk model of Dirks and Leamy [6] in which disks fall randomly onto the surface and then stick where they land or roll into the nearest pocket, where each disk is supported by two other disks which had arrived earlier. This model describes the general appearance of the columnar structure and the behavior of columnar angle in a thin film, but it can only grow low density films and cannot be used to provide more information about film features and formation conditions. During actual condensation, an adatom or admolecule moves some distance over the surface after impact due to transverse momentum and thermal diffusion. [7] This migration of adatoms and admolecules depends on substructure temperature, kinetic energy of incident flux, residual atmosphere, surface topography and the adatom's and admolecule's activation energy.

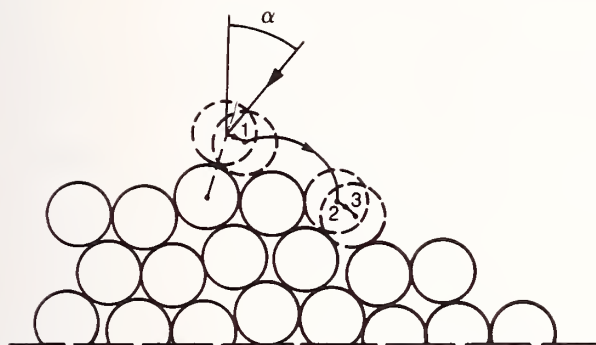
The modified model (Fig. 1) [8,9] includes the migration process such that an incident disk can move over the surface by jumping from one pocket to another after impingement until an eligible site is reached.

The model quantitatively represents the mobility by λ , which is the average distance traveled by the disk divided by the diameter of the disks. This mobility, λ , is derived from the product of the distance traveled and the probability of jumping 1, 2, 3 . . . or N times:

$$\lambda = 0.6R_1 + 1.6R_2 + \dots + nR_n \quad (1)$$

where $R_1, R_2 + \dots R_n$ form a probability distribution function for 1, 2, . . . N jumps. These satisfy,

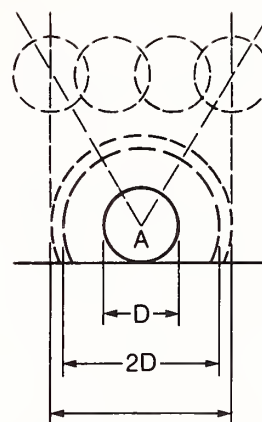
$$\sum_{j=1}^n R_j = 1 \quad (2)$$



α = vapor incidence angle
 λ = average distance jumped by hard disks

G1625

Figure 1 The modified hard disk model allows multiple jumps of an adatom after it impinges on the substrate. In this example the adatom was allowed to jump three times before coming to rest.



$2D \times \text{extending factor}$

G1755

Figure 2 An approximate potential is implemented by extending the capture length of an adatom. In the hard disk model the capture length is just $2 \times$ the diameter of the adatom. In our model we extend this length by a factor ranging from 1 to 1.75.

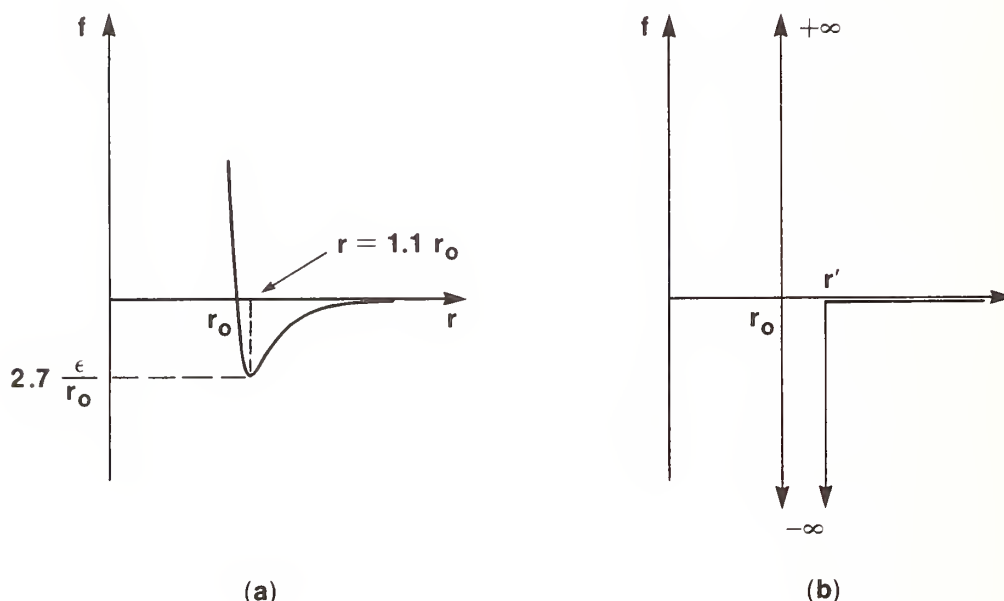
The coefficients 0.6, 1.6, 2.6 . . . are the average distance traveled by a disk for 1, 2, 3 . . . jumps and are determined by another simulation. The number of jumps taken by a disk is determined randomly, but is constrained to follow the probability distribution given by the values for R_1 , R_2 , R_3 which are input during the simulations. The actual value for λ is output after the simulation is complete.

The interaction between atoms or molecules can be generalized by the Lennard-Jones potential. One expression for this potential used by Leamy et al. [10] in their dynamic simulation is,

$$\phi(r) = \epsilon \left(\left(\frac{r_0}{r} \right)^{12} - 2 \left(\frac{r_0}{r} \right)^6 \right) \quad (3)$$

where r is the distance between disks, r_0 is the equilibrium value of r for $\frac{d\phi}{dr} = 0$ and ϵ is the value of $-\phi(r_0)$. Conventionally the negative sign denotes the attractive forces, and the positive sign indicates the repulsive forces so the first and second term in the square bracket correspond to attraction and repulsion, respectively. Figure 3(a) is the curve for the force of the potential function, $f = -d\phi/dr$. The maximum of the attractive forces occurs at $r = 1.1r_0$, and it still has a value of one-fourth of the maximum at $r = 1.5r_0$. This reflects

the behavior of the long range attractive forces. A simplified representation of this interaction can be included in the hard disk model by extending the capture length. The capture length is the diameter of a circle which will cause a passing disk model to be "captured" by the fixed disk (Fig. 2). In the common hard disk model the capture length is two times the diameter of the disk, i.e., the disks must collide in order to be captured. By extending the capture length we create an approximation of the attractive forces. A disk passing within the extended capture length will be attracted to the fixed atom. The force of this simplified potential is shown in Fig. 3(b). In our model we multiply the capture length by an extending factor ranging from 1 to 1.75.



G1754

Figure 3 The force resulting from the Lennard-Jones potential is shown in Figure (a). The approximation to this force as it is used in the simulation program is shown in Figure (b).

Simulation programs have been implemented on IBM-XT and HP9000/200 microcomputers. By choosing various parameters one can create a coating with a nodule in "controlled conditions." One of the programs can trace the dynamic process of a "coating" growth on a computer screen.

Experiments in support of the simulation activities used Al_2O_3 grains, whose diameters were larger than $0.05 \mu\text{m}$, as seeds for nodule growth on polished glass surfaces. The seeded

substrates were overcoated with either a single layer of ZnS or multilayer Ta_2O_5 - SiO_2 stacks. Both normal incidence on stationary substrates and various oblique-incidence angles for rotating substrates were explored. The samples were fractured, and coating cross sections were examined by scanning electron microscopy.

3. The Self-Extending Effects of Clusters and Nodules

Almost all nodule shapes found in thin films are characterized by an inverted cone with a dome or elliptical top. Their diameter increases monotonically with the film thickness, which we describe as a self-extending effect of nodules and clusters. This formation of the nodule can be visualized by examining the effect of the extended capture length on the growth process. We find that nodule-like growth occurs even when the effects of the surrounding film are ignored in structures we call clusters.

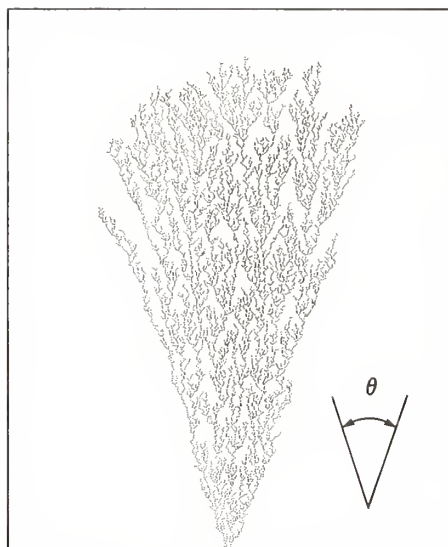
A deposited disk, A, has a capture length greater than its diameter, as shown in Fig. 2. New disks arriving randomly within this capture length will impinge upon A so that the cluster starting at disk A extends its diameter during the growth and forms a cone regardless of seed size or adatom mobility. The cone angle of clusters which form on an individual disk is $36^\circ \pm 2^\circ$ at $\lambda = 0$ as shown in (Fig. 4a), and is almost the same result as P. Ramanlal's disk fan. [11] The cone angles vary from 30° - 40° if clusters initiate at a larger circle seed (Fig. 4b).

The effects of extending the capture length, when adatom mobility is present, are seen in Figs. 4(c) and 4(d). An increase in mobility results in a decrease of the cone angle of the cluster when the capture length is not extended. However, if the capture length of the disks is extended the cone angle of the cluster increases. This suggests that longer range attractive forces between atoms produce larger cone angles on the nodules.

Clusters forming on a smooth substrate will not initiate the self-extending process in the computer simulations because of the competition among adjacent clusters. Nodules will not form spontaneously from homogeneous nucleations on substrate surfaces for similar reasons. Only those clusters which start at protrusive seeds have chances to develop the shapes of nodules.

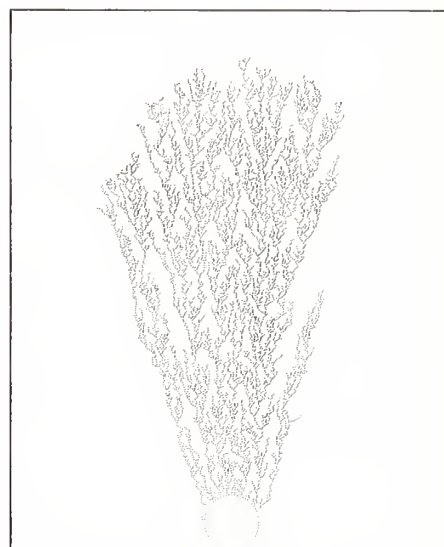
4. The Geometry of Nodule Growth

Nodules take two distinctly different forms depending on whether or not the substrate is rotated in its own plane during deposition. Substrate rotation with an offset vapor source is commonly used to provide thickness uniformity on the substrates.

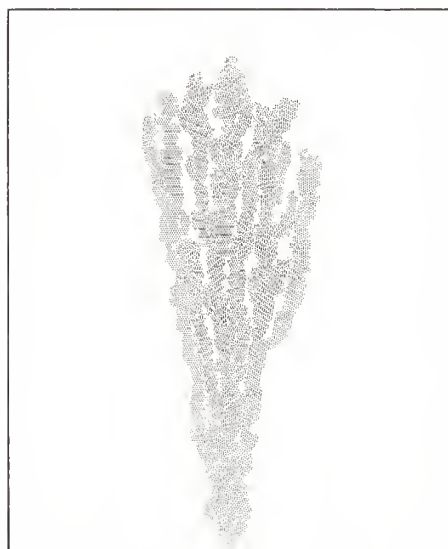


(a) nucleus: single disk
 $\lambda = 0, \theta = 36^\circ \pm 2^\circ$

G1626



(b) nucleus: circle
 $\lambda = 0, \theta = 30^\circ \sim 40^\circ$



(c) $\lambda = 1.9, \theta = 20^\circ$
 extending factor = 1.0

G1627



(d) $\lambda = 2.0, \theta = 45^\circ$
 extending factor = 1.5

Figure 4 Development of the model for simulating cluster growths in "free space." Growths with low adatom mobility are seen in (a) and (b) where the nucleus is a single adatom and a larger circle. Repeated trials of (a) gave consistent values for the cone angle. Allowing some adatom mobility (c) results in a lower cone angle. Extension of the capture length (d) increases the cone angle.

A growth simulation of a nodule on a non-rotating substrate with normal vapor incidence is shown in Fig. 5(a). The structure is characterized by straight sides similar to those of Fig. 5(b) (single layer of ZnS) and Fig. 5(c) (multilayer of Ta₂O₅-SiO₂). The cone angle of the nodule in Fig. 5(c) is 42°, close to the cluster with an extending factor of 1.5 in Fig. 4d. The thickness of the simulated film in Fig. 5(a) is about 1700 Å if a disk represents an atom of diameter 5 Å.

Figure 6(a) is a simplified case of the initial stage of cluster growth on a rotating substrate with oblique vapor incidence ($\alpha = 50^\circ$). Any point on the nodule side is exposed to the incident flux during half of a rotation period so that the seed grows with a cone angle 2γ .

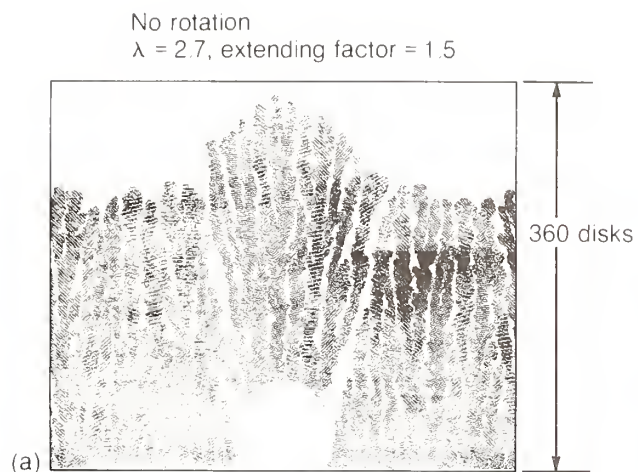
If J is the intensity of incident flux, and α is the incident flux angle, the evolved angle, γ , satisfies:

$$\text{TAN } \gamma = \frac{\int_{-\frac{\pi}{2}}^{\frac{\pi}{2}} J \sin(\alpha - \gamma) d\phi}{\int_0^{2\pi} J \cos \alpha d\phi} \quad . \quad (4)$$

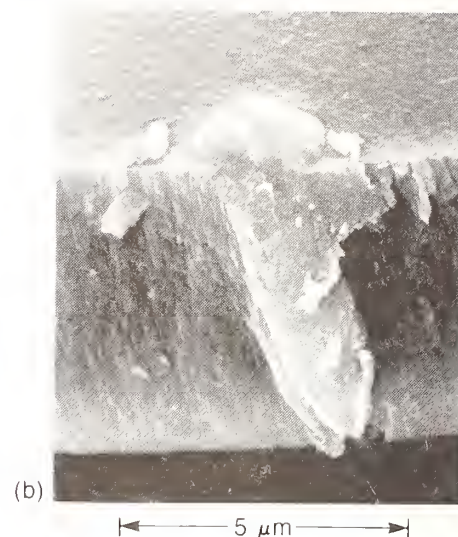
For small γ , the approximation holds:

$$\text{TAN } \gamma \approx \frac{1}{(1+\pi)} \tan \alpha \quad .$$

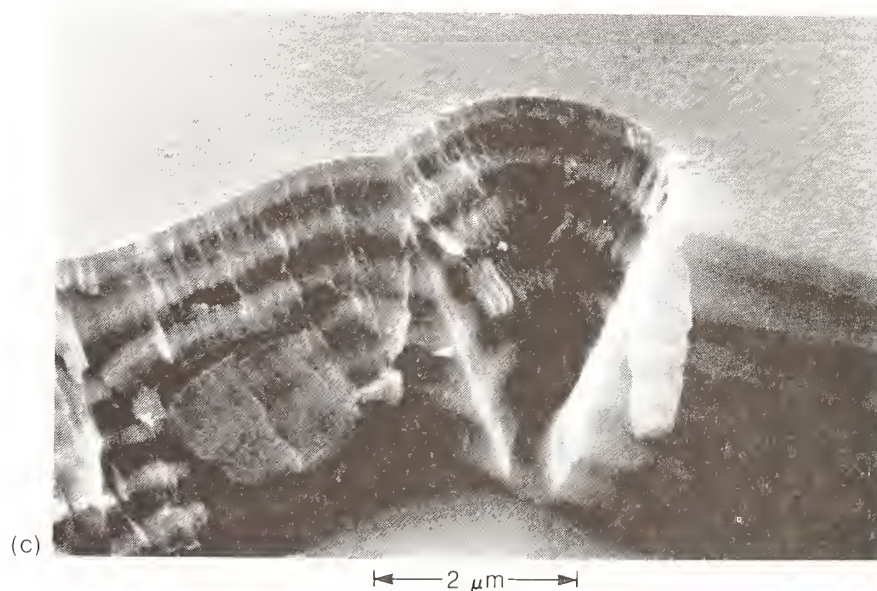
Equation (4) establishes the relation between α and γ in a cluster forming on a rotating substrate. An increase in the incident angle α results in a corresponding increase in the cone angle γ . A cluster enlarges its diameter rapidly (Fig. 6(b)) during the early growth stage. In fact, Eq. (3) holds only at the initial stage of a coating growth. After the step around the seed disappears and the dome on the top of the nodule forms, the increase of the nodule's diameter slows down. As a result, a bowl-like bottom or parabolic sides evolve in contrast with the straight sides of the nodules grown under normal incident flux on stationary substrates (Fig. 7). Nodules in a coating deposited by wide source (for instance, sputtering) exhibit similar shapes due to the spread in angle of incident particles. Figures 8(a) and 9(a) are two nodule simulations growing on 3-dimension rotating substrates (on axis). Note that the diameter



G1629



G1631



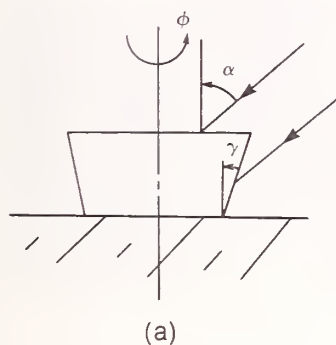
G1630

Figure 5 The characteristic shape of a nodule formed on a fixed substrate with normal vapor incidence is an inverted cone. The model (a) is supported by experiment with single (b) and multiple (c) layer films

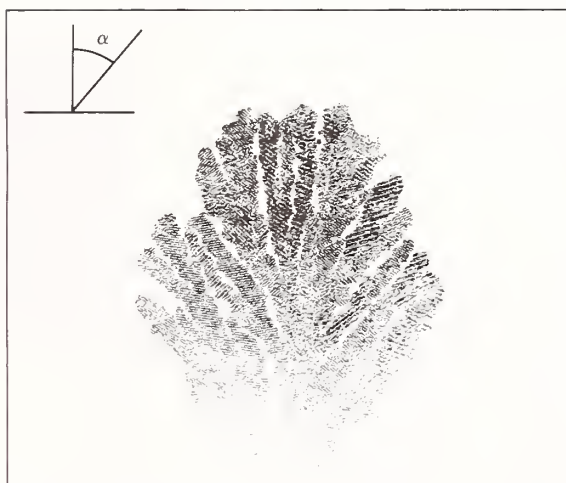
$$\tan \gamma \approx \frac{1}{(1 + \pi)} \tan \alpha$$

$$\alpha = 50^\circ, \lambda = 3.5$$

$$\text{extending factor} = 1.5$$

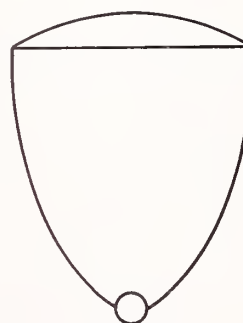
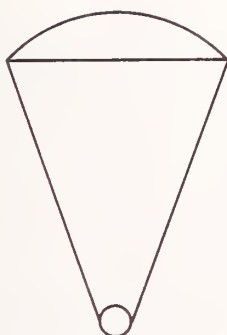


(b)



G1638

Figure 6 Rotation of the substrate and an oblique vapor incidence results in an increase in the nodule cone angle. The simulation in (b) shows this effect for a nodule without the restrictive influence of the surrounding film. This is typical for the initial stages of nodule growth.



G1632

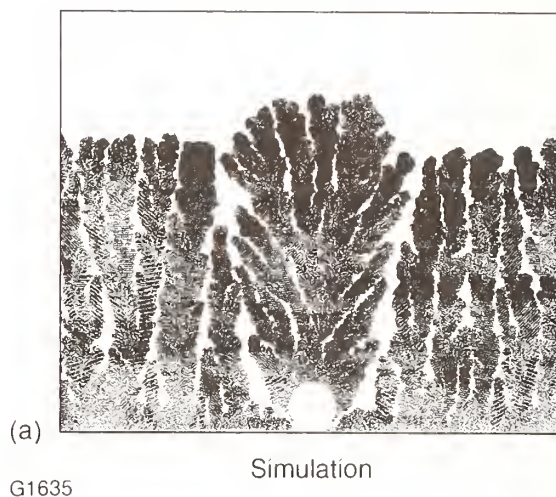
Figure 7 There are two characteristic shapes of nodules in vapor-deposited films. The shape on the left is typical of films deposited with a fixed incident flux. The shape on the right corresponds to a nodule formed on a rotating substrate with an oblique incidence source.

of the nodule grown on incident angle $\alpha = 70^\circ$ is much larger than that on $\alpha = 50^\circ$. In Figs. 8(b) and 8(c) as well as Figs. 9(b) and 9(c) experimental test specimens are shown for comparison. Although the scale lengths are orders of magnitude different between simulations

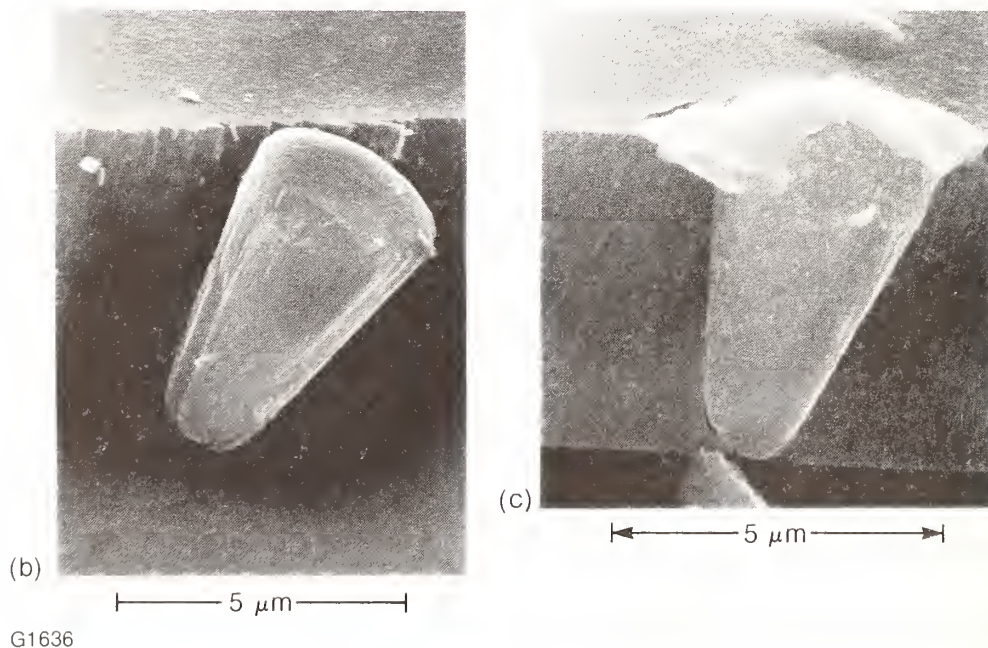
(Figs. 9(a) and 10(a)) and the corresponding micrographs ((b) and (c) of both figures), the visual agreement in geometry is quite good.

Figure 8 Nodule simulations and experiments on rotating substrates at 45 degrees vapor incidence.

$\alpha = 50^\circ$, $\lambda = 3.5$, extending factor = 1.5



45° vapor incidence/single ZnS film



A seed is a necessary condition for the nodule to form. However, while larger seeds tend to generate larger nodules in simulations, not all seeds will grow into nodules. We find that a seed of three disk diameter merges in a film during simulated growth at normal incidence. At

sufficient adatom mobility ($\lambda = 3.4$), disks migrate longer distances along the surface and fill the volume around the small seed. Larger imperfections, such as dust, polishing residue, and rough protrusions on substrate surfaces all act as the starting point for nodules. Smaller defects on substrates, such as impurities, scratches, steps and ledges are the favorable sites for nucleation and may develop into large seeds for nodules under suitable condensation circumstances.

Figure 9 Nodule simulations and experiments at 70 degrees vapor incidence. The size of the nodules varied significantly at this vapor angle.

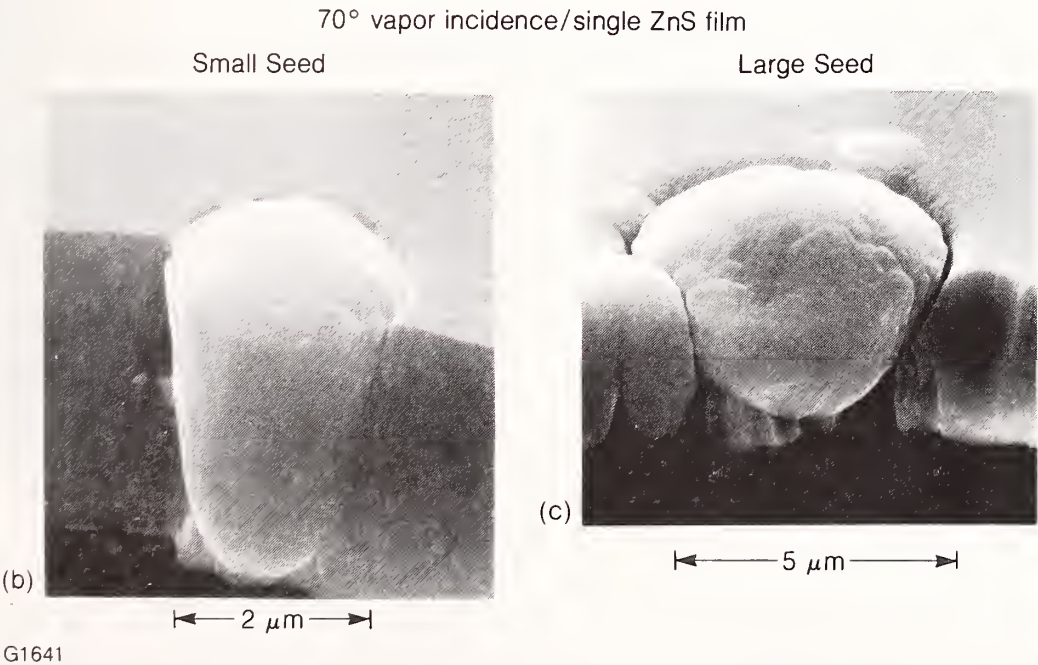
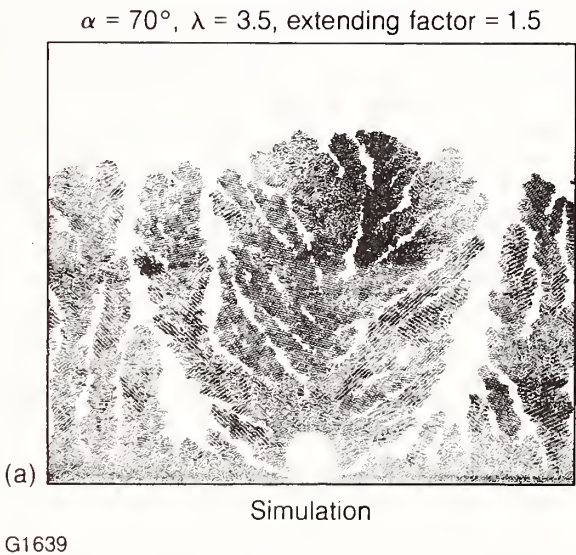
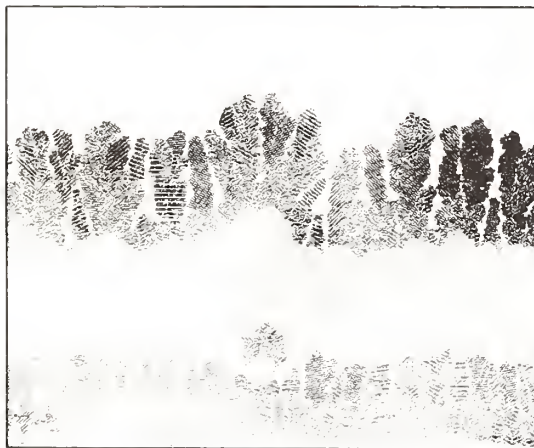


Figure 10 shows the simulation for a three-layer film containing a nodule initiated at a spatter site in first layer. It also shows the nodule growth through the layer interfaces. There are three nodules in Fig. 11. They grew on the same substrate, but apparently have different sizes and shapes, which may originate from the various size seeds, since the simulation has shown that significant differences in nodule sizes follow the various sizes of seeds even if the other conditions are almost the same. A seed significantly higher than the substrate will exhibit growth similar to a cluster. In this sense, the shape of the nodule relates to the size of the seed and the thickness of the film.

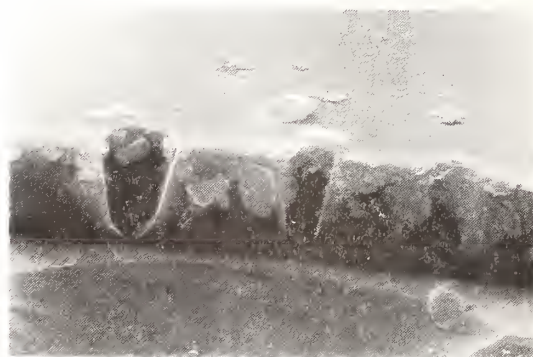
The shadowing effect of a nodule produces an empty area around it during growth that causes a gap if addisks do not have enough migration to fill the area. These gaps, which amount to 50 Å to 100 Å in corresponding simulations, depending on mobility, can be clearly seen around large nodules in the SEM micrographs of the film cross sections (Fig. 9). These gaps represent a significant break in a film's continuity. They also impede thermal conductance away from the nodule if, under high-power laser irradiation, the nodule's absorption should cause local heating.

$\alpha = 50^\circ$, $\lambda = 3.7$, extending factor = 1.25, rotation



G1642

Figure 10 Particles thrown up from the evaporant can act as the nucleus for nodules. The nodule seen here also propagates up through a multilayer.



G1637

Figure 11 Nodule size is related to the size of the seed. The three adjacent nodules in this picture are the result of varying sizes of the seed or agglomerated particles.

5. Conclusion

We have shown that the growth of nodules in coatings is a physical process which depends on the geometry of the coating process. The increasing diameter of the nodules with thickness is due in part to the extension in capture length of the disks. Attractive forces between adatoms are responsible for the extended capture length. Only hard disk models which include this extended capture length will correctly predict nodule shape.

In our study nodule growths only occur at seeds which protrude above the surface of the film. The seeds may take many forms, including dust, preferential nucleation sites, or spatter from the vapor source. The nodules take two distinct shapes: those produced on rotating substrates form a rounded bowl-like bottom, while nodules on stationary substrates form an inverted cone with straight sides.

As one might expect in the rotating substrate case, an increase in the vapor incidence angle results in a large nodule. The self-shadowing effect in this case also generates a gap separating the nodule from the surrounding film. This gap may be seen in both the simulations and experiments and may be responsible for local heating within the nodule. The cone angle is also a function of adatom mobility and decreases as the adatoms become more mobile. Further work will examine techniques to reduce the formation of nodules and modeling defects in different deposition schemes.

Acknowledgment

The work performed at Rochester was supported in part by the New York State Center for Advanced Optical Technology of The Institute of Optics, the U.S. Department of Energy Office of Inertial Fusion under agreement No. DE-FC08-85DP40200 and by the Laser Fusion Feasibility Project at the Laboratory for Laser Energetics which has the following sponsors: Empire State Electric Energy Research Corporation, General Electric Company, New York State Energy Research and Development Authority, Ontario Hydro, Southern California Edison Company, and the University of Rochester.

References

1. T. Spalvins and W.A. Brainard, J. Vac. Sci. Technol., Vol. 11, 1186 (1974).
2. K.H. Guenther, Appl. Opt., Vol. 23, 3806 (1984).
3. J. Murphy, Contemporary Infra-Red Sensors and Instruments, Bellingham, WA, SPIE, 1980, p.64 (SPIE Vol. 246).
4. K.H. Guenther, Appl. Opt., Vol. 20, 1034 (1981).
5. J.W. Patten, Thin Solid Films, Vol. 63, 121 (1979).
6. A.G. Dirk and H.J. Leamy, Thin Solid Films, Vol. 47, 219 (1977).
7. K.L. Chopra, Thin Film Phenomena, Chapter 4, Robt. E. Krieger, Publ., Huntington, NY (1969).

8. Bangjun Liao and H.A. Macleod, Proceedings of the Southwest Conference on Optics of SPIE, Vol. 540, 4-8 March 1985, #TA 118.
9. Bangjun Liao and H.A. Macleod, Thin-Film Microstructure Modeling, Proc. SPIE, Vol. 540, 150 (1985).
10. H.J. Leamy, G.H. Gilmer, and A.G. Dirks, Current Topics in Material Science, North-Holland Publishing Company, 6 (1980), p.309.
11. P. Ramanlal and L.M. Sander, Physical Review Letters, Vol. 54, 1828 (1985).

Interfacial Structure of Ion-Beam Sputter Deposited $\text{SiO}_2/\text{TiO}_2$ Coatings

J. R. Sites and H. Demiryont

Physics Department, Colorado State University
Fort Collins, CO 80523

X-ray photoelectron spectroscopy (XPS) was used to evaluate the interfaces between ion-beam sputter deposited SiO_2 and TiO_2 layers, their free surface, and their interface with a silicon substrate. XPS depth profiles of nominally abrupt $\text{SiO}_2/\text{TiO}_2$ interfaces showed mixing over an 7 nm range, but no valence states other than Si^{+4} and Ti^{+4} . Thus the interfacial region consists of $\text{Si}_{1-x}\text{Ti}_x\text{O}_2$ where x varies from 0 to 1. The free surface of either SiO_2 or TiO_2 extends over 1.5 nm and shows evidence of OH bonds, presumably due to absorbed water. Interfaces between SiO_2 , or TiO_2 , and an optically smooth silicon substrate are about 3 nm wide and exhibit +2 and 0 bonding states for Si, and +2 for Ti, states characteristic of oxygen deficient films. The TiO_2/Si interface also contains Ti-Si bonds, or partial silicide formation.

Key words: optical coatings; interfaces; ion beams; TiO_2 ; SiO_2 ; x-ray photoelectron spectroscopy.

1. Introduction

Multilayer $\text{SiO}_2/\text{TiO}_2$ coatings have long been used to minimize or maximize reflection from optical components. The optical characteristics of such coatings are determined by both the bulk properties of the individual films and those of the interfaces between films. This report examines such interfaces in ion-beam sputter deposited coatings using x-ray photoelectron spectroscopy (XPS).

2. Ion-Beam Sputter Deposition

Silicon and titanium oxide films were deposited by ion-beam sputter deposition techniques, which are described in more detail elsewhere [1-2]. A mixed argon-oxygen beam, 1100 eV in energy and 1 mA/cm² in current density, is neutralized by an equal density of electrons. It strikes either a titanium or a silicon oxide target, and sputters material onto a nearby substrate. The two oxide targets can be switched in situ to produce layered coatings. They can also be partially overlapped to produce $\text{Si}_{1-x}\text{Ti}_x\text{O}_2$ films with any value of x from 0 to 1.

Figure 1 shows schematically the types of structures used for test purposes. The substrates were polished silicon wafers intended for semiconductor fabrication. For the XPS studies, thicknesses were deliberately kept small (10-20 nm/layer) so that interfaces could be reached without excessive etching. The two layer structures of 1a were used for interfacial measurements, the single layers (1b) for bulk reference as well as for free surface and substrate interface studies, and the composite films (1c) for comparison with the interfacial region of 1a.

3. X-ray Photoelectron Spectroscopy

X-rays are used to expel core electrons from the material under study. As seen in figure 2a, the x-ray energy used is 1254 eV, and the measured kinetic energy (KE) of the electrons is simply 1254 eV minus their original binding energy (BE). The escape depth of electrons varies with energy but is typically 1-2 nm, meaning that the measurement technique is very surface sensitive. Energy analysis of the electrons, plus the appropriate sensitivity factors, reveals the relative concentrations of the constituent elements. On a finer energy scale, one can deduce the type and number of neighboring atoms. In many cases, the splitting of peaks will reveal the relative amounts of different bonding states [2-4] and the width of peaks, the distribution of bond angles [5].

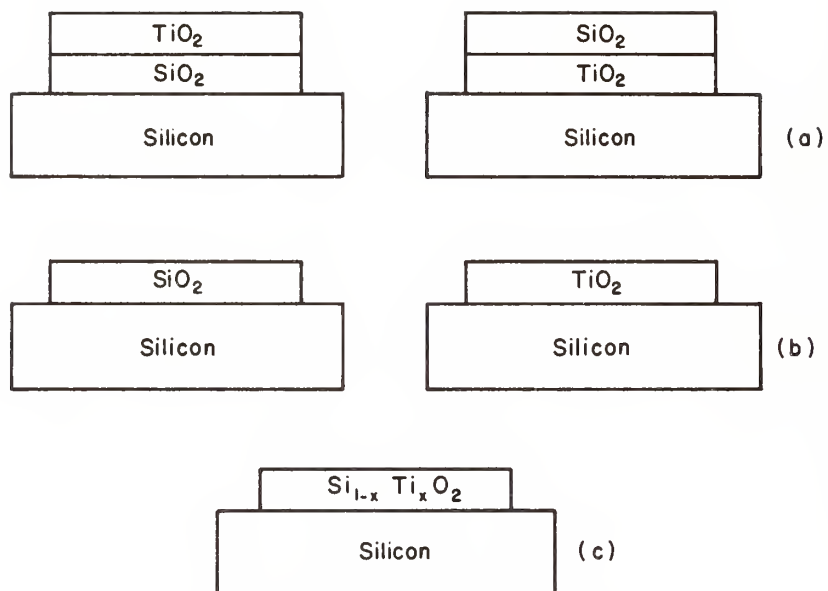


Figure 1. Schematic of test structures used.

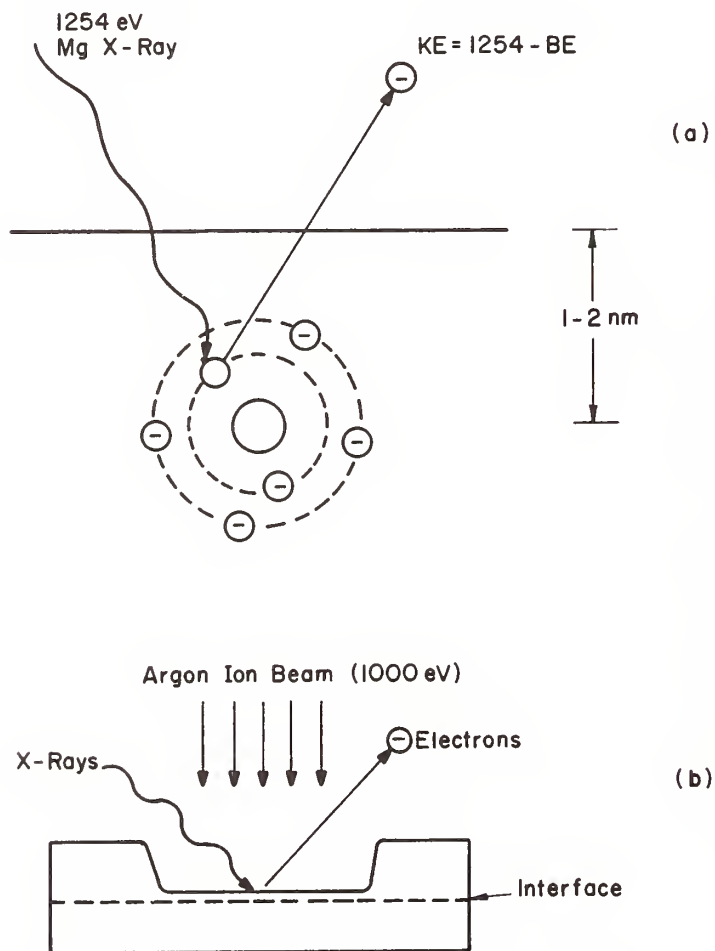


Figure 2. (a) Schematic drawing of the x-ray photoelectron process. (b) Depth profiling using an argon ion beam.

To measure changes in composition as a function of depth, the sample is etched with an argon ion beam (figure 2b). To avoid atomic rearrangement induced by the ion beam, a relatively low energy (1000 eV) is used, and the measured spectra are monitored for signs of peak broadening as a function of etch time. In practice the etching and the XPS measurement are alternated so that the result is a stepwise profile as a function of depth. There is some concern about charging the surface of insulating materials, and hence shifting the observed electron energies. In the present work, however, the thin layers seem to allow a weak, but sufficient, electrical contact to the silicon substrate.

4. $\text{SiO}_2/\text{TiO}_2$ Interface

Figure 3 shows representative spectra taken at different points during an etch through the TiO_2 - SiO_2 structure of figure 1a. Within the nominally TiO_2 top layer (3a), only the Ti 2p

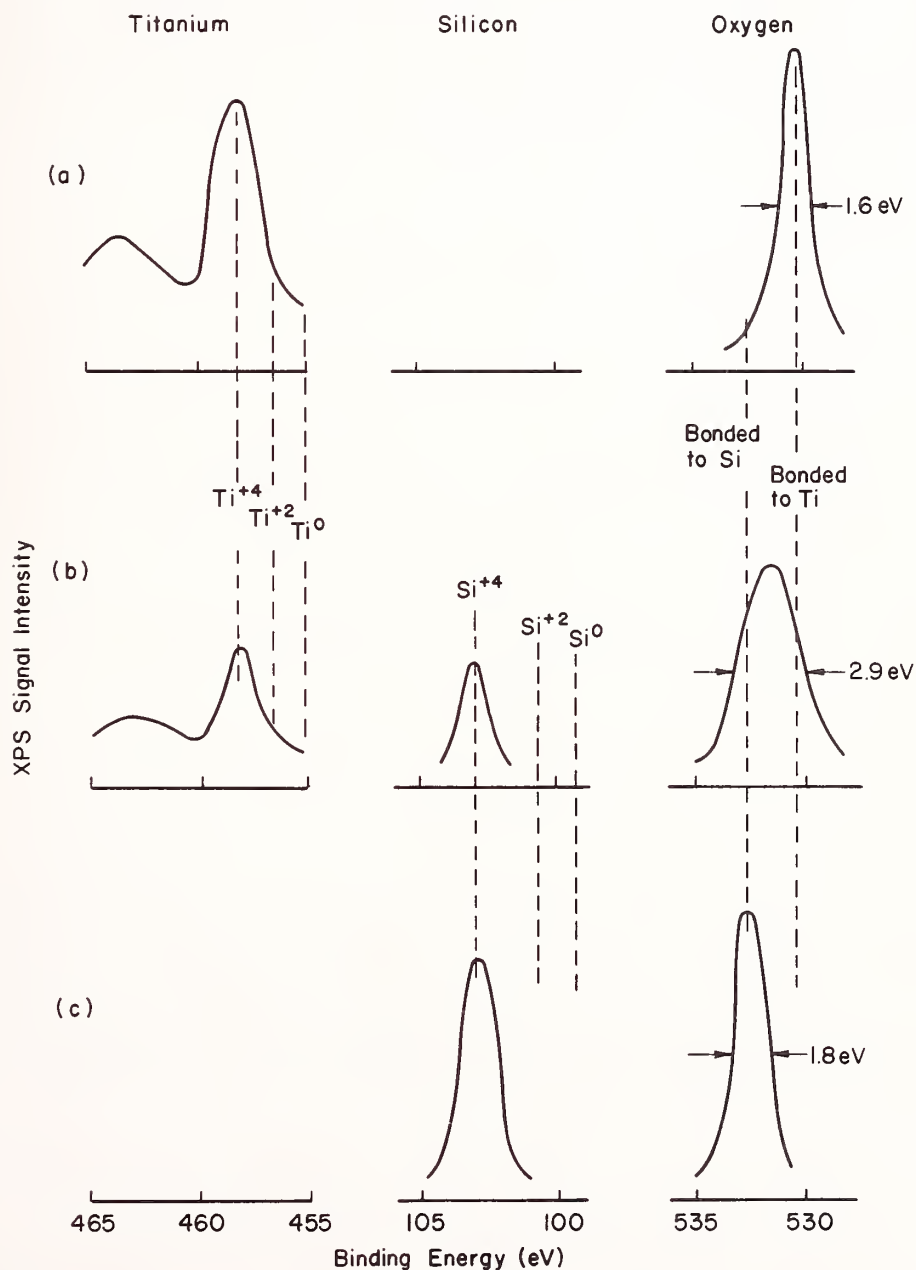


Figure 3. XPS response from (a) TiO_2 top layer, (b) $\text{TiO}_2/\text{SiO}_2$ interface, and (c) SiO_2 lower layer.

doublet and the $O\ 1s$ single line are seen. Furthermore, the titanium spectrum shows only the Ti^{+4} bonding state (four oxygen neighbors), with no evidence of Ti^{+2} or Ti^0 as seen in non-stoichiometric titanium oxides [3].

In the interfacial region (figure 3b), the titanium response is reduced in magnitude, but otherwise unchanged. The $Si\ 2p$ line appears, and like the titanium, only shows the +4 valence state. The oxygen line increases in width and shifts to higher energies, as expected if some of the titanium neighbors are replaced by silicon. The total area of the oxygen line is unchanged. Quite likely, the oxygen peak is actually a superposition of three bonding energies: oxygen bonded to two silicon atoms, oxygen bonded to one silicon and one titanium, and oxygen bonded to two titaniums [2]. This spectrum, midway through the interface, is virtually identical to that from a composite $Si_{1-x}Ti_xO_2$ film (figure 1c) where $x = 0.5$.

Finally in the nominally SiO_2 layer (figure 3c), the titanium line has disappeared, the silicon line is larger, but still shows only one valence state, and the oxygen line has narrowed again, its energy corresponding to silicon neighbors only. Figure 4 shows the normalized areas of the titanium, silicon and oxygen peaks as a function of depth into the coating. The depth calibration is made by measuring the time to etch through single layers (figure 1b) of known thickness, deposited simultaneously with the double layers. The transition from pure TiO_2 to pure SiO_2 takes place over a distance of approximately 7 nm implying considerable mixing of the sputter deposited constituents.

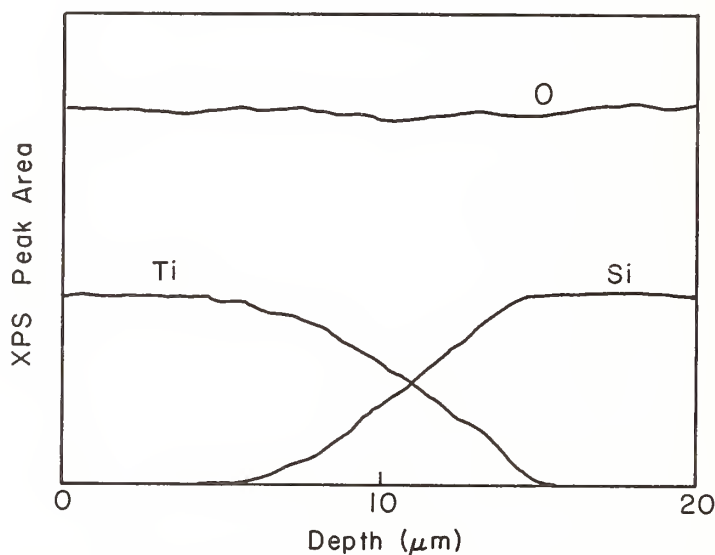


Figure 4. XPS depth profile through TiO_2/SiO_2 interface.

5. Free Surface and Substrate Interfaces

The XPS information for the free surfaces of SiO_2 and TiO_2 , and their interfaces with the silicon substrate are summarized in figure 5. For both oxides, the free surface shows (5a) a high energy shoulder on the oxygen line due to $(OH)^-$ from absorbed water vapor. This shoulder quickly disappears when the depth profile is begun, the distance being about 1.5 nm. In the bulk of the single layers the spectra are identical to those of the double layers discussed above. At the substrate interface, however, the oxygen line is broadened. In the TiO_2/Si case the broadening is due once again to oxygen having both titanium and silicon neighbors; for SiO_2/Si the bond angles have presumably become more distorted.

At the SiO_2/Si interface (figure 5b), the silicon line is split into the three valence states seen in non-stoichiometric silicon. Farther into the substrate, the Si^0 peak becomes dominant. Width of the transition is approximately 3 nm. At the TiO_2/Si interface, there are two features to note. First (figure 5c), the titanium oxide becomes oxygen deficient, and the characteristic +2 sub-oxide valence peak is seen, possibly meaning that the stronger tendency of oxygen to bond with silicon is drawing it away from the titanium. However, no evidence of metallic titanium (Ti^0) or of silicon oxides is seen. Instead the residual titanium forms a Ti-Si bond, or a silicide structure then diminishes to zero, again over a 3 nm distance.

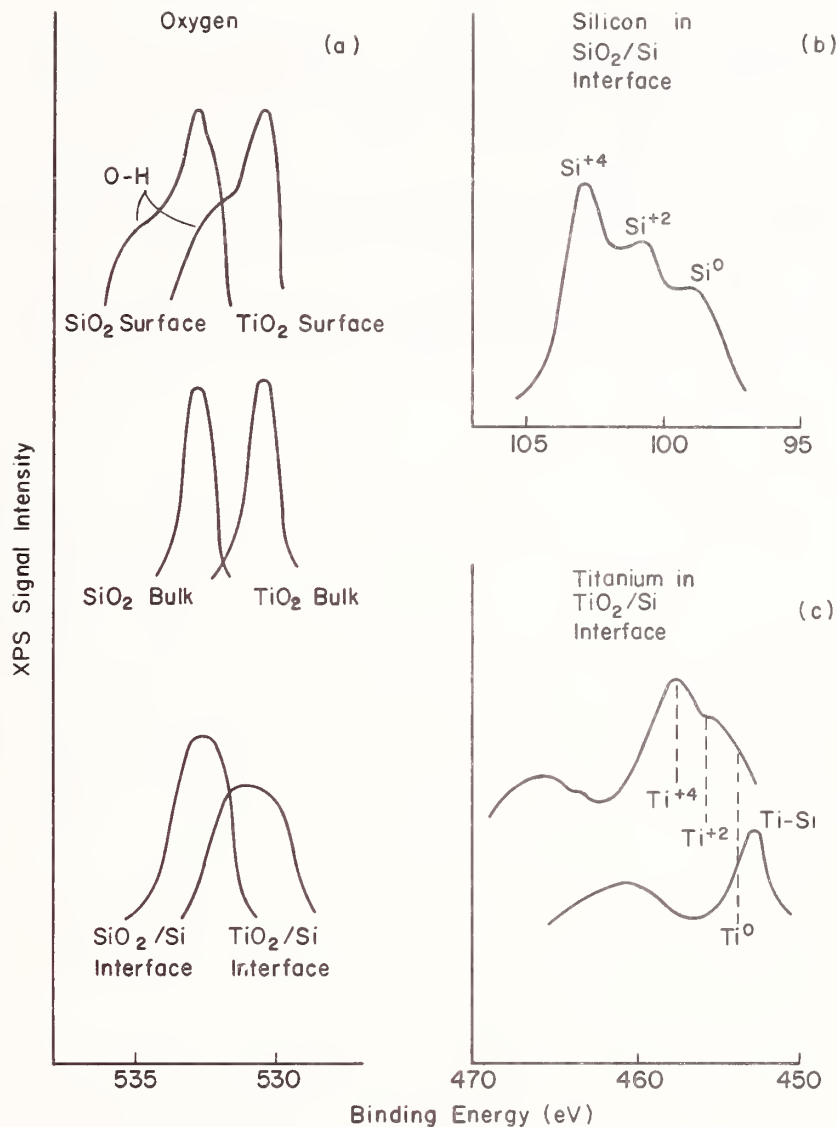


Figure 5. (a) Oxygen XPS response at free surface, bulk and substrate interface for SiO₂ and TiO₂ single layers. (b) Silicon XPS spectrum at SiO₂/Si interface. (c) Titanium XPS spectra just above and just below TiO₂/Si interface.

6. Conclusions

The interfaces between layers of ion-beam sputtered SiO₂ and TiO₂ extended over approximately 7 nm, the free surface over 1.5 nm, and the silicon substrate interface over 3 nm. There was no indication of sub-oxide bonding in either the oxide layers or in the interface between them. The free surface, however, did show substantial water vapor, and the TiO₂/Si interface evidence of silicide formation.

We gratefully acknowledge assistance with the XPS apparatus and from Kent Geib. This work was supported by the Air Force Weapons Laboratory under Contract F29601-83-K-0079.

7. References

- [1] Sites, J.R.; Gilstrap, P.; Rujkorakarn, R. Ion beam sputter deposition of optical coatings. *Optical Engr.* 22(4): 447-449; 1983 July-August.
- [2] Rossnagel, S.M.; Sites, J. R. X-ray photoelectron spectroscopy of ion-beam sputter deposited SiO_2 , TiO_2 , and Ta_2O_5 . *J. Vac. Sci. Technol.* A2(2): 376-379; 1984 April-June.
- [3] Demiryont, H.; Sites, J.R. Effects of oxygen in ion-beam sputter deposition of titanium oxides. *J. Vac. Sci. Technol.* A2(4): 1457-1460; 1984 October-December.
- [4] Demiryont, H.; Sites, J.R.; Geib, K. Effects of oxygen content on the optical properties of tantalum oxide films deposited by ion-beam sputtering. *Appl. Optics* 24(4): 490-495; 1985 15 February.
- [5] Nucho, R.N.; Madhukar, A. in *The Physics of SiO_2 and Its Interfaces*, edited by S.T. Pantelides. New York: Pergamon; 1978. 60-75.

Ion Beam Deposited Oxide Coatings

T. Raj, J.S. Price, and C.K. Carniglia

Martin Marietta Aerospace, Laser Technology Systems
Kirtland Air Force Base, Albuquerque, NM 87119

Single-layer coatings of SiO_2 , Al_2O_3 and ZrO_2 were deposited by ion beam deposition (IBD). IBD is carried out by directing an ion source at a target made of the desired coating material. The material sputtered from the target is directed toward the substrate being coated. The targets chosen for this work were commercially available hot-pressed oxides. To further modify the coating properties, a secondary ion gun was directed toward the substrate to assist the deposition. Thus, ion assisted deposition (IAD) can be combined with IBD. The following coating deposition parameters were varied: composition of the sputter deposition gas mixture, composition of the ion assist gas mixture, and beam voltage and beam current for the ion assist beam. No external heat was applied to the substrates.

Single-layer ZrO_2 coatings were also deposited from a Zr metal target by bombarding this target with an O_2 :Ar ion beam (Reactive Ion Beam Deposition [RIBD]). These depositions were performed with ion assistance (RIBD/IAD) and without. However, filament life of the ion guns was found to be a problem with these coatings because of the presence of oxygen in the ion beam.

The refractive indices for all the coatings were determined by ellipsometry at 633 nm. Representative coatings were analyzed by Auger Electron Spectroscopy (AES) to determine stoichiometry and to provide information on the nature and level of impurities. The RMS surface roughness was determined by TIS (Total Integrated Scatter) measurements. In addition, absorption was determined for a few selected coatings from spectral transmission measurements. The influences of ion beam deposition parameters and ion assist-beam parameters on thin film properties of SiO_2 , Al_2O_3 and ZrO_2 coatings are discussed.

High reflector coatings at 351 nm were deposited on super-polished substrates utilizing the optimum deposition parameters obtained from the single-layer studies. The reflectors were made from ZrO_2 and SiO_2 targets. A peak reflectance greater than 99% was achieved.

Key Words: Al_2O_3 ; ion-beam deposition; ion-beam-assisted deposition; SiO_2 ; thin film coatings; ZrO_2 .

INTRODUCTION

The process of ion beam deposition (IBD) of optical coatings involves directing an ion source at a target made of the desired coating material. The material sputtered from the target is directed toward the substrate being coated. Coatings made using IBD are generally denser than those made using standard evaporation techniques.

In recent research on thin film deposition processes, substantial evidence has been collected that the film growth and the film properties may be significantly influenced if energy and momentum are supplied to the growing films by additional impinging ionized and accelerated species [1-3].¹ The process of direct impingement of the growing film by ions from an ion beam is termed ion assisted deposition (IAD). This technique has been successfully applied in modifying the film properties of evaporated optical coatings (especially dielectric oxides) by a number of researchers [4-9]. Ion assisted coatings are generally denser, less porous and have higher refractive indices than similar films made without IAD. However, the effect of ion assistance on IBD coatings has not been studied in detail. This effect is equivalent to the effect of bias-sputtering on a conventional sputter deposited coating. The technique of using two ion beams (one for deposition and one for ion-assistance) is termed dual-ion beam deposition by several groups [3]. A survey of published literature shows that a group of researchers at Colorado State

*This work was sponsored by the Air Force Weapons Laboratory, Air Force Systems Command, United States Air Force, Kirtland AFB, New Mexico 87117.

¹Numbers in brackets indicate the literature references at the end of the paper.

University has used the dual ion beam technique to deposit SiO_2 , Ta_2O_5 and TiO_2 coatings [10-14].

In the present study, single-layer coatings of Al_2O_3 , SiO_2 and ZrO_2 were deposited by IBD. The targets chosen for this work were commercially available hot-pressed oxides. The ion assistance was performed with a second ion gun. The following coating deposition parameters were varied: composition of the sputter deposition gas mixture, composition of the ion assist gas mixture, and beam voltage and beam current for the ion assist beam. No external heat was applied to the substrates.

Single-layer ZrO_2 coatings were also deposited from a Zr metal target by bombarding this target with an O_2 :Ar ion beam (Reactive Ion Beam Deposition [RIBD]). These depositions were performed with ion assistance (RIBD/IAD) and without. However, filament life of the ion guns was found to be a problem with these coatings because of the presence of oxygen in the ion beam.

The refractive indices and thicknesses for all the coatings were determined by ellipsometry at 633 nm with a Gaertner Null Ellipsometer. The precision for the ellipsometry was about 1 percent.

Representative coatings were analyzed by Auger Electron Spectroscopy (AES) to determine stoichiometry and to provide information on the nature and level of impurities. The Auger spectrometer used was Physical Electronics' Model 590. The detection limits for AES are 0.1 atomic percent for metallic contamination and 0.5-1 atomic percent for carbon contamination.

The RMS surface roughness was determined by TIS (Total Integrated Scatter) measurements. The spatial frequency bandwidth of the TIS measurements is 0.5 μm to 25 μm . The lower surface roughness detection limit of the TIS measurements is about 5 Å.

The ellipsometry, Auger analysis and TIS measurements were all performed on films deposited on Si wafers. In addition, absorption was determined for a few selected coatings on UV grade fused silica substrate from spectral transmission measurements performed with a Varian 2300 spectrophotometer. The precision is about 1% for the refractive index n and 4×10^{-4} for the absorption coefficient k .

SINGLE-LAYER COATINGS

One ion gun (deposition gun) was directed at a target at an incident angle of 45 to 60 degrees. The ion beam parameters for the deposition gun were as follows: ion beam voltage (V_b) = 1000 eV, ion beam current (i_b) = 50 ma, and sputtering gas pressure $\approx 2 \times 10^{-4}$ torr. A second ion gun (assist gun) was directed at the substrate stage at an incident angle of 60°-70°. The beam voltage for the ion assist gun was in the range of 100 to 200 eV.

The sputtering gas in the deposition gun for an IBD coating deposited from an oxide target was either 100% Ar or a mixture of Ar: O_2 . Only 100% Ar was used as a sputtering gas in the deposition gun for ion assisted IBD coatings. The discharge gas mixture, Ar: O_2 , for the ion assist gun had one of the following compositions: 100:0, 70:30, 30:70 or 0:100.

Al_2O_3 Coatings

Single layers of Al_2O_3 were deposited on 5.0 cm semiconductor grade Si wafers by assisted as well as unassisted ion beam deposition from a hot pressed Al_2O_3 target. The thickness of the films was in the range of 50 to 90 nm. The RMS surface roughness, as measured by the TIS technique, for assisted and unassisted Al_2O_3 coatings, was less than 5 Å.

Assistance with a 100 eV/5 ma ion beam (with pure Ar or 10% O_2 in Ar) lowers the refractive index of Al_2O_3 films. The effect of increased beam current is rather insignificant. Assistance with a 300 eV/5 ma ion beam (with pure Ar or 10% O_2 in Ar), lowers the refractive index further. This lowering of the refractive index (away from that of bulk Al_2O_3) could be attributed to the impregnation of the assist gas in the coating. Changing the composition of the deposition gun gas (from pure Ar to 70% O_2 in Ar) produces no significant change in the refractive index of the unassisted Al_2O_3 coatings.

A 100 eV/5 ma assist beam using 70% O_2 /30% Ar produces no significant effect on the refractive index of Al_2O_3 . However, increasing the beam voltage of the assist beam from 100 eV to 300 eV produces a decrease in the refractive index of the Al_2O_3 coatings.

One unassisted (IBD) Al_2O_3 coating and one assisted (300 eV, 5 ma, 90% Ar/10% O_2) Al_2O_3 coating were analyzed by AES. Important observations are as follows:

- 1) Auger and ESCA analyses indicate that the metallic contamination levels in these coatings were below the detection limits of these techniques.
- 2) These sputter-deposited Al_2O_3 coatings are very stable when exposed to an Auger E-beam. Oxygen-deficient Al_2O_3 could not be detected at the surface or inside of these coatings.
- 3) A significant amount of Ar was detected at the surface of the assisted coating, although it was below the detection limit in unassisted coating. The presence of Ar in the assisted coating could be attributed to the gas embedded by the 300 eV ion assist beam.

AES analysis of these two Al_2O_3 coatings is illustrated with the help of the following figures. Figures 1 and 2 indicate AES surveys taken at the surfaces of the unassisted and the assisted coating, respectively. Notice the presence of the Ar Auger peak (212 eV) in the surface spectrum of the assisted coating while it is at noise level in the spectrum for the unassisted coating. Since these spectra were taken without any sputter cleaning, any surface contaminants like carbon should be ignored. Figures 3 and 4 indicate the Auger surveys taken after sputter etching with 2 keV Ar ions about 10 nm of the coatings. These surveys show that carbon and metallic contaminations inside the unassisted, as well as assisted coatings, are below the detection limit of AES.

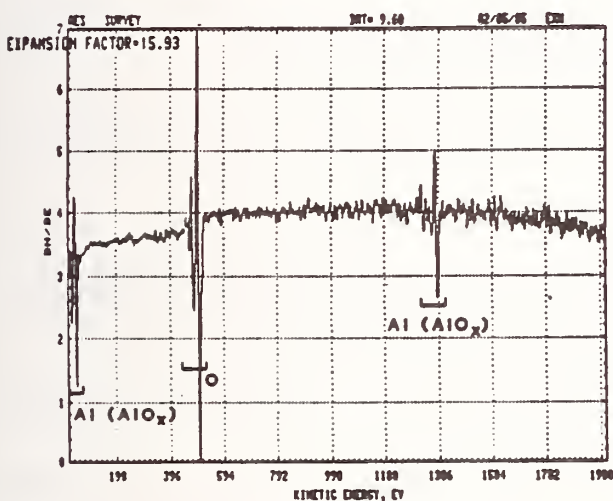


Figure 1. AES survey taken at the surface of unassisted Al_2O_3 coating.

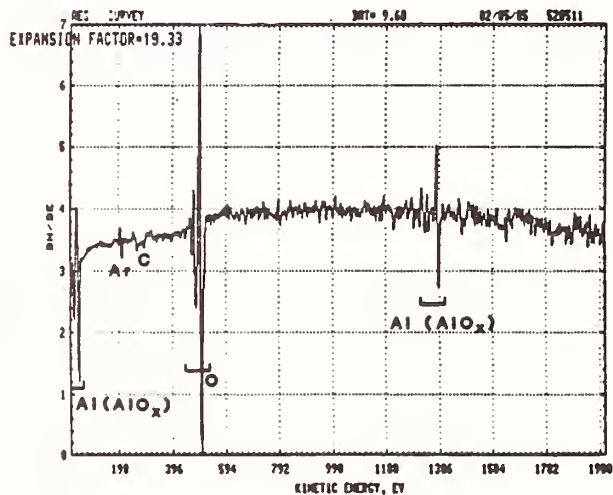


Figure 2. AES survey taken at the surface of ion beam assisted Al_2O_3 .

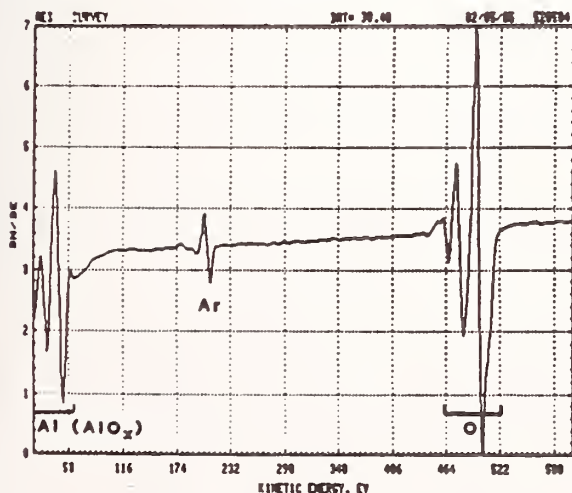


Figure 3. AES survey taken after sputter etching 10 nm of unassisted coating.

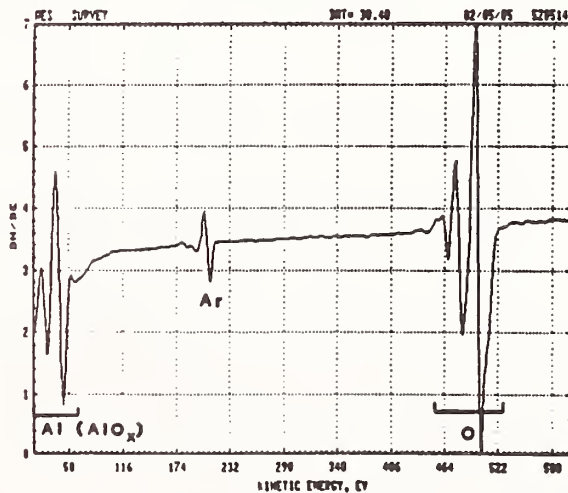


Figure 4. AES survey taken after sputter etching 10 nm of ion assisted coating.

SiO₂ Coatings

The deposition procedure for SiO₂ coatings was the same as for Al₂O₃ coatings. The coating thicknesses were in the range of 40 nm to 90 nm. The RMS surface roughness, as measured by the TIS technique, for assisted and unassisted SiO₂ coatings was low (less than 5 Å).

The effects of ion assist beam voltage and beam current on the refractive index of SiO₂ coatings are as follows:

- 1) The refractive index of unassisted SiO₂ coatings is higher than the refractive index for bulk SiO₂ by about 0.02.
- 2) Ion assistance with a 100 eV beam lowers the index value to 1.475. This decrease in the refractive index is independent of the beam current at 100 eV.
- 3) An increase in assist beam voltage from 100 to 300 eV does not decrease the refractive index any further.

AES analysis of one unassisted (IBD) and one assisted (100 eV, 10 ma, 100%) deposition provided the following information:

The SiO₂ coatings are very clean; the contamination level is below the detection limit of AES. These coatings are not as stable as the Al₂O₃ coatings when exposed to the Auger E-beam. In particular some oxygen can be desorbed leading to oxygen deficient SiO₂.

In summary, the SiO₂ coatings deposited by IBD are clean. However, they are probably non-stoichiometric (oxygen deficient), and their refractive index is higher than that for bulk SiO₂.

ZrO₂ Coatings from an Oxide Target

The deposition procedure for the ZrO₂ coatings was similar to that of the Al₂O₃ coatings. The coating thicknesses were in the range of 50 nm to 100 nm. The surface roughness of ZrO₂ coatings on Si wafers, as measured by the TIS technique was less than 5.3 Å. This is significantly lower than that of ZrO₂ coatings deposited by E-beam evaporation.

The effect of ion assistance on the refractive index at 633 nm of ZrO₂ coatings deposited from a ZrO₂ target was found to be as follows:

- 1) Unassisted IBD ZrO₂ made from a ZrO₂ target with 100% Ar gas has a refractive index which approaches that of the ZrO₂ bulk value (2.15).
- 2) Unassisted IBD ZrO₂ made from a ZrO₂ target with 10% O₂ in Ar gas has a refractive index of 2.11.
- 3) The effect of 100 eV/2 ma ion assistance on the refractive index of IBD ZrO₂ is insignificant.
- 4) As the beam current of the 100 eV ion assist beam is increased from 2 ma to 5 ma, there is a slight decrease in the refractive index of IBD ZrO₂ (2.12).

In summary, ion beam deposited ZrO₂ from a ZrO₂ target without assist or with a small assist can provide ZrO₂ coatings with a refractive index approaching the ZrO₂ bulk value of 2.15.

A typical AES analysis of the IBD ZrO₂ coatings obtained from a ZrO₂ target provided the following information:

- 1) Argon was detected in assisted as well as unassisted ZrO₂ coatings. Though it is not possible to quantify by AES the amount of Ar in these coatings, it can be stated that the amount of Ar trapped in IBD ZrO₂ coatings is significantly larger than that trapped in IBD Al₂O₃ or SiO₂ coatings.
- 2) Carbon was detected below the surface of the ZrO₂ coatings. The amount of carbon was in the range of 2-4 At %. Since Zr is a very reactive element, the presence of carbon could imply nonstoichiometric ZrO₂ coatings.

Refractive Index and Absorption Coefficient for ZrO₂ Coatings

The values for the refractive indices and absorption coefficients of ZrO₂ at 351 nm were determined using thick single-layer depositions and the following methods:

The transmission of a thick ZrO₂ single-layer coating was measured with a Varian 2300 dual beam spectrophotometer in the wavelength range of 200 to 2000 nm. The index values in Figure 5 were obtained by using the value $n_0 = 2.13$ at 633 nm, measured previously by ellipsometry. The indices at the wavelength λ_m of the turning points (maxima and minima) were then determined using

$$n(\lambda_m) = n_0 m \lambda_m / (m_0 \lambda_{m0})$$

where m is the order number (number of quarter-waves) at λ_m , $n(\lambda_m)$ is the index at that wavelength, and m_0 and λ_{m0} are the order number and wavelength of the turning point nearest to 632.8 nm.

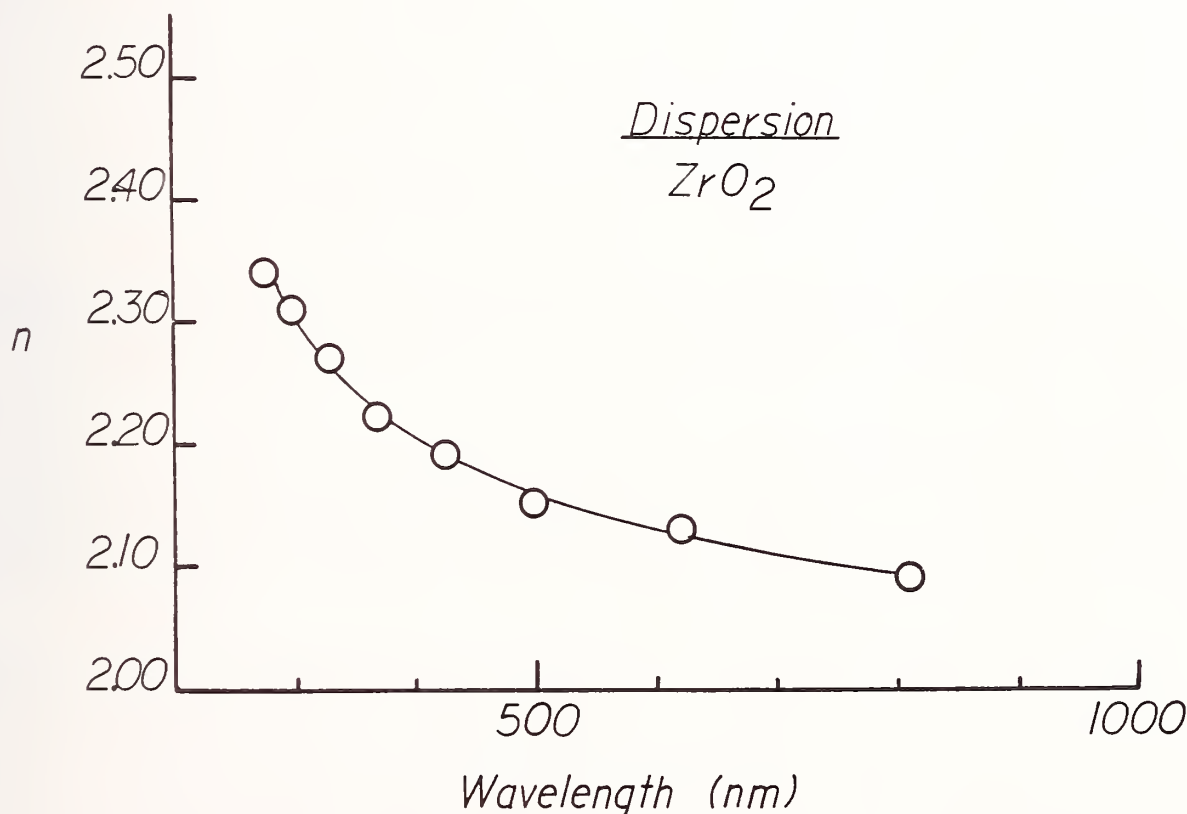


Figure 5. Dispersion curve for an IBD ZrO₂ coating.

The absorption values were also derived from the spectrophotometric scans. The absorption at the wavelength λ_m , where m is an even number, (transmission maximum) was determined using

$$k(\lambda_m) = n(\lambda_m) A(\lambda_m) / (4\pi m)$$

where m is the order number (number of quarter-waves) at λ_m , n_{λ_m} is the index of coating material at that wavelength and $A(\lambda_m)$ is the absorption at that wavelength attributed to the coating. The error in determining k by this method is $\pm 4 \times 10^{-4}$.

Thick ZrO_2 coatings were deposited from a ZrO_2 target on 2.5 cm fused silica substrates using three different deposition techniques: IBD, IBD/IAO and IBD with O_2 backfill. Table 1 lists the deposition parameters along with the refractive indices and absorption values for these coatings at 351 nm. The O_2 backfill pressure (column 3) is the partial pressure of O_2 in the chamber, regardless of whether O_2 was introduced into the chamber through the ion gun or directly into the chamber. For run number IC 445, 10% O_2 sputter gas was introduced through the deposition gun to achieve a chamber pressure of 2×10^{-4} torr. This corresponds to an O_2 partial pressure of 2×10^{-5} torr. In the case of IC 446, pure O_2 was introduced through the etch gun to achieve a chamber pressure of 6×10^{-5} torr. Pure O_2 was introduced directly into the chamber for IC 447 and IC 450 to achieve the respective partial pressures of 2×10^{-5} torr and 6×10^{-5} torr.

Table 1. Effect of O_2 Partial Pressure on Absorption of IBD ZrO_2 Coatings.

Run No.	Depo Gas (O_2 :Ar)	Backfill Gas (100% O_2)	k @ 351nm (10^{-4})	Comments
IC 445	10: 90	2×10^{-5} torr	34	Oxygen introduced through the deposition gun.
IC 446	0:100	6×10^{-5} torr	42	Oxygen introduced through the ion assist gun.
IC 447	0:100	2×10^{-5} torr	34	Oxygen introduced directly into the chamber.
IC 450	0:100	6×10^{-5} torr	42	Oxygen introduced through the ion assist gun.

The values in this table clearly show that the value of $k = 0.0034$ obtained using IBD with an O_2 partial pressure of 2×10^{-5} torr was the lowest absorption obtained. The absorption does not depend on the method of introducing O_2 , but only on the partial pressure of O_2 .

ZrO_2 Coating from a Zr Metal Target

Single-layer ZrO_2 coatings were also deposited from a Zr metal target by bombarding this target with an O_2 :Ar ion beam [Reactive Ion Beam Deposition (RIBD)]. These depositions were performed with ion assistance (RIBD/IAO) and without. The position of the Zr metal target with respect to the deposition gun and the deposition ion beam parameters was similar to the one used for oxide targets, the only exception being that the discharge gas was varied from 70% to 20% O_2 mixed with Ar.

There were a number of experimental problems with the reactive sputter deposition technique. The lifetime of the cathode filaments varied from 15 to 38 min with 70% O_2 discharge gas in the deposition gun. Consequently, some ZrO_2 coatings turned out to be so thin that ellipsometric measurements of the refractive index were not very accurate. Though the average lifetime of the cathode filament was longer with 50% O_2 discharge gas than with 70% O_2 , the cathode filament appeared to be thin, and was therefore replaced at the end of each run. In addition, a yellow deposit appeared on the cathode supports near the filament connections as well as on the inside surface of the grids. This yellow deposit was determined (by AES) to be tungsten oxide. The cathode supports were cleaned before each run. Due to the fragility of the pyrolytic graphite grids and the critical nature of the grid/pair alignment, no attempt was made to clean the grids. These problems were reduced by using 30% and 20% O_2 discharge gas, but they still remained significant when compared to those associated with the use of pure Ar discharge gas.

A study of the refractive indices for unassisted ZrO_2 coatings from a Zr metal target plotted as a function of the deposition gas mixture produced the following conclusions:

- 1) The index is independent of the O_2 concentration in the deposition gas from 20% to 40% O_2 .
- 2) The index decreases as the O_2 concentration increases above 40%.

The effect of ion assistance on ZrO_2 coatings obtained from a Zr metal target is summarized below:

- 1) The refractive index increases slightly by ion assistance with a Ar:O₂ mixture.
- 2) The increase in index is larger when the ion assistance is performed with pure O₂ or a high O₂ content Ar:O₂ mixture. This implies that ion assistance with O₂ improves the stoichiometry of the unassisted ZrO₂ coatings.

HIGH REFLECTOR COATINGS AT 351 nm

A 13 layer ZrO₂/SiO₂ quarter wave reflector coating at 351 nm was deposited on super-polished substrates. No external heat was applied to the substrates. The quarter waves were monitored by a reflection monitor (used at 45°) at 320 nm. Each quarter wave layer was either deposited from the ZrO₂ or the SiO₂ target using an ion source output of 1000 eV beam voltage and 50 ma beam current. One hundred percent Ar was used in the ion sources. No ion assistance was performed, but an O₂ backfill pressure of 2×10^{-5} torr was used. The reflectivity of these coatings was measured to be greater than 99% at 351 nm.

SUMMARY AND CONCLUSIONS

1) Al₂O₃ Coatings

- a. IBD produces Al₂O₃ coatings of a high index (1.65 at 632.8 nm).
- b. These coatings are very clean (free of carbon and metallic contamination).
- c. They are stoichiometric (absence of Al inside the coating).
- d. The amount of Ar trapped in the IBD coating is low.
- e. The effect of an ion assist beam (IAD) is to lower the index of IBD Al₂O₃.
- f. The amount of Ar trapped within an Ar ion beam assisted Al₂O₃ coating is significantly higher than the amount of Ar in an IBD coating. This implies that the ion assist beam embeds Ar into the coating.
- g. The RMS surface roughnesses for IBD Al₂O₃ coatings deposited with and without IAD are low.

IBD Al₂O₃ coatings are the most promising oxide coatings resulting from the IC program.

2) SiO₂ Coatings

- a. IBD produces SiO₂ coatings of an unusually high index. This could be due to a density higher in IBD SiO₂ coatings than in the bulk SiO₂ or due to a lack of stoichiometry.
- b. These coatings are very clean.
- c. They could be slightly oxygen-deficient.
- d. The effect of an ion assist beam is to lower the index and to increase the amount of trapped sputter gas in the coating.
- e. The RMS surface roughness of IBD SiO₂ coatings deposited with and without IAD is low.

3) ZrO₂ Coatings

- a. IBD produces ZrO₂ coatings having index values of almost bulk index value.
- b. These IBD coatings contain significantly larger amounts of trapped Ar gas than do IBD SiO₂ and Al₂O₃ coatings.
- c. These coatings are non-stoichiometric.
- d. The absorption of IBD ZrO₂ coatings at 351 nm is significant.

e. The effect of an O_2 ion assistance at 100 eV is to lower the index slightly and to reduce the absorption.

f. The lowest absorption ($k = 0.0034$ at 335 nm) is obtained using IBD with an O_2 backfill pressure of 2×10^{-5} torr. This low absorption does not depend on the method of introducing O_2 (i.e., whether it is introduced into the sputter gun or directly into the chamber).

g. The surface roughness of IBD ZrO_2 with or without IAD is low -- much lower than the roughness for E-beam evaporated ZrO_2 coatings.

4. Reactive Ion Beam Deposition of ZrO_2 for Ar Targets

a. This technique did not provide any particular advantage over IBD using a ZrO_2 target.

b. The highest index (2.13) for ZrO_2 is obtained by RIBD from a Zr metal target with a mixture of 40% O_2 in Ar.

c. For higher fractions of oxygen in the assist gun, the index increased slightly.

REFERENCES

- [1] Gautherin, G.; Weissmantel, C., "Some Trends in Preparing Film Structures by Ion Beam Methods", *Thin solid Films*, 50, 135 (1978).
- [2] Weissmantel, C., "Ion Beam Deposition of Special Film Structures", *J. Vac. Sci. Tech.* 18 (2), 179 (1981).
- [3] Harper, J.M.E., "Thin Film Processes", Vossen, J.L. and Kern, W. (Eds), Academic Press, New York, 1978, Chapter II-5.
- [4] Martin, P.J.; Macleod, H.A.; Netterfield, R.P.; Pacey, C.G.; Sainty, W.G., "Ion Beam Assisted Deposition of Thin Films", *Appl. Opt.* 22, 178 (1983).
- [5] Martin, P.J.; Netterfield, R.P.; Pacey, C.G.; Sainty, W.G.; Clark, G.J.; Lanford, W.A.; Sie, S.H., "Ion Assisted Deposition of Bulklike ZrO_2 Films", *Appl. Phys. Lett.* 43, 711 (1983).
- [6] Sainty, W.G.; Netterfield, R.P.; Martin, P.J., "Protective Dielectric Coatings Produced by Ion-Assisted Deposition", *Appl. Opt.* 23, 1116 (1984).
- [7] Martin, P.J.; Netterfield, R.P.; Sainty, W.G., "Modifications of the Optical and Structural Properties of Dielectric ZrO_2 Films by Ion Assisted Deposition", *J. Appl. Phys.* 55, 235 (1984).
- [8] McNeil, J.R.; Barron, A.C.; Wilson, S.R.; Hermann, W.C. Jr., "Ion Assisted Deposition of Optical Thin Films: Low Ion Energy vs High Ion Energy", *Appl. Opt.* 23, 552 (1984).
- [9] McNeil, J.R.; Al-Jumaily, G.A.; Jungling, K.C.; Barron, A.C., "Properties of TiO_2 and SiO_2 Thin Films Deposited using Ion-Assisted Deposition", *Appl. Opt.* 24, 486 (1985).
- [10] Demiryont, H.; Kerwin, D.B.; Sites, J.R., "Optical Properties of Ion Beam Sputtered TiO_2 Films", *Nat. Bur. Stand. (U.S.) Spec. Publ.* 688, 311 (1983).
- [11] Sites, J.R.; Gilstrap, P.; Rujkorakarn, "Ion Beam Sputter Deposition of Optical Coatings", *Opt. Engr.* 22, 449 (1983).
- [12] Rossnagel, S.M.; Sites, J.R., "X-ray Photo-electron Spectroscopy of Ion Beam Sputter Deposited SiO_2 , TiO_2 and Ta_2O_5 ", *J. Vac. Sci. Tech.* A2(2), 376 (1984).
- [13] Demiryont, H.; Sites, J.R., "Effects of Oxygen in Ion Beam Sputter Deposition of Titanium Oxide", *J. Vac. Sci. Technol.* A2(4), 1457 (1984).
- [14] Sites, J.R.; Demiryont, H.; Kerwin, D.B., "Ion Beam Sputter Deposition of Oxide Films", *J. Vac. Sci. Tech.* A3(3), 656 (1985).

J.J. McNally

Department of Physics
USAFA/DFP
United States Air Force Academy, CO 80840-5701

and

F.L. Williams, S.R. Wilson and J.R. McNeil
University of New Mexico
Albuquerque, NM 87131

We have investigated the properties of $\text{Al}_2\text{O}_3/\text{SiO}_2$ and $\text{Ta}_2\text{O}_5/\text{SiO}_2$ anti-reflection coatings which have been fabricated using ion-assisted deposition (IAD) techniques. The coatings were deposited with simultaneous O_2 bombardment during film growth. Preliminary laser damage results are presented. We describe the importance of oxygen-ion energy and flux in applying IAD to dielectric materials. Results illustrating increased values of film refractive index, reduction in optical scatter and improved environmental stability are reported.

Key Words: coatings; laser-damage; oxygen-ion assisted deposition.

1. INTRODUCTION

A number of novel deposition techniques have been applied in attempts to improve the properties of thin films. In these techniques, energetic processes are employed to supply sufficient activation energies to increase adatom mobility and eliminate the formation of columnar microstructure. One of these techniques is ion-assisted deposition (IAD). Ion-assisted deposition employs a separate ion source to direct a beam of ions at the growing film during deposition. Thin films deposited using IAD have exhibited increased packing density, improved stability and durability, modifications in stress and improved stoichiometry.¹⁻⁸ Recently, IAD has been applied in the production of optical coatings. Allen applied IAD to obtain increased values of refractive index in TiO_2 films.⁴ Martin et. al. have studied the effects on the properties of ZrO_2 and CeO_2 films bombarded with O_2 and Ar ions during deposition.^{7,9} McNeil et. al.^{6,8} examined the effects of 30 and 500 eV O_2^+ bombardment on the properties of TiO_2 and SiO_2 films deposited using TiO and SiO starting materials. Al-Jumaily et. al. examined the effects of ion energy and flux on optical scatter and crystalline phase in Cu, TiO_2 and SiO_2 films.¹⁰

In this study Kaufman ion sources were used; they are attractive because it is possible to independently control and accurately measure the important experimental parameters involved. The ion beam energy, current density and ion angle of incidence can be varied over a wide range of values independent of the deposition process. The purpose of this work is to systematically investigate the effects of IAD parameters on the properties of Ta_2O_5 and Al_2O_3 thin films. The work is divided into two phases: an initial single-layer parameter optimization study, followed by a multi-layer laser damage study. The optical constants, optical scatter and environmental stability of single-layer coatings are reported. We also report preliminary results from laser damage tests on $\text{Al}_2\text{O}_3/\text{SiO}_2$ anti-reflection coatings.

2. EXPERIMENTAL ARRANGEMENT

The coatings were deposited in a 90-cm diameter, cryogenic-pumped bell jar vacuum system. A schematic of the deposition arrangement is illustrated in Figure 1. The source-to-substrate separation was 35 cm. The Ta_2O_5 and Al_2O_3 coatings were electron-beam evaporated at a rate of $0.30 - 0.40 \text{ nm sec}^{-1}$ with oxygen backfill pressure of 1.0×10^{-4} Torr. The coatings were deposited onto heated substrates (275°C), and were bombarded with oxygen ions during deposition.

A 10-cm Kaufman ion source provided a monoenergetic, neutralized ion beam independent of the material evaporation process. This source has a number of advantages over conventional plasma configurations. These advantages are derived from the basic operating principle of the ion source. This principle is the isolation of ion production and acceleration from the substrates. Briefly, the ion source operates as follows. Gas is introduced into the discharge chamber; electrons emitted from the cathode impact-ionize the gas molecules. The discharge-chamber contains a conducting plasma composed of approximately equal numbers of ions and electrons. The plasma potential is essentially equal to the anode potential, therefore the ions originate at approximately the anode potential. The screen grid aligns the ions that are accelerated from the source by the electric field established in the region between the screen and accelerator grids. The ions travel from the source to the substrates which are held at ground potential. The source provides a low-energy (300-1000 eV) beam of Ar or O_2 ions incident on the film surface at an angle of 45° . A Faraday probe was used to monitor the ion current density at the substrates. Prior to deposition the substrates were cleaned with 300 eV Ar^+ .

The coatings produced in this study were deposited onto a number of different substrates. One inch diameter, 1/4" thick UV-grade fused silica substrates were used for the single-layer coatings. The substrates used for the laser damage coatings were provided by Los Alamos National Laboratory (LANL) and were 2" dia., 3/8" thick fused silica. The substrates were cleaned as follows. Lint and dust particles were removed using dry nitrogen gas. A horse hair brush was used in a circular motion to scrub the substrate surface with a 50-50 mixture of Liquinox soap and deionized water (180M -cm). The substrate was rinsed with de-ionized water (DI), and the scrubbing/rinsing process repeated. The substrate was dried with nitrogen. Kodak lens tissue with ethyl alcohol (200 proof) was used to drag wipe each substrate surface. Two inch diameter polished silicon wafers were coated for optical scatter measurements. The wafers were cleaned using a standard semiconductor industry technique as follows. The wafers were rinsed in DI and degreased in a 3:2 solution of $\text{H}_2\text{SO}_4/\text{H}_2\text{O}_2$ for 10 minutes. A DI rinse was repeated, followed by a 10 minute etch in a 5% HF solution. After a final DI rinse the wafers were blown-dry with nitrogen.

The coatings transmittance and reflectance spectra were measured over the wavelength range $0.185 - 1.2 \mu\text{m}$ using a dual-beam spectrophotometer. The transmittance and reflectance spectra were used to calculate the refractive index (n), the extinction coefficient (k) and the thickness (t) for each coating. They were also used to determine the possible presence of index inhomogeneity in the coatings. A technique due to Manifacier, et. al.¹¹ was used to determine the values of n , k and t . The optical scatter characteristics of the coatings were examined using an angle-resolved scatterometer which is described in detail in Reference 10. When evaluating the scatter characteristics of a dielectric coating it is important to know the

optical thickness of the film. For a film which is an integral number of half-waves in optical thickness, scatter is primarily due to volume effects in the film. The films were deposited onto polished silicon wafers and were multiple half-wave optical thickness at 633 nm. A He-Ne laser illuminated the coated Si wafers; scattered light was collected by a photo-multiplier detector. The detector rotated about the scatter point on the sample in the plane of incidence at a radius of 40 cm.

Humidity cycle tests were conducted in a Vapor-temp controlled humidity chamber to examine film stability properties. The spectral characteristics of conventional coatings are generally unstable, primarily due to porosity and their tendency to adsorb moisture. The coatings were exposed to 97% relative humidity at 35°C for extended periods of time. The film transmittance spectra were examined before and after the humidity exposure to determine the amount of spectral shift.

A number of anti-reflecting (AR) coatings were laser damage tested at Los Alamos National Laboratory by Stephen Foltyn and L. John Jolin. The damage thresholds were measured at 351 nm with 9 nsec pulses. The pulse repetition frequency was 35 pps. The laser beam was focused to give a beam with a mean spot diameter ($1/e^2$) of 0.46 mm at the sample surface. All the testing was n-on-m, where m sites were irradiated at each fluence for a maximum of n pulses. Ten discrete sites were irradiated at each test fluence, and each site was exposed to the laser for 4 sec (140 pulses). Damage was defined as any visible change in the coating observed under 60X microscope examination (microscopic damage). The coatings were tested at several fluence levels between the value at which 0 of 10 sites damaged and the value at which 10 of 10 sites damaged. The fraction of damage sites was plotted as a function of laser fluence, in units of Joules cm^{-2} . A linear regression fit was performed on the data resulting in a sloped, fitted line from a fluence at which all ten sites damaged to a lower fluence at which no damage occurred. The LIDT value was defined as the zero-percent crossing of the fitted line (zero-probability intercept). Note that this is different from another conventional definition of LIDT value which is the average value of the minimum fluence that always causes damage and the maximum fluence at which no damage occurs.

The AR coatings in this study were deposited onto Corning 7940 fused silica substrates with bare surface LIDT values of approximately 8 J cm^{-2} . The coating design was SLLHL where S was the substrate, L was quarter-wave thick SiO_2 and H was quarter-wave thick Al_2O_3 or Ta_2O_5 .

3. RESULTS

The transmittance spectra for two Ta_2O_5 coatings are given in Figure 2. The curve labeled J=0 is for a coating deposited with no ion bombardment; the curve labeled J=5 is for a coating bombarded during deposition with 500 eV O_2^+ at a current density of 5 $\mu\text{A cm}^{-2}$. The curve for the ion assisted coating contains larger differences in transmittance extrema than the curve for the unbombarded coating. These larger differences indicated a larger value of refractive index for the ion assisted coating. Good film stoichiometry was obtained for the ion bombardment conditions employed as indicated by an absence of measurable absorption at wavelengths for which the film is multiple half-wave in optical thickness down to 340 nm. Examination of the reflectance spectra for these coatings indicated the absence of any refractive index inhomogeneity.

The refractive indices of Ta_2O_5 films deposited at 0.3 nm sec^{-1} are plotted in Figure 3 as a function of oxygen-ion current density. The values increase from 2.16 for the unbombarded case ($J=0$) to 2.25 and 2.28 for films bombarded with 500 and 300 eV O_2^+ , respectively. The increase in the values of n with increasing O_2^+ current density indicated that ion bombardment during deposition modified the growth of film columnar microstructure resulting in film densification. Observe for the 500 eV case that the film index values decreased for ion current densities larger than the value at which the maximum index occurred. The decrease in index may be explained as a result of degradation in film stoichiometry, creation of closed isolated voids or oxygen incorporation into the films. A similar dependence of refractive index on bombarding ion flux has been reported for ion assisted ZrO_2 ⁷ and CeO_2 films.⁹ Work is on-going at 300 eV and 200 eV to extend the behavior illustrated in Figure 3.

The coatings bombarded during deposition at oxygen ion current densities up to approximately the value for maximum index exhibited good optical characteristics. For higher levels of bombardment, the optical absorption of the coatings increased. In Figure 4, values of extinction coefficient (k) for Ta_2O_5 coatings bombarded with 500 eV O_2^+ during deposition are shown for different levels of ion current density. The values of k were calculated at $\lambda = 400 \text{ nm}$. As illustrated in Figure 4, film optical absorption increased with higher levels of oxygen ion bombardment. The most probable mechanism for this is the preferential sputtering of oxygen in the Ta_2O_5 molecule. Preferential sputtering would result in oxygen-deficient layers continuously integrated into the coatings as deposition occurs. This mechanism has been observed in other IAD films.⁷

The refractive indices of Al_2O_3 films deposited at 0.4 nm sec^{-1} are plotted in Figure 5 as a function of oxygen-ion density. The values increase from 1.64 for $J=0$ to 1.71 and 1.68 for films bombarded with 1000 and 500 eV O_2^+ , respectively. As illustrated in the case of Ta_2O_5 films (Figure 3), the values increase and then subsequently decrease for increasing level of ion bombardment. The likely mechanism for this behavior is oxygen incorporation in the films. These results illustrate that the effects of ion bombardment on the values of n are material dependent. Work is on-going at 300 eV and 1000 eV to extend the behavior illustrated in Figure 5.

Attempts to measure the values of extinction coefficient for the Al_2O_3 coatings (400 nm thick) were limited due to the minimum sensitivity of the measurement equipment. All computed values of k were less than 2.0×10^{-4} . The low values of k calculated for the Al_2O_3 coatings indicate that for the conditions examined, preferential oxygen sputtering is not a dominant mechanism for Al_2O_3 as was the case for Ta_2O_5 (Figure 4). This result again illustrates that the effects of ion bombardment on film properties are material dependent.

Measurement of the optical scatter characteristic of coatings is a method used to determine the effects of O_2^+ bombardment on film microstructure.¹⁰ The optical scatter characteristics of the coatings were examined using an angle-resolved scatterometer. Figure 6 illustrates the scatter characteristics of two Ta_2O_5 coatings; one deposited with no ion bombardment ($J=0$), and the other bombarded during deposition with 500 eV O_2^+ at a current density of $12 \mu\text{A cm}^{-2}$. The vertical axis is the bidirectional reflectance distribution function (BRDF) of the coating, in units of inverse steradians. The BRDF is proportional to the normalized intensity of scattered light (logarithmic scale). The horizontal axis is the angle from the sample normal, in degrees, at which the scattered light is collected. The scatter characteristic for an uncoated silicon wafer is illustrated for comparison.

As illustrated in Figure 6, the optical scatter from the IAD coating ($J=12$) was less than that from the coating deposited without bombardment. All IAD coatings were compared with coatings deposited without ion bombardment ($J=0$), and a comparable reduction in scatter was observed for other IAD Ta_2O_5 coatings relative to unbombarded coatings except for coatings bombarded with very high levels of current density ($>90 \mu A cm^{-2}$).

Figure 7 illustrates the scatter characteristics of two Al_2O_3 coatings; one deposited without ion bombardment ($J=0$), and the other bombarded during deposition with $500 eV O_2^+$ at a current density of $35 \mu A cm^{-2}$. As illustrated in Figure 7, the optical scatter from the IAD coating ($J=35$) was less than that from the coating deposited without bombardment. Comparable reduction in scatter was observed for other IAD Al_2O_3 coatings relative to unbombarded coatings except for coatings bombarded with very high levels of current density.

These results indicate that moderate levels of ion bombardment during deposition modifies the growth of film columnar microstructure producing a more homogeneous film morphology. These results are similar to the reductions in scatter reported for IAD TiO_2 coatings.¹⁰ Total integrated scatter (TIS) measurements reported for IAD CeO_2 coatings also indicated less optical scatter in coatings deposited under certain conditions of ion bombardment.⁹

The environmental stability of optical coatings is in large part limited by the porosity of the film microstructure. A number of Ta_2O_5 coatings were exposed to humidity testing as described in the previous section to examine the effects of ion bombardment on film stability. Figures 8 and 9 are the transmittance curves for two Ta_2O_5 coatings exposed to humidity testing. The spectra in Figure 8 are for a coating deposited onto a heated silica substrate with no ion bombardment ($J=0$). The spectra in Figure 9 are for a coating bombarded during deposition with $300 eV O_2^+$ at a current density of $20 \mu A cm^{-2}$. The curve labeled AIR is the spectrum measured after the coating has been removed from the vacuum chamber and exposed to the ambient atmosphere. The curve labeled POST HUMIDITY is the spectrum for the same coating remeasured after exposure to 97% relative humidity at $35^\circ C$ for six hours.

The curves in Figure 8 illustrate a spectral shift to longer wavelengths of 1% for the coating deposited without bombardment. The shift was most likely due to water adsorption into the microvoids in the film microstructure. This increased the effective index value of the coating and, in turn, increased the optical thickness (nt). Figure 9 is typical of the results obtained for all IAD coatings examined except one. No spectral shifts within the measurement precision ($\pm 0.5 nm$) of the spectrophotometer were observed. The coating bombarded with $300 eV O_2^+$ at a current density below the critical value exhibited a spectral shift of 0.3%. Similar results have been reported for IAD ZrO_2 and TiO_2 coatings.^{7,3} The Ta_2O_5 results are summarized in Table I.

The spectral shift for the $J=0$ coating indicated the likely existence of columnar microstructure. The shift for the coating bombarded with $300 eV O_2^+$ at a current density of $10 \mu A cm^{-2}$ indicated some columnar microstructure existed although the coating was more stable and had a larger value of n (see Figure 3) than the $J=0$ coating. These humidity test results, as well as the observation of reduced optical scatter and increased refractive index, are consistent with IAD Ta_2O_5 coatings having an increased packing density and being less susceptible to water adsorption.

TABLE I
Spectral Shifts for Ta₂O₅ Coatings After Humidity Exposure

E (eV)	J ($\mu\text{A cm}^{-2}$)	Spectral Shift (%)
0	0	1.0%
300	10	0.3%
300	20	0.0%
300	40	0.0%
500	10	0.0%
500	20	0.0%

A small number of anti-reflection (AR) coatings were laser damage tested at LANL. The coatings were Al₂O₃/SiO₂ and were designed for 351 nm. The damage tests were performed as described in Section 2. The AR coatings deposited with no ion bombardment ($J=0$) had an average damage threshold of 4 J cm^{-2} . The coatings bombarded with 300 eV O₂⁺ at $J=10 \mu\text{A cm}^{-2}$ had an average damage threshold of 6 J cm^{-2} . For the other ion bombardment conditions examined (300 eV, $J=20$ and $J=45$; 500 eV, $J=20$ and $J=40$) the average damage threshold was 3 J cm^{-2} or less. It is premature to draw any firm conclusions from the limited data presented. Further laser damage tests are being conducted on more Al₂O₃/SiO₂ AR coatings and on Ta₂O₅/SiO₂ AR coatings. A report on the completed test results will be made next year.

4. SUMMARY

Oxygen ion bombardment during deposition produced Ta₂O₅ and Al₂O₃ coatings with increased values of refractive index. The increase in n was dependent on ion energy and current density. An increase in optical absorption was observed for IAD Ta₂O₅ coatings. The values of optical absorption increased for bombardment at increasing values of ion current density for a constant ion energy. The increase in optical absorption was attributed to preferential sputtering of oxygen in the Ta₂O₅ molecule. Increases in optical absorption were not observed for Al₂O₃ coatings except for coatings bombarded at very high current densities. The effects on the optical constants of IAD coatings were found to be material dependent. The optical scatter characteristics for IAD coatings were measured. The optical scatter for IAD coatings was lower than the scatter for unbombarded coatings. Improved environmental stability was obtained for IAD Ta₂O₅ coatings exposed to humidity testing.

Preliminary laser damage results indicate comparable, and in certain cases, higher threshold levels for IAD AR coatings. Further damage tests are being conducted and results from these will be reported next year.

REFERENCES

1. J.J. McNally, G.A. Al-Jumaily, S.R. Wilson and J.R. McNeil, "Ion-Beam-Assisted Deposition of Optical Thin Films - Recent Results," Proc. Soc. Photo-Opt. Instrum. Eng. 540, 479 (1985).
2. W.C. Herrmann, Jr. and J.R. McNeil, "Ion Beam Applications for Optical Coating," Proc. Soc. Photo-Opt. Instrum. Eng. 325, 101 (1982).

3. P.J. Martin, H.A. Macleod, R.P. Netterfield, C.G. Pacey and W.G. Sainty, "Ion-Beam-Assisted Deposition of Thin Films," Appl. Opt. 22, 178 (1983).
4. T. Allen, "Properties of Ion Assisted Deposited Silica and Titania Films," Proc. Soc. Photo-Opt. Instrum. Eng. 325, 93 (1982).
5. J.J. Cuomo, J.M.E. Harper, C.R. Guarnieri, D.S. Yee, L.S. Attanasio, J. Angilello, C.T. Wu and R.H. Hammond, "Modification of Nb Film Stress by Low-Energy Ion Bombardment During Deposition," J. Vac. Sci. Technol. 20, 349 (1982).
6. J.R. McNeil, A.C. Barron, S.R. Wilson and W.C. Herrmann, Jr., "Ion-Assisted Deposition of Optical Thin Films: Low Energy vs High Energy Bombardment," Appl. Opt. 23, 552 (1984).
7. P.J. Martin, R.P. Netterfield and W.G. Sainty, "Modification of the Optical and Structural Properties of Dielectric ZrO_2 Films by Ion-Assisted Deposition," J. Appl. Phys. 55, 235 (1984).
8. J.R. McNeil, G.A. Al-Jumaily, K.C. Jungling and A.C. Barron, "Properties of TiO_2 and SiO_2 Thin Films Deposited Using Ion-Assisted Deposition," Appl. Opt. 24, 486 (1985).
9. R.P. Netterfield, W.G. Sainty, P.J. Martin and S.H. Sie, "Properties of CeO_2 Thin Films Prepared by Oxygen-Ion Assisted Deposition," Appl. Opt. 24, 2267 (1985).
10. G.A. Al-Jumaily, J.J. McNally, J.R. McNeil and W.C. Herrmann, Jr., "Effects of Ion-Assisted Deposition on Optical Scatter and Surface Microstructure of Thin Films," J. Vac. Sci. Technol. A3, 651 (1985).
11. J.C. Manifacier, J. Gasiot and J.P. Fillard, "A Simple Method for the Determination of the Optical Constants n, k and the Thickness of a Weakly Absorbing Thin Film," J. Phys. E9, 1002 (1976).

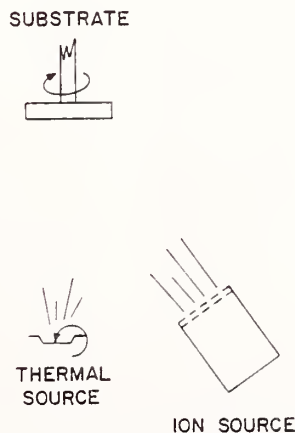


Figure 1. Deposition Arrangement.

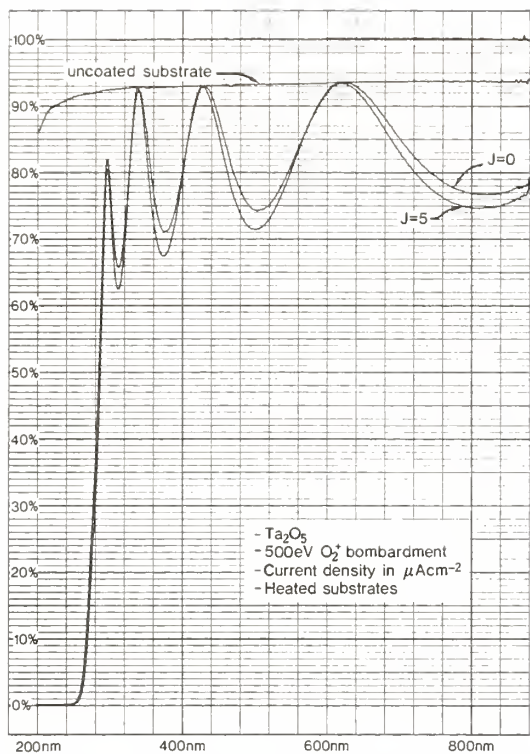


Figure 2. Transmittance spectra for two Ta_2O_5 coatings.

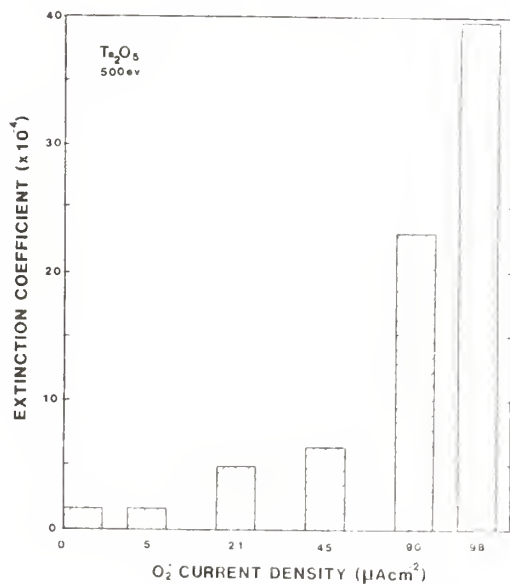


Figure 4. Extinction coefficient vs ion current density for Ta_2O_5 coatings.

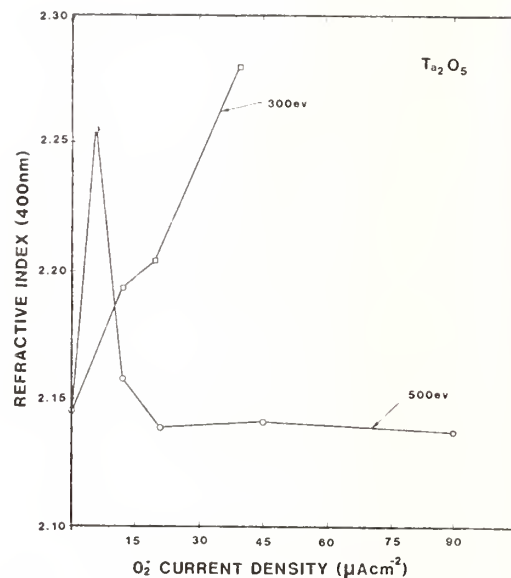


Figure 3. Refractive index vs ion current density for Ta_2O_5 coatings.

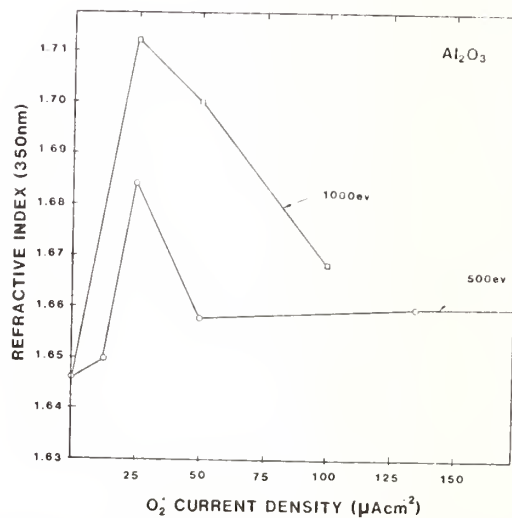


Figure 5. Refractive index vs ion current density for Al_2O_3 coatings.

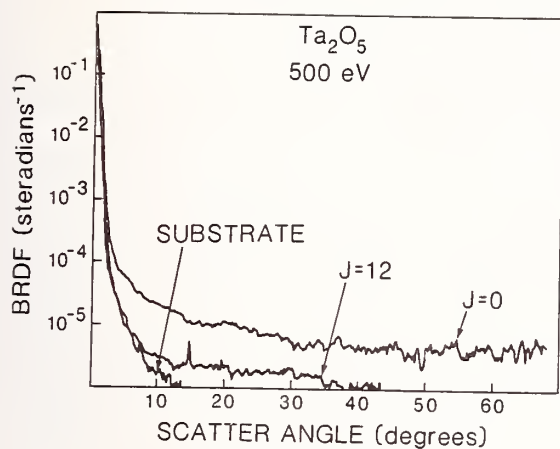


Figure 6.

BRDF vs scatter angle for two Ta_2O_5 coatings.

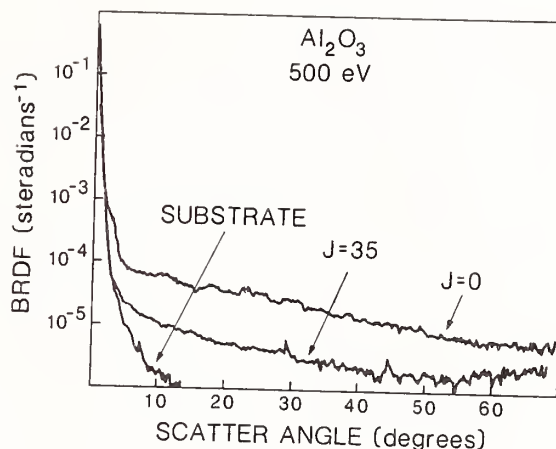


Figure 7.

BRDF vs scatter angle for two Al_2O_3 coatings.

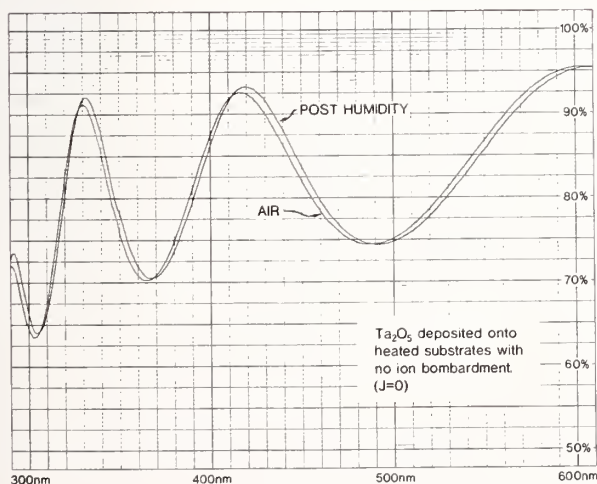


Figure 8.

Transmittance spectra for a Ta_2O_5 coating deposited with no ion bombardment subjected to humidity test.

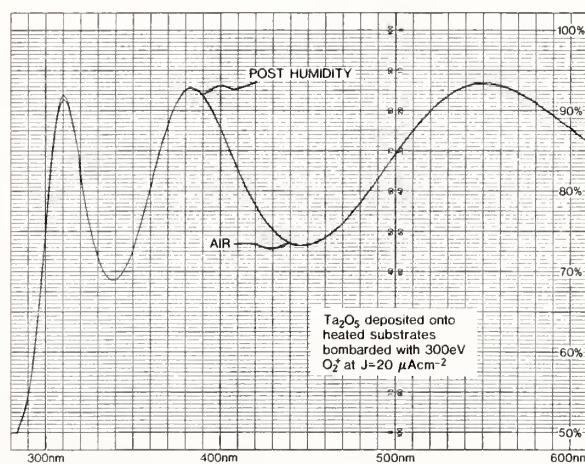


Figure 9.

Transmittance spectra for a Ta_2O_5 coating bombarded during deposition subjected to humidity test.

Ion Assisted Deposition of Optical Films on Heavy Metal Fluoride Glass Substrates

J. J. McNally, G. A. Al-Jumaily and J. R. McNeil

University of New Mexico
Albuquerque, NM 87131

and

B. Bendow^{*}

The BDM Corporation
Albuquerque, NM 87106

Heavy metal fluoride glass materials are attractive for optical applications in the near ultraviolet through infrared wavelength regions. However, many compositions are relatively soft and hygroscopic, and possess low softening temperature (250°C-300°C). We have applied ion assisted deposition (IAD) techniques to deposit MgF_2 , SiO_2 and $\text{Al}_2\text{O}_3/\text{SiO}_2$ thin film structures on fluoride glass substrates at ambient substrate temperature (~100°C). The coatings deposited using IAD improve the environmental durability of the fluoride glass and appear to have reasonably good optical characteristics; without application of IAD, the deposited coatings are not durable and have poor adhesion.

Key Words: coatings; durability; fluoride glass; hermetic; ion-assisted

1. INTRODUCTION

Heavy metal fluoride (HMF) glasses have attracted considerable interest as multispectral transmissive optical components, laser host materials and optical fibers. HMF glasses possess desirable optical properties, including a broad transmittance range from the mid-IR (~7 μm) to near-UV (~0.3 μm), low absorption and scatter losses, low dispersion and index of refraction, and low thermal distortion [1]. However, despite their promising optical characteristics, many compositions are relatively soft and hygroscopic. For example, it has been shown that the solubility of typical fluorozirconates, a category of HMF glass, is many orders of magnitude greater than that of high silicates [2]. Also, measurements of fiber strength reveal that while initial strengths are high, HMF optical fibers degrade rapidly when exposed to high humidity, and that protective Teflon coatings do not serve as effective barriers against the degradation. This susceptibility to attack by moisture indicates that hermetic coatings are required to protect HMF glasses. Moreover, because HMF glasses are chemically sensitive, an additional requirement is that optical coatings must be applied in a non-damaging way.

Ion assisted deposition (IAD) involves the simultaneous bombardment of the growing film with low energy ions during deposition. Ion bombardment can also be used prior to deposition to clean the substrate. IAD has been investigated as a technique for improving the optical and mechanical properties of many materials [3,4]. Thin films deposited using IAD have exhibited increased packing density, improved stability, and reduction in stress [5-7]. In previous publications, [8-12] we described the effects of ion energy and flux on film optical constants, optical scatter characteristics, stoichiometry, stability, impurity content and adhesion for a number of materials. Kaufman ion sources were used in these investigations; they are attractive because it is possible to independently control and accurately measure the important experimental parameters

involved. Reactive or inert gas ions can be employed; ion beam energy, current density and ion angle of incidence can be varied over a wide range of values.

The purpose of this work is to investigate the use of IAD to deposit protective and anti-reflection (AR) coatings on HMF glass substrates, in order to obtain good quality coatings at reduced temperatures. The results are preliminary, as only a limited number of samples and conditions have been investigated. The coating materials selected for this investigation were MgF_2 , SiO_2 and Al_2O_3 . Single-layer coatings of MgF_2 and SiO_2 were deposited onto substrates of HfF_4 - BaF_2 - LaF_3 - AlF_3 (HBLA) glass, and an $\text{Al}_2\text{O}_3/\text{SiO}_2$ AR coating was deposited onto a substrate of ZrF_4 - BaF_2 - LaF_3 - AlF_3 (ZBLA) glass. Tests were performed to determine film and substrate environmental durability, scratch-resistance and adhesion. The optical properties of the coatings were also characterized.

2. EXPERIMENTAL ARRANGEMENT

Details of the film deposition arrangement are given in Reference 12; a schematic of the arrangement is shown in figure 1. A Kaufman ion source is used to provide a monoenergetic, neutralized beam of ions independent of the material evaporation process. It provides a low-energy (300-1500 eV) beam of Ar or O_2 ions incident on the film surface with variable angle of 0-45°. A Faraday probe was used to monitor the ion current density at the substrate. Prior to deposition the substrates were cleaned with 300 eV Ar ions. The MgF_2 film material was evaporated at 0.3 nm/sec using a resistively heated boat, and the growing film was bombarded with 300 eV Ar ions at a current density of $5 \mu\text{A}/\text{cm}^2$ during deposition. The temperature was approximately 100°C due to heating from the boat. The SiO_2 and Al_2O_3 film materials were electron-beam evaporated at rates of 0.3 nm/sec with oxygen backfill pressure of 1.0×10^{-4} Torr. The growing films were bombarded with 300 eV O_2 ions at a current density of $30 \mu\text{A}/\text{cm}^2$ during deposition. The substrate temperature was approximately 150°C.

3. RESULTS

3.1. Environmental Stability

An HBLA glass sample was coated with 0.5 μm IAD MgF_2 film, and another sample was left uncoated. A drop of water was placed on each sample for approximately 16 hours. The samples were then examined using a Nomarski microscope. The two micrographs are shown in figure 2. The results for the uncoated sample illustrate the known susceptibility to aqueous corrosion of an unprotected fluoride glass surface. The result for the coated sample shows that it did not suffer any noticeable degradation, and indicates that an IAD MgF_2 coating might serve as an effective barrier against moisture penetration. Figure 3 is a micrograph of an HBLA glass sample coated with 0.5 μm IAD SiO_2 and subjected to a water drop test. There is no observable difference in the film exposed to the water drop relative to the portion not exposed. We also examined a ZBLA glass sample coated with a two-layer $\text{Al}_2\text{O}_3/\text{SiO}_2$ AR coating. The sample was exposed to a water drop test as described above. Again, there is no noticeable degradation in the film exposed to the water drop; it appears exactly as the portion not exposed. We have also conducted humidity cycle tests to examine film stability properties. Films were exposed to 97% humidity at 35°C for six hours

after removal from the coating chamber. Spectral shifts in film transmittance curves were observed for films deposited without IAD, indicating that the films adsorbed water. However, for all IAD films examined, no spectral shifts were observed in the spectrophotometer traces[13]. These results, as well as previous observations of reduced optical scatter and increased refractive index [8-10], are consistent with IAD films having an increased packing density and being less susceptible to water adsorption. Thus, overcoating a fluoride glass with an IAD coating might protect it from moisture attack and allow the use of HMF glasses in non-ideal environments.

3.2. Abrasion Resistance

We investigated the effect of a coating on the abrasion resistance of HMF glass substrates. Samples were subjected to an eraser-rub test and examined using a Nomarski microscope. A sample was divided into two sections; one section was coated with 0.5 μm IAD MgF_2 , and the other section was left uncoated. The sample was then rubbed a few times with an eraser. Figure 4 is a micrograph of the uncoated HBLA glass section and the IAD coated section. The figure shows that the unprotected HMF glass is soft and subject to abrasion, while the IAD coated section is hard and not subject to abrasion. We investigated the abrasion resistance for two MgF_2 coatings on glass substrates. One sample was coated with 0.5 μm IAD MgF_2 , and the other was coated with 0.5 μm MgF_2 deposited without Ar ion bombardment. The samples were then rubbed a few times with an eraser. Results are shown in figure 5. The unbombarded ($J=0$) sample is scratched, whereas the bombarded sample is much less scratched. This illustrates that the IAD coated sample is more durable than the sample coated without bombardment. We divided another HMF sample into two sections. One section was coated with 0.5 μm IAD SiO_2 , and the other section was left uncoated. Results similar to those obtained for the IAD MgF_2 coated samples were obtained. The coated section is much less scratched than the uncoated section. These results indicate that overcoating a fluoride glass with an IAD coating can enhance the durability of HMF glasses.

3.3. Film Adhesion

All samples were subjected to a tape-pull test to examine the effect of IAD on film adhesion. Coatings deposited without IAD had poor adhesion to the glass substrates. None of the samples coated with ion bombardment during deposition experienced delamination.

3.4. Optical Properties

Transmittance and reflectance spectra for all samples were obtained using a dual-beam spectrophotometer. One important parameter that can be qualitatively characterized from spectrophotometric measurements is film stoichiometry. Poor film stoichiometry leads to a higher UV cutoff wavelength in optical transmittance. The transmittance spectra of the coated and uncoated HMF glass samples were examined, and in no case was the UV cutoff wavelength higher for an IAD coated sample relative to the uncoated substrate. This indicates that ion bombardment at these conditions is not detrimental to film stoichiometry for low temperature coating. Another film property that can be obtained from spectrophotometric measurements is refractive index inhomogeneity.

geneity. The presence of an inhomogeneity can be deduced from the transmittance and reflectance data at wavelengths for which the film is multiple half-wave in optical thickness. Index inhomogeneity can often occur in low temperature coatings. No detectable index inhomogeneity was present in any IAD coating. The transmittance spectra for an uncoated ZBLA glass substrate and a two-layer $\text{Al}_2\text{O}_3/\text{SiO}_2$ AR coating are shown in figure 6. Note that the spectra for the AR coating touches that of the uncoated glass at approximately 500 nm, and that the film optical characteristics are good above 400 nm; note that below 400 nm the film becomes absorbing.

4. CONCLUSIONS

We have successfully applied IAD techniques to deposit MgF_2 , SiO_2 and $\text{Al}_2\text{O}_3/\text{SiO}_2$ thin film structures on HMF glass surfaces at low substrate temperatures (100 - 150°C). The coatings deposited using IAD were hard and dense, and improve the durability of the fluoride glass. Environmental stability and corrosion resistance of the optical surfaces were significantly improved; abrasion resistance was improved; excellent film adhesion was obtained; film optical properties were good and shown to be compatible with the HMF glass material. The demonstrated properties enhance the prospects for the use of HMF glass materials in a variety of applications. Optimization of the coating process should enable further improvements in fluoride glass durability for use in harsh environments.

* This work partially supported by the Air Force Weapons Laboratory under contract no. F 29601-81-C-0012.

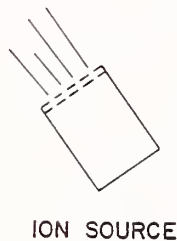
5. REFERENCES

- [1] Tran, D. C., Sigel, G. H., Bendow, B. "Heavy metal fluoride glasses and fibers: A review," IEEE J. Lightwave Tech. 5, 566, 1984.
- [2] Simmons, C. J., Azali, S. A., Simmons, J. H. "Chemical durability studies of heavy metal fluoride glasses," Second Int. Symposium on Halide Glasses, Troy, NY, 1983.
- [3] Herrmann, Jr., W. C., McNeil, J. R. "Ion beam applications for optical coatings," Proc. Soc. Photo-Opt. Instrum. Eng. 325, 101, 1982.
- [4] Martin, P. J., Netterfield, R. P., Sainty, W. G., Clark, G. J., Lanford, W. A., Sie, S. H. "Ion-assisted deposition of bulklike ZrO_2 films," Appl. Phys. Lett. 43, 711, 1983.
- [5] Martin P. J., Macleod, H. A., Netterfield, R. P., Pacey, C. G., Sainty, W. G. "Ion-beam-assisted deposition of thin films," Appl. Opt. 22, 178, 1983.

- [6] Allen, T. H. "Ion assisted deposition of titania and silica films," Proc. Soc. Photo-Opt. Instrum. Eng. 325, 93, 1982.
- [7] Bland, R. D., Kominiak, G. J., Mattox, D. M. "Effect of ion bombardment during deposition of thick metal and ceramic deposits", J. Vac. Sci. Technol. 11, 671, 1974.
- [8] McNally, J. J., Al-Jumaily, G. A., McNeil, J. R. "Ion-assisted deposition of Ta₂O₅ and Al₂O₃ thin films," J. Vac. Sci. Technol. A, to be published, May/June 1986.
- [9] McNally, J. J., Al-Jumaily, G. A., Wilson, S. R., McNeil, J. R. "Ion-beam-assisted deposition of optical thin films - recent results," Proc. Soc. Photo-Opt. Instrum. Eng. 540, 479, 1985.
- [10] Al-Jumaily, G. A., McNally, J. J., McNeil, J. R., "Effect of ion assisted deposition on optical scatter and surface microstructure of thin films," J. Vac. Sci. Technol. A3, 651, 1985.
- [11] McNeil, J. R., Al-Jumaily, G. A., Jungling, K. C., Barron, A. C., "Properties of TiO₂ and SiO₂ thin films deposited using ion assisted deposition," Appl. Opt. 24, 486, 1985.
- [12] McNeil, J. R., Barron, A. C., Wilson, S. R., Herrmann, Jr., W. C. "Ion assisted deposition of optical thin films: low energy vs high energy bombardment," Appl. Opt. 23, 552, 1984.
- [13] McNally, J. J., Al-Jumaily, G. A., McNeil, J. R., "Properties of Ta₂O₅ and Al₂O₃ thin films deposited using ion assisted deposition", to be published.

EXPERIMENTAL ARRANGEMENT

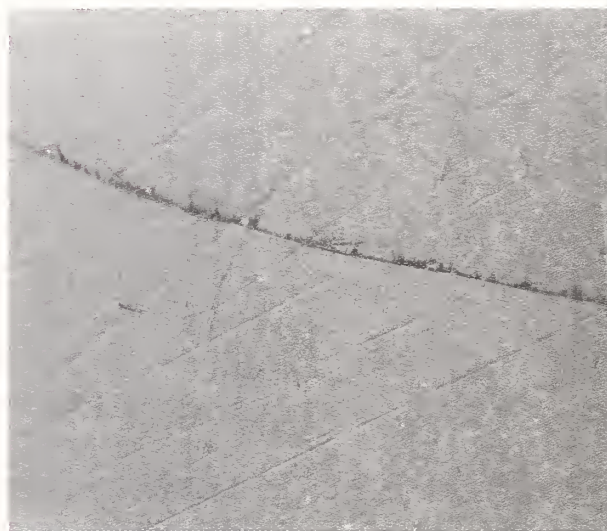
SUBSTRATE



1. Schematic of the experimental arrangement.

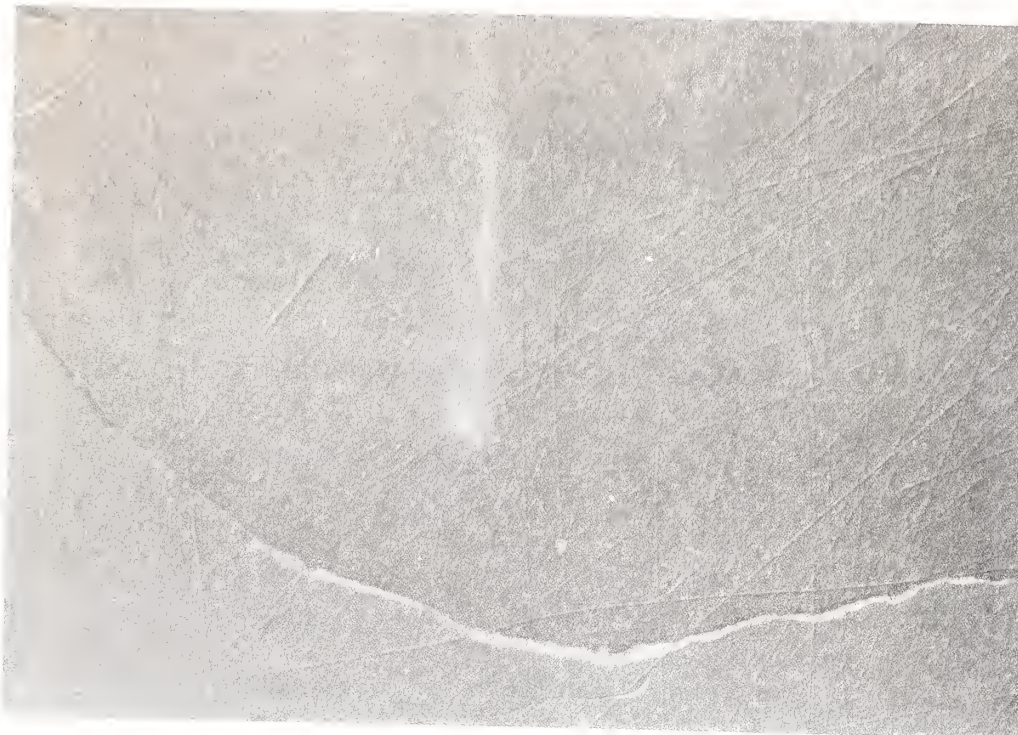


a



b

2. Nomarski micrographs of a) an uncoated HBLA glass sample, and b) a HBLA sample coated with $0.5\text{ }\mu\text{m}$ IAD MgF_2 film after water drop test.



3. Nomarski micrograph of a HBLA sample coated with $0.5\ \mu\text{m}$ IAD SiO_2 after water drop test.



4. Nomarski micrograph of a HBLA sample after eraser rub test. The left side of the figure is the uncoated section, and the right side is the section coated with $0.5\ \mu\text{m}$ IAD MgF_2 .

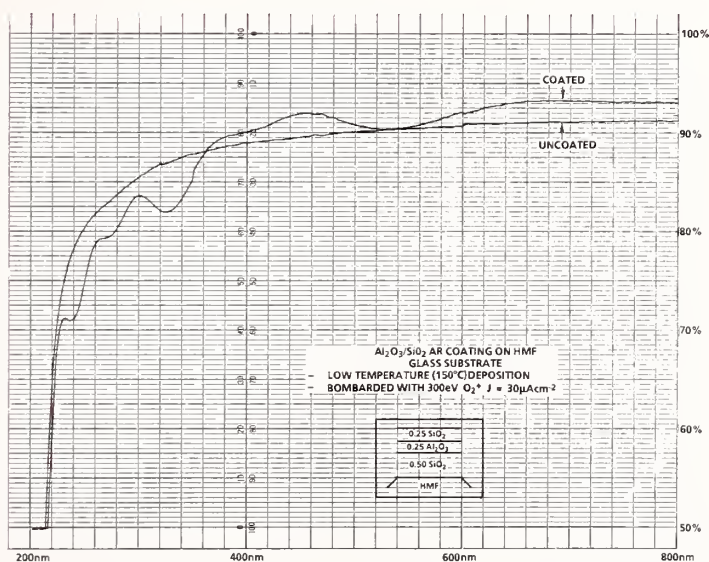


a



b

5. Nomarski micrograph of two MgF_2 coatings after eraser rub test.
 a) Sample coated with $0.5 \mu\text{m}$ MgF_2 deposited without ion bombardment,
 and b) sample coated with $0.5 \mu\text{m}$ IAD MgF_2 .



6. Transmittance spectra for a two-layer $\text{Al}_2\text{O}_3/\text{SiO}_2$ AR coating deposited on a ZBLA sample.

Highly Damage Resistant Porous Dielectric Coating for High Power
Lasers in the Ultraviolet to Near-infrared Wavelength Region

K. Yoshida, H. Yoshida, Y. Kato, and C. Yamanaka

Osaka University
Osaka, Japan

Mechanically hard and broadband gradient refractive index antireflection coating was developed. It has a high damage threshold of $>6 \text{ J/cm}^2$ at 355 nm and 12-13 J/cm^2 in the visible to near-infrared region. It will be applicable to high power pulsed lasers as well as to industrial uses.

Key words: gradient refractive index, porous dielectric AR coating, damage threshold, quartz, mixed thin film, surface roughness.

We have developed a new technique for producing antireflection (AR) coatings on various substrate materials including fused and synthetic quartz and optical glasses. This coating applied on a quartz has a damage threshold of over 6 J/cm^2 at 355 nm. Since the coating is very broadband and mechanically stable, it will be applicable not only to high power lasers, but also to other areas such as optical communications.

Development of high power lasers require damage-resistant AR surfaces. Present multilayer dielectric AR coatings do not have sufficient damage thresholds to pulsed lasers, particularly in the short wavelength region. Graded-index AR surfaces produced by neutral solution processing[1] on bare polished borosilicate crown glass BK-7 have a damage threshold of 12 J/cm^2 at a laser wavelength of 1064 nm with the pulse width (τ_p) of 1 ns[2]. However, the neutral solution processing is not applicable to the surface of silica substrate which is required for ultraviolet lasers. The AR surface produced by this method is susceptible to mechanical damages. Porous silica AR coating was developed for high power ultraviolet lasers[3]. In this method, porosity-graded SiO_2 coating is deposited on a substrate from a polymer solution derived from silicon ethoxide. This method is applicable to a wide variety of substrates including silica and KDP crystals. This porous silica AR coating has an excellent damage threshold of 6-9 J/cm^2 at 351 nm ($\tau_p=1 \text{ ns}$). However, this AR surface is also susceptible to mechanical damages and thus requires careful handling. The AR coating which we report in this letter might exceed the above-mentioned AR coatings in terms of laser damage, mechanical stability, and easiness of coating production.

In the present technique, two dielectric materials A and B having different refractive indices n_A and n_B , where $n_A > n_B$ are simultaneously deposited in vacuum on a substrate such as quartz or optical glasses. Then the mixed thin film is chemically processed in a liquid solution which preferentially dissolves the material B. These processing result in a porous thin film which has gradient refractive index and thus has the AR property over broad bandwidth. Hereafter we call the AR coating produced by this method as porous dielectric AR coating.

In actual production, two dielectric materials SiO_2 and NaF were evaporated from independent evaporation sources and simultaneously deposited in vacuum on one side of a heated quartz substrate. The quartz substrates used in the following tests were standard fused quartz plates for photolithography in semiconductor industry and the synthetic quartz for optical fiber industry, respectively. The porous dielectric AR coating was produced by dissolving NaF in ultrapure water. The wavelength of the minimum reflectivity is controlled by the coating thickness.

The closed circles in Fig. 1 shows the measured reflectivity versus wavelength of the coating after chemical processing. The minimum reflectivity of the porous dielectric AR coating is 0.17% at the optimum wavelength, which is 355 nm in Fig. 1. It has a very broadband characteristic with the reflectance of $<0.5\%$ over 200-nm and $<1\%$ over 300-nm wavelength range. Let us assume that the coating has the refractive indices of $n_f(a)$, $n_f(g)$ on the air side and on the substrate side, respectively. Then the reflectivity versus wavelength at normal incidence is approximately given by

$$R_f \approx 1 - \frac{4n_f(a)n_f(g)n_g}{[n_f(a)n_g + n_f(g)]^2 - [n_f(a)^2 - 1][n_g^2 - n_f(g)^2]\sin^2(\delta/2)} \quad (1)$$

$$\delta = \frac{4\pi}{\lambda} \int_0^{d_f} n(z) dz \approx \frac{2\pi}{\lambda} [n_f(a) + n_f(g)] d_f, \quad (2)$$

where n_g is the refractive index of the substrate, and d_f is the coating thickness[4]. The dashed line in Fig. 1. shows the calculated reflectivities using Eqs. (1) and (2) with the parameters of $n_f(a)=1.220$, $n_f(g)=1.303$, and $d_f=70$ nm, respectively. The solid line is the calculated reflectivity with the homogeneous thin film of $n_f(a)=n_f(g)=1.220$ and $d_f=73$ nm. Thus it is reasonable to assume that the AR coating produced in this method has the gradient refractive index. This refractive index indicates that this AR coating has the density ~46% that of the standard SiO_2 coating.

Figure 2 shows the Nomarski micrographs of the porous dielectric AR coating before and after chemical processing. The roughness of the coated surface after evaporation disappears after chemical processing, and the resultant surface is completely smooth under optical microscope. We have measured the surface roughness of the quartz substrate and the porous dielectric AR coating with digital optical profilometer Wyko Optical Inc. (Type NCP-1000). The results are shown in Fig. 3(a) and (b), respectively. The surface roughness of the substrate and the AR coating were almost the same value of 11Å rms.

The damage threshold of the porous dielectric AR coating was measured at the laser wavelengths of 1053, 527, and 355 nm, respectively. The output from oscillator (a Q-switched Nd: YLF laser or an actively mode-locked Nd: YAG laser) was amplified by two Nd: glass amplifiers of 15-mm aperture and frequency up converted by type II KDP crystals. The amplified laser pulse was focused with a 1-m focal length lens. On the test sample, the laser beam had a smooth Gaussian shape with a spot diameter at $1/e^2$ peak intensity of 400 μm . The laser energy was adjusted with the combination of a half-wave plate and a dielectric polarizer without changing the pumping energies of the amplifiers so as not to change the beam shape on the sample. The laser energy and the pulse shape was monitored with biplanar phototubes which were calibrated with a standard calorimeter. The coating damage was detected by observing before and after laser irradiation with a Nomarski microscope at 200 \times magnification. The test sample was moved after each shot irrespective of the presence or absence of the damage. Therefore the damage thresholds quoted

Table 1. Comparison of the damage threshold between the porous dielectric AR coating, the standard AR coating, and the quartz at $\lambda=355$ nm ($\tau_p=0.4$ ns), 527 nm ($\tau_p=1$ ns), and 1053 nm ($\tau_p=1$ ns), respectively.

AR coatings	Damage Threshold: (J/cm ²)	Laser	coating materials and layers	test
Multilayer	3-4	1053 nm	No undercoat; $\text{TiO}_2/\text{SiO}_2$, 2-6 layers	1-on-1
Multilayer	4-8	1 ns	$\lambda/2$ SiO_2 undercoat; $\text{TiO}_2/\text{SiO}_2$ 3-7, layers	1-on-1
Porous dielectric	12-13			1-on-1
Multilayer	2.5-3.5	527 nm	No undercoat; $\text{TiO}_2/\text{SiO}_2$, 2-6 layers	1-on-1
Multilayer	4-5	1 ns	$\lambda/2$ SiO_2 undercoat; $\text{TiO}_2/\text{SiO}_2$ 3-7, layers	1-on-1
Porous dielectric	12			1-on-1
Monolayer	2-4		$\lambda/4$ SiO_2	1-on-1
	4.4-6.4		$\lambda/4$ SiO_2	N-on-1
Mixed thin film	2.5-3.2	355 nm	$\text{NaF}+\text{SiO}_2$	1-on-1
Multilayer	1-3	0.4 ns	$\lambda/2$ SiO_2 undercoat; $\text{Al}_2\text{O}_3/\text{SiO}_2$, $\text{Sc}_2\text{O}_3/\text{SiO}_2$, 3-7 layers	1-on-1
Porous dielectric	6-9.5			1-on-1
	10.5-11.5			N-on-1
Quartz	9.5-16			1-on-1

hereafter are those for "one-shot damage" (1-on-1 tests). More than 20 samples were tested for the damage measurements.

Table I summarizes the results of the damage thresholds of mixed thin film and the porous dielectric AR coating together with the data of the bare quartz, single layer SiO_2 coating and the standard AR coatings measured at the same experimental conditions. The porous dielectric AR coating has the damage threshold of 6-9.5 J/cm^2 at $\lambda=355$ nm ($\tau_p=0.4$ ns) and 12-13 J/cm^2 at both $\lambda=527$ and 1053 nm ($\tau_p=1$ ns), respectively. Compared with the standard commercial AR coatings, the porous dielectric AR coating has more than twice higher damage threshold at all the tested wavelengths. When same coated site was repeatedly irradiated (N-on-1 tests) at fluence levels below the 1-on-1 threshold, the damage threshold of porous dielectric AR coating was increased from 8 to 11.5 J/cm^2 which is almost the same value of the bare quartz surface. It is interesting to note that the porous dielectric coating has a significantly higher damage threshold compared with the single layer SiO_2 coating.

In Fig. 4 we show the representative pictures of the phase contrast photomicrographs of the damage morphology seen in the porous dielectric AR coatings at different laser fluences at 355 nm. In general, the damaged pattern of this AR coating consists of small pits whose diameters are less than ~ 3 μm . However, at high laser fluences, large damages are produced such as the picture in Fig. 4 at 15.2 J/cm^2 .

✓ The porous dielectric AR coating which we have developed is mechanically hard, since it is physically a single layer hard dielectric coating deposited in vacuum. The AR surface is strong against abrasion by tape peeling test. The surface can be cleaned with, for example, lens tissues to remove dusts and contaminations without causing mechanical damages. Due to the excellent optical and mechanical properties together with the easiness of fabrication, the porous dielectric AR coating might find many applications in various fields including industrial uses.

We have applied the porous dielectric AR coatings on fused quartz optics (aspheric lenses, blast shield glasses, and KDP window glasses) used for third harmonic conversion of our high power glass laser having a 18-cm beam diameter[5]. No damage on the coatings has been produced under the 3 wavelengths irradiation (1052 nm, 526 nm, and 351 nm) with the total fluence of <5 J/cm^2 for the extended period of over 10 months.

In summary, we have developed a new, porous dielectric AR coating. This coating is applicable in various substrates including fused and synthetic quartz. It has gradient refractive index and the broadband AR characteristics. The measured damage threshold of this coating is 6-9.5 J/cm^2 at 355 nm ($\tau_p=0.4$ ns) and 12-13 J/cm^2 at 527 nm and 1053 nm ($\tau_p=1$ ns), respectively. Since the AR surface is mechanically hard, it does not require particular precautions for handling. The reliability has been tested in a high power frequency converted glass laser system.

The authors wish to acknowledge valuable contributions to this work by Dr. Y. Namba of Osaka University and Mr. T. Izawa of Showa Optical Co., Ltd.

References

- [1] L.M. Cook, S. Liolk, and K.H. Mader, American Ceramic Soc. 65, 152 (1982).
- [2] W.H. Lowdermilk and D. Milam, Appl. Phys. Lett. 36, 891 (1980).
- [3] D. Milam, W.H. Lowdermilk, J.G. Wilder and I.M. Thomas, CLEO '84 Technical Digest THB3, 136 (1984).
- [4] H. Schroder, Ann. Physik 39, 55 (1941).
- [5] Y. Kato, K. Yoshida, J. Kuroda, and C. Yamanaka, Appl. Phys. Lett. 38, 72 (1981).

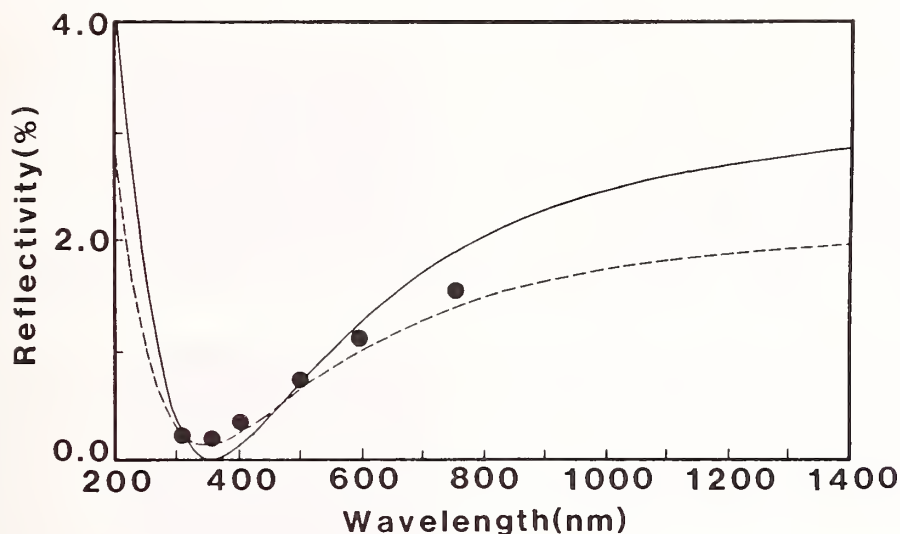
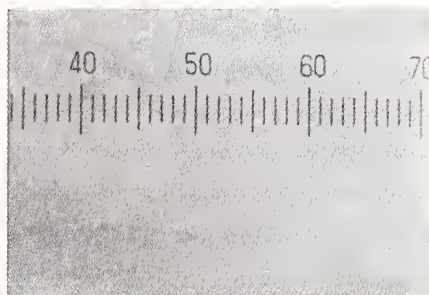
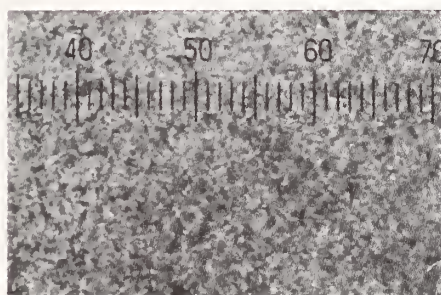


Figure 1. Reflectivity vs wavelength of the porous dielectric AR coating after chemical processing. The closed circles show the measured reflectivities. The dashed line is the calculated reflectivity using Eqs. (1) and (2) with $n_f(a)=1.220$, $n_f(g)=1.303$, and $d_f=70$ nm. The solid line is the calculated reflectivity for the homogeneous monolayer coating with $n_f(a)=n_f(g)=1.220$ and $d_f=73$ nm.



10 μ m

(a) before processing

(b) after processing

Figure 2. Nomarski micrograph of the porous dielectric AR coating before and after chemical processing.

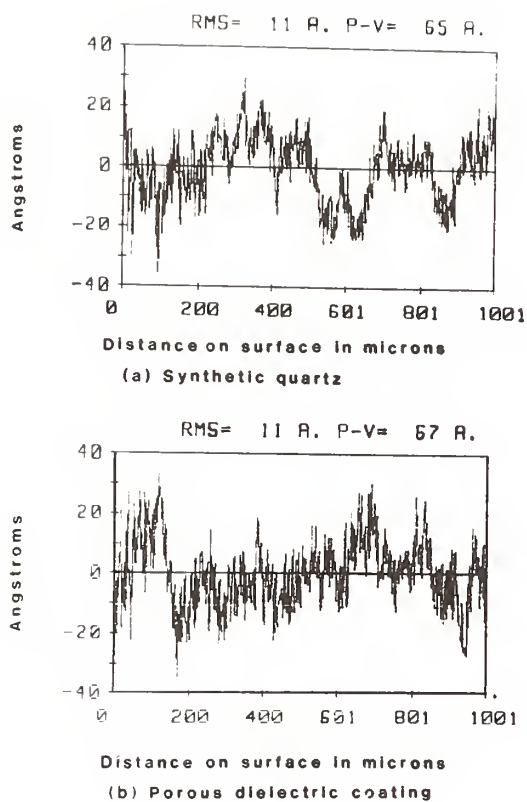


Figure 3. Surface profile by digital optical profilometer.

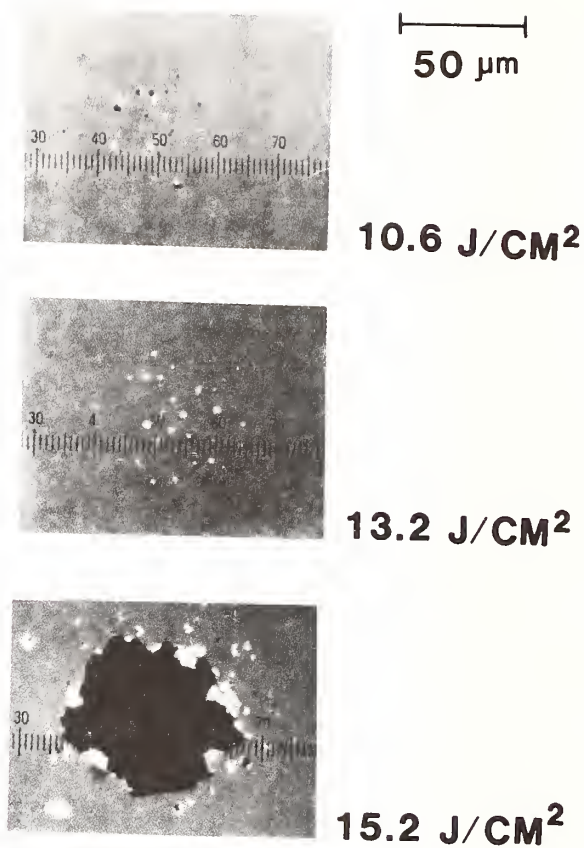


Figure 4. Representative pictures of the phase contrast photomicrograph of the damage morphology at various laser fluences.

Ion Beam Characterization of Multi-Layer Dielectric Reflectors

J. G. Beery, M. G. Hollander, C. J. Maggiore,
A. Redondo, R. T. Westervelt, and T. N. Taylor

Los Alamos National Laboratory
Los Alamos, NM 87545

Energetic ion beams were used to characterize multilayer dielectric reflectors. Alpha-particle beams with beam spot sizes between 10 microns and a few millimeters were scattered from reflectors consisting of 32-layer $\text{SiO}_2/\text{HfO}_2$ and 38-layer $\text{MgF}_2/\text{ThF}_4$. The RBS spectra reveal the nature of the laser damage processes by providing information on diffusion, mixing, and loss of material in the coatings. The particle-induced x-ray emission (PIXE) technique gave complimentary results on low-concentration impurities in the coatings.

Key Words: dielectric reflectors, nuclear microprobe, particle-induced x-ray emission, Rutherford backscattering.

1. Introduction

Considerable work in the damage mechanisms of multilayer dielectric reflectors has previously been reported, using a variety of experimental techniques. The fundamental damage mechanisms are not completely understood because of the complexity of the systems. We have carried out Rutherford backscattering [1] (RBS) and particle-induced x-ray emission [2] (PIXE) experiments using energetic ion beams to characterize high-reflection coatings on laser mirrors before and after damage. These experiments are particularly suitable for measuring the composition as a function of depth, the presence of low concentration impurities, and changes in the structure of the films as a result of the damage processes. The measurements have been made on undamaged coatings with spot sizes of a few square millimeters. Localized structure in the region of individual damage pits has been studied using a nuclear microprobe [3,4], which produces spot sizes as small as ten microns in diameter. The RBS spectra obtained provide information about damage profiles, mixing, diffusion, and loss of material in the coatings. The PIXE technique has been used to measure low concentration levels of impurities in the films.

2. Experimental Method

Rutherford backscattering is a well-established quantitative technique for interface and thin film analysis. It is an analytical technique based on known kinematics and energy loss that can determine the composition and structure in materials to a depth of a few microns.

Figure 1 is a schematic drawing of the general geometry of a backscattering experiment. A beam of light ions from a Van de Graaff accelerator strikes a target, and the scattered particles are detected with a surface barrier detector at a fixed angle. Figure 1a shows a thin film of a heavy element on top of a lighter substrate. The observed energy of the backscattered particles is determined by the kinematics of the elastic scattering and the depth of the scattering event below the surface. Figure 1b shows a typical RBS spectrum. The highest energy, KE_{in} , corresponds to elastic scattering at the surface of the film. The energy E_f is due to elastic scattering from the film at the film-substrate interface and the energy loss of the particles traversing the film. The width of the peak, ΔE , is related to the areal density (atoms/cm²) of the film. The relative masses of the incident and target particles and the scattering geometry determine the kinematic factor, K . The backscattering energy increases with the mass of the target atoms. Thus, RBS is particularly well-suited for measuring the distribution of heavy elements in a lighter matrix.

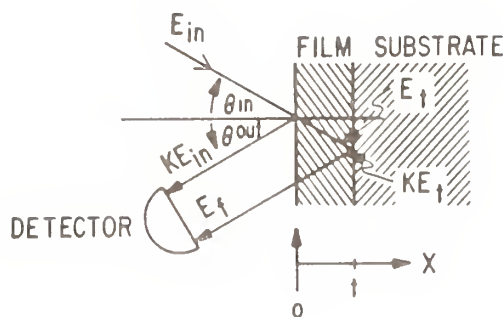


Figure 1a. General backscattering geometry for Rutherford backscattering measurement.

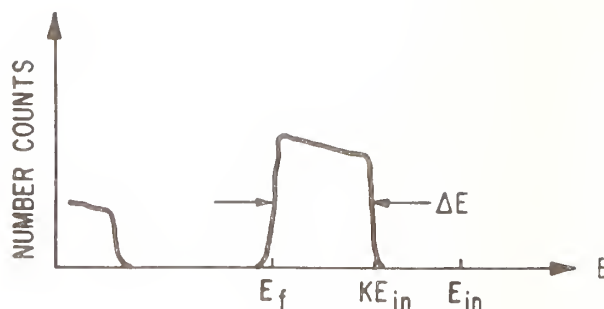


Figure 1b. RBS spectrum obtained from a heavy thin film on a light substrate.

The RBS experiments reported here were carried out with 2.3 and 2.5 MeV α -particles with $\theta_{in} = 0$ and $\theta_{out} = 20$ degrees. We studied 32-layer $\text{SiO}_2/\text{HfO}_2$ and 38-layer $\text{MgF}_2/\text{ThF}_4$ coatings on fused silica. Since the kinematic factor for the lighter elements, Si, O, Mg and F, is much less than that for the Hf or Th, the high energy part of the spectrum characterizes the depth distribution of the heavy elements in the film.

The technique favors high Z elements because the Rutherford backscattering cross section is proportional to Z^2 . If the elemental masses are too close, the kinematic constraints limit the mass resolution and result in overlapping spectra for compound samples. Consequently, the analysis of $\text{Al}_2\text{O}_3/\text{SiO}_2$ coatings is somewhat more difficult. These factors, together with finite detector resolution, limit our depth sensitivity at the surface to approximately 50 angstroms. Energy straggling degrades depth resolution below the surface.

When an energetic ion loses energy in the sample, it induces x-ray emission characteristic of the atoms in the target. Energy analysis of these characteristic lines permits elemental identification at low concentration levels. The PIXE technique is generally applicable to atoms with $Z > 10$. The sensitivity depends on the matrix and the atomic number and is usually in the range of 10 ppm. For the work reported here, the incident beam was 2.0 MeV protons.

These techniques can be applied to the study of localized damage by focusing the incident ion beam into small spatial dimensions. We have studied individual damage pits on multilayer dielectric reflectors using these focused ion beams with both the RBS and PIXE techniques. A nuclear microprobe with spot sizes of a few microns in diameter was used.

We studied $\text{SiO}_2/\text{HfO}_2$ and $\text{MgF}_2/\text{ThF}_4$ multilayer coatings on fused silica substrates. The structure of these films is given in Table 1. Table 2 describes the dimensions of the beam spots and the resulting current densities. For the two larger spot sizes, the RBS and PIXE techniques are non-destructive. For the smallest spot size of ten microns, the current density is high enough to create color centers.

Table 1. Structure of multilayer dielectric reflectors.

HR351-166-SPP	351 nm
(H, L) ¹⁰ H [L(1.429), H(0.705)] ⁵ L(2)	
H: HfO_2	
L: SiO_2	
HR248-213-OC1	248 nm
(HL) ¹⁹ H	
H: ThF_4	
L: MgF_2	

Table 2. α -particle beam parameters.

SPOT SIZE	CURRENT (nA)	CURRENT DENSITY A/m ²
5 mm x 5 mm	20	8×10^{-4}
$r = 100 \mu$	5	6×10^{-1}
$r = 10 \mu$	2	3×10^1

3. Results

Figure 2 shows the experimental RBS energy spectrum from the $\text{SiO}_2/\text{HfO}_2$ coating. One can clearly see 16 separate hafnium peaks. Also evident is the change in layer thickness for the topmost five layers of HfO_2 . The silicon contribution overlaps the lower energy portion of the hafnium peaks extending up to 1.4 MeV, but it does not significantly alter the spectrum due to its lower scattering cross section. The low energy cutoff at 200 keV is due to the discriminator setting in the electronics.

Similar data were also taken on an undamaged $\text{MgF}_2/\text{ThF}_4$ coating. These results are shown in Figure 3. The first 15 layers of this spectrum have been simulated using the model parameters listed in Table 3. The simulation was performed using computer programs based on first principles for the scattering and parameterized energy loss equations. The input consists of average stoichiometric ratios for the individual elements in each layer. The program uses them to calculate the corresponding spectra which are then compared with experiment. The best fit was achieved with a decreasing ratio of thorium to fluorine as one moves toward the substrate (e.g., 1 to 4 for the top layer and 1 to 5 for the eighth layer). In addition, the thorium that is missing from a given ThF_4 layer appears uniformly distributed in the adjacent MgF_2 layer. This can be interpreted as evidence for interlayer mixing during the fabrication process. The thorium fluoride layers are uniform to within 5%. The magnesium fluoride layers appear to be fairly uniform; however, the simulation is not very sensitive to the low mass layers.

Figure 4 is a Nomarski micrograph of a laser damage spot in the silica/hafnia coating. The large oval feature at the center is the visibly damaged region that penetrates to the substrate. The striations to the left and right were made visible during or after the damage process. A relatively clear area

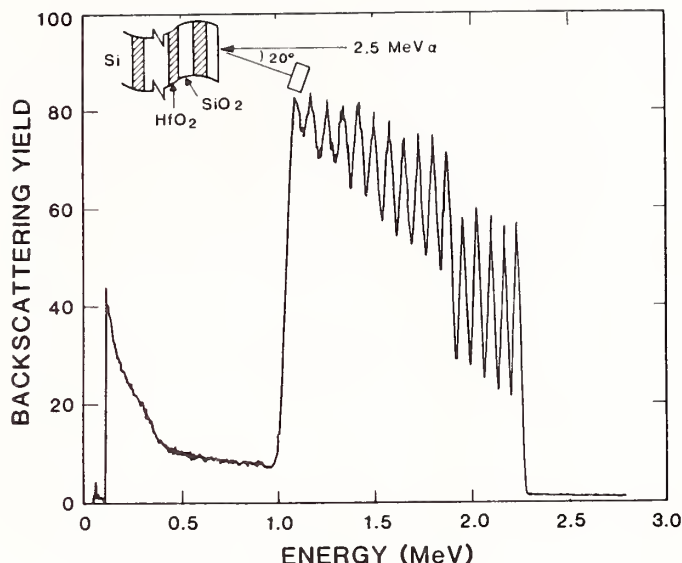


Figure 2. RBS energy spectrum for undamaged region of $\text{SiO}_2/\text{HfO}_2$ reflector.

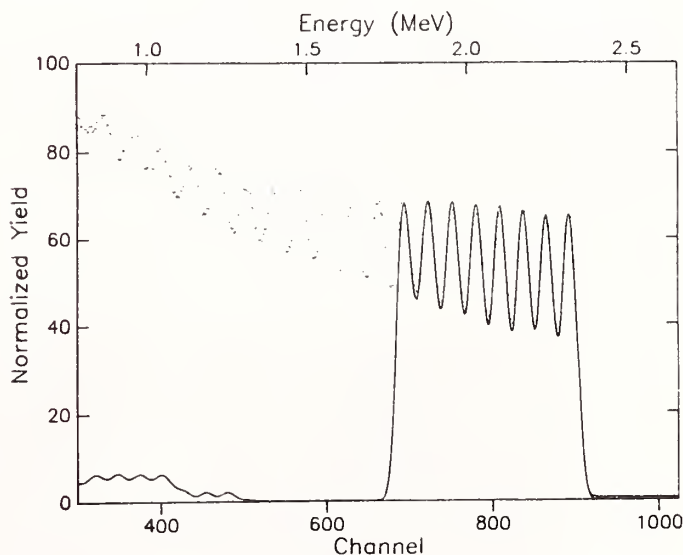


Figure 3. RBS energy spectrum for undamaged region of $\text{MgF}_2/\text{ThF}_4$ reflector (points). Simulated spectrum for fifteen layers nearest surface (solid line).

Table 3. Simulated structure for fifteen layers of $\text{MgF}_2/\text{ThF}_4$. Layer 1 is at the surface.

Layer No.	Thickness (10^{15} atoms/cm ²)	Atomic Concentration (%)		
		Th	F	Mg
1	405	20.0	80.0	
2	430		66.7	33.3
3	410	18.9	81.1	
4	430	1.0	66.0	33.0
5	410	18.5	81.5	
6	430	1.0	66.0	33.0
7	410	18.2	81.8	
8	428	1.6	65.6	32.8
9	405	17.5	82.5	
10	428	2.6	64.9	32.5
11	387	17.4	82.6	
12	428	3.2	64.5	32.3
13	405	16.1	83.9	
14	428	4.2	63.9	31.9
15	410	16.1	83.9	

immediately adjacent to the damage pit suggests that these striations were annealed by thermal processes. To study in detail the damage at a single pit, we focused the ion beam to a spot 10 microns in diameter using the nuclear microprobe. The line of small spots across the lower part of the oval feature is due the microprobe ion beam. We believe that the radiation damage from the ion beam created color centers.



Figure 4. Nomarski micrograph of laser damaged spot and surrounding region.

For the line scan across the laser damage area we obtained RBS spectra, one spectrum at each spot. Figure 5 is a composite of five spectra taken at various positions near or on the laser-damaged area of figure 4. The widest spectrum corresponds to the microprobe analysis at the edge of the damaged region and is similar to that of figure 2 except that the statistics are poorer. In addition, there is a small surface peak corresponding to hafnium that has been ejected from the pit and is on top of the SiO_2 overcoat. As one crosses the crater, the spectra change significantly due to mixing and loss of material. The spectrum corresponding to a spot inside the edge of the crater shows the loss of the overcoat and 5 or 6 pairs of silica/hafnia layers. It also shows that these are the outer layers of the coating. The next spot in the direction toward the bottom of the crater shows additional loss of hafnia and silica. The layered structure is absent indicating interlayer mixing. The last two spectra show successively greater loss of coating material toward the center of the pit.

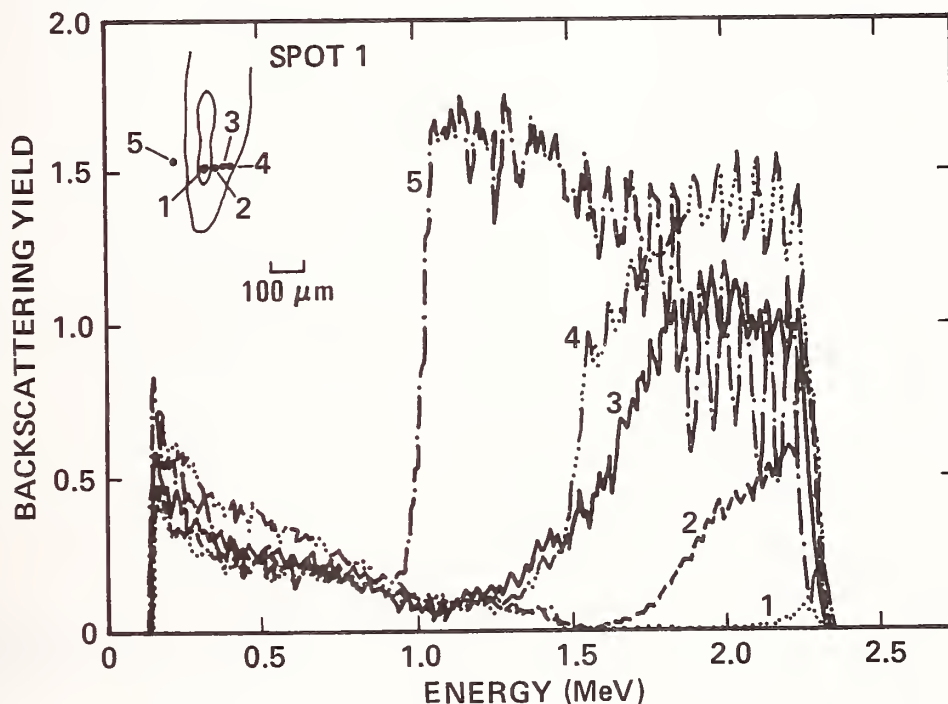


Figure 5. Composite of five RBS energy spectra taken near and on damaged spot. Reflector is $\text{SiO}_2/\text{HfO}_2$.

The RBS technique is sensitive to thin overlayers such as the half-wave overcoat of low-index material commonly applied to these mirrors. For example, figure 6 consists of a spectrum from the undamaged region of the $\text{SiO}_2/\text{HfO}_2$ mirror over-layed with a spectrum near the damaged area. The small shift in the energy of the upper edge of the hafnium corresponds to a 160 Å loss of the SiO_2 overcoat. In addition, the valleys of the undamaged spectrum are deeper than those of the damaged one. This indicates that sub-surface diffusion occurred near the damaged spot. These results suggest that in these hafnia/silica coatings, the damage mechanism proceeds from the top toward the substrate.

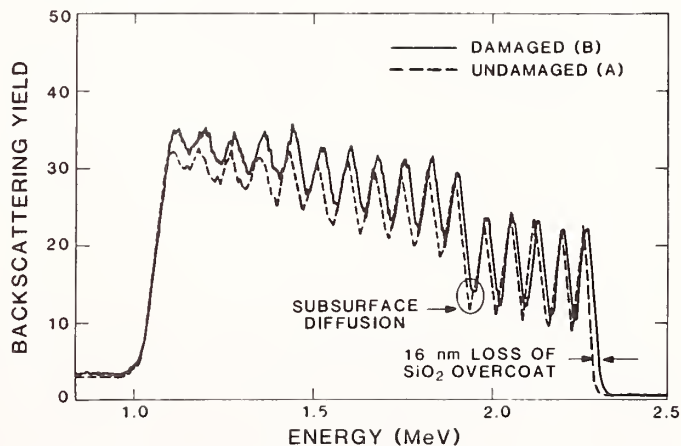


Figure 6. RBS spectra taken from undamaged and slightly damaged regions of $\text{SiO}_2/\text{HfO}_2$ showing partial loss of overcoat and diffusion.

Figure 7 shows the RBS spectrum of an undamaged $\text{MgF}_2/\text{ThF}_4$ coating using a 100-micron spot size. The 19 layers of thorium fluoride are clearly visible. Note the similarity of this spectrum and that of figure 2. As one approaches the laser-damaged area, the differences between the damage behavior of the $\text{SiO}_2/\text{HfO}_2$ and that of the $\text{MgF}_2/\text{ThF}_4$ become evident. These differences are shown in figure 8 for line scan data taken using a 10-micron spot size. The spectrum taken near the edge of the damage region exhibits a loss of layered structure near the substrate whereas the thorium peak is enhanced for the top layer. As we move toward the center of the damage region we observe complete loss of structure and 50% reduction in the amount of thorium. In addition, the surface thorium peak gradually disappears. Changes in the slope of the spectra at 0.9 and 1.2 MeV show the presence of fluorine and magnesium in the damage area. We believe that this indicates mixing of the magnesium fluoride and thorium fluoride films. The behavior of the surface thorium peak in these data, coupled with other spectra from regions which are not visibly altered, indicate that a significant amount of fluorine leaves the surface region. These spectra suggest that the damage mechanism starts from the substrate and progresses outward through the coating.

We have also used PIXE to search for low concentration impurities. Figure 9 shows a spectrum obtained by bombarding the $\text{SiO}_2/\text{HfO}_2$ sample with a beam of 2.0 MeV protons. In addition to the hafnium L lines, K- α lines from iron and zirconium impurities can be seen. The Fe is present at a concentration of 0.14 and the Zr at 0.29 atomic percent relative to the Hf.

4. Conclusions

Spatially resolved RBS provides detailed information about laser damage mechanisms in multi-layer dielectric coatings. Our results show that the fabrication process can result in some interlayer mixing, particularly for those layers closest to the substrate. In addition, the data allow us to identify different damage processes for the two coatings under study. In the case of $\text{SiO}_2/\text{HfO}_2$, the interlayer mixing progresses from the surface toward the substrate. For the $\text{MgF}_2/\text{ThF}_4$ coating the process is more complex, involving subsurface mixing and loss of near-surface fluorine.

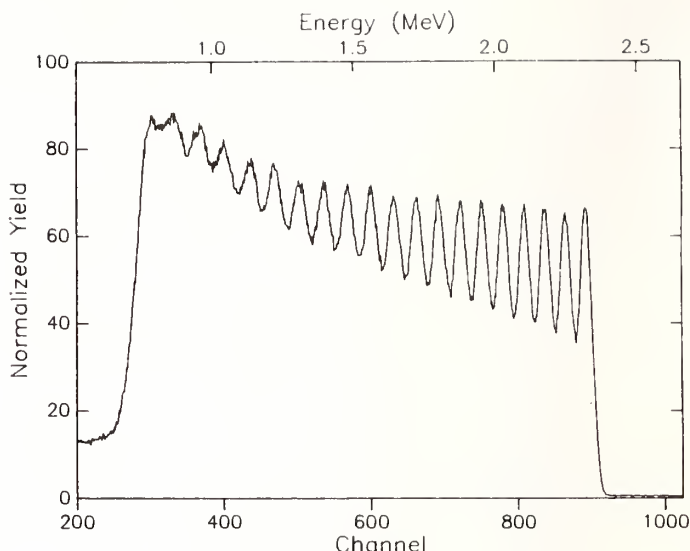


Figure 7. RBS energy spectrum from undamaged region of $\text{MgF}_2/\text{ThF}_4$ reflector.

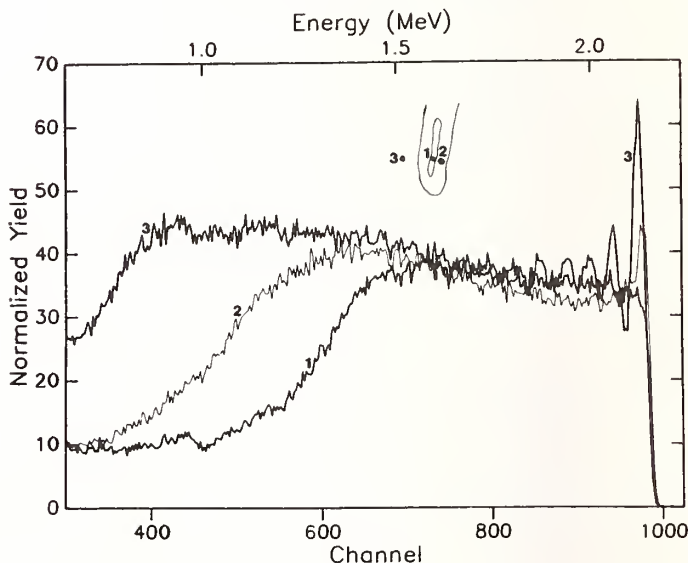


Figure 8. Composite of three energy spectra taken near and on damaged spot. Reflector is $\text{MgF}_2/\text{ThF}_4$.

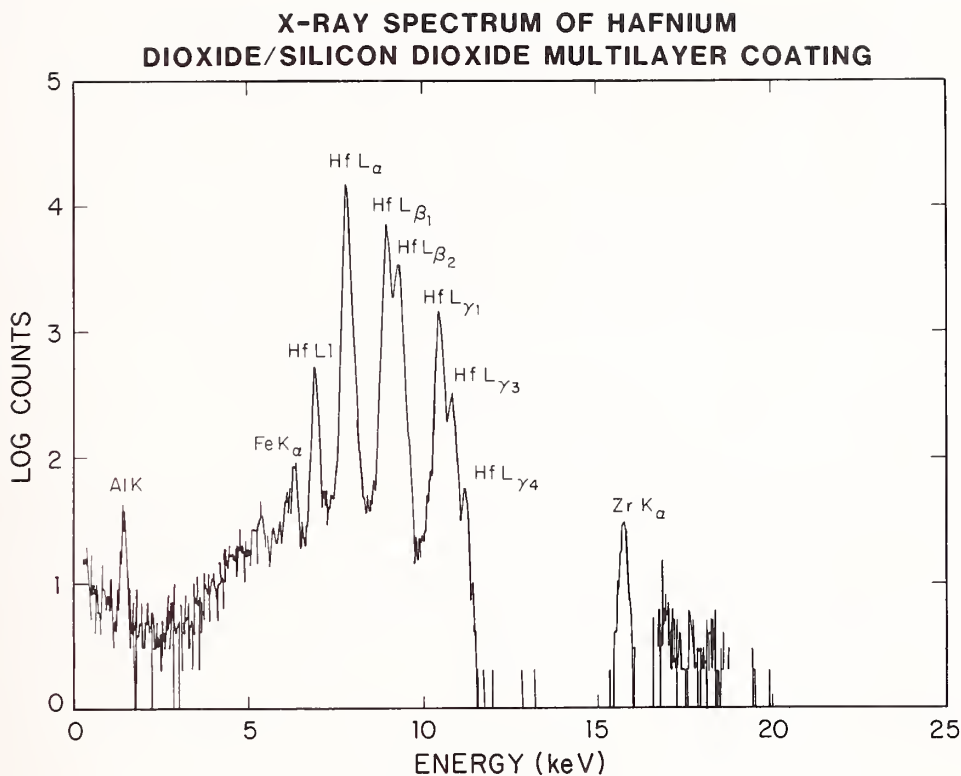


Figure 9. PIXE spectrum from $\text{SiO}_2/\text{HfO}_2$ reflector.

We thank Larry Doolittle for providing us with an RBS simulation code and for guidance in operating the code. We are grateful to Lev Borodovsky for helping with the experimental runs and the computer simulations. The experiment would not have been possible without the assistance of Joe Tesmer and the operating staff of the Van de Graaff facility at Los Alamos National Laboratory.

*This work is supported by the Department of Defense.

5. References

- [1] W-K. Chu, J. W. Mayer, and M-A. Nicolet, Backscattering Spectrometry, (Academic Press, New York, 1978).
- [2] T. B. Johnson, R. Akeleson, and S. A. E. Johansson, Nucl. Instr. Meth. 84, 141 (1970).
- [3] J. A. Cookson, "The Production and Use of A Nuclear Microprobe of Ions at MeV Energies," Nuclear Inst. Methods, 65, 477 (1979).
- [4] C. Maggiore, "Materials Analysis with a Nuclear Microprobe," Scanning Elect. Microsc., 1, 439 (1980).

Raman Scattering Analysis of Thin Film

Coatings Using Guided Waves

Alan F. Stewart

Air Force Weapons Laboratory

Kirtland AFB, New Mexico 87117

and

David R. Tallant and Karen L. Higgins

Sandia National Laboratories

Albuquerque, New Mexico 87185

Selected refractory oxide, thin film coatings have been analyzed using Raman spectroscopy. Diamond and rutile prisms were used to couple the probe beam into the thin film coatings which served as waveguides. Propagation of the probe beam as a guided wave in the thin film increases the probability for Raman scattering by species in the thin film, compared to techniques which depend on a single pass through or probe beam reflection at the film. Because the probe beam is confined entirely within the thin film coating, Raman spectra are obtained which are generally free of vibrational bands due to the substrate. The combination of more efficient coupling between the probe beam and the thin film and the elimination of substrate interferences results in improved sensitivity and the ability to record recognizable Raman spectra of thin films composed even of materials that are relatively inefficient Raman scatterers.

Key words: Thin film coatings, Raman spectroscopy, optical waveguide, prism coupling

1. Introduction

Raman spectroscopy has been used extensively for the determination of the crystalline structure of thin film coatings.¹⁻³ As an optical technique, Raman scattering offers some significant advantages over other analysis methods. Since the Raman effect is the result of atomic motions, local atomic structure in disordered as well as crystalline materials can yield distinctive Raman signatures. However, Raman scattering is intrinsically a weak effect with conversion efficiencies on the order of 10^{-7} . The study of optical thin film coatings compounds the problem of detecting a weak effect, since the interaction volume of the (micrometer or less) coating and a focused laser beam is very small. The supporting substrate may also contribute its own Raman bands, which frequently overwhelm the film's contribution. To improve sensitivity, a variety of experimental techniques including glancing incidence illumination, polarization selectivity and specially designed coating structures have been implemented to enable the spectroscopist to study the structure of thin film coatings.

In this study, we have successfully demonstrated that, by using a thin film coating as a waveguide for the probe beam, significant improvements in sensitivity can be achieved. The interaction between the probe beam and the film is enhanced because the entire probe beam travels along the film rather than passing through it a single time or reflecting at the film's surface. Because the probe beam is confined entirely within the thin film coating, Raman spectra are obtained which are free of Raman bands from the substrate. With the enhanced coupling between the probe beam and the thin film and the elimination of substrate interferences, it is possible to record the Raman spectra of thin films composed even of materials that are relatively inefficient Raman scatterers.

2. Experiment

Raman spectra of thin film coatings were recorded using guided waves as well as glancing incidence illumination. The experimental configuration, as detailed in figure 1, consisted of both argon and krypton ion lasers, collection optics, a double monochromator and cooled photomultiplier. For this study, the spectral resolution of the system was 5 cm^{-1} . Typically, the entrance slit height on the monochromator was set at 1 cm. The collection optics provided a 6X magnification factor so that the system "saw" only 1.5 mm of the guided wave as it propagated through the film.

The probe beam at either 514 or 647 nm was coupled into various thin film coatings using either diamond or rutile prisms. Both prisms were cut at 40, 50, and 90 degree angles to provide the appropriate range of coupling angles.⁴ The sample mount appears in figure 2 with a low-loss film waveguiding less than a milliwatt of 633 nm light. During these experiments, incident beam power levels at 514 nm and 647 nm were typically 300 and 120 milliwatts respectively. The laser power propagating through the film is believed to have been much lower, because of coupling inefficiencies and scattering losses in the films.

The thin film coatings used in this work were of Ta_2O_5 , ZrO_2 , Y_2O_3 , HfO_2 and ThO_2 . These coatings were deposited on superpolished fused silica substrates. The thickness of these coatings ranged from 1/2 to 3/4 wave at 1.06 microns. The Ta_2O_5 thin film coating was fabricated using ion beam sputter deposition. Electron beam deposition in an ultrahigh vacuum (UHV) chamber was used to fabricate the ZrO_2 film under study. The Y_2O_3 , HfO_2 and ThO_2 films were fabricated using conventional electron beam technology.

The ability to couple light into a film and propagate that light over an observable distance depends on a number of factors. The coupling process itself relies on total internal reflection inside the prism with evanescent wave propagation into the waveguide.⁴ In practice, it is difficult to achieve coupling efficiencies as high as the 90% levels predicted by theory. Propagation losses in the waveguide depend on the roughness of the substrate-film and air-film interfaces and the film microstructure. The type of substrate, surface quality of the substrate, temperature and other deposition parameters, in addition to the thermodynamic properties of the coating material itself, all serve to determine the film microstructure. Amorphous films such as those produced by ion sputter deposition typically exhibit the lowest scattering losses and usually make the best waveguides. Thus the films which are the most difficult to study using other analysis techniques are best suited for waveguide studies.

It was observed in the course of this study that film propagation losses were strongly dependent on wavelength as well. Waveguide propagation losses at 514 nm were much higher than at 647 nm. Even though Raman scattering efficiencies decrease as λ^{-4} at longer wavelengths and available laser power was reduced to 30 % of that available at 514 nm, comparable or better spectra could be obtained in some cases using 647 nm light due to reduced propagation losses.

3. Results and Discussion

Initial attempts to use Raman scattering to study thin film structure were not very encouraging. A spectrum obtained on an amorphous Ta_2O_5 coating using glancing incidence illumination appears in figure 3. The spectrum is completely dominated by the Raman signature of the fused silica substrate. After subtraction of the silica bands the remaining spectrum is essentially featureless.

The concept of using guided waves to study thin films had originated much earlier.^{5,6} However, the technique had not been applied to the study of optical thin film coatings. As in earlier work in integrated optics, a rutile (TiO_2) prism was initially used to couple 514 nm light into the same amorphous Ta_2O_5 coating. The spectrum obtained appears in figure 4a. The rutile prism produced its own Raman bands superimposed on those of the Ta_2O_5 . The rutile bands were subtracted out to produce the difference spectrum in figure 4b which resembles the reference standard powder spectrum in figure 4d.

A diamond prism was found to be preferable to the rutile prism as the coupling element. Diamond has a high refractive index (2.41 at 656 nm) for efficient coupling and no Raman bands below 1300 cm^{-1} . The spectrum of diamond has been compared to that of rutile in figure 5. The diamond prism allowed the collection of spectra without the need for digital subtraction of an interfering background spectrum. As demonstrated in figure 4c, the Ta_2O_5 film spectrum obtained with a diamond coupling prism has more clearly defined features and lower noise levels. Peaks in the film spectrum are either missing or broadened compared to the powder spectrum. These are typical differences observed when comparing spectra of crystalline and glassy forms of the same material.

A spectrum obtained on a ZrO_2 film guiding 647 nm light appears in figure 6. This film propagated 647 nm light considerably better than 514 nm light. Weak, but distinct Raman bands due to ZrO_2 in the thin film are shown to correlate with the Raman bands present in both monoclinic and tetragonal zirconia. Thus, both monoclinic and tetragonal local symmetries are found to be present in the film. These observations are confirmed by the x-ray diffraction data plotted in figure 7. The x-ray diffraction data seems to indicate that the film structure is primarily tetragonal with peaks correlating to the 111, 200, and 220 orientations. Secondary maxima appear correlating to the 111 and $\bar{1}\bar{1}\bar{1}$ orientations of the monoclinic structure. Although the Raman

bands of the two forms of ZrO_2 are approximately equal in intensity in Figure 6, the relative concentration of the monoclinic form is much less than that of the tetragonal form. The Raman bands of the two forms have similar intensities because the scattering cross sections of the major monoclinic bands are nearly ten times the scattering cross sections of the major tetragonal bands. Thus, the Raman data also indicates that the film is primarily composed of the tetragonal form of ZrO_2 .

Two of the lowest loss waveguides were films of Y_2O_3 and ThO_2 . The Y_2O_3 spectrum appears in figure 8 with the principal band at 378 cm^{-1} clearly evident. However, this band rests on a broad background with a drop-off at 500 cm^{-1} corresponding to the silica substrate spectrum. This is the only spectra we have recorded using the guided wave technique which clearly shows the influence of the substrate. We believe this results from propagation in a higher order waveguide mode, which couples more strongly to the substrate than a lower order mode. The 378 cm^{-1} band obtained from the film matches, within experimental error, the most intense Raman band obtained from cubic Y_2O_3 reference material.

In figure 9, the spectrum obtained on a ThO_2 film is compared with a reference spectrum of cubic ThO_2 . Clearly, the film spectrum does not resemble that of cubic ThO_2 - the only stable form known for ThO_2 . The thin film ThO_2 spectrum in figure 9 and the monoclinic ZrO_2 spectrum in figure 6 have similar patterns, although the bands are shifted in frequency. This correspondence in spectra suggests that there is also a correspondence in structure between monoclinic ZrO_2 and the ThO_2 in the film.

Hafnia (HfO_2), in bulk and in thin film form, was determined to be a weak Raman scatterer. In figure 10, the thin film spectrum is reminiscent of that observed on ZrO_2 in terms of peak intensities. Both the HfO_2 and ZrO_2 films were relatively low loss waveguides, but neither yielded strong Raman bands. The HfO_2 reference spectrum peaks do match up well with those observed in the thin film spectrum. However, the thin film peaks rest on a broad feature extending out beyond 1000 cm^{-1} which is believed to be due to fluorescence (source unknown).

4. Conclusion

We have demonstrated that Raman analysis of thin film coatings using guided waves can result in significant improvements in sensitivity. Through the use of a diamond prism to couple light into the film, spectra have been obtained which originate solely from the film material. From the Raman spectra, it is possible to determine the local structure associated with the material in the film. Thin film coatings which are amorphous, as determined by x-ray analysis, typically serve as excellent waveguides and thus are ideally suited for study using this technique.

5. References

- [1] Pawlewicz, W.T.; Exarhos, G.J.; Conaway, W.E.; Appl Opt 22, 1837 (1983).
- [2] Hsu, Long-Sheng; She, Chiao-Yao; Exarhos, Gregory J.; Appl Opt 23, 3049 (1984).
- [3] Rujkorakarn, R.; Hsu, L.S.; She, C.Y.; Nat Bur Stand (U.S.) Spec Publ # , pp (1984). Proceedings of the Symposium on Optical Materials for High Power Laser. (To be published).
- [4] Sarid, Dror; Appl. Opt. 18, 2921 (1979).
- [5] Swalen, J.D.; Rabolt, J.F.; Schlotter, N.E.; Knoll, W.; Girlando, A.; Philpott, M.R.; Proc Soc Phot Opt Inst Eng 362, 31 (1982).
- [6] Hetherington III, W.M.; Van Wyck, N.E.; Koenig, E.W.; Stegeman, G.I.; Fortenberry, R.M.; Opt Lett 9, 88 (1984).
- [7] Tallant, D.R., unpublished data

GUIDED WAVE RAMAN EXPERIMENT

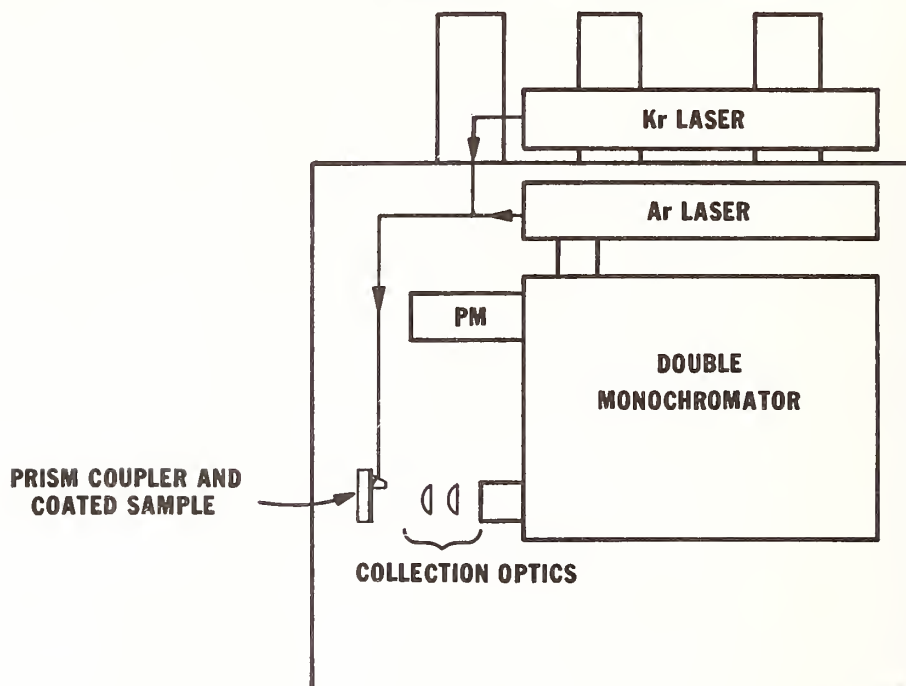


Fig. 1 Experimental arrangement

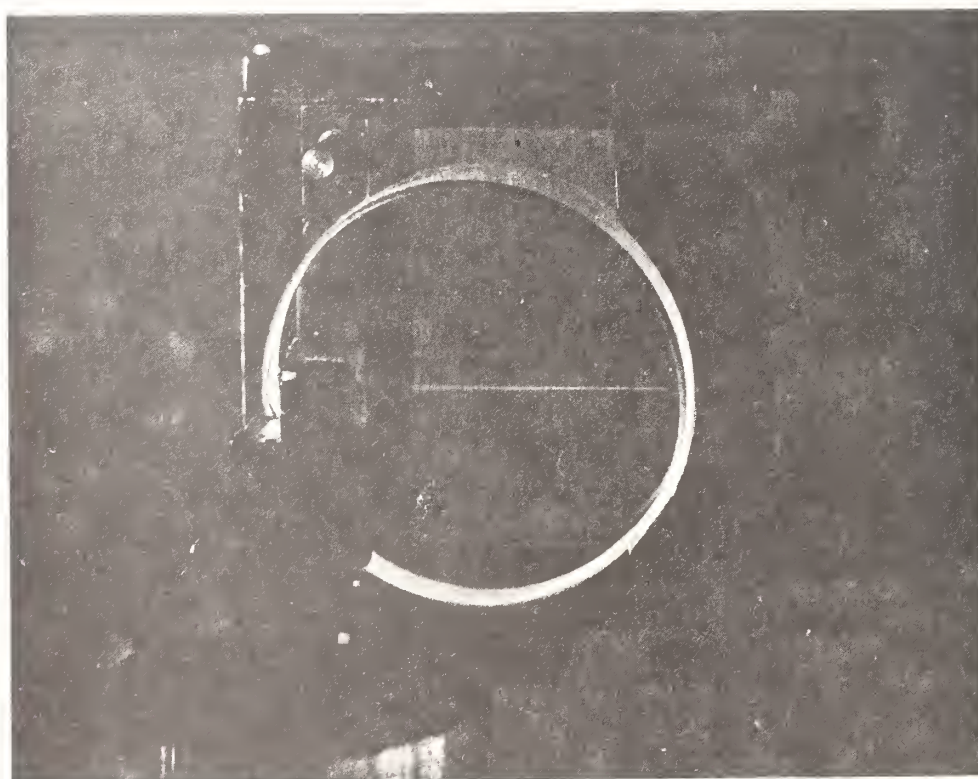


Fig. 2 633 nm light propagation through a Y_2O_3 thin film coating waveguide

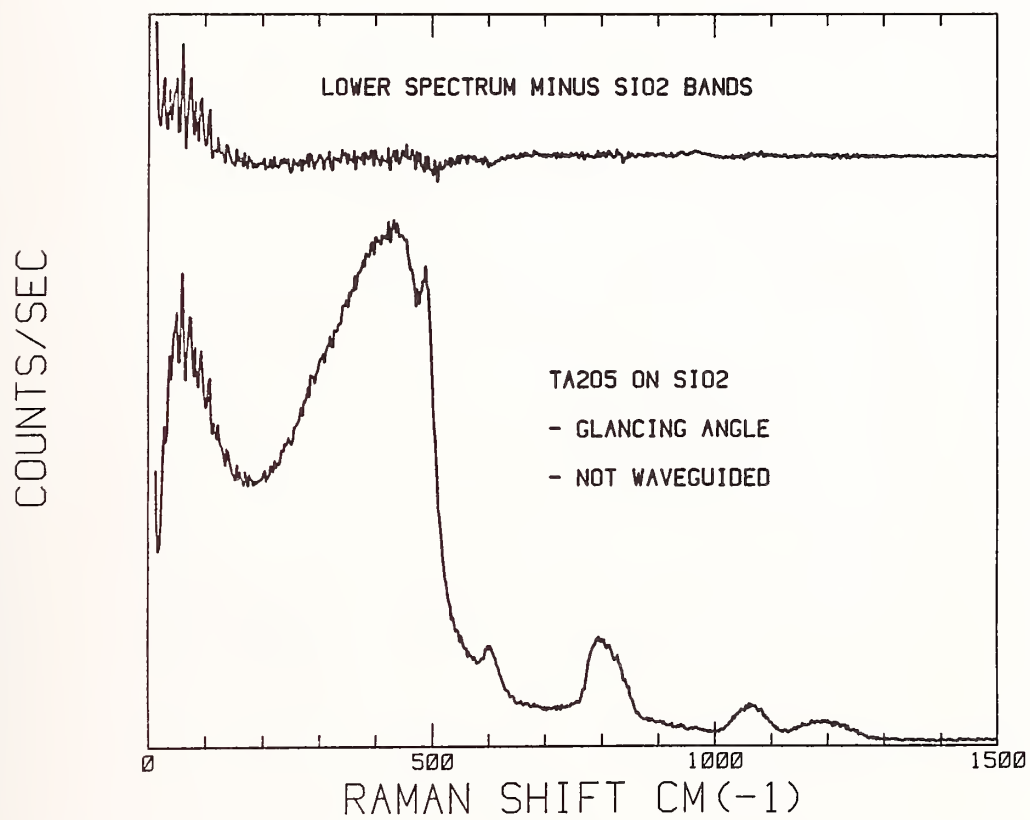


Fig. 3 Raman spectra obtained on an amorphous Ta₂O₅ coating using the glancing incidence technique

GUIDED WAVE SPECTRA OF AMORPHOUS Ta_2O_5 COATING

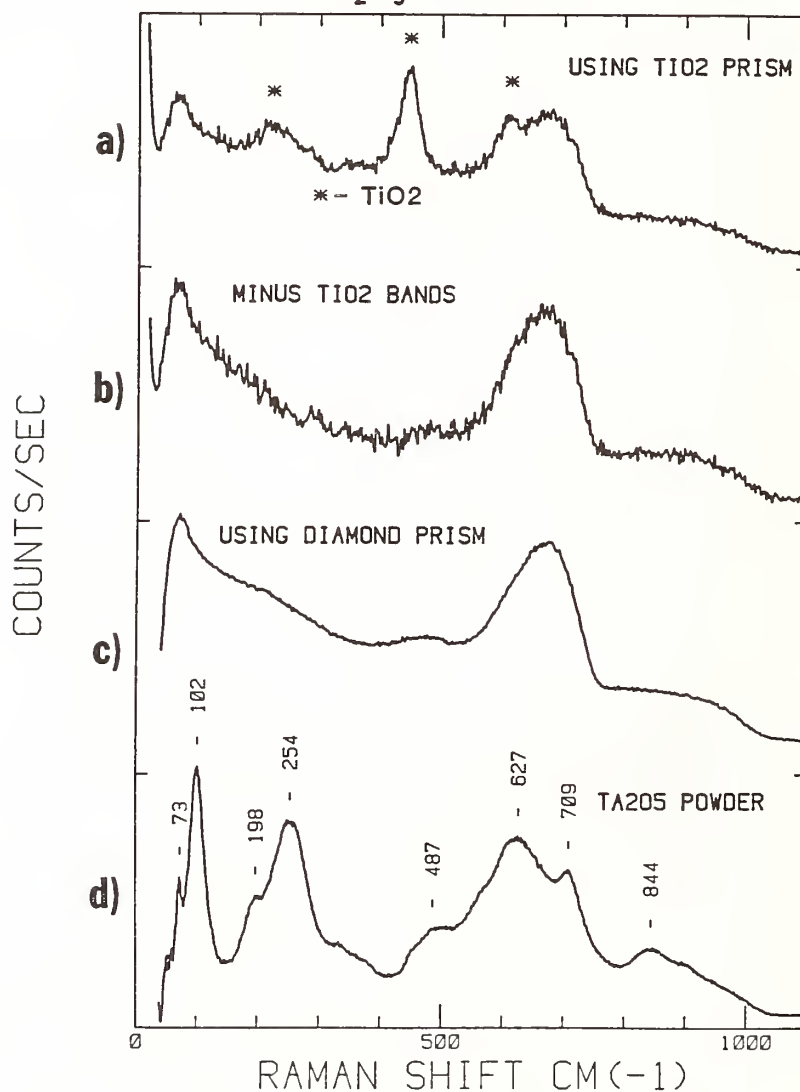


Fig. 4 Raman spectra obtained on an amorphous Ta_2O_5 coating using the guided wave technique: a) Spectrum obtained using a rutile prism for coupling, showing both rutile and Ta_2O_5 bands; b) Difference spectrum obtained after subtraction of rutile bands; c) Spectrum obtained using a diamond prism for coupling; d) Reference spectrum of Ta_2O_5 powder

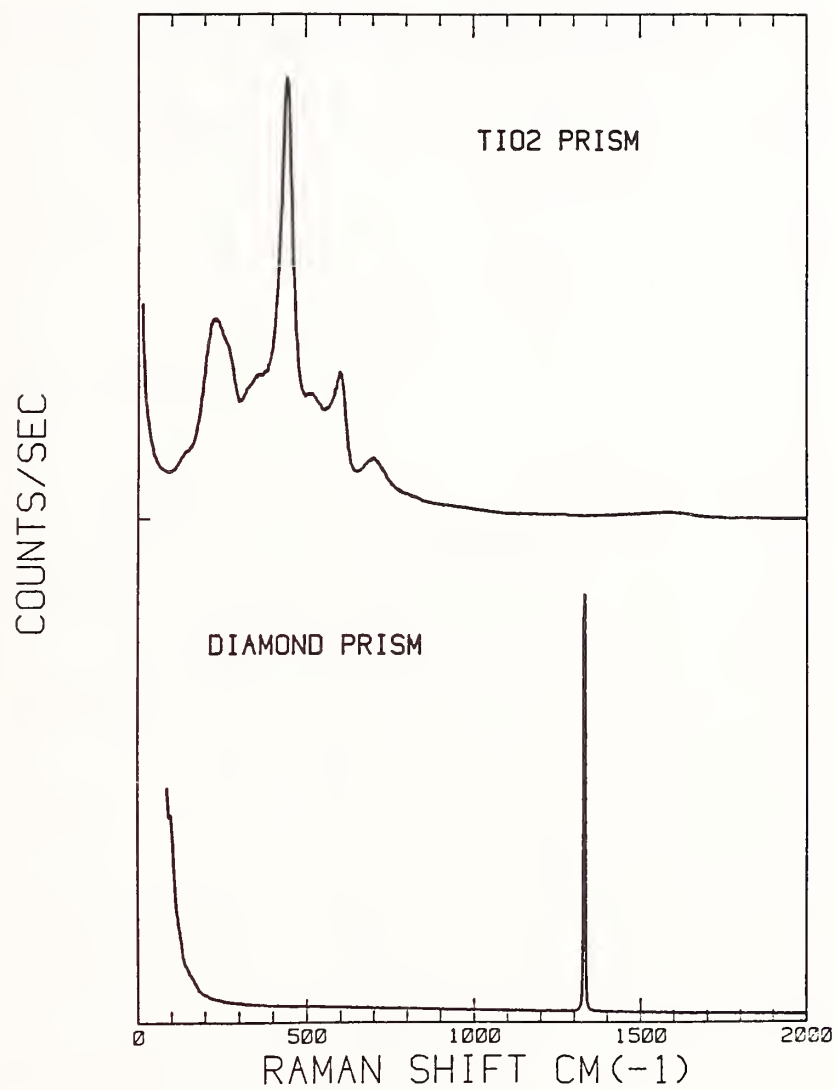


Fig. 5 Raman spectra of diamond and rutile

GUIDED WAVE SPECTRA OF ZrO_2 COATING

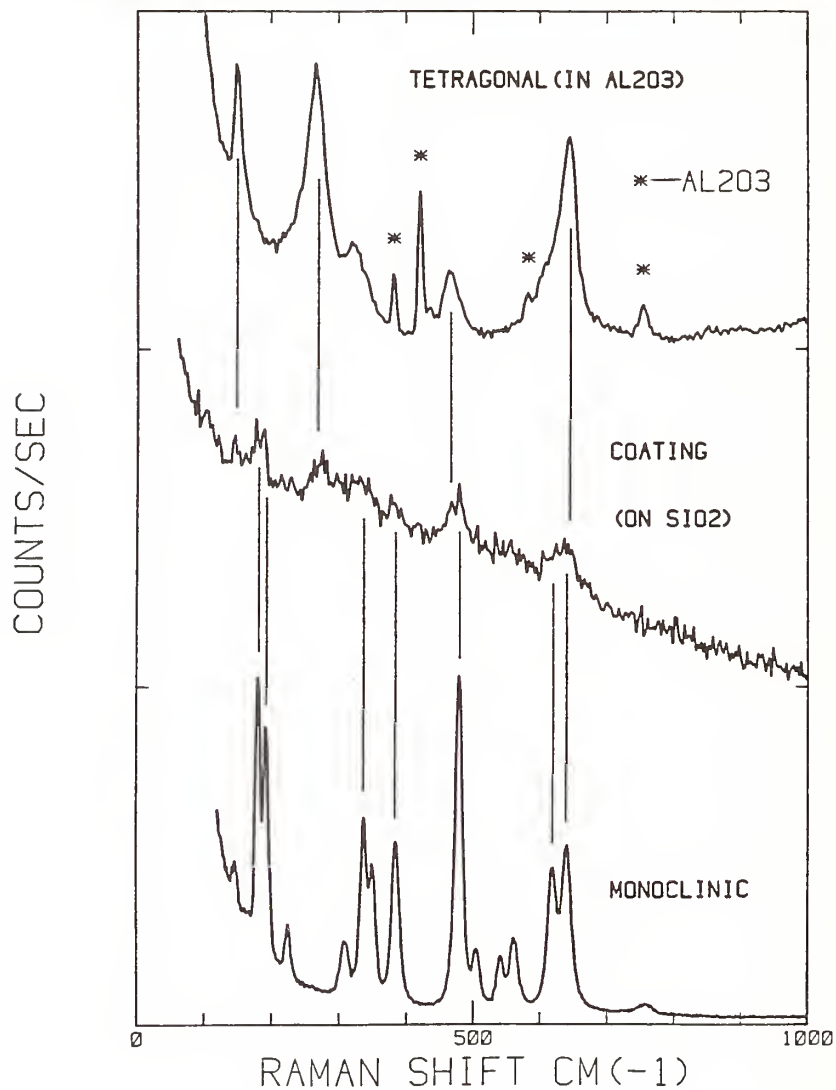


Fig. 6 Spectrum obtained from a ZrO_2 thin film coating showing correlation to monoclinic and tetragonal phases

X-RAY DIFFRACTOMETER DATA **ZrO₂ COATING**

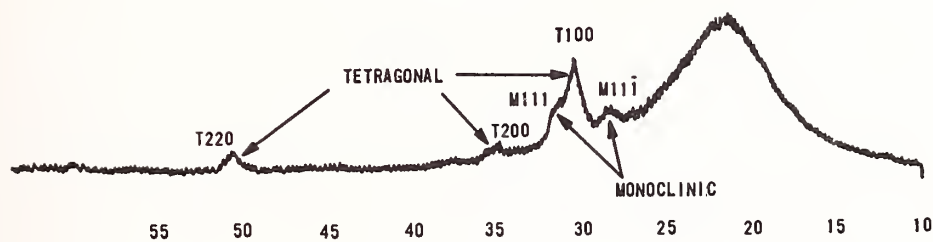


Fig. 7 X-ray diffraction data obtained on ZrO₂ coating.

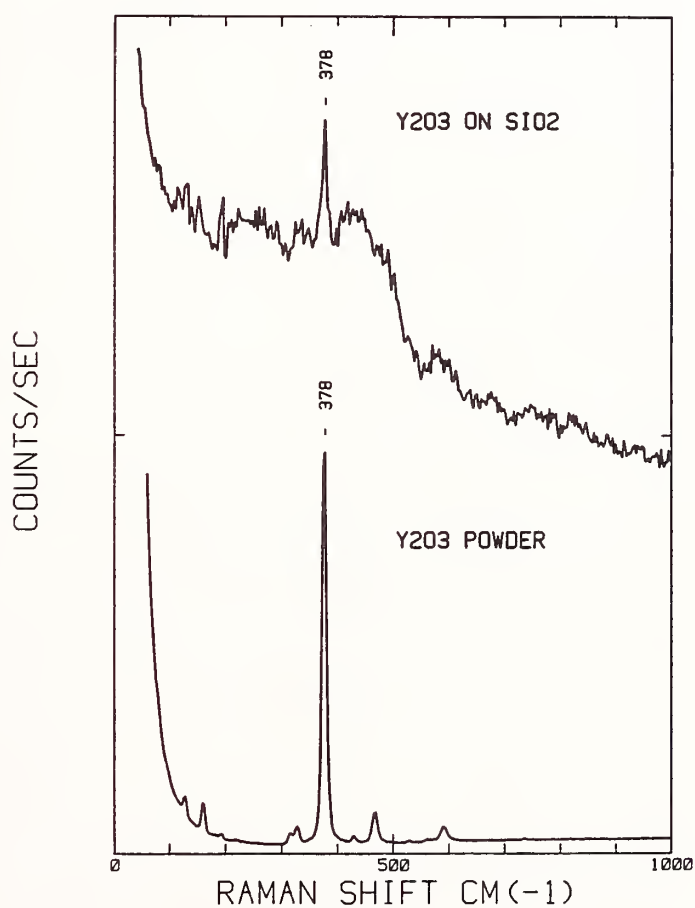


Fig. 8 Raman spectra of a Y₂O₃ thin-film coating and of Y₂O₃ powder

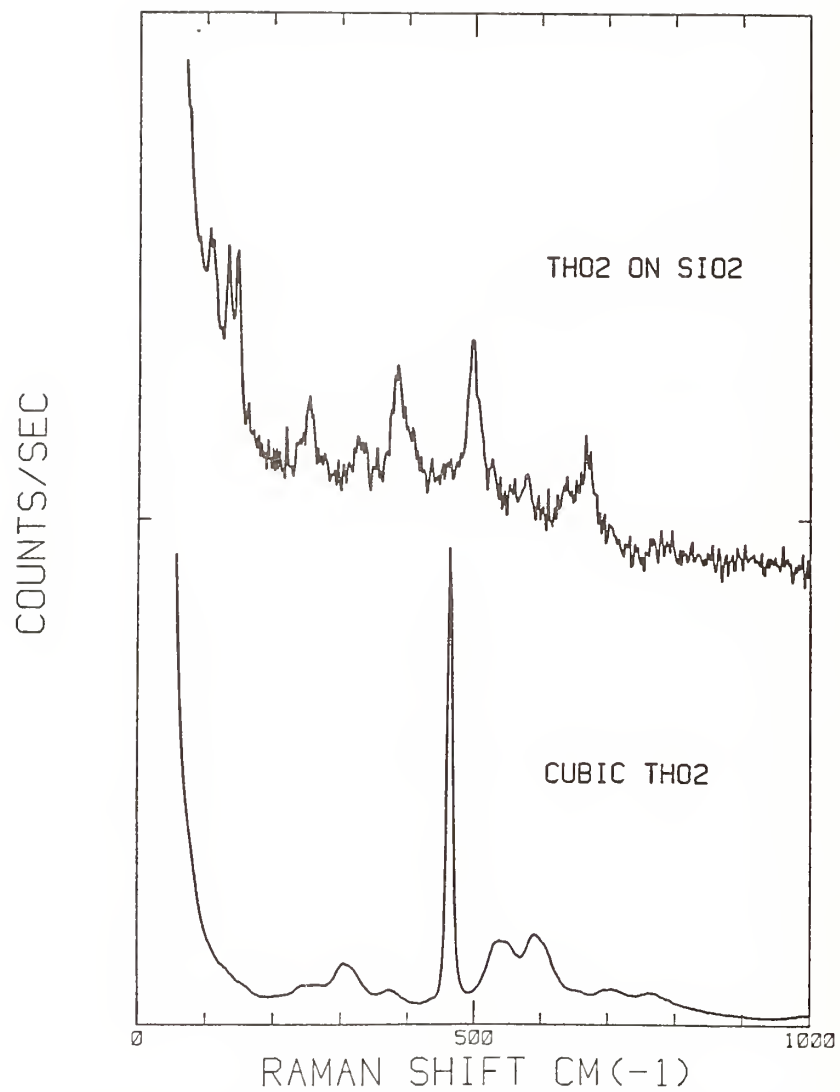


Fig. 9 Raman spectra of a ThO_2 thin-film coating and of cubic ThO_2

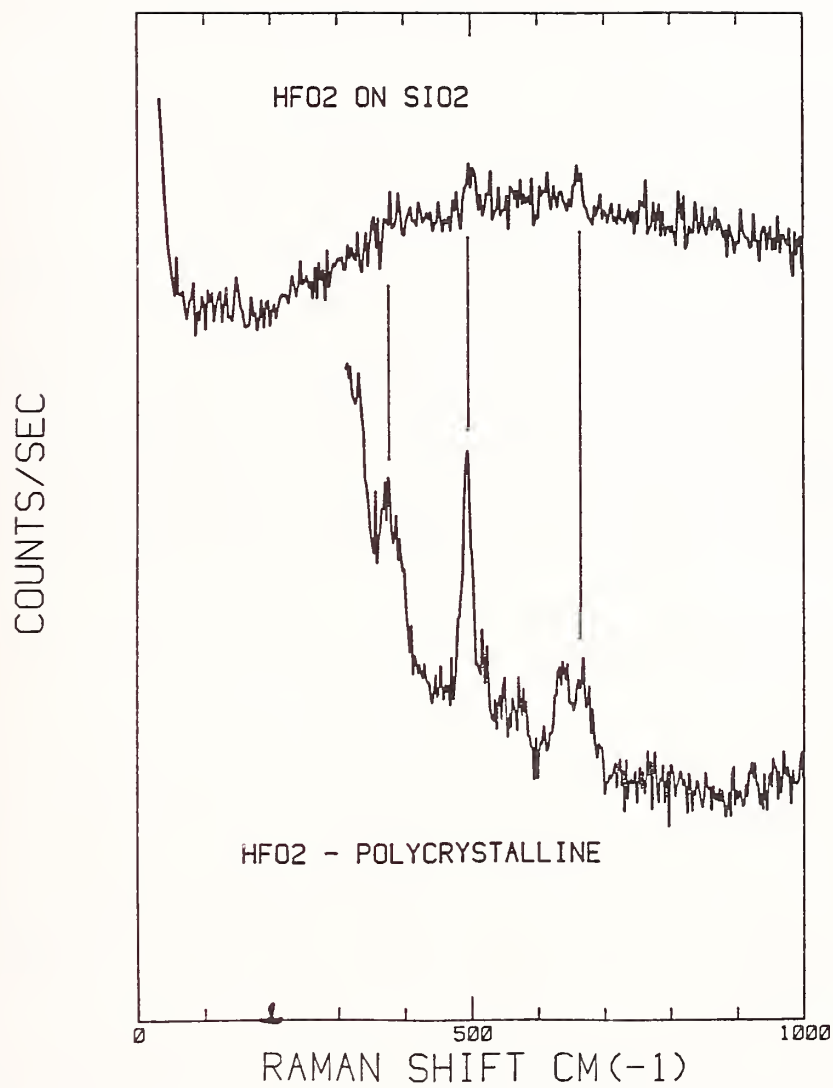


Fig. 10 Raman spectra of a HfO_2 thin-film coating and of polycrystalline HfO_2

Raman Microprobe of Laser-Induced Surface Damage Regions in TiO₂ and ZrO₂ Coatings

Donald M. Friedrich and Gregory J. Exarhos

Pacific Northwest Laboratory*
Richland, Washington 99352

The anatase-to-rutile phase transition, which attends pulsed laser-induced damage of anatase TiO₂ thin films, is studied by simultaneous microphotography and Raman microprobe. The damage is distributed across the damage area in regions of distinct morphology and spectra. In multilayer coatings, a mechanical surface-fracture zone surrounds a set of thin, layered flat rings of distinct but irregular boundaries. These rings surround a rough, pitted transparent central crater in the quartz substrate. Raman difference spectroscopy is used to reveal damage regions containing the rutile phase and regions devoid of TiO₂. Similarly, Raman microprobe spectra reveal the monoclinic crystalline form of ZrO₂ in damaged regions of amorphous ZrO₂ coatings. Finally, frequency shifts of the anatase ν_6 line (nominally 143 cm⁻¹) are used to identify stress in laser-pulse irradiated anatase coatings.

Key words: laser damage; microprobe; Raman spectroscopy; TiO₂ optical coatings; ZrO₂ optical coatings

1. Introduction

Previous time-resolved Raman studies have shown time-dependent reversible and irreversible structural changes in pulse-laser irradiated TiO₂ and ZrO₂ dielectric optical coatings.[1] In single and multilayer anatase TiO₂ coatings, sufficiently intense pulsed laser irradiation at 532 nm led to observation of a partial loss of intensity from anatase Raman lines and concurrent production of an irreversible phase transition from the anatase to the rutile crystalline forms seen in the Raman spectrum. Similarly, Raman spectra from amorphous ZrO₂ coatings revealed phase changes from amorphous to monoclinic crystalline form in the irradiated region of the coating. These measurements and observations are described in references [1] and [2].

In order to investigate in greater detail the nature and distribution of pulsed laser-induced morphological changes in these dielectric optical coatings, we have explored the damage regions with a Raman microprobe. Damage regions range in size from several microns to nearly a millimeter in diameter, depending upon the laser energy, and they vary widely in shape and depth. The Raman microprobe can collect spectra from coating surface areas down to a few microns diameter. The damage topology then can be correlated with observed Raman spectra, which can reveal changes in the morphology of the coating materials. The microprobe also reveals stress conditions of the anatase crystalline form. The stress is observed through frequency changes in the sharp 143 cm⁻¹ (ν_6 (Eg)) line of anatase.

*Pacific Northwest Laboratory is operated by Battelle Memorial Institute for the U. S. Department of Energy under contract DE-AC06-76RLO 1830.

2. Experimental

The damage areas studied were previously induced in the TiO_2 and ZrO_2 dielectric coatings as described in [1]. Briefly, the coatings were prepared by reactive sputtering of Ti or Zr in an Ar/O_2 atmosphere on fused silica substrates [3,4]. These coatings were irradiated with a range of 532 nm pulse energies (0 - 10 mJ) and focused to spot sizes 1 mm or less. The equilibrium and time-resolved Raman measurements from these samples were reported in reference [1]. Selected damage regions from these same samples were studied in detail by the Raman microprobe technique.

The Raman microprobe apparatus consists of a Spex Micramate attached to a Spex 1403 double monochromator with the Datamate photon-counting system. The laser excitation was focused on the sample by a 40X (.60 NA) objective, which also collected the back-scattered Raman light for imaging on the entrance slit of the monochromator. The images, in reflected or transmitted white light, were also relayed to a video camera. The sample damage regions were photographed from the video screen. Good spectral resolution of the sharp 143 cm^{-1} anatase line was achieved with spectral bandpass of 4 cm^{-1} (400μ slits). Spectral line shifts of 0.5 cm^{-1} could be observed reproducibly. Spectral line shifts were further studied at higher resolution (0.5 cm^{-1} bandpass) and confirmed the lower resolution findings.

CW Ar^+ laser lines of 514.5 nm and 488.0 nm were used in these studies with power levels up to 220 mW into the Micramate optics. With regard to effective spatial resolution of surface features, it should be noted that, for a given signal-to-noise ratio, the surface area resolved will increase with increasing laser-probe power. Usable Raman signals could be obtained from the damage regions with powers as low as 30 mW into the Micramate. Less than 40% of the input power finally reaches the sample surface. The high cw-laser powers never damaged the refractory surface of an undamaged coating region. However, the cw probe-laser did occasionally induce damage to darker damage features or coating cracks at probe powers in excess of 100 mW into the Micramate optics. These observations will be described below.

3. Damage Topology and Raman Spectra

Damage spots produced by the higher energy pulses revealed layered topological features in the thin ($<1\mu$) single-layer and multilayer coatings. In the thicker anatase coating, the damage features were qualitatively different and did not show distinct boundaries. Representative damage features in the thin and thick coatings are shown in the photomicrographs (figures 1,3,6) and are now discussed.

3.1. Thick (4μ) Anatase Coating (Sample No. 111J)

A thick, diffuse reflecting anatase coating was studied in order to provide a reference damage behavior most like bulk TiO_2 anatase. In the undamaged state, this coating consisted of a close-packed array of irregular islands of anatase separated by thin cracks. The pattern resembled the cracking pattern appearing in drying mud-flats. The cracks appear to be less than 1μ wide. The anatase islands varied in size, between 10 and 20 microns across, and were designated as "mud-cakes" (figure 1a). The Raman spectrum from these was identical to that of pure TiO_2 powder. In the center of most damage craters, a similar more finely-grained cracking pattern was observed (figure 1b) with mud-cake islands ranging 5 to 10μ across. The Raman spectrum from each of these smaller cakes in the damage center showed no shifting and no evidence for rutile bands, i.e., the spectrum from the damage region was also identical to TiO_2 powder. Surrounding the center damage region is a rippled region resembling sand dunes; and surrounding the dunes region is an irregular topology which appears to consist of melted splashes of coating material (the "melt region", figure 1c). Neither of these regions revealed rutile features in the Raman spectra.

The cw Ar^+ laser caused damage to the coating when the probe laser spot was positioned in one of the cracks, either inside or outside the pulsed laser-induced damage region, and the cw laser power exceeded 100 mW. The coating developed a single black spot (neither reflecting nor transmitting light in the microscope); and concurrently, the anatase was converted to rutile as indicated by loss of anatase lines and strong increase in rutile lines in the Raman spectrum (figure 2). This cw-induced damage is probably thermal in origin and indicates the necessity to use lower cw powers when probing the damage regions even in refractory materials.

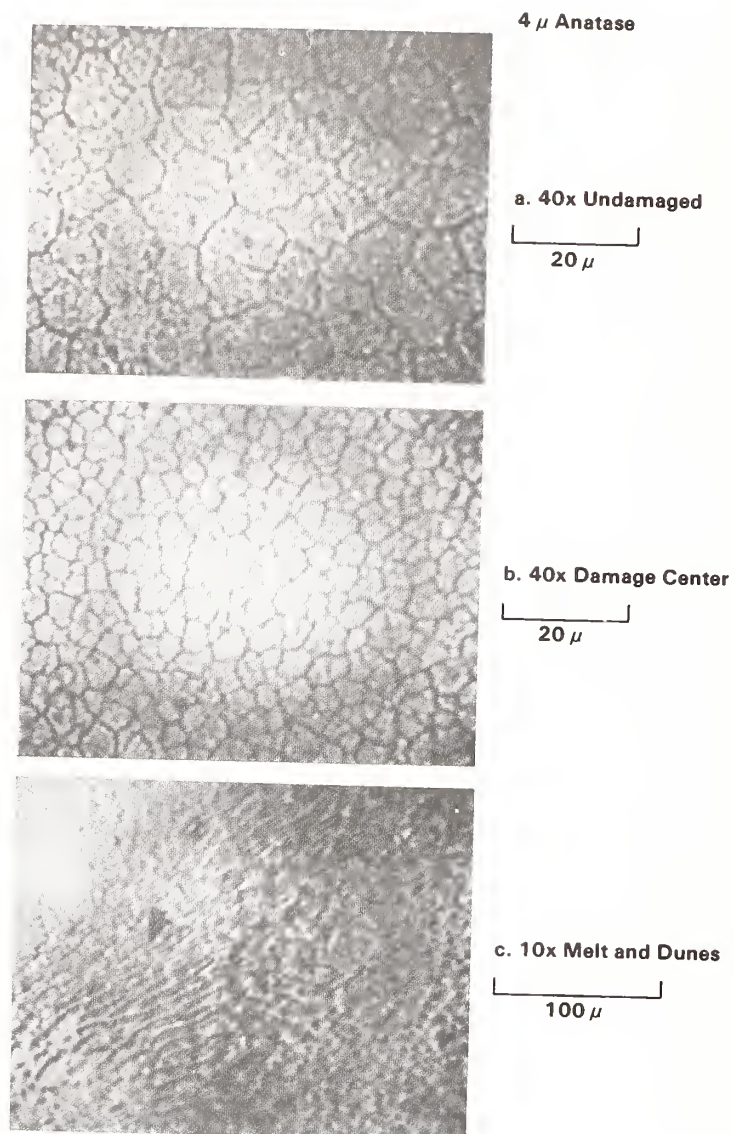


Figure 1. Photomicrographs of a 4 μ -thick anatase sample (#111J).
 (a) Undamaged 4 μ -thick anatase layer showing the larger "mud-cake" topology;
 (b) Center of a large (ca. 1 mm diameter) damage spot showing smaller "mud-cake" forms;
 (c) Transition from melt region to dunes region to central crater in damaged 4 μ -thick anatase (10X).

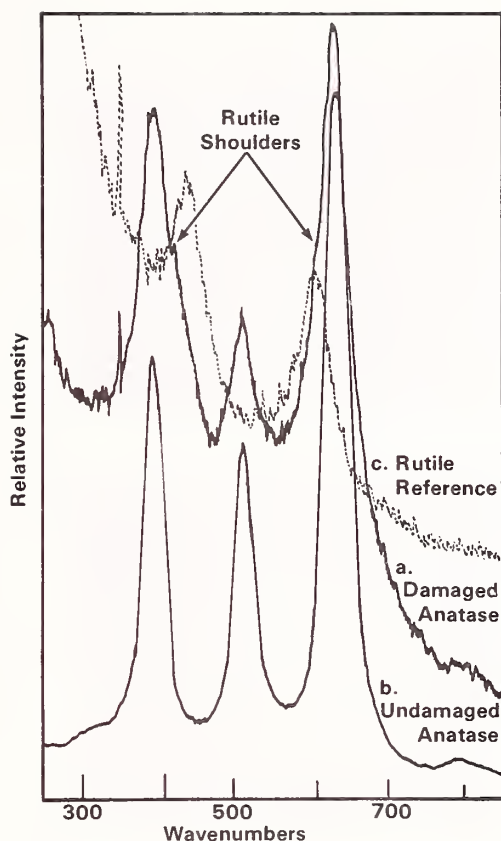


Figure 2. Raman spectrum of cw-laser-induced thermal damage to the 4μ -thick anatase coating (#111J). The 488 nm laser was positioned at a crack between undamaged anatase cakes (see figure 1a). The laser power was 220 mW into the Micramate optics. Rutile shoulders appear at 422 cm^{-1} and 595 cm^{-1} . The anatase ν_6 line (not shown) appears at 148 cm^{-1} . (b) Reference spectrum from undamaged anatase coating. (c) Reference spectrum from undamaged rutile coating.

3.2. Thin and Multilayer Anatase Coatings

Two anatase mirrors were investigated: a single thin layer (0.96μ , sample #111F) and a 17-layer $\text{SiO}_2/\text{TiO}_2$ three-cavity transmission filter for 514.5 nm (sample #115C). The multilayer coating showed remarkably regular damage topology (figure 3). The damage areas consisted of a central dark spot, often rough in texture, frequently with one or more flat, greenish-colored islands in the dark crater. Raman spectra from central damage regions generally showed only two broad, weak bands from amorphous SiO_2 and no TiO_2 spectral features. The dark crater is surrounded by a series of layered shelves, which show little or no TiO_2 content. The shelves tend to be narrow (5 to 20μ wide). The shelf region is surrounded by a severely pockmarked coating surface, which is then surrounded by a region of surface fracturing. The surface fracturing is remarkable in forming an intricate array of angular geometric patterns of high aspect ratio resembling a map of streets and boulevards. The extent of the fracture region varies, but it seems to increase with increasing pulse energy and crater size. The microprobe spectra from selected microscopic areas within these regions show that the anatase is partially or completely depleted and that the anatase ν_6 is often shifted one or two wavenumbers to higher frequency. Evidence for rutile concentrated in microscopic areas of the multilayer coating was below the signal/noise limit of these experiments.

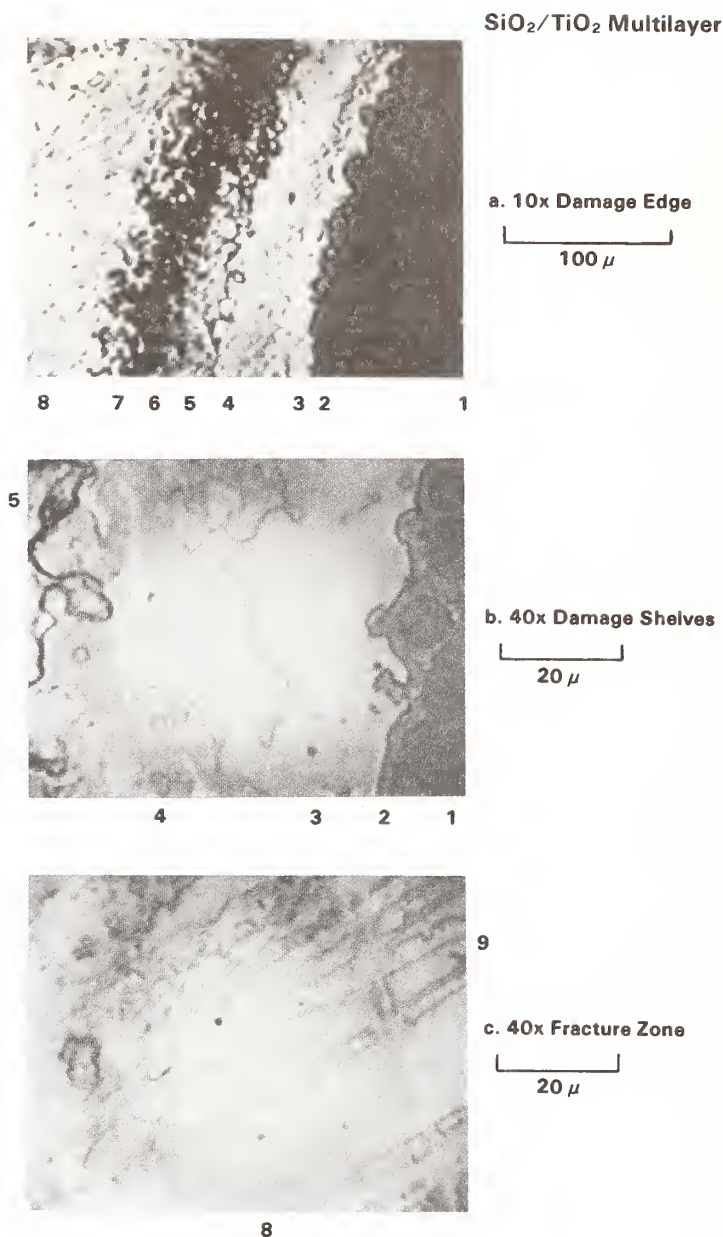


Figure 3. (a) Damage topology in the SiO₂/TiO₂ anatase multilayer (#115C; 10X objective, 0.22 NA). The damage crater is the dark region on the right (1). A series of irregular but distinctly bounded shelves surround the darkened damage crater (2 through 5). These regions are depleted in TiO₂. The transition to the undamaged coating is made through a deeply pitted ring (regions 6-7) and a broad zone of surface fractures (8).

(b) Shelf regions (1-5) shown at higher magnification (40X objective, 0.60 NA).

(c) Surface fracture zone (8) at higher magnification (40X) showing the angular narrow street-like fracturing of the mirror surface.

The thin-layer anatase mirror (#111F) did not show the regular damage topology observed in the multilayer coating. There was no sharp transition from damaged to undamaged regions. The damage craters had a rough and dark surface of irregular shape and no sharp boundaries. At sufficiently low pulse energies, the coating did not form craters but simply darkened by forming a dense array of dark microcraters ($<1\mu$ dia.). As in the multilayer microprobe studies, the rutile Raman lines from microscopic probe areas from the single coating were extremely weak--being at the signal/noise limit.

The anatase-to-rutile conversion following laser-induced damage of coating #111F was recorded earlier [1] by using a cw-probe laser spot, which integrated a much larger surface area (50μ to 100μ probe diameter at focus). Since strong rutile lines are absent from the microprobe spectra, the observed rutile may be distributed at low concentrations over a wide area of the damage region. The microprobe results show that the dominant mechanical damage effect is ablation of TiO_2 from the surface.

3.3. Amorphous ZrO_2

This sample (1.18μ thick, sample #1) shows a featureless Raman spectrum from the undamaged coating. All damaged regions show either the growth of Raman lines from the recrystallized monoclinic form of ZrO_2 (figure 4) or else amorphous fused SiO_2 bands (in strongly damaged craters). These findings are consistent with the spatially unresolved studies in [1]. The ZrO_2 damage topology is similar to that of the anatase mirrors. The crater is surrounded by regions of surface fracture and pockmarks.

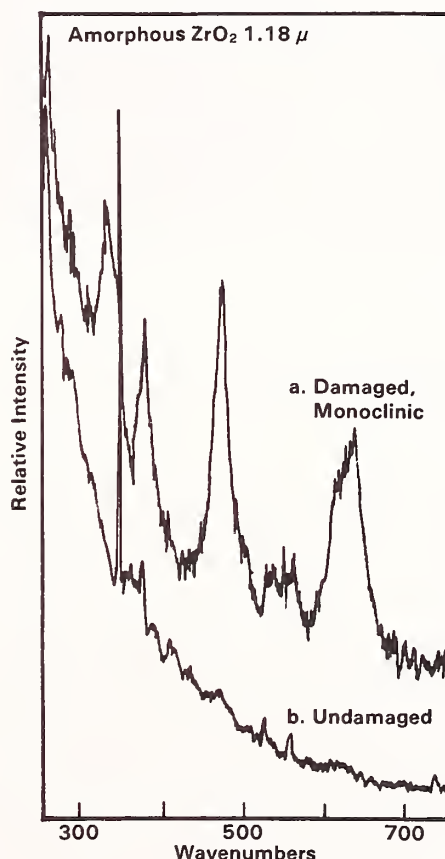


Figure 4. Raman spectrum of amorphous ZrO_2 (1.18μ , sample #1) showing lines from (a) monoclinic crystalline form produced in the damage region; (b) undamaged amorphous coating.

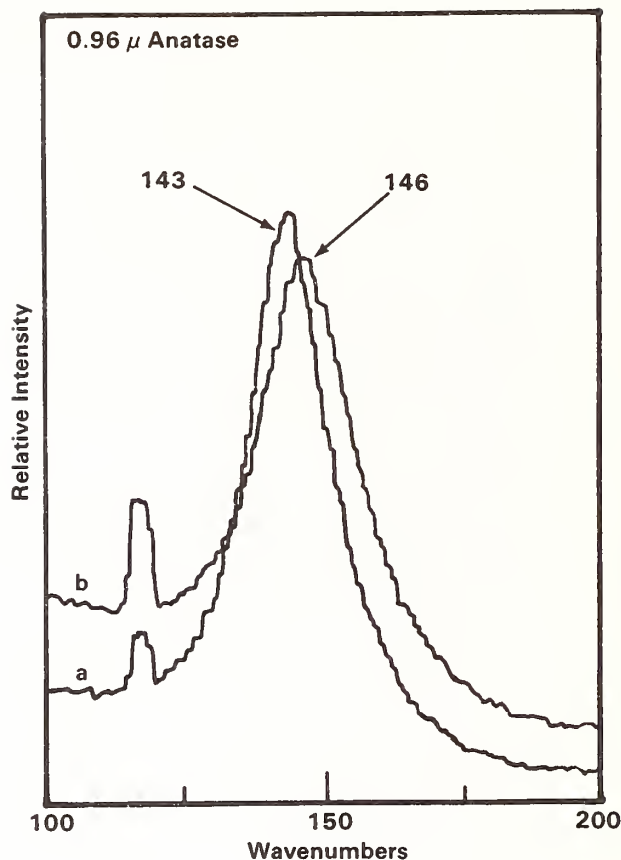


Figure 5. Expanded trace of the ν_6 line in anatase showing (a) unstressed form (143 cm^{-1}) and (b) stressed form (146 cm^{-1})

4. Laser-Induced Stress in Anatase Coatings

It is well-known that the process of coating a substrate can result in stressed coating and substrate. The stress is often estimated by measurement of thin substrate distortion. In a recent study Fauchet, Campbell, and Adar [5] report laser-induced relaxation of stress in thin silicon films on quartz substrates. By contrast, observation of the 143 cm^{-1} line of anatase coatings suggests that high-energy laser pulses induce a compressional stress in dielectric coatings. Ohsaka, et al., [6] report a specific spectral shift of $0.312 \text{ cm}^{-1} \text{ kbar}^{-1}$ for the 143 cm^{-1} ν_6 line of bulk anatase [5]. We always observe an increase in this vibrational frequency in the vicinity of damage in an anatase coating (figure 5). The stress-induced spectral shift is not uniformly or smoothly distributed. In figure 6 the anatase multilayer coating (sample #115C) surrounding a single-shot damage crater reveals two responses to the laser-pulse. On the right-hand side of the crater, the coating has cracked into islands of apparently higher reflectivity. The anatase in these islands shows no compressional stress ($\nu_6 = 143 \text{ cm}^{-1}$). Around the remainder of the periphery, the undamaged coating shows no cracks. Instead, irregular fingers of lower reflectivity fan out into the coating for about 160μ . Figure 7 is a graph of the ν_6 frequency versus distance from the edge of the damage crater along one of these darker fingers. Far from the edge, the anatase is unstressed ($\nu_6 = 143 \text{ cm}^{-1}$). As the edge is approached, the stress suddenly increases about 100μ away from the edge. At the crater edge, the frequency shift is highest ($146\text{--}147 \text{ cm}^{-1}$). This shift corresponds to a bulk compressional stress increase of about 10 kbar. The largest such stress-induced frequency shift was observed inside a small damage crater created by an intense cw-probe laser (514.5 nm) in this coating. The observed ν_6 of 149 cm^{-1} results in a computed bulk compressional stress of 19 kbar.

SiO₂/TiO₂ Multilayer

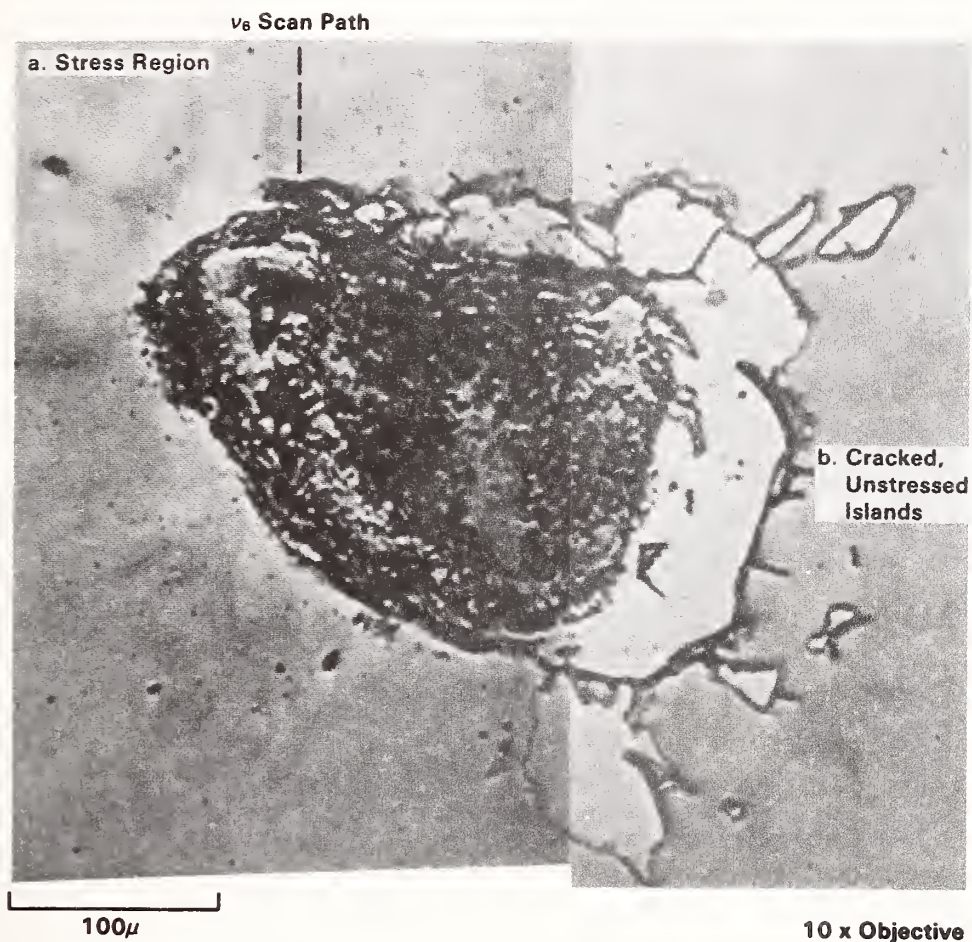


Figure 6. Photomicrograph of (a) stressed and uncracked and (b) unstressed but cracked anatase multilayer coating (#115C) around a damage region.

5. Conclusions

The process of material phase changes, discovered in the time-resolved Raman spectra of pulse-damaged coatings [1], is confirmed by the Raman microprobe technique. The morphology changes are distributed non-uniformly over the damage region. Severe damage spots show complete ablation of TiO₂ as indicated by loss of TiO₂ features in the Raman spectra from the crater regions. The combination of macroscopic probe [1] and microprobe studies indicates that the rutile, produced by pulse damage in anatase coatings, may be distributed at low concentrations throughout the damage regions. Amorphous ZrO₂ shows conversion to the monoclinic crystalline form in the damage zones. Monoclinic damage in amorphous ZrO₂ is easier to detect because the spectrum of undamaged amorphous material is relatively featureless.

Surface fracturing in angular, geometrical patterns and deeply pitted or pocked areas are observed around the larger damage craters in the mirrors. Anatase stress, which may be a precursor to the fracturing, is measured by the frequency shift of the anatase ν_6 line. The typical compressional stress shift observed in these studies was approximately 3 cm⁻¹ or 10 kbar.

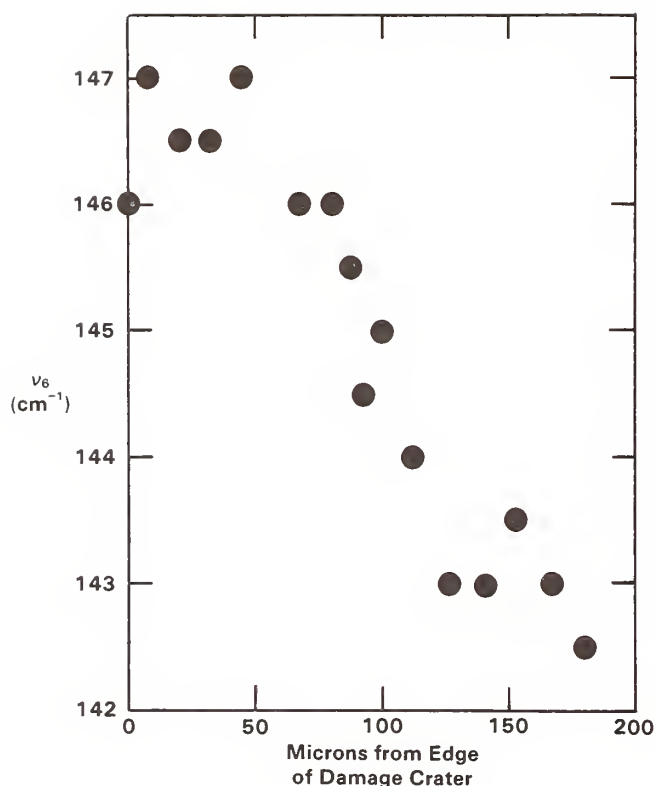


Figure 7. Raman frequency of ν_6 on a track from the edge of the damage crater out to 160 μ away from the edge, along a visible stress line in the coating.

This work was supported by the Air Force Weapons Laboratory, Kirtland, AFB, NM, under Contract PO-85-037. The optical coatings were provided by Dr. W. T. Pawlewicz. The authors also thank Mr. Clark H. Nguyen and Captain P. L. Morse for their assistance and advice during this work.

6. References

- [1] Exarhos, G.J., and Morse, P.L. Raman studies of laser-damaged single- and multi-layer optical coatings. Proceedings of SPIE Southwest Conference on Optics; 1985 March 4-8; Albuquerque, NM.
- [2] Exarhos, G.J., and Pawlewicz, W.T. Raman characterization of all-dielectric multilayer SiO₂/TiO₂ optical coating. Applied Optics 23(12):1986-1988; 1984.
- [3] Pawlewicz, W.T., Martin, P.M., Hays, D.D., and Mann, I.B. Recent developments in reactively sputtered optical thin films; Seddon, R.I., ed. Proceedings of the SPIE conference on optical thin films; 1982 January 26-27; Los Angeles, CA. Proc. Soc. Photo-Opt. Instrument. Eng. 325:105-116; 1982.
- [4] Pawlewicz, W.T., Hays, D.D., and Martin, P.M. High-band-gap oxide optical coatings for 0.25 and 1.06 micron fusion lasers. Thin Solid Films 73:169-175; 1980.
- [5] Fauchet, P.M., Campbell, I.H., and Adar, F. Long-range material relaxation after localized laser damage. Applied Physics Letters 47:479; 1985.
- [6] Ohsaka, T., Yamaoka, S., and Shimomura, O. Effect of hydrostatic pressure on the Raman spectrum of anatase (TiO₂). Solid State Communications 30:345-347; 1979.

Probing Structural Properties of Amorphous Films
With Raman Spectroscopy

C. Y. She and L. S. Hsu*

Physics Department, Colorado State University
Fort Collins, Colorado 80523

Using an oblique geometry, we have previously demonstrated that Raman spectroscopy be used to characterize submicron-thick optical films. With this technique, we have discovered and studied amorphous-crystalline and anatase-rutile transformations in various types of titania films. These studies were however done with treatment and diagnostics carried out in a sequential manner. One objective of this paper is therefore to establish the feasibility of using in-situ Raman spectroscopy to monitor the process of crystallization and structural transformation of optical thin-films in real time. A second objective is to demonstrate that Raman spectroscopy can be used to detect microscopic differences existed in amorphous thin films. We show that the microscopic differences in three otherwise similar types of amorphous titania films may be correlated with their obvious structural differences upon thermal annealing.

Key words: Raman spectroscopy; optical coatings, TiO_2 ; amorphous types; in-situ study; structural transformation.

1. Introduction

We have previously reported the use of Raman spectroscopy for characterization of micron-thick optical films [1]. Raman spectroscopy has not been used much until recently, due perhaps to an obvious fact (or misconception) that a film thinner than one optical wavelength may not scatter enough Raman signal for structure characterization. Recently, using Raman spectroscopy in a 180° backscattering geometry, Pawlewicz et al. [2] were able to characterize crystalline single-layer optical coatings with a measurement time a factor of 100 less than that required for the conventional method of x-ray diffraction, demonstrating Raman spectroscopy as a rapid method for film diagnostics. One of the major factors which limits the sensitivity of their single-layer, Raman technique is the interference resulting from the Raman signal of the substrate. This substrate interference is probably also the reason which renders a commercial Raman microprobe ineffective in characterizing a submicron film, in particular an amorphous film on a transparent substrate. We have devised techniques to improve detection sensitivity by using (1) an oblique-incident geometry to reduce laser light in the substrate and (2) a different collection system, with which the scattered light is collimated before refocussing into a spectrometer, to limit the depth of view mostly to the film of interest. For example, when the substrate interference is suppressed by more than 50-fold in this manner [3], we obtained Raman spectra of titania coating as shown in Fig. 1. The fact that the spectra of three titania films with different structures, but the same stoichiometry, are so dramatically different demonstrates the effectiveness of Raman spectroscopy for structural characterization of thin films. The spectrum of the amorphous film represents its characterization for the first time by any method. Even the time consuming method of x-ray diffraction fails to characterize an amorphous coating.

With our Raman technique, we have discovered and investigated several phase transformations in submicron titania films induced by laser [4] and thermal [5] annealing. The similarity between laser and thermal annealing processes may be seen in Fig. 2 where the spectra of TiO_2 coatings under different laser and thermal annealing conditions are compared. From the thermal annealing results, we have found that all amorphous titania films studied crystallize at around 350°C upon heating. Our Raman data suggest that the exact transformation temperature and the transformed crystalline structure depend upon fabrication method and deposition rate.

*Present Address: Control Laser Corp., 11222 Astronaut Blvd. Orlando, FL 32821

2. Microscopic Differences in Amorphous Titania

What is perhaps more significant is that the outcome of the transformed crystalline structure seems to correlate with the minute differences existed in Raman spectra of the as-deposited amorphous films. Figure 3 shows Raman spectra of three types of amorphous titania films A, B, and C. A and B were prepared by ion-beam sputtering and C by e-beam evaporation. Besides the broad low-frequency shoulder, indicative of amorphous structure, weak rutile peaks of different strengths and widths at 440 and 612 cm^{-1} can be seen in these spectra. By means of Raman spectroscopy, we have established the fact [5] that an amorphous film with weak (broad linewidth) rutile information (Type C) crystallizes at a lower temperature into the anatase structure, while a film with relatively strong (narrower linewidth) rutile formation crystallizes into microcrystalline rutile structure at a higher temperature (Type B). The intermediate Type A films result in a mixed (rutile and anatase) microcrystalline structure. We think that since the anatase structure is energetically more favorable around 350°C, the outcome of the transformation depends upon the competition between the thermodynamically favored anatase and the minute rutile seeds existing in the as-deposited film.

3. In-situ Raman Study

These initial experiments have clearly demonstrated the potential of using spontaneous Raman spectroscopy for optical and electronic film characterization and studies. These studies were done with treatment (by laser or thermal annealing) and diagnostics (with Raman scattering) carried out alternatively in a sequential manner. There is an obvious need for in-situ diagnostics in which Raman spectroscopy is recorded simultaneously as the process of crystallization and/or structural formation is taking place in the film. This way, possible changes or contamination on the film between treatment steps can be avoided; the rate of crystallization and transformation processes can also be determined.

A home-made oven with optical access was constructed to demonstrate the feasibility of in-situ Raman study. As an example, the growth of anatase in a titania film at 400°C is investigated on real-time with this oven. The spectrometer was scanned back and forth around the strongest anatase peak at 150 cm^{-1} and the peak height was monitored as a function of time. This procedure was in fact carried out for a Type C titania film coated on a Si wafer, and the resulting growth of anatase peaks was recorded in Fig. 4(a). For the setting corresponding to annealing at 400°C, anatase growth begins after 20 min. of heating. The process of anatase crystallization is approximately completed after 45 min. of heating at this temperature; its Raman intensity signifies 100% of anatase formation. After the crystallization process is completed, the whole Raman spectrum is also recorded for reference; as shown in Fig. 4(b), the film indeed consists of anatase structure without trace of rutile formation. The peak height may be converted to the percentage of anatase formation giving rise to the experimental points labeled 400°C in Fig. 5. Alternatively, real-time observation of the crystallization process may be made by setting the spectrometer at the peak of the strongest Raman mode, i.e., 150 cm^{-1} for 400°C etc., and recording the Raman intensity as a function of time. This was in fact carried out for annealing at 325°C and 600°C. A different piece of identical Type C film was used for each annealing temperature giving rise to respective anatase growth shown as solid curves in Fig. 5. The effect of annealing temperature on growth rate is also evident. In-situ Raman study of Type A titania films has been published elsewhere [6].

4. Conclusion

We have demonstrated that Raman spectroscopy is a simple and effective diagnostic tool for thin-film studies. Among other things, our Raman technique is capable of distinguishing microscopic differences in amorphous films, analyzing the effect of laser and thermal annealing, and predicting the outcome and exploring the physics of structural phase transitions. The in-situ capability demonstrated here suggests that Raman spectroscopy can be used as a real-time probe for film deposition process as well. Although only titania films are investigated in this report, the approach should be of general interest and can be applied to other thin-film materials [7].

We thank G. Al-Jumaily and J. R. McNeil of UNM, and R. Rujkorakarn and J. R. Sites of CSU for supplying the films for this study. This work was supported by the U.S. Air Force Weapon Laboratory under contract F29601-83-K0079.

5. References

- [1] R. Rujkorakarn, L. S. Hsu and C. Y. She, "Crystallization of titania films by thermal heating," Proc. 16th Annual Symposium on Optical Materials for High Power Lasers, NBS Special Publication (1985).
- [2] W. T. Pawlewicz, G. J. Exarhos and W. E. Conaway, "Structural characterization of TiO_2 optical coatings by Raman spectroscopy," Appl. Opt. 22, 1837 (1983).
- [3] L. S. Hsu, C. Y. She and G. J. Exarhos, "Reduction of substrate interference in Raman spectroscopy of submicron titania coatings," Appl. Opt. 23, 3049 (1984).
- [4] L. S. Hsu, R. Solanki, G. J. Collins and C. Y. She, "Raman study of structural transformations of titania coatings induced by laser annealing," Appl. Phys. Lett. 45, 1065 (1984).
- [5] L. S. Hsu, R. Rujkorakarn, J. R. Sites and C. Y. She, "Thermally induced crystallization of amorphous titania films," J. Appl. Phys. (accepted for publication).
- [6] L. S. Hsu and C. Y. She, "Real-time monitoring of crystallization and structural transformation of titania films with Raman spectroscopy," Opt. Lett. 10, 638 (1985).
- [7] R. Rujkorakarn and J. R. Sites, "Crystallization of zirconia films by thermal annealing," J. Vac. Sci. Technol. (to be published, May 1986).

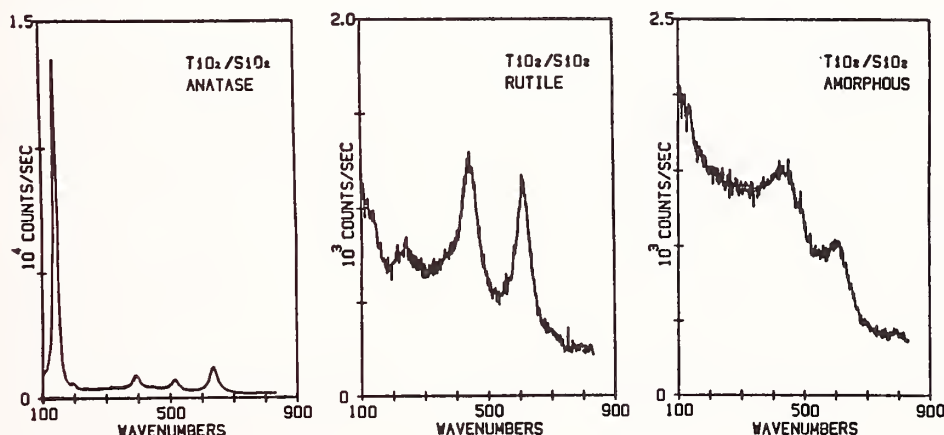


Figure 1. Raman spectra of stoichiometric TiO_2 films with different structures demonstrating the effectiveness of using Raman spectroscopy for thin film characterization. Film thickness is 500 nm.

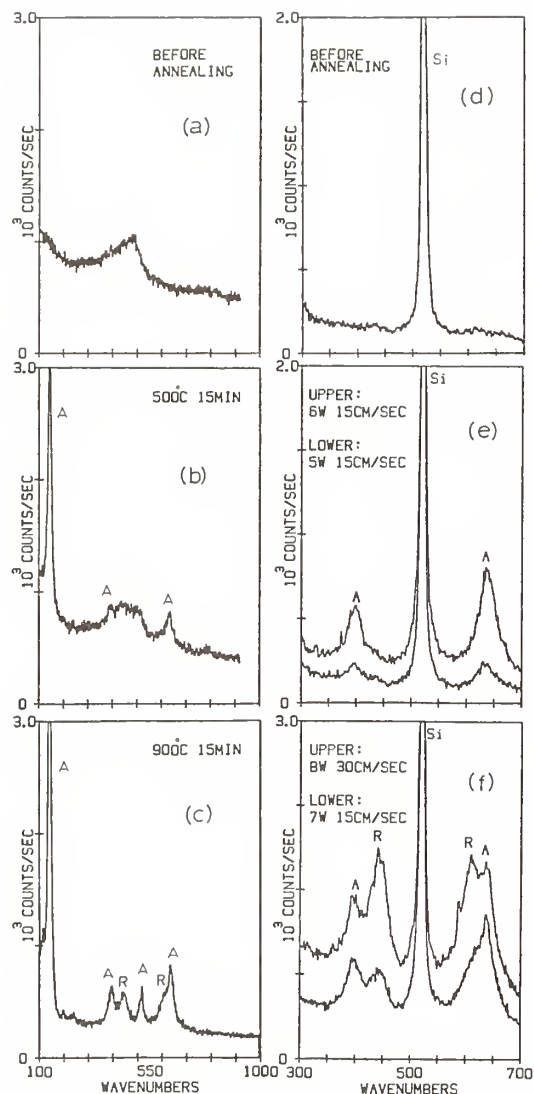


Figure 2. Raman spectra comparing thermal annealing of a titania on silica film and laser annealing of titania on silicon film. Both ion-sputtered films are Type A amorphous as-deposited, and the annealing processes were carried out with fast heating.

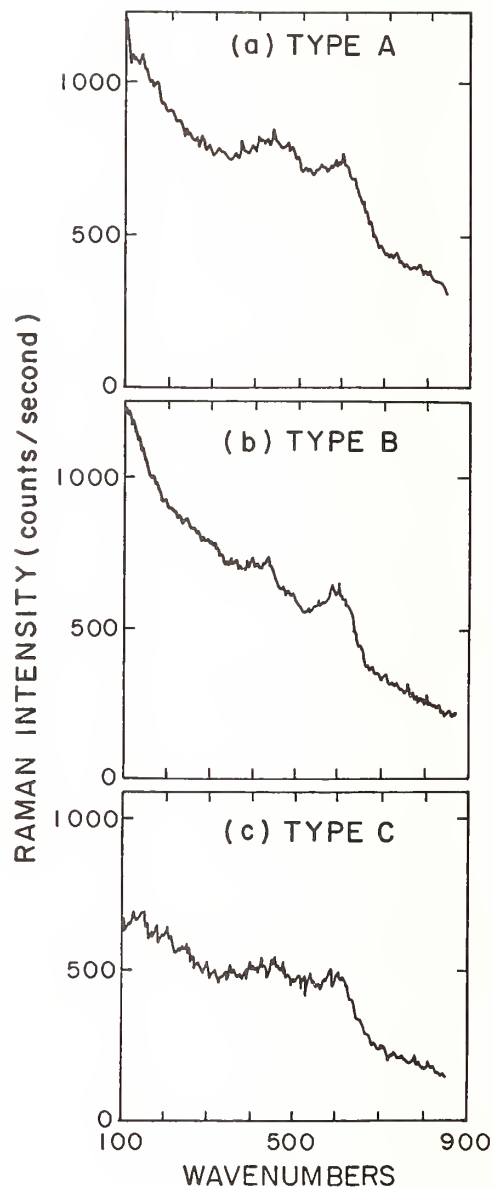


Figure 3. Raman spectra of as-deposited amorphous TiO_2 films (a) Type A, (b) Type B and (c) Type C. All spectra were obtained with oblique-incident geometry along with subtraction technique. Film thickness is again 500 nm.

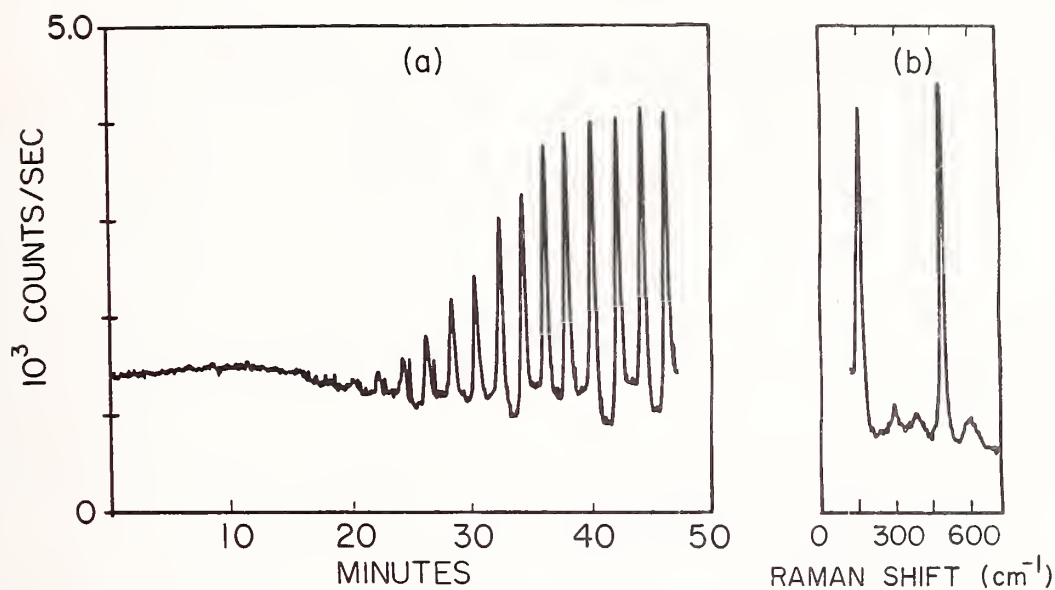


Figure 4. Typical in-situ Raman record of a Type C titania film annealed at 400°C as a function of time showing the amorphous-anatase transformation. (a) Raman intensity of the E_g mode of anatase at 150 cm^{-1} . (b) Entire Raman spectrum scanned after completion of crystallization.

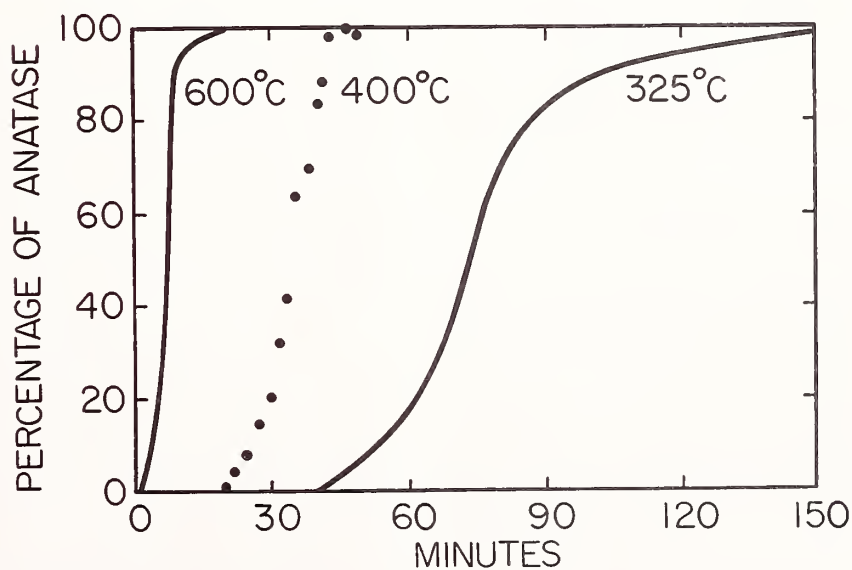


Figure 5. Growth curves of anatase crystallization of Type C titania films. Curves for the annealing temperatures at 325°C and 600°C are derived from the direct records of Raman peak intensity of the E_g anatase mode, while the 400°C curve is deduced from the intensity scans of Fig. 4(a).

Detection of laser damage by Raman microscopy

P.M. Fauchet, I.H. Campbell

Department of Electrical Engineering
Princeton University

F. Adar

Instruments S.A.

ABSTRACT

We demonstrate that Raman microscopy is a sensitive and quantitative tool to detect and characterize laser-induced damage in solids. After damage is induced with single or multiple high power laser pulses, a Raman microprobe maps the surface of the sample with one micron spatial resolution. By performing accurate measurements of the Stokes line, we have been able to measure stress, strain and crystallinity in various samples which had been exposed to high intensity pulses. These results are compared to those obtained using conventional tools such as Nomarski microscopy. Major advantages of Raman microscopy include sensitivity to subtle structural modifications and the fact that it gives quantitative measurements.

Key Words: laser damage; Raman microscopy; silicon.

INTRODUCTION

Many questions regarding the nature of single and multiple pulse laser damage remain unanswered, in large part because of the lack of adequate probes. Detection and characterization of localized laser damage should be performed *in situ*, with nondestructive and sensitive probes having good spatial resolution. Furthermore, quantitative interpretation should be possible and the data acquisition time reasonably short.

Here, we demonstrate that Raman microscopy meets these criteria by investigating the structural modifications that are produced in thin films by high power near infrared and visible pulses. The power of Raman scattering resides in its sensitivity to structural properties such as stress, strain, and microcrystallinity. The use of a microprobe is essential because dramatic changes do occur on a scale of a few microns.

RAMAN MICROSCOPY

To demonstrate the power of Raman microscopy, we elected [1] to first investigate in some detail a well-known material. Silicon was chosen because good quality bulk or thin film samples are conveniently available, and because its Raman line is well characterized. Thin (less than one micron) silicon films on insulator (SOI) grown by low pressure chemical vapor deposition (LPCVD) at 900K have a columnar structure with an average grain size ≤ 50 nm. Damage is produced by pulses at 1064 nm from a Nd:YAG laser, which are weakly absorbed by silicon. The model case under study here is thus relevant for the study of laser damage in thin films and optical coatings. Very recent results obtained with titania films damaged at 532 nm are also presented later and can be discussed in the light of our silicon results.

The Raman Stokes line is characterized by three major parameters:

a: ω_0 the peak frequency

b: Γ the FWHM

c: Γ_a/Γ_b the asymmetry factor

For this study, the influence of stress or strain, and the influence of microcrystallinity on the line must be considered. Uniform stress shifts the peak frequency [2] but leaves the FWHM and the asymmetry factor unchanged. In microcrystalline material, the phonons have a finite spatial extent proportional to the crystallite size [3]. Phonons with wavevector different from 0 thus contribute to the line. In many materials, such as silicon, the phonon frequency decreases with increasing wavevector. Thus, as the crystallite size decreases, the Raman line shifts toward lower frequency, broadens, and becomes asymmetric [4]. Figure 1 compares the line of unstressed single crystal silicon with that of microcrystalline SOI.

Figure 2 is a block diagram of the Raman microprobe [5]. With this apparatus, the spectra consist of points spaced by 0.1 or 0.2 wavenumbers taken with a 1 to 4 seconds exposure time (for Si). The spectral resolution is set at 3 wavenumbers, a convenient compromise between accuracy and data acquisition time. The laser power is kept around 3 mW in a one micron spot on the sample (for Si). The beam is positioned with the help of translation stages and a high resolution display of the surface. A polarizer/analyzer pair is used to take advantage of the polarization selection rules. The various wavelengths available from a krypton laser and an argon laser allow depth profiling. The entire experiment is under computer control.

RESULTS AND DISCUSSION

In a first experiment [1], we exposed SOI to single 40 ps/1064 nm high power pulses. At damage threshold, high resolution Nomarski microscopy reveals a few randomly distributed "wormlike" features 1 to 2 microns in size. The six spectra of Figure 3 were taken, from top to bottom, at the center of one isolated damage site, on the edge, 2, 5, and 9 microns away, and on virgin material. After damage, the material displays good crystalline properties (narrow line = good homogeneity, symmetric line = large grain size) but it is under considerable tensile stress (10^{10} dyne/cm²). The amorphouslike shoulder at 490 wavenumbers is not present, indicating the absence of grain boundary material. The Raman line does not become identical to that of virgin SOI even 10 microns away from the damage site where the surface appears untouched. This long range material relaxation is rather surprising but has been verified in a variety of situations [6].

In a second experiment [1], large (100 microns) heterogeneously damaged regions have been produced by 600 shots at one-half single shot damage. The morphology of the surface appears to be a dense packing of "wormlike" features. At the edge of the damaged area, we observe a smoother annular region. In figure 4, the boundary between virgin and transformed material is at 0. The focused probe beam is scanned from well inside to well outside the damaged area. In the center, where damage is heavy, the surface is very distorted and large variations in stress are observed. The stress becomes uniform in the smooth annular region (from -15 to 0) but the FWHM gradually increases. At the visible boundary, the line is abruptly altered, but takes 20 microns to fully recover. If the probe wavelength is changed, depth profiling can be achieved. We have repeated these experiments at three different wavelengths and obtained similar results. This indicates that a large fraction, if not all of the one micron thick film has been modified.

In figure 5, we plot Γ vs Γ_a/Γ_b and ω_o vs Γ for virgin SOI (0), and at various locations in and around single-shot (■) and multishot (●) damage sites. Closer to the damage site, Γ , ω_o and Γ_a/Γ_b become smaller. The full line results from a calculation which includes the effect of crystal size on the Raman line but neglects the influence of stress. Obviously, the laser irradiated material is now under considerable stress. We also note that Γ , ω_o and Γ_a/Γ_b tend to become smaller on areas damaged by single shots than on areas damaged after multipulse illumination. This difference may come from the fact that complete melting takes place in the former case, leading to regrowth with larger grain size under large tensile stress, whereas in the latter case, the material fails heterogeneously and does not undergo thorough melting. This point deserves further study.

The experiments performed on SOI are now being repeated on titania, zirconia, and other materials used in high power AR and HR coatings. Preliminary results obtained with 662 nm thick titania films on silica indicate that the Raman microscope is also a powerful tool in transparent media. A film was damaged with a several high power 532 nm/30 ps pulses from a Nd:YAG laser system. We took spectra on the edge of the damaged area and compared them with

the spectrum of the virgin film. In figure 6, we show the transformation of the intense 142 wavenumbers line of anatase. The data acquisition rate is approximately 10,000 counts per second at the line center with 10 mW at 514.5 nm focused to 1 micron. Our present interpretation of the data is that there is a stress variation under damage as in silicon. More detailed experiments are now under way.

CONCLUSION

In conclusion, we have shown that Raman microscopy is an excellent probe of the structural modifications produced during laser damage. Material alterations not detected by high resolution Nomarski microscopy or probe light scatter are clearly observed and mapped with one micron resolution. For the first time, significant laser-induced damage was detected up to 20 microns away from the visible damage sites. This finding, which is also important for laser processing, highlights the necessity of using a microprobe. Future studies will be concerned with the role of stress and solid phase transformations in single and multiple pulse damage.

ACKNOWLEDGEMENTS

This research was supported in part by an NSF grant and an equipment loan from LLNL. We thank Dr. N. Johnson (Xerox PARC) and Dr. G. Exarhos (Pacific Northwest Laboratory) for providing the SOI and titania samples respectively.

REFERENCES

1. P.M. Fauchet, I.H. Campbell and F. Adar, "Long range material relaxation after localized laser damage," *Appl. Phys. Lett.* **47**, 479-481 (1985).
2. E. Anastassakis, A. Pinczuk, E. Burstein, F.H. Pollak and M. Cardona, "Effect of static uniaxial stress on the Raman spectrum of silicon," *Solid State Commun.* **8**, 133-138 (1970).
3. H. Richter, Z.P. Wang and L. Ley, "The one phonon Raman spectrum in microcrystalline silicon," *Solid State Commun.* **39**, 625-629 (1981).
4. I.H. Campbell and P.M. Fauchet, "The effects of microcrystal size and shape on the one phonon Raman spectra of crystalline semiconductors," Submitted for publication.
5. P.M. Fauchet, "The Raman microprobe: a quantitative analytical tool to characterize laser-processed semiconductors," *IEEE Circuits and Devices Magazine*, **2**, 37-43 (1986).
6. I.H. Campbell, F. Adar and P.M. Fauchet, "Properties of thin films after focused beam processing," presented at the Annual Fall Meeting of the Materials Research Society (Boston, December 1985), and to be published in *Semiconductor on Insulator and Thin Film Transistor Technology*, MRS Press - 1986.

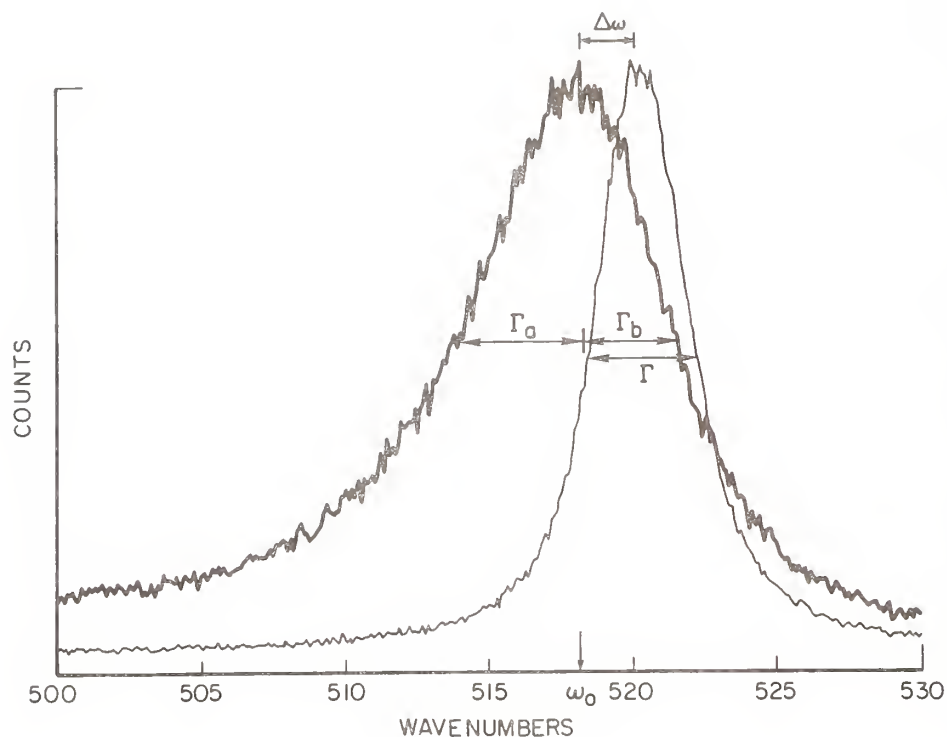


Figure 1

Optic phonon Stokes line of single crystal silicon (fine line) and of polycrystalline silicon thin film (thick line). With the standard operating parameters of our instrument, $\omega_0 = 520 \text{ cm}^{-1}$, $\Gamma \approx 3.8 \text{ cm}^{-1}$, and $\Gamma_a/\Gamma_b \approx 1$ for crystalline silicon, and $\omega_0 \approx 518.5 \text{ cm}^{-1}$, $\Gamma \approx 9 \text{ cm}^{-1}$, and $\Gamma_a/\Gamma_b \approx 1.4$ for the polycrystalline silicon thin films. In these films, the exact parameters of the Raman line are not perfectly identical everywhere (for example, ω_0 varies from 518.5 to 519 cm^{-1} over large distances). These variations reflect stress and homogeneity changes in the film itself.

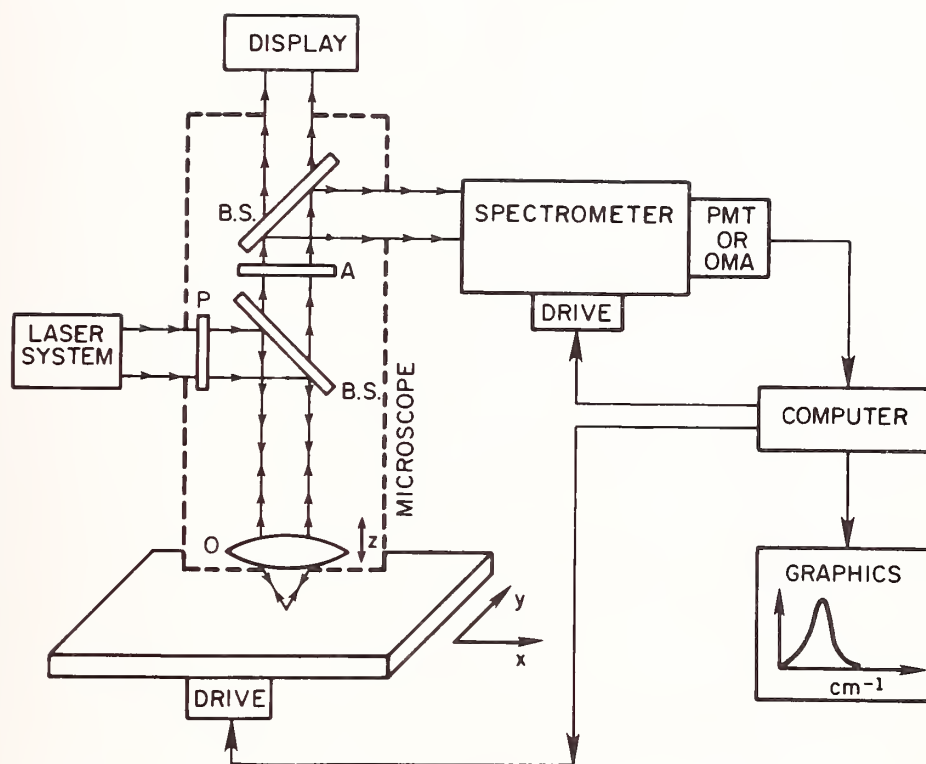


Figure 2

Block diagram of the Raman microprobe. The probe laser beam is focused through the objective O to a one micron spot on the sample surface. The backscattered Raman signal is collimated by the same objective and analyzed by a double-meter spectrometer. The standard optical microscopic image of the surface appears on the display.

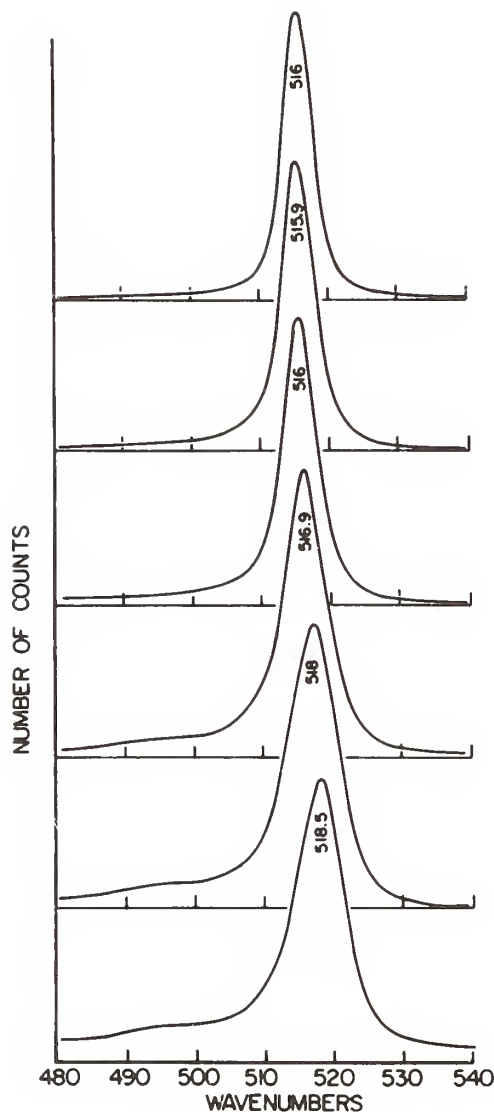


Figure 3

Spectra taken around an isolated ~ 1 micron damage-site formed on a polycrystalline silicon film by a single 40 ps/1064 nm laser pulse at damage threshold. The spectra are taken (from top to bottom) on top of the damage site, on its edge, 2, 5, and 9 microns away, and on virgin, unirradiated material. High resolution Nomarski microscopy suggests that the surface remains unaltered except right at the ~ 1 micron damage site. The amorphous-like shoulder at 495 cm^{-1} , quite apparent in the virgin material, reappears starting at 5 microns away. This shoulder indicates the presence of a relatively large fractional volume of highly distorted material, presumably the grain boundary material. Closer to the damage site, the average grain size has increased, perhaps following melting and recrystallization, and the material is under considerable stress. This extra stress relaxes away from the damage site but has not recovered to the value in the virgin film even after 9 microns.

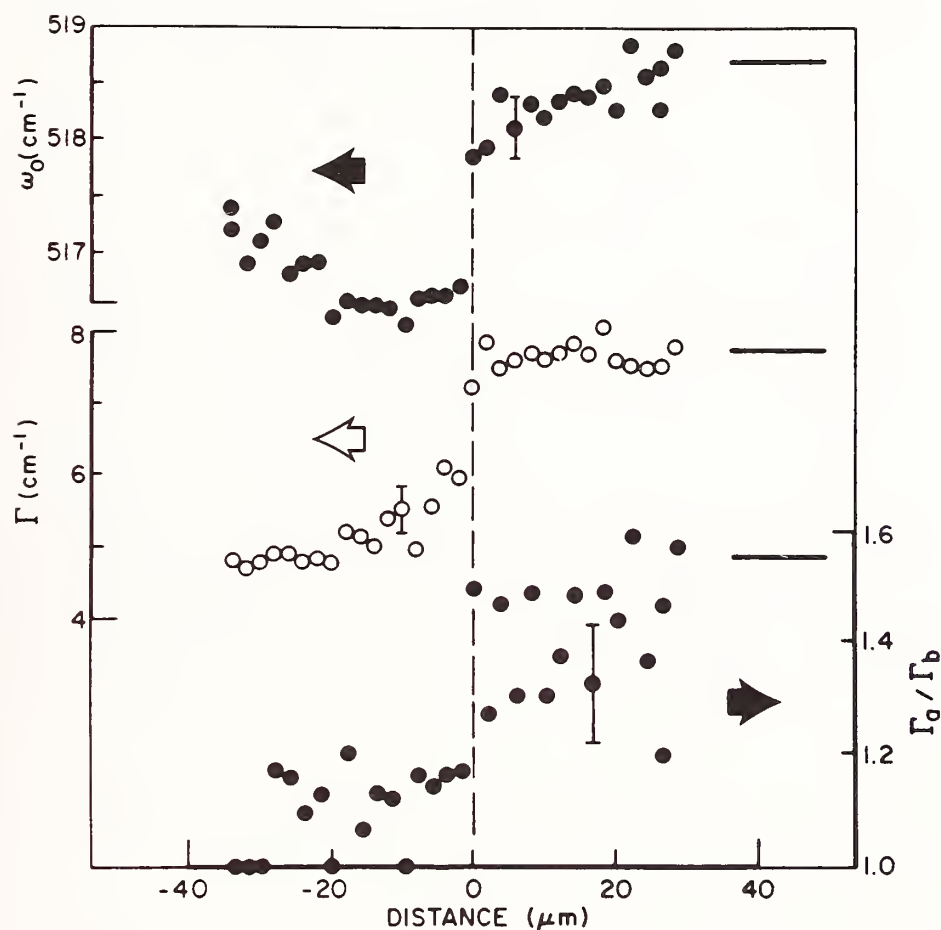


Figure 4

Parameters of the Raman line around a large heterogeneously damaged area formed by repeated illumination (600 shots) at one-half single shot damage. The dashed line indicates the boundary between damaged (left) and undamaged (right) regions as defined by high resolution Nomarski microscopy. The full lines on the right show the parameters of the virgin polycrystalline film. Beyond the visible boundary, it takes ≥ 20 microns for the Raman line to fully recover. (Note however that Γ seems to recover immediately). Inside the damaged region, we observe different parameters depending upon the smoothness of the surface. In the center, the surface is rough and $\omega_0 \sim 517 \text{ cm}^{-1}$ and $\Gamma \simeq 5 \text{ cm}^{-1}$. Around the edge, the surface is smoother and $\omega_0 \lesssim 516.5 \text{ cm}^{-1}$ and $\Gamma \sim 5.5 \text{ cm}^{-1}$.

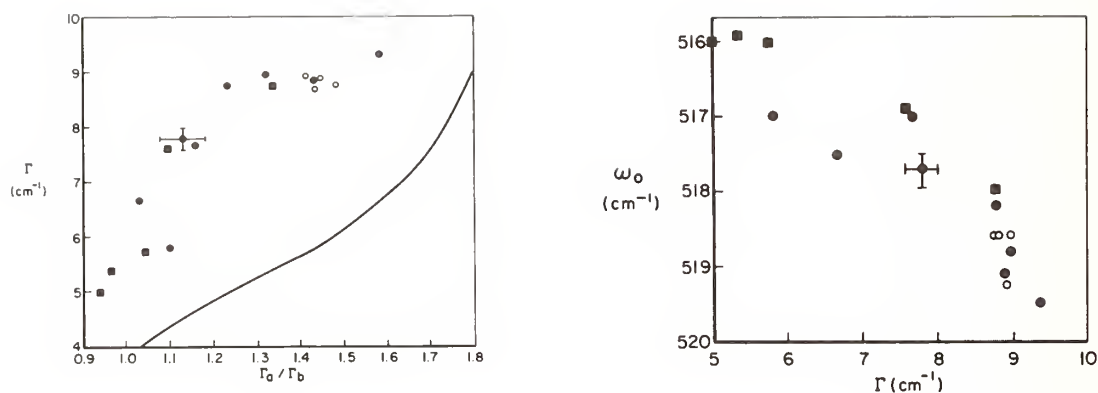


Figure 5

Parameters of the Raman line at various locations in and around single-shot (■) and multishot (●) damage sites, and in virgin polycrystalline silicon films (◐). The full line, which accounts for variations in the grain size only, does not agree with the data. The ω_0 vs Γ data follow a line that actually curves in the opposite direction from that predicted by theory. The stress variations dominate the changes in the Raman line. When ω_0 , Γ and Γ_a/Γ_b are small, the material is made of large grains, and is under large and homogeneous tensile stress. Note that the results on single-shot damage sites tend to show a larger and more homogeneous stress.

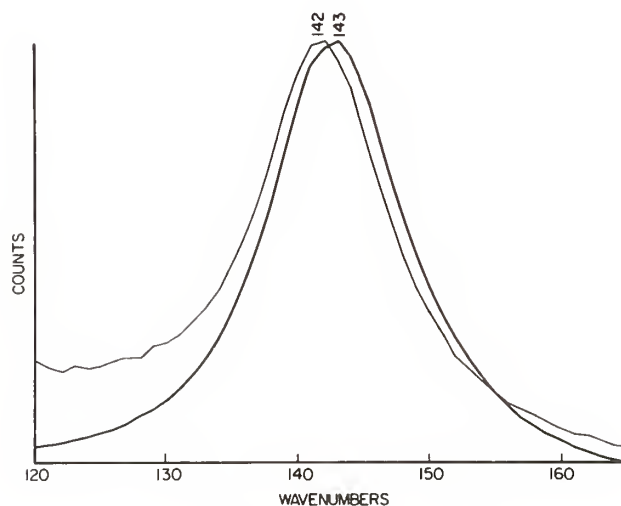


Figure 6

Anatase (TiO_2) before (fine line) and after (thick line) damage with several 30 ps 532 nm pulses, showing a stress variation similar to that observed with silicon.

Time-Resolved Temperature Determinations From Raman Scattering of
TiO₂ Coatings During Pulsed Laser Irradiation

Gregory J. Exarhos

Pacific Northwest Laboratory*
Richland, Washington 99352

Simultaneous measurement of Stokes/anti-Stokes Raman intensities for a particular vibrational mode allows instantaneous surface temperatures to be determined. Time-resolved Raman spectra were measured on a specially constructed spectrometer using pulsed laser excitation and gated detection techniques. Measurements on equilibrated coatings and uncoated substrates at several temperatures served to confirm the utility of the technique for temperature determination as well as calibrate the intensity response of the instrument.

Pulsed irradiated SiO₂ and Y(PO₃)₃ glass substrates yield no temperature increase at laser energies where surface damage is not apparent. At higher pulse energies, an increase in anti-Stokes scattered radiation is observed, signifying a temperature rise. Analogous results are seen in Raman spectra of low energy pulse-irradiated TiO₂ coatings recorded at delays of 0 and 72 nsec from the excitation pulse. At higher energies, increased coating temperatures are observed at these times as well as at short times preceding the peak maximum of the excitation pulse. Raman results are used to model the thermal response of pulsed laser-irradiated dielectric coatings.

Key words: laser heating; molecular vibrational studies; thermal transients;
time-resolved Raman spectroscopy; TiO₂ optical coatings

1. Introduction

Pulsed laser irradiation of insulating solids results in rapid heating of localized areas via single or multiphoton absorption processes and subsequent energy transfer to lattice vibrational modes. Irradiated substrates and dielectric coatings often suffer irreversible changes ranging from subtle microstructural modification to catastrophic structural change. Knowledge of the transient thermal response of the substrate or coating during irradiation is paramount to developing a model for the damage process in a given material.

Conventional methods for measuring temperatures, which include thermal and optical pyrometric techniques, are limited in their application to relatively long time determinations over large sample areas. A viable alternative for temperature determination on ultrashort timescales involves vibrational band intensity analysis of spontaneous Stokes and anti-Stokes Raman scattered radiation, which is excited by the damaging laser pulse or a different wavelength probe laser. Vibrational band intensity ratios are related to the Boltzmann factor by equation (1).

$$\exp [-hc\omega/kt] = A(\omega) \frac{I_a(\omega)/(\omega_0 + \omega)^4}{I_s(\omega)/(\omega_0 - \omega)^4} \quad (1)$$

*Pacific Northwest Laboratory is operated by Battelle Memorial Institute for the U. S. Department of Energy under contract DE-AC06-76RLO 1830.

$I_a(\omega)$ and $I_s(\omega)$ are respectively the anti-Stokes and Stokes band intensities measured at the vibrational frequency ω in wavenumbers. T is the absolute temperature; ω_0 is the laser frequency; and the other constants have their usual meaning.[1,2] The factor $A(\omega)$, a spectrometer response function, takes into account the nonlinearity of spectrometer throughput and detector sensitivity as a function of frequency. Methods to adequately determine this function have been extensively discussed [2] and were used to calibrate the spectrometer used in these studies.

The Raman technique for determining lattice temperatures in pulsed laser annealed silicon has been reported by Compaan, et al., [3] and critically reviewed by Wood and coworkers.[4] This work involved Raman band intensity measurements at the Stokes frequency for the strong silicon mode using a gated photomultiplier detector and then measurement at the anti-Stokes frequency under presumably identical conditions. Relatively low lattice temperatures were determined to ca. $\pm 30\%$. An improvement in the uncertainty of the band intensity ratio is expected if all the Raman data could be collected at the same instant in time. Accurate bandshapes and baselines could also be determined. The presence of spurious fluorescence features, which might accompany the laser pulse, may also be detected and the vibrational band intensities corrected accordingly.

A special spectrometer has been constructed for simultaneous measurement of Stokes and anti-Stokes Raman spectra excited by a single laser pulse. The instrument includes an array detector for parallel signal detection and a special intermediate slit aperture for rejection of the laser excitation line and associated Rayleigh scattering. Spectra of several materials recorded under equilibrium conditions at various temperatures are used to determine the spectrometer response function for band intensity correction. Time-Resolved Raman Spectroscopy (TRRS) has been used to determine surface temperatures during pulsed laser irradiation of high purity bulk anatase (TiO_2) and vitreous silica, and single-layer sputter-deposited anatase coatings. Spectra recorded during the damage pulse and at long delays are used to evaluate the thermal response of these materials.

2. Experimental

All TiO_2 coatings (15 nm grain size and 1μ thick) were made by reactively sputtering Ti in Ar/O_2 atmospheres onto fused silica substrates in an rf diode system.[5] Other samples used for investigation included high purity fused silica substrates and pressure compacted high purity TiO_2 . Fused silica and amorphous $\text{Y(PO}_3)_3$ were used as intensity standards according to Griffiths.[2]

Raman measurements were recorded from samples mounted in a 90° forward scattering geometry. Scattered radiation was collected by a Graflex f/5.6 camera lens and imaged onto the slits of a triple monochromator (.25m focal length). A notch filter served to effectively reject the excitation laser wavelength. The triple monochromator consisted of a subtractive double monochromator with a special intermediate slit as depicted in figure 1 in tandem with a single monochromator, which dispersed the filtered radiation onto the elements of an intensified gated array detector. Interchangeable ruled gratings with different groove densities were used to isolate particular spectral regions on the array detector. This design is essential for simultaneous recording of both Stokes and anti-Stokes Raman spectra due to the six orders of magnitude difference in intensity between the pulsed laser emission and the associated weak Raman scattering.

A pulsed Nd:YAG laser (10 nsec pulse bandwidth at half maximum) operating at 532 nm and from between 1 and 50 mJ/pulse was used for sample irradiation. The focused spot diameter on the sample was approximately 1 mm. Raman spectra were acquired at short time periods preceding the laser pulse maximum, at the laser pulse maximum, and at long delays using ancillary lower energy probe pulses from a pulse train created by the pellicle beamsplitter/delay network. Spectra acquired at detector delays that did not overlap the laser pulse were used to distinguish between induced fluorescence and true vibrational Raman features. Raman spectra were measured as a function of pulse laser energy and detector delay. Static measurements of samples equilibrated in an oven at various temperatures were recorded for spectrometer throughput calculations. For this particular instrument, the $A(\omega)$ factor in equation (1) can vary from .5 to 1 over the spectral bandpass of $\pm 2000 \text{ cm}^{-1}$ centered at the probe laser frequency. Instrumental slitwidth was maintained at 250μ for all measurements.

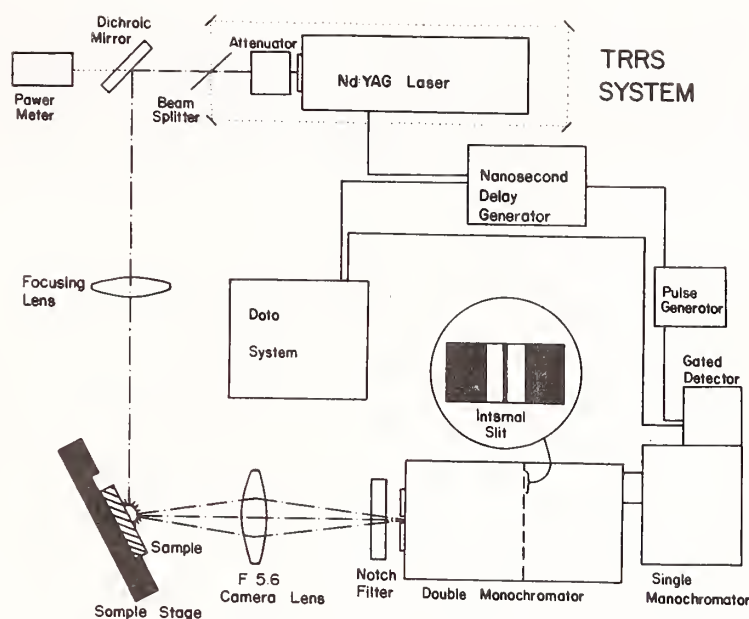


Figure 1. Experimental set-up for measurement of time-resolved Raman spectra (TRRS)

3. Results

Raman measurements were used to determine lattice temperatures of pulsed laser irradiated bulk TiO_2 (anatase) and single-layer anatase coatings on silica. Five prominent vibrational features at 143 cm^{-1} (VS), 199 cm^{-1} (ω), 397 cm^{-1} (S), 515 cm^{-1} (S), and 636 cm^{-1} (S) have been assigned in the bulk crystal [6] and extensive Raman characterization work on single and multilayer anatase coatings has been reported [7,8,9,10]. Figure 2 shows several spectra of an anatase coating measured under thermal equilibrium conditions at several temperatures. The three highest frequency bands are observed in both the Stokes and anti-Stokes spectra in addition to the probe laser line separating them. The strong 143 cm^{-1} band is extinguished since it falls within the rejection band of the notch filter. At a temperature of 742°C , the Stokes/anti-Stokes features are comparable in intensity. Calculated temperatures using a predetermined spectral response function from the standard reference glasses, as described in reference (2), agree to $\pm 2\%$ with measured ambient temperatures of the oven housing the sample. The overall uncertainty in the temperature calculation is principally determined by the uncertainty in the band intensities. These measurements serve to demonstrate the utility of the Raman technique for measuring surface temperatures under equilibrium conditions where the excitation laser produces negligible surface heating.

At higher pulse excitation energies, an appreciable rise in surface temperature is evident from measured Raman spectra. Figure 3 exhibits several representative spectra recorded with the detector gate fully open at the peak of the incident laser pulse. (The gate bandwidth at half maximum was set at 8 nsec.) Samples were irradiated at room temperature, and laser pulse energies were measured for each acquired single-shot spectrum. Unirradiated sample regions were used for each successive pulse, and the spectra recorded in figure 3 are averages of 50 scans each differing in pulse energy by less than $\pm 4\%$.

Spectra depicted in figure 3 were obtained using finer ruled gratings in the monochromator and with the notch filter removed so that the 143 cm^{-1} anatase line appears. At higher pulse energies, extra features appear on either the Stokes or anti-Stokes side of the spectrum and are assigned to laser-induced fluorescence or emission lines. These features are detailed in the top spectrum of figure 3 taken at a detector delay of 31 nsec. No Raman lines are observed at this time, which is longer than the duration of the laser pulse.

Similar results are observed in spectra acquired at a delay of 72 nsec from the primary pulse maximum. Surface temperatures calculated from band intensity ratios average about 60°C lower at this delay when compared with calculated temperatures at the pulse maximum (0 delay).

For such measurements, the primary pulse is split into a pulse train with each separate pulse delayed by the transit time around a fixed delay path (figure 1). The detector is locked onto one of the delayed pulses, which has ca. ten percent of the primary pulse energy. Long-lived emission features induced by the primary pulse can be removed from the spectrum by subtracting the normalized emission spectrum obtained with the delay beam blocked.

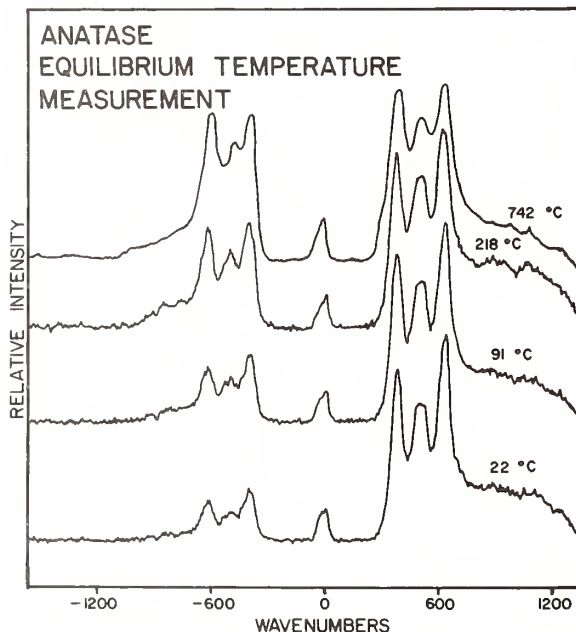


Figure 2. Simultaneous Stokes, anti-Stokes Raman spectra of a 1 μ anatase coating equilibrated at several temperatures (600 g/mm grating with notch rejection filter)

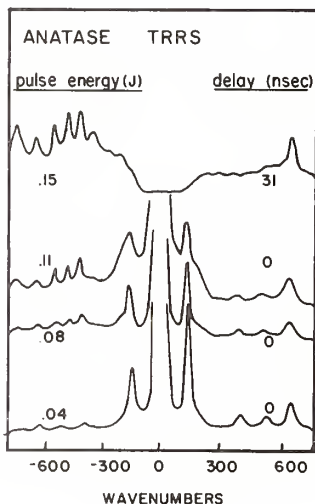


Figure 3. Raman spectra of pulsed-irradiated anatase showing appearance of laser-induced fluorescence features at high pulse energies. The top spectrum was recorded at a detector delay of 31 nsec from the pulse maximum and exhibits pure fluorescence (1200 g/mm grating without notch rejection filter)

The time dependence of the surface temperature rise at the highest pulse energy shown in figure 3 was also studied for irradiated anatase coatings. In this experiment, the detector gate is opened at times preceding the laser pulse maximum as illustrated in figure 4. The hatched regions in figure 4 represent the total integrated laser energy contributing to scattered Raman radiation at two windows prior to the pulse maximum (-15 and -10 nsec). Measured Raman spectra corresponding to these time periods are shown in figure 5. Calculated temperatures from measured Raman intensities are listed in table 1.

Table 1. Calculated Surface Temperatures at Time Periods Preceding the Primary Pulse Maximum

Sample	Calculated Temperature
1 μ Anatase coating	22°C
-15 nsec delay	109°C
-10 nsec delay	134°C

Marked baseline changes accompany the temperature rise, which may result from laser-induced photoluminescence. Previous work [11] concerning pulsed laser-irradiated TiO₂ (rutile) has demonstrated that such emission is induced by multiphoton absorption processes observed in an energy regime where catastrophic damage to the crystal did not occur.

Similar measurements were performed on vitreous silica and bulk anatase samples. Results for bulk anatase were comparable to those seen from 4 μ anatase films. Since the bulk anatase was of extremely high purity, observed results are indicative of the thermal response of the intrinsic material and should not be ascribed to impurities. Stokes/anti-Stokes ratios for vitreous silica exhibited little change as a function of laser pulse energy, indicating that at these energy levels no appreciable rise in temperature had occurred.

4. Discussion

Surface temperatures of pulsed laser-irradiated anatase coatings have been computed from Stokes/anti-Stokes band intensity ratios at zero time delay as a function of pulse energy and are shown in figure 6. Qualitative characterization of three regions are based upon observation of induced surface damage and the functional dependence of temperature on pulse energy. Region I is associated with no observable surface damage and a slight linear increase in temperature with pulse energy. Region II is characterized by "footprints" (darkening) of the coating, the appearance of other non-vibrational features in the spectrum, and a variation of temperature with the square of pulse energy.

Extensive surface damage and cratering is indicative of region III damage, which is also characterized by a nearly complete loss of Raman lines and appearance of intense fluorescence. The temperature dependence on pulse energy follows a higher power law than that exhibited in region II.

Region III is also characterized by a nearly complete loss of intensity at the excitation laser frequency, which was a prominent feature in regions I and II. Self-absorption of the pulse laser wavelength was not observed in regions I or II and probably occurs when available laser energy is sufficient to create a plasma near the surface. Spontaneous Raman scattering is also absorbed by the plasma discharge under these conditions. This plasma results from breakdown of the TiO₂ coating since pulse irradiation of other materials (silica, ZrO₂, aluminum, zirconium) under the same conditions yields markedly different emission features.

The highest surface temperature measured for the anatase coating under high energy pulsed irradiation is ca. 970°C. For higher energy pulses, no vibrational lines ascribable to anatase

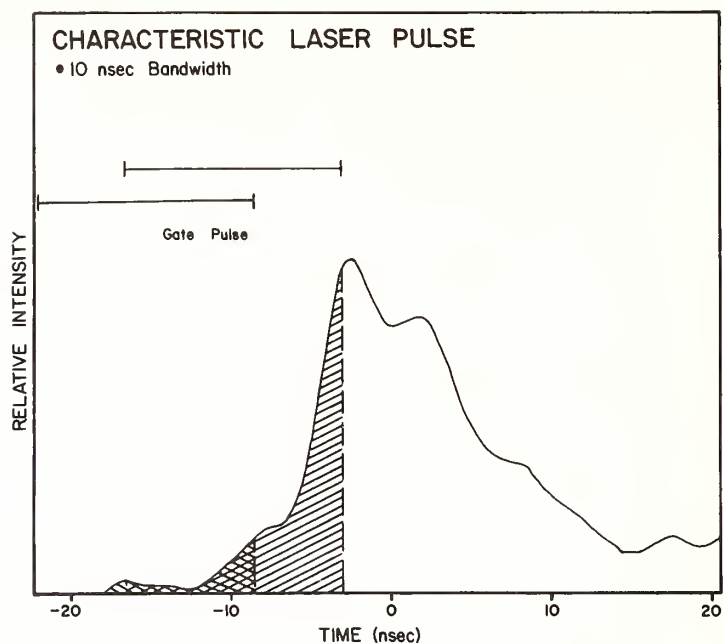


Figure 4. Laser pulse profile in time showing detector gate widths and total integrated laser power delivered at delay times of -15 and -10 nsec.

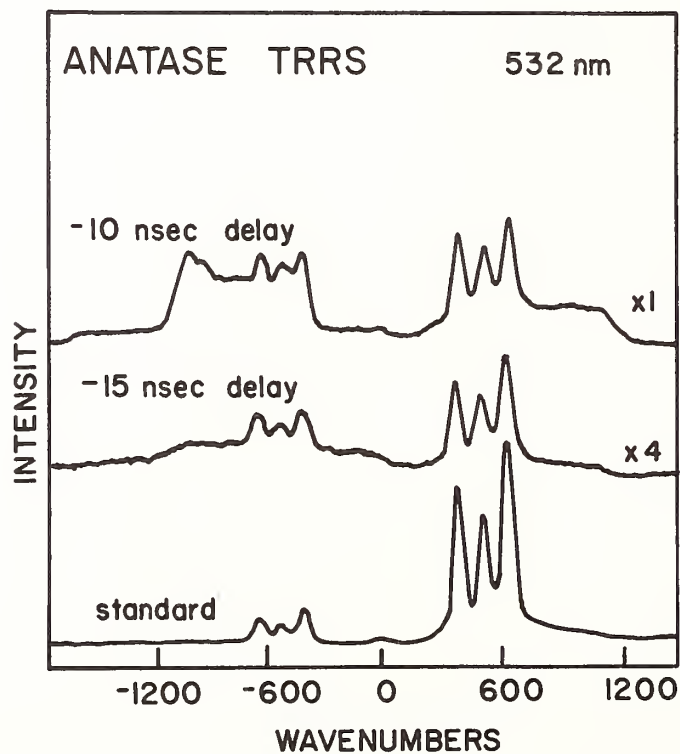


Figure 5. Raman spectra acquired at detector delay settings of -15 and -10 nsec (600 g/mm grating with notch rejection filter).

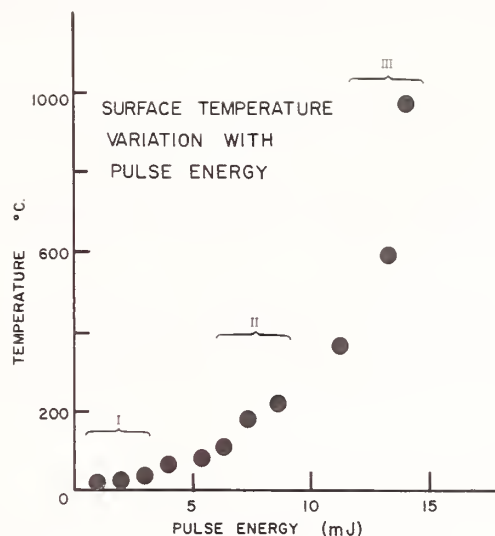


Figure 6. Calculated surface temperature as a function of laser pulse energy for an irradiated 1 μ anatase coating. The three indicated regions correspond to increasing damage to the coating.

are observed. This is reasonable since at these temperatures, anatase irreversibly crystallizes to the rutile modification of TiO₂ with concomitant increase in density.[12] The phase change may be responsible for plasma formation at high pulse energies.

Transient Raman spectra obtained at detector delays preceding the damage pulse maximum (figure 5) indicate a gradual rise in surface temperature with integrated laser pulse energy. Temperature increase results from a combination of linear and nonlinear absorption phenomena and accumulates with deposited laser energy. Thermal diffusion away from the damage region is apparently slower than energy deposition as shown by transient Raman measurements at a detector delay of 72 nsec from the pulse maximum. Surface temperatures are uniformly lower than temperatures determined at zero detector delay in regions I and II.

5. Conclusions

Transient Raman measurements recorded during pulsed laser irradiation of dielectric coatings allow surface temperatures to be calculated from measured intensity data. A unique spectrometer has been constructed that simultaneously measures both Stokes and anti-Stokes vibrational features excited by a single laser pulse at variable times preceding the pulse maximum and at longer times using a lower energy probe pulse. Measurements on anatase coatings demonstrate the viability of the technique for obtaining time-resolved surface temperature information. Laser-induced heating of anatase coatings results from single and multiphoton absorption phenomena and an irreversible phase transition to the rutile phase when the lattice reaches a critical transformation temperature. Additional data is needed from these and similar coatings in order to understand the thermal response of dielectric coatings to laser irradiation. Future work will be directed toward using transient Raman measurements to determine thermal parameters of the coating during irradiation.

This work was supported by the Air Force Weapons Laboratory under Contract P0-85-037. Sputter-deposited coatings have been graciously supplied by Dr. W. T. Pawlewicz. The assistance of Mr. T. C. Nguyen with experimental measurements is gratefully acknowledged.

7. References

- [1] Herzberg, G., *Molecular Spectra and Structure. II. Infrared and Raman Spectra of Polyatomic Molecules*. Princeton; Van Nostrand Press; 1945; p. 261.
- [2] Malyj, M., and Griffiths, J.E. Stokes/anti-Stokes Raman vibrational temperatures: reference materials, standard lamps, and spectro- photometric calibrations. *Applied Spectroscopy* 37(4):315-333; 1983.
- [3] Lo, H.W., and Compaan, A. Raman measurement of lattice temperature during pulsed laser heating of silicon. *Phys. Rev. Lett.* 44(24):1604-1607; 1980.
- [4] Wood, R.F., Lowndes, D.H., Jellison, G.E. Jr., and Modine, F.A. Melting model and Raman scattering during pulsed laser annealing of ion-implanted silicon. *Appl. Phys. Lett.* 41(3):287-290; 1982.
- [5] Pawlewicz, W.T., Martin, P.M., Hays, D.Dk. and Mann, I.B. Recent developments in reactively sputtered optical thin films. Seddon, R.I. ed. *Proceedings of the SPIE conference on optical thin films*; 1982 January 26-27; Los Angeles, CA. *Proc. Soc. Photo-Opt. Instrum. Eng.* 325:105-116; 1982.
- [6] Capwell, R.J., Spagnolo, K., and DeSesa, M.A. A rapid determination of low concentrations of anatase in rutile TiO_2 pigments by Raman spectroscopy. *Appl. Spectrosc.* 26:537-539; 1972.
- [7] Pawlewicz, W.T., Exarhos, G.J., and Conaway, W.E. Structural characterization of TiO_2 optical coatings by Raman spectroscopy. *Applied Optics* 22(12):1837-1840; 1983.
- [8] Exarhos, G.J., and Pawlewicz, W.T. Raman characterization of all-dielectric multilayer $\text{SiO}_2/\text{TiO}_2$ optical coatings. *Applied Optics* 23(12):1986-1988; 1984.
- [9] Long, S.H., She, C.Y., and Exarhos, G.J. Reduction of substrate interference in Raman spectroscopy of submicron titania coatings. *Applied Optics* 23(18):3049-3051; 1984.
- [10] Exarhos, G. J. Substrate signal suppression in Raman spectra of sputter-deposited TiO_2 films. *J. Chem. Phys.* 81(11):5211-5213; 1984.
- [11] Royce, G.A., and Kay, R. B. Multiphoton interactions in rutile. *Applied Optics* 23(12):1975-1979; 1984.
- [12] Parkes, G.D., *Mellor's Modern Inorganic Chemistry, Revised Edition*. London; Longrans Publishing Co.; 1961; 803 p.

- Manuscript Not Received -

=====

EFFECT OF MOLECULAR FLUORINE ON THE PERFORMANCE
OF EXCIMER LASER OPTICS

S. R. Foltyn, L. J. Jolin, and G. Lindholm
Los Alamos National Laboratory

Key Words: Excimer lasers; fluorine degradation; laser damage;
ultraviolet laser coatings.

Thresholds Measured With 350-nm Pulses at 25-100 Hz for Bare Polished
Crystals of CaF_2 and for Silica Sol-gel AR Coatings on Silica Substrates*

M. C. Staggs, D. Milam, I. M. Thomas, and J. G. Wilder
Lawrence Livermore National Laboratory
University of California
P.O. Box 5508, L-490
Livermore, California 94550

An XeF laser-damage experiment was used to measure damage thresholds for bare polished crystals of CaF_2 and porous silica antireflection coatings on fused silica substrates. Damage was induced by applying 1000 350-nm, 25-ns pulses at repetition rates of 25-100 Hz to small (typically 0.12×0.03 cm) sites on the surfaces of the sample. Eight samples of fluorescence-free CaF_2 exhibited both surface and bulk damage at fluences as low as 10 J/cm^2 . Three samples of UV-grade CaF_2 also had surface damage thresholds of 10 J/cm^2 , and bulk damage was not observed in this material. Thresholds for the porous silica coatings were 17-23 J/cm^2 .

Key words: calcium fluoride, multishot damage testing, porous silica antireflection coatings, ultraviolet laser damage.

1. Introduction

We are evaluating solution deposited optical coatings for use at the 350 nm wavelength of XeF lasers. Discharge pumped XeF lasers can operate at repetition rates in excess of 100 Hz, and they emit pulses of short duration, typically 10-30 ns. In available commercial XeF lasers, output single-pulse fluences are less than 0.5 J/cm^2 and laser-induced damage to the optical components in these lasers is not a serious problem. However, many applications of these lasers require concentration of the beam and produce both high peak intensities and moderate average power loadings that damage available UV coatings.

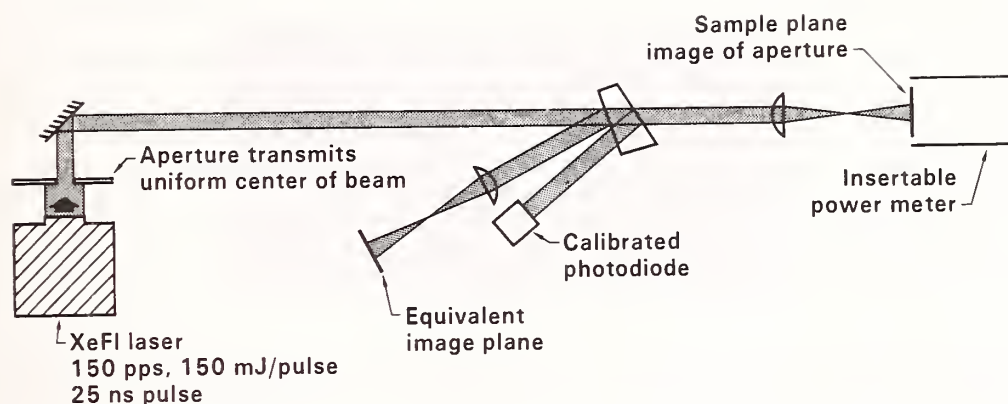
Porous silica antireflection (AR) coatings¹ capable of handling single pulses at fluence of $5\text{-}9 \text{ J/cm}^2$ delivered in 350-nm, 0.6-ns pulses were developed for the Nova laser.² Because of their high single-pulse thresholds, they were obvious candidates as AR coatings for XeF laser components made of UV transmitting materials such as fused silica and CaF_2 . Twelve porous silica AR coatings were deposited on fused silica substrates and tested with a recently assembled XeF laser damage apparatus. We have also tested eleven bare polished CaF_2 crystals to provide a data base that will assist in interpretation of the results of planned tests of porous silica AR coatings on this material.

2. XeF Laser Damage Experiment

The arrangement of our XeF laser-damage experiment is shown in Fig. 1. The laser was manufactured by Lambda Physik (Model EMG 202 MSC). It emits 25-ns, 150 mJ pulses at repetition rates up to 150 Hz. The pulse energy decreases over the life of a gas fill, but is stable to better than 5% over short intervals ($> 10^4$ shots). The output beam is rectangular in cross-section, with approximate dimensions of 0.8×2.6 cm, and the divergences in these two dimensions are respectively, $\sim 1 \text{ mr}$ and $\sim 3 \text{ mr}$ (full angle at half power). In planes near the output mirror the fluence distribution in the center of the beam is uniform to within a few percent over a rectangular area with dimensions of 0.4×2.0 cm.

Image relaying was used to shape the beam incident on the damage samples. We placed an aperture in the beam that transmitted only the central uniform fraction, and used a single plano-convex lens to form a down magnified image of the aperture at the sample surface. Fluence

*Work performed by the Lawrence Livermore National Laboratory under the joint auspices of the Air Force Weapons Laboratory, Kirtland AFB, New Mexico 87117-6008, under P.O. #85-060, and the U.S. Department of Energy under Contract No. W-7405-ENG-48.



Laser, XeF

Pulse energy; 150 mJ, stable within 5%
Pulse duration; 25 ns
Repetition rate; up to 150 HZ
Beam shape; rectangular (.8 × 2.8 cm); uniform to 10% over central .4 × 2.0 cm
Beam divergence, Full angle at half power:
Long dimension 3 mr
Short dimension ~ 1 mr

Figure 1: XeF laser damage experiment.

at the sample's surface was controlled by varying the size of the image. Each site on a sample was irradiated by a sequence of pulses. The number of pulses in the sequence and the pulse repetition rate could be preselected by use of a programmable laser controller. The irradiation sequence began from a single command and could be manually interrupted.

Computation of the single-pulse fluences incident on the sample required measurement of the pulse energy and the beam shape. The energy in single pulses in the sequence was computed by dividing the average power delivered to the sample plane by the pulse repetition rate. Average power was measured by placing a power meter in the sample position. To allow measurement of pulse energies during a damage experiment, a photodiode was placed in a diagnostic beam and the amplitude of the signals from the photodiode was calibrated against the single pulse energies measured by the power meter. We believe the measurements of single pulse energies were accurate to within 3% which was the total difference in power measurements obtained in side-by-side comparisons of three independently calibrated power meters.

The greatest uncertainty in measurement of fluence was that in determining the exact shape of the images relayed to the sample plane. Because the divergence was large in the plane containing the long dimension of the beam, the beam width exceeded the aperture of the available lens. The combination of excluding some edge rays and spherical aberration in the plano-convex lens prevented formation of uniformly illuminated images of the beam limiting aperture. The solution to this problem is use of corrected optics with larger aperture, and an aspheric imaging system with zoom control of magnification has been designed and will soon be available.³

Rather than invest a significant effort in learning to precisely measure the shape of aberrated beams that will not be a permanent aspect of this experiment, we are computing fluences by dividing single-pulse energies by the areas of beam imprints recorded on sections of ultraviolet sensitive paper placed in the sample plane. Imprints of intense 350-nm beams are readily recorded on photocopy papers, a variety of common white papers and highly absorbing optical thin films. An example of an imprint recorded in an impure highly absorbing Ta₂O₅ thin film is shown in Fig. 2. The imaging aberration is apparent by the greater severity of damage in the center of the beam as compared to that at the distantly separated ends of the burn.

Some of the relayed images were also recorded on Kodak I-Z emulsions using a camera with magnification of 17. The magnification was obtained by use of a single plano-convex lens.



Figure 2: Imprint of the beam in the sample plane, recorded in a highly absorbing Ta_2O_5 film. Beam dimensions are $1.3 \times .25$ mm.

Analysis of these photographs indicated that the fluence profile was constant across the lesser dimension of the rectangular images, but smoothly rounded across the longer dimension. Peak fluence values computed from these data were 30-40% greater than those computed assuming that the fluence was uniform across the rectangular area recorded in beam imprints. However, photography of magnified images of small objects placed in the sample plane indicated that the camera lens was responsible for some of the aberration in photographic records of the beam, so our reported fluence values are systematically conservative by an amount less than the 30-40% difference in the two fluence measurements.

The final aspect of the experiment is detection of damage, and we have continued our use of three techniques: observation of laser-induced plasma during irradiation, post-irradiation visual inspection with intense white-light backlighting, and Nomarski microscopy. Damage was defined to be a permanent disruption of the sample detectable by one of the two inspections. We do not yet know whether laser-induced plasmas will be a reliable indicator of damage induced by sequences of 350-nm laser pulses.

Our initial experience with this configuration indicates that image relaying is the optimum technique for irradiating samples with XeF laser beams that are highly divergent and weakly coherent. Use of corrected optics will eliminate the image aberration in our present system, and allow both formation of uniformly intense beams and use of the full power of the laser in all experiments since fluence at the sample can be controlled by varying the size of the image. Corrected optics for photography of beams have also been selected.

3. Test Samples

3.1 Porous Silica AR Coatings

Porous silica films were deposited on fused silica substrates by immersing the substrate in the coating solution and then withdrawing the substrate using a pull rate calibrated to deposit coatings 88 nm in thickness, the quarterwave thickness for the 350-nm wavelength. The coating solutions were either ethanol or methanol containing silica particles with diameters of 10-20 nm. To investigate the effect of aging of the coating solutions, four substrates were coated with an ethanol solution that was prepared 11 months before it was used and four substrates were coated with a freshly prepared methanol solution. The coatings were dried in air at room temperature and required no additional processing.

3.2 CaF_2 Substrates

Bare polished crystals of CaF_2 were purchased from three vendors. One vendor supplied material advertised as UV grade. Two supplied crystals advertised as "fluorescence-free" when irradiated at the ArF wavelength of 190 nm. The polishing processes of two vendors are proprietary; the third used conventional lapping with diamond and ethylene glycol. All crystals were either 2 inch in diameter and 6 mm in thickness or 1.5 inch in diameter and 10 mm in thickness.

4. Damage Thresholds

4.1 Porous Silica AR Coatings

Damage thresholds measured for the porous silica AR coatings on silica substrates are given in Table 1. With 1000 shots applied at 25 Hz to each test site, the thresholds were about 20 J/cm². Within experimental error, thresholds were sharply defined for each sample; fluences below threshold did not cause damage and those above threshold did. Damage consisted of small pits randomly distributed in the irradiated area. Only one or two pits were produced at threshold, and the spatial density of pits increased as the fluence was increased above threshold. Since the area irradiated at 20 J/cm² was 0.226 mm², this indicates that the spatial density of the defects responsible for damage at 20 J/cm² was $\sim 4.4 \text{ mm}^{-2}$.

Because only a few small areas on each sample were tested, one cannot determine from this data whether the coatings contained other widely spaced defects with lower thresholds. The performance of these porous coatings in the Nova laser suggest, however, that the thresholds of coatings measured with mm-diameter beams are probably the same as would be measured with much larger beams. The 46-cm diameter input lenses in the final spatial filter in each arm of Nova are made of fused silica and coated with porous silica films. These lenses are surviving irradiation by 1-ns 1064-nm pulses with spatially averaged fluences of 5-7 J/cm² and local fluence variations of 30-50%. The irradiated area is 1330 cm². In tests with 2-mm diameter 1064-nm beams, we found the median threshold to be 11 J/cm². This correlation between small-spot and large-spot 1064-nm thresholds for these coatings and the consistency of the results observed in our 350-nm tests of several samples give reason to believe that the porous silica coating can withstand about 20 J/cm² applied to areas larger than that of our test beam.

Table 1. Damage thresholds of porous silica coatings on fused silica substrates. Thresholds were measured with 25-ns, 351-nm pulses at 25 Hz.

Sample	Coating Solution	Single-Pulse Damage Thresholds, J/cm ²
3823	Ethanol, aged 11 months	22 \pm 3.5
4019	"	24 \pm 4.0
3818	"	23 \pm 4.0
3433	"	17 \pm 3.0
3328	methanol, freshly prepared	18 \pm 3.0
3368	"	23 \pm 4.0
3369	"	23 \pm 4.0
3330	"	18 \pm 3.0

Our results for solution deposited coatings can be compared with thresholds for coatings made by physical vapor deposition (PVD). Tests at 350-nm of PVD coatings have been made for several years, although single laser pulses were used in most of these studies. Single-shot thresholds of 2-3 J/cm² were observed in 17-ps tests of single layers of ZrO₂, SiO₂ and HfO₂.⁴ Measurements made with single 27-ns 355-nm pulses gave thresholds of 5.9, 7.1 and 9.1 J/cm² for single-layer films of respectively, Al₂O₃, ZrO₂ and ThF₄, a value $> 38 \text{ J/cm}^2$ for a film of NaF, and thresholds of 4.9 and 12.2 J/cm² for multilayer reflectors made of ThO₂/SiO₂ and Al₂O₃/NaF.⁵ In single-layer PVD films with optical thicknesses of 250 nm and 125 nm, respectively, thresholds measured with 355-nm 15-ns pulses were 5 and 19 J/cm² for CaF₂, 12 and 15 J/cm² in SiO₂, 9 and 11 J/cm² in ThF₄, 5 and 6 J/cm² in MgF₂, 6 and 6 J/cm² in Al₂O₃, 4 and 4 J/cm² in MgO, 4 and 3 J/cm² in HfO₂, and 2 and 3 J/cm² in ZrO₂.⁶ Single-shot thresholds that typically were 2-3 J/cm² were measured in several experiments using 350-nm pulses with durations of 0.6-1.0 ns.⁷⁻¹⁰ Coatings tested in those studies were PVD multilayer AR and HR coatings made using a total of 16 different pairings of high-index and low-index materials which included both oxides and fluorides. The largest thresholds reported were 4-5 J/cm².

Fewer multi-shot thresholds measured with repetitively pulsed lasers are available. An $\text{Al}_2\text{O}_3/\text{SiO}_2$ multilayer reflector¹¹ tested with 10-ns, 351-nm XeF pulses at 35 Hz damaged at 8.5 J/cm^2 and thresholds ranging up to 8 J/cm^2 have been measured under the same test conditions on PVD antireflective coatings.¹² The antireflective coating with threshold of 8 J/cm^2 was made of $\text{Al}_2\text{O}_3/\text{Na}_3\text{AlF}_6$.

Our recently measured thresholds of 20 J/cm^2 for porous silica coatings are, therefore, comparable to the largest thresholds reported for single-layer PVD films and considerably larger than thresholds reported for PVD antireflective coatings. It is important to test these porous silica coatings at higher repetition rates and for many shots to insure that they are capable of sustained operation at high fluences.

4.2 Bare Polished CaF_2

In tests of either two or three samples from each of the three vendors, we applied 1000 shots at 25 Hz to each test site. An additional sample from each vendor was tested at 100 Hz. Although damage was usually more severe at 100 Hz, thresholds did not depend on repetition rate, and did not vary significantly from sample to sample. Therefore, all data taken on samples from a particular vendor were combined in a single graph, see Figs. 3-5. We believe that the severity of damage induced at 100 Hz was caused by applying many additional shots to a damaged area before the experiment could be manually interrupted. Further, the equivalence of thresholds at either 25 or 100 Hz indicates that damage resistance was limited by the single-pulse threshold and not by average power loading. For tests at 100 Hz, the average intensity at threshold was about 1 KW/cm^2 while peak power in the individual pulse was about $4 \times 10^8 \text{ W/cm}^2$. A dependence of damage thresholds on average power must eventually appear if the average loading of the crystals is increased by either improving single-pulse thresholds or increasing the repetition rate.

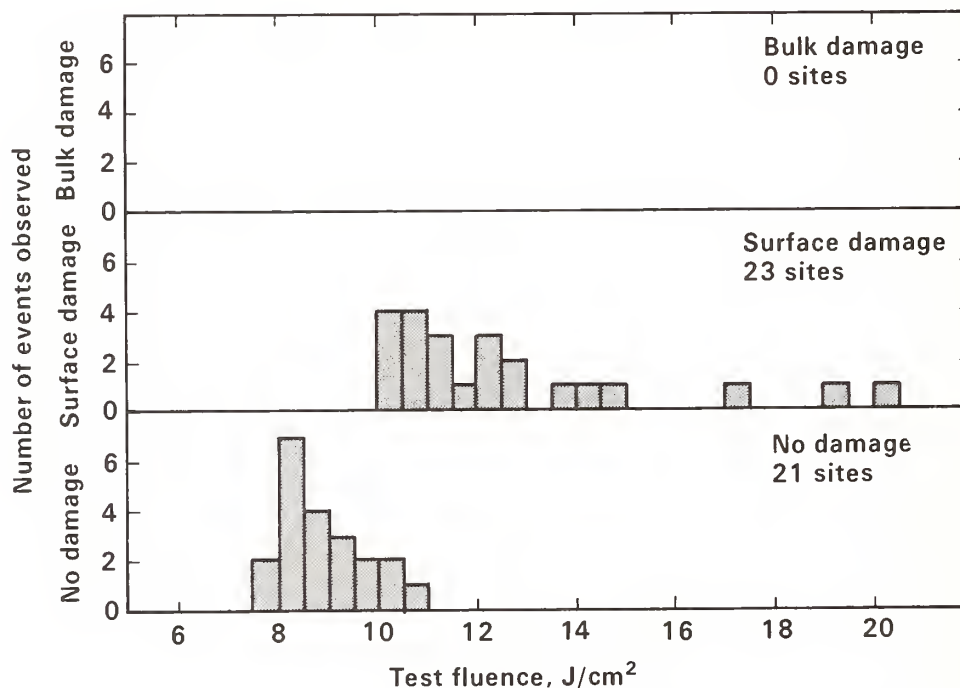


Figure 3: Events observed in tests (25-ns, 350-nm, 25 or 100 Hz) of 44 sites on three bare, polished, UV-grade, CaF_2 crystals.

As is apparent from Fig. 3, the three UV-grade samples had sharply defined surface damage thresholds of about 10 J/cm^2 . At fluences of $10\text{--}14 \text{ J/cm}^2$, damage to these samples consisted of a disturbed area having the rectangular shape of the beam. These disturbed areas had little if any vertical structure, and were more readily visible by visual inspection with intense white-light backlighting than by Nomarski microscopy. This suggests that the damage was an alteration of a surface gel layer that could be eliminated by use of an alternate polishing procedure or removed by etching. Bulk damage was not observed in the UV-grade material.

Thresholds were not sharply defined in the six samples of fluorescence-free CaF_2 , and bulk damage occurred at several test sites (see Figs. 4 and 5). The lack of definition in both surface and bulk thresholds indicates that damages were caused by defects separated by distances comparable to the beam dimension. If tested with a larger beam, the thresholds of the fluorescence-free samples would not exceed 10 J/cm^2 , the least fluence at which damage was observed with the small test beam.

Surface damage in the fluorescence-free samples always consisted of cleavage-like fractures that sometimes covered an area larger than that of the test beam. The shallow beam imprint type of damage was not observed.

From the study of eleven samples we conclude that the threshold for commercially available CaF_2 is about 10 J/cm^2 . Similar tests of UV-grade CaF_2 with 10-ns 355-nm pulses incident at 35 Hz produced surface damage thresholds of $5\text{--}12 \text{ J/cm}^2$.¹³ The fluorescence-free CaF_2 material that we tested was not superior to the UV-grade material for 350-nm applications. However, the observation of bulk damage only in the fluorescence-free crystals could be a misleading result obtained by testing only eleven samples. Elimination of fluorescence induced by UV irradiation was supposedly obtained by improving the purity of the starting materials and growth process. We see no obvious reason why that should lead to production of material with reduced bulk damage thresholds, and believe that testing of many samples from several boules would be required to clearly establish a difference in the bulk quality of the two types of CaF_2 crystals.

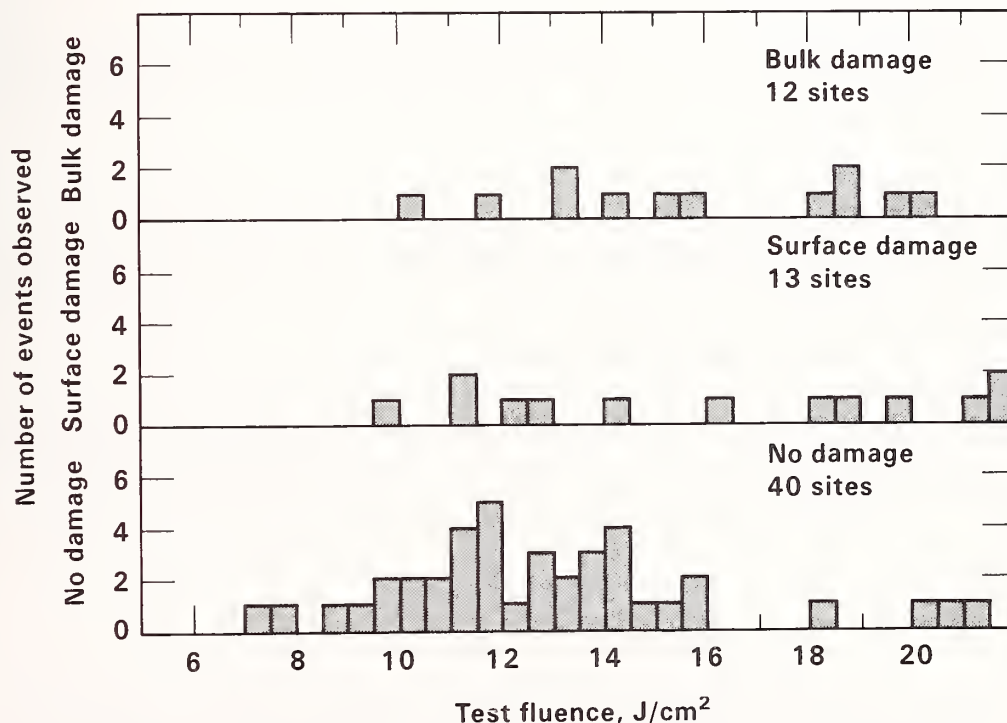


Figure 4: Events observed in tests (25-ns , 350-nm , 25 or 100 Hz) of 65 sites on four bare, polished, fluorescence-free CaF_2 crystals from vendor A.

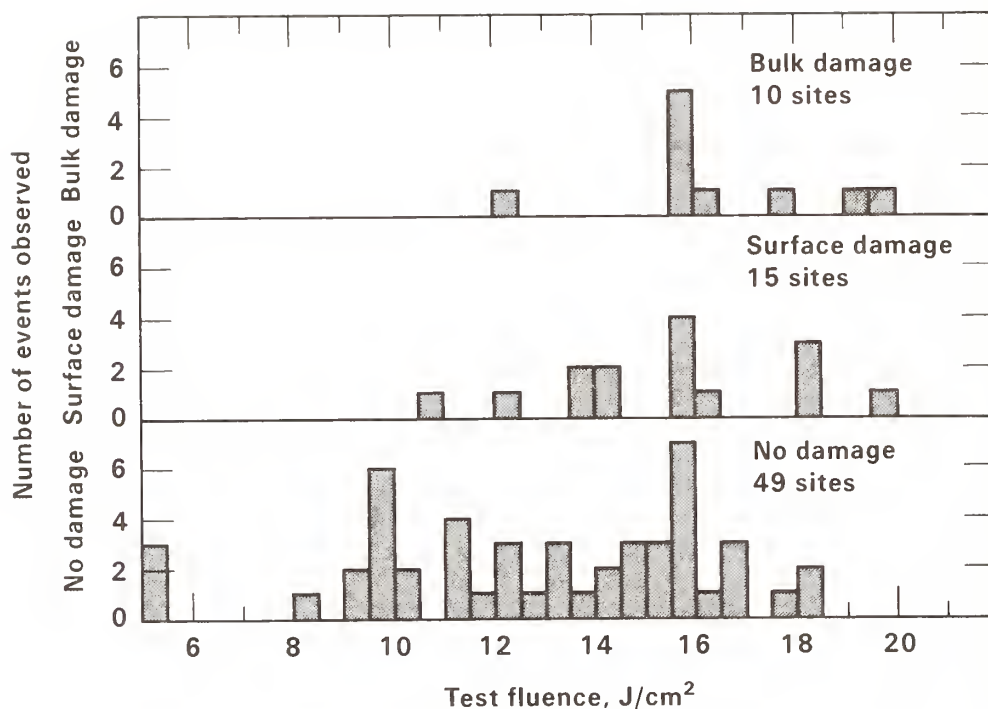


Figure 5: Events observed in tests (25-ns, 350-nm, 25 or 100 Hz) of 74 sites on four bare, polished, fluorescence-free CaF₂ crystals from vendor B.

5. Summary

Porous silica AR films deposited on fused silica substrates had thresholds of 17-23 J/cm² when irradiated by 1000 shot sequences of 350-nm, 25-ns pulses at 25 Hz. These thresholds are about twice as large as the best values previously reported. Because the 1064-nm thresholds measured with 2-mm diameter beams are comparable to the fluence levels at which the coatings survive in large area 1064-nm beams, we believe that 350-nm thresholds of about 20 J/cm² can be realized on areas much larger than our 350-nm test beam.

Bare polished surfaces of commercially available CaF₂ crystals damaged at about 10 J/cm², and the test results indicated that surface damage thresholds might be improved by at least 50% through use of polishing procedures that eliminate gel layers. However, the bulk thresholds of some crystals does not exceed 10 J/cm², so improvements of surface quality may not improve the capability of this material to operate at high fluence. Unless bare CaF₂ can be improved, thresholds of porous silica coatings on CaF₂ substrates will be limited by the performance of the substrate.

We are grateful to several employees of LLNL for assistance in establishing the new XeF damage laboratory. Design and installation of electronic controls for the experiment were supervised by S. E. Peluso and the mechanical aspects of upgrading the building and installing the experiment were supervised by R. E. Wilder. Much of the installation of electronic and mechanical apparatus was done by L. R. Truelsen and G. VonVille.

6. References

- [1] I. M. Thomas, J. G. Wilder, W. H. Lowdermilk and M. C. Staggs, "High damage threshold porous silica antireflective coating", Lawrence Livermore National Laboratory report UCRL-91428, April 25, 1985; to be published in the Proceedings of the 1984 Conference on Laser-Induced Damage in Optical Materials.
- [2] J. F. Holzrichter, "High-power solid-state lasers", Nature, Vol. 316, No. 6026, 25-31, July 1985.
- [3] The zoom magnification system with aspheric lenses was designed by Lynn Seppala of LLNL.
- [4] B. E. Newnam and D. H. Gill, "Spectral dependence of damage resistance of refractory oxide optical coatings", in Laser-Induced Damage in Optical Coatings: 1976, NBS Spec. Publ. 462, pp. 292, issued December 1976.
- [5] B. E. Newnam and D. H. Gill, "Ultraviolet damage resistance of laser coatings", in Laser-Induced Damage in Optical Materials: 1978, NBS Spec. Publ. 541, pp. 190, issued December 1978.
- [6] T. W. Walker, A. H. Guenther, C. G. Fry and P. Nielson, "Pulsed damage thresholds of fluoride and oxide thin films from 0.26 μm to 1.06 μm ", in Laser-Induced Damage in Optical Materials: 1979, NBS Spec. Publ. 568, pp. 405, issued July 1980.
- [7] J. A. Abate and R. Roides, "Laser damage thresholds of optical coatings at 351 nm", in Laser-Induced Damage in Optical Materials: 1982, NBS Spec. Publ. 669, pp. 282, issued January 1984.
- [8] C. K. Carniglia, T. Tuttle Hart, F. Rainer and M. C. Staggs, "Recent damage results on high reflector coatings at 355 nm", to be published in the Proceedings of the 1983 conference on Laser-Induced Damage in Optical Materials.
- [9] T. Tuttle Hart, C. K. Carniglia, F. Rainer and M. C. Staggs, "Recent damage results for antireflection coatings at 355 nm", to be published in the Proceedings of the 1984 conference on Laser-Induced Damage in Optical Materials.
- [10] T. Tuttle Hart, C. K. Carniglia and M. C. Staggs, "Effect of overcoats on 351 nm reflectors", to be published in the Proceedings of the 1984 conference on Laser-Induced Damage in Optical Materials.
- [11] S. R. Foltyn, L. J. Jolin and B. E. Newnam, "Progress in ultraviolet damage testing at Los Alamos", in Laser-Induced Damage in Optical Materials: 1982, NBS Spec. Publ. 669, pp. 266, issued January 1984.
- [12] S. R. Foltyn, Los Alamos National Laboratory, private correspondence.
- [13] S. R. Foltyn, L. J. Jolin, "Catastrophic versus microscopic damage: applicability of laboratory measurements to real systems", to be published in the Proceedings of the 1983 conference on Laser-Induced Damage in Optical Materials.

DISCLAIMER

This document was prepared as an account of work sponsored by an agency of the United States Government. Neither the United States Government nor the University of California nor any of their employees, makes any warranty, express or implied, or assumes any legal liability or responsibility for the accuracy, completeness, or usefulness of any information, apparatus, product, or process disclosed, or represents that its use would not infringe privately owned rights. Reference herein to any specific commercial products, process, or service by trade name, trademark, manufacturer, or otherwise, does not necessarily constitute or imply its endorsement, recommendation, or favoring by the United States Government or the University of California. The views and opinions of authors expressed herein do not necessarily state or reflect those of the United States Government thereof, and shall not be used for advertising or product endorsement purposes.

Study of Temporal and Spatial Intensity Variations and
Intracavity Damage Thresholds of Alexandrite Lasers

D.J. Harter, H. Rainee*, and A.J. Heiney

Allied-Signal Corporation
7 Powder Horn Drive
Mt. Bethel, NJ 07060

The energy densities which can be obtained in a laser resonator before optical damage occurs are usually much lower than the optical damage thresholds measured in extracavity laser experiments. We have measured intracavity optical damage thresholds in an alexandrite laser operating in both single- and multi-transverse mode and found the multi-transverse mode laser has a much lower damage threshold. We studied the temporal and spatial variations of a multi-transverse mode laser and found intensity hot spots which may be an important factor in the difference in the intracavity damage thresholds.

Key Words: alexandrite; antireflection coatings; intracavity optics; laser damage; multimode laser; surface damage.

1. Introduction

Alexandrite is a tunable solid state laser material[1] which has a relatively low emission cross section and therefore a large saturation energy. Thus, to obtain high extraction efficiency from alexandrite, high intracavity fluences are required. Also, because of the low emission cross section and the long excited state lifetime, alexandrite lasers do not experience significant loss from amplified spontaneous emission (ASE). Thus, optical damage is one of the most important limitations on the performance of alexandrite lasers.

Single shot damage measurements of alexandrite have shown that the crystal has a very high bulk damage threshold (1100-4300 J/cm²). With an acid assisted surface polish, the surface damage threshold can approach the damage threshold of the bulk material while mechanically polished surfaces with AR coating have damage thresholds between 50 and 1300 J/cm²[2]. However, in practice, intracavity damage thresholds are much lower than measured damage thresholds and seem to vary widely for different resonator designs. In this paper we describe experiments in which intracavity energy densities were measured accurately just before optical damage. In addition, experiments which show the temporal variations of the intensity profile for a multi-transverse mode laser are described. The temporal variations in the intensity profile appears to contribute to the variation of the intracavity damage threshold for different resonator designs. In addition to knowing the intracavity damage threshold for a specific laser design for a few laser shots, it is necessary to know the damage threshold for longer term operation. The experimental setup for measuring laser parameters preceding optical damage for long operation times will be described.

2. Intracavity Energy Density Measurements

Figure 1 illustrates the experimental setup for measuring the intracavity energy density distribution of the laser beam before optical damage. The energy density distribution is measured at the thin film polarizer since this is the weakest element in the cavity and damages first. Since we are imaging the beam, the energy density at the location where damage occurs can be measured. We find that the beam profiles vary significantly with the direction of passage through the resonator. This is caused by an aperture for limiting the laser to TEM₀₀ operation. The laser beam which has exited from the aperture has near-field Fresnel rings while the beam which has propagated a longer distance appears to be the far field diffraction pattern of an aperture (Airy pattern). The profiles of the beam propagating in the two directions are shown in figure 2. It is interesting to note that in spite of the fact that the total energy in the beam reflected from the output coupler is 37% less than the energy of the other beam, it has a higher peak energy due to its profile. The images of the beam profiles from the two directions are superimposed in order to measure the intracavity energy density at the polarizer. Figure 3 shows the energy density profile of the laser operating in a single transverse mode just before damage. The peak intracavity energy density at the thin film polarizer before damage occurred was measured to be 35 J/cm². The laser resonator is designed so that the beam is smaller on the laser rod. Therefore, the energy density is greater on the rod surface than the polarizer. This measurement was also performed with the laser running in multi-transverse mode; the energy density profile is shown in figure 4. The peak intracavity energy density was 18 J/cm² before damage. We find that the damage threshold

* Present address: Philon Corp. 641 6th Ave. NY, NY 10011

is lower for multi-transverse mode operation compared to single transverse mode. We believe this is due to temporal variations in the beam profile. Measurements of the temporal variation in the intracavity energy profile will now be discussed.

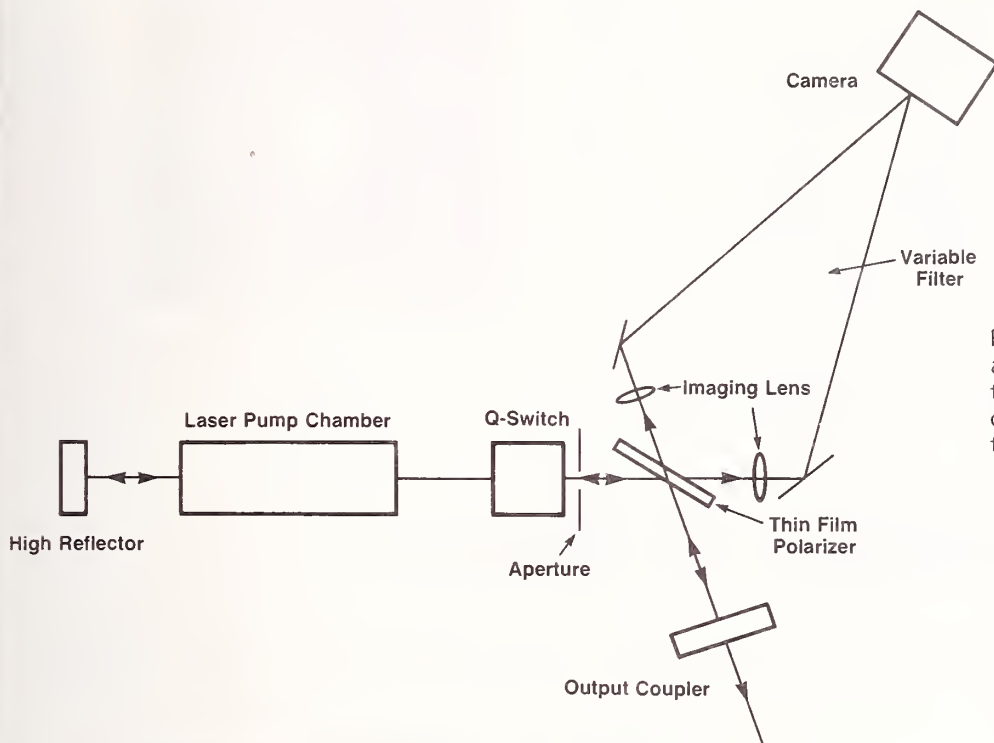


Figure 1: Experimental apparatus for measuring the intracavity energy density profile at the thin film polarizer.

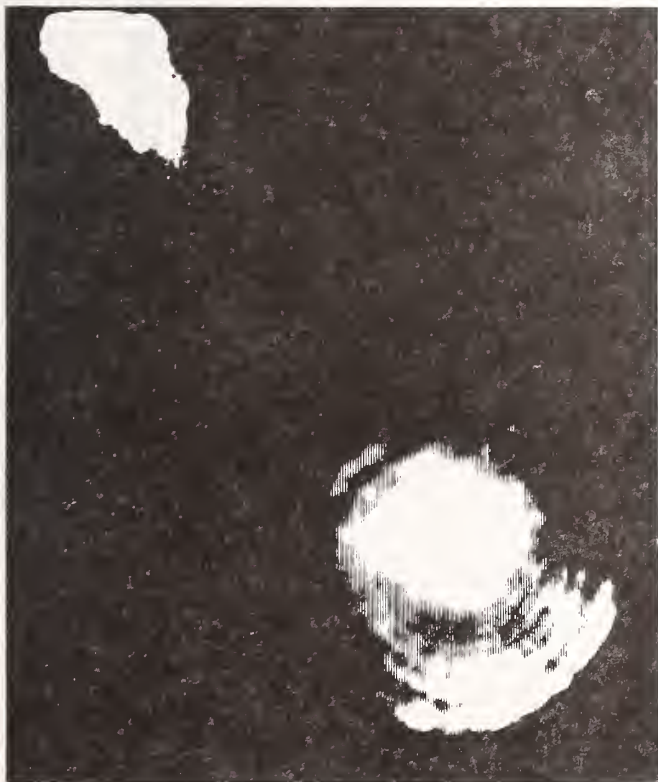


Figure 2: The beam profile at the polarizer from the two directions. The upper beam profile is right out of the aperture and has the near field diffraction pattern of the aperture (Fresnel pattern). The lower pattern has propagated farther and is the far field diffraction of the aperture (Airy pattern).

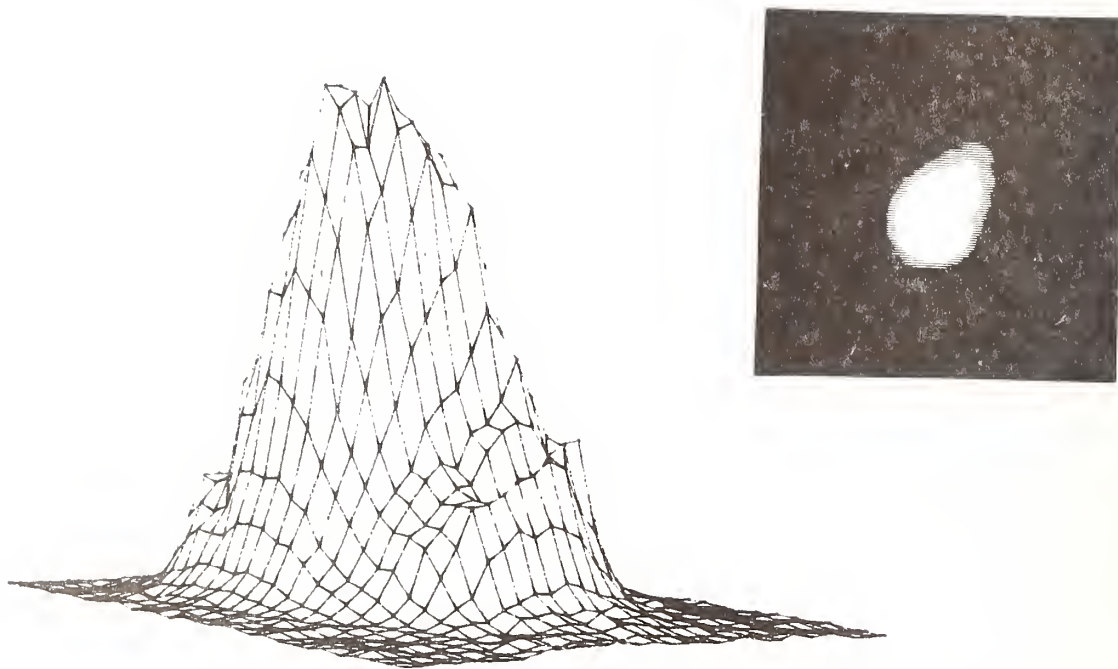


Figure 3: Photograph and three-dimensional plot of the beam profile at the thin film polarizer for a single transverse mode laser. The peak intracavity energy density before damage of the thin film polarizer was 35 J/cm^2 with a 40 ns long pulse.

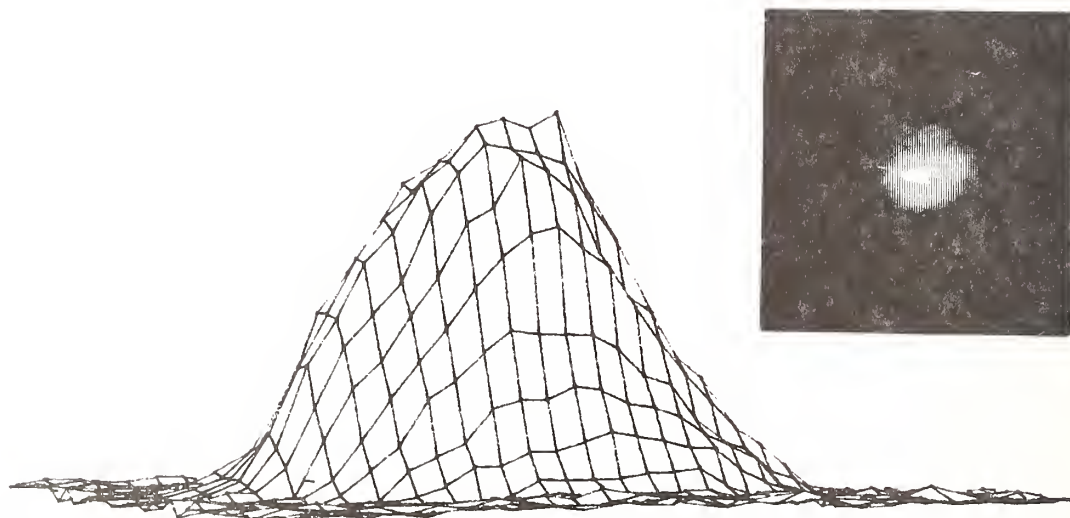


Figure 4: Photograph and three-dimensional plot of the beam profile at the thin film polarizer for a multi-transverse mode laser. The peak intracavity energy density before damage of the thin film polarizer was 18 J/cm^2 with a 40 ns long pulse.

3. Temporal Intensity Variations in Multi-transverse Mode Beam Profiles

The energy density profile for a multi-transverse mode beam as shown in figure 4 is relatively smooth, however, this profile is integrated in time. In this experiment we will study the change in the intensity profile during the temporal evolution of the laser pulse. Figure 5 shows the experimental setup. The beam profile at the output coupler of a pulsed, Q-switched alexandrite laser is imaged onto a camera. In the optical path we place a Pockels cell which transmits light for a 4 nanosecond duration. This device is triggered by the leading edge of the Q-switched pulse and can be delayed with respect to the laser pulse. The temporal profile of a 4 nanosecond slice

from the laser pulse is shown in figure 5b. Figure 5c shows the 4 nanosecond pulse and its temporal relationship with the laser pulse. This profile was obtained by slightly misaligning the electro-optical device to allow the transmission of a portion of the laser pulse. In figure 6 a series of images of the beam profile is shown for various times in the laser pulse; the integrated pulse profile is shown as well. As the laser pulse develops, it starts lasing in a low order mode which has the lowest diffraction loss. At the end of the pulse, the laser is lasing in higher order modes. The intensity profile has hot spots which are not observed in the smooth energy profile shown in figure 4. Qualitatively, we find that the extent of the irregularity in the intensity profile is dependent on the curvature of the resonator mirrors. The temporal variation of the intensity profile most likely contributes to the lower energy damage threshold for multi-transverse mode operation compared to single transverse mode operation and also the variation of the energy damage threshold for different resonator designs for alexandrite lasers. This hypothesis is further supported from experience with a resonator which favored single transverse mode operation. When this resonator was operated in multi-transverse modes, a double Q-switching technique was needed to prevent damage from fast buildup of low order modes.[3]

The previously described experiment raises some additional questions. Does the temporal variation of the intensity profile differ from shot to shot? Another question is how much greater is the intensity in one of the hot spots compared to the average intensity of the pulse? Another experimental method to measure the temporal variation of the intensity at a single point in the laser beam profile is shown in figure 7a. A pinhole is placed in the image plane of the beam profile at the output coupler. A fast photodiode is placed behind the pinhole and measures the temporal variation at that location in the beam. Figure 7b shows the temporal profile of the entire beam. Figure 7c shows the temporal behavior of the pulse at two different spots in the beam. At these two locations the temporal behavior is quite different and the peak intensity is greater than what is expected with the entire pulse profile. The temporal scales are the same in figures 7b-c. We found that the temporal profile at a specific spot in the beam was quite reproducible from shot to shot. The intensity in a hot spot was only about 2X greater than what the average intensity would be at that spot. However, during these experiments the laser was operated at a power much lower than powers when damage occurred. Further experiments close to the damage threshold of the laser would be of interest.

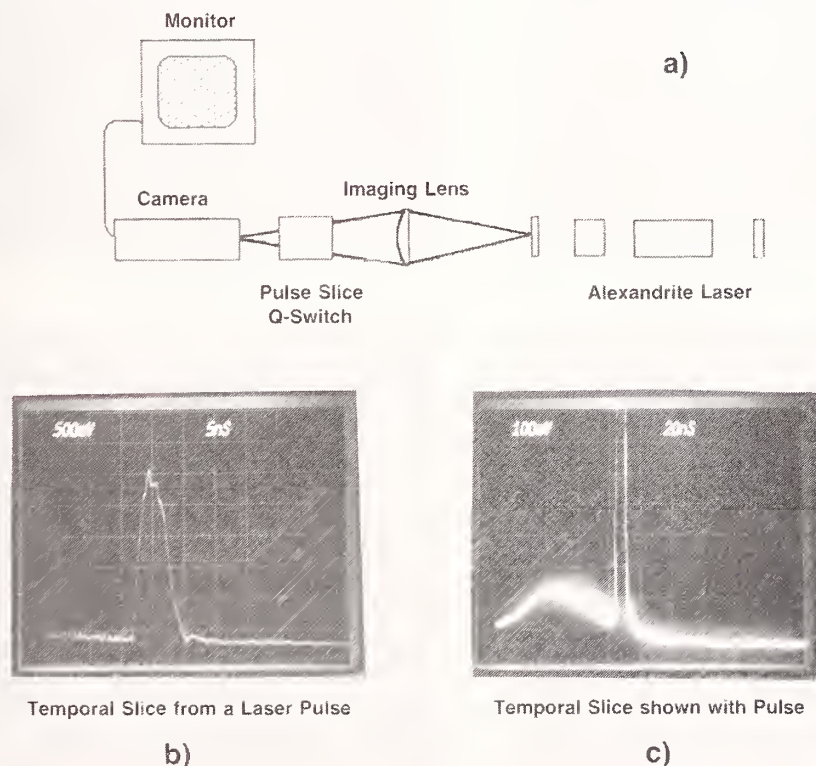
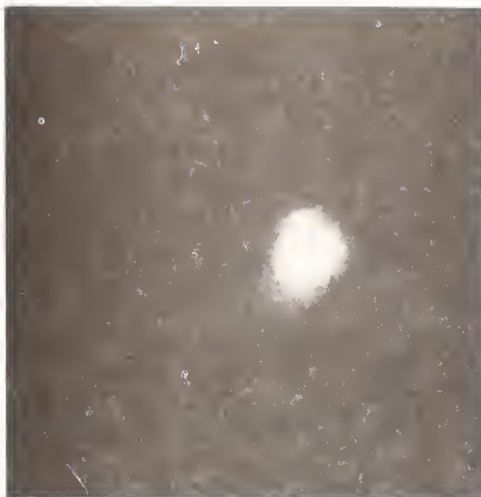


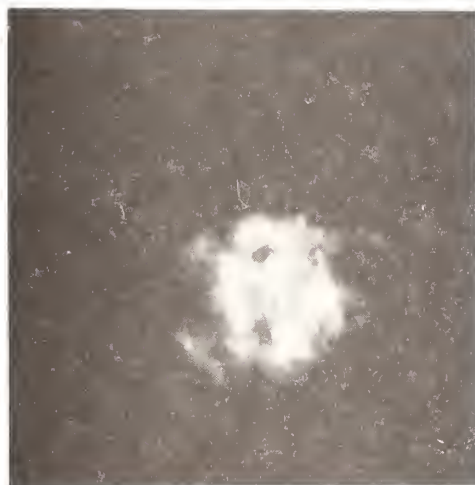
Figure 5a: Experimental apparatus for measuring the temporal evolution of the spatial mode pattern of a multi-transverse mode, pulsed alexandrite laser. b) 4 ns temporal sample from a laser pulse. c) short temporal sample shown with 50 ns Q-switched pulse which transmitted through the pulse slice Q-switch by misaligning this electro-optic device.



Beginning Of Laser Pulse



1/4 Through Pulse



Peak Of The Pulse



3/4 Through Pulse



Spatial Profile Integrated Over Entire Laser Pulse

Figure 6: Series of 4 ns temporal samples from the 50 ns Q-switched pulse. At the beginning of the pulse lasing starts in a low order mode. Near the end of the pulse lasing occurs in higher order modes. Structure in the pulse is not observed in the pulse energy profile.

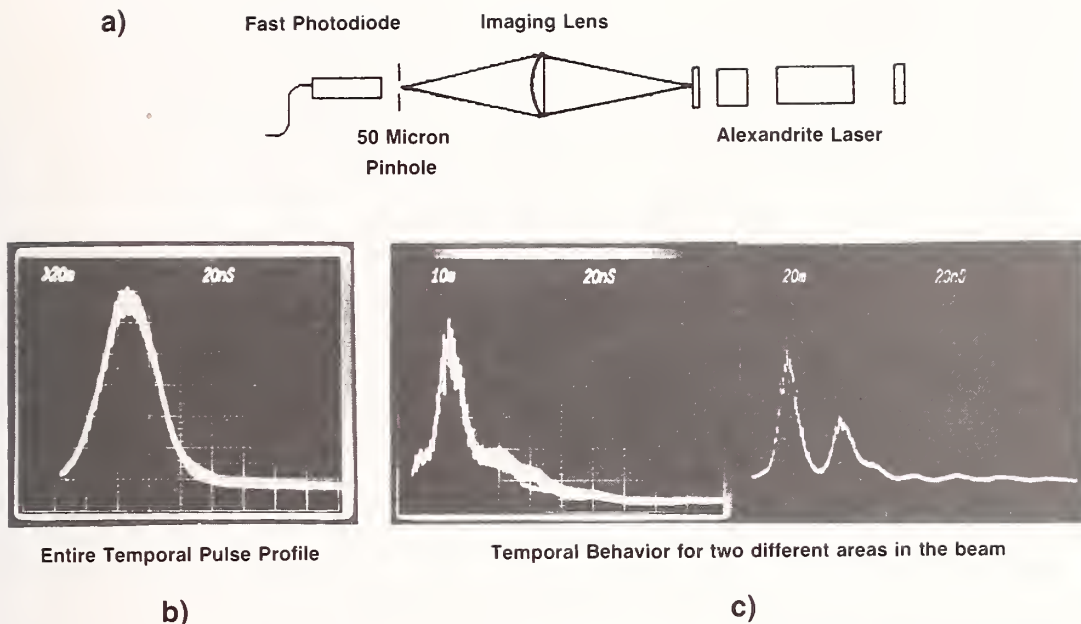


Figure 7a: Experimental apparatus for measuring the temporal behavior of different spatial areas of the laser beam. b) Entire pulse profile. c) and d) Temporal behavior from two different areas of the beam.

4. Computer Controlled Life Time Experiments

Thus far we have discussed our results in measuring intracavity damage thresholds for a few repetitive shots. What is of greater interest is the intracavity energy densities at which the laser can run reliably. Since this will require the accumulation of significant amounts of data, we have set up the computer controller laser lifetime experiment shown in figure 8. The temporal pulse width, spectral linewidth, the wavelength, the pulse energy, and the spatial beam profile are calculated and stored in real time at 10 Hz. The waveforms are displayed every third shot. Figure 9 shows a typical output of the screen.

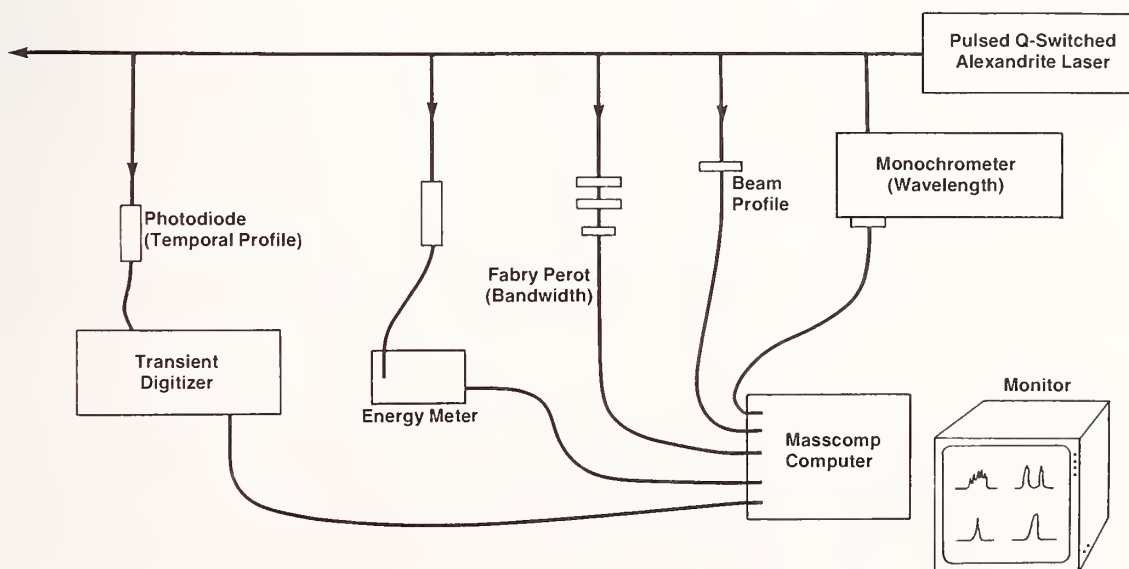


Figure 8: Experimental apparatus for computer controlled lifetime experiments.

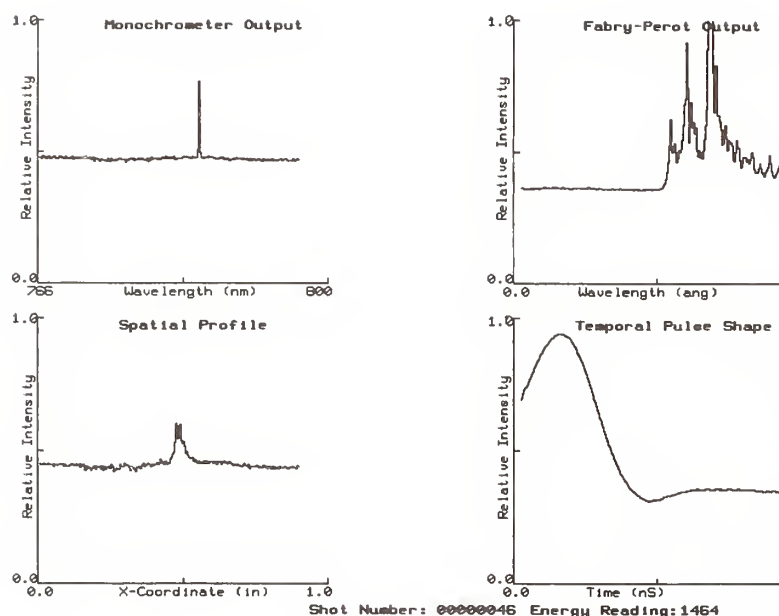


Figure 9: Computer display of laser parameters during lifetime experiment.

5. Conclusion

In conclusion, we have measured peak intracavity energy densities where the damage threshold of the AR coated rod surface is greater than 35 J/cm^2 for a single transverse mode pulse. This was the damage threshold for the intracavity thin film polarizer and during these experiments rod damage did not occur. This fluence is still a factor of 3-10X lower than the damage thresholds measured in single shot measurements on coated surfaces. We find the damage threshold for multi-transverse mode operation to be about a factor of two (18 J/cm^2) lower than for single transverse mode operation. We attribute the lower damage threshold for multi-transverse mode operation partially to the temporal fluctuations in the intensity profile. Even in multi-transverse mode operation the optical damage threshold is greater than the saturation energy of alexandrite at elevated temperatures. At 150°C the saturation energy is between $11\text{-}15 \text{ J/cm}^2$ for the $710\text{-}785 \text{ nm}$ wavelength region.

Optical damage has been the chief limitation of the extraction efficiency for alexandrite lasers. However, as important as having a good correlation between single shot damage thresholds and intracavity damage thresholds, is to have good correlation between intracavity damage thresholds and threshold for long term operation of the laser. We have described the experimental configuration for these measurements.

We wish to thank J. Barrett, H. Samelson, and J. Walling for encouragement and helpful discussions and also K. Whittle and G. Shipp for their technical assistance.

6. References

1. J.C. Walling, O.T. Peterson, H.P. Jenssen, R.C. Morris, and E.W. O'Dell, "Tunable Alexandrite Lasers," IEEE J. of Quantum Electron., QE-16, 1302, (1980).
2. Report to Allied Corporation (unpublished) by S. Seital, Naval Weapons Laboratory, Unpublished results of J.C. Walling and of D.J. Harter, and S.A. Zamor. Some of the uncertainty in the data is due to differences in temporal pulse lengths, damage site spot size, and the wavelength of the laser used in the three different damage threshold experiments.
3. R.C. Sam, R.W. Rappoport, and M.L. Shand, "Design and Performance of a 125 Hz, 50 W Alexandrite Laser," in Proc. Southwest Conf. Opt., Albuquerque, NM, Mar. 4-8, 1985.

Investigation of Metal Coatings for the Free Electron Laser*

Marion L. Scott, Paul N. Arendt, Robert W. Springer,
Richard C. Cordi, and William J. McCreary

Materials Science & Technology Division
Los Alamos National Laboratory
Los Alamos, NM 87545

We are investigating the deposition and characteristics of metal coatings for use in environments such as the Free Electron Laser where the radiation resistance of metal coatings could prove to be of great benefit. We have concentrated our initial efforts on silver laminate coatings due to the high reflectance of silver at 1 micron wavelength. Our initial laminate coatings have utilized thin layers of titanium oxide to break up the columnar structure of the silver during electron-beam deposition on fused silica substrates. Our initial results on equal coating thickness samples indicate an improvement in damage threshold that ranges from 1.07 to 1.71 at 351 nm.

Key Words: metal coatings; silver coatings; coating structure; laminate coatings; laser damage

1. Introduction

The Free Electron Laser is a hostile environment for the optical coatings typically used in a laser cavity. Radiation, such as x-rays, gamma rays, neutrons, and scattered electrons are present in the laser cavity due to collisions of the high energy electrons from the accelerator with magnets, walls, etc. Dielectric materials used in multilayer reflectors are sensitive to this radiation environment and the performance of a multilayer dielectric coating as well as its laser damage threshold can be quickly degraded in response to these radiations.

Previous work at Los Alamos on aluminum films indicate that the physical properties of aluminum films could be improved by interrupting the growth of columns in the aluminum films with pulses of oxygen forming thin oxide layers periodically during the aluminum deposition [1,2,3,4]. Similar work was conducted at Los Alamos with tantalum films and pulsed acetylene gas [5]. A TEM photomicrograph of one of these aluminum laminate structures is shown in figure 1. The yield strength of these aluminum films increased 20 fold from 20 MPa to 400 MPa. In addition, unbacked cylindrical aluminum films only 2,000 Angstroms thick were deposited for the Inertial Confinement Fusion Program [6].

This previous work on aluminum films encouraged us to look for a similar technique to use with the silver films. One difficulty in extending this technique to silver is that the silver film does not readily oxidize in the presence of oxygen. Thus, we were led to depositing a thin layer of another material to interrupt the structure of the silver films. The material we chose to use in this laminate structure is titanium oxide. A thin layer (50 Angstroms) of non-stoichiometric titanium oxide was deposited periodically during the deposition of silver films on fused silica substrates to investigate its effectiveness in improving laser damage threshold (see figure 2).

2. Film Analysis

An Auger depth profile of one of our first silver laminate films is shown in figure 3. The titanium oxide layers are well defined in this structure, though the oxide layers are only 50 to 85 Angstroms thick. A SEM photomicrograph of the cross-section through this laminate structure lacked sufficient resolution to see structure effects in these films. TEM photos have not yet been obtained. SEM photos of the surfaces of silver laminate films and typical silver films indicate that the laminate surfaces are smoother (see figures 4 and 5).

* This work was performed under DOE contract W-7405-ENG-36.

3. Film Fabrication

We prepared our silver films using electron beam deposition in a high vacuum chamber. The deposition rate of the silver layers was relatively high at 25 Angstroms/sec. Thin layers of titanium metal were evaporated periodically and this thin layer was immediately oxidized by introducing a pulse of oxygen into the chamber. All of the samples to be reported here were deposited on highly polished fused silica substrates, 5.08 cm in diameter and 0.995 cm thick.

Two samples each of four coating designs were deposited for this study. The first coating design is a 2,000 Angstrom thick silver film reference, deposited on a 100 Angstrom layer of chromium. The second design is a four layer laminate beginning with a 50 Angstrom titanium oxide layer, followed by a 1,500 Angstrom silver layer. This layer pair is repeated to complete the four layers. The third coating design is similar to the second, except that there are 12 layers, or six pair of titanium oxide and silver layers, instead of two pair. The fourth coating design is a 9,200 Angstrom thick silver reference film deposited on a 100 Angstrom chromium binder layer. This fourth design is a silver reference of equal thickness to the six pair laminate of the third design. Comparison of equal thickness samples is required due to the thermal insulation of the substrate.

4. Surface Roughness Measurements

Surface roughness measurements were performed on these silver samples using a Wyco optical heterodyne profilometer. This non-contact method of determining the microroughness of an optical surface will not affect the subsequent laser damage threshold measurements. The results of these measurements on our eight samples are given in table 1. The thin samples appear to be somewhat rougher than the thicker samples, however, all of the samples are less than nine Angstroms rms along measurement lengths of 1.2 mm.

Table 1. Silver film surface roughness measurements

Sample #	Design	RMS Roughness (Å)
1	100Å Cr/2,000Å Ag	8.4
2	100Å Cr/2,000Å Ag	7.9
3	[50Å TiO _x /1,500Å Ag]*2	7.5
4	[50Å TiO _x /1,500Å Ag]*2	7.7
5	[50Å TiO _x /1,500Å Ag]*6	6.3
6	[50Å TiO _x /1,500Å Ag]*6	5.1
7	100Å Cr/9,200Å Ag	5.9
8	100Å Cr/9,200Å Ag	6.7

5. Reflectance Measurements at 351 nm

Reflectance measurements were made on the eight samples using a W-V attachment on a spectrophotometer from 300 nm to 500 nm. These spectrophotometer measurements are shown in figures 6 to 9. These spectral traces show the emergence of the well known surface plasmon resonance in silver (at 345 nm), particularly in the thicker samples. Since the wavelength of the laser performing the damage tests conducted on these samples is 351 nm, the reflectance values at this wavelength have been summarized in table 2. The silver film absorption (1-R) varies between 18% and 36% in these samples due to the variation in the surface plasmon coupling with film thickness. Surface plasmon coupling variation with surface roughness is well known, but the variation in coupling with thickness is not explainable on this basis.

Table 2. Silver film reflectance measurements at 351 nm

Sample #	Design	Reflectance (%)
1	100Å Cr/2,000Å Ag	77.8
2	100Å Cr/2,000Å Ag	77.8
3	[50Å TiOx/1,500Å Ag]*2	76.0
4	[50Å TiOx/1,500Å Ag]*2	82.2
5	[50Å TiOx/1,500Å Ag]*6	66.6
6	[50Å TiOx/1,500Å Ag]*6	72.5
7	100Å Cr/9,200Å Ag	68.2
8	100Å Cr/9,200Å Ag	64.2

6. Laser Damage Threshold Measurements at 351 nm

Laser damage tests of these samples were conducted at Los Alamos in Steve Foltyn's XeF (351 nm) laser damage laboratory by John Jolin. The absolute laser damage thresholds determined in these tests are not important in our investigation. Thus, the high absorption in the coatings and the substrate being a thermal insulator do not alter the conclusions of our tests. The relative damage performance of the laminate coatings when compared to the reference silver coatings of the same thickness illustrates any improvement due to the laminate design. The results of these laser damage tests are given in table 3.

Table 3. Silver film laser damage thresholds at 351 nm

Sample #	Design	Laser Damage Threshold (mJ/cm ²)
1	100Å Cr/2,000Å Ag	50
2	100Å Cr/2,000Å Ag	50
3	[50Å TiOx/1,500Å Ag]*2	80
4	[50Å TiOx/1,500Å Ag]*2	70
5	[50Å TiOx/1,500Å Ag]*6	150
6	[50Å TiOx/1,500Å Ag]*6	240
7	100Å Cr/9,200Å Ag	140
8	100Å Cr/9,200Å Ag	140

The effect of thin film thickness is clearly evident when one compares the damage thresholds of the last two samples to the first two samples. These samples are identical silver films except for thickness. The first two samples have a total metal film thickness of 2,100 Angstroms each and the last two samples have 9,300 Angstroms each. This increase of 4.5 times in coating thickness results in a factor of three increase in laser damage threshold of the silver reference films.

The most significant results of these laser damage tests are seen in comparing the thresholds measured for the six pair laminate structures (samples 5&6) and the equal thickness reference silver films (samples 7&8). The two thick reference samples each measured 140 mJ/cm², whereas the laminate films measured 150 mJ/cm² and 240 mJ/cm² for samples 5 and 6, respectively. Thus, there is an improvement in the damage threshold of a factor of 1.07 to 1.71 for the laminates over the silver reference films. We cannot account for the large discrepancy between the damage thresholds of samples 5 and 6, except to note that these coatings were deposited in two separate coating runs using the same prescription. Perhaps further investigation of these samples will reveal some difference in the coatings.

7. Conclusions

We have concluded from this preliminary investigation of silver films that laminate structures such as the ones used in this study may prove to be useful in increasing the laser damage thresholds of metal films. This technique could also be extended to dielectric thin films for use in multilayer coatings.

The authors would like to express their appreciation to Steve Foltyn and John Jolin of Los Alamos for performing the laser damage measurements quoted in this paper. We would also like to acknowledge Glen Lindholm and Kathleen Padgett of Los Alamos for performing the spectrophotometer reflectance measurements.

8. References

- [1] Springer, R. W.; Catlett, D. S. Rate and pressure dependence of contaminants in vacuum-deposited aluminum films. *J. Vac. Sci. Tech.* 15(2): 210-214; 1978 March-April.
- [2] Springer, R. W.; Catlett, D. S. Structure and mechanical properties of Al/Al_xO_y vacuum deposited laminates. *Thin Solid Films* 54: 197-205; 1978.
- [3] Springer, R. W.; Barthell, B. L.; Rohr, D. Quantitative characterization of high strength aluminum foils vapor deposited on curved surfaces. *J. Vac. Sci. Tech.* 17(1): 437-439; 1980 January-February.
- [4] Springer, R. W.; Hosford, C. D. Characterization of aluminum-aluminum nitride coatings sputter deposited using the pulsed gas process. *J. Vac. Sci. Tech.* 20(3): 462-465; 1982 March.
- [5] Springer, R. W.; Ott, N. L.; Catlett, D. S. Effect of periodic chemical variation on the mechanical properties of Ta foils. *J. Vac. Sci. Tech.* 16(3): 878-881; 1979 May-June.
- [6] Duchane, D. V.; Barthell, B. L. Unbacked cylindrical metal foils of submicron thickness. *Thin Solid Films* 107: 373-378; 1983.

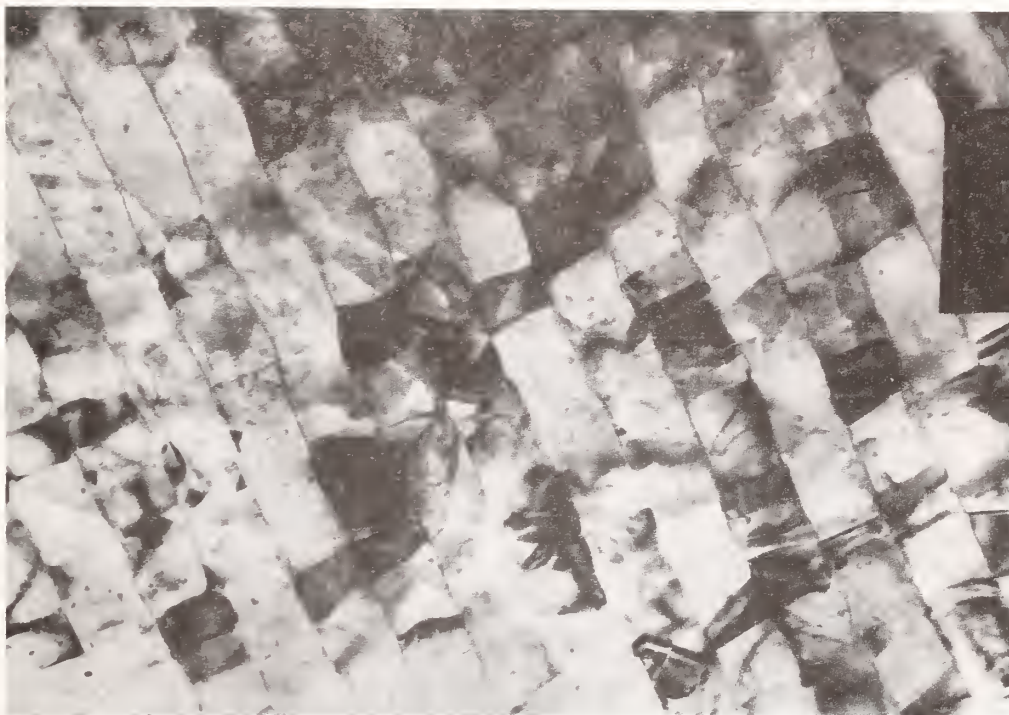


Figure 1. TEM photomicrograph of an aluminum/aluminum oxide laminate film in cross-section. Note the thin oxide layers separating the thick aluminum layers.

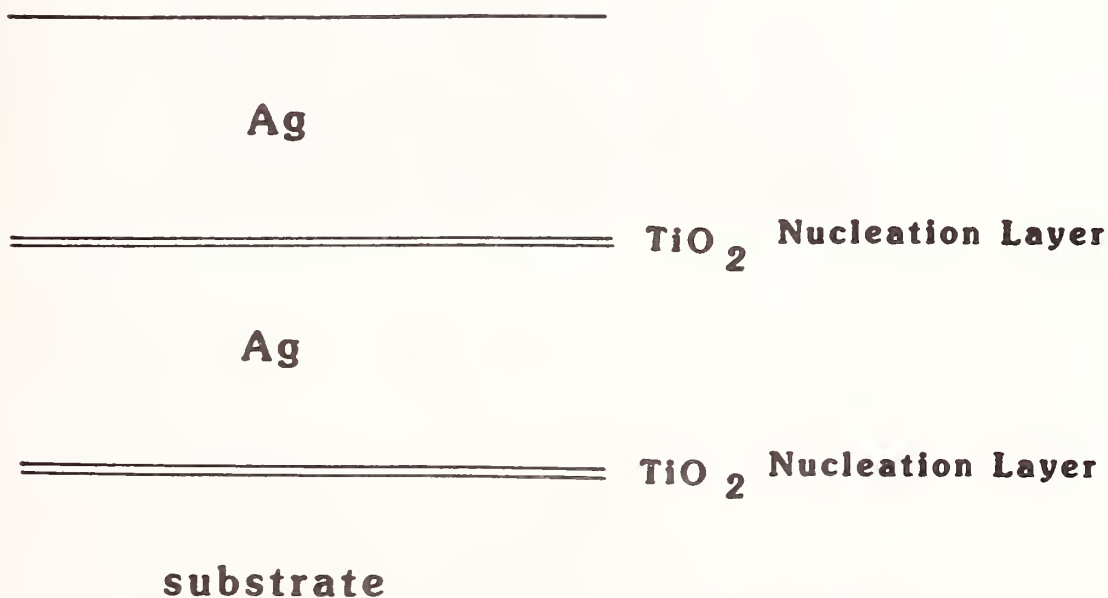


Figure 2. A schematic view of a silver/titanium oxide laminate film with 50 Angstrom titanium oxide layers and 1500 Angstrom silver layers.

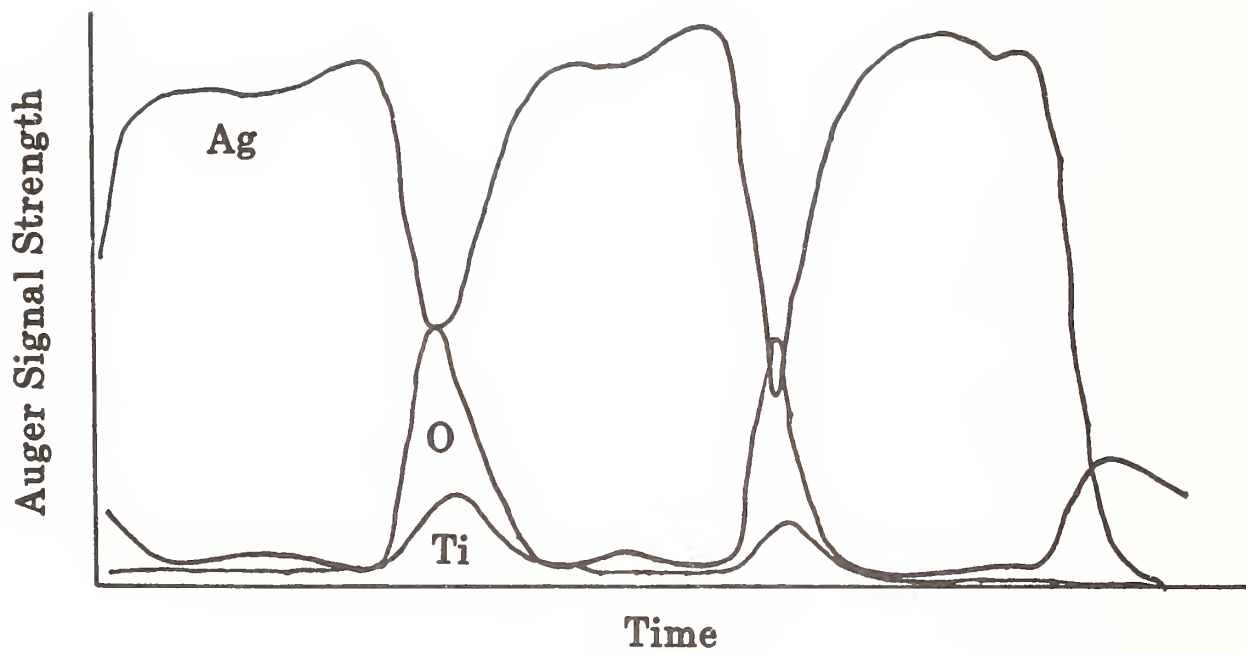


Figure 3. Auger depth profile of a silver/titanium oxide laminate film.

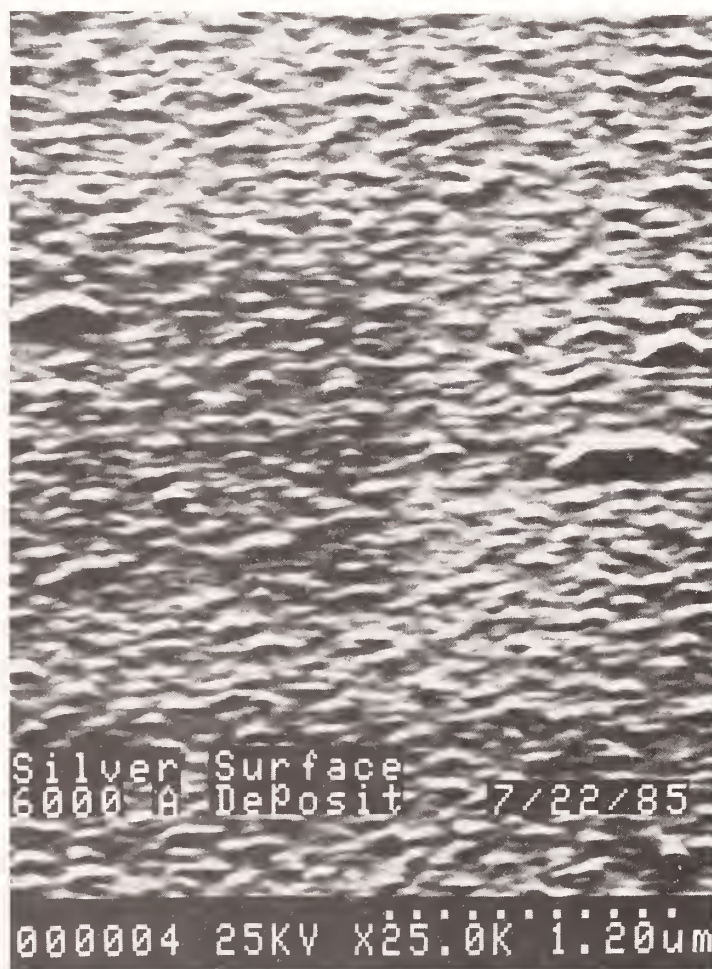


Figure 4. SEM photo of the surface of a typical silver film.



Figure 5. SEM photo of the surface of a silver/titanium oxide film.

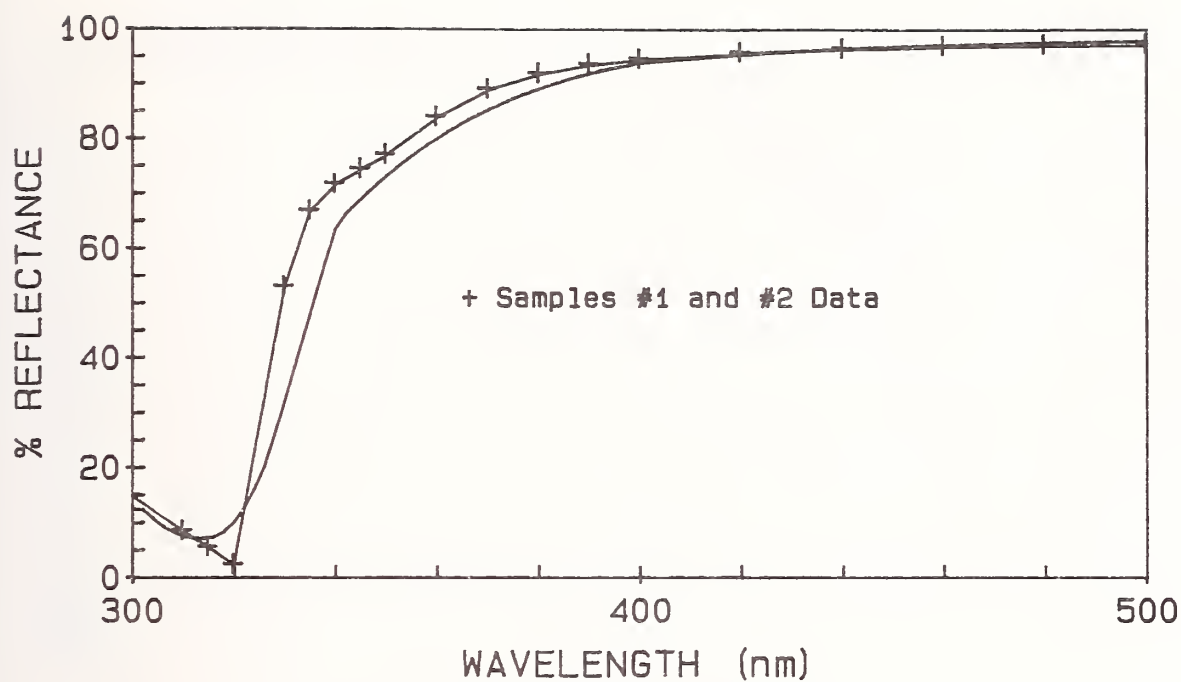


Figure 6. Spectrophotometer reflectance traces of samples 1 & 2 with a reference curve calculated from published optical constants of silver.

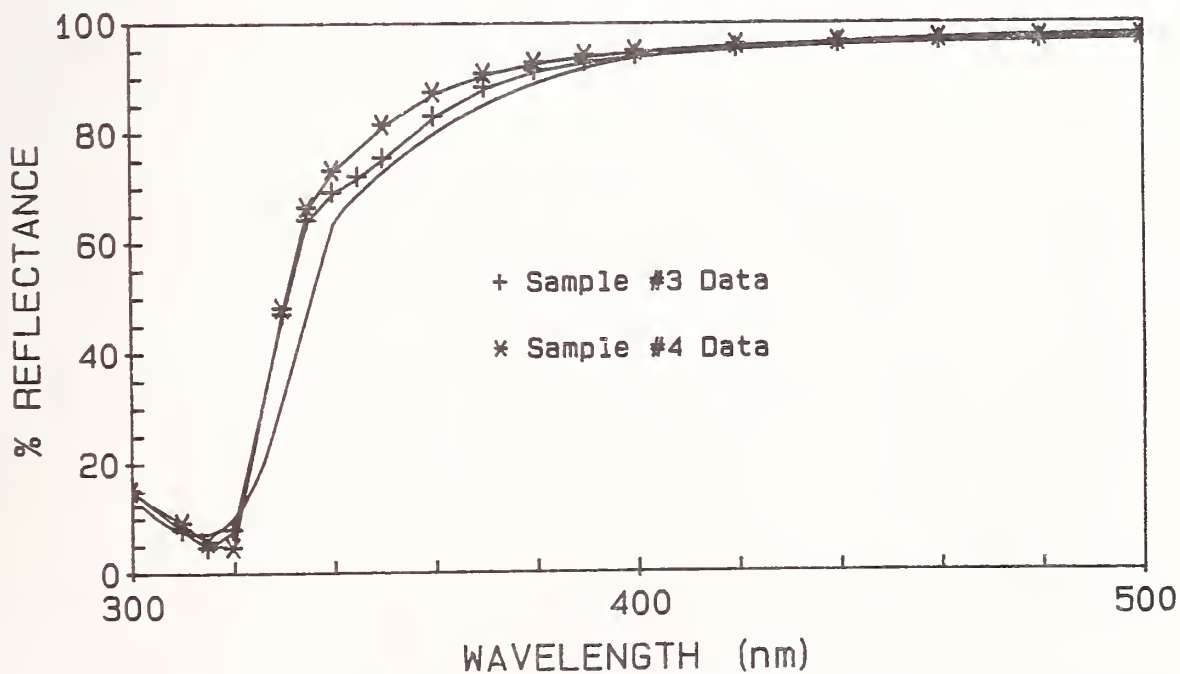


Figure 7. Spectrophotometer reflectance traces of samples 3 & 4 with calculated silver curve.

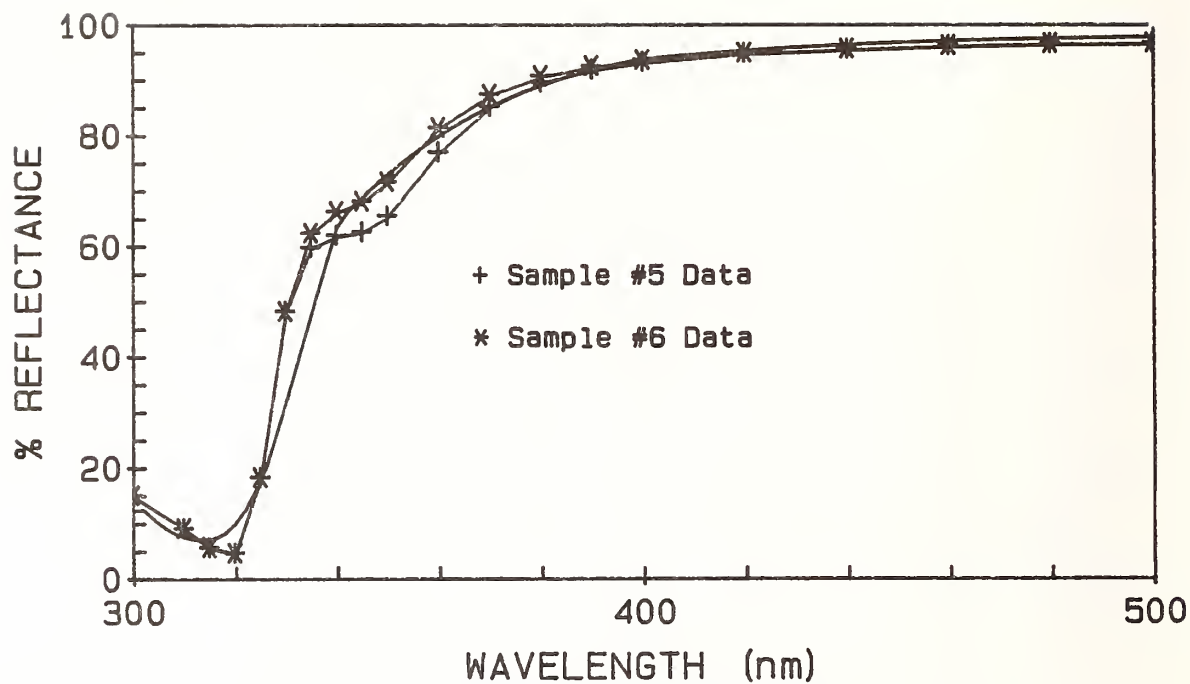


Figure 8. Spectrophotometer reflectance traces of samples 5 and 6 with calculated silver curve.

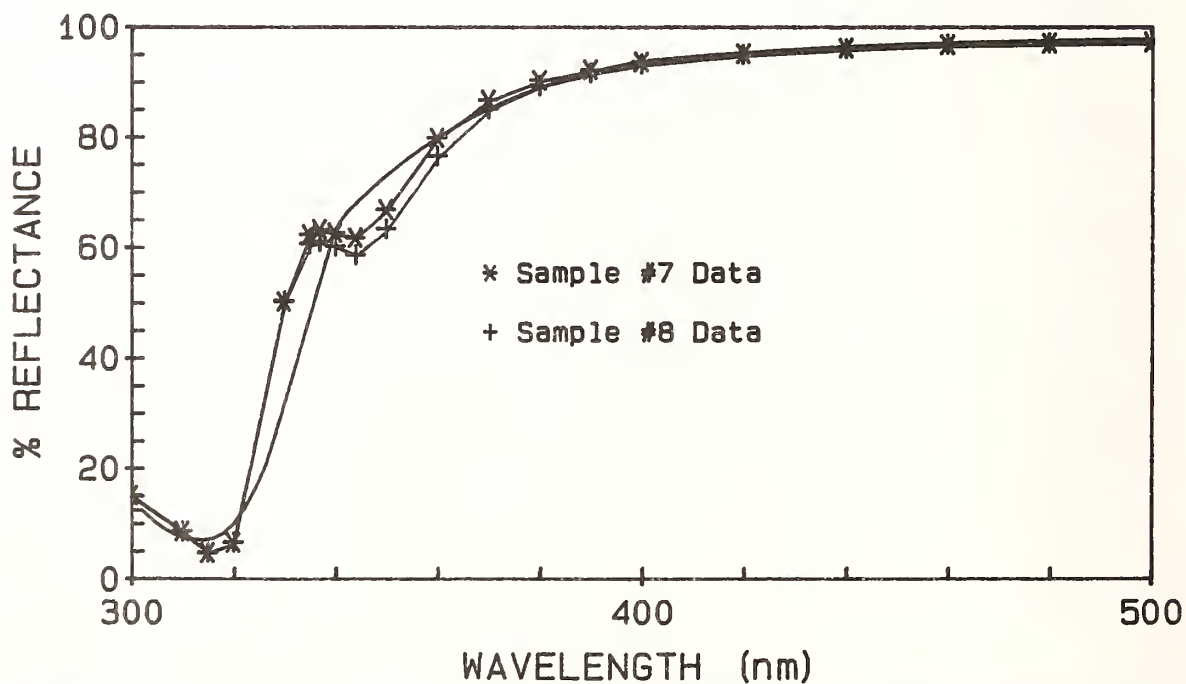


Figure 9. Spectrophotometer reflectance traces of samples 7 and 8 with calculated silver curve.

Influence of Deposition and Post Deposition
Conditions on Laser Induced Damage in Electron
Beam Evaporated TiO_2 and SiO_2 Films

K. Narasimha Rao, M. Adinarayana Murthy, S. Mohan
and M. Ramakrishna Rao

Instrumentation and Services Unit
Indian Institute of Science
Bangalore, Karnataka 560012, India.

Composition and structure of oxide films vary with different deposition techniques, conditions and starting materials, resulting in different damage thresholds. In this investigation, single and multi layer films of TiO_2 and SiO_2 were deposited with TiO and SiO_2 as starting materials. The substrate temperatures were maintained 25, 75, 125 and 175°C and post heat treatment was carried out at 75, 125, 175 and 225°C in air. These films were subjected to laser damage threshold studies, using Q-switched Nd:YAG Laser of 8 to 9ns. pulse width.

Maximum threshold values obtained were 19 J/cm² for TiO_2 films deposited at 25°C and post heated at 75°C; 44J/cm² for SiO_2 film deposited at 25°C and 18J/cm² for multilayer stacks of $\text{TiO}_2/\text{SiO}_2$ deposited at 25°C. Variation in damage threshold values is explained on the basis of film composition, structure and optical properties.

Key words : electron beam evaporation; laser induced damage; multilayers; optical properties; post deposition heat treatment; TiO_2 and SiO_2 films.

1. Introduction

With the increase in application of high power lasers in areas like fusion, microelectronics etc., the necessity of developing high power lasers and their accessories has been seriously felt. The development of lasers is very much interlinked with the laser coatings. New trends in the coating technology are resulting in better, more reliable and high damage threshold coatings.

Though the damage resistance of the coatings depends on laser parameters such as wavelength, spot diameter, pulse width and mode of operation, it has been established that impurities and absorption in coatings which in turn are decided by the deposition techniques and parameters influence the damage resistance of the films [1-5]. Selection of materials is also very important in improving the damage resistance.

Oxides of Titanium and Silicon have been widely used for preparing multi-layer optical coatings for visible and near infrared applications due to their exceptional stability against adverse envi-

ronmental conditions. To obtain films with the required stoichiometry, adhesion and optical properties, a wide variety of techniques such as electron beam evaporation, R.F. Sputtering, Ion assisted deposition, Ion beam sputtering have been used [10-17]. The films have also been subjected to different types of post deposition treatment such as heat treatment in air and vacuum, Ion bombardment, laser annealing, etc.

In this paper, the authors present the results on the studies made on electron beam evaporated films deposited at different ambient substrate temperatures and subjected to post deposition heat treatment in oxygen. The influence of this treatment on the optical properties and damage thresholds of single layer coatings of TiO_2 and SiO_2 , 5-layer partially reflecting and 21-layer fully reflecting laser mirrors is discussed.

2. Experimental Techniques

Single and multilayer films of TiO_2 and SiO_2 were deposited by reactive electron beam evaporation from a four hearth crucible of a 6 KW electron beam gun (Leybold Heraeus). The bell jar (19" dia and 24" height) was pumped by a cheveron baffle - diffusion pump - rotary pump combination to get an ultimate vacuum of 10^{-6} torr. Quartz crystal and optical monitors were used to monitor the film thickness during deposition. The substrates were well polished fused quartz plates of 25mm dia. and glass slides of 2 to 3mm thickness. Substrate rotation was provided to get uniform coatings. The substrates were cleaned with 'Balzers' cleaner 1, rinsed in running water, cleaned with detergent and tap water and then again rinsed in double distilled water. Finally the substrates were subjected to vapour degreasing with iso-propyl alcohol. The substrates were subjected to heat treatment in vacuum prior to depositing the films.

TiO_2 films were prepared by evaporating TiO (Balzers) in a partial oxygen pressure of 2×10^{-4} torr at a rate of 100Å/min. whereas SiO_2 films were prepared by evaporating SiO_2 (Merck) in a partial oxygen pressure of 5×10^{-5} torr at a rate of 240Å/min. The thickness of the single layer films of TiO_2 and SiO_2 was corresponding to the quarter wave thickness for 1.06µm. Partial $[\text{G}(\text{HL})^2\text{HA}]$ and fully reflecting $[\text{G}(\text{HL})^{10}\text{HA}]$ laser mirrors also have been prepared with alternate quarter wave layers of TiO_2 and SiO_2 as high (H) and low (L) refractive index layers. The films were subjected to heat treatment in air at different temperatures upto 225°C after deposition. The transmittance and reflectance of the films before and after heat treatment at different temperatures were recorded with HITACHI 330 Model UV-Vis. and near I.R. double beam spectrophotometer with an accuracy of $\pm 0.2\%$. The refractive index and extinction coefficient of the films were calculated by the envelop technique [18] from the transmission measurements.

Damage threshold measurements on these coatings were carried out with a Quanta Ray DCR-2 Nd:YAG laser with a pulse width of 8 to 9 ns. spot diameter 6.4mm and operating at 1.06µm. The set up used for these measurements is shown in Figure 1. The laser energy density on the sample was varied not only by using neutral density filters but also

by moving the sample towards or away from the focal point of the condensing lens. In this process the spot diameter varied between 0.5mm to 3mm. The influence of the spot diameter on damage threshold was neglected since the spot diameter is well above the minimum diameter [2]. The energy of the laser beam was measured with 'Scientech' calorimeter. The spot size of the laser beam on the test sample was recorded each time on an exposed photographic paper. The damage threshold (J/cm^2) is the ratio between the energy of the laser (in Joules) and the area of the beam (in sq. cm.). A probe beam from a low power He-Ne laser aligned with a switched-Nd:YAG laser has been used to observe the damage by measuring the scattered light. The upper end of the damage threshold is the maximum pulse energy density for which there was no damage.

3. Results and Discussion

3.1 Single Layer TiO_2 Films

The damage thresholds and the extinction coefficient of the single layer TiO_2 films for the substrate temperatures 25, 75, 125 and 175°C and for the post heat treated films in air at temperatures 75, 125, 175°C and 225°C have been presented in table 1. It has been observed that the damage threshold increases with increase in substrate temperature upto 75°C and then starts decreasing. The extinction coefficient measured on these films show that the films with the highest damage threshold has the lowest absorption. It appears that the films deposited at 25°C are not complete oxides and hence have higher absorption. The films deposited at 75°C seems to be the optimum ones with the improved oxidation and hence minimum absorption. This particular substrate temperature seems to provide the necessary activation energy for the oxidation of the material. The films deposited at temperatures higher than 75°C again appear to be incomplete oxides, may be because of the preferential desorption of oxygen molecules during deposition at those temperatures. Hence the extinction coefficient of these films also is more, resulting in decrease in damage thresholds. This explanation on the basis of absorption in films is supported by the insitu optical transmittance studies of these films during deposition shown in Figure 2. in which the film deposited at 75°C shows the highest transmittance for half wave thickness.

The damage thresholds and the extinction coefficient of the films as a function of the post deposition heat treatment have also been presented in the same table. The damage thresholds show an improvement upto a particular temperature which depends on the deposition temperatures and then shows a decrease. The extinction coefficient also shows variation but the variation is exactly opposite in nature but the transition occurring at the same temperature. This shows a direct dependence of the damage threshold on the film absorption. The initial heat treatment upto the transition temperature appears to help in further oxidation, thereby minimising the absorption and improving the damage threshold. Heating above the transition temperature may once again result in desorption of oxygen leading to a slight increase in absorption or scattering due to increase in grain size and decrease in damage threshold. However the films deposited at 75°C show deterioration on further heat treatment. As mentioned already, these films might have been oxidised to the limit

during deposition, further heating resulting only in desorption of oxygen.

3.2 Single Layer SiO_2 Films

The damage thresholds of the single layer SiO_2 films deposited at 25, 75, 125°C and heated to 75, 175, and 225°C are presented in table 2. As deposited films at 25°C showed the maximum damage threshold (44J/cm²). The optical transmission curves showed practically negligible absorption. It appears that the deposition rates and the reactive oxygen pressure during deposition is quite optimum to give the absorption free SiO_2 films at room temperature. The damage threshold of the films deposited at higher temperatures as well as heat treated films were considerably less.

3.3 Multi Layer Films

The damage thresholds of the 5 layer $[\text{G}(\text{HL})^2\text{HA}]$ partial mirrors and 21 layer $[\text{G}(\text{HL})^{10}\text{HA}]$ fully reflecting mirrors are presented in tables 3 and 4 respectively. The variation in the damage threshold both as a function of substrate temperature during deposition and due to heat treatment is very much similar to that observed in the case of single layer TiO_2 films. These observations show that the damage threshold variation can be explained on the basis of absorption in the films and the room temperature deposited films heated to 75°C in the atmosphere have the required oxidation exhibiting the maximum damage threshold to the Nd:YAG laser.

4. Summary and Conclusions

Single layer TiO_2 and SiO_2 and 5 layers and 21 layers of $\text{TiO}_2/\text{SiO}_2$ have been prepared by reactive electron beam evaporation technique. The laser damage thresholds (Nd:YAG laser) and extinction coefficient of these films measured on films deposited at temperatures 25, 75, 125 and 175°C and heat treated in air at temperatures 75, 125, 175 and 225°C showed that damage thresholds are dependent on the absorption films. The films deposited at 25°C and heat treated at 75°C in exhibited minimum absorption and maximum damage threshold.

The authors wish to thank Prof. Y.V.G.S. Murthy and his colleagues, Indian Institute of Technology (IIT), Madras; for their help in making damage threshold measurements. They also thank Prof. E.S. Raja Gopal, Chairman, ISU for his encouragement and keen interest in this study.

5. References

- [1] Desharzer, L.G.; Newnam, B.E.; Leuing, K.M., The Role of Coating Defects in Laser Induced Damage to Dielectric Thin Films. Nat. Bur. Stand. (US) Spec. Publ. 387; 1973, 27-32.
- [2] Newnam, B.E.; Gill, D.H., Spectral Dependence of Damage Resistance of Refractory Oxide Optical Coatings. Nat. Bur. Stand. (US) Spec. Publ. 362; 1976, 292-300.

- [3] Lowder Milk, W.H.; Milam, D.; Rainer, F., Optical Coatings for Laser Fusion Applications. Thin Solid Films, Vol.73; 155-166, 1980.
- [4] Walker, T.W.; Gunther, A.H.; Nielsen, P., Pulsed Laser Damage to Thin Film Optical Coatings Part I-Experimental. IEEE J. Quant. Elect. QE-17, 2041-52, 1981.
- [5] Guenther, K.H.; Humpherys, T.W.; Balmer, J.; Bettis, J.R.; Casparis, E.; Ebert, J.; Eichner, M.; Guenther, A.H.; Kiesel, E.; Kuehnelt, R.; Milam, D.; Ryseck, W.; Seitel, S.C.; Stewart, A.; Weber, H.; Weber, H.P.; Wirtenson, G.; Wood, R.M.; 1.06 Micron Laser Damage on Thin Film Optical Coatings - a Round Robin Experiment Involving Various Pulse Lengths and Beam Diameters.
- [6] Dundenhausen, B.; Mollenstedt, G.; Reactive Vacuum Evaporation of TiO under Stimulated Oxidation of TiO_2 . Z. Angew. Phys., Vol.27; 191, 1969.
- [7] Ritter, E.; SiO and Si_2O_3 Phases in Thin Films, Optica Acta, Vol.9; 197-201, 1962.
- [8] Awarter, M.A., Process for the Manufacture of Thin Films. U.S. Patent, 2920, 002, 1960.
- [9] Pulker, H.K.; Paesold, G.; Ritter, E.; Refractive Indices of TiO_2 Films Produced by Reactive Evaporation of Various Titanium-Oxygen Phases, Appl. Opt., Vol.15; 2986-91, 1976.
- [10] Heitman, W., Reactive Evaporation in an Ionized Gases. Appl. Opt., Vol.10; 1971, 2414-18.
- [11] Kuster, H.; Ebert, J., Activated Reactive Evaporation of TiO_2 Layers and their Absorption Indices. Thin Solid Films, Vol.70; 43-47, 1980.
- [12] Martin, P.J.; Macleod, H.A.; Netterfield, R.P.; Pacey, C.G.; Sainty, W.G., Ion Beam Assisted Deposition of Thin Films, Appl. Opt., Vol.22, 178-184, 1983.
- [13] McNeil, J.R.; Al-Jumaily, G.A.; Jungling, K.C.; Barron, A.C., Properties of TiO_2 and SiO_2 Thin Films Deposited using Ion Assisted Deposition. Appl. Opt., Vol.24; 1985, 486-489.
- [14] Bunshah, R.F.; Deshpandey, C.V., Plasma Assisted Physical Vapour Deposition: A review, J. Vac. Sci. Technol. A3(3) 553-560, 1985.
- [15] Sites, J.R.; Gilstrap, P.; Rujkorakarn, R., Ion Beam Sputter Deposition of Optical Coatings. Opt. Eng. Vol.22; 447-9, 1983.
- [16] Narasimha Rao, K.; Mohan, S.; Ramakrishna Rao, M., Effect of Post Deposition Heat Treatment on Multilayer Hard Coatings for He-Ne Laser. Proceedings of the 3rd Symposium on Lasers and Applications, 1983, Dec. 16-12, Kanpur, India, 81-82.

- [17] Narasimha Rao, K.; Mohan, S.; Ramakrishna Rao, M., Hard Laser Mirrors for 6328A, Efficiency Changes on Heat Treatment. Proceedings of 12th Symposium on Optics and Opto-electronics, 1984, Feb. 1-4, Bangalore, India, 64-68.
- [18] Swane Poel, R., Determination of thickness and Optical Constants of α - Si:H. J. Phys. E: Sci. Instrum. Vol.9; 1214-22, 1983.

Table 1. Damage thresholds in J/cm^2 of TiO_2 films as a function of substrate temperature (T_S) and post deposition heat treatment temperature (T_H).

T_S/T_H	25°C	75°C	125°C	175°C	225°C
25°C	9.0 (0.002)	19.1 (0.001)	12.5 (0.002)	10.1 (0.003)	8.1 (0.003)
75°C	10.1 (0.001)	8.8 (0.001)	8.0 (0.004)	7.9 (0.004)	7.9 (0.004)
125°C	2.1 (0.010)	7.0 (0.005)	9.2 (0.004)	7.9 (0.005)	6.8 (0.005)
175°C	1.2 (0.020)	10.8 (0.010)	12.9 (0.003)	8.8 (0.004)	7.2 (0.005)

Values within the brackets indicate the extinction coefficient of the films.

Table 2. Damage thresholds in J/cm^2 of SiO_2 films as a function of substrate temperature (T_S) and post deposition heat treatment temperature (T_H).

T_S/T_H	25°C	75°C	175°C	225°C
25°C	44.1	16.5	15.2	15.2
75°C	26.0	18.0	16.0	15.0
125°C	25.4	16.0	15.4	12.5

Table 3. Damage thresholds in J/cm^2 of partial mirrors $[\text{G}(\text{HL})^2\text{HA}]$ as a function of substrate temperature (T_S) post deposition heat treatment temperature (T_H).

T_S/T_H	25°C	75°C	125°C	175°C	225°C
25°C	12.5	14.0	10.0	9.7	19.0
75°C	12.5	11.0	10.0	9.5	9.2
125°C	11.0	11.6	10.0	8.7	6.0

Table 4. Damage thresholds in J/cm^2 of high reflecting mirrors $[\text{S}(\text{HL})^{10}\text{HA}]$ as a function of substrate temperature (T_S) and post deposition heat treatment temperature (T_H).

T_S/T_H	25°C	75°C	125°C	175°C	225°C
25°C	18.2	18.0	14.1	12.0	10.6
75°C	11.7	8.3	7.8	8.0	8.0
125°C	3.5	9.9	9.4	9.2	6.9

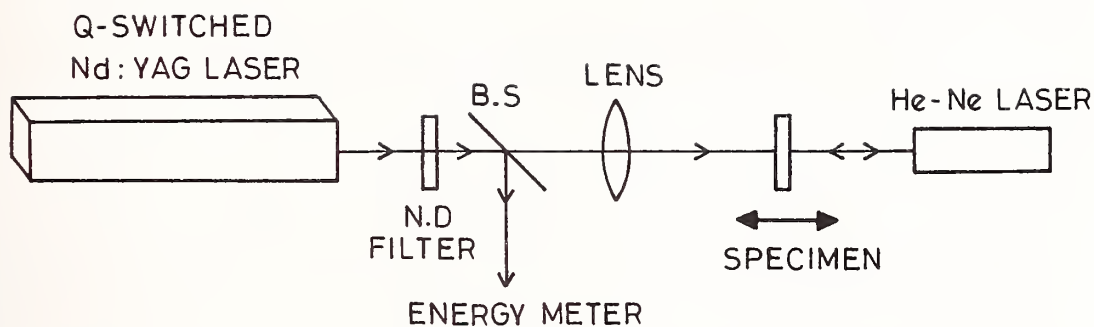


Figure 1. LASER DAMAGE THRESHOLD MEASUREMENT SETUP.

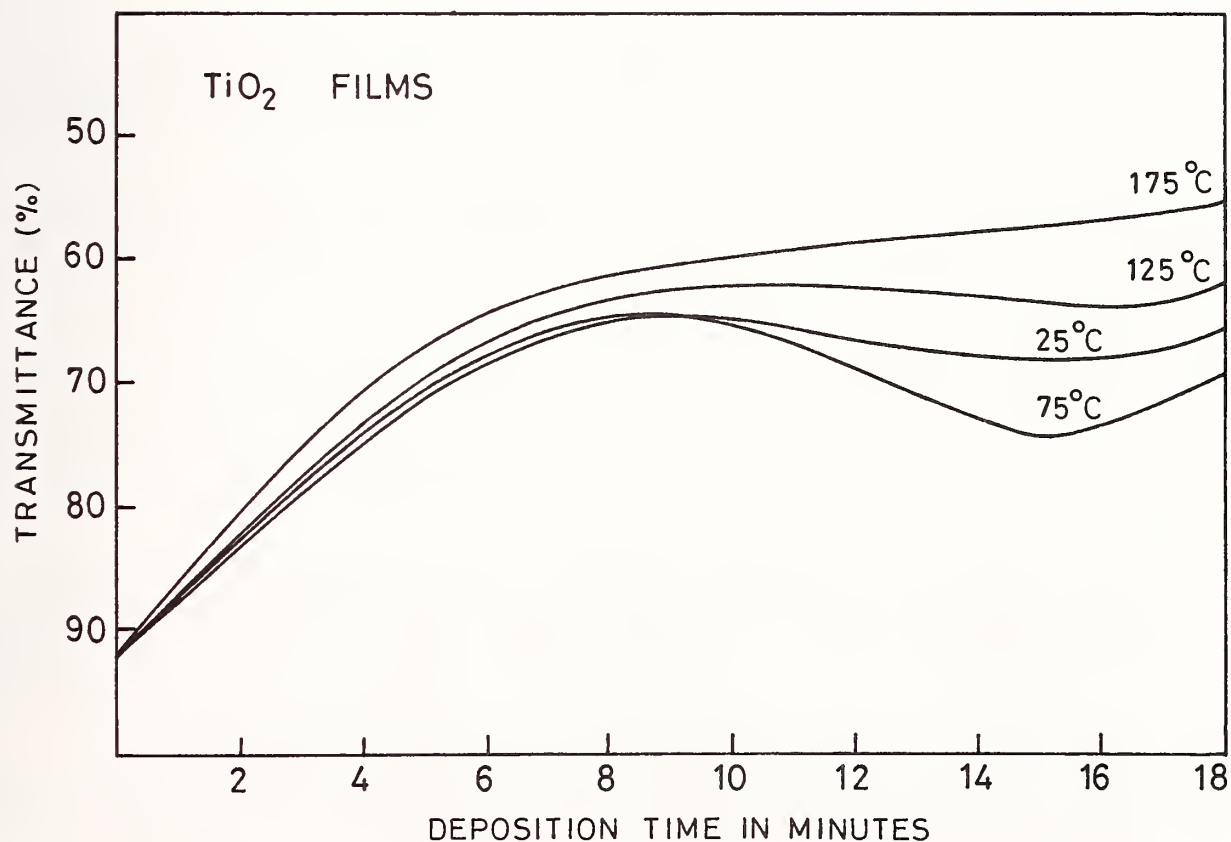


Figure 2. INSITU OPTICAL TRANSMITTANCE WITH THICKNESS FOR DIFFERENT SUBSTRATE TEMPERATURES.

Dependence of Damage Threshold of Anti-Reflection Coatings on Substrate Surface Roughness

Y. Nose, Y. Kato, K. Yoshida
and C. Yamanaka

Institute of Laser Engineering, Osaka University
Suita, Osaka 565, Japan

Geometrical shapes of the damage sites in the 5-layer $\text{SiO}_2/\text{ZrO}_2$ anti-reflection (AR) coatings generated by $1\mu\text{m}$ laser irradiation have been accurately determined. The damages can be classified into two types; deep damage and shallow damage, the former having the lower threshold. Dependence of the damage threshold of the deep damages on substrate surface roughness is given. It is suggested that presence of absorption centers embedded in the substrate is responsible for determining the damage threshold. Possible approaches that will lead to stronger AR coatings are proposed.

Key words: Anti-reflection coating; laser-induced damage; polishing process; surface roughness.

1. Introduction

Previous observations show that transmitting coatings such as anti-reflection (AR) coatings and polarizing beam splitters have lower damage threshold than high-reflectance (HR) coatings [1]. The damage to AR coatings originate at the interface between the first coating layer and the substrate [2]. However the exact process which leads to the laser-induced damage in the AR coating has not been clarified so far.

We report here the results of the detailed observations of the laser-induced damages in the AR coatings. In particular we have studied the correlation between the damages and the surface roughness of the substrate. Based on these observations the most probable mechanism for damage formation in the AR coatings is discussed. Proposals are made which will lead to the improvement of the damage threshold of the AR coatings.

2. Experimental Conditions

2-1. Preparations of the substrates

In order to obtain consistent results in the damage properties of the AR coatings, careful attentions were paid to fabrication of the substrates and the coatings used in the following experiments.

The substrates were high optical quality BK-7 glasses of 30 mm in diameter and 10 mm in thickness. They were polished either by conventional polish or by bowl-feed polish process, respectively [3]. In the latter the substrates were immersed during polishing in the liquid containing the polishing compounds, resulting in smooth surfaces. Ceria compounds were used as the polishing material.

The surface roughness of the polished substrates were measured with a Wyko NCP-1000M optical profilometer. The typical rms (peak-to-valley) surface roughness was 30-35 Å (~ 200 Å) for conventional polish and 5-9 Å (30-60 Å) for bowl-feed polish, respectively. Figure 1 shows the surface profiles of the substrates #1 and #2 which were prepared by conventional and bowl-feed polishes, respectively. As shown in Figure 1, we define two parameters which characterize the lateral scale length of the surface profile: the average distance between the peaks (Δd) whose height exceed the rms roughness and the typical width of these peaks (Δw). Table 1 shows these parameters for the samples #1 and #2. We note that deep and wide rough peaks produced by conventional polish (#1) are smoothed by bowl-feed polish (#2) resulting in smaller value of Δw .

2-2. Coating

Five layer $\text{SiO}_2/\text{ZrO}_2$ AR coatings of quarter-wave design were vacuum deposited on the substrates, with the first SiO_2 layer as the undercoat to increase the damage threshold [4]. The substrates after polish and before coating (typically ~ 1 week) were kept in dry atmosphere to prevent chemical changes on the fresh surface. All the substrates with different surface roughnesses were coated at the same time in order not to introduce uncertainty due to the coating process.

2-3. Laser irradiation

Each sample was irradiated with a laser pulse of $1.064 \mu\text{m}$ wavelength from a Q-switched Nd:YAG laser. The pulse width was 1.5 ns , generated by slicing a Q-switched pulse with a fast Pockels cell switch. After two-stage amplification with Nd: glass amplifiers of 15 mm diameter, the laser pulse was focused with a 500 mm focal length lens. The laser beam on the sample had a smooth Gaussian spatial distribution with the spot diameter of $400 \mu\text{m}$ at $1/e^2$ point. The laser energy was measured with a calibrated photodiode.

The irradiation site was observed in site with a Nomarski microscope before and after each laser irradiation to detect the laser-induced damage. The sample was moved after each laser shot irrespective of the presence or absence of the damage.

2-4. Characterization of the laser-induced damages

The following techniques were used in order to definitely determine the geometrical shapes of the damage sites generated at different experimental conditions.

- 1) Optical microscopy: A Nomarski microscope was used to inspect and record the morphology of the damages.
- 2) Electron microscopy: Enlarged views of the damages were obtained with a scanning electron microscope.
- 3) Surface profilometry: A Talystep surface profilometer was used to determine the surface profile and the depths of the damage sites, since these parameters are difficult to determine with the optical and electron microscopes.
- 4) Material analysis: An electron-probe x-ray microanalyzer (XMA) was used to identify the materials at the damage sites.

3. Experimental results

We have studied the dependences of the laser-induced damages on the surface roughness of the substrates. First we show the results regarding the geometrical shapes of the damage sites generated at typical experimental conditions. Then more quantitative relations between the damages and the surface roughness of the substrates are presented.

3-1. Geometrical shapes of the damage sites

1) Optical microscopy

Morphology of the damages obtained with a Nomarski microscope are shown in Figure 2. The two samples are AR coatings fabricated using the substrates #1 and #2 which have different roughness as shown in Table 1. The damages were produced at the laser fluences (E_L) near the damage threshold ($E_L \sim E_C$) and far above the threshold ($E_L \sim 3E_C$). Note that the damage threshold depends on the surface roughness as will be described later; therefore E_C and E_L are quite different in Figure 2 for the two samples.

Near the threshold, damages which have small diameter (which we call "deep damages" hereafter) are distributed over the irradiated area. When the laser fluence is increased, the number density of the deep damages increases significantly, but the size changes very little. Furthermore when the fluence exceeds approximately twice the threshold of the deep damages, damages covering the large area (which we call "shallow damages" hereafter) are generated.

2) Electron microscopy

Magnified views of the damages obtained with an electron scanning microscope are shown in Figure 3. The deep damages are mostly circular with the diameters of 3-4 μm . The microscope picture for #2 near $E_1 \sim E_{CT}$, which was taken at a tilted angle of 15° , reveals each coating layer at the wall of the crater. It shows that the damage wall has two steps: SiO_2 , $\text{ZrO}_2/\text{SiO}_2$ and $\text{ZrO}_2/\text{SiO}_2$ counted from the outer surface to the substrate. The deep damages have the depth which probably reaches to the substrate, although it is difficult to definitely conclude only with the electron microscopy.

At the higher fluence of $E_1 \sim 3E_{CT}$, shallow damages are produced over the wide area covering the deep damages. In the shallow damages, the top coating layer (SiO_2) is removed from the ZrO_2 layer. However it appears that the top layer remains around the deep damages with the diameter of 20-30 μm even with high fluence irradiation.

3) Surface profilometry

A Talystep was used to measure the depths of the damages. Figure 4 shows the Talystep scans of the samples having the shallow damages. It shows that the depth of the shallow damage corresponds approximately to the thickness of the top coating layer, and the depth of the deep damage is close to the total thickness of the 5 coating layers. However the latter is not accurate since the stylus is not small enough to reach to the bottom of the deep damage which has $\sim 1 \mu\text{m}$ diameter at the bottom. Also this measurement confirms that the top coating layer remains around the deep damage within the shallow damage.

4) Material analysis

Figure 5 shows the results of the XMA analysis at four different sites outside and within the damages. Although XMA does not provide good depth resolution since the probe electrons (25 kV) have $\sim 2 \mu\text{m}$ penetration depths, the result supports the above observations regarding the profiles of the damage sites.

Figure 6 gives the schematic picture of the damage sites based on our experimental observations. At $E_1 \sim E_C$, deep damages which extend to the substrate are generated. At far above threshold like $E_1 \sim 3E_C$, the top coating layer is blown-off resulting in the shallow damage, whereas the top layer remains around the deep damages.

3-2. Dependence of the deep damages on the laser fluence and the surface roughness

Since the deep damage has a lower threshold than the shallow damage, we study here dependences of the deep damage on the two parameters; laser fluence and surface roughness.

1) Dependence on the laser fluence

Here we determine the exact damage threshold of the deep damage using the sample #2 whose substrate has been bowl-feed polished.

The laser beam has the Gaussian spatial distribution on the sample given by

$$E(r) = E_p e^{-2r^2/a^2}, \quad (1)$$

where $a=200 \mu\text{m}$ and E_p is the peak fluence at $r=0$. The damage occurs within the area of radius r_c where $E(r)$ exceeds the threshold fluence E_c ; $E(r_c)=E_c$. We have examined the laser damages with the Nomarski microscope, and determined the critical radius r_c and derived the threshold fluence E_c . For the damages generated at different laser energies up to the peak fluence on the sample of 30 J/cm^2 , the value of E_c thus determined was approximately constant having the value of 7.5 J/cm^2 . Therefore we may conclude that the actual threshold for the deep damages is 7.5 J/cm^2 for the particular sample that we have studied.

The area within r_c is given by

$$S = \pi r_c^2 = (\pi a^2/2) \ln(E_p/E_c), \quad (2)$$

If all the deep damages have the same threshold of E_c , then the number of the deep damages within the area S should increase logarithmically with E_p . Figure 7 shows the experimental results of the total number of the damages and the average distance between the damages plotted against the peak fluence E_p . Since the number of the damages increases with E_p more strongly than logarithmic,² this shows that the deep damages have variation of the thresholds whose lowest value is 7.5 J/cm^2 .

2) Dependence on the surface roughness

It is reasonably well established [1] and our present results support that the damages in the AR coating are caused by some imperfections at or near the boundary between the coating and the substrate. Also there is a set of experimental data that higher damage threshold is obtained with the bowl-feed polish compared with the conventional polish [2].

Figure 8 shows our experimental data of the damage threshold plotted against the rms surface roughness and the peak-to-valley surface roughness. Three bowl-feed polished and one conventional polished samples were used. The damage threshold was determined as the peak fluence at which the damage was detected in situ with the Nomarski microscope. The error bars in the damage threshold show the range of data obtained from many shots on each sample. These data clearly show that the AR coating deposition on the smooth substrate results in higher damage threshold. However it should be noted that the threshold of $E_c \sim 9 \text{ J/cm}^2$ is lower than that obtained with good HR coatings in which the value of $E_c > 12 \text{ J/cm}^2$ has been achieved [1,5].

We have measured the diameters and the average distances of the deep damages produced at high laser fluence of $E_p \sim 3E_c$, and compared them with the lateral scale lengths of the surface roughness of the substrates^c that we have defined in Figure 1. The result is shown in Table 2. Here we find close correlation between the diameter of the deep damage and the width of the surface roughness (Δw), and also between the average distance between the damages and the average distance between the peaks of the surface roughness (Δd). The implications of this results are discussed in the next section.

4. Discussion

First we discuss on the deep damages that give the lower bound of the damage threshold of the AR coating. Lowdermilk and Milam suggested [1] that the damage begins with the generation of very hot spot near the interface with the substrate. The intense heat melts the glass and generates high pressure which lift the coating layers. When the crack reaches to the surface, molten glass is ejected from the center and solidifies quickly.

Our observation of the geometrical shape of the deep damages shows that the damage is extending to the substrate. The damage threshold is related to the surface roughness of the substrate. Also we found close correlation between the geometrical size of the damage and the typical width of the surface roughness, and the correlation between the distance between the damages and the distance between the peaks of the surface roughness. In addition we have other data with the AR coating on a conventional-polished substrate in which deep damages are aligned on a straight line. Close examination of the substrate before coating with the Nomarski microscope reveals the presence of sharp straight scratches on the surface.

Considering these observations, we may propose that the deep damages are generated due to the presence of absorption centers in the substrate. With the bowl-feed polish compared with the conventional polish, the size and also the number density of these absorption centers become less, resulting in higher damage threshold. The nature of the absorption centers is not clear; however they may well be the polishing compounds that are embedded in the valley of the scratches or in the subsurface structure.

It is an intriguing question that how much we can improve the damage threshold when we keep reducing the surface roughness using special techniques. If these new techniques could reduce the absorption centers in the substrate during polishing, then they will result in higher damage threshold. Otherwise it will be difficult to attain significantly better result. We may chemically remove the absorption centers, however it might result in rough surface with high scattering level. Laser annealing of AR coating by repetitive irradiation with low power laser is known to be an effective process to increase the damage threshold [6]. In this case, absorption centers probably spread due to laser heating, resulting in less absorption and thus

higher threshold.

We have another viewpoint which we have derived from our recent work on porous dielectric coating [7]. In this coating, SiO_2 and NaF are coated at the same time on the substrate and NaF is dissolved after coating, leaving porous layer of SiO_2 . This coating has very high damage threshold of 12-13 J/cm^2 at 1 μm even when we use rough substrate. According to our interpretation, the reason for the high damage threshold of the porous coating is that the pressure generated at the absorption centers is not accumulated under the coating layer, but it is quickly released due to the porous nature of the coating [8].

The shallow damages have higher threshold than the deep damages. Although we have not tried to accurately determine the threshold of the shallow damage, it is 20-25 J/cm^2 for the 5-layer $\text{SiO}_2/\text{ZrO}_2$ AR coating on the bowl-feed polished substrate. Therefore if we could completely eliminate the deep damages, there is a possibility that the AR coating could have the damage threshold exceeding 20 J/cm^2 .

It is an interesting observation that the top layer remains around the deep damages located within the shallow damage. One of the possible interpretations is that the plasma ejected from the deep damage refracts and absorbs the laser beam, reducing the laser fluence and thus preventing the damage around the deep damage. There may be interference of the refracted beam with the direct beam near the damage affecting the damage threshold of the shallow damage. Further study will be necessary to clarify various aspects related to the shallow damages.

5. Conclusion

Based on our experimental observations, we have suggested that the presence of absorption centers in the substrate is responsible for determining the damage threshold of the deep damages which give lower bound of the threshold of the AR coating. If this interpretation is correct, then there are two possibilities that we could take to improve the threshold to above 10 J/cm^2 and possibly to 20 J/cm^2 . The first is to reduce the size (and the number) of the absorption centers. Smaller absorption center will result in the reduction of pressure caused by the heating of the absorption center and thus increase in the damage threshold. Further quantitative experimental and theoretical studies are necessary to clarify these relationship. Another possibility is to develop porous coatings which releases the pressure generated at the substrate. The porous AR coatings have already been developed [7,9,10]. However this concept could be extended to other transmitting coatings such as the polarizing beam splitter.

The above discussions are pertinent to the AR coating at 1 μm where the damage is determined by the substrate property. At shorter wavelengths such as in the ultraviolet, the damage is mostly determined by the absorption within the coating layer. In this case selection of the coating materials becomes more important. However porous nature of the coating might help improving the damage threshold also in this wavelength region.

6. Acknowledgement

We appreciate T. Izawa of Showa Optical Company for preparation of the samples used in this study.

7. References

- [1] W.H. Lowdermilk and D. Milam, IEEE J. Quant. Electr. QE-17, 1888 (1981), and references cited therein.
- [2] C.K. Carniglia, J.H. Apfel, G.B. Carrier and D. Milam, NBS Special Pub. 541, 218 (1978).
- [3] R.W. Dietz and J.M. Bennett, Appl. Opt. 5, 881 (1966).
- [4] J.H. Apfel, E.A. Enemark, D. Milam, W.L. Smith and M.J. Weber, NBS Special Pub. 509, 255 (1977).
- [5] T. Izawa, I. Hashimoto and H. Shikakura, Rev. Laser Eng. 11, 662 (1983) (in Japanese).
- [6] J.E. Swain, W.H. Lowdermilk and D. Milam, Appl. Phys. Lett. 41, 782 (1982).

- [7] K. Yoshida, H. Yoshida, Y. Kato and C. Yamanaka, Appl. Phys. Lett. 47, 911 (1985).
- [8] K. Yoshida, T. Yabe, H. Yoshida and C. Yamanaka, J. Appl. Phys. 60, 1545 (1986).
- [9] L.M. Cook, W.H. Lowdermilk, D. Milam and J.W. Swain, Appl. Opt. 21, 1482 (1982).
- [10] I.M. Thomas, Appl. Opt. 25, 1481 (1986).

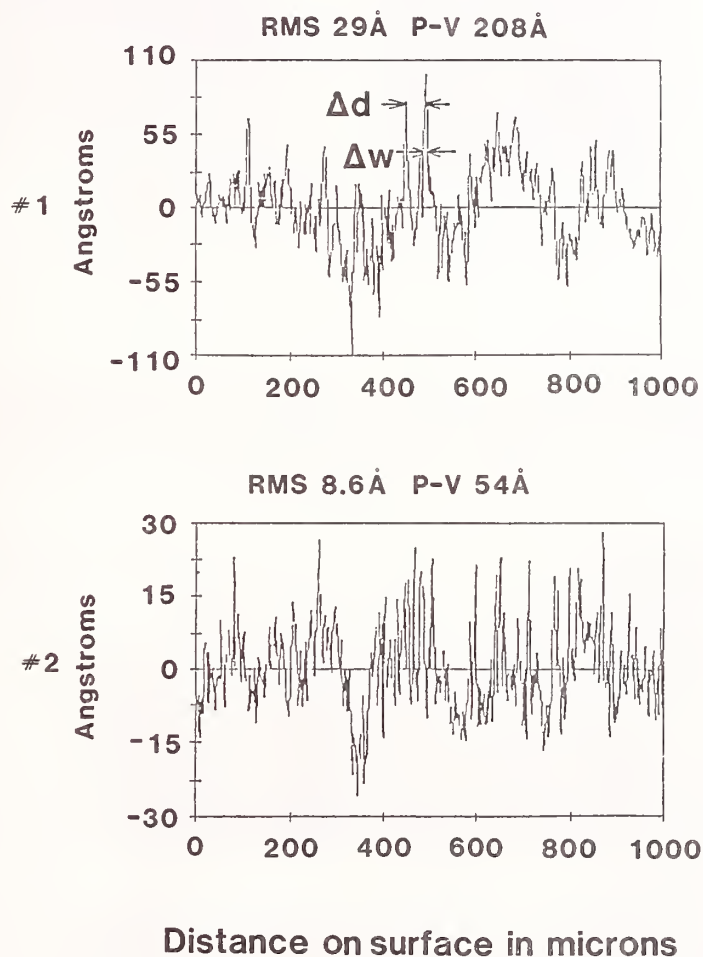


Figure 1 Surface profiles of the substrates prepared with different polishing techniques; conventional polish (#1) and bowl-feed polish (#2). Shown in the figure are definitions of Δw and Δd which characterize lateral scale-lengths of the surface roughness.

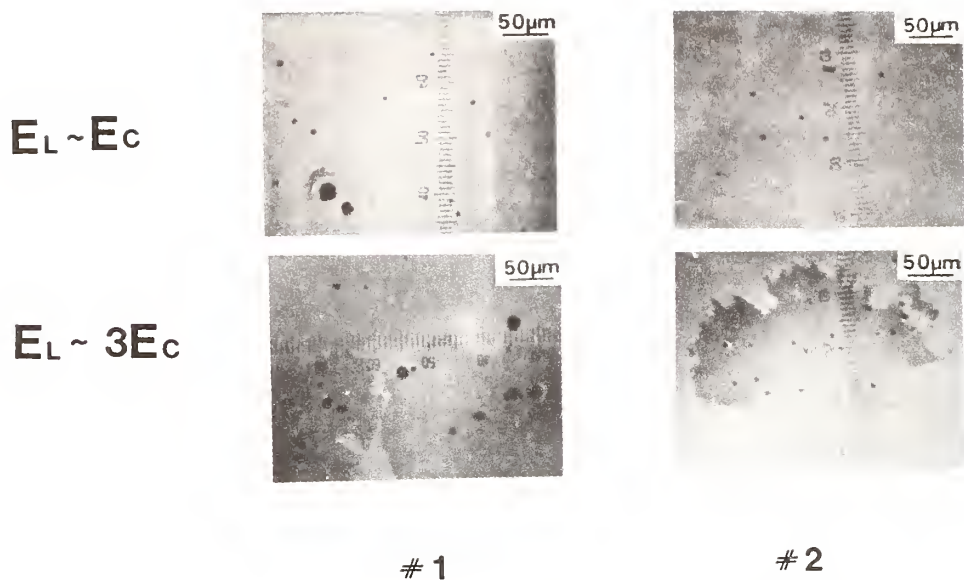


Figure 2 Morphology of the damages of the AR coatings on the substrates #1 and #2 having different surface roughness. Damages near the threshold ($E_L \sim E_c$) and far above the threshold ($E_L \sim 3E_c$) are shown.

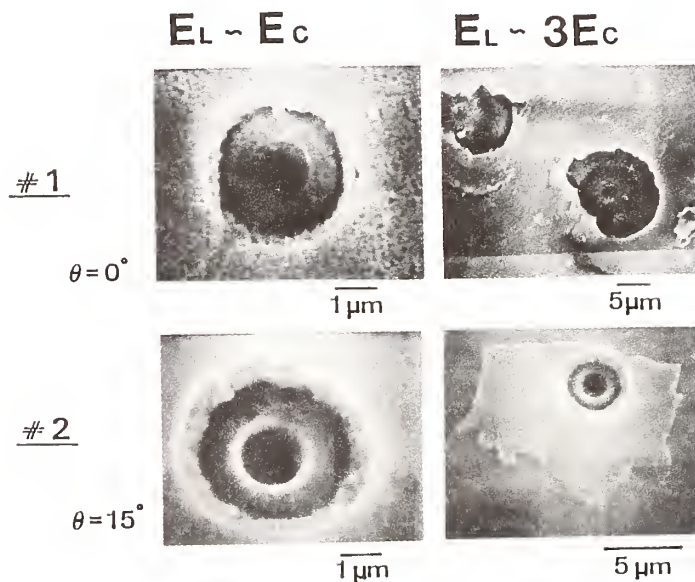


Figure 3 Scanning electron microscope pictures of the deep damages of the AR coatings on the substrates #1 and #2 having different surface roughness. Damages near the threshold ($E_L \sim E_c$) and far above the threshold ($E_L \sim 3E_c$) are shown. For #2 the substrates were tilted at 15° for better observation of the crater walls.

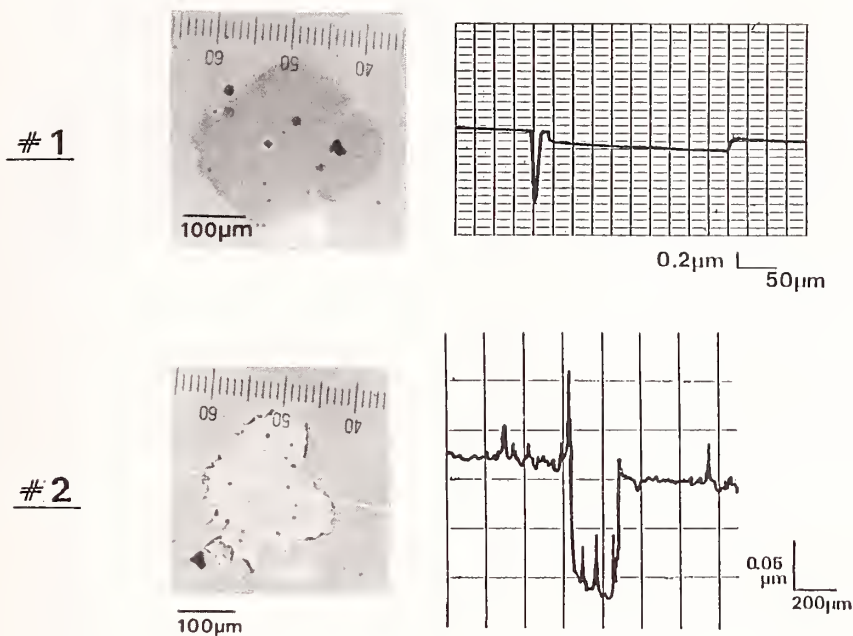


Figure 4 Talystep scans of the damages of the AR coatings on the substrates #1 and #2 having different surface roughness. The scales of the deep damage and the shallow damage are shown in the scan for #1 and #2, respectively.

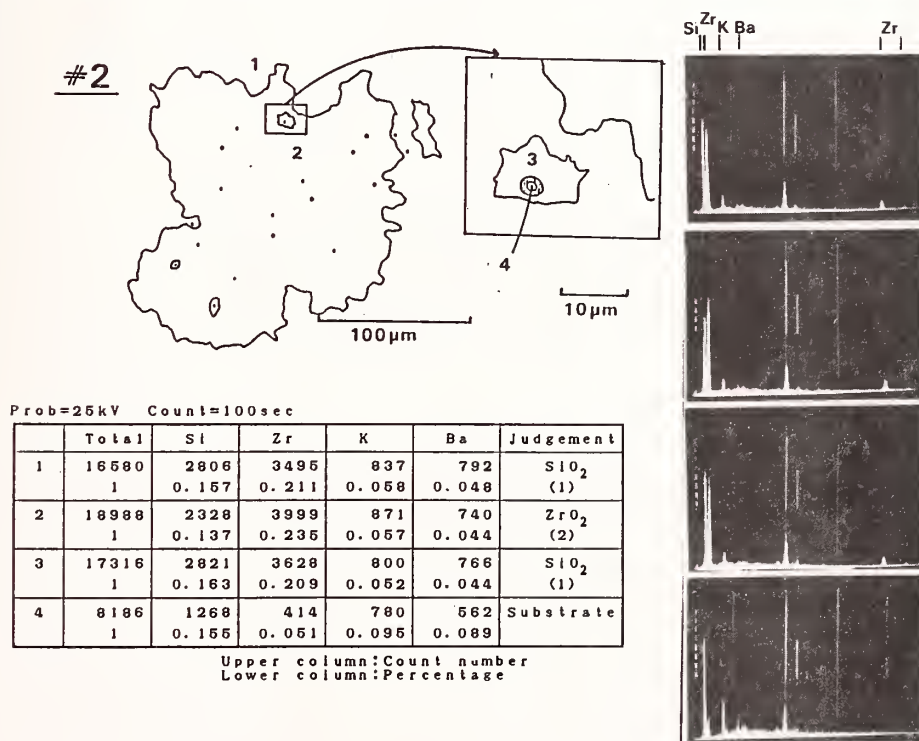


Figure 5 XMA analysis of the sample #2 at four different sites; 1: undamaged site, 2: in the shallow damage, 3: near the deep damage, and 4: in the deep damage.

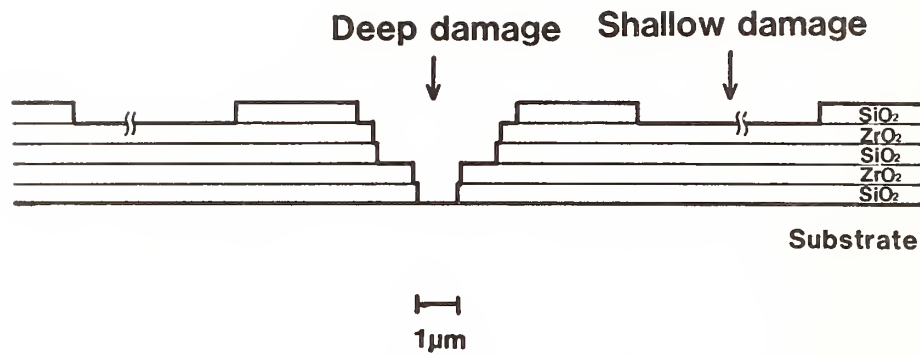


Figure 6 Schematic picture of the damage site of the 5-layer SiO₂/ZrO₂ AR coating.

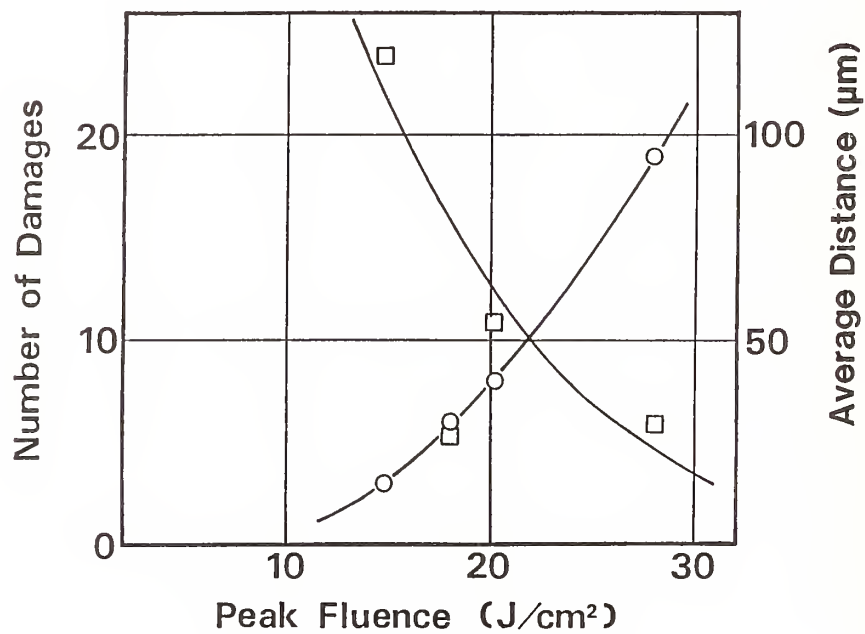


Figure 7 Total number of the deep damages (o) and the average distance between them (□) generated within the laser-irradiated area at different laser fluences.

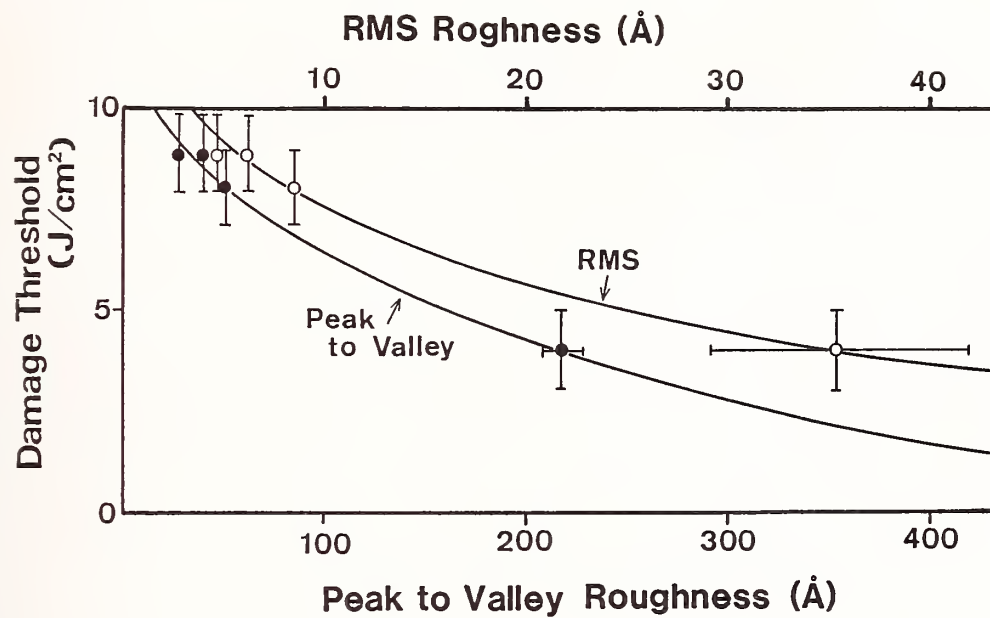


Figure 8 Dependence of the damage threshold of the AR coating on the surface roughness of the substrate.

Table 1. Surface roughness and lateral scale lengths of the two samples prepared by different polishing processes.

Sample	Polish	Surface roughness		Scale length	
		rms	peak-to-valley	Δw	Δd
#1	Conventional	29A	208A	11 μ m	39 μ m
#2	Bowl-feed	8.6A	54A	4 μ m	25 μ m

Table 2. Diameters of and average distances between the deep damages produced at $E_1 \sim 3E_G$. Also shown are lateral scale lengths of the surface roughness of the substrates.

Sample	Polish	Deep damage		Scale length	
		Diameter	Distance	Δw	Δd
#1	Conventional	4-15 μ m	32 μ m	11 μ m	39 μ m
#2	Bowl-feed	3-5 μ m	26 μ m	4 μ m	25 μ m

Correlation Between Local HeNe Scatter and Defect-Initiated
Laser Damage at 2.7 μm

J. O. Porteus, C. J. Spiker, and J. B. Franck

Michelson Laboratory, Physics Division
Naval Weapons Center, China Lake, California 93555-6001

Evidence of a correlation between defect-initiated pulsed laser damage and local pre-damage scatter in multilayer infrared mirror coatings was reported last year at this conference. Analysis of a much larger data base confirms this result on certain sample types over a substantial range of energy densities above the damage onset. Scatter signals from undamaged test sites were obtained using an HeNe scatter-probe damage monitor with a focal spot that nearly coincides with the 150- μm -diameter (D_{1/e^2}) focal spot of the damaging beam. Subsequent damage frequency measurements (1-on-1) were made near normal or at 45-deg incidence with 100-ns pulses at 2.7- μm wavelength. The correlation is characterized by an increase in damage frequency with increasing predamage scatter signal. Characteristics of the correlation are compared with a simple model based on focal spot intensity profiles. Conditions that limit correlation are discussed, including variable scatter from defects and background scatter from diamond-turned substrates. Results have implication for nondestructive defect detection and coating quality control.

Key words: damage correlation; defect scattering; laser-induced damage; multilayer dielectric coatings; nondestructive quality control; optical defects; scatter probe.

Introduction

The importance of defects as initiators of laser-induced damage in optical coatings is well recognized. Defect detection and characterization, particularly when related to laser damage, is therefore of considerable interest to coating development efforts and for quality control. Attempts to correlate damage with photothermal, photoluminescent, and other types of defect signatures have been described in numerous papers at this conference and elsewhere. Our efforts in this area have been based largely on individual defect scattering, which provides relatively simple and rapid detection that can be combined readily with laser damage testing. Association of pulsed visible-wavelength damage with discrete scatterers of the test source radiation has been established using a video microscopy system [1,2].¹ Also, limited evidence of correlation between infrared laser damage and visible wavelength scattering by defects has been reported [3]. The scattered-light detector in this case was a HeNe scatter probe designed to detect damage events automatically. As a result of high sensitivity and spatial resolution better than the mean defect separation, it was possible to detect scattering from individual defects before the damage-probe laser pulse occurred. Close coincidence of the sampling field of the damage probe with that of the scatter probe permitted correlation of damage with the observed defect scattering. The correlation appears as a rise in damage frequency vs pre-damage scatter as shown in figure 11 of [3]. Limitations on the generality of this result must be established before it can be applied to nondestructive quality control. Therefore, a more extensive examination of the available data and its interpretation was performed, as described in this paper.

Scatter Probe

The design and operation of the automated damage test facility used in this work have been described in detail [3]. Essentially, the facility consists of a pulsed laser source, conditioning optics and diagnostics for the laser beam, and a damage test station that includes the sample translation stage and scatter-probe damage monitor. Test sequencing, data acquisition, and maintenance of constant energy density on the sample surface are under computer control. This arrangement provides a convenient means for measuring damage frequency defined as the damaged fraction of a large number of identically tested sites. Such measurements are made for each of several fixed energy densities on a

*Work supported by the Strategic Defense Initiative Organization and Navy Independent Research Funds.

¹Numbers in brackets indicate the literature references at the end of the paper.

given sample, and damage onsets (0% thresholds) are inferred by extrapolating to zero damage frequency using a defect damage model developed for this purpose [4].

A schematic of the scatter probe and its relationship to the pulsed damage probe beam for testing mirror samples at normal incidence is shown in figure 1. For the scatter probe, a high-stability HeNe laser provides a visible plane-polarized CW beam which is brought to a focus by Lens L1 and Mirror M1 at a "negative pinhole" just beyond the reflection at the sample Mirror SM. The position of the HeNe beam and its focus are carefully adjusted to ensure close coincidence at SM with the damage probe beam, which is focused by Lens L3. If the sample surface within the scatter probe field is optically perfect, all of the HeNe beam is specularly reflected and deflected into a dump (not shown) by a tiny diamond-machined mirror on the negative pinhole. However, if the field includes a damaged area, some HeNe radiation is scattered past the negative pinhole, is collected by Lens L2, and is reflected by M2 into the detector, thus indicating a damage event. In a 1-on-1 damage test, the scattered signal is measured at each test site immediately before and immediately after each damage probe pulse, and a damage determination is made when the difference exceeds the combined HeNe source and detector noise fluctuations. One thus discriminates against existing defects that cause the absolute scatter level to vary from site to site across the undamaged sample surface. In performing the damage measurements on certain samples, it was observed that damaged sites often have exhibited an unusually large predamage scatter signal, indicating the presence of a defect. This observation provided the motivation for the present study.

Relationship of Damage Frequency to Localized Scatter

In order to understand the relationship of the predamage scatter signal to damage frequency, one must first understand its relationship to the damage threshold. We treat here the case of a normally incident damage-probe beam with the scatter-probe beam at incidence angle $\theta > 0$, as shown in figure 2. The probe beams are both assumed to be Gaussian, so that the energy density of the damage probe beam at radius r in the sample plane is

$$I(r) = I_a \exp[-(\frac{r}{w})^2] \quad , \quad (1)$$

where I_a is the axial ($r=0$) energy density. Similarly, the intensity of the scatter-probe beam at position (r, ϕ) is

$$J(r, \phi, \theta) = J_a \exp[-(\frac{r}{v})^2 (1 - \cos^2 \phi \sin^2 \theta)] \quad , \quad (2)$$

where ϕ is the azimuth angle measured from the plane of incidence. The scatter probe signal S from a defect with scattering efficiency σ located at (r, ϕ) is

$$S(r, \phi, \theta) = \sigma J(r, \phi, \theta) \quad (3)$$

over and above the background signal S_b . Ideally, there is a threshold scattering level S_0 that corresponds to the onset of damage I_0 , so that the distribution of damage frequency vs scatter is a unity step function at $S = S_0$. This relationship is illustrated in figure 3. From the definition of I_0 , only defects at radial positions $r \leq r_0$, where the damage-probe spatial profile rises above I_0 , will initiate damage [4]. Because of the intensity of the scatter-probe spatial profile in this region [eq. (2)], such defects will scatter with intensity $S \geq S_0$, as shown in the lower part of the figure. However, as a result of the asymmetry when $\theta > 0$, S_0 varies with the azimuth of the defect, ranging from a minimum S_0 at $\phi = \pi/2$ to a maximum S_0' at $\phi = 0$. Combining eqs. (1) through (3) for the conditions $r = r_0$, $I = I_0$, and $S = S_0$, one obtains an explicit expression for S_0 in terms of ϕ and I_0 :

$$S_0(\phi) = \sigma J_a \left(\frac{I_a}{I_0}\right)^{-\left(\frac{w}{v}\right)^2 (1 - \cos^2 \phi \sin^2 \theta)} \quad . \quad (4)$$

Since the defects are random in azimuth, the rise in damage frequency at S_0 is not abrupt, but has a finite slope unless $\theta = 0$. The mid-point S_0 of the rise can be obtained approximately from eq. (4) by replacing $\cos^2 \phi$ by its mean value, giving

$$\bar{S}_0 \approx \sigma J_a \left(\frac{I_a}{I_0}\right)^{-\left(\frac{w}{v}\right)^2 (1 - \frac{1}{2} \sin^2 \theta)} \quad . \quad (5)$$

Observe that \bar{S}_0 decreases as I_a becomes larger. Thus, a downward shift of the distribution to lower scatter levels is to be expected as the incident energy density increases.

The degree of correlation between damage and scatter can be quantified in terms of either the width ΔS_0 or the slope of the rising portion of the distribution. In any practical situation, various sources of broadening can contribute to the width and degrade the correlation. The relative broadening from azimuthal asymmetry associated with nonnormal incidence of the scatter probe can be obtained from eqs. (4) and (5) as

$$\left(\frac{\Delta S_0}{\bar{S}_0}\right)_\theta \approx \frac{\left(\frac{I_a}{I_0}\right)^{\left(\frac{w}{v}\right)^2 \sin^2 \theta} - 1}{\left(\frac{I_a}{I_0}\right)^{\frac{1}{2} \left(\frac{w}{v}\right)^2 \sin^2 \theta}} \quad (6)$$

Poor axial coalignment of the probe beams can introduce additional azimuthal asymmetry and consequent broadening. Broadening also accrues from pulse-to-pulse fluctuations in axial energy density. If ΔI_a represents the maximum deviation from the nominal I_a , the associated full-width broadening contribution averaged over the actual I_a 's is

$$\left(\frac{\Delta S_0}{\bar{S}_0}\right)_{I_a} \approx \left(\frac{w}{v}\right)^2 \left(1 - \frac{1}{2} \sin^2 \theta\right) \left|\frac{2\Delta I_a}{I_a}\right| \quad (7)$$

Similarly, significant broadening can result from excessive fluctuations in the scatter probe laser or detector noise.

Broadening associated with inherent sample properties generally is less straightforward to quantify. Such broadening can arise if all defects do not have the same damage threshold I_0 and the same scattering efficiency σ as assumed in the above analysis. The variation of individual defect damage thresholds can be inferred from the dependence of damage frequency on energy density by a method developed in [4]. Variation of scatter efficiencies can be inferred in a similar way from the frequency distribution $f(S)$ of measured scatter levels. For n randomly sited scatterers per unit area excited at $\theta = 0$ with a Gaussian beam,

$$f(S) = \begin{cases} n\pi v^2 S^{-1} & ; \quad S \leq \sigma J_a \\ 0 & ; \quad S > \sigma J_a \end{cases} \quad (8)$$

In the case of nonidentical σ 's represented by the distribution function $n(\sigma)$, eq. (8) can be generalized to

$$f(S) = \pi v^2 S^{-1} \int_{S/J_a}^{\infty} n(\sigma) d\sigma \quad (9)$$

Here the discontinuity in $Sf(S)$ at $S = \sigma J_a$, which characterizes identical scatterers, is replaced by a more gradual decrease to zero as S increases. The range of the decrease provides an indication of the range of σ variation in terms of S . Because of the standing wave field within a multilayer coating, σ depends on defect depth as well as on inherent defect scattering properties [5]. Since σ can be strongly wavelength dependent as demonstrated in reference [2], correlation between scatter and damage measured at different wavelengths tends to be weakened by variations in defect depth. However, unless the local standing wave field is distorted severely by the defects, depth variations should be apparent from variation of individual defect damage thresholds [6].

Measurement Conditions and Procedure

The damage measurements used for this study were performed to evaluate dielectric-enhanced mirror coatings developed in proprietary efforts, where mirror characteristics and measurement conditions were determined by program requirements. Two distinctly different configurations with respect to damage-probe incidence angle and substrate finish are represented: (1) normal incidence on polished substrates and (2) 45-deg incidence on single-point diamond-turned substrates. Three samples of the first group and six of the second were analyzed for correlation of damage frequency with predamage

scatter. Only three samples are discussed in detail here, two from the first group and one from the second. Significant information on these three samples in their test configurations is given in table 1. The multilayer dielectric coatings were designed for maximum reflectance at 2.7- μ m wavelength and at the damage-probe incidence angle indicated. Mirrors A and C were made from the same coating materials, which differ from those of Mirror B. In the case of Mirror C, a polarizing filter was required in front of the scatter-probe detector to reject a large background component scattered from the diamond-turning tool marks on the substrate. To minimize scattering and damage from dust particles the samples were dusted with boil-off from a liquid N₂ container before mounting in the vacuum test chamber. The 1/e radii of the damage-probe and scatter-probe beams were $w = 53$ and $v = 71$ μ m, respectively, normal to the beam axes at the sample position. The former dimension was measured by pinhole scanning, while the latter was estimated from microscopic inspection of the focal spot. Coalignment of the probe beams was verified on each sample before damage testing by adjusting the scatter-probe beam position for maximum signal from well-developed (uniform) damage produced by the damage probe.

Table 1. Principal samples and test configurations

Mirror	Substrate	Damage probe		Scatter probe	
		Incidence	Polarization	Incidence, θ	Polarization
A	Au/Mo ^a	0°	---	45°	p
B	Ag/ULE ^a	0°	---	45°	p
C	Cu ^b	45°	p ^c	30°	p

^aOptically polished before application of the reflective metal overlayer. ULE is ultra low expansion glass.

^bDiamond-turned, with tool marks nominally normal to incidence plane of probe beams.

^cScatter viewed in s-polarization only.

As described in [3], samples were tested for damage in a matrix of sites. Each site was subjected to a single 100-ns (nominal) pulse of multiline 2.7- μ m radiation having one of several selected energy densities within the limits $\Delta I_a/I_a = \pm 0.2$. The number of sites tested was governed by the requirements for statistical precision in the damage onset determination [4]. Data blocks corresponding to a given energy density include data from ~10 to ~100 sites, a greater number being required to maintain adequate precision at low damage frequencies. Recorded information for each site includes site coordinates, actual energy density, pre- and post-test scatter, and a binary damage/no damage digit used to compute the damage frequency of the entire block. Damage morphology, as later verified by Normarski microscopy, consisted of spatially selective pitting with uniform erosion occurring at the higher energy densities.

Damage frequency vs scatter distributions were obtained at each energy density selected for the damage tests. This was done by sorting the corresponding data blocks into subblocks representing scatter intervals at each level of predamage scatter. The damage frequency for each subblock then was used to construct a histogram of data points representing the distribution at each of the various scatter levels. In order to facilitate comparison with eq. (5) and to evaluate distribution widths, a straight line was fit to the data points in the rising portion of the histogram using a weighted least squares algorithm similar to that described in [4]. The fit was refined by one-by-one exclusion of data points determined to be outside the rising portion. To qualify for exclusion from the fit, a data point must (a) represent a damage frequency of either 0 or 1, (b) represent an extreme scatter level of the group that includes the data point in question, (c) degrade the average fit when included based on the standard error of estimate, and (d) reduce the slope of the fitted line when included. The scatter level corresponding to damage frequency = 0.5 on the fitted line is used to define \bar{S}_0 after subtracting the background scatter S_b . The difference in scatter between the intersections of the line with damage frequencies 0 and 1 is used to define the width ΔS_0 .

Results and Discussion

Generally, all three mirrors of the normal-incidence, polished group showed excellent correlation of damage with scatter, while little or no correlation was found in any of the six diamond-turned mirrors tested at 45 deg. The specific examples of table 1 are discussed below.

Mirror A

Predamage data obtained from Mirror A with the scatter probe is summarized in table 2. Scatter levels S above background given in the top row define the midpoints of half-unit scatter intervals ($\Delta S = 0.5$) comprising the range of observed scatter signals. The second row gives the relative

frequency $f(S)$ ΔS of scatter signals falling within each interval. Corresponding values of $Sf(S)$ given in the third row gradually decrease to zero between $S = 1.35$ and $S = 3.85$, indicating significant variability in σ [see discussion of eq. (9)]. The relatively low value of $Sf(S)$ at $S = 0.35$ apparently is caused by the actual profile being lower in the wings than the assumed Gaussian form. In spite of these complications n can be obtained approximately if $Sf(S)$ is averaged to emphasize intermediate values of S . Appropriate weighting factors are provided by the tabulated $f(S)$ ΔS values. Application of eq. (8) to the weighted average yields $n/\sqrt{2} = 2.4 \times 10^3 \text{ cm}^{-2}$ for the density of scatterers, where the division by $\sqrt{2}$ corrects for the 45° incidence angle.

Table 2. Mirror A scatter frequency data

S^a	0.35	0.95	1.35	1.85	2.35	2.85	3.35	3.85	4.35
$f(S)\Delta S$	0.20	0.34	0.30	0.12	0.02	0.01	0.01	0	0.00
$Sf(S)$	0.14	0.58	0.82	0.45	0.11	0.06	0.03	0	0.02

^aExcludes background $S_b = 12.4$ (arbitrary units)

Results of the damage tests on Mirror A are shown in figure 4. Damage frequencies measured at eight different energy densities are indicated together with standard deviations computed from eq. (26) of [4]. The solid curve shows the power-law defect damage model providing the best representation of the data based on a weighted least-squares fit [4]. The zero-damage intercept of this three-parameter curve gives the damage onset, the slope provides the defect density, and the power (curvature) defines the ensemble of defect failure thresholds. In this case, the power p equals -1 , indicating the degenerate ensemble where all defects initiate damage at the same local energy density. The density of damage-initiating defects is $2 \times 10^{-3} \text{ cm}^{-2}$, in excellent agreement with the density of scatterers obtained with the scatter probe.

Figures 5(a) and (b) show examples of damage frequency vs predamage scatter distributions for two of the eight energy densities of figure 4. Damage frequencies and standard deviations are based on damage data subblocks representing half-unit scatter intervals.* The indicated background $S_b = 12.4$ represents the lowest predamage scatter reading recorded on any site. Parameters obtained as described above from Mirror A distributions such as figure 5 are summarized in table 3. Column 1 gives the relative energy density for each distribution, column 2 gives the slope of the fitted line, column 3 gives the mean threshold scatter level \bar{S}_0 above S_b , and column 4 gives the width ΔS_0 .

Table 3. Mirror A distribution parameters

I_a/I_o	Slope	\bar{S}_0^a	ΔS_0	$\Delta S_0/\bar{S}_0$	
				Observed	Computed ^b
1.38	0.204	3.28	4.90	1.5	0.3
1.75	0.112	4.95	8.93	1.8	0.3
2.50	0.343	1.58	2.92	1.9	0.4
3.00	0.234	2.14	4.27	2.0	0.5
3.50	0.486	1.69	2.05	1.2	0.5
4.00	0.484	1.71	2.07	1.2	0.6
4.50	1.16	1.25	0.86	0.7	0.6
5.00	0.216	2.50	4.60	1.8	0.6

^aWith background, $S_b = 12.4$ subtracted.

^bSum of contributions from eqs. (6) and (7).

*Standard deviations for experimental damage frequencies exactly equal to 0 or 1 are given as $1/(s+1)$ in the figures, where s is the number of test sites represented in the data subblock. This is based on the uncertainty of the result of testing $s+1$ sites. Otherwise, standard deviations were computed from eq. (26) of [4], which gives correct results only at intermediate damage frequencies.

Columns 2 through 4 are expressed in arbitrary scatter units. Column 5 provides the relative width $\Delta S_0/\bar{S}_0$ for comparison with the total known contribution computed from eqs. (6) and (7) given in the last column.

Correlation of damage with predamage scatter is quite evident in all eight distributions of this sample as indicated by the uniformly positive slopes in table 3. Generally, the correlation improves with increasing I_a/I_0 , as is apparent from the correspondingly increasing slopes and decreasing widths ΔS_0 . Comparison of the observed and computed relative widths show the former to be larger in all cases, the difference becoming larger as I_a/I_0 decreases toward unity. Damage with $I_a \approx I_0$ involves defects close to the damage-probe optic axis, where the defect scatter signal is strongest and the asymmetry broadening is minimized, as can be seen from figure 3. This suggests variation in σ as a more important source of broadening than either azimuthal asymmetry or variation in the scatter background. The suggestion is confirmed by the evidence for σ variability from table 2, where the range of S over which $Sf(S)$ goes to zero corresponds roughly to the average ΔS_0 given in table 3. Significant broadening from scatter-probe source instability and detector noise can be eliminated on the basis of excellent reproducibility of the scatter-probe signal from a given site. Also, broadening from defect damage thresholds above I_0 can be largely neglected, since the damage ensemble is degenerate, as discussed in connection with figure 4.

Examination of column 3 of table 3 shows that \bar{S}_0 generally decreases with increasing I_a/I_0 , as predicted by eq. (5). A graphical comparison is given in figure 6, where linear least-squares fits representing the observed and computed shifts in \bar{S}_0 are indicated. Although the observed shift is larger, the difference is within the experimental uncertainty based on distribution widths.

Mirror B

Predamage scatter data for Mirror B is summarized in table 4, which is of the same form as table 2. Variations in $Sf(S)$ are similar to those observed with Mirror A, but decrease more gradually to zero indicating a wider range of σ variability. The density of scatterers obtained by applying eq. (8) to the weighted average of $Sf(S)$ is $n/\sqrt{2} = 2.0 \times 10^3 \text{ cm}^{-2}$, nearly the same as for Mirror A.

Table 4. Mirror B scatter frequency data

S^a	0.15	0.65	1.15	1.65	2.15	2.65	3.15	3.65	4.15	5.15
$f(S)\Delta S$	0.06	0.26	0.29	0.19	0.09	0.05	0.04	0.00	0.02	0.00
$Sf(S)$	0.02	0.34	0.66	0.64	0.39	0.25	0.22	0.02	0.13	0.03

^aExcludes background $S_b = 11.1$

Damage test results from Mirror B, shown in figure 7, are very similar to those from Mirror A in spite of different coating and substrate materials. The best-fit power law model based on the solid data points is again degenerate and gives the same defect density as obtained from the scatter probe. The open data point at $I_a/I_0 = 3.9$ appears to be nonconforming, suggesting intrusion of a secondary damage mechanism at higher energy densities and therefore was excluded from the fit.

Examples of damage frequency vs scatter distributions are shown in figures 8(a) and (b) for two of the eight energy densities of figure 7. Damage frequencies are again based on half-unit scatter intervals, and $S_b = 11.1$. Parameters obtained from these and the other six distributions are summarized in table 5, which is similar to table 3. Although slopes are generally smaller and widths greater than for Mirror A, a definite correlation exists in each case, except for $I_a/I_0 = 2.88$, where the distribution is almost flat. Here, the data indicate several sites with scattering centers unassociated with damage, suggesting excessive substrate scattering in a limited area. A trend to improved correlation with increased I_a/I_0 is less apparent than in Mirror A because of larger fluctuations in the distribution parameters. Observed relative widths are much larger than computed values and do not decrease at small I_a/I_0 as predicted, again pointing to variations in defect scattering as the chief contributor to broadening. This explanation is reconfirmed by the evidence from table 4, where the wider range of σ variability (than for Mirror A) agrees qualitatively with the larger average ΔS_0 .

Observed and computed dependences of S_0 on I_a/I_0 are compared in figure 9. Except for the anomalous data point at $I_a/I_0 = 2.88$, which was excluded from the least-squares fit, the observed shift is again greater than that computed from eq. (5). However, the difference does not exceed the experimental uncertainty when the widths of the distribution are considered.

Table 5. Mirror B distribution parameters

I_a/I_o	Slope	\bar{S}_o^a	ΔS_o	$\Delta \bar{S}_o/S_o$	
				Observed	Computed ^b
1.63	0.091	5.82	11.0	1.9	0.3
1.80	0.053	8.04	18.6	2.3	0.3
2.00	0.376	1.73	2.65	1.5	0.4
2.38	0.169	3.42	5.93	1.7	0.4
2.70	0.267	2.19	3.74	1.7	0.4
2.88	0.009	46.2	115.0	2.5	0.5
3.00	0.256	1.63	3.92	2.4	0.5
3.88	0.183	2.53	5.47	2.2	0.6

^aWith background, $S_b = 11.1$ subtracted.

^bSum of contributions from eqs. (6) and (7).

Mirror C

Figure 10 shows damage test results from Mirror C, which has a somewhat nondegenerate damage ensemble ($p = -0.45$) and a defect density of the same order of magnitude as Samples A and B. Typical scatter distributions are shown in figures 11(a) and (b). Because of the different test configuration and introduction of the polarizing filter, the scatter units are significantly different from those of Samples A and B. Consequently, slopes of the Mirror C distributions cannot be compared numerically with those from the other two samples. However, it is obvious that the present distributions as indicated by the straight-line fits do not rise appreciably over the full range of scatter signals, indicating that the correlation is poor. Consequently, no attempt was made to infer distribution widths or threshold scatter levels for damage on Mirror C.

Evidently, the poor correlation on Mirror C and the other diamond-turned samples is attributable to the polarizing filter required to suppress the strong visible scattering from the tool marks. In another study it was found that visible light scattered from metal surfaces is indeed more highly polarized than that from coating defects [2]. However, the defects scatter a substantial polarized component, which the filter removes, thus reducing the scatter-probe sensitivity. Also, on some of these samples, a systematic dependence on sample position was observed suggesting incomplete suppression of tool-mark scattering. In retrospect, it is unfortunate that the arc-shaped tool marks were essentially normal to the plane of incidence, which maximized the resulting background scatter.

Conclusions

Nine multilayer dielectric mirrors have been studied quantitatively for correlation between the HeNe scatter signal from individual defects and 2.7 μm pulsed-laser damage. After examining over 50 examples of damage frequency vs scatter data, we conclude that a strong correlation can be observed provided certain conditions are satisfied. These include near coincidence of the scatter- and damage-probe spatial profiles, profile dimensions that are smaller than the mean defect separation, adequate stability of the laser sources, and noninterference from scattering unrelated to damage. Also, the correlation is degraded if defects have unequal individual damage thresholds or unequal scattering efficiencies. Variable defect scattering efficiency is the dominant limitation in samples evaluated here, based on evidence from scatter frequency distributions and evaluation of other sources of degradation. A poor correlation observed on diamond-machined dielectric-mirror substrates is attributed indirectly to background scatter from tool marks aligned normal to the incidence plane. Rotation of the sample by 90 deg is expected to alleviate this problem.

For mirrors with good correlation, the mean scatter threshold for damage decreases with increasing energy density above the damage onset. This is consistent with a simple mathematical model that accounts for the different dimensions of the spatial profiles of the two probes, including asymmetry of the scatter-probe profile due to nonnormal incidence. More data would be useful in order to test the model with greater statistical precision.

Overall, the scatter probe shows promise as a simple nondestructive indicator of local laser damage probability when properly implemented and calibrated against damage on representative high-quality mirror samples. Once correlation has been established, the probe could be used to scan large coated areas rapidly to assess the density of damage-initiating defects. Also, defect sites can be identified for more extensive materials analysis or for megashot survivability tests, both of which are inherently time-consuming.

References

- [1] Marrs, C. D.; Porteus, J. O.; Palmer, J. R. "Defect damage precursors in visible-Wavelength mirrors," in Proceedings of the 15th annual symposium on optical materials for high power lasers, Bennett, H. E.; Guenther, A. H.; Milam, D.; Newnam, B. E., ed. 1983 November 14-16; Boulder, CO. Nat. Bur. Stand. (U.S.) Spec. Publ. 688; 1985 Nov. Pp. 378-384.
- [2] Marrs, C. D.; Porteus, J. O.; Palmer, J. R. "Nondestructive defect detection in laser optical coatings." J. Appl. Phys. 57; 1719; 1985.
- [3] Franck, J. B.; Seitel, S. C.; Hodgkin, V. A.; Faith, W. N.; Porteus, J. O. "Automated pulsed testing using a scatter-probe damage monitor," presented at the 16th annual symposium on optical material for high power lasers; 1984 October 15-17; Boulder, CO (proceedings in process).
- [4] Porteus, J. O.; Seitel, S. C. "Absolute onset of surface damage using distributed defect ensembles." Appl. Opt. 23; 3796; 1984.
- [5] Newnam, B. E. "Damage resistance of dielectric reflectors for picosecond pulses," in Proceedings of the 6th annual symposium on optical materials for high power lasers, Glass, A. J.; Guenther, A. H., ed. 1974 May 22-23 Boulder, CO. Nat. Bur. Stand. (U.S.) Spec. Publ. 414; 1974 December. Pp. 39-47.
- [6] Newnam, B. E.; Gill, D. H.; Faulkner, G. "Influence of standing-wave fields on the laser damage resistance of thin films," in Proceedings of the 7th annual symposium on optical materials for high power lasers, Glass, A. J.; Guenther, A. H., ed. 1975 July 29-31; Boulder, CO. Nat. Bur. Stand. (U.S.) Spec. Publ. 435; 1976 April. Pp. 254-271.

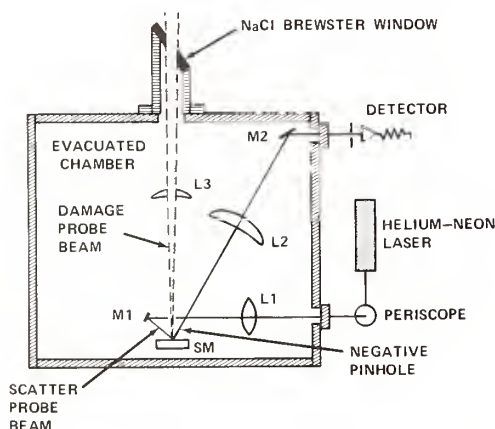


Figure 1. Schematic of scatter probe and damage probe optics in the evacuated test chamber. The scatter-probe optical train runs from the HeNe laser to the detector, incorporating optics L1-M2. The 2.7- μ m damage probe beam enters through the NaCl Brewster window and is focused on the sample Mirror SM by Lens L3.

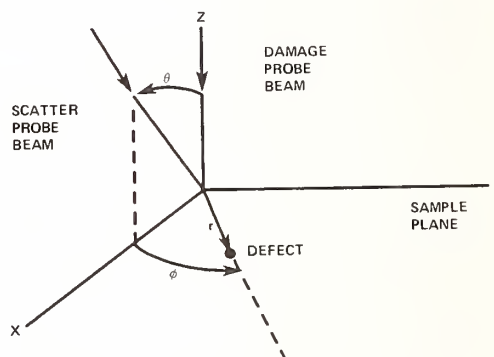


Figure 2. Geometrical relationship of scatter- and damage-probe beams shown for the case of normal incidence damage testing. The scatter-probe beam is incident at angle θ . Defect positions in the sample plane x, y are designated by polar coordinates r, ϕ .

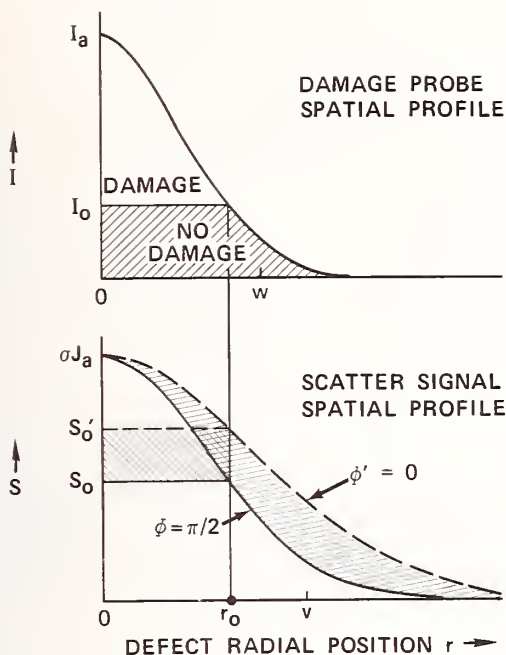


Figure 3. Relationship between the damage onset I_0 and the corresponding scatter threshold for damage S_0 , as governed by the damage- and scatter-probe spatial profiles. The shaded area between the solid and dashed curves indicates the asymmetry of the latter profile in the sample plane, which leads to the shaded variation in S_0 . Symbols are identified in the text.

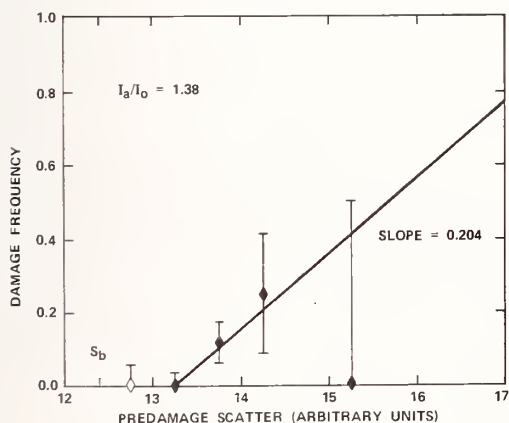


Figure 5(a). Distribution of damage frequency vs. predamage scatter for Mirror A at $I_a/I_0 = 1.38$. Data points indicate damage frequencies at half-unit scatter intervals. solid data points are those included in fitting the straight line representing the rising portion of the distribution.

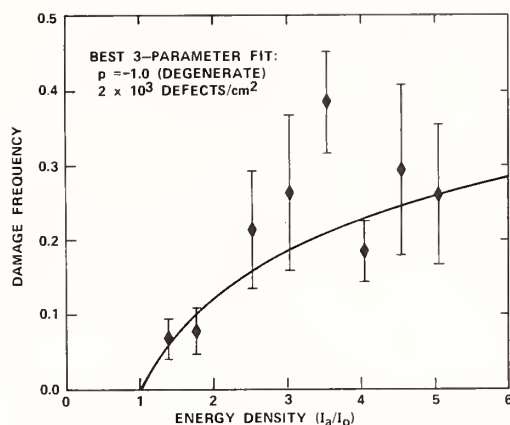


Figure 4. Damage test results for Mirror A. Data points with uncertainties give damage frequencies measured at the energy densities indicated in units of the damage onset. The solid curve represents the best-fit power-law model obtained as described in [4].

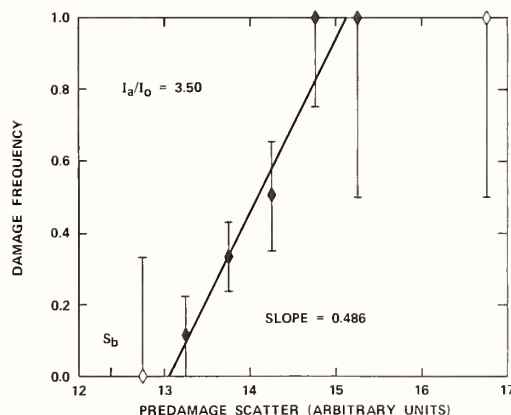


Figure 5(b). Distribution similar to figure 5(a) for Mirror A at $I_a/I_0 = 3.50$.

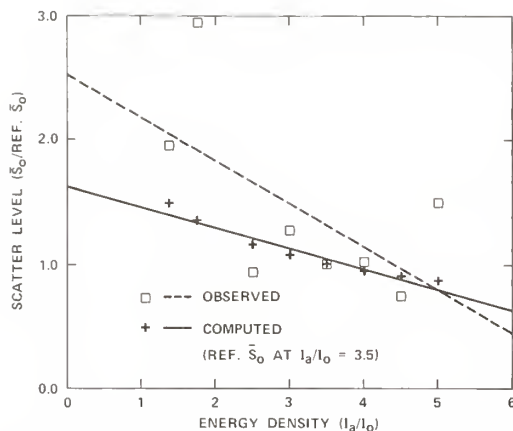


Figure 6. Threshold scatter level \bar{S}_0 vs energy density for Mirror A. Squares represent experimental data and crosses represent values computed from eq. (5). Dashed and solid lines are the respective linear least-squares fits (regression lines). Plotted scatter levels are relative values with \bar{S}_0 at $I_a/I_0 = 3.5$ as an arbitrary reference.

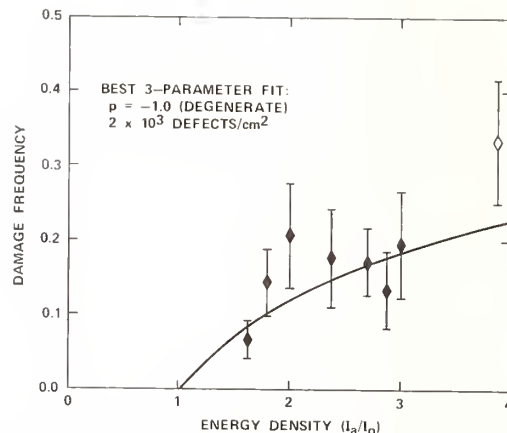


Figure 7. Damage test results for Mirror B presented in the manner of figure 4. Only the seven solid data points were used in fitting the power-law model.

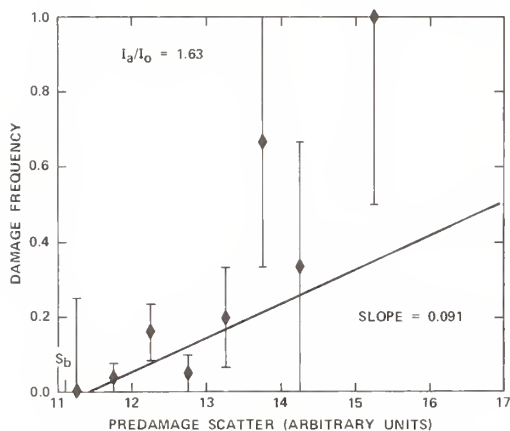


Figure 8(a). Distribution of damage frequency vs predamage scatter for Mirror B at $I_a/I_0 = 1.63$, presented in the manner of figure 5.

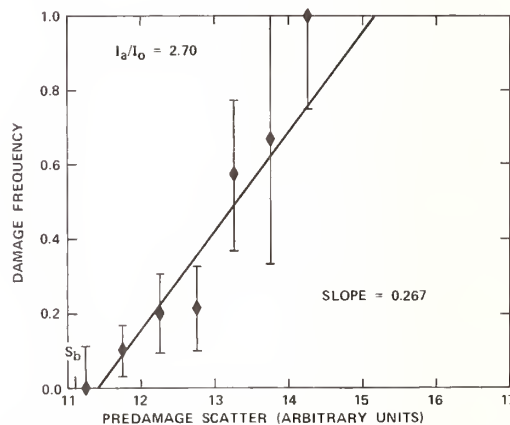


Figure 8(b). Distribution similar to figure 8(a) for Mirror B at $I_a/I_0 = 2.70$.

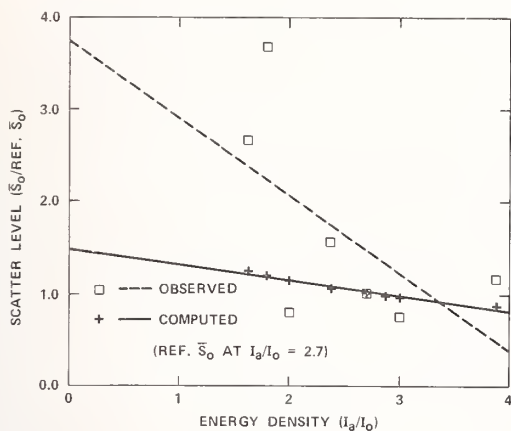


Figure 9. Threshold scatter level \bar{S}_0 vs energy density for Mirror B presented in the manner of figure 6. The value of \bar{S}_0 at $I_a/I_0 = 2.7$ is used as a reference for plotting relative scatter levels.

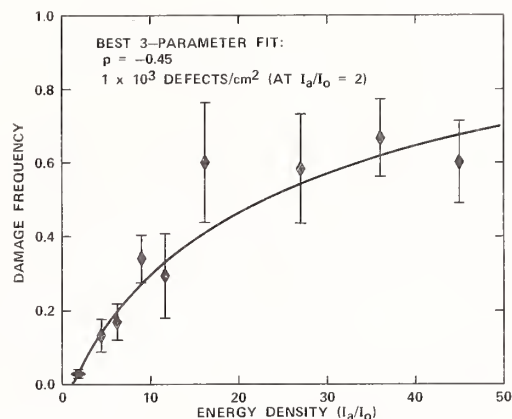


Figure 10. Damage test results for Mirror C presented in the manner of figure 4. The defect density includes all defects that initiate damage at $I_a = 2I_0$ in the nondegenerate ensemble (see [4]).

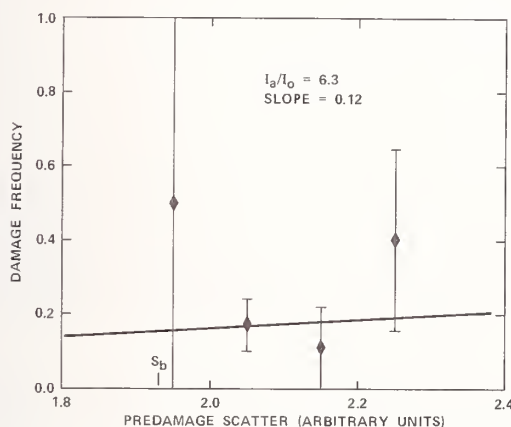


Figure 11(a). Distribution of damage frequency vs predamage scatter for Mirror C at $I_a/I_0 = 6.3$ presented in the manner of figure 5. Data points represent damage frequencies of tenth-unit scatter intervals. The scatter scale differs significantly from that of Samples A and B because of the different test configuration.

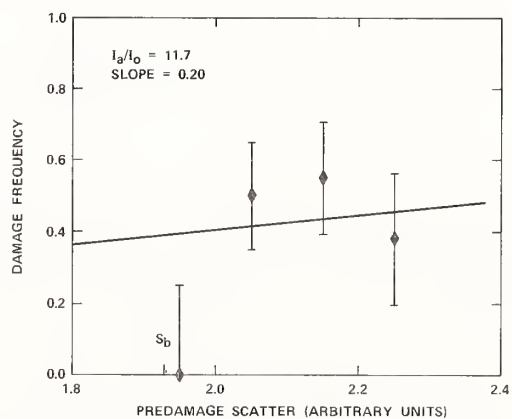


Figure 11(b). Distribution of damage frequency similar to figure 11(a) for Mirror C at $I_a/I_0 = 11.7$.

CO₂ LASER INDUCED DAMAGE IN A MODEL THIN FILM
SYSTEM : ZnS ON Ge

D.R. Gibson and A.D. Wilson

Barr and Stroud Ltd.,
Applied Physics Group,
Caxton Street, Anniesland,
Glasgow G13 1HZ, U.K.

The CO₂ laser absorption and damage characteristics of thermal and electron beam evaporated ZnS films on Ge substrates have been investigated. The substrate temperature during deposition is shown to be an important parameter controlling film porosity and hence water ingress. The role of water is probed by a variety of techniques including laser induced desorption (mass) spectroscopy. Water is shown to lead to high film-substrate and bulk-film absorptances and to low laser damage thresholds (LDTs) with damage originating in the film. Physically dense films, which do not allow water ingress, have high LDTs limited by damage to the Ge substrates. Examination of ZnS films on Si and ZnS substrates indicates that the film absorptances and LDTs are dependent on the substrate material.

KEY WORDS: CO₂ laser damage; film porosity; laser calorimetry; laser desorption spectroscopy; water sorption; ZnS films

1. INTRODUCTION

Thin film coatings are often the parts of infra-red optical elements most susceptible to CO₂ laser induced damage [1]. Currently, there is much interest in obtaining coatings with a high laser damage resistance and to this end, new coating techniques such as molecular beam epitaxy [2] and ion assisted deposition [3] are being investigated. Surprisingly, however, there is only limited information on films produced using conventional vacuum technologies and thus there is an insufficient data base for quantifying improvements effected by the new technologies.

The susceptibility of coatings to laser damage is in the main an artefact of the deposition methodology, which can give rise to coatings with structural defects, impurity inclusions and film structures which are susceptible to atmospheric contamination (e.g. water ingress). In addition, substrate surface quality and pre-coating preparation may also be a contributing factor in lowering or limiting the laser damage resistance of the coating.

Previously, we have examined the laser damage behaviour of ZnS thin films, produced by conventional deposition methods, on Ge substrates. Although in many samples the LDT is limited by the Ge substrate, a significant fraction of the samples are film limited. To resolve the reasons for this behaviour and to increase our general understanding of the damage characteristics of conventionally produced coatings, the CO₂ laser induced damage of this relatively simple thin film system (ZnS films on germanium) has been investigated. The films have been produced using thermal evaporation (at various substrate temperatures) and electron beam evaporation. In addition ZnS films (thermally evaporated) on high laser damage threshold (LDT) substrates (ZnS and Si) have been assessed.

The principal aims of the investigation were to identify the sources of damage within the films in relation to surface and bulk film properties, and to relate these to the deposition conditions. In addition, methods of increasing the laser damage resistance of the films, by optimising the deposition conditions are reported.

The study shows that films deposited at high substrate temperatures have high LDTs and that performance is limited by damage to the Ge substrate. The use of low substrate temperatures can result in films with low LDT values. This is traced to the increase in film porosity which allows water ingress. The water absorbs strongly at 10.59 μm and is the cause of the damage in these "poor" films. The use of pulsed laser induced desorption (mass) spectrometry (PLIDs), pre-pulsed laser calorimetry and pre-pulsed laser damage measurements provide unambiguous evidence of the important role of sorbed water.

2. EXPERIMENTAL

2.1 Samples

ZnS films of various optical thickness ($\sqrt{4}$, $\sqrt{2}$, $3\sqrt{4}$ and λ , where $\lambda = 10.6\mu\text{m}$) on Ge substrates, have been produced using thermal and electron beam evaporation. The Ge substrates were polished using alumina (Linde A, 0.3 micron). Three sets of samples were produced, corresponding to two sets of thermally evaporated ZnS films deposited onto "cold" ($\approx 120^\circ\text{C}$) and "hot" ($\approx 200^\circ\text{C}$) substrates. Since the ZnS sticking coefficient relative to 40°C is 0.93 at 120°C and 0.83 at 200°C [5], it is practicable to produce films at the higher temperature. The third set of samples was produced using electron beam (E.B.) evaporation. In addition, "hot" thermally evaporated ZnS films ($\sqrt{4}$ optical thickness) on ZnS and Si substrates were produced.

In order that coherence effects within the Ge substrates were defeated, each sample had the exit substrate face coated (using the same deposition methodology as the entrance face) with a $\sqrt{4}$ optical thickness ($\lambda = 10.6\mu\text{m}$) ZnS anti-reflection coating. Coherence effects would complicate the results of several of the techniques (laser calorimetry, laser damage assessment) employed to characterise the films.

2.2 CO₂ TEA Laser Damage Test Facility

The CO₂ TEA laser damage facility has been described in detail previously [1, 4]. For this work, a standard spike (100ns FWHM) and tail (2 μs) 10.59 μm pulse was used. The $1/e^2$ spot size was $> 0.9\text{mm}$. The probability method of Foltyn [6] was used to obtain the LDT value which is defined herein as the peak energy density corresponding to the zero probability of damage.

2.3 CO₂ Laser Calorimeter

The basic rate calorimeter has been described previously [4]. For certain measurements involving irradiation of the sample with CO₂ TEA laser pulses prior to measurement (i.e. pre-pulsing) the arrangement sketched in Figure 1 was used.

2.4 CO₂ Pulsed Laser Induced Desorption Spectrometer

Pulsed laser induced desorption (PLID) has been reported by Allen and co-workers [7]. A simplified adaptation of that technique, Figure 2, consists of a (Balzers QMA 064) quadrupole mass analyser (QMA) and positionable sample holder mounted in a UHV chamber fitted with KCl windows, and a CO₂ TEA laser. Before carrying out PLID analysis of the films, the sample was positioned out of the beam and the windows irradiated to drive off any desorbable contaminants. This process was carried out until no increase in system partial pressure was monitored. Unfortunately quantitative information on the number of desorbable molecules cannot be obtained since the collection volume of the QMA is not known and the rise time of the desorption signal is limited by that of the QMA. However, useful qualitative information can be obtained.

3. ZINC SULPHIDE FILMS ON GERMANIUM SUBSTRATES

3.1 Absorbance Data

To determine the interfacial and bulk film contributions to the total absorbance, the absorbance of the various ZnS film thicknesses were determined using CO₂ laser rate calorimetry. Figure 3 shows representative absorbance data for the "cold" thermally deposited ZnS, measured at one week and one month after deposition. For each sample the absorption was determined at three separate sites, so that variation across the sample could be assessed. For the samples measured this variation was typically $\pm 10\%$ of the mean absorbance value.

The difference between the measured and extrapolated zero-thickness absorbances, Figure 3, is due to absorption at the film-air and substrate-film interfaces. The two contributions to the interface absorption were separated using a method, due to Temple [8], which was originally developed for single film coated substrates but has been modified to account for the anti-reflection layer on the exit face of the substrate. It is assumed that the bulk, air-film and film-substrate absorbance within the exit face anti-reflection layer are the same as the front surface film values. This is a reasonable assumption since both films were deposited using the same deposition conditions.

The bulk film absorption coefficient (α_f), and the air-film (a_{af}) and film substrate (a_{fs}) absorbances are given in Table 1 for the films produced by the three deposition conditions. Results are indicated for absorbance data, taken one week and one month after deposition of the

films. The small negative values of a_{af} are considered to be zero within experimental error. The film-substrate absorptance of the "hot" thermally and electron beam evaporated films is comparable to (but, of course, additional to) the surface absorptance of the uncoated alumina polished Ge. The "cold" thermally evaporated films have a significantly higher film-substrate interface absorptance which, as will be shown in section 3.4, is due to water ingress. We note that Donovan et al. [9] detected water, using a nuclear resonant technique at the ZnS film-substrate interface (the substrate material was not specified). The bulk absorption coefficient of the "cold" films exhibited an 8-fold increase after a 3 week exposure to a laboratory environment (due to water ingress) but thereafter remained stable (suggesting the film bulk was saturated with water). The "hot" thermally and electron beam evaporated films showed no such increases in their bulk absorption coefficients. These were, however, an order of magnitude greater than for bulk ZnS at $10.59\mu\text{m}$.

3.2 CO₂ TEA Laser Induced Damage

Figures 4a, b and c show laser damage probability plots (LDPPs) for the "cold" and "hot" thermally evaporated and the electron beam evaporated films. Included in each figure is the LDPP for an uncoated Ge substrate.

The fluence (E) within the substrate surface depends on the interface transmittance (T) of the surface. The ratio of the fluence values for uncoated (u) and coated (c) substrates is $E_c/E_u = T_c/T_u$. Thus an AR coating has the effect of coupling more energy into the substrate surface. It follows that the ratio of the laser damage thresholds will be $\text{LDT}_c/\text{LDT}_u = T_u/T_c$. For Ge, $T_u = 0.64$. For ZnS on Ge, $\lambda/4$ and $3\lambda/4$ films have $T_c \approx 0.99$ whereas $\lambda/2$ and λ films have $T_c \approx 0.64$. Consequently if the LDT of ZnS films on Ge is limited by damage to the Ge, the LDT ratio, $\text{LDT}_c/\text{LDT}_u$, will be ≈ 0.64 for $\lambda/4$ and $3\lambda/4$ films and will be ≈ 1.0 for $\lambda/2$ and λ films. Inspection of Table 2 shows that "hot" thermally and electron beam evaporated films are substrate limited but that the "cold" thermally evaporated films are film limited. Comparison of Nomarski photomicrographs of the damage sites on the coated and uncoated samples revealed "film-like" damage morphology for the "cold" films and "substrate-like" damage for the other samples. Both "cold" and "hot" films showed defect-type damage morphologies with isolated damage sites occurring within the beam area.

3.3 The Effect of Pre-Pulsing on the Laser Damage Threshold

Irradiating at an energy density below the LDT (hereafter called pre-pulsing) has been shown to increase the subsequently measured LDT [7]. This effect is ascribed to desorption of absorbing contaminants leading to a reduction in film absorption.

"Cold" thermally evaporated $\lambda/4$ ZnS films were pre-pulsed at several energy densities up to the LDT value ($\approx 9 \text{ J/cm}^2$). No increase in LDT value was found, most probably due to the low initial LDT value precluding contaminant desorption before film damage. For the $\lambda/2$, $3\lambda/4$ and λ "cold" thermally evaporated films, the effect on the film LDT as a function of pre-pulse energy density (five pulses were used at each energy density), is indicated in Figure 5 where it can be seen that pre-pulse energy densities in excess of $\approx 10 \text{ Jcm}^{-2}$ are required to cause an increase in LDT. The LDPPs for these films after pre-pulsing at $\approx 11 \text{ Jcm}^{-2}$ are shown in Figure 4d. The films now exhibit similar LDPP characteristics and LDTs to the "hot" thermally and electron beam evaporated films. Neither these latter nor the Ge substrates showed any pre-pulsing effects.

This behaviour suggests that the "cold" films contain a desorbable contaminant which limits their LDTs.

3.4 Pre-Pulsed Laser Calorimetry

The effect of pre-pulsing on the absorptance of the "cold" films was investigated using the calorimeter described in Section 2.3. All measurements were made on films four months after their deposition, at which time their absorption properties were not significantly different from those as assessed one month after deposition (see Table 1). Indicated in Figure 6 is the absorption reduction for the "cold" thermally deposited λ thick film as a function of number of pulses, for incident energy densities both below and above the threshold value obtained from pre-pulsed laser damage measurements. The $\lambda/2$ and $3\lambda/4$ films gave similar results. Significant variations in the absorptance reduction for different areas of the film at the same energy density were observed. To eliminate this variation the absorptance reductions shown in Figure 6 are the average values over five separate areas of the film (errors shown in Figure 6 are absolute values).

It can be seen that below $\approx 10 \text{ J/cm}^2$ (peak incident energy density) there is no significant change in the absorptance value. For energy densities above 10 J/cm^2 the total absorptance decrease (over four pulses) is 50%, reducing the absorptance to a value similar to the "hot" thermally and electron beam deposited films (which did not exhibit absorptance reduction on pre-pulsing). Pre-pulsing with more than four pulses led to no further changes in absorptance.

These results suggest that all of the desorbable contaminant within the bulk and at the interfaces of the films is removed.

3.5 Pulsed Laser Induced Desorption (PLID) Analysis

To unambiguously identify the contaminant, PLID analysis was carried out as described in Section 2.4. Irradiating "cold" films at $\approx 11 \text{ Jcm}^{-2}$ led to the increase in partial pressure (QMA tuned to mass 18 i.e. H_2O) shown in Figure 7. Irradiation at $\approx 6.5 \text{ Jcm}^{-2}$ caused no measureable increase in H_2O partial pressure. The number of (11 Jcm^{-2}) pulses required to desorb all of the (desorbable) water is ≈ 4 which is exactly the same as is required to decrease the sample absorptance to the "hot" film value. This demonstrates a very convincing correlation between anomalous film absorptance and the desorbable water content of the film.

4. ZnS FILMS ON HIGH LDT SUBSTRATES

In order that the ultimate laser damage resistance of the best ZnS films could be assessed, $\lambda/4$ ZnS films were thermally deposited onto both faces of high damage resistant substrates (Si and CVD ZnS) at 200°C (i.e. equivalent to the "hot" films discussed previously). Table 3 gives the LDT values and the experimental and theoretical ratios of the coated to uncoated substrate LDT values. Comparison of the experimental and theoretical LDT ratios suggest the ZnS on the Si substrate is film limited and on the ZnS substrate it is substrate limited. This is also evidenced by the damage morphology: for the coated Si substrate, the damage occurs at the substrate-film interface; for the coated ZnS substrates damage occurs on the back coated substrate face, and is a deep crater indicative of an electron avalanche ionisation damage mechanism, as is the case for uncoated ZnS [1]. The important observation is that ZnS films produced conventionally can be as good as bulk ZnS.

A preliminary analysis of the thin film absorptance data indicates that for films on Si, the film-substrate interface absorptance is very large (greater than for good films on Ge) and thus laser damage is most probably initiated at the film-substrate interface. The large interface absorption may indicate reaction between the ZnS and Si. For ZnS films on ZnS, film-substrate interface absorptance cannot be detected. These data indicate that the film growth and hence LDT may be dependent upon the substrate type.

5. SUMMARY AND CONCLUSION

The optical absorptance and laser damage properties at $10.59\mu\text{m}$ of ZnS films on Ge have been related to the deposition conditions. Films deposited on "cold" substrates (120°C) show much higher substrate-film interface absorptances than films deposited on "hot" substrates (200°C) and also have bulk absorption coefficients which increase on exposure to the laboratory atmosphere. Such data indicate that "cold" films are subject to water sorption. The presence of water has been proved unambiguously using pulsed CO_2 laser induced desorption spectroscopy and has been correlated with the anomalous absorptance of "cold" films (cf "hot" films). The water present in "cold" films results in low $10.59\mu\text{m}$ LDT values but can be driven off temporarily by pre-pulsing with a CO_2 TEA laser at energy densities $> 10 \text{ Jcm}^{-2}$. "Hot" films on Ge have stable bulk absorption coefficients and give LDTs which are limited by the substrate rather than the film. The nature of the substrate defects responsible for damage is discussed elsewhere [4].

These observations can be related to the film structure, which is dependent on the energy (i.e. the mobility) of the evaporant adatoms on the substrate surface. The higher the mobility, the greater the degree of structural order and hence film density [10]. For the "cold" thermally evaporated films, there is a relatively low surface mobility, producing a polycrystalline/amorphous structure, which is porous and susceptible to water ingress. For "hot" thermally and electron beam evaporated material, the "hot" substrate surface supplies the energy for crystalline growth and hence higher density films, which preclude water ingress into the film structure. In addition, water adsorbed onto the substrate surface before coating will be significantly reduced by heating the substrate (as in the case for "hot" thermal evaporation). For "cold" thermally evaporated material there may be insufficient energy to desorb substrate surface adsorbed water, leading to a high concentration at the film-substrate interface. Supporting evidence for the higher porosity of the "cold" films has been obtained recently from

two studies; the "cold" films show higher levels of CO₂ laser light scattering from the film bulk confirming their greater degree of inhomogeneity; an electron microprobe analysis of fracture cross-sections of the films indicates a greater decrease in density (as indicated by a decrease in element count rate) for "cold" films as the film thickness is increased [11]. As far as we are aware, this is the first report in which the effect of water sorption in ZnS, caused by film porosity, has been linked unambiguously to anomalously low CO₂ laser damage thresholds.

In addition to the dependence of film properties on the substrate temperature there is also a dependence on the substrate type. For example ZnS films thermally evaporated onto "hot" CVD ZnS have undetectable levels of film-substrate interface absorption and have LDTs equal to the uncoated ZnS even though the ZnS film absorption coefficient is 10 x that of the ZnS substrate. The mechanism of damage in this case is electron avalanche ionisation which is relatively independent of the bulk absorption coefficient e.g. of ZnS and ZnSe [1]. ZnS films on Si show very large values for film-substrate interface absorptance and it is likely that damage is then initiated at the film-substrate interface.

In summary, we have demonstrated that ZnS films produced by conventional thermal evaporation can result in substrate (Ge, ZnS) limited laser damage behaviour. For this to be so, the film density must be sufficiently high to eliminate water ingress. In the present work this has been ensured by using substrate temperatures of $\approx 200^\circ\text{C}$, which value is higher than is conventionally used for ZnS. Ion assisted deposition allows higher density films to be produced at lower substrate temperatures [12]. Epitaxial growth processes are also known to produce void-free high density films. For example, MBE films of ZnS on Ge substrates and ZnSe on ZnSe substrates [2] have been shown to be substrate limited in their CO₂ laser damage behaviour.

The authors wish to thank the Management of Barr and Stroud for permission to publish this paper.

REFERENCES

- [1] D.R. Gibson and A.D. Wilson, "Studies of CO₂ Laser Induced Damage to Infrared Optical Materials and Coatings", paper presented at the 16th Annual Symposium on Optical Materials for High Power Lasers, Boulder, Colo., Oct., 1984.
- [2] K.L. Lewis, J.A. Savage, A.G. Cullis, N.G. Chew, L. Charlwood and D.W. Craig, "Assessment of Optical Coatings Prepared by Molecular Beam Techniques", paper presented at the 16th Annual Symposium on Optical Materials for High Power Lasers, Boulder, Colo., Oct., 1984.
- [3] J.R. Sites, P. Gilstrap and R. Rujkorakarn, NBS Spec. Publ., 669, 243 (1982).
- [4] D.R. Gibson, C.M. MacDonald and A.D. Wilson, "CO₂ Laser Induced Damage to Ge : Relation to Surface Preparation", paper presented at the 17th Annual Symposium on Optical Materials for High Power Lasers, Boulder, Colo., Oct., 1985.
- [5] E. Ritter and R. Hoffmann, J. Vac. Sci. Technol., 16, 733 (1969).
- [6] S.R. Foltyn, NBS Spec. Publ., 669, 368 (1982).
- [7] J.O. Porteus, W.N. Faith and S.D. Allen, NBS Spec. Publ., 638, 273 (1981).
- [8] P.A. Temple, Appl. Phys. Lett., 34, 677 (1979).
- [9] T.M. Donovan, P.A. Temple, S.C. Wu and T.A. Tombrello, NBS Spec. Publ., 568, 237 (1979).
- [10] K.H. Guenther, Appl. Opt., 23, 3806 (1984).
- [11] K. Clarke, D.R. Gibson, C.M. MacDonald and A.D. Wilson, unpublished data.
- [12] S.G. Saxe, M.J. Messerly, B. Bovard, L. De Sandre, F.J. van Milligen and H.A. MacLeod, Appl. Opt., 23, 3633 (1984).

1. ABSORPTANCE OF ZnS FILMS ON Ge

EVAPORATION METHOD	α_f (cm^{-1})		a_{fs} , %		a_{fa} , %	
	1 week	1 month	1 week	1 month	1 week	1 month
Thermal "cold"	1	8	0.54	0.55	-0.07	-0.07
Thermal "hot"	2	2	0.11	0.13	-0.04	-0.01
Electron beam	2	2	0.18	0.15	-0.05	-0.05

α_f , bulk film absorption coefficient, a_{fs} , film-substrate absorptance, a_{fa} , film-air absorptance.
Times are those after deposition.

2. RATIO OF FILM TO SUBSTRATE LASER DAMAGE THRESHOLDS FOR ZnS ON Ge

FILM THICKNESS (NO. OF $\lambda/4$ WAVES)	LDT (FILM)/LDT (SUBSTRATE)		
	THERMAL "COLD"	THERMAL "HOT"	ELECTRON BEAM
1	0.26	0.63	0.60
3	0.48	0.65	0.63
2	0.63	0.92	0.99
4	0.66	0.94	1.05
Probable Damage Source	Film	Substrate	Substrate

3. ZnS FILMS ON HIGH LDT SUBSTRATES

SUBSTRATE TYPE	LDT (Jcm^{-2})		LDT RATIO ($\frac{\text{COATED}}{\text{UNCOATED}}$)	
	SUBSTRATE ONLY	WITH $\lambda/4$ ZnS FILM ON BOTH SIDES	EXPERIMENTAL	THEORETICAL IF SUBSTRATE LIMITED
Si	66	38	0.58	0.7
ZnS	70	69	0.99	1.00

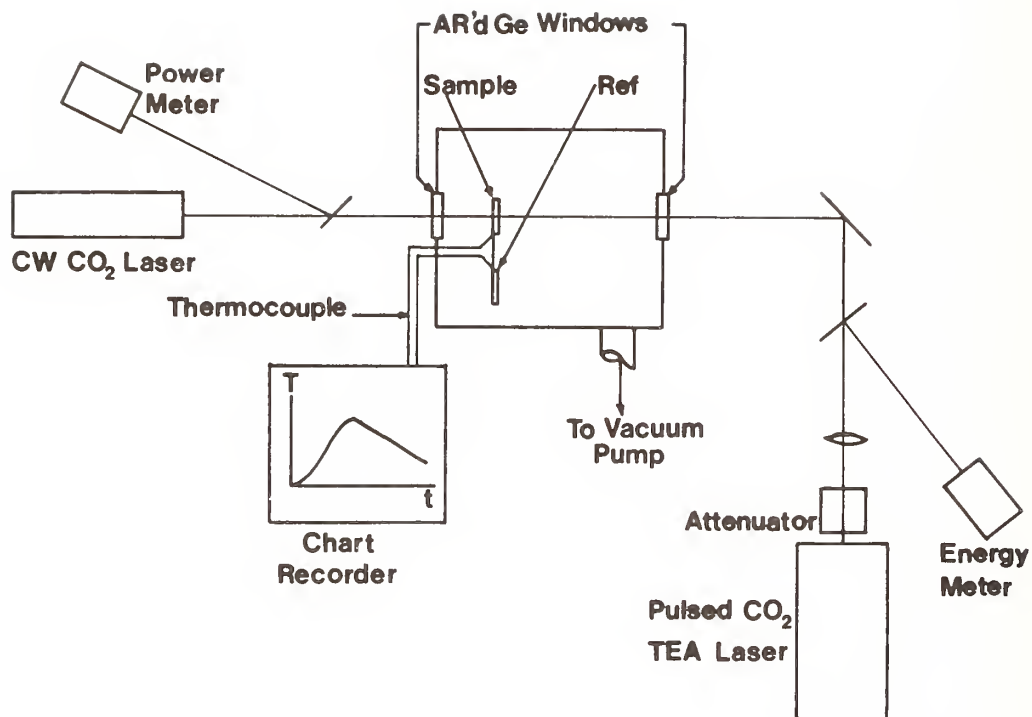


Figure 1. Schematic of CO₂ laser rate calorimeter incorporating a CO₂ TEA laser

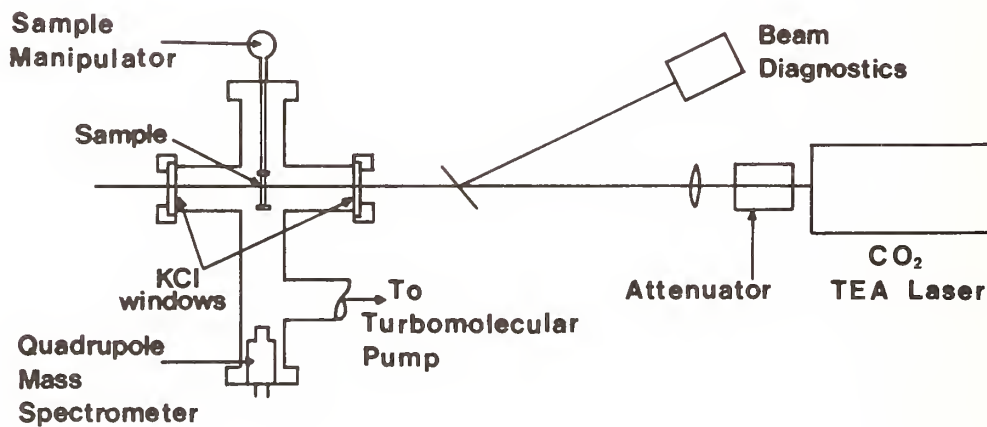


Figure 2. Schematic of CO₂ Pulsed Laser Desorption Mass Spectrometer

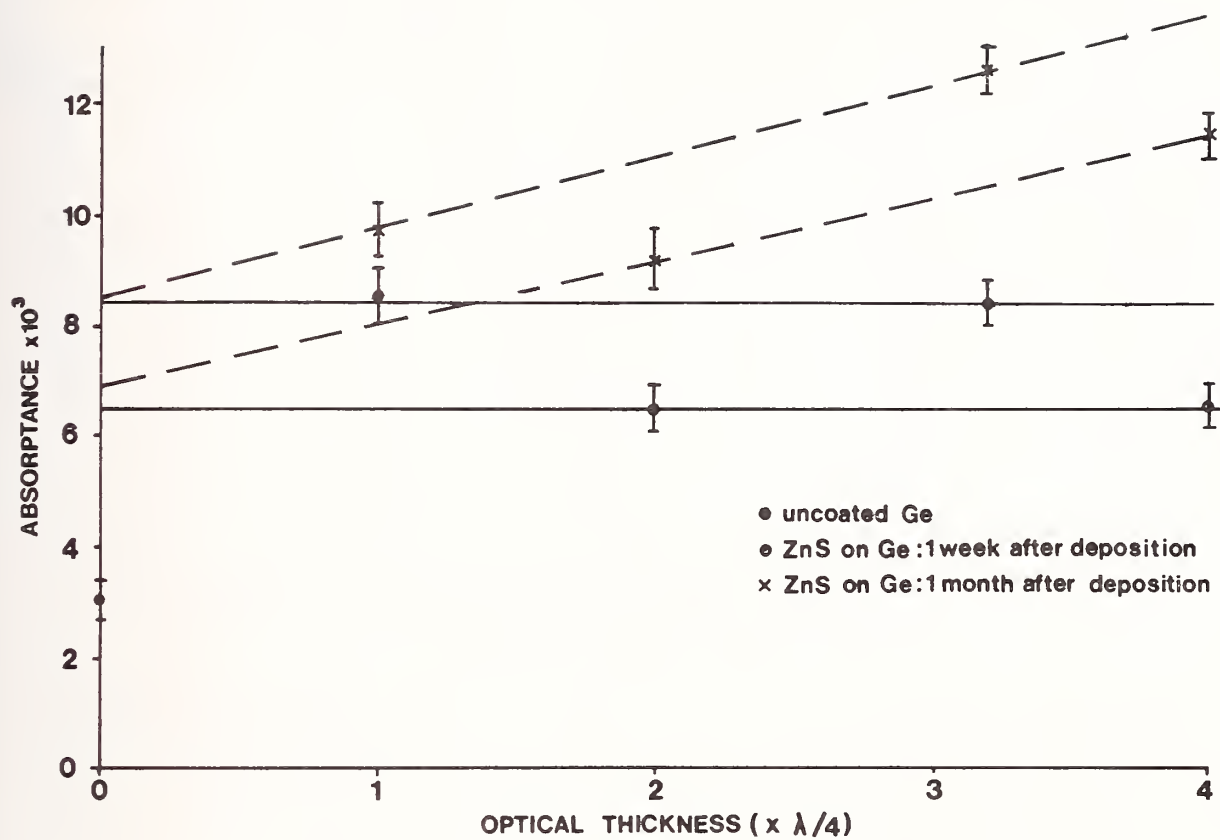


Figure 3. Dependence of absorptance on film thickness for ZnS thermally evaporated onto "cold" Ge substrates

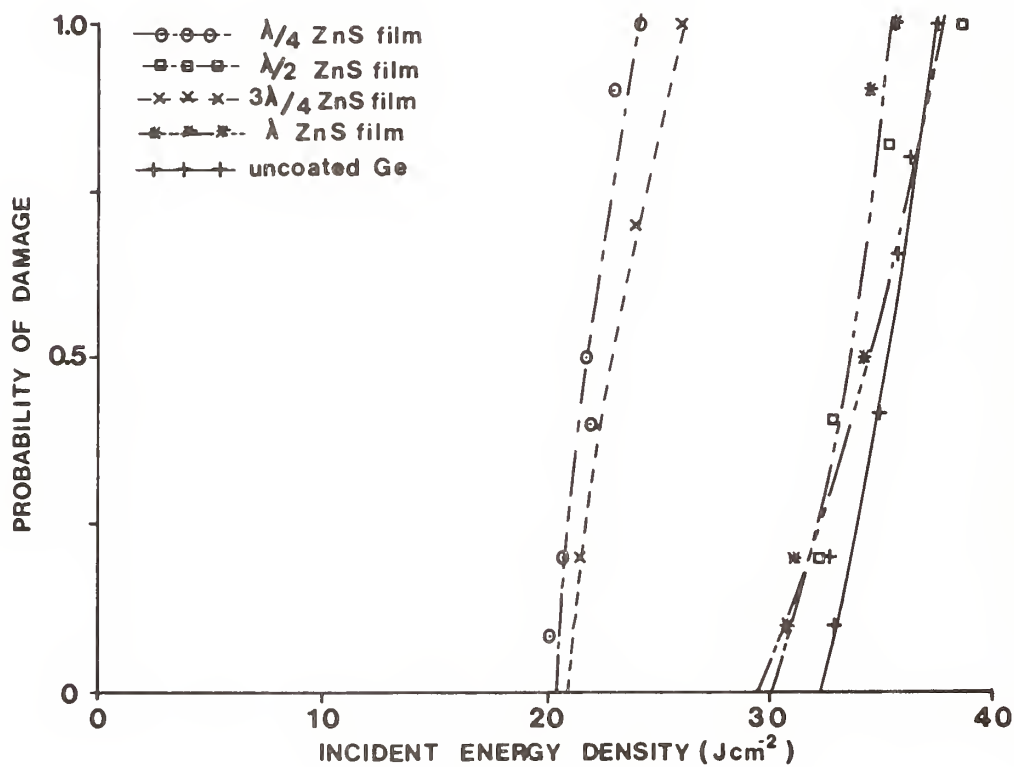
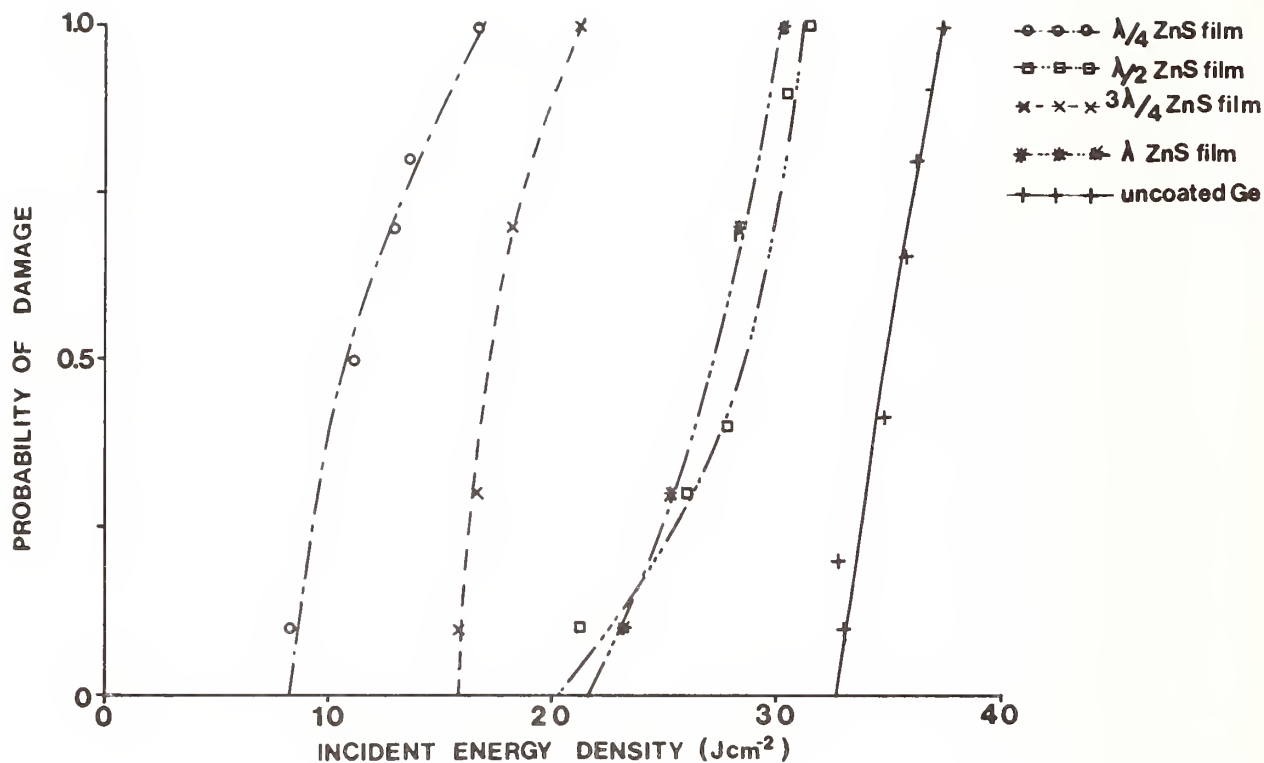


Figure 4. Laser damage probability plots for
a. Thermal evaporated ZnS on "cold" Ge substrates
b. Thermal evaporated ZnS on "hot" Ge substrates

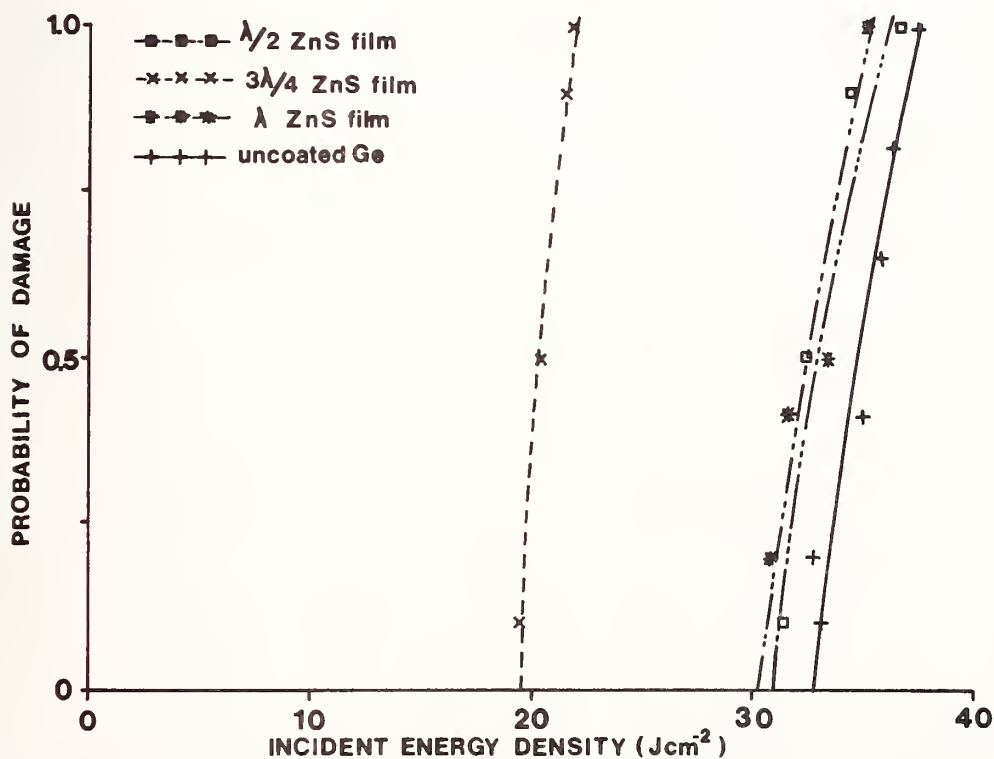
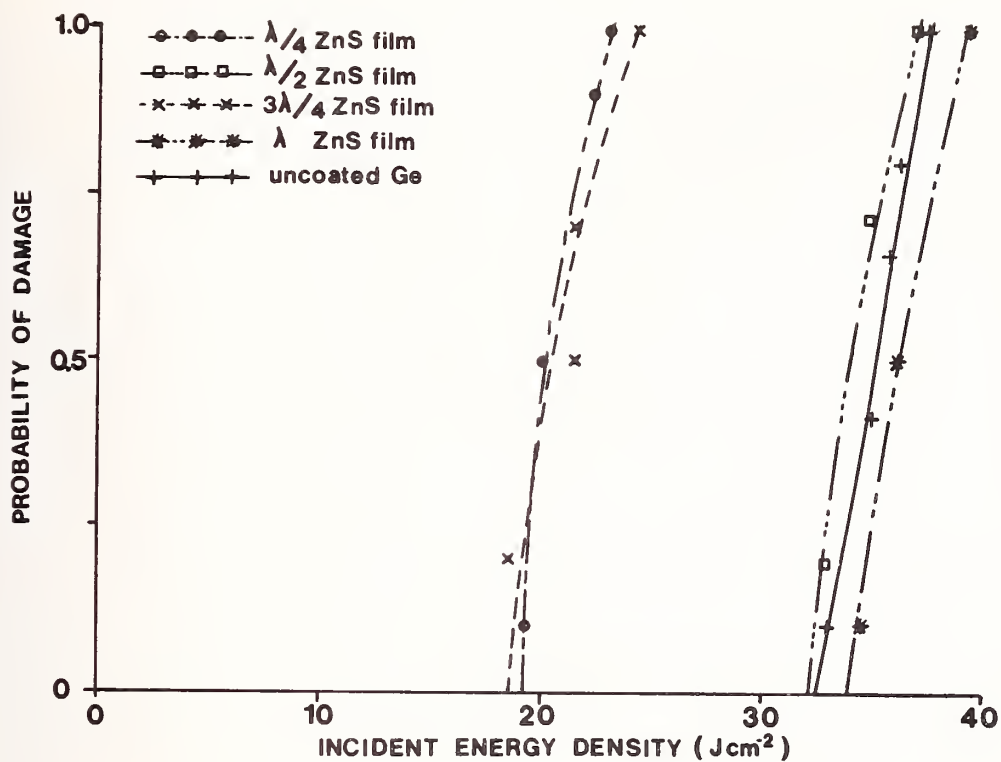


Figure 4 cont'd. Laser damage probability plots for
 c. Electron beam evaporated ZnS
 d. Thermally evaporated ZnS on "cold" Ge substrates after pre-pulsing with 5 pulses at 11 Jcm^{-2} .

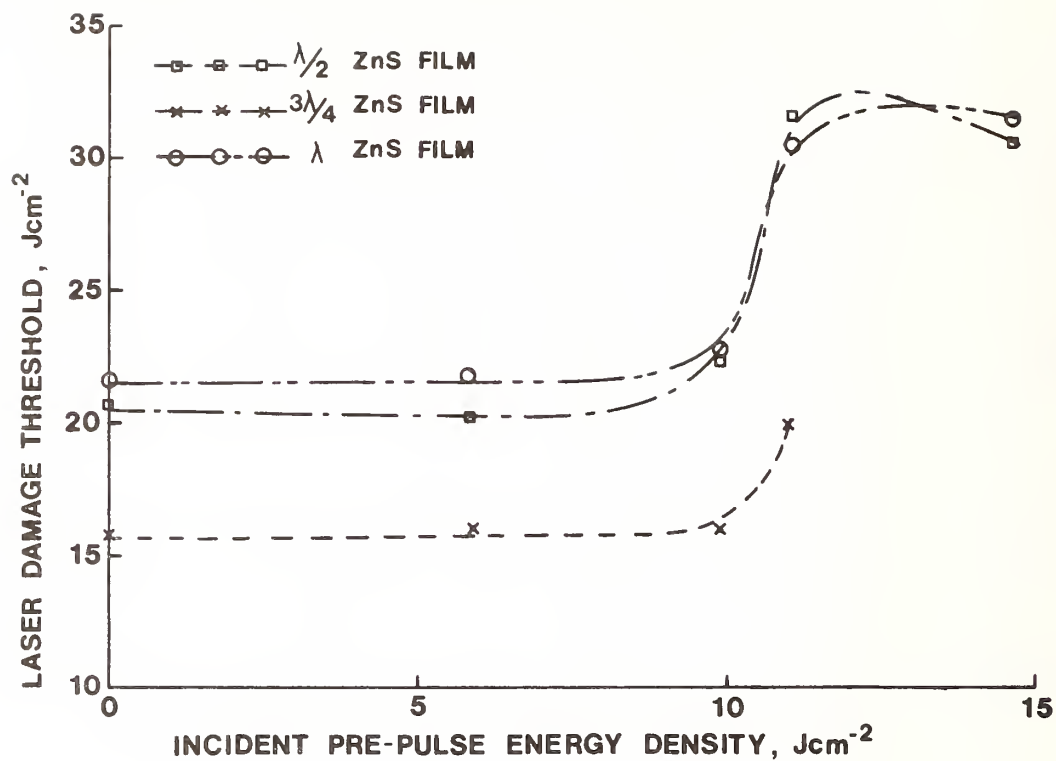


Figure 5. Effect of pre-pulse energy density on subsequently measured laser damage threshold for "cold" ZnS films

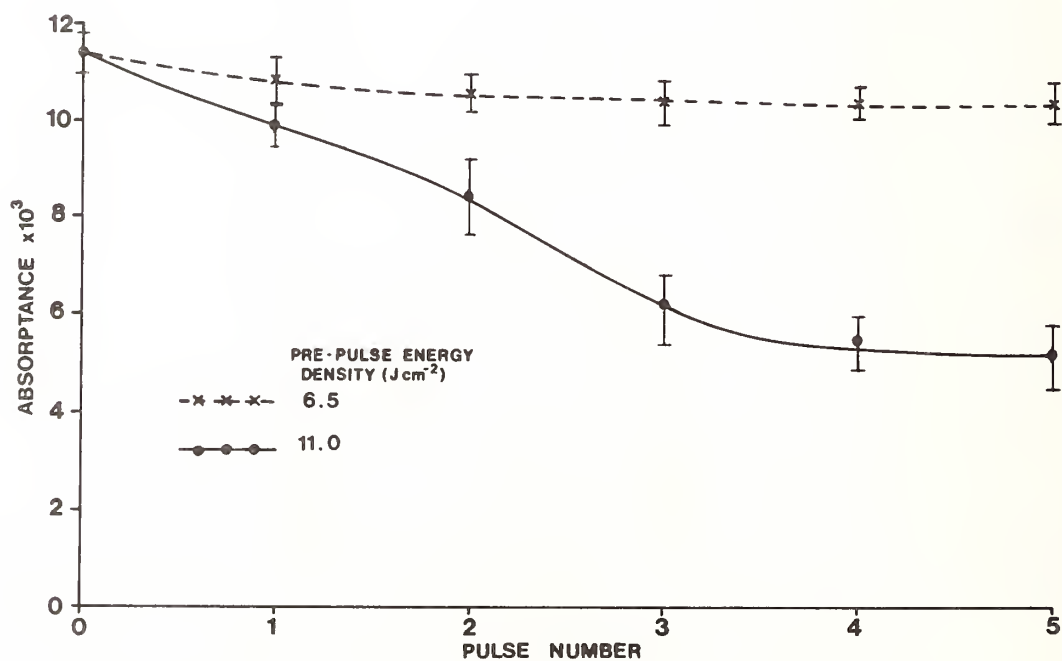


Figure 6. Effect of pre-pulsing on the absorbance of a λ -optical thickness "cold" ZnS film

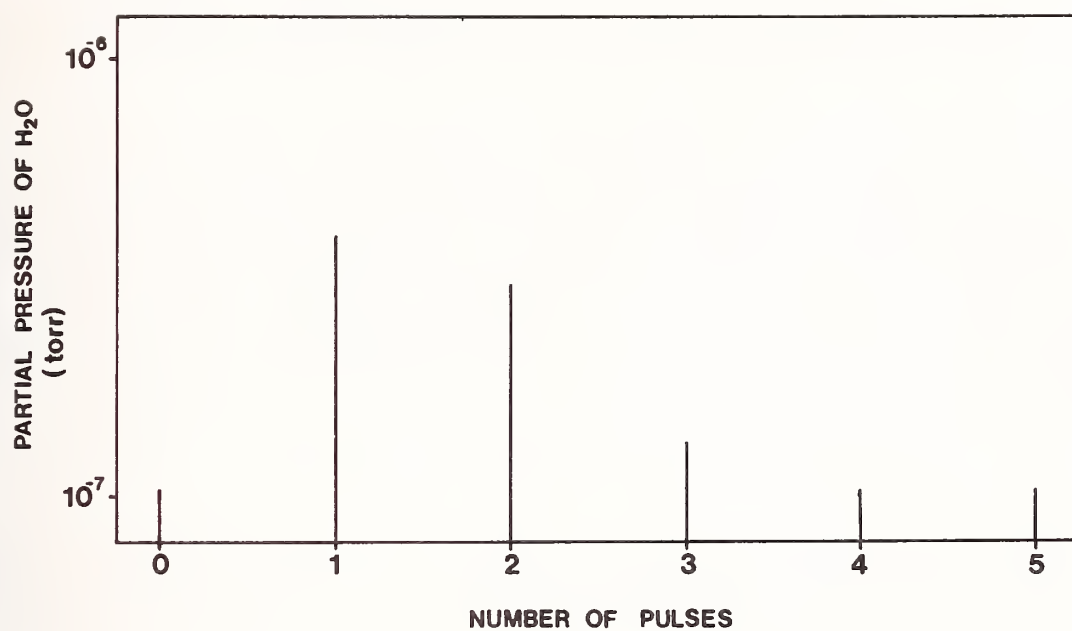


Figure 7. Effect of pre-pulsing at 11Jcm^{-2} on the water desorption signal from a λ -optical thickness "cold" ZnS film

K.L.Lewis, A.M.Pitt, A.G.Cullis, N.G.Chew and L.Charlwood
Royal Signals and Radar Establishment, St. Andrews Road, Malvern, England WR14 3PS

Molecular beam deposition techniques have been used to generate dense optical thin films and film structures for studies which allow the assessment of the onset of laser damage effects, and which explore the control of microstructure. In the first study, ZnS films have been examined on germanium substrates by electron microscopy and the evidence available suggests that damage is initiated by laser beam interactions at dislocation loop clusters in the Ge surface. In the second study the feasibility of using stratified films to control microstructure has been assessed. Damage thresholds in $(\text{ZnS}/\text{ZnSe})_n$ are equivalent to those of uncoated substrates despite the incorporation of 100 or so separate interfaces. A wide range of coatings can be synthesized utilising such structures, which offer the potential of enhanced damage thresholds and broadband optical properties.

Key Words: laser damage; molecular beam deposition; thin films; zinc selenide; zinc

1. Introduction sulfide.

Previous papers^{1,2} presented at this meeting have highlighted the potential afforded by molecular beam techniques in producing optical thin films with a high resistance to laser induced damage. Much of the improvement produced as a result of growth of polycrystalline films in ultra-high vacuum (UHV) appears to be associated with the avoidance of the presence of intergranular voids which renders the film impervious to the ingress of water and other impurities when exposed to the atmosphere. Examples of high resolution transmission micrographs, taken in cross section (XTEM) were presented in reference 2 showing the microstructure achievable. The adoption of UHV environments together with in-situ availability of ion-beam cleaning techniques ensures that the polycrystalline films are of very high purity and essentially free from impurity segregation effects at grain boundaries. In addition the achievement of clean film/substrate and film/film interfaces is routine.

The availability of dense optical thin films allows an assessment of various aspects of damage initiation phenomena. In particular it is possible to explore damage onset in the case where polishing damage is present at the substrate/film interface. This has been assessed for ZnS films on Ge substrates where significant reductions in damage threshold have previously been observed².

This paper also explores the conditions necessary for the modification of the columnar character of thin films by the synthesis of stratified layer configurations in which the thickness of each layer is negligible compared with the wavelength under consideration. In such a film the refractive index of the film is simply a function of the indices (n_1, n_2) and thicknesses (t_1, t_2) of the component materials selected. Specifically, for each layer pair^{3,2}

$$N^2 = \frac{n_1^2 t_1 + n_2^2 t_2}{t_1 + t_2}$$

In the example to be described, ZnSe and ZnS are used as the two component materials with refractive indices 2.5 and 2.3 respectively, and are successively deposited as discrete layers 50 to 300Å thick. Since ZnSe and ZnS have different lattice constants (5.6686Å and 5.4093Å respectively), epitaxial growth of successive layers onto each other should not be possible and propagation of columnar grains should therefore be suppressed at each interface.

2. Experimental

The coatings described in this paper were fabricated in a 3-chambered UHV facility incorporating Knudsen sources, a small RF plasma source, a molecular beam sampling spectrometer, Auger and X-ray photoelectron spectrometers and ion guns for substrate cleaning². The morphology of the coatings was examined in detail by XTEM at 120kV and 400kV using specimens prepared in cross-section by mechanical polishing and subsequent low voltage Ar^+ ion milling. In some instances the Ar^+ ion milling was supplemented by a final polish using an iodine ion beam at low energy. This had been shown in other studies to be useful for the reduction of ion beam damage artifacts in ZnS produced during thinning.

Laser damage thresholds were determined using a short cavity TEA laser at 10.6 μ m (33nsec FWHM with tail extending to 1700nsec) as described previously². The point of damage onset was assessed using a miniature vidicon TV camera mounted on a x10 microscope objective situated close to the sample. The criterion for damage was the threshold production of microscopic surface defects when viewed by the TV camera under oblique tungsten lamp illumination. Beam diameters of 100 μ m $1/e^2$ were measured by the scanning pinhole technique.

3. Microstructure and Optical Properties of Deposited Films

ZnS films deposited on germanium substrates at 50°C have been found to have a microstructure essentially similar to that previously found for ZnSe films². The coatings are dense (figure 1) and no pores are detected, even on the scale of the resolution of the 400kV microscope available for some of the work. However, unlike in the case of ZnSe, the columnar structure of the ZnS does not propagate throughout the thickness of the film and the stacking fault contrast within the columnar grains is no longer perpendicular to the direction of growth. The polycrystalline structure is less ordered and the degree of fibre texture somewhat reduced compared to ZnSe.

A thin amorphous region is present at the surface of the Ge substrate arising from damage induced during ion beam cleaning of the substrate. However, other artifacts some 0.1 to 0.2 μ m in width are also present, which might appear at first sight to be particulate inclusions or polishing rubble. However, close examination of the substrate surface (figure 2) under the correct diffraction conditions reveals that the artifacts are in fact clusters of dislocation loops which have been punched into the surface by the action of abrasive particles and indeed the substrate surface is slightly depressed at the site of these dislocation loops. The electronic structure of the germanium will be considerably modified in the region of such dislocations and may well give rise to regions of enhanced optical absorption, possibly as a result of impurity segregation as has indeed been found at grain boundaries in polycrystalline germanium⁴.

The microstructure of an alloyed $\text{ZnSe}_x\text{S}_{1-x}$ film deposited on a glass cover slip (figure 3) is very similar to that of ZnSe. Here again, columnar grains dominate the microstructure. Surprisingly, in the case of the stratified $(\text{ZnS}/\text{ZnSe})_n$ film the columnar character of the deposit is unchanged (figure 4). The inclusion of 80Å thick sublayers of ZnS is insufficient to prevent propagation of the columnar structure of the film. This may be due to the fact that the lattice parameter mismatch between the ZnSe and ZnS (5%) is too small and the strain imposed by the mismatch is accommodated by a higher density of stacking faults in the region of the interface. The fact that the two sub-layers share a common chemical element (ie Zn) may be a contributing factor in allowing this to happen. At higher resolution, it is apparent that stacking faults are indeed present near the interface and by lattice imaging (figure 5) it is possible to examine the extent to which the strain is being accommodated. Figure 5 shows the otherwise high degree of interface perfection achieved by the absence of voids and inclusions. Close examination of the grain boundary regions shows a similar lack of porosity.

In principle it should be possible to prevent the propagation of columnar grains using mismatched interlayers but it is apparent from the above that a much greater degree of mismatch than 5% is required. A good example would be provided by a BaF_2/ZnS structure where the lattice parameter of BaF_2 ($a_0=6.2001\text{\AA}$) is some 15% greater than ZnS. In addition, the material crystallises in the cubic fluorite structure compared with the cubic zinc blende lattice of ZnS. Should a closer match be required, then it would be possible to examine BaF_2/ZnSe (mismatch 9%) or SrF_2/ZnS (7%).

As a general principle the potential of stratified designs is far reaching. For example, index grading can easily be achieved simply by changing the mark/space ratio of the successive materials being deposited. This has recently been explored by Southwell³. However, graded index designs can also be used to avoid high electric field levels in multilayer dielectrics. For example, Lowdermilk and Mukherjee⁵ found that graded index films prepared by a sol-gel process had laser induced damage thresholds (LIDT) four times greater than those of multilayer A/R films at 1.07 μ m for 1nsec pulses.

4. Effect of Coating Microstructure on Laser Damage Threshold

The results of the assessment of the various combinations of films and substrates examined in this work are summarised in table 1.

4.1 ZnS/germanium specimens

The origin of the low thresholds found in the case of ZnS/Ge have been explored by cross-sectioning the film at near-threshold damage sites and examining the microstructure by TEM. It

has been found that at such threshold fluences, damage only occurs in the central part of the area irradiated by the gaussian beam (figure 6). Since the energy densities at the extremities of the focussed beam waist are significantly lower than those at the peak, it is possible to explore threshold effects by studying the microstructure immediately adjacent to the damage site. The only problem in undertaking such a study is that secondary effects such as film ablation may have occurred and a section of the film in the desired region may no longer be present. In addition the problems of sectioning the specimen near the centre of a laser damage spot some 100µm in diameter to produce a TEM foil 1µm less in thickness are by no means trivial. Some success has been achieved, however, as witnessed by the micrograph shown in figure 7. The centre of the damage site is away to the left hand side of this micrograph, and the coating has been completely removed in that region, with extensive melt back and cratering of the substrate. The most apparent change in the coating is the degree of grain growth that has occurred in the film nearest the air interface. This is clearly a result of localised melting and rapid resolidification as found in the laser annealing of polycrystalline silicon films. Twin bands nucleated during melt recrystallisation are clearly visible in the large grain just to the left of the centre of the micrograph. The average grain size in the recrystallised region is approximately 2500Å and the depth of recrystallisation approximately 4000Å. Although the lower section of the film appears to have been unaffected by the laser pulse, the interface region has and the film is clearly separated from the substrate. The surface of the substrate appears to have melted to a depth of some 240Å.

On the basis of the evidence available, it is argued that the damage process is initiated at the regions of high absorption in the germanium surface at the dislocation loop clusters referred to in section 3. Certainly it has already been suggested by Foley et al⁶ that a direct relationship exists between the LIDT of uncoated germanium and the nature of the damaged sub-surface region. At other damage sites in our specimens where little melt back of the ZnS film has occurred, there are indications of some disturbance at the Ge interface (figure 8) although it is not possible to determine conclusively what this is due to. Once heating has been initiated, absorption levels are rapidly increased and a process of thermal runaway ensues, resulting in ablation of the film above the substrate and plasma formation. It is as a result of this plasma heating that the surface melting of the ZnS film occurs at a position away from the centre of the damage site. ZnS generally sublimates at atmospheric pressure to give zinc and sulphur vapour and it is necessary to impose an overpressure of 150bar to stabilise the liquid phase at the melting point of 1850°C. The plasmas generated through such vapour plumes can have front velocities in the region of 600m/s⁷ and shock wave pressures many orders in excess of 150bar can be generated.

4.2 Zinc Sulpho-selenide Films

The purpose of the study of zinc sulpho-selenide deposition was to assess the conditions necessary for the use of stratified configurations to determine the microstructure of thin films, and to examine the effect that this may have on the laser damage threshold. However, an equally important factor to be determined in such a film is the effect of having introduced a large number of layer interfaces. In the coating considered here, thin films of ZnS 80Å thick were deposited between alternating layers of ZnSe 240Å thick and the configuration repeated to make up a coating 2µm in total thickness. The number of interfaces contained within the coating is therefore 124. Since deposition was entirely carried out in UHV by alternate shuttering of ZnS and ZnSe sources it was hoped that the degree of interface absorption would be low. Indeed transmission values at interference minima both in the stratified design and the alloyed equivalent on ZnSe substrates are very similar with the stratified design being, if anything, 0.8% higher.

As can be seen from Table 1, the laser damage thresholds of both (ZnS/ZnSe)_n and its alloyed equivalent are identical within the limits of experimental error, and are within the range measured for the uncoated substrate. The reason for the slight reduction in LIDT of both sulpho-selenide films compared with that measured for pure ZnSe or pure ZnS films on ZnSe is unclear and further work is underway to assess whether this is typical of other compositions. Since the damage threshold is substrate limited, future work will also explore deposition of stratified films on other substrates of higher LIDT, eg ZnS, KCl. This will allow a more realistic assessment to be made of any enhancement brought about by the stratified concept.

5. Conclusions

The origin of laser damage in dense ZnS films on germanium substrates has been explored by cross-sectional transmission electron microscopy. The evidence available suggests that the seeds for initial absorption of laser radiation are clusters of dislocation loops at the germanium that have been punched into the surface by the action of abrasive particles.

The conditions necessary for the control of microstructure in thin films by the synthesis of

stratified structures are discussed. Despite containing more than 100 film/film interfaces, coatings of $(\text{ZnS}/\text{ZnSe})_n$ have negligible levels of optical absorption and laser damage thresholds identical to the alloyed equivalent. Such film structures have considerable potential for incorporation into gradient index designs where electric field strengths are reduced.

References

1. K.L.Lewis and J.A.Savage: Proc 1983 Boulder Damage Symposium
2. K.L.Lewis, J.A.Savage, A.G.Cullis, N.G.Chew, L.Charlwood and D.W. Craig: Proc 1984 Boulder Damage Symposium
3. W.H.Southwell: Appl Optics, 24, 457 (1985)
4. C.Lewis, R.H.Runalls, G.N.Turner and S.T.Davis: Adv in Optical Production Technology, SPIE, 163, 1 (1979)
5. W.H.Lowdermilk and S.P.Mukherjee: Proc 1981 Boulder Damage Symposium, NBS Special Publ, 638, 432 (1983)
6. J.Foley, S.K.Sharma and R.M.Wood: Proc 1980 Boulder Damage Symposium, Special Publ, 620, 248 (1981)
7. J.E.Field: University of Cambridge, private communication

Table 1 Laser Damage Thresholds of Various UHV-produced Films

Film	Substrate	LIDT/J cm^{-2}
Uncoated	Ge*	25
ZnS	Ge*	15 - 16
Uncoated	ZnSe	50 - 60
ZnSe	ZnSe	60 - 73
ZnS	ZnSe	79
$\text{ZnS}_x\text{Se}_{1-x}$	ZnSe	56 - 57
$(\text{ZnS}/\text{ZnSe})_n$	ZnSe	54 - 60

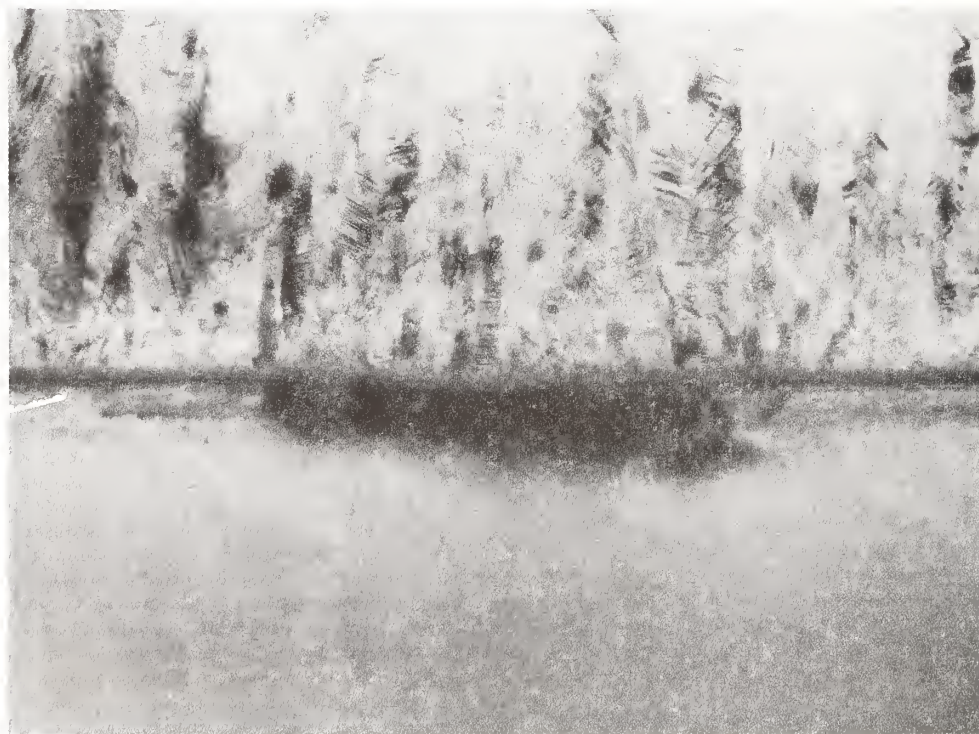
All LIDT values determined for pulse lengths of 32nsec FWHM and $1/e^2$ beam diameters of 100 μm

*Denotes substrates affected by surface work damage - see text



0.2 μ m

Figure 1 Polycrystalline ZnS film deposited in UHV on germanium



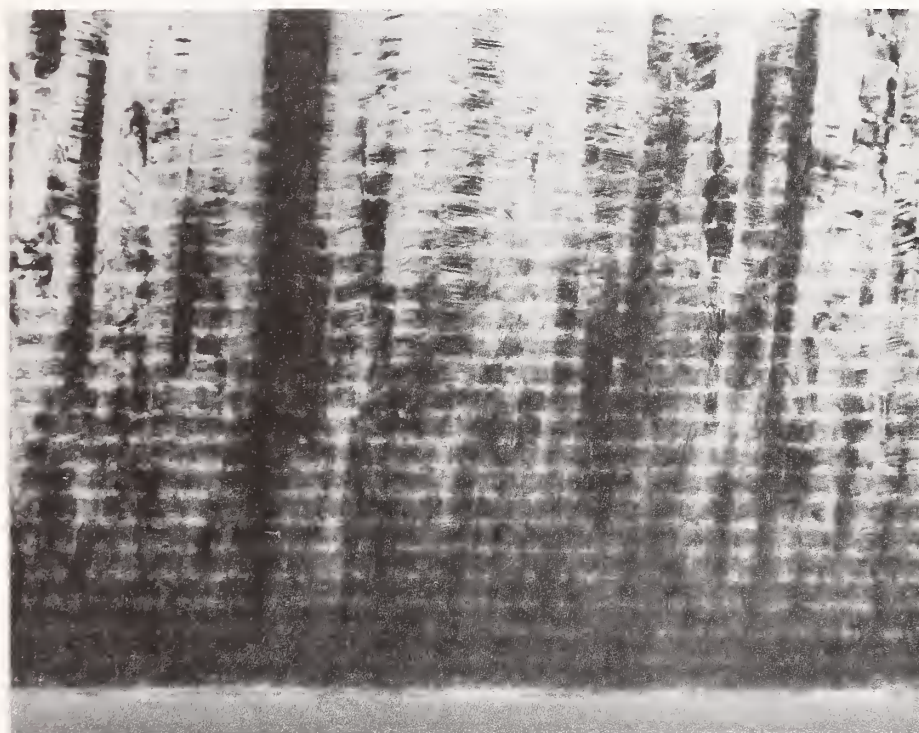
0.1 μ m

Figure 2 Dislocation loop clusters at surface of germanium substrate arising from action of abrasive particles



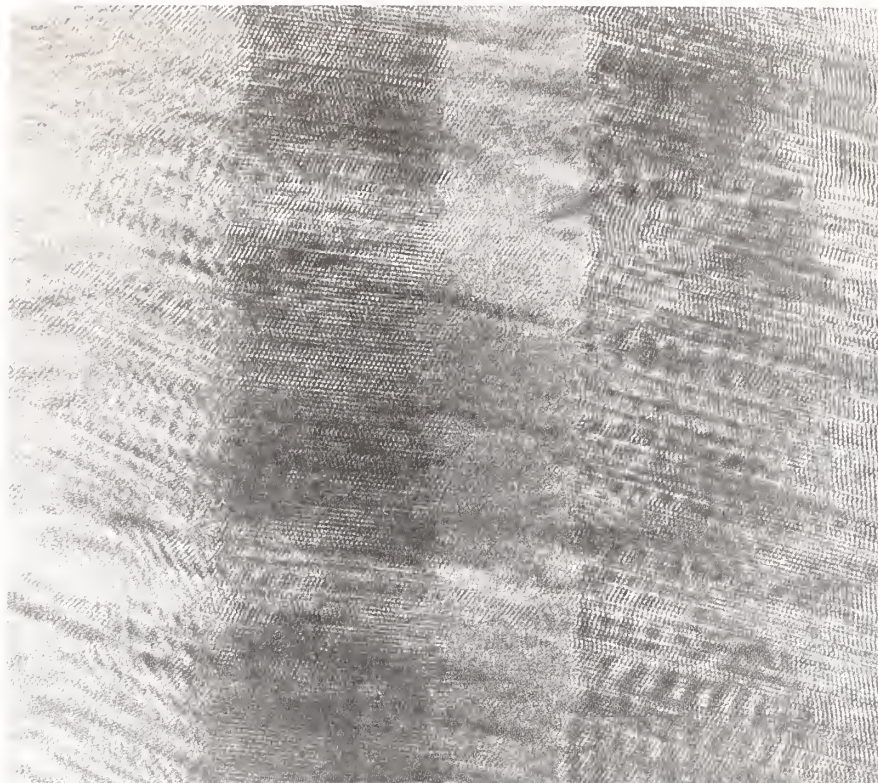
0.2μm

Figure 3 Microstructure of alloyed $\text{ZnS}_x\text{Se}_{1-x}$ film on glass substrate



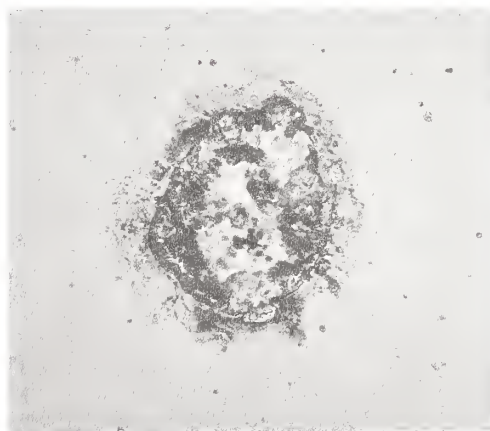
0.2μm

Figure 4 Microstructure of stratified $(\text{ZnS}/\text{ZnSe})_n$ film on glass



10nm

Figure 5 High resolution lattice image of section of stratified $(\text{ZnS}/\text{ZnSe})_n$ film. Four ZnS/ZnSe interfaces are within the field of view. The direction of growth is vertical



100 um

Figure 6 Laser Damage Site at just above threshold fluence in ZnS film grown by MBE on Ge substrate, showing damage artifacts induced by micro-defects at periphery of central crater.



0.5 μ m

Figure 7 Cross sectional TEM image taken of ZnS film at periphery of laser damage site. Degree of melt back of ZnS induced by heating effect of laser driven plasma is clearly shown



0.2 μ m

Figure 8 Micrograph showing disturbance of damage initiators at germanium substrate surface at threshold laser fluences

Transient Absorption of Light
Induced by Radiation

R. Godwin
F. B. Harrison
A. Larson

Los Alamos National Laboratory
Los Alamos, New Mexico, 87454

We have measured two components in the radiation-induced absorption of 250-nm light in fused silica. For the first, the time constant is 48.3 ± 1.3 ns and the absorption coefficient is 6.68 ± 0.37 cm⁻¹ per Mrad. For the second, the time constant is long compared to 3 μ s, and the absorption coefficient is 1.65 ± 0.36 cm⁻¹ per Mrad. The errors quoted are purely statistical.

Key Words: electron irradiation; fused silica; radiation damage; transient absorption.

1. Introduction

We have measured the absorption of 250-nm light in Corning 7940 fused silica, under irradiation by 2-MeV electrons from a Febetron 705 accelerator. The samples were 0.5 mm thick, held at 45° to the electron beam. The light source was a xenon flashlamp excited by a current of 10 kA to an estimated brightness temperature of 25,000° K. The light passed through the sample at an angle of incidence of 45°. The detector was an ITT planar photodiode. In front of the photodiode was an interference filter with a 30 nm wide passband centered at 250 nm.

The radiation dose, as measured by radiochromic film, was 760 krad at the front face of the sample and 410 krad at the back face, giving an average dose of 585 krad. The radiation pulse length was 30 ns.

Because of the 45° angle of incidence, the path length of the light in the sample is 0.565 mm. The data show a radiation-induced absorption with two time constants. One is long compared to the 3 μs duration of the measurement (but short compared to the time between shots, which was a few minutes). The other time constant is short. An analysis of the data is presented below.

2. Derivation of Equations

The fraction of light transmitted

$$\tau = e^{-\sigma_1 n_1(t)\delta} \cdot e^{-\sigma_2 n_2(t)\delta} ; \quad (1)$$

is

$$\begin{aligned} n(t) &= \text{number density of absorption centers (cm}^{-3}\text{)}, \\ \sigma &= \text{absorption cross-section (cm}^2\text{)}, \text{ and} \\ \delta &= \text{window thickness (cm)}. \end{aligned}$$

Subscript (1) refers to centers that recover, subscript (2) to "permanent" damage centers, i.e., with time constants long compared to measurement times. The rate of recovery is given by

$$\dot{n}_1(t) = K_1 \dot{D}(t) - L n_1(t) ; \quad (2)$$

where

$$\begin{aligned} \dot{D}(t) &= \text{dose rate (rads/s)}, \\ K &= \text{production constant (centers/rad) and,} \\ L &= \text{decay rate (s}^{-1}\text{)}. \end{aligned}$$

For the "permanent" term

$$\dot{n}_2(t) = K_2 \dot{D}(t) . \quad (3)$$

Equation (2) has the solution

$$n_1(t) = K_1 e^{-Lt} \int_0^t dt' \dot{D}(t') e^{Lt'} . \quad (4)$$

Let t^* be the time when \dot{D} goes to zero and stays there. Define

$$\hat{D}(L) = \int_{-\infty}^{t^*} dt' \dot{D}(t') e^{Lt} \quad . \quad (5)$$

Then

$$n_1(t) = K_1 \hat{D}(L) e^{-Lt}, \quad t > t^* \quad . \quad (6)$$

Equation (3) has the solution

$$n_2(t) = K_2 \int_0^t dt' \dot{D}(t') = K_2 D(t) \quad . \quad (7)$$

From Eqs. (1), (6), and (7)

$$\ln \tau = -\sigma_1 K_1 \hat{D}(L) e^{-Lt} - \sigma_2 K_2 D(t), \quad t > t^* \quad (8)$$

For $t \rightarrow \infty$, we have

$$\Gamma \equiv \tau(\infty) = e^{-\sigma_2 K_2 D(\infty)} \quad . \quad (9)$$

From Eqs. (8) and (9)

$$\ln \left(\frac{\tau(t)}{\Gamma} \right) = -\sigma_1 K_1 \hat{D}(L) e^{-Lt}, \quad t > t^* \quad . \quad (10)$$

and

$$\ln \Gamma = -\sigma_2 K_2 D(\infty) \delta, \quad t > t^* \quad . \quad (11)$$

Data Analysis

Set

$$f(t) = \ln \left[-\ln \frac{\tau}{\Gamma} \right] = A - Lt, \quad (12)$$

where the zero of time is set at the peak of the dose rate curve, and

$$A \equiv \ln (\sigma_1 K_1 \hat{D} \delta) \quad .$$

Examination of the Febetron pulse shape and the absorption data indicates that the formulas outlined above should apply from about 30 ns after the peak of the radiation pulse, and that 100 ns later the transient absorption is no longer detectable. On this basis, we have performed a least squares fit to the data.

Averaging data for 21 points in 10 ns increments between $t = 150$ and 350 ns, we find

$$\Gamma = 0.947 \pm 0.011 \quad . \quad (13)$$

Using this value of Γ in equation (11), we made a least squares fit to the data from $t = 30$ to 140 ns in 10 ns increments, and found

$$L = (2.07 \pm .05) \times 10^7 \text{ s}^{-1}$$

$$\text{or } L^{-1} = 48.3 \pm 1.3 \text{ ns} \quad . \quad (14)$$

for the attenuation decay constant, and

$$A = -(1.17 \pm 0.05) \quad . \quad (15)$$

The excellent nature of the fit to the data from $t = 30$ to 130 ns is shown in figure 1.

The errors quoted in equations (13), (14) and (15) are those arising from the statistical analysis; these take no account of systematic errors, which will be discussed qualitatively. Carrying the statistical errors forward, we find from equation (11)

$$\sigma_2 K_2 = (1.65 \pm 0.36) / (\text{Mrad cm}); \quad (16)$$

taking the total effective dose to be $D_0 = 0.585$ Mrad.

From equation (12)

$$\sigma_1 K_1 = \frac{1}{\hat{D}\delta} \exp A \quad (17)$$

$\hat{D}\delta$ contains any uncertainties in $D_0\delta$ plus knowledge of the shape and time of the radiation pulse. We estimate that

$$\hat{D} = 1.405 D_0 = 0.822 \text{ Mrad}$$

and that errors due to inaccurate information on the pulse shape and time are less than 10 percent. With this \hat{D} and equations (15) and (17), we find

$$\sigma_1 K_1 = (6.68 \pm 0.37) / (\text{Mrad.cm}) \quad (18)$$

Measurements at Sandia¹ at 257 nm gave an attenuation constant $\beta = 0.045 \text{ cm}^{-1}$ with a radiation dose of 30.3 krad in a pulse about 300 μs long. Using our value for $\beta = \sigma_2 K_2$ (equation 16), we predict for the Sandia measurement.

$$\beta = (0.050 \pm 0.011) \text{ cm}^{-1}$$

in good agreement with their result. This suggests that the recovery time of the "permanent" darkening is at least several hundred microseconds.

$$1.65 \pm 0.36 \text{ cm}^{-1} \text{ per Mrad}$$

Reference

- [1] J. Brannon, private communication

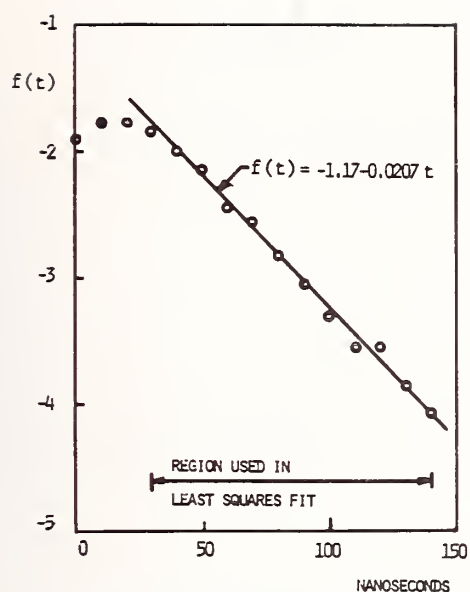


FIGURE 1: $f(t)$ VERSUS TIME (SEE EQUATION 12).
THE CIRCLES ARE DATA POINTS.

EFFECTS OF RADIATION INDUCED DEFECTS ON LASER-INDUCED BREAKDOWN IN SiO_2

M. J. Soileau, Nastaran Mansour, Edesly Canto, and D. L. Griscom*

Center for Applied Quantum Electronics
Department of Physics
North Texas State University
Denton, Texas 76203

The effects of radiation damage on bulk laser-induced breakdown in SiO_2 were investigated. Samples studied included Spectrasil A, B, and WF (water free). Measurements of laser-induced breakdown were conducted with 532 and 1064 nm laser pulses of approximately 20 nsec duration. Reductions of up to 40% in the laser-induced breakdown threshold were observed at 532 nm for samples exposed to 10^8 rads of γ -radiation. The decrease in breakdown threshold for irradiated SiO_2 samples at 532 nm was found to be proportional to the linear absorption of the specimen at 266 nm. These results are in good agreement with a proposed model which suggests that two-photon absorption initiated avalanche process is responsible for laser-induced breakdown for these materials.

Key words: laser-induced breakdown; nsec pulses; two-photon absorption; γ -irradiated SiO_2 ; 1064 nm; 532 nm.

1. Introduction

The effects of radiation damage on the linear optical properties of materials have been extensively studied in many materials and under a variety of conditions [1]. In this paper the effects of γ -radiation damage on nonlinear optical properties, e.g., laser-induced breakdown, of materials are reported.

Laser-induced breakdown in highly transparent materials is known to be an extremely nonlinear process. A detailed quantitative description of the breakdown process (or processes) is not yet available. Recent work [2,3] has indicated that bulk laser-induced damage in wide bandgap dielectrics is due to multiphoton initiated, electron avalanche breakdown. Sample-to-sample variations and focal spot size dependence of the damage [2-5] lead to the conclusion that this optical damage is due to extrinsic factors such as material defects and impurities. However, researchers have had little success in correlating the optical damage with specific impurities and/or defects in good quality optical materials.

The motivation for this work was to study optical damage in samples with known types and densities of defects. The basic idea was to produce various concentrations of E' -centers in fused silica by γ -radiation. The radiation damaged samples were then laser-damage tested at 532 and 1064 nm. This paper is a progress report of this ongoing investigation.

2. Experimental

2.1. Sample Preparation

Single specimens of three types of fused silica were investigated: Spectrasil A, B, and WF (water free). A single sample of each material was sliced into four parts. One quadrant was kept as a control, i.e., was not subjected to any ionizing radiation. The remaining three quadrants were subjected to as much as 10^8 rads of γ -radiation from the Naval Research Laboratory cobalt source.

Figures 1a and 1b are the linear transmission spectra for the witness samples (no radiation) and the samples exposed to 10^8 rads. Note that there is no apparent change in the transmission of the radiation damaged samples at the two laser wavelengths that were used for damage testing (i.e., 532 and 1064 nm). However, there is a substantial increase in the absorption at the 266 nm, the fourth harmonic of the 1064 nm radiation.

*Naval Research Laboratory, Washington, DC 20375-5000

2.2. Laser-Damage Setup

The laser source used in this study was an actively q-switched neodymium:yttrium aluminum garnet (Nd:YAG) oscillator-amplifier laser system operating at 1064 nm. A single pulse of measured Gaussian spatial profile was produced by the oscillator and amplified by a single pass through the amplifier. A KD*P crystal was used with the Nd:YAG laser to produce pulses at 532 nm. The crystal was temperature stabilized for long-term energy stability at the second harmonic. Residual 1064 nm radiation was eliminated by reflection off two dichroic mirrors.

The experiment was performed in similar setups at 1064 and 532 nm as shown in Fig. 2. The temporal pulsewidths were approximately 30 and 18 nsec (FWHM) for 1064 and 532 nm, respectively. The width of each pulse was monitored by a PIN photodiode detector and fast Tektronix storage oscilloscope (Model 7834). The spatial beam spot size (of the unfocused beam) was determined by pinhole scans. A 40 mm focal length lens, designed for minimum spherical aberration, was used to focus the light into the bulk of the materials. A rotating half-wave plate/polarizer combination was used to vary the irradiance on the sample. The energy incident on the sample was continuously monitored by a pyroelectric (Gentec ED-100) detector, and was calibrated with respect to a Gentec (ED-200) pyroelectric energy monitor. Each site was irradiated only once, and damage was determined by the observation of scattered light from a coaxial HeNe laser as viewed through a 10x microscope.

3. Results and Discussion

Table 1 summarizes the results of measurements of the laser-induced breakdown threshold at 532 nm for non-irradiated Spectrasil A, B, WF, and the samples irradiated with γ source of 10^6 , 10^7 , and 10^8 rads. All the data presented in table 1 were taken using linearly polarized laser pulses with a duration of 20 nsec (FWHM) and a calculated $2.2 \mu\text{m}$ focused spot size ($\text{HW1/e}^2\text{M}$ in irradiance). The uncertainties listed in the table of data are relative error obtained by the method used in reference 6. The value given for the electric field are rms fields corresponding to the peak-on-axis irradiance. As indicated in the table of data, the breakdown irradiance decreases significantly for all the irradiated samples. For example, a 40% reduction in breakdown irradiance was measured for 10^8 rads irradiated Spectrasil A compared to the non-irradiated samples.

Table 2 summarizes the results of similar measurement for the same samples at 1064 nm. For this wavelength the pulse duration was 30 nsec (FWHM) and the calculated focused spot size was $3.1 \mu\text{m}$ ($\text{HW1/e}^2\text{M}$ in irradiance). At this wavelength (1064 nm), the laser induced breakdown remains the same for non-irradiated and irradiated Spectrasil A, B, and WF samples.

The effect of self-focusing in our measurements is negligible because the breakdown power is significantly less than its critical power for self-focusing. The critical power for self-focusing for a focused Gaussian beam is obtained from the numerical solution of the nonlinear wave equation and is given by ref. [7]

$$P_2 = 3.77 c \lambda^2 / 32 \pi n_2^2$$

where n_2 is the nonlinear refractive index in esu, λ is the laser wavelength, and c is the speed of light in vacuum. For SiO_2 samples, the values of critical power for self-focusing are ~ 1.7 MW and ~ 6.8 MW at 532 nm and 1064 nm, respectively. These values are obtained using a measured n_2 value of 0.6×10^{-13} esu [8]. In our measurements the breakdown power is two orders of magnitude smaller than the calculated critical power for self-focusing (tables 1 and 2). We performed polarization dependence tests of the breakdown power for these samples [9]. For all samples, the breakdown threshold for linearly polarized and circularly polarized light was equal, confirming that self-focusing was not a major contributor to the observed damage.

Figure 3 is a plot of the results of the laser-induced breakdown measurements at 1064 nm using 30 nsec (FWHM) linearly polarized pulses. Results for the witness samples and the samples exposed to 10^8 rads are shown. The shaded areas are the relative uncertainties in the damage thresholds, i.e., the irradiance region for which the probability of damage was greater than 0 and less than 1. The absolute error bars are estimated to be $\pm 15\%$. The conclusions drawn from this figure are (1) the 1064 nm damage thresholds for the three samples are essentially the same and (2) the damage threshold irradiance at 1064 nm is unaffected by γ -radiation doses up to 10^8 rads.

Figure 4 is a similar plot for the results of the 532 nm measurements. As in the previous figure, the top bars are the results for the unirradiated samples and the bottom bars are the results for the samples exposed to 10^8 rads. The two conclusions drawn from this plot are:

(1) The breakdown irradiance for the witness samples are lower at 532 nm than at 1064 nm. This implies that the laser damage process is not simply avalanche breakdown. (2) The laser damage threshold irradiance at 532 nm is substantially reduced for the samples exposed to 10^8 rads.

Recall that figure 1b showed no observable change in transmission at 532 nm for the γ -irradiated samples. It is not unusual for samples with the same linear transmission to have drastically different breakdown thresholds [5]. To date all attempts to correlate the laser-induced damage threshold to linear absorption have been unsuccessful. Also note that the linear absorption at 266 nm is substantially affected by the γ -radiation. This suggests that the decrease in laser damage threshold for irradiated SiO_2 samples at 532 nm must be related to the linear absorption at 266 nm (the second harmonic of 532 nm). This correlation will be explained by the two-photon assisted electron avalanche breakdown model [10,11] in next paragraph.

Assume that laser-induced breakdown occurs when the density of free carriers generated by a combination of multiphoton and avalanche processes reaches some critical value, N_B (this critical density is assumed to be approximately equal to the density required for the plasma frequency to equal the laser frequency).

In the avalanche process the buildup of free carrier density is given by

$$N_B = N_o e^{\eta_B t} \quad (1)$$

where η_B = net ionization rate

N_o = initial free carrier

The net ionization rate for laser-induced damage is a function of the breakdown field, E_B . Some authors have proposed models [12,13] which predict an ionization rate given by:

$$\eta_B \propto E_B^2$$

Then eq. (1) can be written as:

$$N_B = N_o e^{a E_B^2} \quad (2)$$

where "a" for our experiment is a constant related to many factors such as: frequency of the light, laser pulsewidth, the momentum transfer collision time, effective mass and electron charge.

The model proposed is that free carriers are initially generated by two-photon absorption from defect state within the band gap. Therefore, N_o can be written as:

$$N_o \propto n$$

where n = density of two-photon allowed defect states. Taking the natural log of eq. (2) yields:

$$a E_B^2 = -\ln n + \text{const} \quad (3)$$

The final assumption is that the density of two-photon allowed states (for 532 nm incident radia-

tion) is proportional to the linear absorption at 266 nm (i.e., the second harmonic of the 532 nm radiation). For that assumption eq. (3) gives

$$\left. E_B^2 \right|_{\text{at 532 nm}} \propto \left. -\ln(\alpha \ell) \right|_{\text{at 266 nm}} \quad (4)$$

where α = linear absorption coefficient at the 266 nm

ℓ = length of sample

This analysis [eq. (4)] predicts that the breakdown field at 532 nm should be proportional to the natural log of the absorption at 266 nm. Figures 5, 6, and 7 are the plots of the square of the breakdown field at 532 nm $[(\text{MV}/\text{cm})^2]$ versus the negative natural logarithm of the linear absorption at 532 nm for the Spectrasil A, B, and WF samples exposed to various γ -ray doses up to 10^8 rads. The linear absorption was calculated from the linear spectra of these materials using the assumption that the change in index of refraction is negligible in the wavelength range between 532 and 266 nm. The agreement with the prediction of eq. (4) is quite good considering the relative simplicity of the model and the assumption made.

4. Summary

The effects of γ -radiation on laser-induced breakdown was studied in fused silica at 1064 and 532 nm. The results show no change in the 1064 nm damage thresholds for doses up to 10^8 rads. The 532 nm laser damage threshold irradiance was found to decrease by as much as 40% for samples exposed to 10^8 rads. The reduction of the damage thresholds at 532 nm was found to be related to the increase in linear absorption at 266 nm. These results are consistent with a model that assumes that damage is caused by two-photon absorption initiated avalanche breakdown. The two-photon absorption is assumed to be associated with the defects created by the γ -radiation.

These results indicate that studies of the effects of radiation induced defects can yield important information about the initiation of laser-induced damage in wide bandgap solids. There are practical implications as well. Optical components exposed to ionizing radiation could experience substantial reduction in laser breakdown thresholds, particularly for lasers operating in the visible and ultraviolet spectral regions. This problem could be an important consideration in choosing the optimum laser wavelength for various applications. For example, free electron lasers by their nature produce ionizing radiation which can effect the optical components of the lasers. In that case one may want to choose to operate the laser in the near infrared (e.g., 1000 nm) rather than the visible (e.g., 500 nm) so that the problem of radiation induced defects could be minimized.

The North Texas State University authors acknowledge the support for this work from the Office of Naval Research and the North Texas State University Faculty Research Fund.

5. References

- [1] Friebele, E. J.; Griscom, D. L. "Radiation effects in glass." Glass II. 17; 257-351; eds. New York; Academic Press; 1979.
- [2] Soileau, M. J.; Williams, W. E.; Van Stryland, E. W.; Boggess, T. F.; Smirl, A. L. "Picosecond damage studies at 0.5 and 1 μm ." Opt. Eng. 22(4): 424-430; 1983.
- [3] Soileau, M. J.; Williams, W. E.; Van Stryland, E. W.; Boggess, T. F.; Smirl, A. L. "Temporal dependence of laser-induced breakdown in NaCl." Natl. Bur. Stand. (U.S.) Spec. Pub. 669; 387-405; 1982.
- [4] Van Stryland, E. W.; Soileau, M. J.; Smirl, A. L.; Williams, W. E. "Pulsewidth and focal volume dependences of laser-induced breakdown." Phys. Rev. B 23(5): 2144-2151; 1981.
- [5] Soileau, M. J. "Frequency and focal volume dependence of laser-induced breakdown in wide band gap insulators." Ph.D. Dissertation; University of Southern California; 1979.

- [6] Porteus, J. O.; Jernigan, J. L.; Faith, W. N. "Multi-threshold measurement and analysis of pulsed laser damage on optical surface." Natl. Bur. Stand. (U.S.) Spec. Pub. 568; 507-515; 1979.
- [7] Marburger, J. H. Self-focusing: Theory. Progress in Quantum Electronics, edited by Sanders, J. H.; Stenhold, S. Pergamon. Oxford. 4(1):35-110; 1975.
- [8] Williams, W. E.; Soileau, M. J.; Van Stryland, E. W. "Simple direct measurements of n_2 ." Natl. Bur. Stand. (U.S.) Spec. Pub. 688; 1983.
- [9] Williams, W. E.; Soileau, M. J.; Van Stryland, E. W. "The effect of self-focusing on laser-induced breakdown." Natl. Bur. Stand. (U.S.) Spec. Pub. 688; 1983.
- [10] Soileau, M. J.; Mansour, N.; Canto, E.; Griscom, D. L. "Effect of radiation induced defects on laser-induced breakdown in SiO_2 ." To be published in the Proceedings of the 1985 MRS Meeting.
- [11] Mansour, N.; Guha, S.; Soileau, M. J. "Laser-induced damage in doped and undoped fluorozirconate glass." Natl. Bur. Stand. (U.S.) Spec. Pub.; 1985.
- [12] Yablonovitch, E.; Bloembergen, N. "Avalanche ionization and limiting diameter of filaments induced by light pulses in transparent media." Phys. Rev. Lett. 29(14): 907-910; 1972.
- [13] Sparks, M.; Holstein, T.; Warren, R.; Mills, D. L.; Maradudin, A. A.; Sham, E. L., Jr.; King, F. "Theory of avalanche breakdown in solids." Natl. Bur. Stand. (U.S.) Spec. Pub. 568; 467-478; 1979.

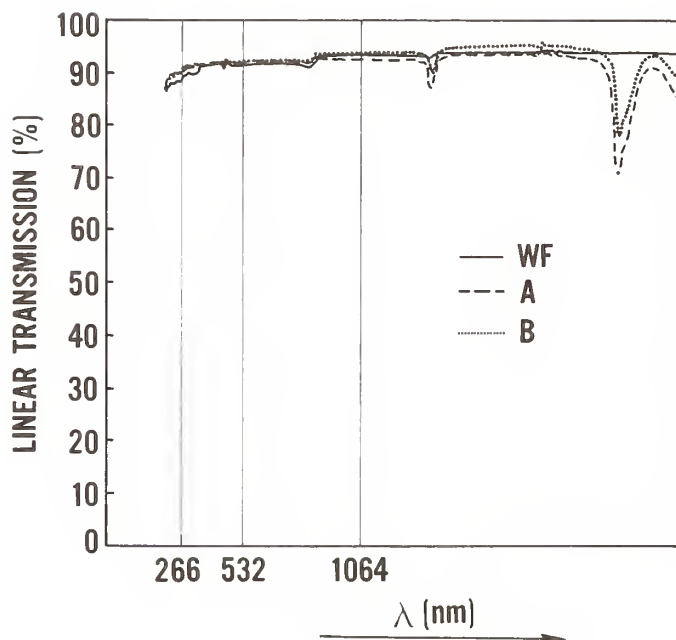


Figure 1a. Linear transmission of unirradiated Spectrasil A, B, and WF used in this work.

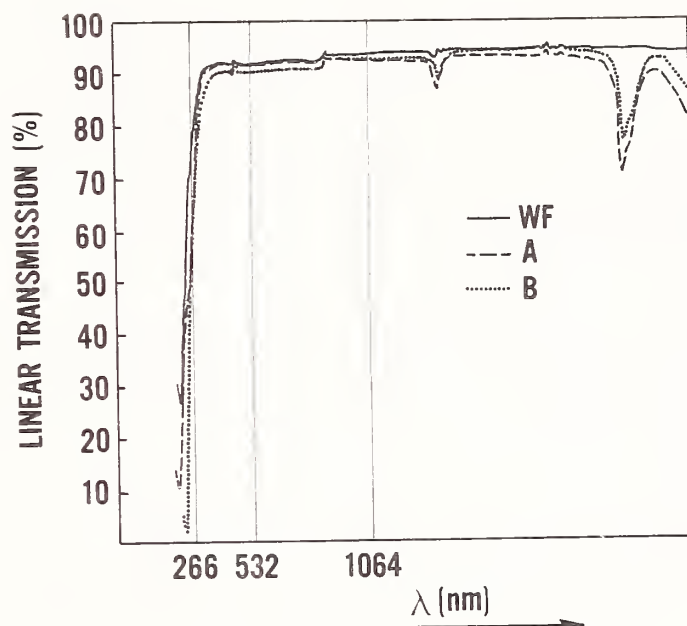


Figure 1b. Linear transmission of samples exposed to 10^8 rads of γ -radiation. Note that there is no detectable change in transmission at 1064 and 532 nm and a substantial reduction in transmission at 266 nm.

Nd: YAG Laser System

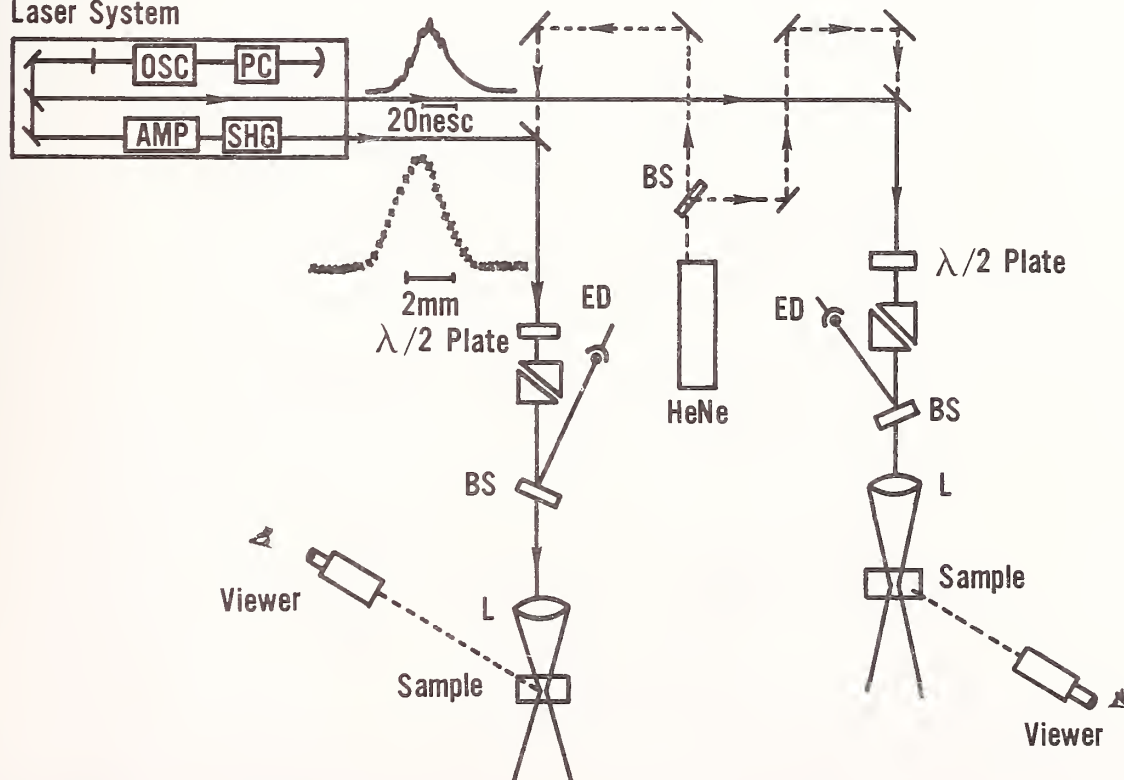


Figure 2. Schematic of the laser-induced damage setup.

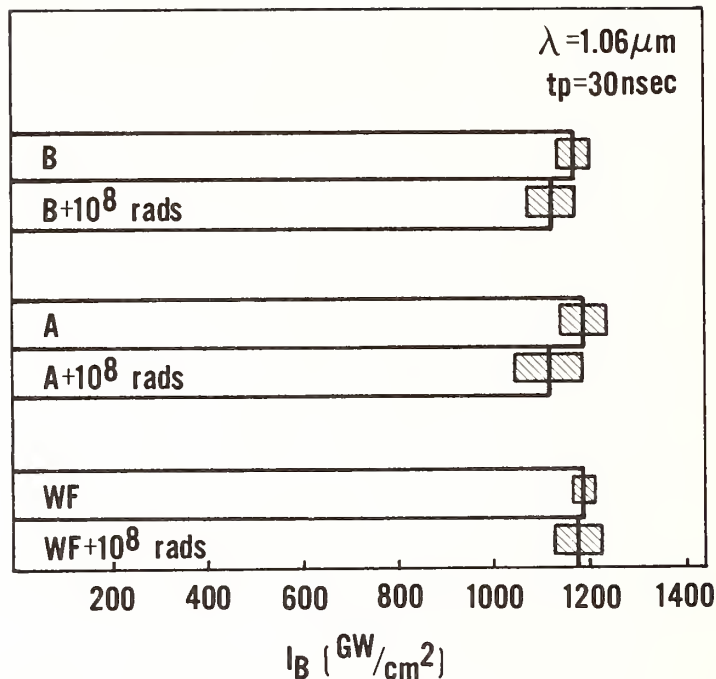


Figure 3. Laser-induced damage results for 30 nsec 1064 nm pulses. The thresholds for damage for the three different specimens are approximately equal and there is no change in the laser damage thresholds for the samples exposed to 10^8 rads.

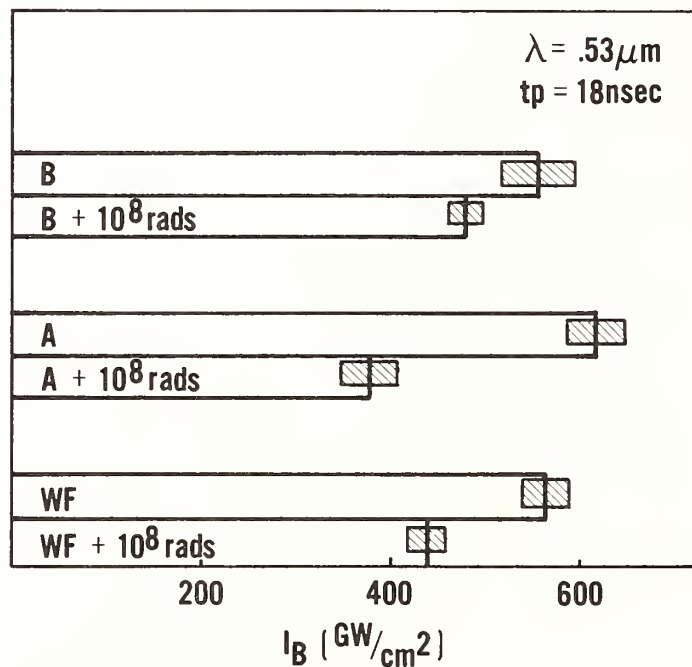


Figure 4. Laser-induced damage results at 532 nm. Note that the laser-induced damage thresholds of the witness samples (i.e., the unirradiated samples) are less at 532 than at 1064. At this wavelength there is a substantial reduction in the optical damage thresholds for the samples exposed to 10^8 rads.

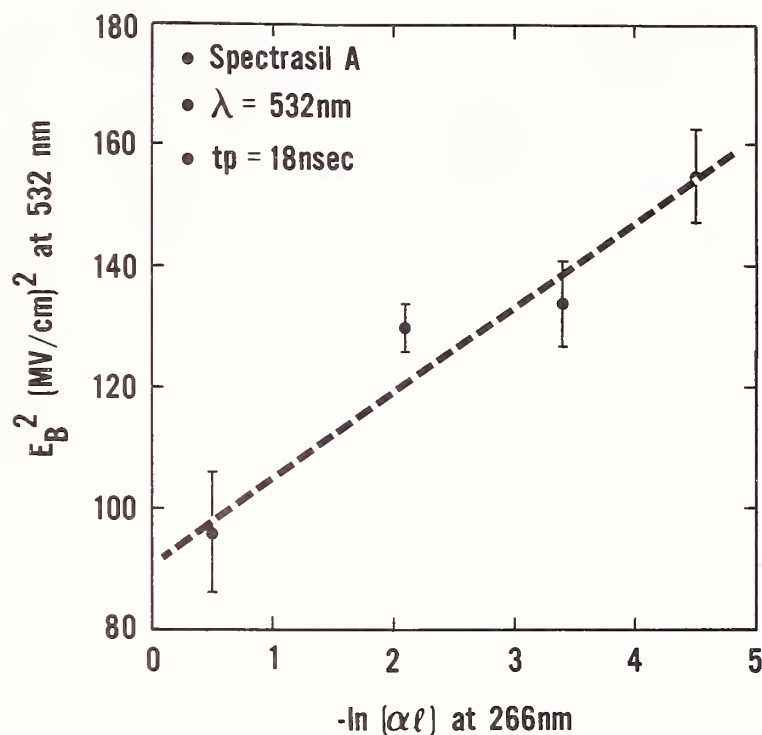


Figure 5. Square of breakdown electric field $(\text{MW/cm})^2$ at 532 nm versus the negative natural logarithm of the linear absorption at 266 nm for non-irradiated and irradiated Spectrasil A samples.

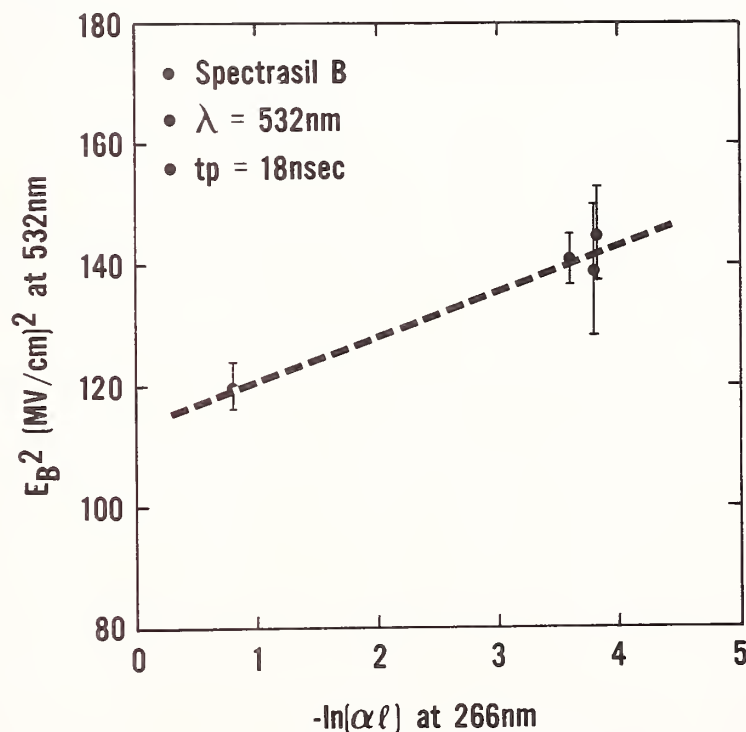


Figure 6. Square of breakdown electric field $(\text{MV/cm})^2$ at 532 nm versus negative natural logarithm of the linear absorption at 266 nm for non-irradiated and irradiated Spectrasil B samples. Recall that for irradiated Spectrasil B sample with the 10^8 rads there is a substantial increase in the absorption at the 266 nm. However, the samples irradiated with 10^6 and 10^7 rads are unaffected and linear transmission spectra remains the same as the non-irradiated sample.

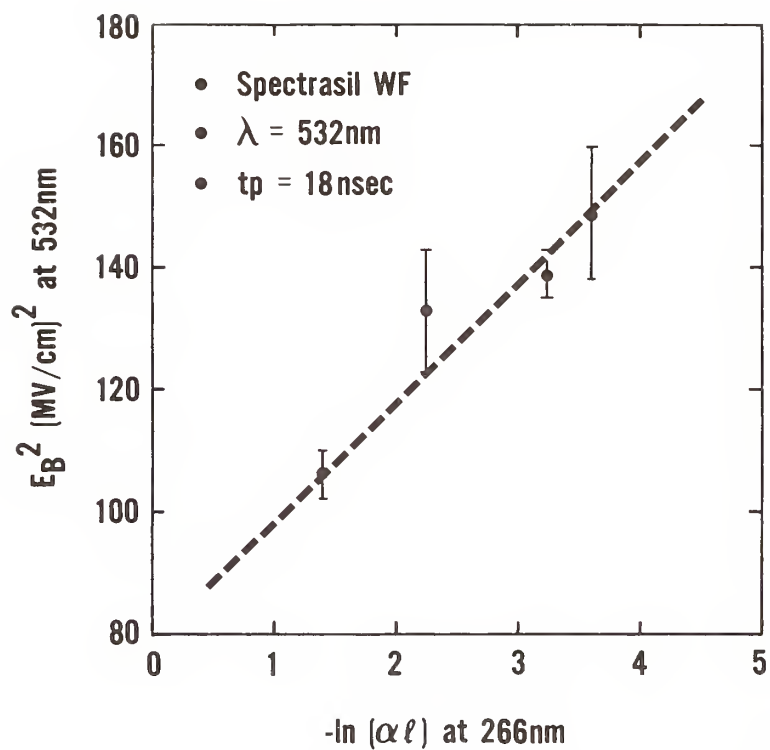


Figure 7. Square of breakdown electric field (MV/cm)² at 532 nm versus the negative natural logarithm of the linear absorption at 266 nm for non-irradiated and irradiated Spectrasil WF samples.

Table 1

Laser induced damage data for non-irradiated and irradiated Spectrasil A, B, and WF samples at 532 nm. The errors shown are relative uncertainties as discussed in the text. The absolute error bars are estimated to be $\pm 15\%$ of the irradiance.

Sample	Radiation rads	I_B GW/cm ²	E_B MV/cm	P_B KW	F_B KJ/cm ²
A	0	614 \pm 30	12.4 \pm 0.3	42.8 \pm 2.1	11.7 \pm 0.6
A	10 ⁶	532 \pm 30	11.6 \pm 0.3	37.1 \pm 2.1	10.1 \pm 0.5
A	10 ⁷	517 \pm 22	11.4 \pm 0.2	36.1 \pm 1.6	9.9 \pm 0.4
A	10 ⁸	382 \pm 37	9.8 \pm 0.5	26.6 \pm 2.6	7.3 \pm 0.7
B	0	554 \pm 45	11.8 \pm 0.5	38.7 \pm 3.1	10.6 \pm 0.9
B	10 ⁶	562 \pm 22	11.9 \pm 0.2	39.2 \pm 1.6	10.7 \pm 0.4
B	10 ⁷	577 \pm 30	12.0 \pm 0.3	40.2 \pm 2.1	11.1 \pm 0.5
B	10 ⁸	480 \pm 22	10.9 \pm 0.2	33.4 \pm 1.6	9.2 \pm 0.4
WF	0	554 \pm 22	11.8 \pm 0.2	38.7 \pm 1.6	10.6 \pm 0.4
WF	10 ⁶	592 \pm 60	12.2 \pm 0.6	41.3 \pm 4.2	11.3 \pm 1.1
WF	10 ⁷	532 \pm 60	11.5 \pm 0.6	37.1 \pm 4.2	10.2 \pm 1.1
WF	10 ⁸	442 \pm 22	10.3 \pm 0.2	30.8 \pm 1.6	8.4 \pm 0.4

I_B = breakdown irradiance (peak on-axis irradiance)
 E_B = breakdown field
 P_B = breakdown power
 F_B = breakdown fluence

Table 2

Laser induced damage data for non-irradiated and irradiated Spectrasil A, B, and WF samples at 1064 nm. The errors shown are relative uncertainties as discussed in the text. The absolute error bars are estimated to be $\pm 15\%$ of the irradiance.

Sample	Radiation rads	I_B GW/cm ²	E_B MV/cm	P_B KW	F_B KJ/cm ²
A	0	1212 \pm 50	17.4 \pm 0.4	180.0 \pm 7.5	38.9 \pm 1.6
A	10 ⁸	1110 \pm 72	16.7 \pm 0.5	164.0 \pm 10.5	35.6 \pm 2.2
B	0	1198 \pm 36	17.4 \pm 0.3	177.0 \pm 5.3	38.5 \pm 1.1
B	10 ⁸	1120 \pm 46	16.8 \pm 0.3	166.0 \pm 6.9	35.9 \pm 1.5
WF	0	1176 \pm 23	17.2 \pm 0.2	174.0 \pm 3.4	37.8 \pm 0.7
WF	10 ⁸	1170 \pm 52	17.1 \pm 0.4	173.0 \pm 7.7	37.6 \pm 1.7

I_B = breakdown irradiance (peak on-axis irradiance)
 E_B = breakdown field
 P_B = breakdown power
 F_B = breakdown fluence

Fundamental Mechanisms Of Optical Damage In Short-Wavelength High-Power Lasers

R.F. Haglund, Jr. and N.H. Tolk

Department of Physics and Astronomy, Vanderbilt University
Nashville, TN 37235

G.W. York

Physics Division, Los Alamos National Laboratory
Los Alamos, NM 87545

Evidence has been accumulating for many years that the physical mechanisms responsible for damage to optical materials in and from high-power, short-wave-length lasers (SWLs) differ in fundamental ways from the thermal processes identified in infrared and visible-wavelength laser damage problems. We propose that this difference stems primarily from the electronic nature of the absorption and excitation processes which occur when SWL photons strike an optical surface, and that electrons, ions and uv photons generated in the laser excitation cycle also contribute to optical damage. In this paper, we present recent experimental results which have pinpointed specific electronic excitation mechanisms which can operate in the high-power laser environment. In many optical materials of interest for SWLs, the deposition of electronic energy creates self-trapped excitons which decay through the energetic expulsion of atoms and molecules from the surface of the material. This erosion process is accompanied by the creation of permanent electronic defects which become nucleation sites for further damage. The relationship between these microscopic mechanisms and observed macroscopic damage phenomenology is discussed, along with evidence for the existence of a surface overlayer which may point the way to radically new techniques for protecting SWL optical elements from laser damage.

Key Words: alkali halides; desorption induced by electronic transitions (DIET); laser desorption; surface damage; surface erosion.

1. Introduction

Early studies of optical damage to laser components at wavelengths of 1 and 10 microns showed that there were two primary causes for catastrophic failure of large optical elements in high-power laser systems: first, the heating of submicron inclusions left from polishing or other manufacturing processes [1]; second, avalanche break-down or field emission at micro-cracks or pores in thin optical coatings [2]. These modes of laser damage have been studied for many years, and this work has brought significant improvements in the performance of optical materials, largely through improved quality control in the fabrication process. However, the very success of these explanations has also created a predisposition to ascribe **all** optical damage to thermal effects, even in the face of experimental evidence that short-wavelength laser photons can induce physical and chemical transitions in pure, structurally-perfect materials by multiphoton or other non-thermal mechanisms [3].

We have been working to identify the fundamental damage limits for short-wavelength lasers set by physics and chemistry of the laser-materials interaction rather than by deficiencies in optical manufacturing practice. Our experimental techniques allow a significant degree of control over and characterization of the incident primary radiation, the substrates and overlayers chosen as model systems, and the dynamical state of atoms, ions and electrons ejected from the target materials following irradiation. Experiments based on these techniques are yielding an increasingly detailed picture of the ways in which microscopic absorption, localization and redistribution of absorbed photon and particle energy triggers macroscopic destructive events such as desorption, erosion, and ablation of optical surfaces.

Building on this evidence, we have argued elsewhere [4] that the **primary** damage mechanisms in short-wavelength lasers are electronic and that they are triggered not only by the laser light itself, but also by electrons and UV photons created in the pumping process and by excited ions and atoms in the laser gas plasma. This picture is consistent with recent experiments indicating the onset of a major change in the morphology of damage to selected dielectrics occurring somewhere in the wavelength region around 250 nanometers [5]. It is our contention that this damage mechanism can be identified with the onset of Desorption Induced by Electronic Transitions (henceforth DIET), a generic category of phenomena implicated in erosion and radiation

damage caused by low-energy electrons, photons and heavy particles (atoms, ions or molecules). Thus, we propose that the catastrophic failure modes of excimer laser optics are precipitated by DIET processes caused by ions, electrons and ultraviolet photons from the laser environment as well as single- and multiple-photon desorption events induced by the laser photons. However, as we shall show, these electronically-induced desorption events also have thermal consequences, particular at laser flux levels above the plasma-formation limit.

In this paper, we first present experimental data from the Large-Aperture laser amplifier Module (LAM) at the Los Alamos National Laboratory, indicating the intensity of the various categories of radiation striking the optical surfaces. We next consider the ways in which DIET processes changes the surface composition and structure of model optical materials, keying our remarks both to specific electronic mechanisms and to the solid-state properties of alkali halides. We then discuss a model for damage-initiating events in a typical large excimer laser, in which not only the laser photons but also uv photons, electrons, ions and neutral atoms created by the laser pumping process can contribute to the destruction of optical surfaces. We shall make a plausible argument, supported by these data, showing how initial low-fluence events induced by an electronic pre-cursors can lead to changes in surface composition which result in catastrophic thermal breakdown when an intense laser pulse impinges on an optical surface. Finally, we adduce experimental evidence for the existence of a protective surface overlayer, the understanding of which may lead to a new class of damage-resistant coatings for short-wavelength lasers.

2. Sources Of Optical Damage In High-Power Excimer Lasers

Figure 1 shows a schematic of the Large-Aperture KrF laser amplifier Module (LAM) now operating at the Los Alamos National Laboratory, a device typical of current and planned large excimer lasers for fusion applications [6]. The LAM has an active volume of some 2 m^3 , and optical surfaces (resonator mirror and windows) exceeding 1 m^2 in size. A population inversion in an Ar-Kr-F₂ mixture is created through electronic excitation of the laser gas by two 400 kA beams of 750 KeV electrons from a cold cathode discharge. The electron trajectories in the gas are constrained to a direction transverse to the optical axis by a 4 kG magnetic field produced by a pair of large Helmholtz coils. The mirror and window have fused-silica or Pyrex substrates, typically coated with multi-layer dielectric thin films of SiO₂, Al₂O₃, or other metal halides or metal oxides.

The design fluence of the LAM is 1 J/cm^2 in a 500-ns pulse; large UV lasers now under design will produce laser fluences ranging up to several J/cm^2 . The significance of these flux levels can be gauged by observing that, for a KrF laser (248 nm), 1 J/cm^2 corresponds to some 10^{14} photons per surface site on the irradiated optical elements. In electron-beam-pumped lasers, *Bremsstrahlung* X-rays produced by the deceleration of near-megavolt pump-beam electrons, as well as scattered or diffusing low-energy electrons, will also irradiate nearby optical surfaces. Each of these sources of radiation efficiently produces neutral atoms and molecules through DIET processes. Moreover, many low-energy ion species in the laser plasma—including oxygen, argon and fluorine—are known to be efficient at producing reactive-ion etching on insulators and semiconductors, particularly in the presence of uv radiation [7]. Thus, in the precursor phase of optical damage, radiation both from the laser environment and the laser photons themselves can play important roles.

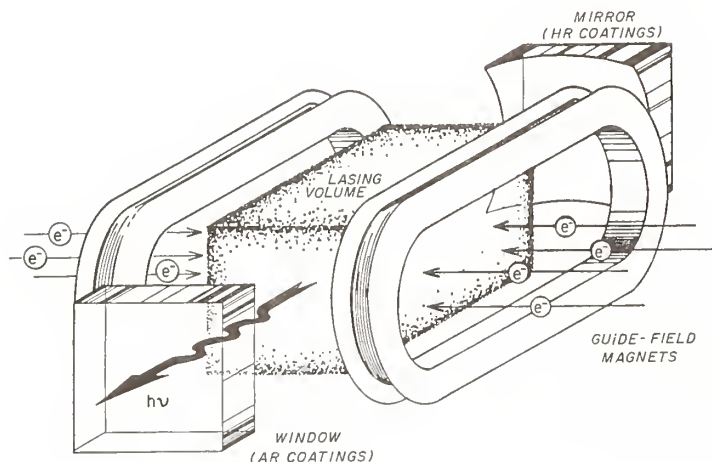


Fig. 1. Schematic of the Large-Aperture KrF Module at Los Alamos. Laser action is initiated by electron-beam pumping of a rare-gas halide mixture in the active volume.

Gross measurements of the radiation flux in the plane of the LAM exit window show that, in spite of the large magnetic guide field, there is substantial leakage of the pump-beam electrons from the active laser volume to the optical surfaces of the chamber. In these experiments, a Faraday cup was placed in the center of the output window, a distance of approximately 40 centimeters from either electron beam cathode and the current was measured during repeated shots from one cathode. It was found that at this center position that the electron current density ranged from 30 to 60 milliamperes per square centimeter, yielding an electron dose on the order of 10 to 100 electrons per surface site per shot. We also measured the total radiation dose at the window at several locations, using lithium fluoride thermal luminescence detectors, and discovered that the average is approximately 2 rads total dose per square centimeter per shot. Thus the laser environment contributes in a major way to optical damage, consistent with anecdotal observations of dramatic reductions in damage threshold for optical materials "inside" high-power lasers.

3. Desorption Induced By Electronic Transitions in Optical Materials

The key to a fundamental understanding of optical damage in optical materials for SWLs is to find the link or links between the microscopic (i.e., atomic-scale) desorption of individual atoms or molecules from the optical material, and macroscopic erosion and large-scale surface damage. This requires dealing both with the detailed mechanisms of desorption and with the surface and solid-state properties of particular optical materials. The key questions revolve around the existence of certain decay channels through which incident energy may be transformed and redistributed to create defects and particle desorption. Hence, in contrast to thermal desorption processes--which depend only on the bulk thermodynamic properties of the optical material--any serious investigation of electronic desorption mechanisms must concern itself with the details of the optical material properties, such as band structure. In this section, we shall discuss DIET processes in a general way, and present representative experimental data used to obtain detailed dynamical information about them.

3.1. Electronically Stimulated Desorption of Neutral Atoms

DIET processes occur when low energy photons, electronics, ions or neutral atoms interact with the atoms in the surface and the near surface layer of bulk material. The DIET process as shown in Figure 2 is characterized by three stages: (1) an **excitation** stage in which the energy of the incoming particle or photon is deposited in the near-surface bulk; (2) the **localization** phase, lasting from 10^{-12} to 10^{-13} second, during which one or more atoms or molecules participating in the excitation arrives at an energy state which is on the repulsive part of the relevant potential energy surface; and (3) **desorption**, as the particle is actually expelled from the surface. During this last phase the particle may also undergo charge exchange or other electronic particle-surface interactions.

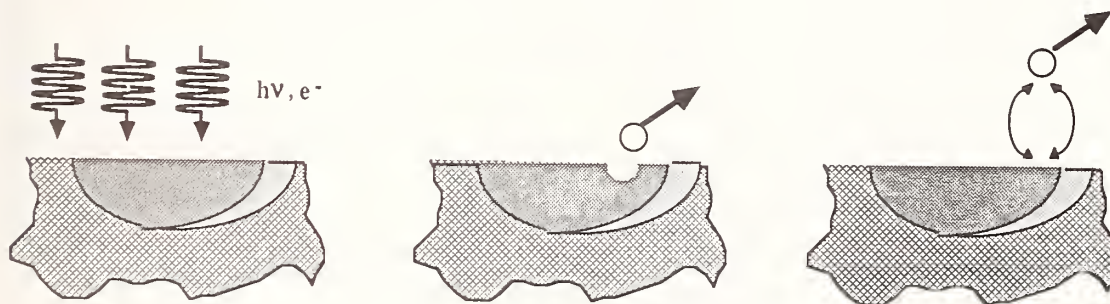


Fig. 2. Illustration of the three stages of a DIET process: (left) excitation; (center) localization of energy leading to desorption; and (right) particle-surface interactions.

DIET spectroscopy of ions has been used for many years to obtain structural and compositional information on a variety of surfaces. Several mechanisms for ion DIET have been proposed, the first of which was the Menzel-Gomer-Redhead model [8], devised to explain the desorption of absorbed gases on metal surfaces. This model, characterized by the assumption that two-body gas-phase potentials can be used to explain the repulsive energy state, accounts in a qualitative way for the desorption of neutral adsorbates such as hydrogen from transition-metal surfaces. In the 1970's, Knotek and Feibelman propounded a different mechanism to explain the desorption of ions from maximally valent covalent solids such as titanium dioxide [9]. In their model, the creation of long-lived hole pairs produced desorption via a Coulomb explosion. By demonstrating explicitly that the formation of hole pairs could increase the stability and lifetime of an

electronic excitation leading to desorption, they pointed to the role of specific solid-state properties of a select class of oxides in desorption phenomena [10]. The link between bond angles and desorption probabilities has been exploited by Madey, Yates and their coworkers to obtain detailed structural and compositional information about adsorbed species on both metal and insulator surfaces [11].

However, neither the Menzel-Gomer-Redhead nor Knotek-Feibelman models are able to explain recent experiments showing conclusively that the DIET phenomenon in insulators (such as the alkali halides and alkaline earth halides) is overwhelmingly dominated by neutral particle production [12]. The predominance of neutral particle yields in electronically stimulated desorption means that in these materials ion desorption is largely irrelevant to studies of the fundamental dynamical mechanisms of desorption, simply because the largest fraction of absorbed energy goes into the production of neutral particles. We now consider representative results from neutral desorption spectroscopy in alkali crystals.

3.2. DIET Experiments on Single-Crystal Alkali Halides

The detection of neutral particles and the study of the desorption mechanism in DIET processes occurs primarily via optical techniques [13]. Figure 3 shows the schematic of a typical DIET experiment in which neutral particles either in the ground state or in excited states desorbing from a surface are observed. The radiation source -- low energy photons, electrons or heavy particles -- is shown as incident from the left. The target surface, generally an insulator, is kept in a sample chamber under ultra-high vacuum, so that the formation of impurity adsorbates on the surface can be controlled or minimized. The target surface is mounted on a micromanipulator stage which can be heated or cooled to study temperature-dependent effects (e.g., defect migration) on desorption dynamics. When the radiation impinges on the target surface, desorption events occur and the desorbing particles begin to move away from the surface. Excited particles among the desorbing atoms and molecules radiate as free particles as they leave the surface. This radiation is detected by a spectrometer whose focal volume is arranged to intersect the volume of the exciting beam immediately in front of the target surface. It is this radiation which is detected by the spectrometer and which gives a characteristic optical signature of particle identity, internal energy state, velocity distribution and dependence on the state of the surface (e.g., temperature).

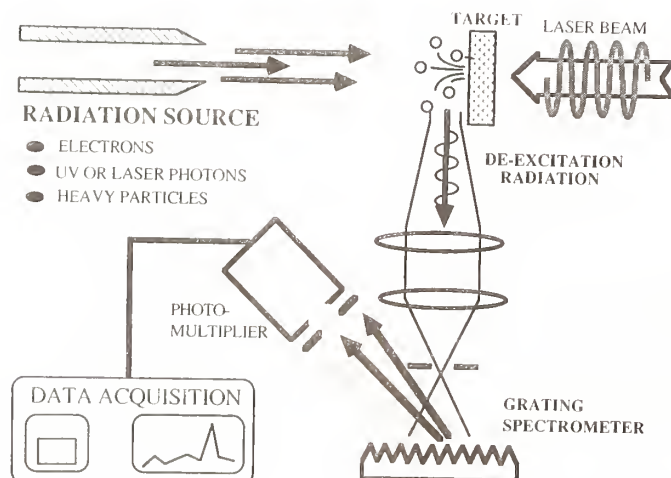


Fig. 3. Schematic of a DIET experiment using optical techniques to detect neutral atoms and molecules.

Ground-state particles leaving the surface, on the other hand, are detected by means of laser-induced fluorescence using a tunable dye laser beam, which is brought to a window in the ultra high vacuum chamber via a fiber-optic link. The light from the laser is collinear with and anti-parallel to the exciting beam so that the particles leaving the surface are excited by the laser into a state from which they can radiate via characteristic spectral lines.

As examples, we consider the results of PSD and ESD experiments [14] on LiF single-crystal surfaces. The excitation source for the PSD experiments was the Tantalus storage ring at the University of Wisconsin Synchrotron Radiation Center, with photons in the energy range from 40-200 eV. In the ESD experiments, the electron source was a high-current, low energy (0-100 eV) gun specially designed for this application.

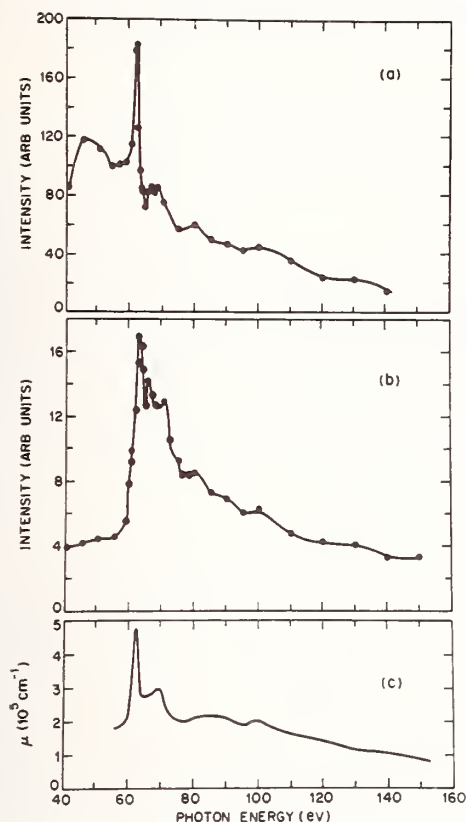


Figure 4 shows the optical emission intensity of (a) desorbed Li^* (excited Li atoms) as a function of the primary-beam photon energy, compared to the similar curve for (b) Li^+ (ions) and (c) the LiF photon absorption coefficient. In all three curves, the main excitonic structure of the Li K-edge is evident. Also, the high yield over a wide range of photon energies suggests that DIET processes are likely to remain efficient even down to relatively low energies, and certainly at energies characteristic of the electron-beam-produced **Bremsstrahlung** in a device such as the LAM. However, the most important feature of these curves is that the Li^* yield exceeds that of the Li^+ by five orders of magnitude. More recent measurements of the PSD yield of Li^0 (ground-state neutral lithium) showed that these yields exceed those of Li^* by at least two orders of magnitude.

Fig. 4. (a) PSD yield of Li^* from LiF.
(b) PSD yield of Li^+ from LiF.
(c) Optical absorption for LiF.

In the alkali halides following electron or photon impact, the halogen neutral atoms are ejected from the surface with a suprathermal energy, while the alkali neutrals are desorbed thermally.

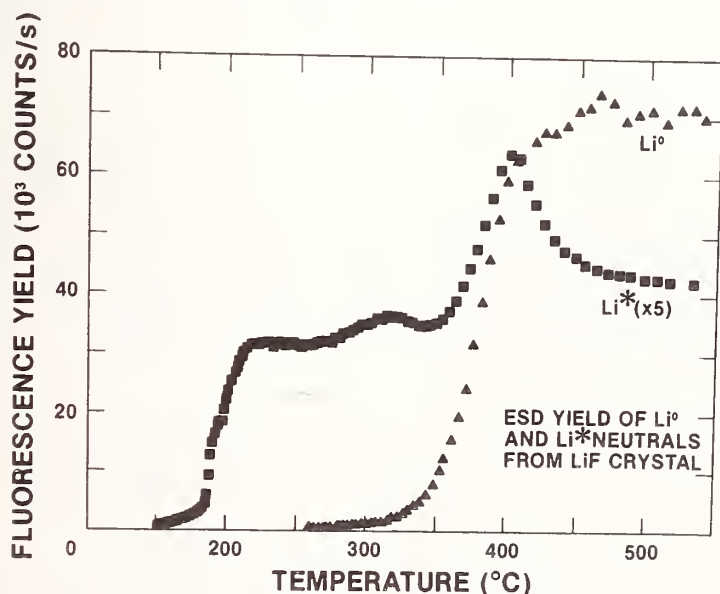


Fig. 5. Fluorescence yields of Li^0 and Li^* desorbed from single-crystal LiF, as a function of temperature.

Figure 5 shows the temperature dependence of the ESD yield of ground-state and excited-state lithium metal atoms from single-crystal lithium fluoride. The desorption yield curve for the ground state neutrals follows the classic Arrhenius desorption shape, increasing as a function of temperature until the yield of lithium metal atoms from the surface is equal to the rate at which they are being produced by the irradiating electrons. The excited state neutrals, on the other hand, are not desorbed thermally; there is other evidence suggesting that the Li^* are in fact not in thermal equilibrium with the surface at the moment of desorption. At temperatures below those required for desorption of either Li^0 or Li^* , then, there are microscopic agglomerations of free alkali metal on the surface of the irradiated alkali halide crystals - a situation fraught with significant implications for optical damage.

Collateral evidence for this picture of ESD/PSD in lithium fluoride comes from measurements on sodium halides showing that the velocities of desorbing ground-state sodium atoms have a Maxwellian distribution at the temperature of the surface. The number versus velocity distribution of the desorbing atoms is given by

$$dn/dv = Cv^2 \exp(-mv^2/2kT), \quad (1)$$

where the velocity v is related to the measured frequency ν of the emitted photons by the first-order Doppler formula

$$\nu = \nu_0 [1 + (v/c) \cos \theta]. \quad (2)$$

The parameter ν_0 is the central frequency for stationary atoms and θ is 0 in the geometry of these experiments. A frequency scan of the tunable dye laser around the characteristic ground-state absorption lines allows desorbing atoms to resonantly absorb laser light at the Doppler-shifted wavelength appropriate to their rest frame. The graph of fluorescence yield vs. frequency is thus equivalent to a scan of dn/dv .

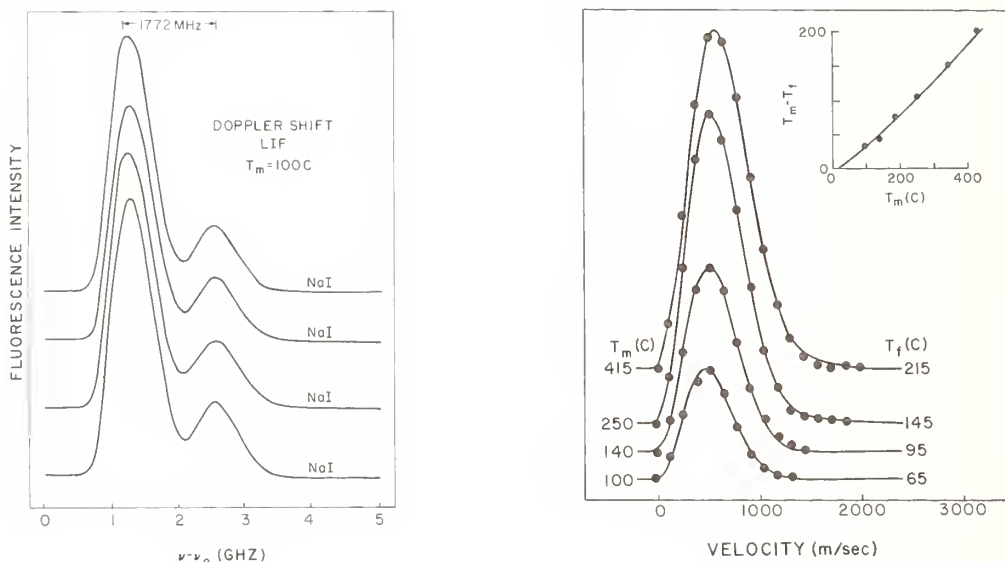


Fig. 6. (Left) Fluorescence yield as a function of laser frequency for ground-state sodium desorbing from various sodium halides. (Right) Velocity distribution derived from the best-fit temperature for the measured Doppler-shifted frequency spectrum.

Figure 6 (Left) shows the measured data in the Doppler scanning configuration of the experiments on a Na-halide crystals, running over the two hyperfine peaks of the Na D₂ line. Figure 6 (Right) compares the fitted Maxwell-Boltzmann temperatures with the measured surface temperatures over the range covered in one set of experiments. The measured surface temperature and the temperature inferred from the fitted velocity distributions differ by a constant amount, probably due to the gradient between the thermocouple probe and the surface. The measured surface and best-fit temperatures were completely consistent with neutral ground-state alkalis desorbing in thermal equilibrium with the surface [15].

Some further clues to the character of the DIET mechanism in alkali halides come from time-resolved ESD measurements carried out on LiF. In these experiments, a chopped electron beam and a time-to-amplitude converter coupled to a multichannel analyzer were employed to measure the desorption yield in the "afterglow" period after the electron beam was turned off. Typical data for ground-state and excited-state neutrals at two different sample temperatures are shown in Figure 7. When the electron beam is turned off, the ground-state fluorescence yield decays slowly, indicating that some kind of diffusive process brings defects to the surface, where they reduce their free energy by participating in desorption events. The same kind of experiment has been carried out looking at the excited-state neutrals desorbed from lithium fluoride. But in this case, the yield of excited state neutral lithium exactly tracks the on-off pattern of the irradiating electron beam, indicating that there is no near-surface bulk contribution to the desorption yield; instead, the neutral excited lithium comes off the surface immediately as it is being irradiated. This shows that we are dealing with quite a different mechanism than that responsible for the desorption of ground state neutral lithium.

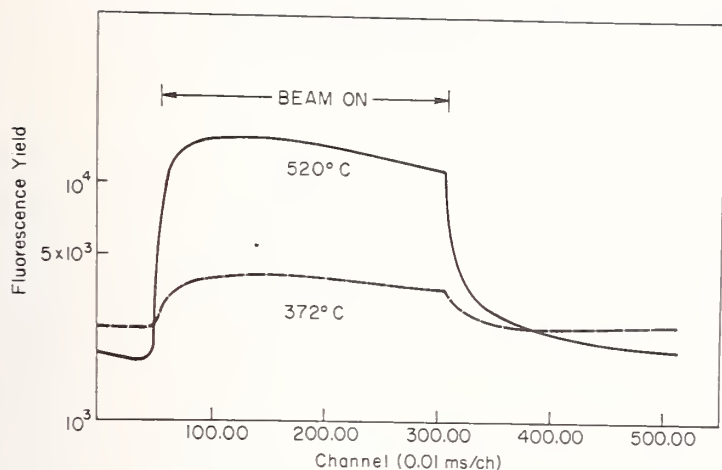


Fig. 7. Time dependence of yield for ground-state Li in ESD from LiF.

3.3. Mechanism for Ground-State Alkali Desorption

Summing up, one can say that electronically-stimulated desorption of ground-state alkalis from alkali halides exhibits features consistent with thermal desorption from the surface and near-surface bulk. In contrast, although the evidence is not so detailed as the results cited here for the alkalis, it has been shown that halogens desorbed from alkali halides under low-energy electron bombardment have suprathermal energies and are emitted in preferred directions along the halogen "strings" in the crystal. This suggests that the formation and relaxation of F-centers, as originally proposed by Pooley and Hersh [16], is a likely mechanism for the ejection of the halogens from the surface and near-surface layer of the bulk. The Pooley-Hersh model involves a specific electronic excitation leading to preferential and energetic ejection of halogens along the $\langle 110 \rangle$ directions (Fig. 9). Simultaneously, by leaving behind an electron to bind to the now undercoordinated alkali atoms near the surface, it provides a mechanism for the generation of neutral alkalis to undergo thermal desorption. Moreover, because the Pooley-Hersh mechanism is a simple one-step process -- involving only the formation and relaxation of an exciton -- the creation of neutral alkalis can occur relatively efficiently.

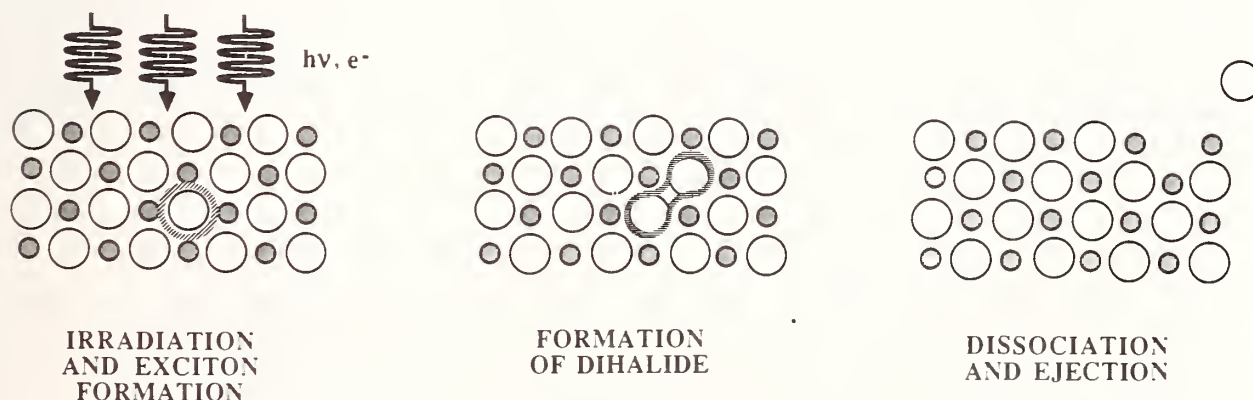


Fig. 8. Schematic of the Pooley-Hersh mechanism. The initial stage localizes the incident electronic energy through the creation of a self-trapped exciton. The transient dihalide molecular ion, formed by the overlap of the excited and a neighboring (normal) halogen ion, is in a predissociative state. When a halogen atom or ion is ejected preferentially along the halogen string directions, it leaves behind an F-center and a defect (halogen vacancy), allowing the undercoordinated alkali ion to be neutralized and desorb thermally.

With respect to optical damage in SWLs, the significance of the Pooley-Hersh mechanism lies in the existence of free alkali metal atoms on the surface following electron or photon irradiation, as long as the surface remains sufficiently cold that thermal desorption does not occur. This implies, as we now discuss, a variety of undesirable consequences for optical materials generically related to the alkali halides.

4. Electronically-Induced Damage in Optical Dielectric Materials

From the microscopic point of view, electronically-induced damage in short wavelength optical materials arises from the ability of these dielectrics to store energy in a highly localized way and then to release that energy through destructive channels. The problem may be seen more clearly by contrasting the situation with that of a pure metal, in which the highly non-localized, conduction-band electrons are able to drain away incident energy from the absorption site and disperse it throughout the metal. In an insulator, such a dispersal of the incident energy is not easily possible, because of the tight binding of the valence-band electrons, reflected in the large size of band-gap energies for typical optical dielectrics. Moreover, in dielectrics there exist a variety of material dependent mechanisms -- including exciton formation and the population of surface states -- through which incident electronic energy can be localized in space and time sufficiently to trigger defect formation, desorption and other destructive events. In the typical laser environment, all materials, including metal mirrors and metal layered structures, are covered either with an oxide or with some other coating due to the presence of air or the laser environment, which renders the surface an insulator or, at best, a semiconductor.

In this section, we discuss one possible scheme for analyzing the susceptibility of optical materials to damage based on generic materials properties. We also discuss evidence for the existence of an as yet uncharacterized overlayer on the surface of most materials, which appears to retard substrate desorption. Finally, we discuss a model of optical damage at short wavelengths, in which an electronic precursor mechanism changes the material composition and structure in ways which lead ultimately to catastrophic damage and failure of the material.

4.1. The Role of Specific Mechanisms

Early thermal models of optical damage were guided by an understanding of the interaction of infrared photons with the phonon spectrum of metals and insulators. Our picture of short wavelength optical damage is likewise guided by a recent characterization of electronic interactions in insulators and semiconductors due to Itoh [17]. This model of different classes of electronic materials allows us to relate experimentally observed desorption dynamics to specific materials properties. By concentrating on specific excitation mechanisms and on the dynamics of energy flow leading to desorption and, ultimately, erosion and material ablation, it is possible to correlate the properties of the incident radiation with the properties of specific optical materials to produce a microscopically detailed picture of the damage process. This understanding of the desorption dynamics leads to a valid description of damage from well below the plasma threshold up to and beyond that limit, and allows the identification of critical rate constants.

The Itoh classification of semiconductors and insulators hinges on an understanding of the ability of materials to support exciton formation, on the one hand, and relaxation to mobile, permanent electronic defects, on the other. The categories of materials together with representative substances which have these various features, are shown in Table 1.

Table 1

<u>Category</u>	<u>Self-Trapped Excitons</u>	<u>Permanent Defects</u>	<u>Materials</u>
I	No	No	Compound semiconductors Some metal oxides
II	Yes	No	α -Quartz
III	Yes	Yes	Alkali halides Alkaline-earth halides Fused silica Other metal oxides (alumina, titania)

It is interesting to note that virtually all optical materials of current interest in short wavelength laser designs fall into either category 2 or 3, forming self-trapped excitons or permanent defects or both.

We have seen that the alkali halides exhibit efficient ESD and PSD through the Pooley-Hersh defect-induced desorption mechanism. Materials in classes II and III of the Itoh taxonomy -- which include virtually all interesting SWL optical materials -- are particularly vulnerable to optical damage because as a class, they can participate in a variety of similar processes. In theory, materials in class I which forms neither self-trapped excitons, nor permanent defects, should be relatively invulnerable to electronical stimulated desorption and erosion of the type we have been considering. However, there is evidence [18] that the compound semiconductors are in fact etched or eroded to a significant degree by electrons and photons or by reactive ions, particularly in the presence of ultraviolet light. This probably means that the Itoh classifications scheme, while helpful, is not yet sufficiently differentiated to account for all the factors which contribute to optical damage. For example, since the Itoh scheme is based on bulk properties of materials, it fails to account for surface states, which are increasingly being implicated in optical damage processes [18]. Therefore, while we shall consider the Itoh taxonomy as a guide to the general phenomenology of electronically-induced optical damage, it is only that at present. In particular, it has little predictive power for extracting rate constants.

4.2. The Protective Overlayer

In early electron-stimulated-desorption experiments on alkali halides, it was found that samples prepared in air and then inserted into the ultra-high vacuum system only exhibited neutral alkali desorption after lengthy irradiation by the electron beam, even when the target was heated to very high temperatures in an ultra-high vacuum environment. Even sputtering by modest doses of noble gas ions failed to produce a virgin surface yielding neutral alkali atoms under electron stimulated desorption. It was not until detailed spectral scans throughout the visible region of the spectrum were taken that it became clear that desorption was in fact occurring, but not desorption of the alkali halides until some significant radiation damage had been done to the surface.

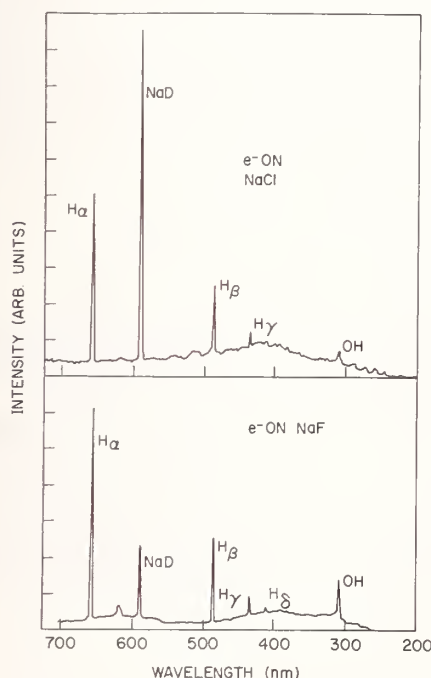


Figure 9 shows a pair of pictures showing electron stimulated desorption on sodium fluoride and sodium chloride. In this experiment the electron beam energy was held fixed while the visible spectrometer (Figure 3) was scanned through the range of wavelengths indicated on the horizontal axis. The peaks in the desorption spectrum were identified from the atomic lines of various elements. In addition to the sodium line, there appears a virtually complete hydrogen spectrum (Balmer series), as well as lines from OH radicals and from a quasi-molecular structure whose exact nature is still under investigation [19]. The crucial item from the standpoint of optical damage is that, in the case of sodium fluoride, the relative yield of sodium is smaller than that of the hydrogen and other contaminant peaks, while in the case of sodium chloride, the sodium yield exceeds that of the contaminant species.

Fig. 9. ESD of Na^* from NaF and NaCl in a hydrogen atmosphere. The electron energy was approximately 500 eV.

This implies that the surface overlayer and the binding of the overlayer to the substrate determine the rate at which substrate material will be ejected by electron irradiation. Similar results have been achieved in preliminary experiments in photon stimulated desorption at the Synchrotron Radiation Center of the University of Wisconsin. One of the tantalizing questions for further research is the extent to which this surface overlayer can be deliberately deposited on an optical surface in such a way that it does not affect the optical properties of the surface, but does influence the rate at which substrate material can be eroded through electron or photon bombardment.

4.3. The Transition from Electronically to Thermally Induced Optical Damage

Using the DIET mechanisms in alkali halides as a model, and considering the effect of the surface overlayer, we now present a model of damage to short wavelength optical materials which takes account of electronically-induced changes in the structure and the composition of the material surface, and of the thermal effects which arise for laser intensities well above the plasma formation limit. In this model, we assume that a Pooley-Hersh type mechanism is operative in a substrate material of Type III, and assume that there is a protective overlayer which erodes at a rate significantly lower than the substrate material. The general scheme for this model is shown in Figures 10a, b, and c.

In Figure 10a, short wavelength laser or other irradiation is incident on an optical element with a protective overlayer and a substrate material forming both self-trapped excitons and permanent electronic defects. In Type III materials, defects produced in the substrate bulk are "gettered" to the interface between the overlayer and the substrate, forming a metallic interlayer. In the early phases of irradiation this metal-rich layer has no effect other than to present a thermal absorption site slightly below the surface of the optical element. It should be noted however, that in multilayer dielectric films, especially where the materials contain metals, it is likely that the existence of these interlayers may lead to serious thermal consequences in the catastrophic phase of laser damage.

In Figure 10b the irradiation has gone on sufficiently long or at sufficient intensities that the protective overlayer has begun to erode, exposing to subsequent irradiation the metal rich interlayer created during the precursor phase. Efficient creation of additional defects in the near surface bulk, and diffusion-dominated migration to the breach in the protective overlayer, begin to occur. It should be noted that the precise location of the breaches or gaps in the protective overlayer will be determined by a number of random events, including, but not limited to: (1) the statistical migration of defects formed in the surface overlayer creating vacancies and under coordinated lattice in the overlayer; (2) surface rearrangements and reconstruction induced by desorption of materials at the surface of the overlayer and (3) the migration of metals from the interlayer into the surface overlayer, producing defects and under-coordinated sites in the lattice structure of the overlayer. Such processes can occur both in crystalline and in amorphous materials; in amorphous materials, the irregularities in the local electron densities simply means that it becomes more difficult to predict the sites at which defects or vacancies will eventually or temporarily come to rest.

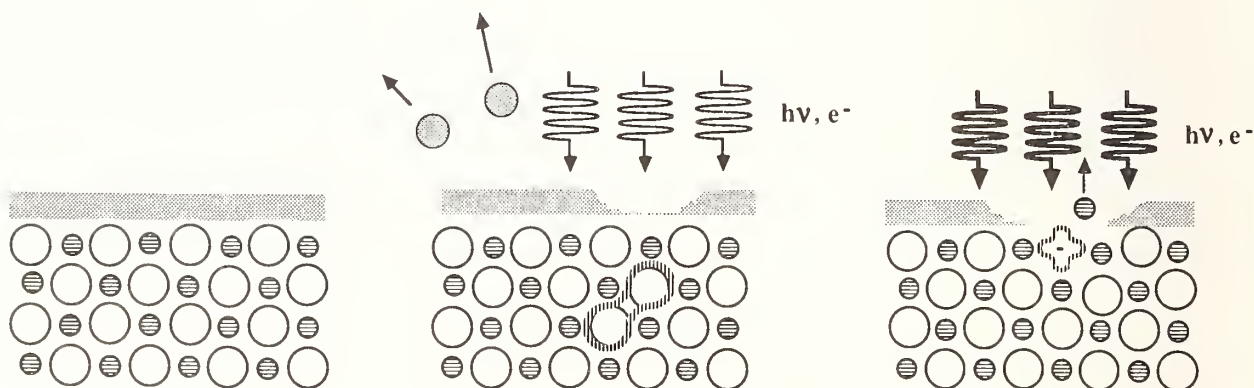


Fig. 10. Phases of electronically induced laser damage. From left to right: (a) Crystal with overlayer. (b) Overlayer erosion. (c) Catastrophic damage.

By far the richest phenomenology and the most damaging events occur with the arrival of a laser pulse on a surface which has gone through the evolutionary phases indicated in Figures 10(a) and 10(b). When the density of metallic atoms is sufficiently high that small agglomerations of metal have actually formed in the breached areas of the overlayer, it is possible for an intense laser pulse to create a metallic plasma, since clusters of even only a few tens of atoms already have essentially metallic properties [20]. The electrons accelerated in the laser field can reach energies sufficient for electron-stimulated-desorption with near unit efficiencies, ejecting additional atoms or molecules from the optical material. The ions accelerated in the plasma by the laser field are even more damaging since, at relatively low energies, they have sputtering

efficiencies greater than unity and produce significant desorption, erosion and cratering of the surface. The acceleration of ions and electrons also produces ultraviolet radiation which can cause photon stimulated desorption. And, finally, the absorption of light in the metal-rich overlayer will also produce thermal cratering and damage typical of the phenomenology already well-known at infrared laser wavelengths.

Thus beginning with a picture of **individual** desorption events initiated by the deposition of electronic energy, we have come full circle to the situation where catastrophic damage is produced collective phenomena, such as plasma formation and thermal absorption at the surface. It is important to understand, however, that while the ultimate damage effects may be thermal in nature, and could perhaps at this stage even be described by a thermal model, the correct description of the microscopic physics (including the determination of the critical rate constants) hinges on understanding electronically stimulated processes induced by short wavelength laser photons, and by hard ultraviolet photons and energetic electrons from the laser pumping process. Moreover, while we have not mentioned surface chemistry explicitly, we should not overlook the fact that reactive ions in laser plasmas, together with metastable neutral species and superthermal atoms from the laser plasma, will also work destructive mischief at the surface.

5. Conclusions

We have argued that DIET processes are likely to be the primary cause of damage to optical materials at short laser wavelengths, say, below 400 nm. The evidence for this point of view rests on a growing body of experimental data from which we are rapidly building a detailed atomic-scale picture of the dynamics of desorption processes. While the materials studied (the alkali halides) are not the specific choices in most SWL's, they are representative of a generic class of wide band-gap insulators which support the creation of self-trapped excitons and relaxation to permanent defects. Because so many SWL optical materials fall into this class, the predictions of our damage model should generally hold true, although the desorption rates (or efficiencies) may well be different in, say, the alkaline-earth halides or metal oxides than in the alkali halides we have studied.

The key steps in the damage process, based on the experimental evidence, are:

- (1) the formation of defects on the surface and in the near-surface bulk;
- (2) changes in surface and near-surface composition (formation of a metal rich overlayer) due to the thermally-driven migration of these defects; and
- (3) the occurrence of catastrophic plasma formation leading to self-reinforcing desorption and sputtering processes.

While we have concentrated on processes occurring on the near-surface bulk induced by relatively high-energy electrons and photons, there is also evidence implicating long-lived surface states in the desorption of excited neutral atoms. Should the photon-energy thresholds for reaching these states prove to be sufficiently low, it would make possible the triggering of DIET processes by low-energy laser photons in efficient, single-photon excitations.

Acknowledgement

The Vanderbilt contribution to this work was partially supported by a research contract from the Los Alamos National Laboratory. The experiment on the KrF LAM was made possible by the diligence and technical skill of the Aurora laser system operating team.

References

- [1] Lowdermilk, W.H.; Milam, D. "Laser-Induced Surface and Coating Damage," J. Quantum Electronics QE-17 (9); 1888-1902; 1981 September.
- [2] Bloembergen, N. "Role of Cracks, Pores, and Absorbing Inclusions on Laser Induced Damage Threshold at Surfaces of Transparent Dielectrics," Appl. Opt. 12 (4); 661-664; 1973 April. See also Bloembergen, N. "Laser-Induced Electric Breakdown in Solids," J. Quantum Electronics QE-10 (3); 1974 March.
- [3] Schmid, A.; Bräunlich, P.; Rol, P.K. "Multiphoton-Induced Directional Emission of Halogen Atoms from Alkali Halides," Phys. Rev. Lett. 35; 1382-1385; 1975 November 17. Bräunlich, P.; Schmid, A.; Kelly, Paul. "Contributions of Multiphoton Absorption to Laser-Induced Intrinsic Damage in NaCl," Appl. Phys. Lett. 26 (4); 150-153; 1975 February 15.

- [4] Haglund, Richard; Tolk, Norman. "Stimulated Desorption as a Potential Damage Mechanism in Ultraviolet Laser Optical Components," in Desorption Induced by Electronic Transitions-DIET II, Brenig, W.; Menzel, D., eds. Heidelberg, Federal Republic of Germany: Springer; 1985. 277-280.
- [5] Rothenberg, J.E.; Kelly, Roger. "Laser Sputtering. Part II. The Mechanism of the Sputtering of Al_2O_3 ," Nucl. Instrum. Methods in Phys. Research B1, (2,3); 291-300; 1984 February.
- [6] Rososcha, L.A.; Bowling, P.S.; Burrows, M.D.; Kang, M.; Hanlon, J.A.; McLeod, J.; York, G.W., Jr. "An Overview of Aurora: A Multikilojoule KrF Laser System for Inertial Confinement Fusion," Lasers and Part. Beams 4; 55-70; 1986 February.
- [7] Chuang, T.J. "Laser-Induced Gas-Surface Interactions," Surf. Sci. Rep. 3; 1-105; 1983.
- [8] Menzel, D.; Gomer, R. "Desorption from Metal Surfaces by Low-Energy Electrons," J. Chem. Phys. 41 (11); 3311-3328; 1964 December 1. Redhead, P.A. "Interaction of Slow Electrons with Chemisorbed Oxygen," Can. J. Phys. 42; 886-905; 1964.
- [9] Knotek, M.L.; Feibelman, P.J. "Ion Desorption by Core-Hole Auger Decay," Phys. Rev. Lett. 40; 964-967; 1978.
- [10] Knotek, M.L. "Stimulated Desorption from Surfaces," Phys. Today 37 (9); 24-32; 1984 September.
- [11] Czyzewski, J.J.; Madey, T.E.; Yates, J.M. "Angular Distributions of Electron-Stimulated Desorption Ions: Oxygen on W(100)," Phys. Rev. Lett. 32 (14); 777-780; 1974 April 8.
- [12] Tolk, N.H.; Feldman, L.C.; Kraus, J.S.; Morris, R.J.; Traum, M.M.; Tully, J.C. "Optical Radiation from Electron-Stimulated Desorption of Excited Particles," Phys. Rev. Lett. 46 (2); 134-137; 1981 January 12.
- [13] Tolk, N.H.; Haglund, R.F., Jr.; Mendenhall, M.H.; Taglauer, E.; Stoffel, N.G. "Electronically Induced Desorption of Neutral Atoms Observed by Optical Techniques," in Desorption Induced by Electronic Transitions: DIET II; 152-159.
- [14] Tolk, N.H.; Traum, M.M.; Kraus, J.S.; Pian, T.R.; Collins, W.E.; Stoffel, N.G.; Margaritondo, G. "Optical Radiation from Photon-Stimulated Desorption of Excited Atoms," Phys. Rev. Lett. 49 (11); 812-815; 1982 September 13.
- [15] Stoffel, N.G.; Riedel, R.; Colavita, E.; Margaritondo, G.; Haglund, R.F., Jr.; Taglauer, E.; Tolk, N.H. "Photon-Stimulated Desorption of Neutral Sodium from Alkali Halides Observed by Laser-Induced Fluorescence," Phys. Rev. B 32; (10); 6805-6808; 1985 November 15.
- [16] Pooley, D. "[110] Anion Replacement Sequences in Alkali Halides and Their Relation to F-Centre Production by Electron-Hole Recombination," Proc. Phys. Soc. 87; 257-262; 1966. Hersh, H.N. "Proposed Excitonic Mechanism of Color-Center Formation," Phys. Rev. 148 (2); 928-932; 1966 August 12.
- [17] Itoh, N.; Nakayama, T. "Electronic Excitation Mechanism of Sputtering and Track Formation by Energetic Ions in the Electronic Stopping Regime," Nucl. Instrum. Methods in Phys. Research B13; 550-555; 1986.
- [18] Nakayama, T.; Itoh, N. "Non-Thermal Laser-Induced Desorption of Compound Semiconductors," in Desorption Induced by Electronic Transitions: DIET II; 237-244.
- [19] Cherry, D.; Mendenhall, M.; Albridge, R.; Cole, R.; Haglund, R.; Heiland, W.; Hudson, L.; Peatman, W.; Pois, H.; Savundararaj, P.; Shea, M.; Tellinghuisen, J.; Tolk, N.; Ye, J. "Broadband Luminescence from Particle Bombardment of Alkali Halides," Nucl. Instrum. Methods in Phys. Research B13; 533-536; 1986.
- [20] Wimmer, E. "All-Electron Local Density Functional Study of Metallic Monolayers: I. Alkali Metals," J. Phys. F: Met. Phys. 13; 2313-2321; 1983.

Temporal Distribution of Electron and Ion Emission Caused by
Laser Excitation of Optical Surfaces in Ultra-high Vacuum*

W. J. Siekhaus, L. L. Chase and D. Milam

Lawrence Livermore National Laboratory
Livermore, California 94550

We have measured electron and ion emission under high vacuum conditions from several semiconductor and insulator surfaces excited by the first and third harmonics of a 1.06 μm Nd laser. The dependence of this emission on laser fluence and wavelength is consistent with a multiphoton excitation process. The dependence on laser pulse length implies, however, that other processes, either diffusive, thermal or thermomechanical, are also involved. Additional information is provided by the temporal and spatial distribution of the charge emission. The most extensive results have been obtained with single crystals of ZnS, for which nearly equal magnitudes of negative and positive charge emission are observed. The results suggest the possibility that the observed charge emission results primarily from the ejection of neutral atoms and molecules from the surface, followed by selective multiphoton ionization of one or more of the neutral species. The irreversible surface modification implied by the observed emission may be the precursor to observable surface damage. Detailed studies of the properties of the emitted particles may be very useful in developing a basic understanding of the damage mechanisms.

Key words: damage precursors; electron and ion emission, multiphoton ionization.

We have measured electron and ion emission resulting from laser excitation of polished surfaces of several amorphous and crystalline optical materials. The objective of this research is to identify the basic mechanisms of optical damage at photon energies much less than the optical bandgap and to identify surface regions that are most susceptible to damage so that these regions can be characterized by surface analytical techniques. The emission of electrons, ions and neutrals resulting from surface bombardment by ions and UV photons has been an active field of research for over two decades [1]. There has, however, been little work of this type involving surface excitation by photons in the transparency region, where the mechanisms for electronic excitation are not generally known. The significance of the information that can be obtained through studies of surface emission is well illustrated by work on alkali halide surfaces reported a decade ago by Schmid, Braunlich and Pol [2], who observed a very efficient surface ablation process caused by multiphoton excitation of trapped excitons by a ruby laser beam at intensities far below the single-shot damage threshold. Those results suggest that surface emission processes may not only contribute to an understanding of surface damage mechanisms, but they may actually be a common initiating factor in optical surface damage. It is therefore important to investigate laser-induced surface emission for a wide range of optical materials.

In order to study intrinsic particle emission processes on clean surfaces, it is necessary to work in an ultra-high-vacuum environment. The present work was performed in a UHV chamber at a residual pressure of 10^{-9} to 10^{-10} torr. The apparatus and experimental procedure have been discussed previously and will not be described here in detail [3]. The polished sample surfaces were cleaned in the evacuated chamber by several laser shots at fluences well below the damage threshold. Large quantities of emitted charge were observed following the first one or two shots due to desorption of contaminants from the surfaces. Subsequent shots gave fairly reproducible charge emission as a function of peak laser fluence. The peak fluence in the 3 mm diameter irradiated area was measured with a vidicon and calorimeter [4]. Laser pulses with nearly rectangular temporal profiles and variable widths from 1 ns to 50 ns were employed. Data were obtained for several materials at both the fundamental and third harmonic of the Nd laser. A two-stage microchannel electron multiplier was used with a fast oscilloscope to record the temporal dependence of the electron and ion emission with a subnanosecond time resolution.

*Work performed under the auspices of the Division of Materials Sciences of the Office of Basic Energy Sciences, U. S. Department of Energy and the Lawrence Livermore National Laboratory under Contract No. W-7405-Eng-48.

The total emitted negative charge as a function of peak laser fluence for several of the materials investigated is shown in figure 1 for 1.06 μm and 0.355 μm laser wavelengths. These data fit power law dependences on the fluence, with power law exponents approximately equal to the order of the multiphoton absorption required to excite electrons across the bandgap of the materials [3]. Although it may be possible to fit the data with other dependences on the fluence, such as an exponentially activated thermal process with a temperature proportional to the fluence [5], it would be difficult to account for the change in slope of the data with laser wavelength with such a model. One possible mechanism that could account for these results is photoelectric emission resulting from multiphoton production of electron-hole pairs, followed by further excitation of the electrons up to the vacuum level, after which they may leave the sample surface. If that is the case, the total charge emission would be expected to depend on the laser fluence F and temporal pulsewidth t_p as

$$Q = KF^{1/N} t_p^{N-1} \quad (1)$$

Then, the ratio of fluences required to produce a given charge emission Q for two pulse durations, t_{p1} and t_{p2} , is given by

$$\frac{F(Q, t_{p1})}{F(Q, t_{p2})} = \left[\frac{t_{p1}}{t_{p2}} \right]^{1-1/N} \quad (2)$$

Data for CdTe, ZnS and NaCl at several pulse durations is shown in figure 2. The logarithm of the ratio in eq (2) is given by the horizontal displacements of the lines for the different pulse lengths. For all three materials this ratio scales approximately as $t_p^{1/2}$. This agrees with eq (2) only for CdS, where $N=2$. For ZnS ($N=4-5$) and NaCl ($N=7$) the behavior expected for the multiphoton photoemission model is clearly not observed [3].

A second indication that a more complex process than photoemission is occurring is that for at least two of the materials investigated, SiO_2 and ZnS, comparable amounts of positive and

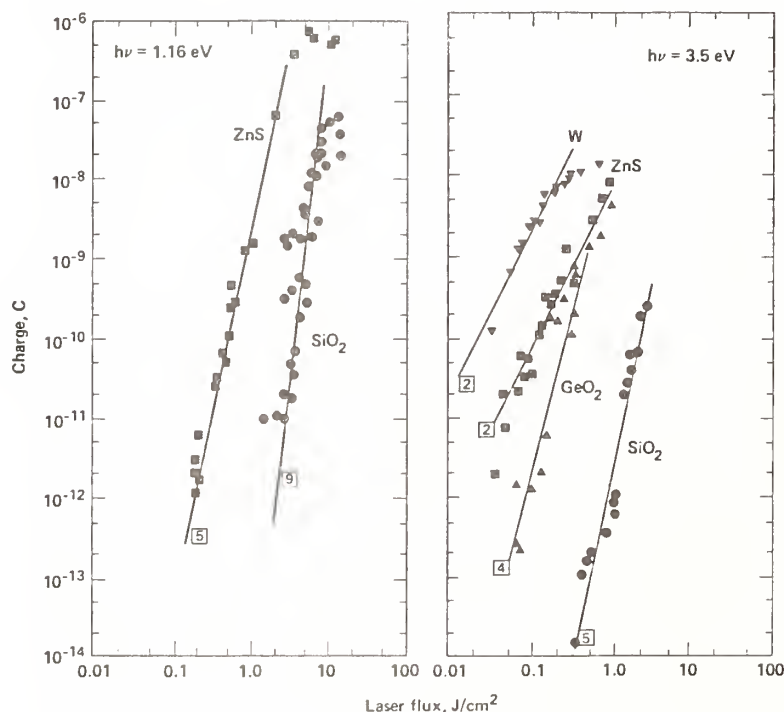


Figure 1. Time-integrated negative charge emission from several optical materials following 1 ns laser pulses at the fundamental and third harmonic of a Nd laser.

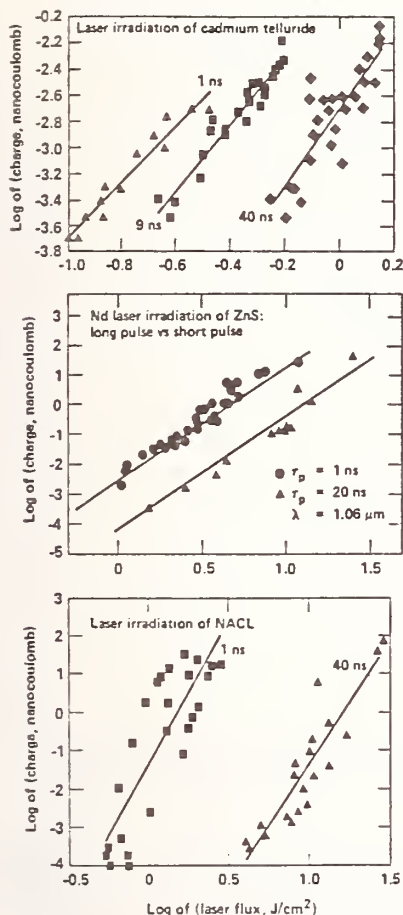


Figure 2. Negative emission produced by 1.06 μ m laser excitation for several laser pulse widths.

negative charge emission were observed. We have investigated the nature of these two emission components for ZnS by measuring the temporal dependence of the charge emission. A two-stage microchannel electron multiplier was placed about 10 cm from the sample in a direction at right angles to the laser beam, so that emission from both the front and back surfaces was detected. Different time delays for detection of the emission from the two surfaces could be obtained by rotating the sample in order to make the path lengths to the detector unequal. The front surface of the detector was biased to potentials of +700 volts or -1800 volts in order to detect the negative and positive emission, respectively.

The negative emission from ZnS is shown in figure 3 for laser pulse lengths of 1 ns and 50 ns. The time delay and duration of this emission are too short for anything but electrons to reach the detector. Measurements on a much longer time scale, shown in the upper part of Figure 4, indicate that there is no identifiable negative ion component, although there is a weak, diffuse emission persisting for several microseconds following the laser pulse. The rise time of the laser pulses is comparable to the 0.5 ns time resolution of the detection system. The response to the 1 ns pulse represents the "impulse response" of the electron emission, which consists of a rapid rise-time of several nanoseconds, followed by a decay time of about 30 ns. This short-pulse response possibly involves geometric time-of-flight factors in addition to any temporal dependence of the emission process itself. We can therefore conclude from these results only that the electron emission occurs within about 30 ns of the laser excitation. If only transit time effects cause the temporal spread of this impulse response, the response to a much longer pulse should be well approximated by a risetime equal to the decay time for the short pulse. The data for a 50 ns pulse are close to these expectations, except for a delay of about 5 ns after the leading edge of the optical pulse, during which the charge emission gradually develops. This is followed by a period, lasting for the duration of the optical pulse, during which the charge emission rises in the expected manner. The initial delay period, which could be caused by cumulative effects, such as heating, may be the cause of the unexpected dependence of the integrated charge emission on the square root of the pulse length.

ZnS electron emission

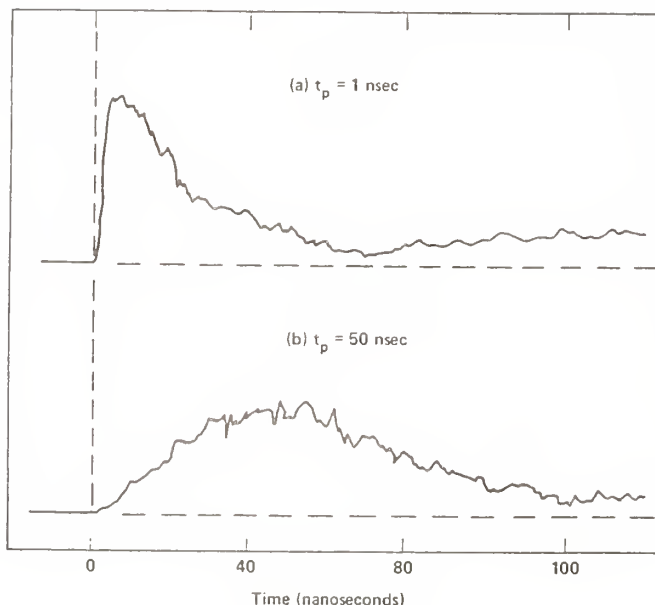


Figure 3. Time dependence of electron emission from a ZnS crystal surface for two laser pulse widths. a) $t_p = 1$ ns, $F = 0.76$ J/cm²; b) $t_p = 50$ ns, $F = 1.1$ J/cm²

Further evidence of the nature of the emission process is provided by the time-of-flight data obtained for emitted positive ions. Typical data for ZnS are shown in figure 4. The ion mass associated with a particular transit time from sample to detector can be obtained from the calibration based on the time delay of the sharp leading edge of the electron emission. The two strongest peaks in figure 4 result from emission of a single mass species from the front and back surfaces of the sample, which was rotated so that the back surface emission had a shorter path to the detector. Assuming a singly charged species, its molecular or atomic weight is about 100. This is approximately the mass of either $(\text{ZnS})^+$ or $(\text{S}_3)^+$, which would be the only reasonably expected products with this mass from a ZnS surface. It should be noted that the only other peaks in figure 4 are two very weak signals from front and back surfaces at a mass corresponding to some hydrocarbon desorption from the surface.

The absence of any peaks in the emission spectra corresponding to ionized Zn or S is notable. Two possible explanations for this behavior are apparent. First, some electronic desorption process may be operative that is rather specific to the release of one of these ionized molecules after the production of initial electrons and holes by multiphoton absorption. It is not clear, however, how to account for the dependence of the emission on laser pulsewidth with such a mechanism. A more plausible hypothesis is that neutral atoms and molecules are emitted from the surface, possibly due to heating by the laser beam, and either ZnS or S_n is preferentially photoionized by the laser after ejection from the surface. It is, in fact, well established for a number of insulating materials that neutral atom and molecule emission is far more probable than ion emission for surface bombardment by ions or UV photons [1]. This mechanism would also account for the observation that only positive ions and electrons are observed.

The evaporation of surface material caused by heating is a possible cause of the observed photoemission. In that case, the composition of the emitted vapor would consist primarily of atomic Zn and S, with ZnS and S_3 present at the one percent level or lower if the available vapor composition data obtained from Knudsen Cell measurements [6] adequately represents the situation of surface heating or melting of the crystalline solid. Since the ionization potentials of Zn and S are on the order of 10 eV, photoionization of this vapor may well favor the production of the molecular ions by a large margin. One problem with a thermal emission model is that a much more complicated dependence of the total emitted charge on the excitation fluence would be expected since the emission from the surface should follow an Arrhenius dependence [5] on the

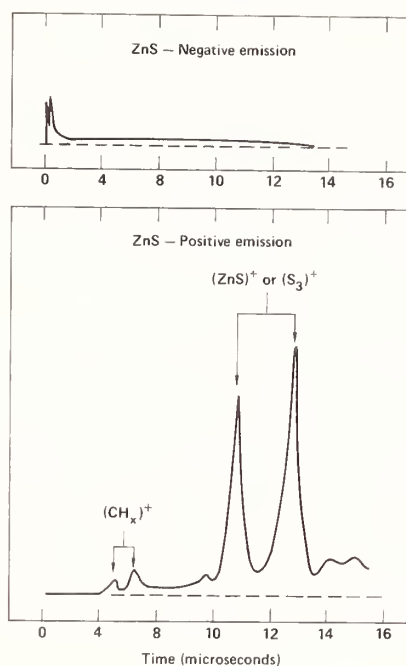


Figure 4. Negative and positive charge emission from ZnS following a 1 ns laser pulse of wavelength 1.06 μm .

surface temperature, which is determined by the laser fluence and pulse duration. As we pointed out earlier, such a behavior is difficult to reconcile with the dependence of the slope of the curves in figure 1 on the laser wavelength. Measurements are planned incorporating an ionizing mass spectrometer in place of the microchannel detector in order to measure the relative abundance of neutral Zn and S atoms and the molecular products. The dependence of this neutral emission on excitation fluence may be of great utility in assessing the roles of thermal evaporation and of multiphoton absorption processes in the solid and in the emitted vapor.

Absorption of laser energy by the plasma resulting from the electron and ion emission is a possible source of energy deposition near the sample surfaces that could lead to optical damage. We have established that, for ZnS, the electron emission occurs within 30 ns of a 1 ns laser pulse. Since the total emitted charge is also known from the data of figure 1, the plasma density near the sample surface can be estimated if the mean velocity and spatial distribution of the emission over the sample surface are known. We have made such estimates assuming a reasonable thermal ion velocity to estimate the plasma expansion rate and find that plasma densities on the order of 10^{19} cm^{-3} or greater, which would be required for significant surface absorption, can only result if the charge emission that we are measuring is localized in regions much smaller than the 3 mm diameter laser spot employed in this investigation. It is therefore important to determine the spatial distribution of the charge emission from optically excited surfaces. We are developing techniques to accomplish this.

In conclusion, these results demonstrate that microscopic damage in the form of surface ablation is occurring at fluences well below the damage threshold for ZnS. This may also be true of the other materials for which we have measured electron and ion emission. [3] The charged and neutral particle emission would appear to be a sensitive way to locate damage susceptible surface regions and to study the mechanisms causing the emission, which may be the initial stage of the processes leading to observable damage.

References

- [1] See, for instance T. E. Madey, J. T. Yates, Jr., J. Vac. Sci. Technol. 8, 525 (1971); D. Menzel, Surf. Sci. 47, 370 (1975).

- [2] A. Schmid, P. Braunlich and P. K. Rol, in Laser Induced Damage in Optical Materials: 1975, ed. by A. J. Glass and A. H. Guenther, National Bureau of Standards Special Publication Number 435, (U.S. Department of Commerce, 1976), p. 366.
- [3] W. J. Siekhaus, J. H. Kinney, D. Milam, and L. L. Chase, Appl. Phys. A39, 163 (1986).
- [4] W. L. Smith, A. J. DeGroot and M. J. Weber, Appl. Opt. 17, 3938 (1978).
- [5] Y. K. Jhee, M. F. Becker, and R. M. Walser, J. Opt. Soc. Am. B 2, 1626 (1985).
- [6] G. DeMaria, P. Goldfinger, L. Malaspina and V. Piacente, Trans. Far. Soc. (GB) 61, 2146 (1965).

DISCLAIMER

This document was prepared as an account of work sponsored by an agency of the United States Government. Neither the United States Government nor the University of California nor any of their employees, makes any warranty, express or implied, or assumes any legal liability or responsibility for the accuracy, completeness, or usefulness of any information, apparatus, product, or process disclosed, or represents that its use would not infringe privately owned rights. Reference herein to any specific commercial products, process, or service by trade name, trademark, manufacturer, or otherwise, does not necessarily constitute or imply its endorsement, recommendation, or favoring by the United States Government or the University of California. The views and opinions of authors expressed herein do not necessarily state or reflect those of the United States Government thereof, and shall not be used for advertising or product endorsement purposes.

Anomalous Absorption in Optical Coatings

M. R. Lange and J. K. McIver

University of New Mexico
Albuquerque, NM, 87131, USA

A. H. Guenther

Air Force Weapons Laboratory
Kirtland AFB, NM, 87117, USA

The observation of isolated damage sites in optical thin films subjected to pulsed laser irradiation has lead to a model based upon localized absorbing regions. This "inclusion initiated" model does not adequately treat several details of the radiation absorption process, but relies principally on thermal conduction as the sole energy transport process. Despite these rather severe shortcomings, qualitative predictions of this theory agree remarkably well with much of the quality experimental data. On the other hand, quantitative agreement can only be achieved if absorption coefficients several orders of magnitude higher than those measured for today's thin films are employed, which themselves are already very high compared to the materials value in bulk form.

In order to explain this apparent discrepancy a detailed theory of the spatial and temporal evolution of the highly absorbing regions must be conceived. In this paper we present our initial steps in this direction. The absorption/thermal diffusion process that leads to damage is modeled by two equations; the evolution equation for the free carrier density and the thermal diffusion equation. In practice these equations are strongly coupled. We decouple the free carrier equation by assuming that all rate constants are independent of the lattice temperature. The solutions of these simplified equations are presented along with their sensitivity to the magnitude of several of the unknown rate constants. Those regions of parameter space in which the original thermal diffusion model is valid are pointed out, as well as the potential implications for more appropriate modeling of the absorption process as functions of experimental and material variables.

Key Words: Anomalous Absorption; Avalanche Ionization; Coatings; Color Centers; Electron Diffusion; Laser Damage; Thermal Diffusion.

1. Introduction

In work set forth to date this paper's authors have stated, with significant morphological evidence [1], their concepts of a localized absorbing region within an optical thin film. These localized absorbing regions are assumed to be due to anomalies of some sort. Heat transfer equations were solved indicating trends in damage thresholds as a function of material and experimental parameters. Thermal diffusion was assumed as the dominant controlling mechanism in the damage process and experimental data has correlated quite well with this model [2]. The thermal diffusion equations incorporate a nonhomogeneous thermal source, which is due to a localized electron density interacting with both the incident field and the lattice structure.

In actuality, there are two coupled nonhomogeneous diffusion processes involved. They are thermal diffusion due to the aforementioned thermal source, and electron diffusion due to a localized electron source. The electron source properties depend, in the main, upon the local optical field and local temperature. These coupled equations are generally untractable and as such are usually decoupled through assumptions which can apply in certain limits.

Assumptions that have been used in previous works are that the operative coefficients and the source for thermal diffusion are independent of temperature, and the electron density has been assumed constant. That is, the electron density is modeled as a step function in time and space such that it evolves instantaneously and does not diffuse. These assumptions are obviously not valid in all cases of interest. Certain refractory oxide film damage [1], for example, exhibits morphology, which grows spatially during irradiation to a size comparable to the incident beam diameter.

In addition to the shortcomings of these previously employed assumptions, the use of an instantaneous electron density must be justified. Thus, mechanisms for the evolution of an electron density had to be investigated.

2. Theory

In an attempt to refine this model in the direction of more comprehensive theory, the concentration of effort is placed upon the evolution of the localized electron density and the absorption processes involved. The approach taken to this end is to write down the classical equation of electron diffusion and solve it for a generalized electron source. Conservation of electromagnetic and thermal energy is then employed with the principal purpose of ascertaining useful scaling laws. The comparison of these scaling laws with experimental data implies certain preferred absorption mechanisms. These mechanisms are then further investigated via the appropriate expressions governing electron diffusion.

The principal findings are that; i) local metallic concentrations supplemented by color centers may be a viable mechanism for the initial electron production in certain optical thin films and ii) very small regions of these anomalies ($\sim 200 \text{ \AA}$) can possibly lead to damage when supplemented by an avalanche ionization. Avalanche ionization is only assumed to occur in optical coatings and serves to expand the region that is absorbing at the anomalously high rate.

The classical equation of electron diffusion is given as:

$$\frac{\partial n}{\partial t} = \frac{1}{r} \frac{\partial^2}{\partial r^2} (r D_e n) + g(n, T, |E|) - (n - n_i) \gamma(n, T) \quad (1)$$

where D_e = electron diffusivity (cm^2/S), $|E|$ = electric field strength (V/cm), g = electron carrier generation ($\text{cm}^{-3}\text{S}^{-1}$), n = electron carrier density (cm^{-3}), n_i = initial carrier density (cm^{-3}), T = temperature (K), and $\gamma(n, T)$ = free carrier decay rate (s^{-1}).

The assumptions made in solution of the above equation are that D_e is independent of n and T (which is not true in general), and g is independent of T . The dependence of g on n and E are incorporated iteratively and the other assumptions will be addressed at a later time.

The solution of the above equation in all space is found via integral transform [2]. n_i is absorbed in n so that n becomes $n = n - n_i$. The general solution is found to be

$$n(r, t) = \frac{2}{\pi r} \int_0^\infty d\beta \sin(\beta r) e^{-(D_e \beta^2 + \gamma)t} \int_0^t dt' \int_0^\infty r' dr' \sin(\beta r') g(r', t') e^{(D_e \beta^2 + \gamma)t'} \quad (2)$$

In order to decide upon a reasonable choice for the electron source generation term $g(r, t)$, attention is diverted to a consideration of the conservation of energy. The morphology of damage suggests a localized source of electron generation, however, it does not imply a mechanism. Scaling laws derived from the conservation of energy consideration may, though.

The Poynting theorem may be written as

$$\frac{\partial w}{\partial t} = \vec{\nabla} \cdot \vec{S} - \left(\vec{J} + \frac{\partial \vec{P}}{\partial t} \right) \cdot \vec{E} + \vec{M} \cdot \frac{\partial \vec{B}}{\partial t} \quad (3)$$

Where w is the field energy, S is the Poynting vector, J is the electron current flux, P is the material polarization and M is the magnetization vector. If the field is in approximate steady state with the absorption process and magnetic transitions are neglected, then

$$\vec{\nabla} \cdot \vec{S} = \vec{J} \cdot \vec{E} + \vec{E} \cdot \frac{\partial \vec{P}}{\partial t} . \quad (4)$$

The $\vec{J} \cdot \vec{E}$ term contains the energy stored in electron acceleration along with electron-phonon collisions and the $\vec{P} \cdot \vec{E}$ term contains the energy stored in polarization along with electronic transitions. The $\vec{J} \cdot \vec{E}$ term is the dominant term in avalanche-ionization and inverse brehmsstrahlung processes while the $\vec{P} \cdot \vec{E}$ term is assumed dominant in single and multiphoton transitions. All of these are possible mechanisms of absorption. In order to avoid restriction to any certain mechanism the $\vec{\nabla} \cdot \vec{S}$ term is used to represent absorption.

For simplicity an incident plane wave is assumed, which gives

$$\vec{\nabla} \cdot \vec{S} = - \frac{I_r \alpha}{\mu} e^{-\alpha z} = - \frac{I_r V \sigma}{\mu} e^{-\alpha z} \quad (5)$$

where I , n_r and μ are the incident field intensity, real index of refraction and magnetic permeability. α is the generalized absorption coefficient and σ is the generalized absorption cross-section with V the volume that is absorbing.

From the first law of thermodynamics the energy balance of an absorbing region is

$$\vec{\nabla} \cdot (-\vec{\nabla}(kT)) + \frac{\partial}{\partial t} (\rho c_V T) = - \vec{\nabla} \cdot \vec{S} , \quad (6)$$

where k = thermal conductivity, c_V = specific heat at constant volume, and ρ = mass density, which leads to

$$E_D (\text{J/cm}^2) = \frac{\mu}{n_r} \int_0^{t_p} \frac{dt}{\alpha} \left\{ \frac{\partial}{\partial t} (\rho c_V T) - \vec{\nabla} \cdot (\vec{\nabla}(kT)) \right\} , \quad (7)$$

where E_D is the energy density of the incident pulse at which the region reaches a critical temperature which causes damage.

The energy depletion from the incident field occurs over a region represented by the length α^{-1} which includes absorption by electrons that immediately thermalize along with those that thermalize after electron diffusion of length δ_e . As pointed out by Meyer et al. [3], the thermal diffusion may be incorporated in the same manner. That is, the energy that is deposited in the lattice is deposited in a region resulting from absorption and thermalization of electrons (both with and without diffusion) along with the thermal diffusion δ_T that occurs after deposition during the pulse. The thermal diffusion length is given by $\delta_T = \sqrt{Dt}$. The two parallel processes may be added to give

$$\delta_{\text{eff}} = \left[\frac{\chi_1}{\left[\alpha^{-1} + \delta_T \right]} + \frac{\chi_2}{\left[\alpha^{-1} + \delta_e + \delta_T \right]} \right]^{-1} . \quad (8)$$

Here χ_1 is the fraction of laser energy deposited directly into the Lattice and χ_2 is the fraction of energy that diffuses before being deposited.

Thus we can write

$$E_D (J/cm^2) \propto \frac{1}{n_r} \int_0^T dT \rho c_v \delta_{eff} \cdot \quad (9)$$

The importance of this procedure is the demonstration of useful scaling laws. For example, when $\delta_T > \delta_e$, α^{-1} ,

$$E_D \propto \frac{1}{n_r} \int_0^T dT \sqrt{\rho c_v k T} \left[\frac{\chi 1}{1 + \frac{\alpha^{-1}}{\delta T}} + \frac{\chi 2}{1 + \frac{\alpha^{-1}}{\delta T} + \frac{\delta_e}{\delta T}} \right]^{-1}, \quad (10)$$

and when $\delta_e, \delta_T < \alpha^{-1}$

$$E_D \propto \frac{1}{n_r} \int_0^T dT \rho c_v \alpha^{-1} \left[\frac{\chi 1}{1 + \alpha \delta T} + \frac{\chi 2}{1 + \alpha \delta_e + \alpha \delta T} \right]^{-1}. \quad (11)$$

The first case exhibits the same scaling law derived for a spherical absorbing region where thermal diffusion dominates [4]. Here, it is much more general in that no specific geometry has been assumed and temperature variation of the constants is incorporated.

The second case demonstrates an absorption dominated process and implies that $E_D \propto \alpha^{-1}$. Thus the wavelength dependence of $\alpha(\lambda)$ should exhibit itself in the damage threshold data roughly as $E_D \propto \alpha^{-1}(\lambda)$.

In addition to the exhibition of wave length dependence in certain cases, an important point of the above scalings is the demonstration of the perspective which they lend to the all important energy transport process. The scales over which energy transformation and transport occur are solely responsible for whether the damage is absorption or diffusion dominated.

The wavelength dependence for damage from reference [1] may be found by averaging over films (λ and $\lambda/2$) for five and fifteen nanoseconds. When this is done it is found that between $\lambda = 0.26 \mu m$ and $0.53 \mu m$ the fluorides damage as $\lambda^{1.95}$ while oxides damage as $\lambda^{2.48}$ and between $\lambda = 0.53 \mu m$ and $1.06 \mu m$ fluorides damages as $\lambda^{0.24}$ and oxides $\lambda^{0.5}$. There is significant statistical deviation from film to film (i.e. for the various coating materials).

In all of the theories investigated, this increasing power of frequency in the absorption function with increasing photon energy was only noted in photo-ionization processes. However, the films and photon energies investigated [1] should not be near band edge transitions. It should be noted that a large density of impurity states can exhibit this same behavior. In addition, the transition between different, but related, processes of absorption at different frequencies is a possibility (i.e., different sorts of impurities). These may occur in the same, or even separate discrete regions.

The α is constituted as $\alpha = \sum_n \alpha_n + \alpha_{FC}$ where $\sum_n \alpha_n$ is the absorption coefficient for n-photon absorption and α_{FC} is the absorption coefficient for free carriers. $\sum_n \alpha_n$ is related to α_{FC} in that n-photon absorption produces free carriers.

Although these processes are generally considered intrinsic they also may apply to the obviously extrinsic damage processes which occur in optical coatings due to localized shallow or impurity states in the coating. These shallow impurity states support photo-ionization and impact

ionization at threshold levels far below those expected of a pure material. These states may occur due to impurity atoms, ions, non-stoichiometric mixtures leading to metallic colloids, color centers or simply because of local disorder. Shallow states due to disorder have been confirmed for D.C. fields by conductivity measurements [5].

Thus, due to the above and the observed morphology it is assumed that there exists the possibility of very small localized regions of impurities.

One obvious choice for an electron source function is a uniform spherical region, of impurities or shallow states, of radius r_0 . The origin of such a region may be a coagulation of centers resulting from dislocations, as discussed below.

This source term is given by

$$g(r', t') = f(t') \{ \theta(r') - \theta(r' - r_0) \} \quad (12)$$

Where for single and multiphoton transitions of shallow states

$$f(t') = \left[\frac{\eta_Q \alpha_1 I}{h\nu} + \frac{I^2 \beta}{2h\nu} \right] \theta(t') \quad (13)$$

Here I is the incident intensity ($\text{ev}/\text{cm}^2\text{-s}$), α_1 is the one photon coefficient ($1/\text{cm}$), β is the two photon coefficient ($\text{cm-s}/\text{ev}$), η_Q is the quantum efficiency (1), $h\nu$ is the photon energy (ev), and the θ 's are step functions. This integral (Eq. (12) into Eq. (2)) is very similar to one done previously [2] and affords a solution of

$$n(r, t) = \frac{2}{\pi} \frac{f(t_p) r_0^3}{D_e r} \int_0^\infty \frac{dy \sin \frac{yr}{r_0} (\sin y - y \cos y) (1 - e^{-(D_e y^2/r_0^2 + \gamma)t})}{y^2 (y^2 + r_0^2 \gamma/D_e)} \quad (14)$$

For the region of parameter space of interest here, the above integral provides numerical problems in its evaluation. However the first term of the integral may be done analytically giving a solution of

$$n(r, t) = \frac{2f(t_p) r_0^3}{\pi r D_e} \left(A - \int_0^\infty \frac{dy \sin(yr/r_0) (\sin y - y \cos y) e^{-(D_e y^2/r_0^2 + \gamma)t}}{y^2 (y^2 + r_0^2 \gamma/D_e)} \right) \quad (15)$$

where

$$A = (r D_e \pi / (2 r_0^3 \gamma)) \{ 1 - \frac{1}{2} (\exp[-(1+r/r_0)c] + \exp[-(1-r/r_0)c]) \\ - (r_0 / (2cr)) (1 + (1-r/r_0)c) \exp[-(1-r/r_0)c] - (1 + (1+r/r_0)c) \exp[-(1+r/r_0)c] \} \quad (16)$$

and where $c^2 = r_0^2 \gamma / D_e$.

This solution is numerically convergent, but only valid for the region of $0 < r/r_0 < 1$. A numerical plot from this solution is given in the next section.

In the far field ($r \gg r_0$) the source may be described as

$$g(r', t') = \frac{\delta(r') f(t') V}{4\pi r'^2} \quad (17)$$

Where $\delta(r')$ is a delta function and V is the characteristic volume of absorption. This gives for the electron density,

$$n(r, t) = \int_0^t dt' \frac{V f(t')}{8(\pi D_e(t-t'))^{3/2}} \exp \frac{-r^2}{4D_e(t-t')} \exp(-\gamma(t-t')) . \quad (18)$$

$f(t')$ is the same as before and α_1 and β are computed from the stimulated transition rates which can be found in terms of the oscillator strengths of the impurity states.

In alkali-halides the shallow impurity states may be provided by a distribution of metallic colloids resulting from poor stoichiometry and various aggregates of color centers. Colloids may be produced in the process of heating to 200 to 350 C [6,7] or even by insufficient heating during film deposition. In addition, mild heating causes the coagulation of F-centers to colloidal particles [6]. With specific reference to alkaline earth fluorides, "F-centres in additively-colored alkaline earth fluoride crystals readily aggregate forming more complex structures" [7]. An example of the sort of distribution that may occur is shown in figure 1.

Where, in optical coatings, the possible localized concentrations of absorption centers such as these, come from is not being assumed here. Dislocation clusters and poor stoichiometry are quite likely in optical coatings. The assumption made is that the conditions of deposition and processing of coatings allow this to be true.

As an illustrative example of one of the materials of interest [1], CaF_2 has an absorption peak at 521 nm in what is called the β band predominantly due to M-centers. It should be pointed out that in CaF_2 the F-centers peak at 376 nm and certain colloids peak at 550 nm. In addition to these are R centers, M_F centers, M^+ centers and many other complex combinations of centers [7]. The definitions of these may be found in references [6,7 and 8].

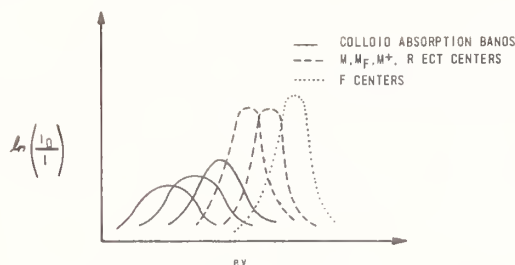
The oscillator strength may be assumed to be ~ 1 [9,10] and the transition rate for single photon transitions is given as [11,12a]

$$W_{ik} = \frac{I g(\nu) e^2 f_{ik}}{m c h \nu} , \quad (19)$$

where $g(\nu)$ is the normalized lineshape, f_{ik} is the oscillator strength and I is the laser intensity. $g(\nu)$ [11,12] can be expressed as follows

$$g(\nu) = \frac{2(\ln 2)^{1/2}}{\pi^{1/2}} \exp[-4(\ln 2) \frac{(\nu - \nu_0)^2}{(\Delta \nu)^2}] \quad (20)$$

One of the wavelengths of interest is 530 nm [2], which is slightly off center of the transition line. Due to the large width of the lines [6,7,8,12b,13], we find $g(\nu) \approx 0.9/\Delta \nu$, however to be conservative a line shape factor of $0.1/\Delta \nu$ will be used.



**A POSSIBLE ABSORPTION STRUCTURE DUE TO COLLOIDS AND CENTERS.
SEE, FOR EXAMPLE, pg 259 AND pg 265 OF REFERENCE 6**

Figure 1. A possible absorption distribution vs. photon energy for a complex aggregate of absorption centers.

From this computation it is found that $W_{ik} = 1.4 \times 10^{11} \text{ s}^{-1}$ from ground state to the first excited state. This first excited state is long lived [9,10] and will easily ionize deeply into the conduction band from here.

3. Results

Assuming an absorption center density of $n_a = 10^{17} \text{ cm}^{-3}$ (which may be conservative for a thin film [13])

$$\frac{n_Q \alpha I}{h\nu} \approx \frac{n_a W_{ic}}{2} = 7 \times 10^{27} \text{ cm}^{-3} \text{ s}^{-1}. \quad (21)$$

Here a factor of 1/2 was included to account for the final ionization step, some of which may occur thermally. This factor may be placed into the quantum efficiency $\eta_Q = 1/2$ and can be considered conservative due to the ionization transition rate approximated from equations in references [11,14 and 15].

Several important points related to table 1 should be mentioned. The results that follow are based upon classical diffusion which should not apply where small numbers of electrons are involved. If one multiplies the electron densities by the impurity region volume it is clear that rather small numbers of electrons are indeed involved. There is no attempt made here to model this situation rigorously. This aspect of the study is used to demonstrate relative orders of magnitudes, and the feasibility of very small local anomaly regions producing large electron densities in the conduction band.

Some of the numerical results from the integration of eq. (14) are shown in Table 1.

$$\alpha_1 = 4.91 \text{ (cm}^{-1}\text{)}, \text{ (for } n_a = 10^{17} \text{ cm}^{-3}, \sigma = 2.1 \times 10^{-17}\text{)}$$

$$\beta = 0.$$

$$\eta_Q = 1/2$$

$$D_e = 0.01 \text{ (cm}^2\text{/s)}$$

$$f_{12} = 1.0 \text{ (oscillator strength)}$$

$$g(\nu) = 0.1/\Delta\nu \text{ (line shape factor)}$$

$$h\nu = 2.34 \text{ eV}$$

$$t_p = 10^{-8} \text{ s}$$

$$r_0 = \text{radius of region of impurities}$$

$$\gamma = \text{conduction electron recombination rate (s}^{-1}\text{)}$$

$$\sigma = \text{absorption cross section (cm}^2\text{)}$$

$$P = \text{probability of electron production within volume of interest}$$

$$n(50\text{\AA}, 0.1\text{ns}) = \text{electron density at } 0.1\text{ns} \text{ and } r = 50 \text{\AA}$$

$$\Delta t = \text{time at which probability of electron production exceeds 1}$$

Table 1. Electron densities achieved at 50 Å within an absorbing region due to photoionization of absorption centers.

$I \left(\frac{\text{GW}}{\text{cm}^2} \right)$	$r_0 \text{ (cm)}$	$\sigma \text{ (cm}^2\text{)}$	$\gamma \text{ (s}^{-1}\text{)}$	P	$n(50\text{\AA}, 0.1\text{ns})$	Δt
0.1	10^{-6}	2.1×10^{-17}	10^{12}	<1		
			10^{11}	<1		
			10^{10}	<1		
	2×10^{-6}	1.6×10^{-17}	10^{12}	<1		
			10^{11}	<1		
			10^{10}	>1	4.2×10^{17}	40 ps
			10^{12}	<1		
			10^{11}	>1	6.5×10^{16}	10 ps
			10^{10}	>1	4.2×10^{17}	8 ps
1.0	10^{-6}	1.6×10^{-16}	10^{12}	<1		
			10^{11}	>1	5.2×10^{17}	6 ps
			10^{10}	>1	3.4×10^{18}	4 ps

For example, the initial color center density for the table above is chosen to be 10^{17} cm^{-3} , however the final electron densities produced from this exceed this number. This number is not chosen to be realistic as much as it is chosen to be conservative. In a region where trap centers are generated by polishing damage or some other process, the trap centers would probably be orders of magnitude greater than 10^{17} cm^{-3} . Thus, 10^{17} is chosen to provide a conservative transition rate, though it is not allowed to limit the number of electrons which transition. Conduction electrons are limited, however, by recombination, or decay. It may further be noted that if 10^{17} cm^{-3} color centers existed in a region of 100 Å in radius, at best one half of an available electron would be in this region. Clearly its only purpose is to give conservative transition rates. As such, the numbers in tables 1 and 2 should not be taken as accurate. They are presented to demonstrate relative orders of magnitudes of conduction electrons that could be produced under the conditions of radiation, decay and diffusion. One primary point of table 1 is the demonstration of the fact that the size of a region and the intensity of radiation dictate a threshold condition due to competing probabilities of transition and decay in the region. What constitutes this region is not assumed here, other than the fact that it contains shallow centers. It may be an inclusion at the base of a nodule [16] or at a grain boundary. It may be a dislocation cluster [17]. It should be noted here that colloidal particles deposit selectively at dislocations [6]. In addition, dislocations are the source of color centers.

This threshold is not, however the damage threshold. The important parameter in damage is the rate at which lattice energy builds in a local region. Even if the electron transition threshold is exceeded, the energy may be harmlessly conducted away by electron and phonon transport. Table 1 also serves to demonstrate that if sufficient numbers of electron trap centers (M-centers, in this case) are present, the transition is quick ($\ll t_p$). The partitioning of such regions where the volume may be smaller than the volume between trap centers is very artificial. It is intended to generalize the table to weaker transitions at higher densities, or perhaps colloidal transitions. This is why the cross section is listed in table 1. Whatever the source of electrons, if the cross section is as given, the table should remain valid in the region of the transitions.

Although the electron densities represented in these small regions are impressively high, they could not alone transfer sufficient energy to the lattice to cause damage. Densities of this sort are required over regions approaching 0.1 to 1. micron in diameter [4]. Since anomaly regions of this size are not observed in optical coatings (except for nodules), these absorbing regions must evolve during irradiation. Since nodules are of the same material as the surrounding film the absorption in and around them must similarly evolve. Of the various mechanisms studied for this process, the only reasonable explanation found is the expansion of the absorbing region via impact ionization. That is, these small local high densities of conduction electrons ionize the surrounding off resonant electron trap centers and impurities. This is commonly termed avalanche ionization, though it usually applies to purely intrinsic processes (ionizing valence electrons). It should be noted that if the absorption center region is on the order of 0.1 to 1. micron, no avalanche is required to produce the appropriate region of high electron densities. This, however, is probably unlikely. A solution of this case is shown in figure 2 which emphasizes the effect of γ .

An avalanche due to impact ionization of impurity, colloidal or trap, states would explain the observation of lower damage thresholds in doped materials regardless of whether or not the doping impurities are in resonance with the field. The photoionization of centers to initiate the process would explain qualitatively the wavelength dependence of damage thresholds in optical coatings.

Although specific numbers are used for a given case in a certain material, this is done for computational purposes. It is felt that the calculation of a specific example is desirable. The concepts are intended to be applied to more general cases through the use of absorption cross sections.

A detailed study of avalanche ionization will not be conducted here. That has been the topic of considerable research by such authors such as [13], [18], [19], and [20]. As reference [19] implies, avalanche-ionization has been confirmed in solids, and as reference [13] indicates, a computational competency has been achieved with the processes involved. It will simply be assumed here that due to shallow trap states, densities in excess of those required [13] to initiate an avalanche have been provided. An exponential growth then follows, which is subsequently limited by ionization of a large fraction of the available atoms, carrier decay and the dynamic Burstein shift [21]. A simple calculation with eq. (22) shows that at optical frequencies ($\sim 500 \text{ nm}$) and damage intensities ($1\text{--}2 \text{ Gw/cm}^2$) in fluoride films a conduction electron can gain energies of one half to two and a half eV in 10^{-10} seconds.

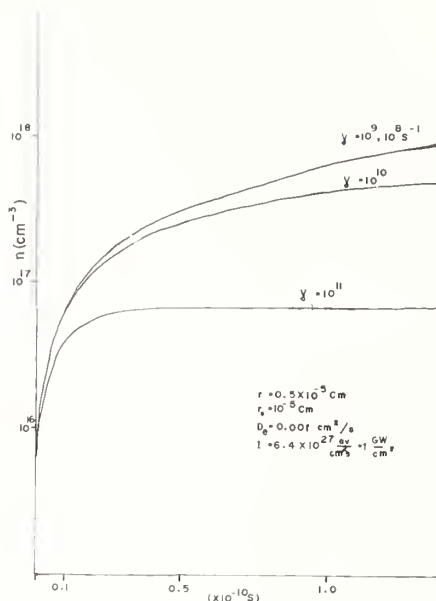


Figure 2. The growth of the electron density at a radius of 500 \AA within an absorbing region of 1000 \AA radius for various γ 's and the parameters given. All unlisted parameters are those given for Table 1.

$$\frac{d\varepsilon}{dt} = |E|^2 \frac{e^2 \tau_k}{m^* (1 + \omega^2 \tau_k^2)} \quad (22)$$

(In eq. (22) ε is the energy transferred to the electron and τ_k is the time between collisions) [13].

The spread in values is due to uncertainties in collision frequencies. These energies are sufficient to ionize many electron trap centers and some impurities [22].

The simple model used herein will produce a conservative estimate of the growth of an electron density initiated by a small region of absorption centers. This relates to previous works [2] which demonstrated a requirement of isolated regions on the order of the film thickness with an average electron density on the order of 10^{18} cm^{-3} .

For this case, the form of $g(r, t)$ chosen is

$$g(r', t') = f(t') e^{-p^2(t') r'^2} \quad (23)$$

where $p(t')$ represents a spatial expansion of the electron source due to the avalanche process. It is assumed from previous studies [19] that an avalanche region's growth is nonlinear, however a conservative estimate of the region's size at a time t is $\delta_e = \sqrt{D_e t}$. That is, the distance

electrons have travelled by diffusion from their initiation point. Thus; $p(t) = 1/\sqrt{D_e t}$ can be used as a trial parameter.

Subsequent integration of eq. (2) affords

$$n(r,t) = \frac{1}{8} \int_0^t \frac{dt' f(t') (D_e t')^{3/2}}{D_e \left((t - t') + \frac{1}{4D_e p^2} \right)^{3/2}} \exp(-\gamma(t-t')) \exp \frac{-r^2}{4 \left(D_e (t-t') + \frac{1}{4D_e p^2} \right)} \quad (24)$$

with

$$f(t') = n_i \alpha_a e^{\alpha_a t'} \quad (25)$$

where α_a is the avalanche coefficient. Equation (25) is simply a means of generating electrons initially at an exponential rate. This growth is terminated at some point due to processes such as the dynamic Burstein shift and ionization of a large fraction of the available electrons.

Table 2

Electron Densities achieved at $12. \times 10^{-6}$ cm from color center initiation due to an electron avalanche for various parameters. The avalanche is assumed to spread via diffusion.

$\alpha_a = 10^{10} (s^{-1})$	Avalanche coefficient
$D_e = 0.01 (cm^2/s)$	Electron diffusion coefficient
$f_{ik} = 1.0$	Oscillator strength
$g(v) = 0.1/\Delta v$	Line shape factor
$h\nu = 2.34$	Photon energy
$t_p = 10^{-8}$	Pulse length
$n_f^* = 10^{20}$	Limiting electron density

* The limiting electron density n_f was chosen as a reasonable value based upon [21].

$I \left(\frac{GW}{cm^2} \right)$	$\sigma / 10^{-17}$	r (cm)	$\gamma \text{ (s}^{-1}\text{)}$	$\alpha_a \text{ (s}^{-1}\text{)}$	$n(r, lns)$
1.0	2.1	12.0×10^{-6}	10^{10}	10^9	4.7×10^{12}
	10^{10}			$6. \times 10^{16}$	
	16.4		10^{11}	10^9	2×10^{10}
				10^{10}	1.2×10^{15}
			10^{10}	10^9	6.3×10^{12}
				10^{10}	$6. \times 10^{16}$

A rigorous justification of eqs. (24) and (25) above is not possible. These expressions are simply a reasonable choice for the purpose of a Gedanken study of a postulated process. It should also be noted that as shown in Ref. [19] avalanche is not a symmetric process. It in fact tends to propagate in the direction of the beam source due to an attenuation of the field. In optical thin films this propagation is modified by encounter of the film surface.

Some of the numerical results are presented in figures 3 and 4 and table 2.

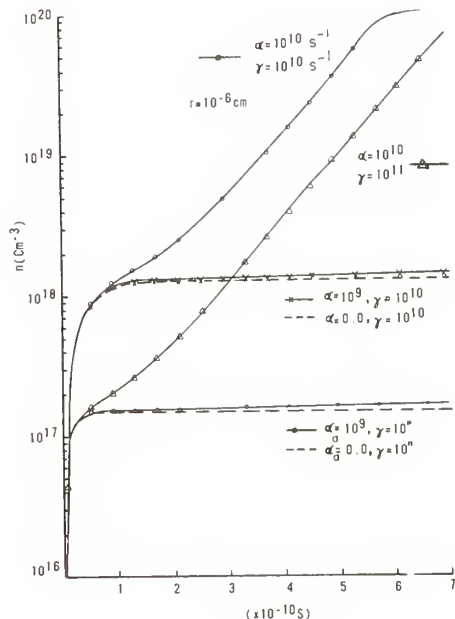


Figure 3. The growth of the electron density at a radius of 100\AA for various parameters. The parameters chosen are considered reasonable. Electron densities become very high at this radius both with and without avalanche ionization. D_e is assumed to be $0.01\text{ cm}^2/\text{s}$.

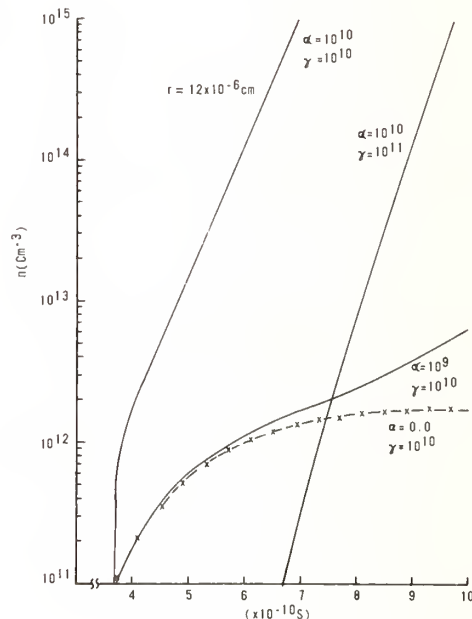


Figure 4. The growth of the electron density at a radius of 1200\AA (1300\AA is the largest radius possible in a half wave film at $0.53\text{ }\mu\text{M}$). Densities of the order of 10^{12} can be achieved by diffusion in the case considered if a sufficient number of electrons are available for photoionization. Otherwise an electron avalanche is required to reach and certainly to exceed this. The assumed $D_e = 0.01\text{ cm}^2/\text{s}$.

4. Discussion

The numerical results presented in the previous section indicate the feasibility of microdamage sites initiated by a localized absorbing anomaly. An avalanche of electrons can produce large, densities of electrons expanding out to diameters on the order of the film thickness.

It should be noted that the field thresholds are lower than those reported previously for avalanche processes in similar materials. However, those were reported in bulk solids. The starting mechanism in thin films should provide lower thresholds for starting the process (colloids and aggregates of high density centers). The large density of shallow states (centers) which may coagulate about colloids, or coagulate about themselves, should provide lower levels required for a sustained avalanche process (i.e., the ionization of the off resonant centers requires significantly less energy than valence electrons).

The avalanche coefficients (10^9 - 10^{10}) were chosen by scaling data from ref. [18] using relations of Epifanov [20] for 2.0 to 2.5 eV impurity states. These numbers were further supported by eq. (22). It should be noted here that eq. (22) is overly simplistic and may not be sufficiently conservative. In addition Epifanov [23] believes that the coefficients determined in ref. [18] may be too high.

The approach taken here may not be considered rigorous. This is intended to be a feasibility study for which more sophistication may be incorporated. The feasibility of this process or a similar one is considered sufficiently demonstrated. The exact processes involved are still considered unknown.

5. Conclusions

It has been shown that due to the non-ideal structure of an optical thin film, large local electron densities may be generated by non-stoichiometric colloids or aggregates of color centers.

These are likely to exist in optical systems due to the conditions of deposition, substrate polishing and subsequent treatment. If avalanche ionization does occur in these films, regions as small as 100 Å in radius of colloids and centers may initiate the process. Otherwise regions closer to the thickness of the film 10^3 - 10^4 Å of colloids and centers may be required.

Since these studies are initial, more investigation will be required to support these theories. It should be pointed out that colloids in the fluoride films would probably be oxidized due to ever present atmospheric oxygen. The process is thus further complicated. Band edge sort of transitions may actually be occurring in oxidized metallic colloids in fluoride films. In addition to this, correct absorption cross sections of metal colloids in the optical region have yet to be computed. Errors or inappropriate assumptions have been found in those reported in the literature.

It is clear that much work remains to be done in this area. Measurements of colloidal absorption bands indicated that it is likely that colloidal absorption at $\gamma = 1.06 \mu\text{m}$ is a strong competitor for the two-photon process which would be required for M-centers in CaF_2 . The two-photon computation produces transition rates significantly less than the one photon at 0.53 μm . However, correct colloidal cross sections need to be computed for comparison. Also, more rigorous avalanche-computations need to be performed for this specialized case, if possible. It may not be possible due to the lack of knowledge of the thin film structure. In addition, complications such as oxidation, temperature effects and electron density variation of D_e and need to be accounted for.

Finally, in order to label this a theory, computation of electron densities would have to be performed in a more rigorous fashion. This list of work to be done can become quite lengthy. It is believed, however, that feasibility has been shown.

This research was sponsored by the Air Force Weapons Laboratory under Contract F29601-84-K-0092.

6. References

- [1] Walker, T. W.; Guenther, A. H.; Nielsen, P. "Pulsed Laser-Induced Damage to Thin-Film Optical Coatings-Part I: Experimental," IEEE J. Quant. Electron, QE-17 (10); 2041; 1981.
- [2] Lange, M. R.; McIver, J. K.; Guenther, A. H. "Pulsed Laser Damage in Thin Film coatings:

- Fluorides and Oxides," *Thin Solid Films*, 125 (1-2); 143; 1985.
- [3] Meyer, J. R.; Bartoli, F. J.; Krueger, M. R. "Optical Heating in Semiconductors" *Physical Review B*, 21 (4); 1559; 1980.
 - [4] Lange, M. R.; McIver, J. K.; Guenther, A. H. "Pulsed Laser Induced Damage of An Optical Material With a Spherical Inclusion: Influence of the Thermal Properties of the Materials" in NBS (U.S.) Spec. Publ. 669. Eds. H. E. Bennett, Guenther, A. H., B. E. Newnam, D. Milam, 1982.
 - [5] Ovshinsky, S. R. "Reversible electrical Switching Phenomena in Disordered Structures," *Physical Review Letters*, 21; (20) 1450; 1968.
 - [6] Schulman, J. H.; Compton, W. D. "Color Centers in Solids," Pergamon Press, 1963.
 - [7] Hayes, W. "Crystals with Fluorite Structures", Oxford: Clarendon Press, 1974.
 - [8] Fowler, W. B. "Physics of Color Centers", Academic Press, N.Y., 1968.
 - [9] Beaumont, J. H.; Hayes, W. "M Centres in Alkaline Earth Fluorides, *Proc. Roy. Soc. A*, 309; 41; 1969.
 - [10] Fowler, W. B. "Relaxation of the Excited F Center," *Phys. Rev.* 135 (6A); 1725; 1964.
 - [11] Yariv, A., *Quantum Electronics*, John Wiley, 1967.
 - [12] (a) A.I.P. Handbook, Sec. 7; 3rd ed.; Ed. Gray, D. E.; McGraw Hill 1973.
(b) A.I.P. Handbook, Sec. 9; 3rd ed.; Ed. Gray, D. E.; McGraw Hill 1973.
 - [13] Sparks, M.; Duthler, C. J. "Theoretical Studies of High-Power Ultra Violet and Infrared Materials," Fifth Tech. Rep. Xonics, Corp. Contract DAHCL5-73-C-0127, 1975.
 - [14] Vaidyanathan, A.; Mitra, S.; Narducci, L.; Shatras, R. "One-Photon Absorption in Direct Gap Semiconductors," *Sol. Stat. Com.* 21; 405-407; 1977.
 - [15] Vaidyanathan, A.; Walker, T.; Guenther, A.; Mitra, S.; Narducci, L. "Comparison Keldysh and Perturbation Formulas for One-Photon Absorption," *Phys. Rev. B* 20(8); 3526-3527; 1979.
 - [16] Lao, B.; Smith, D. "The Development of Nodular Defects in Optical Coatings", NBS Spec. Pub. (this edition); 1985.
 - [17] Lewis, K.; Pitt, A.; Cullis, A.; Chew, N.; Charlwood, L. "Laser Induced Damage in Dense Optical Thin Films", NBS Spec. Pub. (this edition); 1985.
 - [18] Yablonovitch, E.; Bloembergen, N. "Avalanche Ionization and the Limiting Diameter of Filaments Induced by Light Pulse in Transparent Media," *Phys. Rev. Let.* 29 (14); 907; 1972.
 - [19] Fradin, D. W.; Yablonovitch, E.; Bass, M. "Confirmation of an Electron Avalanche Causing Laser-Induced Bulk Damage at 1.06 μ m." *Applied Optics*, 12 (4) 1973.
 - [20] Epifanov, A. S. "Avalanche Ionization Induced in Solid Transparent Dielectrics by Strong Laser Pulses", *Sov. Phys. JETP*, 40 (5); 1974.
 - [21] Burstein, E. "Anomalous Optical Absorption Limit in In Sb," *Phys. Rev.* 93; 632; 1954.
 - [22] Sparks, M.; Duthler, C. J. "9-10 Tech. Rep. Xonics, Corp. Contract DAHCL5-73-C-0127; 1977.
 - [23] Epifanov, A. S.; Private Communications, Nov. 1985.

TIME OF DAMAGE AND THE EFFECT OF THE PULSE REPETITION FREQUENCY ON THE
LASER INDUCED DAMAGE THRESHOLD

R M Wood, S K Sharma, P Waite, E K Gorton* and K Lewis*

GEC Research Ltd., Hirst Research Centre, East Lane, Wembley, Middlesex, United Kingdom

*Royal Signals Research Laboratories, Malvern, Worcestershire, United Kingdom

ABSTRACT

The time of damage has been measured as a function of pulse input energy for a range of i-r windows and mirrors.

More data and understanding of the mechanisms involved has been gained of the effect of laser pulse repetition frequency on the laser induced damage thresholds of infra-red transmitting window materials. Results on Ge, Si, GaAs, ZnS, ZnSe, NaCl and KCl are presented together with comments on the mechanisms which lower the damage threshold from the single shot damage level.

Key Words: CO₂ laser; GaAs; Ge; KCl laser damage; NaCl; repetitive-pulse damages; ZnS; ZnSe.

1 INTRODUCTION

In the search for a reliable measurement of the minimum laser induced damage threshold of a particular component we have investigated the time of damage against input energy for a range of materials. This has resulted in a better understanding of the mechanisms involved.

At previous damage symposia [1,2] the preliminary results of investigations into the effect of pulse repetition frequency on the laser induced damage threshold of infra-red transmitting window materials were presented. This paper reports the results of more experimental measurements on a wider range of infra-red window materials and looks again at the mechanisms which lower the damage threshold from the single shot damage level.

2 APPARATUS

The results in this paper were mainly gained using the LAL hybrid TEA CO₂ pulsed laser, Figure 1. This laser has a Gaussian TEM₀₀ mode, (Figure 2a) has a gain switched spike plus tail (Figure 2b) and can be operated at pulse repetition frequencies from single shot to 100 Hz.

3 MEASUREMENT OF DAMAGE THRESHOLD

Laser induced damage thresholds can be due to a variety of mechanisms:

Dielectric Breakdown

- Bulk Effects
- Surface Effects
- Enhancement by scratches
- Brillouin Scattering
- Self-focussing

Thermal Absorption

- Bulk effects
- Surface effects
- Localised absorption
- Conduction and free-carrier electron absorption
- Transient absorption

and is dependent on both the material parameters and the laser pulse wavelength, and spatial and temporal characteristics. Damage may correlate with either:

- Peak power density (spatial and temporal) in the laser pulse.
- Maximum energy density (spatial) of the laser pulse.
- Average energy density in the pulse spike.
- Average energy density in a pulse with both a spike and a tail.

Total energy density or average power density in a pulse train.
Cw power density (energy in a given time)

It is therefore commonly found that each component or surface may exhibit a range of laser induced damage thresholds (LIDT). A typical graphical record of the percentage of the pulses resulting in damage versus irradiation level is shown in Figure 3. Both the shape of this graph and its absolute position in space is an intimate function of wavelength, spot size and pulse repetition frequency.

4 TIME OF DAMAGE

The damage threshold of a transmitting material such as KCl or NaCl is caused by dielectric breakdown and is expected to occur at or before the peak intensity of the laser pulse. In an absorbing material however the time of damage will be dependent on the energy absorbed and on the thermal properties of the material testunder. Figure 4 shows in schematic form the (a) incident and (b) transmitted pulse shapes of a typical TEA laser. 4c shows damage at the peak irradiance of the pulse and 4d damage at some earlier time. It will be noticed that the plasma is assumed to be formed instantaneously and that consequent transmission (or reflection) is negligible. It will also be realised that these graphs could be gained at just above damage threshold for dielectric breakdown or well above it, in the case of thermal mechanisms. Figures 4e and 4f indicate the onset of damage due to thermal mechanisms alone.

The time of damage has been monitored both in transmission and in reflection for a range of i-r transmitting window materials. The following photographs of the time of damage have been gained using Iwatsu digital storage scopes monitoring both the incident and either the transmitted and/or the reflected beam. It is possible to superimpose both beams on each other and in the cases where this has been done the transmission/reflected beam has been normalised to the incident beam.

Figure 5a shows damage occurring to a Cu mirror in the tail of the TEA laser pulse. This is the minimum damage threshold for this mirror. Figure 5b shows the difference between an unattenuated pulse (lower trace with tail) to an attenuated (damage) pulse which has cut the tail off. Figure 5c shows the normalised incident and reflected beams at higher laser pulse energy showing that the reflection/absorption properties of the mirror change slightly before the main plasma attenuation takes place.

LIDT to a Germanium substrate on the other hand cannot be induced to occur as late in the pulse as late as that to a Cu mirror. Figure 5d shows the latest time of damage to be 20 ns after the peak of the pulse and 5e shows damage at the peak of the pulse. Figure 5f shows the 'latest' time of damage to a Silicon sample (40 ns after the pulsepeak). This photograph indicates that the change of transmission/reflection just before catastrophic breakdown is not so pronounced in Si as in Ge or Cu. Figure 5g indicates the length of time the plasma absorbs the incident radiation.

It will be realised that the time of damage can be used to give guidance both as to the minimum damage threshold which applies and as to the precise mechanisms involved in the damage.

5 PULSE REPETITION FREQUENCY AND DAMAGE THRESHOLD

The preliminary results of our investigations into the effect of pulse repetition frequency on the laser induced damage threshold of infra-red transmitting window materials were presented in 1982 at this conference [1]. In presenting these results we made the comment that the only consistent physical mechanism we could offer to explain the shape of the curve was that of an anomalously low thermal conductivity. L D Merky [3] questioned this explanation but even so did not find another.

We have undertaken more work using the same hybrid TEA CO₂ laser (Figure 1) and have been very careful to ensure that the result is not a system phenomenon. For instance possible changes in sensitivity of the original photon-drag detector have been ruled out by use of a room temperature CMT detector.

A summary of these results is shown in graphical form in Figure 6. The p.r.f. LIDT's are normalised to the single shot value to facilitate comparison between materials. Ge shows a decreasing p.r.f. LIDT with increasing p.r.f. to over 100 Hz. GaAs shows the same general shape but flattens out at lower p.r.f.. ZnSe and ZnS both flatten out earlier and higher (some more evidence will be shown on a range of ZnS samples). Si on the other hand only showed a 10% drop with increasing p.r.f. and a correlation has been found between damage level and number of shots at constant p.r.f.. This behaviour is not unexpected as Si has higher absorption coefficients than

the other i.r. window materials tested and the thermal model is therefore three dimensional rather than the two dimensional model which approximates to the low absorption case. The dielectric substrates KCl and NaCl were found to have steady damage thresholds irrespective of p.r.f..

In all cases damage occurred within 20 shots and it was found that if damage did not occur at a particular pulse energy and p.r.f. within this period then it did not occur within 15 seconds.

In order to check that these prf damage thresholds were not just a short term cumulative effect some long irradiation runs (10^5 shots) were made on all samples at about 70% of the 100 Hz prf threshold value and 10^6 shots at 50% of the 25 Hz threshold value were made using the Ge sample.

It should be noted that these graphs have been found to be consistent over a number of commercially obtained, well polished substrates.

Investigation has been made of the mechanisms which this change in LIDT with p.r.f.. In 1982 we invoked the theory of an anomalously low thermal conductivity/diffusivity to explain the shape of the Ge curve. This could be of bulk or surface origin. The theory of surface origin is favourite at the present time.

Irradiation of a $\lambda/4$ ZnSe overcoated Ge substrate showed that the prf behaviour of the component was changed to be more like a bare ZnSe substrate. Irradiation of the uncoated side showed typical Ge behaviour.

Figure 7a shows the laser damage morphology of a GaAs polycrystalline substrate. This photograph shows line damage around the central damage spot. This line damage was produced consistently during the last two or three shots prior to the catastrophic damage at the centre. It is thought that the lines correspond to cracked grain boundaries. If this is so then the temperature increase during the prf run might be contained within the grain being irradiated. Eventually the grain boundary cracks and the grain raises its temperature up to damage level. Figure 7b shows two damaged areas. The lower damaged area is a grain which was literally blown out of the surface after line damage was produced. Figure 7c shows the central damage spot showing melted material at the edges and typical grain boundary structure within the spot itself.

Once the linedamage appeared on the front surface the central area damaged within two or three shots. This damage occurred all the way through the crystal and damage has been observed on both front and back surfaces simultaneously.

A further series of tests have been made on a series of CVD grown polycrystalline ZnS with distinctive, narrow ranges of crystalite sizes, from RARE Malvern. These varied from 2-5, 35-40, 73, to 148 μm . Samples 2 and 3 reproduced the ZnSe/ZnS band whilst the other two more nearly reproduced the GaAs curve. It was hoped that relationship could be gained between the LIDT's and the p.r.f. behaviour and the grain sizes. This has not been gained unambiguously although variations in behaviour have been observed. These samples are in process of being repolished to a higher standard so as to eliminate differences other than grain size.

6 CONCLUSIONS

Time of damage measurements have been shown to be useful both to determine the minimum damage thresholds and to allow further determination of the mechanisms involved in damage.

Further measurements of the relationship between damage threshold and the laser prf have been made for a range of single crystal and polycrystal i-r transmitting substrates. The favourite mechanism for the observed effect is that of anomalously low thermal conductivity which has been linked to surface condition and grain size.

ACKNOWLEDGEMENTS

This work has been supported by the Procurement Executive, Ministry of Defence (Directorate of Components, Valves and Devices) and sponsored from the RSRE Establishment.

REFERENCES

- 1 R M Wood, S K Sharma and P Waite, NBS Spec. Pub. 669, 1984, p 44
- 2 R M Wood, S K Sharma and P Waite, BDS Symp. 1983
- 3 L D Merkyl, 1985

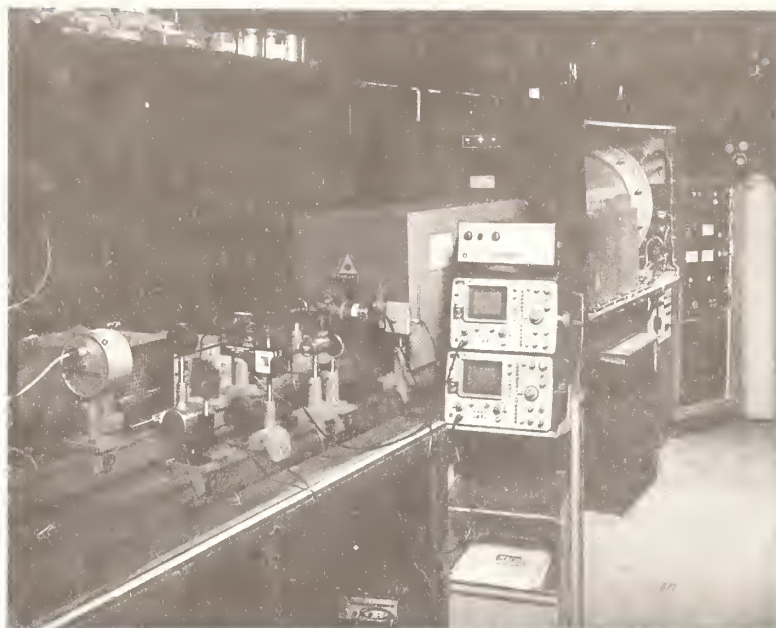


Figure 1: Photograph of damage apparatus

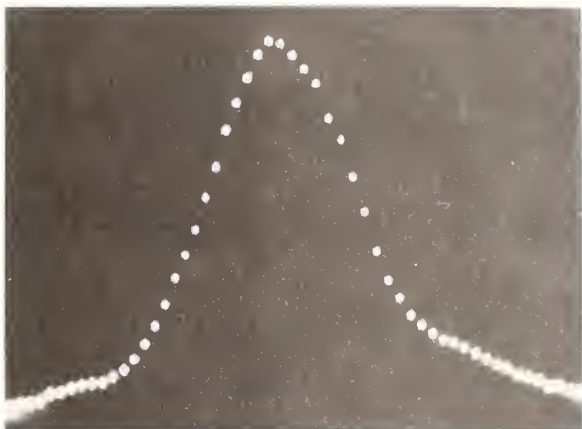


Figure 2a: Spatial profile of beam

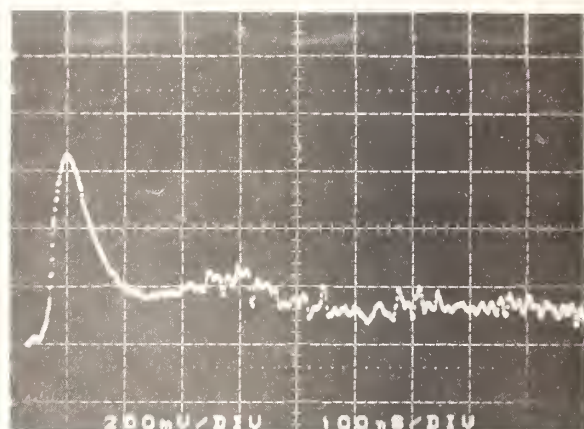


Figure 2b: Temporal profile of beam

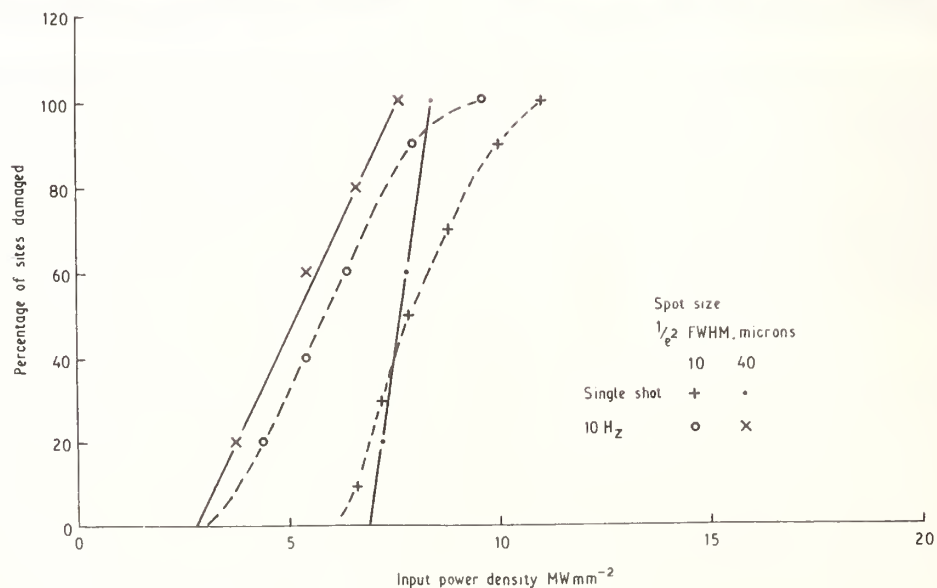


Figure 3: Percentage of area damaged versus irradiation level

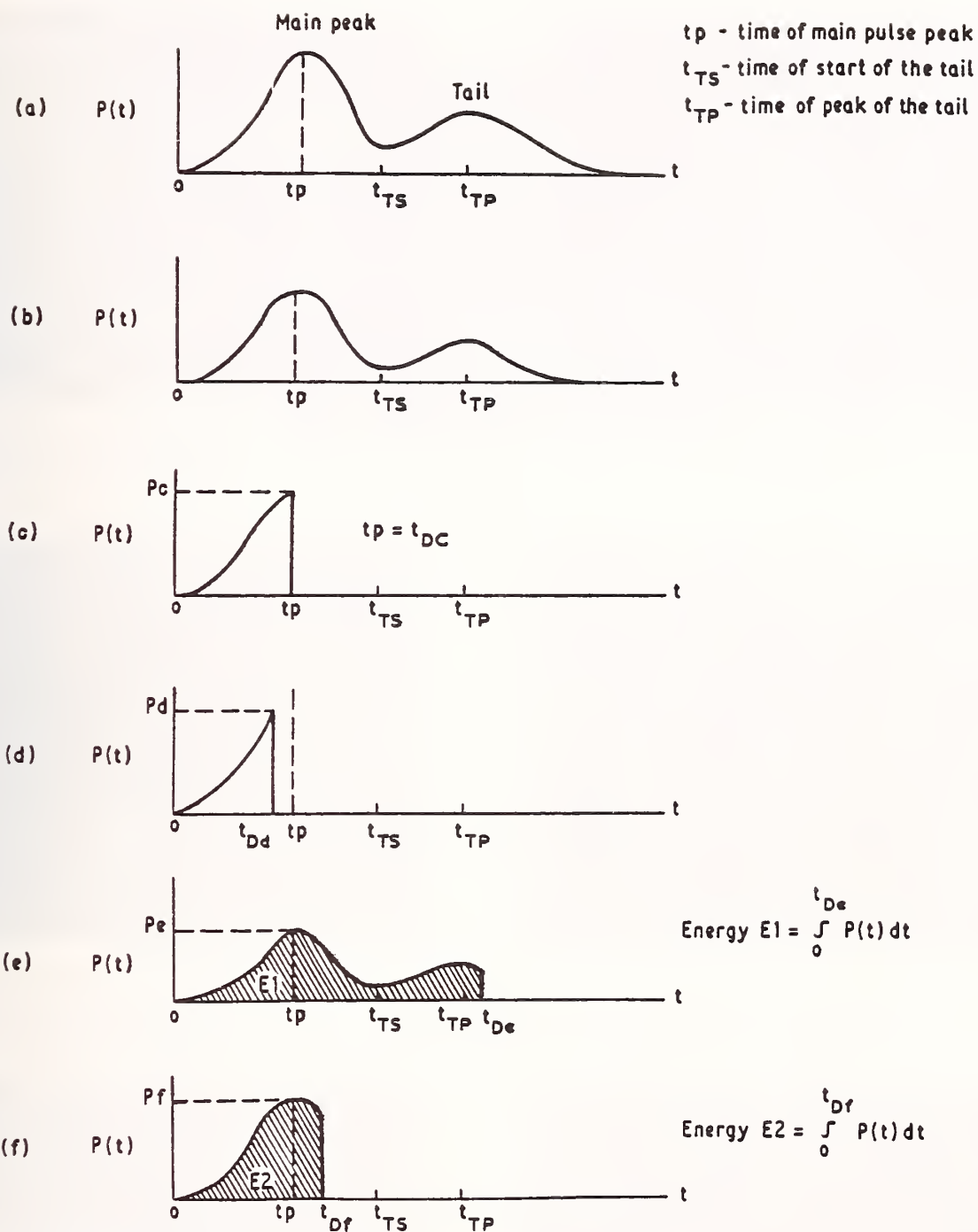


Figure 4: Schematic of the time of damage

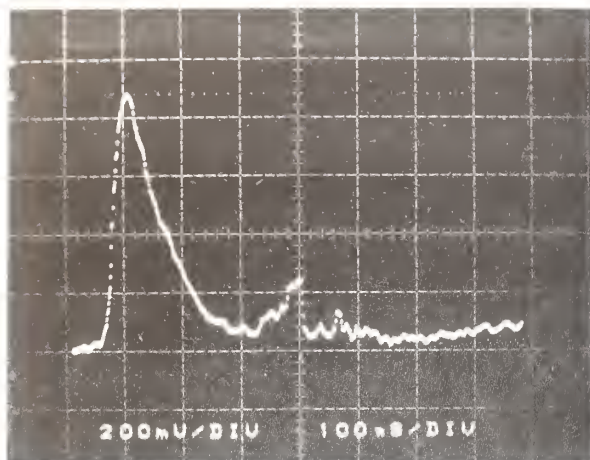


Figure 5a: Cu: showing damage in tail of TEA laser pulse

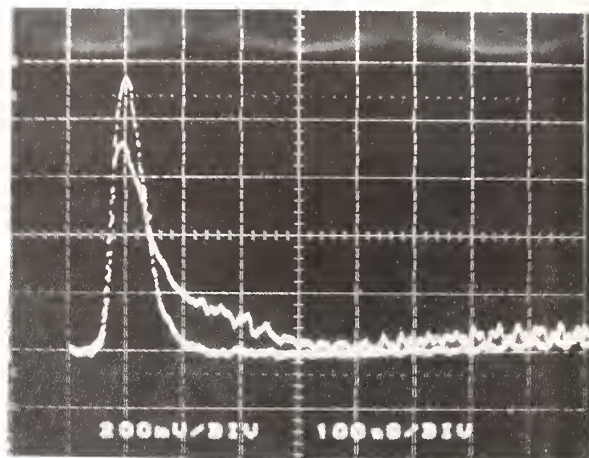


Figure 5b: Cu: showing difference in reflectance with increasing energy in laser pulse

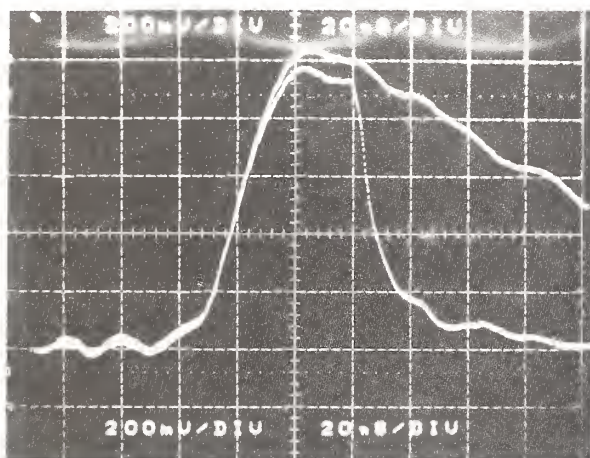


Figure 5c: Ge: normalised incident and reflected beams showing time of damage

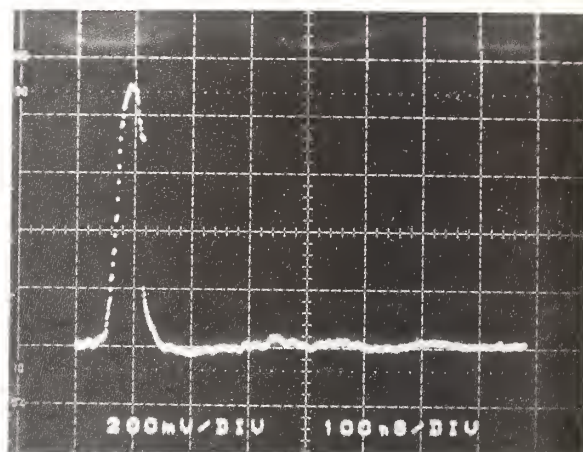


Figure 5d: Cu: normalised incident and reflected beams showing initiation of plasma

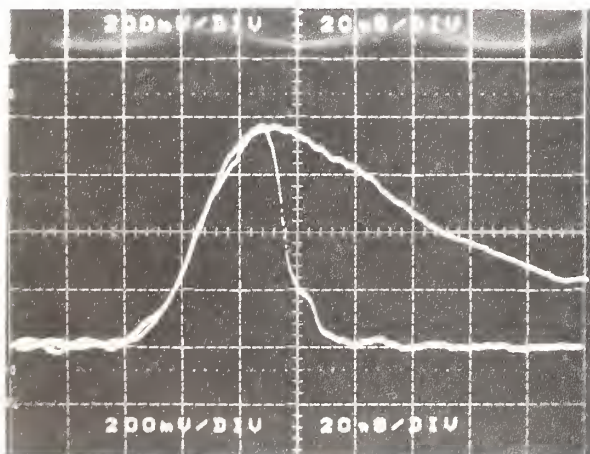


Figure 5e:

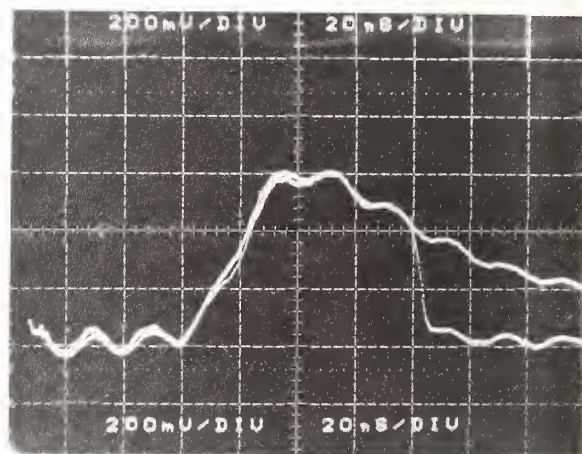


Figure 5f

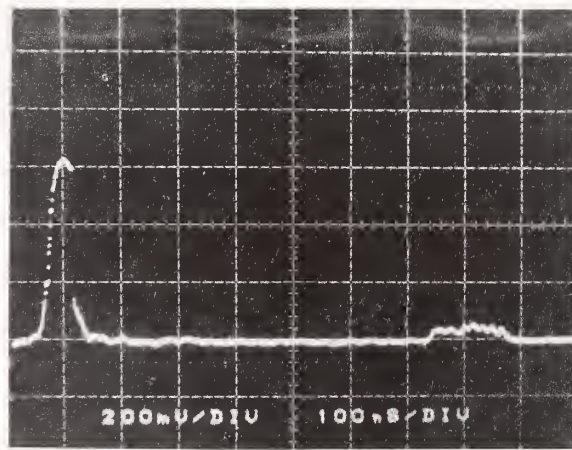


Figure 5g

Figure 5: Time of damage

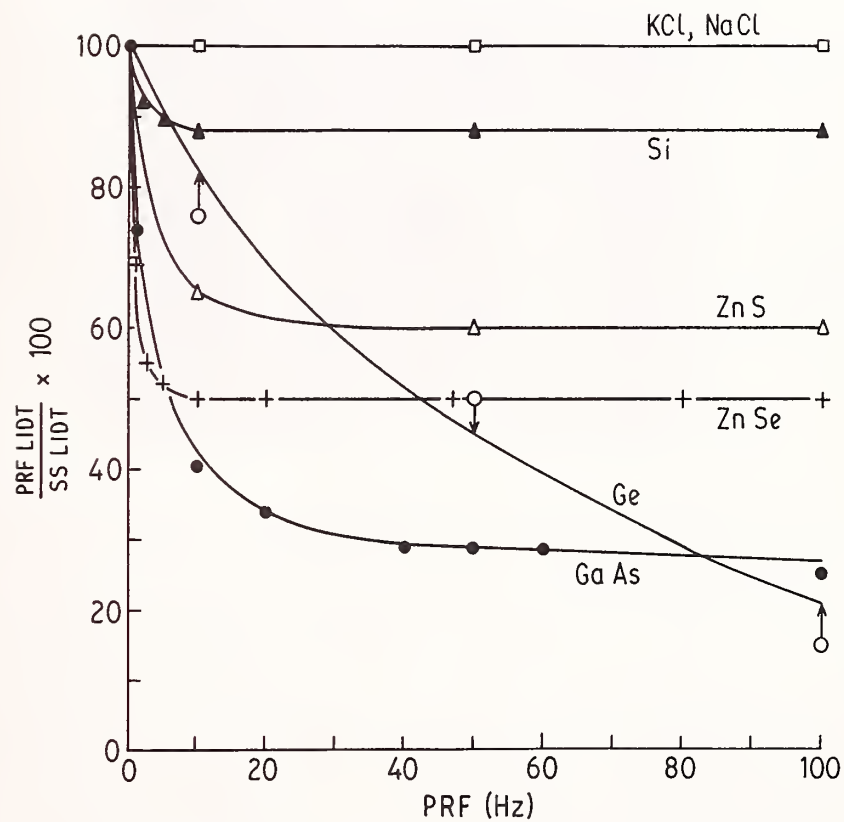


Figure 6: Normalised prf LIDT values as a function of prf for a selection of substrate materials



Figure 7a: Laser damage showing line damage

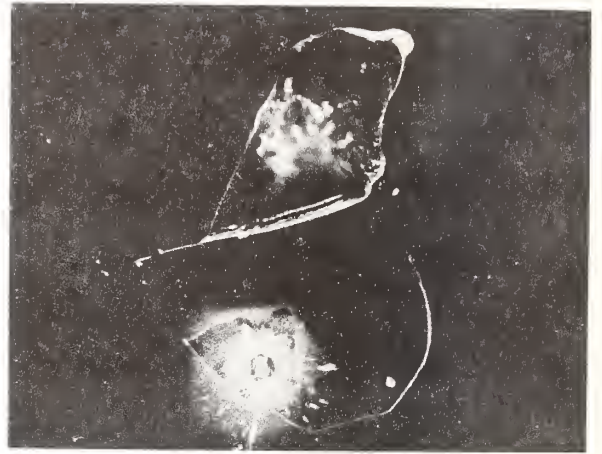


Figure 7b: Two damage areas

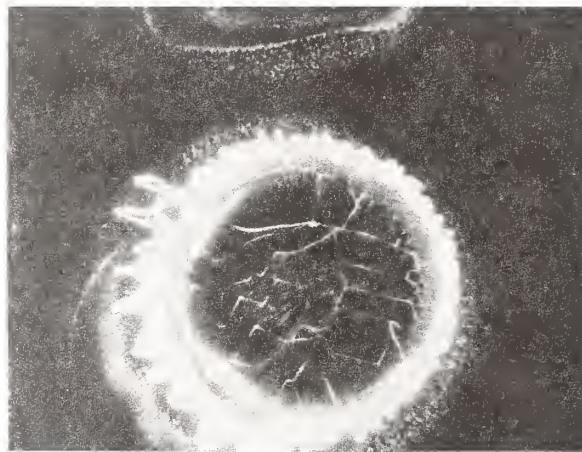


Figure 7c: Central damage spot

Figure 7: prf laser damage morphology in GaAs

Modeling Laser Damage Caused by Platinum
Inclusions in Laser Glass*

John H. Pitts

Lawrence Livermore National Laboratory
P. O. Box 8808, L-480
Livermore, California 94550

A fracture-mechanic theory suggests that crack-propagation rates are proportional to the square root of the inclusion radius and to the three-quarters power of the fluence. The theory does not yet account for pressure loss or convection heat transfer as platinum vapor flows into the crack, and needs to be developed further before accurate propagation rates can be predicted. However, a simple estimate obtained by multiplying the time that the platinum is in the vapor state by the sonic velocity in glass gives a conservative but reasonable result. At fluence levels of 2 J/cm^2 , crack propagation of $4 \text{ }\mu\text{m}$ per shot are predicted.

A crack-development hypothesis, based on shock-wave propagation, successfully predicts the shape of typical damage sites. The sites have an annular crack extending from the equator of the inclusion and planar crack lobes extending from the poles. The lobe at the pole exposed to laser light is larger than the lobe at the unexposed pole.

A numerical heat-transport model predicts temperature profiles in and around a metallic platinum inclusion imbedded in a phosphate laser glass matrix when illuminated with $1\text{-}\mu\text{m}$ laser light. The thermal model predicts that glass damage will occur if the platinum temperature exceeds the boiling point. Predicted fluence-damage limits of 1.4 J/cm^2 for a 1-ns pulse and 4.3 J/cm^2 for a 10-ns pulse agree with experimental data. The damage limit is independent of inclusion size above about $1 \text{ }\mu\text{m}$ in diameter.

Key words: crack propagation rates; damage sites; glass fracture; fluence damage limits; Nova laser; platinum inclusions; thermal modeling.

1. Introduction

Platinum inclusions in neodymium-doped phosphate laser glass on Nova and Novette have been the cause of glass damage when fluence levels greater than about 2 J/cm^2 were reached. Laser light is absorbed by the opaque platinum, causing a thin skin of platinum on the front surface of the inclusion to vaporize. A shock wave propagates through the inclusion and is transmitted to the glass. Glass, being a brittle material, cracks because of the shock wave and the pressure of the vaporized platinum. These cracks propagate until the pressure of the vaporized platinum decreases below that required for further crack propagation.

The phenomena was studied as early as 1970 by Hopper and Uhlmann [1]. They showed photographs of damaged glass and calculated temperatures exceeding $10\,000 \text{ K}$ when fluence levels were 20 J/cm^2 over a 30-ns period. They theorized that very small inclusions were safe because heat losses to the glass kept the temperatures and, hence, stresses within allowable bounds. However, they argued that for sizes above $1000 \text{ }\text{\AA}$ ($0.1 \text{ }\mu\text{m}$), the strength of the glass was exceeded and the glass could fracture. Their thermal modeling suggested that large inclusions were less damaging than intermediate-sized ones (over $1000 \text{ }\text{\AA}$) because the surface-to-volume ratio of the inclusion decreased as the radius increased. Therefore, the larger inclusions had more thermal capacity and hence lower average temperatures and stresses.

Sparks and Duthier [2] also examined the inclusion problem and showed that glass damage was greater with high-intensity, short-pulse lasers than with low-intensity, long-pulse lasers. A number of authors [3-5] have studied heating of a sphere illuminated from one side.

*Work performed under the auspices of the U. S. Department of Energy by the Lawrence Livermore National Laboratory under contract number W-7405-ENG-48.

Their solutions all show that the high temperatures predicted by Hopper and Uhlmann will exist.

We discuss three items in this paper:

- A fracture-mechanics theory suggesting that glass damage will be worse with larger inclusions;
- A hypothesis explaining the shape that typical cracks develop in the glass and that matches many damage sites; and
- Thermal modeling results suggest a fluence threshold of 1.4 J/cm^2 for a 1-ns pulse or 4.3 J/cm^2 for a 10-ns pulse in phosphate glass. This threshold is independent of inclusion size above about $1 \text{ }\mu\text{m}$ in diameter. The thermal modeling results compare favorably with experimental data.

2. Fracture-Mechanics Theory

Consider glass to be a brittle material initially with a penny-shaped crack that is the diameter of the platinum inclusion. The criterion for crack propagation is based on a material property, K_I , called the fracture-toughness (stress-intensity) factor [6]

$$K_I = \sigma \sqrt{\pi a} \quad (1)$$

where

$K_I \equiv$ material fracture toughness ($\text{Pa } \sqrt{\text{m}}$)

$\sigma \equiv$ applied stress (or pressure), Pa

$a \equiv$ crack radius (which we take initially equal to the inclusion radius), m.

If the value of K_I exceeds a critical value, then the crack will propagate. This critical value termed the critical-fracture-toughness or critical-stress-intensity factor, K_{IC} , is a material property, the magnitude of which is normally obtained experimentally.

The Mie-Grüneisen equation of state [7,8] is applicable for shock-wave/high-stress values, where energy is deposited isochorically; it relates stress and specific energy as

$$\sigma = \Gamma \rho e \quad (2)$$

where

$\Gamma \equiv$ Grüneisen constant (dimensionless)

$\rho \equiv$ density (Kg/m^3)

$e \equiv$ specific energy deposition above that required for vaporization (J/Kg).

Following Hopper and Uhlmann's article [1] for an inclusion with finite thermal diffusivity and a 10-J/cm^2 , 1-ns pulse, we have a spatial temperature distribution using their material properties (see their Eqs. (6) and (7b)).

$$\begin{aligned}
\frac{T_1 \text{ ns}}{10 \text{ J/cm}^2} &\approx 4 \times 10^4 \cdot \left(\frac{1 \text{ ns}}{30 \text{ ns}}\right)^{1/2} \cdot \left(\frac{10 \text{ J/cm}^2}{0.7 \text{ J/cm}^2}\right) \\
&\cdot \text{ierfc} \left(\frac{0.6 z}{(1 \text{ ns}/30 \text{ ns})^{1/2}} \right) \\
&\approx 1 \times 10^5 \text{ ierfc} (3.286 z) \quad . \quad (3)
\end{aligned}$$

Here z is the distance into the inclusion from the surface in μm , and T is temperature in K. Values of ierfc , the integral of the complementary error function, are tabulated by Abramovitch and Stegun [9]. The surface temperature drops below the vaporization temperature (4800 K) at $z = 0.307 \mu\text{m}$. If we double the fluence to 20 J/cm^2 , the temperature drops below the vaporization temperature at $z = 0.371 \mu\text{m}$. If we use these values to calculate the power dependence of the fluence, J , on the specific energy deposition (recalling that specific energy deposition is approximately proportional to temperature)

$$\begin{aligned}
\left(\frac{J}{J_0}\right)^m &= \frac{\rho_e}{\rho_{e0}} \approx \frac{T}{T_0} \quad (4) \\
\left(\frac{20 \text{ J/cm}^2}{10 \text{ J/cm}^2}\right)^m &= \frac{20 \text{ J/cm}^2 / 0.371 \mu\text{m}}{10 \text{ J/cm}^2 / 0.307 \mu\text{m}} \\
m &= 3/4 \quad .
\end{aligned}$$

Combining this result with equations (1) and (2) we have

$$K_1 \sim J^{3/4} a^{1/2} \quad . \quad (5)$$

The crack will propagate as long as $K_1 > K_{1C}$. Hence, this model suggests that the extent of crack propagation in the glass per shot is proportional to the square root of the crack radius and the three-quarters power of the fluence. Initially, the crack radius is equal to that of the inclusion but it would increase after each shot. Hence, at constant fluence, the rate of crack propagation would increase after each shot.

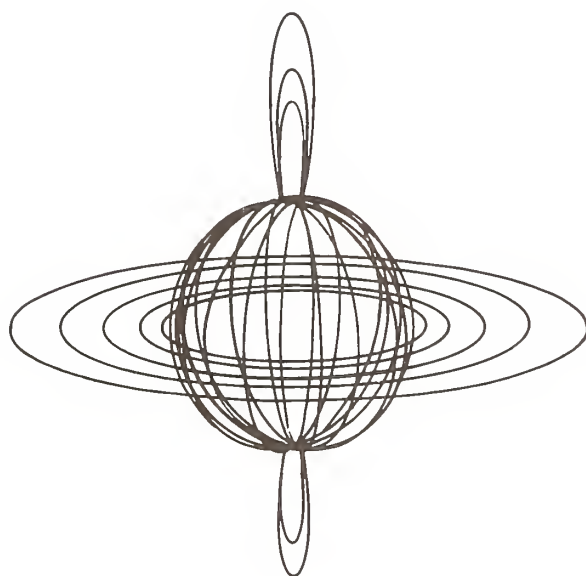
The model does not account for loss of pressure or convection heat transfer as the vaporized platinum flows into the crack, both of which counteract the effect of increasing crack propagation rate in later shots by making it harder to propagate a large crack. Both effects oppose the square root dependence of the crack radius, and could partially account for some experimental data [10,11,12,13], where the amount of crack propagation first increases and then decreases; or alternately propagates and then stops. Another reason cracks could stop propagating in later shots is that all the platinum initially in the inclusion has been deposited in the crack area with a thickness that is now transparent to laser light. Regardless, this model suggests that the larger the inclusion, the worse the damage.

Additional development of this fracture-mechanics theory could lead to a better prediction of how far a crack would propagate during a particular shot. In order to proceed further, we may need to estimate the thickness (width) of a typical crack so that we can calculate the pressure distribution in the crack as a function of time. Further, we may need to account for the change in opacity below unity of platinum deposited in the crack region if the platinum thickness is in the 100-Å, or less, range.

3. Crack-Development Hypothesis

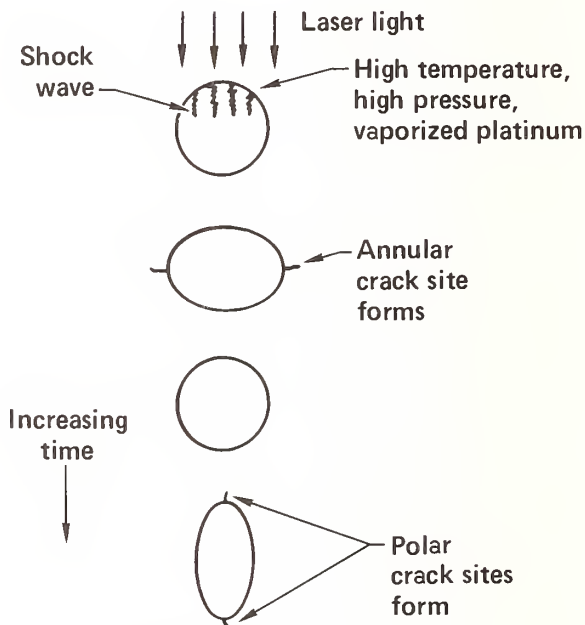
Many damage sites have an annular crack around the equator of the inclusion with an additional planar lobe-shaped crack at each pole [13,14] (see Fig. 1a). The crack at the pole, facing the laser light illumination, is always larger than the crack at the pole hidden from the laser light illumination by the inclusion itself.

During discussions with Hovingh [15], he suggested the phenomena was a result of shock propagation. As energy from laser light is deposited on the surface of the inclusion, a shock wave is developed that propagates through the inclusion (see Fig. 1b), which deforms to an oval shape, putting pressure at the sides of the inclusion. This initiates an annular crack site at the equator. The pressure over the annulus is uniform because of symmetry and a completely symmetric annular crack site is formed.



Typical geometry of many fracture sites

Figure 1a



Deflection of an inclusion with time

Figure 1b

Figure 1. Sketch of a typical damage site and a shock propagation analogy of why this geometry occurs.

It has been asked how pressure can cause a crack site because the pressure forces are compressive. The pressure is applied not only perpendicular to the incoming laser light, but also parallel to it, thereby tending to spread the glass material in tension parallel to the incoming laser light. A similar phenomenon occurs in the walls of a spherical pressure vessel, where the hoop stress is tension and yet there is pressure exerted on the inside wall surface. Further, any compression generated at the crack site changes to tension as the shock passes through the glass material itself.

The shock continues through the inclusion, dissipating energy and becoming weaker with time. The inclusion returns to a circular shape, but then deforms to an oval shape with a major axis parallel (rather than perpendicular) to the direction of the incoming laser light. However, the oval formed has a much more concentrated deformation at the poles because of the concentration of energy deposition there. Crack sites are initiated at the poles only and not as a complete annulus.

An analogy to this type of deformation occurs when a golfer hits a good drive. The golf ball has energy deposited at the surface, deforms to an oval with major axis perpendicular to the direction of the golfer's swing. During flight, the golf ball returns to circular shape and then deforms to an oval with the major axis parallel to the direction of the golfer's swing.

This crack-development hypothesis explains why the form of many crack sites are as shown in Figure 1a. The hypothesis suggests the location of crack initiation sites. However, it is the vaporized platinum and its associated pressure that actually propagate the cracks beyond the initial site. Because the platinum vapor must flow further to reach the crack site at the pole hidden from the laser light, pressure developed there is less than at the opposite pole crack site. Hence, a smaller crack should develop at the hidden pole than at the exposed pole. This is verified in observed glass damage sites.

4. Thermal Modeling

Our thermal model was a half-sphere of platinum surrounded by a half-spherical annulus of glass as shown in Figure 2a. The model represents what could be a typical inclusion, shown in Figure 2b. Vaporization of the platinum is concentrated at the top of the inclusion, which in both cases is normal to the incident laser light. Hence, the spherical model is a good approximation to the more generally shaped inclusion of Figure 2b. We use just a half-sphere in the model because of symmetry. In the model, laser light was absorbed on the upper surface of the platinum sphere with a cosine distribution used to account for the curvature of the surface.

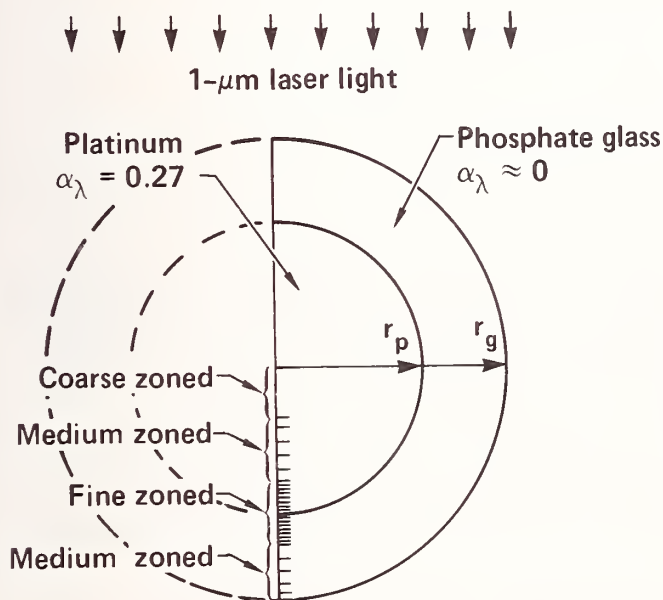


Figure 2a

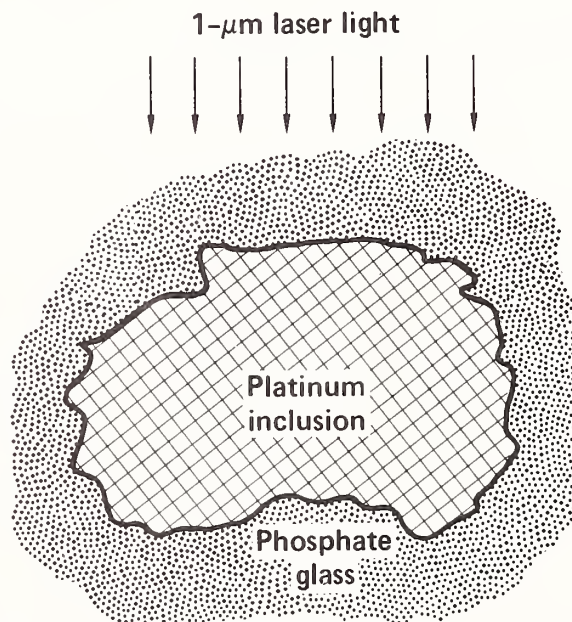


Figure 2b

Figure 2. Hemispherical model of a platinum inclusion in glass illuminated from the top with laser light, and what could be a typical non-spherical inclusion

Thermal properties used in the model for platinum and glass are shown in table 1. Platinum properties were obtained from Touloukian, et. al., [16] and Hampel [17]. The boiling point shown in Table 1 is higher than in some other references (e.g., Weast [18] shows 4100 K) but is used for consistency with other properties taken from Hampel [17]. The key platinum properties are the heat of vaporization and the normal spectral absorptance, so that the difference in the documented boiling point has an insignificant effect. The normal spectral absorptance shown is at room temperature. The absorptance does change with temperature, but it is more a function of the surface itself. Changes of an order of magnitude are feasible depending on whether the

Table 1. Thermal Properties of Materials Used in the Analysis

	Platinum inclusion	LHG-8 phosphate glass
Density, kg/m ³	21,400	2,850
Specific heat, J/kg K	146	263
Thermal conductivity, W/m K	80	0.52
Melting point, K	2,040	---
Heat of fusion, J/kg	101,000	---
Boiling point, K	4,800	---
Heat of vaporization, J/kg	2,260,000	---
Normal spectral absorptance at 1 μ m	0.27	---

surface is polished or not and if the surface is oxidized. We used the room temperature value because no elevated temperature values were available. The equation of state for platinum above the boiling point was that used in the LASNEX Code [19]. Properties of glass were obtained from Stokowski, Saroyan, and Weber [20] for LHG-8 phosphate glass. The surface of the platinum was allowed to radiate to a 300-K surrounding. No absorption was permitted in the glass, but heat was conducted between the glass and the platinum with negligible contact resistance.

Modeling was performed using Shapiro's TOPAZ [21] code with Halquist's MAZE [22] and ORION [23] codes used for preparing the input and processing the output. TOPAZ is a heat conduction code, which is applicable to this problem because inclusion sizes are so small that natural convection is negligible. Problems were run on the CRAY computer with an average run time of about 30 minutes each.

Results are shown in Figure 3 where the fluence damage threshold is plotted against laser pulse length. Comparison with experimental data is excellent. Avizonis and Farrington [24] and Yamanaka [25] included error bars, which are also shown. The theory developed in this paper is the solid line, which has a slope of 1/2 corresponding to a square root dependence on laser pulse length. The slight departure of the theory from the data of Gonzales and Milam [26] at short laser pulse lengths may result from the crack propagation per shot being so small in this region. Hence, it takes a number of shots before any damage can be physically observed.

Temperature profiles at two different times are shown in Figure 4. Peak temperatures are high (electron volt range; 1 ev \approx 10 000 K) and so are the resulting pressures of the vaporized platinum. Note that the temperature contours are all concentrated in the platinum at the exposed surface. There is no change in the temperature profiles when the size of the inclusion is changed above about 1 μ m because the thin layer where the profiles are located is similar to a planar surface. Hence, results are independent of inclusion size above about 1 μ m in diameter. Table 2 lists maximum temperatures, maximum pressures, and the resulting crack propagation per shot for various fluences. The maximum pressures were calculated using eq. (2). We used a Grüneisen constant, Γ , equal to unity; and a value of ρ_e calculated from the TOPAZ results at the time of the peak temperature by dividing the total energy in the vaporized platinum at the exposed pole by the volume of the vaporized platinum.

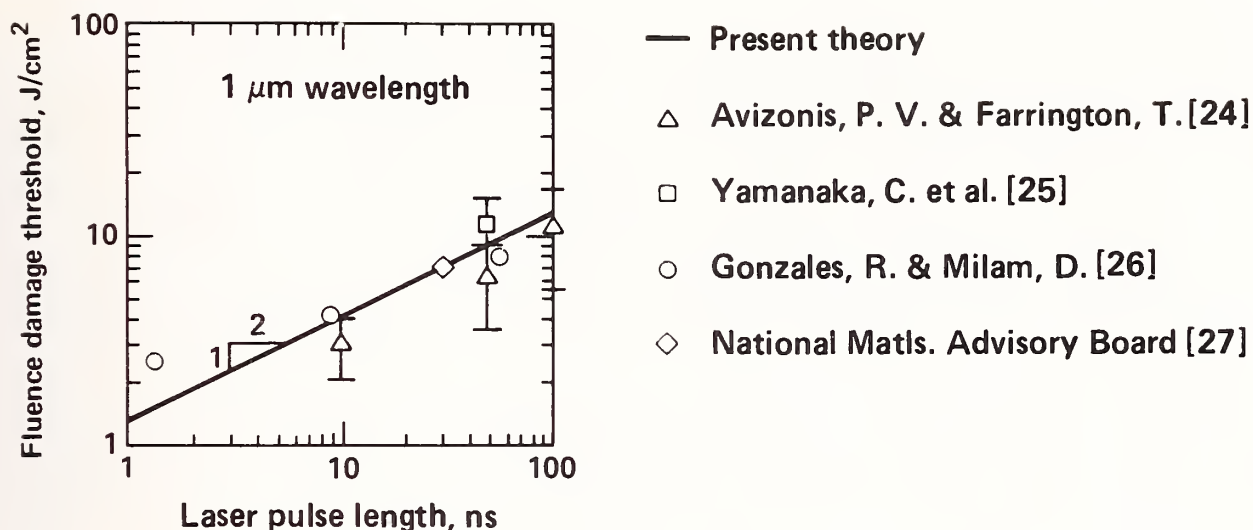


Figure 3. Effect of laser pulse length on the fluence damage threshold. Theoretical results are independent of inclusion size above about $1 \mu\text{m}$ in diameter and are in excellent agreement with experimental data.

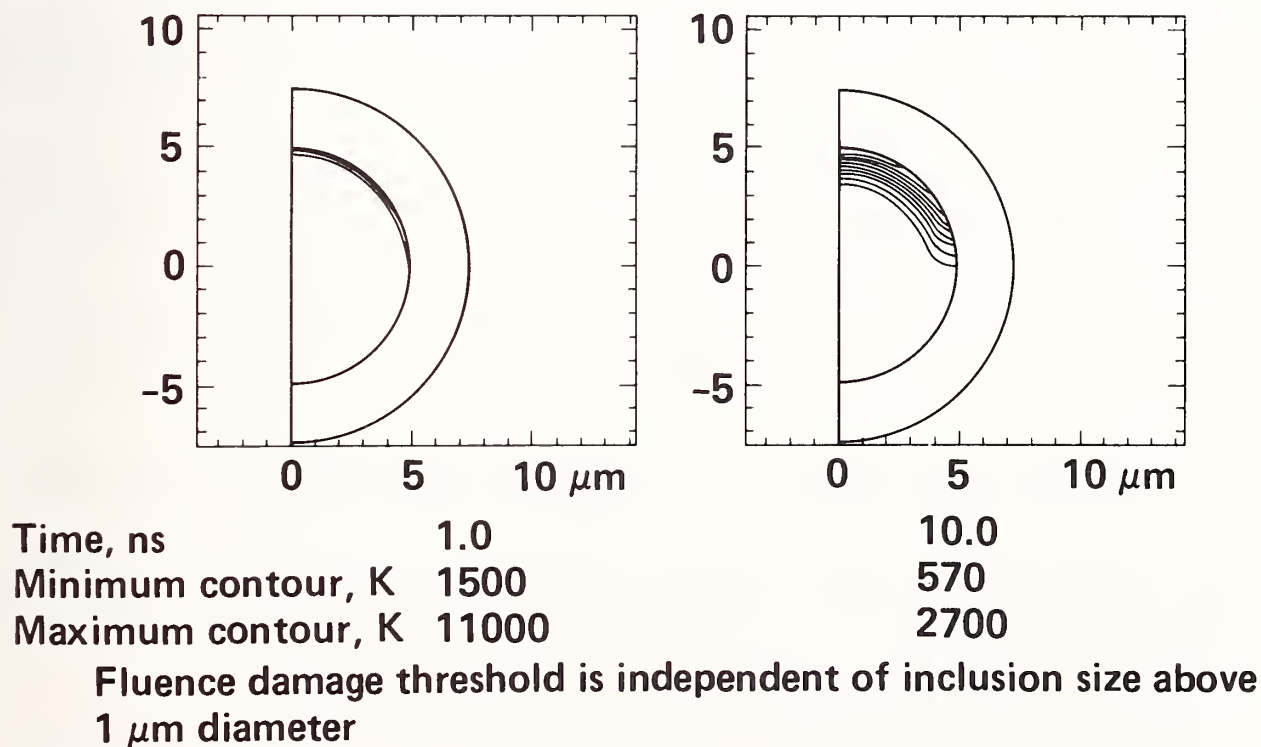


Figure 4. Temperature contours for a $5\text{-}\mu\text{m}$ -radius platinum inclusion surrounded by phosphate glass, and illuminated by $1\text{-}\mu\text{m}$ laser light at an incident fluence of $3.7 \text{ J}/\text{cm}^2$.

Table 2. Calculated Characteristics of Crack Propagation

Incident Fluence (J/cm ²)	Absorbed Fluence (J/cm ²)	Pulse Time (ns)	Maximum Temperature (K)	Maximum Pressure (Pa)	Crack Propagation Per Shot (μm)
37	10	1	1.3×10^5	2.8×10^{11}	500
18	5	1	7.6×10^4	1.5×10^{11}	150
3.7	1	1	1.5×10^4	0.5×10^{11}	8.4
1.8	0.5	1	6.5×10^3	$<0.5 \times 10^{11}$	3.5
1.5	0.4	1	5.3×10^3	$<0.5 \times 10^{11}$	1.5
3.7	1	10	4.5×10^3	-----	----

Fluence damage threshold is 1.4 J/cm² for a 1-ns laser pulse length

We have no doubt that the pressures are high enough to propagate a crack. In conjunction with experimental results [10-14], this suggests that damage will occur if the temperature of the platinum exceeds its boiling point. Experimental data (see Fig. 3) suggests a damage limit of about 2 J/cm² for a 1-ns pulse and 5 J/cm² for a 10-ns pulse. This is in agreement with the calculated values.

The fracture-mechanics theory is not developed enough to predict crack growth. However, crack growth can be conservatively estimated by multiplying the time during which platinum is in a vaporized state by the sound speed in glass. Values of crack growth for fluences close to those of available experiments are reasonable (see Table 2).

The key conclusion of this thermal analysis is that damage will occur if the platinum temperature exceeds the boiling point. Damage is independent of inclusion size (above about 1 μm) and is worse for shorter-duration laser pulses.

5. Conclusions

- Fracture-mechanics theory suggests that crack propagation rates are proportional to the square root of the inclusion radius and the 3/4 power of the fluence. Larger inclusions above about 1 μm in diameter are worse than smaller inclusions.

- A crack-development hypothesis based on shock propagation successfully predicts the shape of many fracture sites. The shape is that of an annular crack around the inclusion equator with planar lobes at the poles. The lobe at the pole exposed to laser light is larger than the lobe at the unexposed pole.

- Thermal modeling predicts that glass damage will occur if the platinum vaporizes and that the fluence damage threshold is both proportional to the square root of the laser pulse length and independent of the inclusion size above about 1 μm in diameter. Predicted fluence damage limits of 1.4 J/cm² for a 1-ns pulse and 4.3 J/cm² for a 10-ns pulse agree with experimental data.

6. Acknowledgement

Besides those people listed in the references, I would like to extend my appreciation to J. H. Campbell at the Lawrence Livermore National Laboratory who directed this effort and reviewed the results.

7. References

- [1] Hopper, R. W. and Uhlmann, D. R., "Mechanism of Inclusion Damage in Laser Glass", Journal of Applied Physics, Vol. 41, No. 10, Sept. 1970, pp. 4023-4037.
- [2] Sparks, M. and Duthier, C. J., "Theory of Infrared Absorption and Material Failure in Crystals Containing Inclusions," Journal of Applied Physics, Vol. 44, No. 7, July 1973, pp. 3038-3045.
- [3] Cheung, J. B., Chen, T. S., and Thirumalai, K., "Transient Thermal Stresses in a Sphere by Local Heating", Journal of Applied Mechanics, Vol. 41, Dec., 1974, pp. 930-934.
- [4] Werley, K. A. and Gilligan, J. G., "The Temperature Distribution of a Sphere Placed in a Directed Uniform Heat Flux", Journal of Heat Transfer, Vol. 103, May 1981, pp. 399-401.
- [5] Duffy, D., "The Temperature Distribution within a Sphere Placed in a Directed Uniform Heat Flux and Allowed to Radiatively Cool", Journal of Heat Transfer, Vol. 107, February 1985, pp. 28-32.
- [6] Rolfe, S. T. and Barsom, J. M., "Fracture and Fatigue Control in Structures - Applications of Fracture Mechanics", Prentice-Hall, Englewood Cliffs, New Jersey, 1977, p. 15ff.
- [7] Baaken, L. H. and Anderson, P. D., "An Equation of State Handbook", Sandia Laboratories, Livermore, Calif., Report SCL-DR-66-123, January 1969, p. 25.
- [8] Zel'dovitch, Ya. B. and Raiser, Yu. P., "Physics of Shock Waves and High-Temperature Hydrodynamic Phenomena", Academic Press, New York, 1967, p. 697ff, and specifically Eq. 11.13.
- [9] Abramovitch, M. and Stegun, I. A., "Handbook of Mathematical Functions," Dover, New York, 1965, p. 317.
- [10] Milam, D. and Gonzales, R., "Damage Tests of Inclusions in a 20.8-cm Disk Taken from Novette", Lawrence Livermore National Laboratory, Livermore, Calif., Internal Memorandum LDG85-34/4080D, April 16, 1985.
- [11] Milam, D. and Gonzales, R., "Additional Tests of Platinum Inclusions," Lawrence Livermore National Laboratory, Livermore, Calif., Internal Memorandum LDG85-56/4667T, July 8, 1985.
- [12] Hatcher, C. W. and Milam, D., "Status of Nova-Hoya Glass Damage Tests," Lawrence Livermore National Laboratory, Livermore, Calif., Internal Memorandum TF85-246, July 23, 1985.
- [13] Milam, D. and Hatcher, C. W., Private communication, Lawrence Livermore National Laboratory, Livermore, Calif., June and July 1985.
- [14] Hopper, R. W., Private communication, Lawrence Livermore National Laboratory, Livermore, Calif., June 1985.
- [15] Hovingh, J., Private communication, Lawrence Livermore National Laboratory, Livermore, Calif., July 1985.
- [16] Touloukian, Y. S. et. al., "Thermophysical Properties of Matter - Thermal Radiative Properties, Metallic Elements and Alloys," IFI/Plemem, Press, New York, 1970.
- [17] Hampel, C. A., "Rare Metals Handbook" Reinhold, 1961, p 319-320.

- [18] Weast, R. C., "CRC Handbook of Chemistry and Physics" CRC Press, Cleveland, Ohio, 65th Edition, 1984.
- [19] Orth, C., Lawrence Livermore National Laboratory, Livermore, Calif., Private communication, July 1985.
- [20] Stokowski, E. E., Saroyan, R. A. and Weber, M. J., "ND-Doped Laser Glass Spectroscopic and Physical Properties," Lawrence Livermore National Laboratory, Livermore, Calif., M-95, Rev. 2, Nov. 1981, Glass #5094.
- [21] Shapiro, A. B., "TOPAZ - A Finite Element Heat Conduction Code for Analyzing 2-D Solids," Lawrence Livermore National Laboratory, Livermore, Calif., UCID 20045, March 1984.
- [22] Hallquist, J. O., "MAZE - A Input Generator for DYNA2D and NIKE2D," Lawrence Livermore National Laboratory, Livermore, Calif., UCID 19029, Rev. 2, June 1983.
- [23] Hallquist, J. O., "ORION: An Interactive Post-Processor for the Analysis Codes NIKE2D, DYNA2D and TACO2D," Lawrence Livermore National Laboratory, Livermore, Calif., UCID 19310, Jan. 1982.
- [24] Avizonis, P. V. and Farrington, T., "Internal Self-Damage of Ruby and Nd-Glass Lasers", Appl. Phys. Ltrs. 7, 1965.
- [25] Yamanaka, C. et. al., "Investigation of Damage in Laser Glass" NBS Special Publication 356, 1971.
- [26] Gonzales, R. P. and Milam, D. "Evolution During Multiple-Shot Irradiation of Damage Surrounding Isolated Platinum Inclusions in Phosphate Laser Glasses" 17th Annual Symposium on Optical Materials for High Power Lasers, Boulder, Colorado, October 28-30, 1985.
- [27] National Materials Advisory Board, "Fundamentals of Damage in Laser Glass". Publication NMAB-271, 1970.

- Manuscript Not Received -
=====

CO₂ LASER-INDUCED AIR BREAKDOWN
NEAR METAL MIRROR SURFACES

Vitaly Konov
Institute of General Physics
Moscow, USSR

Key Words: air breakdown; CO₂ laser; laser-induced damage;
metal mirrors.

BOULDER DAMAGE SYMPOSIUM
Attendees
October 28-30, 1985

Joseph Abate
Hampshire Instruments, Inc.
P.O. Box 10159
250 East River Road
Rochester, NY 14610
(716) 482-4070

Byong H. Ahn
NV & EOL USA CECOM
DELNV-L
Ft. Belvoir, VA 22060-5677
(703) 664-5364

Jonathan W. Arenberg
Hughes Aircraft Co.
P.O. Box 902
Bldg. Ea M/SD126
El Segundo, CA 90245
(213) 616-3090

Tsuyoshi Asaeda
Canon U.S.A.
3191 Red Hill Ave.
Costa Mesa, CA 92626
(714) 556-1036

Bernard Bendow
The BDM Corporation
1801 Randolph Road, SE
Albuquerque, NM 87106
(505) 848-5129

Ralph R. Berggren
Los Alamos National Laboratory
Los Alamos, NM 87545
(505) 667-0593

V. Warren Bircik
Northrop Research & Tech. Center
One Research Park
Palos Verdes Peninsula, CA 90274
(213) 544-5306

James Boyer
Los Alamos National Laboratory
MS J566
P.O. Box 1663
Los Alamos, NM 87544
(505) 667-0041/9222

M. A. Acharekar
Litton Laser Systems
P.O. Box 7300
Orlando, FL 32854-7300
(305) 297-4450

Philip C. Archibald
Naval Weapons Center
Code 3818
China Lake, CA 93555

Paul Arendt
Los Alamos National Laboratory
P.O. Box 1663
MS E-549
Los Alamos, NM 87545
(505) 667-7851

Michael F. Becker
University of Texas at Austin
Electrical Engineering Dept.
133 Engineering Science Bldg.
Austin, TX 78712
(512) 471-3628

Harold E. Bennett
Michelson Laboratory
Naval Weapons Center
Code 38101
China Lake, CA 93555
(714) 939-2869

Jerry Ray Bettis
Rockwell International
Rocketdyne Division
Dept. 631-111 FB33
6633 Canoga Avenue
Canoga Park, CA 91304
(818) 700-6166

Lynn Bonsall
Rockwell International
Rocketdyne Division
6633 Canoga Avenue
Canoga Park, CA 91304
(818) 700-4848

Ernie Braunschweig
RDA
ATO 9377
Albuquerque, NM 87119
(505) 844-8446

Morris Braunstein
Laser Power Corp.
11211 Sorrento Valley Road
San Diego, CA 92121-1325
(619) 455-0751

Dennis Burge
Naval Weapons Center
Code 3816
China Lake, CA 93555
(619) 939-1427

John H. Campbell
Lawrence Livermore National Lab
P.O. Box 5508 L-482
Livermore, CA 94550
(415) 422-6497

Susan D. Carson
BDM Corporation
1801 Randolph Road
Albuquerque, NM 87106
(505) 848-5696

Kathleen A. Cerqua
Laboratory for Laser Energetics
University of Rochester
250 East River Road
Rochester, NY 14623
(716) 275-5101

Jay S. Chivian
LTV Aerospace & Defense Co.
Vought Missiles & Adv. Prog. Div.
P.O. Box 650003
MS TH-67
Dallas, TX 75265-0003
(214) 266-7808

John G. Daly
Litton Laser Systems
P.O. Box 7300
Orlando, FL 32954
(305) 297-4457

Hulya Demiryont
Colorado State Univ.
Physics Dept.
Fort Collins, CO 80523
(303) 491-8452

Dana D. Dlott
School of Chemical Sciences
Noyes Laboratory, Box 37
505 S. Mathews Ave.
Urbana, IL 61801
(217) 333-3574

Robert Brown
Los Alamos National Lab
P.O. Box 1663
Group MP-7, MS H840
Los Alamos, NM 87545
(505) 667-5515

Larry W. Burggraf
AF Office of Scientific Research
AFOSR-NC
Bolling AFB
Washington, DC 20332-6448
(202) 767-4960

Charles K. Carniglia
Martin Marietta Aerospace
P.O. Box 9316
International Airport
Albuquerque, NM 87119
(505) 844-1064

Carlos Casteleiro
Kaman Instruments
1500 Garden of the Gods Road
Colorado Springs, CO 80933
(303) 599-1916

Lloyd L. Chase
Lawrence Livermore National Lab
MS/L-490
P.O. Box 808
Livermore, CA 94550
(415) 422-6270

Don A. Dalton
U.T.R.C.
5301 Central Ave.
Suite 1617
Albuquerque, NM 87111
(505) 266-5828

Donald L. Decker
Code 3816
Naval Weapons Center
China Lake, CA 93555
(619) 939-3247

John A. Detrio
University of Dayton
Research Institute
300 College Avenue
Dayton, OH 45469
(513) 229-3453

Hermann J. Donnert
Kansas State University &
Frank J. Seiler Research Lab.
Ward Hall
Manhattan, KS 66505-7-39
(913) 532-5960

Richard W. Dyer
W. J. Schafer Associates, Inc.
Corporate Place 128
Bldg. 2, Suite 300
Wakefield, MA 01880-1268
(617) 246-0450

David F. Edwards
Lawrence Livermore National Labs.
L-332
Livermore, CA 94550
(415) 422-0747

Alexander Epifanov
Institute of General Physics
Acad. Sc. USSR
Vasilov Str. 38
Moscow
USSR

Ron C. Estler
Fort Lewis College
Durango, CO 81301
(303) 247-7238

Gregory J. Exarhos
Pacific Northwest Laboratory
P.O. Box 999
Richland, WA 99352
(509) 375-2440

Philip M. Fauchet
Princeton University
Dept. of Electrical Engineering
and Computer Science
Princeton, NJ 08544

Albert Feldman
National Bureau of Standards
A257 Materials Bldg.
Gaithersburg, MD 20899
(301) 921-2899

Joseph F. Figueira
Los Alamos National Laboratory
P.O. Box 1663
Los Alamos, NM 87545
(505) 667-6448

Diane M. Fischer
USAF
AFWL/ARAO
Kirtland AFB, NM 87117
(505) 844-1276

Stephen R. Foltyn
Los Alamos National Laboratory
MS-J 566, CHM-5
P.O. Box 1663
Los Alamos, NM 87545
(505) 667-1123

Alan M. Frank
Lawrence Livermore National Lab
Box 808, L-35
Livermore, CA 94550
(415) 422-7271

Donald M. Friedrich
Battelle-Pacific Northwest Labs.
Richland, WA 99352
(509) 375-2440

David Gallant
Rocketdyne Div.
Rockwell International
P.O. Box 5670 KAFB
Albuquerque, NM 87185
(505) 844-5595

Gerald A. Gallegos
Los Alamos National Laboratory
MS J566
P.O. Box 1663
Los Alamos, NM 87545
(505) 667-6448

Ann Genco
Hughes Aircraft
P.O. Box 902 Bldg E4
MS/M133
El Segundo, CA 90245
(213) 616-9182

Adolf Giesen
DFVLR, Institute fur Tech. Physik
Pfaffenwaldring 38-40
7000 Stuttgart 80
FED. REP. OF GERMANY
0711-6862-223

Dennis H. Gill
Los Alamos National Laboratory
Chem. Div. J563
P.O. Box 1663
Los Alamos, NM 87544
(505) 667-8680

Ray Gonzales
Lawrence Livermore National Lab
P.O. Box 5508, L-490
Livermore, CA 94550
(415) 422-6059

George A. Graves
University of Dayton
RM 165 Kettering Labs.
300 College Park
Dayton, OH 45469
(513) 229-4415

Arthur H. Guenther
AFWL/CCN
Kirtland AFB, NM 87117
(505) 844-9856

Gerald A. Gurtman
S-CUBED, Div. of Maxwell Labs, Inc.
P.O. Box 1620
La Jolla, CA 92038-1620
(619) 453-0060 Ext 443

Robert E. Hahn
Optical Coating Laboratory, Inc.
2789 Northpoint Parkway
Santa Rosa, CA 95401-7397
(707) 525-7791

William Hatcher
Lawrence Livermore National Lab
P.O. Box 5508, L-482
Livermore, CA 94550
(415) 422-4375

R. B. Hemphill
LTV Aerospace & Defense Co.
P.O. Box 650003
MS/TH-67
Dallas, TX 75265-0003
(214) 266-7105

Lowell M. Hobrock
Hughes Aircraft Company
2000 E. El Segundo Blvd.
P.O. Box 902
El Segundo, CA 90245
(213) 616-9620

Lonnie Holder
McDonnell Douglas Astronautics Co.
MS-E804/101A/2/230
P.O. Box 516
St. Louis, MO 63166
(314) 234-8436

Alan K. Hopkins
AFWAL/Materials Lab.
Wright-Patterson AFB, OH 45459

George Greiner
Lawrence Livermore National Lab
P.O. Box 5508, L-474
Livermore, CA 94550

Shekhar Guha
Martin Marietta Laboratories
1450 South Rolling Road
Baltimore, MD 21227
(301) 247-0700

Richard F. Haglund, Jr.
Vanderbilt University
Department of Physics & Astronomy
Nashville, TN 37235
(615) 322-2828

Donald J. Harter
Allied Corporation
7 Powderhorn Dr.
Mt. Bethel, NJ 07060
(201) 560-1750

Allan Heiney
Allied Corporation
7 Powderhorn Drive
Mt. Bethel, NJ 07060
(201) 560-1750

Robert L. Hengehold
Air Force Inst. of Technology
Wright-Patterson AFB, OH
(513) 255-2012

Sandra L. Holder
Department of the Navy
Naval Sea Systems Command (PMS-405)
CM2 Room 113
Washington, DC 20362-5101
(202) 692-8641

Samuel J. Holmes
Northrop Research & Technology Center
One Research Park
Palos Verdes Peninsula, CA 90274
(213) 544-5314

Long-Sheng Hsu
Central Laser Corporation
11222 Astronaut Blvd.
Orlando, FL 32819
(305) 851-2540

Austin C. Huang
Electrical & Computer Eng. Dept.
University of Texas at Austin
Austin, TX 78712
(512) 471-3628

Marshall N. Huberman
TRW, Bldg. 01, Room 1051
One Space Park
Redondo Beach, CA 90278
(213) 536-4413

Mark Imus
Optical Coating Laboratory, Inc.
2789 Northpoint Parkway
Santa Rosa, CA 95401-7397
(707) 525-7742

Takao Izawa
Showa Optical Co., LTD
5-3 Shinmachi, 3-Chome
Setagaya-Ko
Tokyo 154
JAPAN
03-429-4131

Stephen D. Jacobs
Laboratory for Laser Energetics
University of Rochester
250 East River Road
Rochester, NY 14623
(716) 275-5101

Yong Jee
Electrical & Computer Eng. Dept.
University of Texas at Austin
Austin, TX 778712
(512) 471-3628

Linda Johnson
Naval Weapons Center
Physics Division, Code 3818
China Lake, CA 93555
(619) 939-1422

George T. Johnston
Optical Coating Laboratory, Inc.
2789 Northpoint Parkway
Santa Rosa, CA 95401-7397
(707) 525-7148

L. John Jolin
Los Alamos National Laboratory
P.O. Box 1663
CHM-5 MS-J566
Los Alamos, NM 87544
(505) 667-7314/2151

Michael P. Joseph
Dynavac Corporation
30 Woodrock Road
Weymouth, MO 02189
(617) 337-4111

Kenneth Jungling
Univ. of New Mexico, EECE
Albuquerque, NM 87131
(505) 277-3317

Doug Jungwirth
Northrop Electronics Div.
2301 West 120th Street
Hawthorne, CA 90250
(213) 606-6744

Austin Kalb
Rockwell International
3370 Miraloma Ave.
MS/GE 14
Anaheim CA 92803/4921
(415) 632-6008

Marvin M. Kaplan
Litton Laser Systems
P.O. Box 7300
Orlando, FL 32854
(301) 297-4528

John A. Kardach
U.S. Air Force
AFWL/CA
Kirtland AFB, NM 87109
(505) 844-7368

Kenneth Kawabata
Hughes Aircraft
P.O. Box 902 E1-F185
E1 Segundo, CA 90245

Geza L. Keller
Los Alamos National Laboratory
M/S E523
P.O. Box 1663
Los Alamos, NM 87545
(505) 667-1537

Wayne D. Kimura
Spectra Technology
2755 Northup Way
Bellevue, WA 98004-1495
(206) 827-3517

Tim F. Kish
Laser Power Optics
11211 Sorrento Valley Road
San Diego, CA 92121
(619) 455-0751

Christopher Klein
The Aerospace Corporation
MY 980,
P. O. Box 92957
Los Angeles, CA 90009
(213) 648-6226

William Koldewyn
Scientech, Inc.
5649 Arapahoe
Boulder, CO 80303
(303) 444-1361

Vitaliy Konov
Institute of General Physics
Acad. Sc. USSR
Vasilov Street 38
Moscow
USSR

Paul Korbin
Rockwell International
1049 Camino Dos Rios
Thousand Oaks, CA 91360
(805) 373-4485

Nessim Lagnado
Hughes Santa Barbara Research Cent.
75 Coromar Drive
Goleta, CA 93117
(805) 968-3511 Ext 2615

Ian Laidler
Loughborough University of Technology
Physics Department
Loughborough
Leicestershire, LE11 3TU
ENGLAND
(0509) 2663171 Ext 5044

Ramin Lalezari
PMS Electro Optics
1855 S. 57th Ct.
Boulder, CO 80301
(303) 443-7100

Michael R. Lange
University of New Mexico
Inst. for Modern Optics
Albuquerque, NM 87131

Joseph R. Latore
Airtron Div. of Litton Systems Inc.
200 E. Hanover Avenue
Morris Plains, NJ 07950
(201) 539-5500

G. David Lawrence
Hughes Aircraft
211 Yacht Club Way #221
Redondo Beach, CA 90277
(213) 616-6237

Paul S. Laybourne
W. J. Schafer Associates, Inc.
1600 Randolph Ct.
Albuquerque, NM 87106

William A. Leamon
Los Alamos National Laboratory
P.O. Box 1663
Los Alamos, NM 87545
(505) 667-7314

Donald H. Leeds
Hughes Aircraft
P.O. Box 902
El Segundo, CA 90245
(213) 616-7695

Thomas A. Leonard
Analytic Decisions Inc.
337 N. Broad Street
Fairborn, OH 45324
(513) 879-4571

Daniel H. Leslie
W.J. Schafer Associates
1901 N. Fort Myer Dr.
Arlington, VA 22209
(703) 558-7900

Keith L. Lewis
Royal Signals & Radar
Establishment
St. Andrews Rd.
Malvern, Worcs. WR14 3PS
UNITED KINGDOM
(06845) 2733 Ext 3062

Hui H. Li
CINDAS
Purdue University
2595 Yeager Rd.
West Lafayette, IN 47906
(317) 494-6300

Bangjun Liao
New York State Center for Advanced
Optical Technology
University of Rochester
Institute of Optics, Wilmot Bldg.
Rochester, NY 14627

Jacques F. Linder
Hughes Aircraft Co.
2000 E. El Segundo Blvd.
El Segundo, CA 90274
(213) 616-6173

Bo Ljung
Singer-Kearfott Div.
1225 McBride Ave.
Little Falls, NJ 07474
(201) 785-2761

Tony Lowderback
Ojai Research Corporation
11554 Ventura Ave.
Ojai, CA 93023

W. Howard Lowdermilk
Lawrence Livermore National Lab
P.O. Box 5508, L-490
Livermore, CA 94550
(415) 422-5498

Samuel Lu
Litton Industries
GCS
5500 Canoga Avenue
Woodland Hills, CA 91365
(818) 715-4565

Donald S. Luczak
Rome Air Dev. Ctr./USAF
Griffiss AFB, NY 13441-5700
(315) 330-3145

David Lunt
Lunt & Co.
P.O. Box 368
Richland, WA 99352
(509) 375-4792

Michael Lunt
Technical Optics Ltd.
Second Avenue,
Onchan, Isle of Man
UNITED KINGDOM O624 4443
O624 74443

H. Angus MacLeod
Optical Sciences Center
University of Arizona
Tucson, AZ 85721
(602) 621-2449

Taaro Mandre
TRW Space & Technology Group
One Space Park
01/1251
Redondo Beach, CA 90278
(213) 535-7139

Diane J. Martin
USAF
AFWL/ARAO
Kirtland AFB, NM 87117-6008
(505) 844-1776

Carl S. Masser
Northrop Research & Technology Center
One Research Park
Palos Verdes Peninsula, CA 90274
(213) 544-5470

Debra A. May
KIGRE, Inc.
5335 Secor Road
Toledo, OH 43623
(419) 473-3157

William J. McCarty
Perkin-Elmer Corp., A00
7421 Orangewood Avenue
P.O. Box 3115
Garden Grove, CA 92642
(714) 895-1667

Fred McClung
Hughes Aircraft Co.
1600 Randolph Ct. S.E.
Albuquerque, NM 87106
(505) 242-9818

Rick L. McGann
Naval Weapons Center
China Lake, CA 93555
(619) 939-3247

James F. McNally
United States Air Force
8808 Camino del Sol
Albuquerque, NM 87111
(505) 277-5502

John R. McNeil
University of New Mexico
Electrical Engineering Dept.
Albuquerque, NM 87131

Larry D. Merkle
Dept. of Physics
Univ. of Arkansas
Fayetteville, AR 72701
(501) 575-6425

David Milam
Lawrence Livermore National Lab
P. O. Box 5508, L-490
Livermore, CA 94550
(415) 422-5499

Mark Mildebrath
Rockwell International
3370 Miraloma
MS GE 14
Anaheim, CA 92803
(714) 752-3411

S. Mohan
Indian Institute of Science
Instrumentation & Services Unit
Bangalore-560 012
INDIA

N. Kent Moncur
KMS Fusion, Inc.
P.O. Box 1567
Ann Arbor, MI 48106
(313) 769-8500

Mark B. Moran
Naval Weapons Center-Physics Div.
Code 3817
China Lake, CA 93555
(619) 939-3827

David Mordaunt
Hughes Aircraft Company
Bldg. El. Mail Station E142
P.O. Box 902
El Segundo, CA 90243
(213) 616-5422

Dennis Morelli
Optical Coating Laboratory, Inc.
2789 Northpoint Parkway
Dept. 428-1
Santa Rosa, CA 95407-7397
(707) 525-7024

Patricia L. Morse
AFWL/ARBE
Optical Components Branch
Kirtland AFB, NM 87117
(505) 844-1776

John D. Myers
Kigre Inc.
5333 Secor Road #10
Toledo, OH 43623
(419) 473-3157

George Nado
Texas Instruments
Box 226015
Mail Stop 3196
Dallas, TX 75266
(214) 480-6412

Yoshiharu Namba
Dept. of Precision Engineering
Osaka University
2-1 Yamadaoka, Suita
Osaka 565
JAPAN
06-877-5111 ext. 4607

Ontario H. Nestor
Harshaw Chemical Company
6801 Cochran Road
Solon, OH 44122
(216) 248-7400

Brian E. Newnam
Los Alamos National Laboratory
MS-J564
Los Alamos, NM 87545
(505) 667-7979

Davis B. Nichols
Boeing Aerospace Co.
Mail Stop 8H-18
P.O. Box 3999
Seattle, WA 98124
(206) 773-8938

Nicholas S. Nogar
Los Alamos National Labs.
CHM2 G-738
Los Alamos, NM 87545
(505) 667-93-5

Robert M. O'Connell
Univ. of Missouri - Columbia
Elect. Engineering Dept.
College of Engineering
Columbia, MO 65201
(314) 882-8373

Takayuki Okamoto
Okamoto Optics Work, Inc.
8-34 Haramachi, Isogo-Ku
Yokohama 235
JAPAN
(045) 752-2233

Yoshiaki Okamoto
Okamoto Optics Work, Inc.
8-34 Haramachi, Isogo-Ku
Yakohama 235
JAPAN
(045) 752-2233

Harumichi Okamoto
Nippon Mining Co., Ltd.
3-17-35 Niizomminami, Toda-shi
Saitama 335
JAPAN
454-42-1811

Richard Owen
Spiricon Inc.
2600 N. Main
Logan, VT 84327
(801) 753-3729

Kathleen M. Padgett
Los Alamos National Laboratory
P.O. Box 1663, MS J566
Los Alamos, NM 87545
(505) 667-7677

James R. Palmer
COMCARO, Inc.
1201 N. China Lake Blvd.
Ridgecrest, CA 93555
(619) 446-7671

Roger A. Paquin
Perkin Elmer Corporation
Electro-Optical Div.
100 Wooster Heights Road
M/S 955
Danbury, CT 06810
(203) 797-6130

Walter T. Pawlewicz
Metallurgy & Coating Section
Battelle Northwest Lab.
2955 George Washington Way
Richland, WA 99352
(509) 375-2074

Samuel F. Pellicori
Santa Barbara Research Center
75 Coromar Drive
Goleta, CA 93117
(805) 968-3511 Ext 2379

Ralph Perkins
Corning
SP-DV-01-1
Corning, NY 14831
(607) 974-3018

John H. Pitts
Lawrence Livermore National Laboratory
P.O. Box 5508, L-480
Livermore, CA 94550
(415) 422-5327

Robert D. Poirier
Perkin Elmer Corp.
761 Main Avenue
Norwalk, CT 06859-0420
(203) 834-4934

Bradley Pond
Martin Marietta
P.O. Box 9316
Albuquerque, NM 87119
(505) 844-1064

James O. Porteus
Naval Weapons Center
Code 3817
China Lake, CA 93555
(619) 999-3827

Shari Powell-Fisher
Optical Coating Laboratory, Inc.
2789 Northpoint Parkway
Santa Rosa, CA 95401-7397
(707) 525-7778

Thomas Price
MIT Lincoln Laboratory
P.O. Box 73 L-218
Lexington, MA 02173-0073
(617) 863-5500

Kopel Rabinovitch
Electro Optics Industries, Ltd.
P.O. Box 1165
Rehovot 76110
ISRAEL
(78) 486253

Tilak Raj
Martin Marietta Denver Aerospace
P.O. Box 9316
International Airport
Albuquerque, NM 87119
(505) 844-1064

John Ranson
Pilkington P.E.
Glascoed Road
St. Asath
Clwyd LL170LL
United Kingdom

Theresa M. Roberts
USAF
RADC/ESMG
Hanscom AFB
Redford, MA 01731-5000
(617) 861-3693

Andrew Romberger
Pennsylvania State University
Berks Campus
P.O. Box 2150
Reading, PA 19608
(215) 320-4817

Carlos Roundy
Spiricon, Inc.
2600 N. Main
Logan, UT 84321
(801) 753-3729

Joseph Sanchez
Optical Coating Laboratory, Inc.
2789 Northpoint Parkway
Santa Rosa, CA 955407-7397
(707) 525-7728

Marion L. Scott
Los Alamos National Laboratory
P.O. Box 1663, MS E549
Los Alamos, NM 877545
(505) 667-4258

Steven C. Seitel
Montana Laser Optics, Inc.
P. O. Box 4151
Bozeman, MT 59772-4151
(406) 586-5100

Keith R. Shillito
AFWAL/MLPJ
Wright-Patterson AFB
Dayton, OH 45433
(415) 423-3508

Dennis R. Sigler
Burleigh Northwest Optical, Inc.
Burleigh Park
Fishers, NY 14453
(716) 924-9355

Herman E. Reedy
Two-Six Inc.
Saxonburg Blvd.
Saxonburg, PA 16056
(412) 352-4455

Raymond S. Robinson
Colorado State University
Ft. Collins, CO 80523
(303) 491-6202

James R. Rotge
Frank J. Seiler Research Laboratory
FJSRL/NH
USAF Academy
Colorado Springs, CO 880840
(303) 472-3122

Theodore T. Saito
Lawrence Livermore National Lab.
P.O. Box 808, L-791
Livermore, CA 944550
(425) 442-7600

Paul Schall
The Aerospace Corporation
M2/321
P.O. Box 920957
Los Angeles, CA 90009
(213) 648-7502

David W. Seegmiller
W.J. Schafer Associates, Inc.
1600 Randolph Ct. S.E.
Suite #202
Albuquerque, NM 87106
(505) 242-9992

C. Y. She
Physics Dept.
Colorado State University
Fort Collins, CO 80523
(303) 491-6261

Wigbert Siekhaus
Lawrence Livermore
National Laboratory
P.O. Box 8081 MS-L311
Livermore, CA 94550
(415) 422-6884

Philip A. Simpson
724.02
National Bureau of Standards
325 Broadway
Boulder, CO 80303
(303) 497-3789

James R. Sites
Physics Department
Colorado State University
Fort Collins, CO 80523
(303) 491-5850

James G. Sliney
Rockwell International
Rocketdyne Division
6633 Canoga Avenue
D/631, 055, FA03
Canoga Park, CA 91304
(818) 700-4900

Thomas Smith
TRW
One Space Park
Redondo Beach, CA 90278
(415) 632-8269

Douglas J. Smith
Institute of Optics
University of Rochester
Wilmot Building
Rochester, NY 14627
(716) 275-4135

Paul G. Snyder
University of Nebraska
Department of Electrical Engineering
W194 Nebraska Hall
Lincoln, NE 68588-0511
(402) 472-3771

M. J. Soileau
North Texas State University
Dept. of Physics
Denton, TX 76303
(817) 565-3263

William H. Southwell
Rockwell Science Center
1049 Camino Dos Rios
Thousand Oaks, CA 91360
(805) 373-4485

Mike C. Staggs
Lawrence Livermore National Lab
P.O. Box 5508, L-490
Livermore, CA 94550
(415) 422-6060

James L. Stanford
Naval Weapons Center, Code 3818
China Lake, CA 93555
(619) 939-1418

James L. Stapp
Rocketdyne
P.O. Box 5670 - M/S RNM1
Kirtland AFB., NM 87185
(505) 844-9013

Alan F. Stewart
Air Force Weapons Lab.
AFWL/ARBE
Kirtland AFB, NM 87117-6008
(505) 844-7368

C. Stonecyper
Litton Laser Systems
P.O. Box 7300
Orlando, FL 32854
(305) 297-4458

W. Kent Stowell
AFWL/AADO-2
Wright-Patterson AFB
Dayton, OH 45433
(513) 255-5147

Jack B. Stubbs
University of Dayton
Research Institute
KL-464
Dayton, OH 45469
(513) 229-3724

Martin R. Sweet
Los Alamos National Laboratory
Los Alamos, NM 87545
(505) 667-7100

Randall T. Swimm
University of Southern California
University Park
Los Angeles, CA
(213) 743-4370

H. Takahashi
Nippon Mining Co., LTD
1868 Dalehurst Ave.
Los Altos, CA 94022
(415) 864-7948

Ian Thomas
Lawrence Livermore National Lab.
P.O. Box 5808, L-483
Livermore, CA 94550
(415) 433-3896

David A. Thompson
Corning Glass Works
Sullivan Park DV-25
Corning, NY 14831
(607) 974-3311

Therese Tillmann
USAF - AFWL/ARBE
Kirtland AFB, NM 87117
(505) 844-1776

Norman Tolk
Vanderbilt University
P.O. Box 1807 Station B
Dept. of Physics & Astronomy
Nashville, TN 37235
(615) 322-2828

H. Toratani
Hoya Optics Inc. Can. LTD
3400 Edison Way
Fremont, CA 94538
(415) 490-1880

John R. Triplett
S-Cubed, A Div. of Maxwell Labs, Inc.
P.O. Box 1620
La Jolla, CA 92038-1620
(619) 453-0060 Ext 407

Stephen Tuenge
Martin Marietta Denver Aerospace
P.O. Box 9316
International Airport
Albuquerque, NM 87119
(505) 844-1064

Trudy Tuttle Hart
OCLI Optical Coating Laboratory, Inc.
2789 Northpoint Parkway,
MS/121-1
Santa Rosa, CA 955407-7397
(707) 525-7181

Marc Von Gunten
Mail Stn. 4-30
Spectra-Physics Inc.
Optics Division
1250 W. Middlefield Road
Mountain View, CA 94039-7013
(415) 961-2550 Ext 3008

Willard R. Wadt
Los Alamos National Laboratory
MS J569
P.O. Box 1663
Los Alamos, NM 87545
(505) 667-7763/2097

Anetta J. Weber
Air Force Weapons Lab/ARA0
Kirtland AFB, NM 87117

William J. Welker
USAF
AFWL/ARBE
Kirtland AFB, NM 87117-6008
(505) 844-1776

Stan Whitcomb
Northrop Electronics Division
2301 West 120th Street
Hawthorne, CA 90250
(213) 606-6768

Frederic H. White III
Rocketdyne Division
Rockwell International
6633 Canoga Ave.
Canoga Park, CA 91304

Keith Wier
Sciencetech Inc.
5649 Arapahoe
Boulder, CO 80303
(303) 444-1361

John G. Wilder
Lawrence Livermore National Laboratory
P.O. Box 5508, L-490
Livermore, CA 94550
(415) 423-3896

Ronald A. Wilklow
Perkin-Elmer
77 Danbury Road
Wilton, CT 06897-420
(203) 834-4450

Jeffrey T. Williams
COMARCO
1201 N. China Lake Blvd.
Ridgecrest, CA 93555
(619) 446-7671

A. D. Wilson
Barr & Stroud Ltd.
Caxton Street
Anniesland
Glasgow, G13 1HZ
SCOTLAND, UK
(041) 954-9601

G. Richard Wirtenson
Lawrence Livermore National Laboratory
P.O. Box 5508, L-491
Livermore, CA 94550
(415) 422-1332

Roger M. Wood
G. E. C. Research Laboratories
East Lane
Wembley, Middx
UNITED KINGDOM
01-904-1262-205

Frank Woodberry
Rocketdyne FA 42
6633 Canoga Ave.
Canoga Park, CA 91304
(818) 700-4931

Kunio Yoshida
Osaka University-Inst. for Laser Eng.
2-6 Yamada-oka
Suita Osaka, 565
JAPAN
(06) 877-5111

Matt Young
724.02
National Bureau of Standards
325 Broadway
Boulder, CO 80303
(303) 497-3223

Rick Zoborowski
OCLI
2789 Northpoint Parkway
Dept. 428-1
Santa Rosa, CA 95407-7397
(707) 525-7010

Thomas G. Zocco
Los Alamos National Laboratory
P.O. Box 1663, MS G730
Los Alamos, NM 87545
(505) 667-4481

U.S. DEPT. OF COMM. BIBLIOGRAPHIC DATA SHEET <i>(See instructions)</i>	1. PUBLICATION OR REPORT NO. NBS/SP-746	2. Performing Organ. Report No.	3. Publication Date July 1988
4. TITLE AND SUBTITLE Laser Induced Damage in Optical Materials: 1985			
5. AUTHOR(S) Harold E. Bennett (NWC), Arthur H. Guenther (AFWL) David Milam (LLNL) and Brian E. Newnam (LANL)			
6. PERFORMING ORGANIZATION <i>(If joint or other than NBS, see instructions)</i> NATIONAL BUREAU OF STANDARDS U.S. DEPARTMENT OF COMMERCE BOULDER, CO 80303		7. Contract/Grant No.	8. Type of Report & Period Covered Final
9. SPONSORING ORGANIZATION NAME AND COMPLETE ADDRESS <i>(Street, City, State, ZIP)</i> National Bureau of Standards (NBS) Defense Advanced Research Project American Society for Testing and Materials (ASTM) Agency (DARPA) Office of Naval Research (ONR) Air Force Office of Scientific Department of Energy (DOE) Research (AFOSR)			
10. SUPPLEMENTARY NOTES Library of Congress Catalog Card Number 88-600557 <input type="checkbox"/> Document describes a computer program; SF-185, FIPS Software Summary, is attached.			
11. ABSTRACT <i>(A 200-word or less factual summary of most significant information. If document includes a significant bibliography or literature survey, mention it here)</i> The Seventeenth Annual Symposium on Optical Materials for High-Power Lasers (Boulder Damage Symposium) was held at the National Bureau of Standards in Boulder, Colorado, October 28-30, 1985. The Symposium was held under the auspices of ASTM Committee F-1, Subcommittee on Laser Standards, with the joint sponsorship of NBS, the Defense Advanced Research Project Agency, the Department of Energy, the Office of Naval Research, and the Air Force Office of Scientific Research. Over 215 scientists attended the Symposium, including representatives from the United States, the United Kingdom, Israel, India, Japan, the Federal Republic of Germany, and the Soviet Union. The Symposium was divided into sessions concerning Materials and Measurements, Mirrors and Surfaces, Thin Films, and Fundamental Mechanisms. As in previous years, the emphasis of the papers presented at the Symposium was directed toward new frontiers and new developments. Particular emphasis was given to materials for high-power apparatus. The wavelength range of prime interest was from 10.6 μm to the uv region. Highlights included surface characterization thin film-substrate boundaries, and advances in fundamental laser-matter threshold interactions and mechanisms. Harold E. Bennett of the Naval Weapons Center, Arthur H. Guenther of the Air Force Weapons Laboratory, David Milam of the Lawrence Livermore National Laboratory, and Brian E. Newnam of the Los Alamos National Laboratory were co-chairmen of the Symposium. The Eighteenth Annual Symposium is scheduled for Nov. 3-5, 1986, at the National Bureau of Standards, Boulder, Colorado.			
12. KEY WORDS <i>(Six to twelve entries; alphabetical order; capitalize only proper names; and separate key words by semicolons)</i> laser damage; laser interaction; optical components; optical fabrication; optical materials and properties; thin film coatings.			
13. AVAILABILITY <input checked="" type="checkbox"/> Unlimited <input type="checkbox"/> For Official Distribution. Do Not Release to NTIS <input checked="" type="checkbox"/> Order From Superintendent of Documents, U.S. Government Printing Office, Washington, D.C. 20402. <input type="checkbox"/> Order From National Technical Information Service (NTIS), Springfield, VA. 22161		14. NO. OF PRINTED PAGES 576 15. Price	

INSTRUCTIONS

FORM NBS-114A: BIBLIOGRAPHIC DATA SHEET. This bibliographic data sheet meets the standards adopted for use by all U.S. Government agencies. It is needed for NTIS processing and must accompany all NBS papers, those appearing in nongovernmental media as well as those in NBS series, since all reports of NBS technical work are normally entered into the NTIS system. For all GPO publications, it becomes an integral part of the document and is widely used by librarians and abstractors.

- Items 1, 2** - Complete if information is available; otherwise Publications Office will complete later. If non-NBS publication, state "see item 10" (Enter other agency sponsor's report number if requested to do so, and enter NBSIR number under item 2).
- Item 3** - Complete if known; otherwise Publications Office will complete.
- Items 4, 5** - Complete as shown on manuscript. When NBS-114A is resubmitted along with NBS-266, following publication of non-NBS media papers, these items must agree with published paper.
- Item 6** - If not NBS, blank out and enter Grantee/Contractor name and address, or if performed jointly, show both.
- Item 7** - Complete when applicable.
- Item 8** - Enter "Interim," "Final," or period covered.
- Item 9** - Enter all sponsors' names and addresses. Include NBS if also a sponsor.
- Item 10** - Enter other relevant information, i.e., related or superseded documents. Also used by Publications Office for Library of Congress catalog number, and entry of non-NBS media citation upon receipt of Form NBS-266 from author. Check block if appropriate and attach SF185.
- Item 11, 12** - Prepare abstract and key words with special care. These are published separately by NBS, NTIS, and other bibliographic services, and are vital elements in guiding readers to your paper. The key words will be used as entries in a subject index. See NBS Communications Manual for additional guidance.
- Item 13** - Indicate "Unlimited" - for open-literature documents cleared under NBS editorial procedures, or "For official distribution. Do not release to NTIS" - for limited, restricted, or need-to-know material (See Communications Manual). Publications Office will mark appropriate "order" box and complete Stock Number when known.
- Items 14, 15** - Leave blank. To be completed by Publications Office or call Printing and Duplicating for NBSIR's.



NBS *Technical Publications*

Periodical

Journal of Research—The Journal of Research of the National Bureau of Standards reports NBS research and development in those disciplines of the physical and engineering sciences in which the Bureau is active. These include physics, chemistry, engineering, mathematics, and computer sciences. Papers cover a broad range of subjects, with major emphasis on measurement methodology and the basic technology underlying standardization. Also included from time to time are survey articles on topics closely related to the Bureau's technical and scientific programs. Issued six times a year.

Nonperiodicals

Monographs—Major contributions to the technical literature on various subjects related to the Bureau's scientific and technical activities.

Handbooks—Recommended codes of engineering and industrial practice (including safety codes) developed in cooperation with interested industries, professional organizations, and regulatory bodies.

Special Publications—Include proceedings of conferences sponsored by NBS, NBS annual reports, and other special publications appropriate to this grouping such as wall charts, pocket cards, and bibliographies.

Applied Mathematics Series—Mathematical tables, manuals, and studies of special interest to physicists, engineers, chemists, biologists, mathematicians, computer programmers, and others engaged in scientific and technical work.

National Standard Reference Data Series—Provides quantitative data on the physical and chemical properties of materials, compiled from the world's literature and critically evaluated. Developed under a worldwide program coordinated by NBS under the authority of the National Standard Data Act (Public Law 90-396).

NOTE: The Journal of Physical and Chemical Reference Data (JPCRD) is published quarterly for NBS by the American Chemical Society (ACS) and the American Institute of Physics (AIP). Subscriptions, reprints, and supplements are available from ACS, 1155 Sixteenth St., NW, Washington, DC 20056.

Building Science Series—Disseminates technical information developed at the Bureau on building materials, components, systems, and whole structures. The series presents research results, test methods, and performance criteria related to the structural and environmental functions and the durability and safety characteristics of building elements and systems.

Technical Notes—Studies or reports which are complete in themselves but restrictive in their treatment of a subject. Analogous to monographs but not so comprehensive in scope or definitive in treatment of the subject area. Often serve as a vehicle for final reports of work performed at NBS under the sponsorship of other government agencies.

Voluntary Product Standards—Developed under procedures published by the Department of Commerce in Part 10, Title 15, of the Code of Federal Regulations. The standards establish nationally recognized requirements for products, and provide all concerned interests with a basis for common understanding of the characteristics of the products. NBS administers this program as a supplement to the activities of the private sector standardizing organizations.

Consumer Information Series—Practical information, based on NBS research and experience, covering areas of interest to the consumer. Easily understandable language and illustrations provide useful background knowledge for shopping in today's technological marketplace.

Order the above NBS publications from: Superintendent of Documents, Government Printing Office, Washington, DC 20402.

Order the following NBS publications—FIPS and NBSIR's—from the National Technical Information Service, Springfield, VA 22161.

Federal Information Processing Standards Publications (FIPS PUB)—Publications in this series collectively constitute the Federal Information Processing Standards Register. The Register serves as the official source of information in the Federal Government regarding standards issued by NBS pursuant to the Federal Property and Administrative Services Act of 1949 as amended, Public Law 89-306 (79 Stat. 1127), and as implemented by Executive Order 11717 (38 FR 12315, dated May 11, 1973) and Part 6 of Title 15 CFR (Code of Federal Regulations).

NBS Interagency Reports (NBSIR)—A special series of interim or final reports on work performed by NBS for outside sponsors (both government and non-government). In general, initial distribution is handled by the sponsor; public distribution is by the National Technical Information Service, Springfield, VA 22161, in paper copy or microfiche form.

U.S. Department of Commerce

National Bureau of Standards

Gaithersburg, MD 20899

Official Business

Penalty for Private Use \$300



Stimulating America's Progress
1913-1988